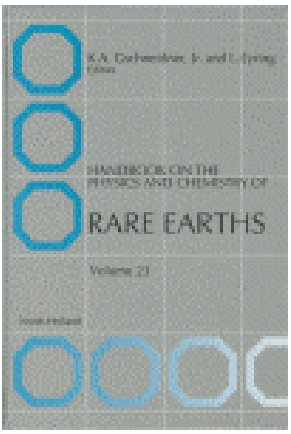

Handbook on the Physics and Chemistry of Rare Earths, volume 23

Elsevier, 1996

Edited by: Karl A. Gschneidner, Jr. and LeRoy Eyring
ISBN: 978-0-444-82507-0

Handbook on the Physics and Chemistry of Rare Earths
Vol. 23
edited by K.A. Gschneidner, Jr. and L. Eyring

PREFACE

Karl A. GSCHNEIDNER, Jr., and LeRoy EYRING

These elements perplex us in our rearches [sic], *baffle us in our speculations, and haunt us in our very dreams. They stretch like an unknown sea before us – mocking, mystifying, and murmuring strange revelations and possibilities.*

Sir William Crookes (February 16, 1887)

In this volume of the Handbook the authors sample the gamut of rare-earth-element involvement on the planet. From the magnetic characteristics of atomic nuclei, to the electronic antenna effects of ligands on encapsulated atoms, to the effects on spectral properties of neighboring atoms in a crystalline array, to the chemical combination of the rare-earth elements with phosphorus, to the chemical constitution of vapor species of their halides, to the distribution of these elements in the waters that envelope the earth.

Forsberg initiates this progression in his review of *NMR studies of paramagnetic lanthanide complexes and shift reagents.* The use of chemical shifts induced in reagents of the rare-earth elements has been studied for 25 years. In this chapter Forsberg summarizes recent developments in this field for paramagnetic lanthanide complexes including the application of several new shift reagents. One of the more important developments that has evolved from the research in this area is the use of lanthanide complexes in magnetic resonance imaging (MRI) in the medical field.

When Eu^{3+} and Tb^{3+} ions are encapsulated in cage-type ligands having chromophoric groups, energy transfer from excitation of the ligand to the metal ions can occur. This *antenna-to-ion energy transfer* results in metal luminescence that is much more intense than could otherwise be obtained. Sabbatini, Guardigli and Manet discuss the theory and application of the consequences of this phenomenon and its relationship to supramolecular chemistry. Applications of these complexes in fluoroimmunoassays and DNA hybridization assays are also discussed.

The *Rationalization of crystal field parametrization* is considered in a pedagogical context by Görller-Walrand and Binnemans. This chapter continues an on-going treatment of the spectroscopic properties of the rare-earth elements in the Handbook. The authors emphasize the symmetry aspects of the crystal field and the parametrization of the energy level scheme. "This parameter set is the greatest possible reduction of the experimental

data and it allows one to reconstruct the energy level scheme of the $4f^n$ configuration and even to make predictions about energy regions which cannot be probed experimentally."

Kuz'ma and Chykhrij present a systematic and encyclopedic discussion of the *phosphides* of the binary, ternary and quaternary rare earths. Their coverage includes preparation, phase diagrams, structure, as well as chemical and physical properties. The crystallochemical regularities, the nature of the interaction between components in ternary systems, and structural relationships also constitute important aspects of this review.

Metal-containing vapor species such as the simple rare-earth *halide vapors* and the vapor complexes $MX–RX_3$ and $MX_2–RX_3$ are finding increasing use in halogen lamps and energy storage media for high-power laser systems and for development of recycling/separation processes. Boghosian and Papatheodorou consider this and pay particular attention to thermodynamic and structural trends, and to characteristic experimental techniques such as absorption and fluorescence spectroscopy.

Byrne and Sholkovitz review the lanthanide composition of the ocean and the processes that control their distribution. Particular attention is given to research on the *lanthanide geochemistry* of marine hydrothermal vent systems. They find that the lanthanides are good indicators of the reactions between hydrothermal fluids and basalt and between iron particles and sea water, but these reactions are not quantitatively significant with respect to river water fluxes and oceanic cycles and inventory.

CONTENTS

CONTENTS OF VOLUMES 1–22

VOLUME 4: Non-metallic compounds – II

1979, 1st repr. 1984; ISBN 0-444-85216-6

VOLUME 5

1982, 1st repr. 1984; ISBN 0-444-86375-3

VOLUME 6

1984; ISBN 0-444-86592-6

VOLUME 7

1984; ISBN 0-444-86851-8

VOLUME 8
1986; ISBN 0-444-86971-9

VOLUME 9
1987; ISBN 0-444-87045-8

VOLUME 10: High energy spectroscopy
1988; ISBN 0-444-87063-6

VOLUME 11: Two-hundred-year impact of rare earths on science
1988; ISBN 0-444-87080-6

VOLUME 12

1989; ISBN 0-444-87105-5

VOLUME 13

1990; ISBN 0-444-88547-1

VOLUME 14

1991; ISBN 0-444-88743-1

VOLUME 15

1991; ISBN 0-444-88966-3

MASTER INDEX, Vols. 1–15
1993; ISBN 0-444-89965-0

VOLUME 16
1993; ISBN 0-444-89782-8

VOLUME 17: Lanthanides/Actinides: Physics – I
1993; ISBN 0-444-81502-3

VOLUME 18: Lanthanides/Actinides: Chemistry
1994; ISBN 0-444-81724-7

VOLUME 19: Lanthanides/Actinides: Physics – II

1994; ISBN 0-444-82015-9

VOLUME 20

1995; ISBN 0-444-82014-0

VOLUME 21

1995; ISBN 0-444-82178-3

VOLUME 22

1996; ISBN 0-444-82288-7

Handbook on the Physics and Chemistry of Rare Earths
Vol. 23
edited by K.A. Gschneidner, Jr. and L. Eyring

Chapter 153

NMR STUDIES OF PARAMAGNETIC LANTHANIDE COMPLEXES AND SHIFT REAGENTS

John H. FORSBERG
Department of Chemistry, Saint Louis University, St. Louis, MO 63103, USA

Contents

List of symbols

A	hyperfine coupling constant	J	resultant spin and orbital angular momentum quantum number
B_0	intensity of external magnetic field		
C_j	Bleaney-factor for metal j	k	Boltzmann constant
G_i	geometric-factor for nucleus i	L	total orbital angular momentum quantum number
g	Landé g-factor		
$\hbar$	Planck constant	N	Avogadro constant
		r	internuclear distance

R	agreement factor	δ_{pc}	pseudocontact shift in ppm
S	total spin angular momentum quantum number	$\delta\nu^{1/2}$	line width at half-height in Hz
$\langle S_z \rangle$	expectation value of electron-spin along the field direction	γ	gyromagnetic ratio
T	temperature in Kelvin	μ_{eff}	effective electron magnetic moment
T_1	longitudinal nuclear relaxation time	τ_c	correlation time
T_2	transverse nuclear relaxation time	τ_e	electron-spin relaxation time
$\mathrm{Tr}\chi$	trace of the magnetic susceptibility tensor	τ_m	residence time of coordinated ligand
β	Bohr magneton	τ_r	rotational correlation time
χ	magnetic susceptibility tensor	θ	angle between r and principal magnetic z-axis
χ'	traceless part of the magnetic susceptibility tensor	ϕ	angle between the principal magnetic x-axis and the projection of r to the plane perpendicular to the magnetic z-axis
χ_{xx}, χ_{yy}, χ_{zz}, χ_{xy}, χ_{xz}, χ_{yz}	components of the magnetic susceptibility tensor	ξ	spin–orbit coupling parameter
δ_c	contact shift in ppm		

1. Introduction

Following Hinckley's (1969) communication, several hundred publications appeared within a few years, demonstrating the ability of $R(thd)_3$ and $R(fod)_3$ chelates[1] to form adducts with a variety of Lewis bases and to induce chemical shifts (LIS) in the proton NMR spectra of the organic substrates. Early studies included qualitative spectral simplification, characterization of the stoichiometry and geometry of the shift reagent adducts in both solution and the solid state, and theoretical studies of the origin of the LIS. By 1973, nine review articles on the application of lanthanide shift reagents had been published (Forsberg 1981), including reports by Sievers (1973), Horrocks (1973), Reuben (1973), and Cockerill et al. (1973). A chapter on shift reagents and NMR of paramagnetic lanthanide complexes appeared in volume 4 of this Handbook (Reuben and Elgavish 1979a). Wenzel (1987) has published a comprehensive review on the use of classical shift reagents, such as $R(fod)_3$ and $R(thd)_3$, used for spectral simplification and the conformational analysis of organic substrates. In this chapter, I provide a summary of recent developments in the field of NMR studies of paramagnetic lanthanide complexes, including the application of several new shift reagents. The review of the literature is selective rather than comprehensive.

The introduction of high-field NMR instrumentation has diminished the need for lanthanide shift reagents for spectral simplification of organic substrates. The commercial

[1] thd, 2,2,6,6-tetramethyl-3,5-heptanedione; fod, 6,6,7,7,8,8,8-heptafluoro-2,2-dimethyl-3,5-octanedione.

development during the 1980's of $Gd(dota)^-$ ($dota^{4-}$, 1,4,7,10-tetraazacyclododecane-1,4,7,10-tetraacetate) and $Gd(dtpa)^{2-}$ ($dtpa^{5-}$, diethylenetriaminepentaacetate) as relaxation agents in magnetic resonance imaging, as well as the recent discovery by Morrow et al. (1992) that lanthanide complexes provide efficient catalytic cleavage of RNA, have stimulated new interest in NMR studies of lanthanide complexes. Whereas the majority of shift reagent adducts are labile on the NMR time scale, the $R(dota)^-$ and $R(dtpa)^{2-}$ complexes, as well as most other lanthanide complexes being investigated as potential MRI agents, are stereochemically rigid in solution. Thus a major focus of this chapter is a review of LIS methodologies for determining three-dimensional structures of stereochemically rigid complexes in solution (sect. 4). A new method of analyzing LIS data has been reported by Kemple et al. (1988), which has been expanded on by Forsberg et al. (1995). These new procedures, which also include new methods of separating the LIS values into their contact and pseudocontact components, are presented in the section on theory (sects. 2.2 and 2.3), together with a review of traditional methods of analyzing LIS data. The applications and limitations of 2D NMR techniques to aid in spectral assignments and to the study of the dynamics of exchange between stereoisomers of paramagnetic lanthanide complexes are presented in sect. 2.5. 2D NMR techniques have proven most useful in the study of stereochemically rigid complexes, thus several applications of these techniques are included in sect. 4. Continuing interest has been maintained in the use of chiral lanthanide shift reagents for determining enantiomeric excess (ee) in asymmetric organic syntheses and the determination of absolute configuration of optically active organic molecules. New developments in this area are reviewed in sect. 5. New lanthanide shift reagents for alkali metal cations have been discovered that allow intra- and extracellular cations to be distinguished by NMR spectroscopy (sect. 6). Although much interest is maintained in the application of paramagnetic lanthanide ions or complexes as probes in other biological systems (see review by Sherry and Geraldes 1989), such as calcium binding proteins (Lee and Sykes 1980, Morishima et al. 1986, Berliner et al. 1987, Marsden et al. 1989, Ming 1993), bile salts (Mukidjam et al. 1986, 1987), nucleotides (Yokoyama et al. 1983, Geraldes and Ascenso 1984), and single-stranded DNA binding domains of gene V proteins (van Duynhoven et al. 1993), these topics are outside the scope of this review.

2. Theory

The binding of a ligand to a paramagnetic lanthanide ion induces frequency shifts in the NMR spectrum (LIS) of the ligand relative to that observed for the corresponding diamagnetic complex. The LIS has two contributions, the Fermi contact (δ_c) and the dipolar or pseudocontact shifts (δ_{pc}):

$$\text{LIS} = \delta_c + \delta_{pc}. \tag{1}$$

Contact shifts are discussed in sect. 2.1, methods of evaluating pseudocontact shifts are presented in sect. 2.2, and methods used to separate the contact and pseudocontact

components of the LIS are presented in sect. 2.3. The goodness of fit obtained in analyzing LIS data for i nuclei is given by the agreement factor, R, defined as (Willcott et al. 1972, Davis and Willcott 1972)

$$R = \left[\frac{\sum_i (\delta_{\text{obs}} - \delta_{\text{obs}})_i^2}{\sum_i (\delta_{\text{obs}})_i^2} \right]^{1/2} \tag{2}$$

2.1. *Contact shifts*

The contact shift is given by

$$\delta_c = \left(\frac{2\pi\beta}{3kT\gamma} \right) \left(\frac{A}{h} \right) \langle S_z \rangle , \tag{3}$$

where β is the Bohr magneton, k is the Boltzmann constant, γ is the gyromagnetic ratio, A/h is the hyperfine coupling constant in frequency units, and $\langle S_z \rangle$ is the electron spin expectation value. Positive contact shifts are to higher frequency (downfield). Since the values of $\langle S_z \rangle$ are used in procedures to separate the contact and pseudocontact components of the LIS (sect. 2.3), a discussion of these values is warranted. The values of $\langle S_z \rangle$ (table 1) reported by Golding and Halton (1972), which take into account population of excited states, are those most commonly used. Pinkerton et al. (1985) recalculated the values of $\langle S_z \rangle$ using the equations given by Golding and Halton, but substituted different sets of values for the spin–orbit coupling parameter, ξ. Except for Sm^{3+} and Eu^{3+}, the values of Pinkerton (table 1) are within 1% agreement of those of Golding and Halton, revealing that the values of $\langle S_z \rangle$ are relatively insensitive to the value of ξ chosen for the calculation. Furthermore, with the exception of Sm^{3+}, Pinkerton reports that the values of $\langle S_z \rangle$ are relatively insensitive to temperature and that the values calculated at 300 K can be used without correction over temperature ranges normally associated with NMR experiments. The value of $\langle S_z \rangle$ calculated for Sm^{3+} is very sensitive to both temperature and the value of ξ. Thus $\langle S_z \rangle$ values for Sm^{3+} must be calculated at the temperature corresponding to that used in recording the NMR spectrum, and then the reliability of the calculated value still depends on the accuracy of ξ. The value of $\langle S_z \rangle$ reported for Eu^{3+} is problematic. The ground state of this ion ($^7F_0$) has no defined g value ($L=S$, $J=0$). The value of $\langle S_z \rangle$ (10.68) reported by Golding and Halton was calculated using an assumed g value of 5.0 for the ground state. Pinkerton determined an average value $\langle S_z \rangle = 7.500$ for Eu^{3+} by fitting experimental LIS data to eq. (12) (see sect. 2.3). This value corresponds to $g=4.4$ for the ground state of the Eu^{3+} ion. The uncertainties associated with values of $\langle S_z \rangle$ for Sm^{3+} and Eu^{3+} can make it difficult to obtain accurate contact shifts for nuclei of complexes derived from the lighter members of the series (Ce–Eu) (see sect. 2.3).

Table 1
Values of $\langle S_z \rangle$ at 300 K

R^{3+}	Golding and Halton[a]		Pinkerton et al., set 1[b]		Pinkerton et al., set 2[b]	
	ζ (cm^{-1})	$\langle S_z \rangle$	ζ (cm^{-1})	$\langle S_z \rangle$	ζ (cm^{-1})	$\langle S_z \rangle$
Ce	737	−0.979	696.41	−0.9736	624.28	−0.9654
Pr	879	−2.972	820.22	−2.956	766.09	−2.939
Nd	1030	−4.487	950.51	−4.452	896.38	−4.425
Pm	1190	−4.014	1091.46	−3.944	1037.33	−3.899
Sm	1361	0.063	1243.60	0.224	1189.47	0.307
Eu	1436	10.682[c]	1407.71	7.569[d]	1353.58	7.658[d]
Gd	1755	31.500	1584.45	31.500	1530.32	31.500
Tb	1965	31.818	1774.46	31.853	1720.33	31.864
Dy	2189	28.545	1998.44	28.565	1944.31	28.572
Ho	2436	22.629	2197.06	22.642	2142.93	22.646
Er	2700	15.374	2431.00	15.382	2376.87	15.384
Tm	2817	8.208	2680.97	8.210	2626.84	8.211
Yb	3288	2.587	2947.69	2.589	2893.56	2.589

[a] From Golding and Halton (1972).
[b] From Pinkerton et al. (1985).
[c] Calculated for $g_J = 5000$ for the ground state.
[d] Calculated for $g_J = 4.4$ for the ground state.

2.2. *Pseudocontact shifts*

Structural information is obtained from the pseudocontact shift, which is given by

$$\delta_{pc} = D_1 \left[\left\langle \frac{(3\cos^2\theta - 1)}{r^3} \right\rangle_{av} \right] + D_2 \left[\left\langle \frac{\sin^2\theta \cos 2\phi}{r^3} \right\rangle_{av} \right], \tag{4}$$

where δ_{pc} is the pseudocontact shift (positive sign is to higher frequency), r, θ, and ϕ are the spherical coordinates of the resonating nucleus in the principal magnetic axis system with the lanthanide ion at the origin; $D_1 = 1/3N \left[\chi_{zz} - \frac{1}{2}(\chi_{xx} + \chi_{yy})\right]$ and $D_2 = 1/2N \left[\chi_{xx} - \chi_{yy}\right]$, where χ_{zz}, χ_{xx}, and χ_{yy} are the principal molecular susceptibilities and N is Avogadro's constant (Horrocks and Sipe 1972). In the case of axial symmetry, $\chi_{xx} = \chi_{yy}$, and $D_2 = 0$. Most studies involving adducts of shift reagents, such as $R(thd)_3$ or $R(fod)_3$, reveal that the first term of eq. (4) adequately describes the pseudocontact shifts induced in the NMR spectrum of the Lewis base substrate, even though it is not likely that the adducts are axially symmetric. Furthermore, it is assumed that the principal magnetic axis coincides with the metal–donor atom bond of the substrate. The coordination numbers and geometries of lanthanide complexes are due primarily to the steric requirements of the ligands. Due to their relatively large size, lanthanide ions generally form complexes having high coordination numbers (7 to 10). The stereochemical lability of these high coordinate complexes is well established, and interconversion between geometrical isomers is generally rapid on the NMR time scale.

Horrocks (1974) showed that if the LSR adducts exist in solution as an ensemble of many (order of 30 or more) rapidly interconverting geometrical isomers, with the additional proviso that the substrate, through its influence on the ligand field in the individual isomers, exhibits a statistical bias to lie in proximity to an axis of maximum or minimum susceptibility, then the net shifts conform reasonably well to the first term of eq. (4). Hawkes et al. (1973a) regarded the question of orientation of the principal magnetic axis in a study of $R(fod)_3$ adducts of stereochemically rigid alcohols ($R(fod)_3$·L; R = Pr, Eu; L = borneol, isoborneol). Assuming an axial model, but without any assumptions regarding the location of the principal magnetic axis, they showed that the best fit between calculated and observed LIS values was obtained when the oxygen–metal bond in the adducts is collinear with the magnetic z-axis.

Recently Kemple et al. (1988) introduced a new procedure for analyzing LIS data, which makes no assumptions regarding the location of the principal magnetic axes or symmetry of the complex. The equation for the pseudocontact shift is written as

$$\delta^{i}_{pc} = \frac{1}{r^3 N}\left\{\frac{1}{2}\left[\left(\chi_{zz} - \frac{1}{3}\mathrm{Tr}\,\boldsymbol{\chi}\right)\left(3\cos^2\theta - 1\right) + \left(\chi_{xx} - \chi_{yy}\right)\left(\sin^2\theta\cos 2\phi\right)\right]\right.$$
$$\left. + \chi_{xy}\left(\sin^2\theta\sin 2\phi\right) + \chi_{xz}\left(\sin 2\theta\cos\phi\right) + \chi_{yz}\left(\sin 2\theta\sin\phi\right)\right\}, \tag{5}$$

where r, θ and ϕ are as defined for eq. (4) and $\boldsymbol{\chi}$, the magnetic susceptibility tensor, is taken to be a symmetric tensor, with $\mathrm{Tr}\,\boldsymbol{\chi} = \chi_{xx} + \chi_{yy} + \chi_{zz}$. In the principal magnetic axis system, the last three terms of eq. (5) vanish ($\boldsymbol{\chi}$ is diagonal in the principal axis system), and becomes equivalent to the expression given in eq. (4). Only the first term remains for the special case of axial symmetry ($\chi_{xx} = \chi_{yy}$). Following the Kemple procedure, geometric factors are calculated in the molecular coordinate system, then a five parameter $\left(\chi_{zz} - \frac{1}{3}\mathrm{Tr}\,\boldsymbol{\chi}\right)$, $\left(\chi_{xx} - \chi_{yy}\right)$, χ_{xy}, χ_{xz}, and χ_{yz} linear least-squares search minimizes the difference between calculated and observed δ_{pc} values according to the agreement factor defined in eq. (2). Since δ_{pc} depends only on the anisotropic (traceless) part ($\boldsymbol{\chi}'$) of the susceptibility tensor $\boldsymbol{\chi}$, the determination of these five fitting parameters is sufficient to determine the principal values of $\boldsymbol{\chi}'$. The principal directions of $\boldsymbol{\chi}'$ (and $\boldsymbol{\chi}$) are then determined by diagonalization of $\boldsymbol{\chi}'$. It should be noted that the procedure used here differs significantly from the procedure employing eq. (4). Since eq. (4) is written in the principal axis system, in addition to using D_1 and D_2 as fitting parameters, it is necessary to vary the principal directions in the molecular fixed frame by using the three Euler angles, which relate the two coordinate systems, as fitting parameters. Thus for a complete fit, the latter operation requires a total of five fitting parameters, the same number used in the Kemple procedure. However, the procedure based on eq. (4) is necessarily nonlinear, since a change in direction of the axes requires recalculating the angular functions. In nonlinear fitting procedures, there are uncertainties regarding whether the true minimum has been found. It is often the case that an unequivocal assignment of the peaks in a spectrum of a paramagnetic complex is not possible, especially when there are a large number of equally intense, featureless peaks. Forsberg et al. (1995) have shown that it

is possible to allow a computer program to permute LIS values over any number of selected nuclei by using a linear least-square fitting of the data according to eq. (5), thereby determining the assignment of peaks that gives the best fit to the LIS data (cf. sect. 4.2.3).

2.3. *Separation of contact and pseudocontact shifts*

Before attempting to use LIS data to determine the geometry of a complex or shift reagent adduct in solution, it is necessary to separate the contact shift contribution from the LIS. In much of the early work reported on the application of shift reagents, contact shifts were assumed to be negligible in proton NMR, and reasonable fits of calculated and observed shifts for the Lewis base were obtained under this assumption. However, Birnbaum and Stratton (1973) reported sizeable contact shifts in their ^{1}H NMR study of solutions of $R(en)_4^{3+}$ complexes in acetonitrile. An awareness of the importance of contact shifts in ^{13}C spectra of lanthanide shift reagent adducts was reported in the same year (Gansow et al. 1973a, Gansow et al. 1973b, Hawkes et al. 1973b). The most commonly used procedure for separating the LIS into contact and pseudocontact components is the temperature independent method introduced by Reilley et al. (1975, 1976). Based on the theoretical approach developed by Bleaney (1972) (for controversy regarding this approach, see Golding and Pyykkö 1973, Stout and Gutowsky 1976, Horrocks 1977), δ_{pc} is expressed as

$$\delta_{pc} = C_j G_i, \tag{6}$$

where C_j are constants (Bleaney factors) characteristic of each Ln^{3+} ion, and G_i for the ith nucleus is given by

$$G_i = \left(\frac{1}{r^3}\right)\left[C\left(3\cos^2\theta - 1\right) + C'\left(\sin^2\theta\cos 2\phi\right)\right], \tag{7}$$

where C and C' are constants, which include the crystal field coefficients, $2A_2^0\langle r^2\rangle = B_0^2$ and $2A_2^2\langle r^2\rangle = B_2^2$, respectively. In the case of axial symmetry, $C' = 0$. δ_c may be expressed as

$$\delta_c = F_i\langle S_z\rangle_j, \tag{8}$$

where F_i represents the collection of constants in eq. (3) for the ith nucleus and $\langle S_z\rangle_j$ is the metal dependent parameter previously defined. Since the LIS is the sum of the contact and pseudocontact components, eqs. (6) and (8) can be combined to give

$$(\mathrm{LIS})_{ij} = G_i C_j + F_i\langle S_z\rangle_j. \tag{9}$$

Equation (9) can be rearranged into two linear forms:

$$\frac{(\mathrm{LIS})_{ij}}{\langle S_z\rangle_j} = G_i\left(\frac{C_j}{\langle S_z\rangle_j}\right) + F_i, \qquad \frac{(\mathrm{LIS})_{ij}}{C_j} = G_i + F_i\left(\frac{\langle S_z\rangle_j}{C_j}\right). \tag{10, 11}$$

If it is assumed that the crystal field coefficients are constant and that the series of lanthanide complexes are isostructural, then a plot of $(\mathrm{LIS})_{ij}/\langle S_z\rangle_j$ versus $C_j/\langle S_z\rangle_j$ or

$(\mathrm{LIS})_{ij}/C_j$ versus $\langle S_z \rangle_j/C_j$ should be linear, with respective slopes of G_i or F_i and respective intercepts of F_i or G_i. Equation (10) is recommended when the pseudocontact shift predominates, whereas eq. (11) is recommended when the contact shift predominates. Provided the assumptions are true, eqs. (10) or (11) can be used for complexes with axial or nonaxial symmetry. Obviously if there are major structural changes across the lanthanide series, then it is not expected that such plots would be linear. Peters (1986) reports that even small variations in the lanthanide–donor atom bond distances resulting from the lanthanide contraction may be sufficient to produce an abrupt break in the plot along the lanthanide series. Even if an abrupt break is not observed, it is prudent to make two plots to compensate for the lanthanide contraction, one for the larger metal ions (Ce–Eu) and one for the smaller ions (Tb–Yb). However, given the uncertainties of the values of $\langle S_z \rangle$ for Sm^{3+} and Eu^{3+} described in sect. 2.1, this leaves only three reliable values (Ce–Nd) for members of the lighter subgroup. Although Bleaney's approximation of expressing the magnetic anisotropy in terms of ligand field parameters of the second degree appears valid, except at low temperatures, i.e., less than 200 K (Stout and Gutowsky 1976), the assumption that the crystal field parameters are independent of the lanthanide ion may not be valid (Reuben 1982). Reilley et al. (1976) noted that the contact contribution to the LIS depends on both the absolute value of the $\langle S_z \rangle_j/C_j$ ratio of the metal ion [Eu (2.638), Pm (2.147), Nd (1.081), Ho (0.574), Er (0.474), Tb (0.373), Dy (0.285), Pr (0.270), Tm (0.157), Ce (0.155), Yb (0.120)], as well as the F_i/G_i ratio for a particular nucleus. Thus shift reagents derived from Yb^{3+} are the best choice if contact shifts are to be ignored, since Yb^{3+} has the smallest $\langle S_z \rangle_j/C_j$ ratio, while its relatively large magnetic anisotropy gives rise to a large dispersion range of LIS values, usually on the order ± 100 ppm in ^1H spectra.

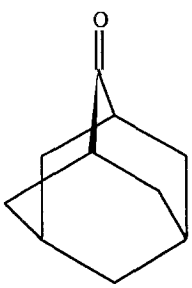

adamantanone Fig. 1.

Peters et al. (1985) reported the LIS values for ^{17}O, ^{13}C, and ^1H for 1:1 adducts of adamantanone (fig. 1) with $R(fod)_3$ shift reagents. Upon calculating the F_i and G_i values using eq. (10), the F_i values obtained for the ^1H nuclei were higher than those for the adjacent ^{13}C nuclei (cf. table 2, F_i values before optimization). Since this is not likely to be the case, they used an iterative procedure based on eq. (10) to optimize three parameters, F_i, G_i, and C_j. In the first step, the value of C_j for each lanthanide was held constant using the Bleaney values, while F_i and G_i were fit to eq. (10) by weighted

Table 2
F_i and G_i values for 1:1 R(fod)$_3$ (R = Pr, Eu, Dy, Yb) adducts with adamantanone (from Peters et al. 1985)

nucleus i	Before opt.		Three-parameter opt.[a]		Two-parameter opt.[b]	
	F_i	G_i	F_i	G_i	F_i	G_i
C=O*	−105.58	22.88	−82.39	23.03	−72.71	19.12
*C=O	1.51	3.51	0.86	4.90	0.51	5.85
C_α	−0.10	2.36	−0.16	2.64	−0.16	2.53
C_β	0.24	1.30	0.20	1.44	0.20	1.36
C_γ	−0.02	0.95	−0.03	1.07	−0.03	1.05
C_δ	−0.02	0.72	−0.03	0.80	−0.03	0.82
H_α	0.49	2.11	−0.01	2.51	0.15	2.20
$H_{\beta syn}$	0.27	1.05	0.02	1.26	0.01	1.27
$H_{\beta anti}$	0.16	0.68	0.00	0.82	−0.01	0.82
H_γ	0.16	0.54	0.03	0.65	0.02	0.67
H_δ	0.12	0.48	0.01	0.58	0.00	0.59

[a] F_i, G_i and C_j were optimized. [b] F_i and C_j were optimized.

least-squares analysis. Then in the second step, the optimized values of F_i and G_i were held constant, while C_j for each lanthanide, scaled to Bleaney's value of −100.0 for Dy^{3+}, was optimized by linear regression analysis. This two step procedure was repeated until no further improvement of the fit between calculated and observed shifts was found. The agreement factor decreased from 0.292 to 0.046 on optimization of C_j. The values of C_j obtained by this procedure (table 3) are in good agreement with the LIS values of H_δ, which are expected to have a negligible contact component (H_δ is six bonds removed from the lanthanide), but are not in agreement with the Bleaney values. The F_i values determined for each ^1H nucleus (cf. table 2, three-parameter optimization) are now significantly smaller than that of the adjacent ^{13}C nucleus. The sign and magnitude of the F value for the ^{17}O nucleus is in good agreement with those observed in other lanthanide complexes. Geometric factors were determined for each nucleus, using the solid state structure reported for the europium complex. The optimization procedure described above was carried out, except that the calculated G_i values were not allowed to vary (cf. table 2, two-parameter optimization). The agreement between these results and those obtained for the three-parameter optimization is very good, with the exception of the carbonyl carbon nucleus and H_α. Since actual geometric factors were used in this procedure, the C_j values obtained on optimization correspond to the anisotropy in the magnetic susceptibility (table 3).

Pinkerton and coworkers reported another method for separating the contact shifts and evaluating the hyperfine coupling constant A for ^{31}P in NMR studies of a series of tetrakis lanthanide complexes derived from dithiophosphinates, $[R\{S_2P(CH_3)_2\}_4]^-$ (Spiliadis and Pinkerton 1982) and esters of dithiophosphoric acid, $[R\{(XO)_2PS_2\}_4]^-$

Table 3
Optimization of C_j for 1:1 adducts of R(fod)$_3$ (R = Pr, Eu, Dy, Yb) with adamantanone (from Peters et al. 1985)

	Pr	Eu	Dy	Yb
δH_δ [a]	−7.04	6.24	−100.0	27.10
C_j (Bleaney)[a]	−11.0	4.0	−100.0	22.0
C_j(opt)[a,b]	−7.31	6.08	−100.0	26.97
C_j(opt)[c]	−1111.0	921.0	−15 048.0	4030.0

[a] Relative values, scaled to a value of −100.0 for Dy.
[b] Three-parameter optimization.
[c] Absolute magnitudes using two-parameter optimization; units are 10^{30} m^3.

(X = C_2H_5, Pinkerton and Earl 1978; X = CH_3, i-C_3H_7, Spiliadis and Pinkerton 1983a). For two nuclei, i and j, in a complex having axial symmetry,

$$\frac{\delta_i \gamma_i}{K\langle S_z\rangle} = \frac{A_i}{h} - \left(\frac{R_{ij} A_j \gamma_i}{h\gamma_j}\right) + R_{ij}\left(\frac{\delta_j \gamma_i}{K\langle S_z\rangle}\right), \tag{12}$$

where δ_i and δ_j are the LIS values, R_{ij} is the ratio of the pseudocontact shifts, $K = 2\pi\beta/3kT$, with the remaining terms defined previously (Pinkerton et al. 1985). For an isostructural series of complexes, a plot of $\delta_i\gamma_i/K\langle S_z\rangle$ versus $\delta_j\gamma_i/K\langle S_z\rangle$ is linear of slope R_{ij} and intercept $A_i/h - (R_{ij}A_j\gamma_i/h\gamma_j)$. If a nucleus j has no contact shift ($A_j = 0$), e.g. a ^{1}H resonance of an alkyl group, then the intercept is A_i/h, and the contact shift of nucleus i, e.g. ^{31}P, is determined. The ^{1}H and ^{31}P spectra of $[R\{(XO)_2PS_2\}_4]^-$ (X = CH_3, i-C_3H_7) in CD_2Cl_2 were recorded at 302 K (Spiliadis and Pinkerton 1983a). The LIS in the ^{1}H spectra were shown to be essentially pseudocontact in origin, whereas the LIS in the ^{31}P spectra have both contact and pseudocontact components (table 4), which were evaluated according to eq. (12). Although single crystal X-ray data (Spiliadis et al. 1983b) revealed that complexes representing both the light and heavy end of the lanthanide series have similar structures, the NMR data were interpreted in terms of two structural types in solution. The dodecahedral geometry observed in the solid state was proposed for the structure in solution for R = La to Dy, whereas square antiprismatic geometry was proposed for R = Ho to Lu. The change in structural type is accompanied by a significant decrease in magnitude of the ^{31}P:^{1}H pseudocontact shift ratios, e.g., 31.7 to 3.0 for X = CH_3 and from 16.4 to 0.55 for X = i-C_3H_7. The change in structural type is also accompanied by a reduction in the hyperfine coupling to phosphorus (A/h in MHz): 1.62 to 0.82 for X = CH_3; 1.57 to 0.85 for X = i-C_3H_7. It is important to note, as in the case of most high coordinate lanthanide complexes, that these molecules are fluxional on the NMR time scale.

Given the assumptions inherent in the separation procedure proposed by Reilley, we (Forsberg et al. 1995) sought an alternative procedure for separating the contact component of the LIS. If we write δ_{ij} as the LIS for the ith nucleus on the jth metal, for axial symmetry,

$$\delta_{ij} = G_i A_j + F_i \langle S_z\rangle_j \tag{13}$$

Table 4
LIS data (in ppm) for $[C_6H_5)_4As][\{R(XO)_2PS_2\}_4]$ at 302 K (from Spiliadis and Pinkerton 1983a)

R	X = CH_3			X = i-C_3H_7		
	δP_{obs} [a]	δP_c	δP_{pc}	δP_{obs} [a]	δP_c	δP_{pc}
Ce	−104.0	−74.5	−29.5	−99.0	−68.6	−30.4
Pr	−254.9	−217.2	−37.7	−243.2	−203.5	−39.7
Nd	−333.0	−303.2	−29.8	−334.0	−294.7	−39.3
Tb	1375.0	2289.9	−914.9	1413.0	2147.0	−734.0
Dy	1099.7	2151.8	−1052.1	1121.4	1997.6	−876.2
Ho	790.0	830.0	−40.0	825.0	836.9	−11.9
Er	535.0	505.0	30.0	571.5	562.9	8.6
Tm	306.0	257.1	48.9	321.0	306.1	14.9
Yb	56.0	42.1	13.9	98.8	94.6	4.2

[a] δP_{obs} measured relative to the corresponding lanthanum complex. Downfield shifts are positive.

where G_i is the geometric factor for the ith proton and A_j represents $\chi_{zz}^j - \mathrm{Tr}\chi^j$ for the jth metal from eq. (5), and F_i and $\langle S_z \rangle_j$ are defined in eq. (8). The idea is to find a set of optimum values of A_j, G_i, and F_i that minimize R (eq. 2) for the resulting matrix of $i \times j$ simultaneous equations. We showed that there exist linear transformations, eqs. (14)–(16), dependent on two continuous parameters (a, c), which leave the right-hand side of eq. (13) invariant:

$$G_i' = aG_i, \tag{14}$$

$$F_i' = F_i + cG_i, \tag{15}$$

$$A_j' = \frac{1}{a}A_j - \frac{c}{a}\langle S_z \rangle_j, \tag{16}$$

Consequently, any fitting method, such as least-squares, will give an infinite number of solution sets for each of the variables, A_j, G_i, and F_i. However, if values are preassigned to any two of the variables, say $G_1 = G_1^0$ (geometric factor for H_1) and $A_1 = A_1^0$ ($A_1^0 = \chi_{zz} - \frac{1}{3}\mathrm{Tr}\chi$ for metal 1), then the parameters a and c are determined, and any solution set (G_i', F_i' and A_j') can be brought by the linear transformations to the set that is scaled to G_1^0 and A_1^0, namely G_i^0, A_j^0 and F_i^0. Although this method of separating LIS values into the contact and pseudocontact components is theoretically sound, there appear to be two problems if the goal of analyzing LIS data is to provide an independent means to determine the structure of a complex in solution. First, the geometric factor for one nucleus is assumed to be known, which is only the case if the structure is known. Secondly, the magnetic anisotropy ($\chi_{zz} - \frac{1}{3}\mathrm{Tr}\chi$) for one lanthanide complex is also assumed to be known from analyzing the LIS data for that complex according to eq. (5), which requires knowledge of the contact shifts for accuracy. Although it may be reasonable to assume that the contact shifts are negligible for protons on a ligand

coordinated to Yb^{3+}, as discussed above, it is best not to make such an assumption. The efficacy of the procedure lies in the fact that only the product of A_jG_i must be known precisely in order to give a reliable set of F_i values. Thus the analysis is carried out, using as a first approximation for G_1^0, that value obtained from a solid state structure or a molecular mechanics calculation, then varying A_1^0 to obtain a minimum value of R. The same value of R and set of F_i^0 values are obtained by choosing an approximate value of A_1^0 and varying G_1^0. As the structure of the complex is modified to represent the true structure in solution, a correlation will exist between geometric factors determined from the separation procedure and those calculated from the structure. Furthermore, a correlation will exist between the magnetic anisotropy values obtained by analyzing the LIS data according to eq. (5), and the values obtained using eqs. (13)–(16). An application of this procedure is given in sect. 4.2.3.

2.4. *Nuclear relaxation in paramagnetic lanthanide complexes*

In addition to acting as shift reagents, it is well established that paramagnetic lanthanide complexes are effective relaxation agents. Due to the relatively long electron-spin relaxation time of Gd^{3+}, complexes of Gd^{3+} are most effective as relaxation agents, as evidenced by their commercial development as MRI contrast agents. Paramagnetic lanthanide ions affect both the longitudinal relaxation rate (decay of the z-component of magnetization, with a rate constant T_1^{-1}) and the transverse relaxation rate (loss of coherence of magnetization in the xy-plane, with a rate constant T_2^{-1}). Transverse relaxation determines the line width of the resonance ($\delta\nu^{1/2} = 1/\pi T_2$, where $\delta\nu^{1/2}$ is the line width at half-height). The ability of paramagnetic lanthanide ions to induce nuclear relaxation through either a dipolar or Curie mechanism (or a combination of both) provides information regarding internuclear distances. Lanthanide ions generally are not effective at inducing relaxation in ^1H and ^{13}C nuclei through a contact interaction. Equations for lanthanide-induced relaxation, in terms of T_1^{-1} and T_2^{-1}, for all three contributions, are available in the literature (see Kemple et al. 1988). Both the dipolar and Curie contributions to T_1^{-1} and T_2^{-1} have an r^{-6} dependency on the R^{3+}-nucleus distance. The dipolar contribution to T_1^{-1} and T_2^{-1} is also a function of the correlation time, τ_c, where $\tau_c^{-1} = \tau_e^{-1} + \tau_r^{-1} + \tau_m^{-1}$ (τ_e is the electron-spin relaxation time; τ_r is the rotational correlation time; τ_m is the residence time of the ligand in the coordination sphere). The correlation time is dominated (except for Gd^{3+}) by the very short electron-spin relaxation times, which are on the order of 10^{-13} s (Alsaadi et al. 1980a, 1980b). Thus, in addition to the r^{-6} dependency, the values of T_1^{-1} and T_2^{-1} for various nuclei in lanthanide complexes relaxing via a dipolar interaction are dictated by the electron-spin relaxation time. Although difficult to measure for individual lanthanide complexes, the electron-spin relaxation times for the lighter members of the lanthanide series (Ce–Eu) are generally smaller than those for the heavier members (Tb–Yb). Thus line-broadening (smaller T_2^{-1} values) is less severe in spectra of complexes of the lighter lanthanides than in those of the heavier lanthanides (reasonably narrow line widths are observed for Yb^{3+} complexes). The larger electron-spin relaxation times of the heavier

members of the series also make it difficult to observe 2D spectra of complexes of these metal ions (see sect. 2.5). Curie relaxation depends on the rotational correlation time, τ_r. It is often assumed that the Curie contribution to T_1^{-1} and T_2^{-1} is negligible compared to the dipolar contribution for relatively small paramagnetic lanthanide complexes, since $\tau_e \ll \tau_r$, i.e., $\tau_c^{-1} = \tau_e^{-1}$, therefore, $\tau_c \gg \tau_r$. However, the Curie contribution to both T_1^{-1} and T_2^{-1} is also proportional to B_o^2 (B_o is the magnetic field strength) and T^{-2}. Thus at higher field strengths and lower temperatures, the Curie contribution to both longitudinal and transverse relaxation becomes more important. Kemple et al. (1988) estimate that the dipolar and Curie contributions to T_1^{-1} and T_2^{-1} are about equal for ^{1}H nuclei in lanthanide complexes derived from edta-type ligands (see sect. 4.1) at field strengths of ~7 T (300 MHz) at room temperature.

It is difficult to use lanthanide-induced relaxation data to obtain accurate distances between various nuclei and the lanthanide ion. If it can be shown that the dipolar contribution to either T_1^{-1} or T_2^{-1} is dominant, then the difficulty is related to a means to determine accurate values of the electron-spin relaxation times. If the Curie contribution can be shown to dominate, then the problem is measuring accurate correlation times. However, the major difficulty is that the relative dipolar and Curie contributions to T_1^{-1} and T_2^{-1} are generally not known. However, since both the Curie and dipolar contributions to T_1^{-1} and T_2^{-1} have an r^{-6} dependency on the R^{3+}-nucleus distance, ratios of T_1 or T_2 values for various nuclei can be used to determine accurate ratios of the internuclear distances.

2.5. *2D-NMR techniques*

Jenkins and Lauffer (1988a,b) introduced 2D NMR spectroscopy, namely COSY and EXSY (exchange spectroscopy), of paramagnetic lanthanide complexes in their report on ^{1}H NMR studies of $R(dtpa)^{2-}$ complexes in aqueous solution. The results of their study are presented in sect. 4.3. In their papers, Jenkins and Lauffer point out some of the difficulties associated with the use of these techniques in paramagnetic systems. The major limitation in the use of EXSY spectroscopy to resolve exchange partners is that of short T_1 values (effective longitudinal relaxation). EXSY spectroscopy uses the same three-pulse sequence as used in NOESY spectroscopy ($\frac{1}{2}\pi$–t_1–$\frac{1}{2}\pi$–τ_m–$\frac{1}{2}\pi$–t_2). Due to chemical exchange, a nucleus whose z-magnetization was modulated by one chemical shift during t_1 may have the opportunity to migrate to another site during τ_m, referred to as the mixing time, and appear with a different chemical shift during t_2 acquisition. Thus the spectrum has a COSY-like appearance, with cross peaks between the shifts of exchanging sites. For short T_1 values, as observed in paramagnetic systems, substantial cross peak intensity can develop only at very short mixing times relative to diamagnetic systems. In a simple two-site interchange between symmetry related species, in which case k_{ex}(forward) = k_{ex}(reverse), where the protons have similar T_1 values, the diagonal and cross peak intensities can be described as

$$I(\text{diag}) = \tfrac{1}{2}\,[1 + \exp(-2k_{ex}\tau_m)]\exp\left(-\frac{\tau_m}{T_1}\right) I_0, \tag{17}$$

$$I(\text{cross}) = \tfrac{1}{2}\,[1 - \exp(-2k_{ex}\tau_m)]\exp\left(-\frac{\tau_m}{T_1}\right) I_0. \tag{18}$$

Based on these equations, considerable cross peak intensity can develop for mixing times between $1/k_{ex}$ and T_1. Since k_{ex} is generally not known, a range of τ_m values is usually used in an effort to detect cross peaks. However, there are two practical limitations to consider. If the exchange rate is too slow (small k_{ex}), the frequency-labeled z-magnetization will disappear due to a relatively short T_1 characteristic of paramagnetic systems (see sect. 2.4) before it has a chance to migrate. On the other hand, if the inherent exchange rate is sufficiently fast (large k_{ex}) to allow for the detection of cross peaks for nuclei with very short T_1 values, then it may not be possible to reach the slow exchange regime of the NMR time scale, a prerequisite for EXSY spectroscopy. Thus EXSY spectroscopy may not be possible for complexes of those lanthanides (Tb–Tm) that most effectively induce nuclear relaxation.

Similar limitations apply to 2D COSY spectra of paramagnetic complexes, where short T_2 values (transverse relaxation) lead to rapid decay of phase coherence, which attenuates cross peak intensity. Since the amount of magnetization transfer is proportional to $[\exp(-t_1/T_2)]\sin \pi J t_1$ (J is the nuclear spin–spin coupling constant), once t_1 (the evolution time) becomes on the order of T_2, little cross peak intensity will accumulate. As noted by Jenkins and Lauffer, cross peaks should be detected if $T_2 \geqslant 1/5J$. If transverse relaxation has a Curie component (see sect. 2.4), which is proportional to $\mu_{eff}^2 B_0^2/T^2 r^6$, the detection of cross peaks becomes problematic at low temperatures, high fields, short metal–proton distances, and for complexes derived from metal ions with large effective magnetic moments, such as the heavier lanthanides, Tb–Tm. An additional problem is the wide dispersion range of chemical shifts observed in paramagnetic systems, which may result in inadequate digitization of the cross peaks due to limitation of computer storage of the data matrix.

3. NMR studies of shift reagents and labile complexes

Although lanthanide shift reagents, such as $R(fod)_3$ and $R(thd)_3$, found widespread use in separating overlapping multiplets in spectra of organic substrates, the resulting Lewis base adducts are labile on the NMR time scale. Early work to deduce the structure of lanthanide shift reagent adducts in solution employed certain assumptions as noted by Horrocks (1974). Namely, (1) the LIS is pseudocontact in origin; (2) the adduct exists as a single, stoichiometric species having axial symmetry; (3) only a single geometrical isomer of the adduct is present and that the substrate ligand exists as a single conformation; and (4) the principal magnetic axis has a known orientation with respect to the substrate. If any of the above criteria are not met (as a generalization, none of these criteria are usually met), then geometric inferences drawn will not be strictly valid. Since the majority of the adducts are labile on the NMR time scale, the observed shifts are a weighted average of the shifts of the substrate in the complexed and free states. Therefore, evaluation of the bound

shifts requires knowledge of the equilibria involved in complexation of the substrate with the shift reagent. Shift reagents (LR) are known to form several complexes, generally formulated as LR_nS_m, where S represents the organic substrate with $n \geqslant 1$ and $m \geqslant 1$. As noted by Bovée et al. (1982), it is difficult to extract reliable values for the bound shifts and equilibrium constants from measured shift data if two or more equilibria are involved.

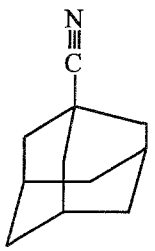

adamantane-1-carbonitrile Fig. 2.

The problems encountered in structural analysis are well illustrated with the adducts formed between $R(fod)_3$ and adamantane-1-carbonitrile (fig. 2), a highly structured ligand. Raber et al. (1981) reported a procedure for the evaluation of the structure of the $Eu(fod)_3$ adduct using LIS data. Best fit of the LIS data was obtained with a Eu–N bond distance of 2.1 Å. However, using ^1H and ^{13}C spin-lattice relaxation rates induced by $Gd(fod)_3$, Peters et al. (1982) determined a Gd–N bond distance of 2.6 Å, which is more in line with values expected for R^{3+}–N bond distances. Peters suggested that the values of the bound shifts obtained for the europium adduct were inaccurate due to the presence of complex equilibria involving the mono and bis adducts, and free substrate, all in fast exchange on the NMR time scale.

The importance of including both terms of eq. (4) in analyzing LIS data of shift reagent adducts became clear in a report by Horrocks and Sipe (1972), who used magnetic anisotropy measurements obtained on single crystals of a series of eight-coordinate adducts, $R(thd)_3 \cdot L_2$ (L = 4-picoline), together with geometric factors determined from the solid state structure, to reproduce the pseudocontact shifts observed experimentally in solution. This study was followed by a series of papers by Cramer and coworkers (Cramer et al. 1974, 1975, Cramer and Maynard 1978), who showed that a good fit between experimental and calculated LIS values for a series of bis adducts, $R(thd)_3 \cdot L_2$ (L = pyridine, 3-picoline, 4-picoline, 3,5-lutidine), could only be obtained using the full expression given in eq. (4). In these studies, geometric factors for all the protons were calculated using the solid state crystal structure of the pyridine adduct, which was shown to have a two-fold symmetry axis. The principal magnetic z-axis was assumed to coincide with the molecular symmetry axis, while the location of the magnetic x-axis, as well as D_1 and D_2, were used as fitting parameters. It is important to note that the values found for D_2 are generally two to three times larger than the values for D_1, indicating the importance of the second term in eq. (4).

Complexes derived from a single multidentate ligand, in which the denticity of the ligand is incapable of satisfying the high coordination number demanded of the lanthanide ions or totally encapsulating the metal ion, are typically labile on the NMR time scale. ^{1}H NMR studies of paramagnetic R(edta)$^-$ complexes, which have been used as aqueous shift and relaxation reagents (Elgavish and Reuben 1976, 1977, Reuben 1976, Sherry et al. 1981), for example, reveal an equivalent AX quartet pattern for each of the acetate protons and a singlet for the ethylene protons, indicating that the R^{3+}–O interactions are short-lived on the NMR time scale, whereas the R^{3+}–N donor interactions are long-lived with the ethylenediamine chelate ring undergoing rapid interconversion between its two puckered conformations (Siddall and Stewart 1969, Southwood-Jones and Merbach 1978). However, given sufficient steric hindrance, stereochemical interconversions that might otherwise be assumed to be rapid may become slow on the NMR time scale. A case in point is the 60 MHz ^{1}H NMR study reported by Evans and de Villardi (1978) on 1:1 adducts of *N*-tetraalkyl substituted ethylenediamines and 1,2-propanediamines with Pr(fod)$_3$ in deuterated toluene. These ligands are coordinated in a bidentate manner to the lanthanide ion, forming a puckered five-membered chelate ring that is chiral, existing in two enantiomeric forms, λ and δ. Generally, ethylenediamine chelate ring interconversion between the two conformers is rapid on the NMR time scale. However, the spectra of adducts derived from *N,N,N′,N′*-tetramethylethylenediamine revealed separate resonances for the axial and equatorial protons of the chelate at –60°C, indicating that chelate ring interconversion is slow at this temperature. The free energy barrier to ring interconversion was determined to be 10.1 kcal mol^{-1} at –36°C. An even larger barrier to interconversion is suggested for the adduct derived from *N,N,N′,N′*-tetramethylpropylene-1,2-diamine, since separate resonances for the four CH_3(N) groups, the CH_3(C) group, and the three ethylenediamine chelate ring protons were observed at 20°C.

Several paramagnetic lanthanide complexes derived from macrocyclic ligands have been investigated as potential shift reagents. Horrocks and Wong (1976) investigated the organic solvent soluble lanthanide complexes of tetraarylporphine (tap) having the general formulation, R(tap)(acac) (acac = acetylacetonate). Paramagnetic shifts (mostly downfield) are observed for the tap protons of the Eu^{3+} and Yb^{3+} complexes, whereas the acac proton resonances are shifted upfield. The pseudocontact shifts induced in the ^{1}H spectra of the ligands were analyzed using an axial model. The metal ions lie significantly out of the phorphyrin plane, ~1.8 Å (Eu^{3+}) and ~1.6 Å (Yb^{3+}), along the C_4 axis of the macrocycle, with the acac ligand coordinating the lanthanide ion in a bidentate fashion in the axial position. The ytterbium complex serves as a downfield shift reagent toward heterocyclic amines and alcohols. An eight-coordinate model was proposed to account for the fact that the resonance shifts of the substrate are in the same direction as those of the tap ligand, i.e., the substrate protons also lie in the equatorial region. Horrocks and Hove (1978) reported the synthesis of water soluble lanthanide complexes derived from tetra-*p*-sulfonatophenylporphine (tpps), with the general formula, R(tpps)(imidazole)$_x$ ($x \leqslant 2$; R = Gd–Lu). The LIS ^{1}H data for the thulium complex were analyzed using an axial model, and it was determined that the metal ion lies ~1.6 Å out of the porphyrin plane along the C_4 axis of the macrocycle. The tpps complexes of the latter

lanthanides (Ho–Yb) serve as potent aqueous solution shift reagents for nuclei of neutral and cationic substrates (the 4-picoline molecule and *N*-methylpyridinium cation were examined) and, to a lesser extent, for the water proton resonance and anionic substrates, such as the *p*-toluidate anion. More recently, monophthalocyanine complexes of Pr^{3+} and Eu^{3+} have been reported as selective shift reagents for primary aliphatic amines (Komarov et al. 1993).

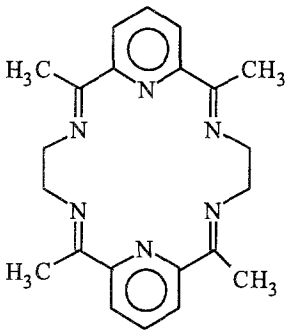

Fig. 3.

Vallarino and coworkers investigated complexes derived from the macrocyclic hexaimine ligand (fig. 3) as potential shift reagents (Fonda et al. 1993, Benetollo et al. 1990, Bombieri et al. 1991). The interaction of $[Eu(CH_3COO^-)_2L]Cl$ with sodium carboxylates (formate, acetate, propanoate, butanoate, benzoate, and succinate), in aqueous solution, produced sizable ^1H shifts in the spectrum of the substrate. Substitutional equilibrium is established between the carboxylate substrate and the acetate ligands of the shift reagent, with rapid exchange between coordinated and free carboxylate ions on the NMR time scale. However, neither neutral oxygen donors (acetone, methanol, 1-butanol, 2-methyl butanol) (Fonda et al. 1993) or *N*-donor ligands (aminobutane, ethylenediamine, aniline, pyridine, 1,10-phenanthroline and 2,2′-bipyridyl) (Bombieri et al. 1991) revealed shifts in the ^1H NMR spectrum of the substrate, indicating that the neutral donors could not compete with the acetate ion for coordination to the lanthanide ion. Interestingly, the LIS in the ^1H spectra of $[R(CH_3COO^-)_2L]^+$ (R = Nd, Eu) are strongly solvent dependent (Benetollo et al. 1990). For example, the ethylene CH_2 ^1H resonance in the europium complex appears at −7.65 ppm in D_2O, at 1.47 ppm in DMSO-d, and at 0.62 ppm in $CDCl_3$. It was concluded that the folding of the macrocycle is affected by the nature of the exocyclic ligands (anions or solvent molecules), resulting in different spatial positions of the hydrogen atoms of the macrocyclic ligand relative to the metal ion. In an earlier study, Arif et al. (1987) recorded the ^1H spectra of the series of $RL(NO_3)_3$ complexes. The contact and pseudocontact components of the LIS of the various protons were separated according to eq. (10). Linear plots were observed only for nuclei of complexes derived for the first three members of the series (Ce–Nd), with poor fitting results for other members of the series, indicating that a structural change occurs as the lanthanide series is traversed. It could not be ascertained whether the structural change is by means of a rapid equilibrium between two or more distinct structures, which is

progressively displaced across the series, or whether only one structure is present for each metal ion, but progressively alters with ionic radius. In a latter ^1H and ^{13}C NMR study of $Eu(CH_3COO^-)_2L^+$ at room temperature, Smith et al. (1989) noted that the effective symmetry of the complex in solution is D_{2h}, suggesting that the bending of the two diiminopyridine portions of the macrocycle about the diamine bridges is rapid on the NMR time scale.

As noted above for adducts of shift reagents, labile complexes that are not axially symmetric may often give reasonable fits of LIS data by assuming axial symmetry. As an example, the symmetry of the ligand dictates that the complexes, $R(bdoda)_n^{(3-2n)+}$ (R = Pr, Eu, Yb; bdoda = benzene-1,2-dioxyacetate; $n = 1, 2$), have C_2 symmetry. However, using only the first term of eq. (4), ^1H and ^{13}C LIS data for both the mono and bis complexes were fit to a geometrical model in which the principal magnetic axis was taken as collinear with the C_2-symmetry axis of the ligand, with the lanthanide ion lying along the axis in the plane defined by the benzene ring and ether oxygen atoms (Kullberg and Choppin 1977).

It is not surprising that good fits of LIS data are obtained for labile lanthanide complexes derived from nonrigid ligands, in which the structural model has axial symmetry. Peters et al. (1988a) determined the bound shifts for ^1H, ^{13}C and ^{17}O resonances of eleven paramagnetic complexes derived from the bidentate glycolate anion, $HOCH_2COO^-$. Plots of the LIS data according to either eqs. (10) or (11) were reasonably linear, allowing separation of the contact and pseudocontact components in terms of the F_i and G_i parameters. Peters and co-workers had previously shown that the values of the F parameter for lanthanide bound oxygen atoms were all in a rather small range of -70 ± 11 at 73°C (Vijverberg et al. 1980). Based on the F_i values obtained for the glycolate complexes, it was proposed that three water molecules are coordinated to the lanthanide ion in addition to three glycolate ligands, each coordinating in a bidentate fashion by one carboxyl oxygen and the hydroxylic oxygen. An optimum fit of experimental and calculated G values was obtained for a tricapped trigonal prismatic geometry, in which all coordinated carboxylate oxygens are in the capping positions ($\theta = 92°$) and the OH oxygens are at one set of prism vertices ($\theta = 52°$), with the water oxygen atoms occupying the other set of prism vertices ($\theta = 138°$) (average metal–oxygen bond distances are 2.47 Å). Peters (1988b) reported ^1H, ^{13}C and ^{17}O NMR studies of the series of $[R(oda)_3]^{3-}$ (oda = oxydiacetate, $^-OOCCH_2OCH_2COO^-$) complexes. Plots of the ^{13}C and ^1H LIS data according to eqs. (10) or (11) revealed a break between the lighter (Ce–Eu) and the heavier members of the series. The plots for the lighter members of the series were relatively linear, allowing separation of the contact and pseudocontact components of the shifts in terms of the F_i and G_i values, whereas the plots for the heavier members of the series were more irregular. The experimental and calculated G_i values were in good agreement with structures having D_3 symmetry, corresponding to the crystal structure of $Na_3[Ce(oda)_3] \cdot 2NaClO_4 \cdot 6H_2O$. The crystal structure reveals that the lanthanide cation is nine coordinate, located in a twisted tricapped trigonal prismatic coordination polyhedron in which the ether oxygens bond at the capping positions. Although the complexes are isostructural in the solid state, the break in the plots of the

LIS data, noted above, suggest that a structural change occurs in solution for heavier members of the series. Peters proposed that a carboxylate group of one of the oda ligands is expelled from the coordination sphere on going to the heavier lanthanides, giving an eight-coordinate complex. Although the eight-coordinate complex should have low symmetry, no separation of oda signals was observed in the NMR spectra, suggesting that the ligands are rapidly reorienting on the NMR time scale. Interestingly, though, separation of the geminal protons of the methylene group are observed for complexes of Ho–Yb when the temperature is lowered to 6°C.

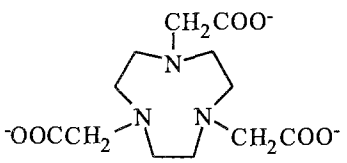

nota Fig. 4.

Sherry et al. (1986) reported ^{1}H and ^{13}C NMR studies of R(nota) (nota^{3-} = 1,4,7-triazacyclononane-*N,N′,N″*-triacetate) (fig. 4). Whereas other complexes derived from macrocyclic ligands with acetate groups as pendant arms, such as dota (sect. 4.2.1) and teta (sect. 4.2.4) are structurally rigid on the NMR time scale, the nota complexes are not rigid. Thus the ^{1}H spectra at 25°C (pH 6) revealed a single resonance for the ethylene protons, indicating that a rapid interconversion occurs between the λ and δ conformers of the ethylenediamine chelate rings, and a single ^{1}H resonance for the acetate protons, indicating that the carboxyl groups are fluxional in these complexes. With one exception (R = Pr), the ^{13}C spectra revealed single resonances for the ethylene, carboxyl and acetate carbons at 25°C. The spectrum of Pr(nota) revealed two ^{13}C resonances for the ethylene group, suggesting that nota forms mixed complexes with early members of the lanthanide series, perhaps a pentadentate chelated species in equilibrium with a hexadentate chelated species. The contact and pseudocontact components of the LIS were separated using eq. (10). A distinct break in the plots occurs between terbium and dysprosium, indicating a structural change that may result from a combination of changes in hydration number, conversion to only a hexachelated complex for the smaller ions, or the ability of the smaller ions to make a closer approach to the triazamacrocycle cavity. Based on ^{17}O data, Peters (1986) proposed that the number of water molecules coordinated to the complexes changes from 3 to 2 near the middle of the series. The experimentally determined *G* parameters are presented in table 5 for the Pr–Tb and Dy–Yb subgroups, together with values calculated using the axial symmetry model (eq. 4, $D_2 = 0$) (Sherry et al. 1986). The position of the lanthanide ion relative to the center of the triangle formed by the three nitrogen donor atoms was varied from 2.6 to 1.8 Å, corresponding to R^{3+}–N bond distances of 3.1 and 2.4 Å (table 5). For the Pr–Tb subgroup, the agreement is better for the longer R^{3+}–N distance, whereas for the Dy–Yb subgroup, the agreement is better for the shorter R^{3+}–N bond distance. The ability of the R(nota) complexes

Table 5
Calculated and observed pseudocontact shift ratios for the R(nota) complexes (Sherry et al. 1986)

Nucleus	Relative G values (calculated)[a,b]			Relative G values (exp.)	
	D=2.6 Å	D=2.2 Å	D=1.8 Å	Pr–Tb	Dy–Yb
C_N	−1.42	−1.39	−1.27	−2.19	−0.51
$H_{N'}$	−0.57	−0.36	−0.11	−0.17	−0.08
$H_{N''}$	−1.00	−1.00	−1.00	−1.00	−1.00
H_A	0.36	0.60	0.77	−0.13	0.06
	(0.94)	(1.24)	(1.34)		
C_A	0.31	0.88	1.33	0.42	0.53
C_O	4.67	4.18	2.84	2.50	3.42
	(1.25)	(1.47)	(1.49)		

[a] Shift ratios calculated using axial symmetry model. The ratios are reported relative to $H_{N''}$ because this nucleus is least sensitive to the R–N distance. G values for H_A and C_O are given for both gauche and eclipsed (parentheses) rotamers of the acetate protons relative to the $-CH_2-N-CH_2-$ bonds of the macrocyclic ring.
[b] D is the distance between the lanthanide cation and the center of a triangle formed by the three nitrogen atoms of nota. These distances correspond to R–N bond lengths of 3.1, 2.7, and 2.4 Å, respectively.

to act as aqueous shift reagents and relaxation probes is demonstrated with mixed complexes formed with the mononucleotide adenosine 5′-monophosphate and endo-*cis*-bicyclo-[2.2.1]hept-5-ene-2,3-dicarboxylic acid (Geraldes et al. 1987). The use of R(nota) complexes as aqueous shift reagents for $^{23}Na^+$ nuclei is presented in sect. 6.

4. Studies of stereochemically rigid complexes

It is apparent that reliable structural information would be best obtained on those complexes that are not only thermodynamically stable, but more importantly, also stereochemically rigid on the NMR time scale. Furthermore, studies of stereochemically rigid systems best provide support for theoretical models used in explaining the origin of the LIS, as well as separation of the contact and pseudocontact components of the LIS. Although steric hindrance is probably the most important factor in dictating stereochemical rigidity in lanthanide complexes, it is now recognized that high denticity ligands, such as the octadentate ligands dota (sect. 4.2.1) and dtpa (sect. 4.3) that are capable of totally encapsulating the metal ion, are rigid on the NMR time scale. Other complexes in which the lanthanide ion is totally encapsulated, such as the [2.2.1] cryptates (Gansow et al. 1979, Gansow and Kausar 1983, 1985) and the amine cage complexes prepared by Raymond and coworkers (Smith et al. 1988), appear to be rigid on the NMR time scale. However, a complete analysis of the LIS data has not been carried out on these systems. Stereochemical rigidity also can be imparted by constraints on the ligand to bind the metal, e.g., dpa (sect. 4.4.1) or hbpz (sect. 4.4.2), or the rigid nature of the ligand itself, e.g., texaphyrins (sect. 4.4.3) or porphyrins (sect. 4.4.4). NMR studies representing each of these types of stereochemically rigid systems are summarized in the

following sections. Each system is presented with sufficient detail to provide an insight to the potential of using paramagnetic lanthanide ions as NMR probes for determining the structure of complexes in solution and to characterize the dynamic intramolecular reorientation of ligands that occurs in the coordination sphere.

4.1. *Complexes derived from indole-edta (1) and benzyl-edta (2)*

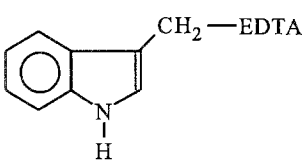

1

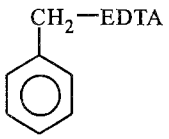

2

Fig. 5.

Kemple et al. (1988) reported ^{1}H NMR studies of lanthanide complexes derived from indole-edta (R = La, Pr, Nd, Eu, Yb) and benzyl-edta (R = La, Pr, Yb, Lu) (fig. 5) in D_2O over the temperature range 5–60°C. Although the LIS data are limited to three paramagnetic lanthanide ions (R = Pr, Nd, Eu), the new method introduced for analyzing the LIS data, which uses a linear least-squares fitting of the data to expressions involving elements of the magnetic susceptibility tensor, is an important contribution to the field (sect. 2.2). All proton resonances were resolved in the spectra of the diamagnetic and paramagnetic complexes derived from the lighter lanthanides (line broadening precluded complete resolution of peaks in the case of ytterbium). No proton equivalencies were observed, indicating that the complexes are totally asymmetric in solution and presumably rigid on the NMR time scale (the authors note that the contribution of molecular motion to the structural studies, which are described below, is difficult to ascertain). It is interesting to note that the stereochemical rigidity proposed for these systems is not observed in paramagnetic lanthanide complexes derived from edta (Elgavish and Reuben 1976, 1977, Reuben 1976, Sherry et al. 1981). The assignment of the resonances, which are presented in the original literature, were based on proton decoupling experiments, 2D COSY spectra, T_1 and T_2 measurements, and LIS analyses. The structures for the complexes were determined by molecular mechanics calculations using the MM2 force field (see fig. 6). Since MM2 parameters are not defined for lanthanide–donor atom bonds, crystal structure data for the lanthanum complex derived from edta provided atomic coordinates for the heavy atoms. The carboxylate oxygen atoms and the lanthanum ion were held fixed at the crystallographic coordinates, while the remainder of the system, including all hydrogen atoms, was allowed to fully relax during energy minimization. The structures reveal that the metal ion is located approximately at the center of a nearly planar trapezoid of four oxygen atoms (O-2, O-8, O-9 and O-15). The z-axis of the molecular coordinate system was chosen to pass through the metal ion, perpendicular to a plane that was least-squares fit to the four oxygen atoms. The x- and y-axes in the molecular coordinate system were taken to be roughly bisecting the sides of the trapezoid. The coordinates of the

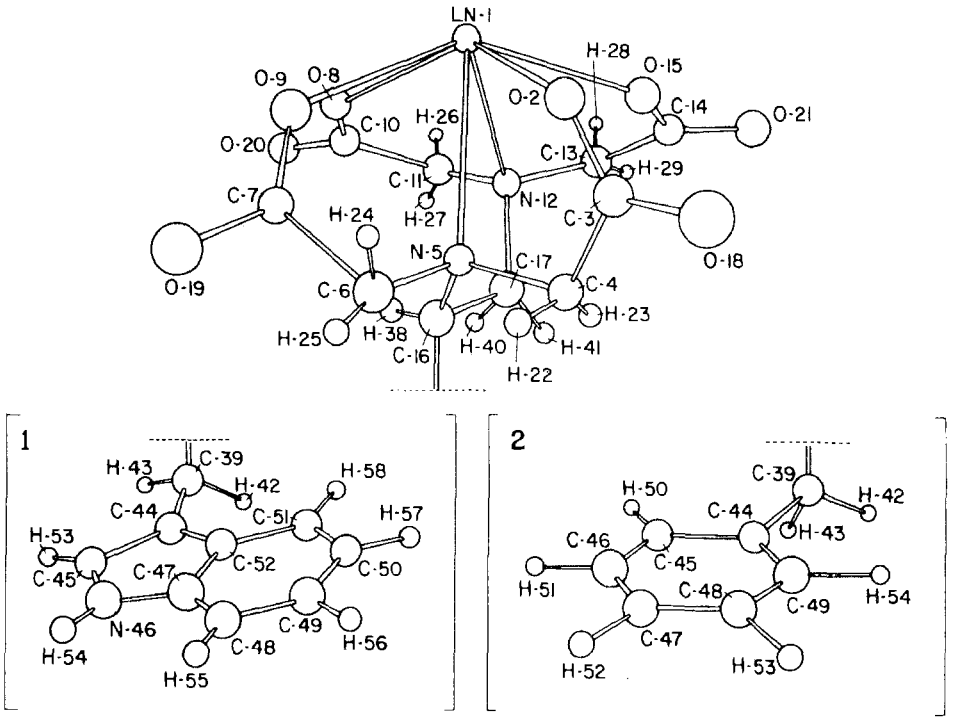

Fig. 6. Structures of La-1 and La-2 from molecular mechanics calculations showing the atom numbering system used (Kemple et al. 1988).

hydrogen atoms in the molecular axis system, obtained from the molecular mechanics calculations, were used in the LIS analysis. Initially the LIS values were assumed to be purely pseudocontact in origin. Analyses were carried out using the expression given in eq. (5), with the 13 aliphatic protons, 22–29, 38, 40–43, serving as the basis. The aromatic moieties were not included in the analyses, since these groups are subject to rotation about the bond connecting C-39 and C-44 (see fig. 6). No assumptions were made regarding the orientation of the molecular coordinate system and the principal magnetic axis system. As noted in sect. 2.2, the pseudocontact shifts depend only on the traceless part χ' of the susceptibility tensor χ. Diagonalization of χ' gives a set of Euler angles that relates the principal axis system of χ' (and χ) to the arbitrarily defined molecular coordinate system. The fits obtained for complexes derived from indole-edta, without correcting the LIS for contact shifts, were not deemed reasonable [$R = 0.143$–0.158 (Pr^{3+}), 0.348–0.349 (Nd^{3+}), and 0.685–0.825 (Eu^{3+})]. Introducing contact shift parameters into the fitting procedure requires consideration of the following factors. Unless required by symmetry, each proton in the molecule could have a different contact shift. On the other hand, no more than eight contact shift parameters may be introduced in order that the total number of fitting parameters (including the five susceptibility parameters) does not exceed the number of LIS values, which is 13. Otherwise, fits of the LIS values with reduced deviations will

Table 6
Magnetic susceptibility parameters for fits of R-1 and R-2 complexes to the LIS data (from Kemple et al. 1988)

T (°C)	χ'_{ww} [a]	χ'_{uu} [a]	η	θ_{uz} (°)	θ_{vz} (°)	θ_{wz} (°)	R
Pr-1							
5	−2112	1797	0.702	94.2	84.2	7.2	0.026
30	−1837	1566	0.704	93.5	84.4	6.6	0.032
60	−1563	1320	0.689	92.4	84.8	5.7	0.043
Nd-1							
5	−1520	1499	0.973	101.3	72.6	21.0	0.039
30	−1249	1209	0.936	100.4	73.8	19.4	0.031
60	−981	909	0.854	98.9	75.0	17.5	0.024
Eu-1							
5	−2512	1431	0.139	29.3	61.1	94.8	0.052
30	−1850	1012	0.093	11.4	98.3	97.8	0.031
60	−1339	870	0.299	33.4	120.9	101.5	0.092
Pr-2							
5	−2242	1962	0.750	92.9	82.5	8.0	0.031
30	−1962	1723	0.756	92.2	82.6	7.8	0.038
60	−1671	1451	0.737	91.2	83.0	7.1	0.048

[a] In units of ppm Å^3. Uncertainties in the susceptibility parameters are ~10%.

result without improving the determination of the susceptibility parameters and thus the flexibility needed for accurate evaluation of the geometry-dependent parameters is lost. To limit the number of contact shift parameters, the authors divided the eight acetate protons into two groups of four, 22–25 and 26–29, the rationale being that, although both sets have the same bonding network to the lanthanide ion, the attachment of the indolyl or benzyl fragment at C-16 introduces asymmetry into the molecule, which might lead to differing contact shifts for the acetate protons on the two sides of the ligand. Similar rationale was used to assign separate contact shift parameters to the bridge protons 38, 40, and 41. The results of the fitting procedure (table 6) are expressed in terms of the susceptibility parameters and principal directions u, v, w of χ', where u, v, and w are chosen such that $|\chi'_{ww}| > |\chi'_{uu}| > |\chi'_{vv}|$. An asymmetry parameter, defined as $\eta = (\chi'_{vv} - \chi'_{uu})/\chi'_{ww}$, is also presented, together with values of θ_{uz}, θ_{vz}, θ_{wz}, the angles between the u-, v-, w-axes and the molecular z-axis. Contact shifts obtained from the analyses are recorded in table 7. From the data in table 6, it is clear that axial symmetry ($\eta = 0$) does not hold for these complexes in solution. Furthermore, there are deviations of the directions of each of the principal axes of χ' from the initially chosen x-, y-, and z-axes. In addition, the directions of the principal axes are not coincident among the different complexes derived from the same ligand and also show some variation with temperature. The asymmetry parameter, which is equivalent to the quotient C/C' in eq. (7) (cf. sect. 2.3), varies considerably

Table 7
Contact shifts determined as fitting parameters from LIS analysis of R-1 and R-2 (from Kemple et al. 1988)[a]

T (°C)	Protons 22–25	Protons 26–29	Proton 38	Proton 40	Proton 41
Pr-1					
5	3.32 (1.17)	5.13 (1.96)	−3.80 (1.99)	−0.75 (1.93)	3.64 (1.92)
30	3.37 (1.27)	3.54 (2.12)	−3.65 (2.15)	−1.57 (2.09)	2.65 (2.08)
60	3.37 (1.46)	2.15 (2.43)	−3.14 (2.47)	−2.38 (2.39)	1.88 (2.38)
Nd-1					
5	5.70 (1.04)	7.31 (1.74)	−9.68 (1.77)	6.42 (1.71)	7.05 (1.70)
30	5.35 (0.70)	5.44 (1.17)	−7.39 (1.19)	4.27 (1.15)	5.93 (1.14)
60	4.77 (0.44)	3.71 (0.73)	−5.44 (0.75)	2.20 (0.72)	4.85 (0.72)
Eu-1					
5	−16.54 (1.57)	−13.30 (2.63)	6.51 (2.67)	−1.74 (2.58)	−14.28 (2.57)
30	−15.17 (0.76)	−10.47 (1.27)	7.76 (1.29)	−0.49 (1.25)	−12.83 (1.25)
60	−14.08 (1.95)	−8.10 (3.26)	8.50 (3.31)	0.80 (3.21)	−11.48 (3.19)
Pr-2					
5	3.19 (1.49)	6.65 (2.38)	−2.42 (2.43)	1.45 (2.39)	5.58 (2.36)
30	3.23 (1.58)	4.94 (2.53)	−2.31 (2.58)	0.48 (2.54)	4.40 (2.50)
60	3.23 (1.74)	3.24 (2.78)	−1.97 (2.83)	−0.67 (2.79)	3.27 (2.75)

[a] Standard errors in the parameters based on the fits are given in parentheses.

among the three ions examined. Since the susceptibility tensor of a paramagnetic ion is dependent on the energy levels and states of the particular ion of the complex, the observation that the principal values and directions of χ' bear no particular relation from one ion to the next, even in an isostructural series of complexes, may be due to changes in the crystal field parameters. Although the author's rationale used to assign contact shift parameters to groups of protons is reasonable, the resulting improvement in the agreement factor does not necessarily reflect better definition of the susceptibility tensor or geometrical parameters. The conclusion that the principal values and directions of χ' have no relation from one complex to another would be better supported if the contact shifts had been determined by an independent method. The authors applied Reilley's separation procedure (eq. 10), but had data for only three complexes, one of which is the europium complex, for which the $\langle S_z \rangle$ value is not well-defined (see sect. 2.1). The resulting contact shifts did not agree with the values obtained as fitting parameters. However, the latter are meaningful only if the susceptibility tensor is well-defined. Uncertainties in the geometric factors, which were determined by molecular mechanics calculations, or uncertainties introduced due to reorientation of the ligand in the coordination sphere, lead to uncertainties in the components of the susceptibility tensor.

4.2. *Complexes derived from macrocyclic ligands with pendant arms*

The commercial development of $Gd(dota)^-$ as a magnetic resonance imaging relaxation agent, as well as the demonstrated ability of lanthanide complexes to catalytically cleave RNA, have stimulated research into the synthesis of complexes derived from macrocyclic ligands with pendant arms. NMR studies have been carried out on many of the paramagnetic complexes derived from this class of ligands, which are reviewed in the following sections.

4.2.1. *R(dota)$^-$ complexes*[2]

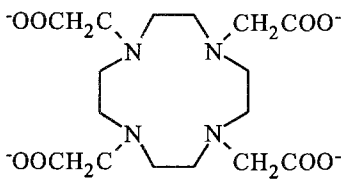

dota Fig. 7.

The crystal structure of $[Eu(dota)H_2O]^-$ revealed that the europium ion is nine coordinate, encapsulated by the octadentate dota ligand, which binds through the four nitrogen atoms and four carboxyl oxygen atoms (fig. 7) (Spirlet et al. 1984a). The coordination polyhedron is described as a distorted capped square antiprism, with the water molecule forming the cap. The ^1H spectra of the $R(dota)^-$ (R = Pr, Eu, Yb) complexes in aqueous solution at 0°C revealed six equally intense resonances, four of which are assigned to the ethylenic groups and two to the acetate groups (Desreux 1980). These observations indicate that, in solution, the complex has a C_4 symmetry axis, which is consistent with the solid state structure, and that the interconversion between the λ and δ forms (fig. 8) of the ethylenediamine chelate rings is slow on the NMR time scale. As the temperature is increased, interconversion of the λ and

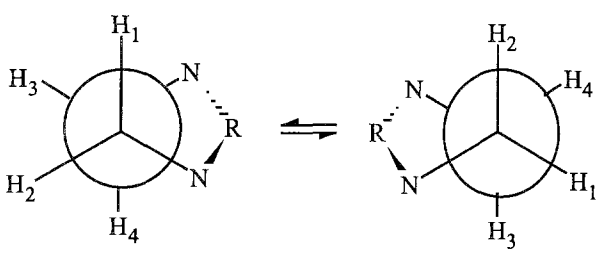

λ δ Fig. 8.

[2] $dota^{4-}$ = 1,4,7,10-tetraazacyclododecane-*N,N',N'',N'''*-tetraacetate.

δ conformers exchanges the axial proton H_1 with the equatorial proton H_3 and the axial proton H_4 with the equatorial proton H_2, leading to two signals in the fast exchange limit. At the same time, the two acetate protons become equivalent and appear as a singlet. Two ^{13}C resonances are observed for the ethylenic groups in the slow exchange limit, which coalesce on increasing the temperature. The following kinetic parameters at 300 K were obtained by line-shape analysis of the coalescence of the ^{13}C resonances in the diamagnetic lanthanum complex: $\Delta G^{\ddagger} = 60.7 \pm 1.2$ kJ mol^{-1}; $\Delta H^{\ddagger} = 59.4 \pm 0.8$ kJ mol^{-1}; $\Delta S^{\ddagger} = -4.6 \pm 3.3$ J K^{-1} mol^{-1}; $E_a = 61.9 \pm 1.2$ kJ mol^{-1}. Using the geometric factors calculated from the solid state structure of the europium complex, the LIS values (not corrected for contact shifts) of the ytterbium complex were fit to the first term of eq. (4) (Brittain and Desreux 1984). The value of the agreement factor ($R = 0.036$) indicates that the solid state structure is a good approximation for the structure observed in solution. In the analysis, the value of D_1 was determined as 5082 ± 209 ppm Å^3. Aime et al. (1992a) obtained an agreement factor of $R = 0.009$, with $D_1 = 5300 \pm 24$ ppm Å^3, in their analysis of the LIS ^1H data for the ytterbium complex, in which they allowed the internal coordinates of the ligand to change within a relatively narrow range around the average values obtained from the crystal structure of the europium complex. In another study, Aime et al. (1992b) assumed relaxation occurred via the Curie mechanism (cf. sect. 2.4) and used longitudinal and transverse relaxation times of the ^1H resonances of the terbium, dysprosium, and holmium complexes, together with rotational correlation times τ_r, to determine proton–R^{3+} distances in the complexes. The values are in accord with those obtained for the crystal structure of the europium complex. Low-temperature limiting ^1H and ^{13}C NMR spectra of 12 R(dota)$^-$ complexes (R = La, Pr, Nd, Sm, Eu, Tb, Dy, Ho, Er, Tm, Yb, Lu) revealed the presence in aqueous solution of a small concentration of a second isomer (Aime et al. 1992a), which supported the observations of Brittain and Desreux (1984). 2D EXSY spectra of the ytterbium system, recorded at 25°C ($\tau_m = 5$ ms), revealed three cross peaks for each signal, one cross peak showing correlation between two protons in a given isomer, e.g., H_1 with H_3 (fig. 8), and two cross peaks showing correlation to the corresponding protons in the other isomer. At 0°C, the 2D EXSY spectrum revealed only those cross peaks correlating the acetate protons of the two isomers. Based on these observations, Aime and coworkers concluded that two isomerization processes were involved, one involving a concerted interconversion of all the ethylenediamine rings of the macrocycle, which was slower on the NMR time scale, and a more rapid process involving a concerted motion of the acetate arms, which changes the rotation of the pendant arms from clockwise to counterclockwise (or vice versa) around the C_4 symmetry axis. These workers also reported analysis of the LIS data obtained for the minor isomer of the ytterbium complex, supposedly locating the protons of the acetate groups. However, as noted by Jacques and Desreux (1994), the values of the shifts calculated for the acetate protons of the minor isomer cannot be reproduced using the geometric factors and the D_1 values reported by Aime and coworkers. In their paper, Jacques and Desreux (1994) reported on the kinetics of exchange within and between the two isomeric forms of the ytterbium complex, which were measured using 2D EXSY spectroscopy. Although the EXSY spectrum (fig. 9) at

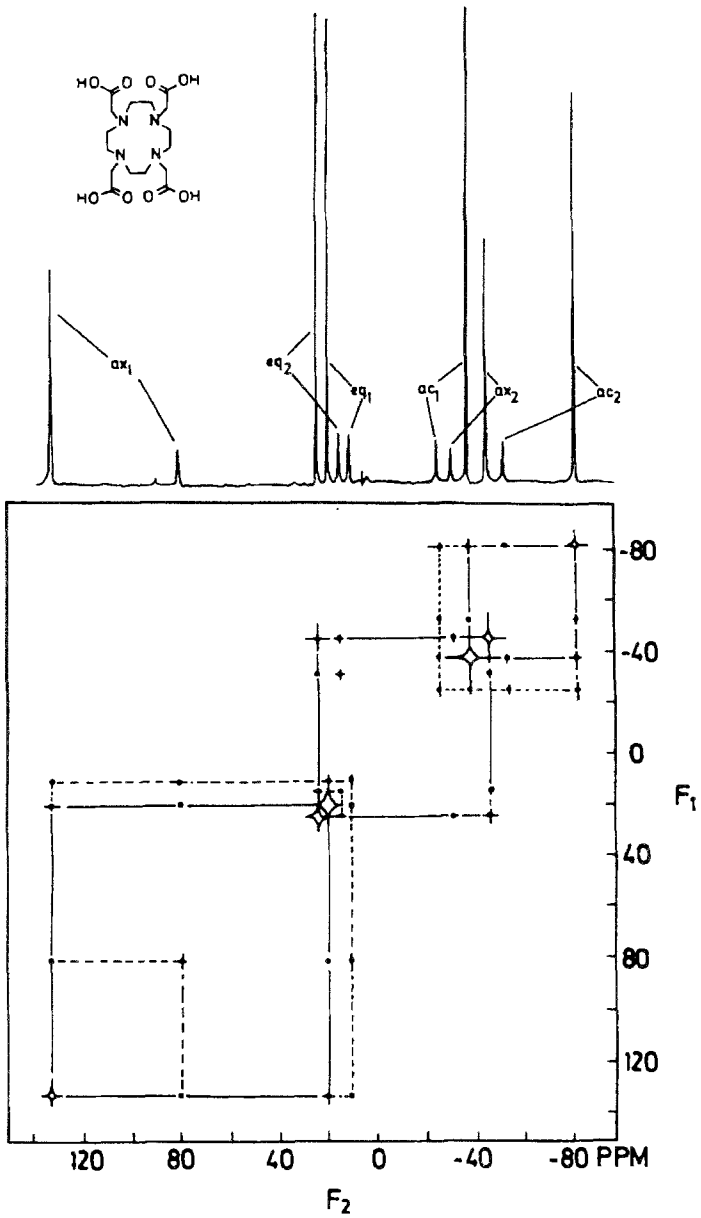

Fig. 9. EXSY spectrum of Yb(dota)$^-$ at 303 K (Jacques and Desreux 1994). The assignments are from Brittain and Desreux (1984).

303 K is similar to that reported by Aime and coworkers, the kinetics measurements suggest that no distinction can be made between the dynamic behavior of the macrocyclic ring and acetate arms. Furthermore, these authors proposed that both isomers exist as a

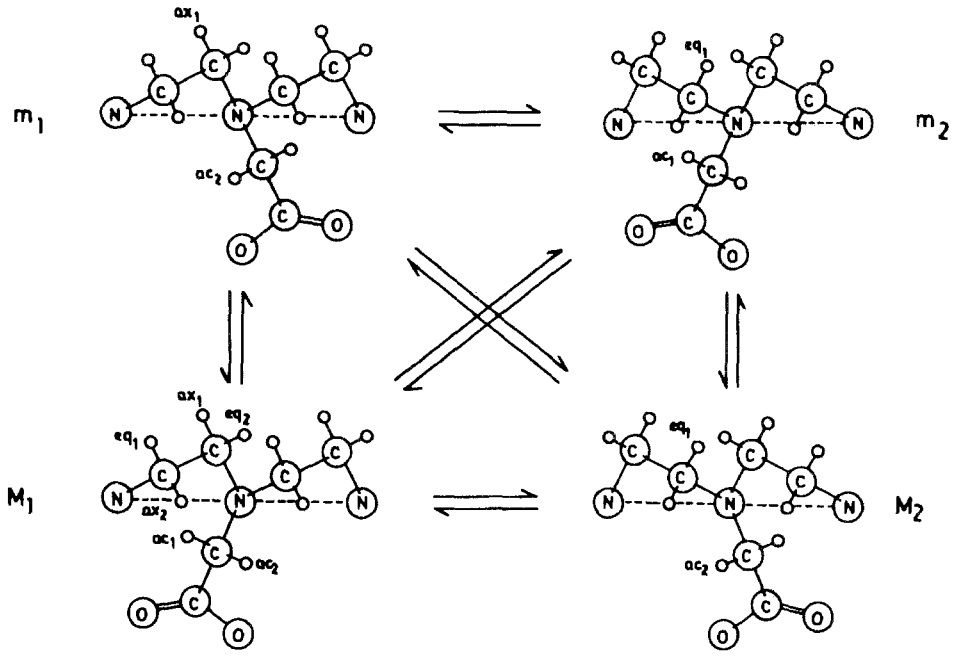

Fig. 10. Schematic presentation of the conformational processes in the Yb(dota)$^-$ chelate. The symbols M and m designate the major and the minor isomers, respectively. The metal ions are left off for clarity (Jacques and Desreux 1994). The atom labeling is taken from Brittain and Desreux (1984).

pair enantiomers, and that exchange can occur between either mirror images or major and minor isomers (fig. 10). The activation energy for the major to minor exchange is higher than that for the minor to major exchange ($\Delta G^{\ddagger} = 65.6$ vs $61.4\,\mathrm{kJ\,mol^{-1}}$), presumably because of the greater steric crowding in the minor isomer. However, no detailed geometrical analysis of the LIS data for the minor isomers was reported.

4.2.2. *R(dotp)$^{5-}$ complexes*[3]

Geraldes et al. (1992) recorded ^{1}H, ^{13}C, and ^{31}P LIS spectra for eleven paramagnetic R(dotp)$^{5-}$ complexes (fig. 11) in aqueous solution at 298 K. The high structural rigidity of these complexes is evidenced by an activation energy for ethylenediamine chelate ring interconversions of approximately $100\,\mathrm{kJ\,mol^{-1}}$, which is considerably higher than the value of $61.9\,\mathrm{kJ\,mol^{-1}}$ reported for the analogous R(dota)$^-$ complexes (sect. 4.2.1). The contact and pseudocontact contributions to the LIS values were separated by the Reilley procedure using eqs. (10) or (11). F_i values are in the ranges of 0.56 to −1.17 for protons and −1.95 to −3.68 for ^{13}C, while the value for ^{31}P is −4.63. Geometric factors for each nucleus were determined from molecular mechanics calculations using the MMX force field. Since lanthanide parameters for empirical force fields remain

[3] dotp^{8-} = 1,4,7,10-tetraazacyclododecane-*N,N',N'',N'''*-tetra-(methylene phosphonate).

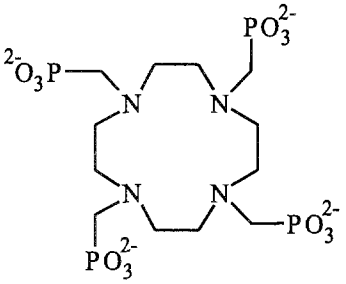

dotp

Fig. 11.

undetermined, the R–N and R–O bond distances of 2.70 and 2.35 Å used in the molecular mechanics calculations were based on the crystal structure of the analogous $Eu(dota)^-$ complex. A comparison of calculated and experimental LIS values, given in the original literature, showed good agreement.

The host–guest complex formed in aqueous solution between γ-cyclodextrin (γ-CD) and $Tm(dotp)^{5-}$ was examined by ^1H NMR (Sherry et al. 1994). The γ-cyclodextrin molecule is a cyclic oligosaccharide consisting of eight D-glucose units. The molecules are pail-shaped with the two secondary hydroxyl groups (2- and 3-positions) on each glucose ring situated at the mouth of the wider opening and the one primary hydroxyl group (6-position) on each ring situated at the mouth of the narrower opening. When $Tm(dotp)^{5-}$ was titrated into a D_2O solution of γ-CD, the proton resonances of the host were shifted. The magnitude of the shift was sensitive to the amount of $Tm(dotp)^{5-}$ added, indicating that free and bound γ-CD were in rapid exchange on the NMR time scale. The LIS ratio for each γ-CD proton relative to a reference proton (H_2) was used to determine the best position of the $Tm(dotp)^{5-}$ complex relative to the host. A best fit ($R = 0.054$) was obtained when the complex was situated above the wider opening along the C_8 symmetry axis of the cyclodextrin, with the hydrophobic ethylenediamine protons of the complex nestled inside the γ-CD basket. After locating the position of the complex, geometric factors for each proton of γ-CD in the host–guest complex were determined using the published crystal structure data. Multiplying the geometric factors by D_1 ($D_1 = 17\,854$ ppm Å^3) gives the fully bound LIS value for each proton in γ-CD (H_n, LIS in ppm): H_1 (−7.48), H_2 (−16.32), H_3 (−43.65), H_4 (−6.55), H_5 (29.10), H_6 (22.10), $H_{6'}$ (11.09).

4.2.3. *Complexes with 1,4,7,10-tetrakis(N,N-diethylacetamido)-1,4,7,10-tetraazacyclododecane*

Recently we reported ^1H and ^{13}C NMR studies of the diamagnetic and paramagnetic lanthanide complexes derived from 1,4,7,10-tetrakis(*N,N*-diethylacetamido)-1,4,7,10-tetraazacyclododecane (fig. 12; referred to as **3** below) in deuterated acetonitrile (Forsberg et al. 1995). The complexes demonstrate dynamic behavior that is similar to the analogous dota complexes, with slow interconversion between the two enantiomeric conformers of each ethylenediamine chelate ring of the macrocycle (cf. sect. 4.2.1).

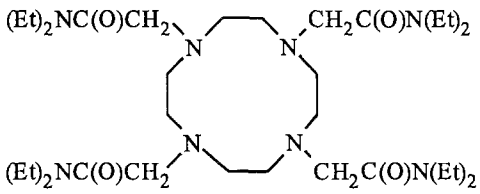

3

Fig. 12.

The ^{13}C spectrum confirms the structurally rigid nature of the lanthanum complex at room temperature: δ (ppm) C_1, 50.3; C_2, 55.2; C_3, 58.3; C_4, 173.4; C_5, 43.3; C_6, 44.1; C_7, 14.4; C_8, 13.4 (see fig. 13 for atom assignments). As the temperature is increased, the two resonances assigned to the macrocyclic ring carbon atoms coalesce. Complete lineshape analysis yielded the activation parameters: $\Delta G^{\ddagger}$, 58.8 kJ mol^{-1}; $\Delta H^{\ddagger}$, 52.1 kJ mol^{-1}; $\Delta S^{\ddagger}$, −22.5 J K^{-1} mol^{-1}; $k = 300\ s^{-1}$ at 298 K). Comparison of these data with that obtained for [Ladota]$^-$ ($\Delta G^{\ddagger}$, 60.7 kJ mol^{-1} at 300 K) reveals that increasing the steric bulk of the pendant arms has little effect on the dynamics of interconversion between the λ and δ conformers of the chelate rings.

The ^1H NMR spectrum of solutions of each paramagnetic 1:1 chelate (R = Pr, Nd, Sm, Eu, Tb, Dy, Ho, Er, Tm, Yb) in deuterated acetonitrile revealed 12 peaks, consistent with a sterically rigid, eight-coordinate complex having a C_4 symmetry axis, suggesting that the donor atoms are located at the vertices of a square antiprism. Interestingly, each of the methylene protons (H_7, H_8, H_9, H_{10}) of the ethyl groups are also nonequivalent, indicating that sufficient steric hindrance exists between the pendant arms to restrict free rotation about the N–C(5) and N–C(6) bonds. The LIS values for the ten protons are given in table 8. 2D COSY spectra (R = Pr, Nd, Sm, Eu, Yb) revealed cross peaks for each pair of geminal protons and, in addition, the methylene protons of the ethyl group also revealed cross peaks to the methyl protons, which allow H_7, H_8, H_9, and H_{10} to be distinguished from the other, equally intense, proton resonances. Cross peaks were not observed in the COSY spectra of complexes derived from the other lanthanide ions (Tb^{3+}–Tm^{3+}) due to effective transverse relaxation. The ^{13}C spectra (R = Pr, Nd, Sm, Eu) revealed eight peaks, consistent with complexes having C_4 symmetry.

Following the procedure of Kemple et al. (1988) (cf. sect. 2.2), we have written a program SHIFT ANALYSIS, which takes advantage of the graphical interface of the Macintosh computers, to analyze the LIS data. As is often the case in the spectra of paramagnetic complexes, several, equally intense, featureless peaks were observed, precluding an unequivocal assignment. By using a linear least-squares fitting of the data, we showed it is possible to allow the program to permute LIS values over any number of selected nuclei using a suboptimal procedure (described in the original literature) that we termed the JOLT method, thereby determining which particular assignment of peaks gives the best fit to the LIS data. In order to achieve a correct assignment of peaks using the JOLT method, the contact shifts must be small and a reasonable geometrical model must be chosen for the complex. Thus the LIS analysis was initiated with the

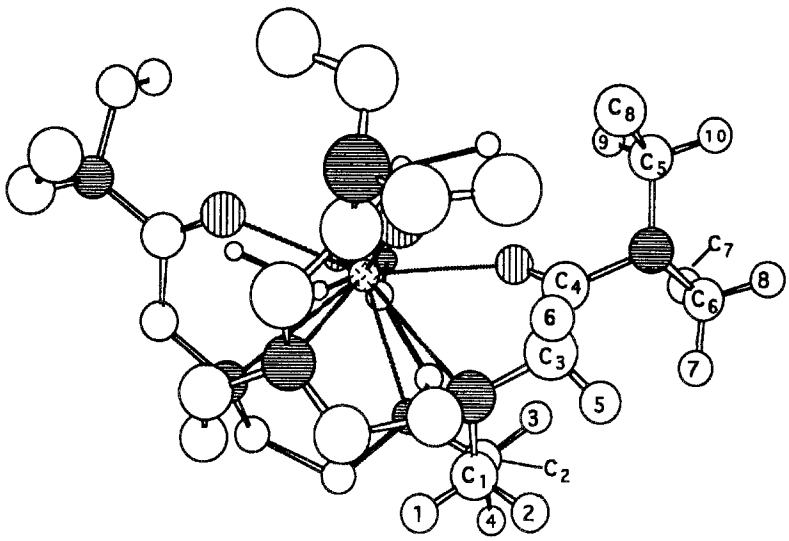

Fig. 13. Structure of $R(3)^{3+}$ complexes from molecular mechanics calculations showing numbering scheme for carbon and hydrogen atoms. The symmetry related hydrogen atoms are not shown for clarity (Forsberg et al. 1995).

ytterbium complex, since ytterbium has the largest ratio of pseudocontact to contact shifts. Cartesian coordinates for each of the protons were determined using molecular mechanics calculations based on Allinger's MM2 force field, which had been augmented to include parameters for the ytterbium ion. However, since the coordination numbers and geometries of lanthanide complexes are dictated by the steric requirements of the ligands, it is unlikely that a set of parameters involving lanthanide ions will provide reliable minimizations for all complexes. Thus, for a first approximation, the atomic positional coordinates reported for the structure of $Na[Eu(dota)H_2O)]\cdot 4H_2O$ (Spirlet et al. 1984a) were used to locate the donor atoms at the vertices of a distorted square antiprism (see fig. 13). The donor atoms were kept locked in position during energy minimization, while the rest of the ligand molecule was allowed to relax. The resulting coordinates for H_1–H_{10} were entered into the SHIFT ANALYSIS program and the LIS analysis was carried out using the JOLT method to assign the LIS values to the 40 hydrogen atoms of the ligand. Criteria for a correct assignment are that the symmetry-related protons are assigned the same LIS value, that the LIS values for geminal protons are consistent with the 2D COSY spectrum, and that the assignments are consistent with the longitudinal (T_1^{-1}) and transverse (T_2^{-1}) relaxation rates, which reveal an r^{-6} dependency on the proton–metal distance. Since the calculations were carried out using the full expression given in eq. (5) (five parameter fit), the results prove that the complex is axially symmetric, e.g., for the ytterbium complex, $\chi_{xy} = 0.10$, $\chi_{xz} = 0.07$, $\chi_{yz} = -0.07$, $\chi_{xx} = \chi_{yy} = -1969$ VVk mol^{-1}, $(\chi_{zz} - \mathrm{Tr}\,\chi) = 3269$ VVk mol^{-1}. Furthermore, diagonalization of the tensor provided a set of Euler angles that relate the principal magnetic axis system to the molecular coordinate

Table 8
^{1}H LIS data for lanthanide complexes derived from **3** (from Forsberg et al. 1995)[a]

R	H=	1	2	3	4	5	6	7	8	9	10	R=
Pr	LIS_{obsv}	−47.7	−5.3	16.6	−2.3	14.7	28.6	8.9	6.7	1.2	3.4	0.051
	LIS_{calc}	−47.5	−5.8	15.2	−1.3	15.1	29.4	9.6	6.4	−0.9	2.4	
	δ_c [b]	−0.9	4.9	0.6	6.3	3.4	0.4	0.2	0.4	0.0	−0.3	
Nd	LIS_{obsv}	−22.2	2.4	7.8	5.2	9.3	11.7	4.1	3.3	9.7	1.9	0.104
	LIS_{calc}	−21.5	2.8	7.2	6.1	10.2	13.3	4.4	3.2	−0.3	0.7	
	δ_c [b]	−1.3	7.4	0.9	9.4	5.1	0.7	0.3	0.6	0.1	−0.5	
Sm	LIS_{obsv}	−3.89	−0.94	1.30	−0.80	1.10	2.55	0.68	0.51	−0.09	0.48	0.066
	LIS_{calc}	−3.91	−0.90	1.29	−0.67	1.02	2.59	0.81	0.50	0.00	0.23	
	δ_c [b]	1	−0.05	−0.01	−0.06	−0.03	0.00	0.00	0.00	0.00	0.00	
Eu	LIS_{obsv}	21.6	−8.5	−8.2	−12.5	−13.6	−13.4	−4.1	−3.6	−0.5	−0.5	0.062
	LIS_{calc}	21.0	−8.5	−8.0	−13.1	−14.0	−14.1	−4.1	−3.6	−0.5	−0.5	
	δ_c [b]	2.2	−12.5	−1.5	−15.9	−8.6	−1.1	−0.5	−1.0	−0.1	0.8	
Tb	LIS_{obsv}	−454.1	−118.4	166.5	−113.6	114.5	315.6	86.6	61.2	−1.3	14.6	0.037
	LIS_{calc}	−463.5	−117.5	150.4	−108.1	112.2	310.5	86.6	61.2	−1.3	14.6	
	δ_c [b]	−7.4	−39.3	−22.4	−51.7	−33.5	−2.7	7.7	10.2	16.2	14.0	
Dy	LIS_{obsv}	−490.2	−112.3	190.5	−106.7	136.8	349.5	91.2	66.7	−8.3	9.9	0.042
	LIS_{calc}	−504.2	−115	175.8	−102.9	132.5	336.9	103.7	61.0	−6.5	9.8	
	δ_c [b]	−6.7	−35.3	−20.1	−46.4	−30.2	−2.4	6.6	9.3	14.5	12.7	
Ho	LIS_{obsv}	−233.3	−55.1	94.0	−53.0	62.9	163.0	42.5	30.2	−5.0	3.3	0.058
	LIS_{calc}	−242.3	−57.9	86.8	−56.4	57.8	153.7	50.5	29.7	−3.6	6.6	
	δ_c [b]	−5.3	−27.9	−15.9	−36.7	−23.9	−1.9	5.5	7.4	11.5	10.1	

continued on next page

Table 8, *continued*

R	H=	1	2	3	4	5	6	7	8	9	10	*R*=
Er	LIS_{obsv}	292.3	38.3	−129.0	15.2	−109.8	−208.1	−48.4	−31.4	17.3	12.2	0.033
	LIS_{calc}	295.5	32.2	−124.1	11.9	−111.5	−206.1	−54.9	−26.9	19.7	7.5	
	δ_c [b]	−3.6	−19.0	−10.8	−25.0	−16.2	−1.3	3.7	5.0	7.8	6.8	
Tm	LIS_{obsv}	789.7	105.5	−363.0	80.6	−290.1	−577.2	−134.4	−84.4	46.5	5.5	0.046
	LIS_{calc}	815.6	107.3	−344.4	67.1	−283.8	−549	−156.0	−78.5	49.9	13.8	
	δ_c [b]	−2.1	−10.2	−5.7	−13.4	−8.6	−0.6	2.1	2.7	4.2	5.1	
Yb	LIS_{obsv}	100.6	14.9	−46.4	8.7	−37.6	−70.2	−16.4	−10.3	5.6	4.4	0.044
	LIS_{calc}	101.5	12.2	−43.5	6.6	−37.4	−70.6	−19.8	−9.8	6.4	2.0	
	LIS_{calc} [c]	99.2	12.2	−45.6	7.2	−36.8	−70.8	−21.5	−9.7	17.6	2.3	0.100
	δ_c [b]	−0.6	−3.2	−1.8	−4.2	−2.7	−0.2	0.6	0.8	1.3	1.1	

[a] LIS values in ppm. Positive shifts are to higher frequency (downfield). LIS values for R = Pr–Eu referenced to the lanthanum complex; values for R = Tb–Yb referenced to the lutetium complex. Calculated values obtained for optimal geometries with clockwise rotation of the pendant arms about the C_4 axis (viewed from the plane of oxygen atoms) with each chelate ring of the macrocycle in the λ conformation.

[b] From linear least squares analysis of the data set using eqs. (13)–(16).

[c] Calculated for counterclockwise rotation of the pendant arms about the C_4 axis, retaining the λ conformation of each chelate ring of the macrocycle.

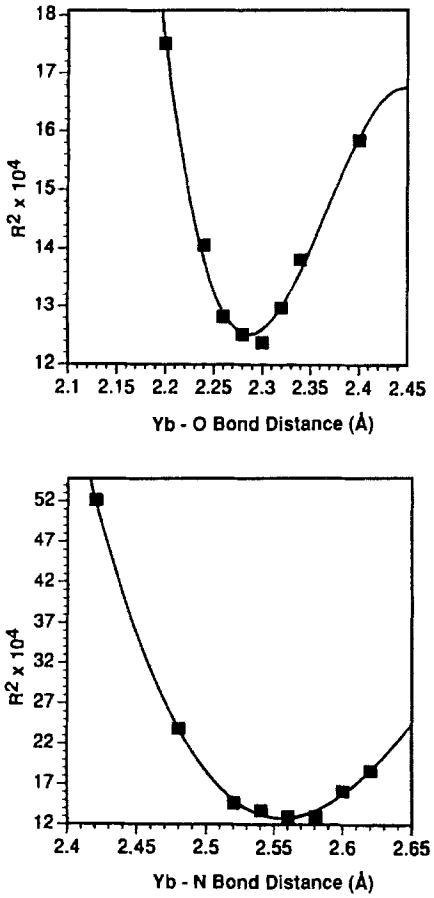

Fig. 14. Plots of R^2 versus R–donor atom bond distances for the $Yb(3)^{3+}$ complex (Forsberg et al. 1995).

system: $\theta = 0.001°$ (tilt of C_4 symmetry axis from the principal magnetic z-axis), and $\phi = 45°$, $\gamma = -72°$ (the combined values of ϕ and γ indicate that the principal magnetic x- and y-axes are rotated $-27°$ from the molecular x- and y-axes (the molecular x- and y-axes were chosen to coincide with the projection of the R–N bonds in a plane containing the R^{3+} ion, which is perpendicular to the C_4 symmetry axis). The assignments of H_1–H_{10} in the spectra of the other complexes can be based on the observation that most spectra reveal the same pattern of peaks as observed in the spectrum of the ytterbium complex. However, it is interesting to note that, with the exception of the neodymium and europium complexes, which have the largest contact to pseudocontact shift ratios, the JOLT method also gave a consistent set of assignments for each of the complexes without correcting the LIS values for a contact shift. In order to refine the molecular geometry, the contact shifts must be separated from the LIS values. The contact shifts were determined by a linear least-squares analysis of the data according to eqs. (13)–(16) (cf. sect. 2.3) and the results are given in table 8. Molecular mechanics calculations were then carried out using a range

Table 9
Lanthanide–donor atom bond distances and bond angles (from Forsberg et al. 1995)

R	R–N (Å)	R–O (Å)	N–R–N (°)	O–R–O (°)	R–N (plane) (Å)	R–O (plane) (Å)	R[a]
Pr	2.82	2.47	102	153	1.74	0.63	0.033
Nd	2.82	2.47	102	153	1.74	0.63	0.078
Sm	2.78	2.41	103	150	1.73	0.64	0.026
Eu	2.74	2.30	104	147	1.69	0.68	0.053
Tb	2.64	2.30	109	145	1.54	0.70	0.030
Dy	2.60	2.28	110	142	1.49	0.75	0.035
Ho	2.62	2.30	109	143	1.46	0.78	0.050
Er	2.64	2.33	109	145	1.46	0.79	0.027
Tm	2.54	2.26	112	137	1.41	0.83	0.042
Yb	2.56	2.21	111	138	1.45	0.79	0.034

[a] Agreement factor using H_1–H_6.

of metal–donor atom bond distances. After each minimization, the resulting coordinates of H_1–H_6 (H_7–H_{10} were used to refine the position of the pendant arms) were entered into the SHIFT ANALYSIS program and the goodness of fit of the calculated and observed LIS values, as measured by R^2, was determined. Plots of R^2 vs. R–N and R–O bond distances reveal minima corresponding to the bond distances that best fit the LIS data (fig. 14). A summary of the metal–donor atom bond distances for each of the complexes and the corresponding values of R obtained by this procedure are given in table 9. Although not monotonic, a general decrease in M–L donor bond distance is noted across the lanthanide series. Furthermore, the decrease corresponds roughly to that expected for the decrease in ionic radius across the series for eight-coordinate lanthanide ions: Nd^{3+}–N = 2.82 Å, Yb^{3+}–N = 2.56 Å (9.2% decrease), Nd^{3+}–O = 2.47 Å, Yb^{3+}–O = 2.21 Å (10.5% decrease) versus an 11.2% decrease in ionic radius. With decreasing radius, the metal ion sinks further into the cavity of the macrocyclic ring, allowing the pendant arms to further encapsulate the ion. The result is a decrease in the distance of the metal ion to the mean plane of the nitrogen atoms, with a concomitant increase in the N–R–N bond angles, while the distance to the mean plane of the oxygen atoms increases producing smaller O–R–O angles (table 9). Since the donor atoms were locked in place during minimization, it was also necessary to vary the R–N–C(3)–C(4) dihedral angle, which effects rotation of the square pyramid containing the oxygen atoms relative to the square pyramid containing the nitrogen atoms about their common vertex (the R^{3+} ion). In the optimal structures, this angle is 32±1° for each complex, producing a rotational angle of 47° (versus 45° in the square antiprism). Note that on refining the molecular structure, good agreement is observed between both the sets of G_i^0 values (table 10) and $A_j^0 = \chi_{zz} - \frac{1}{3}\mathrm{Tr}\,\chi$ values (table 11) obtained by the two independent methods of analysis, i.e., least-squares analysis of the data using eqs. (13)–(16) and those obtained from the SHIFT ANALYSIS program. The self-consistency of the results provides support for

Table 10
Geometric factors for complexes derived from **3** obtained by two methods of analysis (from Forsberg et al. 1995)

Method	$G_i(H_i)$ (10^3 Å^3)									
	$i=1$	$i=2$	$i=3$	$i=4$	$i=5$	$i=6$	$i=7$	$i=8$	$i=9$	$i=10$
Pr–Eu										
Linear least squares[a,b]	27.9	5.90	−8.79	4.34	−7.78	−19.1	−5.80	−3.52	1.26	−0.72
SHIFT ANALYSIS[d]	27.9	6.16	−9.50	5.10	−6.62	−16.6	−5.20	−3.76	−0.67	−2.30
Tb–Yb										
Linear least squares[a,c]	31.1	5.01	−12.3	3.48	−10.3	−21.4	−6.30	−3.28	2.10	0.53
SHIFT ANALYSIS[d]	31.1	4.83	−13.6	3.80	−10.8	−22.4	−5.40	−3.50	1.50	0.15

[a] Obtained using the method of linear least squares analysis (eqs. 13–16) of the LIS data normalized to the geometric factor for H_1.
[b] Normalized to the anisotropy parameter for the praseodymium complex.
[c] Normalized to the anisotropy parameter for the ytterbium complex.
[d] Obtained using the SHIFT ANALYSIS program.

Table 11
Values of $\chi_{zz} - \frac{1}{3}\mathrm{Tr}\,\chi$ (from Forsberg et al. 1995)[a]

Method	$\chi_{zz} - \frac{1}{3}\mathrm{Tr}\,\chi$ (VVk/mol)[a]									
	Pr	Nd	Sm	Eu	Tb	Dy	Ho	Er	Tm	Yb
SHIFT[b]	−1690	−729	−141	684	−15 100	−16 200	−7790	9960	25 800	3250
LLS[c]	−1690	−730	−143	703	−14 300	−15 600	−7400	9370	25 700	3250

[a] Values normalized to the geometric factor of H_1 and the $\chi_{zz} - \frac{1}{3}\mathrm{Tr}\,\chi$ values of Pr (R = Pr, Nd, Sm, Eu) or Yb (R = Tb, Dy, Ho, Er, Tm, Yb).
[b] Using the SHIFT ANALYSIS program.
[c] Linear least squares analysis of the data set using eqs. (13)–(16).

the efficacy of the new method introduced for computing contact shifts. In principle, ^{13}C LIS values can be included with ^{1}H data when computing the contact shifts using eqs. (13)–(16). However, the fit of the LIS data was slightly poorer when ^{13}C data were included in the computation of the contact shifts for the larger metal ions (^{13}C data could not be obtained for the smaller ions due to line broadening). Thus the contact shifts for ^{13}C were determined as fitting parameters by incorporating the ^{13}C LIS values in the SHIFT ANALYSIS program with the proton data for H_1–H_{10}. Any nucleus assigned a contact shift as a fitting parameter produced an exact fit between the observed and calculated LIS values, which means that the resulting contact shifts are meaningful only if the elements of the susceptibility tensor are well-defined. Plots of the ^{13}C contact shifts versus $\langle S_z \rangle$ are linear (cf. eq. 3), suggesting that the values obtained in this manner (table 12) are reliable.

Table 12
LIS values and contact shifts (ppm) for selected ^{13}C nuclei of complexes derived from **3** (from Forsberg et al. 1995)

C	Pr		Nd		Sm		Eu	
	LIS[a]	δ_c	LIS[a]	δ_c	LIS[a]	δ_c	LIS[a]	δ_c
C(1)	−51.6	−15.2	−38.8	−18.5	−1.58	+1.07	+50.5	+27.2
C(2)	−27.3	−15.5	−26.5	−19.9	+0.40	+1.26	+36.4	+29.3
C(3)	+17.8	−17.6	−5.6	−25.3	+3.58	+0.91	+19.8	+45.2
C(4)	+19.7	−34.0	−8.6	−38.5	+6.15	+2.11	+10.2	+53.1

[a] Referenced to the lanthanum complex.

Each complex has two independent structural features that are sources of chirality for the complexes. The pendant arms may be oriented around the C_4 symmetry axis of the complex in a propeller-like manner in either a clockwise (A) or counterclockwise (B) direction (fig. 15). Secondly, as noted above, each ethylenediamine ring of the

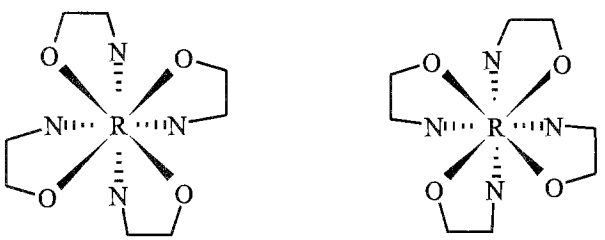

A B Fig. 15.

macrocycle can adopt two different conformations (λ or δ) when coordinated to the metal ion. The observation of only 12 peaks in the spectrum of each paramagnetic complex suggests that all the ethylenediamine rings in a particular ligand molecule adopt either the λ or δ conformation, and that for a given conformation of the macrocycle, the pendant arms are rotated in only one direction, i.e. the complex exists as a single pair of enantiomers in solution. If the ethylenediamine rings were to adopt both λ and δ conformations within a single ligand molecule, then diastereomers would be observed, giving rise to a set of 12 additional peaks in the spectrum for each diastereomer. Likewise, diastereomers would be observed if the pendant arms were to rotate in either a clockwise or counterclockwise manner about the C_4 axis for a fixed conformation of the macrocyclic ring. Three dihedral angles are required to define the position of the two sets of methylene hydrogen atoms (H_6–H_{10}) of the ethyl groups on the pendant arms: A = C(5)NC(4)C(3), B = C(7)C(6)NC(4) and C = C(8)C(5)NC(4). The results reported in table 8 were obtained using a clockwise rotation of the pendant arms (λ conformation for each of the ethylenediamine rings in the macrocycle) with $A = -141°$, $B = 74°$, $C = 95°$ for R = Pr, Nd, Sm, Eu, and $A = -147°$, $B = 79°$, $C = 62°$ for R = Tb, Dy, Ho, Er, Tm, Yb. Analysis of the

LIS data was also carried out with the pendant arms rotated counterclockwise about the C_4 axis, keeping the ethylenediamine rings in the λ conformation. Although the R–N and R–O bond distances in the optimized structures were the same as those obtained in the corresponding complexes with clockwise rotation of the arms, the value of the rotational angle between the two square pyramids was determined to be 28° vs. 47° with clockwise rotation of the arms. The results of the analysis for the ytterbium complex are presented in table 8. Although a comparison of the R values for the ytterbium complex (0.10 for counterclockwise rotation vs. 0.047 for clockwise rotation) suggests that the clockwise rotation of the arms provides the better fit of the data, it is important to determine at what confidence level the two models are being distinguished based on their respective agreement factors. Richardson et al. (1979) reported a statistical method, which is based on the jack-knife test, that establishes whether two structural models are significantly different based on *R* values. Applying Richardson's procedure to our data for the ytterbium complex revealed that a model with counterclockwise rotation of the pendant arms can be rejected at the 93% confidence level relative to a model with clockwise rotation of the arms. Similar results were obtained for the other complexes. It should also be noted that the larger value of *R* obtained for the counterclockwise rotation of the pendant arms is due primarily to disagreement between the observed and calculated LIS values for H_7–H_{10}, i.e., the methylene protons of the pendant arms.

Our results are also consistent with those of Morrow et al. (1993), who also reported only a single pair of enantiomers in the NMR spectrum of the lanthanum complex derived from dota analogues with $-CH_2CH_2C(O)NH_2$ pendant arms. The crystal structure of this complex revealed that the pendant arms are rotated clockwise about the C_4 symmetry axis when each ethylenediamine ring of the macrocycle is in the λ conformation. In another study, using dota analogues with 2-hydroxypropyl groups as pendant arms, Morrow and coworkers observed that the europium complex crystallized with two diastereomers in the unit cell, differing in rotation of the pendant arms (Chin et al. 1994). Interestingly, NMR studies of these complexes in d_4-methanol revealed the presence of only one diastereomer (single pair of enantiomers) in solution. It was proposed that the isomer with clockwise rotation of the pendant arms was favored based on steric considerations. This conclusion is consistent with our results for complexes derived from **3**. It is interesting to note that NMR studies revealed the existence of two isomers for $[R(dota)]^-$, differing in rotation of the pendant arms (cf. sect. 4.2.1). Based both on our observations and those reported by others, it is apparent that the steric requirements of the pendant arms in dota analogues dictate the stereochemistry observed in this class of lanthanide complexes.

4.2.4. *R(teta)⁻ complexes*[4]

The ^1H spectra of $R(teta)^-$ (R = Eu, Yb) (fig. 16) in aqueous solution at 3°C revealed 14 equally intense resonances, indicating that the complexes are structurally rigid in solution at this temperature and that the complexes adopt a structure having a

[4] $teta^{4-}$ = 1,4,8,11-tetraazacyclotetradecane-*N,N',N'',N'''*-tetraacetate.

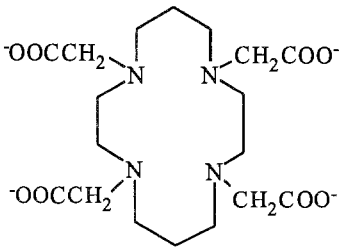

teta Fig. 16.

C_2 symmetry axis (Desreux and Loncin 1986). The NMR data are consistent with the solid state structure of the terbium complex (Spirlet et al. 1984b), which showed that the terbium ion was encapsulated by an octadentate teta ligand, with four nitrogen and four oxygen atoms coordinating to the metal ion at the vertices of a dodecahedron (fig. 17). As depicted in fig. 17, two nitrogen and two oxygen atoms are higher than the mean N_4 and O_4 planes, while the other two nitrogen and two oxygen atoms are lower than the mean planes. Each acetate arm of teta links nitrogen and oxygen atoms belonging to a low or to a high group of atoms. The LIS data obtained for the ytterbium complex were analyzed using the complete expression given in eq. (4). In their analysis, Desreux and Loncin assumed the principal magnetic z-axis was collinear with the C_2 symmetry axis, but the position of the principal magnetic x- and y-axes were allowed to vary in the fitting procedure. Geometric factors were computed from the crystallographic data for each modification of the position of the x- and y-axes, then a least-squares analysis was carried out using D_1 and D_2 as fitting parameters to determine the best-fit between the calculated and observed shifts. An agreement factor of $R=0.089$, with $D_1=3237\pm520$ and $D_2=-2526\pm73$ ppm Å^3, was obtained when the x (or y) axis makes an angle of $9\pm0.5°$ with the line joining the two central methylene groups of the propylenic chains. The value of the agreement factor suggests that the solution structure of the ytterbium complex is closely approximated by the solid state structure of the terbium complex. Due to a larger contact component in the LIS, the ordering of peaks in the spectrum of the europium complex is not the same as that observed in the ytterbium complex. As the temperature is increased to 98°C, coalescence of the proton resonances was observed, which was attributed to an intramolecular exchange process in which a group of atoms labeled high in fig. 17 is moved down, while the opposite translation is performed with the low group of atoms. The result is a new dodecahedral configuration that is identical with the original geometry, but has been rotated by 90° along the C_2 axis of symmetry. In this process, the geometric factors of all protons are modified, except those of the central methylene group of the propylenic chains. For the latter, the polar coordinates are identical in absolute value in the two conformations and as a result, these two peaks remain well-resolved under all experimental conditions. Whereas the dynamic behavior of the dota complexes (sect. 4.2.1) was attributed to interconversion of the ethylenic moieties of the macrocyclic ring without substantial motion of the ligating atoms, the

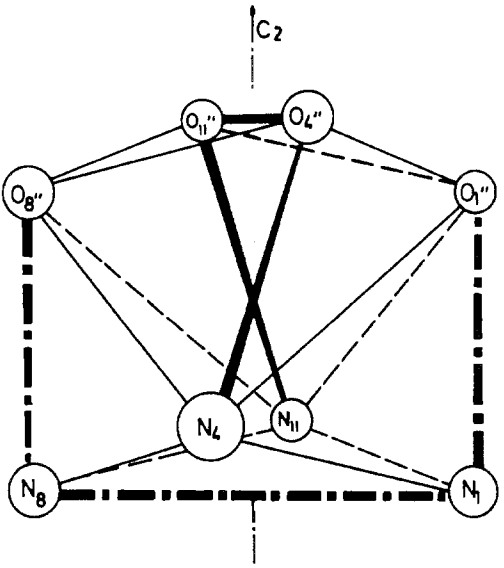

Fig. 17. Schematic presentation of the dodecahedral structure of the Tb(teta)$^-$ complex in the solid state. The coordination sphere of the Tb^{3+} ion is divided into two groups of atoms that are distinguished by connecting them with solid and dash-dotted lines for the "high" and "low" groups, respectively (Desreux and Loncin 1986).

donor groups in the coordination sphere of the teta complexes are exchanging between two different locations, thus leading to complete rearrangement of the complex. Lineshape analysis of ^{13}C data obtained for the diamagnetic lutetium complex yielded the following kinetic parameters: $\Delta G^{\ddagger} = 63.7 \pm 7.5$ kJ mol^{-1} (25°C), $\Delta H^{\ddagger} = 71.7 \pm 5.3$ kJ mol^{-1}, $\Delta S^{\ddagger} = 27 \pm 8$ J K^{-1} mol^{-1}, $E_a = 74.4 \pm 5.0$ kJ mol^{-1}. Whereas the limiting slow-exchange spectra of the europium and ytterbium teta complexes are similar, the spectrum of the Pr(teta)$^-$ complex revealed that the complex is totally asymmetric at the low temperature limit.

4.3. *Complexes with diethylenetriamine-N,N,N',N',N''-pentaacetate (dtpa^{5-}) and amide derivatives of dtpa^{5-}*

The commercial development of $[Gd(dtpa)H_2O]^{2-}$ as a magnetic resonance imaging agent has prompted NMR studies of lanthanide complexes derived from dtpa (fig. 18) and its amide derivatives. Jenkins and Lauffer (1988a,b) were the first to report on the ^1H NMR studies of the paramagnetic R(dtpa)$^{2-}$ complexes. Their studies revealed that all 18 proton resonances of the ligand were resolved at 5°C in spectra obtained in aqueous media, indicating that the complexes are structurally rigid at this temperature on the NMR time scale. On increasing the temperature to 95°C, rapid exchange produces nine resonances, indicating that exchange is occurring between two conformational isomers. 2D EXSY spectra were recorded for the R(dtpa)$^{2-}$ (R = Pr, Eu, Yb) complexes in D_2O at 25°C (a representative spectrum of the praseodymium complex is shown in fig. 19). The cross peaks connecting all exchange pairs were resolved in these spectra. From the simple coalescence behavior (18 peaks to 9) observed in the spectrum of

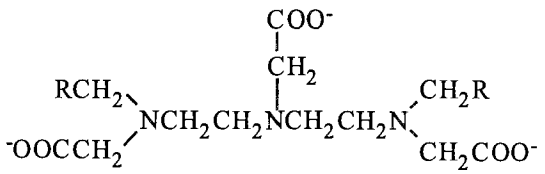

R = COO^- = dtpa

R = $C(O)NHCH_2CH_2CH_3$ = dtpa-pa_2

R = $C(O)NHCH_2CH_2NHCH_2CH_2NH(O)C$ = dtpa-dien

Fig. 18.

each complex, it was proposed that exchange is occurring between two enantiomers as shown in fig. 20. The crystal structure of the neodymium complex (Stezowski and Hoard 1984) showed that the coordination polyhedron may be viewed as a monocapped square antiprism, with three nitrogen and one oxygen from a terminal acetate forming the bottom square face and the four remaining acetate oxygen atoms forming the top face; a water molecule occupies the ninth coordination site in the capping position. The exchange process involves the shuffling of coordinated acetates as shown in fig. 20. In addition, the ethylene groups of the backbone flip between staggered conformations. Exchange rates between enantiomers were calculated using the expression $k_{ex} = \pi\delta\nu/2^{1/2}$, where $\delta\nu$ is the frequency separation (in Hz) between the two exchange partners at the coalescence temperature. In addition, exchange rates were determined for the praseodymium complex from the EXSY spectra. The values of $\Delta G^{\ddagger}$ (kJ mol^{-1}), $\Delta H^{\ddagger}$ (kJ mol^{-1}) and $\Delta S^{\ddagger}$ (J K^{-1} mol^{-1}) for the conformational interchange at 298 K are: 56.5±3.6, 35.2±2.0, −71.4±5.8 for Pr; 55.4±4.6, 38.5±2.4, −56.8±7.0 for Eu; and 49.4±10.0, 37.0±5.0, −41.7±16.2 for Yb. The similarities in activation enthalpies suggest that the same mechanism for conformational interconversion is operative in all three complexes. The authors noted that the rate of conformational interconversions of the dtpa complexes are only an order of magnitude larger than the dynamic processes observed in the dota chelates (sect. 4.2.1), even though the dota chelates require a concerted conformational interconversion of four ethylenediamine-type chelate rings, as opposed to only two such rings in the dtpa chelates. They further proposed that structural rigidity will likely be observed on the NMR time scale for lanthanide complexes derived from highly multidentate ligands, where the ligand is capable of realizing its full denticity.

No cross peaks were observed in the COSY spectrum of the $Pr(dtpa)^{2-}$ complex under conditions of slow exchange ($\leqslant$25°C at 500 MHz). However, the COSY spectrum recorded at 90°C and 250 MHz, under conditions of fast exchange, revealed cross peaks between some of the geminal partners. Although higher temperatures and lower field strength reduce the problems due to Curie relaxation (sect. 2.4), broadening (relaxation) due to chemical exchange still exists at 90°C between some of the exchange pairs,

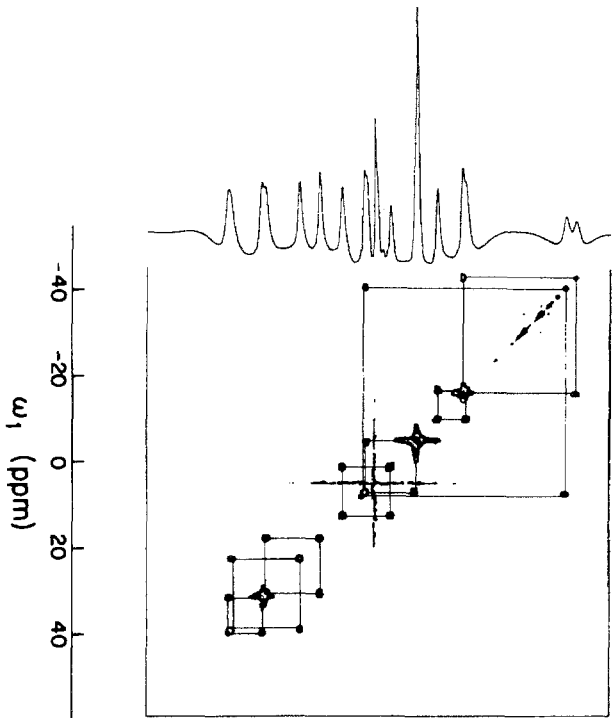

Fig. 19. The EXSY spectrum of 0.3 M $Pr(dtpa)^{2-}$ at 500 MHz and 25°C. Mixing time was 15 ms (Jenkins and Lauffer 1988a).

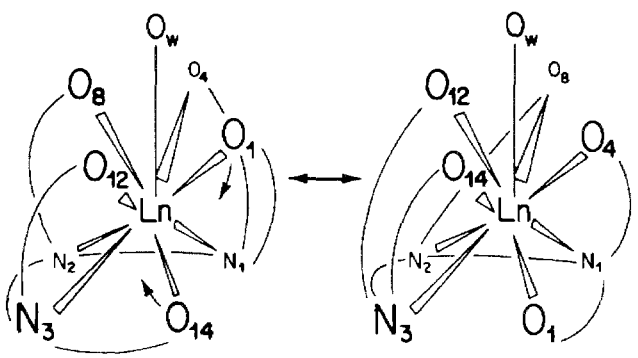

Fig. 20. Schematic for the conformational rearrangement taking place in $R(dtpa)^{2-}$ showing movement of coordinated acetates (Jenkins and Lauffer 1988b).

precluding observation of cross peaks between all geminal pairs. The COSY spectra indicate that at lower temperatures, transverse relaxation occurs predominantly through the Curie mechanism, whereas at higher temperatures, transverse relaxation is dictated by the rate of chemical exchange. This conclusion is based on the observation that cross

peaks were not detected at lower temperatures, and by the fact that, although Yb^{3+} has a μ_{eff} greater than that of Pr^{3+} by a factor of 1.3 (thus its Curie contribution should be a factor of $(1.3)^4$ or 2.86 greater), the COSY spectrum of $Yb(dtpa)^{2-}$ has as many cross peaks as the spectrum of $Pr(dtpa)^{2-}$ at a similar temperature. Analyses of the LIS data for the praseodymium and ytterbium complexes were carried out using the full expression given in eq. (4), with no corrections for contact shifts. Geometric factors were determined from proton coordinates reported for the crystal structure of $Nd(dtpa)^{2-}$. In the case of the praseodymium complex, an agreement factor $R = 0.16$ was obtained, with the best fit axes corresponding to the metal ion–water vector making an angle of 16.0° with the z-axis and the projection of that vector making an angle of 10.0° with the x-axis (i.e. $\theta = 16.0°$ and $\phi = 10.0°$ for the vector); $D_1 = -1250 \pm 125$ ppm Å^3 and $D_2 = -1250 \pm 300$ ppm Å^3. For the ytterbium complex, $R = 0.094$, with $\theta = 19.6°$ and $\phi = 57.2°$; $D_1 = 3880 \pm 99$ ppm Å^3 and $D_2 = 3397 \pm 307$ ppm Å^3. The authors noted that the source of discrepancy between the observed and calculated shifts in the case of the $Pr(dtpa)^{2-}$ complex is probably due to contact shift contributions. Since Pr^{3+} is closer in size to Nd^{3+} (the metal ion used in the crystal structure determination) than Yb^{3+}, it is not likely that these differences arise from discrepancies between the crystal structure of $Nd(dtpa)^{2-}$ and the solution structure of $Pr(dtpa)^{2-}$, since $Yb(dtpa)^{2-}$ gave a good fit. This line of reasoning is consistent with the fact that Yb^{3+} produces the smallest contact contribution to the observed LIS.

Peters (1988c) reported on ^{13}C NMR studies of the $R(dtpa)^{2-}$ complexes in aqueous media. At 21°C, the ^{13}C resonances observed in the spectra of the paramagnetic chelates are broad and featureless. Increasing the temperature to 73°C resulted in three carboxylate resonances, with an integral ratio of 2:2:1, and five methylene signals, with an integral ratio of 2:2:2:2:1, in the spectra of the complexes derived from the lighter metals (R = Ce, Pr, Nd, Sm, Eu), whereas the spectra of complexes derived from the heavier metals (R = Tb–Yb) were still rather broad, precluding unambiguous assignments. The number of ^{13}C signals (8) observed in the fast exchange limit is consistent with the number of ^1H signals observed (9), suggesting that the ligand remains bound in an octadentate fashion under conditions of fast intramolecular reorientation. Using the iterative procedure described in sect. 2.3, which is based on Reilley's separation method (see eq. 10), optimum values of the geometric factors (G_i) for exchange related pairs of ^{13}C atoms were determined (Peters et al. 1985). Only data for R = Ce–Eu were included in the analysis. The resulting G_i values were fit to a set of G_i values that were determined using eq. (7) by substituting coordinates for the carbon atoms obtained from the crystallographic data of $Nd(dtpa)^{2-}$and then varying the orientation of the magnetic axes and the ratio of C/C'. Only a moderate fit between the calculated and experimental G_i values was obtained (see the original literature), leading the authors to conclude that the solid state structure of the neodymium complex is not an adequate model for the solution structure. In their method of analysis, it is necessary to assume that the values of C and C' (cf. eq. 7) are the same for each of the lanthanide complexes. As reported in sect. 4.1, Kemple and coworkers (1988) provide evidence to the contrary that the values of C and C' remain constant in complexes that are inherently asymmetric. However, Aime and Botta (1990), based on ^1H and ^{13}C NMR spectra and longitudinal relaxation times of $R(dtpa)^{2-}$ (R = La, Pr,

Eu) chelates, concluded that their data are in agreement with a solution structure that is similar to that observed for the neodymium complex in the solid state. Peters (1988c) recorded the ^{17}O spectra of the series of $R(dtpa)^{2-}$ chelates. Although it was not possible to observe ^{17}O signals of coordinated dtpa in the paramagnetic complexes due to extreme line broadening, an average ^{17}O signal due to water, which is undergoing fast exchange between the coordination sphere and bulk solution, was observed. The ^{17}O shifts were extrapolated to a R^{3+}/H_2O ratio of 1.0 to obtain the bound shifts of water in each of the complexes [R^{3+} (δ in ppm)]: La (152), Ce (247), Pr (305), Nd (452), Sm (99), Eu (−304), Gd (−1634), Tb (−2144), Dy (−1983), Ho (−1232), Er (−520), Tm (177), Yb (155), Lu (279). A plot of LIS/C_j versus $\langle S_z \rangle / C_j$ (eq. 11) yielded a straight line, indicating that no change in the number of coordinated waters occurs along the series. The slope of the line yields $F = -53$, suggesting the coordination of one water molecule in each complex of the series (cf. Peters et al. 1985, Vijverberg et al. 1980, Nieuwenhuizen et al. 1985).

Geraldes et al. (1991, 1993) reported on the structure and dynamics of lanthanide(III) complexes derived from dtpa-pa_2 in aqueous solution using ^{13}C and ^{17}O NMR. With the use of the longitudinal ^{13}C relaxation times of the neodymium complex, it was shown that the ligand is bound to the lanthanide ion in an octadentate fashion via the three nitrogens of the diethylenetriamine backbone, the three carboxylate groups, and the two amide oxygen atoms. Upon the addition of Dy^{3+} to a solution of dtpa-pa_2 in D_2O, the water ^{17}O shift decreases linearly as the molar ratio Dy^{3+}/dtpa-pa_2 (ρ_L) increases. A sharp break in the plot is noted at $\rho_L = 1.0$, indicating that water molecules are quantitatively displaced by the dtpa-pa_2 ligand. The slope of the plot of the Dy^{3+}-induced ^{17}O shift versus the molar ratio Dy^{3+}/H_2O (ρ_w) was used to determine that one water molecule resides in the inner sphere of the dysprosium complex, giving a total coordination number of nine. The ^{17}O shifts obtained for the various R(dtpa-pa_2) complexes at 73°C were extrapolated to $\rho_w = 1.0$, yielding in ppm: La (338), Ce (381), Pr (511), Nd (648), Sm (297), Eu (−320), Tb (−1901), Dy (−1960), Ho (−1051), Er (−238), Tm (464), Yb (314), Lu (421). At room temperature, ^{13}C NMR spectra of the paramagnetic complexes exhibited very broad and featureless signals. Increasing the temperature to 75°C resulted in appreciable sharpening of the signals in the spectra of the lighter lanthanides (R = Ce–Eu), but the spectra of complexes derived from the heavier lanthanides (R = Tb–Yb) remained broad. The spectrum of the neodymium complex in CD_3OD/D_2O (1:1 v/v) at −30°C revealed eight β-methylene and eight methyl ^{13}C resonances, indicating the presence of four geometric isomers in solution. Attempts to fit the LIS data to calculated models failed due to the complexity of the spectra, which hampered a full assignment of the resonances to various isomers. X-ray analysis of the gadolinium complex (Konings et al. 1990) revealed that the coordination polyhedron of the nine-coordinate complex could best be described as a tricapped trigonal prism, with the two terminal nitrogen atoms of the diethylenetriamine backbone and the water molecule capping the rectangular faces of the prism. Based on this structure, Geraldes and coworkers showed, by examining molecular models, that the ligand can be arranged around the metal ion forming four pairs of enantiomers, each pair of enantiomers giving rise to a separate set of ^{13}C resonances. This model is in agreement with the observation of, for example, eight peaks for the methylene carbons of the two

propyl groups of the Nd(dtpa-pa$_2$) complex at −30°C. Three dynamic processes were identified by means of variable-temperature NMR measurements: (i) rapid rotations of the carboxylate groups; (ii) racemization at the middle nitrogen atom via interconversions between the two possible conformations of the ethylene bridges; and (iii) racemization at the terminal nitrogen atoms of the diethylenetriamine backbone via decoordination–inversion–coordination. A schematic showing the interconversion between the various isomers is shown in the original literature and is similar to that depicted in fig. 21, taken from a report by Franklin and Raymond (1994). The barriers of the interconversions for these processes were determined by line-shape analyses and from coalescence temperatures: $\Delta G^{\ddagger}$ at 283 K for (i) $< 43\ \mathrm{kJ\,mol^{-1}}$, measured for the lanthanum complex; (ii) $53\ \mathrm{kJ\,mol^{-1}}$, measured for the neodymium complex; and (iii) 71 and $67\ \mathrm{kJ\,mol^{-1}}$, measured for the lanthanum and lutetium complexes, respectively.

Franklin and Raymond (1994) reported the variable temperature ^{1}H NMR study of paramagnetic lanthanide complexes derived from dtpa-dien in D_2O. The ligand dtpa-dien, named for the diethylenetriamine linking moiety, is an 18-membered macrocyclic analog of dtpa-pa$_2$ containing a heteroatom (N-atom) in the amide link. The structures of the lanthanum and europium complexes were determined by X-ray crystallography. $[La(dtpa\text{-}dienH^+)H_2O]_2(CF_3SO_3)_2 \cdot 18\ H_2O$ crystallizes as a carboxylate-bridged dimer. Each lanthanum ion is 11-coordinate, with octadentate ligand coordination, an η^2-bridging carboxylate, and one water. $[Eu(dtpa\text{-}dienH^+)]_4(CF_3SO_3)_4 \cdot 6NaCF_3SO_3 \cdot 20\ H_2O$ crystallizes as a carboxylate-bridged tetramer with two crystallographically independent Eu^{3+} positions. The coordination geometries about each europium ion are nearly identical, and were described as nine-coordinate tricapped trigonal prisms, with octadentate ligand coordination plus an η^1-bridging carboxylate. The proton spectrum of each paramagnetic complex revealed the existence of two isomers in solution, with one isomer dominating (major isomer) for each lanthanide. Assuming that the coordination geometry of each complex in solution is the tricapped trigonal prism observed for the europium complex in the solid state, with a water molecule replacing the bridging carboxylate group, then only the l_1SR, d_1SR, l_2RR and d_2SS isomers (two pairs of enantiomers) will accommodate binding of the macrocyclic ligand (fig. 21). [In figure 21, the eight possible isomers are designated d or l below each pictogram by the chirality of the metal (named for the "handedness" of the carboxylates when viewed down the H_2O–R bond) and of the two chiral nitrogens. The four pairs of d, l enantiomers are numbered (1–4).] The solid state structure of the europium complex corresponds to the d_1SR, l_1SR isomer pair. At low temperatures (0–25°C), each isomer produced 26 peaks in the NMR spectrum, which is equal to the number of protons in the ligand. As the temperature is raised, the peaks of the minor isomer broaden and recoalesce to 13 peaks at 97°C (referred to as the dynamic isomer), whereas the major isomer peaks remain essentially unchanged (static isomer). Integration of signal intensities revealed that there is a distinct trend toward the static isomer across the lanthanide series, with the dynamic isomer comprising 5% of the Yb(dtpa-dien) solution structure, while the Eu(dtpa-dien) complex is present as ~20% of the dynamic isomer at 5°C, and is well resolved to 26 peaks at this temperature. The dynamic isomer of Pr(dtpa-dien) is both more abundant (50%) and more fluxional at this

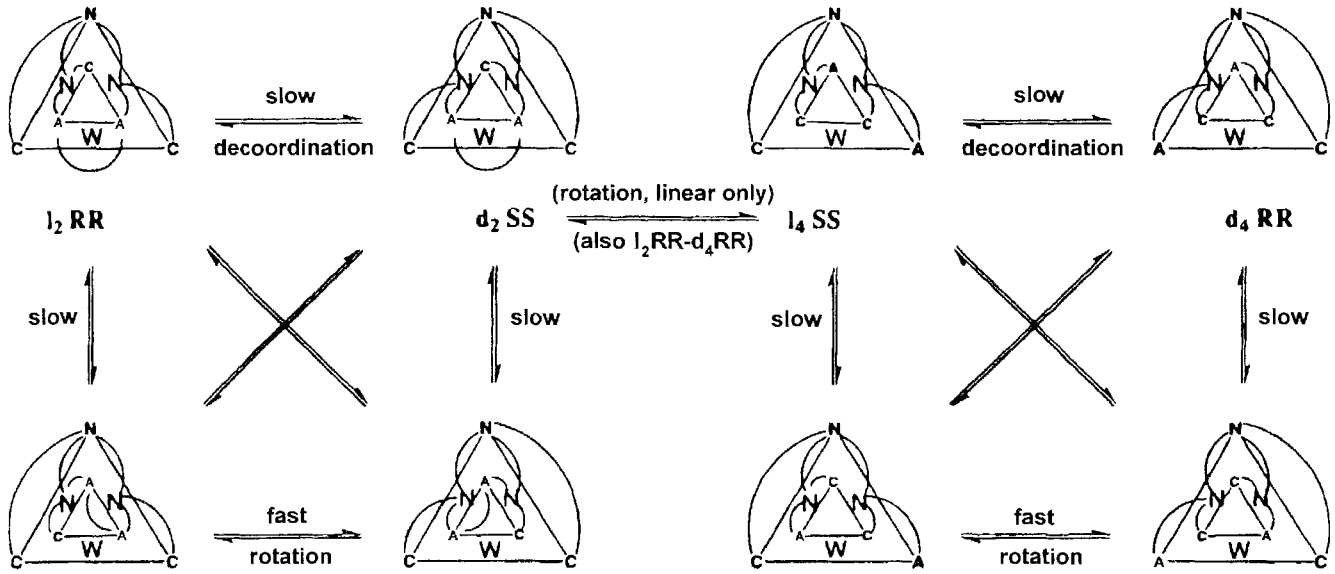

Fig. 21. Possible isomers for [R(dtpa-bis(amide)·H_2O], assuming octadentate chelation and tricapped trigonal prismatic geometry. The backbone amine N atoms cannot span the three face caps, so the central amine N atom must sit on a vertex with the terminal amine N atoms on two of the three caps. The water molecule caps the third face. Nomenclature: A, amide oxygen; C, carboxylate oxygen; W, water oxygen. Isomers are designated by chirality at the metal center and at the two terminal N atoms (Franklin and Raymond 1994).

temperature. The 2D EXSY spectra at 0 and 26°C were taken under conditions where there is no detectable exchange involving the static isomer. However, the EXSY spectra of the dynamic isomer revealed single cross peaks between pairs of protons, suggesting that the exchange process is occurring between a pair of enantiomers. A rate constant for this dynamic process was determined to be $555 \pm 70\,s^{-1}$ at 26°C, corresponding to $\Delta G^{\ddagger} = 57.5 \pm 0.3\,kJ\,mol^{-1}$. This value is similar to that observed for the low energy barrier in the isomerization of the dtpa chelates, involving pseudorotation through a mirror plane, without changing the chirality of the nitrogens. Since this mechanism is only available between the d_1SR and l_1SR isomers of the R(dtpa-dien) complexes, it follows that the dynamic isomer has these configurations. The other isomeric forms available to the macrocyclic ligand (d_2SS, l_2RR) are incapable of rotational isomerization. The only mechanism for enantiomeric isomerization in this case involves successive decoordination and subsequent change in backbone amine chirality. This mechanism would involve a much higher barrier to isomerization than rotation, which would be reflected in a relatively slower rate of exchange. The static isomer was assigned to this pair of enantiomers. Peak assignments for the europium spectrum, given in the original literature, are based on deuteration studies, 2D COSY and 2D EXSY spectroscopy. No analysis of the LIS values is presented.

4.4. *Complexes with sterically rigid ligands or ligands with binding constraints*

4.4.1. *$[R(dpa)_3]^{3-}$ and $[R(mdpa)_3]^{3-}$ complexes*[5]

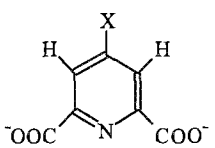

X = H = dpa

X = Me = mdpa

Fig. 22.

The Reilley et al. (1975) report, which involved the ^1H and ^{13}C NMR study of the series of $[R(dpa)_3]^{3-}$ and $[R(mdpa)_3]^{3-}$ chelates in aqueous solution (fig. 22), established that Bleaney's (1972) theory for pseudocontact shifts and Golding and Halton's (1972) theory of contact shifts could be combined as a basis for separating the contribution each makes to the experimental LIS (sect. 2.3). The studies of Reilley and coworkers were stimulated by Donato and Martin (1972), who had established that the $[R(dpa)_3]^{3-}$ chelates, which were known to be thermodynamically stable in aqueous solution, were also stereochemically rigid on the NMR time scale (100 MHz) at 35°C. For R = Tb–Yb, two resonances were observed, corresponding to the pair of meta protons and the para proton, with a shift ratio of 1.14 ± 0.02, indicating that these complexes are isostructural and that the LIS is predominately pseudocontact in origin. The data were interpreted in terms of a tricapped trigonal prismatic geometry having D_3 symmetry, with the aromatic rings canted at an angle of 49° with respect to the equatorial plane containing

[5] dpa^{2-} = pyridine-2,6-dicarboxylate; $mdpa^{2-}$ = 4-methylpyridine-2,6-dicarboxylate.

Table 13
G_i and F_i values for $R(dpa)_3$ and $R(mpda)_3$ (from Reilley et al. 1975)[a]

nucleus i	F_i[b]	G_i	R_i[c]
C_α	−0.022	1.575	0.09
C_β	−2.623	0.554	0.17
C_γ	1.279	0.510	0.04
COO	−1.159	0.470	0.27
C(Me)	−0.206	0.225	0.12
H_β	0.009	0.339	0.09
H_γ	0.013	0.299	0.08
H(Me)	0.026	0.196	0.10

[a] Both series of complexes have the same LIS values.
[b] The contact shift is $F_i\langle S_z\rangle_j$, where the sign of $\langle S_z\rangle_j$ is the opposite of that given in table 1. A positive shift is upfield with this sign convention.
[c] The R value is as defined in eq. (2), except that the sum is taken over the series of metal complexes for each nucleus, rather than the sum over the nuclei of an individual complex.

the nitrogen atoms. The structure proposed for the complexes in solution is similar to that observed in the solid state (Albertsson 1970, 1972). For common nuclei, the series of $[R(mpda)_3]^{3-}$ and $[R(dpa)_3]^{3-}$ chelates gave the same ^1H and ^{13}C LIS values (Reilley et al. 1975), indicating that the two series of complexes are isostructural with each other. The LIS data were incorporated into eq. (10) to give a series of simultaneous equations, which were solved for the G_i and F_i values, effecting separation of the pseudocontact and contact components of the LIS. The computed values of F_i, given in table 13, show that the contact contribution is very small for the ^1H and C_α resonances, whereas large contact contributions exist for C_β, C_γ, CH_3, and COO^-. In addition, an alternation in the sign of the contact shift occurs as one goes from C_β to C_γ to CH_3. The magnitude of the contact shift is largest for C_β and follows the trend $C_\beta > COO^- > C_\gamma > CH_3$. The values of $A/h \times 10^3$ Hz for the $R(mpda)_3$ chelates are: C_β : 44, C_γ : −17, CH_3 : 3 (Desreux and Reilley 1976). The geometric factors, G_i, given in table 13, were shown to correspond to either a clockwise or counterclockwise helical arrangement of the ligands around the C_3 symmetry axis (Reilley et al. 1975).

Interestingly, below room temperature, spectra of the bis complexes $[R(dpa)_2]^-$ (R = Tb, Dy, Ho, Er, Tm, Yb) in 50% v/v CD_3OD/D_2O revealed two resonances for the meta protons and a single resonance for the para protons, indicating that the ligands are mobile on the surface of the metal ion, but that the two meta protons have different dispositions relative to the lanthanide ion (Alsaadi et al. 1980c). The structure of the bis complexes in solution was proposed to be that of a tricapped trigonal prism, with three water molecules completing the coordination sphere. Proton relaxation data were used to determine hydration numbers of six and three, respectively, for the $[R(dpa)]^+$ and $[R(dpa)_2]^-$ complexes in D_2O (Alsaadi et al. 1980d).

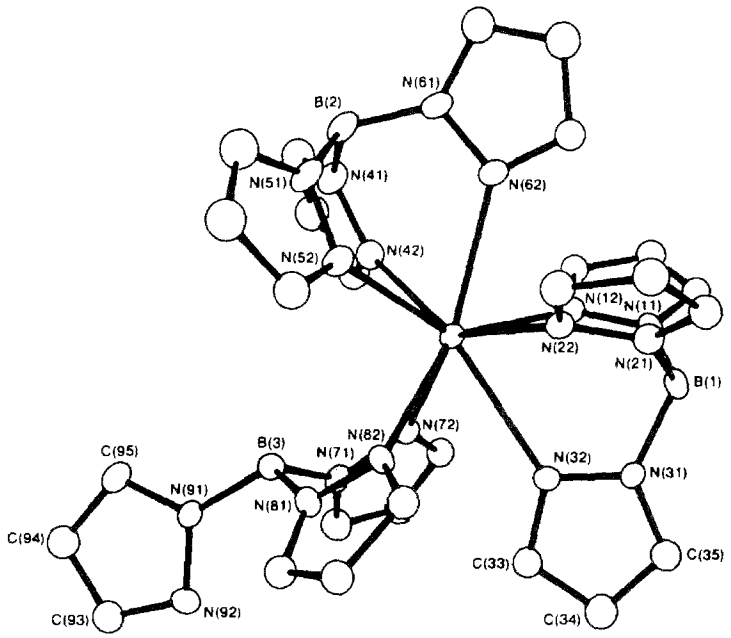

Fig. 23. Perspective view of the solid-state structure of $Yb(hbpz)_3$ perpendicular to the approximate molecular mirror plane (Stainer and Takats 1982).

4.4.2. *$Yb(hbpz)_3$ complexes*[6]

Stainer and Takats (1983) recorded the ^1H, ^{13}C, and ^{11}B spectra of $Yb(hbpz)_3$ in CD_2Cl_2 at 25°C. The ^1H spectrum revealed 21 resonances (18 from the pyrazolyl protons and 3 from the B–H protons) dispersed over a chemical shift range of ~200 ppm. The ^{13}C NMR spectrum has 18 resonances; 9 resonances of relative intensity 2, and 9 resonances of relative intensity 1. The ^{11}B spectrum has three well-separated resonances integrating as a 1:1:1 ratio. The number and relative intensities of the signals indicate that the complexes are stereochemically rigid in solution at room temperature and have C_s symmetry. The crystal structure of the complex revealed an eight-coordinate, bicapped trigonal prismatic geometry, with two tridentate ligands, each spanning one height and capping one rectangular face of the prism, while the bidentate ligand spans the remaining prism height, with the uncoordinated pyrazolyl group directed away from the ytterbium ion, as shown in fig. 23 (Stainer and Takats 1982). The LIS data were least-squares fit to the full form of eq. (4). The C_s symmetry of the molecule fixes the principal magnetic z-axis perpendicular to the mirror plane containing Yb, B(1), B(2) and B(3), while an angle ϕ (defined as the angle between the magnetic x-axis and the Yb–B(1) bond vector), together with D_1 and D_2, were used as fitting parameters in the least-squares analysis. Analysis of the ^1H data gave $R = 0.084$, $D_1 = 8.8 \times 10^2$ Å^3 ppm, $D_2 = 43.6 \times 10^2$ Å^3 ppm, and $\phi = -10.1°$. The close agreement between calculated and observed shifts suggests that

[6] $hbpz^-$ = tris-(pyrazol-1-yl)borate.

the solution structure approximates that observed in the solid state and that the contact contribution to the ^{1}H shifts is small. Analysis of the LIS data for the 18 ^{13}C and 3 ^{11}B resonances gave $R=0.101$, $D_1=8.8\times10^2$ Å^3 ppm, $D_2=42.6\times10^2$ Å^3 ppm, and $\phi=-11.2°$. The relatively good agreement factor suggests that the ^{13}C and ^{11}B resonances also have only small contact shifts. Including all the ^{1}H, ^{13}C and ^{11}B resonances in the analysis gave $R=0.099$, $D_1=8.9\times10^2$ Å^3 ppm, $D_2=42.6\times10^2$ Å^3 ppm, and $\phi=-10.9°$. The structural rigidity of these eight-coordinate complexes may be due to the fortuitous wrapping of the hbpz ligands around the metal, in which one pyrazolyl group is directed away from the metal center in a manner that appears to preclude its participation in an intramolecular ligand reorientation process.

4.4.3. *Complexes with texaphyrins, (tx), R(tx)*$^{2+}$[7]

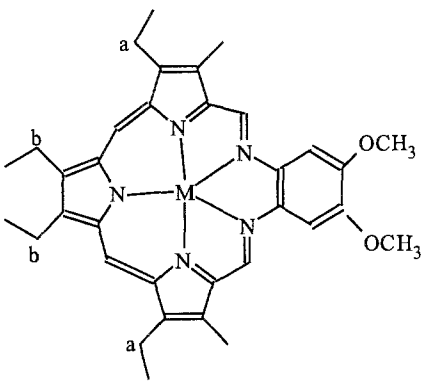

Fig. 24.

A series of lanthanide complexes derived from texaphyrins (fig. 24) have been synthesized by Sessler and coworkers (1993a,b). Texaphyrins are aromatic pentadentate ligands that belong to the general class of compounds known as expanded porphyrins. The binding cavity in texaphyrins is ~20% larger than in porphyrins. As a result, the texaphyrins form stable 1:1 complexes with the tripositive lanthanides, in which the R^{3+} ions are closer to the plane of nitrogen atoms than in the porphyrin complexes. The crystal structure of the gadolinium nitrate complex, $Gd(tx)(NO_3)_2$, derived from the texaphyrin with methoxy substituents on the benzo group, for example, reveals that the metal ion is 0.694 Å above the plane of five nitrogen atoms (Sessler et al. 1993a). Two distinct structures were found in the unit cell for this complex. One structure contained a nine-coordinate gadolinium ion, with one bidentate nitrate ion and one methanol molecule occupying one "axial" position and a second molecule of methanol binding through the opposite axial position. The second structure contained a ten-coordinate gadolinium ion, with two bidentate nitrate ions occupying one "axial" position and one molecule

[7] Htx = 4,5,9,24-tetraethyl-16,17-dimethoxy-10,23-dimethyl-13,20,25,26,27-pentaazapentacyclo-[20.2.1^{3,6}.1^{8,11}.0^{14,19}]heptacosa-1,3,5,7,9,11(27),12,14,16,18,20,22(25),23-tridecaene.

of methanol binding in the opposite axial position. Lisowski et al. (1995) reported on the ^{1}H NMR studies of the series of paramagnetic nitrate complexes derived from tx in methanol-d_4 and $CDCl_3$. Nine proton resonances are observed at 296 K, corresponding to effective C_{2v} symmetry. However, at lower temperatures (below 273 K), each of the nonequivalent methylene groups (a and b in fig. 24) split into two peaks, indicating that the complexes have nominal C_s symmetry. The effective C_{2v} symmetry observed at higher temperatures can be accounted for by fast rotation of the ethyl substituents or, alternatively, from exchange of nitrate ligands from one side of the macrocyclic plane to the other side, i.e., exchange between axial sites, with metal flip-flop averaging of out-of-plane structures. While the NMR data do not allow a distinction between these two possibilities, the latter mechanism was favored based on the relatively low activation free energies associated with the process responsible for signal averaging (less than 56 and 48 kJ mol^{-1} for the neodymium and terbium complexes, respectively). Based on data available in the literature, the activation free energy barrier for rotation of the ethyl groups is expected to exceed 70 kJ mol^{-1}. Unequivocal peak assignments in the spectra of the complexes derived from the lighter lanthanides were based on 2D COSY and ROESY experiments, and 1D NOE difference experiments. Plots of LIS versus C_j were used to correlate the chemical shifts of complexes derived from the heavier metals (Tb–Yb) with those of the lighter metals. The LIS values were then fit to eq. (4) using D_1, D_2, and an angle α (defined as the angle between the principal x-axis and the R^{3+}–N bond vector lying in the symmetry plane; an α value of $-16°$ corresponds to the z-axis being perpendicular to the macrocycle plane in the X-ray structure of the gadolinium complex) as fitting parameters in a nonlinear least-squares analysis. The principal magnetic z- and x-axes were taken to lie in the symmetry plane (the xz-symmetry plane passes through the lanthanide ion and the nitrogen atom of the central tripyrrane pyrrole and a point midway between the two imino nitrogen atoms). The geometric factors for each proton were derived from the coordinates of the solid state structure of the nine-coordinate $Gd(tx)(NO_3)_2$ structure. The results of the analyses, presented in table 14, gave agreement factors (R) ranging from 0.053 for $Yb(tx)(NO_3)_2$ to 0.412 for $Eu(tx)(NO_3)_2$. Since the LIS values have not been corrected for contact shifts, good fits are observed for those metal ions (Tm^{3+} and Yb^{3+}) that have the lowest theoretical contact to pseudocontact shift ratios. On the other hand, less acceptable fits are observed for those metal ions (Nd^{3+} and Eu^{3+}) that have relatively large contact to pseudocontact shift ratios. Rather than use contact shifts as fitting parameters to reduce the value of R, the authors elected to factor out contact shifts by selecting, in an iterative fashion, LIS values for certain protons to be explicitly excluded from the fitting procedure. While many calculations were carried out for various single positions, the dramatic improvements in the R factors were obtained only when the imino protons were excluded from the fitting procedure (cf. table 14). Once good fits were obtained in this manner, the resulting parameters (D_1, D_2, and α) were used to calculate the pseudocontact shift for the omitted imino protons. Subsequently, the contact shifts of the imino protons were obtained by subtracting the calculated pseudocontact shift from the observed LIS (table 14). Plots of the contact shifts of the imino proton versus theoretical $\langle S_z \rangle$ values proved linear, indicating that

Table 14
Fitting results for the R(tx)$(NO_3)_2$ complexes (from Lisowski et al. 1995)

R	D_1 [a]	D_2 [a]	α (°)	R [b]	R' [c]	δ_c [d]
Ce	209	−214	−16.2	0.195	0.282	3.50
Pr	493	−696	−29.7	0.125	0.282	9.61
Nd	363	−597	−19.9	0.168	0.362	13.14
Eu	−364	557	−22.6	0.259	0.421	−25.9
Tb	8024	−6489	−19.1	0.084	0.274	−74.39
Dy	11 588	−13 360	−19.1	0.096	0.212	−66.88
Ho	7036	−7523	−21.6	0.075	0.212	−41.04
Er	−3039	1159	−4.8	0.114	0.258	−35.73
Tm	−6005	3398	−17.2	0.072	0.076	−13.09
Yb	−4196	1931	−19.2	0.066	0.053	−4.18

[a] ppm Å^3.
[b] Agreement factor for a model excluding the imino protons from the calculation.
[c] Agreement factor for a model including all the protons.
[d] Contact shift in ppm for the imino proton.

the contact shifts obtained in this manner were reliable (it also means the magnetic anisotropy parameters, D_1 and D_2, are well defined). The authors noted that the values of the magnetic anisotropy parameters are the same when the contact shifts of the imino protons are used as fitting parameters in the least-squares analysis, however, the R values are smaller, e.g., $R = 0.044$ for Yb(tx)$(NO_3)_2$ and $R = 0.080$ for Tb(tx)$(NO_3)_2$. The smaller R values result because inclusion of a contact shift as a fitting parameter produces an exact fit between the calculated and observed LIS, making one term in the numerator of eq. (2) exactly zero, while the sum in the denominator of eq. (2) becomes larger due to an additional term, namely $(\delta_{obsv})^2$ for the imino protons. Thus inclusion of contact shifts as fitting parameters in the analysis has not improved the accuracy of the components of the susceptibility tensor. Fits obtained excluding the imino proton data gave values of α close to −16°, suggesting that the magnetic z-axis is nearly perpendicular to the macrocyclic plane. The χ tensors are, however, highly rhombic. Thus the axial and rhombic contributions to the pseudocontact shifts, given by the first and second terms of eq. (4), respectively, are comparable in absolute magnitude, but of opposite sign. None of the principal χ values is particularly unique in the complexes derived from Ce–Ho, i.e., $|\chi_{zz} - \chi_{xx}|$ is similar to $|\chi_{xx} - \chi_{yy}|$, whereas for complexes derived from Er–Yb, $|\chi_{zz} - \chi_{xx}| \gg |\chi_{xx} - \chi_{yy}|$. For the Ce–Ho complexes, the y-axis could equally well be chosen as being unique rather than the z-axis. However, defining the z-axis as being roughly perpendicular to the macrocycle plane provides a unique choice for the principal axis system in the case of complexes derived from Er–Yb. According to Bleaney's theory (1972) (cf. sect. 2.3), the ratio of D_1 to D_2 should equal the ratio of the crystal field coefficients B_0^2/B_2^2 for a series of isostructural complexes. The ratios of D_1 to D_2 for the R(tx)$(NO_3)_2$ complexes are −0.98 (Ce), −0.71 (Pr), −0.61 (Nd), −0.65 (Eu), −1.27 (Tb),

Table 15
Fitting results for the diphenyl phosphate complexes $R(tx)(P_1)_2$[a] (from Lisowski et al. 1995)

R	D_1[b]	D_2[b]	α (°)	R[c]	δ_c[d]
Tb	−2054	−7466	−12.1	0.204	11.52
Dy	−2618	−15222	−9.6	0.046	−50.74
Ho	1815	−9764	−20.3	0.084	−39.87
Er	776	1791	3.9	0.119	−24.76
Tm	−1343	5715	−0.8	0.086	−10.94
Yb	−54	3512	2.4	0.061	−2.92

[a] Geometric factors determined from the crystal structure of $Dy(tx)(p_1)_2$.
[b] ppm Å^3.
[c] Excluding the LIS values for the imino protons.
[d] Contact shifts of the imino protons in ppm.

−0.87 (Dy), −0.94 (Ho), −2.62 (Er), −1.77 (Tm), and −2.17 (Yb). The significant change in the D_1 to D_2 ratio noted for the Er–Yb complexes may reflect changes in metal-centered axial ligation in solution across the lanthanide series. Replacement of the axial nitrate ligands with diphenylphosphate mono anion $[(C_6H_5)_2PO_4^- = P_1]$ to form $R(tx)(P_1)_2$ complexes in solution resulted in a totally altered ^1H spectrum for each of the paramagnetic complexes. The crystal structure of the dysprosium complex revealed that the metal ion is seven-coordinate, with five donor atoms being provided by the texaphyrin ligand and two by monodentate diphenyl phosphate anions. The dysprosium ion is 0.073 Å from the plane of five nitrogen atoms of the macrocycle, with the diphenyl phosphate anions bonding on the opposite sides of the macrocyclic ring in the two axial positions. The LIS values obtained for $R(tx)(P_1)_2$ (R = Tb–Yb) were analyzed in the manner described above for the $R(tx)(NO_3)_2$ complexes. The fitting results (table 15) reveal that the D_1 and D_2 values change completely in comparison with those obtained for the corresponding nitrate complexes (cf. table 14), with the absolute value of D_2 now greater than D_1. The changes in D_1 and D_2 parameters were attributed to changes in the crystal field coefficients, which result from binding of the phosphate rather than nitrate ligands in the axial positions.

4.4.4. *Sandwich complexes derived from phthalocyanine (pc) and octaethylporphyrinate (oep)*

^1H NMR studies of the series of sandwich complexes derived from phthalocyanine, $R(pc)_2^-$, revealed only two resonances for the aromatic ring, suggesting a highly symmetrical structure for the complexes in solution (Konami et al. 1989). The authors noted that the high symmetry could be caused by spinning of the pc rings, although they proposed that the rings are staggered and that the complexes have D_{4d} symmetry in solution. The G_i and F_i parameters, which were determined by Reilley's method (eq. 10), are 0.284 and −0.659, respectively, for the ortho protons, and 0.143 and -0.360, respectively, for the meta protons of the aromatic ring. The average distance between the

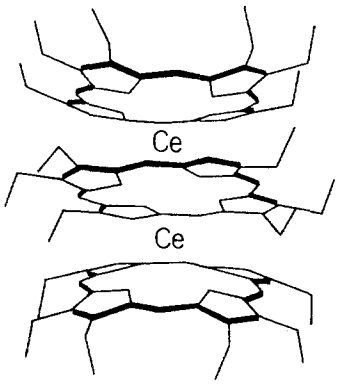

Fig. 25. Line drawing of $Ce_2(oep)_3$, showing doming of the outer oep rings. Some of the ethyl groups have been omitted for clarity (Buchler et al. 1992).

two phthalocyanine rings was determined to be 2.54 Å, with a mean R^{3+}–N bond distance of 2.31 Å.

Buchler et al. (1989, 1992) reported the ^1H and ^{13}C spectra of an interesting series of triple-decker $R_2(oep)_3$ (oep = octaethylporphyrinate) complexes. The X-ray structure (Buchler et al. 1986) of the Ce^{3+} complex revealed that each Ce^{3+} ion is sandwiched between two ocatethylporphyrin rings. The outer rings show strong C_{4v} doming, while the internal ring is planar (the adjacent rings are staggered by 24.5° to relieve inter-ring alkyl crowding) (see fig. 25). Four ^1H resonances were observed for the outer oep ring at 3.47 ppm (meso), 0.72 and −0.15 ppm (α-CH_2), and 2.08 ppm (β-CH_3), while three resonances are observed at −8.12, −5.33, and −5.00 ppm for the meso, α-CH_2 and β-CH_3 protons, respectively. Since the outer rings do not possess a symmetry plane, the outer ring α-CH_2 protons are diastereotopic, giving rise to two resonances. The resonance for the outer ring methyl group is shifted in a direction opposite to that of the two CH_2 proton resonances, suggesting that there is limited rotation of the alkyl groups. Using the solid state structure, geometric factors for each proton were calculated, taking into account both components G(1) and G(2) for proximal and distal Ce^{3+} ions, respectively. The ethyl groups were allowed to rotate about the α-C to pyrrole-C bond using an angle ϕ, defined as the angle between the α-C to β-C bond vector and the pyrrole ring ($\phi = 0$ represents the rotamer in which the β-CH_3 groups are above the outer oep ring, with the z-projection of the α-C to β-C bond parallel to the C_4 rotation axis). While the best static fit of relative geometric factors and LIS values were obtained for the three outer ring alkyl resonances at $\phi = 30°$, the authors felt that some rotational freedom must exist. Allowing free rotation of the ethyl groups provided no satisfactory fit to the observed pseudocontact shifts. However, average geometric factors for an equally populated set of rotamers with $\phi = 0 \pm 60°$ gave good agreement (within 10%) of the experimental pseudocontact shift ratios. The best fit of the alkyl resonances of the inner oep ring were obtained for average geometric factors corresponding to $\phi = 270 \pm 130°$. It is noted that the shifts for R = Pr, Nd, and Sm are qualitatively similar to those obtained for the cerium complex, but their magnitudes were too small to allow modeling of the geometry. Two sets of five ^{13}C resonances are observed for the outer and inner oep

rings in the cerium complex. Since the ^{13}C resonances may have a significant contact component, an interesting approach was taken to evaluate the pseudocontact component of the ^{13}C resonances. A plot of the ^{1}H LIS values versus the geometric factors for each of the protons is linear, with a slope $D_1 = 2980 \times 10^{-6}$ cm^3/mol cerium (cf. eq. (4) with $D_2 = 0$), suggesting that the ^{1}H shifts are purely pseudocontact. The pseudocontact shifts of the ^{13}C resonances were then calculated using this value of D_1 and the geometric factors of the carbon atoms, which were calculated from the solid state structure. Except for the α-C of the pyrrole ring, good agreement is obtained between experimental and calculated shifts for the inner ring, whereas the agreement is not as good for the outer ring. Differences between the observed and calculated values presumably correspond to the contact shift component.

5. Chiral shift reagents

The chiral europium shift reagent, Eu(t-cam)$_3$, derived from the β-diketonate derivative of camphor, 3-(*tert*-butylhydroxymethylene)-d-camphor, H(t-cam,) (fig. 26; X = *t*-butyl) was first reported by Whitesides and Lewis (1970) to resolve enantiomeric resonances in ^{1}H NMR. There are two mechanisms that can lead to enantiomeric resolution in the NMR spectra of chiral substrates in the presence of chiral shift reagents. First, the geometry of the complex between each enantiomer and the shift reagent are diastereomers, giving rise to different pseudocontact shifts. Secondly, there is a difference in the association constants between the enantiomers and the shift reagent (stereoselectivity). Among the several other camphor derivatives that were studied as potential chiral shift reagents, those with X = $-CF_3$ and $-C_3F_7$ proved to be quite effective (Goering et al. 1974). Wenzel (1987) provides an excellent review of the use of these and other chiral shift reagents to determine optical purity or enantiomeric excess in organic solvents. Procedures for assigning absolute configurations to substrates using chiral shift reagents in organic solvents have met with only limited success.

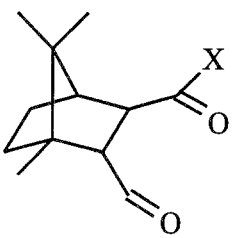

Fig. 26.

Reuben (1979b, 1980) reports NMR spectral resolution of enantiomeric nuclei of α-hydroxycarboxylates by paramagnetic lanthanide ions in aqueous solution. Addition of $PrCl_3$ or $EuCl_3$ to nonracemic mixtures of lactate ion results in resolution of the methyl resonances of the two optical isomers of lactate. The "self"-resolution of the spectra of nonracemic mixtures by the mere addition of a lanthanide salt is due to a chemical shift

difference between an optically pure tris complex, ML_3 (or its enantiomer MD_3), and the mixed MD_2L complex, a diastereomer, where the chirality of the ligands is indicated. Under the condition of fast exchange observed in these systems, the contribution of the 3:1 complexes to the chemical shift differences is given by

$$\delta_L = \frac{3ML_3\Delta_3}{L_t} + \frac{2MDL_2\Delta_2}{L_t} + \frac{MD_2L\Delta_1}{L_t}, \tag{19}$$

$$\delta_D = \frac{3MD_3\Delta_3}{D_t} + \frac{2MLD_2\Delta_2}{D_t} + \frac{ML_2D\Delta_1}{D_t}, \tag{20}$$

where the subscript t indicates total concentration, and Δ_n is the chemical shift of the possible pairs of enantiomers, $ML_nD_{(3-n)}$ and $MD_nL_{(3-n)}$. The square brackets denoting concentrations are omitted. As long as $L_t \neq D_t$ (nonracemic mixture), then $\delta_L - \delta_D \neq 0$. Resolution of a racemic mixture is obtained by addition of a molar excess of the pure enantiomer, C, of some other chiral α-hydroxycarboxylate. In this case, the resonances of the L and D forms of the racemic mixture of one α-hydroxycarboxylate are distinguished due to formation of diastereomers, such as MC_2L and MC_2D.

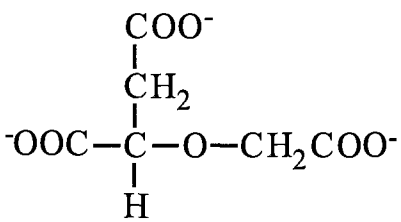

cmos

Fig. 27.

Peters et al. (1983) reported the use of R(cmos) (R = Eu, Yb; $cmos^{3-}$ = (*S*)-carboxymethyloxysuccinate, fig. 27) as chiral shift reagents in aqueous solution. In aqueous solution, cmos can form both 1:1 and 2:1 ligand:R^{3+} chelates with high stability constants ($\log K_1 \approx 8$; $\log K_2 \approx 4$), in which the ligand binds in a quadridentate fashion. Since R^{3+} ions usually have coordination numbers of eight or nine, the R(cmos) complexes have several coordination sites available for binding an additional substrate. Addition of Eu(cmos) resulted in ^1H spectral resolution of the two enantiomers in racemic oxydilactate and of the enantiotopic CH_2 protons of oxydiacetate and nitrilotriacetate. Yb(cmos) was used to resolve the enantiomers of the two amino acids, alanine and 3-hydroxyphenylalanine.

In a series of papers, Kabuto and colleagues (Kabuto and Sasaki 1984, 1987, 1989, 1990, Kabuto et al. 1992) reported the ability of [Eu(R- or S-pdta)]$^-$ ($pdta^{4-}$ = 1,2-propanediaminetetraacetate) to act as chiral shift reagents in aqueous solution and the usefulness of the reagents in assigning the absolute configuration of a number of different substrates. The R(pdta)$^-$ complexes are thermodynamically stable in aqueous

solution, with the ligand binding in a hexadentate fashion. Addition of a small amount of Eu(R-pdta)$^-$ (<0.1 mol ratio) to solutions of α-amino acid enantiomers shifted the H_α signal upfield, giving separate signals for the pair of enantiomers. Unambiguous assignment of the separate signals was accomplished by using a nonracemic mixture of enantiomers. In 22 examples of a wide variety of α-amino acids, the H_α signal due to the L-enantiomer always showed larger upfield shifts than those due to the D-isomer (Kabuto and Sasaki 1987). Furthermore, the Eu(R-pdta)$^-$ reagent causes larger upfield shifts than the Eu(S-pdta)$^-$ reagent. In a latter paper, Kabuto and Sasaki (1990) showed that the methyl resonance of the S-isomer of a series of eleven α-methyl amino acids shifted upfield relative to the methyl resonance of the R-isomer in the presence of Eu(R-pdta)$^-$. Consistent correlation was also observed between absolute configuration of fifteen α-hydroxy carboxylic acids (Kabuto and Sasaki 1989) and seventeen aldonic acids (Kabuto et al. 1992) and their ^{1}H shifts induced by Eu(R-pdta)$^-$. Kido et al. (1990, 1991) reported on the utility of the europium(III) derivative of (*S,S*)-ethylenediamine-*N,N'*-disuccinic acid as a chiral shift reagent for ^{1}H spectral resolution of enantiomers of five α-amino acids in aqueous media.

Wenzel et al. (1994) synthesized a novel chiral lanthanide shift reagent by the reaction of diethylenetriaminepentaacetic dianhydride with 6-mono- and 2-mono(ethylenediamine) derivatives of β-cyclodextrin to produce cd-en-dtpa (fig. 28). The β-cyclodextrin is a cyclic

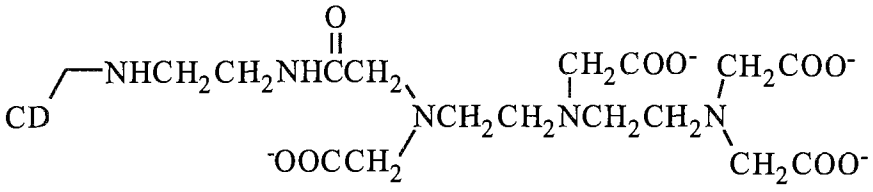

cd-en-dtpa

Fig. 28.

oligosaccharide consisting of seven D-glucose units. The molecules are pail-shaped with the two secondary hydroxyl groups (2- and 3-positions) on each glucose ring situated at the mouth of the wider opening and one primary hydroxyl group (6-position) on each ring situated at the mouth of the narrower opening. Adding Dy^{3+} to cd-en-dtpa enhances the enantiomeric resolution in the ^{1}H NMR spectra of carbinoxamine maleate, doxylamine succinate, pheniramine maleate, propranolol hydrochloride and tryptophan. The enhancement is more pronounced with the secondary derivative (2-β-cd-en-dtpa-Dy). In each case, the substrate is associated with the cyclodextrin cavity as an inclusion complex, with the dysprosium ion coordinated in an octadentate fashion by the dtpa group. It is proposed that the lanthanide ion is disposed to the side of the cyclodextrin cavity in both the 6-β-cd-en-dtpa-Dy and 2-β-cd-en-dtpa-Dy complexes. As a result, the largest lanthanide induced shifts are observed for substrate nuclei imbedded within the cyclodextrin cavity.

6. Shift reagents for biologically important cations

Although the direct NMR detection of physiologically important cations, such as $^{7}Li^{+}$, $^{23}Na^{+}$, $^{39}K^{+}$ or $^{25}Mg^{2+}$, is possible, the study of transport of such ions across cell membranes requires a lifting of the degeneracy of NMR signals due to intra- and extracelluar cations. This may be accomplished by designing a paramagnetic lanthanide shift reagent that remains extracelluar and binds to the cation of interest, thereby inducing a shift in the extracelluar cation, with the intracellular ions maintaining their characteristic shifts. Several reports of lanthanide complexes (all are anionic except those derived from nota) that produce substantial shifts in $^{23}Na^{+}$ resonances appeared within a few months of each other. Bryden et al. (1981) reported on the use of R(dota)$^{-}$, R(nota) and R(edta)$^{-}$ (R = Pr, Nd, Eu, Gd–Yb). The sign of the ^{23}Na shifts in R(dota)$^{-}$ solutions follow those predicted by Bleaney's model for pseudocontact shifts, which means that the sodium ion must have a preferred orientation with respect to the R(dota)$^{-}$ complex. If there were no preferred orientation of the sodium ion, the pseudocontact shifts would average to zero. It was proposed that the Na^{+} ion associates with the carboxylate groups in a cone about the C_4 symmetry axis of the complex, making the angle θ in the geometric factor (cf. eq. (4); $D_2 = 0$) substantially greater than zero, but less than 54.7° (the geometric factor is zero at this angle). The ^{23}Na shifts in R(edta)$^{-}$ and R(nota) solutions also follow the Bleaney model, but with a change in sign relative to the ^{23}Na shifts observed in the R(dota)$^{-}$ solutions. In the case of the edta and nota complexes, it was proposed that the Na^{+} ion associates with the carboxylate groups, with an effective angle $\theta > 54.7°$ from the principal magnetic axis (effective axial symmetry is observed in both the R(edta)$^{-}$ and R(nota) chelates). Pike and Springer (1982) reported that Dy(dpa)$_3^{3-}$ and Dy(nta)$_2^{3-}$ produced larger LIS (upfield) for $^{23}Na^{+}$ than Dy(edta)$^{-}$, presumably due to the larger charge and ability of the former complexes to form stronger ion pairs with the sodium ion. Although the nature of the ion binding was not reported, graphical analysis of titration curves of LIS versus the mole ratio of shift reagent indicated that Dy(nta)$_2^{3-}$ forms both 1:1 and 2:1 Na^{+}:shift reagent ion pairs.

Of the shift reagents studied to date, the Dy(ppp)$_2^{7-}$ (ppp = triphosphate ion = $P_3O_{10}^{5-}$) introduced by Gupta and Gupta (1982) has attracted the most attention. These workers resolved resonances from intra- and extracellular ^{23}Na ions in NMR studies of human red blood cells and a frog skeletal muscle. As an example, the ^{23}Na NMR spectrum of a suspension of red blood cells in a medium containing 140 mM Na^{+}, 10 mM K^{+} and 2 mM or 5 mM Dy(ppp)$_2^{7-}$, at pH 7.5, revealed two well-resolved ^{23}Na resonances. An upfield resonance corresponds to extracelluar $^{23}Na^{+}$ ions, which interact with the shift reagent, while the downfield resonance is due to intracellular $^{23}Na^{+}$ ions (the chemical shift of the latter resonance is essentially unaffected by the presence of the paramagnetic shift reagent). The solution structure of R(ppp)$_2^{7-}$ and the number of binding sites for monovalent ions remains a subject of controversy and investigation. The crux of the problem appears to be the multiple equilibria involving the R(ppp)$_2^{7-}$ chelates (Szklaruk et al. 1990), including dissociation of the complex and competition of H^{+} and M^{+} for oxygen atoms of the carboxylate groups (Chu et al. 1990). Furthermore, the LIS observed

in ^{31}P, ^{17}O, or M^+ spectra are usually obtained under conditions of rapid exchange on the NMR time scale, making it difficult to extract reliable structural information. Based on the molecular structure of the ppp^{5-} ion, as determined in the crystal structure of $Na_5(ppp)$, and the way the Na^+ ions are coordinated in the crystal, Springer's group postulated the equilibrium shown in fig. 29 for the binding of Na^+ ion to $R(ppp)_2^{7-}$ (Chu et al. 1984).

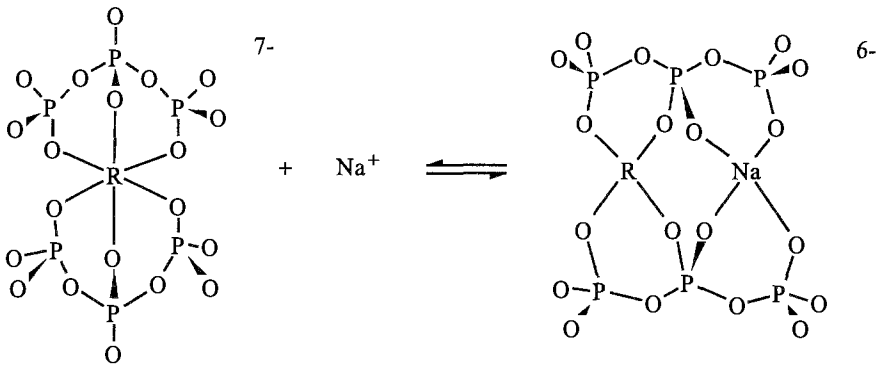

Fig. 29.

The structure on the right features a specific Na^+ binding site close to the lanthanide ion, which would account for the relatively large LIS observed for $^{23}Na^+$ (37.9 ppm at $[Dy(ppp)_2^{7-}]/[Na^+] = 0.1$, $[Na^+] = 150$ mM, pH 7.36). In a later study of the thermodynamics of the interaction, this group showed that the $^{23}Na^+$ binding data for $R(ppp)_2^{7-}$ (R = Tb, Dy, Tm) can be fitted well by assuming only a single binding site for the Na^+ cation (Chu et al. 1990). A limiting $^{23}Na^+$ shift of -435 ± 15 ppm was determined for the dysprosium complex at 30°C, with a formation constant of 8744 ± 4063. Nieuwenhuizen et al. (1985) reported ^{31}P, ^{17}O, and $^{23}Na^+$ studies of the $R(ppp)_2^{7-}$ shift reagents. Except for R = Ce and Sm, slow exchange was observed at 25°C in the ^{31}P spectra of D_2O solutions containing an excess of ligand (>2:1 ppp:R^{3+} mol ratio). Integrals in the slow exchange region confirmed the stoichiometry of the $R(ppp)_2^{7-}$ complexes. Geometric factors (G_i) were determined for the phosphorus atoms using Reilley's procedure (sect. 2.3) to separate the contact and pseudocontact components of the ^{31}P LIS. That the magnitudes of the G_i values of the two different phosphorus nuclei are about the same can be explained by positioning the principal magnetic axis perpendicular to the plane defined by the two central phosphorus atoms and the lanthanide ion, in a manner similar to that depicted in fig. 30 (fig. 30 is taken from Ramasamy et al. 1991). The phosphorus atoms then occupy the equatorial region ($55° < \theta < 125°$), where θ is the angle between the principal axis and the R^{3+}–P vector). Based on F_i values (eq. 11) determined from LIS data of ^{17}O resonances of the phosphate groups in complexes derived from the lighter lanthanides, under conditions of fast exchange, at 73°C, it was proposed that each triphosphate ion is quadridentate, coordinating through two oxygen atoms of one of the terminal PO_3 groups, one oxygen atom of the other terminal PO_3 group, and one oxygen atom of the central PO_2 group, as shown in fig. 30 (^{17}O signals could not be observed for complexes derived from the

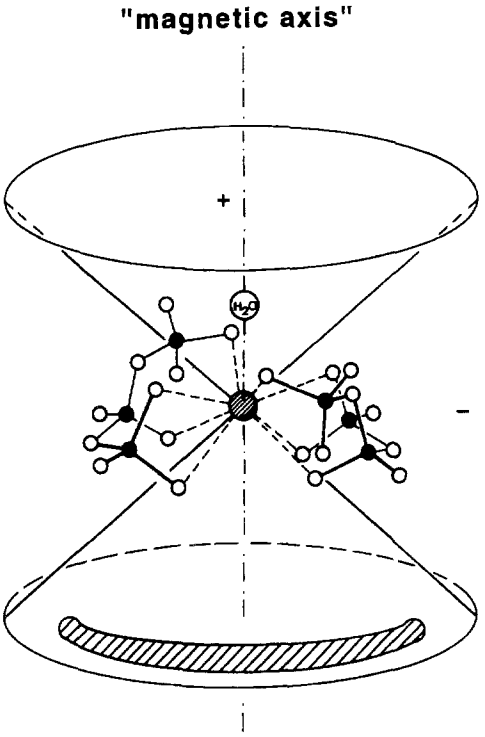

Fig. 30. Schematic representation of the structure of the $R(ppp)_2^{7-}$–alkali metal ion adduct. A tricapped trigonal prismatic coordination of the R^{3+} ion is assumed (Ramasamy et al. 1991).

heavier lanthanides due to severe line broadening under conditions of slow exchange that prevailed in these systems at 73°C). Although quadridentate ligation of the ligand is reasonable, the LIS values used in these calculations were not directly observed, but derived from the slopes of plots of LIS versus $[R^{3+}]/[Na_5(ppp)]$ ($[Na_5(ppp)] = 0.35$ M). Analysis of the ^{17}O LIS of D_2O indicated the coordination of one water molecule in the axial region ($-55° < \theta < +55°$). It was further proposed that seven Na^+ cations bind to the oxygen atoms of the carboxylate groups in the axial region. In a later investigation, Ramasamy et al. (1989) monitored a titration of 5 mM $Dy(ppp)_2^{7-}$ (as the tetramethylammonium salt) with Li^+ or Na^+ at pH 7.5 using ^7Li and ^{23}Na NMR. Extrapolation of the linear portion of the curve, obtained at large $[M^+]:[Dy(ppp)_2^{7-}]$ ratios, revealed a break at approximately a 7:1 mole ratio, which indicates that seven monovalent cations bind to the shift reagent. A second break in the curve is observed at approximately a 1:1 mole ratio, characterized by a sharp increase in the ^7Li or ^{23}Na paramagnetic shifts. This observation suggests that the first equivalent of M^+ added to $Dy(ppp)_2^{7-}$ occupies a preferential binding site, which has a specific θ value, and therefore, a specific pseudocontact shift. Further addition of M^+ leads to exchange between the M^+ on the preferred site and those on other locations in the second coordination sphere. Since each M^+ ion has its own θ value and corresponding pseudocontact shift, averaging leads to a decrease in the geometric factor and therefore a decrease in the average pseudocontact

shift. After addition of seven equivalents of M^+, rapid exchange occurs between M^+ in the second coordination sphere and bulk solution, resulting in a decrease in the paramagnetic shift, which asymptotically approaches zero. It was also shown that the relative order of cation competition for $Dy(ppp)_2^{7-}$ is $Ca^{2+} > Mg^{2+} > Li^+ > Na^+ > K^+$. In a follow-up study, Ramasamy et al. (1991) used paramagnetic ion-induced relaxation rate enhancements of ^6Li in adducts of Li^+ with $R(ppp)_2^{7-}$ (R = Dy, Tm) in aqueous solution to show that up to seven Li^+ cations can coordinate to the outer oxygens of the triphosphate ligands. The estimated R^{3+}–Li^+ distances range from 5.1 to 5.9 Å for $[Li^+]/[R(ppp)_2^{7-}]$ ratios of 0.2 to 7. Using the structural model first proposed by Nieuwenhuizen et al. (1985), it was proposed that the water molecule and the oxygen atoms of the central phosphate group of the triphosphate ligands occupy the capping positions of a tricapped trigonal prism, while the oxygen atoms of the terminal phosphate groups occupy the remaining positions (see fig. 30). The principal magnetic axis is proposed to pass through the water molecule, with the preferred site of coordination of M^+ ions to oxygen atoms in the axial site opposite the water molecule. In a later study, based on luminescence lifetime measurements of $Tb(ppp)_2^{7-}$ in D_2O/H_2O solutions, Anson et al. (1987) reported that two water molecules are coordinated to the lanthanide ion. Since terbium is adjacent to dysprosium, they proposed that the shift reagent be formulated as $[Dy(ppp)_2(H_2O)_2]^{7-}$, in which each triphosphate ligand coordinates the lanthanide ion in a terdentate manner, giving a total coordination number of eight. Using ^{31}P LIS data, they determined G values that also place the phosphorus atoms in the equatorial region, with the two water molecules in the axial region. Apart from a different mode of coordination of the ligand, and the addition of one more water molecule to the coordination sphere, their model is structurally similar to that proposed by Nieuwenhuizen et al. (1985). However, based on plots of $1/\delta_{obs}(^{23}Na)$ versus $[Na^+]$, they concluded that only one Na^+ ion is associated with the shift reagent, with a limiting shift of –477 ppm at 25°C, pH 8, which agrees reasonably well with the value (–435 ppm) reported by Chu et al. (1990), taking into account the experimental differences of 5°C in temperature and in pH. Based on the value of G determined by Reilley's method, these workers concluded that the Na^+ ion occupies an axial site opposite the water molecules, binding to the negatively charged carboxylate oxygen atoms.

Although $Dy(ppp)_2^{7-}$ is a very effective shift reagent, Springer notes that it is also quite toxic to animals (Szklaruk et al. 1990, and references therein). In addition to the effects of the equilibrium competitions of the biological metal cations Mg^{2+} and Ca^{2+} with Na^+ for $Dy(ppp)_2^{7-}$, the Springer group proposes that the toxicity is most likely due to irreversible, perhaps enzymatic, degradation of free ligand (from dissociation of $Dy(ppp)_2^{7-}$) *in vivo*. In order to avoid this latter problem, the Springer group synthesized DyL^{5-}, where L^{8-} = *o*-bis((3-(tripolyphosphato)propyl)oxy)benzene anion (fig. 31), which covalently links two triphosphate groups. *In vitro* ^{23}Na NMR experiments showed that DyL^{5-}shifts the ^{23}Na signal upfield about one-third as well as $Dy(ppp)_2^{7-}$, while maintaining approximately the same pH profile as $Dy(ppp)_2^{7-}$ toward binding Na^+, but offers the advantage of less severe competition from Mg^{2+} and Ca^{2+} for the Na^+ binding site. Furthermore, although catalytic amounts of alkaline phosphatase promote hydrolysis of DyL^{5-}, the reaction is not as rapid nor as extensive as the hydrolysis of $Dy(ppp)_2^{7-}$. Preliminary experiments

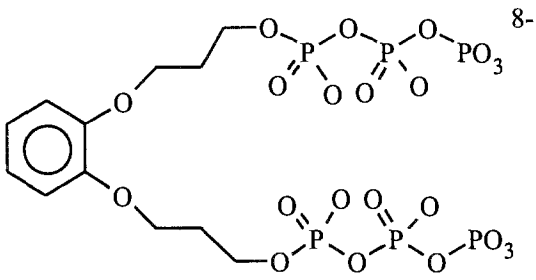

L^{8-} = o-bis((3-(tripolyphosphato)propyl)oxy)benzene

Fig. 31.

with beating rat hearts show that when hearts are perfused at only slightly subnormal flow rates with buffer solutions that are 5.7 mM in DyL^{5-}, they continue to beat and the extracelluar sodium resonance is shifted upfield by 4 ppm.

Pike et al. (1983) reported on the use $R(ca)_3^{6-}$ (R = Dy, Tm; H_3ca = 4-hydroxy-2,6-dicarboxylic acid) as shift reagents for $^{25}Mg^{2+}$, $^{39}K^+$, $^{23}Na^+$, $^{87}Rb^+$ and the ^{14}N resonance of NH_4^+. As observed for most other anionic shift reagents, the dysprosium complex produces upfield shifts and the thulium complex produces downfield shifts. However, the magnitude of the ^{23}Na shift produced by $Dy(ca)_3^{6-}$ is approximately four times smaller than that observed for the $Dy(ppp)_2^{7-}$ complexes under similar conditions. Chu et al. (1984) reported that the shifts produced by complexes derived from $Dy(ttha)^{3-}$ and $Tm(ttha)^{3-}$ (H_6ttha = triethylenetetraminehexaacetic acid) are in the opposite direction as those produced by most other anionic shift reagents. This observation suggests that the sodium ion binding site is in the equatorial region of the dipolar field created in the $R(ttha)^{3-}$ complexes. A limiting value of +159±8 ppm is reported for ^{23}Na shifts induced by $Dy(ttha)^{3-}$, which is significantly smaller than the limiting shift (–435 ppm) reported for the $Dy(ppp)_2^{7-}$ shift reagent (Chu et al. 1990). However, $R(ttha)^{3-}$ reagents offer the advantage that the induced shifts are relatively pH independent in the pH range 5.5–12 and not as sensitive to competition from Ca^{2+} and Mg^{2+} cations. ^{23}Na spectra of the gastrocnemius muscle in a living rat infused with $Dy(ttha)^{3-}$ were recorded at field strengths of 1.5, 4.7, 8.4 T (Balschi et al. 1989; see references therein for other *in vivo* studies using $Dy(ttha)^{3-}$ as a shift reagent). The spectra revealed little change in resolution as the field strength increased, suggesting that the observed line widths are determined primarily by bulk magnetic susceptibility shifts. A comparison of the paramagnetic shifts induced in $^7Li^+$ resonances by the shift reagents $R(ppp)_2^{7-}$, $R(ttha)^{3-}$, $R(nta)_2^{3-}$, $R(dpa)_3^{3-}$, and $R(Hca)_3^{3-}$ (R = Dy, Tm) was reported by Ramasamy et al. (1989). The results of this study show that the $R(ppp)_2^{7-}$ complexes produce the largest shifts, which are highly pH dependent. Sherry et al. (1988) reported on the use of $Dy(dotp)^{5-}$ as an upfield ^{23}Na shift reagent (see sect. 4.2.2 for NMR studies of $R(dotp)^{5-}$ complexes). The shifts induced in the ^{23}Na spectrum of gently packed human red blood cells (80% hematocrit) in the presence of $Dy(dotp)^{5-}$ are about 83% as large as those induced

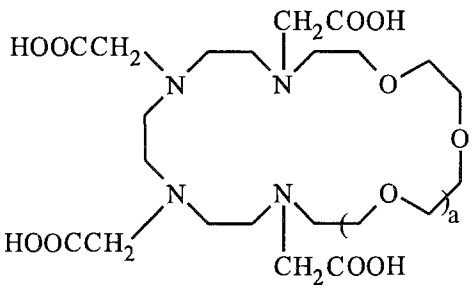

O_3N_4 $(a = 1)$ O_5N_4 $(a = 3)$

O_4N_4 $(a = 2)$ O_6N_4 $(a = 4)$

Fig. 32.

by $Dy(ppp)_2^{7-}$. Although this shift reagent is nearly as effective as $Dy(ppp)_2^{7-}$, it is unfortunately more susceptible to competition from Ca^{2+}. Time-dependent changes in ^{23}Na and ^{31}P spectra of $Dy(dotp)^{5-}$ in the presence of rat abdominal wall muscle were similar to those observed for $Dy(ppp)_2^{7-}$. The latter reagent had been shown to undergo irreversible hydrolysis to inorganic phosphate in this muscle tissue. However, in the case of $Dy(dotp)^{5-}$, the decrease in intensity of the signal due to extracelluar $^{23}Na^+$ that is bound to the shift reagent was shown to be due to sequestering (50%) of the shift reagent by the muscle tissue, rather than degradation of the reagent by hydrolysis.

One of the major problems with alkali metal cation shift reagents is their nonspecificity for a particular biological cation such as Na^+. Removal of calcium ion from solution by complexation and or precipitation of the Ca^{2+}–SR salt may have a detrimental effect upon those tissues which depend upon low Ca^{2+} concentrations for survival. Sherry's group provides an interesting approach to solving the problem of competition between ions by designing shift reagents that are more specific for certain cations (Sink et al. 1990). In their initial attempt, they synthesized a new series of polyoxa tetraaza macrocyclic tetraacetates (fig. 32), in which the tetraaza tetraacetate portion of the molecule is similar to dota and encapsulates the paramagnetic lanthanide ion, leaving a polyoxa crown ether-type cavity available for binding to alkali metal cations. Paramagnetic-induced shifts for aqueous solutions containing alkali metal cations (32 mM) and DyL^- shift reagents (8.1 mM) at pH 7 and 25°C are recorded in table 16. The results show that in all cases the paramagnetic shifts are small and the trends show little correlation with cavity size from $Dy(O_3N_4)^-$ to $Dy(O_6N_4)^-$. A plot of the ^{23}Na shift versus $[Dy(O_4N_4)^-]/[Na^+]$ was fit to a 1:1 binding model, with a Na^+ binding constant of 7.59 M^{-1}. A reasonable explanation for the small shifts is related to the geometrical interaction of the alkali metal cations with the $Dy(O_nN_4)^-$ complexes. Whereas the Na^+ ion is proposed to be located in the axial region of the $Dy(dota)^-$ complex, about 3.9 Å from the dysprosium ion, the preferred sodium ion binding site in $Dy(O_4N_4)^-$, based on molecular mechanics calculations, places the Na^+ ion in the center of the polyoxa cavity, in the equatorial region, roughly 106° from

Table 16
Paramagnetic induced shifts (ppm) induced by DyL^- for alkali metal cations in aqueous solution at pH 7[a] (from Sink et al. 1990)

Shift reagent	Shift			
	Li^+	Na^+	K^+	Cs^+
$Dy(O_3N_4)^-$	0.23	0.12	0.63	2.57
$Dy(O_4N_4)^-$	0.32	0.65	0.63	2.16
$Dy(O_5N_4)^-$	0.18	0.46	0.42	1.92
$Dy(O_6N_4)^-$	0.20	0.42	0.21	1.80

[a] All solutions contained 8.1 mM DyL^- and 32 mM alkali metal cation.

an axis perpendicular to the four nitrogen atoms and 5.3 Å from the dysprosium ion. The authors concluded that although these shift reagents do appear to have a greater selectivity for Na^+ over Ca^{2+}, the paramagnetic shifts induced in the alkali metal cation spectra are too small to make these reagents useful candidates for *in vivo* NMR studies.

7. Concluding remarks

The introduction of high-field NMR instrumentation has diminished the need for lanthanide shift reagents for qualitative spectral simplification of organic molecules. Interest remains in developing new chiral shift reagents for determining enantiomeric excess in asymmetric organic synthesis and for determining the absolute configuration of optically active substrates. Research continues for development of nontoxic shift reagents to study the transport of biologically active cations across cell membranes *in vivo*. With the commercial development of $Gd(dota)^-$ and $Gd(dtpa)^{2-}$ as MRI-relaxation agents, recent NMR studies have focused on paramagnetic complexes that are sterically rigid on the NMR time scale. Structural rigidity is observed in complexes derived from multidentate ligands, in which the denticity of the ligand provides a coordinatively saturated lanthanide ion, or may be imposed by ligands with special binding constraints. Two-dimensional NMR spectra, which aid in spectral assignments and characterization of the dynamics of exchange between stereoisomers, are now routinely recorded for complexes derived from the lighter members of the series (Ce–Eu), as well as those of ytterbium. An improved method of analyzing pseudocontact shifts has been introduced, which uses a linear least-squares fitting of the LIS data to expressions involving elements of the magnetic susceptibility tensor. Furthermore, by using a linear least-squares fitting of the data, it is possible to allow a computer program to permute LIS values over any number of nuclei, thereby determining the assignment of peaks that gives the best fit to the LIS data. Molecular modeling techniques have been combined with analyses of LIS data to obtain three-dimensional structures of complexes in solution. Since geometrical information is obtained only from the pseudocontact shift, the degree to which a structure can be refined using molecular modeling and analysis of LIS data, is

limited to the accuracy of determining the contact shift component of the LIS. Reilley's temperature-independent method is most commonly used to determine the contact shift, but is applicable only for an isostructural series of complexes in which the crystal-field parameters remain constant. However, small variations in geometry due to the lanthanide contraction can lead to relatively large errors in the contact shifts determined by this procedure. Furthermore, there is evidence that the crystal-field coefficients may not be constant across the lanthanide series. A new method of determining contact shifts based on a linear least-squares analysis of the LIS data has been introduced, which eliminates assumptions regarding crystal-field coefficients, but is limited to complexes having axial symmetry and also requires that the complexes be isostructural. Lacking a reliable method for determining contact shifts, one approach for determining a structure in solution is prompted by the strategy introduced by Sessler and coworkers in their NMR study of lanthanide texaphyrin complexes (sect. 4.4.3). An initial LIS analysis can be carried out by selecting only those nuclei having a large pseudocontact to contact shift ratio to define the elements of the susceptibility tensor, e.g., ^{1}H nuclei in a series of complexes, excluding Nd and Eu, having large LIS values. Contact shifts for other nuclei (^{13}C and ^{1}H) in the series of complexes then can be determined as fitting parameters. If the resulting contact shifts are linearly related to the $\langle S_z \rangle$ values for the various lanthanides, then it follows that the components of the susceptibility tensor are likely well-defined. Subsequently, the structure can be refined using molecular mechanics calculations to minimize the agreement factor R. To date, analyses of LIS data for a relatively complete series of complexes have been reported only for complexes derived from dotp (sect. 4.2.2), an amide derivative of dota (sect. 4.4.3), dpa and mdpa (sect. 4.4.1), and tx (sect. 4.4.3). Although the data are limited, these studies prove the potential to use paramagnetic lanthanide ions as probes to determine three-dimensional structures of complexes in solution.

References

Aime, S., and M. Botta, 1990, Inorg. Chim. Acta **177**, 101.

Aime, S., M. Botta and G. Ermondi, 1992a, Inorg. Chem. **31**, 4291.

Aime, S., L. Barbero, M. Botta and G. Ermondi, 1992b, J. Chem. Soc. Dalton Trans., p. 225.

Albertsson, J., 1970, Acta Chem. Scand. **24**, 1213.

Albertsson, J., 1972, Acta Chem. Scand. **26**, 985.

Alsaadi, B.M., F.J.C. Rossotti and R.J.P. Williams, 1980a, J. Chem. Soc. Dalton Trans., p. 2147.

Alsaadi, B.M., F.J.C. Rossotti and R.J.P. Williams, 1980b, J. Chem. Soc. Dalton Trans., p. 2151.

Alsaadi, B.M., F.J.C. Rossotti and R.J.P. Williams, 1980c, J. Chem. Soc. Dalton Trans., p. 597.

Alsaadi, B.M., F.J.C. Rossotti and R.J.P. Williams, 1980d, J. Chem. Soc. Dalton Trans., p. 813.

Anson, S.M., R.B. Homer and P.S. Belton, 1987, Inorg. Chim. Acta **138**, 241.

Arif, A.M., J.D.J. Backer-Dirks, C.J. Gray, F.A. Hart and M.B. Hursthouse, 1987, J. Chem. Soc. Dalton Trans., p. 1665.

Balschi, J.A., S.J. Kohler, J.A. Bittl, C.S. Springer and J.S. Ingwall, 1989, J. Magn. Reson. **83**, 138.

Benetollo, F., A. Polo, G. Bombieri, K.K. Fonda and L.M. Vallarino, 1990, Polyhedron **9**, 1411.

Berliner, L.J., K. Koga, H. Nishikawa and J.E. Scheffler, 1987, Biochemistry **26**, 5769.

Birnbaum, E.R., and S. Stratton, 1973, Inorg. Chem. **12**, 379.

Bleaney, B., 1972, J. Magn. Reson. **8**, 91.
Bombieri, G., F. Benetollo, A. Polo, K.K. Fonda and L.M. Vallarino, 1991, Polyhedron **10**, 1385.
Bovée, W.M.M.J., J.H. Alberts, J.A. Peters and J. Smidt, 1982, J. Am. Chem. Soc. **104**, 1632.
Brittain, H.G., and J.F. Desreux, 1984, Inorg. Chem. **23**, 4459.
Bryden, C.C., C.N. Reilley and J.F. Desreux, 1981, Anal. Chem. **53**, 1418.
Buchler, J.W., A.D. Cian, J. Fischer, M. Kihn-Botulinski, H. Paulus and R. Weiss, 1986, J. Am. Chem. Soc. **108**, 3652.
Buchler, J.W., M. Kihn-Botulinski, J. Löffler and M. Wicholas, 1989, Inorg. Chem. **28**, 3770.
Buchler, J.W., J. Löffler and M. Wicholas, 1992, Inorg. Chem. **31**, 524.
Chin, K.O.A., J.R. Morrow, C.H. Lake and M.R. Churchill, 1994, Inorg. Chem. **33**, 656.
Chu, S.C., M.M. Pike, E.T. Fossel, T.W. Smith, J.A. Balschi and C.S. Springer, 1984, J. Magn. Reson. **56**, 33.
Chu, S.C., H.Z. Qiu, C.S. Springer and A. Wishnia, 1990, J. Magn. Reson. **87**, 287.
Cockerill, A.F., G.L.O. Davies, R.C. Harden and D.M. Rakham, 1973, Chem. Rev. **73**, 553.
Cramer, R.E., and R.B. Maynard, 1978, J. Magn. Reson. **31**, 295.
Cramer, R.E., R. Dubois and K. Seff, 1974, J. Am. Chem. Soc. **96**, 4125.
Cramer, R.E., R. Dubois and C.K. Furuike, 1975, Inorg. Chem. **14**, 1005.
Davis, R.E., and M.R. Willcott, 1972, J. Am. Chem. Soc. **94**, 1744.
Desreux, J.F., 1980, Inorg. Chem. **19**, 1319.
Desreux, J.F., and M.F. Loncin, 1986, Inorg. Chem. **25**, 69.
Desreux, J.F., and C.N. Reilley, 1976, J. Am. Chem. Soc. **98**, 2105.
Donato, H., and R.B. Martin, 1972, J. Am. Chem. Soc. **94**, 4129.
Elgavish, G.A., and J. Reuben, 1976, J. Am. Chem. Soc. **98**, 4755.
Elgavish, G.A., and J. Reuben, 1977, J. Am. Chem. Soc. **99**, 1762.
Evans, D.F., and G.C. de Villardi, 1978, J. Chem. Soc. Dalton Trans., p. 315.
Fonda, K.K., D.L. Smailes, L.M. Vallarino, G. Bombieri, F. Benetollo, A. Polo and L. De Cola, 1993, Polyhedron **12**, 549.
Forsberg, J.H., 1981, in: Gmelin Handbook of Inorganic Chemistry, 8th Ed., Syst. No. 39, Part D4 (Springer, Berlin) ch. 5.
Forsberg, J.H., R.M. Delaney, Q. Zhao, G. Harakas and R. Chandran, 1995, Inorg. Chem. **34**, 3705.
Franklin, S.J., and K.N. Raymond, 1994, Inorg. Chem. **33**, 5794.
Gansow, O.A., and A.R. Kausar, 1983, Inorg. Chim. Acta **72**, 39.
Gansow, O.A., and A.R. Kausar, 1985, Inorg. Chim. Acta **95**, 1.
Gansow, O.A., P.A. Loeffler, R.E. Davis, M.R. Willcott and R.E. Lenkinski, 1973a, J. Am. Chem. Soc. **95**, 3389.
Gansow, O.A., P.A. Loeffler, R.E. Davis, M.R. Willcott and R.E. Lenkinski, 1973b, J. Am. Chem. Soc. **95**, 3392.
Gansow, O.A., D.J. Pruett and K.B. Triplett, 1979, J. Am. Chem. Soc. **101**, 4408.
Geraldes, C.F.G.C., and J.R. Ascenso, 1984, J. Chem. Soc. Dalton Trans., p. 267.
Geraldes, C.F.G.C., M.P.M. Marques and A.D. Sherry, 1987, Inorg. Chim. Acta, **139**, 311.
Geraldes, C.F.G.C., A.M. Urbano, M.C. Alpoim, M.A. Hoefnagel and J.A. Peters, 1991, J. Chem. Soc. Chem. Commun., p. 656.
Geraldes, C.F.G.C., A.D. Sherry and G.E. Kiefer, 1992, J. Magn. Reson. **97**, 290.
Geraldes, C.F.G.C., A.M. Urbano, M.A. Hoefnagel and J.A. Peters, 1993, Inorg. Chem. **32**, 2426.
Goering, H.L., J.N. Eikenberry, G.S. Koermer and C.J. Lattimer, 1974, J. Am. Chem. Soc. **96**, 1493.
Golding, R.M., and M.P. Halton, 1972, Aust. J. Chem. **25**, 2577.
Golding, R.M., and P. Pyykkö, 1973, Mol. Phys. **26**, 1389.
Gupta, R.K., and P. Gupta, 1982, J. Magn. Reson. **47**, 344.
Hawkes, G.E., D. Leibfritz, D.W. Roberts and J.D. Roberts, 1973a, J. Am. Chem. Soc. **95**, 1659.
Hawkes, G.E., C. Marzin, S.R. Johns and J.D. Roberts, 1973b, J. Am. Chem. Soc. **95**, 1661.
Hinckley, C.C., 1969, J. Am. Chem. Soc. **98**, 1331.
Horrocks, W.DeW., 1973, NMR of Paramagnetic Molecules: Principles and Applications (Academic Press, New York, London) ch. 12.
Horrocks, W.DeW., 1974, J. Am. Chem. Soc. **96**, 3022.
Horrocks, W.DeW., 1977, J. Magn. Reson. **26**, 333.
Horrocks, W.DeW., and E.G. Hove, 1978, J. Am. Chem. Soc. **100**, 4386.

Horrocks, W.DeW., and J.P. Sipe, 1972, Science, **177**, 994.

Horrocks, W.DeW., and C.P. Wong, 1976, J. Am. Chem. Soc. **98**, 7157.

Jacques, V., and J.F. Desreux, 1994, Inorg. Chem. **33**, 4048.

Jenkins, B.G., and R.B. Lauffer, 1988a, J. Magn. Reson. **80**, 328.

Jenkins, B.G., and R.B. Lauffer, 1988b, Inorg. Chem. **27**, 4730.

Kabuto, K., and Y. Sasaki, 1984, J. Chem. Soc. Chem. Commun., p. 316.

Kabuto, K., and Y. Sasaki, 1987, J. Chem. Soc. Chem. Commun., p. 670.

Kabuto, K., and Y. Sasaki, 1989, Chem. Lett., p. 385.

Kabuto, K., and Y. Sasaki, 1990, Tetrahedron Lett. **31**, 1031.

Kabuto, K., K. Sasaki and Y. Sasaki, 1992, Tetrahedron Asymmetry **3**, 1357.

Kemple, M.D., B.D. Ray, K.B. Lipkowitz, F.G. Prendergast and B.D.N. Rao, 1988, J. Am. Chem. Soc. **110**, 8275.

Kido, J., Y. Okamoto and H.G. Brittain, 1990, J. Coord. Chem. **21**, 107.

Kido, J., Y. Okamoto and H.G. Brittain, 1991, J. Org. Chem. **56**, 1412.

Komarov, I.V., V.N. Nemykin and N.B. Subbotin, 1993, Appl. Magn. Reson. **4**, 377.

Konami, H., M. Hatano and A. Tajiri, 1989, Chem. Phys. Lett. **160**, 163.

Konings, M.S., W.C. Dow, D.B. Love, K.N. Raymond, S.C. Quay and S.M. Rocklage, 1990, Inorg. Chem. **29**, 1488.

Kullberg, L., and G.R. Choppin, 1977, Inorg. Chem. **16**, 2926.

Lee, L., and B.D. Sykes, 1980, Biophys. J. **32**, 193.

Lisowski, J., J.L. Sessler, V. Lynch and T.D. Mody, 1995, J. Am. Chem Soc. **117**, 2273.

Marsden, B.J., R.S. Hodges and B.D. Sykes, 1989, Biochemistry **28**, 8839.

Ming, L.J., 1993, Magn. Reson. Chem. **31**, S104.

Morishima, I., M. Kurono and Y. Shiro, 1986, J. Biol. Chem. **261**, 9391.

Morrow, J.R., L.A. Buttrey, V.M. Shelton and K.A. Berback, 1992, J. Am. Chem. Soc. **114**, 1903.

Morrow, J.R., S. Amin, C.H. Lake and M.R. Churchill, 1993, Inorg. Chem. **32**, 4566.

Mukidjam, E., S. Barnes and G.A. Elgavish, 1986, J. Am. Chem. Soc. **108**, 7082.

Mukidjam, E., G.A. Elgavish and S. Barnes, 1987, Biochemistry **26**, 6785.

Nieuwenhuizen, M.S., J.A. Peters, A. Sinnema, A.P.G. Kieboom and H. van Bekkum, 1985, J. Am. Chem. Soc. **107**, 12.

Peters, J.A., 1986, J. Magn. Reson. **68**, 240.

Peters, J.A., 1988b, J. Chem. Soc. Dalton Trans., p. 961.

Peters, J.A., 1988c, Inorg. Chem. **27**, 4686.

Peters, J.A., H. van Bekkum and W.M.M.J. Bovée, 1982, Tetrahedron **38**, 331.

Peters, J.A., C.A.M. Vijverberg, A.P.G. Kieboom and H. van Bekkum, 1983, Tetrahedron Lett. **24**, 3141.

Peters, J.A., M.S. Nieuwenhuizen and D.J. Raber, 1985, J. Magn. Reson. **65**, 417.

Peters, J.A., M.S. Nieuwenhuizen and A.P.G. Kieboom, 1988a, J. Chem Soc. Dalton Trans., p. 717.

Pike, M.M., and C.S. Springer, 1982, J. Magn. Reson. **46**, 348.

Pike, M.M., D.M. Yarmush, J.A. Balschi, R.E. Lenkinski and C.S. Springer, 1983, Inorg. Chem. **22**, 2388.

Pinkerton, A.A., and W.L. Earl, 1978, J. Chem. Soc. Dalton Trans., p. 267.

Pinkerton, A.A., M. Rossier and S. Spiliadis, 1985, J. Magn. Reson. **64**, 420.

Raber, D.J., C.M. Janks, M.D. Johnston and N.K. Raber, 1981, Org. Magn. Reson. **15**, 57.

Ramasamy, R., M.C. Espanol, K.M. Long, D.M. de Freitas and C.F.G.C. Geraldes, 1989, Inorg. Chim. Acta **163**, 41.

Ramasamy, R., D.M. de Freitas, C.F.G.C. Geraldes and J.A. Peters, 1991, Inorg. Chem. **30**, 3188.

Reilley, C.N., B.W. Good and J.F. Desreux, 1975, Anal. Chem. **47**, 2110.

Reilley, C.N., B.W. Good and R.D. Allendoerfer, 1976, Anal. Chem. **48**, 1446.

Reuben, J., 1973, Progr. NMR Spectosc. **9**, 1.

Reuben, J., 1976, J. Am. Chem. Soc. **98**, 3726.

Reuben, J., 1979b, J. Chem. Soc. Chem. Commun., p. 68.

Reuben, J., 1980, J. Am. Chem. Soc. **102**, 2232.

Reuben, J., 1982, J. Magn. Reson. **50**, 233.

Reuben, J., and G.A. Elgavish, 1979a, in: Handbook on the Physics and Chemistry of Rare Earths, Vol. 4, eds K.A. Gschneidner Jr and L. Eyring (North-Holland, Amsterdam) ch. 38.

Richardson, M.F., S.M. Rothstein and W.K. Li, 1979, J. Magn. Reson. **36**, 69.

Sessler, J.L., T.D. Mody, G.W. Hemmi and V. Lynch, 1993a, Inorg. Chem. **32**, 3175.

Sessler, J.L., T.D. Mody, G.W. Hemmi, V. Lynch, S.W. Young and R.A. Miller, 1993b, J. Am. Chem. Soc. **115**, 10368.

Sherry, A.D., and C.F.G.C. Geraldes, 1989, in: Lanthanide Probes in Life, Chemical and Earth Sciences: Theory and Practice, eds J.-C.G. Bünzli and G.R. Choppin (Elsevier, Amsterdam) ch. 4.

Sherry, A.D., C.A. Stark, J.R. Ascenso and C.F.G.C. Geraldes, 1981, J. Chem. Soc. Dalton Trans., p. 2078.

Sherry, A.D., M. Singh and C.F.G.C. Geraldes, 1986, J. Magn. Reson. **66**, 511.

Sherry, A.D., C.R. Malloy, F.M.H. Jeffrey, W.P. Cacheris and C.F.G.C. Geraldes, 1988, J. Magn. Reson. **76**, 528.

Sherry, A.D., R. Zarzycki and C.F.G.C. Geraldes, 1994, Magn. Reson. Chem. **32**, 361.

Siddall, T.H., and W.E. Stewart, 1969, Inorg. Nucl. Chem. Letters **5**, 421.

Sievers, R.E., ed., 1973, Nuclear Magnetic Shift Reagents (Academic Press, New York).

Sink, R.M., D.C. Buster and A.D. Sherry, 1990, Inorg. Chem. **29**, 3645.

Smith, P.H., Z.E. Reyes, C.W. Lee and K.N. Raymond, 1988, Inorg. Chem. **27**, 4154.

Smith, P.H., J.R. Brainard, D.E. Morris, G.D. Jarvinen and R.R. Ryan, 1989, J. Am. Chem. Soc. **111**, 7437.

Southwood-Jones, R.V., and A.E. Merbach, 1978, Inorg. Chim. Acta **30**, 77.

Spiliadis, S., and A.A. Pinkerton, 1982, J. Chem. Soc. Dalton Trans., p. 1815.

Spiliadis, S., and A.A. Pinkerton, 1983a, Inorg. Chim. Acta **75**, 125.

Spiliadis, S., A.A. Pinkerton and D. Schwarzenbach, 1983b, Inorg. Chim. Acta **75**, 115.

Spirlet, M.R., J. Rebizant, J.F. Desreux and M.F. Loncin, 1984a, Inorg. Chem. **23**, 359.

Spirlet, M.R., J. Rebizant, M.F. Loncin and J.F. Desreux, 1984b, Inorg. Chem. **23**, 4278.

Stainer, M.V.R., and J. Takats, 1982, Inorg. Chem. **21**, 4050.

Stainer, M.V.R., and J. Takats, 1983, J. Am. Chem. Soc. **105**, 410.

Stezowski, J.J., and J.L. Hoard, 1984, Isr. J. Chem. **24**, 323.

Stout, E.W., and H.S. Gutowsky, 1976, J. Magn. Reson. **24**, 389.

Szklaruk, J., J.F. Marecek, A.L. Springer and C.S. Springer, 1990, Inorg. Chem. **29**, 660.

van Duynhoven, J.P.M., I.M.A. Nooren, D.W. Swinkels, P.J.M. Folkers, B.J.M. Harmsen, R.N.H. Konings, G.J. Tesser and C.W. Hilbers, 1993, Eur. J. Biochem. **216**, 507.

Vijverberg, C.A.M., J.A. Peters, A.P.G. Kieboom and H. van Bekkum, 1980, Rec. Trav. Chim. Pays-Bas **99**, 403.

Wenzel, T.J., 1987, NMR Shift Reagents (CRC Press, Boca Raton, FL).

Wenzel, T.J., M.S. Bogyo and E.L. Lebeau, 1994, J. Am. Chem. Soc. **116**, 4858.

Whitesides, G.M., and D.W. Lewis, 1970, J. Am. Chem. Soc. **92**, 6979.

Willcott, M.R., R.E. Lenkinski and R.E. Davis, 1972, J. Am. Chem. Soc. **94**, 1742.

Yokoyama, S., T. Oida, S. Uesugi, M. Ikehara and T. Miyazawa, 1983, Bull. Chem. Soc. Jpn. **56**, 375.

Handbook on the Physics and Chemistry of Rare Earths
Vol. 23
edited by K.A. Gschneidner, Jr. and L. Eyring

Chapter 154

ANTENNA EFFECT IN ENCAPSULATION COMPLEXES OF LANTHANIDE IONS

NANDA SABBATINI, MASSIMO GUARDIGLI AND ILSE MANET
Dipartimento di Chimica "G. Ciamician", Università di Bologna, Via Selmi 2, 40126 Bologna, Italy

Contents

Symbols

$biqO_2$	3,3′-biisoquinoline-*N,N′*-dioxide
bpy	2,2′-bipyridine
$bpyO_2$	2,2′-bipyridine-*N,N′*-dioxide
FIAs	fluoroimmunoassays
$k_{nr}(OH)$	rate constant of the nonradiative decay process via vibronic coupling with solvent OH oscillators
k_{nr}(other vibr.)	rate constant of the nonradiative decay process via vibronic coupling with oscillators different from solvent OH oscillators
$k_{nr}(T)$	rate constant of the nonradiative thermally activated decay process
k_r	radiative decay rate constant
LMCT	ligand-to-metal charge transfer
n	number of solvent molecules coordinated to the metal ion
phen	1,10-phenanthroline
TR-FIAs	time-resolved fluoroimmunoassays
ε_{max}	maximum molar absorption coefficient value of an absorption band
$\eta_{en.tr.}$	ligand-to-metal energy-transfer efficiency
η_{isc}	intersystem-crossing efficiency
$\eta_{singlet \rightarrow triplet}$	singlet → triplet energy-transfer efficiency
$\eta_{triplet \rightarrow metal}$	triplet → metal energy-transfer efficiency
λ_{max}	wavelength corresponding to the maximum molar absorption coefficient
$\tau_D^{300\,K}$	lifetime in deuterated solvent at 300 K
$\tau_D^{77\,K}$	lifetime in deuterated solvent at 77 K
$\tau_H^{300\,K}$	lifetime in hydrogenated solvent at 300 K
τ_H^{77K}	lifetime in hydrogenated solvent at 77 K
Φ	metal luminescence quantum yield upon ligand excitation

Φ_D	metal luminescence quantum yield upon ligand excitation in deuterated solvent	Φ_M	metal luminescence quantum yield upon excitation in the metal emitting state
Φ_H	metal luminescence quantum yield upon ligand excitation in hydrogenated solvent		

1. Introduction

In this chapter we will discuss Eu^{3+} and Tb^{3+} complexes obtained upon encapsulation of these ions by cage-type ligands exhibiting, in solution, metal luminescence upon ligand excitation. Recent developments in the field of supramolecular chemistry revealed that cage-type ligands are capable of encapsulating lanthanide ions, giving rise to the formation of complexes stable in solution. This is of particular interest since, as is known, lanthanide ions do not exhibit strong coordination ability towards conventional ligands, especially in aqueous solution where water molecules compete efficiently to occupy the coordination sites of the metal ion. If the cage-type ligand incorporates chromophoric groups, it can play the role of *antenna* in the complex by absorbing light and transferring the excitation energy to the metal ion which eventually emits (fig. 1)

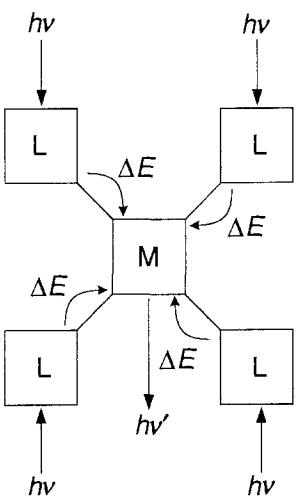

Fig. 1. Schematic representation of the *antenna effect* in the complex: light is absorbed by the chromophores of the ligand and electronic energy is transferred to the luminescent metal ion (Alpha et al. 1990).

(Sabbatini et al. 1993). An efficient *antenna* is expected to lead to metal luminescence much more intense than that obtained upon metal excitation since lanthanide ions are characterized by very low molar absorption coefficients. These complexes can be considered light-conversion molecular devices because they are able to transform light absorbed by the ligand into light emitted by the ions via an intramolecular energy transfer (Balzani and Scandola 1991).

Our study focuses on complexes of Eu^{3+} and Tb^{3+} because among the lanthanide ions these show intense emission in the visible and possess long-lived emitting states. These characteristics render Eu^{3+} and Tb^{3+} complexes important for time-resolved luminescence bioaffinity assays, the application we are particularly interested in, since they allow a sensitivity enhancement of the assay via minimizing interference of the short-lived, background luminescence in the UV of the biological species and of scattered excitation light. In sect. 2 of this chapter we will illustrate some general concepts of supramolecular chemistry dealing with the encapsulation of cations by cage-type ligands. In sect. 3 we will give an overview of the processes involving electronically excited states, which occur in some Eu^{3+} and Tb^{3+} complexes of cage-type ligands after light absorption. In sect. 4 these complexes will be presented in different classes defined by the nature of the ligands. Further, we discuss in sect. 5 the complexes from the point of view of the ligand absorption, the ligand-to-metal energy transfer, the metal luminescence efficiency and, finally, the metal luminescence intensity. The last section treats the applications of Eu^{3+} and Tb^{3+} complexes in fluoroimmunoassays and DNA hybridization assays.

2. Encapsulation of metal ions

In this section we summarize the fundamentals of supramolecular chemistry dealing with encapsulation of cations by cage-type ligands (Lehn 1985, 1988).

Generally, a supermolecule is thought of as a species containing different partners, the *molecular receptor* and the *substrate,* the component whose binding is looked for. The formation of a supermolecule depends on a process called *molecular recognition* which consists in selective binding of the substrate by the receptor on the basis of the information stored in the interacting components. Binding of substrate by receptor to form the supermolecule involves intermolecular, noncovalent bonds driven by electrostatic forces, van der Waals forces, hydrogen bonds, and so on. Molecular recognition is possible only if the two species are complementary in size, shape, and binding sites. From this point of view, supramolecular chemistry may be considered generalized coordination chemistry, since it aims at extending to all kinds of substrates, i.e., cationic, anionic, and neutral species of inorganic, organic, and biological nature. Natural and synthetic ligands consisting of macrocycles and macropolycycles are revealed suitable for the complexation of alkali, alkaline-earth, and lanthanide ions. Pedersen's macrocyclic polyethers (fig. 2) combine the complexation ability of the ether functions towards cations of the hard type and the capacity of ion enclosure by the macrocycle (Pedersen 1988). Lehn's macrobicyclic ligands such as the cryptands shown in fig. 2 form even more stable complexes with several cations (Lehn and Sauvage 1975). The cryptates have stability constants several orders of magnitude higher than those of the complexes of macrocyclic ligands. The strong complexation ability of the cryptands results from their macrobicyclic nature giving rise to a three-dimensional cavity well fitted for binding of cations. This type of complexation defines the *cryptate effect* characterized by high stability and selectivity, slow exchange rates, and efficient shielding of the ion from the environment.

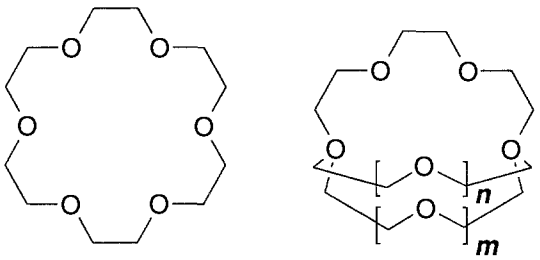

18C6 2.1.1: $n = 1, m = 1$
2.2.1: $n = 1, m = 2$
2.2.2: $n = 2, m = 2$

Fig. 2. Schematic representation of the 18C6 crown ether and the 2.1.1, 2.2.1, and 2.2.2 cryptands.

The cryptands show pronounced selectivity as a result of size complementarity between the cation and the intramolecular cavity of the ligand. For example, as the strands of the cryptands are lengthened from 2.1.1 to 2.2.2 (fig. 2) the most strongly bound ions are Li^+, Na^+, and K^+, respectively. Cryptand 2.2.2 also displays a higher selectivity for Sr^{2+} and Ba^{2+} than for Ca^{2+}. Another important aspect of the encapsulation of cations is the amount of *preorganization* of the ligand (Cram 1988). Crystal structures of cryptands (Weiss et al. 1970, Metz et al. 1973) and crown ethers (Dobler and Phizackerly 1974a,b, Dobler et al. 1974, Dunitz and Seiler 1974, Dunitz et al. 1974, Seiler et al. 1974) show that they contain neither cavities nor convergently arranged binding sites prior to cation complexation. Other types of cage-type ligands, e.g., spherands, are completely preorganized after their synthesis for the cation complexation (Trueblood et al. 1981). Comparison of the binding free energies for complexation of different cations by several types of cage-type ligands led to the conclusion that the more highly hosts and guests are organized for binding and the lower their solvation is prior to complexation, the more stable their complexes will be.

Also for d-block metal ions, encapsulation led to several innovations related to, e.g., the syntheses and properties of their complexes (Balzani and Scandola 1991). These metal ions can govern *template* syntheses of cage-type complexes by organizing around themselves some organic fragments according to the coordination symmetry required by the cation. For example, Ni(II) promoted syntheses of tetraazamacrocycles by exerting both kinetic and thermodynamic effects and remained firmly trapped inside the ring. Demetallation and recovery of the free macrocycle could only be achieved under drastic conditions. Interestingly, several properties of cage-type complexes are significantly modified with respect to similar, uncaged complexes. For example, ligand dissociation requiring extensive nuclear motions is prevented. This is clearly illustrated by the following case. $[Co(sep)]^{3+}$ (fig. 3) (Creaser et al. 1977) and $[Co(NH_3)_6]^{3+}$ have the same composition and symmetry of the first coordination sphere, but show a completely different behavior upon excitation in the ligand-to-metal charge-transfer (LMCT) bands and one-electron reduction in pulse radiolysis experiments. $[Co(NH_3)_6]^{3+}$ undergoes ligand dissociation which results in decomposition of the complex, while $[Co(sep)]^{3+}$

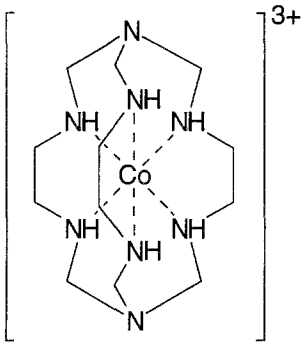

[Co(sep)]$^{3+}$

Fig. 3. Schematic representation of the $[Co(sep)]^{3+}$ complex (Creaser et al. 1977).

gives rise to $[Co(sep)]^{2+}$. This is explained considering that the lability of $[Co(NH_3)_6]^{2+}$ is overcome in the cage-type complex because the coordinating amino groups cannot be removed.

In conclusion, the properties illustrated above show that encapsulation of cations by cage-type ligands can give rise to complexes exhibiting a variety of new properties. Nowadays, these complexes are widely studied because of their importance for applications. These aspects characterize the study presented here, which, as described in sect. 1, focuses on obtaining intense luminescence in solution upon encapsulation of the Eu^{3+} and Tb^{3+} ions by suitable cage-type ligands and on the applications one can develop on the basis of this luminescence.

3. Light conversion in Eu^{3+} and Tb^{3+} complexes

As mentioned in sect. 1, encapsulation of the Eu^{3+} and Tb^{3+} ions by cage-type ligands incorporating chromophoric groups aims at the design of light-conversion molecular devices built up of distinct absorbing (ligand) and emitting (metal ion) components (fig. 1) (Alpha et al. 1990, Sabbatini et al. 1993). In these systems, *ligand-to-metal energy transfer* gives rise to metal luminescence (fig. 4). The metal emissions we consider are those originating from the Eu^{3+} $^5D_0$ and Tb^{3+} $^5D_4$ excited states because they are the most intense and these states possess the longest lifetimes. In this light-conversion process, the quantities that contribute to the metal luminescence intensity are (i) the efficiency of the ligand absorption, (ii) the efficiency of the ligand-to-metal energy transfer, and (iii) the efficiency of the metal luminescence.

It must be pointed out that the experimentally determined quantities are the molar absorption coefficients and the metal luminescence quantum yield upon ligand excitation (hereafter indicated as quantum yield). The molar absorption coefficients of the ligand in the complex are related to the efficiency of the absorption and the quantum yield is

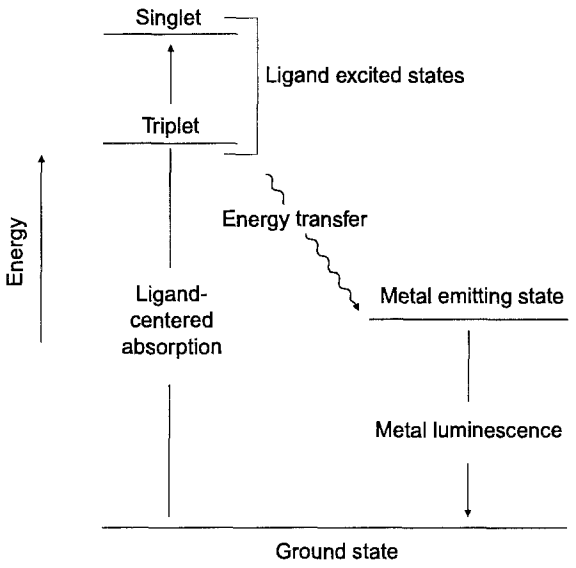

Fig. 4. Schematic representation of the conversion of absorbed light into emitted light in Eu^{3+} and Tb^{3+} complexes.

proportional to the efficiencies of both the ligand-to-metal energy transfer and the metal luminescence.

The efficiency of the ligand-to-metal energy transfer, $\eta_{\text{en.tr.}}$, can be obtained from the ratio between the quantum yield upon ligand excitation, Φ, and the quantum yield upon metal excitation, Φ_{M}:

$$\eta_{\text{en.tr.}} = \frac{\Phi}{\Phi_{\text{M}}}. \tag{1}$$

If Φ_{M} cannot be measured, it may be substituted, as in eq. (2), by the efficiency of the metal luminescence, η_{M}, obtained from eq. (3). Since in this study the radiative and nonradiative rate constants are calculated from the experimental lifetimes, eq. (3) may be replaced by eq. (4) on the assumption that the decay of the metal emitting state in D_2O at 77 K is purely radiative:

$$\eta_{\text{en.tr.}} = \frac{\Phi}{\eta_{\text{M}}}, \qquad \eta_{\text{M}} = \frac{k_{\text{r}}}{k_{\text{r}} + k_{\text{nr}}}, \qquad \eta_{\text{M}} = \frac{\tau_{\text{exp.}}}{\tau_{\text{D}}^{77\,\text{K}}}. \tag{2,3,4}$$

It must be pointed out that in the presence of equilibria involving the metal emitting state and other excited states which decay to the ground state, eq. (4) is not valid and substitution of $\tau_{\text{exp.}}/\tau_{\text{D}}^{77\,\text{K}}$ for η_{M} in eq. (2) gives only a lower limiting value of $\eta_{\text{en.tr.}}$. Let us now discuss the type of ligand excited state involved in the energy transfer. Ligand absorption causes population of the ligand singlet excited states which deactivate to the ligand triplet excited states via intersystem crossing. In principle, both singlet and triplet ligand excited states may be involved in the energy transfer to the metal ion. It is known,

however, that the lifetimes of the singlet excited states of aromatic compounds like the ligand chromophores presented in this study are of the order of 10^{-9} s so that energy transfer processes from these states should be very fast (rate constants greater than 10^9 s^{-1}) in order to be effective. The triplet excited states of aromatic systems have much longer lifetimes and therefore, more than the singlet excited states, are expected to be involved in the energy transfer to the metal ion. Therefore, it is interesting to know the efficiency of the triplet → metal energy transfer, $\eta_{\text{triplet} \rightarrow \text{metal}}$, because it may reflect the ligand–metal interaction. The involvement of a ligand triplet excited state in the ligand-to-metal energy transfer was proved experimentally only for the Tb^{3+} complex of ligand **2**, for which $\eta_{\text{triplet} \rightarrow \text{metal}}$ was measured (sect. 5.2). The relationship between $\eta_{\text{en.tr.}}$ and $\eta_{\text{triplet} \rightarrow \text{metal}}$ is expressed by

$$\eta_{\text{en.tr.}} = \eta_{\text{singlet} \rightarrow \text{triplet}} \eta_{\text{triplet} \rightarrow \text{metal}}, \tag{5}$$

where $\eta_{\text{singlet} \rightarrow \text{triplet}}$ is the efficiency of singlet → triplet conversion in the complex.

In the absence of decay processes of the ligand singlet excited state to excited states different from the ligand triplet excited state, $\eta_{\text{singlet} \rightarrow \text{triplet}}$ is at least equal to the intersystem crossing efficiency of the free ligand, η_{isc}, considering the heavy atom effect. When in the complex the singlet excited state undergoes deactivation processes related to the presence of the metal, $\eta_{\text{singlet} \rightarrow \text{triplet}}$ may be lower than η_{isc} of the ligand, thus giving a lower limiting value of $\eta_{\text{en.tr.}}$ if $\eta_{\text{singlet} \rightarrow \text{triplet}}$ is substituted by η_{isc} in eq. (5).

Now, we discuss the metal luminescence efficiency in the complex on the basis of the radiative and nonradiative decay processes of the Eu^{3+} $^5D_0$ and Tb^{3+} $^5D_4$ emitting states lying at 17 260 cm^{-1} and 20 400 cm^{-1}, respectively. According to the theory on nonradiative transitions in lanthanide complexes (Reisfeld 1975, Carnall 1979, Strek 1982), nonradiative decay between various states may occur by coupling of the electronic levels of the lanthanide ion with suitable vibrational modes of the coordination environment. The efficiency of these processes depends on the energy gap between the electronic levels involved and the vibrational energy of the oscillators (Reisfeld 1975, Freed 1976, Reisfeld and Jørgensen 1977, Carnall 1979). When lanthanide ions coordinate solvents containing high-energy OH oscillators nonradiative deactivation takes place via vibronic coupling with their vibrational states (Haas and Stein 1971, Stein and Wurzberg 1975). If the OH oscillators are replaced by the low-frequency OD ones, this deactivation process becomes much less efficient. By carrying out experiments in H_2O and D_2O solutions, Horrocks and Sudnick (1979, 1981) have shown that for the Eu^{3+} and Tb^{3+} complexes the number, n, of water molecules coordinated to the metal ion is given, with an estimated uncertainty of 0.5, by

$$n = q\left(\frac{1}{\tau_{\text{H}}} - \frac{1}{\tau_{\text{D}}}\right), \tag{6}$$

where τ_{H} and τ_{D} are the experimental lifetimes (in ms) of the Eu^{3+} $^5D_0$ and Tb^{3+} $^5D_4$ emitting states (hereafter shortly referred to as lifetimes) in H_2O and D_2O, and q is 1.05

and 4.2 for the Eu^{3+} and Tb^{3+} compounds, respectively. The q values show that vibronic coupling is more efficient for Eu^{3+} than Tb^{3+}, as expected on the basis of the energy gap between the emitting state and the highest level of the ground state multiplet (12 260 cm^{-1} and 14 400 cm^{-1} for Eu^{3+} and Tb^{3+}, respectively).

On the assumption that methanol behaves like half a water molecule, Holz et al. (1991) have proposed the use of the following equation to determine the number of coordinated methanol molecules:

$$n = r\left(\frac{1}{\tau_{\mathrm{MeOH}}} - \frac{1}{\tau_{\mathrm{MeOD}}}\right), \tag{7}$$

where τ_{MeOH} and τ_{MeOD} are the experimental lifetimes (in ms) of the metal emitting states in MeOH and MeOD and r is 2.1 and 8.4 for the Eu^{3+} and Tb^{3+} compounds, respectively.

The emitting state may also deactivate nonradiatively via thermally activated crossing to short-lived, upper-lying excited states of other configurations (e.g., LMCT states for the Eu^{3+} complexes) (Blasse 1979), which decay nonradiatively to the ground state.

Taking into account the radiative and nonradiative deactivation processes described above, the overall decay rate constant of the emitting state of the metal ion can be expressed as

$$k = \frac{1}{\tau} = k_{\mathrm{r}} + k_{\mathrm{nr}} + k_{\mathrm{nr}}(T), \tag{8}$$

where k_{r} is the radiative rate constant, and k_{nr} and $k_{\mathrm{nr}}(T)$ are the nonradiative temperature independent and temperature dependent decay rate constants, respectively.

In OH-containing solvents the most important contribution to k_{nr} comes from the vibronic coupling with the high-energy OH oscillators. The overall decay rate constant can thus be rewritten as

$$k = \frac{1}{\tau} = k_{\mathrm{r}} + k_{\mathrm{nr}}(T) + k_{\mathrm{nr}}(\mathrm{OH}) + k_{\mathrm{nr}}(\text{other vibr.}), \tag{9}$$

where the term k_{nr}(other vibr.) accounts for the nonradiative decay via vibronic coupling with vibrations different from those of the OH oscillators. The decay rate constants may be obtained from the lifetimes in hydrogenated (τ_{H}) and deuterated (τ_{D}) solvents at different temperatures. On the basis of eq. (9), assuming that the term k_{nr}(other vibr.) is negligible and the coupling with the OD oscillators is completely inefficient, and recalling the previous assumption on $\tau_{\mathrm{D}}^{77\,\mathrm{K}}$, the radiative rate constant k_{r} is given by

$$k_{\mathrm{r}} = \frac{1}{\tau_{\mathrm{D}}^{77\,\mathrm{K}}} \tag{10}$$

and the nonradiative rate constants $k_{\mathrm{nr}}(T)$ and $k_{\mathrm{nr}}(\mathrm{OH})$ at room temperature (hereafter indicated by 300 K) are given by

$$k_{\mathrm{nr}}(T) = \frac{1}{\tau_{\mathrm{D}}^{300\,\mathrm{K}}} - \frac{1}{\tau_{\mathrm{D}}^{77\,\mathrm{K}}}, \qquad k_{\mathrm{nr}}(\mathrm{OH}) = \frac{1}{\tau_{\mathrm{H}}^{300\,\mathrm{K}}} - \frac{1}{\tau_{\mathrm{D}}^{300\,\mathrm{K}}}. \tag{11, 12}$$

When the emitting state is in equilibrium with other excited states a more complex, non-exponential decay is expected, but an exponential decay is generally used in the first

approximation. It must be pointed out that in the presence of an equilibrium eq. (11) does not give $k_{nr}(T)$, but a number which reflects the effect of the equilibrium on the decay of the metal emitting state (sect. 5.3).

4. Eu^{3+} and Tb^{3+} complexes of cage-type ligands

In this section we review some photophysical properties of Eu^{3+} and Tb^{3+} complexes of cage-type ligands. In the following, the complexes are named by formulas consisting of the symbol of the metal ion followed by the number used for the ligand. The complexes are presented in different classes defined by the nature of the ligand. The different classes are schematized in fig. 5.

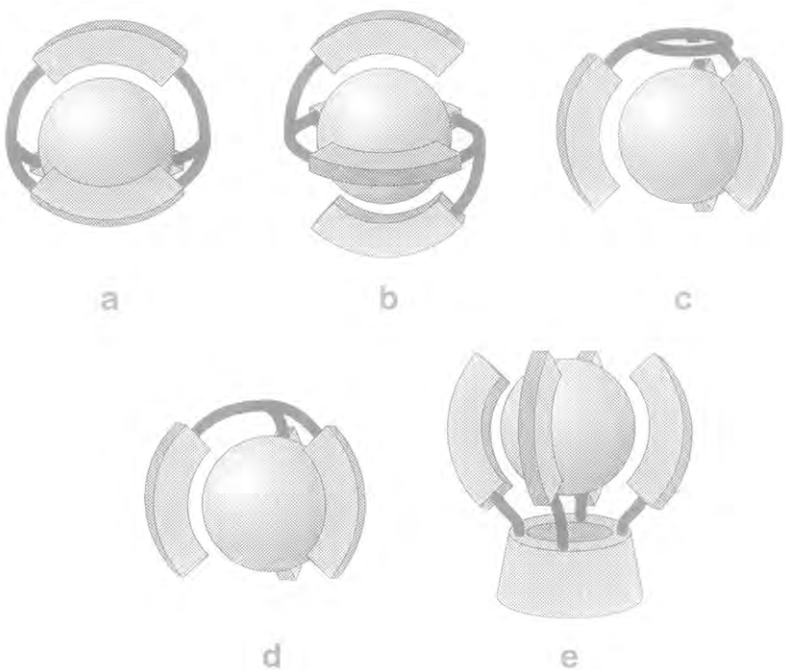

Fig. 5. Schematic representation of different classes of Eu^{3+} and Tb^{3+} complexes with encapsulating ligands: (a) cryptates; (b, c) complexes of branched-macrocyclic ligands; (d) podates; (e) complexes of functionalized calixarenes.

4.1. *Cryptates*

Figure 6 shows schematically the ligands of the Eu^{3+} and Tb^{3+} cryptates examined. Some photophysical data and the number of coordinated solvent molecules of these complexes are gathered in table 1.

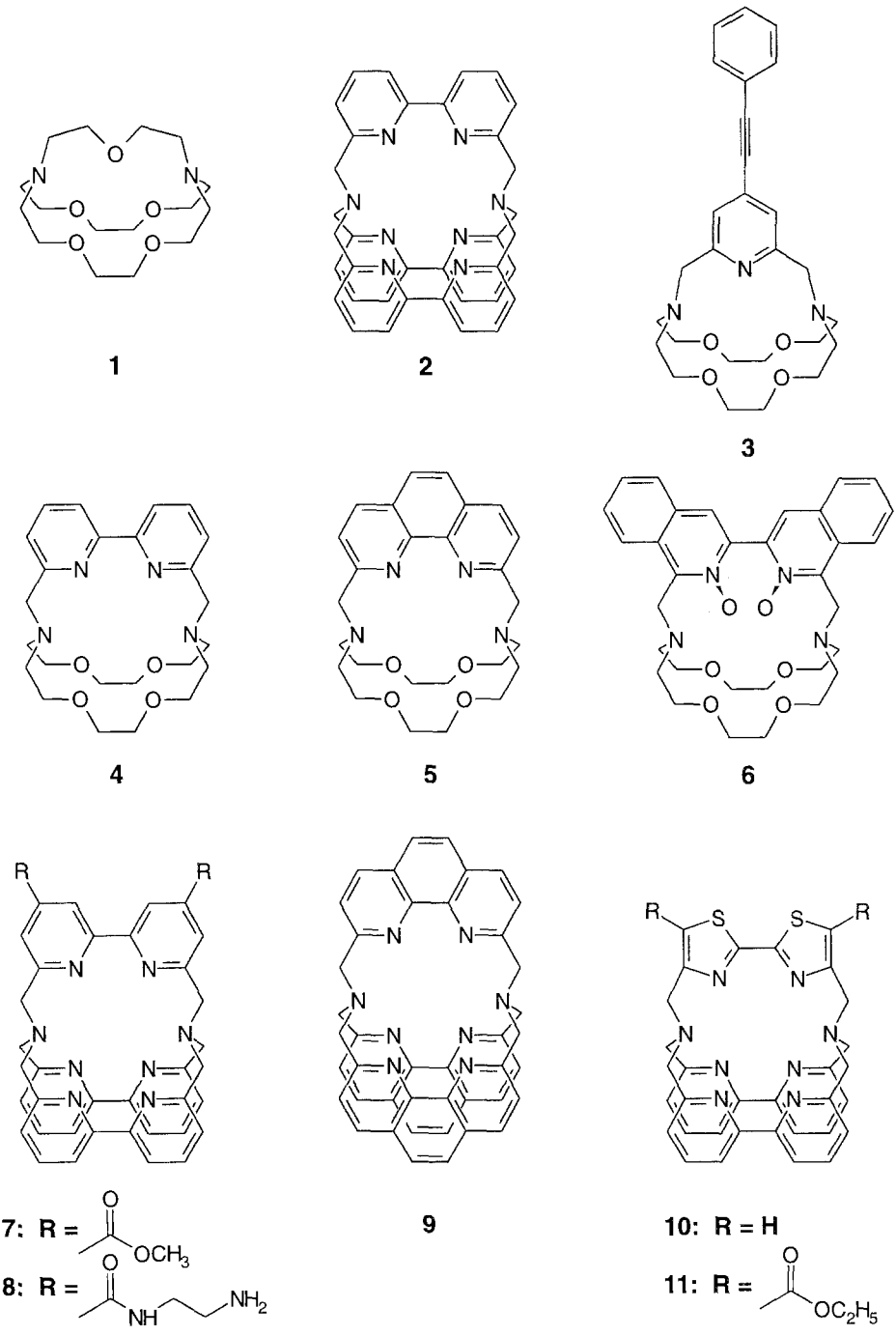

Fig. 6. Schematic representation of the ligands of the cryptates examined.

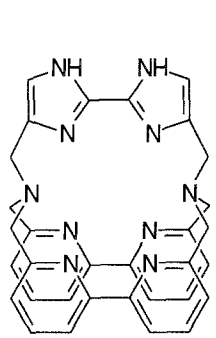

12

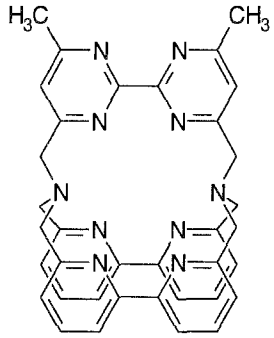

13

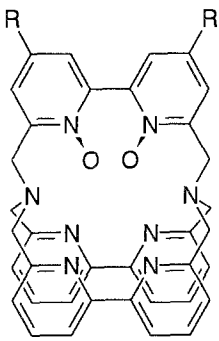

14: R = H

15: R = 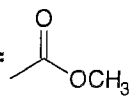

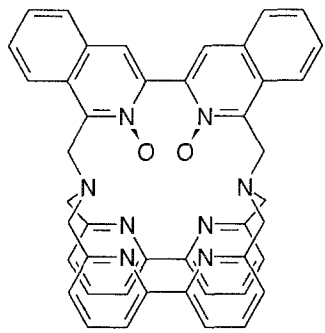

16

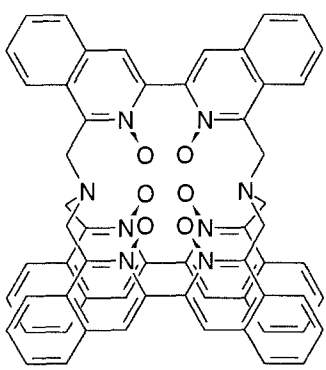

17

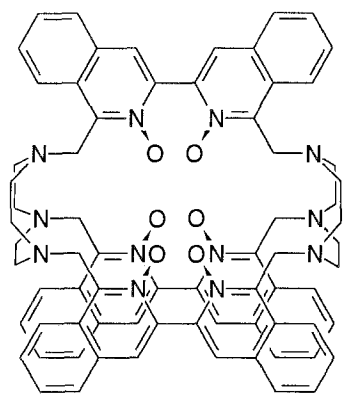

18

Fig. 6 (continued).

Table 1
Photophysical data and number of solvent molecules coordinated to the metal ion for some Eu^{3+} and Tb^{3+} cryptates

Compound	Solvent	Absorption		Emission[a]						n[b]	Reference
		λ_{max} (nm)	ε_{max} ($M^{-1} cm^{-1}$)	$\tau_H^{300\,K}$ (ms)	$\tau_D^{300\,K}$ (ms)	$\tau_H^{77\,K}$ (ms)	$\tau_D^{77\,K}$ (ms)	$\Phi_H^{300\,K}$	$\Phi_D^{300\,K}$		
Eu**1**	H_2O	298	111[c]	0.22	0.64	0.34	1.2		0.003	3.1	Sabbatini et al. (1984)
Tb**1**	H_2O	368	~0.3[d]	1.3	3.1	1.3	3.1	0.3		1.9	Sabbatini et al. (1986)
Eu**2**	H_2O	303	28000	0.34	1.7	0.81	1.7	0.02	0.10	2.5	Alpha et al. (1990)
Tb**2**	H_2O	304	29000	0.33	0.43	1.7	3.8	0.03	0.03	3.0	Alpha et al. (1990)
Eu**4**[e]	H_2O			0.41				>0.01			Alpha et al. (1987b)
Tb**4**[e]	H_2O			0.72				>0.01			Alpha et al. (1987b)
Eu**5**[f]	H_2O			0.27				>0.01			Alpha et al. (1987b)
Eu**6**[g]	CH_3CN			0.70[h]				0.17[h]			Pietraszkiewicz et al. (1993)
				0.62[i]				0.057[i]			
Eu**7**	H_2O	305	26000	0.35	1.5	0.73	1.5	0.02	0.08	2.3	Guardigli (1993)
Eu**14**	H_2O	304	20000	0.46	1.15	1.2	1.3	0.15	0.30	1.4	Prodi et al. (1991)
Eu**15**	H_2O	306	17000	0.40	0.70	0.80	1.1	0.09	0.17	1.1	Sabbatini et al. (1993)
Eu**16**	H_2O	304	20000	0.39	0.66	1.0	1.1	0.20	0.30	1.1	Prodi et al. (1991)
Eu**18**[g]	CH_3CN			0.14				0.001			Pietraszkiewicz et al. (1993)

[a] Excitation in the ligand at the λ_{max} values indicated in this table, unless otherwise noted. The lifetimes are measured in correspondence with the $^5D_0 \rightarrow {}^7F_2$ and $^5D_4 \rightarrow {}^7F_5$ emissions for Eu^{3+} and Tb^{3+}, respectively.
[b] Calculated using eq. (6).
[c] LMCT absorption.
[d] Metal-centered absorption.
[e] Excitation at 310 nm.
[f] Excitation at 280 nm.
[g] Excitation at 337 nm.
[h] Counterion $CF_3SO_3^-$.
[i] Counterion Cl^-.

Cryptands containing polyoxyethylene chains as the 2.2.1 cryptand **1** can be considered three-dimensional analogues of crown ethers, and were originally designed for complexation of alkali metal cations (Lehn 1985, 1988). The complexes of these ligands, called cryptates, showed a substantial gain in stability and selectivity in comparison with complexes of related non-cryptand ligands, which has been attributed to the so-called *cryptate effect* (sect. 2). Due to the similarities between the alkali cations and the trivalent lanthanide ions it is not surprising that ligand **1** formed stable complexes with the latter ions as well. These complexes presented important characteristics like kinetic inertness in water and efficient shielding of the metal ion from solvent molecules. The first photophysical studies on luminescent Eu^{3+} and Tb^{3+} complexes of cage-type ligands have been performed on complexes of ligand **1** (Sabbatini et al. 1984, 1986, Blasse et al. 1986). The absorption spectrum of Eu**1** presented two bands in the UV ($\varepsilon_{max} \approx 100\,M^{-1}\,cm^{-1}$), attributed to LMCT transitions involving the ether oxygens and the amine nitrogens of the ligand. Analogous bands appeared in the metal luminescence excitation spectrum, together with the metal-centered bands of the Eu^{3+} ion. In this spectrum, the relatively high intensity of the metal-centered bands compared to that of the LMCT bands indicated that conversion of absorbed light into light emitted by the metal is more efficient when excitation is performed in the metal-centered bands. The absorption spectrum of Tb**1** did not differ appreciably from that of the Tb^{3+}_{aq} ion. Comparison of the lifetimes in H_2O and D_2O of both complexes indicated the presence of efficient nonradiative decay via vibronic coupling with the OH oscillators of the water molecules coordinated to the metal ion. This process is less efficient for Tb**1**, as expected considering that the energy gap between the metal emitting state and the ground state is higher in Tb^{3+} complexes than in Eu^{3+} complexes (sect. 3). By using eq. (6), 3.1 and 1.9 water molecules were calculated to coordinate the metal ion for Eu**1** and Tb**1**, respectively, showing that the ligand partially shields the metal ion from the solvent (as is known, the Eu^{3+}_{aq} and Tb^{3+}_{aq} ions coordinate 9 to 10 water molecules). For Eu**1** the temperature dependence of the lifetime of the metal emitting state indicated that a thermally activated nonradiative decay of this state occurs. This process was ascribed to the population of LMCT excited states from the Eu^{3+} emitting state followed by efficient nonradiative deactivation of these states to the ground state. It has been suggested that the LMCT excited states are in equilibrium with the emitting state. Considering that the quantum yield upon LMCT excitation is one order of magnitude lower than that obtained upon excitation in the metal-centered $^5L_6$ state, the effect of the equilibrium is presumably small (Sabbatini et al. 1993). For Tb**1** the lifetime values of the metal emitting state indicated that no thermally activated nonradiative decay of this state is present, as expected considering that this complex does not possess low-lying, excited-configuration states. Further, 1:1 and 1:2 (complex:anion) ion pairs between the Eu**1** and Tb**1** cryptates and fluoride anions were studied (Sabbatini et al. 1987c). The fluoride anions were found to replace partially the water molecules coordinated to the metal ion and to increase the lifetimes and quantum yields. The photophysical behavior of these ion pairs confirmed the conclusions drawn for the complexes on the role played by the nonradiative decays of the metal emitting states. Formation of ion pairs with phosphate anions showing properties analogous to those of ion pairs with fluoride anions has been

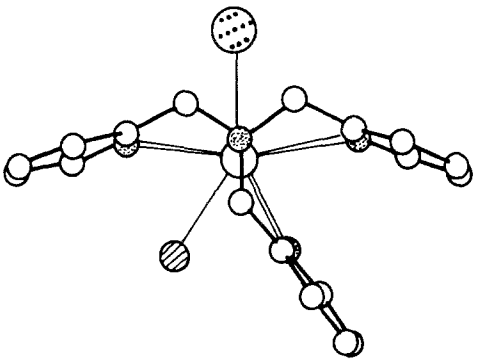

Fig. 7. Crystal structure of [Tb**2**]$Cl_3 \cdot 4H_2O$. The view is perpendicular to the mirror plane passing through the cation. N atoms, small dotted circles; O atoms, dashed circles; Cl^- anions, large dotted circles (Bkouche-Waksman et al. 1991).

reported (Sabbatini et al. 1992). In conclusion, the Eu**1** and Tb**1** complexes gave low metal luminescence intensity because of their weak absorption and, in the case of Eu**1**, of the low quantum yield.

In order to obtain more intense metal luminescence further research was directed at the design of cryptates containing chromophores in the ligand, whose excitation would lead, possibly, to intense metal luminescence via an efficient ligand-to-metal energy transfer.

Some lanthanide complexes of ligand **2** which contains three 2,2′-bipyridine (bpy) units as chromophores were synthesized from the Na**2** complex upon substitution of the Na^+ ion by the lanthanide ion (Rodríguez-Ubis et al. 1984, Alpha 1987, Alpha et al. 1987b). The crystal structure of the [Tb**2**]$Cl_3 \cdot 4H_2O$ complex (fig. 7) showed that the cation is encapsulated by the ligand via binding by the eight nitrogens (Bkouche-Waksman et al. 1991). The complex has wide open faces which are filled up by water and counterions, thus completing the first coordination sphere of the metal ion. The photophysical properties of the Eu**2** and Tb**2** complexes were extensively studied in water (Alpha et al. 1987a,b, 1990, Lehn 1987, Sabbatini et al. 1987b). Among the complexes studied up to now, these have been most investigated; therefore we will consider them prototypes of the Eu^{3+} and Tb^{3+} complexes with encapsulating ligands incorporating chromophoric units. Some photophysical data and the number of water molecules coordinated to the metal ion are shown in table 1. The absorption spectra of Eu**2** and Tb**2** showed bands corresponding to $\pi\pi^*$ transitions in the bpy's (for free bpy $\varepsilon_{max} = 13\,000\,M^{-1}\,cm^{-1}$ at $\lambda_{max} = 281$ nm, Alpha et al. 1990). Analogous bands were observed for the Na**2** complex ($\varepsilon_{max} = 34\,000\,M^{-1}\,cm^{-1}$ at $\lambda_{max} = 291$ nm, Alpha et al. 1990). The bands were red-shifted in comparison with the free bpy and the molar absorption coefficients were lower than the values corresponding to the sum of three free bpy's. Both effects have been attributed to the coordination of the bpy to the metal ion. The large red shift has been considered indicative of a rather strong interaction between the bpy and the metal ion (Sabbatini et al. 1993). Similarity of the absorption and the metal luminescence excitation spectra indicated that energy transfer from the ligand excited states to the metal emitting state takes place. On the basis of the lifetime values in H_2O and D_2O it was found that an important decay process of the metal emitting states takes

place via vibronic coupling with the OH oscillators of the coordinated water molecules. About three water molecules were estimated to coordinate the metal ion. Interestingly, the shielding of the metal ion in these cryptates is comparable with that of the cryptates of ligand **1**. No temperature dependence of the lifetime was observed for Eu**2**, indicating that excited states of other configurations are too high in energy to deactivate the Eu^{3+} emitting state at room temperature. The strong temperature dependence of the lifetime of Tb**2** suggested that an important thermally activated nonradiative decay of the metal emitting state takes place. It was proved that the excited state thermally populated via this process is the ligand triplet excited state which lies ~1200 cm^{-1} above the Tb^{3+} $^5D_4$ emitting state. The presence of an equilibrium between these states has been suggested, which could explain the quenching of the metal emitting state by oxygen (the lifetimes are 0.33 ms and 0.45 ms in aerated and deaerated water solution, respectively). In fact, the quenching should not take place by interaction of oxygen with the metal emitting state, as suggested by the absence of any oxygen effect on the luminescence of the Tb^{3+} ion, and could reflect the quenching of ligand triplet excited states by oxygen observed in Gd**2**. Both Tb**2** and Eu**2** gave low quantum yields. The low value of Tb**2** has been ascribed mainly to the efficient metal-to-ligand back energy transfer (sect. 5.2). In the case of Eu**2** the low value has been explained by low efficiency of the ligand-to-metal energy transfer due to deactivation of the ligand excited states via LMCT excited states (sect. 5.2) and deactivation of the emitting state via vibronic coupling with the OH oscillators of the water molecules coordinated to the metal ion. The luminescence of the Eu**2** and Tb**2** complexes was investigated also in the solid state (Blasse et al. 1988a,b). High quantum yield, 0.5, was found at 300 K for Eu**2**, while for Tb**2** high values were obtained only at low temperatures. In the latter case the quantum yield decreased on raising the temperature, as expected considering the above mentioned metal-to-ligand back energy transfer.

Results concerning other cryptates incorporating chromophoric groups are presented in the remainder of this subsection. The synthesis of the Eu^{3+} complex of ligand **3** has been reported (Takalo and Kankare 1988). This complex was stable in neutral aqueous solution and showed metal luminescence upon ligand excitation. The metal luminescence intensity was 56 000 times higher than that obtained for an equimolar solution of the Eu^{3+}_{aq} ion upon excitation at the same wavelength. Ligands **4** and **5** incorporating as chromophores one bpy and one 1,10-phenanthroline (phen), respectively, were obtained (Rodríguez-Ubis et al. 1984). Preliminary photophysical results have been reported for Eu**4**, Tb**4**, and Eu**5** (Alpha et al. 1987b). These complexes were found to be stable in water where they showed strong metal emission upon excitation in the bpy and phen chromophores of the ligand. The lifetimes of Eu**4** and Eu**5** were longer than that of Eu**1**. This has been attributed, at least in part, to a better shielding of the metal ion by the ligands. However, since lifetimes in heavy water were not reported this hypothesis is not confirmed. The lifetime of Tb**4** was shorter than that of Tb**1**. In this case, the effect on the lifetime due to a better shielding of the metal ion could be masked by efficient deactivation of the metal emitting state via thermally activated nonradiative decay involving the lowest triplet excited state of the phen unit. The quantum yields were of the order of 10^{-2}, i.e., similar

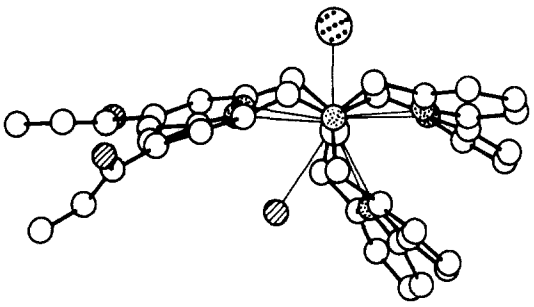

Fig. 8. Crystal structure of [Tb**7**]$Cl_3 \cdot 4H_2O$. The view is perpendicular to the mirror plane passing through the cation. N atoms, small dotted circles; O atoms, dashed circles; Cl^- anions, large dotted circles (Bkouche-Waksman et al. 1991).

to those of Eu**2** and Tb**2**. The 3,3′-biisoquinoline-*N*,*N*′-dioxide ($biqO_2$) chromophore coordinating the metal ion via the oxygens was used to obtain ligand **6**. *N*-oxides were found to be more powerful ligating groups for lanthanide ions than the corresponding amines and more efficient sensitizers of metal luminescence (Musumeci et al. 1982). The photophysical properties of the Eu^{3+} complex of ligand **6** with several counterions were studied in acetonitrile (Lehn et al. 1990, Pietraszkiewicz et al. 1993). It was found that this ligand forms luminescent 1:1 complexes with various Eu^{3+} salts. The lifetimes and quantum yields depended on the nature of the counterion, the dependence being more pronounced for the quantum yields than for the lifetimes. This behavior may be due to different amounts of interaction between the counterion and the Eu^{3+} ion. For example, the highest quantum yield value was found in the case of $CF_3SO_3^-$ while in the presence of weakly coordinating anions like perchlorate and chloride the quantum yields were lower. The Eu**6** complex was reported to be stable also in water, but no luminescence data were given in this solvent.

Ligand **7** (Alpha et al. 1988), obtained upon introduction of carboxymethyl substituents in the 4 and 4′ positions of one bpy of ligand **2**, was synthesized. The Eu**7** complex was obtained (Alpha et al. 1988) and its photophysical properties were studied (Sabbatini et al. 1992, Guardigli 1993). The absorption spectrum of Eu**7** in water was similar to that of the parent Eu**2**. Comparison of the metal emission spectra of Eu**7** and Eu**2** indicated that the carboxymethyl substituents do not affect the symmetry of the first coordination sphere of the Eu^{3+} ion. This is confirmed by the crystal structure of the analogous complex [Tb**7**]$Cl_3 \cdot 4H_2O$ shown in fig. 8 (Bkouche-Waksman et al. 1991). The lifetimes and quantum yields were similar to those of the parent Eu**2**, indicating that the presence of the carboxymethyl substituent slightly affects the photophysical properties. Likewise, in the case of Eu**8** (Mathis 1993) introduction of substituents did not cause relevant changes in the photophysical properties with respect to those of Eu**2**. The Eu^{3+} complex of ligand **9** containing three phen's was prepared (Rodríguez-Ubis et al. 1984). It has been reported that its behavior in water is similar to that of Eu**2**, but quantitative data were not given (Roth 1992). Interestingly, the crystal structure of [Na**9**]Br·$2CHCl_3$ (fig. 9) (Caron et al. 1985) showed that the symmetry is higher than that of Tb**2**. This may be due to the rigidity of the phen unit. Ligands **10**–**13** containing the heterocyclic chromophores 2,2′-bithiazole, 2,2′-biimidazole, and 2,2′-bipyrimidine were prepared (Lehn and Regnouf de Vains 1992).

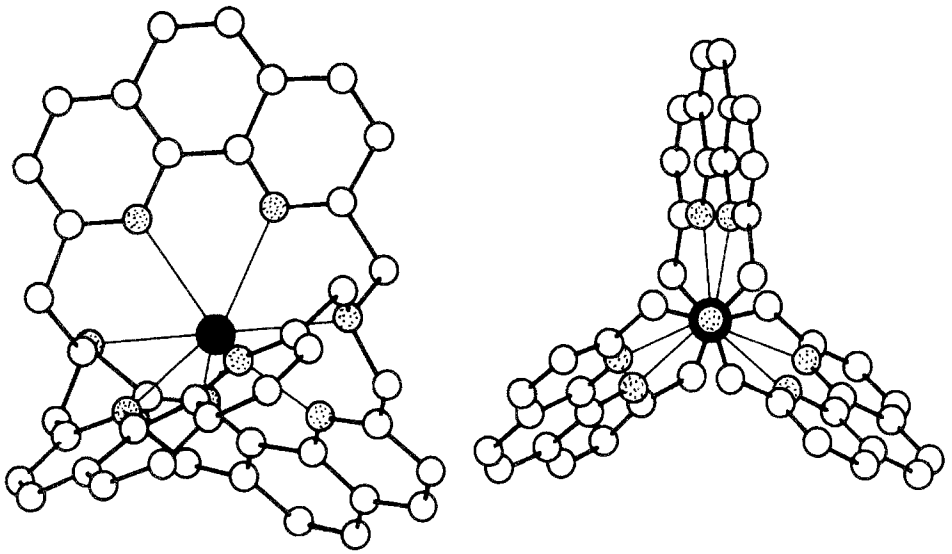

Fig. 9. Two views of the crystal structure of the sodium cryptate Na**9**. Left: view into the cavity, showing the coordination of the Na^+ ion to the eight N sites. Right: projection upon a plane perpendicular to the axis connecting the two aliphatic nitrogens of the ligand (Caron et al. 1985).

The Eu^{3+} complexes of these ligands were obtained and preliminary photophysical results in water have been reported for some of them (Lehn and Regnouf de Vains 1992). For the Eu^{3+} complexes of ligands **10**–**12** luminescence was much less intense than for Eu**2**, while Eu**13** showed luminescence intensity similar to that of Eu**2**.

Other cryptands incorporating *N*-oxides in one or more chromophores were obtained. First, ligand **14** containing one 2,2′-bipyridine-*N*,*N*′-dioxide ($bpyO_2$) and two bpy's was synthesized and its Eu^{3+} complex was obtained (Lehn and Roth 1991). The photophysical properties of Eu**14** were studied in water (Lehn and Roth 1991, Prodi et al. 1991). Significant changes in the absorption spectrum with respect to that of Eu**2** were observed. The number of water molecules coordinated to the metal ion was ~1.4, i.e., smaller than that of Eu**2**, showing improvement of the shielding ability of the ligand upon introduction of *N*-oxides. The lifetimes showed that nonradiative decay of the metal emitting state takes place via both the vibronic coupling and the thermally activated processes. The thermally activated nonradiative decay, which is absent in Eu**2**, has been attributed to the population of LMCT excited states lying at lower energies in Eu**14** than in Eu**2**. This has been related to the weaker electron-donating properties of $bpyO_2$ compared to bpy, which leaves the europium ion more positive in Eu**14** than in Eu**2**. Most interestingly, the quantum yield of Eu**14** was much higher than that of Eu**2**. This has been ascribed to a more efficient ligand-to-metal energy transfer (sect. 5.2) and the more efficient shielding of the metal ion mentioned above. Carboxymethyl groups were introduced in the $bpyO_2$ chromophore of ligand **14**, thus obtaining ligand **15**. The Eu**15** complex was synthesized (Roth 1992) and its photophysical properties were studied in water (Sabbatini et al. 1993). Analogously to

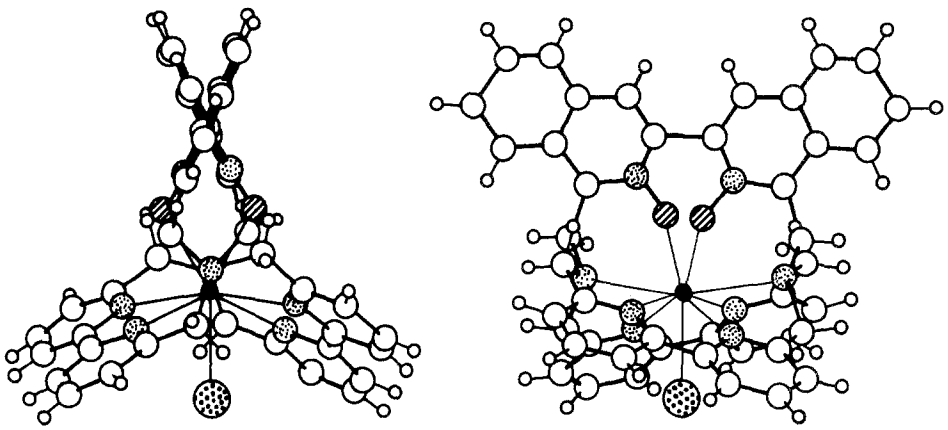

Fig. 10. Crystal structure of [Eu**16**]Cl_3. N atoms, small dotted circles; O atoms, dashed circles; Cl^- anions, large dotted circles (Paul-Roth et al. 1995).

what was found for Eu**7** and its parent Eu**2**, the symmetry of the first coordination sphere, obtained from high-resolution metal emission spectra, and the number of coordinated water molecules were similar for Eu**15** and Eu**14**. The lifetime and quantum yield values were lower for Eu**15** than for Eu**14** and the decrease of the lifetime when going from 77 K to 300 K was higher for Eu**15**. This has been explained considering that the carboxymethyl substituents, due to their electron-withdrawing character, lower the energy of the LMCT excited states. Further, ligand **16** which contains one $biqO_2$ and two bpy's was synthesized and the Eu**16** complex was obtained (Lehn and Roth 1991). The crystal structure of the chloride salt of Eu**16** was determined (fig. 10) (Paul-Roth et al. 1995). This structure revealed that the two isoquinoline moieties of $biqO_2$ are not coplanar and the two oxygens block two faces of the macrobicyclic structure preventing the approach of solvent molecules to the metal ion. The photophysical properties of Eu**16** were studied in water (Prodi et al. 1991). The absorption spectrum presented a band at 304 nm due to the bpy's and additional bands at about 270 and 360 nm, which have been attributed to absorption of the $biqO_2$ chromophore. The luminescence properties were similar to those of Eu**14** and Eu**15**. The temperature dependence of the lifetimes indicated that the thermally activated nonradiative decay of the metal emitting state is more efficient than in Eu**14** and Eu**15**. It has been proposed on the basis of the energy estimated for the lowest ligand triplet excited state that this decay involves an equilibrium between this state and the metal emitting state. The quantum yield in H_2O was higher than those of Eu**14** and Eu**15**, thanks to the more efficient ligand-to-metal energy transfer (sect. 5.2). Analogously to what was found for Eu**14** and Eu**15**, the number of water molecules coordinated to the metal ion was low, ~1.1. For the Eu^{3+} complexes of ligands **17** and **18** incorporating three $biqO_2$ units short lifetimes and low quantum yields (of the order of 10^{-3}) were obtained in acetonitrile (Pietraszkiewicz et al. 1993). The low values have been attributed to inefficient complexation, and therefore bad ligand–metal interaction, because the cavities of ligands **17** and **18** do not fit the size of the Eu^{3+} ion.

4.2. *Complexes of macrocycles*

Complexes of the Eu^{3+} and Tb^{3+} ions with different types of macrocyclic ligands have been obtained and their properties, in particular luminescence, have been reported by different authors (Bünzli 1987, Holz et al. 1991, Sabbatini et al. 1993, Frey et al. 1994, Alexander 1995). For this class of complexes we discuss only the complexes of macrocyclic ligands incorporating chromophores since they can play the role of antennas. Figure 11 shows schematically the macrocyclic ligands of the Eu^{3+} and Tb^{3+} complexes examined. Some photophysical data and the number of coordinated solvent molecules of these complexes are gathered in table 2.

One of the first approaches to the introduction of chromophores in macrocyclic ligands consisted of the synthesis of ligand **19** (Pedersen 1967a,b). For its Eu^{3+} and Tb^{3+} complexes metal emission following an energy transfer from the ligand excited states to the metal emitting states has been reported (Costa et al. 1980). Ligands **20** and **21** incorporate the 3-aroylcoumarine chromophore in the 15C5 and 18C6 crown ethers, respectively. Metal luminescence was observed for the Eu^{3+} and Tb^{3+} complexes of these ligands upon ligand excitation (Alonso et al. 1993). A template synthesis gave the Eu^{3+} complex of ligand **22**, a hexaazamacrocycle containing two pyridines as chromophores (De Cola et al. 1986). A complete photophysical study has been reported for Eu**22** in water (Sabbatini et al. 1987a). The excitation spectrum of Eu**22** showed the same pattern as the absorption spectrum, consisting of ligand-centered transitions. This indicated that light absorption in the ligand was followed by an energy transfer to the metal emitting state. This state was quenched by vibronic coupling with the OH oscillators. In fact, one water molecule was found to be coordinated to the Eu^{3+} ion in the complex. Both the macrocyclic ligand and the coordinated acetate counterion account for the efficient shielding of the ion from the solvent molecules. Comparison between the quantum yields obtained upon ligand and metal excitation suggested that the energy transfer from the ligand excited states to the metal emitting state does not compete efficiently with the other deactivation processes of the ligand excited states. The Eu^{3+} complex of ligand **23** was obtained upon template synthesis and its metal luminescence was investigated (Benetollo et al. 1991). The complex, which was not luminescent itself, developed Eu^{3+} luminescence upon addition of a β-diketonate in methanol. This luminescence has been attributed to replacement of counterions and/or solvent molecules by the sensitizer β-diketonate without disruption of the Eu^{3+} complex. The Eu^{3+} complexes of ligands **24** and **25** were prepared (Pietraszkiewicz et al. 1989, 1993). Eu**24**, sparingly soluble in water, showed in this solvent metal luminescence upon ligand excitation with a quantum yield of the order of 10^{-3} (Pietraszkiewicz et al. 1989). Eu**25** was not stable in water and was studied in acetonitrile. Metal luminescence was observed upon excitation of the ligand. The quantum yield was of the order of 10^{-2} (Pietraszkiewicz et al. 1993).

The bpy chromophore has been used to synthesize several branched-macrocyclic ligands. Let us first discuss the complexes of the ligands incorporating the macrocycle **26**. Ligands **27** and **28** containing four bpy's were synthesized (Ziessel and Lehn 1990). Complexes of these ligands with Eu^{3+} and Tb^{3+} were prepared and their photophysical

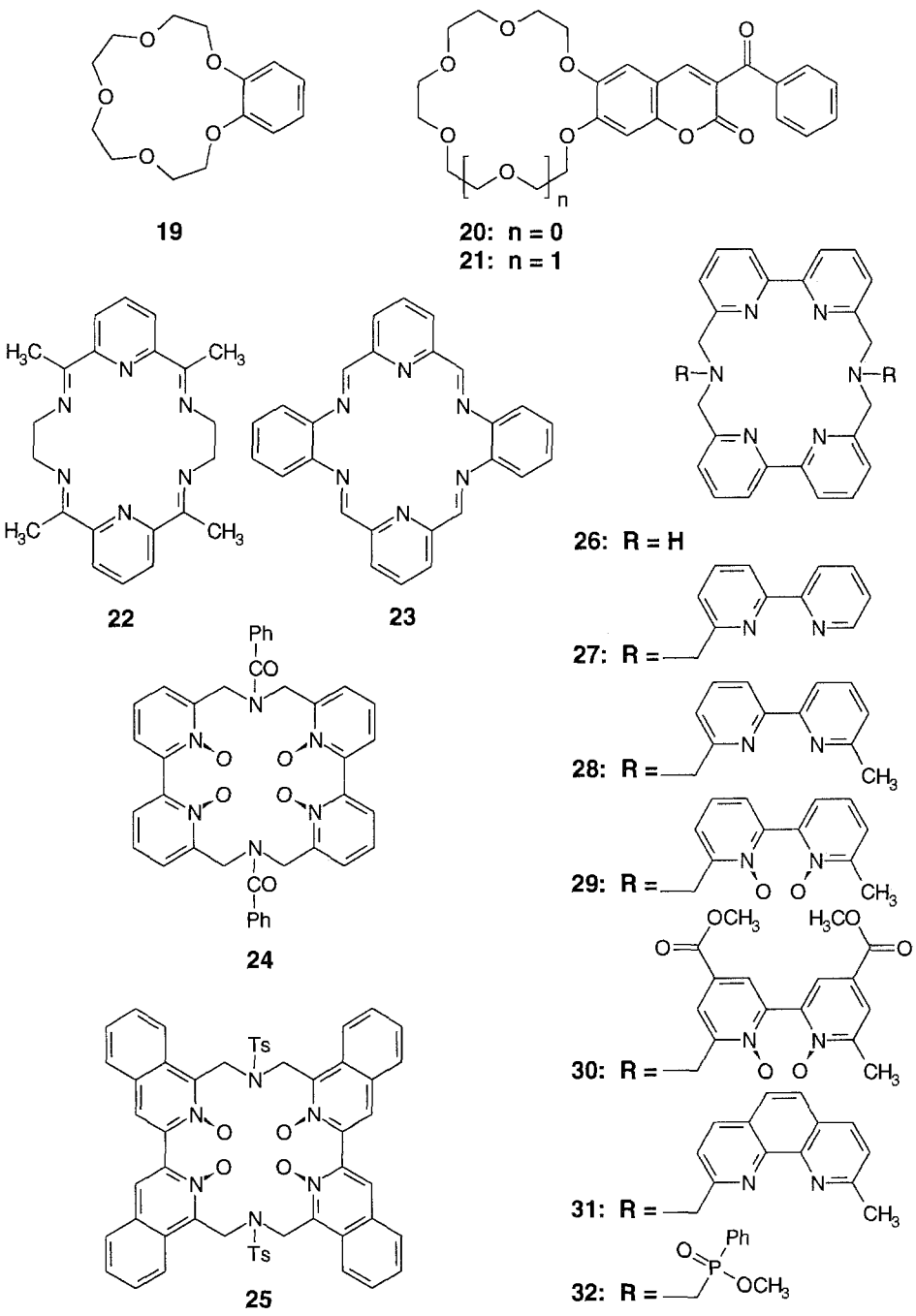

Fig. 11. Schematic representation of the macrocyclic ligands of the complexes examined.

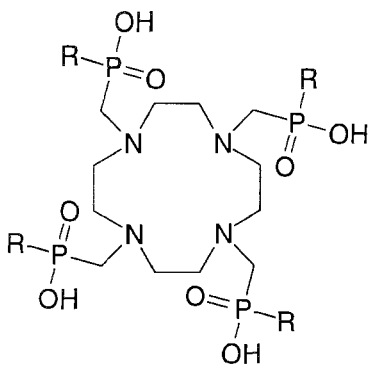

33: R = CH_3
34: R = CH_2Ph

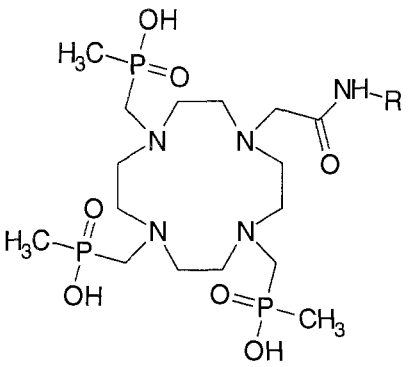

35: R = CH_3

36: R =

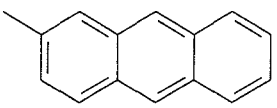

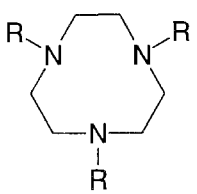

37: R =

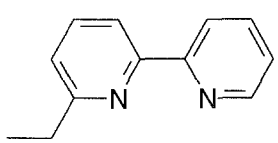

38: R =

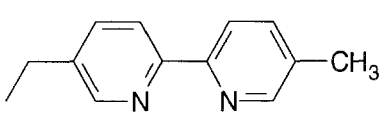

39: R =

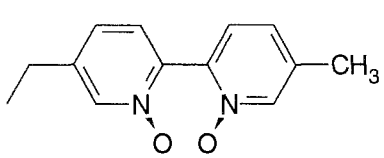

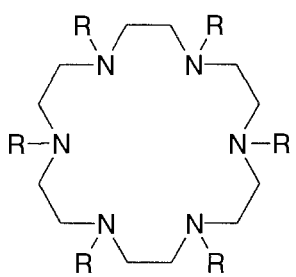

R =

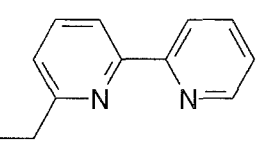

40

Fig. 11 (continued).

properties were studied in water and methanol (Balzani et al. 1991). Similarity of absorption and metal luminescence excitation spectra indicated the presence of ligand-to-metal energy transfer. For Eu**27** the lifetime and quantum yield values showed little

Table 2
Photophysical data and number of solvent molecules coordinated to the metal ion for some Eu^{3+} and Tb^{3+} complexes of macrocyclic ligands

Compound	Solvent	Absorption		Emission[a]						n[b]	Reference
		λ_{max} (nm)	ε_{max} (M^{-1} cm^{-1})	$\tau_H^{300\,K}$ (ms)	$\tau_D^{300\,K}$ (ms)	$\tau_H^{77\,K}$ (ms)	$\tau_D^{77\,K}$ (ms)	$\Phi_H^{300\,K}$	$\Phi_D^{300\,K}$		
Eu22	H_2O	300	10000	0.70	2.0	1.4	2.1		0.006	1.0	Sabbatini et al. (1987a)
Eu27	H_2O	312	36000	1.5	1.9	1.8	1.9	0.10	0.20	<0.5	Balzani et al. (1991)
Tb27	MeOH	312	44000	1.1	1.2	2.0	2.9	0.14	0.35	0.6	Balzani et al. (1991)
Eu28	MeOH	299	39000	1.0	1.8	1.3	2.0	0.01	0.01	0.9	Balzani et al. (1991)
Eu29	H_2O	310	15500	0.5	1.2	1.2	1.45	0.015	0.035	1.2	Sabbatini et al. (1993)
Eu30	H_2O	286	34000	0.13[c]	0.13[c]	1.05	1.3	0.01	0.01		Guardigli (1993)
Eu31	H_2O	278	46000	0.27	1.85	0.3	1.9	0.013	0.09	3.3	Sabbatini et al. (1994b)
								0.016[d]	0.10[d]		
Tb31	H_2O	278	43000	0.06	0.06	1.4	2.6	0.007[e]	0.007	2.7[f]	Sabbatini et al. (1994b)
								0.007[d,e]	0.007[d]		
Eu32	H_2O	307	15100	0.6	2.1	1.2	2.0	0.08	0.30	1.3	Sabbatini et al. (1994a)
Tb32	H_2O	306	15300	0.43	0.50	1.8	2.4	0.08	0.09	1.4	Sabbatini et al. (1994a)
Eu33[g]	H_2O			1.25	1.85			0.0006	0.001	0.3	Murru et al. (1993)
Tb33[g]	H_2O			2.96	3.71			0.01	0.009	0.3	Murru et al. (1993)
Eu34[g]	H_2O			1.59	2.07			0.0009	0.0015	0.2	Murru et al. (1993)
Tb34[g]	H_2O			4.13	4.44			0.44	0.49	0.1	Murru et al. (1993)
Eu35[g]	H_2O			0.76	1.85			0.0005	0.0013	0.8	Murru et al. (1993)
Tb35[g]	H_2O			3.2	4.3			0.16	0.28	0.3	Murru et al. (1993)
Eu36[h]	H_2O			0.07,[i] 0.60[i]	0.17,[i] 1.21[i]			0.0007	0.0032	0.9	Murru et al. (1993)
Tb36[h]	H_2O			0.17,[i] 0.63[i]	0.26,[i] 0.80[i]			0.0006	0.004	1.4	Murru et al. (1993)
Eu37	H_2O	311	24500	0.50	0.57	0.87	1.1	0.05	0.07	<0.5	Prodi et al. (1991)
Tb37	H_2O	311	20400	1.5	1.5	1.4	1.5	0.37	0.38	<0.5	Prodi et al. (1991)

continued on next page

Table 2, *continued*

Compound	Solvent	Absorption		Emission[a]						n[b]	Reference
		λ_{max} (nm)	ε_{max} ($M^{-1}\,cm^{-1}$)	$\tau_H^{300\,K}$ (ms)	$\tau_D^{300\,K}$ (ms)	$\tau_H^{77\,K}$ (ms)	$\tau_D^{77\,K}$ (ms)	$\Phi_H^{300\,K}$	$\Phi_D^{300\,K}$		
Eu**38**	CH_3CN	304	30500	1.74				0.36			Manet (1995)
Tb**38**	CH_3CN	303	31200	0.42				0.08			Manet (1995)
Eu**39**	MeOH	260	38000	0.52	0.71	0.58	0.79	0.05	0.05	<0.7	Manet (1995)
Tb**39**	MeOH	260	38000			0.90	1.00				Manet (1995)
Eu**40**	CH_3CN	306	49000	0.73		1.02		0.020			Ziessel et al. (1993)
Tb**40**	CH_3CN	306	60400	1.36		1.74		0.015			Ziessel et al. (1993)

[a] Excitation in the ligand at the λ_{max} values indicated in this table, unless otherwise noted. The lifetimes are measured in correspondence with the $^5D_0 \rightarrow {}^7F_2$ and $^5D_4 \rightarrow {}^7F_5$ emissions for Eu^{3+} and Tb^{3+}, respectively.

[b] Calculated using eqs. (6) and (7).

[c] The effects of the vibronic coupling with the OH oscillators are, most likely, masked by the thermally activated nonradiative decay.

[d] Excitation at 310 nm.

[e] In deaerated solution the values 0.040 and 0.028 were obtained for the quantum yields upon excitation at 310 nm and 278 nm, respectively.

[f] From lifetime values 0.35 ms and 0.45 ms obtained in deaerated H_2O and D_2O solution, respectively.

[g] Excitation at 250 nm.

[h] Excitation at 303 nm.

[i] No explanation has been reported for the presence of two lifetime values.

deactivation via vibronic coupling with OH oscillators of coordinated water molecules and no temperature dependence. For Tb**27**, metal-to-ligand back energy transfer was found to be an important decay pathway of the metal emitting state, in analogy with Tb**2** (sect. 4.1). Interestingly, the good quantum yield of Tb**27** indicated that this process plays a less important role than in Tb**2**. As concerns Eu**28**, lifetimes similar to those of the parent Eu**27** complex were obtained, but the quantum yields were much smaller (Balzani et al. 1991). This has been attributed to the methyl groups preventing the approach of the bpy's in the branches to the metal ion (Sabbatini et al. 1993). This interpretation is supported by the presence of a residual ligand phosphorescence (Balzani et al. 1991). Less than one solvent molecule was coordinated to the Eu^{3+} and Tb^{3+} ions complexed by ligands **27** and **28**. Interestingly, in these complexes the ion was more efficiently shielded than in the cryptates Tb**2** and Eu**2** which still contained about 3 water molecules coordinated to the metal ion. The efficient shielding offered by ligands **27** and **28** towards solvent interaction suggested that, as envisaged by space-filling models, the metal ion is enclosed in the macrocyclic ring and encapsulated by the two branches of the ligand. *N*-oxides were introduced in the bpy's of the branches of ligand **28**, thus obtaining ligand **29** (Roth 1992). Remarkably, Eu**29** and Tb**29** were stable in water, differently from Eu**28**. The stabilization introduced by the *N*-oxides has been explained considering that the oxygens of these groups may approach the ion better than the bpy nitrogens, thus reducing the influence of steric hindrance by the methyl groups (Sabbatini et al. 1993). The absorption spectra of Eu**29** and Tb**29** showed the same bands of the parent complexes containing only bpy's and shoulders on the red side of the lowest energy bands due, most likely, to $bpyO_2$-localized ligand excited states. For Eu**29**, comparison of the lifetimes at 300 K and 77 K in D_2O indicated that thermally activated nonradiative decay of the metal emitting state takes place. It has been proposed that this process involves LMCT excited states lying at lower energy than in Eu**27**, containing only bpy's. As suggested for the cryptates the lower energy of the LMCT excited states may be due to the weaker basicity of $bpyO_2$ which leaves the europium ion with a higher formal positive charge (Sabbatini et al. 1993). Tb**29** showed metal emission only at 77 K (Sabbatini et al. 1993). The lack of metal luminescence at room temperature has been ascribed to nonradiative deactivation via the lowest ligand triplet excited state, which on the basis of the phosphorescence spectrum of the Gd**29** complex is localized at almost the same energy as the metal emitting state. Ligand **30** was obtained upon introduction of carboxymethyl substituents in the $bpyO_2$ branches of ligand **29**, and the photophysics of its Eu^{3+} complex was studied in water (Guardigli 1993). Both lifetime and quantum yield values of Eu**30** were lower than those of Eu**29** and the temperature dependence of the lifetime is stronger for Eu**30**. This behavior has been attributed to efficient thermally activated nonradiative decay via LMCT excited states lying at lower energy because of the presence of the electron-withdrawing carboxymethyl substituents.

In order to enhance the absorption efficiency, ligand **31** containing 1,10-phenanthroline in the branches was synthesized and the photophysics of its Eu^{3+} and Tb^{3+} complexes was studied (Sabbatini et al. 1994b). Interestingly, these complexes did not decompose in water, differently from those of ligand **28** containing bpy's instead of phen's. This

has been related to the rigidity of the phen moiety. Similarity of the absorption and metal luminescence excitation spectra of the complexes indicated that ligand-to-metal energy transfer takes place from both the bpy and phen chromophores. As to the quantum yields upon excitation in the bpy or phen chromophores, lower values were obtained for the phen units indicating a lower efficiency of the ligand-to-metal energy transfer for this chromophore. The lifetimes and quantum yields of Eu**31** indicated that nonradiative deactivation via vibronic coupling with the OH oscillators of the coordinated water molecules is very efficient. Indeed, about 3.3 water molecules were found to coordinate the metal ion. The lack of any temperature dependence of the lifetime in heavy water suggested that thermally activated decay processes do not play an important role in the deactivation of the metal emitting state. As to Tb**31**, the strong increase of the lifetime upon lowering the temperature indicated that thermally activated nonradiative decay of the Tb^{3+} emitting state via short-lived, upper-lying excited states is very efficient. In analogy with the Tb**2** complex it has been suggested that the thermally activated decay may involve an equilibrium between the metal emitting state and the lowest ligand triplet excited state which was found to lie at 20 800 cm^{-1} on the basis of the phosphorescence spectrum of the Gd^{3+} complex. In aerated solutions the very efficient thermally activated nonradiative decay of the metal emitting state masked the quenching via vibronic coupling with OH oscillators, which could only be detected in deaerated solutions. By using eq. (6), about 2.7 water molecules were calculated to coordinate the metal ion. The photophysics of these complexes was also studied in methanol (Sabbatini et al. 1994b). The analysis of the photophysical data suggested that the complexation of the lanthanide ion is worse in methanol than in water. This has been ascribed to a weaker interaction in methanol between the phen branches and the metal ion. An approach to optimize the stability in water of complexes of branched-macrocyclic ligands consisted in the introduction of phosphinate esters in the branches of macrocycle **26** (Sabbatini et al. 1994a), since they have good ligating properties towards lanthanide ions. In fact, the Eu^{3+} and Tb^{3+} complexes of ligand **32** were found to be stable in water (Sabbatini et al. 1994a). The absorption spectra of the complexes showed the typical bpy transitions and shoulders at 260 nm most likely due to the phenyl moiety. Comparison of the absorption spectra with the metal luminescence excitation spectra indicated that ligand-to-metal energy transfer takes place. This process clearly involved the bpy's while energy transfer from the phenyl moiety could not be unequivocally assessed. Anyway, the involvement of phenyl or benzyl units attached to phosphonic or phosphinic groups in efficient energy transfer to Eu^{3+} and Tb^{3+} ions has been recently reported (Murru et al. 1993, Sato et al. 1993b). For both Eu**32** and Tb**32** the lifetimes and quantum yields in H_2O and D_2O indicated that some vibronic coupling with the OH oscillators occurs. The number of water molecules coordinated to the metal ion was about 1.5. For Tb**32**, the strong temperature dependence of the lifetime indicated that a thermally activated nonradiative decay process plays an important role. In analogy with the other Tb^{3+} complexes containing the bpy chromophore, such a process most likely involved an equilibrium between the lowest bpy triplet excited state and the metal emitting state. Interestingly, the quantum yields were rather high compared to those of

the prototypes Eu**2** and Tb**2**, and similar to those of the complexes of ligand **27**. As suggested for the latter, the branched-macrocyclic structure provided better shielding from water molecules and, most likely, better complexation leading to more efficient ligand-to-metal energy transfer (sect. 5.2).

Phosphinate esters were also attached to the tetraazacyclododecane macrocycle, thus obtaining ligands **33–36** (Cole et al. 1992). The Eu^{3+} and Tb^{3+} complexes of these ligands were obtained and their photophysics was studied in water (Murru et al. 1993). The lifetimes of the Eu^{3+} and Tb^{3+} complexes of ligands **33** and **34** in water and heavy water were consistent with there being no water molecules bound to the metal ion as suggested also by the ^{17}O NMR and Gd-relaxivity measurements. Low quantum yields were obtained for the Eu^{3+} and Tb^{3+} complexes of ligand **33**, and stronger luminescence was observed for Tb**34** upon excitation in the phenyl moiety. As to Tb**35**, it has been reported that the absorption and metal luminescence excitation spectra match well and the complex exhibits a relatively high quantum yield upon ligand excitation. The Eu^{3+} and Tb^{3+} complexes of ligand **36** containing the anthryl chromophore exhibited metal luminescence upon ligand excitation. It has been claimed that the ligand-to-metal energy transfer involves the anthryl moiety (Murru et al. 1993). However, considering that this chromophore has triplet excited states at energies lower than those of the Eu^{3+} and Tb^{3+} emitting states, they are expected to quench the metal luminescence. Indeed, the very low values of the quantum yields showed that the anthryl moiety is not a good sensitizer for Eu^{3+} and Tb^{3+} emission.

The Eu^{3+} and Tb^{3+} ions were also encapsulated by the triazacyclononane-based ligand **37**, carrying bpy's ligated to the ring through C^6 (Ziessel and Lehn 1990), and the photophysical properties of the complexes obtained were investigated in water (Prodi et al. 1991). The lifetimes of both complexes were almost the same in H_2O and D_2O, showing that no water molecules are coordinated to the metal ions. For Eu**37**, the short lifetime, its temperature dependence and the low quantum yield have been explained on the basis of low-lying LMCT excited states involving the aliphatic nitrogens. The lifetime of Tb**37** did not depend on the temperature. This was in agreement with the observation of the lowest ligand triplet excited state at 22 800 cm^{-1}, a value significantly higher than that of the Tb^{3+} emitting state. The lack of any thermally activated nonradiative decay and of coordinated water molecules led to a high quantum yield. Recently three bpy units were also ligated to the triazacyclononane through C^5 thus obtaining ligand **38**, and its Eu^{3+} and Tb^{3+} complexes were prepared (Ziessel 1994). Interestingly, a different behavior was observed for the complexes of this ligand (Manet 1995) compared to the complexes of ligand **37**. The complexes of ligand **38** were found to be unstable in water, differently from those of ligand **37**, and to be stable in anhydrous acetonitrile. Moreover, Eu**38** exhibited a much longer lifetime and much higher quantum yield than Eu**37**. It is worthwhile noting that the quantum yield of Eu**38**, 0.36, is the highest value found up to now for Eu^{3+} complexes with cage-type ligands. Further, the quantum yield of Tb**38** is much lower than that of Tb**37**.

The following observations on the nonradiative deactivations may explain the different photophysical behavior of the complexes of ligands **37** and **38**. From the phosphorescence

of the Gd^{3+} complexes of ligands **37** and **38**, the lowest ligand triplet excited states have been localized at 22 800 cm^{-1} and 22 200 cm^{-1}, respectively, so that back energy transfer from the Tb^{3+} emitting state to the lowest ligand triplet excited state did not occur in Tb**37**, but may be present in Tb**38**. In the case of Eu**38**, deactivation via LMCT excited states involving the aliphatic nitrogens may be less efficient than for Eu**37**. Indeed, such LMCT excited states are expected to lie at higher energies as a consequence of a longer distance between the Eu^{3+} ion and the aliphatic nitrogens as appears also from the CPK models. Ligand **39** was obtained upon attachment of $bpyO_2$ units via C^5 to the triazacyclononane and the Eu^{3+} and Tb^{3+} complexes of this ligand were synthesized (Ziessel 1995). Their photophysics was studied in MeOH, where the complexes were stable (Manet 1995). For Eu**39** metal luminescence was observed at room temperature. Differently, Tb**39** showed metal luminescence only at 77 K. The latter behavior has been attributed to nonradiative decay of the metal emitting state via the lowest ligand triplet excited state, which on the basis of the ligand phosphorescence spectrum of Gd**39** is localized at almost the same energy as the Tb^{3+} emitting state.

Ligand **40** containing the hexaazacyclooctadecane ring carrying six pendant bpy's was synthesized (Ziessel and Lehn 1990), and the properties of its Eu^{3+} and Tb^{3+} complexes were studied (Ziessel et al. 1993). A 2:1 (metal:ligand) stoichiometry for the solid homonuclear Eu^{3+} and Tb^{3+} complexes of this ligand was found. These complexes decomposed in water and methanol and were stable in acetonitrile where they showed low quantum yields.

4.3. *Podates*

The bpy unit was used as chromophore in the podands **41–44**. Figure 12 shows schematically the podand ligands of the Eu^{3+} complexes examined. Some photophysical data and the number of coordinated solvent molecules of these complexes are gathered in table 3.

The tripode and tetrapode ligands **41** and **42** were synthesized (Lehn and Ziessel 1987). The Eu^{3+} complexes of these ligands were prepared and their photophysical properties were studied (Balzani et al. 1990). The complexes were stable in MeOH and underwent decomposition in water, which was very slow for Eu**42**. The lifetimes showed that thermally activated nonradiative decay of the emitting state is negligible for both complexes and deactivation via vibronic coupling with the OH oscillators of the solvent is very efficient. The latter deactivation pathway played a more important role for Eu**42** than for Eu**41**, suggesting that the smaller ligand **41** leaves less room for solvent molecules in the first coordination sphere. It is interesting to notice that for Eu**42** in D_2O the lifetime is nearly the same as in MeOD, while the quantum yield is one order of magnitude lower. This behavior has been attributed to a lower ligand-to-metal energy-transfer efficiency in water than in methanol due, most likely, to a longer distance in water between the Eu^{3+} ion and the bpy's (sect. 5.2). The tetrapode ligands **43** and **44** and their Eu^{3+} complexes were synthesized (Ziessel 1994). These complexes decomposed in water and methanol and were stable in anhydrous acetonitrile. The lifetimes of both

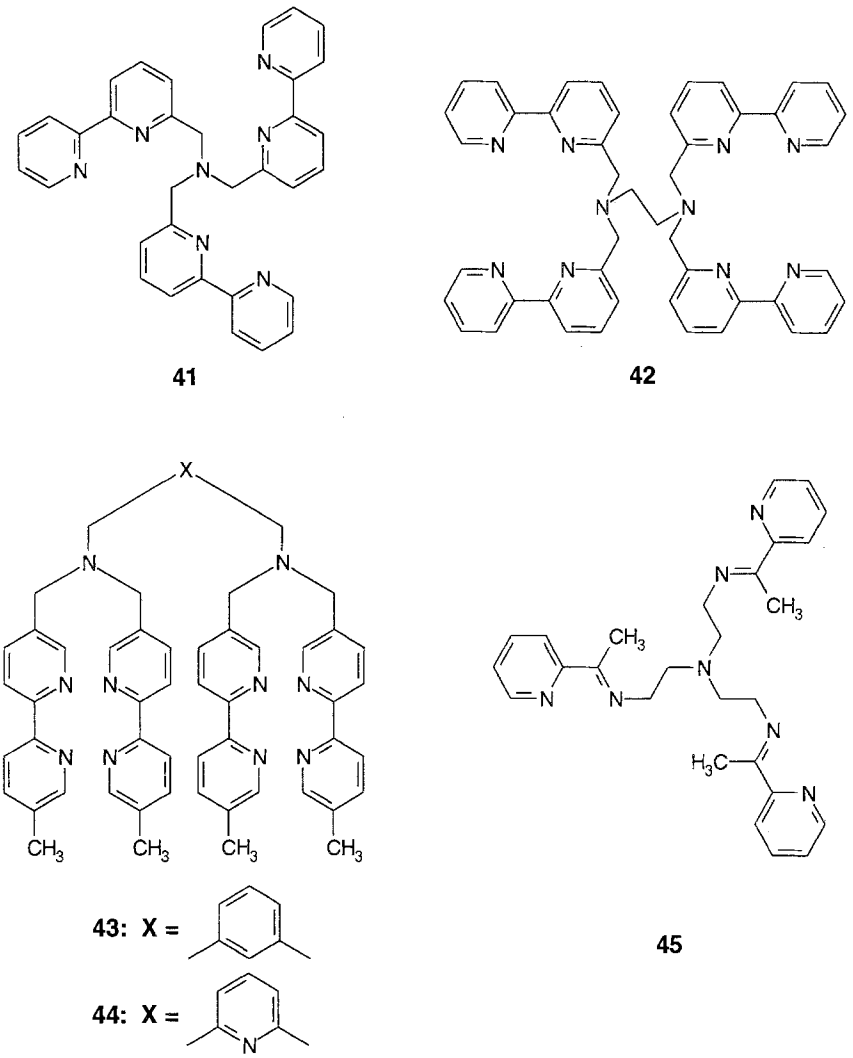

Fig. 12. Schematic representation of the ligands of the podates examined.

complexes were rather long and temperature independent and the quantum yields were good (Manet 1995).

Some lanthanide complexes of ligand **45** were obtained, but the free ligand could not be isolated (Carugo and Bisi-Castellani 1994). These complexes were insoluble in the most common solvents, with the exception of DMSO and DMF. In DMF, weak Eu^{3+} and Tb^{3+} luminescence was observed upon ligand excitation, and lifetimes and quantum yields were given. However, since the complexes underwent partial decomposition, one has to be cautious with the values reported.

Table 3
Photophysical data and number of solvent molecules coordinated to the metal ion for some Eu^{3+} and Tb^{3+} podates

Compound	Solvent	Absorption		Emission[a]						n[b]	Reference
		λ_{max} (nm)	ε_{max} (M^{-1} cm^{-1})	$\tau_H^{300\,K}$ (ms)	$\tau_D^{300\,K}$ (ms)	$\tau_H^{77\,K}$ (ms)	$\tau_D^{77\,K}$ (ms)	$\Phi_H^{300\,K}$	$\Phi_D^{300\,K}$		
Eu**41**	MeOH	301	32 000	0.95	1.80	0.94	2.0	0.06	0.10	1.0	Balzani et al. (1990)
Eu**42**	MeOH	301	42 000	0.81	1.70	1.10	1.8	0.07	0.20	1.4	Balzani et al. (1990)
Eu**43**	CH_3CN	304	26 500	1.2		1.12		0.04			Manet (1995)
Eu**44**	CH_3CN	308	43 500	1.0		1.1		0.04			Manet (1995)

[a] Excitation in the ligand at the λ_{max} values indicated in this table. The lifetimes are measured in correspondence with the $^5D_0 \rightarrow {}^7F_2$ and $^5D_4 \rightarrow {}^7F_5$ emissions for Eu^{3+} and Tb^{3+}, respectively.
[b] Calculated using eq. (7).

4.4. *Complexes of calixarenes*

Encapsulation of the Eu^{3+} and Tb^{3+} ions by cage-type ligands was also achieved using functionalized calixarenes. Metal luminescence properties were studied mostly for complexes of calix[4]arenes, while few results are available for complexes of calix[6]arenes and calix[8]arenes, the latter being dinuclear complexes. Figure 13 shows schematically the calixarene ligands of the Eu^{3+} and Tb^{3+} complexes examined. Some photophysical data and the number of coordinated solvent molecules of these complexes are gathered in table 4.

First, complexes of the *p-tert*-butyl-calix[4]arene tetraacetamide ligand **46** were studied. Interestingly, Eu**46** and Tb**46** were water soluble, differently from the free ligand and the K^+ complex, and their photophysics was studied in water (Sabbatini et al. 1990). The absorption spectra of the complexes presented two bands due to ligand-centered transitions ($\lambda_{max} = 273$ and 282 nm, $\varepsilon_{max} = 1100\,M^{-1}\,cm^{-1}$). Comparison of the absorption and metal luminescence excitation spectra indicated that ligand-to-metal energy transfer from the calix[4]arene moiety to the metal ion takes place. About one water molecule was found to coordinate the metal ion, showing that ligand **46** efficiently shields the metal ion from solvent molecules. For Eu**46** the lifetimes showed that the thermally activated nonradiative decay process of the Eu^{3+} emitting state is not efficient. The very low quantum yield was due to inefficient ligand-to-metal energy transfer, which has been attributed to deactivation of the ligand excited states via LMCT excited states (sect. 5.2). The lifetimes of Tb**46** showed no temperature dependence and a small effect of solvent deuteration. The former observation has been explained considering that the energy of the lowest ligand triplet excited state, which is about $4000\,cm^{-1}$ higher than that of the metal emitting state, renders metal-to-ligand back energy transfer inefficient. Interestingly, the quantum yields of Tb**46** were much higher than those of Eu**46** as a result of much more efficient ligand-to-metal energy transfer (sect. 5.2). The synthesis of ligands **47**–**50** and their complexation of Eu^{3+} and Tb^{3+} in methanol has been recently reported (Georgiev et al. 1994). The Tb^{3+} complexes were strongly luminescent, while the Eu^{3+} complexes showed only weak emission. In all cases addition of water caused quenching of the luminescence, the quenching being less efficient for complexes of ligands **49** and **50** based on calix[6]arenes. This effect has been explained considering that the larger, more flexible calix[6]arenes encapsulate the metal ion more efficiently. Some photophysical properties of the Tb^{3+} complexes of ligands **51**–**53** in water have been reported (Sato et al. 1993a). 1:1 and 2:1 (metal:ligand) stoichiometries were found for the complexes of ligands **52** and **53** and of ligand **51**, respectively. Comparison of the metal luminescence excitation spectra with the absorption spectra indicated that metal emission followed energy transfer from the phenol moiety of the ligand to the metal ion. The luminescence intensities were pH dependent and reached the highest values at $pH > 11$. Interestingly, a high quantum yield was obtained for Tb**53**. As concerns Tb**51** and Tb**52**, the quantum yields were determined in the presence of a free ligand excess which affects the efficiencies of light absorption by the complex and therefore the quantum yields.

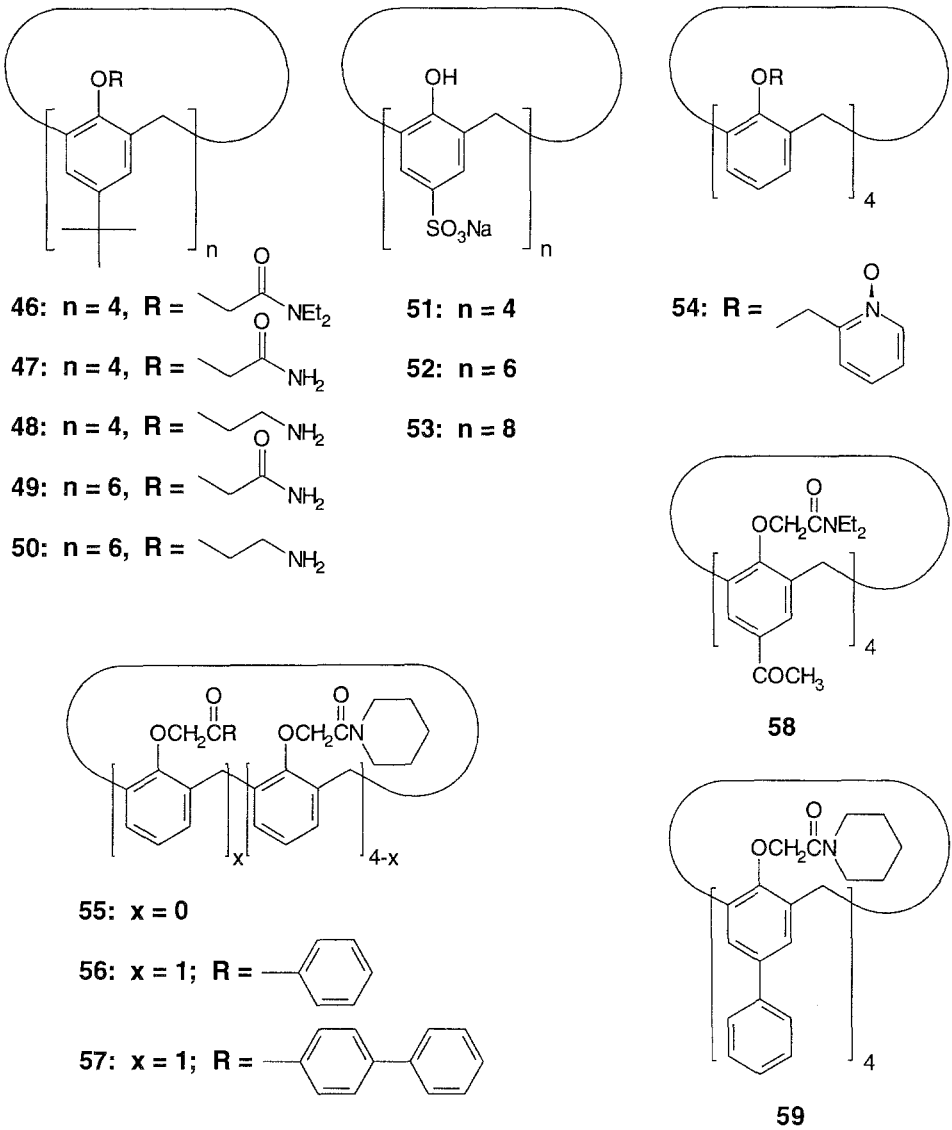

Fig. 13. Schematic representation of the calixarene-based ligands of the complexes examined (*continued on next page*).

Considering that calixarenes have rather low molar absorption coefficients, more efficient chromophores were attached to calixarene moieties in order to obtain strongly absorbing ligands for Eu^{3+} and Tb^{3+} complexation. Complexes of ligand **54** containing four pyridine-*N*-oxide units as chromophores showed metal luminescence upon ligand excitation in methanol (Pappalardo et al. 1991). The luminescence was completely

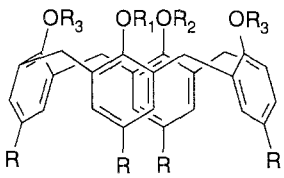

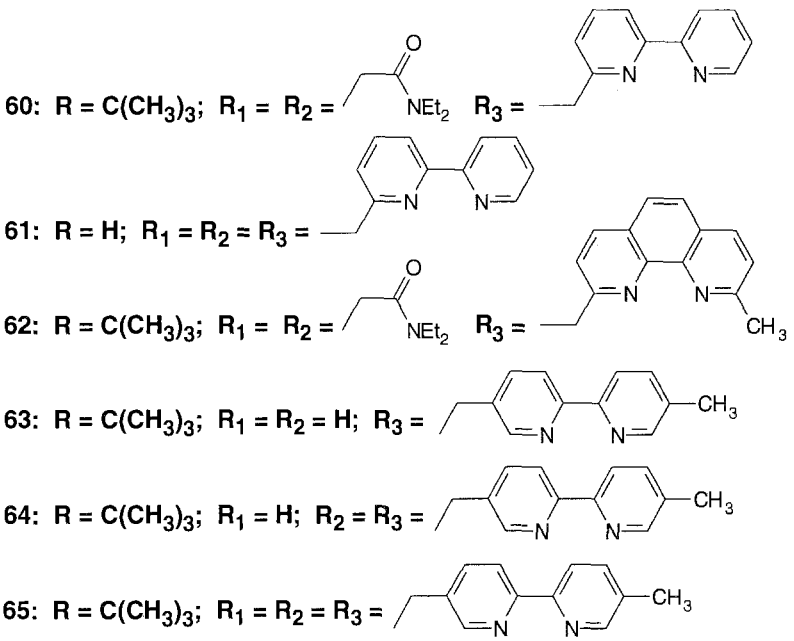

Fig. 13 (continued).

quenched upon addition of water, suggesting the lability of the complexes in water. The quantum yields in methanol were of the order of 10^{-3} for both Eu**54** and Tb**54**. The Eu^{3+} and Tb^{3+} complexes of ligands **55–59** containing phenyl and diphenyl groups as chromophores were prepared in order to investigate the correlation between the metal luminescence intensity and the nature of the ligand and the chromophore (Sato and Shinkai 1993, Matsumoto and Shinkai 1994). For all complexes 1:1 stoichiometries were found in both acetonitrile and methanol. Metal luminescence upon ligand excitation was observed for almost all the complexes studied. High quantum yields, e.g. 0.27 for Tb**56**, and rather long lifetimes have been reported for some of the complexes in acetonitrile. However, it must be noticed that the method (Haas and Stein 1971) used to obtain the quantum yields foresees that the quantum yield of the standard is considered at the excitation wavelength used also for the sample. Since this is not the case for the quantum yields reported, one has to be cautious with these values.

Table 4
Photophysical data for some Eu^{3+} and Tb^{3+} complexes of functionalized calixarenes

Compound	Solvent	Absorption		Emission[a]			Reference
		λ_{max} (nm)	ε_{max} (M^{-1} cm^{-1})	$\tau_H^{300\,K}$ (ms)	$\tau_H^{77\,K}$ (ms)	$\Phi_H^{300\,K}$	
Eu**46**	H_2O	273	1100	0.65[b]	1.8[b]	0.0002	Sabbatini et al. (1990)
Tb**46**	H_2O	273	1100	1.5[c]	1.6[c]	0.20	Sabbatini et al. (1990)
Tb**53**	H_2O	~290	~25000			0.20[d]	Sato et al. (1993a)
Eu**60**	CH_3CN	305	28000	0.65		0.04	Casnati et al. (1996)
Tb**60**	CH_3CN	306	29000	1.9		0.12	Casnati et al. (1996)
Eu**61**	CH_3CN	307	50000	0.65		<0.01	Casnati et al. (1996)
Tb**61**	CH_3CN	305	46700	1.4		0.02	Casnati et al. (1996)
Eu**63**	CH_3CN	309	22500	1.2		0.03	Sabbatini et al. (1995)
Tb**63**	CH_3CN	301	23400	0.52	1.03	0.001	Sabbatini et al. (1995)
Eu**64**	CH_3CN	306	26700	1.26		0.14	Sabbatini et al. (1995)
Tb**64**	CH_3CN	305	30000	0.81	0.98	0.0013	Sabbatini et al. (1995)
Eu**65**	CH_3CN	305	39600	1.6		0.16	Sabbatini et al. (1995)
Tb**65**	CH_3CN	302	42800	0.57	1.18	0.007	Sabbatini et al. (1995)

[a] Excitation in the ligand at the λ_{max} values indicated in this table, unless otherwise noted. The lifetimes are measured in correspondence with the $^5D_0 \rightarrow {}^7F_2$ and $^5D_4 \rightarrow {}^7F_5$ emissions for Eu^{3+} and Tb^{3+}, respectively.
[b] The values 1.9 ms and 2.0 ms are obtained in D_2O at 300 K and 77 K, respectively.
[c] The values 2.6 ms and 2.8 ms are obtained in D_2O at 300 K and 77 K, respectively.
[d] Excitation at 255 nm.

Several calix[4]arenes carrying the bpy chromophore were synthesized. Ligands **60** and **61** containing two bpy's and two amides and four bpy's, respectively, in which the bpy's are ligated to the calixarene moiety through C^6 were obtained (Sabbatini et al. 1995, Casnati et al. 1996). These ligands gave 1:1 complexes with Eu^{3+} and Tb^{3+} in acetonitrile with formation constants of the order of 10^5 M^{-1}. The photophysical properties of these complexes were studied in solutions containing the ligand and an excess of the Eu^{3+} or Tb^{3+} salts (Sabbatini et al. 1995, Casnati et al. 1996). The absorption spectra of the ligands and the complexes were characterized by intense bands in the UV due to bpy absorption. Comparison of the absorption spectra and the metal luminescence excitation spectra indicated that energy transfer from the bpy moiety to the metal ion takes place. Good quantum yields were obtained for the complexes of ligand **60**. The lower quantum yields of the complexes of ligand **61** were attributed to a less efficient ligand-to-metal energy transfer due to steric hindrance which the four bpy's may undergo when approaching the metal ion (sect. 5.2). No metal luminescence upon ligand excitation was found in acetonitrile solutions containing the Eu^{3+} or Tb^{3+} ions and ligand **62** (Casnati et al. 1996). Ligands **63–65**, in which the bpy's are ligated to the calixarene moiety through C^5, were synthesized and their Eu^{3+} and Tb^{3+} complexes were isolated (Ulrich and Ziessel 1994). The photophysical properties were studied in anhydrous acetonitrile (Sabbatini et al. 1995). For all complexes metal luminescence upon bpy excitation was

observed. The Eu^{3+} complexes showed longer lifetimes and higher quantum yields than the Tb^{3+} complexes. Interestingly, Eu**64** and Eu**65** gave particularly high quantum yields.

5. Discussion

The results obtained for the different classes of complexes clearly demonstrate that the nature of the ligand is determining in obtaining metal luminescence. Next, we would like to draw out the different roles the ligand can play. First, the ligand is responsible for the absorption of the complex, the bands observed corresponding to those of the free ligand slightly modified upon complexation. Further, the complexation ability of the ligand influences the ligand-to-metal energy transfer. This depends also on the energies of the ligand excited states and, in the case of the Eu^{3+} complexes, the LMCT excited states, related to the redox properties of the ligand. Finally, the ligand influences the deactivation processes of the metal emitting states. Shielding of the metal ion by the ligand accounts for the nonradiative deactivation involving solvent molecules coordinated to the metal ion. The energies of the ligand excited states and, for the Eu^{3+} complexes, the LMCT excited states determine the nonradiative deactivations via these states.

Some general conclusions can also be drawn on the effects of the metal ion on the photophysical properties of the complexes. In the Eu^{3+} complexes, low-lying LMCT excited states are thought to be responsible for the thermally activated nonradiative decay of the Eu^{3+} emitting state (sect. 5.3) and for some low $\eta_{en.tr.}$ values (sect. 5.2). For the Tb^{3+} complexes there are no low-lying excited states different from the ligand and metal excited states, and high $\eta_{en.tr.}$ values are usually obtained (sect. 5.2). The energy of the Tb^{3+} emitting state, higher than that of the Eu^{3+} emitting state, renders more probable nonradiative deactivation of the former state via the lowest ligand triplet excited state. This process is present in almost all the Tb^{3+} complexes containing the bpy and phen chromophores and is responsible, most likely, for the lack of metal luminescence at room temperature of several Tb^{3+} complexes with ligands incorporating heterocyclic *N*-oxide chromophores.

In the following sections we discuss several quantities in detail. In sections 5.1 and 5.2 we focus on the antenna effect of the ligand, discussing the efficiencies of the ligand absorption in the complexes and the energy transfer from the ligand excited states to the metal emitting states (table 5). In sect. 5.3 the efficiency of the metal luminescence in the complexes is treated on the basis of the rate constants of the decay processes of the metal emitting states (table 6). Finally, in sect. 5.4 we compare the intensities of the metal luminescence using the molar absorption coefficients and the quantum yields (table 7). Only the complexes for which the necessary experimental data are available will be treated.

5.1. *Ligand absorption*

The absorption properties of the complexes (table 5) and, for the sake of comparison, of the free chromophores incorporated in the ligands are discussed. We focus on the

Table 5
Absorption data and ligand-to-metal energy-transfer efficiencies[a]

Compound	λ_{max} (nm)	ε_{max} (M^{-1} cm^{-1})	$\eta_{en.tr.}$ [b]
Eu**2**	303	28000	0.10
Eu**7**	305	26000	0.08
Eu**14**	304	20000	0.40[c]
Eu**15**	306	17000	0.25[c]
Eu**16**	304	20000	0.55[c]
Eu**27**	312	36000	0.20
Eu**28**[d]	299	39000	0.02
Eu**29**	310	15500	0.05[c]
Eu**30**	286	34000	0.10[c]
Eu**31**	278	46000	0.09
Eu**32**	307	15100	0.27
Eu**37**	311	24500	0.14[c,e]
Eu**38**[f]	304	30500	n.a.[g]
Eu**39**[d]	260	38000	0.08
Eu**41**[d]	301	32000	0.12
Eu**42**[d]	301	42000	0.20
Eu**46**	273	1100	0.0006
Tb**2**	304	29000	0.34[h]
Tb**27**[d]	312	44000	0.80[h]
Tb**31**	278	43000	0.30[h]
Tb**32**	306	15300	0.45[h]
Tb**37**	311	20400	0.40[c]
Tb**38**[f]	303	31200	n.a.[g]
Tb**39**[d]	260	38000	n.a.[i]
Tb**46**	273	1100	0.35

[a] In water solution, unless otherwise noted. The λ_{max} and ε_{max} values are those reported in tables 1–4.
[b] Obtained from eqs. (2)–(4), using the lifetime and quantum yield values reported in tables 1–4.
[c] Calculated on the assumption that the thermally activated decay process does not involve any equilibrium between the metal emitting state and other excited states (sect. 3).
[d] In methanol solution.
[e] A higher value is expected considering that the radiative lifetime may be longer than τ_D^{77K} introduced in eq. (4) if vibronic coupling involving CH bonds occurs (sect. 5.2).
[f] In acetonitrile solution.
[g] The value cannot be calculated because lifetime values at 77 K are not reliable.
[h] The value reported is a lower limiting value because of the equilibrium between the emitting state of the Tb^{3+} ion and the triplet excited state of the ligand (sect. 3).
[i] The value cannot be calculated because no metal luminescence is observed at room temperature.

absorption bands at lowest energy because they are important for applications (sect. 6). In all cases where the ligands contain only the bpy chromophore, complexation gives rise to a red shift of the bpy absorption (for free 2,2′-bipyridine $\lambda_{max} = 281$ nm in water). The observed differences may be related to the amount of ligand–metal interaction in the complex. The effect is similar for complexes of the cryptands and podands and the branched-macrocyclic ligands **28** and **38** while a more pronounced shift is observed for complexes of the branched-macrocyclic ligands **27** and **37**. This may be explained considering that in the complexes of the last two ligands the approach between the chromophore and the metal ion may be closer than in the other complexes, as illustrated by the space-filling models. This hypothesis is supported by the kinetic behavior in solution (sect. 4.2).

A decrease of the molar absorption coefficients of the bpy is observed upon complexation of the metal ion. The ε_{max} values obtained span the range of 7000–11 000 M^{-1} cm^{-1} for one bpy, while for the free 2,2′-bipyridine ε_{max} is 13 000 $M^{-1}cm^{-1}$. The ε_{max} decrease and the λ_{max} shift show the same trend, as expected considering that both factors reflect the amount of metal coordination by the ligand. In the complexes of ligand **31** only a small red shift of the phen absorption is observed (for free 1,10-phenanthroline $\lambda_{max} = 270$ nm in water). The small shift may be attributed to scarce metal coordination due to steric hindrance induced by the presence of the methyl substituents in the phen moiety. This hypothesis is supported by the luminescence data (sect. 4.2).

A decrease of the molar absorption coefficients upon metal complexation is observed in correspondence with the phen absorption. This decrease cannot be unequivocally attributed to complexation of the phen moiety because in the spectral region corresponding to the maximum phen absorption also the bpy absorption is present which is more red-shifted than the phen absorption. The introduction of *N*-oxides in the bpy's gives rise to substantial changes in the absorption spectra of the complexes with respect to those of the analogous complexes containing only bpy's. For the complexes of ligands **14**, **15**, **29**, and **30** the intensities of the absorption maxima at about 305 nm decrease. This is due to the low absorption intensity of the 6,6′-dimethyl-2,2′-bipyridine-*N,N′*-dioxide chromophore at 305 nm. Note that the latter chromophore shows an absorption band at higher energy and less intense ($\lambda_{max} = 260$ nm and $\varepsilon_{max} = 8000$ M^{-1} cm^{-1}, Guardigli 1992) compared to the bpy chromophore.

The absorption spectra of the Eu^{3+} and Tb^{3+} complexes of ligand **39** and of the analogous ligand containing four 5′-methyl-2,2′-bipyridine-*N,N′*-dioxide units attached to the tetraazacyclododecane ring have maxima at 260 nm, as the free chromophore, with very high molar absorption coefficients (Manet 1995). As to the Eu^{3+} and Tb^{3+} complexes of the calix[4]arene-based ligand **46**, their absorption spectra are characterized by low molar absorption coefficients, $\varepsilon_{max} = 1100\ M^{-1}cm^{-1}$ at $\lambda_{max} = 270$ nm. Importantly, complexes of ligands **60**, **61** and **63–65** obtained upon attachment of chromophores to the calix[4]arene moiety have much more intense absorption, with ε_{max} values in the range of 20 000–50 000 M^{-1} cm^{-1}.

5.2. *Ligand-to-metal energy-transfer efficiency*

The efficiencies of the energy transfer from the singlet excited state of the ligand populated upon absorption to the emitting state of the metal ion, $\eta_{en.tr.}$, obtained from eqs. (2)–(4) (sect. 3) are presented in table 5.

The Tb^{3+} complexes of ligands **2**, **27**, **31**, and **32** are characterized by high values of $\eta_{en.tr.}$. It must be pointed out that these values are lower limiting values since the equilibrium between the lowest ligand triplet excited state and the Tb^{3+} $^5D_4$ emitting state plays an important role in the deactivation of the metal emitting state (sect. 3). Indeed, one has to be cautious when comparing the $\eta_{en.tr.}$ values for these complexes. For example, the value of Tb**27**, higher than the other ones, is most likely related to the lower value of $k_{nr}(T)$ and thus to an equilibrium playing a less important role. Therefore, the lower $\eta_{en.tr.}$ values corresponding to higher $k_{nr}(T)$ values are not necessarily connected with a lower energy-transfer efficiency but could reflect a more important role of the equilibrium in the deactivation of the metal emitting state. For the Tb**2** complex the value of $\eta_{triplet \rightarrow metal}$ has been obtained experimentally (Alpha et al. 1990). This value is about unity, showing that in this complex the energy transfer to the metal overcomes the other deactivation processes of the lowest ligand triplet excited state. A value close to unity is also obtained for $\eta_{en.tr.}$ using eq. (5) if $\eta_{singlet \rightarrow triplet}$ is substituted by the η_{isc} value of the free bpy (~1). This substitution appears to be justified if one considers that the Tb^{3+} ion should not introduce low-lying excited states deactivating the bpy singlet excited state and the heavy metal ion could only increase the intersystem-crossing efficiency. Noticeably, $\eta_{en.tr.}$ equal to unity is three times higher than the value calculated using eqs. (2)–(4). This shows how the latter is affected by the presence of the equilibrium. For the Tb**37** complex, whose lifetime is not temperature dependent, $\eta_{en.tr.}$ is lower than for the other Tb^{3+} complexes. In this case, however, the lifetime in D_2O at 77 K used in eq. (4) may be shorter than the radiative lifetime because of a vibronic coupling contribution due to the CH oscillators of the ligand (Prodi et al. 1991). If the value commonly obtained for the radiative lifetime of Tb^{3+} complexes is used, $\eta_{en.tr.}$ and $\eta_{triplet \rightarrow metal}$ increase by a factor of two. For Tb**46** $\eta_{en.tr.}$ is 0.35. Since η_{isc} of the free ligand is not known, using eq. (5) we can only estimate that $\eta_{triplet \rightarrow metal} \geqslant 0.35$.

Let us now consider the Eu^{3+} complexes. First of all, it is noticeable that the energy-transfer efficiency of Eu**2** is lower than that of Tb**2**. Such a behavior has been explained by possible deactivation of the ligand singlet and triplet excited states via low-lying LMCT excited states in Eu**2**. Analogous considerations may be valid for the other Eu^{3+} complexes. Complexes containing only bpy's and phen's show similar efficiencies, with the exception of Eu**28** for which the much lower value may be ascribed to steric hindrance of the methyl groups. For the cryptates incorporating *N*-oxides $\eta_{en.tr.}$ is considerably higher. Note that this quantity is never unity, suggesting that LMCT excited states still play a role. However, this may be less important because of a more efficient population of the lowest ligand triplet excited state due to the presence of $bpyO_2$- and $biqO_2$-localized levels or because a closer approach between the ligand and the metal ion could give rise to a higher value of $\eta_{triplet \rightarrow metal}$. Analogously to the cryptates,

introduction of the $bpyO_2$ chromophore in Eu**29** and Eu**30** gives rise to an increase of $\eta_{en.tr.}$ compared to the parent Eu**28**. Anyway, for these three complexes the $\eta_{en.tr.}$ values are rather low, most likely, because of steric hindrance of the methyl groups in the branches. The exceedingly low value of $\eta_{en.tr.}$ of Eu**46** suggests a very efficient deactivation of the ligand excited states via LMCT excited states considering that $\eta_{en.tr.}$ of Tb**46** is about three orders of magnitude higher.

5.3. *Metal luminescence efficiency*

In order to discuss the efficiency of the metal luminescence in the complex, the radiative and nonradiative decay rate constants of the Eu^{3+} $^5D_0$ and Tb^{3+} $^5D_4$ emitting states (table 6) have been calculated using eqs. (10)–(12).

The radiative rate constants are higher for the Eu^{3+} than for the Tb^{3+} complexes. This is in line with what usually observed, because of the mixing of the $^5D_0$ emitting state with LMCT excited states in Eu^{3+} complexes and the much less efficient mixing of the $^5D_4$ emitting state with f–d excited states in Tb^{3+} complexes (Blasse 1979). The k_r values differ from one another more for Eu^{3+} than for Tb^{3+} complexes, with the exception of Tb**37**, in agreement with the larger effect of the ligand on the energy of the LMCT excited states in Eu^{3+} complexes than on the energy of the f–d states in Tb^{3+} complexes. In particular, the Eu^{3+} complexes containing $bpyO_2$, $biqO_2$, and electron-withdrawing substituents in the ligand show higher k_r values than the analogous complexes containing only bpy's, as expected on the basis of the lower energies of their LMCT excited states (sect. 4.1). The values of k_r for Eu**37** and Tb**37** may be overestimated because the lifetimes at 77 K could be shortened by the contribution of vibronic coupling involving the CH oscillators in the ligand (Prodi et al. 1991).

As to the rate constant of the thermally activated nonradiative decay, it is worthwhile to recall that in the presence of equilibria between the emitting states and other excited states its values cannot be obtained from eq. (11). Nevertheless, we think that for homogeneous series of complexes the values obtained from this equation may be used to discuss the relative importance of the thermally activated nonradiative decay. Following this approach, the values obtained from eq. (11) are presented in table 6 regardless of whether the equilibrium is present or not. The cases in which the equilibrium may be present are indicated. Among the Eu^{3+} complexes, the $k_{nr}(T)$ term is negligible for complexes containing only bpy's or phen's, with the exception of Eu**37**, and becomes important in complexes containing *N*-oxides. This has been related to the effects of the deactivation of the Eu^{3+} emitting state via low-lying LMCT excited states. For the complexes of ligands containing *N*-oxides the LMCT excited states are expected to lie at lower energies than in complexes containing only bpy's, because the reduced electron donor capability of the *N*-oxide-containing moiety leaves the europium ion more positive. An analogous hypothesis may account for the increase of $k_{nr}(T)$ caused by the presence in the ligand of the electron-withdrawing carboxymethyl substituent (Sabbatini et al. 1993). The high $k_{nr}(T)$ value of Eu**37** has been explained by efficient deactivation via low-lying LMCT excited states involving the aliphatic nitrogens of the macrocycle (Prodi et al. 1991). In

Table 6
Decay rate constants of the metal emitting states and number of solvent molecules coordinated to the metal ion[a]

Compound	k_r[b] (s^{-1})	$k_{nr}(T)$[c] (s^{-1})	$k_{nr}(OH)$[d] (s^{-1})	n[e]
Eu**2**	590	<50	2400	2.5
Eu**7**	670	<50	2200	2.3
Eu**14**	770	100[f]	1300	1.4
Eu**15**	900	500[f]	1100	1.1
Eu**16**	900	600[f]	1000	1.1
Eu**27**	530	<50	140	<0.5
Eu**28**[g]	500	50	450	0.9
Eu**29**	700	150[f]	1200	1.2
Eu**30**	770	6900[f]	n.a.[h]	n.a.[h]
Eu**31**	530	<50	3200	3.3
Eu**32**	500	<50	1200	1.3
Eu**37**	900[i]	850[f]	250	<0.5
Eu**39**[g]	1250	140	520	1.1
Eu**41**[g]	500	50	500	1.0
Eu**42**[g]	550	<50	650	1.4
Eu**46**	500	<50	1000	1.1
Tb**2**	260	2100[j]	700	3.0
Tb**27**[g]	350	500[f]	80	0.6
Tb**31**	390	16000[f]	630[k]	2.7
Tb**32**	420	1600[f]	330	1.4
Tb**37**	670[i]	<50	<50	<0.5
Tb**46**	360	<50	280	1.2

[a] In water solution, unless otherwise noted. The lifetime values used to calculate the k and n values are those reported in tables 1–4.
[b] Obtained from eq. (10).
[c] Obtained from eq. (11), regardless of the presence of equilibria (sect. 3). Cases in which the equilibrium may be present are indicated.
[d] Obtained from eq. (12).
[e] Obtained from eqs. (6) and (7).
[f] It cannot be excluded that the excited state involved in the thermally activated nonradiative decay is in equilibrium with the metal emitting state.
[g] In methanol solution.
[h] The lifetimes in H_2O and D_2O are equal (table 2). However, the effects of the vibronic coupling with the OH oscillators are, most likely, masked by the very fast thermally activated nonradiative decay.
[i] A lower value is expected considering that vibronic coupling involving CH oscillators may occur (sect. 5.3).
[j] From kinetic data in deaerated solution a value of $1.6\times10^5\ s^{-1}$ was obtained for the rate constant of the thermally activated back energy transfer from the $^5D_4\ Tb^{3+}$ emitting state to the lowest triplet excited state of the ligand (sect. 4.1).
[k] In deaerated solution. No deuteration effect on the lifetimes is observed in aerated solution.

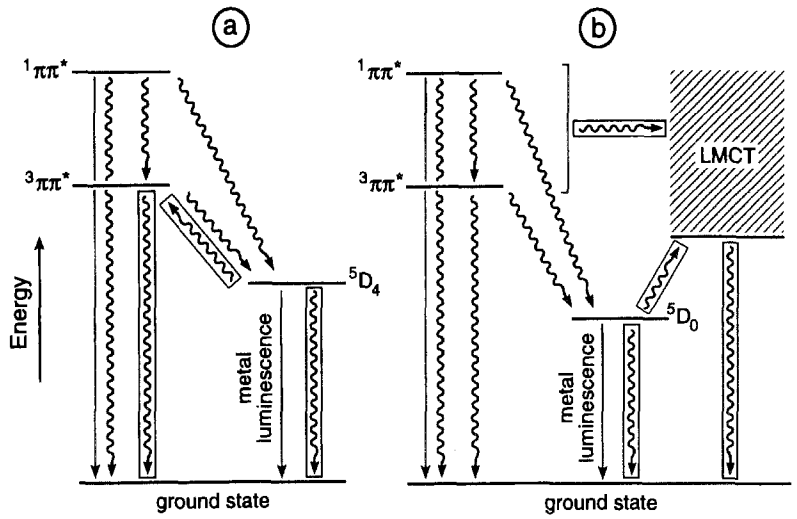

Fig. 14. Scheme of the deactivation processes involved in the conversion of the light absorbed by the ligand into light emitted by the metal ion in (a) Tb^{3+} and (b) Eu^{3+} complexes. The $^1\pi\pi^*$ state is the ligand excited state populated upon excitation and the $^3\pi\pi^*$ state is the ligand excited state populated upon intersystem crossing from the $^1\pi\pi^*$ state. The $^5D_4$ and $^5D_0$ excited states are the luminescent states of Tb^{3+} and Eu^{3+}, respectively. The LMCT excited states are the ligand-to-metal charge-transfer states. The pathways responsible for the most important nonradiative losses are boxed.

the case of the Tb^{3+} complexes, the thermally activated nonradiative decay, which consists of the deactivation of the metal emitting state via the lowest triplet excited state of the ligand, is important for all complexes containing bpy's or phen's, with the exception of Tb**37** where the lowest triplet excited state of the ligand lies at higher energy than in the other Tb^{3+} complexes (sect. 4.2). For complexes of the calixarene ligand **46** $k_{nr}(T)$ is negligible, showing that this ligand does not introduce excited states which can be thermally populated from the metal emitting states.

Finally, we discuss the importance of the nonradiative decay via vibronic coupling with the OH oscillators of the solvent, considering the number of solvent (water or methanol) molecules coordinated to the metal ion obtained from the decay rate constants (table 6). First of all, it is interesting to notice that the numbers of coordinated water molecules, inferior to three, indicate efficient shielding of the metal ion by the cage-type ligands. The Eu^{3+} and Tb^{3+} cryptates containing only bpy's have about 2.5 water molecules in the first coordination sphere of the metal ion. The presence of *N*-oxides in the bpy cryptands causes a decrease of the number of coordinated water molecules, suggesting that steric hindrance of the *N*-oxide groups and the charge of the oxygens may hamper water coordination. The branched-macrocyclic ligands incorporating the macrocycle **26** shield the metal ion very efficiently, which may be attributed to the presence of four coordinating units and the flexible structure of these ligands. Steric hindrance due to the methyl groups in the branches leads to less efficient shielding. In fact, in the complexes of ligand **31** about 3 water molecules are coordinated to the metal ion and Eu**28** decomposes in

water. As to the branched-macrocyclic ligands incorporating the triazacyclononane ring, their shielding ability towards water molecules strongly depends on the position of the attachment of the bpy to the ring, which may give rise to different structures of the complexes, as also suggested by the CPK models. As a matter of fact, in the Eu^{3+} and Tb^{3+} complexes of ligand **37** no water molecule is present in the first coordination sphere of the metal ion while the analogous complexes of ligand **38** decompose in water. The podands **41**–**44** are so inefficient in competing with water molecules for lanthanide complexation that their complexes decompose in water. Ligand **46** shields the metal ion from water molecules relatively well, but its complexes are rather unstable in water. Differently from what observed for complexes in water, the numbers of coordinated methanol molecules are similar to one another. This may be related to weaker coordination and larger size of methanol molecules compared to water molecules.

The scheme presented in fig. 14 summarizes the processes involved in the conversion of light absorbed by the ligands into light emitted by the metal ions for the complexes discussed. The pathways responsible for the most important nonradiative losses are boxed.

5.4. *Metal luminescence intensity*

In this part we discuss the intensity of the metal luminescence obtained upon ligand excitation on the basis of the product of the metal luminescence quantum yield upon excitation at a certain wavelength and the molar absorption coefficient of the ligand in the complex at the same wavelength (table 7). We would like to recall that the metal luminescence intensity is the photophysical property of main interest in this research dealing with the antenna effect in Eu^{3+} and Tb^{3+} complexes. Further, this quantity is determining for some applications of these compounds (sect. 6).

First, complexes containing only the bpy chromophore will be considered. The prototypes Eu**2** and Tb**2** showed strong absorption but gave rather low quantum yields so that high values were not obtained for the luminescence intensity. This quantity was not affected by the presence of substituents, as found in Eu**7** and Eu**8**. The Eu^{3+} and Tb^{3+} complexes of the branched-macrocyclic ligand **27** containing one bpy more than the cryptand **2** gave much more intense luminescence thanks to the higher molar absorption coefficients and the good quantum yields. As to the analogous complex Eu**28**, the luminescence intensity is one order of magnitude lower than that of Eu**27**. This is accounted for by the lower quantum yield caused, most likely, by worse metal–ligand interaction due to the methyl groups. Eu**31** and Tb**31** gave low luminescence intensities in spite of the high molar absorption coefficients, because of the low quantum yields. Concerning Eu**32** and Tb**32**, the presence of only two chromophores results in relatively low molar absorption coefficients. The quantum yields are good so that the luminescence intensities are still rather high. Substitution of the weakly absorbing phenyl units in the phosphinate groups by efficient chromophores is expected to give rise to more intense luminescence if absorption in these chromophores is followed by efficient ligand-to-metal energy transfer (Sabbatini et al. 1994a). The Eu^{3+} and Tb^{3+} complexes of the

Table 7
Metal luminescence intensities[a]

Compound	ε_{max} (M^{-1} cm^{-1})	Φ	$\varepsilon_{max} \times \Phi$
Eu2	28000	0.02	560
Eu7	26000	0.02	520
Eu14	20000	0.15	3000
Eu15	17000	0.09	1500
Eu16	20000	0.20	4000
Eu27	36000	0.10	3600
Eu28	39000	0.01	390
Eu29	15500	0.015	230
Eu30	34000	0.01	340
Eu31	46000	0.013	600
Eu32	15100	0.08	1200
Eu37	24500	0.05	1200
Eu38	30500	0.36	11000
Eu39	38000	0.05	1900
Eu40	49000	0.02	980
Eu41	32000	0.06	1900
Eu42	42000	0.07	2900
Eu43	26500	0.04	1100
Eu44	43500	0.04	1700
Eu46	1100	0.0002	0.2
Eu60	28000	0.04	1100
Eu61	50000	<0.01	<500
Eu63	22500	0.03	680
Eu64	26700	0.14	3700
Eu65	36900	0.16	5900
Tb2	29000	0.03	870
Tb27	44000	0.14	6200
Tb31	43000	0.007	300
Tb32	15300	0.08	1200
Tb37	20400	0.37	7500
Tb38	31200	0.08	2500
Tb40	60400	0.015	900
Tb46	1100	0.20	220
Tb60	29000	0.12	3500
Tb61	46700	0.02	930
Tb63	23400	0.001	23
Tb64	30000	0.0013	39
Tb65	42800	0.007	300

[a] The ε_{max} and Φ values (in hydrogenated solvents) are those reported in tables 1–4.

branched-macrocyclic ligands **37** and **38**, where the triazacyclononane ring carries three bpy's, have molar absorption coefficients similar to those of the Eu**2** and Tb**2** prototypes. Most interestingly, Eu**38** and Tb**37** gave the highest luminescence intensities among the complexes examined, thanks to their high quantum yields. It is worthwhile pointing out that for these complexes the LMCT and lowest ligand triplet excited states lie at energy levels sufficiently high not to interfere with the ligand-to-metal energy transfer nor to deactivate the metal emitting states. Tb**38** and Eu**37** show less intense luminescence because they have much lower quantum yields. The luminescence intensities of the binuclear Eu^{3+} and Tb^{3+} complexes of ligand **40** are rather low, in spite of the high molar absorption coefficients resulting from the presence of six bpy's in the ligand, because of the low quantum yields. The Eu^{3+} and Tb^{3+} complexes of the podands **41–44** show rather intense luminescence because the molar absorption coefficients are high and the quantum yields relatively good.

Further, complexes of some ligands analogous to those mentioned above but containing one to three $bpyO_2$ and one $biqO_2$ chromophores instead of the bpy chromophore will be discussed. The Eu^{3+} complexes of the cryptands **14** and **15**, containing two bpy's and one $bpyO_2$, and cryptand **16**, containing two bpy's and one $biqO_2$, gave rather good molar absorption coefficients and high quantum yields so that good luminescence intensities were obtained. In comparison with the Eu**2** prototype these values are significantly higher. As discussed before, the different behavior is mainly due to a more efficient ligand-to-metal energy transfer. The gain of luminescence intensity upon introduction of *N*-oxides was not observed for Eu**29** and Eu**30**, the values being similar to that of Eu**28**. Most likely, for these three complexes bad interaction between the metal ion and the branches containing methyl groups is responsible for the low quantum yields. Eu**39**, containing three $bpyO_2$ chromophores, gave good luminescence intensity thanks to high molar absorption coefficients and good quantum yields.

Finally, we discuss the Eu^{3+} and Tb^{3+} complexes of ligands based on substituted calix[4]arenes. The complexes of ligand **46** show low luminescence intensities due to the weak absorption of the calixarene. Most interestingly, the introduction of two to four bpy's in the calix[4]arene moiety as in the complexes of ligands **60**, **61** and **63-65** gives rise in most cases to substantial increase of the luminescence intensity thanks to the significant enhancement of the molar absorption coefficients and, for the Eu^{3+} complexes, of the quantum yields.

6. Applications

In this section we will present the applications in immunoassays and DNA hybridization assays of Eu^{3+} and Tb^{3+} complexes exhibiting intense metal luminescence in solution. We will illustrate some general aspects of immunoassays and DNA hybridization assays and discuss in more detail the application of some luminescent Eu^{3+} and Tb^{3+} complexes in these assays.

Immunoassays are based on the immunoreaction occurring between an antibody used as detection reagent and the antigen to be analyzed (Hemmilä 1991). Immunoassays are most interesting as analytical tool thanks to the high specificity with which the antibody recognizes a certain antigen among several other biomolecules, even if these differ very little from the antigen at the molecular level. In order to detect the immunocomplex a label capable of generating a signal is attached to the antibody. Adequate choice of the label can render immunoassays very sensitive. Nowadays analytes present in concentrations down to femtomolar can be quantified. Thanks to their high sensitivity and specificity immunoassays are far superior to almost all other methods for *in vitro* determination of biomolecules. Immunoassays are classified according to several criteria. One of them is based on either the presence or absence of a separation step, thus defining heterogeneous and homogeneous immunoassays, respectively (Stryer 1988). Up to now, the heterogeneous immunoassays have been used more because of their high sensitivity, obtained via the physical separation of the fraction carrying the labelled immunocomplex from other interfering biological species in the sample.

The heterogeneous immunoassays schematized in fig. 15, also called sandwich assays, make use of a liquid phase containing the antigen to be analyzed and a solid phase. A specific antibody immobilized on the solid phase binds the antigen. Washing is performed in order to eliminate other biological species present in the sample, which can interfere during the detection step. A solution of a labelled antibody is added in order to mark the antigen. In this way, the antigen is captured between the antibody immobilized on the solid phase and the labelled antibody. Then the signal of the label is detected. The field of immunoassays is huge, both in respect to variations in compounds to be analyzed and to concentration ranges, which may vary from millimolar to subpicomolar. The very optimal label should fulfill a number of requirements among which the high sensitivity is the most important.

Initially, immunoassays relying on labelling with radioisotopes gained wide acceptance as clinical analyses (Miles and Hales 1968, Weeks et al. 1986). The unquestionable disadvantages of the use of radioisotopes created a strong demand to obtain non-radioisotopic labels. In order to be competitive with radioisotopes, the alternative tracers should enable the detection of the labelled immunoreagent down to 10^{-15}–10^{-18} moles. Among the alternative tracers, enzymatic and luminogenic labels have been studied in particular.

In enzymatic immunoassays (Rubenstein et al. 1972, Mayer and Neuenhofer 1994) the enzyme used as label does not generate any detection signal, but produces the signal-generating species upon the enzyme-catalyzed reaction. High turnover of the enzyme-catalyzed reaction gives rise to efficient amplification of the detection signal so that high sensitivities are achieved for this type of assays. However, these assays present some drawbacks. The detection signal depends very much on incubation time, temperature, and other physical and chemical conditions during substrate incubation. Enzymes can also be sensitive to interfering substances in the sample, such as endogenic enzymes or inhibitors. Enzymes are molecules with a relatively large molecular weight which can cause steric repulsions during the coupling of the antibody to the antigen.

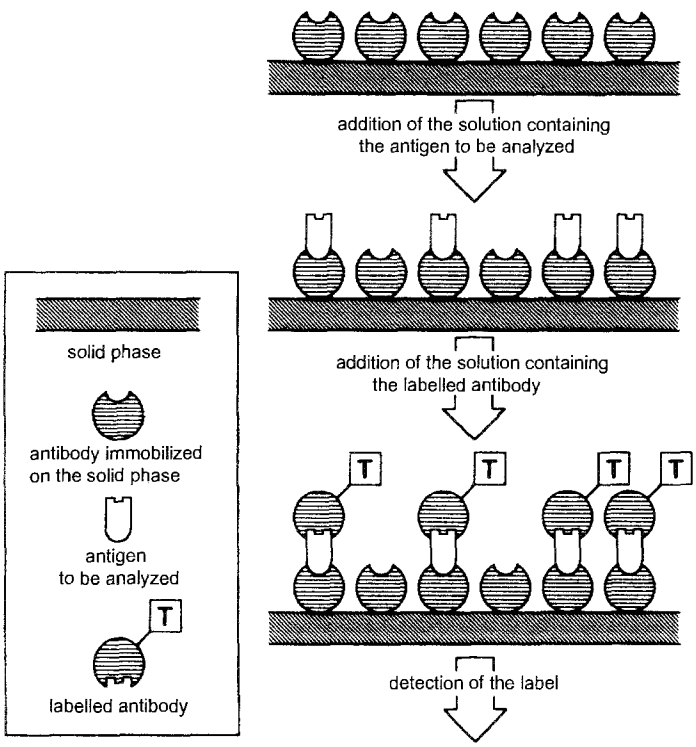

Fig. 15. Scheme of a heterogeneous immunoassay.

The immunological analyses based on the use of luminogenic labels are called fluoroimmunoassays, FIAs (Schroeder et al. 1976, Hemmilä 1991). This kind of labelling is relatively inexpensive and harmless, and luminescence can be measured quickly and simply. Luminogenic labels are usually divided into (i) photoluminescent species, which emit upon photonic excitation, (ii) bioluminescent species, which emit upon an enzymatic reaction, and (iii) chemiluminescent species, which emit upon a chemical reaction. The photoluminescent labels will be treated in more detail because they are of interest for our research. The use of photoluminescent labels instead of radioisotopes involves the disadvantage of decreased sensitivity due to light scattering and short-lived background fluorescence (lifetimes of the order of nanoseconds) of most biological species. A significant improvement has been obtained via FIAs based on time-resolved measurements, TR-FIAs, which make use of labels characterized by long-lived luminescent states. Eu^{3+} and Tb^{3+} compounds are most interesting for TR-FIAs because the Eu^{3+} $^5D_0$ and Tb^{3+} $^5D_4$ luminescent states are particularly long-lived (lifetimes of the order of milliseconds). Moreover, their line-like emission bands lie in the visible, so that these bands can be distinguished from the background fluorescence usually characterized by broad bands in the UV. In order to minimize absorption of interfering biological species and to avoid the use in the instrumentation of deuterium lamps and expensive optical parts

in fused silica, excitation of the Eu^{3+} and Tb^{3+} complexes used as labels should occur at wavelengths longer than 300 nm.

Chelates of lanthanide ions revealed to be particularly suitable for heterogeneous FIAs. According to the way the lanthanide chelates are used, the assays can be divided into (i) assays relying on a separate fluorescence enhancement step, (ii) assays using stabilization techniques, and (iii) assays using *in situ* fluorescent, stable chelates. Among these, fluorescence enhancement assays were the first practical, lanthanide-chelate based fluoroimmunoassays. Two ways to perform the fluorescence enhancement, either by forming mixed-ligand chelates or by completely dissociating the labelling chelate prior to the formation of the fluorescent chelate, have been described. The latter approach was found to be more rapid and practical because this technique allows separate optimization of the immunoreagent labelling with the lanthanide chelate and of the conditions for the fluorimetric detection of the luminescent lanthanide chelate. This technique is available commercially under the trade name DELFIA (Dissociation-Enhanced Lanthanide FluoroImmunoAssay) and has been used for a great number of analytes (Hemmilä et al. 1984, Hemmilä and Dakubu 1986). This analysis is performed as follows. The Eu^{3+} chelate of a polycarboxylic acid is linked to an immunoreagent at pH 7–9. After the immunoreaction and the separation of the labelled immunocomplex, the Eu^{3+} ion is released upon lowering the pH and the solution is treated with the fluorescence enhancement solution containing β-diketones which form highly luminescent complexes with the Eu^{3+} ion. In order to make these complexes soluble in water solution the non-ionic detergent Triton X-100 is added, which dissolves the Eu^{3+} complex in a micellar phase. Shielding of Eu^{3+} from water molecules causing quenching of the luminescence is obtained by the addition of trioctylphosphine oxide which occupies the coordination sites of the Eu^{3+} ion still available in the chelate. Finally, the Eu^{3+} luminescence is measured in a time-resolved mode. The CyberFluor system (Diamandis 1988, Evangelista et al. 1988) is an example of an assay using an *in situ* fluorescent, stable chelate. This system employs the 4,7-bis(chlorosulfophenyl)-1,10-phenanthroline-2,9-dicarboxylic acid chelating ligand capable of sensitizing the Eu^{3+} luminescence. The photosensitizer is attached to an immobilized antibody and after saturation with the metal ion the Eu^{3+} luminescence, obtained upon ligand-to-metal energy transfer, is detected. Of course, neither DELFIA nor CyberFluor can be used for homogeneous assays.

Much research has been dedicated to the development of simultaneously stable and luminescent Eu^{3+} and Tb^{3+} chelates in order to develop simplified heterogeneous FIAs and, possibly, to apply these chelates in homogeneous FIAs. A schematic representation of a luminescent Eu^{3+} and Tb^{3+} chelate suitable as label for FIAs is shown in fig. 16. It consists of (i) the Eu^{3+} or Tb^{3+} ion, (ii) an aromatic structure acting as antenna, (iii) additional chelating groups, e.g. carboxylic acid moieties, and (iv) a functional group allowing the formation of a covalent linkage between the chelate and the target biomolecule. Luminescent Eu^{3+} or Tb^{3+} chelates studied up to now comprise, mostly, aromatic nitrogen heterocycles as energy-absorbing and transferring moieties. The 4-(arylethynyl)pyridine (Takalo et al. 1993), 2,2′-bipyridine (Mukkala and Kankare 1992), 1,10-phenanthroline (Templeton Gudgin and Pollak 1989, Sammes et al. 1992)

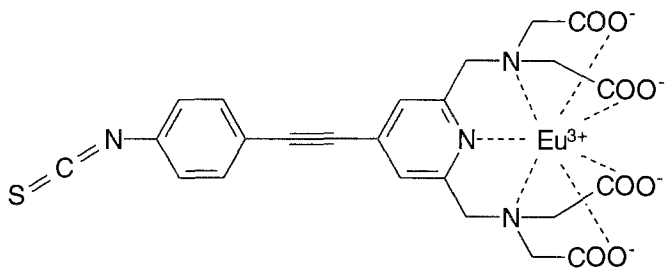

Fig. 16. Schematic representation of a luminescent Eu^{3+} chelate suitable as label for FIAs.

and 2,2′:6′2″-terpyridine (Toner 1990, Mukkala et al. 1993) moieties have been extensively used as energy-absorbing and transferring units. Additional chelating groups to obtain stable complexes are dicarboxylic acids, (methylenenitrilo)bis(acetic acids) and (methylenenitrilo)bis(methylphosphonic acids).

A different approach to obtain Eu^{3+} and Tb^{3+}-based labels for TR-FIAs consists of the use of luminescent cage-type complexes of these ions such as those described in the previous sections. This kind of complexes offers the possibility to obtain luminescent complexes stable in aqueous medium. Further, these systems render the development of highly sensitive assays possible thanks to the intense metal luminescence, which can be achieved via (i) efficient shielding of the metal ion by appropriate cage-type ligands from the solvent molecules quenching the metal luminescence, (ii) substitution of solvent molecules in the first coordination sphere of the complexed metal ion by anions like fluorides and phosphates, and (iii) introduction of efficient chromophores in the ligand acting as antenna. The prototypes Eu**2** and Tb**2** were tested as luminescent labels for TR-FIAs in spite of their rather low metal luminescence intensities because they were stable in water and did not decompose upon attachment to the biomolecule. Anyway, a demand for complexes characterized by higher metal luminescence intensities emerged. As a matter of fact, other complexes studied subsequently (sect. 4) exhibited satisfactory metal luminescence intensities but, up to now, drawbacks related to instability of the complexes in water or their decomposition upon attachment to the biomolecule rendered their application in TR-FIAs impossible. Recently the application of the Eu**8** complex, similar to Eu**2**, in homogeneous FIAs has been reported (Mathis 1993, Lehn 1995). This application is based on the luminescence of an allophycocyanin molecule, sensitized by Eu**8**. The antigen to be analyzed reacts with two different antibodies, one carrying the europium complex and the other the allophycocyanin molecule. In the sandwich immunocomplex, allophycocyanin luminescence is observed as a consequence of an energy transfer from the excited Eu^{3+} ion.

Time-resolved measurements of Eu^{3+} or Tb^{3+} luminescence have been used in DNA hybridization assays for the detection of DNA sequences (Landegren et al. 1988, Oser and Valet 1990). Rapid and precise registration of a DNA sequence is of importance in the characterization of genetic material and, in particular, to recognize the presence or absence of mutations. Most available methods involve the labelling of a probe DNA single strand complementary to a target DNA single strand and the separation of the resulting hybridized double strand from the excess probe. Up to now heterogeneous assays are most frequently used. The target DNA is immobilized on a solid matrix and then incubated with the labelled DNA probe to obtain the hybridized duplex. Afterwards washing is performed to eliminate the excess probe DNA and the detection is carried out. Recently, the application of Eu**8** in a DNA hybridization assay has been reported (Prat et al. 1991). This assay is based on the time-resolved measurement of the Eu^{3+} luminescence of Eu**8** bound to streptavidin capable of recognizing biotinylated probe DNA. Nowadays much research aims at the development of homogeneous assays because the hybridization kinetics is more favorable and simplified analytical procedures are attained. Homogeneous assays require special labelling of the DNA probes because the measurable signal is to be obtained only after hybridization occurred. Here we describe some different approaches to homogeneous assays for the detection of point mutations in DNA sequences via time-resolved fluorescence measurements of Eu^{3+} and Tb^{3+} complexes. Oser and Valet (1990) described an assay involving a suitable pair of single-stranded DNA probes carrying the components for the formation of a Tb^{3+} complex after hybridization with the single-stranded target DNA. One probe carries a diethylenetriaminepentaacetate group complexing the Tb^{3+} ion, and the second probe carries a salicylate group that can coordinate to the Tb^{3+} ion only after hybridization has taken place, and act as antenna in order to obtain metal luminescence. More recently Coates et al. (1994, 1995) developed a new homogeneous assay involving a single-stranded DNA probe carrying a Eu^{3+} chelate of EDTA and a single-stranded DNA target. Hybridization results in the formation of the DNA duplex but no metal luminescence is observed yet. Addition of a third component, incorporating a metal-luminescence sensitizer attached to an intercalating group, can give rise to the formation of a luminescent Eu^{3+} complex after intercalation occurred. The approach capitalizes on the presence of mismatches of the probe with certain targets not having completely complementary nucleic-acid sequences in the sites where intercalation preferably occurs. Then, the presence of mismatches in the duplex causes a reduced binding of the intercalator compared to the binding in a matching duplex. As a consequence the Eu^{3+} luminescence intensities are lower for duplexes with mismatches since a minor amount of the luminescent complex is achieved. The molecules used are the intercalating phenanthridinium linked to 2,9-dicarboxy-1,10-phenanthroline derivatives capable of coordinating the metal ion and acting as antenna. At 295 K only modest discriminations in luminescence intensities could be made between matched and mismatched duplexes, while raising the temperature up to 305 K led to a better discrimination between the two species. Finally we would like to mention an approach consisting of distance measurements in DNA sequences on the basis of the Förster theory on energy transfer. Selvin et al. (1994) have reported an assay in which energy transfer

occurs between a Eu^{3+} complex exhibiting metal luminescence upon ligand excitation and an acceptor molecule. Depending on the position of these two species on the DNA double strand, energy transfer occurs and distances can be determined.

Acknowledgements

This work was supported by M.U.R.S.T. (Ministero dell'Università e della Ricerca Scientifica e Tecnologica) and by the Progetto Strategico "Tecnologie Chimiche Innovative (Sottoprogetto A)" of C.N.R. (Consiglio Nazionale delle Ricerche).

References

Alexander, V., 1995, Chem. Rev. **95**, 273.

Alonso, M.T., E. Brunet, C. Hernandez and J.-C. Rodríguez-Ubis, 1993, Tetrahedron Lett. **34**, 7465.

Alpha, B., 1987, Ph.D. Thesis (University of Strasbourg).

Alpha, B., V. Balzani, J.-M. Lehn, S. Perathoner and N. Sabbatini, 1987a, Angew. Chem. Int. Ed. Engl. **26**, 1266.

Alpha, B., J.-M. Lehn and G. Mathis, 1987b, Angew. Chem. Int. Ed. Engl. **26**, 266.

Alpha, B., E. Anklam, R. Deschenaux, J.-M. Lehn and M. Pietraszkiewicz, 1988, Helv. Chim. Acta **71**, 1042.

Alpha, B., R. Ballardini, V. Balzani, J.-M. Lehn, S. Perathoner and N. Sabbatini, 1990, Photochem. Photobiol. **52**, 299.

Balzani, V., and F. Scandola, 1991, Supramolecular Photochemistry (Ellis Horwood Limited, Chichester).

Balzani, V., E. Berghmans, J.-M. Lehn, N. Sabbatini, R. Terörde and R. Ziessel, 1990, Helv. Chim. Acta **73**, 2083.

Balzani, V., J.-M. Lehn, J. van de Loosdrecht, A. Mecati, N. Sabbatini and R. Ziessel, 1991, Angew. Chem. Int. Ed. Engl. **30**, 190.

Benetollo, F., G. Bombieri, K.K. Fonda, A. Polo, J.R. Quagliano and L.M. Vallarino, 1991, Inorg. Chem. **30**, 1345.

Bkouche-Waksman, I., J. Guilhem, C. Pascard, B. Alpha, R. Deschenaux and J.-M. Lehn, 1991, Helv. Chim. Acta **74**, 1163.

Blasse, G., 1979, Chemistry and physics of R-activated phosphors, in: Handbook on the Physics and Chemistry of Rare Earths, Vol. 4, eds K.A. Gschneidner Jr and L. Eyring (North-Holland, Amsterdam) pp. 237–274.

Blasse, G., M. Buys and N. Sabbatini, 1986, Chem. Phys. Lett. **124**, 538.

Blasse, G., G.J. Dirksen, N. Sabbatini, S. Perathoner, J.-M. Lehn and B. Alpha, 1988a, J. Phys. Chem. **92**, 2419.

Blasse, G., G.J. Dirksen, D. van der Voort, N. Sabbatini, S. Perathoner, J.-M. Lehn and B. Alpha, 1988b, Chem. Phys. Lett. **146**, 347.

Bünzli, J.-C.G., 1987, Complexes with synthetic ionophores, in: Handbook on the Physics and Chemistry of Rare Earths, Vol. 9, eds K.A. Gschneidner Jr and L. Eyring (North-Holland, Amsterdam) pp. 321–394.

Carnall, W.T., 1979, The absorption and fluorescence spectra of rare earth ions in solution, in: Handbook on the Physics and Chemistry of Rare Earths, Vol. 3, eds K.A. Gschneidner Jr and L. Eyring (North-Holland, Amsterdam) pp. 171–208.

Caron, A., J. Guilhem, C. Riche, C. Pascard, B. Alpha, J.-M. Lehn and J.-C. Rodríguez-Ubis, 1985, Helv. Chim. Acta **68**, 1577.

Carugo, O., and C. Bisi-Castellani, 1994, Monatsh. Chem. **125**, 647.

Casnati, A., C. Fischer, M. Guardigli, A. Isernia, I. Manet, N. Sabbatini and R. Ungaro, 1996, J. Chem. Soc. Perkin Trans. **2**, 395.

Coates, J., P.G. Sammes, G. Yahioglu, R.M. West and A.J. Garman, 1994, J. Chem. Soc. Chem. Commun., p. 2311.

Coates, J., P.G. Sammes, R.M. West and A.J. Garman, 1995, J. Chem. Soc. Chem. Commun., p. 1107.

Cole, E., C.J. Broan, K.J. Jankowski, P.K. Pulukkody, D. Parker, A.T. Millikan, N.R.A. Beeley, K. Millar and B.A. Boyce, 1992, Synthesis, 67.

Costa, Silvia M. deB., M.M. Queimado and J.J.R. Frausto da Silva, 1980, J. Photochem. **12**, 31.

Cram, D.J., 1988, Angew. Chem. Int. Ed. Engl. **27**, 1009.

Creaser, I.I., J.M. Harrowfield, A.J. Herlt, A.M. Sargeson, J. Springborg, R.J. Geue and M.R. Snow, 1977, J. Am. Chem. Soc. **99**, 3181.

De Cola, L., D.L. Smailes and L.M. Vallarino, 1986, Inorg. Chem. **25**, 1729.

Diamandis, E.P., 1988, Clin. Biochem. **21**, 139.

Dobler, M., and R.P. Phizackerly, 1974a, Acta Crystallogr. Sect. B **30**, 2746.

Dobler, M., and R.P. Phizackerly, 1974b, Acta Crystallogr. Sect. B **30**, 2748.

Dobler, M., J.D. Dunitz and P. Seiler, 1974, Acta Crystallogr. Sect. B **30**, 2741.

Dunitz, J.D., and P. Seiler, 1974, Acta Crystallogr. Sect. B **30**, 2739.

Dunitz, J.D., M. Dobler, P. Seiler and R.P. Phizackerly, 1974, Acta Crystallogr. Sect. B **30**, 2733.

Evangelista, R.A., A. Pollak, B. Allore, E.F. Templeton, R.C. Morton and E.P. Diamandis, 1988, Clin. Biochem. **21**, 173.

Freed, F.K., 1976, Top. Appl. Phys. **15**, 23.

Frey, S.T., C.A. Chang, J.F. Carvalho, A. Varadarajan, L.M. Schultze, K.L. Pounds and W.DeW. Horrocks Jr, 1994, Inorg. Chem. **33**, 2882.

Georgiev, E.M., J. Clymire, G.L. McPherson and D.M. Roundhill, 1994, Inorg. Chim. Acta **227**, 293.

Guardigli, M., 1992, unpublished results.

Guardigli, M., 1993, Ph.D. Thesis (University of Bologna).

Haas, Y., and G. Stein, 1971, J. Phys. Chem. 75, 3677.

Hemmilä, I.A., 1991, Applications of fluorescence in immunoassays, in: Chemical analysis, Vol. 117, eds J.D. Winefordner and I.M. Kolthoff (Wiley, New York).

Hemmilä, I.A., and S. Dakubu, 1986, US Patent No. 4 565 790.

Hemmilä, I.A., S. Dakubu, V.-M. Mukkala, H. Siitari and T. Lövgren, 1984, Anal. Biochem. **137**, 335.

Holz, R.C., C. Allen Chang and W.DeW. Horrocks Jr, 1991, Inorg. Chem. **30**, 3270.

Horrocks Jr, W.DeW., and D.R. Sudnick, 1979, J. Am. Chem. Soc. **101**, 334.

Horrocks Jr, W.DeW., and D.R. Sudnick, 1981, Acc. Chem. Res. **14**, 384.

Landegren, U., R. Kaiser, C.T. Caskey and L. Hood, 1988, Science **242**, 229.

Lehn, J.-M., 1985, Science **227**, 849.

Lehn, J.-M., 1987, Photophysical and photochemical aspects of supramolecular chemistry, in: Supramolecular Photochemistry, ed. V. Balzani (Reidel, Dordrecht) pp. 29–43.

Lehn, J.-M., 1988, Angew. Chem. Int. Ed. Engl. **27**, 89.

Lehn, J.-M., 1995, Supramolecular Chemistry (VCH, Weinheim).

Lehn, J.-M., and J.-B. Regnouf de Vains, 1992, Helv. Chim. Acta **75**, 1221.

Lehn, J.-M., and C.O. Roth, 1991, Helv. Chim. Acta **74**, 572.

Lehn, J.-M., and J.P. Sauvage, 1975, J. Am. Chem. Soc. **97**, 6700.

Lehn, J.-M., and R. Ziessel, 1987, J. Chem. Soc. Chem. Commun., p. 1292.

Lehn, J.-M., M. Pietraszkiewicz and J. Karpiuk, 1990, Helv. Chim. Acta **73**, 106.

Manet, I., 1995, unpublished results.

Mathis, G., 1993, Clin. Chem. **39**, 1953.

Matsumoto, H., and S. Shinkai, 1994, Chem. Lett., 901.

Mayer, A., and S. Neuenhofer, 1994, Angew. Chem. Int. Ed. Engl. **33**, 1044.

Metz, B., D. Moras and R. Weiss, 1973, Acta Crystallogr. Sect. B **29**, 1377.

Miles, L.E.M., and C.N. Hales, 1968, Nature **219**, 186.

Mukkala, V.-M., and J.J. Kankare, 1992, Helv. Chim. Acta **75**, 1578.

Mukkala, V.-M., M. Helenius, I.A. Hemmilä, J. Kankare and H. Takalo, 1993, Helv. Chim. Acta **76**, 1361.

Murru, M., G. Williams, A. Beeby and D. Parker, 1993, J. Chem. Soc. Chem. Commun., p. 1116.

Musumeci, A., R.P. Bonomo, V. Cucinotta and A. Seminara, 1982, Inorg. Chim. Acta **59**, 133.

Oser, A., and G. Valet, 1990, Angew. Chem. Int. Ed. Engl. **29**, 1167.

Pappalardo, S., F. Bottino, L. Giunta, M. Pietraszkiewicz and J. Karpiuk, 1991, J. Incl. Phenom. **10**, 387.

Paul-Roth, C.O., J.-M. Lehn, J. Guilhem and C. Pascard, 1995, to be published.

Pedersen, C.J., 1967a, J. Am. Chem. Soc. **89**, 2495.

Pedersen, C.J., 1967b, J. Am. Chem. Soc. **89**, 7017.

Pedersen, C.J., 1988, Angew. Chem. Int. Ed. Engl. **27**, 1021.

Pietraszkiewicz, M., S. Pappalardo, P. Finocchiaro, A. Mamo and J. Karpiuk, 1989, J. Chem. Soc. Chem. Commun., p. 1907.

Pietraszkiewicz, M., J. Karpiuk and A.K. Rout, 1993, Pure Appl. Chem. **65**, 563.

Prat, O., E. Lopez and G. Mathis, 1991, Anal. Biochem. **195**, 283.

Prodi, L., M. Maestri, V. Balzani, J.-M. Lehn and C.O. Roth, 1991, Chem. Phys. Lett. **180**, 45.

Reisfeld, R., 1975, Struct. Bonding (Berlin) **22**, 123.

Reisfeld, R., and C.K. Jørgensen, 1977, Inorg. Chem. Concepts **1**, 1.

Rodríguez-Ubis, J.-C., B. Alpha, D. Plancherel and J.-M. Lehn, 1984, Helv. Chim. Acta **67**, 2264.

Roth, C.O., 1992, Ph.D. Thesis (University of Strasbourg).

Rubenstein, K.E., R.S. Schneider and E.F. Ullman, 1972, Biochem. Biophys. Res. Commun. **47**, 846.

Sabbatini, N., S. Dellonte, M. Ciano, A. Bonazzi and V. Balzani, 1984, Chem. Phys. Lett. **107**, 212.

Sabbatini, N., S. Dellonte and G. Blasse, 1986, Chem. Phys. Lett. **129**, 541.

Sabbatini, N., L. De Cola, L.M. Vallarino and G. Blasse, 1987a, J. Phys. Chem. **91**, 4681.

Sabbatini, N., S. Perathoner, V. Balzani, B. Alpha and J.-M. Lehn, 1987b, Antenna effect in Eu^{3+} and Tb^{3+} cryptates, in: Supramolecular Photochemistry, ed. V. Balzani (Reidel, Dordrecht) pp. 187–206.

Sabbatini, N., S. Perathoner, G. Lattanzi, S. Dellonte and V. Balzani, 1987c, J. Phys. Chem. **91**, 6136.

Sabbatini, N., M. Guardigli, A. Mecati, V. Balzani, R. Ungaro, E. Ghidini, A. Casnati and A. Pochini, 1990, J. Chem. Soc. Chem. Commun., p. 878.

Sabbatini, N., M. Guardigli, J.-M. Lehn and G. Mathis, 1992, J. All. Comp. **180**, 363.

Sabbatini, N., M. Guardigli and J.-M. Lehn, 1993, Coord. Chem. Rev. **123**, 201.

Sabbatini, N., M. Guardigli, F. Bolletta, I. Manet and R. Ziessel, 1994a, Angew. Chem. Int. Ed. Engl. **33**, 1501.

Sabbatini, N., M. Guardigli, I. Manet, F. Bolletta and R. Ziessel, 1994b, Inorg. Chem. **33**, 955.

Sabbatini, N., M. Guardigli, I. Manet, R. Ungaro, A. Casnati, C. Fischer, R. Ziessel and G. Ulrich, 1995, New. J. Chem. **19**, 137.

Sammes, P.G., G. Yahioglu and G.D. Yearwood, 1992, J. Chem. Soc. Chem. Commun., p. 1282.

Sato, N., and S. Shinkai, 1993, J. Chem. Soc. Perkin Trans. **2**, 621.

Sato, N., M. Goto, S. Matsumoto and S. Shinkai, 1993a, Tetrahedron Lett. **34**, 4847.

Sato, N., I. Yoshida and S. Shinkai, 1993b, Chem. Lett., 1261.

Schroeder, H.R., P.O. Vogelhut, R.J. Carrico, R.C. Boguslaski and R.T. Buckler, 1976, Anal. Chem. **48**, 1933.

Seiler, P., M. Dobler and J.D. Dunitz, 1974, Acta Crystallogr. Sect. B **30**, 2744.

Selvin, P.R., T.M. Rana and J.E. Hearst, 1994, J. Am. Chem. Soc. **116**, 6029.

Stein, G., and E. Wurzberg, 1975, J. Chem. Phys. **62**, 208.

Strąk, W., 1982, J. Chem. Phys. **76**, 5856.

Stryer, L., 1988, Biochemistry (Freeman, New York).

Takalo, H., and J. Kankare, 1988, Finn. Chem. Lett. **15**, 95.

Takalo, H., E. Hänninen and J. Kankare, 1993, Helv. Chim. Acta **76**, 877.

Templeton Gudgin, E.F., and A. Pollak, 1989, J. Lumin. **43**, 195.

Toner, J.L., 1990, Lanthanide chelates as luminescent probes, in: Inclusion Phenomena and Molecular Recognition, ed. J. Atwood (Plenum Press, New York) pp. 185–197.

Trueblood, K.N., C.B. Knobler, E. Maverick, R.C. Helgeson, S.B. Brown and D.J. Cram, 1981, J. Am. Chem. Soc. **103**, 5594.

Ulrich, G., and R. Ziessel, 1994, Tetrahedron Lett. **35**, 6299.

Weeks, I., M. Sturgess, R.C. Brown and J.S. Woodhead, 1986, Methods Enzymol. **133**, 366.

Weiss, R., B. Metz and D. Moras, 1970, Proc. 13th Int. Conf. Coord. Chem. **2**, 85.

Ziessel, R., 1994, unpublished results.

Ziessel, R., 1995, unpublished results.

Ziessel, R., and J.-M. Lehn, 1990, Helv. Chim. Acta **73**, 1149.

Ziessel, R., M. Maestri, L. Prodi, V. Balzani, J.-M. Lehn and A. Van Dorsselaer, 1993, Inorg. Chem. **32**, 1237.

Handbook on the Physics and Chemistry of Rare Earths
Vol. 23
edited by K.A. Gschneidner, Jr. and L. Eyring

Chapter 155

RATIONALIZATION OF CRYSTAL-FIELD PARAMETRIZATION

Christiane Görller-Walrand and Koen Binnemans
University of Leuven, Department of Chemistry,
Coordination Chemistry Division, Celestijnenlaan 200F,
B-3001 Heverlee-Leuven, Belgium

Contents

List of symbols and abbreviations

A_{SO}	angular part of the spin–orbit interaction
$A_k^q\langle r^k\rangle$	operator-equivalent crystal-field parameters
B_q^k, B'^k_q, B_0^k	crystal-field parameters
CCF	correlation crystal field
CN	coordination number
Cp	η^5-cyclopentadienyl
C_q^k	tensor operator
Dod	dodecahedron
dpa	pyridine-2,6-dicarboxylate
e	elementary charge
$\boldsymbol{E}$	electric field vector of the light
E^k	electron repulsion parameters (Racah parameters)
e_k	electron repulsion operator associated with the Racah parameters
E_{AVE}	parameter shifting the energy of the whole $4f^n$ configuration
ED	(induced) electric dipole
EPR	electron paramagnetic resonance
F^k	electron repulsion parameters (Slater parameters)
f_k	electron repulsion operator associated with the Slater parameters
g_A	degeneracy of level A
$G(G_2)$	Casimir's operator for group G_2
$G(R_7)$	Casimir's operator for group R_7
$\boldsymbol{H}$	magnetic field vector of the light
$\mathcal{H}$	total Hamiltonian (free-ion and crystal-field)
$\mathcal{H}_{CF}$	crystal-field Hamiltonian
$\mathcal{H}_{CCF}$	correlation crystal-field Hamiltonian
$\mathcal{H}_{OCCF}$	orthogonal correlation crystal-field Hamiltonian
$\mathcal{H}_{free\ ion}$	free-ion Hamiltonian
HSM	hard-sphere model
J	total angular momentum
L	total orbital angular momentum
L	ligand number
LCCF	orbitally correlated crystal field
M	magnetic quantum number
MCD	magnetic circular dichroism
MD	magnetic dipole
MFP	most favorable polyhedron
MSAP	monocapped square antiprism
M^k	Marvin integral
m_k	operator associated with the Marvin integrals
N_v	scalar crystal-field strength parameter
O	electric dipole or magnetic dipole operator
OCCF	orthogonal correlation crystal field
ODA	oxydiacetate

P^k	electrostatic correlated spin–orbit interaction parameter	(x, y, z)	basis functions transforming as the electric dipole operator
p_k	operators associated with P^k parameters	Y_k^q	spherical harmonics
$P_k(\cos\omega)$	Legendre polynomials	Z	atomic number
PCEM	point charge electrostatic model	$-Ze$	electric charge of a (negative) ligand
(R_x, R_y, R_z)	basis functions transforming as the magnetic dipole operator	$Z^c_{k0}, Z^c_{kq}, Z^s_{kq}$	tesseral harmonics (c, cosine; s, sine)
R	radial distance between the central metal ion and a ligand	α, β, γ	two-particle configuration interaction parameters (Trees' parameters)
$\boldsymbol{R}$	position vector for a general point in the environment	α, σ, π	polarization direction in polarized spectra
$\boldsymbol{r}_i$	position vector for electron i	ϕ	distortion angle
$\langle r^k \rangle$	expectation value of the k-th power of the ionic or atomic radius	Γ	irreducible representation
		ξ_{4f}	spin-orbit coupling constant
S	total spin angular momentum	μ	crystal-field quantum number
SAP	square antiprism	σ	root mean square (r.m.s.) deviation
SCCF	spin-correlated crystal field		
SP	square prism	(θ, φ)	polar coordinates of the ligand positions
T^i	three-particle parameter		
t_i	three-particle operator	(θ_i, φ_i)	polar coordinates of the position of electron i
TPA	two-photon absorption		
TP	tricapped prism	$\Psi_{l^n\tau SLJM}$	wave function
TTP	tricapped trigonal prism	$\begin{pmatrix} J & k & J' \\ -M & q & M' \end{pmatrix}$	3-j symbol
U	repulsive energy		
U^k_q	unit tensor	$\begin{pmatrix} J & J' & K \\ L' & L & S \end{pmatrix}$	6-j symbol
$\overline{U}^k$	reduced matrix element $\langle \Psi_{l^n\tau SLJ} \Vert U^k \Vert \Psi_{l^n\tau' SL'J'} \rangle$	$\langle \Vert \Vert \rangle$	reduced matrix element
V	crystal-field potential	$\otimes$	direct product

1. Introduction

The spectroscopic properties of lanthanide ions have already been the subject of several chapters in this series. The atomic lanthanide spectra and the theoretical methods for free-ion energy level calculation were reviewed by Goldschmidt (1978). Fulde (1979) considered the crystal fields in rare-earth metallic compounds. Attention was given to the determination of crystal-field parameters in opaque materials, for which no optical methods can be used. In a chapter concerning the complexes of the rare earths, Thompson (1979) paid attention to the spectroscopic properties of coordination compounds. Carnall (1979) discussed the absorption and fluorescence spectra of rare-earth ions in solution. Weber's contribution (1979) treated rare-earth lasers and that of Blasse (1979) treated phosphors activated by lanthanide ions. Morrison and Leavitt (1982)

published a comprehensive review of the energy levels of the trivalent lanthanide ions in transparent host crystals. The intensities of absorption and luminescence spectra of lanthanide ions in glasses and the energy transfer in those vitreous matrices are the subjects of a chapter by Reisfeld and Jørgensen (1987). Judd (1988) outlined the history of lanthanide optical spectroscopy, with emphasis on the development of theoretical models which enabled an understanding of the properties of the atomic 4f shell. Applications of laser spectroscopy to lanthanide systems can be found in the contribution by Yen (1989). Beitz (1994) compared the experimental and theoretical studies of the absorption and luminescence spectra of lanthanide and actinide compounds in solution. Recently, Garcia and Faucher (1995) reviewed and discussed the fitting of phenomenological parameters, the correlated crystal field and the *ab initio* calculations of crystal-field parameters. Spectroscopic methods also find application for the quantitative and qualitative analysis of rare-earth ions. O'Laughlin (1979) discussed spectrophotometric methods for the analysis of lanthanide ions in solution. Optical atomic emission and absorption methods are described by DeKalb and Fassel (1979). D'Silva and Fassel (1979) treated X-ray excited optical luminescence of the rare earths as a method for trace analysis.

In this chapter, special emphasis will be given to the symmetry aspects of the crystal field and the parametrization of the energy level scheme. Four parts can be distinguished. First we give an overview of the experimental data of trivalent lanthanide ions doped into crystalline host matrices. We find such a list is useful, since a large number of papers concerning the spectroscopic properties of trivalent lanthanide ions have been published since the review article of Morrison and Leavitt (1982). The references are not classified according to the host crystal, but according to the lanthanide ion. Because of this alternative classification, together with the fact that many more host matrices are tabled, references before 1982 are also presented. How the experimental data can be interpreted in the framework of crystal-field theory is discussed in the second part. A thorough description is given of the crystal-field perturbation and the calculation of the crystal-field matrix elements. The selection rules for induced electric dipole (ED) and magnetic dipole (MD) transitions for systems with even or odd numbers of f electrons in different site symmetries are presented. Methods for the assignment of crystal-field levels are discussed. From the knowledge of the crystal structure of the host or more precisely from the knowledge of the symmetry of the rare-earth site, it is possible to predict the spectroscopic characteristics of the lanthanide ion in a qualitative way. In the third part, the determination of phenomenological crystal-field parameters is discussed. Such a set of crystal-field parameters in combination with a suitable set of free-ion parameters allows calculation of crystal-field energy levels and to reconstruct the energy diagram of the $4f^n$ configuration. In this way, it is not only possible to check the validity of the crystal-field model but also to get information about energy levels which cannot be detected experimentally. A parameter set is compact, but it contains all the information about the electronic structure of the 4f shell of trivalent lanthanide ions. Some attention is also paid to the correlation crystal-field model, by which one is able to remove, for a large part, the discrepancies between the experimental crystal-field levels and the energy position calculated in the framework of a one-electron crystal field model. The

strength of the crystal field can be represented by a single scalar crystal-field strength parameter. In the fourth part we will reverse the order, i.e., we consider whether it is possible to determine the symmetry and the structure of the rare-earth site from the absorption and emission spectra of the trivalent lanthanide ions and more particularly of the Eu^{3+} ion. We investigate the influence of the shape of the coordination polyhedron around the lanthanide ion on the crystal-field parameters. A correlation is made between the crystal-field splitting of the $^{2S+1}L_J$ free-ion levels of the Eu^{3+} ion and the symmetry of its surrounding. Finally, we present a procedure to determine the point symmetry group of the rare-earth site using the Eu^{3+} ion as a crystal-field probe. We have written this text as didactically as possible, so that it is not only readable for those who are familiar with lanthanide spectroscopy, but also for people from other domains of rare-earth research. The crystal-field theory is presented as seen through the eyes of a chemist. We give therefore special attention to simple models and to the relation between spectroscopic properties and structural aspects of lanthanide compounds. Examples are given whenever it is possible.

It may be helpful to explain the use of the terms "rare earths" and "lanthanides" throughout the text. By convenience, the term lanthanides refers to the elements La ($Z=57$) to Lu ($Z=71$). The term rare earths is commonly used for the lanthanides with inclusion of the elements Y ($Z=39$) and Sc ($Z=21$). Although one speaks often about rare-earth spectroscopy, the term lanthanide spectroscopy is preferable. The main objects of study in lanthanide spectroscopy are the trivalent lanthanide ions from Ce^{3+} ($4f^1$) to Yb^{3+} ($4f^{13}$), since these ions have unpaired f electrons and can interact with ultraviolet, visible or near-infrared radiation. Divalent ions like Eu^{2+} have gained less interest and will not be discussed here. The trivalent lanthanide ions La^{3+} ($4f^0$) and Lu^{3+} ($4f^{14}$) are not spectroscopically active, because of an empty or filled 4f shell. The same is true for Y^{3+} and Sc^{3+}. Yttrium, lanthanum and to a lesser extent lutetium compounds are used as transparent host crystals in which other trivalent lanthanide ions can be doped. The trivalent lanthanide ions can readily substitute for Y^{3+}, La^{3+} and Lu^{3+}. Expressions like "point group of the rare-earth site" and "the crystal field in rare-earth compounds" are thus meaningful.

2. Experimental data

Spectra of trivalent lanthanide ions are much more complicated than those of transition metal ions, which show only a few broad bands. Because the partially filled 4f shell is shielded by the filled 5s and 5p orbitals, the lanthanide ion is only moderately influenced by its environment. Therefore it behaves to a large extent like a free ion. The crystal field is a weak perturbation compared to the electron repulsion and spin–orbit coupling. The optical absorption spectra of 4f systems in single crystals are similar to atomic spectra in the sense that they may sometimes show a large number of very narrow lines. The abundance of lines in the spectra of trivalent lanthanide ions has puzzled earlier spectroscopists. It was J. Becquerel (Becquerel 1907, Becquerel and Kamerlingh Onnes

1908, Becquerel et al. 1925) who discovered that at low temperatures the transitions of lanthanide ions are not bands, but line transitions. He and other workers were unable to explain this spectroscopic behavior, because the necessary theoretical background was lacking at that time. Moreover, most measurements were done on minerals, which contain a mixture of the different lanthanide ions (mainly praseodymium and neodymium as absorbing centers). One had to wait until the discovery of quantum mechanics by Bohr, Dirac, Heisenberg, Slater and others. In 1929 Bethe (Bethe 1929) introduced the crystal-field theory. The fundamental idea is that the splitting of absorption lines of an ion in an electric crystal field is closely related to the symmetry of that field. Group theory has been important in spectroscopy ever since. It became clear that the sharp lines in the absorption and emission spectra of trivalent lanthanide ions are forbidden transitions within the 4f shell (Freed 1931, Tomaschek 1932a,b, Van Vleck 1937). A serious problem was also that high-purity rare-earth compounds were not widely available until after World War II. These impurities resulted in many spurious lines. The development of theories explaining the spectroscopic behavior of the lanthanide ions has been reviewed by Judd (1988).

From the beginning of the 1950s onwards, a lot of experimental data were gathered by research groups like those of K.H. Hellwege (Darmstadt, Germany) and Dieke (Johns Hopkins University, Baltimore). The trivalent lanthanide ions were in the first place doped into host single crystals which could be easily grown from aqueous solutions: the ethylsulphates $R(C_2H_5SO_4)_3 \cdot 9H_2O$, the nonahydrated bromates $R(BrO_3)_3 \cdot 9H_2O$, the double nitrates $R_2M_3(NO_3)_{12} \cdot 24H_2O$ (R = Ce–Eu, M = Mg, Zn) and the hexahydrated chlorides $RCl_3 \cdot 6H_2O$. Anhydrous salts were also studied. We can mention here lanthanum trichloride $LaCl_3$. This matrix has the advantage that it has a high point symmetry, C_{3h} (which can be approximated by D_{3h}). The host $LaCl_3$ has a large optical window, i.e., is transparent to a large wavelength interval. Anhydrous salts are desired for absorption measurements in the near-infrared, because otherwise the electronic transitions are masked by the strong O–H vibrations of the water molecules. The peaks are small and only a few vibronic satellite lines are present. A disadvantage is the hygroscopic character, so that special precautions have to be taken during the preparation, storage and handling of these crystals. The early papers contain only a list of experimental energy levels, grouped according to the $^{2S+1}L_J$ free-ion label. It was not tried to parametrize the spectrum, because an adequate translation of Bethe's crystal-field theory to lanthanide systems was not available. Stevens and Elliot (Stevens 1952, Elliot and Stevens 1953a,b) and Judd (1955, 1957) began to rationalize the raw experimental data by determining crystal-field parameters. This was a difficult task in that pre-computer era, but remarkable results were achieved. The spectroscopic data of the trivalent lanthanide ions have been reviewed by Dieke (1968). A few years earlier, Wybourne (1965) wrote his famous book describing the theory behind calculating free-ion and crystal-field energy levels.

The development of solid state lasers in the 1960s stimulated lanthanide spectroscopy, after it became clear that the trivalent lanthanide ions have promising lasing characteristics. The use of rare-earth ions in laser crystals has been discussed by Weber (1979) and by Kaminskii (1981). Crystals which came under examination are $CaWO_4$, $LiYF_4$, LaF_3,

$YAlO_3$, the rare-earth garnets $A_3B_5O_{12}$ (A = Y, R; B = Al, Ga) and many others. Another class of materials are the rare-earth phosphors which are used in lighting devices and cathode ray tubes (e.g. television screens): Y_2O_2S, ROX (R = Y, La, Gd; X = Cl, Br, I), Y_2O_3, YPO_4, YVO_4, ... These compounds are often only available as polycrystalline samples and have been studied mainly by luminescence techniques. We would also like to mention two host crystals, which are studied from theoretical interest and because large single crystals can be grown relatively easily: the elpasolites A_2BRX_6 (A = Rb, Cs; B = Li, Na, K; X = F, Cl, Br) and the oxydiacetates $Na_3[R(C_4H_4O_5)_3]\cdot 2NaClO_4\cdot 6H_2O$ (or RODA for short). The elpasolite matrix is one of the few examples in which a lanthanide ion is in a site with O_h symmetry. RODA crystallizes out from an aqueous solution. These crystals have been used for testing intensity models and circular dichroism (CD) studies. The oxydiacetates are optically active, because of the D_3 point group. From theoretical viewpoint, crystals with a high site symmetry are desirable, because only few parameters are required for describing the crystal-field splitting. Host matrices with the lanthanide ion at an inversion center are not widely investigated (except the elpasolites). If the point group has an inversion center, the 4f–4f transitions can only gain transitions by vibronic coupling and the zero-phonon lines are often absent (see sect. 3.3). This vibronic structure does not make the interpretation of the spectra easy.

In table 1, an overview is given of the literature concerning the experimental data on the spectroscopic properties of trivalent lanthanide ions doped into crystalline host matrices. The systems are ordered according to the lanthanide ion. Further classification is done alphabetically. We do not claim completeness, since this would be an utopia. We want to present a range of lanthanide-doped crystals as broad as possible. It is our hope that this table can be helpful for spectroscopists who want to make comparative studies. Only crystal-field studies are presented. Papers which are solely concerned with intensity calculations are omitted.

Table 1
Overview of the literature concerning experimental studies of the spectroscopic properties of trivalent lanthanide ions doped into crystalline host matrices

Compound	Reference(s)
Ce^{3+}	
CeF_3	Buchanan et al. (1966)
$CsCdBr_3:Ce^{3+}$	Blasse et al. (1985)
$Cs_2NaCeCl_6$	Amberger et al. (1976)
$LaCl_3:Ce^{3+}$	Hellwege et al. (1965)
$LaF_3:Ce^{3+}$	Buchanan et al. (1966), Gerlinger and Schaack (1986), Carnall et al. (1989)
$YAlO_3:Ce^{3+}$	Weber (1973)
$YPO_4:Ce^{3+}$	Briffaut and Denis (1970), Hoshina and Kuboniwa (1971), Nakazawa and Shianoya (1974)
$Y_2O_3:Ce^{3+}$	Chang et al. (1982)

Continued on next page

Table 1, *continued*

Compound	Reference(s)
$Y_3Ga_5O_{12}:Ce^{3+}$	Herrmann et al. (1966)
Pr^{3+}	
$BaY_2F_8:Pr^{3+}$	Kaminskii and Sarkisov (1986)
$BiLiF_4:Pr^{3+}$	Schultheiss et al. (1987)
$Bi_4Ge_3O_{12}:Pr^{3+}$	Kaminskii et al. (1984a)
$CaF_2:Pr^{3+}$	Bhola (1975)
$CaWO_4:Pr^{3+}$	Aizenberg et al. (1966), Wortman et al. (1975a), Morrison and Leavitt (1982)
$[(C_4H_9)_4N]_3Pr(NCS)_6$	Maghrawy et al. (1993)
$Cp_3Pr{\cdot}CNC_6H_{11}$	Amberger et al. (1986a)
$CsBr:Pr^{3+}$	Radhakrishna and Sivasankar (1977)
$CsCdBr_3:Pr^{3+}$	Chaminade et al. (1991), Ramaz et al. (1993), Neukum et al. (1994), Antic-Fidancev et al. (1995b)
$Cs_2NaPrCl_6$	Amberger et al. (1975), Schwartz (1976), Cheng and Dorain (1976), Amberger (1978a), Morrison et al. (1980a), Reid et al. (1987), Tanner et al. (1994b)
Cs_2NaPrF_6	Amberger (1978b), Tanner et al. (1994b)
$Cs_2NaYBr_6:Pr^{3+}$	Tanner et al. (1994b)
$Cs_2NaYCl_6:Pr^{3+}$	Morley et al. (1982), Tanner et al. (1994b)
$GdCl_3:Pr^{3+}$	Rana et al. (1988)
$Gd_2SiO_5:Pr^{3+}$	Kuleshov et al. (1994)
$Gd_2Te_4O_{11}:Pr^{3+}$	Cascales et al. (1992b)
$Gd_3Ga_5O_{12}:Pr^{3+}$	Antic-Fidancev et al. (1992b)
$KY_3F_{10}:Pr^{3+}$	Morrison et al. (1980b), Abdulsabirov et al. (1987)
$LaAlO_3:Pr^{3+}$	Pelletier-Allard and Martin-Brunetière (1969)
$LaBr_3:Pr^{3+}$	Wong and Richman (1962), Kiess and Dieke (1966), Dieke (1968), Chivian et al. (1979), Schmid et al. (1987)
$LaCl_3:Pr^{3+}$	Sayre et al. (1955), Sarup and Crozier (1965), Rana and Kaseta (1983), Rana et al. (1984), Schmid et al. (1987)
$LaF_3:Pr^{3+}$	Wong et al. (1963a), Yen et al. (1964), Caspers et al. (1965b), Carnall et al. (1969), Elias et al. (1973), Matthies and Welsch (1975), Cordero-Montalvo and Bloembergen (1984, 1985), Levy et al. (1984), Carnall et al. (1988, 1989)
$LiLuF_4:Pr^{3+}$	Kaminskii (1986)
$LiYF_4:Pr^{3+}$	Caspers and Rast (1975), Esterowitz et al. (1979a), Esterowitz et al. (1979b), Renfro et al. (1980), Adam et al. (1985), Schultheiss et al. (1987)
$LuPO_4:Pr^{3+}$	Hayhurst et al. (1982)
$Lu_3Al_5O_{12}:Pr^{3+}$	Kustov and Ryabchenkov (1988)
$PbMoO_4:Pr^{3+}$	Morozov et al. (1966)
$PbWO_4:Pr^{3+}$	Singh et al. (1986)
$Pr(AP)_6I_3$	Jayasankar and Richardson (1989)

Table 1, *continued*

Compound	Reference(s)
$Pr(CCl_3COO)_3 \cdot 2H_2O$	Legendziewicz et al. (1995)
$Pr(C_2H_5SO_4)_3 \cdot 9H_2O$	Kato and Takada (1979)
PrF_3	Koningstein and Grünberg (1971), Dahl and Schaack (1984)
$PrGaO_3$	Podlesnyak et al. (1994)
PrI_3	Clifton et al. (1971)
PrOCl	Antic-Fidancev et al. (1991a)
PrODA	Schwartz et al. (1980)
$Pr(OH)_3$	Chirico et al. (1979)
$Pr_2Mg_3(NO_3)_{12} \cdot 24H_2O$	Hellwege and Hellwege (1953), Kato and Takada (1979), Hens and Görller-Walrand (1995)
$Pr_2(SeO_4)_3 \cdot 8H_2O$	Nandi and Neogy (1988)
$Pr_2Te_4O_{11}$	Cascales et al. (1992b)
$Pr_3Ga_5O_{12}$	Antic-Fidancev et al. (1989, 1992b)
$Pr_3Sb_5O_{12}$	Saez-Puche et al. (1989)
$ThBr_4:Pr^{3+}$	Conway et al. (1981)
$ThCl_4:Pr^{3+}$	Malek et al. (1986)
$YAlO_3:Pr^{3+}$	Arsenev et al. (1974), Kaminskii et al. (1988), Malinowski et al. (1995)
$Y(CCl_3COO)_3 \cdot 2H_2O:Pr^{3+}$	Legendziewicz et al. (1995)
$YPO_4:Pr^{3+}$	Hayhurst et al. (1982)
$Y_3Al_5O_{12}:Pr^{3+}$	Hooge (1966), Gourley (1972), Antic-Fidancev et al. (1987a), Kustov and Ryabchenkov (1988)
$Y_3Ga_5O_{12}:Pr^{3+}$	Hooge (1966), Antic-Fidancev et al. (1989, 1992b, 1994a)
Nd^{3+}	
$BaMoO_4:Nd^{3+}$	Morozov et al. (1967)
$BaWO_4:Nd^{3+}$	Morozov et al. (1967)
$Ba_{0.25}Mg_{2.75}Y_2Ge_3O_{12}:Nd^{3+}$	Miller et al. (1972)
$Ba_2MgGe_2O_7:Nd^{3+}$	Horowitz et al. (1972)
$Ba_2ZnGe_2O_7:Nd^{3+}$	Horowitz et al. (1972)
$Ba_3LaNb_3O_{12}:Nd^{3+}$	Antonov et al. (1986)
$Bi_4Ge_3O_{12}:Nd^{3+}$	Kaminskii et al. (1976e), Morrison and Leavitt (1981)
$Bi_4Si_3O_{12}:Nd^{3+}$	Kaminskii et al. (1976b)
$CaAl_4O_7:Nd^{3+}$	Lindop and Goodwin (1973)
$CaF_2:Nd^{3+}$	Han et al. (1993)
$CaF_2:Nd^{3+}$	Voron'ko et al. (1966), Toledano (1972)
$CaLa_4(SiO_4)_3O:Nd^{3+}$	Ivanov et al. (1977)
$CaMoO_4:Nd^{3+}$	Morozov et al. (1967)
$CaNa(MoO_4)_2:Nd^{3+}$	Morozov et al. (1967)
$Ca(NbO_3)_2:Nd^{3+}$	Kaminskii and Li (1970), Kaminskii et al. (1973a)
$CaO \cdot 2Al_2O_3:Nd^{3+}$	Lindop and Goodwin (1973)

Continued on next page

Table 1, *continued*

Compound	Reference(s)
$CaWO_4:Nd^{3+}$	Kariss et al. (1964), Farrar (1965), Morozov et al. (1967), Morrison and Leavitt (1982)
$CaY_2Mg_2Ge_3O_{12}:Nd^{3+}$	Sharp et al. (1974), Tucker and Birnbaum (1979)
$CaY_4(SiO_4)_3O:Nd^{3+}$	Ivanov et al. (1977)
$Ca_3Ga_2Ge_4O_{14}:Nd^{3+}$	Kaminskii et al. (1984b)
$Ca_5(PO_4)_3F:Nd^{3+}$	Morozov et al. (1970), Maksimova and Sobol' (1974), Gruber et al. (1996)
$CdMoO_4:Nd^{3+}$	Morozov et al. (1967)
$CeF_3:Nd^{3+}$	Dmitruk et al. (1968)
$CeNa(WO_4)_2:Nd^{3+}$	Morozov et al. (1967)
$Cp_3Nd{\cdot}CNC_6H_{11}$	Amberger et al. (1986b)
$CsCdBr_3:Nd^{3+}$	Barthem et al. (1987, 1989), Barthou and Barthem (1990), Ramaz et al. (1992)
$Cs_2NaGdCl_6:Nd^{3+}$	Tanner et al. (1991)
$GaS:Nd^{3+}$	Tagiev et al. (1985), Babaev et al. (1989)
$GdAlO_3:Nd^{3+}$	Arsenev and Bienert (1974)
$GdVO_4:Nd^{3+}$	Anderson et al. (1994)
$Gd_{2-x}Nd_x(WO_4)_3:Nd^{3+}$	Berenberg et al. (1984)
$Gd_2Ti_2O_7:Nd^{3+}$	Antonov et al. (1977a)
$Gd_3Ga_5O_{12}:Nd^{3+}$	Bagdasarov et al. (1974), Nekvasil (1978)
$Gd_3Sc_2Al_3O_{12}:Nd^{3+}$	Bagdasarov et al. (1975a)
$Gd_3Sc_2Ga_3O_{12}:Nd^{3+}$	Gruber et al. (1988), Gruber et al. (1990b)
$Gd_3Sc_2Ga_3O_{12}:Nd^{3+}$	Kaminskii et al. (1976a)
$KLa(MoO_4)_2:Nd^{3+}$	Kaminskii et al. (1973c)
$KY(MoO_4)_2:Nd^{3+}$	Kaminskii et al. (1970)
$KY(WO_4)_2:Nd^{3+}$	Kaminskii et al. (1972)
$KY_3F_{10}:Nd^{3+}$	Abdulsabirov et al. (1987)
$K_5Bi_{1-x}Nd_x(MoO_4)_4$	Kaminskii et al. (1977a)
$(La_{1-x}Nd_x)_3Ga_5SiO_{14}$	Kaminskii et al. (1983b)
$La_{1-x}Nd_xMgAl_{11}O_{19}$	Saber et al. (1985)
$LaBr_3:Nd^{3+}$	Richman and Wong (1962)
$LaCl_3:Nd^{3+}$	Eisenstein (1963b), Crosswhite et al. (1976), Rana et al. (1982)
$LaF_3:Nd^{3+}$	Wong et al. (1963b), Caspers et al. (1965a), Voron'ko et al. (1973), Kumar et al. (1976), Carnall et al. (1988, 1989)
$LaNa(WO_4)_2:Nd^{3+}$	Morozov et al. (1967)
$LaNbO_4:Nd^{3+}$	Godina et al. (1967)
$LaTaO_4:Nd^{3+}$	Godina et al. (1967)
$LaVO_4:Nd^{3+}$	Antic-Fidancev et al. (1991b)
$La_2Be_2O_5:Nd^{3+}$	Jenssen et al. (1976)
$La_2O_2S:Nd^{3+}$	Alves et al. (1971)
$La_2O_3:Nd^{3+}$	Henderson et al. (1967a)

Table 1, *continued*

Compound	Reference(s)
$La_3Lu_2Ga_3O_{12}$	Allik et al. (1988), Gruber et al. (1990b)
$LiGd(MoO_4)_2:Nd^{3+}$	Kaminskii (1981)
$LiKYF_5:Nd^{3+}$	Kaminskii et al. (1994)
$LiLa(MoO_4)_2:Nd^{3+}$	Kaminskii et al. (1973b)
$LiLuF_4:Nd^{3+}$	Kaminskii (1986)
$LiNbO_3:Nd^{3+}$	Gabrielyan et al. (1970), Johnson and Ballman (1969)
$LiNdP_4O_{12}$	Saruwatari et al. (1977), Mazurak and Gruber (1992)
$LiYF_4:Nd^{3+}$	Harmer et al. (1969), Sengupta and Artman (1970a,b), Wortman (1972), da Gama et al. (1981b), Song et al. (1984), Görller-Walrand et al. (1989b), Faucher et al. (1989b), Malinowski et al. (1990), De Leebeeck and Görller-Walrand (1995)
$LiYO_2:Nd^{3+}$	Antonov et al. (1977b)
$LuAlO_3:Nd^{3+}$	Kaminskii et al. (1976c), Faucher et al. (1989a)
$LuPO_4:Nd^{3+}$	Hayhurst et al. (1982)
$Lu_2SiO_5:Nd^{3+}$	Tkachuk et al. (1986)
$Lu_2Si_2O_7:Nd^{3+}$	Tkachuk et al. (1986)
$Lu_3Al_5O_{12}:Nd^{3+}$	Azamatov et al. (1970), Kaminskii et al. (1975)
$Lu_3Ga_5O_{12}:Nd^{3+}$	Bagdasarov et al. (1975b), Nekvasil (1978)
$NaBi(MoO_4)_2:Nd^{3+}$	Kaminskii et al. (1989)
$NaBi(WO_4)_2:Nd^{3+}$	Kaminskii et al. (1989)
$NaLa(MoO_4)_2:Nd^{3+}$	Morozov et al. (1967), Kaminskii (1981), Stevens et al. (1991)
$NaYGeO_4:Nd^{3+}$	Kaminskii et al. (1984a)
$Na_5YSi_4O_{12}:Nd^{3+}$	Kaminskii et al. (1983a)
$NdAlGe_2O_7$	Kaminskii et al. (1987)
$NdAlO_3$	Antic-Fidancev et al. (1980)
$NdBO_3$	Antic-Fidancev et al. (1992c)
$Nd(BrO_3)_3 \cdot 9H_2O$	Ewald (1939)
$Nd(C_2H_5SO_4)_3 \cdot 9H_2O$	Dieke (1968), Kato et al. (1977)
$[Nd(C_3H_7NO)(NO_3)_3(H_2O)_3] \cdot H_2O$	Oczko and Legendziewicz (1993)
$NdCl_3 \cdot 6H_2O$	Ewald (1939), Dieke (1968), Voloshin et al. (1976)
NdF_3	Caro et al. (1981)
$Nd(NO_3)_3 \cdot 6H_2O$	Ewald (1939), Caro et al. (1977b)
NdOCl	Beaury (1988)
NdODA	May et al. (1989)
NdP_5O_{14}	Krühler (1974), Tofield et al. (1975), Kaminskii (1981)
$NdPO_4$	Antic-Fidancev et al. (1991b)
$NdVO_4$	Antic-Fidancev et al. (1991b)
$Nd_2(SeO_4)_3 \cdot 8H_2O$	Neogy and Nandi (1985)
$Nd_2(SO_4)_3 \cdot 8H_2O$	Ewald (1939)
Nd_2BaZnO_5	Taibi et al. (1989)

Continued on next page

Table 1, *continued*

Compound	Reference(s)
$Nd_2Mg_3(NO_3)_{12}\cdot 24H_2O$	Ewald (1939), Tinsley (1963), Dieke (1968), Görller-Walrand et al. (1993a)
Nd_2O_2S	Beaury and Caro (1990)
A-Nd_2O_3	Henderson et al. (1967a), Faucher et al. (1980)
$Nd_2P_5O_{11}$	Danielmeyer and Weber (1972)
γ-Nd_2S_3	Gruber et al. (1983)
$Nd_2Te_4O_{11}$	Cascales et al. (1992b)
$Nd_2Zn_3(NO_3)_{12}\cdot 24H_2O$	Ewald (1939), Dieke (1968)
$Nd_3Ga_5O_{12}$	Nutter and Harrison (1963)
$PbMoO_4:Nd^{3+}$	Kariss and Feofilov (1964), Shekun (1966), Morozov et al. (1967), Minhas et al. (1973)
$PbWO_4:Nd^{3+}$	Morozov et al. (1967), Singh et al. (1986)
$Pb_5(PO_4)_3F:Nd^{3+}$	Morozov et al. (1975)
$Pb_5Ge_3O_{11}:Nd^{3+}$	Kaminskii et al. (1982)
$Sc_2O_3:Nd^{3+}$	Zverev et al. (1967)
$Sc_2SiO_5:Nd^{3+}$	Tkachuk et al. (1986)
$Sc_2Si_2O_7:Nd^{3+}$	Tkachuk et al. (1986)
$SrF_2:Nd^{3+}$	Han et al. (1993)
$SrMoO_4:Nd^{3+}$	Morozov et al. (1967)
$SrWO_4:Nd^{3+}$	Morozov et al. (1967)
$Sr_3Ga_2Ge_4O_{14}:Nd^{3+}$	Kaminskii et al. (1984b)
$Sr_5(PO_4)_3F:Nd^{3+}$	Maksimova and Sobol' (1974), Gruber et al. (1996)
$YAlO_3:Nd^{3+}$	Weber and Varitimos (1971), Kaminskii (1981), Aminov et al. (1985)
$YAl_3(BO_3)_4:Nd^{3+}$	Huang and Luo (1991)
$YF_3:Nd^{3+}$	Davydova et al. (1978)
$YGaO_3:Nd^{3+}$	Kaminskii et al. (1976d)
$YNbO_4:Nd^{3+}$	Godina et al. (1967)
$YP_5O_{14}:Nd^{3+}$	Kaminskii (1981)
$YPO_4:Nd^{3+}$	Hayhurst et al. (1982)
$YScO_3:Nd^{3+}$	Bagdasarov et al. (1975c)
$YTaO_4:Nd^{3+}$	Godina et al. (1967)
$YVO_4:Nd^{3+}$	Karayianis et al. (1975), Kaminskii (1981), Anderson et al. (1994)
$Y_2O_3:Nd^{3+}$	Chang (1966), Zverev et al. (1967)
$Y_2SiO_5:Nd^{3+}$	Tkachuk et al. (1986)
$Y_2Si_2O_7:Nd^{3+}$	Tkachuk et al. (1986)
$Y_2Ti_2O_7:Nd^{3+}$	Antonov et al. (1977a)
$Y_3Al_5O_{12}:Nd^{3+}$	Koningstein and Geusic (1964), Feofilov et al. (1965), Koningstein (1966), Bogomolova et al. (1977), Nekvasil (1978), Gorban et al. (1985a), Gorban et al. (1985b), Hua et al. (1988), Song et al. (1988), Gruber et al. (1990b), Lupei et al. (1995), Burdick et al. (1994)

Table 1, *continued*

Compound	Reference(s)
$Y_3Ga_5O_{12}:Nd^{3+}$	Koningstein (1966), Nekvasil (1978), Kaminskii et al. (1976d)
$Y_3Sc_2Al_3O_{12}:Nd^{3+}$	Allik et al. (1990), Gruber et al. (1990b)
Pm^{3+}	
$LaCl_3:Pm^{3+}$	Baer et al. (1973), Carnall et al. (1976)
Sm^{3+}	
$CaF_2:Sm^{3+}$	Ewanizky et al. (1965), Rabbiner (1967)
$CdF_2:Sm^{3+}$	Rabbiner (1967)
$Cs_2NaSmCl_6$	Amberger et al. (1977), Banerjee and Schwartz (1981), Richardson et al. (1985)
$Cs_2NaYCl_6:Sm^{3+}$	Tanner et al. (1994b)
$KY_3F_{10}:Sm^{3+}$	Abdulsabirov et al. (1987)
$LaCl_3:Sm^{3+}$	Magno and Dieke (1962)
$LaF_3:Sm^{3+}$	Rast et al. (1967a), Dieke (1968), Neogy and Purohit (1987), Carnall et al. (1988)
$Sm(AP)_6(ClO_4)_3$	Berry and Richardson (1989)
$Sm(AP)_6I_3$	Berry and Richardson (1989)
$SmCl_3 \cdot 6H_2O$	Lämmermann (1958), Friederich et al. (1960a)
$Sm(C_2H_5SO_4)_3 \cdot 9H_2O$	Lämmermann (1958), Dieke (1968)
$Sm(NO_3)_3 \cdot 6H_2O$	Lämmermann (1958), Friederich et al. (1960a)
SmODA	May et al. (1987, 1992)
$Sm_2Mg_3(NO_3)_{12} \cdot 24H_2O$	Friederich et al. (1960b), Hens (1996)
$Sm_3Ga_5O_{12}$	Veyssie and Dreyfus (1967)
$Y_2O_2S:Sm^{3+}$	Babkina et al. (1974)
$Y_2O_3:Sm^{3+}$	Chang et al. (1982)
$Y_3Al_5O_{12}:Sm^{3+}$	Grünberg (1969)
$Y_3Ga_5O_{12}:Sm^{3+}$	Grünberg (1969), Grünberg et al. (1969a)
Eu^{3+}	
$BaEu(CO_3)_2F$	Antic-Fidancev et al. (1995a)
$BaGd_2O_4:Eu^{3+}$	Taibi et al. (1994)
$BaSO_4:Eu^{3+}$	Lange (1938)
$BaY_2O_4:Eu^{3+}$	Taibi et al. (1994)
$CaC_4H_4O_6 \cdot 4H_20:Eu^{3+}$	Capobianco et al. (1989)
$CaSO_4:Eu^{3+}$	Lange (1938), Danby and Manson (1984)
$Ca_2B_2O_5:Eu^{3+}$	Capobianco et al. (1970)
$CdF_2:Eu^{3+}$	Kingsley and Prener (1962), Louart et al. (1981)
$CsCdBr_3:Eu^{3+}$	Pellé et al. (1995)
$Cs_2AgEuCl_6$	Kuo et al. (1995)
$Cs_2KYF_6:Eu^{3+}$	Amberger (1980)
$Cs_2NaEuCl_6$	Schwartz (1975)

Continued on next page

Table 1, *continued*

Compound	Reference(s)
$Cs_2NaYCl_6:Eu^{3+}$	Tanner et al. (1994b)
$D\text{-}Lu_2Si_2O_7:Eu^{3+}$	Chateau et al. (1990a)
$D\text{-}Y_2Si_2O_7:Eu^{3+}$	Chateau et al. (1990a)
$Eu(AP)_6(ClO_4)_3$	Berry et al. (1989)
$EuAlO_3$	Kajiura and K. Shinagawa (1970)
$Eu(AP)_6I_3$	Berry et al. (1989)
$Eu(BrO_3)_3 \cdot 9H_20$	Lange (1938), Hellwege and Kahle (1951b), Hasunuma et al. (1984), Moret et al. (1991), Binnemans and Görller-Walrand (1996a)
$Eu(C_2H_3O_2)_3 \cdot 4H_2O$	Lange (1938)
$Eu(C_2H_5SO_4)_3 \cdot 9H_2O$	Sayre and Freed (1956), Dieke (1968), Ohaka and Kato (1983)
$EuCl_3 \cdot 6H_2O$	Hellwege and Kahle (1951a), Bel'skii and Struchkov (1965)
$Eu(DBM)_3 \cdot 3H_2O$	Kirby and Richardson (1983)
EuF_3	Caspers et al. (1967), Jayasankar et al. (1985)
$Eu(NO_3)_3 \cdot 6H_2O$	Lange (1938)
$[Eu(NO_3)_2(18\text{-}6)]_3[Eu(NO_3)_6]$	Bünzli and Pradervand (1986)
$Eu(NO_3)_3(C_{10}H_{20}O_5)$	Bünzli et al. (1982)
EuODA	Berry et al. (1988)
$Eu(OH)_3$	Cone and Faulhaber (1971)
$EuPO_4 \cdot 4H_2O$	Lange (1938)
$Eu(PyNO)_8(ClO_4)_3$	Thompson and Kuo (1989)
EuP_5O_{14}	Brecher (1974)
$Eu_2(C_2O_4)_3 \cdot 10H_2O$	Lange (1938)
$Eu_2Mg_3(NO_3)_{12} \cdot 24H_2O$	Lange (1938), Bünzli and Pradervand (1986), Görller-Walrand et al. (1989a)
$Eu_2(SO_4)_3 \cdot 8H_2O$	Lange (1938)
$Eu_2Zn_3(NO_3)_{12} \cdot 24H_2O$	Hellwege and Schröck-Vietor (1954), Hölsä (1991a), Görller-Walrand et al. (1992)
$Eu_3Ga_5O_{12}$	Boal et al. (1973)
Eu_6WO_{12}	Beaury et al. (1978)
$GdAl_3(BO_3)_4:Eu^{3+}$	Görller-Walrand et al. (1994)
$GdAsO_4:Eu^{3+}$	Linarès et al. (1977)
$GdBGeO_5:Eu^{3+}$	Antic-Fidancev et al. (1994b)
$GdOBr:Eu^{3+}$	Hölsä and Porcher (1982a)
$GdOCl:Eu^{3+}$	Hölsä and Porcher (1981)
$GdOF:Eu^{3+}$	Hölsä and Kestilä (1995a,b)
$GdONO_3:Eu^{3+}$	Hölsä et al. (1994)
$GdVO_4:Eu^{3+}$	Linarès et al. (1977)
$Gd_2(SiO_4)O:Eu^{3+}$	Hölsä et al. (1986)
$Gd_2MoO_6:Eu^{3+}$	Huang et al. (1982)
$Gd_2O_2S:Eu^{3+}$	Sovers and Yoshioka (1969)
$Gd_2O_2SO_4:Eu^{3+}$	Porcher et al. (1983)

Table 1, *continued*

Compound	Reference(s)
$Gd_2O_3:Eu^{3+}$	Rosenberger (1962), Dexpert-Ghys et al. (1981), Daly et al. (1983)
$In_2O_3:Eu^{3+}$	Antic-Fidancev et al. (1992a)
$In_2Si_2O_7:Eu^{3+}$	Chateau et al. (1990b)
$KGd(CO_3)F_2:Eu^{3+}$	Mercier et al. (1995)
$KLu_3F_{10}:Eu^{3+}$	Valon et al. (1977)
$KMgLa(PO_4)_2:Eu^{3+}$	Tie et al. (1995)
$KY_3F_{10}:Eu^{3+}$	Porcher and Caro (1976)
$La_{1-x}Eu_xMgAl_{11}O_{19}$	Saber et al. (1985)
$LaBGeO_5:Eu^{3+}$	Antic-Fidancev et al. (1994b)
$LaBO_3:Eu^{3+}$	Capobianco et al. (1970)
$LaCl_3:Eu^{3+}$	DeShazer and Dieke (1963)
$LaF_3:Eu^{3+}$	Kumar et al. (1977), Carnall et al. (1988, 1989)
$LaMgB_5O_{10}:Eu^{3+}$	Hölsä and Leskelä (1985)
$LaOBr:Eu^{3+}$	Hölsä and Porcher (1982a)
$LaOCl:Eu^{3+}$	Hölsä and Porcher (1981)
$LaOF:Eu^{3+}$	Hölsä (1991b), Hölsä and Kestilä (1995a,b), Wang et al. (1995)
$LaOI:Eu^{3+}$	Hölsä and Porcher (1982a)
$LaONO_3:Eu^{3+}$	Hölsä and Karppinen (1991), Hölsä et al. (1994)
$LaPO_4:Eu^{3+}$	Linarès et al. (1977), Antic-Fidancev et al. (1991b), Tie et al. (1995)
$LaVO_4:Eu^{3+}$	Linarès et al. (1977), Antic-Fidancev et al. (1991b)
$LaWO_4Cl:Eu^{3+}$	Cascales et al. (1992a)
$La_2BaZnO_5:Eu^{3+}$	Taibi et al. (1989)
$La_2MoO_6:Eu^{3+}$	Huang et al. (1982)
$La_2O_2S:Eu^{3+}$	Sovers and Yoshioka (1969), Alves et al. (1970)
$La_2O_2SO_4:Eu^{3+}$	Porcher et al. (1983)
$La_3WO_6Cl_3:Eu^{3+}$	Cascales et al. (1992a)
$LiNbO_3:Eu^{3+}$	Arizmendi and Cabrera (1985)
$LiYF_4:Eu^{3+}$	Görller-Walrand et al. (1985, 1993b), Bihari et al. (1990)
$Li_6Gd(BO_3)_3:Eu^{3+}$	Hölsä and Leskelä (1991)
$Li_6Y(BO_3)_3:Eu^{3+}$	Hölsä and Leskelä (1991)
$LuAsO_4:Eu^{3+}$	Linarès et al. (1977)
$LuOOH:Eu^{3+}$	Chateau and Hölsä (1985), Hölsä (1990)
$LuPO_4:Eu^{3+}$	Linarès et al. (1977)
$LuVO_4:Eu^{3+}$	Linarès et al. (1977)
$Lu_2(SiO_4)O:Eu^{3+}$	Hölsä et al. (1986)
$Lu_2O_2S:Eu^{3+}$	Sovers and Yoshioka (1969)
$Lu_2Si_2O_7:Eu^{3+}$	Chateau et al. (1990b)
$MgSO_4:Eu^{3+}$	Lange (1938)
$Na_3La_2(CO_3)_4F:Eu^{3+}$	Antic-Fidancev et al. (1995a)
$Na_5Eu(MoO_4)_4$	Huang et al. (1984)

Continued on next page

Table 1, *continued*

Compound	Reference(s)
$Na_5Eu(WO_4)_4$	Huang et al. (1984)
Rb_2NaEuF_6	Thompson et al. (1991)
$ScLiO_2:Eu^{3+}$	Gaume-Mahn et al. (1971)
$Sc_2Si_2O_7:Eu^{3+}$	Chateau et al. (1990b)
$SrEu_2O_4$	Taibi et al. (1993)
$SrGd_2O_4:Eu^{3+}$	Taibi et al. (1993)
$SrIn_2O_4:Eu^{3+}$	Taibi et al. (1993)
$SrSO_4:Eu^{3+}$	Lange (1938)
$SrY_2O_4:Eu^{3+}$	Taibi et al. (1993)
$ThO_2:Eu^{3+}$	Hubert et al. (1993)
$YAl_3(BO_3)_4:Eu^{3+}$	Görller-Walrand and Vandevelde (1985), Görller-Walrand et al. (1988)
$YAsO_4:Eu^{3+}$	Linarès et al. (1977)
$YOBr:Eu^{3+}$	Hölsä and Porcher (1982a)
$YOCl:Eu^{3+}$	Hölsä and Porcher (1981)
$YOF:Eu^{3+}$	Hölsä and Kestilä (1995a,b)
$YOOH:Eu^{3+}$	Hölsä (1990)
$YPO_4:Eu^{3+}$	Brecher et al. (1968), Linarès et al. (1977)
$YVO_4:Eu^{3+}$	Brecher et al. (1967), Linarès et al. (1977)
$Y_2BaZnO_5:Eu^{3+}$	Taibi et al. (1989)
$Y_2MoO_6:Eu^{3+}$	Huang et al. (1982)
$Y_2O_2S:Eu^{3+}$	Sovers and Yoshioka (1968, 1969), Alves et al. (1970)
$Y_2O_2SO_4:Eu^{3+}$	Porcher et al. (1983)
$Y_2O_3:Eu^{3+}$	Chang (1963), Chang and Gruber (1970)
$Y_2Si_2O_7:Eu^{3+}$	Chateau et al. (1990b)
$Y_3Al_5O_{12}:Eu^{3+}$	Koningstein (1964), Asano and Koningstein (1979), Gross et al. (1993), Binnemans and Görller-Walrand (1996b)
$Y_3Ga_5O_{12}:Eu^{3+}$	Koningstein (1965a)
Gd^{3+}	
$BaF_2:Gd^{3+}$	Makovsky (1967)
$Bi_2Mg_3(NO_3)_{12}\cdot 24H_2O:Gd^{3+}$	Trenam (1953)
$CaF_2:Gd^{3+}$	Makovsky (1966)
$CaWO_4:Gd^{3+}$	Gil'fanov et al. (1967)
$Ce_2Mg_3(NO_3)_{12}\cdot 24H_2O:Gd^{3+}$	Trenam (1953)
$Cs_2NaGdCl_6$	de Vries and Blasse (1988), Bouazaoui et al. (1991a,b)
$d(C_2H_5SO_4)_3\cdot 9H_2O$	Dieke (1968)
$GdCl_3$	Schwiesow and Crosswhite (1969a)
$GdCl_3\cdot 6H_20$	Dieke and Leopold (1957), Hellwege et al. (1963), Carnall et al. (1971), Antic et al. (1975)
GdF_3	Jayasankar et al. (1985)
$Gd(OH)_3$	Schwiesow and Crosswhite (1969a)

Table 1, *continued*

Compound	Reference(s)
GdODA	Kundu et al. (1990a,b), Stephens et al. (1991)
C-Gd_2O_3	Antic-Fidancev et al. (1982)
$Gd_3Sc_2Ga_3O_{12}$	Gruber et al. (1988)
KY_3F_{10}:Gd^{3+}	Abdulsabirov et al. (1987)
$LaBr_3$:Gd^{3+}	Schwiesow and Crosswhite (1969a)
$LaCl_3$:Gd^{3+}	Piksis et al. (1967), Schwiesow and Crosswhite (1969a)
LaF_3:Gd^{3+}	Caspers et al. (1969), Schwiesow and Crosswhite (1969b), Carnall et al. (1971, 1988, 1989)
$LiNaY_2F_8$:Gd^{3+}	Aamili et al. (1991)
SrF_2:Gd^{3+}	Makovsky (1967)
YF_3:Gd^{3+}	Orlov and Stolov (1975)
$Y(OH)_3$:Gd^{3+}	Schwiesow and Crosswhite (1969a)
YVO_4:Gd^{3+}	Kahle et al. (1968)
$Y_3Al_5O_{12}$:Gd^{3+}	Kaminskii (1975)
Tb^{3+}	
CaF_2:Tb^{3+}	Chrysochoos (1983)
$CaWO_4$:Tb^{3+}	Wortman (1968), Leavitt et al. (1974)
$CsCdBr_3$:Tb^{3+}	Berdowski et al. (1985), Lammers and Blasse (1986)
$Cs_2NaTbCl_6$	Thompson et al. (1977), Tanner et al. (1994a,b)
Cs_2NaYCl_6:Tb^{3+}	Thompson et al. (1977)
DyF_3:Tb^{3+}	Bumagina et al. (1977)
GdF_3:Tb^{3+}	Bumagina et al. (1977)
GdOCl:Tb^{3+}	Hölsä and Porcher (1982b)
La_2O_2S:Tb^{3+}	Alves et al. (1970)
$LaBr_3$:Tb^{3+}	Joshi et al. (1973)
$LaCl_3$:Tb^{3+}	Thomas et al. (1963)
LaF_3:Tb^{3+}	Carnall et al. (1987, 1988)
LaOCl:Tb^{3+}	Hölsä and Porcher (1982b)
$LiTbF_4$	Christensen (1978)
$LiYF_4$:Tb^{3+}	Morrison and Leavitt (1982), Liu et al. (1994)
$Na_3[Tb(dpa)_3]\cdot NaClO_4\cdot 10H_2O$	Bolender et al. (1992)
$TbAl_3(BO_3)_4$	Kellendonk and Blasse (1982), Görller-Walrand et al. (1987)
$TbCl_3\cdot 6H_2O$	Dieke (1968)
$Tb(C_2H_5SO_4)_3\cdot 9H_20$	Dieke (1968)
TbF_3	Krupka and Guggenheim (1969), Bumagina et al. (1977)
TbODA	Saxe et al. (1982)
$Tb(OH)_3$	Scott et al. (1969)
$Tb_3Al_5O_{12}$	Boal et al. (1973), Koningstein and Schaack (1970)
$YAlO_3$:Tb^{3+}	Berg (1973), Morrison and Leavitt (1982)
YF_3:Tb^{3+}	Bumagina et al. (1977)

Continued on next page

Table 1, *continued*

Compound	Reference(s)
$YOCl:Tb^{3+}$	Hölsä and Porcher (1982b)
$YPO_4:Tb^{3+}$	Ionka et al. (1973)
$Y(OH)_3:Tb^{3+}$	Scott et al. (1969)
$Y_2O_2S:Tb^{3+}$	Rossat-Mignod et al. (1974a,b)
$Y_3Al_5O_{12}:Tb^{3+}$	Koningstein (1964), Bayerer et al. (1986), Richter et al. (1991)
$Y_3Ga_5O_{12}:Tb^{3+}$	Joshi and Page (1977)
Dy^{3+}	
$BaY_2F_8:Dy^{3+}$	Johnson and Guggenheim (1973)
$CaWO_4:Dy^{3+}$	Wortman and Sanders (1971)
$Cs_2NaDyCl_6$	Tanner et al. (1988)
$Cs_2NaGdCl_6:Dy^{3+}$	Tanner et al. (1988)
$Dy(C_2H_5SO_4)_3 \cdot 9H_2O$	Gramberg (1960), Hellwege et al. (1961a,b), Dieke (1968)
DyODA	Metcalf et al. (1995)
$Dy(OH)_3$	Scott (1970), Morrison and Leavitt (1982)
Dy_2O_3	Henderson et al. (1967b)
$Dy_3Al_5O_{12}$	Grünberg et al. (1967), Faulhaber and Hüfner (1969), Gehring et al. (1969), Aoyagi et al. (1969)
$Dy_3Ga_5O_{12}$	Veyssie and Dreyfus (1967), Grünberg et al. (1967, 1969b), Wadsack et al. (1971), Blanc et al. (1970)
$DyAlO_3$	Hüfner et al. (1967)
$DyCl_3 \cdot 6H_2O$	Dieke and Singh (1956), Dieke (1968)
$KY_3F_{10}:Dy^{3+}$	Abdulsabirov et al. (1987)
$LaCl_3:Dy^{3+}$	Crosswhite and Dieke (1961), Axe and Dieke (1962), Dieke (1968)
$LaF_3:Dy^{3+}$	Fry et al. (1968), Goodman et al. (1986), Carnall et al. (1988), Neogy and Purohit (1988)
$LiYF_4:Dy^{3+}$	Davydova et al. (1977)
$YAlO_3:Dy^{3+}$	Antonov et al. (1973)
$YF_3:Dy^{3+}$	Davydova et al. (1978)
$Y_2O_2S:Dy^{3+}$	Rossat-Mignod et al. (1974b)
$Y_2O_3:Dy^{3+}$	Chang et al. (1982)
$Y_3Al_5O_{12}:Dy^{3+}$	Gehring et al. (1969), Grünberg et al. (1969b)
$Y_3Ga_5O_{12}:Dy^{3+}$	Grünberg et al. (1969b)
Ho^{3+}	
$BaY_2F_8:Ho^{3+}$	Johnson and Guggenheim (1974)
$CaF_2:Ho^{3+}$	Zhang et al. (1994)
$CaWO_4:Ho^{3+}$	Wortman and Sanders (1970)
$CsCdBr_3:Ho^{3+}$	Mujaji et al. (1993)
$Cs_2NaGdCl_6:Ho^{3+}$	Tanner et al. (1994b)
$Cs_2NaHoBr_6$	Tanner et al. (1994b)
$Cs_2NaHoCl_6$	Morley et al. (1981), Tanner et al. (1994b)

Table 1, *continued*

Compound	Reference(s)
$GdAlO_3:Ho^{3+}$	Arsenev and Bienert (1972c)
$HoAsO_4$	Bischoff et al. (1991)
$Ho(C_2H_5SO_4)_3 \cdot 9H_2O$	Grohmann et al. (1960), Hellwege et al. (1961c), Dieke (1968)
$HoCl_3 \cdot 6H_2O$	Kahle (1956a), Dieke (1968), Stöhr and Gruber (1971), Stöhr et al. (1971)
HoF_3	Blinde (1974), Sharipov et al. (1975), Morrison and Leavitt (1982)
HoODA	Moran et al. (1989, 1990a,b)
$HoPO_4$	Enderle et al. (1990c), Bischoff et al. (1991), Loong et al. (1993)
$HoVO_4$	Barakat and Finn (1988), Bischoff et al. (1991)
$Ho_2(SO_4)_3 \cdot 8H_2O$	Stöhr and Gruber (1975)
$Ho_3Al_5O_{12}$	Ashurov et al. (1979), Ivanov et al. (1975)
$Ho_3Ga_5O_{12}$	Sievers and Tinkham (1963), Belyaeva et al. (1969)
$LaCl_3:Ho^{3+}$	Dieke and Pandey (1964), Rajnak and Krupke (1967), Crosswhite et al. (1977)
$LaF_3:Ho^{3+}$	Caspers et al. (1970), Carnall et al. (1987, 1988)
$LaNbO_4:Ho^{3+}$	Kaminskii (1981)
$LiNbO_3:Ho^{3+}$	Johnson and Ballman (1969), Antonov and Arsenev (1975)
$LiYF_4:Ho^{3+}$	Karayianis et al. (1976)
$NaLa(MoO_4)_2:Ho^{3+}$	Kaminskii (1981)
$PbMoO_4:Ho^{3+}$	Kanskaya et al. (1967)
$YAlO_3:Ho^{3+}$	Weber et al. (1973), Antonov et al. (1973)
$YAsO_4:Ho^{3+}$	Enderle et al. (1990b)
$Y(OH)_3:Ho^{3+}$	Scott (1970), Morrison and Leavitt (1982), Pilawi (1990), Bischoff et al. (1991)
$YPO_4:Ho^{3+}$	Becker et al. (1969), Loong et al. (1993)
$YVO_4:Ho^{3+}$	Wunderlich (1977), Morrison and Leavitt (1982), Enderle et al. (1990a)
$Y_2O_2S:Ho^{3+}$	Rossat-Mignod et al. (1974a,b)
$Y_3Al_5O_{12}:Ho^{3+}$	Johnson et al. (1966), Zverev et al. (1970), Ashurov et al. (1979), Gruber et al. (1991)
$Y_3Fe_5O_{12}:Ho^{3+}$	Johnson et al. (1970)
$Y_3Ga_5O_{12}:Ho^{3+}$	Johnson et al. (1969, 1970)
Er^{3+}	
$BaY_2F_8:Er^{3+}$	Johnson and Guggenheim (1971), Antipenko et al. (1985)
$Bi_4Ge_3O_{12}:Er^{3+}$	Kaminskii et al. (1979b), Morrison and Leavitt (1981)
$Ca_5(PO_4)_3F:Er^{3+}$	Gruber et al. (1994)
$CaF_2:Er^{3+}$	Pollack (1964), Rector et al. (1966), Freeth et al. (1982)
$CaWO_4:Er^{3+}$	Bernal (1971)
$CsCdBr_3:Er^{3+}$	Cockcroft et al. (1989, 1992), McPherson and Meyerson (1990), Pellé and Goldner (1993)
$Cs_2LiErCl_6$	Tanner et al. (1994b)
$Cs_2NaErCl_6$	Meyer and Gaebell (1978), Tanner (1986a, 1988), Tanner et al. (1994b)

Continued on next page

Table 1, *continued*

Compound	Reference(s)
$Cs_3Lu_2Br_9:Er^{3+}$	Hehlen et al. (1994)
$Er(BrO_3)_3 \cdot 9H_2O$	Petty (1956)
$Er(C_2H_5SO_4)_3 \cdot 9H_2O$	Hellwege et al. (1960), Erath (1961), Kato et al. (1977)
$ErCl_3 \cdot 6H_2O$	Kahle (1956b), Dieke (1968), Carnall et al. (1972), Couture and Rajnak (1984)
$ErFeO_3$	Faulhaber et al. (1967)
$Er(NO_3)_3 \cdot 6H_2O$	Petty (1956)
ErODA	Schoene et al. (1991)
$Er(OH)_3$	Cone (1972)
$ErPO_4$	Loong et al. (1993)
$C\text{-}Er_2O_3$	Gruber et al. (1966)
$Er_2(SO_4)_3 \cdot 8H_2O$	Petty (1956)
$GdAlO_3:Er^{3+}$	Arsenev and Bienert (1972a)
$HfSiO_4:Er^{3+}$	Hayhurst et al. (1981)
$KEr(WO_4)_2$	Kaminskii et al. (1979a)
$KGd(WO_4)_2:Er^{3+}$	Kaminskii et al. (1977b)
$KY(WO_4)_2:Er^{3+}$	Kaminskii et al. (1979a)
$KY_3F_{10}:Er^{3+}$	Abdulsabirov et al. (1987)
$LaBr_3:Er^{3+}$	Kiess and Dieke (1966)
$LaCl_3:Er^{3+}$	Dieke and Singh (1961), Varsanyi and Dieke (1962), Eisenstein (1963a)
$LaF_3:Er^{3+}$	Krupke and Gruber (1963, 1964, 1965a), Carnall et al. (1972, 1988)
$LaOBr:Er^{3+}$	Yang et al. (1991)
$LaOCl:Er^{3+}$	Yang et al. (1991)
$LiErP_4O_{12}$	Mazurak and Gruber (1992)
$LiLuF_4:Er^{3+}$	Kaminskii (1986)
$LiNbO_3:Er^{3+}$	Gabrielyan et al. (1970)
$LiYF_4:Er^{3+}$	Brown et al. (1969), Kulpa (1975), Petrov and Tkachuk (1978), da Gama et al. (1981a)
$LuPO_4:Er^{3+}$	Hayhurst et al. (1981)
$Lu_3Al_5O_{12}:Er^{3+}$	Kaminskii et al. (1977c)
$NaLa(MoO_4)_2:Er^{3+}$	Stevens et al. (1991)
$Tb(OH)_3:Er^{3+}$	Cone (1972)
$YAlO_3:Er^{3+}$	Donlan and Santiago (1972)
$YCl_3:Er^{3+}$	Rakestraw and Dieke (1965)
$YF_3:Er^{3+}$	Kuroda et al. (1972), Davydova et al. (1978)
$Y(OH)_3:Er^{3+}$	Cone (1972)
$YPO_4:Er^{3+}$	Kuse (1967)
$YVO_4:Er^{3+}$	Kuse (1967)
$Y_2O_2S:Er^{3+}$	Rossat-Mignod et al. (1973), Linarès and Souillat (1970)
$Y_2O_3:Er^{3+}$	Rosenberger (1962), Kisliuk et al. (1964)
$Y_3Al_5O_{12}:Er^{3+}$	Koningstein and Geusic (1964), Gruber et al. (1993a)

Table 1, *continued*

Compound	Reference(s)
$Y_3Ga_5O_{12}:Er^{3+}$	Pappalardo (1963), Dieke (1968), Ashurov et al. (1976)
$Y_3Sc_2Al_3O_{12}:Er^{3+}$	Gruber et al. (1990a, 1993a)
$Y_3Sc_2Ga_3O_{12}:Er^{3+}$	Gruber et al. (1993a)
Tm^{3+}	
$BaYb_2F_8:Tm^{3+}$	Antipenko et al. (1986)
$CaF_2:Tm^{3+}$	Muko (1973)
$CaWO_4:Tm^{3+}$	Wortman et al. (1975b)
$Cs_2NaTmCl_6$	Schwartz et al. (1979), Morrison et al. (1980a), Tanner (1985a, 1986b), Tanner et al. (1994b)
$Cs_2NaYBr_6:Tm^{3+}$	Tanner (1985b)
$Gd_3Ga_5O_{12}:Tm^{3+}$	Lupei et al. (1994)
$GdAlO_3:Tm^{3+}$	Arsenev and Bienert (1972b)
$GdOCl:Tm^{3+}$	Hölsä et al. (1995)
$GSGG:Tm^{3+}$	Seltzer et al. (1994)
$LaCl_3:Tm^{3+}$	Gruber et al. (1981)
$LaF_3:Tm^{3+}$	Carnall et al. (1970, 1988), Carnall and Crosswhite (1983)
$LaOBr:Tm^{3+}$	Mazurak et al. (1994)
$LiNbO_3:Tm^{3+}$	Johnson and Ballman (1969)
$LiTmF_4$	Christensen (1979)
$LiYF_4:Tm^{3+}$	Jenssen et al. (1975), Dulick et al. (1991)
$LuPO_4:Tm^{3+}$	Becker et al. (1984)
$NaLa(MoO_4)_2:Tm^{3+}$	Merkle et al. (1992)
$NaLa(MoO_4)_2:Tm^{3+}$	Merkle et al. (1992)
$TmCl_3 \cdot 6H_2O$	Stöhr and Gruber (1971), Stöhr et al. (1971)
$Tm(C_2H_5SO_4)_3 \cdot 9H_2O$	Johnson (1958), Gruber and Conway (1960a,b), Krupke and Gruber (1965b), Dieke (1968), Kato and Takada (1979)
$Tm_2(SO_4)_3 \cdot 8H_2O$	Karlow and Gruber (1971, 1975), Karlow et al. (1975)
$Tm_3Al_5O_{12}$	Milward (1967), Koningstein and Grünberg (1971)
$Tm_3Ga_5O_{12}$	Pearson et al. (1968), Koningstein and Kane-Maguire (1974)
$YAlO_3:Tm^{3+}$	Antonov et al. (1973)
$YCl_3 \cdot 6H_2O:Tm^{3+}$	Olsen and Gruber (1971)
$YCl_3:Tm^{3+}$	Dieke (1968)
$YPO_4:Tm^{3+}$	Knoll (1971), Becker et al. (1984)
$YSAG:Tm^{3+}$	Gruber et al. (1993b)
$YSGG:Tm^{3+}$	Seltzer et al. (1993)
$YVO_4:Tm^{3+}$	Knoll (1971), Wortman et al. (1974)
$Y_2O_3:Tm^{3+}$	Gruber et al. (1964)
$Y_3Al_5O_{12}:Tm^{3+}$	Zverev et al. (1970), Gruber et al. (1989)
$Y_3Ga_5O_{12}:Tm^{3+}$	Pearson et al. (1968), Ralph (1969), Buchanan et al. (1969)
$ZnS:Tm^{3+}$	Zimmermann and Boyn (1985)

Continued on next page

Table 1, *continued*

Compound	Reference(s)
Yb^{3+}	
$BaYb_2F_8$	Antipenko et al. (1985)
$Bi_4Ge_3O_{12}:Yb^{3+}$	Kaminskii et al. (1979b)
$CaF_2:Yb^{3+}$	Low (1962), Kirton and McLaughlan (1967)
$CaWO_4:Yb^{3+}$	Jones (1967)
$CdF_2:Yb^{3+}$	Weller (1967)
$Cs_2NaHoBr_6:Yb^{3+}$	Tanner (1986c)
$Cs_2NaYbCl_6$	Schwartz (1977), Amberger et al. (1977), Kanellakopulas et al. (1977)
$Cs_3Yb_2Br_9$	Hehlen and Güdel (1993)
$KY_3F_{10}:Yb^{3+}$	Abdulsabirov et al. (1987)
$LaF_3:Yb^{3+}$	Rast et al. (1967b), Carnall et al. (1989)
$LiYF_4:Yb^{3+}$	Brown (1980), Morrison and Leavitt (1982)
$YAlO_3:Yb^{3+}$	Weber (1971), Antonov et al. (1973)
$Yb(C_2H_5SO_4)_3 \cdot 9H_2O$	Wong (1963), Dieke (1968), Wheeler et al. (1968)
$YbCl_3 \cdot 6H_2O$	Dieke and Crosswhite (1956)
$Yb_3Al_5O_{12}$	Buchanan et al. (1967), Koningstein and Grünberg (1971)
$Yb_3Ga_5O_{12}$	Buchanan et al. (1967), Koningstein (1968), Argyle et al. (1971)
$YF_3:Yb^{3+}$	Kuroda et al. (1972), Davydova et al. (1978)
$Y_2O_3:Yb^{3+}$	Chang et al. (1982)
$Y_3Al_5O_{12}:Yb^{3+}$	Wood (1963), Koningstein (1965b), Bogomolova et al. (1976)
$Y_3Ga_5O_{12}:Yb^{3+}$	Herrmann et al. (1966), Argyle et al. (1971), Koningstein (1965b)

Figure 1 shows the number of host crystals for each of the trivalent lanthanide ions. From this figure it is clear that the most thoroughly spectroscopically investigated lanthanide ions are Nd^{3+} and Eu^{3+}, followed by Er^{3+} and Pr^{3+}. The reasons for this are simple. Pr^{3+} and Eu^{3+} are both theoretically attractive. Pr^{3+} has a $4f^2$ configuration. This configuration is only 91-fold degenerated (compare this with a total degeneration of 3432 for the $4f^7$ configuration of Gd^{3+}). Eu^{3+} is interesting because of the non-degenerate ground state $^7F_0$ and because of the well-spaced ^7F_J ($J=0$ to 6) and ^5D_J ($J=0$ to 4) states. Furthermore, Eu^{3+}-doped phosphors have several applications, especially as the red phosphor in television screens. Eu^{3+} will be discussed in detail in sects. 5.6–5.8. The reason why Tm^{3+} has been studied less extensively than Pr^{3+}, although the $4f^{12}$ configuration of Tm^{3+} has the same free-ion levels as the $4f^2$ configuration of Pr^{3+}, is probably a financial one. Abundance of Tm^{3+} in nature is much less than that of Pr^{3+}, making Tm^{3+} compounds expensive. During the last years, the number of papers dealing with the spectroscopic properties of Tm^{3+} ions has increased considerably, however. The thulium ion can find application in up-converters. Nd^{3+} is important for solid state lasers (e.g. YAG:Nd^{3+}). The same can be said for Er^{3+}. Spectroscopic data for Pm^{3+} doped into crystalline host matrices are very sparse and to our knowledge only $LaCl_3:Pm^{3+}$ has

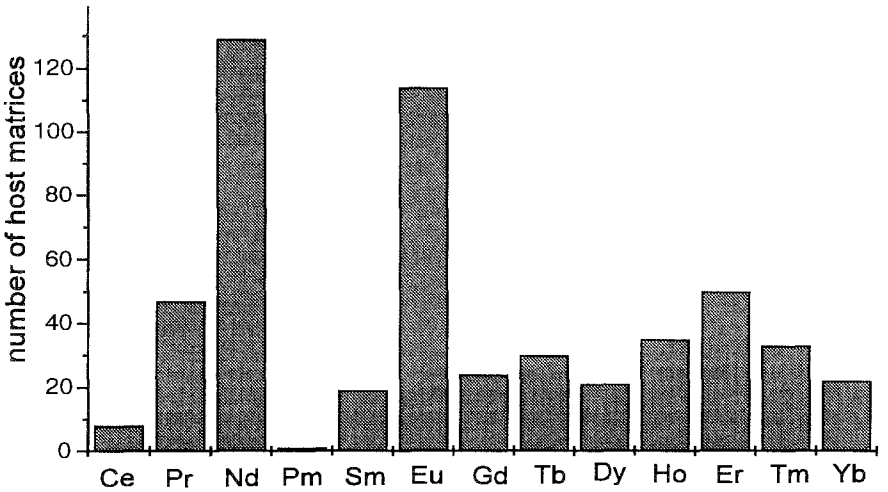

Fig. 1. For each lanthanide ion the number of crystalline host matrices for which spectroscopy studies are available, is plotted. The data are taken from table 1. The importance of Nd^{3+} and Eu^{3+} is very distinct.

been studied (Baer et al. 1973, Carnall et al. 1976). Pm^{3+} is highly radioactive and single crystals are often quickly darkened by radiation effects. For Gd^{3+} and Tb^{3+} only a small part of the $4f^n$ configuration can be studied, because of the large energy gap between the ground term and the excited terms. Sm^{3+} and Dy^{3+} are also problematic because of the very high density of states, which causes a strong violation of the intermediate coupling scheme. It is very difficult to adhere a $^{2S+1}L_J$ label to the free-ion levels. Ho^{3+} has a 17-fold degenerate ground state ($^5I_8$), making a spectroscopic study arduous. The $4f^{10}$ configuration of Ho^{3+} is however rather well investigated. Ce^{3+} ($4f^1$) and Yb^{3+} ($4f^{13}$) have too few crystal-field levels to permit determination of reliable crystal-field parameters.

3. The crystal-field perturbation

3.1. *Crystal-field potential*

The crystal-field interaction is a perturbation of the electron cloud of the central lanthanide ion by all the electrons of the system, other than those of the lanthanide ion itself. The crystal-field Hamiltonian $\mathcal{H}_{CF}$ is defined as:

$$\mathcal{H}_{CF} = -e \sum_{i=1}^{n} V(\boldsymbol{r}_i), \tag{1}$$

where $V(\boldsymbol{r}_i)$ is the potential felt by the electron, and $\boldsymbol{r}_i$ is the position vector of the electron. The summation runs over all the electrons i of the central metal ion. e is the

elementary charge. If the crystal-field perturbation on the $4f^n$ electrons is caused by a time-independent charge distribution $\rho(\boldsymbol{R})$, the crystal-field potential will be given by:

$$V(\boldsymbol{r}_i) = \int \frac{\rho(\boldsymbol{R})}{|\boldsymbol{R} - \boldsymbol{r}_i|} \mathrm{d}\tau. \tag{2}$$

$\boldsymbol{R}$ is the position vector of a general point of the environment, $\mathrm{d}\tau$ is a volume element. Note that the product of a charge distribution and a volume element has the dimension of a charge. The integral is over the whole space. Instead of integration, one can also sum over discrete point charges $-Ze$ at the atomic positions R_L. One can consider the formal charge of the ligands (e.g. $Z=2$ for O^{2-}):

$$V(\boldsymbol{r}_i) = \sum_L \frac{(-Ze)_L}{|\boldsymbol{R}_L - \boldsymbol{r}_i|}. \tag{3}$$

The summation is over the surrounding ions contributing to the crystal field experienced by the rare-earth ion. This equation will be used in the point-charge electrostatic model (PCEM), which is discussed in sect. 5.3. Although a charge distribution is more general than discrete charges, the latter have the advantage that they are easier to visualize.

The potential in eq. (2) can be expanded using the expression

$$\frac{1}{|\boldsymbol{R} - \boldsymbol{r}_i|} = \sum_{k=0}^{\infty} \frac{r_<^k}{r_>^{k+1}} P_k(\cos\omega), \tag{4}$$

where $P_k(\cos\omega)$ are the *Legendre polynomials* and ω is the angle between $\boldsymbol{R}$ and $\boldsymbol{r}_i$. $r_<$ is the smaller distance of (r_i, R) and $r_>$ is the larger distance. If the charge distribution of the crystal does not penetrate that of the 4f electrons, we can assume $r_i < R$:

$$\frac{1}{|\boldsymbol{R} - \boldsymbol{r}_i|} = \sum_{k=0}^{\infty} \frac{r_i^k}{R^{k+1}} P_k(\cos\omega). \tag{5}$$

$P_k(\cos\omega)$ can be expanded further by the *spherical harmonic addition theorem* (Griffith 1961) which expresses the angle ω between $\boldsymbol{R}$ and $\boldsymbol{r}_i$ in terms of the polar angles (θ, φ) and (θ_i, φ_i). Thus (θ, φ) characterizes the angular distribution of the disturbing charges and (θ_i, φ_i) represents the angular position of electron i:

$$P_k(\cos\omega) = \frac{4\pi}{2k+1} \sum_{q=-k}^{k} Y_k^{q*}(\theta, \varphi) Y_k^q(\theta_i, \varphi_i), \tag{6}$$

Y_k^q are the spherical harmonics and they are given up to $k=7$ in Appendix 1. $Y_k^{q*}(\theta, \varphi)$ is the complex conjugate of $Y_k^{-q}(\theta, \varphi)$ and is defined as:

$$Y_k^{q*}(\theta, \varphi) = (-1)^q Y_k^{-q}(\theta, \varphi). \tag{7}$$

Thus:

$$P_k(\cos\omega) = \frac{4\pi}{2k+1} \sum_{q=-k}^{k} (-1)^q\, Y_k^{-q}(\theta, \varphi)\, Y_k^{q}(\theta_i, \varphi_i). \tag{8}$$

The $Y_k^{-q}(\theta, \varphi)$ can be seen as expansion coefficients and the $Y_k^q(\theta_i, \varphi_i)$ as operators. $Y_k^{-q}(\theta, \varphi)$ and $Y_k^q(\theta_i, \varphi_i)$ will be shortened to Y_k^{-q} and $Y_k^q(i)$, respectively. We can work out the summation of eq. (8):

$$P_k(\cos\omega) = \frac{4\pi}{2k+1} \left[(-1)^0\, Y_k^0 Y_k^0(i) + \sum_{q=1}^{k} \left((-1)^q\, Y_k^{-q} Y_k^q(i) + (-1)^{-q}\, Y_k^q Y_k^{-q}(i) \right) \right], \tag{9}$$

Since $(-1)^0 = 1$ and $(-1)^{-q} = (-1)^q$:

$$P_k(\cos\omega) = \frac{4\pi}{2k+1} \left[Y_k^0 Y_k^0(i) + \sum_{q=1}^{k} (-1)^q \left(Y_k^{-q} Y_k^q(i) + Y_k^q Y_k^{-q}(i) \right) \right]. \tag{10}$$

The expansion coefficient Y_k^0 is real, but Y_k^q and Y_k^{-q} are complex quantities. It is more convenient to replace the *spherical harmonics* Y_k^0, Y_k^q and Y_k^{-q} by the *tesseral harmonics* Z_{k0}^{c}, Z_{kq}^{c} and Z_{kq}^{s}, which are real. The relations between the spherical and tesseral harmonics are:

$$\text{spherical harmonic } Y_k^0 = Z_{k0}^{c}, \tag{11}$$

$$\text{spherical harmonic } Y_k^q = \frac{(-1)^q}{\sqrt{2}} \left(Z_{kq}^{c} + \mathrm{i} Z_{kq}^{s} \right), \tag{12}$$

$$\text{spherical harmonic } Y_k^{-q} = \frac{1}{\sqrt{2}} \left(Z_{kq}^{c} - \mathrm{i} Z_{kq}^{s} \right), \tag{13}$$

and

$$\text{tesseral harmonic } Z_{k0}^{c} = Y_k^0, \tag{14}$$

$$\text{tesseral harmonic } Z_{kq}^{c} = \frac{1}{\sqrt{2}} \left(Y_k^{-q} + (-1)^q\, Y_k^q \right), \tag{15}$$

$$\text{tesseral harmonic } Z_{kq}^{s} = \frac{\mathrm{i}}{\sqrt{2}} \left(Y_k^{-q} - (-1)^q\, Y_k^q \right). \tag{16}$$

The superscripts c and s stand for the presence of the factors $\cos(q\varphi)$ and $\sin(q\varphi)$ in the tesseral harmonics. The expressions for the tesseral harmonics in polar coordinates can be calculated easily with eqs. (14)–(16) from the expressions of the spherical harmonics.

The tesseral harmonics in cartesian coordinates for $k=0$ to $k=6$ have been tabulated by Prather (1961). His results together with the tesseral harmonics for $k=7$ are given in Appendix 2. Equation (10) can be rewritten as:

$$P_k(\cos\omega) = \frac{4\pi}{2k+1}\left[Z^{\mathrm{c}}_{k0}Y^0_k(i) + \sum_{q=1}^{k}(-1)^q\left(\frac{1}{\sqrt{2}}\left(Z^{\mathrm{c}}_{kq} - \mathrm{i}Z^{\mathrm{s}}_{kq}\right)Y^q_k(i) + \frac{(-1)^q}{\sqrt{2}}\left(Z^{\mathrm{c}}_{kq} + \mathrm{i}Z^{\mathrm{s}}_{kq}\right)Y^{-q}_k(i)\right)\right], \tag{17}$$

and after rearrangement:

$$P_k(\cos\omega) = \frac{4\pi}{2k+1}\left[Z^{\mathrm{c}}_{k0}Y^0_k(i) + \sum_{q=1}^{k}\left(Z^{\mathrm{c}}_{kq}\frac{1}{\sqrt{2}}\left(Y^{-q}_k(i) + (-1)^q Y^q_k(i)\right) + Z^{\mathrm{s}}_{kq}\frac{\mathrm{i}}{\sqrt{2}}\left(Y^{-q}_k(i) - (-1)^q Y^q_k(i)\right)\right)\right]. \tag{18}$$

Notice that in eq. (18) one has

$$\left(Y^{-q}_k(i) + (-1)^q Y^q_k(i)\right) = \sqrt{2}Z^{\mathrm{c}}_{kq}(i), \qquad \left(Y^{-q}_k(i) - (-1)^q Y^q_k(i)\right) = \frac{\sqrt{2}}{\mathrm{i}}Z^{\mathrm{s}}_{kq}(i),$$
$$Y^0_k(i) = Z^{\mathrm{c}}_{k0}(i).$$

An equivalent way to write eq. (18) is thus

$$P_k(\cos\omega) = \frac{4\pi}{2k+1}\left[Z^{\mathrm{c}}_{k0}Z^{\mathrm{c}}_{k0}(i) + \sum_{q=1}^{k}\left(Z^{\mathrm{c}}_{kq}Z^{\mathrm{c}}_{kq}(i) + Z^{\mathrm{s}}_{kq}Z^{\mathrm{s}}_{kq}(i)\right)\right]. \tag{19}$$

The spherical harmonics $Y^q_k(i)$ can be replaced by the tensor operators $C^k_q(i)$, which have the same transformation properties as the spherical harmonics:

$$C^k_q(i) = \sqrt{\frac{4\pi}{2k+1}}Y^q_k(i). \tag{20}$$

So we find:

$$P_k(\cos\omega) = \sqrt{\frac{4\pi}{2k+1}}\left[Z^{\mathrm{c}}_{k0}C^k_0(i) + \sum_{q=1}^{k}\left(Z^{\mathrm{c}}_{kq}\frac{1}{\sqrt{2}}\left(C^k_{-q}(i) + (-1)^q C^q_k(i)\right) + Z^{\mathrm{s}}_{kq}\frac{\mathrm{i}}{\sqrt{2}}\left(C^k_{-q}(i) - (-1)^q C^q_k(i)\right)\right)\right]. \tag{21}$$

After combination of eq. (5) and eq. (21), the following expression is found for the crystal-field potential $V(\boldsymbol{r}_i)$ in eq. (2):

$$V(\boldsymbol{r}_i) = \sum_{k=0}^{\infty} \sqrt{\frac{4\pi}{2k+1}} \left[Z^{\mathrm{c}}_{k0} C^k_0(i) + \sum_{q=1}^{k} \left(Z^{\mathrm{c}}_{kq} \frac{1}{\sqrt{2}} \left(C^k_{-q}(i) + (-1)^q C^q_k(i) \right) + Z^{\mathrm{s}}_{kq} \frac{\mathrm{i}}{\sqrt{2}} \left(C^k_{-q}(i) - (-1)^q C^q_k(i) \right) \right) \right] \times \int \rho(\boldsymbol{R}) \frac{r_i^k}{R^{k+1}} \mathrm{d}\tau. \tag{22}$$

To simplify this expression, we introduce the coefficients B^k_0, B^k_q and B'^k_q:

$$\text{coefficient } B^k_0 = \sqrt{\frac{4\pi}{2k+1}} Z^{\mathrm{c}}_{k0} \int \rho(\boldsymbol{R}) \frac{r^k}{R^{k+1}} \mathrm{d}\tau, \tag{23}$$

$$\text{coefficient } B^k_q = \sqrt{\frac{4\pi}{2k+1}} \frac{Z^{\mathrm{c}}_{kq}}{\sqrt{2}} \int \rho(\boldsymbol{R}) \frac{r^k}{R^{k+1}} \mathrm{d}\tau, \tag{24}$$

$$\text{coefficient } B'^k_q = \sqrt{\frac{4\pi}{2k+1}} \frac{Z^{\mathrm{s}}_{kq}}{\sqrt{2}} \int \rho(\boldsymbol{R}) \frac{r^k}{R^{k+1}} \mathrm{d}\tau, \tag{25}$$

or if discrete negative charges are considered:

$$\text{coefficient } B^k_0 = \sqrt{\frac{4\pi}{2k+1}} Z^{\mathrm{c}}_{k0} \sum_L (-Ze)_L \frac{r^k}{R^{k+1}_L}, \tag{26}$$

$$\text{coefficient } B^k_q = \sqrt{\frac{4\pi}{2k+1}} \frac{Z^{\mathrm{c}}_{kq}}{\sqrt{2}} \sum_L (-Ze)_L \frac{r^k}{R^{k+1}_L}, \tag{27}$$

$$\text{coefficient } B'^k_q = \sqrt{\frac{4\pi}{2k+1}} \frac{Z^{\mathrm{s}}_{kq}}{\sqrt{2}} \sum_L (-Ze)_L \frac{r^k}{R^{k+1}_L}. \tag{28}$$

All these coefficients are real numbers and contain both an angular and a radial part. The radial dependence is considered to be the same for all states, so that we write r^k and not r^k_i. The coefficients may not be confused with the crystal-field parameters which will be defined further on. The notations are the same as those given by Wybourne (1965). The

coefficients B_0^k, B_q^k and B'^k_q can also be defined in terms of the real and imaginary part of Y_k^q instead of Z_{kq}^0, Z_{kq}^c and Z_{kq}^s:

$$\text{coefficient } B_0^k = \sqrt{\frac{4\pi}{2k+1}}\, Y_k^0 \sum_L (-Ze)_L \frac{r^k}{R_L^{k+1}}, \tag{29}$$

$$\text{coefficient } B_q^k = \sqrt{\frac{4\pi}{2k+1}}\, (-1)^q \,\mathrm{Re} Y_k^q \sum_L (-Ze)_L \frac{r^k}{R_L^{k+1}}, \tag{30}$$

$$\text{coefficient } B'^k_q = \sqrt{\frac{4\pi}{2k+1}}\, (-1)^q \,\mathrm{Im} Y_k^q \sum_L (-Ze)_L \frac{r^k}{R_L^{k+1}}. \tag{31}$$

Notice that the factor $1/\sqrt{2}$ disappears in the expressions for B_q^k and B'^k_q. From the *formula of de Moivre,* $\exp(iq\varphi) = \cos(q\varphi) + i\sin(q\varphi)$, it is clear that B_q^k contains a cosine and B'^k_q a sine part. This could also be deduced of course from the terms Z_{kq}^c and Z_{kq}^s in the definition of these coefficients. Equation (22) can be rewritten as:

$$V(\boldsymbol{r}_i) = \sum_{k=0}^{\infty} \left[B_0^k C_0^k(i) + \sum_{q=1}^{k} \left(B_q^k \left(C_{-q}^k(i) + (-1)^q C_k^q(i) \right) + B'^k_q \mathrm{i} \left(C_{-q}^k(i) - (-1)^q C_k^q(i) \right) \right) \right]. \tag{32}$$

In practice, k runs only over a limited number of terms. For f systems $k = 0, 1, \ldots, 7$. The crystal-field potential V can be divided into an even (k = even) part and an odd part (k = odd). The even part ($k = 0, 2, 4, 6$) is responsible for the crystal-field splitting, while the odd part ($k = 1, 3, 5, 7$) is responsible for the intensity of induced electric dipole transitions (Judd 1962, Ofelt 1962). The values of q are limited by the point group of the rare-earth site, since the crystal-field Hamiltonian has to be invariant under all symmetry operations of the point group. The Hamiltonian transforms as the totally symmetric representation Γ_1, because symmetry operations cannot change the energy of the ion. The non-zero (k, q) combinations can be determined by checking which of the coefficients B_0^k, B_q^k and B'^k_q contain the same symmetry elements as the point group in question. The symmetry elements of the coefficients B_0^k, B_q^k and B'^k_q are of course the same as those for the tesseral harmonics Z_{k0}^c, Z_{kq}^c and Z_{kq}^s. The symmetry elements of the tesseral harmonics with $k = 0$ to 6 have been listed by Prather (1961) and his results together with those for $k = 7$ are listed in table 2. The effect of the symmetry elements on reducing the number of (k, q) combinations are summarized in table 3. One has to be aware that all the symmetry operations generated by a C_n rotation axis are also symmetry operations generated by a C_m axis, where m is a multiple of n (e.g. C_3 and C_6, C_2 and C_4). For instance, the symmetry operations C_3^1 and C_3^2 generated by a C_3 axis,

are equivalent to the C_6^2 and C_6^4 operations generated by a C_6 axis. Tesseral harmonics which contain a C_6 axis as symmetry element, are invariant under the C_3 operations and will be present in the expansion of the crystal-field potential. Vertical planes of symmetry arising from Z_{kq}^c are denoted as σ_v and those arising from Z_{kq}^s as σ_d. In the absence of any symmetry 28 non-zero coefficients occur, or 27 if B_0^0 is excluded. The term $B_0^0 C_0^0$ is spherically symmetric and responsible for the greater part of the lattice energy and the heat of solution (Wybourne 1965). This coefficient can be ignored if only the crystal field splitting is considered, because it gives in first approximation only a uniform shift of all levels of the $4f^n$ configuration. In energy level calculations, B_0^0 is absorbed in the free-ion parameter E_{AVE} (see sect. 4.1) together with other spherically symmetric interactions. One may not forget that the spherical part of the crystal-field interaction is much larger than the non-spherical part. The non-spherical part on the other hand is responsible for a partial or total removal of the $2J+1$ fold degeneration of the J terms in the free ion. Total removal of the degeneracy can be found for systems with an even number of f electrons and a low site symmetry. Systems with an odd number of f electrons (*Kramers' ions*) and a symmetry lower than cubic, have invariably twofold degenerated crystal-field levels (in the absence of an external magnetic field).

We will illustrate the development of the even part of the crystal-field potential for the symmetries C_4 and D_3. First of all we determine which tesseral harmonics have the same symmetry elements as the point group C_4. In C_4, only a fourfold rotation axis is present. This axis can generate the symmetry operations C_4^1, C_4^2 (=C_2), C_4^3 and the identity. The tesseral harmonics Z_{20}^c, Z_{40}^c and Z_{60}^c have cylindrical symmetry and are present in the even part of every crystal-field potential. The C_4 axis is a symmetry element for the harmonics Z_{44}^c, Z_{44}^s, Z_{64}^c and Z_{64}^s. We have thus the following coefficients in the even part of the crystal-field potential for C_4: B_0^2, B_0^4, B_4^4, B'^4_4, B_0^6, B_4^6 and B'^6_4. The potential can be written as

$$\begin{aligned} V^{\text{even}}(C_4) = {} & B_0^2 C_0^2(i) + B_0^4 C_0^4(i) + B_4^4 \left(C_{-4}^4(i) + C_4^4(i)\right) + B'^4_4 \mathrm{i} \left(C_{-4}^4(i) - C_4^4(i)\right) \\ & + B_0^6 C_0^6(i) + B_4^6 \left(C_{-4}^6(i) + C_4^6(i)\right) + B'^6_4 \mathrm{i} \left(C_{-4}^4(i) - C_4^4(i)\right). \end{aligned} \tag{33}$$

The symmetry elements in D_3 are C_3 and C_2'. It is easy to see that the tesseral harmonics Z_{20}^c, Z_{40}^c, Z_{43}^c, Z_{60}^c and Z_{63}^c have the same symmetry elements as D_3. But, we have already mentioned that a C_6 axis will also generate the symmetry operations C_3^1 (=C_6^2) and C_3^2 (=C_6^4) present in D_3. Therefore, Z_{66}^c is invariable under the symmetry operations of D_3. The tesseral harmonics Z_{kq}^s are absent, because C_2' is not a symmetry element for the tesseral harmonics with k = even. The coefficients in $V^{\text{even}}(D_3)$ are B_0^2, B_0^4, B_3^4, B_0^6, B_3^6 and B_6^6. The potential is

$$\begin{aligned} V^{\text{even}}(D_3) = {} & B_0^2 C_0^2(i) + B_0^4 C_0^4(i) + B_3^4 \left(C_{-3}^4(i) - C_3^4(i)\right) + B_0^6 C_0^6(i) \\ & + B_3^6 \left(C_{-3}^6(i) - C_3^6(i)\right) + B_6^6 \left(C_{-6}^6(i) + C_6^6(i)\right). \end{aligned} \tag{34}$$

Pay attention to the phase convention for combining $C_{-q}^k(i)$ and $C_q^k(i)$. In Appendix 3 the crystal-field potentials for the 32 crystallographic point groups are given, together

Table 2
Symmetry elements in tesseral harmonics

q	0	1	2	3	4	5	6	7
Z^c_{1q}	C_∞, σ_v	σ_h, σ_v						
Z^c_{2q}	C_∞, i, C'_2, S_4, σ_h	σ_v, i, C'_2	C_2, i, C'_2, σ_h, σ_v					
Z^c_{3q}	C_∞, σ_v	σ_h, σ_v	C_2, σ_v, S_4	C_3, σ_h, σ_v				
Z^c_{4q}	C_∞, i, C'_2, S_4, σ_h	σ_v, i, C'_2	C_2, i, C'_2, σ_h, σ_v	C_3, i, C'_2, σ_v, S_6	C_4, i, C'_2, σ_h, σ_v, S_4			
Z^c_{5q}	C_∞, σ_v	σ_h, σ_v	C_2, σ_v, S_4	C_3, σ_h, σ_v	C_4, σ_v	C_5, σ_h, σ_v		
Z^c_{6q}	C_∞, i, C'_2, S_4, σ_h	σ_v, i, C'_2	C_2, i, C'_2, σ_h, σ_v	C_3, i, C'_2, σ_v, S_6	C_4, i, C'_2, σ_h, σ_v, S_4	C_5, i, C'_2, σ_v	C_6, i, C'_2, σ_h, σ_v, S_6	
Z^c_{7q}	C_∞, σ_v	σ_h, σ_v	C_2, σ_v, S_4	C_3, σ_h, σ_v	C_4, σ_v	C_5, σ_h, σ_v	C_6, σ_v	C_7, σ_h, σ_v
Z^s_{1q}		σ_h, σ_d, C'_2						
Z^s_{2q}		σ_d, i	C_2, i, σ_h, σ_d					
Z^s_{3q}		σ_h, σ_d, C'_2	C_2, C'_2, σ_d, S_4	C_3, C'_2, σ_h, σ_d				
Z^s_{4q}		σ_d, i	C_2, i, σ_h, σ_d	C_3, i, σ_d, S_6	C_4, i, σ_h, σ_d, S_4			
Z^s_{5q}		σ_h, σ_d, C'_2	C_2, C'_2, σ_d, S_4	C_3, C'_2, σ_h, σ_d	C_4, C'_2, σ_d	C_5, C'_2, σ_h, σ_d		
Z^s_{6q}		σ_d, i	C_2, i, σ_h, σ_d	C_3, i, σ_d, S_6	C_4, i, σ_h, σ_d, S_4	C_5, i, σ_d	C_6, i, σ_h, σ_d, S_6	
Z^s_{7q}		σ_h, σ_d, C'_2	C_2, C'_2, σ_d, S_4	C_3, C'_2, σ_h, σ_d	C_4, C'_2, σ_d	C_5, C'_2, σ_h, σ_d	C_6, C'_2	C_7, C'_2, σ_h, σ_d

Table 3
Symmetry element restrictions on the number of allowed q values in the expansion of the crystal-field potential

Symmetry element	Restrictions on q
C_n (parallel to main axis)	q is integer multiple of the rotation number n, but $q \leqslant k$
σ_h (xy-plane)	no terms with q=even or $q=0$ for odd k values; no terms q=odd for even k values
σ_v (xz-plane)	no imaginary terms
i (inversion center)	no odd k values, thus no induced electric dipole intensity by mixing states of opposite parity
C_2' (parallel to x-axis)	no terms with $q=0$ for odd k values; no real terms with $k + \|q\|$ odd; no imaginary terms with $k + \|q\|$ even
C_2' (parallel to y-axis)	no terms with $q=0$ for odd k values; no real terms with $k + \|q\|$ odd; no imaginary terms with $k + \|q\|$ even
S_n (parallel to main crystal axis)	no terms with $q=0$ for odd k values; no terms with $q=n$-fold and $k + \|q\|$ odd; no terms with $q = (2x+1)n/2$ ($x = 0, 1, 2, \ldots$) and $k + \|q\|$ even

with potentials for point groups which may be observed in molecular complexes. In the appendix, $C^k_{-q}(i)$ and $C^k_q(i)$ will be shortened to C^k_{-q} and C^k_q. The expressions for the potentials are the same for both even and odd f systems, since a double group (for f systems with an odd number of electrons) contains the same symmetry elements as the corresponding single group. The crystal fields can be divided first of all into the cubic and non-cubic crystal fields. According to the smallest q-value different from zero, the non-cubic crystal fields can be divided into the following classes (in order of descending symmetry): hexagonal ($q=6$), tetragonal ($q=4$), trigonal ($q=3$), orthorhombic ($q=2$), monoclinic ($q=2$), triclinic ($q=1$). The difference between orthorhombic and monoclinic crystal fields is that for orthorhombic crystal fields only real crystal-field parameters have to be considered, while for monoclinic crystal fields imaginary parameters also occur. The division of the different point groups into the different symmetry classes can be found in table 4. Although the icosahedral symmetry is not compatible with the crystallographic point groups, we will consider that symmetry also, because of the theoretical interest. Distinction between the different symmetries can be made on the basis of the selection rules for induced electric dipole (ED) and magnetic dipole (MD) transitions. This will be discussed in sect. 3.3. It is however not possible for systems with an odd number of f electrons to discriminate for instance between a D_{3h} and a C_{3h} symmetry on the basis of the selection rules.

Because values of the B^k_q coefficients of the expansion of the crystal-field potential depend upon the choice of the coordinate system, conventions for settling the positions of the coordinate axes are required. We use the conventions of Prather (1961). The z-direction is the direction of the principal symmetry axis. The y-axis is chosen to coincide with a twofold symmetry axis. The x-axis is perpendicular to both y- and z-axis, but in such a way that the three axes form a right-handed coordinate system. Such a choice will

Table 4
Division of the 32 crystallographic point symmetry groups into the different symmetry classes

Class	Point symmetry groups
Cubic	O_h, T_d, O, T_h, T
Hexagonal	D_{6h}, C_{6v}, D_6, C_{6h}, C_6, D_{3h}, C_{3h}
Trigonal	D_{3d}, C_{3v}, D_3, S_6 (=C_{3i}), C_3
Tetragonal	D_{4h}, D_{2d}, C_{4v}, D_4, C_{4h}, S_4, C_4
Orthorhombic	D_{2h}, C_{2v}, D_2
Monoclinic	C_{2h}, C_s, C_2
Triclinic	C_i, C_1

result in the simplest description of the crystal field. Another choice of the quantization axis yields a more complicated expansion, and the symmetry will be apparently lower. The symmetry is not actually lower, since the choice of the coordinate system cannot influence the eigenvalues (= energy levels) of the system, as mentioned for the determination of the non-vanishing (k, q) values in the crystal-field potential. The eigenfunctions (= wave functions) depend however on the position of the coordinate axes. In an apparently lower symmetry more tensor operators will be present, but the number of expansion coefficients remains the same. These coefficients are linear combinations of the coefficients found in the coordinate system with the z-axis parallel to the principal symmetry axis. Another consequence of this more complicated description of the crystal field is that more off-diagonal matrix elements will be present in the energy matrix. A rotation of the x- and y-axis in the xy-plane, can change the sign of the coefficients, or can make one parameter equal to zero or transform B_q^k into B'^k_q coefficients.

3.2. *Crystal-field matrix elements and crystal-field parameters*

The crystal-field energy levels can be found by diagonalizing the crystal-field matrix. A general matrix element can be written as:

$$\langle \Psi_{l^n \tau SLJM} | \mathcal{H}_{CF} | \Psi_{l^{n'} \tau' S' L' J' M'} \rangle , \tag{35}$$

or

$$\left\langle \Psi_{l^n \tau SLJM} \left| -e \sum_{i,k} \left[B_0^k C_0^k(i) + \sum_{q=1}^{k} \left(B_q^k \left(C_{-q}^k(i) + (-1)^q C_q^k(i) \right) + B'^k_q \mathrm{i} \left(C_{-q}^k(i) - (-1)^q C_q^k(i) \right) \right) \right] \right| \Psi_{l^{n'} \tau' S' L' J' M'} \right\rangle . \tag{36}$$

The coefficient B_q^k will be transformed into the crystal-field parameter B_q^k if the coefficient is brought outside the matrix element together with the radial parts of the wave functions. The radial part of the wave function is represented by $R_{nl}(r)$. The tensor operators are acting only on the angular part of the wave functions. The use of the same notation for both the coefficient and the parameter is confusing, but we shall adopt this notation

because it is commonly accepted in the literature. The crystal-field parameters can be defined as:

$$\text{parameter } B_0^k = -e \int_{r=0}^{\infty} R_{nl}^2(r) r^k \, \mathrm{d}r \sqrt{\frac{4\pi}{2k+1}} Z_{k0}^{\mathrm{c}} \int \frac{\rho(\boldsymbol{R})}{R^{k+1}} \mathrm{d}\tau, \tag{37}$$

$$\text{parameter } B_q^k = -e \int_{r=0}^{\infty} R_{nl}^2(r) r^k \, \mathrm{d}r \sqrt{\frac{4\pi}{2k+1}} \frac{Z_{kq}^{\mathrm{c}}}{\sqrt{2}} \int \frac{\rho(\boldsymbol{R})}{R^{k+1}} \mathrm{d}\tau, \tag{38}$$

$$\text{parameter } B'^k_q = -e \int_{r=0}^{\infty} R_{nl}^2(r) r^k \, \mathrm{d}r \sqrt{\frac{4\pi}{2k+1}} \frac{Z_{kq}^{\mathrm{s}}}{\sqrt{2}} \int \frac{\rho(\boldsymbol{R})}{R^{k+1}} \mathrm{d}\tau, \tag{39}$$

or in terms of discrete charges:

$$\text{parameter } B_0^k = \int_{r=0}^{\infty} R_{nl}^2(r) r^k \, \mathrm{d}r \sqrt{\frac{4\pi}{2k+1}} Z_{k0}^{\mathrm{c}} \sum_L \frac{Z_L e^2}{R_L^{k+1}}, \tag{40}$$

$$\text{parameter } B_q^k = \int_{r=0}^{\infty} R_{nl}^2(r) r^k \, \mathrm{d}r \sqrt{\frac{4\pi}{2k+1}} \frac{Z_{kq}^{\mathrm{c}}}{\sqrt{2}} \sum_L \frac{Z_L e^2}{R_L^{k+1}}, \tag{41}$$

$$\text{parameter } B'^k_q = \int_{r=0}^{\infty} R_{nl}^2(r) r^k \, \mathrm{d}r \sqrt{\frac{4\pi}{2k+1}} \frac{Z_{kq}^{\mathrm{s}}}{\sqrt{2}} \sum_L \frac{Z_L e^2}{R_L^{k+1}}. \tag{42}$$

The crystal-field parameter contains both a radial and an angular part. The electron charge $-e$ is also included. The expressions for the parameters if discrete charges are considered, will be discussed in sect. 5.3. It is convenient to determine the B_q^k parameters semi-empirically, since the radial parts cannot be calculated exactly. Initial values for the crystal-field parameters are varied in such an extent that the sum of the squared differences between the experimental and calculated crystal-field levels is minimized, as will be shown in sect. 4.1. For the 4f systems which have been studied up to the present time, the B_q^k parameter values lie between $-2500\,\mathrm{cm}^{-1}$ and $2500\,\mathrm{cm}^{-1}$. From now on in the text, the notations B_0^k, B_q^k and B'^k_q represent crystal-field parameters and not coefficients.

The angular parts (containing the coordinates of the electron) of the matrix element in eq. (36) can be calculated exactly using standard techniques of tensor algebra. We will illustrate this. Consider the matrix element

$$\left\langle \Psi_{l^n \tau S L J M} \left| \sum_i C_q^k(i) \right| \Psi_{l^{n'} \tau' S' L' J' M'} \right\rangle. \tag{43}$$

The summation over the tensor operators $C_q^k(i)$ can be rewritten in terms of a unit tensor U_q^k (Wybourne 1965, Weissbluth 1978, Edmonds 1974).

$$\left\langle \Psi_{l^n \tau S L J M} \left| U_q^k \right| \Psi_{l^{n'} \tau' S' L' J' M'} \right\rangle \left\langle l \left\| C^k \right\| l' \right\rangle. \tag{44}$$

The matrix elements in U_q^k are diagonal in the spin S. The reduced matrix element $\langle l \| C^k \| l' \rangle$ contains the l-state dependence of the electrons. By applying the *Wigner–Eckart theorem* (Weissbluth 1978), one finds:

$$\langle \Psi_{l^n \tau SLJM} | U_q^k | \Psi_{l^{n'} \tau' SL'J'M'} \rangle = (-1)^{J-M} \begin{pmatrix} J & k & J' \\ -M & q & M' \end{pmatrix} \langle \Psi_{l^n \tau SLJ} \| U^k \| \Psi_{l^{n'} \tau' SL'J'} \rangle . \tag{45}$$

$\langle \Psi_{l^n \tau SLJ} \| U^k \| \Psi_{l^{n'} \tau' SL'J'} \rangle$ is a reduced matrix element and is independent of M, q and M'. Further reduction results in:

$$\langle \Psi_{l^n \tau SLJ} \| U^k \| \Psi_{l^{n'} \tau' SL'J'} \rangle = (-1)^{S+L'+J+k} [(2J+1)(2J'+1)]^{1/2} \begin{Bmatrix} J & J' & k \\ L & L & S \end{Bmatrix} \langle \Psi_{l^n \tau SL} \| U^k \| \Psi_{l^{n'} \tau' SL'} \rangle . \tag{46}$$

$\langle \Psi_{l^n \tau SL} \| U^k \| \Psi_{l^{n'} \tau' SL'} \rangle$ is a *doubly reduced matrix element* and can be calculated by a recursion formula in terms of the *coefficients of fractional parentage* (Racah 1949, Judd 1963). They are tabulated in the work of Nielson and Koster (1963). The doubly reduced matrix elements are constants for a given lanthanide ion and thus independent of the local surroundings. The actual value of the (single) reduced matrix element depends however on the applied coupling scheme: Russell–Saunders coupling, intermediate coupling or J-mixing[1]. It may also vary slightly from system to system, because of small variations in the free-ion parameters, which are due to for instance nephelauxetic effects. The 3-j symbol $\begin{pmatrix} J & k & J' \\ -M & q & M' \end{pmatrix}$ and the 6-j symbol $\begin{Bmatrix} J & J' & k \\ L & L & S \end{Bmatrix}$ represent the coupling of two and three angular momenta, respectively. The n-j symbols can be found in the work of Rotenberg et al. (1959). The reduced matrix element $\langle l \| C^k \| l' \rangle$ can be worked out:

$$\langle l \| C^k \| l' \rangle = (-1)^l [(2l+1)(2l'+1)]^{1/2} \begin{pmatrix} l & k & l' \\ 0 & 0 & 0 \end{pmatrix} . \tag{47}$$

Equation (44) is rewritten as:

$$\begin{aligned} \left\langle \Psi_{l^n \tau SLJM} \left| \sum_i C_q^k(i) \right| \Psi_{l^{n'} \tau' SL'J'M'} \right\rangle = {} & (-1)^{2J-M+S+L'+k+l} [(2J+1)(2J'+1)]^{1/2} [(2l+1)(2l'+1)]^{1/2} \\ & \times \begin{pmatrix} l & k & l' \\ 0 & 0 & 0 \end{pmatrix} \begin{pmatrix} J & k & J' \\ -M & q & M' \end{pmatrix} \begin{Bmatrix} J & J' & k \\ L' & L & S \end{Bmatrix} \\ & \times \langle \Psi_{l^n \tau SL} \| U^k \| \Psi_{l^{n'} \tau' SL'} \rangle . \end{aligned} \tag{48}$$

Because in first approximation the splitting of a J level is independent of the splitting in other J levels, matrix elements are evaluated within one multiplet. Furthermore, only the 4f configuration ($l=3$) is considered:

$$\begin{aligned} \left\langle \Psi_{l^n \tau SLJM} \left| \sum_i C_q^k(i) \right| \Psi_{l^n \tau SLJM'} \right\rangle = {} & (-1)^{2J-M+S+L+k+3} 7(2J+1) \\ & \times \begin{pmatrix} 3 & k & 3 \\ 0 & 0 & 0 \end{pmatrix} \begin{pmatrix} J & k & J \\ -M & q & M' \end{pmatrix} \begin{Bmatrix} J & J & k \\ L & L & S \end{Bmatrix} \langle \Psi_{l^n \tau SL} \| U^k \| \Psi_{l^n \tau SL} \rangle . \end{aligned} \tag{49}$$

[1] In Russell–Saunders coupling S and L remain good quantum numbers. In intermediate coupling only J is a good quantum number. By J-mixing, several J terms with different J values can mix under the influence of the crystal-field Hamiltonian.

Based on the properties for 3-j symbols, one can deduce selection rules for k from eq. (49). k is even because the 3-j symbol $\begin{pmatrix} 3 & k & 3 \\ 0 & 0 & 0 \end{pmatrix}$ is zero, unless $k+6$ is even. Indeed, otherwise a contradiction will be found after a permutation of the first and third column:

$$\begin{pmatrix} 3 & k & 3 \\ 0 & 0 & 0 \end{pmatrix} = (-1)^{k+6} \begin{pmatrix} 3 & k & 3 \\ 0 & 0 & 0 \end{pmatrix}. \tag{50}$$

In combination with the triangle condition $k \leqslant 6$, it is clear that for the crystal-field splitting only the k values 0, 2, 4, 6 have to be considered. It is already mentioned that the parameter B_0^0 shifts the whole configuration. For high symmetric systems, even fewer k values will occur:

cubic symmetry : $k = 0, 4, 6,$ icosahedral symmetry : $k = 0, 6,$

spherical symmetry : $k = 0$ (no crystal-field splitting, free-ion case).

The 3-j symbol $\begin{pmatrix} J & k & J \\ -M & q & M' \end{pmatrix}$ is zero unless $-M+q+M'=0$. From the triangular conditions for this 3-j symbol, one can find the selection rule:

$$k \leqslant 2J. \tag{51}$$

Not all parameters are therefore responsible for the crystal field splitting of multiplets with small J values. For instance, the splitting of $^5D_1$ ($J=1$) in Eu^{3+} is in a good approximation described only by the crystal-field parameters with $k=2$, and the splitting of $^5D_2$ ($J=2$) by the parameters with $k=2$, 4. This selection rule is only strictly valid in the case of intermediate coupling.

When J-mixing is considered, a $^{2S+1}L_J$ term may have contributions from terms with other J values. When in this way a small part of the $J=2$ wave functions are mixed with the $J=1$ wave functions of $^5D_1$, the parameters will also be necessary for a rigorous description of the crystal-field splitting of the $^5D_1$ term. For the crystal-field splitting, the intermediate coupling scheme is a good approximation, so long as the crystal-field interaction is not too strong. We can make a difference between weak-field and strong-field lanthanide systems. The terms "*weak field*" and "*strong field*" here have another meaning than for transition metal complexes. For a strong-field transition metal system, the crystal-field perturbation is a stronger interaction than the electron repulsion. For lanthanide systems, the crystal-field interaction is always weaker than the electron repulsion. In a strong-field lanthanide system, the intermediate coupling scheme is not appropriate for the description of the energy levels. J-mixing has to be taken into account. The intermediate coupling scheme remains a good model for weak-field lanthanide systems. Examples of weak-field systems are the ethylsulphates $R(C_2H_5SO_4)_3 \cdot 9H_2O$, the oxydiacetates $Na_3[R(C_4H_4O_5)_3] \cdot 2NaClO_4 \cdot 6H_2O$ and $LaCl_3$. Examples of strong-field complexes are the rare-earth garnets $A_3B_5O_{12}$ (A = Y, R; B = Al, Ga), the oxychlorides ROCl and KY_3F_{10}.

The *operator-equivalent method*, the oldest formalism for the interpretation of crystal-field splitting in lanthanide spectra, originally neglected J-mixing (Stevens 1952, Elliot and Stevens 1953a,b, and Judd 1955). The neglect of J-mixing and the diagonalization of the energy matrix within one $^{2S+1}L_J$ multiplet is useful for obtaining estimates of the crystal-field parameters from experimental measurements on isolated multiplets. This will be illustrated further for the ^7F_J and ^5D_J multiplets of Eu^{3+}. In high symmetries, it is often possible to obtain good approximate crystal-field parameters from analytical expressions without the need for a least-squares fit. This method cannot be used if the Russell–Saunders coupling scheme and even the intermediate coupling scheme are highly violated. The different $^{2S+1}L_J$ multiplets are then thoroughly mixed and the concept of a free-ion level has no meaning.

The condition $-M+q+M'=0$ determines which non-diagonal matrix elements will occur in the energy matrix for a given symmetry (the q-values are constrained by symmetry). The non-diagonal matrix elements are responsible for the fact that M will not remain a good quantum number for a lanthanide ion in a crystal field. The wave function of a crystal-field level will be a sum of states $M+mq$ (m is an integer). To classify the M states which can be mixed by the crystal-field Hamiltonian, the *crystal quantum number* μ has been introduced by Hellwege (1949):

$$M = \mu \pmod{q}. \tag{52}$$

In the definition mod q simply means the addition or subtraction of multiples of q to the crystal quantum number μ. For q, the minimum q-value in the crystal-field potential different from zero is taken. The crystal-field quantum numbers for a given symmetry can be found in practice by writing down different series $M+mq$, so that these series together contain every integer between $-J'$ and J' (J' is the highest value for the J quantum number in the system under study). The number with the lowest absolute value in each series will be considered as a crystal quantum number μ. This can be illustrated for the C_3 symmetry ($q=3$). The crystal quantum numbers for a C_3 symmetry in systems with an even number of electrons are $\mu=0^+$, 0^- and $\mu=\pm1$.

$M=$	-12	-9	-6	-3	**0**	3	6	9	12	$(\mu=0^+,0^-)$;
	-11	-8	-5	-2	**1**	4	7	10		$(\mu=1)$;
	-10	-7	-4	$-$**1**	2	5	8	11		$(\mu=-1)$.

The crystal quantum numbers for systems with an even number of electrons are:

$q=2$: $\mu=0^+,0^-,1^+,1^-$;
$q=3$: $\mu=0^+,0^-,\pm1$;
$q=4$: $\mu=0^+,0^-,\pm1;,2^+,2^-$;
$q=5$: $\mu=0^+,0^-,\pm1,\pm2$;
$q=6$: $\mu=0^+,0^-,\pm1,\pm2,3^+,3^-$.

and for systems with an odd number of electrons:

$$q = 2: \quad \mu = \pm\tfrac{1}{2};$$
$$q = 3: \quad \mu = \pm\tfrac{1}{2}, \pm\tfrac{3}{2};$$
$$q = 4: \quad \mu = \pm\tfrac{1}{2}, \pm\tfrac{3}{2};$$
$$q = 5: \quad \mu = \pm\tfrac{1}{2}, \pm\tfrac{3}{2}, \pm\tfrac{5}{2};$$
$$q = 6: \quad \mu = \pm\tfrac{1}{2}, \pm\tfrac{3}{2}, \pm\tfrac{5}{2}.$$

States characterized by a different crystal quantum number cannot be mixed by the crystal-field Hamiltonian. The energy matrix can therefore be broken up into different submatrices, one for each μ quantum number. Each submatrix (also called μ matrix) can be diagonalized separately. States characterised by $-\mu$ and $+\mu$ will be degenerate in the absence of a magnetic field. The crystal-field quantum number μ can be used to label the crystal-field levels of systems with an odd number of electrons in a symmetry lower than cubic, since there is a one to one correspondence between the crystal quantum numbers and the irreducible representations of the point group in question. For systems with an even number of f electrons, the irreducible representations are preferable as labels, since some of the submatrices characterised by a crystal quantum number are reducible. Submatrices which contain for every M value also every $-M$ value, will give, after diagonalization, wave functions transforming as one of two possible irreducible representations. These crystal quantum numbers have to be distinguished by the superscripts (+) and (−): μ^+ corresponds to states of one irreducible representation and μ^- to the states of the other irreducible representation (e.g. 0^+ and 0^-).

For cubic groups one has to work with irreducible representations. The crystal quantum numbers are not useful to classify the states, because of the occurrence of triplet and quartet states. Quartet states are found in the double groups O_h^*, O^* and T_d^*.

3.3. *Assignment of crystal-field transitions*

Spectral assignment is the labelling of energy levels with the irreducible representations of the point group. For the symbols of the irreducible representations, two different nomenclatures are used in lanthanide spectroscopy. The Γ_i symbols have been introduced by Bethe (1929). The representations are numbered sequentially. These symbols are preferable for theoretical work, but the disadvantage is that these symbols tell nothing about the degeneracy of the representation. Since these symbols are used by Koster et al. (1963), we also use these symbols. Another nomenclature has been proposed by Mulliken. One-dimensional representations are designated A or B; two-dimensional representations are designated E and three-dimensional representations are designated T. These symbols are used in the character tables of Cotton (1971). In Appendix 4, the correlation between the Bethe and Mulliken symbols is given for the different point groups. Assignments can be made on the basis of the selection rules for induced electric dipole (ED) and magnetic

dipole (MD) transitions. The selection rules tell us whether a transition is allowed or forbidden, but nothing about the intensity.

A transition between a crystal-field level i of the initial state and a crystal-field level f of the final state is allowed if the matrix element $\langle \Psi_i | O | \Psi_f \rangle$ is non-zero. O stands for both the ED and the MD operator. $\langle \Psi_i | O | \Psi_f \rangle$ is identical to the integral $\int \Psi_i^* O \Psi_f \, d\tau$, which is called the transition moment integral. Assume that Ψ_i, Ψ_f and O have the respective symmetry labels Γ_i, Γ_f and Γ. The matrix element $\langle \Psi_i | O | \Psi_f \rangle$ will not vanish if the direct product $\Gamma_i \otimes \Gamma \otimes \Gamma_f$ contains the totally symmetric irreducible representation Γ_1. Another formulation is that Γ has to be contained in the direct product $\Gamma_i \otimes \Gamma_f$.

The electric dipole operator O_{ED} transforms like $\boldsymbol{x}$, $\boldsymbol{y}$ and $\boldsymbol{z}$, since an electric dipole operator induces a linear displacement of electric charge in the ion. The magnetic dipole operator O_{MD} transforms like $\boldsymbol{R_x}$, $\boldsymbol{R_y}$ and $\boldsymbol{R_z}$, because a magnetic dipole transition can be seen as a rotational displacement of electric charge.

In a cubic symmetry the directions x, y and z are equivalent in the sense that they are interchangeable by the symmetry operations of the point group. This is noted as (x, y, z) and (R_x, R_y, R_z). For symmetries lower than cubic, the x, y and z directions are no longer equivalent. In other words, x, y and z do not belong to the same irreducible representation. For uniaxial crystals (hexagonal, tetragonal and trigonal) x and y remain interchangeable, which is noted as (x, y) and (R_x, R_y). Only for orthorhombic, monoclinic and triclinic symmetries the three directions are independent. For uniaxial and lower symmetries, the phenomenon of polarization is encountered. A transition will be allowed only in certain directions and forbidden in other directions. For uniaxial crystals, three different polarized spectra can be recorded, depending on the vibration direction of the electric field vector $\boldsymbol{E}$ and the magnetic field vector $\boldsymbol{H}$ with respect to the crystallographic c-axis:

$$\begin{aligned} &\alpha \text{ spectrum}: \quad \boldsymbol{E} \perp \boldsymbol{c}, \quad \boldsymbol{H} \perp \boldsymbol{c}; \\ &\sigma \text{ spectrum}: \quad \boldsymbol{E} \perp \boldsymbol{c}, \quad \boldsymbol{H} \parallel \boldsymbol{c}; \\ &\pi \text{ spectrum}: \quad \boldsymbol{E} \parallel \boldsymbol{c}, \quad \boldsymbol{H} \perp \boldsymbol{c}. \end{aligned}$$

In an α spectrum or axial spectrum, the light propagates along the c-axis, which has the same direction as the optic axis. Both $\boldsymbol{E}$ and $\boldsymbol{H}$ are perpendicular to c. An α spectrum is recorded with unpolarized light. In a σ and a π spectrum, the light propagates perpendicular to the c-axis. These spectra are therefore also called orthoaxial spectra. In a σ spectrum, the electric field vector $\boldsymbol{E}$ is perpendicular to the c-axis, which incorporates that $\boldsymbol{H}$ is parallel to the c-axis. In a π spectrum, the electric field vector is parallel to the c-axis and the magnetic field vector is perpendicular to the c-axis. An ED transition which is seen in both the α and σ spectra corresponds to a transition caused by the (x,y) components of the electric field. An ED transition in the π spectrum is induced by the z component of the electric field. A MD transition in the σ spectrum is due to the R_z operator. A MD transition detected in both the α and π spectra is caused by the (R_x, R_y) operators. This implies that the nature of an intraconfigurational 4f–4f transition can by determined by comparing the three polarized spectra. For an ED transition the α and

σ spectra are identical, while for a MD transition the α and π spectra are the same (Sayre et al. 1955). For orthorhombic, monoclinic and triclinic crystal fields the labels α, σ and π cannot be used. Here the nomenclature is that an ED transition is allowed in x, y or z polarization and a MD transition in R_x, R_y or R_z polarization.

According to the Judd–Ofelt theory (Judd 1962, Ofelt 1962) induced electric dipole (ED) transitions can be observed only if the point group of the site contains no center of symmetry. Only in this case, the odd part of the crystal-field potential will be non-zero and intensity can be achieved by mixing configurations of opposite parity into the 4f wave functions. Of the 32 crystallographic point groups, 21 are non-centrosymmetric: C_{6v}, C_6, D_6, D_{3h}, D_3, C_{3v}, C_{3h}, C_3, D_4, C_{4v}, C_4, S_4, D_{2d}, D_2, C_{2v}, C_2, C_s, C_1, O, T_d and T. The 11 centrosymmetric point groups are: O_h, T_h, D_{6h}, C_{6h}, D_{4h}, C_{4h}, D_{3d}, C_{3i}, D_{2h}, C_{2h} and C_i. Electric dipole transitions are however observed in centrosymmetric systems. This is due to vibronic coupling, i.e. coupling of the electronic and vibrational wave functions. The vibrations under consideration can be molecular vibrations or vibrations of the crystal lattice as a whole. The transition moment integral, $\int \Psi_i^* O \Psi_f \, d\tau$, is non-vanishing if there are normal vibrations whose first excited states belong to irreducible representations which also occur in the direct product $\Gamma_i \otimes \Gamma \otimes \Gamma_f$ of the irreducible representations of the wave function of the ground state, the dipole operator and the wave function of the final state. One can say alternatively that an ED transition is allowed by vibronic coupling with a vibrational mode of symmetry Γ_{phonon}, if the direct product $\Gamma_i \otimes \Gamma_{\text{phonon}} \otimes \Gamma \otimes \Gamma_f$ contains the totally symmetric representation Γ_1. All 4f crystal field levels of an even electron system have a gerade (g or +) parity and all crystal field levels of an odd electron system have ungerade (u or −) parity. The ED operator is ungerade. Therefore, only ungerade vibrational modes will couple with the electronic wave functions. Since the ED transition can only occur as long as there is a simultaneous excitation of a vibration, no peak will be found at the zero-phonon line, but at a wavenumber which is equal to the sum of the transition energies of both the electronic and the vibrational transition. Shifts to lower energy are not so often found and are due to transitions starting from an excited vibrational level of the ground state. Vibronic transitions can be observed also in non-centrosymmetric systems, especially for Pr^{3+} systems. Here the zero-phonon line will be observed. The vibrations transform like the irreducible representations of the point group of the crystal itself, whereas the selection rules for the electronic transitions are determined by the symmetry of the site. The site symmetry is often lower than the symmetry of the crystal as a whole. By means of a correlation diagram, one can find out how the irreducible representations of the vibrations correspond to the irreducible representations of the site symmetry. A model for calculating the intensities of 4f–4f transitions in trivalent lanthanides with O_h site symmetry has been worked out by Faulkner and Richardson (1978).

Magnetic dipole (MD) transitions are allowed in both centrosymmetric and non-centrosymmetric point groups. The magnetic dipole operator has a gerade parity. Transitions allowed by the magnetic dipole mechanism are however sparse, because of the selection rule $\Delta J = 0$ or $\Delta J = 1$ (but not $0 \leftrightarrow 0$). The best-known MD transitions are $^5D_0 \leftarrow {}^7F_1$ and $^5D_1 \leftarrow {}^7F_0$ of Eu^{3+}.

The selection rules for the crystallographic point groups are given in Appendix 5. From these tables, one can check whether an ED or MD transition between two crystal-field levels is forbidden or allowed and in which polarization the transition will be observed. Since transitions in cubic point groups are not polarized, it is simply indicated whether the transition is allowed or forbidden. In Appendix 6 the full-rotational group compatibility tables are presented. From these tables it can be deduced how a free-ion J-level is broken up into crystal-field levels when the ion is placed in a crystalline environment with a distinct point group.

The first act in the assignment of a level is the determination of the irreducible representation of the ground crystal-field level. This is very easy for Eu^{3+}, since the ground state is non-degenerate ($^7F_0$) and has symmetry label Γ_1. For the other trivalent lanthanide ions, spectra have to be recorded under cryogenic conditions, so that only the ground crystal-field level is populated. Cryogenic conditions also have the advantage that the linewidths are much smaller than at room temperature. Liquid nitrogen (77 K) or liquid helium (4.2 K) are used as refrigerants. For many systems one has indeed to cool to liquid helium temperature to get sufficient resolution. At 4.2 K, crystal-field levels more than $10\,cm^{-1}$ above the ground state will not give rise to detectable transitions. It is helpful to consider a transition to a non-degenerate excited state. Examples are the $^3P_0$ level in Pr^{3+} and the $^2P_{1/2}$ level in Nd^{3+}. Energy level calculations with a set of crystal-field parameters of a lanthanide ion in the same host matrix can be of great help. After the determination of the symmetry label of the ground state and eventually of the first excited crystal-field levels of the ground multiplet, the assignment of the other crystal-field levels can begin. This is often like doing puzzles. Only transitions starting from the lower crystal-field levels within the ground multiplet can be used for spectral assignments. The higher crystal-field levels will only be sufficiently populated to give detectable transitions at temperatures not far below room temperature. At these temperatures the spectral lines will broaden and overlap, so that interpretation is difficult. The restriction that only the lowest crystal-field levels can be used as starting levels, has as a consequence that not all crystal-field levels of the excited state can be observed experimentally. An example will make this clear. If the ground level has symmetry Γ_1 and if the $\Gamma_1 \leftarrow \Gamma_1$ transition is not allowed for that particular point group, no Γ_1 level of the excited $^{2S+1}L_J$ multiplet can be observed at low temperatures. This can be a problem, for instance, for Eu^{3+} with its Γ_1 ground state ($^7F_0$). Only if $^7F_1$, which is ca. $350\,cm^{-1}$ above the ground state, is thermally sufficiently populated, more transitions will be seen.

If the symmetry is high, more transitions are forbidden by symmetry restrictions than for systems with a low site symmetry. Thus, in a spectrum of a trivalent lanthanide ion in a low symmetry site more peaks within a spin–orbit coupling band will be found than in the spectrum of the same lanthanide ion occupying a site of high symmetry. For the symmetries C_s, C_2 and C_1 no transitions are forbidden and $2J + 1$ peaks are found in an even electron system for transitions between a crystal-field level of the ground state and the crystal-field levels of an excited multiplet.

Based on the number of transitions and their polarization, the site symmetry can be determined. This is worked out below in sect. 5.8 for Eu^{3+}. The method cannot be used for

centrosymmetric systems, because several vibronic transitions are possible to one single crystal-field level. This makes the spectrum very congested.

If the intensity of a transition is low, it is possible that it cannot be seen in the spectrum and fewer peaks are detected than predicted by the selection rules. Sometimes more peaks are found than expected on the basis of the selection rules. These peaks are called *satellite lines.* One reason for this is the vibronic transitions which are discussed above. Another reason is the occurrence of sites which are not optically equivalent. This is for instance the case for crystals in which a trivalent lanthanide ion replaces a divalent cation. A typical example is CaF_2. But the occupation of different sites can also occur if the lanthanide ion replaces a trivalent ion. In the rare-earth garnet $A_3B_5O_{12}$ (A = Y, Lu, Gd; B = Al, Ga), the lanthanide ion preferentially enters the A site with D_2 symmetry, but it can also take place in the B site with C_{3i} symmetry, especially when the doping concentration is high. The method of crystal preparation also influences the distribution of the lanthanide ions over the different sites. Another cause of satellite lines are crystal imperfections, such as interstitial lanthanide ions. Nearest-neighbor and next-nearest-neighbor interactions can also result in additional peaks (Prinz 1966a,b). It is evident that if impurities of other lanthanide ions are present in the crystal, these impurities will give rise to lines in the spectrum. This was a severe problem in the early days of rare-earth spectroscopy (before World War II), when rare-earth compounds were not readily available in high purity. Now it is still possible that neodymium impurities are found in a praseodymium spectrum and vice-versa, because of the difficulties in separating these two elements. It is a good advice to keep in mind the possibility of impurities if one finds unexpected lines in spectral regions where no transitions should be observed.

Besides absorption and emission measurements, other techniques (optical, magnetic or magneto-optical) can also be used for determination and assignment of crystal-field energy levels inside the 4f shell: two-photon absorption (TPA), Zeeman effect spectroscopy, electron paramagnetic resonance (EPR) and magnetic circular dichroism (MCD).

Two-photon absorption (TPA) provides spectroscopic information which is complementary to that of the classical one-photon absorption spectroscopy. Although the principle of two-photon absorption has been formulated more than half a century ago (Göppert-Mayer 1931), it was not before the availability of high intensity lasers that this technique became useful. Denning (1991) has published the TPA-spectrum of Tb^{3+} in the elpasolite matrix $Cs_2NaTbCl_6$ and reviewed the possibilities of this new technique. It is an advantageous technique for 4f systems in centrosymmetric systems with a high symmetry (e.g. O_h), since the $4f \leftarrow 4f$ transitions are allowed by the two-photon transition mechanism. The electric dipole forbidden transitions (the zero-phonon lines) in a O_h symmetry can be detected in a two-photon spectrum. The two-photon spectrum is not blurred by vibronic structure. The one-photon transitions in a cubic host matrix are unpolarized, but the two-photon spectra show a polarization dependence which can be helpful to determine the symmetry labels. Since two-photon processes are in competition with one-photon processes, the non-stationary intermediate state of the two-photon process may not coincide with an energy level to which a one-photon absorption can take place. Otherwise the one-photon absorption will occur and not the two-photon

absorption. This requirement and the energy range of available light sources restrict the use of two-photon absorption mainly to systems in the middle of the lanthanide series (Eu^{3+}, Gd^{3+} and Tb^{3+}), where a large energy gap exists between the ground ^{2S+1}L term and the first excited ^{2S+1}L term, although TPA spectra for other lanthanide ions have also been recorded: Ce^{3+} (Gayen and Hamilton 1983, Gayen et al. 1984, Gayen et al. 1986, Leavitt 1987), Pr^{3+} (Yen et al. 1981, Cordero-Montalvo and Bloembergen 1984, Rana et al. 1984, Malinowski et al. 1995), Nd^{3+} (Kramer and Boyd 1981, Chase and Payne 1986), Eu^{3+} (Skripko et al. 1976, Kholodenkov and Makhanek 1982, 1984, Kholodenkov et al. 1984, Makhanek et al. 1984), Gd^{3+} (Dagenais et al. 1981, Downer et al. 1982, Downer and Bivas 1983, Bloembergen 1984, Cordero-Montalvo 1985, Kundu et al. 1990a,b, Mahiou et al. 1985, Jacquier et al. 1987a, 1989), Tb^{3+} (Skripko et al. 1976, Jacquier et al. 1987b, Huang et al. 1989, Denning 1991), Ho^{3+} (Rao et al. 1983), Er^{3+} (Gintoft and Skripko 1972), Tm^{3+} (Bleijenberg et al. 1980). Considerable theoretical work on two-photon spectroscopy of lanthanide ions has been done by Axe (1964), Judd and Pooler (1982), Downer et al. (1982), Downer and Bivas (1983), Downer (1989), Reid and Richardson (1984), Sztucki and Stręk (1986a,b) and by Ceulemans and Vandenberghe (1993, 1994).

When a crystal is placed in an external magnetic field, all crystal-field degeneracies are removed. This is called the Zeeman effect and can be studied by different techniques: Zeeman spectroscopy, electron paramagnetic resonance (EPR) and magnetic circular dichroism (MCD).

Zeeman spectroscopy can be considered as absorption spectroscopy in the presence of an external magnetic field. In uniaxial crystals, we can make a distinction between the parallel and the perpendicular Zeeman effect, depending on the orientation of the magnetic field with respect to the main crystal axis (*c*-axis). In the parallel Zeeman spectrum, twofold degenerate levels are split and the wave functions are diagonal in the magnetic quantum number M. The magnitude of the splitting is linearly proportional to the strength of the magnetic field. If the light beam is along the main crystal axis (and thus parallel to the magnetic field), the transitions to the two Zeeman components will be circularly polarized. If the light beam is perpendicular to the main crystal axis, the transitions will be π, σ polarized. The Zeeman effect is useful to determine the M quantum number of crystal-field levels in odd electron systems, since the splitting is proportional to M. The splitting of a level with $M = \pm\frac{3}{2}$ will be three times as large as the splitting of a level with $M = \pm\frac{1}{2}$. In the perpendicular Zeeman effect, the crystal-field degeneracy is removed, but the splitting is not linearly proportional to the strength of the magnetic field. Non-degenerate crystal-field levels will be affected too by the magnetic field. The matrix elements are no longer diagonal in M. The Zeeman effect in lanthanide compounds has been discussed by Wybourne (1965), Dieke (1968), Hellwege (1976) and Hüfner (1978).

In electron paramagnetic resonance (EPR) experiments transitions between the Zeeman components of the ground state of the lanthanide ion are studied. These transitions are found in the microwave region of the spectrum. With EPR the crystal-field levels of the ground state can be determined with a much higher accuracy than is possible with optical methods. A clear introduction to EPR and its instrumentation has been given by

Stephens (1989). EPR is more extensively discussed by Abragam and Bleaney (1970). Mishra and Upretti (1986) review the literature from 1977 to 1983, with some emphasis on the crystal-field parameters for lanthanide ions extracted from single crystals and powdered samples.

Magnetic circular dichroism (MCD) is the difference in absorption of left and right circularly polarized light by a compound in a magnetic field. A MCD spectrum gives the same information as a Zeeman spectrum, but is has the advantage that the effect can also be measured if there is a considerable line broadening. MCD measurements are however restricted to cubic and uniaxial samples. In a uniaxial crystal, the magnetic field and the light beam are parallel to the optic axis. In cubic crystals, MCD can be recorded in all directions. The magnetic field and the light beam are here also parallel. Selection rules for MCD in lanthanide systems are given by Görller-Walrand and coworkers (Görller-Walrand and Godemont 1977, Görller-Walrand 1985, Görller-Walrand and Fluyt-Adriaens 1985). Schwartz (Schwartz 1975, 1976, Schwartz et al. 1977, 1979, Banerjee and Schwartz 1981) has used MCD for the spectral study of lanthanide ions in the cubic elpasolite matrices Cs_2NaRCl_6. Amberger et al. (Amberger and Jahn 1984, Amberger et al. 1985, Amberger and Yünlü 1986, Amberger and Schultz 1991, Amberger et al. 1992) made spectral assignments in crystalline organolanthanoid(III) compounds with the aid of MCD spectroscopy.

In metallic compounds, optical methods cannot be used to determine the crystal-field levels. The determination of crystal field levels in such compounds has been reviewed by Fulde (1979) and is only mentioned here. These are primarily based on measurements of the magnetic susceptibility, magnetization in high magnetic field, specific heat (Schottky anomaly), Mössbauer effect, electron paramagnetic resonance, and inelastic neutron scattering.

3.4. *Nephelauxetic effect*

The total or partial removal of the $2J+1$ degeneracy of the $4f^n\ ^{2S+1}L_J$ free-ion levels is only one consequence of the crystal field felt by the lanthanide ion. Another consequence is a shift of the barycenter of the $^{2S+1}L_J$ level. This effect has been called "nephelauxetic effect" by Jørgensen (1962) and was interpreted as caused by a covalent contribution to the bonding between the lanthanide ions and the ligands (Jørgensen 1962, Jørgensen et al. 1964, 1965). *Nephelauxetic* means *cloud expanding* and this suggests that the size of the electron cloud around the lanthanide ion increases by transferring electron density to bonding molecular orbitals. An increase of the cloud size results in a decrease of the interelectronic repulsion. This is reflected by a diminution of the values of the Racah parameters (or Slater integrals) compared to the values for the free ion. Newman (1973, 1977) has however suggested that this change of the Slater integrals cannot be due to covalency effects, but due to dielectric effects caused by the local polarizability within the crystalline host matrix. A review of the nephelauxetic effect is given by Reisfeld and Jørgensen (1977). Caro and coworkers investigated systematically the nephelauxetic effect in lanthanide systems (Caro et al. 1976, 1977a, Antic-Fidancev et al. 1987b). Main

attention was given to non-degenerate levels, because here no crystal-field splitting occurs: $^2P_{1/2}$ of Nd^{3+} ($4f^3$), $^5D_0$ of Eu^{3+} ($4f^6$). Another level of interest was $^6P_{7/2}$ of Gd^{3+} ($4f^7$). It has been tried to use this effect for the determination of structural characteristics, namely lanthanide–ligand distances and the coordination number. For neodymium and gadolinium, there is experimental evidence for a sensitivity of the energetic position of $^2P_{1/2}$ and the $^6P_{7/2}$ level, respectively, to the distance between the lanthanide and its nearest neighbors. The shorter the metal–ligand distance, the lower the energetic position. A same sensitivity is however not found for the $^5D_0$ level of Eu^{3+}. There is no correlation between the crystal-field parameters and the nephelauxetic effect. Recently Frey and Horrocks (1995) have studied the nephelauxetic effect in Eu^{3+}, by measuring the wavenumber of the $^5D_0 \leftarrow {}^7F_0$ transition in various complexes. They concluded that the nephelauxetic effect depends on the covalency of the metal–ligand bond and on the coordination number (the lower the coordination number, the larger the nephelauxetic effect). A satisfying explanation for the nephelauxetic effect has still to be found and may be a challenge to both theoreticians and experimentalists.

4. Determination of phenomenological crystal-field parameters

4.1. *Calculation of free-ion and crystal-field energy levels*

The energy levels of trivalent lanthanide ions can be calculated by diagonalizing the energy matrix. The matrix elements are of the type $\langle \Psi_{l^n\tau SLJM} | \mathcal{H} | \Psi_{l^{n'}\tau'S'L'J'M'} \rangle$, where $\mathcal{H}$ is the Hamiltonian, $\Psi_{l^n\tau SLJM}$ and $\Psi_{l^{n'}\tau'S'L'J'M'}$ are basis functions of the $4f^n$ configuration. The angular part of the matrix elements can be calculated exactly, whereas the radial parts are treated as adjustable parameters. The parameter set is optimized in a general least-squares fitting by minimizing the squares of the differences between the experimental and calculated energy levels. The root mean square (r.m.s.) deviation σ is used as a figure of merit to describe the quality of the fit.

$$\sigma = \left(\frac{\sum \left(E_{\text{exp}} - E_{\text{calc}}\right)^2}{N - P} \right)^{1/2}, \tag{53}$$

where E_{exp} and E_{calc} are the experimental and calculated energy levels, respectively. N is the number of experimental energy levels and P is the number of variable parameters. It is tried to reduce the value of σ as much as possible. If σ is less than $20\,\text{cm}^{-1}$, it is believed that the parameter set can give a rather good description of the system.

Because of the large dimension of the energy matrices for $4f^n$ systems, calculations are done with the aid of special computer fitting programs. Indeed, the degeneracy will rapidly increase towards the middle of the lanthanide series. The degeneracy is equal to 14, 91, 364, 1001, 2002, 3003, 3432 for $n=1$ to $n=7$ (the same degeneracies are found for the f^{14-n} systems). This means that for Gd^{3+} ($4f^7$) a 3432×3432 matrix has to be

diagonalized. If the system has a symmetry higher than C_1, the energy matrix can be blocked out in submatrices, one for each crystal-field quantum number μ (see sect. 3.2). Every submatrix can be diagonalized separately. The best-known fitting programs are those written by H. Crosswhite (Argonne National Laboratory, Argonne, IL) and by M.F. Reid (University of Canterbury, Christchurch, New Zealand).

The different perturbations in the free-ion Hamiltonian, with corresponding operators and parameters will only be summarized here. The reader can find more detailed information in Wybourne (1965), Judd (1966), Judd et al. (1968) and in Crosswhite and Crosswhite (1984). The crystal-field Hamiltonian has been discussed in sect. 3.

The spherically symmetric part of the free-ion and crystal-field perturbations are taken together in the parameter E_{AVE}. A change of this parameter will result in a uniform shift of the total $4f^n$ configuration. E_{AVE} varies between ca. 1300 cm^{-1} for Ce^{3+} ($Z=58$, $4f^1$) and ca. 87000 cm^{-1} for Gd^{3+} ($Z=64$, $4f^7$). E_{AVE} then decreases again to ca. 4600 cm^{-1} for Yb^{3+} ($Z=70$, $4f^{14}$).

The electrostatic repulsion between electrons of the $4f^n$ configuration is described parametrically by the term $\sum_{k=2,4,6} F^k f_k$. The F^k parameters are the electrostatic radial integrals, the f_k represent the angular part of the electrostatic interaction. The F^0 parameter is not considered here, because it is incorporated in E_{AVE}. The F^k decrease as k increases. The F^4 and F^6 parameters can be expressed approximately as functions of F^2: $F^4=0.668\,F^2$ and $F^6=0.495\,F^2$ (Carnall et al. 1988). These ratios are those of the hydrogenic wave functions and are applied if the amount of experimental data is insufficient to vary the three electrostatic parameters independently. For instance, if for Eu^{3+} only data of the ^7F and ^5D terms are available only one parameter can be varied. This does not imply that the f-orbitals are hydrogenic, but that the ratios F^4/F^2 and F^6/F^2 are rather insensitive to the exact composition of the wave functions (Wybourne 1965). F^2 increases from ca. 69000 cm^{-1} for Pr^{3+} to ca. 100000 cm^{-1} for Tm^{3+}. Sometimes, F_k parameters are used instead of F^k: $F^2=225\,F_2$, $F^4=1089\,F_4$ and $F^6=(184041/25)F_6$ (Hüfner 1978). The f_k are invariant with regard to the group R_3, but not with regard to the groups R_7 and G_2 (which are used to label the states). It is possible to introduce operators e_k, which are linear combinations of the f_k operators and which have the same transformation properties as the groups R_7 and G_2. The corresponding parameters are E^k ($k=1$, 2, 3). E^0 can be included in an E_{AVE} parameter. The relations between the operators e_k and f_k and between the parameters F^k and E^k have been given by several authors (Racah 1949, Griffith 1961, Wybourne 1965, Caro 1976, Hüfner 1978, Morrison and Leavitt 1982).

Another perturbation is the spin–orbit coupling. Spin–orbit coupling results from the interaction between the spin magnetic moment of the electron and the magnetic field created by the movement of the electron around the nucleus. This interaction is described by the term $\zeta_{4f}A_{SO}$ in the Hamiltonian. ζ_{4f} is the spin–orbit coupling constant. A_{SO} represents the angular part of the spin–orbit interaction. ζ_{4f} increases over the lanthanide series from ca. 650 cm^{-1} for Ce^{3+} ($Z=58$) to ca. 2900 cm^{-1} for Yb^{3+} ($Z=70$) (Carnall et al. 1989).

Although the electrostatic and spin–orbit interactions are by far the most important terms in the Hamiltonian, other smaller interactions have to be considered in order to get a good agreement between experimental and calculated energy levels. Diagonalization of the energy matrix which incorporates only the electrostatic and spin–orbit interaction, often results in discrepancies between experimental and calculated levels of several hundred cm^{-1} (Wybourne 1965).

Additional parameters and operators are required to describe the configuration interaction. Configuration interaction is the spin-independent interaction between configurations of equal parity. The new operators are two-particle and three-particle operators working within the $4f^n$ configuration. They result in an adaptation of the basis functions. In this way, no increase of the dimension of the energy matrix is required, only a relatively small increase in the number of parameters. Another consequence is that the F^k integrals can no longer be considered as pure Hartree–Fock integrals, but they will incorporate configuration interaction effects which transform as f_k.

The two-particle correction term in the free-ion Hamiltonian is $\alpha L(L+1)+\beta G(G_2)+\gamma G(R_7)$ (Rajnak and Wybourne 1963). α, β and γ are the parameters which account for the radial interactions not transforming as f_k. $G(G_2)$ and $G(R_7)$ are the Casimir's operators for the groups G_2 and R_7, respectively. L is the total angular momentum. Morrison and Rajnak (1971) have calculated these electrostatic configuration interaction parameters for Pr^{3+}. The values of α, β and γ are rather stable over the lanthanide series, because processes such as excitation of one or two particles to the high energy continuum states have large contributions to the parameters and the energies of these continuum states relative to the $4f^n$ configurations do not change significantly with the atomic number Z (Carnall et al. 1989).

For $4f^n$ configurations with three or more f electrons, the Hamiltonian is expanded with the term $\sum_i t_i T^i$ ($i=2, 3, 4, 6, 7, 8$) to take the three-particle configuration interaction into account. t_i are the three-particle operators and T^i are the parameters (Judd 1966). Variation of the T^i parameters in a fitting procedure has to be done carefully, since these parameters are only sensitive to particular $^{2S+1}L_J$ levels. If the level for which a T^i parameter shows a great sensitivity, is not found in the experiment, a variation of that T^i parameter will result in a meaningless parameter value. The parameter has to be constrained in that case. A systematic investigation of the sensitivity has not been done yet, although some preliminary data have been published (Caro et al. 1977a, Görller-Walrand et al. 1994). The values of the T^i parameters have been calculated for Pr^{2+} ($4f^3$) by Balasubramanian et al. (1975) using *ab initio* methods. The parameters are fairly constant over the lanthanide series. Judd and Lo (1994) have found some erroneous values for the t_i matrix elements for the $4f^6$ and $4f^7$ configurations in the input files of the computer program written by H. Crosswhite; these errors luckily have negligible effect on the calculations.

Magnetically correlated corrections such as spin–spin and spin–other-orbit interactions are represented by the term $\sum_{k=0,2,4} m_k M^k$ in the Hamiltonian, where m_k are the operators (Judd et al. 1968). The parameters M^k are also called Marvin-integrals after

H.H. Marvin (Marvin 1947). In the calculations, these parameters are mostly maintained by the pseudo-relativistic Hartree–Fock ratios $M^2/M^0 = 0.56$ and $M^4/M^0 = 0.38$, allowing only M^0 to vary freely (Crosswhite and Crosswhite 1984).

The electrostatic correlated spin–orbit interactions are described by the $\sum_{k=2,4,6} p_k P^k$ term, with p_k as the operators and P^k as the parameters (Judd et al. 1968, Goldschmidt et al. 1968). The parameters can be varied in the ratios $P^4/P^2 = 0.75$, $P^6/P^2 = 0.5$ (Crosswhite and Crosswhite 1984).

Since the introduction of new parameters may alter the values of the parameters already fitted, Judd and Crosswhite (1984) have introduced orthogonalized operators. These yield parameters which are more precisely defined and more stable than the conventional ones.

The free-ion Hamiltonian can thus be written as

$$\mathcal{H}_{\text{free ion}} = E_{\text{AVE}} + \sum_{k=2,4,6} F^k f_k + \zeta_{4f} A_{\text{SO}} + \alpha L(L+1) + \beta G(G_2) + \gamma G(R_7) + \sum_{i=2,3,4,6,7,8} t_i T^k + \sum_{k=0,2,4} m_k M^k + \sum_{k=2,4,6} p_k P^k. \tag{54}$$

The number of free-ion parameters is 2 for Ce^{3+} and Yb^{3+} (only E_{AVE} and ζ_{4f}), 14 for Pr^{3+} and Tm^{3+} (no T^i parameters) and 20 for the rest of the lanthanide series. The total Hamiltonian is the sum of the free-ion and crystal-field Hamiltonians:

$$\mathcal{H} = \mathcal{H}_{\text{free ion}} + \mathcal{H}_{\text{CF}}. \tag{55}$$

For each lanthanide ion, a mean value was calculated for the different free-ion parameters available in the literature. The parameter sets are given in table 5.

A very recent theoretical development is the quark model of the 4f shell (Judd 1991, 1994, Judd and Lister 1991, 1992a–c, 1993a–c). The quark model is an alternative way of classifying the atomic levels in the 4f shell. Instead of 15 different $4f^n$ configurations (n runs from 0 to 14), one considers only one single quark configuration $(s+f)^4$, augmented by two parity labels.

4.2. *Pitfalls in the fitting procedure*

A problem with the present parametrization scheme in terms of 20 free ion parameters and a symmetry-dependent number of crystal-field parameters is that, although a good agreement between experiment and theory can be obtained, the parameter sets for different systems are difficult to compare with each other. It was already noticed by D.J. Newman (Newman 1971) that there is very little relationship between sets of parameters for the same ion in host crystals with different site symmetry or even for the same ion in isomorphic hosts. The same is true for the parameters for the different lanthanide ions in the same matrix.

There are several causes for these comparison problems. First of all, one can expect problems when fitting such a large set of adjustable parameters. The optimized parameter

Table 5
Mean free-ion parameters (cm^{-1}) for the trivalent lanthanide ions

Ion	E_{AVE}	F^2	F^4	F^6	α	β	γ	T^2	T^3	T^4	T^6	T^7	T^8	ζ_{4f}	M^0	M^2	M^4	P^2	P^4	P^6
Pr^{3+}	9818	68323	49979	32589	21.11	−644	1413	–	–	–	–	–	–	747	1.88	1.05	0.71	244	186	122
Nd^{3+}	24059	72295	52281	35374	21.08	−606	1526	303	41	66	−289	317	301	879	1.85	1.04	0.70	232	174	116
Pm^{3+}	36709	75842	54319	38945	20.92	−645	1410	306	45	34	−314	557	407	1023	1.97	1.10	0.75	280	210	140
Sm^{3+}	45675	79012	56979	40078	20.50	−616	1565	282	26	71	−257	314	328	1170	2.38	1.33	0.90	336	252	168
Eu^{3+}	63736	82786	59401	42644	19.80	−617	1460	370	40	40	−330	380	370	1332	2.38	1.33	0.90	303	227	152
Gd^{3+}	87446	85300	60517	44731	18.95	−620	1658	308	43	51	−298	338	335	1504	2.99	1.67	1.14	542	407	271
Tb^{3+}	68237	89540	63485	44998	17.57	−581	1792	330	40	45	−365	320	349	1705	2.70	1.51	1.03	482	362	241
Dy^{3+}	55893	92373	65281	47642	17.86	−628	1170	326	23	83	−294	403	340	1915	4.46	2.50	1.69	610	458	305
Ho^{3+}	48831	95772	67512	48582	17.22	−596	1839	365	37	95	−274	331	343	2142	2.99	1.67	1.14	582	437	291
Er^{3+}	35863	97909	70349	48861	15.86	−541	1572	286	48	14	−319	203	333	2358	5.58	3.12	2.12	730	548	365
Tm^{3+}	17677	101381	70230	51827	17.25	−665	1936	–	–	–	–	–	–	2644	4.93	2.76	1.87	730	548	365

set is very dependent on the chosen starting values. The free-ion parameters will not vary much for a lanthanide ion in different systems, in contrast to the crystal-field parameters, which may show a large variation dependent on the host crystal. Starting values for crystal-field parameters can be obtained from *ab initio* calculations, like the calculation of *point charge lattice sums* (see Garcia and Faucher 1995). Another method is the initial use of a higher symmetry to reduce the number of parameters. This is the so called "*descent of symmetry*" method (Wybourne 1965). One can also try to extract parameters directly from the experimental data. Antic-Fidancev et al. (1982) have determined the second-rank parameters ($k=2$) for gadolinium compounds by plotting the calculated overall splitting and intermediate crystal-field levels of the $^6P_{7/2}$ multiplet in function of B_0^2 and B_2^2. The parameter set for which the agreement between calculated and experimental energy levels was the best, has been retained. Once a reliable set of parameters is obtained, it can be used as starting values for another lanthanide ion in the same matrix, or for the same ion in an isomorphic matrix. Parameters can only be changed over a limited interval and the fitting procedure will stop if a local minimum in the r.m.s. σ function is reached. This local minimum is not necessarily equal to the absolute minimum. The σ function is a smooth function. This means that relatively large changes of the parameters can be made without considerably changing the r.m.s. value σ. A particular set of parameters may be suitable to calculate the total splitting of a J term exactly, but not the position of the intermediate crystal-field levels. For another set the calculation of the intermediate levels may be good, but not the overall splitting. Both parameter sets can have the same σ value, although their values are different. To handle the large matrices for f^5 to f^9 systems, one can truncate the basis set. This means that J terms above an arbitrarily chosen energy value are omitted in the calculation. The truncation has only a small influence on the lower energy levels, but the deviation enlarges towards the truncation edge. The influence of truncation effects on crystal-field calculations has been studied by Teste de Sagey et al. (1982). The calculated values are also dependent on the applied coupling scheme: Russell–Saunders coupling, the intermediate coupling scheme or J-mixing. Another problem is that different research groups do not use the same levels of a particular lanthanide ion in the fitting procedure. This can be due to the fact that some levels cannot be seen in a crystal which is only weakly doped with the lanthanide ion. Some systems have been studied only by luminescence methods, and others only by absorption spectroscopy. A combined treatment is favorable, since the two methods are complementary. Comparable results can only be expected if the systems under study are treated in exactly the same manner: the same levels and the same starting values. If an inappropriate starting value for a particular parameter is chosen, the other parameters will be influenced, because they will try to compensate for this inadequacy. One has to be sure that the calculated barycenter of the multiplet agrees with the experimental one, otherwise an incorrect crystal-field splitting pattern will be simulated, giving incorrect crystal-field parameters. The experimental barycenter can be determined only if all the crystal-field levels within a $^{2S+1}L_J$ level are detected. The barycenter is found by multiplying each crystal-field level of a multiplet by its degeneracy and making the sum. The barycenter is then equal to that sum divided by $2J+1$. On the

other hand, J-mixing will also influence the position of the calculated barycenter (Görller-Walrand et al. 1994).

The fact that the different research groups do not use the same expansion for the crystal-field potential does not enhance the easiness of a comparison. It is useless to report crystal-field parameters without giving the expansion of the crystal-field potential, because in that case one cannot convert the parameter values to another formalism. The B_q^k parameters with $q \neq 0$ are not invariant under rotation, their value and sign depend on the choice of the coordinate system. One can always make one of the B'^k_q parameters equal to zero by an appropriate rotation of the coordinate system. Special attention has to be paid to the rare-earth garnets. The garnets $A_3B_5O_{12}$ (A = Y, Gd, Lu; B = Al, Ga) possess six sites with D_2 symmetry. The sites have different orientations in order to be compatible with the cubic symmetry of the crystal. In the absence of a magnetic field, all the sites are equivalent. For each site, one can determine a set of crystal-field parameters. If one set of parameters is available, the crystal-field parameters for the other sites can be found by applying transformation formulas (Morrison and Leavitt 1982). Each set of parameters will give the same calculated crystal-field levels, although the actual sets may look very different.

Table 6 (Stewart 1985) lists the conversion factors to convert parameters $A_k^q \langle r^k \rangle$ of the operator-equivalent method (Stevens 1952, Elliot and Stevens 1953a,b and Judd 1955) into B_q^k parameters. Although the $A_k^q \langle r^k \rangle$ are out of use now, they are often encountered in the older literature.

If the unit tensor U_q^k is chosen as operator and not the C_q^k tensor, the conversion can be done by:

$$B_q^k \text{ (as function of } C_q^k) = (-1)^q \left(\langle 3 \| C^k \| 3 \rangle \right)^{-1} B_q^k \text{ (as function of } U_q^k). \tag{56}$$

The reduced matrix elements $\langle 3 \| C^k \| 3 \rangle$ can be calculated according to eq. (30). The values of the matrix elements are also given in sect. 4.6. The phase factor $(-1)^q$ has to be introduced if in the crystal-field potential the U_{-q}^k and U_q^k operators are combined as $\left(U_q^k + (-1)^q U_{-q}^k\right)$ for the real part and $\left(U_q^k - (-1)^q U_{-q}^k\right)$ for the imaginary part.

A totally different cause for the difficulty in comparison between the different sets of crystal field parameters, is the fact that for f^n systems the parameters do not only depend on the radial coordinates of the ligands, but also on the angular coordinates. This is not the case for most d^n transition metal complexes, since they have a coordination polyhedron which is an octahedron (CN = 6), a tetrahedron (CN = 4) or a derived structure (plane square, CN = 4; tetragonal bipyramid, CN = 6; ...). In these complexes, the angular positions of the ligands are restricted by symmetry. There are no degrees of freedom for the angular coordinates, only for the radial position. For rare-earth systems as will be discussed below in sect. 5.1, the most common coordination polyhedra are the dodecahedron (CN = 8), (distorted) square antiprism (CN = 8), monocapped square antiprism (CN = 9) and tricapped trigonal prism (CN = 9). These polyhedra have a degree of freedom for the angular coordinates.

Table 6
Relations between the B_q^k and $A_k^q\langle r^k\rangle$ crystal-field parameters (for k = even)

$$B_0^2 = 2A_2^0\langle r^2\rangle$$

$$B_1^2 = \frac{-1}{\sqrt{6}}A_2^1\langle r^2\rangle$$

$$B_2^2 = \frac{2}{\sqrt{6}}A_2^2\langle r^2\rangle$$

$$B_0^4 = 8A_4^0\langle r^4\rangle$$

$$B_1^4 = \frac{-2}{\sqrt{5}}A_4^1\langle r^4\rangle$$

$$B_2^4 = \frac{4}{\sqrt{10}}A_4^2\langle r^4\rangle$$

$$B_3^4 = \frac{-2}{\sqrt{35}}A_4^3\langle r^4\rangle$$

$$B_4^4 = \frac{8}{\sqrt{70}}A_4^4\langle r^4\rangle$$

$$B_6^0 = 16A_6^0\langle r^6\rangle$$

$$B_1^6 = \frac{-8}{\sqrt{42}}A_6^1\langle r^6\rangle$$

$$B_2^6 = \frac{16}{\sqrt{105}}A_6^2\langle r^6\rangle$$

$$B_3^6 = \frac{-8}{\sqrt{105}}A_6^3\langle r^6\rangle$$

$$B_4^6 = \frac{16}{3\sqrt{14}}A_6^4\langle r^6\rangle$$

$$B_5^6 = -\frac{-8}{3\sqrt{77}}A_6^5\langle r^6\rangle$$

$$B_6^6 = \frac{16}{\sqrt{231}}A_6^6\langle r^6\rangle$$

Rudowicz (1985, 1986a,b) discussed the determination of "imaginary" crystal-field parameters. Three different approaches are considered for the determination of crystal-field parameters for symmetries with imaginary terms in the Hamiltonian. One approach is the complete fitting in which all parameters admissible by the point group are taken into account. In a second approach one of the imaginary parameters is set to zero by a suitable rotation of the coordination systems. In the third approach, the symmetry of the system is approximated by a higher symmetry so that only real parameters have to be considered. Imaginary parameters are a source of great confusion and Rudowicz pointed on several inadequate parameter fittings which can be found in the literature. Since our parameters are derived from tesseral harmonics, they are all real.

We want to give here also some comments on the definitions of the crystal-field parameters by Wybourne (1965). His crystal-field formalism is sometimes a little bit confusing. First, he introduces the parameters which have the same transformation properties as spherical harmonics. These parameters are in general complex numbers. Both B_0^k, B_q^k and B_{-q}^k occur. Moreover, his parameters transform as tesseral harmonics, like our parameters do. It is therefore easy to confuse B_{-q}^k and B'^k_q. Prather (1961) always uses tesseral harmonics for his parameters and also for his operators.

4.3. *Sensitivity of calculated crystal-field levels towards parameter change*

The tendency in lanthanide spectroscopy is to use as many levels as possible to determine a set of phenomenological B_q^k crystal-field parameters. It is commonly thought that the larger the number of experimental levels used in the fitting procedure, the more reliable the parameter set will be. This is because in statistics a larger data set represents better the total population than a small one. Such a large number of levels is indeed required if one wants to deduce a set of free-ion parameters together with the crystal-field parameters. But are all crystal-field levels appropriate to determine a set of crystal-field parameters? The answer is no. It was already observed by Görller-Walrand et al. (1994) that some crystal-field levels are more sensitive to a particular parameter than others. A level is very sensitive to a parameter, if a small change of that parameter will cause a great change of the calculated energy of the level in question. It is preferable to select those levels to determine the parameter, since this sensitivity will lead to a higher accuracy.

So much emphasis is put on the crystal-field parameters by the description of the crystal field felt by a lanthanide ion that it is often forgotten that the reduced matrix elements $\langle \Psi_{l^n\tau SLJ} | U^k | \Psi_{l^{n'}\tau'SL'J'} \rangle$, (or $\overline{U}^k$ for short) are also responsible for the crystal-field splitting of a J level. The magnitude of the crystal-field splitting is proportional to the $\overline{U}^k$, in the sense that levels with large values for the $\overline{U}^k$ will show a greater crystal-field splitting than levels with small $\overline{U}^k$ values. If two multiplets with the same J value show a great difference in crystal-field splitting, it is because their values are very different. A calculated crystal-field level is very sensitive to a change of a B_q^k parameter, if the $\overline{U}^k$ value is large. In order to determine the B_q^k parameters with a particular k-value, one has to select levels with a large value for the $\overline{U}^k$ in question, while the other $\overline{U}^k$ have to be small or equal to zero. Due to the selection rule $k \leqslant 2J$ not every $\overline{U}^k$ will have the same contribution to the splitting of levels with small J values. Although the doubly reduced matrix elements (depend on S and L) can be found tabulated in the literature (Rotenberg et al. 1959), the $\overline{U}^k$ (depend on S, L and J) cannot. They can be calculated with the knowledge of the doubly reduced matrix elements and the composition of the free-ion wave functions. The squares of the $\overline{U}^k$ are given by Carnall et al. (1977). Since the $\overline{U}^k$ are relatively insensitive to the chemical nature and symmetry of the host matrix, they can be regarded in a good approximation as constants for a given trivalent lanthanide ion.

Not only must the $^{2S+1}L_J$ manifold, which is used to determine a particular B_q^k, have a large reduced matrix element $\overline{U}^k$ for one particular k-value, while the other two reduced matrix elements must have a small value or be equal to zero, other conditions must be fulfilled also. The $^{2S+1}L_J$ manifold may not overlap with other $^{2S+1}L_J$ manifolds, otherwise an unambiguous assignment of the crystal-field levels is not possible. J-mixing is also much stronger for levels which are close to each other. This means that one is restricted to the lower lying free-ion levels (roughly speaking $<25\,000\,\mathrm{cm}^{-1}$), since at higher energies the density of states is so high that overlap will very often occur. High values for the reduced matrix elements are of course of no use if the intensities of the transitions to the selected J level are very low, so that the transitions cannot be observed experimentally.

It is also important to choose $^{2S+1}L_J$ levels for which all or nearly all crystal-field levels can be experimentally found. Crystal-field levels which are not observed may result in an unrealistic set of crystal-field parameters. It must also be noticed that although f^n and f^{14-n} systems have the same $^{2S+1}L_J$ levels, one cannot use the same levels to extract the crystal-field parameters, because of the above conditions. For some lanthanide ions, it is really difficult to select an appropriate set of levels. It is problematic to determine the sixth-rank crystal field parameters of Gd^{3+}, since none of the levels is very sensitive to the $k=6$ parameters. This is due to a small value of the $\overline{U}^6$ matrix element. Some levels which show all characteristics required to select them as levels to be used in the fitting procedure, have to be rejected, because of the fact that their energy positions are badly simulated by the crystal-field calculations. These levels will be discussed in sect. 4.5. The best levels for each lanthanide ion and each k-value are summarized in table 7. It is meaningless to carry insensitive levels through the fitting procedure. They will only result in parameter sets which are very difficult to compare with each other. It is advisable to determine first the parameters with $k=2$, then those with $k=4$ and eventually the $k=6$ parameters. Here, the selection rule $k \leqslant 2J$ is very helpful. After this stepwise determination of the crystal field parameters, one can vary at the end all the parameters simultaneously. This is only important if J-mixing is taken into account.

4.4. *Systematic trends of the crystal-field parameters over the lanthanide series*

The expected trend is a decrease of the parameter values over the lanthanide series due to the increased nuclear charge which is felt by the f electrons (Carnall et al. 1989). As the electron orbits are pulled closer to the nucleus, the crystal-field effect should be reduced. This effect is greater than that of a contraction of the crystal lattice by a decrease of the ionic radius of the lanthanide ion (reduction of the central ion–ligand distance). The expected trend is however not always observed. In some cases the crystal-field parameters remain fairly constant over the lanthanide series, in other cases there is a lot of scatter of the values of the parameters or the parameters even increase. This is maybe due to the difficulty of obtaining consistent sets of parameters, as described earlier. The parameters for the trivalent lanthanide ions doped in the host matrices LaF_3, $LaCl_3$, $LiYF_4$, $R(C_2H_5SO_4)_3{\cdot}9H_2O$, $Na_3[R(C_4H_4O_5)_3]{\cdot}2NaClO_4{\cdot}6H_2O$ and Cs_2NaRCl_6 are given in table 8. The B_0^2, B_0^4 and B_0^6 parameters are plotted in figs. 2–4.

There is a remarkable discontinuity in magnitude of the crystal field parameters, especially the sixth-rank parameters ($k=6$), between the first and second half of the lanthanide series in systems like LaF_3 and $LaCl_3$ (Carnall et al. 1989). According to Judd (1979) the drop in the $k=6$ parameters in going from $LaCl_3{:}Eu^{3+}$ to $LaCl_3{:}Tb^{3+}$ is an indication for the need to include two-electron operators in the crystal-field Hamiltonian (which is done in correlation crystal-field theory, see sect. 4.5).

The relative position of the crystal-field levels in a $^{2S+1}L_J$ state will be in general not the same for a f^n and a f^{14-n} system, because of a change of the crystal-field parameters over the lanthanide series and because of an opposite sign for the reduced matrix elements.

Table 7
The most sensitive $^{2S+1}L_J$ multiplets for the determination of the B_q^k crystal-field parameters for each of the lanthanide ions (except Pm^{3+})[a]

Ion	$k=2$		$k=4$		$k=6$	
	Multiplet	Position (cm^{-1})	Multiplet	Position (cm^{-1})	Multiplet	Position (cm^{-1})
Pr^{3+}	$^3P_1$[b]	21500	$^1D_2$[c]	17000	$^3H_4$	ground state
			$^7F_2$	5200	$^3F_3$	6500
					$^3H_6$	4600
Nd^{3+}[d]	$^4F_{3/2}$	11600	$^4F_{9/2}$	14900	$^4I_{9/2}$	ground state
	$^3P_{3/2}$	26400			$^4I_{15/2}$	6200
	$^2D_{5/2}$	24000				
Sm^{3+}	$^4F_{3/2}$	18900	$^6F_{5/2}$	7200	$^6H_{7/2}$	1100
			$^4F_{5/2}$	22200	$^6H_{9/2}$	2300
			$[^6H_{5/2}]$	ground state	$^6F_{7/2}$	8000
Eu^{3+}	$^7F_1$	400	$^7F_2$	1000	$^7F_4$	2900
	$[^5D_1]$	19000	$[^5D_2]$	21400	$^7F_3$	1900
					$^5L_6$	25100
					$[^5D_4]$	27600
Gd^{3+}	$^6P_{7/2}$	32200	$^6I_{9/2}$	36300	–[e]	
	$^6P_{3/2}$	33400	$^6I_{11/2}$	36600		
Tb^{3+}	$^7F_1$	5600	$^7F_2$	5100	$^7F_4$	3400
					$^5G_6$	26500
Dy^{3+}	$^6F_{3/2}$	13300	$^6F_{5/2}$	12500	$^6F_{7/2}$	11100
					$^4F_{9/2}$	21100
Ho^{3+}	$^5I_5$[f]	11300	$^5F_2$	21200	$^5I_8$	ground state
			$^5F_5$	15500	$^5G_4$	26100
Er^{3+}	$^4S_{3/2}$	18600	$^4F_{5/2}$	22400	$^4I_{9/2}$	12600
	$^4F_{3/2}$	22700				
Tm^{3+}	$^3P_1$	36500	$^3F_2$	15200	$^3H_4$	12700
	$[^1D_2]$	28000			$[^3F_3]$	14600

[a] The selection criteria are high values for the reduced matrix element U^k, no overlap with other multiplets, and sufficiently high intensities of the transitions in question. Less favorable choices are placed in brackets. The approximate energetic position of each multiplet is given (rounded to the nearest hundred).

[b] The $^3P_1$ multiplet overlaps in some crystals with the $^1I_6$ multiplet.

[c] According to all criteria, $^1D_2$ is the best multiplet for the determination of the fourth-rank crystal-field parameters of Pr^{3+}, but it is very often a troublesome one in the fitting procedure.

[d] Many apparent good choices for Nd^{3+} have to be omitted, because of a strong overlap between different multiplets, e.g. ($^4H_{5/2}$, $^2H_{9/2}$), ($^4F_{7/2}$, $^4S_{3/2}$), ...

[e] The determination of the sixth-order crystal-field parameters for Gd^{3+} is really problematic, because none of the levels which can be determined by spectroscopic measurements have sufficiently high values for the U^6 reduced matrix element. The crystal-field splitting is in a good approximation determined by the second- and fourth-rank parameters only.

[f] No multiplet in Ho^{3+} is sensitive to the second-rank parameters alone. The splitting in the $^5I_5$ multiplet has also considerable contributions from the fourth-rank parameters.

Table 8

Crystal-field parameters (cm^{-1}) for trivalent lanthanide ions doped into host crystals $LaCl_3$, LaF_3, $LiYF_4$, Cs_2NaRCl_6, $Na_3[R(C_4H_4O_5)_3]\cdot 2NaClO_4\cdot 6H_2O$ (RODA), and $R(C_2H_5SO_4)_3\cdot 9H_2O$ (RES)[a,b]

R^{3+}	B_0^2	B_0^4	B_0^6	B_2^2	B_2^4	B_3^4	B_3^6	B_4^4	B_2^6	B_4^6	B_6^6	Ref.
$LaCl_3:R^{3+}$												
Ce^{3+}	127	−319	−1047								−427	1
Pr^{3+}	108	−332	−653								−445	1
Nd^{3+}	168	−340	−734								−460	1
Pm^{3+}	151	−410	−667								−460	1
Sm^{3+}	188	−173	−695								−467	1
Eu^{3+}	193	−296	−818								−521	1
Gd^{3+}	208	−266	−482								−411	1
Tb^{3+}	184	−295	−459								−284	1
Dy^{3+}	205	−352	−413								−225	1
Ho^{3+}	246	−252	−500								−316	1
Er^{3+}	199	−317	−402								−240	1
Tm^{3+}	225	−241	−447								−254	1
Yb^{3+}	–	–	–								–	1
$LaF_3:R^{3+}$												
Ce^{3+}	[−218]	[738]	[679]	[−120]	[431]			[616]	[−921]	[−348]	[−788]	2
Pr^{3+}	−218	738	679	−120	431			616	−921	−348	−788	2
Nd^{3+}	−256	496	641	−48	521			563	−839	−408	−831	2
Pm^{3+}	−245	470	640	−50	525			490	−750	−450	−760	2
Sm^{3+}	−224	452	649	[−50]	597			408	−706	−508	−692	2
Eu^{3+}	−217	413	558	[−50]	597			408	[−706]	[−508]	[−692]	2
Gd^{3+}	[−231]	[604]	[280]	[−99]	[340]			[452]	[−721]	[−204]	[−509]	2
Tb^{3+}	−231	604	280	−99	340			452	−721	−204	−509	2
Dy^{3+}	−244	506	367	−65	305			523	−590	−236	−556	2
Ho^{3+}	[−240]	560	376	−107	250			466	−576	−227	−546	2
Er^{3+}	−238	453	373	−91	308			417	−489	−240	−536	2
Tm^{3+}	−249	457	282	−105	320			428	−482	−234	−492	2
Yb^{3+}	[−249]	[457]	[282]	[−105]	[320]			[428]	[−482]	[−234]	[−492]	2

continued on next page

Table 8, *continued*

R^{3+}	B_0^2	B_0^4	B_0^6	B_2^2	B_2^4	B_3^4	B_3^6	B_4^4	B_2^6	B_4^6	B_6^6	Ref.
$LiYF_4$:R^{3+}												
Ce^{3+}	–	–	–					–		–		3
Pr^{3+}	481	−1150	−89					−1228		−1213		3
Nd^{3+}	409	−1135	27					−1216		−1083		3
Pm^{3+}	–	–	–					–		–		3
Sm^{3+}	–	–	–					–		–		3
Eu^{3+}	348	−775	−80					−1045		−772		4
Gd^{3+}	–	–	–					–		–		3
Tb^{3+}	400	−802	−57					−1055		−754		5
Dy^{3+}	340	−784	−7					−951		−850		3
Ho^{3+}	408	−629	−18					−835		−673		3
Er^{3+}	352	−820	−134					−1000		−617		3
Tm^{3+}	348	−639	−182					−864		−641		3
Yb^{3+}	–	–	–					–		–		3
Cs_2NaRCl_6:R^{3+}												
Ce^{3+}		2119	261									6
Pr^{3+}		1938	290									6
Nd^{3+}		1966	258									6
Pm^{3+}		–	–									6
Sm^{3+}		–	–									6
Eu^{3+}		2055	308									6
Gd^{3+}		1776	136									6
Tb^{3+}		1624	150									6
Dy^{3+}		1614	148									6
Ho^{3+}		1593	171									6
Er^{3+}		1492	163									6
Tm^{3+}		1498	159									6
Yb^{3+}		1471	[0]									6

continued on next page

Table 8, *continued*

R^{3+}	B_0^2	B_0^4	B_0^6	B_2^2	B_2^4	B_3^4	B_3^6	B_4^4	B_2^6	B_4^6	B_6^6	Ref.
RODA												
Ce^{3+}	–	–	–			–	–				–	7
Pr^{3+}	–90	–1340	–413			–943	–332				–299	7
Nd^{3+}	–22	–1030	–503			–808	–1035				–636	7
Pm^{3+}	–	–	–			–	–				–	7
Sm^{3+}	14	–834	–474			–742	–870				–622	7
Eu^{3+}	41	–893	–337			–696	–799				–635	7
Gd^{3+}	64	–844	–629			–749	–937				–752	8
Tb^{3+}	–	–	–			–	–				–	7
Dy^{3+}	–	–	–			–	–				–	7
Ho^{3+}	64	–741	–416			–512	–608				–526	9
Er^{3+}	104	–766	–324			–557	–485				–433	7
Tm^{3+}	176	–431	–155			397	472				–420	7
Yb^{3+}	–	–	–			–	–				–	7
RES												
Ce^{3+}	18	–336	–720								–716	10
Pr^{3+}	8	–791	–772								–686	7
Nd^{3+}	161	–644	–733								–685	7
Pm^{3+}	–	–	–								–	10
Sm^{3+}	120	–509	–640								–605	10
Eu^{3+}	122	–427	–597								–600	7
Gd^{3+}	200	–552	–544								–523	10
Tb^{3+}	220	–598	–544								490	10
Dy^{3+}	288	–681	–531								564	10
Ho^{3+}	250	–630	–478								–412	10
Er^{3+}	220	–648	–494								–416	7
Tm^{3+}	260	–568	–457								–456	10
Yb^{3+}	310	–464	–416								–498	10

continued on next page

Table 8, notes

[a] The literature values are transformed to the C_q^k formalism and to our choice of the coordination axes (conventions of Prather).

[b] Values in brackets are parameters which were constrained during the fitting. The parameters for $LaF_3:Pm^{3+}$ are interpolated values.

References

(1) Jayasankar et al. (1989a)
(2) Carnall et al. (1989)
(3) Jayasankar et al. (1989b)
(4) Görller-Walrand et al. (1993b)
(5) Liu et al. (1994)
(6) Tanner et al. (1994b)
(7) Hammond et al. (1989)
(8) Stephens et al. (1991)
(9) Moran et al. (1990a)
(10) Morrison and Leavitt (1982)

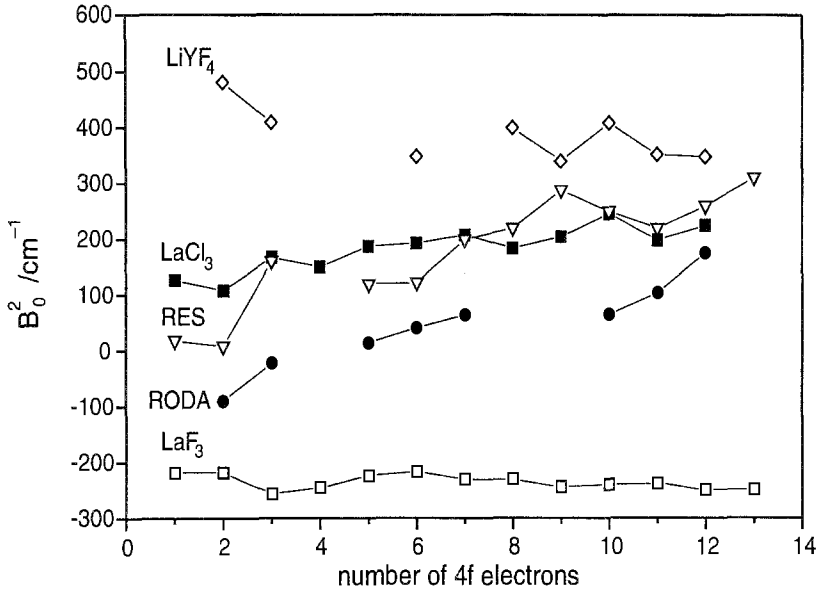

Fig. 2. Change of the B_0^2 crystal-field parameter over the lanthanide series for different crystalline host matrices.

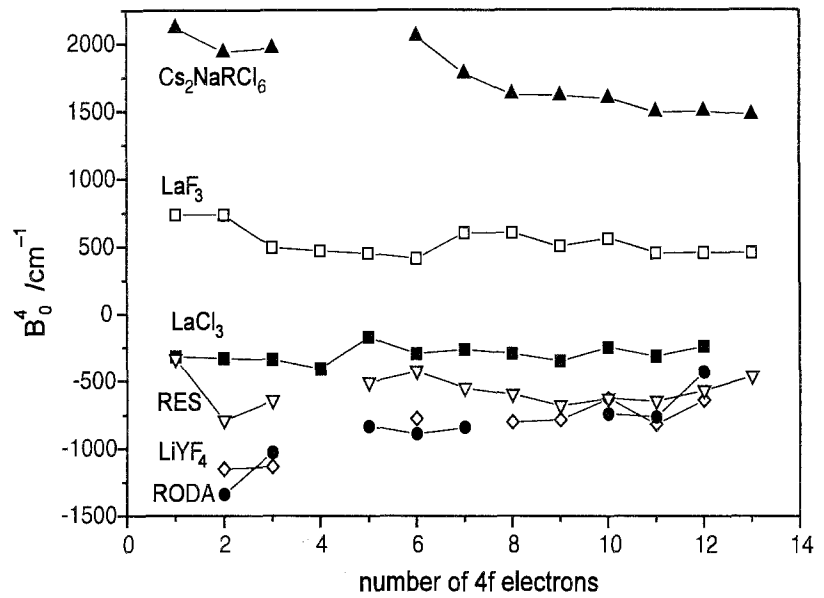

Fig. 3. Change of the B_0^4 crystal-field parameter over the lanthanide series for different crystalline host matrices.

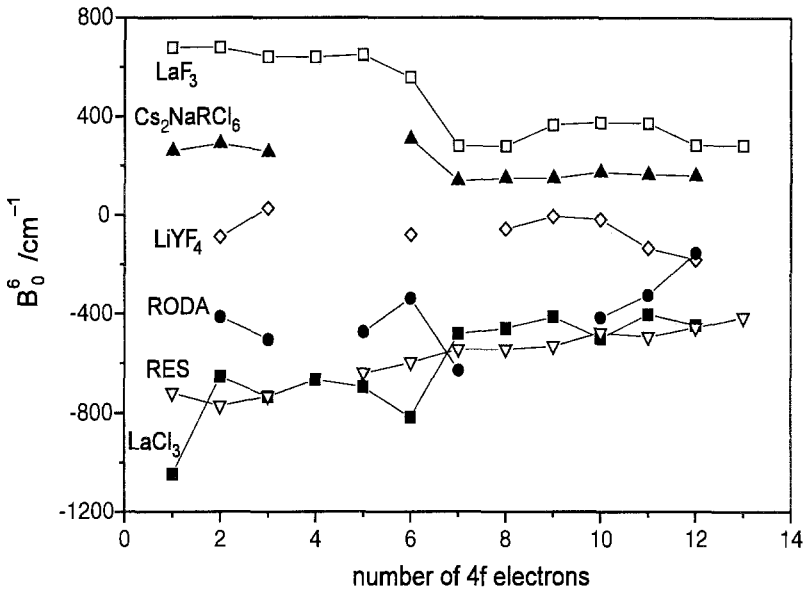

Fig. 4. Change of the B_0^6 crystal-field parameter over the lanthanide series for different crystalline host matrices.

4.5. *Correlation crystal field*

The use of the one-electron crystal-field model results in a good agreement between experimental and calculated crystal-field levels for most systems. However, the splitting of some $^{2S+1}L_J$ multiplets often cannot be well simulated. Anomalous multiplets are $^1D_2$ of Pr^{3+} (Judd 1979), $^2H(2)_{11/2}$ of Nd^{3+} (Faucher et al. 1989b), ^5D_J of Eu^{3+} (Moune and Caro 1989), $^6I_{17/2}$ of Gd^{3+} (Judd 1979), $^3K_8$ of Ho^{3+} (Judd 1979) and $^1G_4$ and $^1D_2$ of Tm^{3+} (Jayasankar et al. 1989b).

To remove these discrepancies, the Hamiltonian is extended to account for the effects of the electron correlation on the anisotropic crystal-field interactions in the 4f shell. Two-body operators are necessary to describe the correlation effects. The expression *correlation crystal field* is used for the two-electron part of the crystal-field perturbation. A review of the theoretical development of correlation crystal-field theory is given by Garcia and Faucher (1995). A practical problem for taking the correlation effects into account is the enormous number of parameters required.

Judd (1977a) proposed that a large part of the correlation effects may be parametrized as a spin-correlated crystal field (SCCF). SCCF is based on the observation that crystal-field parameters seem to be dependent on the spin multiplicity of a ^{2S+1}L term, and considers correlations which result from a difference in the crystal field seen by 4f electrons with different spins s_i relative to the direction of the total spin S $\left(S = \sum_i s_i\right)$. The strong attractive exchange forces between 4f electrons whose spins are parallel result

in less extended radial wave functions and thus in smaller crystal-field parameters. The one-electron crystal-field Hamiltonian (expressed in spherical harmonics) is modified to

$$\mathcal{H}_{\mathrm{CF}} = \sum_{k,q,i} B_q^k (1 + c_k s_i \cdot S) C_q^k(i). \tag{57}$$

The c_k ($k=2$, 4, 6) are adjustable parameters, s_i is the spin operator for the i-th electron and S is the total spin operator. The c_k parameters must be negative if the contraction of the radial wave functions corresponds to parallel spins. Positive values for c_6 have been reported however (Newman et al. 1982) and were explained to be due to a charge-transfer mechanism and to covalent effects. Only three additional parameters have to be introduced. The calculations can be done in practice by replacing in the expression for the crystal-field matrix element (eq. 49) the double reduced matrix element $\langle \Psi_{l^n \tau SL} \| U^k \| \Psi_{l^{n'} \tau' SL'} \rangle$, by

$$\langle \Psi_{l^n \tau SL} \| U^k \| \Psi_{l^{n'} \tau' SL'} \rangle + c_k \left[\frac{S(S+1)}{(2S+1)} \right]^{1/2} \langle \Psi_{l^n \tau SL} \| V^{1k} \| \Psi_{l^{n'} \tau' SL'} \rangle. \tag{58}$$

V^{1k} is a unit double tensor. The corresponding reduced matrix elements can be calculated in a similar way as the reduced matrix elements for the unit tensor U^k.

Jayasankar et al. (1987) reported a SCCF study of the crystal-field interaction in NdF_3, LaF_3:Nd^{3+} and $LiYF_4$:Nd^{3+}. Jayasankar et al. (1989b) included SCCF effects in a comparative crystal-field analysis of trivalent lanthanide ions in $LiYF_4$. An SCCF study of $LaCl_3$:R^{3+} can be found in Jayasankar et al. (1989a).

The orbitally correlated crystal field (LCCF) is an effect analogue to SCCF, but LCCF considers correlations which are due to a difference in the crystal field felt by 4f electrons with different orientations of the orbital angular momentum l_i relative to the direction of the total angular momentum L $\left(L = \sum_i l_i\right)$. On the basis of a study of the SCCF and LCCF effects of Pr^{3+} and Er^{3+} in $LaCl_3$, Yeung and Newman (1987) concluded that the SCCF effects are more important than the LCCF effects.

A general correlation crystal-field (CCF) parametrization accounts for all possible CCF operators, whereas SCCF and LCCF are restricted models (Newman and Ng 1988, Reid 1992). The Hamiltonian can be extended with the term

$$\mathcal{H}_{\mathrm{CCF}} = \sum_{k_1,k_2,k} B_q^k(k_1,k_2) \sum_{i>j} \left[u^{(k_1)}(i)\, u^{(k_2)}(j) \right]_q^{(k)}, \tag{59}$$

with $u^{(k_1)}$ and $u^{(k_2)}$ unit tensor operators. i and j label the 4f electrons. k_1 and k_2 can range from 0 to 6, $k=0$, 2, 4, 6, 8, 10 or 12. In principle q can take all values between $-k$ and k, but it is restricted by the point group in the same way as in the one-electron case. The $B_q^k(k_1,k_2)$ are phenomenological two-particle crystal-field parameters. This parametrization can be seen as an extension of Slater's F^k ($k=2,4,6$) parameters in the free-ion Hamiltonian and it accounts for the non-spherically symmetric effects.

Judd (1977b) proposed an alternative parametrization which is an extension of Racah's E^i ($i=1,2,3$) parameters. The operators in this parametrization scheme are orthogonal over the 4f configuration and have well-defined transformation properties under Racah's parentage groups. This makes that the reduced matrix elements are rather easy to evaluate. The Hamiltonian describing the orthogonal correlation crystal field (OCCF) is given by (Judd 1977b, Reid 1987):

$$\mathcal{H}_{\mathrm{OCCF}} = \sum_{i,k,q} G^k_{iq} g^{(k)}_{iq}. \tag{60}$$

G^k_{iq} are the parameters and $g^{(k)}_{iq}$ are the operators. There are 43 CCF or OCCF parameters. This large number of parameters does not facilitate the practical use of correlation crystal-field theory. An approach to make the parametrization scheme practicable, is to check to which parameters the anomalous levels are sensitive and to include only these sensitive parameters in the fitting, omitting the other parameters. Reid (1987) studied the CCF effects in $LaCl_3$:Ho^{3+} and in $LaCl_3$:Gd^{3+}. He found that the operator $g^{(6)}_3$ could correct for discrepancies in the calculated splitting of the anomalous multiplets $^3K_8$ of Ho^{3+} and $^6I_{17/2}$ of Gd^{3+}. The parameters $G^{(4)}_2$, $G^{(4)}_{10A}$ and $G^{(4)}_{10B}$ resulted in a better fit of the $^2H(2)_{11/2}$ multiplet of Nd^{3+} in YAG, $LaCl_3$, LaF_3, $LiYF_4$, $NdAlO_3$ and NdODA (Li and Reid 1990). Rukmini et al. (1994) came to the same conclusion for Nd^{3+} in other crystalline host matrices. Devi et al. (1994) published a CCF analysis of SmODA. Although the total σ value did not change much compared to the one-electron parametrization, CCF improved the σ value of several individual multiplets markedly.

Another way to remove the large discrepancies in the crystal field splitting in the anomalous multiplets, are term-dependent crystal-field parameter sets. This means that more than one parameter set is used to describe the crystal-field splitting within one lanthanide ion in a particular host crystal. Grünberg et al. (1969a,b) have used different parameter sets to calculate the crystal-field splitting of the ^6H and the ^6F terms of Sm^{3+} in $Y_3Ga_5O_{12}$ and $Y_3Al_5O_{12}$. A good fit has also been obtained by a mathematical trick, namely by modifying the reduced matrix elements of the troublesome multiplet $^2H(2)_{11/2}$ of Nd^{3+} (Faucher et al. 1989b). The other multiplets and the crystal-field parameters were not affected.

4.6. *Crystal-field strength parameters*

Several authors have tried to simplify the description of the crystal field by reducing the number of parameters. Auzel (Auzel 1979, Auzel and Malta 1983) has defined a scalar crystal-field strength parameter N_v:

$$N_v = \left[\sum_{k,q} \frac{4\pi}{2k+1} \left(B^k_q\right)^2 \right]^{1/2}. \tag{61}$$

N_v is a norm and represents a distance in the space spanned by the spherical harmonics Y^q_k. In this way, the crystal field can be characterized by one single number.

Auzel had first introduced a slightly different definition for N_v, omitting the factor $\frac{4\pi}{2k+1}$. It can be shown that under some assumptions N_v can be correlated to the maximum crystal field splitting of distinct $^{2S+1}L_J$ multiplets. The relation between N_v and the maximum splittings of the $^4I_{9/2}$, $^4I_{11/2}$, $^4I_{13/2}$ and $^4I_{15/2}$ multiplets of Nd^{3+} is linear in a good approximation.

The relation between the maximum crystal-field splitting ΔE of a $^{2S+1}L_J$ multiplet and the scalar crystal-field strength parameter N_v is:

$$\Delta E = \left[\frac{3g_A^2}{g(g_A+2)(g_A+1)\pi}\right]^{1/2} \left[\prod_{k=2,4,6} |\langle \Psi_{4f^n\tau SLJ} \| U^k \| \Psi_{4f^n\tau SLJ}\rangle \langle 3 \| C^k \| 3\rangle|\right]^{1/3} N_v, \tag{62}$$

g_A is the degeneracy effectively removed by the crystal field:

$$g_A = 2J+1 \quad \text{for} \quad J = \text{even}, \qquad g_A = J + \tfrac{1}{2} \quad \text{for} \quad J = \text{odd}, \tag{63,64}$$

g is the total degeneracy of the $^{2S+1}L_J$ multiplet:

$$g = g_A \quad \text{for} \quad J = \text{even}, \qquad g = 2g_A \quad \text{for} \quad J = \text{odd}. \tag{65,66}$$

$g_A = 2J+1$ (for J = even) is strictly only valid for orthorhombic and lower symmetries for which all crystal-field degeneracy is removed.

The reduced matrix elements $\langle 3 \| C^k \| 3\rangle$ are given by:

$$\langle 3 \| C^2 \| 3\rangle = \frac{-14}{\sqrt{105}} \approx -1.37, \tag{67}$$

$$\langle 3 \| C^4 \| 3\rangle = \frac{\sqrt{14}}{\sqrt{11}} \approx 1.13, \tag{68}$$

$$\langle 3 \| C^6 \| 3\rangle = \frac{-70}{\sqrt{3003}} \approx -1.28. \tag{69}$$

These factors are relatively invariable with regard to k. Equation (62) can be considered as a geometrical rotational-invariant average for the maximum crystal-field splitting in any point symmetry. This approximation is good if the $\overline{U}^k$ are stationary in k, i.e. if the $\overline{U}^2$, $\overline{U}^4$ and $\overline{U}^6$ have nearly the same value (or at least the same order of magnitude). Based on the stationarity of the squares of the reduced matrix elements, Auzel (Auzel and Malta 1983) has selected for the lanthanide ions $^{2S+1}L_J$ levels which should theoretically provide the best crystal-field probe: $^3H_4$ and $^3H_6$ for Pr^{3+}, $^4I_{13/2}$ and $^4I_{9/2}$ for Nd^{3+}, $^4I_{13/2}$ and $^6H_{15/2}$ for Sm^{3+}, $^7F_5$ for Eu^{3+}, $^7F_5$ for Tb^{3+}, $^6F_{9/2}$, $^4F_{9/2}$, $^6F_{11/2}$, $^4I_{13/2}$, $^6H_{15/2}$ and $^4H_{15/2}$ for Dy^{3+}, $^5I_4$ and $^5I_6$ for Ho^{3+}, $^4F_{9/2}$, $^4I_{11/2}$ and $^4I_{13/2}$ for Er^{3+}, $^3H_4$ and $^3H_6$ for Tm^{3+}. These levels have the common feature that $J \geqslant 3$ (for J = even) and $J \geqslant 7/2$ (for J = odd), because otherwise not every B_q^k crystal field parameter will contribute to the

splitting of the given $^{2S+1}L_J$ level. A procedure for the case of small J values has been described by Malta et al. (1995).

A characterization of the crystal field by only one parameter is however a rather drastic reduction of the parameter formalism. One has to be cautious if one wants to relate the concept "*crystal field strength*" with the maximum crystal-field splitting of a $^{2S+1}L_J$ multiplet and if one wants to classify the different crystalline systems in order of increasing crystal-field strength parameters. Although a system A has a larger crystal-field strength parameter than a system B, there is however no guarantee that the maximum crystal-field splitting of every $^{2S+1}L_J$ multiplet of A will be greater than the maximum crystal-field splitting of the corresponding multiplet of B. The crystal-field strength parameter is in fact the square root of the sum of the squares of the B_q^k parameters. By taking this sum, it is no longer clear which rank (k value) of parameters has the largest contribution to the sum. For instance, systems which have large values for the fourth-rank parameters and only small values for the sixth-rank parameters can have the same crystal-field strength parameter as a system with small contributions from the B_q^4 parameters, but large contributions from the B_q^6 parameters. Assume that the crystal-field strength parameter for a particular ion in host matrix A (= system A) is greater than for the same lanthanide ion in host matrix B (= system B). So one would expect that in the first instance the maximum crystal-field splitting will be greater for the multiplets in system A than in system B. Select a $^{2S+1}L_J$ multiplet, which has a very small value for $\overline{U}^4$ and a large value for $\overline{U}^6$. If system A has large B_q^4 parameters and only small B_q^6, whereas the opposite is the case for system B (but $N_v(\mathrm{A}) > N_v(\mathrm{B})$), then it is easy to understand that it is possible that the maximum crystal-field splitting of that $^{2S+1}L_J$ multiplet is smaller in system A than in system B. A condition for the probes to predict the maximum crystal-field splitting $^{2S+1}L_J$ multiplets is therefore $\overline{U}^2 \approx \overline{U}^4 \approx \overline{U}^6$.

Chang et al. (1982) have introduced a *strength parameter* S, which is defined in terms of rotational invariants of the crystal field as follows:

$$S = \left[\frac{1}{3} \sum_k \frac{1}{2k+1} \left(\left(B_0^k\right)^2 + 2 \sum_{q>0} \left(\left(\mathrm{Re}\, B_q^k\right)^2 + \left(\mathrm{Im}\, B_q^k\right)^2 \right) \right) \right]^{1/2} . \tag{70}$$

Kibler (1983) has proposed another crystal-field strength parameter:

$$s = (2l+1) \left[\sum_{k,q} \frac{1}{2k+1} \begin{pmatrix} l & k & l \\ 0 & 0 & 0 \end{pmatrix}^2 \left(B_q^k\right)^2 \right]^{1/2} . \tag{71}$$

The parameters provide an indication of the maximum crystal-field splitting of the nl shell.

5. The way back: deducing symmetry and structure information from lanthanide spectra

5.1. *Structural chemistry of lanthanide compounds*

The most often observed coordination numbers (CN) in lanthanide complexes or rare-earth complexes in general are 8 and 9, although many systems with a lower or higher CN are known. The stereochemistry of inorganic complexes with coordination numbers between 6 and 12 has been reviewed by Kepert and Favas (Kepert 1977, 1979, Favas and Kepert 1980, 1981). Other studies are by Muetterties and Wright (1981), Drew (1977), Lippard and Cotton (1967), Hoard and Silverton (1962), Day and Hoard (1967), and Burdett et al. (1978). The structures of lanthanide complexes have been reviewed by Sinha (1976) and Thompson (1979). The coordination polyhedra for the different coordination numbers are given in table 9. Most of them are however hypothetical or have been found until now in a very limited number of compounds. The dodecahedron, square antiprism, tricapped trigonal prism, monocapped square antiprism or structures derived from these, are most often found. These coordination polyhedra together with the tetrahedron, trigonal prism, octahedron, cube and icosahedron are shown in figs. 5 and 6. The lanthanide compounds show a greater diversity in coordination polyhedra than the d-block transition metals. This is because for transition metals the metal–ligand bonding shows a considerably covalent character so that the geometry of the coordination polyhedron is determined to a large extent by the demand for orbital overlap. The orbital overlap is only favorable in certain directions. In lanthanide compounds the bonding has a high degree of ionic character. The shape of the coordination polyhedron is largely determined by the electrostatic repulsion between the ligands around the central lanthanide ion. If a lanthanide ion is however doped into a crystalline host matrix, the ion will be forced into a site with geometry which is determined by the crystal lattice itself.

5.2. *Prediction of the coordination polyhedron on basis of electrostatic considerations*

Calculations of the most stable geometries on the basis of electrostatic repulsion between the ligands have been done by Kepert (1965, 1977, 1979) and by Favas and Kepert (1980, 1981). The repulsive energy u_{ij} between two ligands i and j is given by Pauling (1960):

$$u_{ij} = u_0 + u_B, \tag{72}$$

where u_0 is the energy due to the Coulombic repulsion. If Z_i and Z_j are the (effective) charges of the two ligands, e the elementary charge and d_{ij} the distance between them, the Coulombic repulsion energy will be equal to

$$u_0 = \frac{Z_i Z_j e^2}{d_{ij}}. \tag{73}$$

Table 9
Coordination polyhedra for the coordination numbers (CN) 6–12. For each polyhedron the point group is given

Polyhedron	Symmetry	CN
Octahedron (Oct)	O_h	6
Trigonal prism (TP)	D_{3h}	6
Trigonal antiprism (TAP)	D_{3d}	6
Tetragonal bipyramid (TBP)	D_{4h}	6
Capped trigonal prism (CTP)	C_{2v}	7
Monocapped octahedron (MO)	C_{3v}	7
End-capped trigonal prism (ETP)	C_{3v}	7
Cube	O_h	8
Square prism (SP)	D_{4h}	8
Square antiprism (SAP)	D_{4d}	8
Dodecahedron (Dod)	D_{2d}	8
Bicapped octahedron (BOct)	C_{2v}	8
Bicapped trigonal prism (BTP)	C_{2v}	8
End-bicapped trigonal prism (EBTP)	D_{3h}	8
End-bicapped trigonal antiprism (EBTAP)	D_{3d}	8
Hexagonal bipyramid (HBP)	D_{6h}	8
Tricapped trigonal prism (TTP)	D_{3h}	9
Monocapped square antiprism (MSAP)	C_{4v}	9
Bicapped square antiprism (BSAP)	D_{4d}	10
Tetracapped trigonal prism (FTP)	C_{3v}	10
Pentagonal antiprism (PAP)	D_{5d}	10
Pentagonal prism (PP)	D_{5h}	10
Bicapped square prism (BSP)	D_{4h}	10
Pentacapped trigonal prism (PTP)	D_{3h}	11
Monocapped pentagonal prism (MPP)	C_{5v}	11
Monocapped pentagonal antiprism (MPAP)	C_{5v}	11
Icosahedron	I_h	12
Cuboctahedron	O_h	12
Truncated tetrahedron	T_d	12
Hexagonal prism (HP)	D_{6h}	12
Hexagonal antiprism (HAP)	D_{6d}	12
Bicapped pentagonal prism (BPP)	D_{5h}	12
Anticuboctahedron	D_{3h}	12

u_B arises from the repulsion between the outer electrons of the atoms. It is also called the *Born* term:

$$u_B = \frac{b_{ij}e^2}{d_{ij}^n}, \tag{74}$$

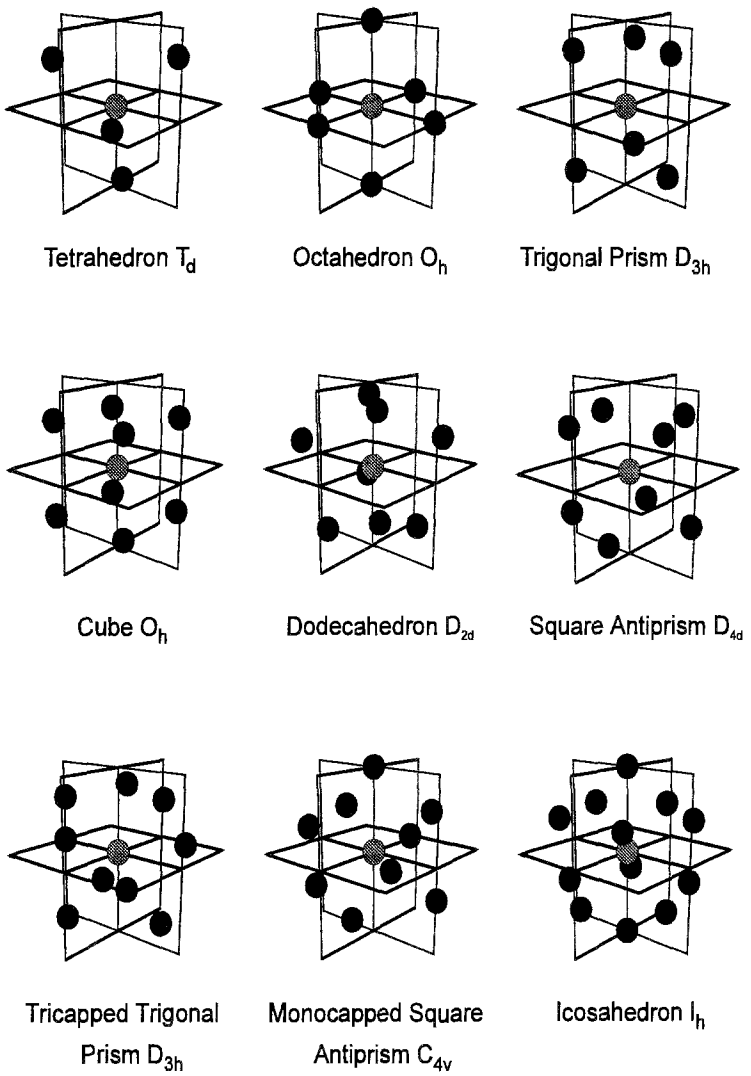

Fig. 5. Different ligand surroundings in rare-earth compounds. The same perspective and metal–ligand distance is chosen for all drawings.

where b_{ij} is a constant and n is some positive number. The value of n must lie between two extremes: from $n=1$ corresponding to the Coulombic model, to $n=\infty$ corresponding to the interaction between incompressible spheres. Actual values of n are between 6 (for the lighter elements, with a neon-like filled valence shell) and 12 (for the heavy elements). The model in which the ligand atoms are considered as incompressible spheres is called the *Hard-Sphere Model* (HSM).

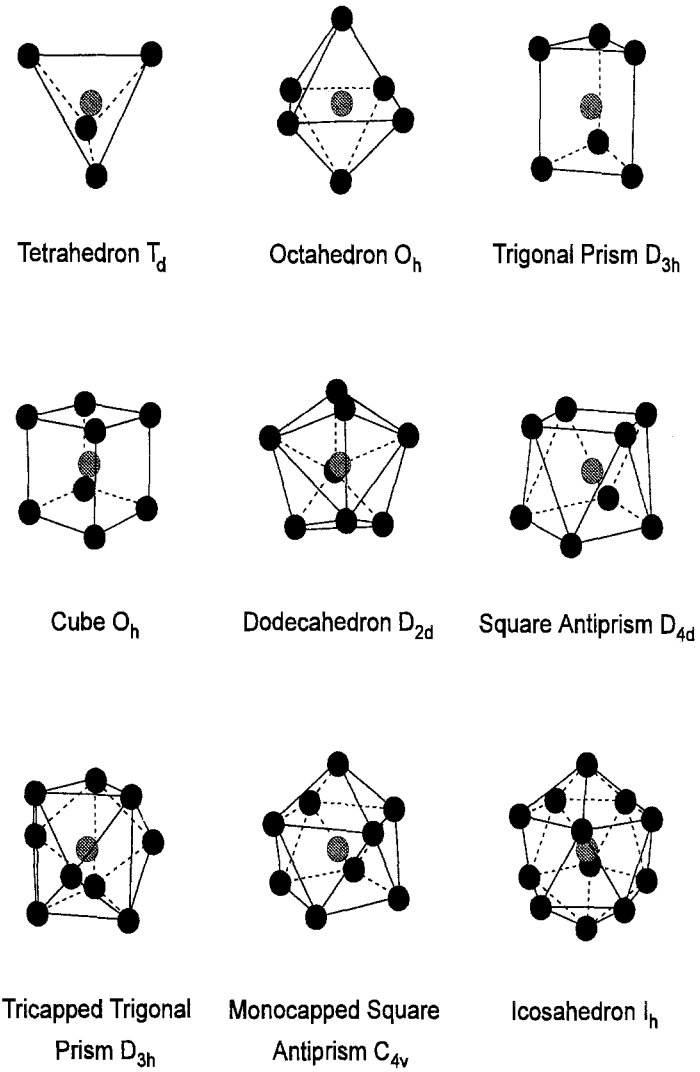

Fig. 6. Coordination polyhedra for rare-earth compounds. For all the polyhedra, the same perspective and metal–ligand distance is chosen.

If in a first approximation all metal–ligand distances are set equal to r (e.g. all ligands are lying on a sphere with radius r) d_{ij} can be calculated and the total repulsive energy U for identical monodentate ligands can be expressed as

$$U = \sum_{i,j} u_{ij} \equiv X\frac{Ze^2}{r} + Y\frac{be^2}{r^n}. \tag{75}$$

X and Y are numerical coefficients and are calculated as a function of the angular coordinates of the ligands. By minimizing the repulsive energy U, the *most favorable polyhedron* (MFP) can be predicted. In general, the angular coordinates for the HSM ($n=\infty$) are calculated somewhat different from those calculated for the MFP. If for a polyhedron two radial distances r_A and r_B can occur, the energy can be further minimized by allowing the ratio r_A/r_B to be different from unity.

5.3. *General PCEM expressions for the crystal-field parameters*

The *point charge electrostatic model* (PCEM) is the oldest of the additive crystal-field models. It was introduced by Bethe (1929) and has been described by, e.g. Hutchings (1964) and Figgis (1966). In an additive crystal-field model, the contributions of each ligand are taken into account separately. The basic assumption of the PCEM is that the electric field felt by the central metal ion is generated by negative point charges, which are situated around the central metal ion according to the symmetry of the site. The negative charges are placed on the atomic positions of the ligands. The perturbation of the central metal ion is considered as purely electrostatic, neglecting every covalent contribution. The expression for the B_q^k parameters in the PCEM model does not contain an integral over the charge distribution, but a summation over discrete point charges situated on the positions of the ligands:

$$B_0^k = \sum_{L=1}^{N} Z_L e^2 \frac{\langle r^k \rangle}{R_L^{k+1}} \sqrt{\frac{4\pi}{2k+1}}\, Y_k^0(\theta_L, \varphi_L), \tag{76}$$

$$B_q^k = \sum_{L=1}^{N} Z_L e^2 \frac{\langle r^k \rangle}{R_L^{k+1}} \sqrt{\frac{4\pi}{2k+1}}\, (-1)^q \,\mathrm{Re}\, Y_k^q(\theta_L, \varphi_L), \tag{77}$$

$$B'^k_q i = \sum_{L=1}^{N} Z_L e^2 \frac{\langle r^k \rangle}{R_L^{k+1}} \sqrt{\frac{4\pi}{2k+1}}\, (-1)^q \,\mathrm{Im}\, Y_k^q(\theta_L, \varphi_L). \tag{78}$$

The Y_k^q are the spherical harmonics. They represent the angular part of the crystal-field parameter. The coordinates are those from the point charges representing the ligands. N is the number of ligands. $\langle r^k \rangle$ is the expectation value of the k-th power of the radius of the lanthanide ion:

$$\langle r^k \rangle = \int_{r=0}^{\infty} R_{nl}^2(r) r^k \, \mathrm{d}r. \tag{79}$$

For a crude calculation of the crystal-field parameters, the values reported by Freeman and Watson (1962) or by Freeman and Desclaux (1979) can be used. R_L is the distance from the central lanthanide ion to the L-th ligand. $-Z_L e$ represents the (effective) charge of the L-th ligand, multiplication with the electron charge $-e$ gives the factor $Z_L e^2$. Although

the PCEM is only a coarse approximation, it is attractive because of its simplicity and it has some interesting features. It is helpful in predicting the sign of the crystal-field parameters. It can be used to reduce the number of adjustable parameters in a fitting procedure to determine the phenomenological B_q^k parameters.

The signs of the crystal-field parameters are merely determined by their angular part. Indeed, the radial part has to be positive. By filling in the angular positions of the ligands in eqs. (76)–(78), one can predict the sign of the B_q^k crystal-field parameters. One has to be aware that the choice of the coordination axes will effect the value and sign of the crystal-field parameters. The conventions of Prather (1961) are therefore always applied. Only the ions in the first coordination sphere around the central lanthanide ion are considered, because otherwise the simple relation between the geometry of the coordination polyhedron and the crystal-field splitting pattern will be lost. For qualitative predictions this is a good approximation, since the splitting is in agreement with the point group of the coordination polyhedron. It is remarkable that with such a simple model good agreement can be reached between experiment and theory for the prediction of the sign of the crystal-field parameters. Although it is unrealistic to assume the interaction between the central metal ion and the surrounding anions as purely electrostatic, the distribution of point charges reflects the symmetry of the crystal field. If one wants to make quantitative predictions, and especially when the crystal-field parameters are calculated by *ab initio* methods, the other ions in the crystal lattice have to be considered too. This is what is done in lattice sums. And even then the PCEM will give often no satisfying values for the crystal-field parameters. More sophisticated models have to be used (Garcia and Faucher 1995). For crystals however, it is sometimes difficult to determine the nearest neighbors, since some ions can be at a little further distance from the central metal ion than those in the first coordination sphere and these will also contribute to the crystal field felt by the lanthanide ion. In fact all ions in the crystal will contribute to the crystal field, but because of the $1/R^{k+1}$ dependence, ions at a greater distance will be of much less importance than those closer to the lanthanide ion. Problems may also occur if an atom is a ligand of more than one metal ion. The sign of the parameters with $k=4$ and $k=6$ are well predicted by the PCEM, taking only the coordination polyhedron around the lanthanide ion into account. Agreement is less for parameters with $k=2$, because the function $1/R^3$ ($k=2$) decreases much slower than $1/R^5$ ($k=4$) and $1/R^7$ ($k=6$). The non-nearest neighbor ions have therefore a greater contribution to the parameters with $k=2$, than to those with $k=4$ and 6. The sign prediction of the B_q^k crystal-field parameters for lanthanide ions in different surroundings will be discussed below in this section. The predicted signs are of great value to check the sign of the parameters obtained by the fitting procedure. Some sign combinations are impossible or a given sign corresponds to a coordination polyhedron with angles for the ligands which are physically meaningless.

It is often a good approximation to consider only one distance from the lanthanide ion to the ligands. If the distances are somewhat different, it is however better to take these differences into account by choosing a reference distance and relating all other distances to the reference. The ligands can then be regarded as point charges on a sphere. We choose the mean distance $\overline{R}_0$ as the reference distance. If two distances R_1 (N ligands)

and R_2 (M ligands) have to be considered for the coordination polyhedron ($R_1 < R_2$), the radial and angular parts in the PCEM expressions are separated in the following way (applied to B_q^k):

$$B_q^k = \sum_{L=1}^{N} Z_L e^2 \frac{\langle r^k \rangle}{R_1^{k+1}} \sqrt{\frac{4\pi}{2k+1}} (-1)^q \operatorname{Re} Y_k^q(\theta_L, \varphi_L) + \sum_{L=1}^{M} Z_L e^2 \frac{\langle r^k \rangle}{R_2^{k+1}} \sqrt{\frac{4\pi}{2k+1}} (-1)^q \operatorname{Re} Y_k^q(\theta_L, \varphi_L). \tag{80}$$

$$B_q^k = Ze^2 \frac{\langle r^k \rangle}{R_0^{k+1}} \left(\sum_{L=1}^{N} \frac{R_0^{k+1}}{R_1^{k+1}} \sqrt{\frac{4\pi}{2k+1}} (-1)^q \operatorname{Re} Y_k^q(\theta_L, \varphi_L) + \sum_{L=1}^{M} \frac{R_0^{k+1}}{R_2^{k+1}} \sqrt{\frac{4\pi}{2k+1}} (-1)^q \operatorname{Re} Y_k^q(\theta_L, \varphi_L) \right). \tag{81}$$

Here it is also presumed that the effective charge $-Z_L e$ is the same for all ligands. This presumption was necessary because the effective charges are not known, in contradistinction to the distances R_L. And for many crystalline matrices only one kind of ligand occurs around the central metal ion (oxygen or halides).

Since the parameters B_q^k and B_0^k have the same radial part, this radial part will vanish in the ratio B_q^k/B_0^k. In this way, it is possible to reduce the number of adjustable parameters in the fitting procedure to only three: B_0^2, B_0^4 and B_0^6. The other B_q^k parameters are then constrained to the ratio which was calculated by applying the PCEM. This is interesting for trigonal systems. As will be shown in sect. 5.7.2, the B_3^4 and B_3^6 parameters which represent the trigonal distortion of a hexagonal crystal field do not result in a further splitting of the levels compared to the hexagonal crystal field, but influence, in the first place, the composition of the wave functions. It is therefore advisable to hold them in the PCEM ratios, as long as no additional information, like spectral intensities, is available. Otherwise these parameters will be only fitting by-products. In general, it will be found that the ratio B_q^k/B_0^k found from the case where all crystal-field parameters are adjustable parameters, are not the same as the ratio calculated by the PCEM. Rajnak and Wybourne (1964) pointed out that a deviation of the experimental ratio from the predicted ratio is due to configuration interaction by the crystal field. A disadvantage of the procedure is that the ligand coordinates have to be known. This is not a great problem for crystalline systems since the atomic coordinates can be determined by diffraction methods. In crystalline systems, one has to be aware that if the doping ion has a substantially different radius than the radius of the ion which will be replaced by the doping ion, a distortion in the lattice can occur. Then both radial and angular coordinates may change.

PCEM expressions for the B_q^k crystal-field parameters can be written down for the different coordination polyhedra. By filling in the angular coordinates calculated for the HSM or the MFP, one can predict the sign of the B_q^k parameters and the B_q^k/B_0^k ratios.

To derive general PCEM expressions it is instructive to consider a coordination polyhedron as consisting of a prismatic body and a variable number of equatorial and axial ligands. The only polyhedra which are difficult to describe in this simple scheme are the dodecahedron and the icosahedron (along the threefold axis). It will be shown that a dodecahedron can be considered as two interpenetrating tetrahedra. An icosahedron described along the fivefold axis gives no problems.

The simplest case is one ligand on the positive z-axis (CN = 1). The angular position of the ligand is $\theta = 0°$. The point group is $C_{\infty v}$. Three parameters are required to describe the crystal field: B_0^2, B_0^4 and B_0^6. The PCEM expressions for these parameters are:

$$B_0^2 = Ze^2 \frac{\langle r^2 \rangle}{R^3}, \tag{82}$$

$$B_0^4 = Ze^2 \frac{\langle r^4 \rangle}{R^5}, \tag{83}$$

$$B_0^6 = Ze^2 \frac{\langle r^6 \rangle}{R^7}. \tag{84}$$

An axial position is the most destabilizing of all angular ligand positions, because $\cos\theta$ reaches a maximum value for $\theta = 0°$. Ligands on the z-axis have the largest contribution to the crystal-field parameters.

The PCEM expressions for two ligands on the z-axis (CN = 2) are analogous to the case of one axial ligand because of the additivity of the contributions to the PCEM expressions of the crystal-field parameters. The point group of a ligand arrangement with two ligands on the z-axis is $D_{\infty h}$. A crystal field with $D_{\infty h}$ is described by the same parameters as a $C_{\infty v}$ symmetry (B_0^2, B_0^4, B_0^6). The values of the parameters in a system with two ligands on the z-axis are twice the values of the parameters in the case of one ligand on the z-axis.

$$B_0^2 = 2Ze^2 \frac{\langle r^2 \rangle}{R^3}, \tag{85}$$

$$B_0^4 = 2Ze^2 \frac{\langle r^4 \rangle}{R^5}, \tag{86}$$

$$B_0^6 = 2Ze^2 \frac{\langle r^6 \rangle}{R^7}. \tag{87}$$

All crystal-field parameters have a positive sign in both $C_{\infty v}$ and $D_{\infty h}$.

The simplest coordination polyhedron with CN = 3 is an equilateral triangle, situated in the equatorial plane; the point group is D_{3h}. The y-axis is parallel to the twofold axis and the x-axis is perpendicular to it, so that the x-, y- and z-axes form a right-handed coordination system. The (θ, φ) coordinates for the three ligands are (90°, 90°), (90°, 210°)

and (90°, 330°). The non-zero parameters are B_0^2, B_0^4, B_0^6 and B_6^6. The PCEM expressions for this case are:

$$B_0^2 = -\frac{3}{2}Ze^2\frac{\langle r^2\rangle}{R^3}, \tag{88}$$

$$B_0^4 = \frac{9}{8}Ze^2\frac{\langle r^4\rangle}{R^5}, \tag{89}$$

$$B_0^6 = -\frac{15}{16}Ze^2\frac{\langle r^6\rangle}{R^7}. \tag{90}$$

$$B_6^6 = -\frac{3\sqrt{231}}{32}Ze^2\frac{\langle r^6\rangle}{R^7}. \tag{91}$$

It is clear that the crystal-field parameters do not have the same sign. B_0^2 and B_0^6 are positive, B_0^4 is negative. It is possible to generalize the PCEM expressions of the B_0^k parameters for planar coordination polyhedra with a coordination number larger than 3. The number of B_q^k parameters with $q \neq 0$ will of course be symmetry-dependent. All these planar polyhedra have a D_{nh} symmetry. The B_0^k parameters are:

$$B_0^2 = -\frac{n}{2}Ze^2\frac{\langle r^2\rangle}{R^3}, \tag{92}$$

$$B_0^4 = \frac{3n}{8}Ze^2\frac{\langle r^4\rangle}{R^5}, \tag{93}$$

$$B_0^6 = -\frac{5n}{16}Ze^2\frac{\langle r^6\rangle}{R^7}. \tag{94}$$

Specific for a D_{4h} symmetry (CN=4), a B_4^4 and a B_4^6 parameter are present. The angular (θ, φ) coordinates for the ligands are (90°, 45°), (90°, 135°), (90°, 225°) and (90°, 335°). One can derive the following PCEM expressions:

$$B_4^4 = -\frac{\sqrt{35}}{4}Ze^2\frac{\langle r^4\rangle}{R^5}, \tag{95}$$

$$B_4^6 = -\frac{21}{4\sqrt{14}}Ze^2\frac{\langle r^6\rangle}{R^7}. \tag{96}$$

A rotation of the x- and y-axes over 45° around the z-axis will change the sign of the B_4^4 and B_4^6 parameters. The ligand coordinates are then (90°, 0°), (90°, 90°), (90°, 180°) and (90°, 270°). This also results in an interchanging of the Γ_3 and Γ_4 symmetry labels. Every other rotation in the xy-plane will result in non-zero B'^4_4 and B'^6_4 parameters.

By combining the PCEM expressions for axial and equatorial ligands, one can build PCEM expressions for pyramids (C_{nv}) and bipyramids (D_{nh}). In this model the lanthanide

ion is situated in the base plane of the pyramid. This is a very exotic case since for normal pyramidal arrangements the central metal ion is placed in the center of the pyramid. However, one can imagine a hypothetical case in which one axial ligand has been removed from a bipyramid, leaving a pyramid. For the bipyramids, the model can give an adequate description. We consider here only one metal–ligand distance. An increase of a radial distance results in a decrease of the crystal-field parameters. Based on the additivity principle the following PCEM expressions are found for the bipyramids:

$$B_0^2 = Ze^2 \frac{\langle r^2 \rangle}{R^3} \left[2 - \frac{n}{2}\right], \tag{97}$$

$$B_0^4 = Ze^2 \frac{\langle r^4 \rangle}{R^5} \left[2 + \frac{3n}{8}\right], \tag{98}$$

$$B_0^6 = Ze^2 \frac{\langle r^6 \rangle}{R^7} \left[2 - \frac{5n}{16}\right], \tag{99}$$

with n the number of equatorial ligands.

The signs of the crystal-field parameters can be predicted. B_0^2 is positive for a trigonal bipyramid, zero for a tetragonal bipyramid (with one metal–ligand distance) and positive for all other bipyramids (pentagonal bipyramid, hexagonal bipyramid, ...). B_0^4 is always positive. B_0^6 is positive for all bipyramids with $n \leqslant 6$, otherwise it is negative.

A next step is the study of the prismatic (D_{nh}) and antiprismatic (D_{nd}) coordination polyhedra. The simplest prismatic polyhedron is the trigonal prism (D_{3h}, CN=6) and the simplest antiprismatic polyhedron is the tetragonal disphenoid (D_{2d}, CN=4). The tetrahedron is a special case of this tetragonal disphenoid. The PCEM expression for the B_0^2, B_0^4 and B_0^6 parameters are:

$$B_0^2 = mZe^2 \frac{\langle r^2 \rangle}{R^3} \left(3\cos^2\theta - 1\right), \tag{100}$$

$$B_0^4 = \frac{m}{4} Ze^2 \frac{\langle r^4 \rangle}{R^5} \left(35\cos^4\theta - 30\cos^2\theta + 3\right), \tag{101}$$

$$B_0^6 = \frac{m}{8} Ze^2 \frac{\langle r^6 \rangle}{R^7} \left(231\cos^6\theta - 315\cos^4\theta + 105\cos^2\theta - 5\right), \tag{102}$$

where m is the number of ligands in the base plane of the prism.

By combining the expressions for axial, equatorial and prismatic ligands, one can derive the general PCEM expressions for the B_0^2, B_0^4 and B_0^6 crystal-field parameters:

$$B_0^2 = Ze^2 \frac{\langle r^2 \rangle}{R^3} \left[p - \frac{n}{2} + m\left(3\cos^2\theta - 1\right)\right], \tag{103}$$

$$B_0^4 = Ze^2 \frac{\langle r^4 \rangle}{R^5} \left[p + \frac{3n}{8} + \frac{m}{4}\left(35\cos^4\theta - 30\cos^2\theta + 3\right)\right], \tag{104}$$

$$B_0^6 = Ze^2 \frac{\langle r^6 \rangle}{R^7} \left[p - \frac{5n}{16} + \frac{m}{8} \left(231\cos^6\theta - 315\cos^4\theta + 105\cos^2\theta - 5 \right) \right], \tag{105}$$

where

p, number of axial ligands (1 or 2);

n, number of equatorial ligands;

m, number of ligands in base plane of prism ($\frac{1}{2}$ total ligands in prism).

By applying these formulas it is easy to write down PCEM expressions for every polyhedron which can be thought of as being composed of prismatic, axial and equatorial ligands. Examples are the tricapped trigonal prism ($p=0$, $n=3$, $m=3$), monocapped square antiprism ($p=1$, $n=0$, $m=4$), bicapped pentagonal antiprism ($p=2$, $n=0$, $m=5$), ... One may however not forget that these expressions are valid for only one radial distance. For the prismatic polyhedra it is assumed that if the ligands of the top plane are found at θ, the ligands of the base plane are situated at $180-\theta°$. In reality, this condition is often not fulfilled for monocapped prismatic or antiprismatic polyhedra (C_{nv} symmetry).

For the B_q^k parameters with $q \neq 0$ the PCEM expressions have to be derived by filling in the ligand coordinates and summing over all ligands. These parameters depend on the choice of the x- and y-axes, as already mentioned. Notice that axial ligands only have contributions to $q=0$ parameters, because in all expressions for the B_q^k parameters with $q \neq 0$ a $\sin\theta$ dependence is found and $\sin 0° = 0$.

Using eqs. (103)–(105) it is possible to determine the θ-values for which the B_0^2, B_0^4 and B_0^6 parameters will become equal to zero. Thus $B_0^2 = 0$ if

$$p - \frac{n}{2} + m\left(3\cos^2\theta - 1\right) = 0, \tag{106}$$

thus

$$\cos\theta = \left(\frac{2m - 2p + n}{6m} \right)^{1/2}, \tag{107}$$

or

$$\theta = \arccos\left(\frac{2m - 2p + n}{6m} \right)^{1/2}. \tag{108}$$

The symbols m, n and p have been defined above.

If $p=n=0$, the coordination polyhedron is a simple prism. The zero-condition for the B_0^2 parameter is

$$\theta = \arccos\sqrt{\tfrac{1}{3}} = 54.74°. \tag{109}$$

This formula has a general validity, this means that for a trigonal, tetragonal, pentagonal, hexagonal, ..., prism or antiprism $B_0^2 = 0$ if $\theta = 54.74°$. This angle will be met again below, and will be named the "*cubic angle*".

Table 10
Predicted sign for the B_q^k crystal-field parameters in some selected geometries[a]

Polyhedron	B_0^2	B_0^4 [b]	B_3^4	B_4^4 [c]	B_0^6 [d]	B_3^6	B_4^6 [e]	B_6^6
Octahedron[f]	0	+	0	+	+	0	−	0
Cube[f]	0	−	0	−	+	0	−	0
Square prism (SP), prolate[g]	+	−	0	−	+	0	−	0
Square prism (SP), oblate[g]	−	−	0	−	+	0	−	0
Square antiprism (SAP)	−	−	0	0	+	0	0	0
Dodecahedron (Dod)	+	−	0	−	−	0	−	0
Tricapped trigonal prism (TTP)	+	−	0	0	−	0	0	−
Monocapped square antiprism (MSAP)	−	−	0	+	+	0	−	0
Icosahedron[h]	0	0	0	0	−	−	0	+

[a] The sign is calculated by filling in the angular coordinates of the HSM in the PCEM expressions. Only one radial distance is considered. The coordination numbers and point symmetry groups can be found in table 9. A zero means that the parameter is not present in the symmetry in question.
[b] B_0^4 will be negative for $30.56° < \theta < 70.12°$.
[c] B_4^4 will be negative for all angles θ.
[d] B_0^6 will be positive if $\theta < 21.2°$ or $48.6° < \theta < 76.2°$.
[e] B_4^6 is negative if $\theta < 76.2°$.
[f] The fourfold rotation axis is chosen as the quantization axis.
[g] The most stable SP is the cube. Therefore a difference is made between an oblate and prolate SP.
[h] The trifold rotation axis is chosen as the quantization axis.

The signs of the B_0^k parameters for different coordination polyhedra are predicted within the PCEM formalism. The angular coordinates are those for the HSM given by Kepert (1977, 1979) and by Favas and Kepert (1980, 1981). The results are summarized in table 10.

5.4. *Influence of distortions on the crystal-field parameters*

Crystal-field parameters which describe the distortion of an ideal coordination polyhedron with a high site symmetry towards a lower symmetry, will be small if the distortion is small. This is the basis of the "*descent of symmetry*" method for finding starting values for the parameters. In many cases the simulation of an energy level scheme has been successful by using a higher symmetry than the real one, so that fewer parameters are required. This is very advantageous, since most lanthanide systems have only a low site symmetry at the place of the rare-earth ion. Typical examples are the approximation of the real S_4 symmetry of the scheelite-type crystals by a D_{2d} symmetry (Görller-Walrand et al. 1993b, Huang et al. 1984, Brown et al. 1969, Jenssen et al. 1975, da Gama et al. 1981b), the C_{3h} symmetry of the ethylsulphates by D_{3h} (Urland 1979) and the C_3 symmetry of the double nitrates by a C_{3v} symmetry (Tinsley 1963, Görller-Walrand et al. 1992). Monoclinic and triclinic site symmetries are often approximated by the orthorhombic C_{2v} symmetry (Brecher 1974), because this is the point group with the

highest symmetry for which no crystal-field degeneracy exists (for systems with an even number of f electrons). C_{2v} has the advantage that only real parameters have to be considered. For instance, the C_2 symmetry of LaF_3 has been approximated by a C_{2v} symmetry (Carnall et al. 1989).

In the "descent of symmetry" method the small parameters describing the distortion are set equal to zero, so that the system is approximated by a higher symmetry. Only as the parameters of this higher symmetry have been refined, additional parameters are included to account for the symmetry lowering. Although the crystal-field splitting can be described in a higher symmetry, it is necessary for the calculation of transition intensities to consider the point group of low symmetry.

The B_0^k parameters only depend on the θ-coordinates, whereas the B_q^k parameters ($q \neq 0$) depend on both the θ- and φ-coordinates (Binnemans and Görller-Walrand 1995a). Distortions which only change the φ-coordinates of the ligands, will have no influence on the parameters. Distortions which incorporate a change of the θ-coordinates, will change all parameters. Distortion schemes with no influence on the B_0^k parameters are: $D_{nh} \rightarrow D_n \rightarrow D_{nd}$, $D_{nh} \rightarrow C_{nh}$, $D_{2d} \rightarrow S_4$ and $C_{nv} \rightarrow C_n$. Distortions which will change all parameters are: $D_{nh} \rightarrow C_{nv}$ and $D_{nh} \rightarrow C_n$. These distortions, except $D_{2d} \rightarrow S_4$, can be illustrated by means of a tricapped trigonal prism (TTP). A TTP has CN = 9 and a D_{3h} symmetry. It is composed of a trigonal prism and three equatorial ligands. A $D_{3h} \rightarrow D_3 \rightarrow D_{3d}$ distortion corresponds to a φ-rotation of the base and top of the prism until the TTP has been transformed into a tricapped trigonal antiprism (D_{3d}). By a φ-rotation of the equatorial triangle of the TTP, the D_{3h} symmetry will be lowered to C_{3h}. A C_{3v} symmetry can be achieved by lifting the three equatorial ligands out of the equatorial plane over the same θ-angle. An additional φ-rotation of the triangle formed by these three ligands, will lower the symmetry to C_3. A $D_{3h} \rightarrow C_3$ distortion is a combination of a $D_{3h} \rightarrow C_{3v}$ distortion and a $C_{3v} \rightarrow C_3$ distortion. All these distortions can be seen as a subgroup decomposition of the D_{3h} point group (Koster et al. 1963). The symmetry lowering of D_{2d} to S_4 in a dodecahedron is a φ-distortion which destroys the σ_d mirror plane. If the symmetry of the rare-earth site is lowered, there is not only a change of the crystal-field parameters present in the higher symmetry, additional parameters will also occur.

5.5. *Detailed discussion of coordination polyhedra*

5.5.1. *Octahedron (CN = 6)*

Although the octahedron is frequently found as a coordination polyhedron in transition metal complexes, it is much less common for lanthanides, because of their large ionic radii. A well known example for lanthanides in an octahedral surrounding is the elpasolite structure, Cs_2NaRCl_6 (Morrison et al. 1980a, Tanner et al. 1994b). Another example is ThO_2 (Hubert et al. 1993). If the fourfold rotation axis is chosen as the main axis, the crystal field in an octahedron will be described by the parameters B_0^4, B_4^4, B_0^6, and B_4^6. The reason why no B_0^2 parameter is present in a O_h symmetry is because the contributions of each ligand to this parameter will cancel each other (the sum of the contributions is zero). The coordination axes coincide with the fourfold rotation axes. The angular coordinates

Table 11
Angular coordinates (θ_i, φ_i) for the ligands in an octahedron (O_h) with regard to the fourfold and threefold rotation axes

i	Fourfold axis[a,b]		Threefold axis[a,b]	
	θ_i (°)	φ_i (°)	θ_i (°)	φ_i (°)
1	0	–	54.74	120
2	180	–	54.74	240
3	90	0	54.74	0
4	90	90	125.26	60
5	90	180	125.26	180
6	90	270	125.26	300

[a] If a fourfold rotation axis is chosen as the quantization axis (z-axis), the x- and y-axes will coincide with the other fourfold axes. If a threefold rotation axis is chosen as the z-axis, the y-axis will be in the direction of a twofold rotation axis and the x-axis is perpendicular to it.
[b] $54.74° = \theta_{\text{cubic}}$; $125.26° = 180° - \theta_{\text{cubic}}$.

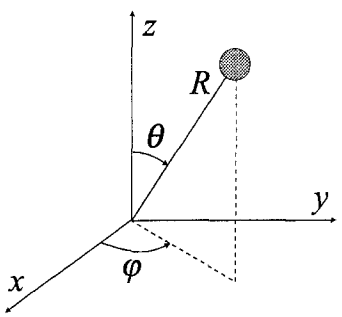

Fig. 7. Polar coordinates (θ, φ).

of the ligands are given in table 11. The conventions for measuring the polar coordinates are given in fig. 7.

The expressions for the crystal-field parameters in the PCEM formalism are:

$$B_0^4 = \frac{7}{2} Ze^2 \frac{\langle r^4 \rangle}{R^5}, \tag{110}$$

$$B_4^4 = \frac{\sqrt{70}}{4} Ze^2 \frac{\langle r^4 \rangle}{R^5}, \tag{111}$$

$$B_0^6 = \frac{3}{4} Ze^2 \frac{\langle r^6 \rangle}{R^7}, \tag{112}$$

$$B_4^6 = -\frac{21}{4\sqrt{14}} Ze^2 \frac{\langle r^6 \rangle}{R^7}. \tag{113}$$

There are only two independent parameters in an O_h symmetry (B_0^4 and B_0^6). B_4^4 and B_4^6 are restricted by the ratios B_4^4/B_0^4 and B_4^6/B_0^6:

$$\frac{B_4^4}{B_0^4} = \sqrt{\frac{5}{14}}, \tag{114}$$

$$\frac{B_4^6}{B_0^6} = -\sqrt{\frac{7}{2}}. \tag{115}$$

These ratios are the "*cubic ratios*" and are also reported by Morrison and Leavitt (1982) and by Caro (1976). The ratios reported by Prather (1961) are a factor $\sqrt{2}$ larger, because his operators are also tesseral harmonics. Both B_0^4 and B_0^6 will be positive.

An alternative description of the octahedral crystal field is possible by choosing the threefold rotation axis as the quantization axis (*z*-axis). The angular coordinates for the ligands according to the threefold rotation axis can also be found in table 11. The *y*-axis coincides with the twofold rotation axis and the *x*-axis is perpendicular to both the *y*- and *z*-axis, forming a right-handed coordinate system. θ is restricted to the *cubic angle* $\theta_{\text{cubic}} = \arccos\left(1/\sqrt{3}\right) = 54.74°$ (54°44′). The crystal field is described by the parameters B_0^4, B_3^4, B_0^6, B_3^6, B_6^6. The PCEM expressions are:

$$B_0^4 = -\frac{7}{3}Ze^2\frac{\langle r^4\rangle}{R^5}, \tag{116}$$

$$B_3^4 = \frac{\sqrt{70}}{3}Ze^2\frac{\langle r^4\rangle}{R^5}, \tag{117}$$

$$B_0^6 = \frac{4}{3}Ze^2\frac{\langle r^6\rangle}{R^7}, \tag{118}$$

$$B_3^6 = \frac{\sqrt{210}}{18}Ze^2\frac{\langle r^6\rangle}{R^7}, \tag{119}$$

$$B_0^6 = \frac{\sqrt{231}}{18}Ze^2\frac{\langle r^6\rangle}{R^7}. \tag{120}$$

Only the B_0^4 and the B_0^6 are independent parameters, since the B_3^4/B_0^4, B_3^6/B_0^6, B_6^6/B_0^6 ratios are symmetry restricted.

$$\frac{B_3^4}{B_0^4} = -\sqrt{\frac{10}{7}}, \tag{121}$$

$$\frac{B_3^6}{B_0^6} = \frac{\sqrt{210}}{24}, \tag{122}$$

$$\frac{B_6^6}{B_0^6} = \frac{\sqrt{231}}{24}. \tag{123}$$

Figure 8 shows an octahedron with the fourfold rotation axis as the quantization axis and an octahedron with the threefold rotation axis as the quantization axis.

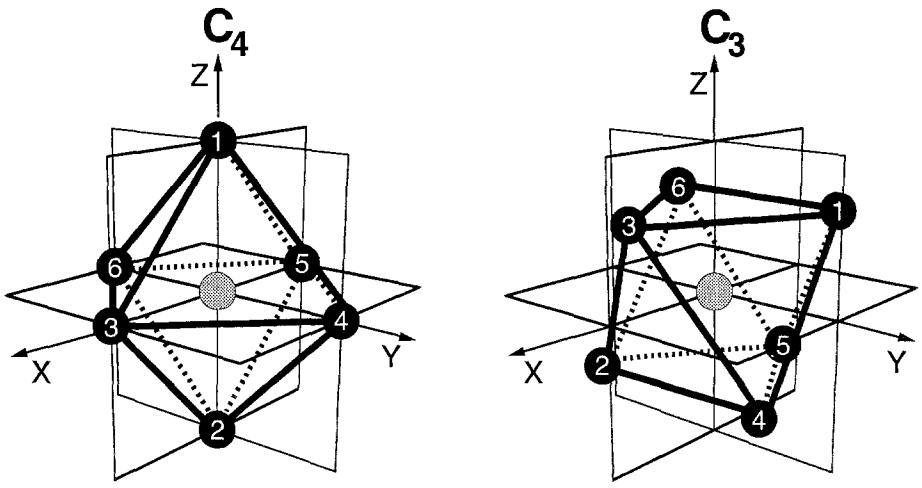

Fig. 8. Octahedron (O_h).

5.5.2. *Tetrahedron (CN = 4)*

The tetrahedron (T_d) is considered here only theoretically, since CN = 4 is too low for lanthanide systems. But it is interesting to compare both octahedron, cube and tetrahedron. The fourfold inversion axis or the threefold rotation axis can be chosen as z-axis. The angular coordinates are given in table 12. The PCEM expressions for the parameters with regard to the fourfold rotation axis are:

$$B_0^4 = -\frac{14}{9} Ze^2 \frac{\langle r^4 \rangle}{R^5}, \tag{124}$$

$$B_4^4 = -\frac{\sqrt{70}}{9} Ze^2 \frac{\langle r^4 \rangle}{R^5}, \tag{125}$$

$$B_0^6 = \frac{8}{9} Ze^2 \frac{\langle r^6 \rangle}{R^7}, \tag{126}$$

$$B_4^6 = -\frac{66}{9\sqrt{14}} Ze^2 \frac{\langle r^6 \rangle}{R^7}. \tag{127}$$

B_4^4/B_0^4 and B_4^6/B_0^6 are restricted to the cubic ratios. The B_q^k parameters for the tetrahedron can be related to those for the octahedron:

$$B_q^4 \text{ (tetrahedron)} = -\frac{4}{9} B_q^4 \text{ (octahedron)}, \tag{128}$$

$$B_q^6 \text{ (tetrahedron)} = \frac{32}{27} B_q^6 \text{ (octahedron)}. \tag{129}$$

Compare eq. (128) with the well known relation $\Delta_{\text{tetrahedron}} = -\frac{4}{9}\Delta_{\text{octahedron}}$ for transition metal complexes ($\Delta = 10\,\text{Dq}$). Equations (128) and (129) can be used to derive the

Table 12
Angular coordinates (θ_i, φ_i) for the ligands in a tetrahedron (T_d) with respect to the fourfold inversion axis and the threefold axis

i	With respect to S_4 axis[a]		With respect to C_3 axis[a]	
	θ_i (°)	φ_i (°)	θ_i (°)	φ_i (°)
1	54.74	315	0	0
2	54.74	135	109.48	120
3	125.26	45	109.48	0
4	125.26	225	109.48	240

[a] $54.74° = \theta_{cubic}$; $109.48° = 2\theta_{cubic}$.

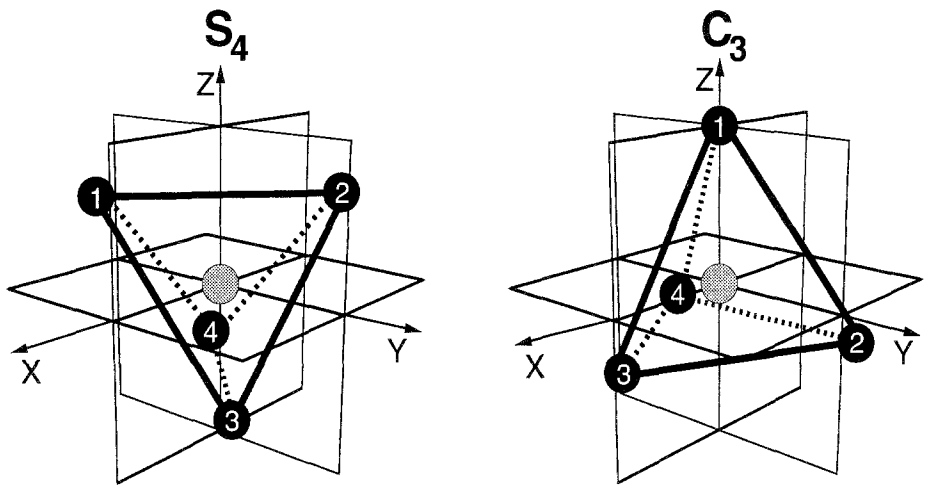

Fig. 9. Tetrahedron (T_d).

expressions for the crystal-field parameters in a tetrahedron with the threefold rotation axis as quantization axis from the expressions of those for the octahedron. The parameters are in the cubic ratios (eqs. 132–134). It should be noted that both Prather (1961) and Caro (1976) report wrong values for these ratios in a tetrahedron along the threefold axis. In fig. 9, a tetrahedron is shown for both the choices of the quantization axis (fourfold and threefold).

5.5.3. *Cube (CN = 8)*

Until now no systems are known where the coordination polyhedron around the lanthanide ion is a perfect cube. This is mainly due to the unfavorable electrostatic interaction or steric repulsion in such an arrangement of ligands. Among the 5f compounds there are however some examples of complexes with a nearly cubic geometry: $(Et_4N)_4[U(NCS)_8]$ (Countryman and McDonald 1971) and $U(bpy)_4$ (Del Piero et al. 1975). The cube is attractive from theoretical viewpoint, because of its high symmetry and because many

Table 13
Angular coordinates (θ_i, φ_i) for the ligands in a cube (O_h). The fourfold rotation axis is chosen as the quantization axis

i	θ_i (°)[a]	φ_i (°)
1	54.74	45
2	54.74	135
3	54.74	225
4	54.74	315
5	125.26	45
6	125.26	135
7	125.26	225
8	125.26	315

[a] $\theta_{\text{cubic}} = 54.74°$ (or 54°44′).

coordination polyhedra for systems with CN = 8 can be considered as originating from a distorted cube. The coordinate axes coincide with the fourfold rotation axes. Since in a cube the directions x, y and z are equivalent, the labels x, y and z can be interchanged. The angular coordinates of the ligands in a cube can be found in table 13.

Because the octahedron and cube have the same symmetry (O_h), the crystal field generated inside a cube is described by the same crystal-field parameters as the octahedron (B_0^4, B_4^4, B_0^6 and B_4^6). The actual PCEM expressions for the parameters will be different, because of the difference in coordination number:

$$B_0^4 = -\frac{28}{9} Ze^2 \frac{\langle r^4 \rangle}{R^5}, \tag{130}$$

$$B_4^4 = -\frac{2\sqrt{70}}{9} Ze^2 \frac{\langle r^4 \rangle}{R^5}, \tag{131}$$

$$B_0^6 = \frac{16}{9} Ze^2 \frac{\langle r^6 \rangle}{R^7}, \tag{132}$$

$$B_4^6 = -\frac{112}{9\sqrt{14}} Ze^2 \frac{\langle r^6 \rangle}{R^7}. \tag{133}$$

For a cube, one also has to consider only two independent parameters B_0^4 and B_0^6. B_4^4 and B_4^6 are restricted by the cubic ratios for B_4^4/B_0^4 and B_4^6/B_0^6 as in the octahedron.

In a cube the B_0^4 parameter is negative and the B_0^6 is positive (in the octahedron both parameters are positive). It is possible to discriminate between an octahedron (CN = 6) and a cube (CN = 8) in a cubic symmetry on the basis of the sign of the B_0^4 parameters. B_0^4 will be in general larger than B_0^6. This may give the impression that the fourth-rank parameters will dominate in coordination polyhedra with CN = 8.

The cube can be seen as composed of two interpenetrating tetrahedra. Therefore

$$B_q^k \text{ (cube)} = 2B_q^k \text{ (tetrahedron)}. \tag{134}$$

The relation between the B_q^k of the octahedron and those of the cube are:

$$B_q^4 \text{ (cube)} = -\frac{8}{9}B_q^4 \text{ (octahedron)}, \tag{135}$$

$$B_q^6 \text{ (cube)} = \frac{64}{27}B_q^6 \text{ (octahedron)}. \tag{136}$$

In principle, the crystal field generated inside a cubic arrangement of ligands can also be described with the threefold rotation axis as the quantization axis, but that is not advantageous.

5.5.4. *Cuboctahedron (CN = 12)*

A cuboctahedron (O_h) can be obtained by truncating either an octahedron or a cube. It contains the eight equilateral triangular faces of the octahedron and the six square faces of a cube. All vertices are identical and all edge lengths are equal to the metal–ligand bond length. The angle between two adjacent metal–ligand bonds is 60°. Favas and Kepert (1981) have shown that the cuboctahedron is less stable than the icosahedron, which will be discussed in sect. 5.5.6. The cuboctahedron with CN = 12 is however the coordination polyhedron around the spheres in a cubic closest packing. Since the cuboctahedron has O_h symmetry, the crystal field can be described with the fourfold or the threefold rotation axis as the quantization axis. The ligand coordinates are given in table 14. A cuboctahedron is illustrated in fig. 10.

The PCEM expressions for the fourfold axis as the quantization axis are:

$$B_0^4 = -\frac{7}{4}Ze^2\frac{\langle r^4\rangle}{R^5}, \tag{137}$$

$$B_4^4 = -\frac{\sqrt{70}}{8}Ze^2\frac{\langle r^4\rangle}{R^5}, \tag{138}$$

$$B_0^6 = -\frac{39}{16}Ze^2\frac{\langle r^6\rangle}{R^7}, \tag{139}$$

$$B_4^6 = \frac{237}{16\sqrt{14}}Ze^2\frac{\langle r^6\rangle}{R^7}. \tag{140}$$

The y-axis is chosen to coincide with a fourfold axis and not a twofold axis. The cubic ratios are found for B_4^4/B_0^4 and B_4^6/B_0^6. The cuboctahedron can be considered as a special case of the tetracapped square prism, namely one for which $B_0^2 = 0$ ($\theta = 45°$).

Table 14
Angular coordinates (θ_i, φ_i) for the ligands in a cuboctahedron (O_h) with respect to a fourfold and threefold rotation axis

i	Fourfold axis		Threefold axis	
	θ_i (°)	φ_i (°)	θ_i (°)[a]	φ_i (°)
1	45	0	35.26	120
2	45	90	90	150
3	45	180	90	210
4	45	270	35.26	240
5	135	0	90	30
6	135	90	144.74	60
7	135	180	144.74	300
8	135	270	90	330
9	90	315	35.26	0
10	90	45	90	90
11	90	135	144.74	180
12	90	225	90	270

[a] $35.26° = 90° - \theta_{cubic}$.

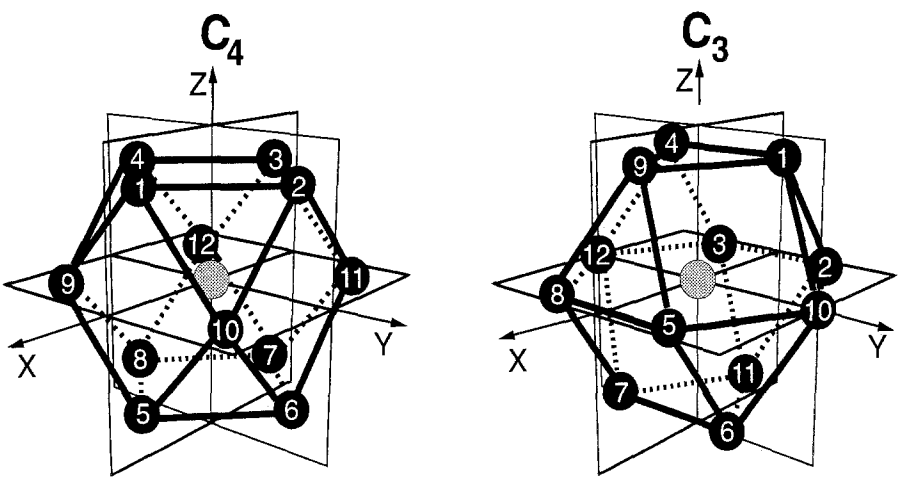

Fig. 10. Cuboctahedron (O_h).

If the threefold rotation axis is chosen as the quantization axis, the PCEM expressions are:

$$B_0^4 = \frac{7}{6} Ze^2 \frac{\langle r^4 \rangle}{R^5}, \tag{141}$$

$$B_3^4 = -\frac{\sqrt{70}}{6} Ze^2 \frac{\langle r^4 \rangle}{R^5}, \tag{142}$$

$$B_0^6 = -\frac{13}{3}Ze^2\frac{\langle r^6\rangle}{R^7}, \tag{143}$$

$$B_3^6 = -\frac{13\sqrt{210}}{72}Ze^2\frac{\langle r^6\rangle}{R^7}, \tag{144}$$

$$B_6^6 = -\frac{13\sqrt{231}}{72}Ze^2\frac{\langle r^6\rangle}{R^7}. \tag{145}$$

Once again, it can be shown that B_3^4/B_0^4, B_3^6/B_0^6 and B_6^6/B_0^6 are in the cubic ratios. By rotating the upper triangle over 60° with regard to the lower triangle, the cuboctahedron will be transformed into an anticuboctahedron (D_{3h}). The anticuboctahedron is the coordination polyhedron found around the spheres in a hexagonal closest packing. As long as $\theta = 35.26°$, the six square side faces will remain and $B_0^2 = 0$. A θ-distortion will transform the square faces in trapezia, but the D_{3h} symmetry will be preserved.

The parameters describing the crystal field in a cuboctahedron can be related to those of an octahedron:

$$B_q^4 \text{ (cuboctahedron)} = -\frac{1}{2}B_q^4 \text{ (octahedron)}, \tag{146}$$

$$B_q^6 \text{ (cuboctahedron)} = -\frac{13}{4}B_q^6 \text{ (octahedron)}. \tag{147}$$

5.5.5. *Tetrakishexadron (CN = 14)*

The tetrakishexadron (O_h) can be considered as the combination of a cube and an octahedron. The coordination number is 14. Every face of the original cube is transformed into a tetragonal pyramid, so that the total number of faces is 24. The tetrakishexadron is thus a hexacapped cube (fig. 11). We consider only one radial distance, so that the points of the cube and the octahedron are lying on one sphere. Different tetrakishexadra are possible, the general formula is $\{0hk\}$ (in Miller-indices). The coordinates of the ligands are the same as those of the cube and the octahedron together. Both the fourfold or the threefold rotation axis can be chosen as the quantization axis.

For the fourfold rotation axis, the PCEM expressions are:

$$B_0^4 = \frac{7}{18}Ze^2\frac{\langle r^4\rangle}{R^5}, \tag{148}$$

$$B_4^4 = \frac{\sqrt{70}}{36}Ze^2\frac{\langle r^4\rangle}{R^5}, \tag{149}$$

$$B_0^6 = \frac{273}{108}Ze^2\frac{\langle r^6\rangle}{R^7}, \tag{150}$$

$$B_4^6 = -\frac{637}{36\sqrt{14}}Ze^2\frac{\langle r^6\rangle}{R^7}. \tag{151}$$

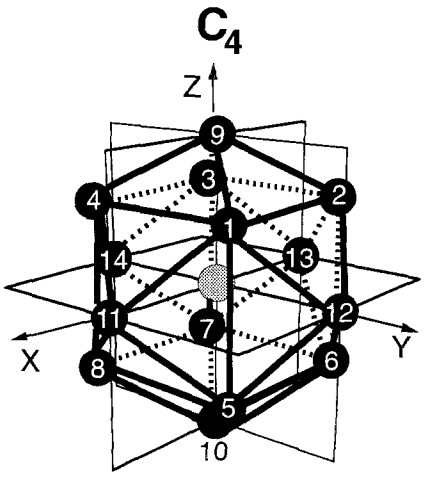

Fig. 11. Tetrakishexadron (O_h).

The cubic ratios are found for B_4^4/B_0^4 and B_4^6/B_0^6. The PCEM expression are simply the sum of those of the cube and the octahedron.

$$B_q^4 \text{ (tetrakishexahedron)} = \frac{1}{9} B_q^4 \text{ (octahedron)}, \tag{152}$$

$$B_q^6 \text{ (tetrakishexahedron)} = \frac{91}{27} B_q^6 \text{ (octahedron)}. \tag{147}$$

With the aid of these relations and the expressions for the crystal-field parameters of the octahedron, it is easy to build the PCEM expressions for the tetrakishexadron along the threefold rotation axis.

5.5.6. *Icosahedron (CN = 12)*

The icosahedron (I_h symmetry) is composed of 20 identical equilateral triangles. All 12 vertices are identical and linked to 5 other vertices. Since the icosahedron possesses a fivefold rotation axis, it is not compatible with the crystallographic space groups. So only distorted icosahedra can occur in real crystals.

Theoretical studies of lanthanide ions in an icosahedral symmetry can be found in Judd (1957) and Golding et al. (1985). The angle α between two adjacent metal–ligand bonds is (Favas and Kepert 1981)

$$\alpha = \arccos\left(\frac{\cos 72^\circ}{1 - \cos 72^\circ}\right) = 63.43^\circ, \tag{154}$$

For the description of the crystal field both the fivefold and the threefold rotation axis can be chosen as the quantization axis (fig. 12). The angular coordinates for a lanthanide complex with icosahedral symmetry are given in table 15. The simplest description is along the fivefold axis. The icosahedron can then be considered as a special case of a

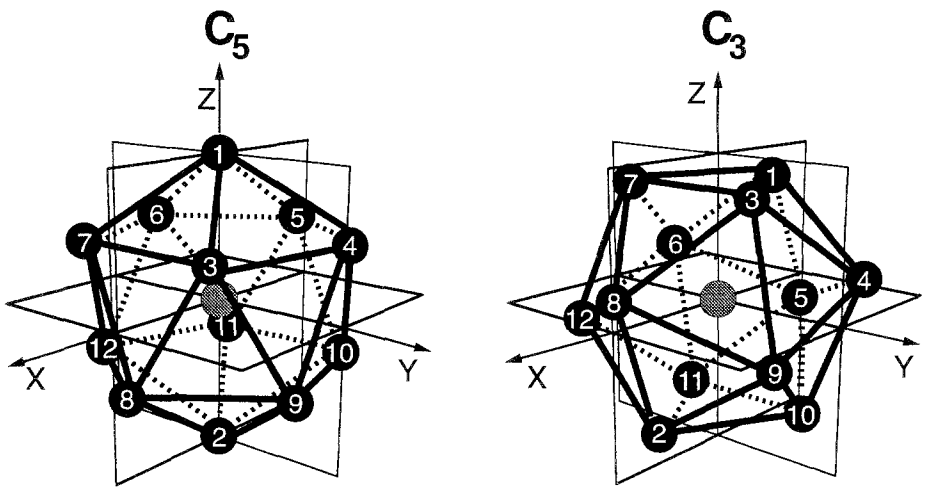

Fig. 12. Icosahedron (I_h).

Table 15
Angular coordinates (θ_i, φ_i) for the ligands in an icosahedron (I_h)[a]

i	Fivefold axis		Threefold axis	
	θ_i (°)	φ_i (°)	θ_i (°)	φ_i (°)
1	0	–	37.38	180
2	180	–	142.62	0
3	63.43	36	37.38	60
4	63.43	108	79.19	120
5	63.43	180	100.81	180
6	63.43	252	79.19	240
7	63.43	324	37.38	300
8	116.57	0	79.19	0
9	116.57	72	100.81	60
10	116.57	144	142.42	120
11	116.57	216	142.62	240
12	116.57	288	100.81	300

[a] Both the fivefold and threefold rotation axis can be chosen as the quantization axis.

bicapped pentagonal antiprism (D_{5d}). Because $\theta = 63.43°$, both the second and fourth-rank parameters will be equal to zero. The icosahedral crystal-field is described by the sixth-rank crystal-field parameters only. Levels for which $J < 3$ cannot be split by the I_h crystal field. The PCEM expressions for the B_0^6 and B_5^6 parameters are:

$$B_0^6 = \frac{132}{25} Ze^2 \frac{\langle r^6 \rangle}{R^7}, \tag{155}$$

$$B_5^6 = \frac{12\sqrt{77}}{25} Ze^2 \frac{\langle r^6 \rangle}{R^7}. \tag{156}$$

There is only one independent parameter, since the two parameters are restricted to the icosahedral ratio:

$$\frac{B_5^6}{B_0^6} = \sqrt{\frac{7}{11}}. \tag{157}$$

It is more advantageous to choose a threefold rotation axis as the quantization axis than a fivefold axis, because it is useful for understanding distortion schemes like $I_h \rightarrow C_{3v} \rightarrow C_3$, which are found in the rare-earth double nitrates $R_2M_3(NO_3)_{12}{\cdot}24H_2O$ (R = Ce–Eu; M = Mg, Zn). Although the real site symmetry is C_3, it is very close to I_h. The symmetry can be lowered from I_h to C_{3v} by a distortion of the θ coordinates. A further symmetry lowering to C_3 is possible by taking a distortion of the φ coordinates into account. Three crystal-field parameters have to be taken into account (B_0^6, B_3^6 and B_6^6). The icosahedral ratios are in this case (Judd 1957, Wybourne 1965):

$$\frac{B_3^6}{B_0^6} = \sqrt{\frac{7}{3}}, \tag{158}$$

$$\frac{B_6^6}{B_0^6} = -\frac{14}{\sqrt{231}}. \tag{159}$$

If the coordination polyhedron approximates the icosahedron, the crystal-field parameters of rank $k = 2$ and $k = 4$ will be small. The parameters with $k = 6$ will be almost in the icosahedral ratio. By observing that in the rare-earth double nitrates the B_3^6/B_0^6 and B_6^6/B_0^6 ratios are close to the icosahedral ratios, Judd (1957) concluded that the coordination polyhedron of these compounds can be considered as a slightly distorted icosahedron. It is remarkable that Judd came to this result, before the structure of the double nitrates was solved by X-ray diffraction. For $Eu_2Zn_3(NO_3)_{12}{\cdot}24H_2O$ (Görller-Walrand et al. 1992) the B_3^4/B_0^6 and B_6^6/B_0^6 ratios are 1.492 and −1.097, respectively (fitting in a C_{3v} symmetry). Compare these values to the ratios predicted for the ideal icosahedron: 1.527 and −0.921.

5.5.7. *Square prism – square antiprism (CN = 8)*

The *tetragonal prism* or *square prism (SP)* is the simplest coordination polyhedron with tetragonal symmetry. The point group is D_{4h}. The angular coordinates of the ligands in a tetragonal prism (CN = 8) are the same as for the cube, except that θ is now not restricted to θ_{cubic}. There is thus a degree of freedom for the angular coordinates. The radial distance from the ligand to the central metal ion is the same for all ligands. If $\theta = \theta_{cubic}$ (54.74°), the square prism will be transformed into a cube. According to the HSM and MFP, the cube is the most stable form of a square prism. If the square prism is compressed ($\theta > \theta_{cubic}$), one speaks of an *oblate* square prism. If it is elongated ($\theta < \theta_{cubic}$), it is called a *prolate* square

Table 16
Angular coordinates (θ_i, φ_i) for the ligands in a distorted square prism (CN = 8) with D_4 symmetry[a]

i	θ_i (°)	φ_i (°)
1	θ	$45+\phi$
2	θ	$135+\phi$
3	θ	$225+\phi$
4	θ	$315+\phi$
5	$180-\theta$	$45-\phi$
6	$180-\theta$	$135-\phi$
7	$180-\theta$	$225-\phi$
8	$180-\theta$	$315-\phi$

[a] ϕ is the distortion angle. If $\phi=0$, the symmetry will be D_{4h} (square prism) and if $\phi=22.5°$, the symmetry will be D_{4d} (square antiprism). For $\theta=54.74°$ and $\phi=0$, the coordinates of the cube are obtained. According to the hard-sphere model, the most stable square antiprism is predicted for $\theta=59.2°$.

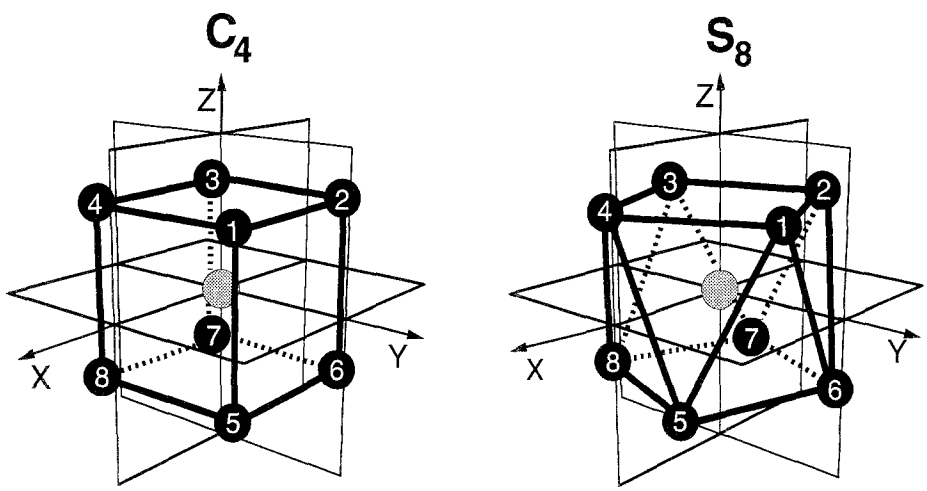

Fig. 13. Distortion of a cube (O_h) (left) towards a square antiprism (D_{4d}) (right).

prism. An angular twist of the top with regard to the base will lower the symmetry to D_4. Notice that in fact the top is twisted over an angle $+\phi$ and the base over an angle $-\phi$ with respect to the D_{4h} SP. The total distortion angle is therefore 2ϕ. This way of presenting the problem is necessary, because the twofold rotation axis has to stay parallel to the y-axis. The angular coordinates for the distorted square prism can be found in table 16. After a 45° twist the coordination polyhedron will however be the highly symmetric *Archimedean antiprism* (D_{4d}), which is also called *square antiprism* (SAP). The distortion of a cube to a square antiprism is shown in fig. 13. In the HSM, the most stable SAP is found for $\theta=59.2°$. The angles for the different n values in the MFP are $\theta=55.9°$ ($n=1$), $\theta=57.1°$ ($n=6$) and $\theta=57.9°$ ($n=12$). The decrease of θ for the MFP

compared to the HSM corresponds to an elongation along the eightfold inversion axis. In the distortion scheme the same θ value is taken for both SP and SAP, although for the two geometries the θ values for the most stable polyhedra are different. The $D_{4h} \rightarrow D_4 \rightarrow D_{4d}$ distortion scheme has been considered also by Korol'kov and Makhanek (1972, 1977). A D_{4d} symmetry is not compatible with the crystallographic space groups, because it shows in fact an octagonal (eightfold) symmetry. In crystalline systems, only a subgroup of D_{4d} can be present. The coordination polyhedron around Y^{3+} in KY_3F_{10} (Pierce and Hong 1974) is for instance a distorted square antiprism (C_{4v}). Couture and Le Paillier-Malécot (1984) pointed out that the crystal field at the rare-earth ion site in the monoclinic hexahydrated trichlorides $RCl_3 \cdot 6H_2O$ (C_2 symmetry) can be approximated by a D_{4d} symmetry. This method has been applied in the interpretation of the spectrum of $ErCl_3 \cdot 6H_2O$ (Couture and Rajnak 1984). A square antiprism with D_{4d} symmetry can be found however in molecular complexes. Symmetry lowering from D_{4h} to its subgroups D_4, D_2, C_4, C_{2v}, D_{2d} and S_4 has been discussed in some detail by Lempicki et al. (1968). Note that D_{2d} is the point group of a dodecahedron and will be discussed below. S_4 is the symmetry of a distorted dodecahedron.

The crystal-field splitting in a tetragonal symmetry is described by the parameters B_0^2, B_0^4, B_4^4, B_0^6 and B_4^6. These parameters are thus the same as for a cubic symmetry, except that there is an additional parameter, B_0^2. The expressions for the crystal-field parameters according to the PCEM are

$$B_0^2 = Ze^2 \frac{\langle r^2 \rangle}{R^3} 4 \left(3\cos^2\theta - 1\right), \tag{160}$$

$$B_0^4 = Ze^2 \frac{\langle r^4 \rangle}{R^5} \left(35\cos^4\theta - 30\cos^2\theta + 3\right), \tag{161}$$

$$B_4^4 = -\frac{\sqrt{70}}{2} Ze^2 \frac{\langle r^4 \rangle}{R^5} \sin^4\theta \cos 4\phi, \tag{162}$$

$$B_0^6 = \frac{1}{2} Ze^2 \frac{\langle r^6 \rangle}{R^7} \left(231\cos^6\theta - 315\cos^4\theta + 105\cos^2\theta - 5\right), \tag{163}$$

$$B_4^6 = -\frac{21}{2\sqrt{14}} Ze^2 \frac{\langle r^6 \rangle}{R^7} \sin^4\theta \left(11\cos^2\theta - 1\right) \cos 4\phi. \tag{164}$$

These expressions are valid for a D_4 symmetry. D_{4h} and D_{4d} are then special cases: $\phi = 0$ for D_{4h} and $2\phi = 45°$ for D_{4d}. The B_0^2 parameter will be zero for $\theta = \theta_{\text{cubic}}$ (54.74°) and positive for $\theta < \theta_{\text{cubic}}$. This means that the sign of the B_0^2 can be used to make predictions about the shape of the coordination polyhedron. A positive sign for B_0^2 is an indication that the tetragonal prism is prolate ($\theta < \theta_{\text{cubic}}$), a negative sign is an indication for oblateness ($\theta > \theta_{\text{cubic}}$). If the tetragonal prism is nearly a cube, B_0^2 will be small. In this sense, the absolute value of the B_0^2 parameter is a measure for the tetragonal distortion of a cube. If the symmetry is lowered further to orthorhombic, the B_2^k parameters will be in the

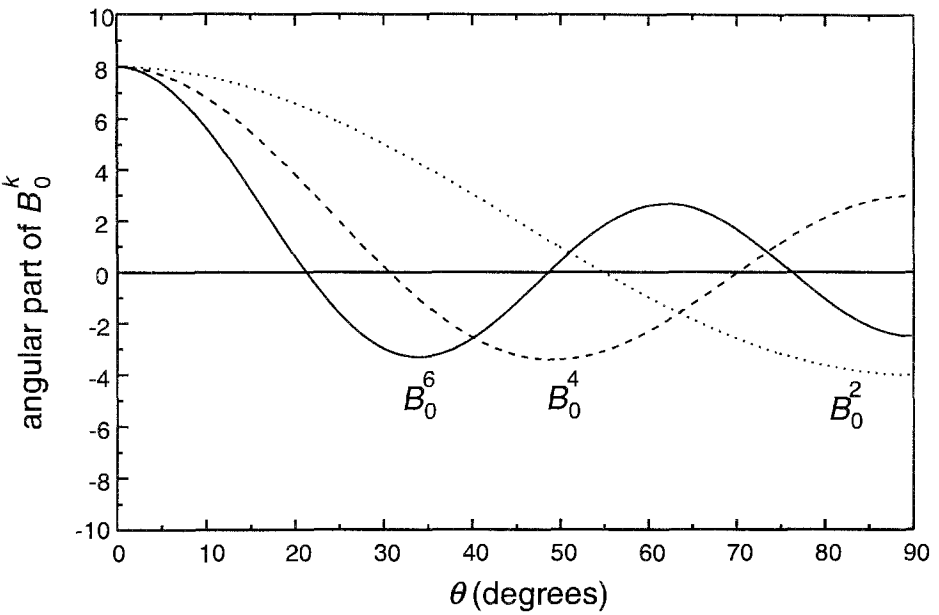

Fig. 14. Angular θ-dependence of the B_0^k crystal-field parameters in a D_{4h} symmetry.

same sense a measure of the orthorhombic distortion. The B_0^4 parameter will be negative for $30.6° < \theta < 70.1°$. Since the θ values for most real structures will be in this range, it is expected that the B_0^4 parameters for systems with a D_{4h} or derived symmetries will be negative. The B_0^6 parameter will be positive if $\theta < 21.2°$ or $48.6° < \theta < 76.2°$. The angular dependence of the B_0^k parameters is visualized in fig. 14. The B_4^4 and B_4^6 parameters will reach a maximum absolute value for a D_{4h} symmetry. Their values are reduced by a distortion to a D_4 symmetry and will vanish for a D_{4d} symmetry.

The crystal-field splitting by a *square antiprism* (D_{4d}) is described by only three parameters (B_0^2, B_0^4 and B_0^6). Due to the absence of parameters with $q \neq 0$, there will be no off-diagonal matrix elements in the crystal-field energy matrix. States with a different M value cannot be mixed by the crystal-field Hamiltonian and M will remain a good quantum number for all $^{2S+1}L_J$ levels. If $\theta = \theta_{\text{cubic}}$, the crystal field is described by no more than two crystal-field parameters (B_0^4 and B_0^6). This polyhedron can thus be formed from a cube by a 45° rotation of one square face relative to the parallel one.

Other coordination polyhedra with D_{4h} symmetry are the tetragonal bipyramid (CN = 6), which can be seen as a distortion of the octahedron, and the bicapped square prism (CN = 10). The tetragonal bipyramid is not discussed here, because an angular distortion cannot lower the symmetry to D_4. The distortion scheme of a bicapped square prism (BSP, D_{4h}) to a bicapped square antiprism (BSAP, D_{4d}) is analogue to the one described above. The PCEM expressions for the B_4^4 and B_4^6 parameters will be exactly the same as for the SP–SAP distortion scheme, since axial ligands do not have an influence on

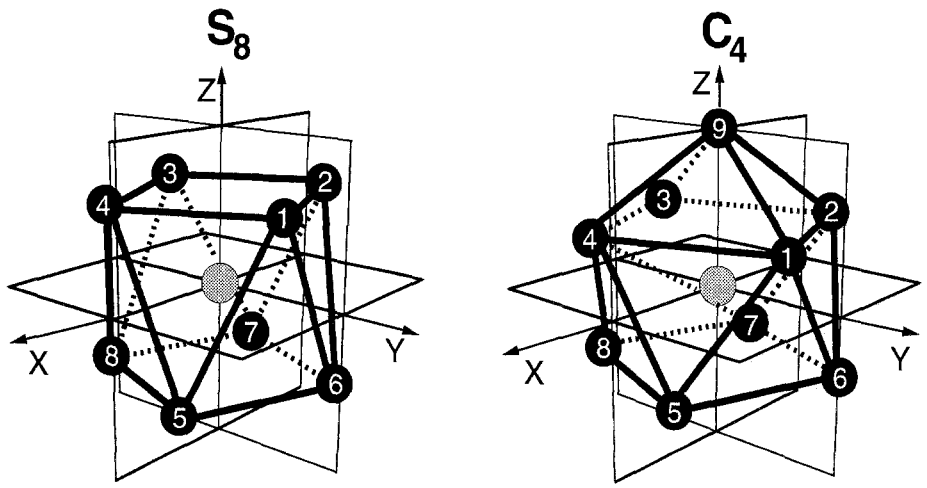

Fig. 15. Square antiprism (D_{4d}) (left) and monocapped square antiprism (C_{4v}) (right).

B_q^k parameters with $q \neq 0$. The expressions for the B_0^2, B_0^4 and B_0^6 parameters are somewhat different.

Adding only one axial ligand to a square antiprism will result in a monocapped square antiprism (MSAP). The CN is 9 and the symmetry C_{4v}. For the most stable MSAP $\theta_A = 70.1°$ and $\theta_B = 125.7°$ in the hard sphere model. Two θ values are necessary to describe the structure. Because of the axial ligand, the (capped) square top face is larger than the square bottom face. Examples of rare-earth systems with a MSAP coordination polyhedron are the oxyhalogenides ROX (R = La, Y, Gd and X = Cl, Br, I) (Hölsä and Porcher 1981, 1982a). A square antiprism and a monocapped square antiprism are shown in fig. 15.

5.5.8. *Dodecahedron (CN = 8)*

A dodecahedron (CN = 8) forms the coordination polyhedron for many lanthanide systems. In crystalline systems the ideal dodecahedron (D_{2d}) is found for the zircon structure (e.g. YPO_4 and YVO_4), while a slightly distorted dodecahedron (S_4) is observed in scheelite-type matrices (e.g. $CaWO_4$ and $LiYF_4$). A dodecahedron can be derived from a cube. As already mentioned, a cube can be considered as composed of two interpenetrating tetrahedra. By compressing one tetrahedron along the S_4 axis and elongating the other, the dodecahedron will be formed (fig. 16). The dodecahedron has 12 trigonal faces. There are two degrees of freedom for the angular coordinates and also two degrees of freedom for the radial coordinates, although the latter is not necessary. The choice of the coordinate system together with the ligand numbering is given in fig. 17. The x and y axes coincide with the twofold rotation axes of the dodecahedron. The coordinates of the ligands can be found in table 17. Only one radial distance is considered. If the ions are approximated by hard spheres and $R_A/R_B = 1$, the shape characteristics for the ideal dodecahedron are $\theta_A = 36.9°$ and $\theta_B = 69.5°$ (Favas and

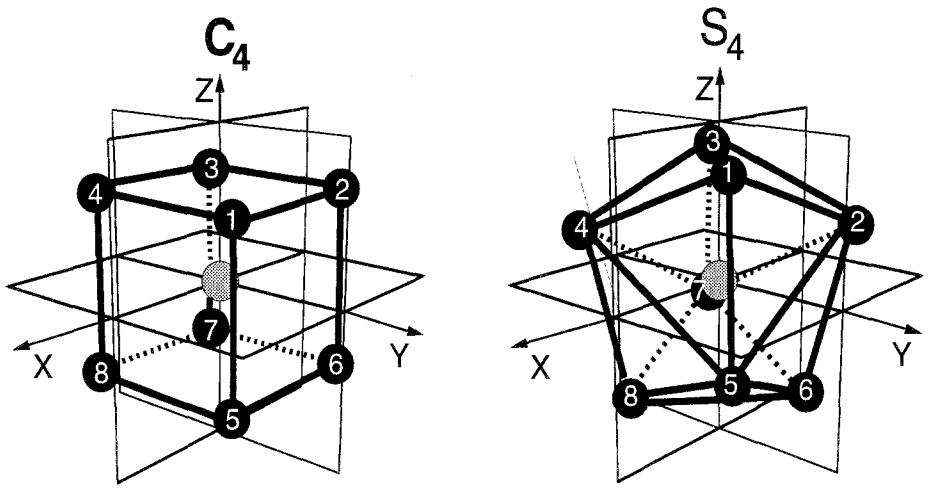

Fig. 16. Distortion of a cube towards a dodecahedron. The dodecahedron is considered as composed of two interpenetrating tetrahedra.

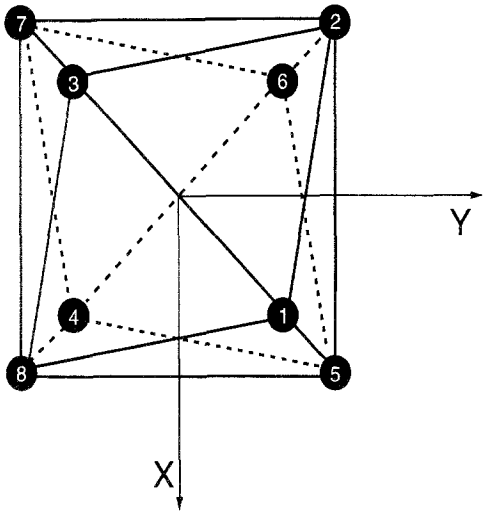

Fig. 17. Choice of the coordinate axes in a dodecahedron (D_{2d}).

Kepert 1980). If θ_A is larger than the ideal value and θ_B smaller, the dodecahedron is oblate, otherwise it is prolate. According to Hoard and Silverton (1962), the values for the most favorable dodecahedron are $\theta_A = 35.2°$ and $\theta_B = 73.5°$, with $R_A/R_B = 1.03$. For molecular complexes, θ_A and θ_B are in the ranges 34.3°–48.6° and 73.7°–88.2°, respectively (Drew 1977). In crystalline systems θ_A can be as low as 30° and R_A/R_B up to 1.08 (Linarès et al. 1977). The dodecahedron which is defined here, may not be confused with the regular geometric dodecahedron, which is composed of 12 pentagonal faces and

Table 17
Coordinates (R_i, θ_i, φ_i) for the ligands in a dodecahedron (D_{2d})[a]

i	R_i	θ_i (°)	φ_i (°)
1	R_A	θ_A	45
2	R_B	θ_B	135
3	R_A	θ_A	225
4	R_B	θ_B	315
5	R_B	$180-\theta_B$	45
6	R_A	$180-\theta_A$	135
7	R_B	$180-\theta_B$	225
8	R_A	$180-\theta_A$	315

[a] The ratio R_A/R_B is between 1.0 and 1.1. For the most favorable dodecahedron: $\theta_A = 35.2°$, $\theta_B = 73.5°$ and $R_A/R_B = 1.03$.

has icosahedral (I_h) symmetry. Another dodecahedron is the rhombic dodecahedron of the cubic crystal system.

Since a dodecahedron possesses a tetragonal symmetry, the crystal-field splitting will be described by the parameters B_0^2, B_0^4, B_0^6 and B_4^6. The formal expressions of the parameters in an additive model are:

$$B_0^2 = Ze^2 \frac{\langle r^2 \rangle}{R^3} 2\left(3\cos^2\theta_A + 3\cos^2\theta_B - 2\right), \tag{165}$$

$$B_0^4 = Ze^2 \frac{\langle r^4 \rangle}{R^5} \frac{1}{2}\left(35\cos^4\theta_A + 35\cos^4\theta_B - 30\cos^2\theta_A - 30\cos^2\theta_B + 6\right), \tag{166}$$

$$B_4^4 = -Ze^2 \frac{\langle r^4 \rangle}{R^5} \frac{\sqrt{70}}{4}\left(\sin^4\theta_A + \sin^4\theta_B\right), \tag{167}$$

$$B_0^6 = Ze^2 \frac{\langle r^6 \rangle}{R^7} \frac{1}{4}\left(231\cos^6\theta_A + 231\cos^6\theta_B - 315\cos^4\theta_A - 315\cos^4\theta_B + 105\cos^2\theta_A + 105\cos^2\theta_B - 10\right), \tag{168}$$

$$B_4^6 = -Ze^2 \frac{\langle r^6 \rangle}{R^7} \frac{21}{4\sqrt{14}}\left(\sin^4\theta_A\left(11\cos^2\theta_A - 1\right) + \sin^4\theta_B\left(11\cos^2\theta_B - 1\right)\right). \tag{169}$$

If $\theta_A = \theta_B$, the expressions will be the same as for D_{4h} symmetry. B_0^2 is zero if $\theta_A = \arccos\left[\left(2 - 3\cos^2\theta_B\right)/3\right]^{1/2}$. This relation is only valid if the two radial coordinates are the same. Since for most dodecahedra $\theta_A < \theta_{cubic}$, $\theta_B > \theta_{cubic}$ and $(\theta_A + \theta_B)/2 \approx \theta_{cubic}$, it is difficult to predict the sign of the B_0^2 parameter, especially when the two radial coordinates are somewhat different. But it seems to be a rule of thumb that B_0^2 is positive if $(\theta_A + \theta_B)/2 \approx \theta_{cubic}$. This is illustrated in table 18 for Eu^{3+} in different zircon-type host matrices. The angular coordinates and B_0^2 crystal-field parameters are

Table 18
Sign prediction for the B_0^2 crystal-field parameter for Eu^{3+} in zircon-type host matrices (D_{2d} symmetry)[a]

Compound	R_A/R_B	θ_A (°)	θ_B (°)	$\frac{1}{2}(\theta_A+\theta_B)$ (°)	B_0^2	
					Predicted sign	Exp. value (cm^{-1})
YPO_4	1.03	30.22	76.33	53.28	+	+300
$LuPO_4$	1.04	30.95	76.53	53.74	+	+200
YVO_4	1.06	32.83	78.10	55.47	−	−110
$LuVO_4$	1.07	33.18	78.18	55.68	−	−212
$GdVO_4$	1.05	32.45	77.89	55.17	−	−66
$YAsO_4$	1.05	31.88	77.80	54.84	−	−122
$LuAsO_4$	1.06	32.27	78.03	55.15	−	−212
$GdAsO_4$	1.04	31.44	77.72	54.58	−	−24

[a] Coordinates and experimental B_0^2 values from Linarès et al. (1977).

those reported by Linarès et al. (1977). The values of the parameters were converted to our formalism. All signs are predicted correctly. Small values for B_0^2 are found if the mean of the two angles is nearly equal to the cubic angle. The B_0^2 sign inversion of Eu^{3+} in YVO_4 and YPO_4 was also observed by Brecher et al. (1967, 1968) and interpreted in terms of oblate and prolate dodecahedra. But speaking of the oblateness or prolateness of a dodecahedron could give the suggestion that both the tetrahedra are compressed (oblate) or elongated (prolate) relative to their position in the cube. In fact, one tetrahedron is elongated and the other is compressed. A positive sign for the B_0^2 parameter is an indication that one tetrahedron has been compressed to a larger extent than the other tetrahedron has been elongated. If the coordinates are filled in eq. (165), the signs of the B_0^2 parameter for some compounds are calculated incorrectly.

For the other B_q^k one can predict that B_0^4 will be negative if both θ_A and θ_B are between 31.9° and 68.4°. B_0^6 will be negative if $21.2° < \theta_A < 48.6°$ and $\theta_B > 76°$. In intermediate cases where only one of the two conditions are fulfilled, predictions about the sign are difficult to make. The same is true for the sign of the B_4^6 parameter, although for most realistic angles, B_4^6 is negative. The sign of the B_4^4 however is restricted by symmetry and has to be negative in a D_{2d} symmetry for our choice of the coordinate axes. For the ideal dodecahedron ($\theta_A = 36.9°$, $\theta_B = 69.5°$ and $R_A/R_B = 1$), all B_q^k parameters, except the B_0^2, will be negative.

5.5.9. *Tricapped trigonal prism and related polyhedra (CN = 9)*

The tricapped trigonal prism TTP (CN = 9) is one of the most frequently observed coordination polyhedra for lanthanide systems, although not often in its full D_{3h} symmetry.

When top and base of the TTP are twisted relative to each other over a distortion angle 2ϕ, the symmetry will be lowered to D_3. D_3 molecules are optically active (because the sixfold inversion axis of the D_{3h} has been destroyed). Two enantiomorphic forms are

Table 19
Coordinates (R_i, θ_i, φ_i) for the ligands in a distorted tricapped trigonal prism (D_3)[a]

i	R_i	θ_i (°)	φ_i (°)
2	R_A	θ	$210+\phi$
3	R_A	θ	$330+\phi$
4	R_A	$180-\theta$	$90-\phi$
5	R_A	$180-\theta$	$210-\phi$
6	R_A	$180-\theta$	$330-\phi$
7	R_B	90	30
8	R_B	90	150
9	R_B	90	270

[a] ϕ is the distortion angle. For the tricapped trigonal prism TTP (D_{3h}) $\phi=0°$. For the most favorable polyhedra, θ_A is around 45° and the ratio R_A/R_B is between 1.0 and 1.1.

possible, depending on the sign of the distortion angle 2ϕ. If $\phi=30°$, the symmetry will be D_{3d}. In a hexagonal D_{3h} symmetry, the crystal field is described by the parameters B_0^2, B_0^4, B_0^6 and B_6^6. By lowering the symmetry to D_3 two additional parameters will appear: B_3^4 and B_3^6. These two parameters can be seen as a measure for the distortion angle ϕ. The sign of the parameters will be opposite for the two enantiomers. A MCD study of the $D_{3h} \rightarrow D_3$ distortion in EuODA can be found in L. Fluyt et al. (1994). The D_{3h} symmetry is lowered to C_{3v} if the three capping ligands are removed out of the equatorial plane, but all in the same direction and with the same distortion angle ϕ. D_{3h} is on the other hand lowered to C_{3h} if the equatorial triangle with the three capping ligands is twisted over an angle ϕ with regard to the base and the top of the prism. A combined effect of the C_{3v} and C_{3h} distortions will result in a C_3 symmetry (see also sect. 5.4).

The coordinates of the ligands in a distorted TTP can be found in table 19 and the choice of the coordination axis in fig. 18. According to the HSM, $\theta=41.8°$. The θ value for the MFP is however larger: $\theta=45.3°$ ($n=1$), $\theta=44.7°$ ($n=6$) and $\theta=43.9°$ ($n=12$). If the ratio R_B/R_A is allowed to vary, the θ value will increase further and R_B/R_A will be between 1.0 and 1.1. R_A represents the distance between the central metal ion and the ligands of the prism (top and base), R_B is the distance between the metal ion and the equatorial ligands.

The PCEM expressions for the tricapped trigonal prism are:

$$B_0^2 = Ze^2 \frac{\langle r^2 \rangle}{R^3} \frac{9}{2} \left(2\cos^2\theta - 1\right), \tag{170}$$

$$B_0^4 = Ze^2 \frac{\langle r^4 \rangle}{R^5} \frac{3}{8} \left(70\cos^4\theta - 60\cos^2\theta + 9\right), \tag{171}$$

$$B_3^4 = Ze^2 \frac{\langle r^4 \rangle}{R^5} \frac{3\sqrt{35}}{2} \sin^3\theta \cos\theta \sin 3\phi, \tag{172}$$

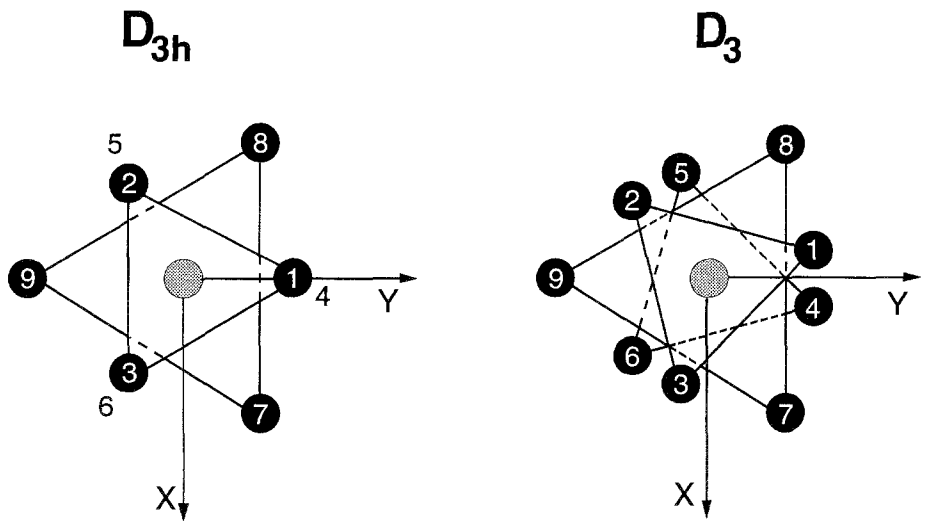

Fig. 18. Choice of the coordinate axes in a tricapped trigonal prism TTP (D_{3h}) and trigonal prism TP (D_3).

$$B_0^6 = Ze^2 \frac{\langle r^6 \rangle}{R^7} \frac{3}{16} \left(462\cos^6\theta - 630\cos^4\theta + 210\cos^2\theta - 15\right), \tag{173}$$

$$B_3^6 = Ze^2 \frac{\langle r^6 \rangle}{R^7} \frac{3\sqrt{105}}{8} \sin^3\theta \left(11\cos^3\theta - 3\cos\theta\right) \sin 3\phi, \tag{174}$$

$$B_6^6 = -Ze^2 \frac{\langle r^6 \rangle}{R^7} \frac{3\sqrt{231}}{32} \left(2\sin^6\theta \cos 6\phi + 1\right). \tag{175}$$

Only one radial distance is considered. The B_0^2 parameter will be zero for $\theta = 45°$. For the HSM a positive sign is predicted. This is also true for the MFP ($n = 6$ and $n = 12$). For the MFP ($n = 1$) a negative sign is predicted for B_0^2 ($\theta = 45.3°$). One can therefore expect a small B_0^2 parameter for an ion in a nine-coordination with a TTP as coordination polyhedron. Exceptions can occur if the ratio R_B/R_A is substantially different from unity or if the symmetry is lowered by a distortion. For $Eu(C_2H_5SO_4)_3 \cdot 9H_2O$ $\theta_A = 44.5°$ and $R_B/R_A = 0.92$ (Kuroda et al. 1981). The B_0^2 parameter for Eu^{3+} in this crystal is 168 cm^{-1} (Ohaka and Kato 1983). For $Na_3[Eu(ODA)_3] \cdot 2NaClO_4 \cdot 6H_2O$ $\theta_A = 46.1°$ and $R_A/R_B = 0.96$ (Kuroda et al. 1981). Here the value for the parameter is 41 cm^{-1} (Berry et al. 1988). The sign of B_0^2 for EuODA is only predicted correctly if the two distances R_A and R_B are taken into account.

It can be checked that the zero B_0^2 condition for a TP (CN = 6) is given by $\theta = \theta_{cubic}$. So one would therefore predict a small value for B_0^2 if $\theta \approx \theta_{cubic}$. But, for Eu^{3+} in $GdAl_3(BO_3)_4$ $\theta = 54.2°$ (Kuroda et al. 1981) and B_0^2 has a large value (530 cm^{-1}) (Görller-Walrand et al. 1994). A possible explanation is that the six coordinating oxygens (which belong to the borate groups) cannot shield the large lanthanide ion effectively from its environment. The ions in the crystal lattice which are not the nearest neighbors of the

lanthanide ion will therefore have important contributions to the B_0^2. The crystal field generated by the ligands in the first coordination polyhedron is in this case not a good approximation for the crystal-field perturbation which is felt by the lanthanide ion. The structure of $GdAl_3(BO_3)_4$ (Görller-Walrand et al. 1988) can be seen as layers of borate groups. The positive ions (Gd^{3+} and Al^{3+}, together with the Eu^{3+} ions as dopants) are situated between these layers. The electron density at the equatorial positions is not high, which explains a poor shielding of the more distant ions. Note the difference with the elpasolite matrix Cs_2NaRCl_6 (Morrison et al. 1980a). Here the CN = 6 also. Based on the octahedral arrangement of the chloride ions in the first coordination sphere a zero value for B_0^2 is predicted. This is proved experimentally. The elpasolite matrix is cubic so that the contributions to the B_0^2 parameter of the ions outside the first coordination will also sum to zero.

The effect of an addition of an axial or equatorial ligand to a trigonal prism will be reflected in the crystal-field parameters. Axial ligands will increase the B_0^2 parameter. The effect of additional equatorial ligands is a decrease of the B_0^2 parameter.

For a TTP, B_0^4 will be negative if $35.8° < \theta < 63.9°$. According to the HSM and MFP, B_0^4 is expected to be negative. The signs of B_3^4 and B_3^6 will, as already mentioned, depend on the configuration of the optical isomers. With our choice of the coordinate axes, a negative sign is predicted for both the B_0^6 and B_6^6 parameters. It has to be noticed that most B_6^6 parameters reported in the literature for systems with a tricapped trigonal prism as the coordination polyhedron have a negative sign. This corresponds to a coordinate system which has been rotated over $\pm 30°$ in the xy-plane, relative to our coordinate system.

The effect of an addition of an axial or equatorial ligand to a trigonal prism will be reflected in the crystal-field parameters. Axial ligands will increase the B_0^2 and B_0^4 parameters and decrease the B_0^6 parameter. The effect of additional equatorial ligands is an increase of the B_0^4 parameter and a decrease of the B_0^2 and B_0^6 parameters.

If in a D_{3d} symmetry with CN = 6 and $\theta = \theta_{cubic}$ (54.74°), one has in fact an octahedron (O_h). For a cubic symmetry, the B_0^2 parameter will of course vanish. The octahedron (O_h) can thus be seen as a special case of a trigonal antiprism (D_{3d}). A trigonal prism and a tricapped trigonal prism are illustrated in fig. 19.

Caro et al. (1977a) have investigated the correlation between the magnitude of the crystal-field parameters and the local surrounding of the lanthanide ion. They came to the conclusion that the experimental values of the crystal-field parameters depend mostly on the coordination number (CN) of the lanthanide ion. The shape of the coordination polyhedron and not the site symmetry determines the magnitude of the crystal-field parameters. They stated that for CN > 9, the parameters of rank $k = 6$ are large, for CN = 9, all parameters are small, for CN < 9 such as 8, 7 and 6, first the parameters of rank $k = 4$, than the parameters of rank $k = 2$ increase. These rules are however only valid in certain cases. For instance the crystal-field parameters for systems with CN = 9 are small if the coordination polyhedron around the lanthanide ion is a tricapped trigonal prism, but are large if the coordination polyhedron is a monocapped square antiprism (Binnemans and Görller-Walrand 1995b). The fact that the crystal-field parameters are small for a tricapped trigonal prism seems to be a rule (Binnemans and Görller-Walrand 1996a). The lanthanide crystal-field parameters are far more complex. The magnitude of

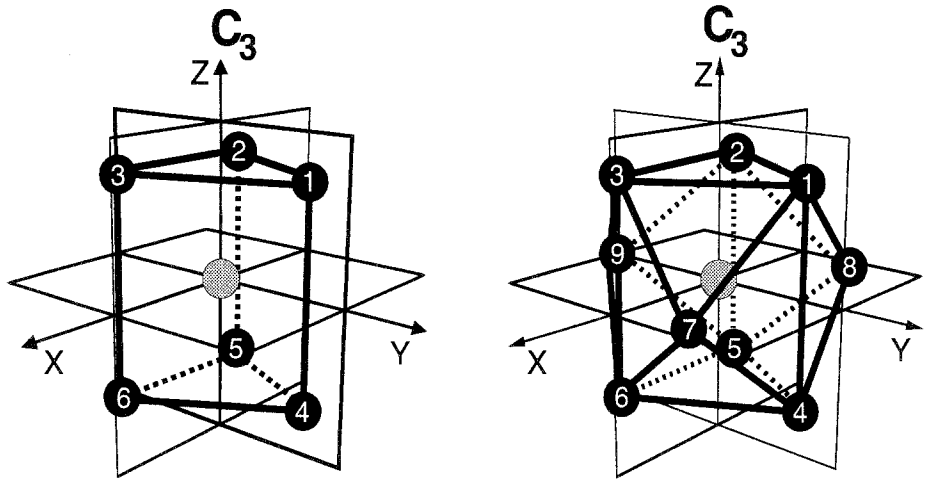

Fig. 19. Trigonal prism (D_{3h}) (left) and tricapped trigonal prism (D_{3h}) (right).

the parameters is not only a function of the shape of the coordination polyhedron, the parameter values depend also strongly on the ligand–central ion distance, on the nature of the ligands itself, on the bonding characteristics, ... The shape of the coordination polyhedron cannot be used to predict the value of the crystal-field parameters, it can be used on the other hand to predict the signs of the parameters (see sect. 5.3).

5.6. *Advantages and disadvantages of the use of the Eu^{3+} ion in crystal-field studies*

Every lanthanide ion can be used in principle to investigate the crystal-field interaction at the rare-earth ion site in a particular host matrix. For some ions, more transitions will be observed in the energy region which is studied by optical spectroscopy (near infrared/visible/ultraviolet) than for others. Not all lanthanide ions however are suitable as probe for the site symmetry around the central metal ion, especially if one wants to study distortions of an ideal high symmetric coordination polyhedron. Systems with an odd number of f electrons (Nd^{3+}, Sm^{3+}, ...) are out of the question, because for a symmetry lower than cubic every $^{2S+1}L_J$ level will be split in $J + 1/2$ crystal-field levels. All crystal-field levels will be doubly degenerate in the absence of an external magnetic field (*Kramers' degeneracy*). A progressive lowering of the site symmetry will thus not result in a progressive removal of the $2J + 1$ fold degeneracy of the $^{2S+1}L_J$ level.

The best choice for a "*crystal-field probe*" is the Eu^{3+} ion, for the following reasons:

(1) The ground state $^7F_0$ is non-degenerate. This simplifies the interpretation of the spectra to a great extent. The $^7F_0$ state will transform as the total symmetric representation Γ_1 of the point group. If the weak $^5D_0 \leftarrow {}^7F_0$ transition (ca. 17 250 cm^{-1}) can be observed (in C_s, C_n and C_{nv} symmetries), it will be possible to determine the number of non-equivalent sites in the host matrix. For each site only one transition is expected.

(2) $^{2S+1}L_J$ levels with small J values can be found in the spectral region which can be studied by optical spectroscopy. These levels are interesting, because there is a straightforward relation between the crystal-field splitting and the crystal-field parameters (especially for $J = 1$ and 2). In this case, the crystal-field parameters can be deduced directly from experiment.

(3) The different J levels in the energetic low-lying ^7F and ^5D terms are well separated from each other. There is no overlap between crystal-field levels belonging to different J states.

Especially the ^7F_J levels are very suitable to be used in a crystal-field study, because of the extra advantage that the reduced matrix elements have large values. Moreover, the ^7F_J states can still be described rather well in a Russell–Saunders basis (Ofelt 1963), in contrast to the levels at high energy. The ^5D_J states are less suitable than the ^7F_J, because of their small value for the reduced matrix elements. Moune and Caro (1989) pointed out that the crystal-field splittings of the ^5D_J levels are often difficult to fit, especially when a large basis set is used. But the ^5D_J levels have on the other hand the advantage that they can be observed in the absorption spectrum. Most ^7F_J levels can be detected only in the luminescence spectrum. The typical features of the $^5D_{0,1} \rightarrow {}^7F_J$ transitions in the luminescence spectrum of Eu^{3+} have been discussed by Bünzli (1989). The $^7F_6$ level (ca. 5000 cm^{-1}) can be observed in the near infrared absorption spectrum, if the host crystal is a rigid matrix. Otherwise overtones of the ligand vibrations prevent or hinder the detection of the weak 4f–4f transitions. In hydrated crystals, it will be difficult to record crystal-field transitions to the $^7F_6$ level. In the optical absorption spectra at room temperature, one can observe transitions starting from $^7F_1$, and in crystals with a high Eu^{3+} concentration even transitions starting from the $^7F_2$ level can be observed (Görller-Walrand et al. 1994). The magnitude of the crystal-field splitting of the $^7F_1$ multiplet can be determined from the $^5D_0 \leftarrow {}^7F_1$ transition (ca. 16 900 cm^{-1}). The absolute energetic position of the crystal-field levels of $^7F_1$ can be found from this transition only if the position of the $^5D_0$ level is known from the $^5D_0 \leftarrow {}^7F_0$ transition. If the latter position cannot be detected (symmetry forbidden in some point groups), the energetic positions of the $^7F_1$ level have to be determined from the $^5D_1 \leftarrow {}^7F_1$ transition (ca. 18 650 cm^{-1}). The crystal-field levels of the $^5D_1$ multiplet can be determined by the magnetic dipole transition $^5D_1 \leftarrow {}^7F_0$ (ca. 19 000 cm^{-1}). The $^5D_2 \leftarrow {}^7F_0$ transition (ca. 21 450 cm^{-1}) and the $^5D_2 \leftarrow {}^7F_1$ transition (ca. 21 100 cm^{-1}) are useful for the determination of the crystal-field levels of the $^5D_2$ multiplet. The former is an induced electric dipole transition, whereas the latter is allowed by the selection rules of both magnetic and induced electric dipole transitions. In most cases, the crystal-field levels of the $^5D_3$ level can only be probed by the $^5D_3 \leftarrow {}^7F_1$ transition (ca. 24 000 cm^{-1}). The $^5D_3 \leftarrow {}^7F_0$ transition (ca. 24 350 cm^{-1}) is forbidden by the selection rules for induced electric dipole transitions (Judd 1962, Ofelt 1962), because $|\Delta J| = 3$. The latter transition is only found for crystals with a strong crystal field (e.g. the rare-earth garnets), where J-mixing is important. The $^5D_4$ level is also interesting for crystal-field studies. The $^5D_4 \leftarrow {}^7F_0$ transition is found at ca. 27 600 cm^{-1} and the $^5D_4 \leftarrow {}^7F_1$ transition at ca. 27 250 cm^{-1}. The knowledge of the energetic position of the $^5L_6$ multiplet (ca. 25 100 cm^{-1}) is important for the determination

Table 20
Free-ion levels of Eu^{3+} between 0 and 40000 cm^{-1}, calculated with the mean free-ion parameters for Eu^{3+} (table 5)

$^{2S+1}L_J$	E_{calc} (cm^{-1})	$^{2S+1}L_J$	E_{calc} (cm^{-1})
$^7F_0$	0	$^3P_0$	32790
$^7F_1$	379	$^5F_2$	33055
$^7F_2$	1043	$^5F_3$	33092
$^7F_3$	1896	$^5F_1$	33366
$^7F_4$	2869	$^5F_4$	33513
$^7F_5$	3912	$^5F_5$	34040
$^7F_6$	4992	$^5I_4$	34057
$^5D_0$	17227	$^5I_5$	34388
$^5D_1$	18973	$^5I_6$	34966
$^5D_2$	21445	$^5I_7$	35429
$^5D_3$	24335	$^5I_8$	35453
$^5L_6$	25125	$^5K_5$	36168
$^5L_7$	26177	$^3K_6$	37320
$^5G_2$	26269	$^3P_1$	38132
$^5G_3$	26493	$^5K_7$	38247
$^5G_4$	26611	$^5G_2$	38616
$^5G_5$, $^5G_6$	26642	$^5K_8$	38667
$^5L_8$	27095	$^3K_6$, $^3I_6$	38780
$^5D_4$	27583	$^5G_3$	39143
$^5L_9$	27844	$^5K_9$	39518
$^5L_{10}$	28341	$^5G_4$	39726
$^5H_3$	30870		
$^5H_7$	31070		
$^5H_4$	31292		
$^5H_6$, $^5H_5$	31511		

of the free-ion parameter α (Görller-Walrand et al. 1994). The $^5L_6 \leftarrow {}^7F_0$ transition is the most intense transition in the ultraviolet–visible spectrum of Eu^{3+}. Only the spin-allowed transition $^7F_6 \leftarrow {}^7F_0$ in the infrared can be more intense.

A disadvantage of Eu^{3+} is the low intensity of transitions to ^5D_J ($\varepsilon < 1\ mol^{-1}\ L\ cm^{-1}$), which require relatively high doping concentrations of the single crystals (a few %). Another disadvantage is its tendency to be reduced to Eu^{2+}. The allowed f–d transitions of Eu^{2+} have a much higher intensity than the forbidden f–f transitions of Eu^{3+}. There will be, even at a low Eu^{2+} concentration, such a strong absorption in the blue and ultraviolet region that no $4f^n$ levels above $^5D_2$ can be observed.

The references with experimental data for Eu^{3+} doped into crystalline host matrices are summarized in table 1. The mean free-ion parameters of Eu^{3+} (table 6) were used to calculate the free-ion levels between 0 and 40000 cm^{-1} (table 20). The density of states

above 25 000 cm^{-1} is high. In practice, only the crystal-field levels of the multiplets ^7F_J, ^5D_J and $^5L_6$ can be assigned without detailed energy-level calculations. Only a few studies report transitions to other multiplets (Berry et al. 1988, Görller-Walrand et al. 1993b). Although a large number of crystal-field levels is calculated in the 25 000–40 000 cm^{-1} region, a rather small number of transitions will be observed in the spectrum. The reason is that most other transitions do not obey the selection rules for induced electric dipole transitions ($|\Delta J| = 2$, 4 or 6 for transitions starting from $^7F_0$).

5.7. *Splitting of multiplets with small J-values*

5.7.1. $J = 1$

The observed number of crystal-field levels in a $J = 1$ level ($^7F_1$ and $^5D_1$) gives an indication for the symmetry class of the rare-earth ion site. This is especially useful for polycrystalline samples. A $J = 1$ level will not be split in a cubic crystal field. The threefold degeneracy remains. It will be split in two levels (a non-degenerate and a twofold degenerate crystal-field level) in the presence of a hexagonal, trigonal or tetragonal crystal field. An orthorhombic, monoclinic or triclinic crystal field will remove all crystal-field degeneracies and three crystal-field levels can be observed. In this way it is possible to detect distortions in the crystal lattice at the rare-earth ion site. The $^7F_1$ and $^5D_1$ levels are suitable for this, because normally all crystal-field levels of these multiplets can be observed experimentally. This is in general not the case for multiplets with a larger J value for which some crystal-field levels are often experimentally missed, due to the low intensities of the transition which has to be used to locate them. Binnemans and Görller-Walrand (1995b) have related small crystal-field splittings of the $^7F_1$ and $^5D_1$ manifolds to the structure of the coordination polyhedron.

The sign of the second-rank ($k = 2$) crystal-field parameters can be determined from the splitting pattern of the $^7F_1$ and $^5D_1$ multiplets, after assignment of the crystal-field levels. For a hexagonal, trigonal and tetragonal symmetry, only the B_0^2 parameter has to be considered. If the non-degenerate level $|0\rangle$ is at a higher energy than the twofold degenerate level $|\pm 1\rangle$, the sign of the B_0^2 parameter is positive. There is a linear relationship between the magnitude of the B_0^2 parameter and the total splitting of the $^7F_1$ level, so that it is possible to determine this parameter directly from experiment. The linear relationship is less distinct for the $^5D_1$, because of the small crystal-field splitting due to the small value of the reduced matrix element $\overline{U}^2$. A larger relative error in the determination of the crystal-field splitting, will result in a larger uncertainty for the B_0^2 parameter. The total splitting of the $^7F_1$ and the $^5D_1$ levels of Eu^{3+} in different host crystals (trigonal symmetry or higher) together with the corresponding B_0^2 parameters are given in table 21. A least-squares fitting gave a non-zero intercept, due to the errors on the crystal-field parameters: $|B_0^2| = 4.47\Delta E\,(^7F_1) - 44.41$. The regression coefficient is 0.99792 (see fig. 20). Since a zero intercept is expected in the absence of a crystal field (free-ion case), an alternative least-squares fitting has been done by forcing the straight line to go through the origin: $|B_0^2| = 4.04\Delta E\,(^7F_1)$.

Table 21
Total crystal-field splitting ΔE (cm^{-1}) of the $^7F_1$ and $^5D_1$ multiplets for Eu^{3+} in different host crystals[a]

Compound	ΔE ($^7F_1$)	ΔE ($^5D_1$)	B_0^2 (cm^{-1})	Refs.
$Cs_2NaEuCl_6$	0	0	0	Schwartz (1975)
$GdAsO_4$	0	0	−12	Linarès et al. (1977)
LaOF	3	0	−1	Hölsä and Kestilä (1995b)
GdOF	3	4	−3	Hölsä and Kestilä (1995b)
YOF	10	3	−28	Hölsä and Kestilä (1995b)
EuODA	18	4	41	Berry et al. (1988)
$GdVO_4$	18	2	−66	Linarès et al. (1977)
La_2O_2S	26	7	106	Sovers and Yoshioka (1969)
$YAsO_4$	27	6	−122	Linarès et al. (1977)
Gd_2O_2S	33	8	91	Sovers and Yoshioka (1969)
Y_2O_2S	38	8	101	Sovers and Yoshioka (1969)
$Eu(C_2H_5SO_4)_3 \cdot 9H_2O$	39	4	168	Ohaka and Kato (1983)
YVO_4	42	9	−122	Brecher et al. (1967)
Lu_2O_2S	46	6	114	Sovers and Yoshioka (1969)
$Eu_2Zn_3(NO_3)_{12} \cdot 24H_2O$	49	11	−146	Görller-Walrand et al. (1992)
$LaCl_3$	50	8	178	DeShazer and Dieke (1963)
$Eu(BrO_3)_3 \cdot 9H_2O$	52	8	202	Hasunuma et al. (1984)
$Na_5Eu(WO_4)_4$	53	16	180	Huang et al. (1984)
$LuAsO_4$	58	10	−212	Linarès et al. (1977)
$Na_5Eu(MoO_4)_4$	60	18	200	Huang et al. (1984)
$LuPO_4$	61	15	200	Linarès et al. (1977)
$LuVO_4$	74	14	−212	Linarès et al. (1977)
$LiYF_4$	96	22	349	Görller-Walrand et al. (1993b)
YPO_4	97	21	293	Brecher et al. (1968)
$Eu(OH)_3$	101	18	422	Cone and Faulhaber (1971)
$GdAl_3(BO_3)_4$	130	30	530	Görller-Walrand et al. (1994)
$YAl_3(BO_3)_4$	130	36	493	Görller-Walrand et al. (1988)
KY_3F_{10}	133	32	−551	Porcher and Caro (1976)
YOCl	192	42	−813	Hölsä and Porcher (1981)
GdOCl	218	48	−907	Hölsä and Porcher (1981)
YOBr	225	53	−964	Hölsä and Porcher (1982a)
GdOBr	251	61	−1098	Hölsä and Porcher (1982a)
LaOCl	290	75	−1281	Hölsä and Porcher (1981)
LaOI	338	81	−1482	Hölsä and Porcher (1982a)
LaOBr	346	83	−1499	Hölsä and Porcher (1982a)

[a] The splittings are proportional to the B_0^2 parameter. Systems with orthorhombic or lower symmetry are not considered, because an addititional B_2^2 parameter is required to describe the crystal-field splitting. The absolute values of the splittings are given. The sign of the B_0^2 is determined by the relative position of the degenerate and the non-degenerate crystal-field level. Entries are given in the order of increasing splitting of the $^7F_1$ level.

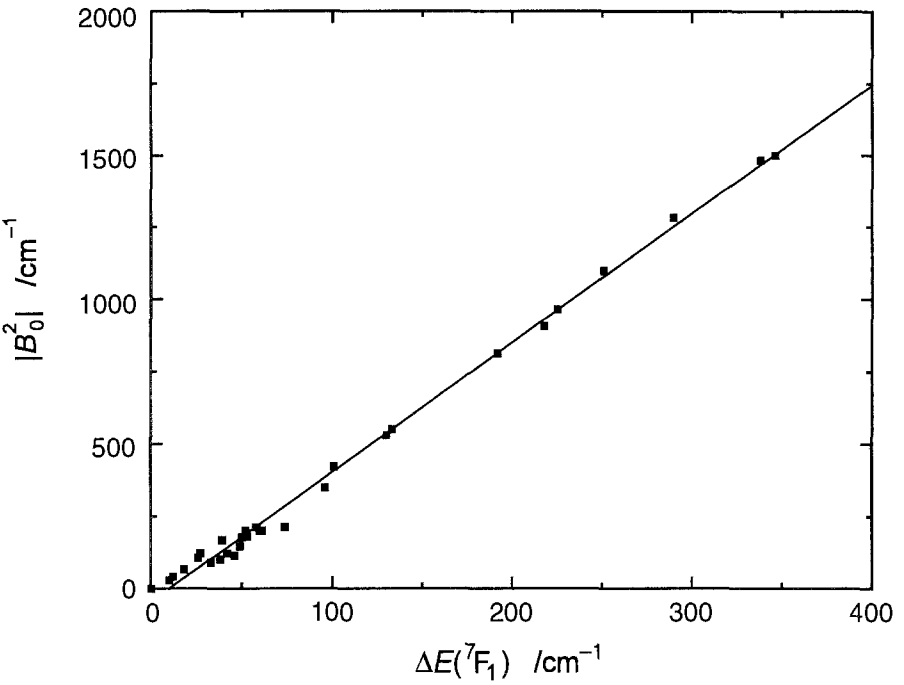

Fig. 20. Correlation between the splitting of the $^7F_1$ level in Eu^{3+} and the absolute value of the B_0^2 crystal-field parameter.

These rules can be proved by diagonalization of the crystal-field energy matrix within a $J = 1$ multiplet. The matrix elements can be calculated using the method described above. The reduced matrix elements are left unspecified, because we want to consider a general case. The non-zero matrix elements are $H_{11} = H_{-1-1} = -\frac{\sqrt{14}}{15}\bar{U}^2 B_0^2$ and $H_{00} = \frac{2\sqrt{14}}{15}\bar{U}^2 B_0^2$. There are no off-diagonal matrix elements. Diagonalization of the matrix is therefore very easy and will give the following eigenvalues (energies):

$$E_{|+1\rangle} = E_{|-1\rangle} = -\frac{\sqrt{14}}{15}\bar{U}^2 B_0^2, \tag{176}$$

$$E_{|0\rangle} = \frac{2\sqrt{14}}{15}\bar{U}^2 B_0^2. \tag{177}$$

From these relations it is directly clear that if the B_0^2 parameter is positive, the $|0\rangle$ level will be at a higher energy than the degenerate $|\pm 1\rangle$. $\bar{U}^2$ is positive for both $^7F_1$ and $^5D_1$. The total crystal-field splitting of the $J = 1$ multiplet is $\frac{\sqrt{14}}{5}\bar{U}^2 B_0^2$. After inserting a value for the reduced matrix element, the total splitting can be calculated. The barycenter of the crystal-field level is the same as the free-ion level. This will be in general true for each calculation in an intermediate coupling scheme, but not when J mixing is considered (Görller-Walrand et al. 1994).

In an orthorhombic, monoclinic or triclinic symmetry the twofold degeneracy of the level is removed and this further splitting is described by an additional parameter, B_2^2. By applying the PCEM model, the relation between the B_0^2 and the B_2^2 parameter can be calculated. Now the energy matrix will contain two non-diagonal matrix elements, $H_{1-1} = H_{-11} = -\frac{7\sqrt{2}}{5\sqrt{3}}\overline{U}^2 B_2^2$. After diagonalization, one can find the following energy levels:

$$E_{|0\rangle} = \frac{2\sqrt{14}}{15}\overline{U}^2 B_0^2, \tag{178}$$

$$E_{|-1,1\rangle^-} = \frac{-\sqrt{14}}{15}\overline{U}^2 B_0^2 + \frac{7\sqrt{2}}{5\sqrt{3}}\overline{U}^2 B_2^2, \tag{179}$$

$$E_{|-1,1\rangle^+} = \frac{-\sqrt{14}}{15}\overline{U}^2 B_0^2 - \frac{7\sqrt{2}}{5\sqrt{3}}\overline{U}^2 B_2^2. \tag{180}$$

$|-1,1\rangle^-$ is an abbreviation for $\frac{i}{\sqrt{2}}(|-1\rangle + |+1\rangle)$ and $|-1,1\rangle^+$ for $\frac{1}{\sqrt{2}}(|-1\rangle - |+1\rangle)$. These relations are valid within the usual *Condon–Shortley* phase convention. M does not remain a good quantum number. Since the orthorhombic C_{2v} symmetry is often used as an approximation for monoclinic and triclinic symmetries, we will discuss this case. The symmetry labels for the wave functions in a C_{2v} symmetry are Γ_3 for $|0\rangle$, Γ_2 for $|-1,1\rangle^-$ and Γ_4 for $|-1,1\rangle^+$. Γ_2 and Γ_4 correlate with the twofold degenerate representations in hexagonal, trigonal or tetragonal symmetry. The sign of the B_0^2 parameter determines the relative position of the Γ_3 level with respect to the barycenter of the Γ_2 and Γ_4 levels. If B_0^2 is positive, the Γ_3 level will be at a higher energy. The magnitude of the B_0^2 parameter is proportional to the difference in energy between the Γ_3 level and the barycenter of the Γ_2 and Γ_4 levels. The sign of the B_2^2 parameter determines the relative position of the Γ_2 and Γ_4 levels. The Γ_2 level will be at a higher energy than the Γ_4 level, if B_2^2 is positive. The magnitude of that parameter is proportional to the energy difference between the Γ_2 and Γ_4 levels. Moreover, the Γ_2 and the Γ_4 level will have the same relative position in both the $^7F_1$ and the $^5D_1$ multiplet. One has to be careful when applying these rules, since they will not be valid if the C_2 axis is not parallel with the main crystal axis. In that case one has to work with rotated coordinate systems. A typical example is Eu^{3+} in the tysonite structure (LaF_3) (Görller-Walrand 1993).

For symmetries lower than orthorhombic, no further crystal-field splitting will be observed, since all crystal-field splitting is already removed. The additional parameters will have an influence on the calculated energy levels, but this change could also be taken into account by the two parameters B_0^2 and B_2^2. It is indeed perfectly possible to describe the two energy differences between the three crystal-field levels by only two parameters. For the calculation of the spectral intensities the additional parameters are required to modify the crystal-field wave functions. In a C_1 symmetry for instance, every wave function of the $^5D_1$ multiplet is a linear combination of the $|0\rangle$, $|+1\rangle$ and $|-1\rangle$ functions.

Table 22
Matrix elements for the $J=2$ levels of Eu^{3+}

$H_{00} = \frac{2\sqrt{2}}{5\sqrt{3}}\overline{U}^2 B_0^2 + \frac{2}{\sqrt{55}}\overline{U}^4 B_0^4$	$H_{2-2} = H_{-22} = \frac{\sqrt{14}}{3\sqrt{11}}\overline{U}^4 B_4^4$
$H_{11} = H_{-1-1} = \frac{\sqrt{2}}{5\sqrt{3}}\overline{U}^2 B_0^2 - \frac{4}{3\sqrt{55}}\overline{U}^4 B_0^4$	$H_{2-1} = H_{-21} = \frac{-\sqrt{7}}{3\sqrt{11}}\overline{U}^4 B_3^4$
$H_{22} = H_{-2-2} = \frac{-2\sqrt{2}}{5\sqrt{3}}\overline{U}^2 B_0^2 + \frac{1}{3\sqrt{55}}\overline{U}^4 B_0^4$	$H_{-12} = H_{1-2} = \frac{\sqrt{7}}{3\sqrt{11}}\overline{U}^4 B_3^4$

5.7.2. $J=2$

The $J=2$ levels of interest in Eu^{3+} are $^7F_2$ and $^5D_2$. The crystal-field splitting of these levels is in first approximation described by the second- and fourth-rank parameters ($k=2$ and 4) only. The different matrix elements can be found in table 22. The $J=2$ levels are split in a cubic environment (O_h) in the same way as the d orbitals of the transition metals, namely in a twofold degenerate (E_g or Γ_3^+) and a threefold degenerate (T_{2g} or Γ_5^+) level. As described above (sects. 5.5.1 and 5.7.1), the B_0^2 parameter will be absent in a cubic symmetry. The crystal field is described by the parameters B_0^4, B_4^4, B_0^6 and B_4^6, but one has to take the cubic ratios B_0^4/B_4^4 and B_4^6/B_0^6 into account (see sect. 5.5). After diagonalization of the energy matrix, one can find the following eigenvalues:

$$E(E_g) = \frac{2}{\sqrt{55}}\overline{U}^4 B_0^4, \tag{181}$$

$$E(T_{2g}) = -\frac{4}{3\sqrt{55}}\overline{U}^4 B_0^4. \tag{182}$$

The E_g level of $^5D_2$ will be found at a higher energy than the T_{2g} level, if the B_0^4 parameter is positive (because $\overline{U}^4$ is positive). This is the case for an octahedron. Experimental evidence is given by Eu^{3+} in the elpasolite matrix $Cs_2NaEuCl_6$ (Schwartz 1975). For a cube, the B_0^4 parameter is negative and the relative position of the two levels is $E(T_{2g}) > E(E_g)$. If $^7F_2$ is considered, the situation is reversed, because $\overline{U}^4$ is negative.

Although the crystal-field splitting of the $J=1$ levels is the same for both hexagonal, trigonal and tetragonal crystal fields, the splitting of the $J=2$ levels will be different in each of those symmetries. The simplest case is the hexagonal crystal field ($q=6$), for which only the B_0^2 and B_0^4 parameters have to be considered. Since there are no off-diagonal matrix elements, states with a different M quantum number will not be mixed. There are two degenerate levels ($|\pm1\rangle$ and $|\pm2\rangle$) and one non-degenerate level ($|0\rangle$). After diagonalization of the energy matrix, one finds the following energy levels:

$$E_{|0\rangle} = \frac{2\sqrt{2}}{5\sqrt{3}}\overline{U}^2 B_0^2 + \frac{2}{\sqrt{55}}\overline{U}^4 B_0^4, \tag{183}$$

$$E_{|\pm1\rangle} = \frac{\sqrt{2}}{5\sqrt{3}}\overline{U}^2 B_0^2 - \frac{4}{3\sqrt{55}}\overline{U}^4 B_0^4, \tag{184}$$

$$E_{|\pm2\rangle} = -\frac{2\sqrt{2}}{5\sqrt{3}}\overline{U}^2 B_0^2 + \frac{1}{3\sqrt{55}}\overline{U}^4 B_0^4. \tag{185}$$

Since the position of the levels is a function of two parameters, no simple relationship can be deduced for the relative position of the crystal-field levels. If B_0^2 is accidentally equal to zero, an equal spacing will be found between the three levels. The degenerate $|\pm2\rangle$ level will be at the intermediate position in all cases. Because one can determine the B_0^2 parameter from the splitting of a $J=1$ level, the experimental position of two of the three crystal-field levels in the $J=2$ level is in theory sufficient to determine B_0^4. The position of the crystal-field levels in the octagonal D_{4d} symmetry ($q=8$), is the same as in the hexagonal crystal field, due to the absence of non-zero off-diagonal matrix elements.

In a tetragonal symmetry ($q=4$), non-zero off-diagonal matrix elements are found between the $\langle+2|$ and the $|-2\rangle$ states, so these states will be mixed by the tetragonal crystal-field Hamiltonian. The two wave functions have the form $|2,-2\rangle^+ = \frac{1}{\sqrt{2}}(|-2\rangle + |+2\rangle)$ and $|2,-2\rangle^- = \frac{i}{\sqrt{2}}(|-2\rangle - |+2\rangle)$. The behavior of the $|0\rangle$ and $|\pm1\rangle$ levels will be the same as in the hexagonal field. In a tetragonal crystal field, a $J=2$ level is split into three non-degenerate and one twofold degenerate crystal-field level. After diagonalization, the following relations are found for the energy levels:

$$E_{|0\rangle} = \frac{2\sqrt{2}}{5\sqrt{3}}\overline{U}^2 B_0^2 + \frac{2}{\sqrt{55}}\overline{U}^4 B_0^4, \tag{186}$$

$$E_{|\pm1\rangle} = \frac{\sqrt{2}}{5\sqrt{3}}\overline{U}^2 B_0^2 - \frac{4}{3\sqrt{55}}\overline{U}^4 B_0^4, \tag{187}$$

$$E_{|2,-2\rangle^+} = -\frac{2\sqrt{2}}{5\sqrt{3}}\overline{U}^2 B_0^2 + \frac{1}{3\sqrt{55}}\overline{U}^4 B_0^4 + \frac{\sqrt{14}}{3\sqrt{11}}\overline{U}^4 B_4^4, \tag{188}$$

$$E_{|2,-2\rangle^-} = -\frac{2\sqrt{2}}{5\sqrt{3}}\overline{U}^2 B_0^2 + \frac{1}{3\sqrt{55}}\overline{U}^4 B_0^4 - \frac{\sqrt{14}}{3\sqrt{11}}\overline{U}^4 B_4^4. \tag{189}$$

B_4^4 can be determined directly from the splitting between the $E_{|2,-2\rangle^+}$ and the $E_{|2,-2\rangle^-}$ level, since the energy difference between the two levels is equal to $\frac{2\sqrt{14}}{3\sqrt{11}}\overline{U}^4 B_4^4$. The sign of the B_4^4 parameter determines the relative position of the two levels. The sign of the B_4^4 parameter will change if the x- and y-axes are rotated over $\pm45°$ around the z-axis.

In a trigonal symmetry ($q=3$), the crystal-field Hamiltonian will mix $|+1\rangle$ into $|-2\rangle$ and $|-1\rangle$ into $|+2\rangle$. One degenerate level will have mainly a $|\pm1\rangle$ character and the other will be mainly $|\pm2\rangle$. Compared to the hexagonal crystal fields, there is no further splitting

of the $J=2$ levels. The non-diagonal matrix elements are $H_{-12} = H_{1-2} = -\frac{\sqrt{77}}{3\sqrt{11}}\overline{U}^4 B_3^4$ and $H_{-21} = H_{2-1} = \frac{\sqrt{7}}{3\sqrt{11}}\overline{U}^4 B_3^4$. The corresponding energies are:

$$E_{|0\rangle} = \frac{2\sqrt{2}}{5\sqrt{3}}\overline{U}^2 B_0^2 + \frac{2}{\sqrt{55}}\overline{U}^4 B_0^4, \tag{190}$$

$$E_{|1,-2\rangle^+} = E_{|-1,2\rangle^+} = \frac{(H_{11}+H_{22}) + \sqrt{(H_{11}+H_{22})^2 - 4(H_{22}H_{11} - H_{1-2}H_{-21})}}{2}, \tag{191}$$

$$E_{|1,-2\rangle^-} = E_{|-1,2\rangle^-} = \frac{(H_{11}+H_{22}) - \sqrt{(H_{11}+H_{22})^2 - 4(H_{22}H_{11} - H_{1-2}H_{-21})}}{2}. \tag{192}$$

According to McGlynn et al. (1972), the wave functions for the mixed $|+1,-2\rangle$ and $|-1,+2\rangle$ states can be written in trigonometric form. The mixing of two states Ψ_A and Ψ_B can be described as:

$$|\Psi_-\rangle = \sin\alpha\,|\Psi_A\rangle - \cos\alpha\,|\Psi_B\rangle, \tag{193}$$

$$|\Psi_+\rangle = \cos\alpha\,|\Psi_A\rangle + \sin\alpha\,|\Psi_B\rangle. \tag{194}$$

with $\tan 2\alpha = 2H_{AB}/(H_{AA} - H_{BB})$, where H_{AA} and H_{BB} are diagonal matrix elements, and H_{AB} is a non-diagonal matrix element. The mixing parameter α is restricted to $45° < \alpha < 135°$. The $^5D_2$ wave functions except $|0\rangle$ are therefore:

$$|+1,-2\rangle^- = \sin\alpha\,|+1\rangle - \cos\alpha\,|-2\rangle, \tag{195}$$

$$|+1,-2\rangle^+ = \cos\alpha\,|+1\rangle + \sin\alpha\,|-2\rangle, \tag{196}$$

$$|-1,+2\rangle^- = \sin\alpha\,|-1\rangle - \cos\alpha\,|+2\rangle, \tag{197}$$

$$|-1,+2\rangle^+ = \cos\alpha\,|-1\rangle + \sin\alpha\,|+2\rangle, \tag{198}$$

and

$$\tan 2\alpha = \frac{2H_{1-2}}{H_{11} - H_{-2-2}} = \frac{2H_{-12}}{H_{-1-1} - H_{22}}. \tag{199}$$

$|+1,-2\rangle^+$ and $|-1,+2\rangle^+$ are degenerate. The same is true for $|+1,-2\rangle^-$ and $|-1,+2\rangle^-$.

It is not easy to extract the B_q^4 parameters for trigonal crystal fields directly from experimental data. It is therefore advisable to restrict B_3^4/B_0^4 to the PCEM ratio. If all the crystal-field levels of the $J=2$ multiplet are known, so that the experimental barycenter can be obtained, it is possible to determine the B_0^4 parameter by the shift of the $|0\rangle$ state from the barycenter. The B_0^2 parameter can be extracted from the splitting of a $J=1$ level.

For lower symmetries it is in general not possible to extract the B_q^4 parameters directly from experiment, because of the large number of non-diagonal matrix elements. If $q=2$, there will be a mixing of the $|0\rangle$ state with the $|+2\rangle$ and $|-2\rangle$ levels on one side and the $|-1\rangle$ and $|+1\rangle$ levels on the other. A fitting procedure is then required.

5.7.3. $J>2$

The above rules for an extraction of the B_q^k crystal-field parameters directly from experimental data cannot be applied for most symmetries to J levels for which $J>2$, because of the presence of a large number of off-diagonal matrix elements. Every level is in this case a function of at least three parameters. It is more difficult to determine the B_6^k parameters than the second- or fourth-rank parameters. One can first determine the B_0^6 parameter and subsequently the B_q^6 parameters ($q \neq 0$). In the end both B_0^6 and B_q^6 are varied in order to remove discrepancies. An alternative approach is to restrict B_q^6/B_0^6 to the PCEM ratio, because in this way only one sixth-rank parameter will remain.

5.8. *The Eu^{3+} ion as probe for point group determination*

By making use of the selection rules for induced electric dipole (ED) and magnetic dipole (ED) transitions (see Appendix 5), it is in principle possible to discriminate between the different point groups. This has been explored by several authors, like Sinha and Butter (1969). These authors determined the symmetry of europium complexes, but their symmetry discriminating table contains unfortunately many errors. Bünzli (1989) has discussed the use of the $^5D_{0,1} \rightarrow {}^7F_J$ luminescent transitions of Eu^{3+} for the point group determination of complexes in solution. He gave ED and MD selection rules for the $^5D_0 \rightarrow {}^7F_J$ transitions ($J=0$ to $J=4$) of Eu^{3+} in numerous point groups, both centrosymmetric and non-centrosymmetric. Polarization is not taken into account.

We have developed a procedure to determine the point group of the lanthanide site on the basis of selected transitions in the absorption spectrum of the Eu^{3+} ion doped into the system under study. The method can be applied also to the luminescence spectrum, so that it is usable in different circumstances. Only the 18 non-cubic crystallographic point groups, which have no center of inversion, are taken into account: D_3, C_{6v}, C_6, D_{3h}, C_{3h}, C_{3v}, C_3, D_3, D_4, C_{4v}, C_4, S_4, D_{2d}, D_2, C_{2v}, C_2, C_s and C_1. The centrosymmetric point groups are not considered, because in this case induced electric dipole transitions cannot gain intensity by mixing of configurations of opposite parity in the $4f^n$ configuration by the odd part of the crystal-field potential. Electric dipole transitions can here occur only by vibronic coupling. The cubic point groups with no center of inversion (O, T_d and T) are not found for lanthanide systems.

The most interesting transitions in the Eu^{3+} absorption spectrum are: $^5D_0 \leftarrow {}^7F_0$, $^5D_1 \leftarrow {}^7F_0$, $^5D_2 \leftarrow {}^7F_0$, $^5D_4 \leftarrow {}^7F_0$ and $^5L_6 \leftarrow {}^7F_0$. All these transitions are induced electric dipole (ED) transitions, except the $^5D_1 \leftarrow {}^7F_0$, which is a magnetic dipole (MD) one. The corresponding transitions in the luminescence spectrum are $^5D_0 \rightarrow {}^7F_0$, $^5D_1 \rightarrow {}^7F_0$ (or $^5D_0 \rightarrow {}^7F_1$), $^5D_0 \rightarrow {}^7F_2$ and $^5D_0 \rightarrow {}^7F_4$ (or $^5D_0 \rightarrow {}^7F_6$ if observed). The

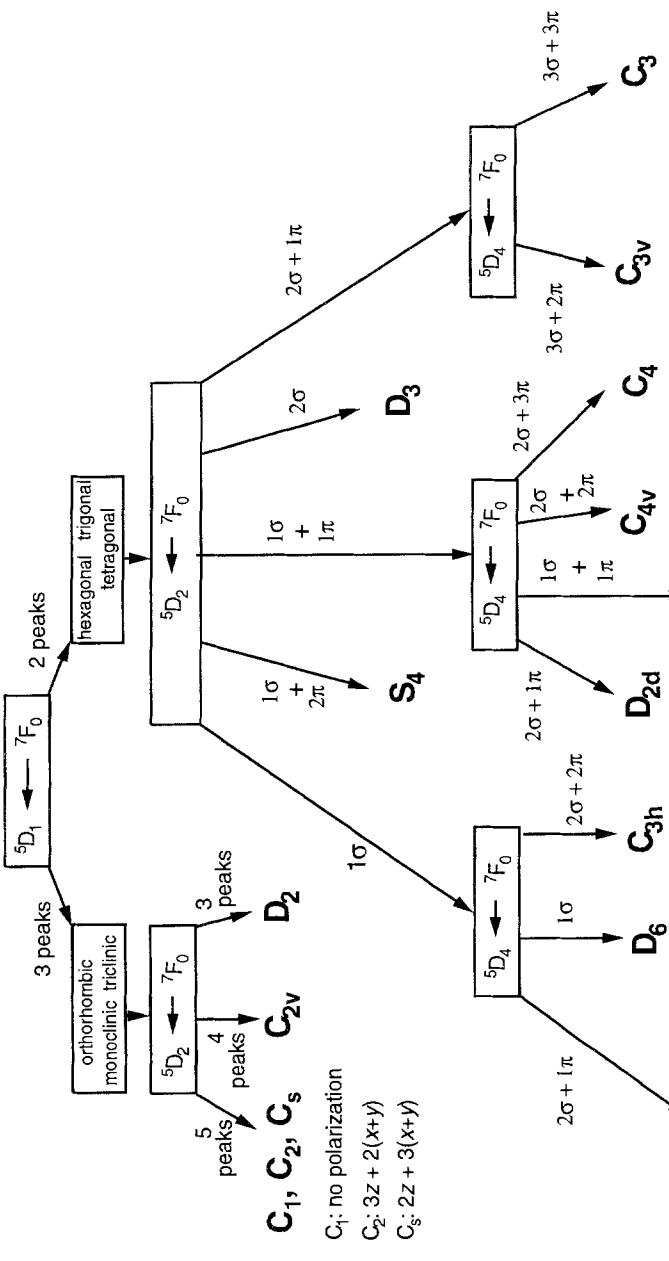

Fig. 21. Scheme for point group determination in single crystals, based on selected transitions in the Eu^{3+} ion.

procedure will be given for the absorption spectrum. The $^5D_1 \leftarrow {}^7F_0$ transition allows one to make a first crude separation. If three peaks are observed for this transition, the point group is orthorhombic, monoclinic or triclinic. Two peaks are an indication that the point group is hexagonal, trigonal or tetragonal.

If the symmetry is found to be orthorhombic (D_2, C_{2v}), monoclinic (C_2, C_s) or triclinic (C_1), a further division can be made on the basis of the $^5D_2 \leftarrow {}^7F_0$ transition. Three peaks indicate that the point group is D_2, four peaks that the symmetry is C_{2v}. If five peaks are detected, three possible symmetries are still left: C_s, C_2 and C_1. These can only be separated in single crystals, where polarized spectra can be obtained. The transitions of a system with C_2 or C_s symmetry are polarized: 3 $(x+y)+2z$ for C_s and 2 $(x+y)+3z$ for C_2. This is not the case for C_1, since all crystal-field transitions are allowed in all polarizations (no symmetry restrictions).

A discrimination between the hexagonal, trigonal and tetragonal point groups is also possible. If the $^5D_2 \leftarrow {}^7F_0$ transition shows only one peak in the σ spectrum and none in the π spectrum (1σ), the point group is D_6, D_{3h}, C_{3h} or D_4. According to Bünzli (1989), no ED transition is expected for a $J=0$ to $J=2$ transition in D_4. The $A_1(\Gamma_1) \rightarrow E(\Gamma_5)$ transition is however allowed, since the (x,y) components of the ED operator transform as E. Next, one has to check the $^5D_4 \leftarrow {}^7F_0$ transition. One peak in the σ spectrum (1σ) proves that the symmetry is D_6. If two peaks are observed in the σ spectrum and two peaks in the π spectrum ($2\sigma+2\pi$), the symmetry is C_{3h}. The presence of two peaks in the σ spectrum and one peak in the π spectrum ($2\sigma+2\pi$) shows that the symmetry is D_{3h} or D_4. In order to determine whether the point group is D_{3h} or D_4, the peaks of the $^5L_6 \leftarrow {}^7F_0$ have to be checked. For a D_{3h} symmetry, two peaks in the σ spectrum and one peak in the π spectrum ($2\sigma+1\pi$) are expected. For D_4, three peaks in the σ spectrum and one peak in the π spectrum are forecast, thus ($3\sigma+1\pi$) for short.

Two peaks in the σ spectrum and none in the π spectrum (2σ) of the $^5D_2 \leftarrow {}^7F_0$ transition are the spectroscopic signature for a D_3 symmetry. One peak in the σ spectrum and two in the π spectrum ($1\sigma+2\pi$) are an indication for a S_4 symmetry. If one peak is found in the σ spectrum and one in the π spectrum ($1\sigma+1\pi$), the point group can be C_{6v}, C_6, C_{4v}, C_4or D_{2d}. Then the $^5D_4 \leftarrow {}^7F_0$ transition has to be considered again. ($2\sigma+1\pi$) is an indication for D_{2d}, ($2\sigma+2\pi$) for C_{4v} and ($2\sigma+3\pi$) for C_4. If one peak is detected in the σ spectrum and one in the π spectrum ($\sigma+\pi$), two possible point groups are left: C_{6v} and C_6. A discrimination is possible by considering the peaks in the $^5L_6 \leftarrow {}^7F_0$ transition: two peaks in the σ spectrum and two peaks in the π spectrum ($2\sigma+2\pi$) for C_{6v}, two peaks in the σ spectrum and three peaks in the π spectrum ($2\sigma+3\pi$) for C_6.

A $^5D_2 \leftarrow {}^7F_0$ transition with two peaks in the σ spectrum and one peak in the π spectrum ($2\sigma+1\pi$) is an indication for a C_{3v} or a C_3 symmetry. The $^5D_4 \leftarrow {}^7F_0$ transition will give exclusion: ($3\sigma+2\pi$) for C_{3v} and ($3\sigma+3\pi$) for C_3. The point group determination scheme is given in fig. 21. In table 23 the point groups of the rare-earth sites in the most common crystalline host matrices are summarized.

The $^5D_1 \leftarrow {}^7F_0$ and $^5D_2 \leftarrow {}^7F_0$ transitions alone can already give a lot of information. The $^5D_1 \leftarrow {}^7F_0$ allows the discrimination between the low and high symmetric point groups. The $^5D_2 \leftarrow {}^7F_0$ provides a unique spectroscopic signature for the S_4, D_3, D_2

Table 23
Point group of the rare-earth site in crystalline host matrices[a]

Point group	Host crystal
O_h	Elpasolites A_2BRX_6 (A=Cs, Rb; B=Li, Na, K; R=Ce–Lu, Y; X=F, Cl, Br) e.g. Cs_2NaYCl_6
D_{3h}	$R(BrO_3)_3 \cdot 9H_2O$
C_{3h}	$LaCl_3$, $LaBr_3$, $La(OH)_3$, ethylsulphates $R(C_2H_5SO_4)_3 \cdot 9H_2O$
C_{3i}	Y_2O_3[b]
C_{4v}	KY_3F_{10}, KLu_3F_{10}, ROX (R=La, Gd, Y; X=Cl, Br, I)
D_{2d}	YPO_4, YVO_4, $YAsO_4$, RPO_4, RVO_4, $RAsO_4$
S_4	AXO_4 (A=Ca, Ba, Sr, Pb, Cd; X=W, Mo), e.g. $CaWO_4$ (scheelite) $LiYF_4$, $LiLuF_4$
D_3	Oxydiacetates $Na_3[R(C_4H_4O_5)_3] \cdot 2NaClO_4 \cdot 6H_2O$, borates $R_3Al(BO_3)_4$ (R=Ce–Lu, La, Y)
C_{3v}	R_2O_2S (R=Ce–Lu, La, Y,); ROF (R=La, Gd, Y)
C_3	Double nitrates $R_2M_3(NO_3)_{12} \cdot 24H_2O$ (R=Ce–Eu; M=Mg, Zn); $Eu(DBM)_3 \cdot H_2O$
D_2	Rare-earth garnets $A_3B_5O_{12}$ (A=Ce–Lu, Y; B=Al, Ga) e.g. $Y_3Al_5O_{12}$ (YAG)
C_{2v}	CdF_2[c]
C_2	LaF_3, RF_3, $RCl_3 \cdot 6H_2O$, Y_2O_3[b]
C_s	ROOH (R=La, Gd, Lu, Y); $LaWO_4Cl$, $La_3WO_6Cl_3$
C_1	$Li_6R(BO_3)_3$

[a] The hosts are classified according to the crystallographic point groups. However, for several point groups, no examples are known. These point groups are not mentioned. The exact point group of the host is reported, not the point group of higher symmetry which can be used to describe the site symmetry approximately.
[b] In Y_2O_3 both C_{3i} and C_2 sites occur.
[c] In CdF_2, C_{4v} and C_{3v} sites are also present.

and C_{2v} point groups (in combination with the splitting of the $^5D_1 \leftarrow {}^7F_0$), while this transition gives a strong indication for the other point groups. A C_{4v} symmetry can be distinguished from a D_{2d} symmetry on the basis of the sign of the *A*-term in the MCD spectrum (Görller-Walrand and Fluyt-Adriaens 1985). These two transitions can be observed in most cases, whereas this is not always true for the $^5D_4 \leftarrow {}^7F_0$ transition. The $^5D_4 \leftarrow {}^7F_0$ transition cannot be detected if a strong absorption of the ligands is found in the near ultraviolet spectral region or if a part of Eu^{3+} is reduced to Eu^{2+}. Eu^{2+} shows strong absorption bands, due to allowed f–d transitions, which can mask the $^5D_4 \leftarrow {}^7F_0$. Often the $^5L_6 \leftarrow {}^7F_0$ cannot be recorded either. Luminescence measurements can give relief.

Besides the problems of absorption by the ligands or Eu^{2+} absorption of transitions, other problems may also occur. Although some transitions are allowed by the selection rules, it is possible that they are not found experimentally because their intensity is weak. This is especially a problem if the doping concentration is low or if the optical path length is small. A small crystal-field splitting can also be problematic. If the separation between two crystal-field levels is small, the absorption or luminescence peaks will overlap. As long as the second peak can be observed as a shoulder of the first peak,

it is still possible to determine the symmetry. It is however worse if the splitting is so small that only one peak is observed. The line width of transitions in single crystals is fortunately small, but this is not the case for solutions. In solutions and glasses, the inhomogeneous line broadening can even mask the whole crystal-field splitting fine structure, making a symmetry determination impossible. Inhomogeneous line broadening occurs if a distribution of sites with little different energies is present. Symmetry determination in solutions is therefore to a large extent restricted to molecular complexes, which have a well-defined first coordination sphere. If the $^5D_0 \leftarrow {}^7F_0$ transition shows more than one peak, it is an indication that more than one non-equivalent site is present. The peaks of the transitions from each site are superposed on the spectrum, so that a simple straightforward point-group determination is not possible in this case. We also assume that the $^5D_2 \leftarrow {}^7F_0$ and the $^5D_4 \leftarrow {}^7F_0$ transitions are pure ED transitions, neglecting all MD contributions. Hasunuma et al. (1984) report some MD lines for the $^5D_0 \rightarrow {}^7F_2$ and $^5D_0 \rightarrow {}^7F_4$ transitions in $Eu(BrO_3)_3 \cdot 9H_2O$.

For solutions and polycrystalline samples no polarized spectra can be recorded. The procedure will be the same, but now only the number of peaks found for a particular transition have to be considered. Now it is not possible to distinguish a C_1 from a C_2 or C_s symmetry. The S_4 symmetry has the same spectrum for the $^5D_2 \leftarrow {}^7F_0$ transition as the C_{3v} and C_3 symmetries. The $^5D_4 \leftarrow {}^7F_0$ transition can give a solution: four peaks for S_4, five peaks for C_{3v} and six peaks for C_3. A similar problem is found for the D_3 symmetry, which cannot be distinguished from a C_{6v}, C_6, C_{4v}, D_{2d} or C_4 symmetry. Even the $^5D_4 \leftarrow {}^7F_0$ will give no unambiguous answer, since for both D_3 and C_{4v} four peaks are predicted. Here, the $^5D_0 \leftarrow {}^7F_0$ transition will give a way out, because this transition is allowed for C_{4v}, but forbidden for D_3. Another check is the fact the D_3 molecules are optically active, while C_{4v} molecules are not. D_3 molecules give a CD signal, if the sample is not a racemic mixture.

6. Conclusion

Enormous progress has been made since the discovery by J. Becquerel in the first decade of this century that the low temperature absorption spectra of the trivalent lanthanide ions consist of a great of number very small lines resembling atomic spectra. Spectroscopists are not only able to explain the features of a spectrum in a qualitative way, they can also extract a set of free-ion and crystal-field parameters. This parameter set is the greatest possible reduction of the experimental data and it allows one to reconstruct the energy level scheme of the $4f^n$ configuration and even to make predictions about energy regions which cannot be probed experimentally. Powerful theoretical tools for this work are group theory and tensor algebra. High-speed computers enable the handling of large matrices which are necessary in accurate energy calculations. Computers make it possible to work with a considerable number of parameters in order to reach a very good agreement between experiment and theory. The tendency in lanthanide spectroscopy is to introduce new parameters every time discrepancies between experiment and theory are found. Such

large parameter sets do not of course enhance a physical understanding of the problem. The question about the reliability of these parameter sets is a criticism often heard from non-spectroscopists and even from transition-metal spectroscopists. We have tried in this chapter to clarify the description of the crystal field felt by a trivalent lanthanide ion in a crystalline host matrix. The concept of the coordination polyhedron was used to rationalize the crystal-field parameters and to make a close connection between structure and spectroscopic behavior. We are conscious of the fact that describing the crystal field by taking only the first coordination sphere into account, is a very simple presentation of the reality. Physicists and especially those who want to calculate the crystal-field parameters by *ab initio* methods, may feel somewhat unhappy with our model. But a simple model is more suited for an understanding of the crystal-field perturbation, since it allows one to explain many features of the crystal-field splitting in a qualitative way. We do agree that for an accurate simulation of the energy level scheme elaborate calculations and a great number of parameters are necessary. Special attention was therefore also given to the determination of phenomenological parameters and the energy level calculation. Although many spectroscopic studies of trivalent lanthanide ions are available in the literature and the theory has reached a mature level, one does not have to fear that lanthanide spectroscopy will soon become a closed chapter in science. A lot of work has still to be done. For most systems only the lower $^{2S+1}L_J$ levels of the highly degenerate $4f^n$ configurations have been investigated. Spectroscopic studies span the 0–40 000 cm^{-1} spectral region for only a few transparent host crystals with a relatively high symmetry for the rare-earth site. Intense broad band absorptions due to, for instance, charge transfer or allowed f–d transitions prevent the detection of the weak 4f–4f transitions in the high energy range by conventional optical absorption methods. If the sample does not show luminescence, only scarce spectroscopic information will be available in the 0–5000 cm^{-1} range. Restrictions by the selection rules also reduce the number of crystal-field levels which can be detected. Assistance can be expected from exotic spectroscopic methods which can cover a broader energy range than absorption and luminescence spectroscopy and for which other selection rules are applicable. A step in that direction are two-photon absorption (TPA) and spectroscopic methods based on the Zeeman effect (MCD, EPR). Who knows what other methods will be available in the future? The study of crystal-field effects in opaque materials has received only limited interest, because optical methods cannot be used for those systems. Until now, the interpretation of the spectra has been restricted to a large extent to the energy level scheme alone. A lot of additional information can be gained from a study of the intensities of the transitions between crystal-field levels. Parametrization of the transition intensities is a more formidable task than the parametrization of the energy level scheme, so that this subject is considered by only a few research groups. A goal to be reached in lanthanide spectroscopy is the reconstruction of the spectrum by *ab initio* calculations without the need of parameter sets. There has to be a one-to-one agreement between the experimental and the calculated spectrum, both in energetic positions of the peaks and spectral intensities. At this moment, we are still far from that. It can be asked what the impact of the quark model developed by Judd will be when it has been totally worked out. The use of spectroscopy for structural

investigations in solid compounds has not been explored totally yet. Instead of explaining the spectral features with the aid of structural data from X-ray and other diffraction methods, spectroscopy has been complementary to these. An advantage of spectroscopy is that it is very sensitive to small distortions of the ideal structure. The need of methods for structural study of systems in solutions including biological systems, assures that lanthanide spectroscopy will be a field of study in the 21th century.

Acknowledgments

Koen Binnemans (aspirant N.F.W.O.) thanks the "Nationaal Fonds voor Wetenschappelijk Onderzoek" for financial support. Financial support from the Geconcerteerde Onderzoeksakties (Konventie Nr. 87 93-110) and from the I.I.K.W. (4.0007.94 and G.0124.95) is also gratefully acknowledged. We wish to thank H. Crosswhite (Argonne National Laboratory, Argonne, IL) and M.F. Reid (University of Canterbury, Christchurch, New Zealand) for their crystal-field diagonalization programs, which are used in our laboratory. We would also like to thank I. Couwenberg, L. Fluyt and K. Heyde for critically reading the manuscript.

Appendix 1. Spherical harmonics Y_k^q

$$Y_0^0 = \frac{1}{\sqrt{4\pi}}$$

$$Y_1^0 = \frac{\sqrt{3}}{\sqrt{4\pi}}\cos\theta$$

$$Y_1^{\pm 1} = \mp\frac{\sqrt{3}}{\sqrt{2}\sqrt{4\pi}}\sin\theta\, e^{\pm i\varphi}$$

$$Y_2^0 = \frac{\sqrt{5}}{2\sqrt{4\pi}}\left(3\cos^2\theta - 1\right)$$

$$Y_2^{\pm 1} = \mp\frac{\sqrt{3}\sqrt{5}}{\sqrt{2}\sqrt{4\pi}}\cos\theta\sin\theta\, e^{\pm i\varphi}$$

$$Y_2^{\pm 2} = \frac{\sqrt{3}\sqrt{5}}{\sqrt{8}\sqrt{4\pi}}\sin^2\theta\, e^{\pm i2\varphi}$$

$$Y_3^0 = \frac{\sqrt{7}}{2\sqrt{4\pi}}\left(2\cos^3\theta - 3\cos\theta\sin^2\theta\right)$$

$$Y_3^{\pm 1} = \mp \frac{\sqrt{3}\sqrt{7}}{4\sqrt{4\pi}} \left(4\cos^2\theta \sin\theta - \sin^3\theta\right) e^{\pm i\varphi}$$

$$Y_3^{\pm 2} = \frac{\sqrt{15}\sqrt{7}}{\sqrt{8}\sqrt{4\pi}} \cos\theta \sin^2\theta \, e^{\pm i2\varphi}$$

$$Y_3^{\pm 3} = \mp \frac{\sqrt{5}\sqrt{7}}{4\sqrt{4\pi}} \sin^3\theta \, e^{\pm i3\varphi}$$

$$Y_4^0 = \frac{\sqrt{9}}{8\sqrt{4\pi}} \left(35\cos^4\theta - 30\cos^2\theta + 3\right)$$

$$Y_4^{\pm 1} = \mp \frac{\sqrt{5}\sqrt{9}}{4\sqrt{4\pi}} \sin\theta \cos\theta \left(7\cos^2\theta - 3\right) e^{\pm i\varphi}$$

$$Y_4^{\pm 2} = \frac{\sqrt{5}\sqrt{9}}{\sqrt{32}\sqrt{4\pi}} \sin^2\theta \left(7\cos^2\theta - 1\right) e^{\pm i2\varphi}$$

$$Y_4^{\pm 3} = \mp \frac{\sqrt{35}\sqrt{9}}{4\sqrt{4\pi}} \sin^3\theta \cos\theta \, e^{\pm i3\varphi}$$

$$Y_4^{\pm 4} = \frac{\sqrt{35}\sqrt{9}}{\sqrt{128}\sqrt{4\pi}} \sin^4\theta \, e^{\pm i4\varphi}$$

$$Y_5^0 = \frac{\sqrt{11}}{8\sqrt{4\pi}} \left(63\cos^5\theta - 70\cos^3\theta + 15\cos\theta\right)$$

$$Y_5^{\pm 1} = \mp \frac{\sqrt{15}\sqrt{11}}{\sqrt{128}\sqrt{4\pi}} \left(21\cos^4\theta - 14\cos^2\theta + 1\right) \sin\theta \, e^{\pm i\varphi}$$

$$Y_5^{\pm 2} = \frac{\sqrt{105}\sqrt{11}}{\sqrt{32}\sqrt{4\pi}} \left(3\cos^2\theta - 1\right) \cos\theta \sin^2\theta \, e^{\pm i2\varphi}$$

$$Y_5^{\pm 3} = \mp \frac{\sqrt{35}\sqrt{11}}{16\sqrt{4\pi}} \left(9\cos^2\theta - 1\right) \sin^3\theta \, e^{\pm i3\varphi}$$

$$Y_5^{\pm 4} = \frac{3\sqrt{35}\sqrt{11}}{\sqrt{128}\sqrt{4\pi}} \cos\theta \sin^4\theta \, e^{\pm i4\varphi}$$

$$Y_5^{\pm 5} = \mp \frac{3\sqrt{7}\sqrt{11}}{16\sqrt{4\pi}} \sin^5\theta \, e^{\pm i5\varphi}$$

$$Y_6^0 = \frac{\sqrt{13}}{16\sqrt{4\pi}} \left(231\cos^6\theta - 315\cos^4\theta + 105\cos^2\theta - 5\right)$$

$$Y_6^{\pm 1} = \mp \frac{\sqrt{21}\sqrt{13}}{\sqrt{128}\sqrt{4\pi}} \sin\theta \left(33\cos^5\theta - 30\cos^3\theta + 5\cos\theta\right) e^{\pm i\varphi}$$

$$Y_6^{\pm 2} = \frac{\sqrt{105}\sqrt{13}}{32\sqrt{4\pi}} \sin^2\theta \left(33\cos^4\theta - 18\cos^2\theta + 1\right) e^{\pm i2\varphi}$$

$$Y_6^{\pm 3} = \mp \frac{\sqrt{105}\sqrt{13}}{16\sqrt{4\pi}} \sin^3\theta \cos\theta \left(11\cos^2\theta - 3\right) e^{\pm i3\varphi}$$

$$Y_6^{\pm 4} = \frac{3\sqrt{7}\sqrt{13}}{\sqrt{512}\sqrt{4\pi}} \sin^4\theta \left(11\cos^2 - 1\right) e^{\pm i4\varphi}$$

$$Y_6^{\pm 5} = \mp \frac{3\sqrt{77}\sqrt{13}}{16\sqrt{4\pi}} \sin^5\theta \cos\theta \, e^{\pm i5\varphi}$$

$$Y_6^{\pm 6} = \frac{\sqrt{231}\sqrt{13}}{32\sqrt{4\pi}} \sin^6\theta \, e^{\pm i6\varphi}$$

$$Y_7^0 = \frac{\sqrt{15}}{16\sqrt{4\pi}} \cos\theta \left(429\cos^6\theta - 693\cos^4\theta + 315\cos^2\theta - 35\right)$$

$$Y_7^{\pm 1} = \mp \frac{\sqrt{14}\sqrt{15}}{64\sqrt{4\pi}} \sin\theta \left(429\cos^6\theta - 495\cos^4\theta + 135\cos^2\theta - 5\right) e^{\pm i\varphi}$$

$$Y_7^{\pm 2} = \frac{\sqrt{21}\sqrt{15}}{32\sqrt{4\pi}} \cos\theta \left(143\cos^6\theta - 253\cos^4\theta + 125\cos^2\theta - 15\right) e^{\pm i2\varphi}$$

$$Y_7^{\pm 3} = \mp \frac{\sqrt{42}\sqrt{15}}{64\sqrt{4\pi}} \sin\theta \left(143\cos^6\theta - 209\cos^4\theta + 69\cos^2\theta - 3\right) e^{\pm i3\varphi}$$

$$Y_7^{\pm 4} = \frac{\sqrt{231}\sqrt{15}}{32\sqrt{4\pi}} \cos\theta \left(13\cos^6\theta - 29\cos^4\theta + 19\cos^2\theta - 3\right) e^{\pm i4\varphi}$$

$$Y_7^{\pm 5} = \mp \frac{\sqrt{231}\sqrt{15}}{64\sqrt{4\pi}} \sin\theta \left(13\cos^6\theta - 27\cos^4\theta + 15\cos^2\theta - 1\right) e^{\pm i5\varphi}$$

$$Y_7^{\pm 6} = \frac{\sqrt{3003}\sqrt{15}}{32\sqrt{4\pi}} \cos\theta \sin^6\theta \, e^{\pm i6\varphi}$$

$$Y_7^{\pm 7} = \mp \frac{\sqrt{858}\sqrt{15}}{64\sqrt{4\pi}} \sin^7\theta \, e^{\pm i7\varphi}$$

Appendix 2. Normalized tesseral harmonics ($r^2 = x^2 + y^2 + z^2$)

$$Z_{00}^{c} = \frac{1}{\sqrt{4\pi}}$$

$$Z_{10}^{c} = \frac{\sqrt{3}}{\sqrt{4\pi}}\frac{z}{r}$$

$$Z_{11}^{c} = \frac{\sqrt{3}}{\sqrt{4\pi}}\frac{x}{r}$$

$$Z_{11}^{s} = \frac{\sqrt{3}}{\sqrt{4\pi}}\frac{y}{r}$$

$$Z_{20}^{c} = \frac{\sqrt{5}}{2\sqrt{4\pi}}\frac{1}{r^2}\left(2z^2 - x^2 - y^2\right)$$

$$Z_{21}^{c} = \frac{\sqrt{3}\sqrt{5}}{\sqrt{4\pi}}\frac{1}{r^2}xz$$

$$Z_{21}^{s} = \frac{\sqrt{3}\sqrt{5}}{\sqrt{4\pi}}\frac{1}{r^2}yz$$

$$Z_{22}^{c} = \frac{\sqrt{3}\sqrt{5}}{2\sqrt{4\pi}}\frac{1}{r^2}\left(x^2 - y^2\right)$$

$$Z_{22}^{s} = \frac{\sqrt{3}\sqrt{5}}{2\sqrt{4\pi}}\frac{1}{r^2}2xy$$

$$Z_{30}^{c} = \frac{\sqrt{7}}{2\sqrt{4\pi}}\frac{1}{r^3}\left(2z^3 - 3x^2z - 3y^2z\right)$$

$$Z_{31}^{c} = \frac{\sqrt{6}\sqrt{7}}{4\sqrt{4\pi}}\frac{1}{r^3}\left(4z^2x - x^3 - xy^2\right)$$

$$Z_{31}^{s} = \frac{\sqrt{6}\sqrt{7}}{4\sqrt{4\pi}}\frac{1}{r^3}\left(4z^2y - x^2y - y^3\right)$$

$$Z_{32}^{c} = \frac{\sqrt{15}\sqrt{7}}{2\sqrt{4\pi}}\frac{1}{r^3}\left(zx^2 - zy^2\right)$$

$$Z_{32}^{s} = \frac{\sqrt{15}\sqrt{7}}{2\sqrt{4\pi}}\frac{1}{r^3}2xyz$$

$$Z_{33}^{c} = \frac{\sqrt{10}\sqrt{7}}{4\sqrt{4\pi}} \frac{1}{r^3} \left(x^3 - 3xy^2\right)$$

$$Z_{33}^{s} = \frac{\sqrt{10}\sqrt{7}}{4\sqrt{4\pi}} \frac{1}{r^3} \left(3x^2y - y^3\right)$$

$$Z_{40}^{c} = \frac{\sqrt{9}}{8\sqrt{4\pi}} \frac{1}{r^4} \left(8z^4 + 3x^4 + 3y^4 - 24x^2y^2 - 24y^2z^2 + 6x^2y^2\right)$$

$$Z_{41}^{c} = \frac{\sqrt{10}\sqrt{9}}{4\sqrt{4\pi}} \frac{1}{r^4} \left(4z^2 - 3x^2 - 3y^2\right) xy$$

$$Z_{41}^{s} = \frac{\sqrt{10}\sqrt{9}}{4\sqrt{4\pi}} \frac{1}{r^4} \left(4z^2 - 3x^2 - 3y^2\right) yz$$

$$Z_{42}^{c} = \frac{\sqrt{5}\sqrt{9}}{4\sqrt{4\pi}} \frac{1}{r^4} \left(6z^2 - x^2 - y^2\right) \left(x^2 - y^2\right)$$

$$Z_{42}^{s} = \frac{\sqrt{5}\sqrt{9}}{4\sqrt{4\pi}} \frac{1}{r^4} \left(6z^2 - x^2 - y^2\right) 2xy$$

$$Z_{43}^{c} = \frac{\sqrt{70}\sqrt{9}}{4\sqrt{4\pi}} \frac{1}{r^4} \left(x - 3y^2\right) xz$$

$$Z_{43}^{s} = \frac{\sqrt{70}\sqrt{9}}{4\sqrt{4\pi}} \frac{1}{r^4} \left(3x^2 - y^2\right) yz$$

$$Z_{44}^{c} = \frac{\sqrt{35}\sqrt{9}}{8\sqrt{4\pi}} \frac{1}{r^4} \left(x^4 - 6x^2y^2 + y^4\right)$$

$$Z_{44}^{s} = \frac{\sqrt{35}\sqrt{9}}{8\sqrt{4\pi}} \frac{1}{r^4} 4xy \left(x^2 - y^2\right)$$

$$Z_{50}^{c} = \frac{\sqrt{11}}{8\sqrt{4\pi}} \frac{1}{r^5} \left(8z^5 - 40z^3 \left(x^2 + y^2\right) + 15 \left(x^2 + y^2\right)^2 z\right)$$

$$Z_{51}^{c} = \frac{\sqrt{15}\sqrt{11}}{8\sqrt{4\pi}} \frac{1}{r^5} \left(8z^4 + x^4 + y^4 + 2x^2y^2 - 12x^2z^2 - 12y^2z^2\right) x$$

$$Z_{51}^{s} = \frac{\sqrt{15}\sqrt{11}}{8\sqrt{4\pi}} \frac{1}{r^5} \left(8z^4 + x^4 + y^4 + 2x^2y^2 - 12x^2z^2 - 12y^2z^2\right) y$$

$$Z_{52}^{c} = \frac{\sqrt{105}\sqrt{11}}{4\sqrt{4\pi}} \frac{1}{r^5} \left(2z^2 - x^2 - y^2\right) \left(x^3 - y^3\right) z$$

$$Z_{52}^{s} = \frac{\sqrt{105}\sqrt{11}}{4\sqrt{4\pi}} \frac{1}{r^5} \left(2z^2 - x^2 - y^2\right) 2xyz$$

$$Z_{53}^{c} = \frac{\sqrt{70}\sqrt{11}}{16\sqrt{4\pi}} \frac{1}{r^5} \left(8z^2 - x^2 - y^2\right) \left(x^3 - 3xy^2\right)$$

$$Z_{53}^{s} = \frac{\sqrt{70}\sqrt{11}}{16\sqrt{4\pi}} \frac{1}{r^5} \left(8z^2 - x^2 - y^2\right) \left(3x^2y - y^3\right)$$

$$Z_{54}^{c} = \frac{3\sqrt{35}\sqrt{11}}{8\sqrt{4\pi}} \frac{1}{r^5} \left(x^4 - 6x^2y^2 + y^4\right) z$$

$$Z_{54}^{s} = \frac{3\sqrt{35}\sqrt{11}}{8\sqrt{4\pi}} \frac{1}{r^5} \left(x^2 - y^2\right) 4xyz$$

$$Z_{55}^{c} = \frac{3\sqrt{14}\sqrt{11}}{16\sqrt{4\pi}} \frac{1}{r^5} \left(x^5 - 10x^3y^2 + 5xy^4\right)$$

$$Z_{55}^{s} = \frac{3\sqrt{14}\sqrt{11}}{16\sqrt{4\pi}} \frac{1}{r^5} \left(y^5 - 10y^3x^2 + 5yx^4\right)$$

$$Z_{60}^{c} = \frac{\sqrt{13}}{16\sqrt{4\pi}} \frac{1}{r^6} \left[16z^6 - 120\left(x^2 + y^2\right) z^4 + 90\left(x^2 + y^2\right)^2 z^2 - 5\left(x^2 + y^2\right)^3\right]$$

$$Z_{61}^{c} = \frac{\sqrt{21}\sqrt{13}}{8\sqrt{4\pi}} \frac{1}{r^6} \left[8z^5 - 20z^3\left(x^2 + y^2\right) + 5z\left(x^2 + y^2\right)^2\right] x$$

$$Z_{61}^{s} = \frac{\sqrt{21}\sqrt{13}}{8\sqrt{4\pi}} \frac{1}{r^6} \left[8z^5 - 20z^3\left(x^2 + y^2\right) + 5z\left(x^2 + y^2\right)^2\right] y$$

$$Z_{62}^{c} = \frac{\sqrt{210}\sqrt{13}}{32\sqrt{4\pi}} \frac{1}{r^6} \left[16z^4 - 16\left(x^2 + y^2\right) z^2 + \left(x^2 + y^2\right)^2\right] \left(x^2 - y^2\right)$$

$$Z_{62}^{s} = \frac{\sqrt{210}\sqrt{13}}{32\sqrt{4\pi}} \frac{1}{r^6} \left[16z^4 - 16\left(x^2 + y^2\right) z^2 + \left(x^2 + y^2\right)^2\right] 2xy$$

$$Z_{63}^{c} = \frac{\sqrt{210}\sqrt{13}}{16\sqrt{4\pi}} \frac{1}{r^6} \left(8z^2 - 3x^2 - 3y^2\right) \left(x^2 - 3y^2\right) xz$$

$$Z_{63}^{s} = \frac{\sqrt{210}\sqrt{13}}{16\sqrt{4\pi}} \frac{1}{r^6} \left(8z^2 - 3x^2 - 3y^2\right) \left(3x^2 - y^2\right) \left(3z^2 - y^2\right) yz$$

$$Z_{64}^{c} = \frac{3\sqrt{7}\sqrt{13}}{16\sqrt{4\pi}} \frac{1}{r^6} \left(10z^2 - x^2 - y^2\right) \left(x^4 - 6x^2y^2 + y^4\right)$$

$$Z_{64}^{s} = \frac{3\sqrt{7}\sqrt{13}}{16\sqrt{4\pi}}\frac{1}{r^6}\left(10z^2 - x^2 - y^2\right)\left(4x^3y - 4xy^3\right)$$

$$Z_{65}^{c} = \frac{3\sqrt{154}\sqrt{13}}{16\sqrt{4\pi}}\frac{1}{r^6}\left(x^5 - 10x^3y^2 + 5xy^4\right)z$$

$$Z_{65}^{s} = \frac{3\sqrt{154}\sqrt{13}}{16\sqrt{4\pi}}\frac{1}{r^6}\left(y^5 - 10y^3x^2 + 5yx^4\right)z$$

$$Z_{66}^{c} = \frac{\sqrt{462}\sqrt{13}}{32\sqrt{4\pi}}\frac{1}{r^6}\left(x^6 - 15x^4y^2 + 15x^2y^4 - y^6\right)$$

$$Z_{66}^{s} = \frac{\sqrt{462}\sqrt{13}}{32\sqrt{4\pi}}\frac{1}{r^6}\left(3x^2 - y^2\right)\left(x^2 - 3y^2\right)2xy$$

$$Z_{70}^{c} = \frac{\sqrt{15}}{16\sqrt{4\pi}}\frac{1}{r^7}\left[16z^7 - 168z^5\left(x^2+y^2\right) + 210z^3\left(x^2+y^2\right)^2 - 35z\left(x^2+y^2\right)^3\right]$$

$$Z_{71}^{c} = \frac{\sqrt{7}\sqrt{15}}{32\sqrt{4\pi}}\frac{1}{r^7}\left[-5\left(x^2+y^2\right)^3 + 120z^2\left(x^2+y^2\right)^2 - 240z^4\left(x^2+y^2\right) + 64z^6\right]x$$

$$Z_{71}^{s} = \frac{\sqrt{7}\sqrt{15}}{32\sqrt{4\pi}}\frac{1}{r^7}\left[-5\left(x^2+y^2\right)^3 + 120z^2\left(x^2+y^2\right)^2 - 240z^4\left(x^2+y^2\right) + 64z^6\right]y$$

$$Z_{72}^{c} = \frac{\sqrt{42}\sqrt{15}}{32\sqrt{4\pi}}\frac{1}{r^7}\left[48z^5 - 80z^3\left(x^2+y^2\right) + 15z\left(x^2+y^2\right)^2\right]\left(x^2 - y^2\right)$$

$$Z_{72}^{s} = \frac{\sqrt{42}\sqrt{15}}{32\sqrt{4\pi}}\frac{1}{r^7}\left[48z^5 - 80z^3\left(x^2+y^2\right) + 15z\left(x^2+y^2\right)^2\right]2xy$$

$$Z_{73}^{c} = \frac{\sqrt{21}\sqrt{15}}{32\sqrt{4\pi}}\frac{1}{r^7}\left[80z^4 - 60z^2\left(x^2+y^2\right) + 3\left(x^2+y^2\right)^2\right]\left(x^2 - 3y^2\right)x$$

$$Z_{73}^{s} = \frac{\sqrt{21}\sqrt{15}}{32\sqrt{4\pi}}\frac{1}{r^7}\left[80z^4 - 60z^2\left(x^2+y^2\right) + 3\left(x^2+y^2\right)^2\right]\left(3x^2 - y^2\right)y$$

$$Z_{74}^{c} = \frac{\sqrt{462}\sqrt{15}}{32\sqrt{4\pi}}\frac{1}{r^7}\left[10z^3 - 3z\left(x^2+y^2\right)\right]\left(x^4 - 6x^2y^2 + y^4\right)$$

$$Z_{74}^{s} = \frac{\sqrt{462}\sqrt{15}}{32\sqrt{4\pi}}\frac{1}{r^7}\left[10z^3 - 3z\left(x^2+y^2\right)\right]\left(x^2 - y^2\right)4xy$$

$$Z_{75}^{c} = \frac{\sqrt{462}\sqrt{15}}{64\sqrt{4\pi}}\frac{1}{r^7}\left[12z^2 - \left(x^2+y^2\right)\right]\left(x^5 - 5xy^4 - 10x^3y^2\right)$$

$$Z_{75}^{s} = \frac{\sqrt{462}\sqrt{15}}{64\sqrt{4\pi}} \frac{1}{r^7} \left[12z^2 - \left(x^2 + y^2\right)\right] \left(5x^4y - 10x^2y^3 + y^5\right)$$

$$Z_{76}^{c} = \frac{\sqrt{6006}\sqrt{15}}{32\sqrt{4\pi}} \frac{1}{r^7} \left[x^6 - 15x^4y^2 + 15x^2y^4 - y^6\right] z$$

$$Z_{76}^{s} = \frac{\sqrt{6006}\sqrt{15}}{32\sqrt{4\pi}} \frac{1}{r^7} \left(3x^2 - y^2\right) \left(x^2 - 3y^2\right) 2xyz$$

$$Z_{77}^{c} = \frac{\sqrt{1716}\sqrt{15}}{64\sqrt{4\pi}} \frac{1}{r^7} \left(x^7 - 21x^5y^2 + 35x^3y^4 - 7xy^6\right)$$

$$Z_{77}^{s} = \frac{\sqrt{1716}\sqrt{15}}{64\sqrt{4\pi}} \frac{1}{r^7} \left(7x^6y - 35x^4y^3 + 21x^2y^5 - y^7\right)$$

Appendix 3. Crystal-field potentials

A3.1. D_{nh} *groups*

$$V^{\text{even}}(D_{2h}) = B_0^2 C_0^2 + B_2^2 (C_{-2}^2 + C_2^2) + B_0^4 C_0^4 + B_2^4 (C_{-2}^4 + C_2^4) + B_4^4 (C_{-4}^4 + C_4^4) + B_0^6 C_0^6 + B_2^6 (C_{-2}^6 + C_2^6) + B_4^6 (C_{-4}^6 + C_4^6) + B_6^6 (C_{-6}^6 + C_6^6)$$

$$V^{\text{odd}}(D_{2h}) = 0$$

$$V^{\text{even}}(D_{3h}) = B_0^2 C_0^2 + B_0^4 C_0^4 + B_0^6 C_0^6 + B_6^6 (C_{-6}^6 + C_6^6)$$

$$V^{\text{odd}}(D_{3h}) = B'^3_3 \mathrm{i}(C_{-3}^3 + C_3^3) + B'^5_3 \mathrm{i}(C_{-3}^5 + C_3^5) + B'^7_3 \mathrm{i}(C_{-3}^7 + C_3^7)$$

$$V^{\text{even}}(D_{4h}) = B_0^2 C_0^2 + B_0^4 C_0^4 + B_4^4 (C_{-4}^4 + C_4^4) + B_0^6 C_0^6 + B_4^6 (C_{-4}^6 + C_4^6)$$

$$V^{\text{odd}}(D_{4h}) = 0$$

$$V^{\text{even}}(D_{5h}) = B_0^2 C_0^2 + B_0^4 C_0^4 + B_0^6 C_0^6$$

$$V^{\text{odd}}(D_{5h}) = B'^5_5 \mathrm{i}(C_{-5}^5 + C_5^5) + B'^7_5 \mathrm{i}(C_{-5}^7 + C_5^7)$$

$$V^{\text{even}}(\mathrm{D_{6h}}) = B_0^2 C_0^2 + B_0^4 C_0^4 + B_0^6 C_0^6 + B_6^6 (C_{-6}^6 + C_6^6)$$

$$V^{\text{odd}}(\mathrm{D_{6h}}) = 0$$

$$V^{\text{even}}(\mathrm{D_{\infty h}}) = B_0^2 C_0^2 + B_0^4 C_0^4 + B_0^6 C_0^6$$

$$V^{\text{odd}}(\mathrm{D_{\infty h}}) = 0$$

A3.2. D_{nd} *groups*

$$V^{\text{even}}(\mathrm{D_{2d}}) = B_0^2 C_0^2 + B_0^4 C_0^4 + B_4^4 (C_{-4}^4 + C_4^4) + B_0^6 C_0^6 + B_4^6 (C_{-4}^6 + C_4^6)$$

$$V^{\text{odd}}(\mathrm{D_{2d}}) = B'^3_2 \mathrm{i}(C_{-2}^3 - C_2^3) + B'^5_2 \mathrm{i}(C_{-2}^5 - C_2^5) + B'^7_2 \mathrm{i}(C_{-2}^7 - C_2^7) + B'^7_6 \mathrm{i}(C_{-6}^7 - C_6^7)$$

$$V^{\text{even}}(\mathrm{D_{3d}}) = B_0^2 C_0^2 + B_0^4 C_0^4 + B_3^4 (C_{-3}^4 - C_3^4) + B_0^6 C_0^6 + B_3^6 (C_{-3}^6 - C_3^6) + B_6^6 (C_{-6}^6 + C_6^6)$$

$$V^{\text{odd}}(\mathrm{D_{3d}}) = 0$$

$$V^{\text{even}}(\mathrm{D_{4d}}) = B_0^2 C_0^2 + B_0^4 C_0^4 + B_0^6 C_0^6$$

$$V^{\text{odd}}(\mathrm{D_{4d}}) = B'^5_4 \mathrm{i}(C_{-4}^5 - C_4^5) + B'^7_4 \mathrm{i}(C_{-4}^7 - C_4^7)$$

$$V^{\text{even}}(\mathrm{D_{5d}}) = B_0^2 C_0^2 + B_0^4 C_0^4 + B_0^6 C_0^6 + B_5^6 (C_{-5}^6 - C_5^6)$$

$$V^{\text{odd}}(\mathrm{D_{5d}}) = 0$$

$$V^{\text{even}}(\mathrm{D_{6d}}) = B_0^2 C_0^2 + B_0^4 C_0^4 + B_0^6 C_0^6$$

$$V^{\text{odd}}(\mathrm{D_{6d}}) = B'^7_6 \mathrm{i}(C_{-6}^7 - C_6^7)$$

A3.3. D_n *groups*

$$V^{\text{even}}(D_2) = B_0^2 C_0^2 + B_2^2(C_{-2}^2 + C_2^2) + B_0^4 C_0^4 + B_2^4(C_{-2}^4 + C_2^4) + B_4^4(C_{-4}^4 + C_4^4) + B_0^6 C_0^6 + B_2^6(C_{-2}^6 + C_2^6) + B_4^6(C_{-4}^6 + C_4^6) + B_6^6(C_{-6}^6 + C_6^6)$$

$$V^{\text{odd}}(D_2) = B'^3_2\mathrm{i}(C_{-2}^3 - C_2^3) + B'^5_2\mathrm{i}(C_{-2}^5 - C_2^5) + B'^5_4\mathrm{i}(C_{-4}^5 - C_4^5) + B'^7_2\mathrm{i}(C_{-2}^7 - C_2^7) + B'^7_4\mathrm{i}(C_{-4}^7 - C_4^7) + B'^7_6\mathrm{i}(C_{-6}^7 - C_6^7)$$

$$V^{\text{even}}(D_3) = B_0^2 C_0^2 + B_0^4 C_0^4 + B_3^4(C_{-3}^4 - C_3^4) + B_0^6 C_0^6 + B_3^6(C_{-3}^6 - C_3^6) + B_6^6(C_{-6}^6 + C_6^6)$$

$$V^{\text{odd}}(D_3) = B'^3_3\mathrm{i}(C_{-3}^3 + C_3^3) + B'^5_3\mathrm{i}(C_{-3}^5 + C_3^5) + B'^7_3\mathrm{i}(C_{-3}^7 + C_3^7) + B'^7_6\mathrm{i}(C_{-6}^7 - C_6^7)$$

$$V^{\text{even}}(D_4) = B_0^2 C_0^2 + B_0^4 C_0^4 + B_4^4(C_{-4}^4 + C_4^4) + B_0^6 C_0^6 + B_4^6(C_{-4}^6 + C_4^6)$$

$$V^{\text{odd}}(D_4) = B'^5_4\mathrm{i}(C_{-4}^5 - C_4^5) + B'^7_4\mathrm{i}(C_{-4}^7 - C_4^7)$$

$$V^{\text{even}}(D_5) = B_0^2 C_0^2 + B_0^4 C_0^4 + B_0^6 C_0^6 + B_5^6(C_{-5}^6 - C_5^6)$$

$$V^{\text{odd}}(D_5) = B'^5_5\mathrm{i}(C_{-5}^5 + C_5^5) + B'^7_5\mathrm{i}(C_{-5}^7 + C_5^7)$$

$$V^{\text{even}}(D_6) = B_0^2 C_0^2 + B_0^4 C_0^4 + B_0^6 C_0^6 + B_6^6(C_{-6}^6 + C_6^6)$$

$$V^{\text{odd}}(D_6) = B'^7_6\mathrm{i}(C_{-6}^7 - C_6^7)$$

A3.4. C_{nv} *groups*

$$V^{\text{even}}(C_{2v}) = B_0^2C_0^2 + B_2^2(C_{-2}^2 + C_2^2) + B_0^4C_0^4 + B_2^4(C_{-2}^4 + C_2^4) + B_4^4(C_{-4}^4 + C_4^4) + B_0^6C_0^6 + B_2^6(C_{-2}^6 + C_2^6) + B_4^6(C_{-4}^6 + C_4^6) + B_6^6(C_{-6}^6 + C_6^6)$$

$$V^{\text{odd}}(C_{2v}) = B_0^1C_0^1 + B_0^3C_0^3 + B_2^3(C_{-2}^3 + C_2^3) + B_0^5C_0^5 + B_2^5(C_{-2}^5 + C_2^5) + B_4^5(C_{-4}^5 + C_4^5) + B_0^7C_0^7 + B_2^7(C_{-2}^7 + C_2^7) + B_4^7(C_{-4}^7 + C_4^7) + B_6^7(C_{-6}^7 + C_6^7)$$

$$V^{\text{even}}(C_{3v}) = B_0^2C_0^2 + B_0^4C_0^4 + B_3^4(C_{-3}^4 - C_3^4) + B_0^6C_0^6 + B_3^6(C_{-3}^6 - C_3^6) + B_6^6(C_{-6}^6 + C_6^6)$$

$$V^{\text{odd}}(C_{3v}) = B_0^1C_0^1 + B_0^3C_0^3 + B_3^3(C_{-3}^3 - C_3^3) + B_0^5C_0^5 + B_3^5(C_{-3}^5 - C_3^5) + B_0^7C_0^7 + B_3^7(C_{-3}^7 - C_3^7) + B_6^7(C_{-6}^7 + C_6^7)$$

$$V^{\text{even}}(C_{4v}) = B_0^2C_0^2 + B_0^4C_0^4 + B_4^4(C_{-4}^4 + C_4^4) + B_0^6C_0^6 + B_4^6(C_{-4}^6 + C_4^6)$$

$$V^{\text{odd}}(C_{4v}) = B_0^1C_0^1 + B_0^3C_0^3 + B_0^5C_0^5 + B_4^5(C_{-4}^5 + C_4^5) + B_0^7C_0^7 + B_4^7(C_{-4}^7 + C_4^7)$$

$$V^{\text{even}}(C_{5v}) = B_0^2C_0^2 + B_0^4C_0^4 + B_0^6C_0^6 + B_5^6(C_{-5}^6 - C_5^6)$$

$$V^{\text{odd}}(C_{5v}) = B_0^1C_0^1 + B_0^3C_0^3 + B_0^5C_0^5 + B_5^5(C_{-5}^5 - C_5^5) + B_0^7C_0^7 + B_5^7(C_{-5}^7 - C_5^7)$$

$$V^{\text{even}}(C_{6v}) = B_0^2C_0^2 + B_0^4C_0^4 + B_0^6C_0^6 + B_6^6(C_{-6}^6 + C_6^6)$$

$$V^{\text{odd}}(C_{6v}) = B_0^1C_0^1 + B_0^3C_0^3 + B_0^5C_0^5 + B_0^7C_0^7 + B_6^7(C_{-6}^7 + C_6^7)$$

$$V^{\text{even}}(C_{\infty v}) = B_0^2C_0^2 + B_0^4C_0^4 + B_0^6C_0^6$$

$$V^{\text{odd}}(C_{\infty v}) = B_0^1C_0^1 + B_0^3C_0^3 + B_0^5C_0^5 + B_0^7C_0^7$$

A3.5. C_{nh} *groups*

$$\begin{aligned} V^{\text{even}}(C_{2h}) = {} & B_0^2 C_0^2 + B_2^2 (C_{-2}^2 + C_2^2) + B'^2_2 \mathrm{i}(C_{-2}^2 - C_2^2) \\ & + B_0^4 C_0^4 + B_2^4 (C_{-2}^4 + C_2^4) + B'^4_2 \mathrm{i}(C_{-2}^4 - C_2^4) \\ & + B_4^4 (C_{-4}^4 + C_4^4) + B'^4_4 \mathrm{i}(C_{-4}^4 - C_4^4) \\ & + B_0^6 C_0^6 + B_2^6 (C_{-2}^6 + C_2^6) + B'^6_2 \mathrm{i}(C_{-2}^6 - C_2^6) \\ & + B_4^6 (C_{-4}^6 + C_4^6) + B'^6_4 \mathrm{i}(C_{-4}^6 - C_4^6) \\ & + B_6^6 (C_{-6}^6 + C_6^6) + B'^6_6 \mathrm{i}(C_{-6}^6 - C_6^6) \end{aligned}$$

$$V^{\text{odd}}(C_{2h}) = 0$$

$$V^{\text{even}}(C_{3h}) = B_0^2 C_0^2 + B_0^4 C_0^4 + B_0^6 C_0^6 + B_6^6 (C_{-6}^6 + C_6^6) + B'^6_6 \mathrm{i}(C_{-6}^6 - C_6^6)$$

$$\begin{aligned} V^{\text{odd}}(C_{3h}) = {} & B_3^3 (C_{-3}^3 - C_3^3) + B'^3_3 \mathrm{i}(C_{-3}^3 + C_3^3) + B_3^5 (C_{-3}^5 - C_3^5) + B'^5_3 \mathrm{i}(C_{-3}^5 + C_3^5) \\ & + B_3^7 (C_{-3}^7 - C_3^7) + B'^7_3 \mathrm{i}(C_{-3}^7 + C_3^7) \end{aligned}$$

$$\begin{aligned} V^{\text{even}}(C_{4h}) = {} & B_0^2 C_0^2 + B_0^4 C_0^4 + B_4^4 (C_{-4}^4 + C_4^4) + B'^4_4 \mathrm{i}(C_{-4}^4 - C_4^4) \\ & + B_0^6 C_0^6 + B_4^6 (C_{-4}^6 + C_4^6) + B'^6_4 \mathrm{i}(C_{-4}^6 - C_4^6) \end{aligned}$$

$$V^{\text{odd}}(C_{4h}) = 0$$

$$V^{\text{even}}(C_{5h}) = B_0^2 C_0^2 + B_0^4 C_0^4 + B_0^6 C_0^6 + B_5^6 (C_{-5}^6 - C_5^6) + B'^6_5 \mathrm{i}(C_{-5}^6 + C_5^6)$$

$$V^{\text{odd}}(C_{5h}) = B_5^5 (C_{-5}^5 - C_5^5) + B'^5_5 \mathrm{i}(C_{-5}^5 + C_5^5) + B_5^7 (C_{-5}^7 - C_5^7) + B'^7_5 \mathrm{i}(C_{-5}^7 + C_5^7)$$

$$V^{\text{even}}(C_{6h}) = B_0^2 C_0^2 + B_0^4 C_0^4 + B_0^6 C_0^6 + B_6^6 (C_{-6}^6 + C_6^6) + B'^6_6 \mathrm{i}(C_{-6}^6 - C_6^6)$$

$$V^{\text{odd}}(C_{6h}) = 0$$

A3.6. C_n *groups*

$$V^{\text{even}}(C_2) = B_0^2 C_0^2 + B_2^2(C_{-2}^2 + C_2^2) + B'^2_2\mathrm{i}(C_{-2}^2 - C_2^2)$$
$$+ B_0^4 C_0^4 + B_2^4(C_{-2}^4 + C_2^4) + B'^4_2\mathrm{i}(C_{-2}^4 - C_2^4) + B_4^4(C_{-4}^4 + C_4^4) + B'^4_4\mathrm{i}(C_{-4}^4 - C_4^4)$$
$$+ B_0^6 C_0^6 + B_2^6(C_{-2}^6 + C_2^6) + B'^6_2\mathrm{i}(C_{-2}^6 - C_2^6) + B_4^6(C_{-4}^6 + C_4^6) + B'^6_4\mathrm{i}(C_{-4}^6 - C_4^6)$$
$$+ B_6^6(C_{-6}^6 + C_6^6) + B'^6_6\mathrm{i}(C_{-6}^6 - C_6^6)$$

$$V^{\text{odd}}(C_2) = B_0^1 C_0^1 + B_0^3 C_0^3 + B_2^3(C_{-2}^3 + C_2^3) + B'^3_2\mathrm{i}(C_{-2}^3 - C_2^3)$$
$$+ B_0^5 C_0^5 + B_2^5(C_{-2}^5 + C_2^5) + B'^5_2\mathrm{i}(C_{-2}^5 - C_2^5) + B_4^5(C_{-4}^5 + C_4^5) + B'^5_4\mathrm{i}(C_{-4}^5 - C_4^5)$$
$$+ B_0^7 C_0^7 + B_2^7(C_{-2}^7 + C_2^7) + B'^7_2\mathrm{i}(C_{-2}^7 - C_2^7) + B_4^7(C_{-4}^7 + C_4^7) + B'^7_4\mathrm{i}(C_{-4}^7 - C_4^7)$$
$$+ B_6^7(C_{-6}^7 + C_6^7) + B'^7_6\mathrm{i}(C_{-6}^7 - C_6^7)$$

$$V^{\text{even}}(C_3) = B_0^2 C_0^2 + B_0^4 C_0^4 + B_3^4(C_{-3}^4 - C_3^4) + B'^4_3\mathrm{i}(C_{-3}^4 + C_3^4)$$
$$+ B_0^6 C_0^6 + B_3^6(C_{-3}^6 - C_3^6) + B'^6_3\mathrm{i}(C_{-3}^6 + C_3^6) + B_6^6(C_{-6}^6 + C_6^6) + B'^6_6\mathrm{i}(C_{-6}^6 - C_6^6)$$

$$V^{\text{odd}}(C_3) = B_0^1 C_0^1 + B_0^3 C_0^3 + B_3^3(C_{-3}^3 - C_3^3) + B'^3_3\mathrm{i}(C_{-3}^3 + C_3^3)$$
$$+ B_0^5 C_0^5 + B_3^5(C_{-3}^5 - C_3^5) + B'^5_3\mathrm{i}(C_{-3}^5 + C_3^5)$$
$$+ B_0^7 C_0^7 + B_3^7(C_{-3}^7 - C_3^7) + B'^7_3\mathrm{i}(C_{-3}^7 + C_3^7) + B_6^7(C_{-6}^7 + C_6^7) + B'^7_6\mathrm{i}(C_{-6}^7 - C_6^7)$$

$$V^{\text{even}}(C_4) = B_0^2 C_0^2 + B_0^4 C_0^4 + B_4^4(C_{-4}^4 + C_4^4) + B'^4_4\mathrm{i}(C_{-4}^4 - C_4^4)$$
$$+ B_0^6 C_0^6 + B_4^6(C_{-4}^6 + C_4^6) + B'^6_4\mathrm{i}(C_{-4}^6 - C_4^6)$$

$$V^{\text{odd}}(C_4) = B_0^1 C_0^1 + B_0^3 C_0^3 + B_0^5 C_0^5 + B_4^5(C_{-4}^5 + C_4^5) + B'^5_4\mathrm{i}(C_{-4}^5 - C_4^5)$$
$$+ B_0^7 C_0^7 + B_4^7(C_{-4}^7 + C_4^7) + B'^7_4\mathrm{i}(C_{-4}^7 - C_4^7)$$

$$V^{\text{even}}(C_5) = B_0^2 C_0^2 + B_0^4 C_0^4 + B_0^6 C_0^6 + B_5^6(C_{-5}^6 - C_5^6) + B'^6_5\mathrm{i}(C_{-5}^6 + C_5^6)$$

$$V^{\text{odd}}(C_5) = B_0^1 C_0^1 + B_0^3 C_0^3 + B_0^5 C_0^5 + B_5^5(C_{-5}^5 - C_5^5) + B'^5_5\mathrm{i}(C_{-5}^5 + C_5^5)$$
$$+ B_0^7 C_0^7 + B_5^7(C_{-5}^7 - C_5^7) + B'^7_5\mathrm{i}(C_{-5}^7 + C_5^7)$$

$$V^{\text{even}}(C_6) = B_0^2 C_0^2 + B_0^4 C_0^4 + B_0^6 C_0^6 + B_6^6(C_{-6}^6 + C_6^6) + B'^6_6\mathrm{i}(C_{-6}^6 - C_6^6)$$

$$V^{\text{odd}}(C_6) = B_0^1 C_0^1 + B_0^3 C_0^3 + B_0^5 C_0^5 + B_0^7 C_0^7 + B_6^7(C_{-6}^7 + C_6^7) + B'^7_6\mathrm{i}(C_{-6}^7 - C_6^7)$$

A3.7. S_n *groups*

$$V^{\text{even}}(S_4) = B_0^2 C_0^2 + B_0^4 C_0^4 + B_4^4(C_{-4}^4 + C_4^4) + B'^4_4\mathrm{i}(C_{-4}^4 - C_4^4) + B_0^6 C_0^6 + B_4^6(C_{-4}^6 + C_4^6) + B'^6_4\mathrm{i}(C_{-4}^6 - C_4^6)$$

$$V^{\text{odd}}(S_4) = B_2^3(C_{-2}^3 + C_2^3) + B'^3_2\mathrm{i}(C_{-2}^3 - C_2^3) + B_2^5(C_{-2}^5 + C_2^5) + B'^5_2\mathrm{i}(C_{-2}^5 - C_2^5) + B_2^7(C_{-2}^7 + C_2^7) + B'^7_2\mathrm{i}(C_{-2}^7 - C_2^7) + B_6^7(C_{-6}^7 + C_6^7) + B'^7_6\mathrm{i}(C_{-6}^7 - C_6^7)$$

$$V^{\text{even}}(S_6) = B_0^2 C_0^2 + B_0^4 C_0^4 + B_3^4(C_{-3}^4 - C_3^4) + B'^4_3\mathrm{i}(C_{-3}^4 + C_3^4) + B_0^6 C_0^6 + B_3^6(C_{-3}^6 - C_3^6) + B'^6_3\mathrm{i}(C_{-3}^6 + C_3^6) + B_6^6(C_{-6}^6 + C_6^6) + B'^6_6\mathrm{i}(C_{-6}^6 - C_6^6)$$

$$V^{\text{odd}}(S_6) = 0$$

$$V^{\text{even}}(S_8) = B_0^2 C_0^2 + B_0^4 C_0^4 + B_0^6 C_0^6$$

$$V^{\text{odd}}(S_8) = B_4^5(C_{-4}^5 + C_4^5) + B'^5_4\mathrm{i}(C_{-4}^5 - C_4^5) + B_4^7(C_{-4}^7 + C_4^7) + B'^7_4\mathrm{i}(C_{-4}^7 - C_4^7)$$

A3.8. *Low-symmetry groups*

$$V^{\text{even}}(C_s) = B_0^2 C_0^2 + B_2^2(C_{-2}^2 + C_2^2) + B'^2_2\mathrm{i}(C_{-2}^2 - C_2^2) + B_0^4 C_0^4 + B_2^4(C_{-2}^4 + C_2^4) + B'^4_2\mathrm{i}(C_{-2}^4 - C_2^4) + B_4^4(C_{-4}^4 + C_4^4) + B'^4_4\mathrm{i}(C_{-4}^4 - C_4^4) + B_0^6 C_0^6 + B_2^6(C_{-2}^6 + C_2^6) + B'^6_2\mathrm{i}(C_{-2}^6 - C_2^6) + B_4^6(C_{-4}^6 + C_4^6) + B'^6_4\mathrm{i}(C_{-4}^6 - C_4^6) + B_6^6(C_{-6}^6 + C_6^6) + B'^6_6\mathrm{i}(C_{-6}^6 - C_6^6)$$

$$V^{\text{odd}}(C_s) = B_1^1(C_{-1}^1 - C_1^1) + B'^1_1\mathrm{i}(C_{-1}^1 + C_1^1) + B_1^3(C_{-1}^3 - C_1^3) + B'^3_1\mathrm{i}(C_{-1}^3 + C_1^3) + B_3^3(C_{-3}^3 - C_3^3) + B'^3_3\mathrm{i}(C_{-3}^3 + C_3^3) + B_1^5(C_{-1}^5 - C_1^5) + B'^5_1\mathrm{i}(C_{-1}^5 + C_1^5) + B_3^5(C_{-3}^5 - C_3^5) + B'^5_3\mathrm{i}(C_{-3}^5 + C_3^5) + B_5^5(C_{-5}^5 - C_5^5) + B'^5_5\mathrm{i}(C_{-5}^5 + C_5^5) + B_1^7(C_{-1}^7 - C_1^7) + B'^7_1\mathrm{i}(C_{-1}^7 + C_1^7) + B_3^7(C_{-3}^7 - C_3^7) + B'^7_3\mathrm{i}(C_{-3}^7 + C_3^7) + B_5^7(C_{-5}^7 - C_5^7) + B'^7_5\mathrm{i}(C_{-5}^7 + C_5^7) + B_7^7(C_{-7}^7 - C_7^7) + B'^7_7\mathrm{i}(C_{-7}^7 + C_7^7)$$

$$
\begin{aligned}
V^{\text{even}}(\mathrm{C_i}) = {} & B_0^2 C_0^2 + B_1^2 (C_{-1}^2 - C_1^2) + B'^2_1 \mathrm{i}(C_{-1}^2 + C_1^2) + B_2^2 (C_{-2}^2 + C_2^2) + B'^2_2 \mathrm{i}(C_{-2}^2 - C_2^2) \\
& + B_0^4 C_0^4 + B_1^4 (C_{-1}^4 - C_1^4) + B'^4_1 \mathrm{i}(C_{-1}^4 + C_1^4) + B_2^4 (C_{-2}^4 + C_2^4) + B'^4_2 \mathrm{i}(C_{-2}^4 - C_2^4) \\
& + B_3^4 (C_{-3}^4 - C_3^4) + B'^4_3 \mathrm{i}(C_{-3}^4 + C_3^4) + B_4^4 (C_{-4}^4 + C_4^4) + B'^4_4 \mathrm{i}(C_{-4}^4 - C_4^4) \\
& + B_0^6 C_0^6 + B_1^6 (C_{-1}^6 - C_1^6) + B'^6_1 \mathrm{i}(C_{-1}^6 + C_1^6) + B_2^6 (C_{-2}^6 + C_2^6) + B'^6_2 \mathrm{i}(C_{-2}^6 - C_2^6) \\
& + B_3^6 (C_{-3}^6 - C_3^6) + B'^6_3 \mathrm{i}(C_{-3}^6 + C_3^6) + B_4^6 (C_{-4}^6 + C_4^6) + B'^6_4 \mathrm{i}(C_{-4}^6 - C_4^6) \\
& + B_5^6 (C_{-5}^6 - C_5^6) + B'^6_5 \mathrm{i}(C_{-5}^6 + C_5^6) + B_6^6 (C_{-6}^6 + C_6^6) + B'^6_6 \mathrm{i}(C_{-6}^6 - C_6^6)
\end{aligned}
$$

$$
V^{\text{odd}}(\mathrm{C_i}) = 0
$$

$$
\begin{aligned}
V^{\text{even}}(\mathrm{C_1}) = {} & B_0^2 C_0^2 + B_1^2 (C_{-1}^2 - C_1^2) + B'^2_1 \mathrm{i}(C_{-1}^2 + C_1^2) + B_2^2 (C_{-2}^2 + C_2^2) + B'^2_2 \mathrm{i}(C_{-2}^2 - C_2^2) \\
& + B_0^4 C_0^4 + B_1^4 (C_{-1}^4 - C_1^4) + B'^4_1 \mathrm{i}(C_{-1}^4 + C_1^4) + B_2^4 (C_{-2}^4 + C_2^4) + B'^4_2 \mathrm{i}(C_{-2}^4 - C_2^4) \\
& + B_3^4 (C_{-3}^4 - C_3^4) + B'^4_3 \mathrm{i}(C_{-3}^4 + C_3^4) + B_4^4 (C_{-4}^4 + C_4^4) + B'^4_4 \mathrm{i}(C_{-4}^4 - C_4^4) \\
& + B_0^6 C_0^6 + B_1^6 (C_{-1}^6 - C_1^6) + B'^6_1 \mathrm{i}(C_{-1}^6 + C_1^6) + B_2^6 (C_{-2}^6 + C_2^6) + B'^6_2 \mathrm{i}(C_{-2}^6 - C_2^6) \\
& + B_3^6 (C_{-3}^6 - C_3^6) + B'^6_3 \mathrm{i}(C_{-3}^6 + C_3^6) + B_4^6 (C_{-4}^6 + C_4^6) + B'^6_4 \mathrm{i}(C_{-4}^6 - C_4^6) \\
& + B_5^6 (C_{-5}^6 - C_5^6) + B'^6_5 \mathrm{i}(C_{-5}^6 + C_5^6) + B_6^6 (C_{-6}^6 + C_6^6) + B'^6_6 \mathrm{i}(C_{-6}^6 - C_6^6)
\end{aligned}
$$

$$
\begin{aligned}
V^{\text{odd}}(\mathrm{C_1}) = {} & B_0^1 C_0^1 + B_1^1 (C_{-1}^1 - C_1^1) + B'^1_1 \mathrm{i}(C_{-1}^1 + C_1^1) \\
& + B_0^3 C_0^3 + B_1^3 (C_{-1}^3 - C_1^3) + B'^3_1 \mathrm{i}(C_{-1}^3 + C_1^3) + B_2^3 (C_{-2}^3 + C_2^3) + B'^3_2 \mathrm{i}(C_{-2}^3 - C_2^3) \\
& + B_3^3 (C_{-3}^3 - C_3^3) + B'^3_3 \mathrm{i}(C_{-3}^3 + C_3^3) \\
& + B_0^5 C_0^5 + B_1^5 (C_{-1}^5 - C_1^5) + B'^5_1 \mathrm{i}(C_{-1}^5 + C_1^5) + B_2^5 (C_{-2}^5 + C_2^5) + B'^5_2 \mathrm{i}(C_{-2}^5 - C_2^5) \\
& + B_3^5 (C_{-3}^5 - C_3^5) + B'^5_3 \mathrm{i}(C_{-3}^5 + C_3^5) + B_4^5 (C_{-4}^5 + C_4^5) + B'^5_4 \mathrm{i}(C_{-4}^5 - C_4^5) \\
& + B_5^5 (C_{-5}^5 - C_5^5) + B'^5_5 \mathrm{i}(C_{-5}^5 + C_5^5) + B_0^7 C_0^7 \\
& + B_1^7 (C_{-1}^7 - C_1^7) + B'^7_1 \mathrm{i}(C_{-1}^7 + C_1^7) + B_2^7 (C_{-2}^7 + C_2^7) + B'^7_2 \mathrm{i}(C_{-2}^7 - C_2^7) \\
& + B_3^7 (C_{-3}^7 - C_3^7) + B'^7_3 \mathrm{i}(C_{-3}^7 + C_3^7) + B_4^7 (C_{-4}^7 + C_4^7) + B'^7_4 \mathrm{i}(C_{-4}^7 - C_4^7) \\
& + B_5^7 (C_{-5}^7 - C_5^7) + B'^7_5 \mathrm{i}(C_{-5}^7 + C_5^7) + B_6^7 (C_{-6}^7 + C_6^7) + B'^7_6 \mathrm{i}(C_{-6}^7 - C_6^7) \\
& + B_7^7 (C_{-7}^7 - C_7^7) + B'^7_7 \mathrm{i}(C_{-7}^7 + C_7^7)
\end{aligned}
$$

A3.9. *Cubic groups*

A3.9.1. *W.r.t. the fourfold rotation axis*

$$V^{\text{even}}(\mathrm{O_h}) = B_0^4\left[C_0^4 + \frac{\sqrt{5}}{\sqrt{14}}\left(C_{-4}^4 + C_4^4\right)\right] + B_0^6\left[C_0^6 - \frac{\sqrt{7}}{\sqrt{2}}\left(C_{-6}^6 + C_6^6\right)\right]$$

$$V^{\text{odd}}(\mathrm{O_h}) = 0$$

$$V^{\text{even}}(\mathrm{T_d}) = B_0^4\left[C_0^4 + \frac{\sqrt{5}}{\sqrt{14}}\left(C_{-4}^4 + C_4^4\right)\right] + B_0^6\left[C_0^6 - \frac{\sqrt{7}}{\sqrt{2}}\left(C_{-6}^6 + C_6^6\right)\right]$$

$$V^{\text{odd}}(\mathrm{T_d}) = B'^3_2\mathrm{i}\left(C_{-2}^3 - C_2^3\right) + B'^7_2\mathrm{i}\left[\left(C_{-2}^7 - C_2^7\right) - \frac{\sqrt{11}}{\sqrt{117}}\left(C_{-6}^7 - C_6^7\right)\right]$$

A3.9.2. *W.r.t. the threefold rotation axis*

$$V^{\text{even}}(\mathrm{O_h}) = B_0^4\left[C_0^4 - \frac{\sqrt{10}}{\sqrt{7}}\left(C_{-3}^4 - C_3^4\right)\right] + B_0^6\left[C_0^6 - \frac{\sqrt{210}}{24}\left(C_{-3}^6 - C_3^6\right) + \frac{\sqrt{231}}{24}\left(C_{-6}^6 + C_6^6\right)\right]$$

$$V^{\text{odd}}(\mathrm{O_h}) = 0$$

$$V^{\text{even}}(\mathrm{T_d}) = B_0^4\left[C_0^4 - \frac{\sqrt{10}}{\sqrt{7}}\left(C_{-3}^4 - C_3^4\right)\right] + B_0^6\left[C_0^6 - \frac{\sqrt{210}}{24}\left(C_{-3}^6 - C_3^6\right) + \frac{\sqrt{231}}{24}\left(C_{-6}^6 + C_6^6\right)\right]$$

$$V^{\text{odd}}(\mathrm{T_d}) = B_0^3\left[C_0^3 + \frac{\sqrt{2}}{\sqrt{5}}\left(C_{-3}^3 - C_3^3\right)\right] + B_0^5C_0^5 + B_0^7\left[C_0^7 + \frac{2}{\sqrt{21}}\left(C_{-3}^3 - C_3^3\right) - \frac{4\sqrt{11}}{\sqrt{273}}\left(C_{-3}^7 - C_3^7\right)\right]$$

A3.10. *Icosahedral group* (I_h)

A3.10.1. *W.r.t. the threefold rotation axis*

$$V^{\text{even}}(I_h) = B_0^6 \left[C_0^6 + \frac{\sqrt{7}}{\sqrt{3}} \left(C_{-3}^6 - C_3^6 \right) - \frac{14}{\sqrt{231}} \left(C_{-6}^6 + C_6^6 \right) \right]$$

$$V^{\text{odd}}(I_h) = 0$$

A3.10.2. *W.r.t. the fivefold rotation axis*

$$V^{\text{even}}(I_h) = B_0^6 \left[C_0^6 + \frac{\sqrt{7}}{\sqrt{11}} \left(C_{-5}^6 - C_5^6 \right) \right]$$

$$V^{\text{odd}}(I_h) = 0$$

Appendix 4. Correlation between Bethe and Mulliken symbols for irreducible representations

The correlation between the Bethe and the Mulliken symbols for the irreducible representations in the non-centrosymmetric point groups is given in the following table. The labels for the centrosymmetric point groups can be found easily by adding the labels *u* and *g* to the Mulliken symbols or + and – to the Bethe symbols of the corresponding point group lacking the inversion center.

	Γ_1	Γ_2	Γ_3	Γ_4	Γ_5	Γ_6
O	A_1	A_2	E	T_1	T_2	–
T_d	A_1	A_2	E	T_1	T_2	–
T	A	E		T	–	–
D_6	A_1	A_2	B_1	B_2	E_1	E_2
C_{6v}	A_1	A_2	B_1	B_2	E_1	E_2
D_{3h}	A_1'	A_2'	A_1''	A_2''	E''	E'
C_6	A	E_2		B	E_1	
C_{3h}	A'	E'		A''	E''	

continued

	Γ_1	Γ_2	Γ_3	Γ_4	Γ_5	Γ_6
D_3	A_1	A_2	E	–	–	–
C_{3v}	A_1	A_2	E	–	–	–
C_3	A	E		–	–	–
D_4	A_1	A_2	B_1	B_2	E	–
C_{4v}	A_1	A_2	B_1	B_2	E	–
D_{2d}	A_1	A_2	B_1	B_2	E	–
C_4	A	B	E		–	–
S_4	A	B	E		–	–
C_{2v}	A_1	B_1	A_2	B_2	–	–
D_2	A	B_2	B_1	B_3	–	–
C_2	A′	A″	–	–	–	–
C_1	A	–	–	–	–	–

Appendix 5. Selection rules for induced electric dipole (ED) and magnetic dipole (MD) transitions

The selection rules for induced electric dipole (ED) and magnetic dipole transitions are presented. The irreducible representations are labelled according to the notations of Koster et al. (1963). The double groups are indicated by an asterisk. The definitions of the polarization directions α, σ, π, x, y, z, R_x, R_y and R_z have been given in sect. 3.3. The selection rules for the orthorhombic, monoclinic and triclinic double groups are not given, because all transitions are allowed. The selection rules for the centrosymmetric point groups are not specifically reported, since these can be easily deduced from the tables of the non-centrosymmetric point groups. The ED selection rules do not have to be considered, since the induced electric dipole transitions for these point groups are strictly forbidden if no vibronic coupling is considered. The MD selection rules for the centrosymmetric point groups are the same as those for the subgroup missing the inversion center, with that difference that each representation becomes a parity label and that only transitions between representations with (+) parity have to be considered. The 11 centrosymmetric point groups with the corresponding non-centrosymmetric point groups (in parentheses) are O_h (O), T_h (T), D_{6h} (D_6), C_{6h} (C_6), D_{4h} (D_4), C_{4h} (C_4), D_{3d} (D_3), C_{3i} (C_3), D_{2h} (D_2), C_{2h} (C_2) and C_i (C_1). There are, of course, also 11 centrosymmetric double groups. For the cubic point groups, only the MD selection rules for O_h are given. ED transition are forbidden and the other cubic point groups are not expected for lanthanide compounds.

A5.1. *Cubic groups*

O_h	MD				
	Γ_1^+	Γ_2^+	Γ_3^+	Γ_4^+	Γ_5^+
Γ_1^+	–	–	–	R_x, R_y, R_z	–
Γ_2^+	–	–	–	–	R_x, R_y, R_z
Γ_3^+	–	–	–	R_x, R_y, R_z	R_x, R_y, R_z
Γ_4^+	R_x, R_y, R_z	–	R_x, R_y, R_z	R_x, R_y, R_z	R_x, R_y, R_z
Γ_5^+	–	R_x, R_y, R_z	R_x, R_y, R_z	R_x, R_y, R_z	R_x, R_y, R_z

O_h^*	MD		
	Γ_6^-	Γ_7^-	Γ_8^-
Γ_6^-	R_x, R_y, R_z	–	R_x, R_y, R_z
Γ_7^-	–	R_x, R_y, R_z	R_x, R_y, R_z
Γ_8^-	R_x, R_y, R_z	R_x, R_y, R_z	R_x, R_y, R_z

A5.2. *Hexagonal groups*

D_6	ED						MD					
	Γ_1	Γ_2	Γ_3	Γ_4	Γ_5	Γ_6	Γ_1	Γ_2	Γ_3	Γ_4	Γ_5	Γ_6
Γ_1	–	π	–	–	α, σ	–	–	σ	–	–	α, π	–
Γ_2	π	–	–	–	α, σ	–	σ	–	–	–	α, π	–
Γ_3	–	–	–	π	–	α, σ	–	–	–	σ	–	α, π
Γ_4	–	–	π	–	–	α, σ	–	–	σ	–	–	α, π
Γ_5	α, σ	α, σ	–	–	π	α, σ	α, π	α, π	–	–	σ	–
Γ_6	–	–	α, σ	α, σ	α, σ	π	α, π	α, π	–	–	–	σ

D_6^*	ED			MD		
	Γ_7	Γ_8	Γ_9	Γ_7	Γ_8	Γ_9
Γ_7	α, σ, π	–	α, σ	α, σ, π	–	α, π
Γ_8	–	α, σ, π	α, σ	–	α, σ, π	α, π
Γ_9	α, σ	α, σ	π	α, π	α, π	σ

C_{6v}	ED						MD					
	Γ_1	Γ_2	Γ_3	Γ_4	Γ_5	Γ_6	Γ_1	Γ_2	Γ_3	Γ_4	Γ_5	Γ_6
Γ_1	π	–	–	–	α, σ	–	–	σ	–	–	α, π	–
Γ_2	–	π	–	–	α, σ	–	σ	–	–	–	α, π	–
Γ_3	–	–	π	–	–	α, σ	–	–	–	σ	–	α, π
Γ_4	–	–	–	π	–	α, σ	–	–	σ	–	–	α, π
Γ_5	α, σ	α, σ	–	–	π	α, σ	α, π	α, π	–	–	σ	–
Γ_6	–	–	α, σ	α, σ	α, σ	π	α, π	α, π	–	–	–	σ

C_{6v}^*	ED			MD		
	Γ_7	Γ_8	Γ_9	Γ_7	Γ_8	Γ_9
Γ_7	α, σ, π	–	α, σ	α, σ, π	–	α, π
Γ_8	–	α, σ, π	α, σ	–	α, σ, π	α, π
Γ_9	α, σ	α, σ	π	α, π	α, π	σ

C_6	ED				MD			
	Γ_1	$\Gamma_{2,3}$	Γ_4	$\Gamma_{5,6}$	Γ_1	$\Gamma_{2,3}$	Γ_4	$\Gamma_{5,6}$
Γ_1	π	–	–	α, σ	σ	–	–	α, π
$\Gamma_{2,3}$	–	α, σ, π	–	–	–	α, σ, π	–	–
Γ_4	–	–	α, σ, π	–	–	–	α, σ, π	–
$\Gamma_{5,6}$	α, σ	–	–	π	α, π	–	–	σ

C_6^*	ED			MD		
	Γ_7	Γ_8	Γ_9	Γ_7	Γ_8	Γ_9
Γ_7	π	α, σ	α, σ	σ	α, π	α, π
Γ_8	α, σ	π	α, σ	α, π	σ	α, π
Γ_9	α, σ	α, σ	π	α, π	α, π	σ

D_{3h}	ED						MD					
	Γ_1	Γ_2	Γ_3	Γ_4	Γ_5	Γ_6	Γ_1	Γ_2	Γ_3	Γ_4	Γ_5	Γ_6
Γ_1	–	–	–	π	–	α, σ	–	σ	–	–	α, π	–
Γ_2	–	–	π	–	–	α, σ	σ	–	–	–	α, π	–
Γ_3	–	π	–	–	α, σ	–	–	–	–	σ	–	α, π
Γ_4	π	–	–	–	α, σ	–	–	–	σ	–	–	α, π
Γ_5	–	–	α, σ	α, σ	α, σ	π	α, π	α, π	–	–	σ	α, π
Γ_6	α, σ	α, σ	–	–	π	α, σ	–	–	α, π	α, π	α, π	σ

D_{3h}^*	ED			MD		
	Γ_7	Γ_8	Γ_9	Γ_7	Γ_8	Γ_9
Γ_7	–	α, π, σ	α, σ	α, σ, π	–	α, π
Γ_8	α, π, σ	–	α, σ	–	α, σ, π	α, π
Γ_9	α, σ	α, σ	π	α, π	α, π	σ

C_{3h}	ED				MD			
	Γ_1	$\Gamma_{2,3}$	Γ_4	$\Gamma_{5,6}$	Γ_1	$\Gamma_{2,3}$	Γ_4	$\Gamma_{5,6}$
Γ_1	–	α, σ	π	–	σ	–	–	α, π
$\Gamma_{2,3}$	α, σ	α, σ	–	π	–	σ	α, π	α, π
Γ_4	π	–	–	α, σ	–	α, π	σ	–
$\Gamma_{5,6}$	–	π	α, σ	α, σ	α, π	α, π	–	σ

C_{3h}^{*}	ED			MD		
	$\Gamma_{7,8}$	$\Gamma_{9,10}$	$\Gamma_{11,12}$	$\Gamma_{7,8}$	$\Gamma_{9,10}$	$\Gamma_{11,12}$
$\Gamma_{7,8}$	–	α, π, σ	α, σ	α, σ, π	–	α, π
$\Gamma_{9,10}$	α, π, σ	–	α, σ	–	α, σ, π	α, π
$\Gamma_{11,12}$	α, σ	α, σ	π	α, π	α, π	σ

A5.3. *Trigonal groups*

C_{3v}	ED			MD		
	Γ_1	Γ_2	Γ_3	Γ_1	Γ_2	Γ_3
Γ_1	π	–	α, σ	–	σ	α, π
Γ_2	–	π	α, σ	σ	–	α, π
Γ_3	α, σ	α, σ	α, σ, π	α, π	α, π	α, σ, π

$C_{3v}*$	ED		MD	
	Γ_4	$\Gamma_{5,6}$	Γ_4	$\Gamma_{5,6}$
Γ_4	α, π, σ	α, σ	α, σ, π	α, π
$\Gamma_{5,6}$	α, σ	π	α, π	σ

D_3	ED			MD		
	Γ_1	Γ_2	Γ_3	Γ_1	Γ_2	Γ_3
Γ_1	–	π	α, σ	–	σ	α, π
Γ_2	π	–	α, σ	σ	–	α, π
Γ_3	α, σ	α, σ	α, σ, π	α, π	α, π	α, σ, π

D_3^*	ED		MD	
	Γ_4	$\Gamma_{5,6}$	Γ_4	$\Gamma_{5,6}$
Γ_4	α, π, σ	α, σ	α, σ, π	α, π
$\Gamma_{5,6}$	α, σ	π	α, π	σ

C_3	ED		MD	
	Γ_1	$\Gamma_{2,3}$	Γ_1	$\Gamma_{2,3}$
Γ_1	π	α, σ	σ	α, π
$\Gamma_{2,3}$	α, σ	α, σ, π	α, π	σ

C_3^*	ED		MD	
	$\Gamma_{4,5}$	Γ_6	$\Gamma_{4,5}$	Γ_6
$\Gamma_{4,5}$	α, π, σ	α, σ	α, σ, π	α, π
Γ_6	α, σ	π	α, π	σ

A5.4. *Tetragonal groups*

D_4	ED					MD				
	Γ_1	Γ_2	Γ_3	Γ_4	Γ_5	Γ_1	Γ_2	Γ_3	Γ_4	Γ_5
Γ_1	–	π	–	–	α, σ	–	σ	–	–	α, π
Γ_2	π	–	–	–	α, σ	σ	–	–	–	α, π
Γ_3	–	–	–	π	α, σ	–	–	–	σ	α, π
Γ_4	–	–	π	–	α, σ	–	–	σ	–	α, π
Γ_5	α, σ	α, σ	α, σ	α, σ	π	α, π	α, π	α, π	α, π	σ

D_4^*	ED		MD	
	Γ_6	Γ_7	Γ_6	Γ_7
Γ_6	α, σ, π	α, σ	α, σ, π	α, π
Γ_7	α, σ	α, σ, π	α, π	α, σ, π

C_{4v}	ED					MD				
	Γ_1	Γ_2	Γ_3	Γ_4	Γ_5	Γ_1	Γ_2	Γ_3	Γ_4	Γ_5
Γ_1	π	–	–	–	α, σ	–	σ	–	–	α, π
Γ_2	–	π	–	–	α, σ	σ	–	–	–	α, π
Γ_3	–	–	π	–	α, σ	–	–	–	σ	α, π
Γ_4	–	–	–	π	α, σ	–	–	σ	–	α, π
Γ_5	α, σ	α, σ	α, σ	α, σ	π	α, π	α, π	α, π	α, π	σ

C_{4v}^*	ED		MD	
	Γ_6	Γ_7	Γ_6	Γ_7
Γ_6	α, σ	α, σ, π	α, σ, π	α, π
Γ_7	α, σ, π	α, σ	α, π	α, σ, π

D_{2d}	ED					MD				
	Γ_1	Γ_2	Γ_3	Γ_4	Γ_5	Γ_1	Γ_2	Γ_3	Γ_4	Γ_5
Γ_1	–	–	–	π	α, σ	–	σ	–	–	α, π
Γ_2	–	–	π	–	α, σ	σ	–	–	–	α, π
Γ_3	–	π	–	–	α, σ	–	–	–	σ	α, π
Γ_4	π	–	–	–	α, σ	–	–	σ	–	α, π
Γ_5	α, σ	α, σ	α, σ	α, σ	π	α, π	α, π	α, π	α, π	σ

D_{2d}^*	ED		MD	
	Γ_6	Γ_7	Γ_6	Γ_7
Γ_6	α, σ	α, σ, π	α, σ, π	α, π
Γ_7	α, σ, π	α, σ	α, π	α, σ, π

S_4	ED			MD		
	Γ_1	Γ_2	$\Gamma_{3,4}$	Γ_1	Γ_2	$\Gamma_{3,4}$
Γ_1	–	π	α, σ	σ	–	α, π
Γ_2	π	–	α, σ	–	σ	α, π
$\Gamma_{3,4}$	α, σ	α, σ	π	α, π	α, π	σ

S_4^*	ED		MD	
	$\Gamma_{5,6}$	$\Gamma_{7,8}$	$\Gamma_{5,6}$	$\Gamma_{7,8}$
$\Gamma_{5,6}$	α, σ	α, σ, π	α, σ, π	α, π
$\Gamma_{7,8}$	α, σ, π	α, σ	α, π	α, σ, π

C_4	ED			MD		
	Γ_1	Γ_2	$\Gamma_{3,4}$	Γ_1	Γ_2	$\Gamma_{3,4}$
Γ_1	π	–	α, σ	σ	–	α, π
Γ_2	–	π	α, σ	–	σ	α, π
$\Gamma_{3,4}$	α, σ	α, σ	π	α, π	α, π	σ

C_4^*	ED		MD	
	$\Gamma_{5,6}$	$\Gamma_{7,8}$	$\Gamma_{5,6}$	$\Gamma_{7,8}$
$\Gamma_{5,6}$	α, σ, π	α, σ	α, σ, π	α, π
$\Gamma_{7,8}$	α, σ	α, σ, π	α, π	α, σ, π

A5.5. *Orthorhombic groups*

D_2	ED				MD			
	Γ_1	Γ_2	Γ_3	Γ_4	Γ_1	Γ_2	Γ_3	Γ_4
Γ_1	–	y	z	x	–	R_y	R_z	R_x
Γ_2	y	–	x	z	R_y	–	R_x	R_z
Γ_3	z	x	–	y	R_z	R_x	–	R_y
Γ_4	x	z	y	–	R_x	R_z	R_y	–

C_{2v}	ED				MD			
	Γ_1	Γ_2	Γ_3	Γ_4	Γ_1	Γ_2	Γ_3	Γ_4
Γ_1	z	x	–	y	–	R_y	R_z	R_x
Γ_2	x	z	y	–	R_y	–	R_x	R_z
Γ_3	–	y	z	x	R_z	R_x	–	R_y
Γ_4	y	–	x	z	R_x	R_z	R_y	–

A5.6. *Monoclinic groups*

C_2	ED		MD	
	Γ_1	Γ_2	Γ_1	Γ_2
Γ_1	z	x,y	R_z	R_x,R_y
Γ_2	x,y	z	R_x,R_y	R_z

C_s	ED		MD	
	Γ_1	Γ_2	Γ_1	Γ_2
Γ_1	x,y	z	R_x,R_y	R_z
Γ_2	z	x,y	R_z	R_x,R_y

A5.7. *Triclinic group*

C_1	ED Γ_1	MD Γ_1
Γ_1	x,y,z	R_x,R_y,R_z

Appendix 6. Full-rotational group compatibility tables

The full-rotational group compatibility tables show how a free-ion J level is broken up into crystal-field levels when the ion is placed in a crystalline environment with a distinct point symmetry. The irreducible representations (irreps) are labelled according to the notations of Koster et al. (1963). The tables are given up to $J=8$ for even-electron systems and up to $J=17/2$ for odd-electron systems. The double groups are marked by an asterisk. Although higher J values may occur for trivalent lanthanide ions, they are of less importance for the study of the energy levels in the ultraviolet, visible and near-infrared parts of the spectra.

O_h		O_h^*	
J	Irreducible representations	J	Irreducible representations
0	Γ_1^+	1/2	Γ_6^-
1	Γ_4^+	3/2	Γ_8^-
2	$\Gamma_3^+ + \Gamma_5^+$	5/2	$\Gamma_7^- + \Gamma_8^-$
3	$\Gamma_2^+ + \Gamma_4^+ + \Gamma_5^+$	7/2	$\Gamma_6^- + \Gamma_7^- + \Gamma_8^-$
4	$\Gamma_1^+ + \Gamma_3^+ + \Gamma_4^+ + \Gamma_5^+$	9/2	$\Gamma_6^- + 2\Gamma_8^-$
5	$\Gamma_3^+ + 2\Gamma_4^+ + \Gamma_5^+$	11/2	$\Gamma_6^- + \Gamma_7^- + 2\Gamma_8^-$
6	$\Gamma_1^+ + \Gamma_2^+ + \Gamma_3^+ + \Gamma_4^+ + 2\Gamma_5^+$	13/2	$\Gamma_6^- + 2\Gamma_7^- + 2\Gamma_8^-$
7	$\Gamma_2^+ + \Gamma_3^+ + 2\Gamma_4^+ + 2\Gamma_5^+$	15/2	$\Gamma_6^- + 2\Gamma_7^- + 3\Gamma_8^-$
8	$\Gamma_1^+ + 2\Gamma_3^+ + 2\Gamma_4^+ + 2\Gamma_5^+$	17/2	$2\Gamma_6^- + \Gamma_7^- + 3\Gamma_8^-$

D_6		D_6^*	
J	Irreducible representations	J	Irreducible representations
0	Γ_1	1/2	Γ_7
1	$\Gamma_2 + \Gamma_5$	3/2	$\Gamma_7 + \Gamma_9$
2	$\Gamma_1 + \Gamma_5 + \Gamma_6$	5/2	$\Gamma_7 + \Gamma_8 + \Gamma_9$
3	$\Gamma_2 + \Gamma_3 + \Gamma_4 + \Gamma_5 + \Gamma_6$	7/2	$\Gamma_7 + 2\Gamma_8 + \Gamma_9$
4	$\Gamma_1 + \Gamma_3 + \Gamma_4 + \Gamma_5 + 2\Gamma_6$	9/2	$\Gamma_7 + 2\Gamma_8 + 2\Gamma_9$
5	$\Gamma_2 + \Gamma_3 + \Gamma_4 + 2\Gamma_5 + 2\Gamma_6$	11/2	$2\Gamma_7 + 2\Gamma_8 + 2\Gamma_9$
6	$2\Gamma_1 + \Gamma_2 + \Gamma_3 + \Gamma_4 + 2\Gamma_5 + 2\Gamma_6$	13/2	$3\Gamma_7 + 2\Gamma_8 + 2\Gamma_9$
7	$\Gamma_1 + 2\Gamma_2 + \Gamma_3 + \Gamma_4 + 3\Gamma_5 + 2\Gamma_6$	15/2	$2\Gamma_7 + 3\Gamma_8 + 3\Gamma_9$
8	$2\Gamma_1 + \Gamma_2 + \Gamma_3 + \Gamma_4 + 3\Gamma_5 + 3\Gamma_6$	17/2	$3\Gamma_7 + 3\Gamma_8 + 3\Gamma_9$

C_{6v}		C_{6v}^*	
J	Irreducible representations	J	Irreducible representations
0	Γ_1	1/2	Γ_7
1	$\Gamma_2 + \Gamma_5$	3/2	$\Gamma_7 + \Gamma_9$
2	$\Gamma_1 + \Gamma_5 + \Gamma_6$	5/2	$\Gamma_7 + \Gamma_8 + \Gamma_9$
3	$\Gamma_2 + \Gamma_3 + \Gamma_4 + \Gamma_5 + \Gamma_6$	7/2	$\Gamma_7 + 2\Gamma_8 + \Gamma_9$
4	$\Gamma_1 + \Gamma_3 + \Gamma_4 + \Gamma_5 + 2\Gamma_6$	9/2	$\Gamma_7 + 2\Gamma_8 + 2\Gamma_9$
5	$\Gamma_2 + \Gamma_3 + \Gamma_4 + 2\Gamma_5 + 2\Gamma_6$	11/2	$2\Gamma_7 + 2\Gamma_8 + 2\Gamma_9$
6	$2\Gamma_1 + \Gamma_2 + \Gamma_3 + \Gamma_4 + 2\Gamma_5 + 2\Gamma_6$	13/2	$3\Gamma_7 + 2\Gamma_8 + 2\Gamma_9$
7	$\Gamma_1 + 2\Gamma_2 + \Gamma_3 + \Gamma_4 + 3\Gamma_5 + 2\Gamma_6$	15/2	$2\Gamma_7 + 3\Gamma_8 + 3\Gamma_9$
8	$2\Gamma_1 + \Gamma_2 + \Gamma_3 + \Gamma_4 + 3\Gamma_5 + 3\Gamma_6$	17/2	$3\Gamma_7 + 3\Gamma_8 + 3\Gamma_9$

D_{3h}		D_{3h}^*	
J	Irreducible representations	J	Irreducible representations
0	Γ_1	1/2	Γ_8
1	$\Gamma_2 + \Gamma_5$	3/2	$\Gamma_8 + \Gamma_9$
2	$\Gamma_1 + \Gamma_5 + \Gamma_6$	5/2	$\Gamma_7 + \Gamma_8 + \Gamma_9$
3	$\Gamma_2 + \Gamma_3 + \Gamma_4 + \Gamma_5 + \Gamma_6$	7/2	$2\Gamma_7 + \Gamma_8 + \Gamma_9$
4	$\Gamma_1 + \Gamma_3 + \Gamma_4 + \Gamma_5 + 2\Gamma_6$	9/2	$2\Gamma_7 + \Gamma_8 + 2\Gamma_9$
5	$\Gamma_2 + \Gamma_3 + \Gamma_4 + 2\Gamma_5 + 2\Gamma_6$	11/2	$2\Gamma_7 + 2\Gamma_8 + 2\Gamma_9$
6	$2\Gamma_1 + \Gamma_2 + \Gamma_3 + \Gamma_4 + 2\Gamma_5 + 2\Gamma_6$	13/2	$2\Gamma_7 + 3\Gamma_8 + 2\Gamma_9$
7	$\Gamma_1 + 2\Gamma_2 + \Gamma_3 + \Gamma_4 + 3\Gamma_5 + 2\Gamma_6$	15/2	$3\Gamma_7 + 2\Gamma_8 + 3\Gamma_9$
8	$2\Gamma_1 + \Gamma_2 + \Gamma_3 + \Gamma_4 + 3\Gamma_5 + 3\Gamma_6$	17/2	$3\Gamma_7 + 3\Gamma_8 + 3\Gamma_9$

C_6		C_6^*	
J	Irreducible representations	J	Irreducible representations
0	Γ_1	1/2	$\Gamma_{7,8}$
1	$\Gamma_1 + \Gamma_{5,6}$	3/2	$\Gamma_{7,8} + \Gamma_{11,12}$
2	$\Gamma_1 + \Gamma_{2,3} + \Gamma_{5,6}$	5/2	$\Gamma_{7,8} + \Gamma_{9,10} + \Gamma_{11,12}$
3	$\Gamma_1 + \Gamma_{2,3} + 2\Gamma_4 + \Gamma_{5,6}$	7/2	$\Gamma_{7,8} + 2\Gamma_{9,10} + \Gamma_{11,12}$
4	$\Gamma_1 + 2\Gamma_{2,3} + 2\Gamma_4 + \Gamma_{5,6}$	9/2	$\Gamma_{7,8} + 2\Gamma_{9,10} + 2\Gamma_{11,12}$
5	$\Gamma_1 + 2\Gamma_{2,3} + 2\Gamma_4 + 2\Gamma_{5,6}$	11/2	$2\Gamma_{7,8} + 2\Gamma_{9,10} + 2\Gamma_{11,12}$
6	$3\Gamma_1 + 2\Gamma_{2,3} + 2\Gamma_4 + 2\Gamma_{5,6}$	13/2	$3\Gamma_{7,8} + 2\Gamma_{9,10} + 2\Gamma_{11,12}$
7	$3\Gamma_1 + 2\Gamma_{2,3} + 2\Gamma_4 + 3\Gamma_{5,6}$	15/2	$2\Gamma_{7,8} + 3\Gamma_{9,10} + 3\Gamma_{11,12}$
8	$3\Gamma_1 + 3\Gamma_{2,3} + 2\Gamma_4 + 3\Gamma_{5,6}$	17/2	$3\Gamma_{7,8} + 3\Gamma_{9,10} + 3\Gamma_{11,12}$

C_{3h}		C_{3h}^*	
J	Irreducible representations	J	Irreducible representations
0	Γ_1	1/2	$\Gamma_{9,10}$
1	$\Gamma_1 + \Gamma_{5,6}$	3/2	$\Gamma_{9,10} + \Gamma_{11,12}$
2	$\Gamma_1 + \Gamma_{2,3} + \Gamma_{5,6}$	5/2	$\Gamma_{7,8} + \Gamma_{9,10} + \Gamma_{11,12}$
3	$\Gamma_1 + \Gamma_{2,3} + 2\Gamma_4 + \Gamma_{5,6}$	7/2	$2\Gamma_{7,8} + \Gamma_{9,10} + \Gamma_{11,12}$
4	$\Gamma_1 + 2\Gamma_{2,3} + 2\Gamma_4 + \Gamma_{5,6}$	9/2	$2\Gamma_{7,8} + \Gamma_{9,10} + 2\Gamma_{11,12}$
5	$\Gamma_1 + 2\Gamma_{2,3} + 2\Gamma_4 + 2\Gamma_{5,6}$	11/2	$2\Gamma_{7,8} + 2\Gamma_{9,10} + 2\Gamma_{11,12}$
6	$3\Gamma_1 + 2\Gamma_{2,3} + 2\Gamma_4 + 2\Gamma_{5,6}$	13/2	$2\Gamma_{7,8} + 3\Gamma_{9,10} + 2\Gamma_{11,12}$
7	$3\Gamma_1 + 2\Gamma_{2,3} + 2\Gamma_4 + 3\Gamma_{5,6}$	15/2	$2\Gamma_{7,8} + 3\Gamma_{9,10} + 3\Gamma_{11,12}$
8	$3\Gamma_1 + 3\Gamma_{2,3} + 2\Gamma_4 + 3\Gamma_{5,6}$	17/2	$3\Gamma_{7,8} + 3\Gamma_{9,10} + 3\Gamma_{11,12}$

D_3		D_3^*	
J	Irreducible representations	J	Irreducible representations
0	Γ_1	1/2	Γ_4
1	$\Gamma_2 + \Gamma_3$	3/2	$\Gamma_4 + \Gamma_{5,6}$
2	$\Gamma_1 + 2\Gamma_3$	5/2	$2\Gamma_4 + \Gamma_{5,6}$
3	$\Gamma_1 + 2\Gamma_2 + 2\Gamma_3$	7/2	$3\Gamma_4 + \Gamma_{5,6}$
4	$2\Gamma_1 + \Gamma_2 + 3\Gamma_3$	9/2	$3\Gamma_4 + 2\Gamma_{5,6}$
5	$\Gamma_1 + 2\Gamma_2 + 4\Gamma_3$	11/2	$4\Gamma_4 + 2\Gamma_{5,6}$
6	$3\Gamma_1 + 2\Gamma_2 + 4\Gamma_3$	13/2	$5\Gamma_4 + 2\Gamma_{5,6}$
7	$2\Gamma_1 + 3\Gamma_2 + 5\Gamma_3$	15/2	$5\Gamma_4 + 3\Gamma_{5,6}$
8	$3\Gamma_1 + 2\Gamma_2 + 6\Gamma_3$	17/2	$6\Gamma_4 + 3\Gamma_{5,6}$

C_{3v}		C_{3v}^*	
J	Irreducible representations	J	Irreducible representations
0	Γ_1	1/2	Γ_4
1	$\Gamma_2 + \Gamma_3$	3/2	$\Gamma_4 + \Gamma_{5,6}$
2	$\Gamma_1 + 2\Gamma_3$	5/2	$2\Gamma_4 + \Gamma_{5,6}$
3	$\Gamma_1 + 2\Gamma_2 + 2\Gamma_3$	7/2	$3\Gamma_4 + \Gamma_{5,6}$
4	$2\Gamma_1 + \Gamma_2 + 3\Gamma_3$	9/2	$3\Gamma_4 + 2\Gamma_{5,6}$
5	$\Gamma_1 + 2\Gamma_2 + 4\Gamma_3$	11/2	$4\Gamma_4 + 2\Gamma_{5,6}$
6	$3\Gamma_1 + 2\Gamma_2 + 4\Gamma_3$	13/2	$5\Gamma_4 + 2\Gamma_{5,6}$
7	$2\Gamma_1 + 3\Gamma_2 + 5\Gamma_3$	15/2	$5\Gamma_4 + 3\Gamma_{5,6}$
8	$3\Gamma_1 + 2\Gamma_2 + 6\Gamma_3$	17/2	$6\Gamma_4 + 3\Gamma_{5,6}$

C_3		C_3^*	
J	Irreducible representations	J	Irreducible representations
0	Γ_1	1/2	$\Gamma_{4,5}$
1	$\Gamma_1 + \Gamma_2 + \Gamma_3$	3/2	$\Gamma_{4,5} + 2\Gamma_6$
2	$\Gamma_1 + 2\Gamma_2 + 2\Gamma_3$	5/2	$2\Gamma_{4,5} + 2\Gamma_6$
3	$3\Gamma_1 + 2\Gamma_2 + 2\Gamma_3$	7/2	$3\Gamma_{4,5} + 2\Gamma_6$
4	$3\Gamma_1 + 3\Gamma_2 + 3\Gamma_3$	9/2	$3\Gamma_{4,5} + 4\Gamma_6$
5	$3\Gamma_1 + 4\Gamma_2 + 3\Gamma_3$	11/2	$4\Gamma_{4,5} + 4\Gamma_6$
6	$5\Gamma_1 + 4\Gamma_2 + 4\Gamma_3$	13/2	$5\Gamma_{4,5} + 4\Gamma_6$
7	$5\Gamma_1 + 5\Gamma_2 + 5\Gamma_3$	15/2	$5\Gamma_{4,5} + 6\Gamma_6$
8	$5\Gamma_1 + 6\Gamma_2 + 6\Gamma_3$	17/2	$6\Gamma_{4,5} + 6\Gamma_6$

D_4		D_4^*	
J	Irreducible representations	J	Irreducible representations
0	Γ_1	1/2	Γ_6
1	$\Gamma_2 + \Gamma_5$	3/2	$\Gamma_6 + \Gamma_7$
2	$\Gamma_1 + \Gamma_3 + \Gamma_4 + \Gamma_5$	5/2	$\Gamma_6 + 2\Gamma_7$
3	$\Gamma_2 + \Gamma_3 + \Gamma_4 + 2\Gamma_5$	7/2	$2\Gamma_6 + 2\Gamma_7$
4	$2\Gamma_1 + \Gamma_2 + \Gamma_3 + \Gamma_4 + 2\Gamma_5$	9/2	$3\Gamma_6 + 2\Gamma_7$
5	$\Gamma_1 + 2\Gamma_2 + \Gamma_3 + \Gamma_4 + 3\Gamma_5$	11/2	$3\Gamma_6 + 3\Gamma_7$
6	$2\Gamma_1 + \Gamma_2 + 2\Gamma_3 + 2\Gamma_4 + 3\Gamma_5$	13/2	$3\Gamma_6 + 4\Gamma_7$
7	$\Gamma_1 + 2\Gamma_2 + 2\Gamma_3 + 2\Gamma_4 + 4\Gamma_5$	15/2	$4\Gamma_6 + 4\Gamma_7$
8	$3\Gamma_1 + 2\Gamma_2 + 2\Gamma_3 + 2\Gamma_4 + 4\Gamma_5$	17/2	$5\Gamma_6 + 4\Gamma_7$

C_{4v}		C_{4v}^{*}	
J	Irreducible representations	J	Irreducible representations
0	Γ_1	1/2	Γ_6
1	$\Gamma_2 + \Gamma_5$	3/2	$\Gamma_6 + \Gamma_7$
2	$\Gamma_1 + \Gamma_3 + \Gamma_4 + \Gamma_5$	5/2	$\Gamma_6 + 2\Gamma_7$
3	$\Gamma_2 + \Gamma_3 + \Gamma_4 + 2\Gamma_5$	7/2	$2\Gamma_6 + 2\Gamma_7$
4	$2\Gamma_1 + \Gamma_2 + \Gamma_3 + \Gamma_4 + 2\Gamma_5$	9/2	$3\Gamma_6 + 2\Gamma_7$
5	$\Gamma_1 + 2\Gamma_2 + \Gamma_3 + \Gamma_4 + 3\Gamma_5$	11/2	$3\Gamma_6 + 2\Gamma_7$
6	$2\Gamma_1 + \Gamma_2 + 2\Gamma_3 + 2\Gamma_4 + 3\Gamma_5$	13/2	$3\Gamma_6 + 4\Gamma_7$
7	$\Gamma_1 + 2\Gamma_2 + 2\Gamma_3 + 2\Gamma_4 + 4\Gamma_5$	15/2	$4\Gamma_6 + 4\Gamma_7$
8	$3\Gamma_1 + 2\Gamma_2 + 2\Gamma_3 + 2\Gamma_4 + 4\Gamma_5$	17/2	$5\Gamma_6 + 4\Gamma_7$

D_{2d}		D_{2d}^{*}	
J	Irreducible representations	J	Irreducible representations
0	Γ_1	1/2	Γ_7
1	$\Gamma_2 + \Gamma_5$	3/2	$\Gamma_6 + \Gamma_7$
2	$\Gamma_1 + \Gamma_3 + \Gamma_4 + \Gamma_5$	5/2	$2\Gamma_6 + \Gamma_7$
3	$\Gamma_2 + \Gamma_3 + \Gamma_4 + 2\Gamma_5$	7/2	$2\Gamma_6 + 2\Gamma_7$
4	$2\Gamma_1 + \Gamma_2 + \Gamma_3 + \Gamma_4 + 2\Gamma_5$	9/2	$2\Gamma_6 + 3\Gamma_7$
5	$\Gamma_1 + 2\Gamma_2 + \Gamma_3 + \Gamma_4 + 3\Gamma_5$	11/2	$3\Gamma_6 + 3\Gamma_7$
6	$2\Gamma_1 + \Gamma_2 + 2\Gamma_3 + 2\Gamma_4 + 3\Gamma_5$	13/2	$4\Gamma_6 + 3\Gamma_7$
7	$\Gamma_1 + 2\Gamma_2 + 2\Gamma_3 + 2\Gamma_4 + 4\Gamma_5$	15/2	$4\Gamma_6 + 4\Gamma_7$
8	$3\Gamma_1 + 2\Gamma_2 + 2\Gamma_3 + 2\Gamma_4 + 4\Gamma_5$	17/2	$4\Gamma_6 + 5\Gamma_7$

C_4		C_4^{*}	
J	Irreducible representations	J	Irreducible representations
0	Γ_1	1/2	$\Gamma_{5,6}$
1	$\Gamma_1 + \Gamma_{3,4}$	3/2	$\Gamma_{5,6} + \Gamma_{7,8}$
2	$\Gamma_1 + 2\Gamma_2 + \Gamma_{3,4}$	5/2	$\Gamma_{5,6} + 2\Gamma_{7,8}$
3	$\Gamma_1 + 2\Gamma_2 + 2\Gamma_{3,4}$	7/2	$2\Gamma_{5,6} + 2\Gamma_{7,8}$
4	$3\Gamma_1 + 2\Gamma_2 + 2\Gamma_{3,4}$	9/2	$3\Gamma_{5,6} + 2\Gamma_{7,8}$
5	$3\Gamma_1 + 2\Gamma_2 + 3\Gamma_{3,4}$	11/2	$3\Gamma_{5,6} + 3\Gamma_{7,8}$
6	$3\Gamma_1 + 4\Gamma_2 + 3\Gamma_{3,4}$	13/2	$3\Gamma_{5,6} + 4\Gamma_{7,8}$
7	$3\Gamma_1 + 4\Gamma_2 + 4\Gamma_{3,4}$	15/2	$4\Gamma_{5,6} + 4\Gamma_{7,8}$
8	$5\Gamma_1 + 4\Gamma_2 + 4\Gamma_{3,4}$	17/2	$5\Gamma_{5,6} + 4\Gamma_{7,8}$

S_4		S_4^*	
J	Irreducible representations	J	Irreducible representations
0	Γ_1	1/2	$\Gamma_{7,8}$
1	$\Gamma_1 + \Gamma_{3,4}$	3/2	$\Gamma_{5,6} + \Gamma_{7,8}$
2	$\Gamma_1 + 2\Gamma_2 + \Gamma_{3,4}$	5/2	$2\Gamma_{5,6} + \Gamma_{7,8}$
3	$\Gamma_1 + 2\Gamma_2 + 2\Gamma_{3,4}$	7/2	$2\Gamma_{5,6} + 2\Gamma_{7,8}$
4	$3\Gamma_1 + 2\Gamma_2 + 2\Gamma_{3,4}$	9/2	$2\Gamma_{5,6} + 3\Gamma_{7,8}$
5	$3\Gamma_1 + 2\Gamma_2 + 3\Gamma_{3,4}$	11/2	$3\Gamma_{5,6} + 3\Gamma_{7,8}$
6	$3\Gamma_1 + 4\Gamma_2 + 3\Gamma_{3,4}$	13/2	$4\Gamma_{5,6} + 3\Gamma_{7,8}$
7	$3\Gamma_1 + 4\Gamma_2 + 4\Gamma_{3,4}$	15/2	$4\Gamma_{5,6} + 4\Gamma_{7,8}$
8	$5\Gamma_1 + 4\Gamma_2 + 4\Gamma_{3,4}$	17/2	$4\Gamma_{5,6} + 5\Gamma_{7,8}$

D_2		D_2^*	
J	Irreducible representations	J	Irreducible representations
0	Γ_1	1/2	Γ_5
1	$\Gamma_2 + \Gamma_3 + \Gamma_4$	3/2	$2\Gamma_5$
2	$2\Gamma_1 + \Gamma_2 + \Gamma_3 + \Gamma_4$	5/2	$3\Gamma_5$
3	$\Gamma_1 + 2\Gamma_2 + 2\Gamma_3 + 2\Gamma_4$	7/2	$4\Gamma_5$
4	$3\Gamma_1 + 2\Gamma_2 + 2\Gamma_3 + 2\Gamma_4$	9/2	$5\Gamma_5$
5	$2\Gamma_1 + 3\Gamma_2 + 3\Gamma_3 + 3\Gamma_4$	11/2	$6\Gamma_5$
6	$4\Gamma_1 + 3\Gamma_2 + 3\Gamma_3 + 3\Gamma_4$	13/2	$7\Gamma_5$
7	$3\Gamma_1 + 4\Gamma_2 + 4\Gamma_3 + 4\Gamma_4$	15/2	$8\Gamma_5$
8	$5\Gamma_1 + 4\Gamma_2 + 4\Gamma_3 + 4\Gamma_4$	17/2	$9\Gamma_5$

C_{2v}		C_{2v}^*	
J	Irreducible representations	J	Irreducible representations
0	Γ_1	1/2	Γ_5
1	$\Gamma_2 + \Gamma_3 + \Gamma_4$	3/2	$2\Gamma_5$
2	$2\Gamma_1 + \Gamma_2 + \Gamma_3 + \Gamma_4$	5/2	$3\Gamma_5$
3	$\Gamma_1 + 2\Gamma_2 + 2\Gamma_3 + 2\Gamma_4$	7/2	$4\Gamma_5$
4	$3\Gamma_1 + 2\Gamma_2 + 2\Gamma_3 + 2\Gamma_4$	9/2	$5\Gamma_5$
5	$2\Gamma_1 + 3\Gamma_2 + 3\Gamma_3 + 3\Gamma_4$	11/2	$6\Gamma_5$
6	$4\Gamma_1 + 3\Gamma_2 + 3\Gamma_3 + 3\Gamma_4$	13/2	$7\Gamma_5$
7	$3\Gamma_1 + 4\Gamma_2 + 4\Gamma_3 + 4\Gamma_4$	15/2	$8\Gamma_5$
8	$5\Gamma_1 + 4\Gamma_2 + 4\Gamma_3 + 4\Gamma_4$	17/2	$9\Gamma_5$

C_2		C_2^*	
J	Irreducible representations	J	Irreducible representations
0	Γ_1	1/2	$\Gamma_{3,4}$
1	$\Gamma_1 + 2\Gamma_2$	3/2	$2\Gamma_{3,4}$
2	$3\Gamma_1 + 2\Gamma_2$	5/2	$3\Gamma_{3,4}$
3	$3\Gamma_1 + 4\Gamma_2$	7/2	$4\Gamma_{3,4}$
4	$5\Gamma_1 + 4\Gamma_2$	9/2	$5\Gamma_{3,4}$
5	$5\Gamma_1 + 6\Gamma_2$	11/2	$6\Gamma_{3,4}$
6	$7\Gamma_1 + 6\Gamma_2$	13/2	$7\Gamma_{3,4}$
7	$7\Gamma_1 + 8\Gamma_2$	15/2	$8\Gamma_{3,4}$
8	$9\Gamma_1 + 8\Gamma_2$	17/2	$9\Gamma_{3,4}$

C_s		C_s^*	
J	Irreducible representations	J	Irreducible representations
0	Γ_1	1/2	$\Gamma_{3,4}$
1	$\Gamma_1 + 2\Gamma_2$	3/2	$2\Gamma_{3,4}$
2	$3\Gamma_1 + 2\Gamma_2$	5/2	$3\Gamma_{3,4}$
3	$3\Gamma_1 + 4\Gamma_2$	7/2	$4\Gamma_{3,4}$
4	$5\Gamma_1 + 4\Gamma_2$	9/2	$5\Gamma_{3,4}$
5	$5\Gamma_1 + 6\Gamma_2$	11/2	$6\Gamma_{3,4}$
6	$7\Gamma_1 + 6\Gamma_2$	13/2	$7\Gamma_{3,4}$
7	$7\Gamma_1 + 8\Gamma_2$	15/2	$8\Gamma_{3,4}$
8	$9\Gamma_1 + 8\Gamma_2$	17/2	$9\Gamma_{3,4}$

C_1		C_1^*	
J	Irreducible representations	J	Irreducible representations
0	Γ_1	1/2	Γ_2
1	$3\Gamma_1$	3/2	$2\Gamma_2$
2	$5\Gamma_1$	5/2	$3\Gamma_2$
3	$7\Gamma_1$	7/2	$4\Gamma_2$
4	$9\Gamma_1$	9/2	$5\Gamma_2$
5	$11\Gamma_1$	11/2	$6\Gamma_2$
6	$13\Gamma_1$	13/2	$7\Gamma_2$
7	$15\Gamma_1$	15/2	$8\Gamma_2$
8	$17\Gamma_1$	17/2	$9\Gamma_2$

References

Aamili, A., R. Mahiou, C. Linarès, D. Zambon, D. Avignant and J.C. Cousseins, 1991, J. Solid State Chem. **95**, 307.

Abdulsabirov, R.Y., A.V. Vinokurov, V.A. Ivanshin, I.N. Kurkin, E.A. Pudovik, A.L. Stolov and S.I. Yagudin, 1987, Opt. Spectrosc. (USSR) **63**, 55.

Abragam, A., and B. Bleaney, 1970, Electron Paramagnetic Resonance of Transition Ions (Clarendon Press, Oxford).

Adam, J.L., W.A. Sibley and D.R. Gabbe, 1985, J. Lumin. **33**, 391.

Aizenberg, I.B., F.Z. Gil'fanov and A.L. Stolov, 1966, Sov. Phys. J. **9**, 29.

Allik, T.H., S.A. Stewart, D.K. Sardar, G.J. Quarles, R.C. Powell, C.A. Morrison, G.A. Turner, M.R. Kokta, W.W. Hovis and A.A. Pinto, 1988, Phys. Rev. B **37**, 9129.

Allik, T.H., C.A. Morrison, J.B. Gruber and M.R. Kokta, 1990, Phys. Rev. B **41**, 21.

Alves, R.V., J.J. Pearson, K.A. Wickersheim and R.A. Buchanan, 1970, in: Proc. 8th RERC, April 19–22, Reno, NV, p. 703.

Alves, R.V., R.A. Buchanan, K.A. Wickersheim and E.A. Yates, 1971, J. Appl. Phys. **42**, 3043.

Amberger, H.-D., 1978a, Z. Anorg. Allg. Chem. **439**, 48.

Amberger, H.-D., 1978b, Inorg. Nucl. Chem. Lett. **14**, 491.

Amberger, H.-D., 1980, Z. Anorg. Allg. Chem. **467**, 231.

Amberger, H.-D., and W. Jahn, 1984, Spectrochim. Acta A **40**, 1025.

Amberger, H.-D., and H. Schultz, 1991, Spectrochim. Acta A **47**, 233.

Amberger, H.-D., and K. Yünlü, 1986, Spectrochim. Acta A **42**, 393.

Amberger, H.-D., R.D. Fischer and G.G. Rosenbauer, 1975, Ber. Bunsenges. Physik. Chem. **79**, 1226.

Amberger, H.-D., G.G. Rosenbauer and R.D. Fischer, 1976, Mol. Phys. **32**, 1291.

Amberger, H.-D., G.G. Rosenbauer and R.D. Fischer, 1977, J. Chem. Phys. Solids **38**, 379.

Amberger, H.-D., W. Jahn and N.M. Edelstein, 1985, Spectrochim. Acta A **41**, 465.

Amberger, H.-D., K. Yünlü and N.M. Edelstein, 1986a, Spectrochim. Acta A **42**, 27.

Amberger, H.-D., H. Schultz and N.M. Edelstein, 1986b, Spectrochim. Acta A **42**, 657.

Amberger, H.-D., C. Hagen, G. Shalimoff and N.M. Edelstein, 1992, Spectrochim. Acta A **48**, 1107.

Aminov, L.K., A.A. Kaminskii and M.I. Chertanov, 1985, Phys. Status Solidi b **130**, 757.

Anderson, F.G., P.L. Summers, H. Weidner, P. Hong and R.E. Peale, 1994, Phys. Rev. B **50**, 14802.

Antic, E., M. Lemaître-Blaise and P. Caro, 1975, C.R. Acad. Sci. Paris **280**, C407.

Antic-Fidancev, E., M. Lemaître-Blaise, L. Beaury, G. Teste de Sagey and P. Caro, 1980, J. Chem. Phys. **73**, 4613.

Antic-Fidancev, E., M. Lemaître-Blaise and P. Caro, 1982, J. Chem. Phys. **76**, 2906.

Antic-Fidancev, E., M. Lemaître-Blaise, P. Caro and J.-C. Krupa, 1987a, Inorg. Chim. Acta **139**, 281.

Antic-Fidancev, E., M. Lemaître-Blaise and P. Caro, 1987b, New. J. Chem. **11**, 467.

Antic-Fidancev, E., M. Lemaître-Blaise, P. Caro, P. Porcher and J.-C. Krupa, 1989, J. Less-Common Met. **148**, 167.

Antic-Fidancev, E., M. Lemaître-Blaise, P. Porcher and J. Hölsä, 1991a, J. Chem. Soc. Faraday Trans. **87**, 3625.

Antic-Fidancev, E., J. Hölsä, M. Lemaître-Blaise and P. Porcher, 1991b, J. Phys.: Condens. Matter **3**, 6829.

Antic-Fidancev, E., J. Aride, M. Lemaître-Blaise, P. Porcher and M. Taibi, 1992a, J. Alloys & Compounds **188**, 242.

Antic-Fidancev, E., J. Hölsä, J.-C. Krupa, M. Lemaître-Blaise and P. Porcher, 1992b, J. Phys. Condens. Matter **4**, 8321.

Antic-Fidancev, E., J. Aride, J.-P. Chaminade, M. Lemaître-Blaise and P. Porcher, 1992c, J. Solid State Chem. **97**, 74.

Antic-Fidancev, E., M. Lemaître-Blaise and P. Porcher, 1994a, J. Alloys & Compounds **207/208**, 90.

Antic-Fidancev, E., K. Serhan, M. Taibi, M. Lemaître-Blaise, P. Porcher, J. Aride and A. Boukhari, 1994b, J. Phys.: Condens. Matter **6**, 6852.

Antic-Fidancev, E., M. Lemaître-Blaise, P. Porcher, N. Mercier and M. Leblanc, 1995a, J. Solid State Chem. **116**, 286.

Antic-Fidancev, E., M. Lemaître-Blaise, J.-P. Chaminade and P. Porcher, 1995b, J. Alloys & Compounds **225**, 95.

Antipenko, B.M., S.P. Voronin, S.N. Gifeisman, R.V. Dubravyanu, Y.E. Perlin, T.A. Privalova and O.B. Raba, 1985, Opt. Spectrosc. (USSR) **58**, 780.

Antipenko, B.M., S.I. Boldyrev, S.P. Voronin, Y.E. Perlin and T.A. Privalova, 1986, Opt. Spectrosc. (USSR) **60**, 470.

Antonov, V.A., and P.A. Arsenev, 1975, Z. Prikl. Spektrosk. **22**, 341.

Antonov, V.A., P.A. Arsenev, K.E. Bienert and A.V. Potemkim, 1973, Phys. Status Solidi a **19**, 289.

Antonov, V.A., P.A. Arsenev and D.S. Petrova, 1977a, Phys. Status Solidi a **41**, K127.

Antonov, V.A., P.A. Arsenev, S.A. Vakhidov, E.M. Ibragimova and D.S. Petrova, 1977b, Phys. Status Solidi a **41**, 45.

Antonov, V.A., P.A. Arsenev, A.A. Evdokimov, E.K. Kopylova, A.M. Starikov and K.G. Tadzhi-Aglaev, 1986, Opt. Spectrosc. (USSR) **60**, 57.

Aoyagi, K., K. Tsushima and M. Vesugi, 1969, J. Phys. Soc. Jpn. **27**, 49.

Argyle, B.E., R.L. Wadsack and R.K. Chang, 1971, J. Appl. Phys. **42**, 1478.

Arizmendi, L., and J.M. Cabrera, 1985, Phys. Rev. B **31**, 7138.

Arsenev, P.A., and K.E. Bienert, 1972a, Phys. Status Solidi a **10**, K85.

Arsenev, P.A., and K.E. Bienert, 1972b, Phys. Status Solidi a **13**, K125.

Arsenev, P.A., and K.E. Bienert, 1972c, Phys. Status Solidi a **13**, K129.

Arsenev, P.A., and K.E. Bienert, 1974, J. Appl. Spectrosc. (USSR) **17**, 1623.

Arsenev, P.A., K.E. Bienert and A.V. Potemkin, 1974, Phys. Status Solidi a **26**, K113.

Asano, M., and J.A. Koningstein, 1979, Chem. Phys. **42**, 369.

Ashurov, M.K., Y.K. Voron'ko, V.V. Osiko, A.A. Sobol', B.P. Starikov, M.I. Timoshechkin and A.Y. Yablonskii, 1976, Phys. Status Solidi a **35**, 645.

Ashurov, M.K., Y.K. Voron'ko, E.V. Zharikov, A.A. Kaminskii, V.V. Osiko, A.A. Sobol', M.I. Timoshechkin, V.A. Federov and A.A. Shabaltal, 1979, Inorg. Mater. (USSR) **15**, 979.

Auzel, F., 1979, Mater. Res. Bull. **14**, 223.

Auzel, F., and O.L. Malta, 1983, J. Phys. (France) **44**, 201.

Axe, J.D., 1964, Phys. Rev. **136**, A42.

Axe, J.D., and G.H. Dieke, 1962, J. Chem. Phys. **37**, 2364.

Azamatov, Z.T., P.A. Arsenev and M.V. Chukichev, 1970, Sov. Phys. Crystallogr. **15**, 713.

Babaev, M.M., G.M. Niftiev and B.G. Tagiev, 1989, Opt. Spectrosc. (USSR) **66**, 766.

Babkina, T.V., M.I. Gaiduk, L.N. Zorina and N.P. Soshin, 1974, Opt. Spectrosc. (USSR) **37**, 401.

Baer, W., J.G. Conway and S.P. Davis, 1973, J. Chem. Phys. **59**, 2294.

Bagdasarov, K.S., G.A. Bogomolova, M.M. Gritsenko, A.A. Kaminskii, A.M. Kevorkov, A.M. Prokhorov and S.E. Sarkisov, 1974, Sov. Phys. Dokl. **19**, 353.

Bagdasarov, K.S., G.A. Bogomolova, A.A. Kaminskii, A.M. Kevorkov, L. Li, A.M. Prokhorov and S.E. Sarkisov, 1975a, Sov. Phys. Dokl. **19**, 584.

Bagdasarov, K.S., A.A. Kaminskii, A.M. Kevorkov and A.M. Prokhorov, 1975b, Sov. Phys. Dokl. **19**, 671.

Bagdasarov, K.S., A.A. Kaminskii, A.M. Kevorkov, L. Li, A.M. Prokhorov, T.A. Tevosyan and S.E. Sarkisov, 1975c, Sov. Phys. Dokl. **20**, 681.

Balasubramanian, G., M.M. Islam and D.J. Newman, 1975, J. Phys. B **8**, 2601.

Banerjee, A.K., and R.W. Schwartz, 1981, Chem. Phys. **58**, 255.

Barakat, M., and C.B.P. Finn, 1988, J. Phys. C **21**, 6123.

Barthem, R.B., R. Buisson, F. Madeores, J.C. Vial and J.P. Chaminade, 1987, J. Phys. (Paris) **48**, 379.

Barthem, R.B., R. Buisson and R.L. Cone, 1989, J. Chem. Phys. **91**, 627.

Barthou, C., and R.B. Barthem, 1990, J. Lumin. **46**, 9.

Bayerer, R., J. Heber and D. Mateika, 1986, Z. Phys. B **64**, 201.

Beaury, L., 1988, Ph.D. Thesis (Université de Paris-Sud, Orsay).

Beaury, L., and P. Caro, 1990, J. Phys. (France) **51**, 471.

Beaury, O., M. Faucher and P. Caro, 1978, Mat. Res. Bull. **13**, 175.

Becker, P.C., T. Hayhurst, G. Shalimoff, J.G. Conway, N.M. Edelstein, L.A. Boatner and M.M. Abraham, 1984, J. Chem. Phys. **81**, 2872.

Becker, P.J., H.G. Kahle and D. Kuse, 1969, Phys. Status Solidi **36**, 695.

Becquerel, J., 1907, Le Radium **4**, 328.

Becquerel, J., and H. Kamerlingh Onnes, 1908, Proc. Acad. Amsterdam **10**, 592.

Becquerel, J., H. Kamerlingh Onnes and W.J. de Haas, 1925, Comm. Leiden **177**.

Beitz, J.V., 1994, Similarities and differences in trivalent lanthanide-ion and actinide-ion solution absorption spectra and luminescence, in: Handbook on the Physics and Chemistry of Rare Earths,

Vol. 18, eds K.A. Gschneidner Jr, L. Eyring, G.R. Choppin and G.H. Lander (North-Holland, Amsterdam) ch. 120, p. 159.

Bel'skii, N.K., and Y.T. Struchkov, 1965, Sov. Phys. Crystall. **10**, 15.

Belyaeva, A.I., V.N. Pavlov and A.V. Antonov, 1969, Opt. Spectrosc. (USSR) **27**, 151.

Berdowski, P.A.M., M.J.J. Lammers and G. Blasse, 1985, J. Chem. Phys. **83**, 476.

Berenberg, V.A., A.O. Ivanov, L.I. Krutova, I.V. Mochalov and V.S. Terpugov, 1984, Opt. Spectrosc. (USSR) **57**, 274.

Berg, J.L., 1973, M.S. Thesis (Air Force Institute of Technology, Wright Patterson Air Force Base, OH).

Bernal, E.G., 1971, J. Chem. Phys. **55**, 2538.

Berry, M.T., and F.S. Richardson, 1989, Mol. Phys. **66**, 703.

Berry, M.T., C. Schwieters and F.S. Richardson, 1988, Chem. Phys. **122**, 105.

Berry, M.T., A.F. Kirby and F.S. Richardson, 1989, Mol. Phys. **66**, 723.

Bethe, H.A., 1929, Ann. Phys. **3**, 133.

Bhola, V.P., 1975, Phys. Status Solidi b **68**, 667.

Bihari, B., K. Sharma and L.E. Erickson, 1990, J. Phys.: Condens. Matter **2**, 5703.

Binnemans, K., and C. Görller-Walrand, 1995a, in: Proc. 3rd Int. Conf. on Rare Earth Development and Applications, Batou, Inner-Mongolia, China, 21–25 August 1995, organized by the Chinese Society of Rare Earths (Metallurgical Industry Press, Beijing) pp. 202–205.

Binnemans, K., and C. Görller-Walrand, 1995b, Chem. Phys. Lett. **245**, 75.

Binnemans, K., and C. Görller-Walrand, 1996a, J. Phys.: Condens. Matter **8**, 1267.

Binnemans, K., and C. Görller-Walrand, 1996b, J. Chem. Soc. Faraday Trans. **92**, 2487.

Bischoff, H., B. Pilawi, A. Kasten and H.G. Kahle, 1991, J. Phys.: Condens. Matter **3**, 10057.

Blanc, J., D. Brochier and A. Ribeyron, 1970, Phys. Lett. **33A**, 201.

Blasse, G., 1979, Chemistry and physics of R-activated phosphors, in: Handbook on the Physics and Chemistry of Rare Earths, Vol. 4, eds K.A. Gschneidner Jr and L. Eyring (North-Holland, Amsterdam) ch. 34, p. 237.

Blasse, G., A. Wolfert and G.L. McPherson, 1985, J. Solid State Chem. **57**, 396.

Bleijenberg, K.C., F.A. Kellendonk and C.W. Struck, 1980, J. Chem. Phys. **73**, 3586.

Blinde, D.R., 1974, M.S. Thesis (Iowa State University).

Bloembergen, N., 1984, J. Lumin. **31&32**, 23.

Boal, D., P. Grünberg and J.A. Koningstein, 1973, Phys. Rev. B **7**, 4757.

Bogomolova, G.A., D.N. Vylegzhanin and A.A. Kaminskii, 1976, Sov. Phys. JETP **42**, 440.

Bogomolova, G.A., L.A. Bumagina, A.A. Kaminskii and B.Z. Malkin, 1977, Sov. Phys. Solid State **19**, 1428.

Bolender, J.P., D.H. Metcalf and F.S. Richardson, 1992, J. Alloys & Compounds **180**, 177.

Bouazaoui, M., B. Jacquier, C. Linarès, W. Stręk and R.L. Cone, 1991a, J. Lumin. **48&49**, 318.

Bouazaoui, M., B. Jacquier, C. Linarès and W. Stręk, 1991b, J. Phys.: Condens. Matter **3**, 921.

Brecher, C., 1974, J. Chem. Phys. **61**, 2297.

Brecher, C., H. Samelson, A. Lempicki, R. Riley and T. Peters, 1967, Phys. Rev. **155**, 178.

Brecher, C., H. Samelson, R. Riley and A. Lempicki, 1968, J. Chem. Phys. **49**, 3303.

Briffaut, J.P., and J.P. Denis, 1970, Phys. Status Solidi b **41**, 781.

Brown, E.A., 1980, Harry Diamond Laboratories Reports TR-1932 and TR-1934.

Brown, M.R., K.G. Roots and W.A. Shand, 1969, J. Phys. C **2**, 593.

Buchanan, R.A., H.E. Rast and H.H. Caspers, 1966, J. Chem. Phys. **44**, 4063.

Buchanan, R.A., K.A. Wickersheim, J.J. Pearson and G.F. Herrmann, 1967, Phys. Rev. **159**, 245.

Buchanan, R.A., J.J. Pearson and G.F. Herrmann, 1969, Solid State Comm. 7, 195.

Bumagina, L.A., B.N. Kazakov, B.Z. Malkin and A.L. Stolov, 1977, Sov. Phys. Solid State **19**, 624.

Bünzli, J.-C.G., 1989, Luminescent probes, in: Lanthanide Probes in Life, Chemical and Earth Sciences, eds J.-C.G. Bünzli and G.R. Choppin (Elsevier, Amsterdam) p. 219.

Bünzli, J.-C.G., and G.-O. Pradervand, 1986, J. Chem. Phys. **85**, 2489.

Bünzli, J.-C.G., B. Klein, G. Chapuis and K.J. Schenk, 1982, Inorg. Chem. **21**, 808.

Burdett, J.K., R. Hoffmann and R.C. Fay, 1978, Inorg. Chem. **17**, 2553.

Burdick, G.W., C.K. Jayasankar, F.S. Richardson and M.F. Reid, 1994, Phys. Rev. B **50**, 16309.

Capobianco, J.A., P.P. Proulx, N. Raspa, D.J. Simkin and D. Krashkevich, 1970, J. Chem. Phys. **90**, 2857.

Capobianco, J.A., P.P. Proulx and N. Raspa, 1989, Chem. Phys. Lett. **161**, 151.

Carnall, W.T., 1979, The absorption and fluorescence spectra of rare earth ions in solution, in: Handbook on the Physics and Chemistry of Rare Earths, Vol. 3, eds K.A. Gschneidner Jr and L. Eyring (North-Holland, Amsterdam) ch. 24.

Carnall, W.T., and H. Crosswhite, 1983, J. Less-Common Met. **93**, 127.

Carnall, W.T., P.R. Fields and R. Sarup, 1969, J. Chem. Phys. **51**, 2587.

Carnall, W.T., P.R. Fields, J. Morrison and R. Sarup, 1970, J. Chem. Phys. **52**, 4054.

Carnall, W.T., P.R. Fields and R. Sarup, 1971, J. Chem. Phys. **54**, 1476.

Carnall, W.T., P.R. Fields and R. Sarup, 1972, J. Chem. Phys. **57**, 43.

Carnall, W.T., H. Crosswhite, H.M. Crosswhite and J.G. Conway, 1976, J. Chem. Phys. **64**, 3582.

Carnall, W.T., H. Crosswhite and H.M. Crosswhite, 1977, Energy Level Structure and Transition Probabilities in the Spectra of the Trivalent Lanthanides in LaF_3 (Argonne National Laboratory, Argonne, IL).

Carnall, W.T., G.L. Goodman, R.S. Rana, G.M. Jursich, R.S. Rana, P. Vandevelde, L. Fluyt and C. Görller-Walrand, 1987, Inorg. Chim. Acta **139**, 275.

Carnall, W.T., G.L. Goodman, K. Rajnak and R.S. Rana, 1988, A Systematic Analysis of the Spectra of the Lanthanides Doped into Single Crystal LaF_3, ANL-88-8 report (Argonne National Laboratory, Argonne, IL).

Carnall, W.T., G.L. Goodman, K. Rajnak and R.S. Rana, 1989, J. Chem. Phys. **90**, 3443.

Caro, P., 1976, Structure Electronique des Elements de Transition (PUF, Paris).

Caro, P., O. Beaury and E. Antic, 1976, J. Phys. (France) **37**, 671.

Caro, P., E. Antic, L. Beaury, O. Beaury, J. Derouet, M. Faucher, C. Guttel, O.K. Moune and P. Porcher, 1977a, Colloq. CNRS **255**, 71.

Caro, P., D.-R. Svoronos, E. Antic and M. Quarton, 1977b, J. Chem. Phys. **66**, 5284.

Caro, P., J. Derouet, L. Beaury, G. Teste de Sagey, J.P. Chaminade, J. Aride and M. Pouchard, 1981, J. Chem. Phys. **74**, 2698.

Cascales, C., E. Antic-Fidancev, M. Lemaître-Blaise and P. Porcher, 1992a, J. Solid State Chem. **89**, 118.

Cascales, C., E. Antic-Fidancev, M. Lemaître-Blaise and P. Porcher, 1992b, J. Phys.: Condens. Matter **4**, 2721.

Caspers, H.H., and H.E. Rast, 1975, J. Lumin. **10**, 347.

Caspers, H.H., H.E. Rast and R.A. Buchanan, 1965a, J. Chem. Phys. **42**, 3214.

Caspers, H.H., H.E. Rast and R.A. Buchanan, 1965b, J. Chem. Phys. **43**, 2124.

Caspers, H.H., H.E. Rast and J.L. Fry, 1967, J. Chem. Phys. **47**, 4505.

Caspers, H.H., S.A. Miller, H.E. Rast and J.L. Fry, 1969, Phys. Rev. **180**, 329.

Caspers, H.H., H.E. Rast and J.L. Fry, 1970, J. Chem. Phys. **53**, 3208.

Ceulemans, A., and G.M. Vandenberghe, 1993, J. Chem. Phys. **98**, 9372.

Ceulemans, A., and G.M. Vandenberghe, 1994, J. Alloys & Compounds **207/208**, 102.

Chaminade, J.P., R.M. McFarlane, F. Ramaz and J.C. Vial, 1991, J. Lumin. **48/49**, 531.

Chang, N.C., 1963, J. Appl. Phys. **34**, 3500.

Chang, N.C., 1966, J. Chem. Phys. **44**, 4044.

Chang, N.C., and J.B. Gruber, 1970, J. Chem. Phys. **41**, 3227.

Chang, N.C., J.B. Gruber, R.P. Leavitt and C.A. Morrison, 1982, J. Chem. Phys. **76**, 3877.

Chase, L.L., and S.A. Payne, 1986, Phys. Rev. B **34**, 8883.

Chateau, C., and J. Hölsä, 1985, J. Less-Common Met. **112**, 131.

Chateau, C., J. Hölsä and P. Porcher, 1990a, Z. Phys. Chem. Neue Folge **166**, 211.

Chateau, C., J. Hölsä and P. Porcher, 1990b, J. Chem. Soc. Dalton Trans., p. 1579.

Cheng, C., and P.B. Dorain, 1976, J. Chem. Phys. **65**, 785.

Chirico, R.D., E.F. Westrum Jr, J.B. Gruber and J. Warmkessel, 1979, J. Chem. Thermodyn. **11**, 835.

Chivian, J.S., N.J. Krasutsky and W.E. Case, 1979, J. Opt. Soc. Am. **69**, 1622.

Christensen, H.P., 1978, Phys. Rev. B **17**, 4060.

Christensen, H.P., 1979, Phys. Rev. B **19**, 6573.

Chrysochoos, J., 1983, J. Less-Common Met. **93**, 73.

Clifton, J.R., M. Gruen and A. Ron, 1971, J. Mol. Spectrosc. **39**, 202.

Cockcroft, N.J., G.D. Jones and R.W.G. Syme, 1989, J. Lumin. **43**, 275.

Cockcroft, N.J., G.D. Jones and D.C. Nguyen, 1992, Phys. Rev. B **45**, 5187.

Cone, R.L., 1972, J. Chem. Phys. **57**, 4893.

Cone, R.L., and R. Faulhaber, 1971, J. Chem. Phys. **55**, 5198.
Conway, J.G., J.-C. Krupa, P. Delamoye and M. Genet, 1981, J. Chem. Phys. **74**, 849.
Cordero-Montalvo, C.D., 1985, Phys. Rev. B **31**, 5433.
Cordero-Montalvo, C.D., and N. Bloembergen, 1984, Phys. Rev. B **30**, 438.
Cordero-Montalvo, C.D., and N. Bloembergen, 1985, Phys. Rev. B **31**, 613.
Cotton, F.A., 1971, Chemical Applications of Group Theory, 2nd Ed. (Wiley-Interscience, New York).
Countryman, R., and W.S. McDonald, 1971, J. Inorg. Nucl. Chem. **33**, 2213.
Couture, L., and A. Le Paillier-Malécot, 1984, Chem. Phys. **85**, 307.
Couture, L., and K. Rajnak, 1984, Chem. Phys. **85**, 315.
Crosswhite, H.M., and H. Crosswhite, 1984, J. Opt. Soc. Am. B **1**, 246.
Crosswhite, H.M., and G.H. Dieke, 1961, J. Chem. Phys. **35**, 1535.
Crosswhite, H.M., H. Crosswhite, F.W. Kaseta and R. Sarup, 1976, J. Chem. Phys. **64**, 1981.
Crosswhite, H.M., H. Crosswhite, N. Edelstein and K. Rajnak, 1977, J. Chem. Phys. **67**, 3002.
da Gama, A.A.S., G.F. da Sá, P. Porcher and P. Caro, 1981a, J. Phys. Chem. Solids **42**, 701.
da Gama, A.A.S., G.F. da Sá, P. Porcher and P. Caro, 1981b, J. Chem. Phys. **75**, 2583.
Dagenais, M., M.C. Downer, R. Newman and N. Bloembergen, 1981, Phys. Rev. Lett. **46**, 561.
Dahl, M., and G. Schaack, 1984, Z. Phys. B **56**, 279.
Daly, J.G., J.A. Schmidt and J.B. Gruber, 1983, Phys. Rev. B **27**, 5250.
Danby, R.J., and N.B. Manson, 1984, J. Chem. Phys. **81**, 5462.
Danielmeyer, H.G., and H.P. Weber, 1972, IEEE J. Quantum Electron. **QE-8**, 805.
Davydova, M.P., S.B. Zdanovich, B.N. Kazakov, S.L. Korableva and A.L. Stolov, 1977, Opt. Spectrosc. (USSR) **42**, 327.
Davydova, M.P., B.N. Kazakov and A.L. Stolov, 1978, Sov. Phys. Solid State **20**, 1378.
Day, V.W., and J.L. Hoard, 1967, J. Am. Chem. Soc. **52**, 109.
De Leebeeck, H., and C. Görller-Walrand, 1995, J. Alloys & Compounds **225**, 75.
de Vries, A.J., and G. Blasse, 1988, J. Chem. Phys. **88**, 7312.
DeKalb, E.L., and V.A. Fassel, 1979, Optical atomic emission and absorption methods, in: Handbook on the Physics and Chemistry of Rare Earths, Vol. 4, eds K.A. Gschneidner Jr and L. Eyring (North-Holland, Amsterdam) ch. 37D, p. 405.
Del Piero, G., G. Perego, A. Zazetta and G. Brandi, 1975, Cryst. Struct. Comm. **4**, 521.
Denning, R.G., 1991, Eur. J. Solid State Inorg. Chem. **28**, 33.
DeShazer, L.G., and G.H. Dieke, 1963, J. Chem. Phys. **38**, 2190.
Devi, A.R., C.K. Jayasankar and M.F. Reid, 1994, Phys. Rev. B **49**, 12551.
Dexpert-Ghys, J., M. Faucher and P. Caro, 1981, Phys. Rev. B **23**, 607.
Dieke, G.H., 1968, Spectra and Energy Levels of Rare Earth Ions in Crystals (Interscience, New York).
Dieke, G.H., and H.M. Crosswhite, 1956, J. Opt. Soc. Am. **46**, 885.
Dieke, G.H., and L. Leopold, 1957, J. Opt. Soc. Am. **47**, 944.
Dieke, G.H., and B. Pandey, 1964, J. Chem. Phys. **41**, 1952.
Dieke, G.H., and S. Singh, 1956, J. Opt. Soc. Am. **46**, 495.
Dieke, G.H., and S. Singh, 1961, J. Chem. Phys. **41**, 1952.
Dmitruk, M.V., A.A. Kaminskii and I.A. Shcherbakov, 1968, Sov. Phys. JETP **27**, 900.
Donlan, V.L., and A.A. Santiago Jr, 1972, J. Chem. Phys. **57**, 4717.
Downer, M.C., 1989, Top. Appl. Phys. **65**, 29.
Downer, M.C., and A. Bivas, 1983, Phys. Rev. B **28**, 3677.
Downer, M.C., A. Bivas and N. Bloembergen, 1982, Opt. Comm. **41**, 335.
Drew, M.G.B., 1977, Coord. Chem. Rev. **24**, 179.
D'Silva, A.P., and V.A. Fassel, 1979, X-ray excited optical luminescence of the rare earths, in: Handbook on the Physics and Chemistry of Rare Earths, Vol. 4, eds K.A. Gschneidner Jr and L. Eyring (North-Holland, Amsterdam) ch. 37E, p. 441.
Dulick, M., G.E. Faulkner, N.J. Cockcroft and D.C. Nguyen, 1991, J. Lumin. **48&49**, 517.
Edmonds, A.R., 1974, Angular Momentum in Quantum Mechanics (Princeton University Press, Princeton, NJ).
Eisenstein, J.C., 1963a, J. Chem. Phys. **39**, 2128.
Eisenstein, J.C., 1963b, J. Chem. Phys. **39**, 2134.

Elias, L.R., W.S. Heaps and W.M. Yen, 1973, Phys. Rev. B **8**, 4989.

Elliot, R.J., and K.W.H. Stevens, 1953a, Proc. R. Soc. London A **215**, 437.

Elliot, R.J., and K.W.H. Stevens, 1953b, Proc. R. Soc. London A **218**, 553.

Enderle, M., B. Pilawi, W. Schlaphof and H.G. Kahle, 1990a, J. Phys.: Condens. Matter **2**, 4685.

Enderle, M., B. Pilawi, M. Schwab and H.G. Kahle, 1990b, J. Phys.: Condens. Matter **2**, 4701.

Enderle, M., B. Pilawi and H.G. Kahle, 1990c, J. Phys.: Condens. Matter **2**, 4711.

Erath, E.H., 1961, J. Chem. Phys. **34**, 1985.

Esterowitz, L., F.J. Bartoli and R.E. Allen, 1979a, J. Lumin. **21**, 1.

Esterowitz, L., F.J. Bartoli, R.E. Allen, D.E. Wortman, C.A. Morrison and R.P. Leavitt, 1979b, Phys. Rev. B **19**, 6442.

Ewald, H., 1939, Ann. Phys. 5. Folge **34**, 14.

Ewanizky, T.F., P.J. Caplan and J.R. Pastore, 1965, J. Chem. Phys. **43**, 4351.

Farrar, R.T., 1965, Harry Diamond Laboratories Report TR-1309.

Faucher, M., J. Dexpert-Ghys and P. Caro, 1980, Phys. Rev. B **21**, 3689.

Faucher, M., D. Garcia, E. Antic-Fidancev and M. Lemaître-Blaise, 1989a, J. Phys. Chem. Solids **50**, 1227.

Faucher, M., D. Garcia, P. Caro, J. Derouet and P. Porcher, 1989b, J. Phys. (France) **50**, 219.

Faulhaber, R., and S. Hüfner, 1969, Z. Phys. **228**, 235.

Faulhaber, R., S. Hüfner, E. Orlich and H. Schuchert, 1967, Z. Phys. **204**, 101.

Faulkner, T.R., and F.S. Richardson, 1978, Mol. Phys. **35**, 1141.

Favas, M.C., and D.L. Kepert, 1980, Proc. Inorg. Chem. **26**, 325.

Favas, M.C., and D.L. Kepert, 1981, Proc. Inorg. Chem. **28**, 309.

Feofilov, P.P., V.A. Timofeeva, M.N. Tolstoi and L.M. Belyaev, 1965, Opt. Spectrosc. (USSR) **19**, 451.

Figgis, B.N., 1966, Introduction to Ligand Fields (Wiley, New York).

Fluyt, L., P. Verhoeven, H. Lambaerts, K. Binnemans and C. Görller-Walrand, 1994, J. Alloys & Compounds **207/208**, 51.

Freed, S., 1931, Phys. Rev. **38**, 2122.

Freeman, A.J., and J.P. Desclaux, 1979, J. Magn. Magn. Mater. **12**, 11.

Freeman, A.J., and R.E. Watson, 1962, Phys. Rev. **127**, 2058.

Freeth, C.A., G.D. Jones and R.W.G. Syme, 1982, J. Phys. C **15**, 5667.

Frey, S.T., and W.DeW. Horrocks Jr, 1995, Inorg. Chim. Acta **229**, 383.

Friederich, A., K.H. Hellwege and H. Lämmermann, 1960a, Z. Phys. **158**, 251.

Friederich, A., K.H. Hellwege and H. Lämmermann, 1960b, Z. Phys. **159**, 524.

Fry, J.L., H.H. Caspers, H.E. Rast and S.A. Miller, 1968, J. Chem. Phys. **48**, 2342.

Fulde, P., 1979, Crystal fields, in: Handbook on the Physics and Chemistry of Rare Earths, Vol. 2, eds K.A. Gschneidner Jr and L. Eyring (North-Holland, Amsterdam) ch. 17.

Gabrielyan, V.T., A.A. Kaminskii and L. Li, 1970, Phys. Status Solidi a **3**, K37.

Garcia, D., and M. Faucher, 1995, Crystal field in non-metallic (rare earth) compounds, in: Handbook on the Physics and Chemistry of Rare Earths, Vol. 21, eds K.A. Gschneidner Jr and L. Eyring (North-Holland, Amsterdam) ch. 144, p. 263.

Gaume-Mahn, F., C. Linarès and M. Blanchard, 1971, in: Proc. 9th RERC, October 10–14, Blacksburg, VA, p. 478.

Gayen, S.K., and D.S. Hamilton, 1983, Phys. Rev. B **28**, 3706.

Gayen, S.K., G.J. Pogatschnik and D.S. Hamilton, 1984, J. Lumin. **31&32**, 260.

Gayen, S.K., D.S. Hamilton and R.H. Bartram, 1986, Phys. Rev. B **34**, 7517.

Gehring, K.A., M.J.M. Leask and J.H.M. Thornley, 1969, J. Phys. C **2**, 484.

Gerlinger, H., and G. Schaack, 1986, Phys. Rev. B **33**, 7438.

Gil'fanov, F.Z., A.M. Levshin and A.L. Stolov, 1967, Opt. Spectrosc. (USSR) **23**, 323.

Gintoft, R.I., and G.A. Skripko, 1972, J. Appl. Spectrosc. (USSR) **17**, 1480.

Godina, N.A., M.N. Tolstoi and P.P. Feofilov, 1967, Opt. Spectrosc. (USSR) **23**, 411.

Golding, R.M., R.O. Pascual and I.C. Hoare, 1985, Theoret. Chim. Acta (Berlin) **67**, 157.

Goldschmidt, Z.B., 1978, Atomic properties (free ion), in: Handbook on the Physics and Chemistry of Rare Earths, Vol. 1, eds K.A. Gschneidner Jr and L. Eyring (North-Holland, Amsterdam) ch. 1, p. 1.

Goldschmidt, Z.B., A. Pasternak and Z.H. Goldschmidt, 1968, Phys. Lett. A **28**, 265.

Goodman, G.L., W.T. Carnall, R.S. Rana, P. Vandevelde, L. Fluyt and C. Görller-Walrand, 1986, J. Less-Common Met. **126**, 283.

Göppert-Mayer, M., 1931, Ann. Phys. **9**, 273.

Gorban, I.S., A.F. Gumenyuk and V.Ya. Degoda, 1985a, Opt. Spectrosc. (USSR) **58**, 131.

Gorban, I.S., A.F. Gumenyuk and V.Ya. Degoda, 1985b, Opt. Spectrosc. (USSR) **58**, 278.

Görller-Walrand, C., 1985, Chem. Phys. Lett. **115**, 333.

Görller-Walrand, C., 1993, Radiochim. Acta **61**, 221.

Görller-Walrand, C., and L. Fluyt-Adriaens, 1985, J. Less-Common Met. **112**, 175.

Görller-Walrand, C., and J. Godemont, 1977, J. Chem. Phys. **66**, 48.

Görller-Walrand, C., and P. Vandevelde, 1985, Chem. Phys. Lett. **122**, 276.

Görller-Walrand, C., M. Behets, P. Porcher, O.K. Moune-Minn and I. Laursen, 1985, Inorg. Chim. Acta **109**, 83.

Görller-Walrand, C., P. Vandevelde, P. Porcher and J.-C. Krupa, 1987, Inorg. Chim. Acta **139**, 277.

Görller-Walrand, C., P. Vandevelde, I. Hendrickx, P. Porcher, J.-C. Krupa and G.S.D. King, 1988, Inorg. Chem. Acta **143**, 259.

Görller-Walrand, C., I. Hendrickx, L. Fluyt, P. Porcher, O.K. Moune-Minn and G. Blasse, 1989a, J. Lumin. **42**, 349.

Görller-Walrand, C., L. Fluyt, P. Porcher, A.A.S. da Gama, G.F. da Sá, W.T. Carnall and G.L. Goodman, 1989b, J. Less-Common Met. **148**, 339.

Görller-Walrand, C., I. Hendrickx, L. Fluyt, M.P. Gos, J. D'Olieslager and G. Blasse, 1992, J. Chem. Phys. **96**, 5650.

Görller-Walrand, C., L. Fluyt, J. D'Olieslager, M.P. Gos and I. Hendrickx, 1993a, J. Chem. Phys. **99**, 3182.

Görller-Walrand, C., K. Binnemans and L. Fluyt, 1993b, J. Phys.: Condens. Matter **5**, 8359.

Görller-Walrand, C., E. Huygen, K. Binnemans and L. Fluyt, 1994, J. Phys.: Condens. Matter **6**, 7797.

Gourley, J.T., 1972, Phys. Rev. B **5**, 22.

Gramberg, G., 1960, Z. Phys. **159**, 125.

Griffith, J.S., 1961, The Theory of Transition-Metal Ions (Cambridge University Press, London).

Grohmann, I., K.H. Hellwege and H.G. Kahle, 1960, Z. Phys. **160**, 149.

Gross, H., J. Neukum, J. Heber, D. Mateika and Tang Xiao, 1993, Phys. Rev. B **48**, 9264.

Gruber, J.B., and J.G. Conway, 1960a, J. Chem. Phys. **32**, 1178.

Gruber, J.B., and J.G. Conway, 1960b, J. Chem. Phys. **32**, 1531.

Gruber, J.B., W.F. Krupke and J.M. Pointdexter, 1964, J. Chem. Phys. **41**, 3363.

Gruber, J.B., J.R. Henderson, M. Muramoto, K. Rajnak and J.G. Conway, 1966, J. Chem. Phys. **45**, 477.

Gruber, J.B., R.P. Leavitt and C.A. Morrison, 1981, J. Chem. Phys. **74**, 2705.

Gruber, J.B., R.P. Leavitt and C.A. Morrison, 1983, J. Chem. Phys. **79**, 1664.

Gruber, J.B., M.E. Hills, C.A. Morrison, G.A. Turner and M.R. Kokta, 1988, Phys. Rev. B **37**, 8564.

Gruber, J.B., M.E. Hills, R.M. Macfarlane, C.A. Morrison, G.A. Turner, G.J. Quarles, G.J. Kintz and L. Esterowitz, 1989, Phys. Rev. B **40**, 9464.

Gruber, J.B., M.E. Hills, M.D. Seltzer, G.A. Turner, C.A. Clyde and M.R. Kokta, 1990a, Chem. Phys. **144**, 327.

Gruber, J.B., M.E. Hills, T.H. Allik, C.K. Jayasankar, J.R. Quagliano and F.S. Richardson, 1990b, Phys. Rev. B **41**, 7999.

Gruber, J.B., M.E. Hills, M.D. Seltzer, S.B. Stevens, C.A. Morrison, G.A. Turner and M.R. Kokta, 1991, J. Appl. Phys. **69**, 8183.

Gruber, J.B., J.R. Quagliano, M.F. Reid, F.S. Richardson, M.E. Hills, M.D. Seltzer, S.B. Stevens, C.A. Morrison and T.H. Allik, 1993a, Phys. Rev. B **48**, 15561.

Gruber, J.B., M.D. Seltzer, M.E. Hills, S.B. Stevens and C.A. Morrison, 1993b, J. Appl. Phys. **73**, 1929.

Gruber, J.B., M.D. Seltzer, M.E. Hills, T.H. Allik, J.A. Hutchinson, C.A. Morrison and B.H.T. Chai, 1994, Opt. Mater. **3**, 99.

Gruber, J.B., C.A. Morrison, M.D. Seltzer, A.O. Wright, M.P. Nadler, T.H. Allik, J.A. Hutchinson and B.T.H. Chai, 1996, J. Appl. Phys. **79**, 1746.

Grünberg, P., 1969, Z. Phys. **225**, 376.

Grünberg, P., K.H. Hellwege and S. Hüfner, 1967, Phys. Kondens. Materie **6**, 95.

Grünberg, P., S. Hüfner, E. Orlich and J. Schmitt, 1969a, J. Appl. Phys. **40**, 1501.

Grünberg, P., S. Hüfner, E. Orlich and J. Schmitt, 1969b, Phys. Rev. **184**, 285.

Hammond, R.M., M.F. Reid and F.S. Richardson, 1989, J. Less-Common Met. **148**, 311.

Han, T.P.J., G.D. Jones and R.W.G. Syme, 1993, Phys. Rev. B **47**, 14706.

Harmer, A.L., A. Linz and D.R. Gabbe, 1969, J. Phys. Chem. Solids **30**, 1483.

Hasunuma, M., K. Okada and Y. Kato, 1984, Bull. Chem. Soc. Jpn. **57**, 3036.

Hayhurst, T., G. Shalimoff, N.M. Edelstein, L.A. Boatner and M.M. Abraham, 1981, J. Chem. Phys. **74**, 5449.

Hayhurst, T., G. Shalimoff, J.G. Conway, N.M. Edelstein, L.A. Boatner and M.M. Abraham, 1982, J. Chem. Phys. **76**, 3960.

Hehlen, M.P., and H.U. Güdel, 1993, J. Chem. Phys. **98**, 1768.

Hehlen, M.P., H.U. Güdel and J.R. Quagliano, 1994, J. Chem. Phys. **101**, 10303.

Hellwege, A.M., and K.H. Hellwege, 1953, Z. Phys. **135**, 92.

Hellwege, K.H., 1949, Ann. Physik **4**, 95.

Hellwege, K.H., 1976, Einführung in die Festkörperphysik (Springer, Berlin).

Hellwege, K.H., and H.G. Kahle, 1951a, Z. Physik **129**, 62.

Hellwege, K.H., and H.G. Kahle, 1951b, Z. Physik **129**, 85.

Hellwege, K.H., and W. Schröck-Vietor, 1954, Z. Phys. **138**, 449.

Hellwege, K.H., G. Hess and H.G. Kahle, 1960, Z. Phys. **333**, 159.

Hellwege, K.H., G. Horstick, S. Hüfner and H. Lämmermann, 1961a, Z. Phys. **165**, 253.

Hellwege, K.H., G. Horstick, S. Hüfner and H. Lämmermann, 1961b, Z. Phys. **165**, 259.

Hellwege, K.H., S. Hüfner and D. Kuse, 1961c, Z. Phys. **164**, 243.

Hellwege, K.H., S. Hüfner and H. Schmidt, 1963, Z. Phys. **172**, 460.

Hellwege, K.H., E. Orlich and G. Schaack, 1965, Phys. Kondens. Mater. **4**, 196.

Henderson, J.R., M. Muramato and J.B. Gruber, 1967a, J. Chem. Phys. **46**, 2515.

Henderson, J.R., M. Muramato, T.M. Henderson and J.B. Gruber, 1967b, J. Chem. Phys. **47**, 5097.

Hens, E., 1996, Ph.D. Thesis (Katholieke Universiteit Leuven, Belgium).

Hens, E., and C. Görller-Walrand, 1995, J. Alloys & Compounds **225**, 66.

Herrmann, G.F., J.J. Pearson, K.A. Wickersheim and R.A. Buchanan, 1966, J. Appl. Phys. **37**, 1312.

Hoard, J.L., and J.V. Silverton, 1962, Inorg. Chem. **2**, 235.

Hölsä, J., 1990, Z. Naturforsch. **45a**, 173.

Hölsä, J., 1991a, Z. Phys. Chem. **172**, 253.

Hölsä, J., 1991b, J. Rare Earths **1**, 91.

Hölsä, J., and M. Karppinen, 1991, Eur. J. Solid State Inorg. Chem. **28**, 135.

Hölsä, J., and E. Kestilä, 1995a, J. Alloys & Compounds **225**, 89.

Hölsä, J., and E. Kestilä, 1995b, J. Chem. Soc. Faraday Trans. **91**, 1503.

Hölsä, J., and M. Leskelä, 1985, Mol. Phys. **54**, 657.

Hölsä, J., and M. Leskelä, 1991, J. Lumin. **48&49**, 497.

Hölsä, J., and P. Porcher, 1981, J. Chem. Phys. **75**, 2108.

Hölsä, J., and P. Porcher, 1982a, J. Chem. Phys. **76**, 2790.

Hölsä, J., and P. Porcher, 1982b, J. Chem. Phys. **76**, 2798.

Hölsä, J., K. Jyrkäs and M. Leskelä, 1986, J. Less-Common Met. **126**, 215.

Hölsä, J., M. Karppinen and E. Kestilä, 1994, J. Alloys & Compounds **207/208**, 64.

Hölsä, J., R.-J. Lamminmäki, E. Antic-Fidancev, M. Lemaître-Blaise and P. Porcher, 1995, J. Phys.: Condens. Matter **7**, 5127.

Hooge, F.N., 1966, J. Chem. Phys. **45**, 4504.

Horowitz, D.J., L.F. Gillespie, J.E. Miller and E.J. Sharp, 1972, J. Appl. Phys. **43**, 3527.

Hoshina, T., and S. Kuboniwa, 1971, J. Phys. Soc. Jpn. **31**, 828.

Hua, D., Z. Song, S. Wang and Z. Rong, 1988, J. Chem. Phys. **89**, 5398.

Huang, J., J. Loriers and P. Porcher, 1982, J. Solid State Chem. **43**, 87.

Huang, J., J. Loriers, P. Porcher, G. Teste de Sagey, P. Caro and C. Levy-Clement, 1984, J. Chem. Phys. **80**, 6204.

Huang, J., G.K. Liu and R.L. Cone, 1989, Phys. Rev. B **39**, 6348.

Huang, Y., and Z. Luo, 1991, Phys. Status Solidi b **167**, K117.

Hubert, S., P. Thouvenot and N. Edelstein, 1993, Phys. Rev. B **48**, 5751.

Hüfner, S., 1978, Optical Spectra of Transparent Rare Earth Compounds (Academic Press, New York).

Hüfner, S., H. Schuchert and N. Skribanowitz, 1967, Z. Naturforsch. **22a**, 573.

Hutchings, M.T., 1964, Solid State Phys. **16**, 227.

Ionka, E.A., N.N. Morozov, E.N. Murav'ev, V.P. Orlovskii and V.P. Repko, 1973, Inorg. Mater. (USSR) **9**, 1130.

Ivanov, A.O., I.V. Mochalov, A.M. Tkachuk, V.A. Federov and P.P. Feofilov, 1975, Sov. Quantum Electron. **5**, 115.

Ivanov, A.O., L.G. Morozova, I.V. Mochalov and V.A. Federov, 1977, Opt. Spectrosc. (USSR) **42**, 331.
Jacquier, B., Y. Salem, C. Linarès, J.C. Gacon, R. Mahiou and R.L. Cone, 1987a, J. Lumin. **38**, 258.
Jacquier, B., J.C. Gacon, J.F. Marceron, M.F. Joubert and R.L. Cone, 1987b, J. Lumin. **40&41**, 517.
Jacquier, B., J.C. Gacon, Y. Salem, C. Linarès and R.L. Cone, 1989, J. Phys.: Condens. Matter **1**, 7385.
Jayasankar, C.K., and F.S. Richardson, 1989, J. Less-Common Met. **148**, 281.
Jayasankar, C.K., E. Antic-Fidancev, M. Lemaître-Blaise and P. Porcher, 1985, Phys. Status Solidi b **133**, 345.
Jayasankar, C.K., F.S. Richardson, M.F. Reid, P. Porcher and P. Caro, 1987, Inorg. Chim. Acta **139**, 287.
Jayasankar, C.K., F.S. Richardson and M.F. Reid, 1989a, J. Less-Common Met. **148**, 289.
Jayasankar, C.K., M.F. Reid and F.S. Richardson, 1989b, Phys. Status Solidi b **155**, 559.
Jenssen, H.P., A. Linz, R.P. Leavitt, C.A. Morrison and D.E. Wortman, 1975, Phys. Rev. B **11**, 92.
Jenssen, H.P., R.F. Begley, R. Webb and R.C. Morris, 1976, J. Appl. Phys. **47**, 1496.
Johnson, L.F., and A.A. Ballman, 1969, J. Appl. Phys. **40**, 297.
Johnson, L.F., and H.J. Guggenheim, 1971, Appl. Phys. Lett. **19**, 44.
Johnson, L.F., and H.J. Guggenheim, 1973, Appl. Phys. Lett. **23**, 96.
Johnson, L.F., and H.J. Guggenheim, 1974, IEEE J. Quantum Electron. **QE-10**, 442.
Johnson, L.F., J.E. Geusic and L.G. Van Uitert, 1966, Appl. Phys. Lett. **8**, 200.
Johnson, L.F., J.F. Dillon and J.P. Rameika, 1969, J. Appl. Phys. **40**, 1499.
Johnson, L.F., J.F. Dillon and J.P. Rameika, 1970, Phys. Rev. B **1**, 1935.
Johnson, U., 1958, Z. Phys. **152**, 454.
Jones, G.R., 1967, J. Chem. Phys. **47**, 4347.
Jørgensen, C.K., 1962, Progress Inorg. Chem. **4**, 73.
Jørgensen, C.K., R. Pappalardo and E. Ritterhaus, 1964, Z. Naturforsch. Teil A **19**, 424.
Jørgensen, C.K., R. Pappalardo and E. Ritterhaus, 1965, Z. Naturforsch. Teil A **20**, 54.
Joshi, B.D., and A.G. Page, 1977, J. Lumin. **15**, 29.
Joshi, B.D., B.M. Patel, A.G. Page, T.R. Bangia and R.N. Saxena, 1973, J. Lumin. **6**, 125.
Judd, B.R., 1955, Proc. R. Soc. London Ser. A **227**, 552.
Judd, B.R., 1957, Proc. R. Soc. London Ser. A **241**, 122.
Judd, B.R., 1962, Phys. Rev. **127**, 750.
Judd, B.R., 1963, Operator Techniques in Atomic Spectroscopy (McGraw-Hill, New York).
Judd, B.R., 1966, Phys. Rev. **141**, 4.
Judd, B.R., 1977a, Phys. Rev. Lett. **39**, 242.
Judd, B.R., 1977b, J. Chem. Phys. **66**, 3163.
Judd, B.R., 1979, J. Lumin. **18/19**, 604.
Judd, B.R., 1988, Atomic theory and optical spectroscopy, in: Handbook on the Physics and Chemistry of Rare Earths, Vol. 11, eds K.A. Gschneidner Jr and L. Eyring (North-Holland, Amsterdam) ch. 74, p. 81.
Judd, B.R., 1991, Eur. J. Solid State Inorg. Chem. **28**, 17.
Judd, B.R., 1994, Comments At. Mol. Phys. **30**, 27.
Judd, B.R., and H. Crosswhite, 1984, J. Opt. Soc. Am. B **1**, 255.
Judd, B.R., and G.M.S. Lister, 1991, Phys. Rev. Lett. **67**, 1720.
Judd, B.R., and G.M.S. Lister, 1992a, J. Phys. B **25**, 577.
Judd, B.R., and G.M.S. Lister, 1992b, J. Phys. B **25**, L205.
Judd, B.R., and G.M.S. Lister, 1992c, J. Phys. A **25**, 2615.
Judd, B.R., and G.M.S. Lister, 1993a, J. Phys. B **26**, 193.
Judd, B.R., and G.M.S. Lister, 1993b, J. Phys. B **26**, 3177.
Judd, B.R., and G.M.S. Lister, 1993c, J. Alloys & Compounds **193**, 155.
Judd, B.R., and E. Lo, 1994, J. Phys.: Condens. Matter **6**, L799.
Judd, B.R., and D.R. Pooler, 1982, J. Phys. C. **15**, 591.
Judd, B.R., H.M. Crosswhite and H. Crosswhite, 1968, Phys. Rev. **169**, 130.
Kahle, H.G., 1956a, Z. Phys. **145**, 347.
Kahle, H.G., 1956b, Z. Phys. **145**, 361.
Kahle, H.G., V. Joch, J. Plamper and W. Urban, 1968, J. Chem. Phys. **49**, 2702.
Kajiura, M., and K. Shinagawa, 1970, J. Phys. Soc. Jpn. **28**, 1041.
Kaminskii, A.A., 1975, Lazernye Kristalli (Izd. Nauka, Moscow).
Kaminskii, A.A., 1981, Laser Crystals (Springer, Berlin).
Kaminskii, A.A., 1986, Phys. Status Solidi a **97**, K53.

Kaminskii, A.A., and L. Li, 1970, Inorg. Mater. (USSR) **6**, 254.

Kaminskii, A.A., and S.E. Sarkisov, 1986, Phys. Status Solidi a **97**, K163.

Kaminskii, A.A., A.A. Pavlyuk and P.V. Klevtsov, 1970, Opt. Spectrosc. (USSR) **28**, 157.

Kaminskii, A.A., P.V. Klevtsov, L. Li and A.A. Pavlyuk, 1972, Inorg. Mater. (USSR) **8**, 1896.

Kaminskii, A.A., S.E. Sarkisov and L. Li, 1973a, Phys. Status Solidi a **15**, K141.

Kaminskii, A.A., A.A. Mayer, M.V. Provotorov and S.E. Sarkisov, 1973b, Phys. Status Solidi a **17**, K115.

Kaminskii, A.A., P.V. Klevtsov, L. Li, A.A. Pavlyuk and S.E. Sarkisov, 1973c, Inorg. Mater. (USSR) **9**, 1824.

Kaminskii, A.A., G.A. Bogomolova, K.S. Bagdasarov and A.G. Petrosyan, 1975, Opt. Spectrosc. (USSR) **39**, 643.

Kaminskii, A.A., K.S. Bagdasarov, G.A. Bogomolova, M.M. Gritsenko, A.M. Kevorkov and S.E. Sarkisov, 1976a, Phys. Status Solidi a **34**, K109.

Kaminskii, A.A., S.E. Sarkisov, A.A. Maier, V.A. Lomonov and V.A. Balashov, 1976b, Sov. Tech. Phys. Lett. **2**, 59.

Kaminskii, A.A., A.O. Ivanov, S.E. Sarkisov, I.V. Mochalov, V.A. Federov and L. Li, 1976c, Sov. Phys. JETP **44**, 516.

Kaminskii, A.A., G.A. Bogomolova, D.N. Vylegzhanin, K.S. Bagdasarov, A.M. Kevorkov and M.M. Gritsenko, 1976d, Phys. Status Solidi a **38**, 409.

Kaminskii, A.A., D. Schultze, B. Hermoneit, S.E. Sarkisov, L. Li, J. Bohm, P. Reiche, R. Ehlert, A.A. Mayer, V.A. Lomonov and V.A. Bazlashov, 1976e, Phys. Status Solidi a **33**, 737.

Kaminskii, A.A., S.E. Sarkisov, J. Bohm, P. Reiche, D. Schultze and R. Uecker, 1977a, Phys. Status Solidi a **43**, 71.

Kaminskii, A.A., A.A. Pavlyuk, T.I. Butaeva, V.A. Federov, I.F. Balashov, V.A. Berenberg and V.V. Lubchenko, 1977b, Inorg. Mater. (USSR) **13**, 1251.

Kaminskii, A.A., T.I. Butaeva, V.A. Federov, K.S. Bagdasarov and A.G. Petrosyan, 1977c, Phys. Status Solidi a **39**, 541.

Kaminskii, A.A., A.A. Pavlyuk, T.I. Butaeva, L.I. Bobovich, I.F. Balashov, V.A. Berenberg and V.V. Lubchenko, 1979a, Inorg. Mater. (USSR) **15**, 424.

Kaminskii, A.A., S.E. Sarkisov, T.I. Butaeva, G.A. Denisenko, B. Hermoneit, J. Bohm, W. Grosskreutz and D. Schultze, 1979b, Phys. Status Solidi a **56**, 725.

Kaminskii, A.A., S.E. Sarkisov, H.D. Kürsten and D. Schultze, 1982, Phys. Status Solidi a **72**, 207.

Kaminskii, A.A., V.A. Timofeeva, N.R. Agamalyan, A.B. Bykov, S.E. Sarkisov and Yu.M. Gerasimov, 1983a, Phys. Status Solidi a **76**, 777.

Kaminskii, A.A., I.M. Silvestrova, S.E. Sarkisov and G.A. Denisenko, 1983b, Phys. Status Solidi a **80**, 607.

Kaminskii, A.A., V.A. Timofeeva, A.B. Bykov and S.E. Sarkisov, 1984a, Phys. Status Solidi a **83**, K165.

Kaminskii, A.A., E.L. Belokoneva, B.V. Mill, Yu.V. Pisarevskii, I.M. Silvestrova, A.V. Butashin and G.G. Khodzhabagyan, 1984b, Phys. Status Solidi a **86**, 345.

Kaminskii, A.A., B.V. Mill, A.V. Butashin, E.L. Belokoneva and K. Kurbanov, 1987, Phys. Status Solidi a **103**, 575.

Kaminskii, A.A., K. Kurbanov, K.L. Ovanesyan and A.G. Petrosyan, 1988, Phys. Status Solidi a, **105**, K155.

Kaminskii, A.A., A. Kholov, P.V. Klevtsov and S.K. Khafizov, 1989, Phys. Status Solidi a **114**, 713.

Kaminskii, A.A., V.S. Mironov, S.N. Bagaev, N.M. Khaidukov, M.F. Joubert, B. Jacquier and G. Boulon, 1994, Phys. Status Solidi a **145**, 177.

Kanellakopulas, B., H.-D. Amberger, G.G. Rosenbauer and R.D. Fischer, 1977, J. Inorg. Nucl. Chem. **39**, 607.

Kanskaya, L.M., A.I. Ryskin and A.M. Tkachuk, 1967, Opt. Spectrosc. (USSR) **22**, 177.

Karayianis, N., C.A. Morrison and D.E. Wortman, 1975, J. Chem. Phys. **62**, 4125.

Karayianis, N., D.E. Wortman and H.P. Jenssen, 1976, J. Phys. Chem. Solids **37**, 675.

Kariss, Y.E., and P.P. Feofilov, 1964, Opt. Spectrosc. (USSR) **17**, 387.

Kariss, Y.E., A.M. Morozov and P.P. Feofilov, 1964, Opt. Spectrosc. (USSR) **17**, 481.

Karlow, E.A., and J.B. Gruber, 1971, J. Chem. Phys. **55**, 4730.

Karlow, E.A., and J.B. Gruber, 1975, J. Chem. Phys. **62**, 1606.

Karlow, E.A., J. Stöhr and J.B. Gruber, 1975, Chem. Phys. **10**, 131.

Kato, Y., and H. Takada, 1979, Bull. Chem. Soc. Jpn. **52**, 990.

Kato, Y., T. Nagai and A. Saika, 1977, Bull. Chem. Soc. Jpn. **50**, 862.
Kellendonk, F., and G. Blasse, 1982, J. Chem. Phys. Solids **43**, 481.
Kepert, D.L., 1965, J. Chem. Soc., p. 4736.
Kepert, D.L., 1977, Proc. Inorg. Chem. **23**, 1.
Kepert, D.L., 1979, Proc. Inorg. Chem. **25**, 41.
Kholodenkov, L.E., and A.K. Makhanek, 1982, Phys. Status Solidi b **112**, K149.
Kholodenkov, L.E., and A.K. Makhanek, 1984, Phys. Status Solidi b **125**, 365.
Kholodenkov, L.E., A.K. Makhanek and A.A. Kaminskii, 1984, Phys. Status Solidi b **126**, 659.
Kibler, M., 1983, Phys. Rev. Lett. **98A**, 343.
Kiess, N.H., and G.H. Dieke, 1966, J. Chem. Phys. **45**, 2729.
Kingsley, J.K., and J.S. Prener, 1962, Phys. Rev. **126**, 458.
Kirby, A.F., and F.S. Richardson, 1983, J. Phys. Chem. **87**, 2544.
Kirton, J., and S.D. McLaughlan, 1967, Phys. Rev. **155**, 279.
Kisliuk, P., W.F. Krupke and J.B. Gruber, 1964, J. Chem. Phys. **40**, 3606.
Knoll, K.D., 1971, Phys. Status Solidi b **45**, 553.
Koningstein, J.A., 1964, Phys. Rev. **136**, A717.
Koningstein, J.A., 1965a, J. Chem. Phys. **42**, 3195.
Koningstein, J.A., 1965b, Theor. Chim. Acta **3**, 271.
Koningstein, J.A., 1966, J. Chem. Phys. **44**, 3957.
Koningstein, J.A., 1968, Appl. Spectrosc. **22**, 438.
Koningstein, J.A., and J.E. Geusic, 1964, Phys. Rev. **136**, A711.
Koningstein, J.A., and P. Grünberg, 1971, Can. J. Chem. **49**, 2336.
Koningstein, J.A., and C.J. Kane-Maguire, 1974, Can. J. Chem. **52**, 3445.
Koningstein, J.A., and G. Schaack, 1970, Phys. Rev. B **2**, 1242.
Korol'kov, V.S., and A.G. Makhanek, 1972, Zh. Prikl. Spektrosk. **17**, 828.
Korol'kov, V.S., and A.G. Makhanek, 1977, Phys. Status Solidi b **81**, 387.
Koster, G.F., J.O. Dimmock, R.G. Wheeler and H. Statz, 1963, Properties of the Thirty-Two Point Groups (MIT Press, Cambridge, MA).
Kramer, M.A., and R.W. Boyd, 1981, Phys. Rev. B **23**, 986.
Krühler, W., 1974, Ph.D. Thesis (Universität Stuttgart).
Krupka, D.C., and H.J. Guggenheim, 1969, J. Chem. Phys. **51**, 4006.
Krupke, W.F., and J.B. Gruber, 1963, J. Chem. Phys. **39**, 1024.
Krupke, W.F., and J.B. Gruber, 1964, J. Chem. Phys. **41**, 1225.
Krupke, W.F., and J.B. Gruber, 1965a, J. Chem. Phys. **42**, 1134.
Krupke, W.F., and J.B. Gruber, 1965b, Phys. Rev. **139**, A2008.
Kuleshov, V.V., V.P. Mikhailov, S.A. Radkevich, V.N. Boikov, D.S. Umreiko and B.I. Minkov, 1994, Opt. Spectrosc. (USSR) **77**, 539.
Kulpa, S.M., 1975, J. Phys. Chem. Solids **36**, 1317.
Kumar, U.V., H. Jagannath, D.R. Rao and P. Venkateswarlu, 1976, Ind. J. Phys. **50**, 90.
Kumar, U.V., D.R. Rao and P. Venkateswarlu, 1977, J. Chem. Phys. **66**, 2019.
Kundu, T., A.K. Banerjee and M. Chowdhury, 1990a, Phys. Rev. B **41**, 10911.
Kundu, T., A.K. Banerjee and M. Chowdhury, 1990b, Phys. Rev. B **42**, 7769.
Kuo, S.C., L.C. Thompson and H.-D. Amberger, 1995, J. Alloys & Compounds **225**, 60.
Kuroda, H., S. Shionoya and T. Kushida, 1972, J. Phys. Soc. Jpn. **33**, 125.
Kuroda, R., S.F. Mason and C. Rosini, 1981, J. Chem. Soc. Faraday Trans. 2 **77**, 2125.
Kuse, D., 1967, Z. Phys. **203**, 49.
Kustov, E.F., and V.V. Ryabchenkov, 1988, Sov. Phys. Crystallogr. **33**, 533.
Lämmermann, H., 1958, Z. Phys. **150**, 551.
Lammers, M.J.J., and G. Blasse, 1986, Chem. Phys. Lett. **126**, 405.
Lange, H., 1938, Ann. Phys. 5. Folge **32**, 361.
Leavitt, R.P., 1987, Phys. Rev. B **35**, 9271.
Leavitt, R.P., C.A. Morrison and D.E. Wortman, 1974, J. Chem. Phys. **61**, 1250.
Legendziewicz, J., G. Oczko, W. Stręk and J. Hanuza, 1995, Eur. J. Solid State Inorg. Chem. **32**, 95.
Lempicki, A., H. Samelson and C. Brecher, 1968, J. Mol. Spectrosc. **27**, 375.
Levy, C.G., T.J. Glynn and W.M. Yen, 1984, J. Lumin. **31&32**, 245.
Li, C.L., and M.F. Reid, 1990, Phys. Rev. B **42**, 1903.
Linarès, C., and J.C. Souillat, 1970, C.R. Acad. Sc. Paris **271**, 861.
Linarès, C., A. Louat and M. Blanchard, 1977, Struct. Bonding (Berlin) **33**, 179.
Lindop, A.J., and D.W. Goodwin, 1973, J. Phys. C **6**, 1818.
Lippard, S.L., and F.A. Cotton, 1967, Progr. Inorg. Chem. **8**, 109.

Liu, G.K., W.T. Carnall, R.P. Jones, R.L. Cone and J. Huang, 1994, J. Alloys & Compounds **207/208**, 69.

Loong, C.-K., L. Soderholm, J.P. Hammonds, M.M. Abraham, L.A. Boatner and N.M. Edelstein, 1993, J. Phys.: Condens. Matter **5**, 5121.

Louart, J.P., C. Bissieux, M. Egee, G. Mary and M. de Murcia, 1981, J. Phys. C **14**, 4923.

Low, W., 1962, J. Chem. Phys. **37**, 30.

Lupei, A., V. Lupei, S. Grecu, C. Tiseani and G. Boulon, 1994, J. Appl. Phys. **75**, 4652.

Lupei, V., A. Lupei, C. Tieanu, S. Georgescu, C. Stoicescu and P.M. Nanau, 1995, Phys. Rev. B **51**, 8.

Maghrawy, H., W. Stręk, J. Legendziewicz, J. Hanuza and E. Lukowiak, 1993, Pol. J. Chem. **67**, 1959.

Magno, M.S., and G.H. Dieke, 1962, J. Chem. Phys. **37**, 2354.

Mahiou, R., B. Jacquier and R.L. Cone, 1985, J. Phys. (France) **46**, C7–119.

Makhanek, A.K., R.I. Gintoft, L.A. Dzhuguryan, V.S. Korol'kov and L.E. Kholodenkov, 1984, Zh. Prikl. Spektrosk. **40**, 964.

Makovsky, J., 1966, Phys. Lett. **19**, 647.

Makovsky, J., 1967, J. Chem. Phys. **46**, 390.

Maksimova, G.V., and A.A. Sobol', 1974, in: Proc. P.N. Lebedev Phys. Inst. [Acad. Sci. USSR], Vol. 60, ed. D.V. Skobeltsin (Consultants Bureau, New York) pp. 59–73.

Malek, C.K., J.-C. Krupa and M. Genet, 1986, Inorg. Chim. Acta **115**, 115.

Malinowski, M., B. Jacquier, M. Bouazaoui, M.F. Joubert and C. Linarès, 1990, Phys. Rev. B **41**, 31.

Malinowski, M., C. Garapon, M.F. Joubert and B. Jacquier, 1995, J. Phys.: Condens. Matter 7, 199.

Malta, O.L., E. Antic-Fidancev, M. Lemaître-Blaise, A. Milicic-Tang and M. Taibi, 1995, J. Alloys & Compounds **228**, 41.

Marvin, H.H., 1947, Phys. Rev. **71**, 102.

Matthies, S., and D. Welsch, 1975, Phys. Status Solidi b **68**, 125.

May, P.S., M.F. Reid and F.S. Richardson, 1987, Mol. Phys. **61**, 1455.

May, P.S., C.K. Jayasankar and F.S. Richardson, 1989, Chem. Phys. **138**, 123.

May, P.S., D.H. Metcalf, F.S. Richardson, R.C. Carter, C.E. Miller and R.A. Palmer, 1992, J. Lumin. **51**, 249.

Mazurak, Z., and J.B. Gruber, 1992, J. Phys.: Condens. Matter **4**, 3453.

Mazurak, Z., A. Garcia and C. Fouassier, 1994, J. Phys.: Condens. Matter **6**, 2031.

McGlynn, S.P., L.G. Vanquickenborne, M. Konishita and D.G. Carroll, 1972, Introduction to Applied Quantum Chemistry (Holt, Rinehart and Winston, New York).

McPherson, G.L., and S.L. Meyerson, 1990, Chem. Phys. Lett. **167**, 471.

Mercier, N., M. Leblanc, E. Antic-Fidancev, M. Lemaître-Blaise and P. Porcher, 1995, J. Alloys & Compounds **225**, 198.

Merkle, L.D., J.B. Gruber, M.D. Selzer, S.B. Stevens and T.H. Allik, 1992, J. Appl. Phys. **72**, 4269.

Metcalf, D.H., T.A. Hopkins and F.S. Richardson, 1995, Inorg. Chem. **34**, 4868.

Meyer, G., and H.-C. Gaebell, 1978, Z. Anorg. Allg. Chem. **445**, 147.

Miller, J.E., E.J. Sharp and D.J. Horowitz, 1972, J. Appl. Phys. **43**, 462.

Milward, R.C., 1967, Phys. Lett. A **25**, 19.

Minhas, I.S., K.K. Sharma and J.B. Gruber, 1973, Phys. Rev. B **8**, 385.

Mishra, S.K., and G.C. Upretti, 1986, Magn. Reson. Rev. **10**, 333.

Moran, D.M., A. De Piante and F.S. Richardson, 1989, J. Less-Common Met. **148**, 297.

Moran, D.M., A. De Piante and F.S. Richardson, 1990a, Phys. Rev. B **42**, 3317.

Moran, D.M., A. De Piante and F.S. Richardson, 1990b, Phys. Rev. B **42**, 3331.

Moret, E., F. Nicolo, J.-C.G. Bünzli and G. Chapuis, 1991, J. Less-Common Met. **171**, 273.

Morley, J.P., T.R. Faulkner, F.S. Richardson and R.W. Schwartz, 1981, J. Chem. Phys. **75**, 539.

Morley, J.P., T.R. Faulkner, F.S. Richardson and R.W. Schwartz, 1982, J. Chem. Phys. 77, 1734.

Morozov, A.M., E.G. Reut and A.I. Ryskin, 1966, Opt. Spectrosc. (USSR) **21**, 314.

Morozov, A.M., M.N. Tolstoi and P.P. Feofilov, 1967, Opt. Spectrosc. (USSR) **22**, 139.

Morozov, A.M., L.G. Morozova, A.K. Trofimov and P.P. Feofilov, 1970, Opt. Spectrosc. (USSR) **29**, 590.

Morozov, A.M., L.G. Morozova, V.A. Federov and P.P. Feofilov, 1975, Opt. Spectrosc. (USSR) **39**, 343.

Morrison, C.A., and R.P. Leavitt, 1981, J. Chem. Phys. **74**, 25.

Morrison, C.A., and R.P. Leavitt, 1982, Spectroscopic properties of triply ionized lanthanides in transparent host crystals, in: Handbook on the Physics and Chemistry of Rare Earths, Vol. 5, eds

K.A. Gschneidner Jr and L. Eyring (North-Holland, Amsterdam) ch. 46.
Morrison, C.A., R.P. Leavitt and D.E. Wortman, 1980a, J. Chem. Phys. **73**, 2580.
Morrison, C.A., D.E. Wortman, R.P. Leavitt and H.P. Jenssen, 1980b, Harry Diamond Laboratories Report TR-1897, 28pp.
Morrison, J.C., and K. Rajnak, 1971, Phys. Rev. A **4**, 536.
Moune, O.K., and P. Caro, 1989, J. Less-Common Met. **148**, 181.
Muetterties, M.C., and C.M. Wright, 1981, Q. Rev. Chem. Soc. **21**, 109.
Mujaji, M., G.D. Jones and R.W.G. Syme, 1993, Phys. Rev. B **48**, 710.
Muko, K., 1973, J. Phys. Chem. Solids **34**, 2029.
Nakazawa, E., and S. Shianoya, 1974, J. Phys. Soc. Jpn. **36**, 504.
Nandi, J., and D. Neogy, 1988, Phys. Status Solidi b **149**, 275.
Nekvasil, V., 1978, Phys. Status Solidi b **87**, 317.
Neogy, D., and J. Nandi, 1985, J. Chem. Phys. **83**, 4093.
Neogy, D., and T. Purohit, 1987, Phys. Status Solidi b **139**, 519.
Neogy, D., and T. Purohit, 1988, Phys. Status Solidi b **146**, 181.
Neukum, J., N. Bodenschatz and J. Heber, 1994, Phys. Rev. B **50**, 3536.
Newman, D.J., 1971, Adv. Phys. **20**, 197.
Newman, D.J., 1973, J. Phys. Chem. Solids **34**, 541.
Newman, D.J., 1977, Aust. J. Phys. **30**, 315.
Newman, D.J., and B. Ng, 1988, Rep. Prog. Phys. **52**, 699.
Newman, D.J., G.G. Siu and W.Y.P. Fung, 1982, J. Phys. C **15**, 3113.
Nielson, C.W., and J.F. Koster, 1963, Spectroscopic Coefficients for the p^n, d^n and f^n Configurations (MIT Press, Cambridge, MA).
Nutter, P.B., and M.L. Harrison, 1963, Progress Report No. 1, NTIS #475607 (Raytheon Company).
Oczko, G., and J. Legendziewicz, 1993, Acta Phys. Polonica A **84**, 925.
Ofelt, G.S., 1962, J. Chem. Phys. **37**, 511.
Ofelt, G.S., 1963, J. Chem. Phys. **38**, 2171.
Ohaka, T., and Y. Kato, 1983, Bull. Chem. Soc. Jpn. **56**, 1289.
O'Laughlin, J.W., 1979, Chemical spectrophotometric and polarographic methods, in: Handbook on the Physics and Chemistry of Rare Earths, Vol. 4, eds K.A. Gschneidner Jr and L. Eyring (North-Holland, Amsterdam) ch. 37A, p. 341.
Olsen, D.N., and J.B. Gruber, 1971, J. Chem. Phys. **54**, 2077.
Orlov, M.S., and A.L. Stolov, 1975, Opt. Spectrosc. (USSR) **39**, 640.
Pappalardo, R., 1963, Z. Phys. **173**, 374.
Pauling, L., 1960, The Nature of the Chemical Bond, 3rd Ed. (Cornell University Press, Ithaca, NY).
Pearson, J.J., G.F. Herrmann and R.A. Buchanan, 1968, J. Appl. Phys. **39**, 980.
Pellé, F., and P. Goldner, 1993, Phys. Rev. B **48**, 9995.
Pellé, F., N. Gardant, M. Genotelle, P. Goldner and P. Porcher, 1995, J. Phys. Chem. Solids **56**, 1003.
Pelletier-Allard, N., and F. Martin-Brunetière, 1969, J. Phys. (France) **30**, 849.
Petrov, M.V., and A.M. Tkachuk, 1978, Opt. Spectrosc. (USSR) **41**, 81.
Petty, C.C., 1956, Dissertation (The Johns Hopkins University, Baltimore, MD).
Pierce, J.W., and H.Y.-P. Hong, 1974, in: Proc. 10th Rare Earth Res. Conf., Carefree, p. 527.
Piksis, A.H., G.H. Dieke and H.M. Crosswhite, 1967, J. Chem. Phys. **47**, 5083.
Pilawi, B., 1990, J. Phys.: Condens. Matter **2**, 5555.
Podlesnyak, A., S. Rosenkranz, F. Fauth, W. Marti, H.J. Scheel and A. Furrer, 1994, J. Phys.: Condens. Matter **6**, 4099.
Pollack, S.A., 1964, J. Chem. Phys. **40**, 2751.
Porcher, P., and P. Caro, 1976, J. Chem. Phys. **65**, 89.
Porcher, P., D.R. Svoronos, L. Leskelä and J. Hölsä, 1983, J. Solid State Chem. **46**, 101.
Prather, J.L., 1961, Atomic Energy Levels in Crystals, National Bureau of Standards Monograph 19 (NBS, Washington).
Prinz, G.A., 1966a, Phys. Lett. **20**, 323.
Prinz, G.A., 1966b, Phys. Rev. **152**, 474.
Rabbiner, N., 1967, J. Opt. Soc. Am. **57**, 1376.
Racah, G., 1949, Phys. Rev. **76**, 1352.
Radhakrishna, S., and V.S. Sivasankar, 1977, J. Chem. Phys. **66**, 5645.
Rajnak, K., and W.F. Krupke, 1967, J. Chem. Phys. **46**, 3532.
Rajnak, K., and B.G. Wybourne, 1963, Phys. Rev. **132**, 280.
Rajnak, K., and B.G. Wybourne, 1964, J. Chem. Phys. **41**, 565.
Rakestraw, J.W., and G.H. Dieke, 1965, J. Chem. Phys. **42**, 873.
Ralph, J.E., 1969, Solid State Comm. **7**, 1065.

Ramaz, F., R.M. McFarlane and J.C. Vial, 1992, J. Lumin. **53**, 244.
Ramaz, F., R.M. McFarlane, J.C. Vial, J.P. Chaminade and F. Madeores, 1993, J. Lumin. **55**, 173.
Rana, R.S., and F.W. Kaseta, 1983, J. Chem. Phys. **79**, 5280.
Rana, R.S., F.W. Kaseta and R.H. Garvey, 1982, J. Chem. Phys. **77**, 4400.
Rana, R.S., C.D. Cordero-Montalvo and N. Bloembergen, 1984, J. Chem. Phys. **81**, 2951.
Rana, R.S., J. Shertzer and F.W. Kaseta, 1988, Lanth. Act. Res. **2**, 295.
Rao, D.N., J. Prasad and P.N. Prasad, 1983, Phys. Rev. B **28**, 20.
Rast, H.E., Fry J.L. and H.H. Caspers, 1967a, J. Chem. Phys. **46**, 1460.
Rast, H.E., H.H. Caspers and S.A. Miller, 1967b, J. Chem. Phys. **47**, 3874.
Rector, C.W., B.C. Pandey and H.W. Moos, 1966, J. Chem. Phys. **45**, 171.
Reid, M.F., 1987, J. Chem. Phys. **87**, 2875.
Reid, M.F., 1992, J. Alloys & Compounds **180**, 93.
Reid, M.F., and F.S. Richardson, 1984, Phys. Rev. B **29**, 2830.
Reid, M.F., F.S. Richardson and P.A. Tanner, 1987, Mol. Phys. **60**, 881.
Reisfeld, R., and C.K. Jørgensen, 1977, Lasers and Excited States of Rare Earths (Springer, Berlin).
Reisfeld, R., and C.K. Jørgensen, 1987, Excited state phenomena in vitreous materials, in: Handbook on the Physics and Chemistry of Rare Earths, Vol. 9, eds K.A. Gschneidner Jr and L. Eyring (North-Holland, Amsterdam) ch. 58, p. 1.
Renfro, G.M., J.C. Windscheif, W.A. Sibley and R.F. Belt, 1980, J. Lumin. **22**, 51.
Richardson, F.S., M.F. Reid, J.J. Dallara and R.D. Smith, 1985, J. Chem. Phys. **83**, 3813.
Richman, I., and E.Y. Wong, 1962, J. Chem. Phys. **37**, 2270.
Richter, K., R. Wannemacher, J. Heber and D. Mateika, 1991, J. Lumin. **47**, 169.
Rosenberger, D., 1962, Z. Phys. **167**, 360.
Rossat-Mignod, J., J.C. Souillat and C. Linarès, 1973, J. Phys. Chem. Solids **34**, 371.
Rossat-Mignod, J., J.C. Souillat and G. Quézel, 1974a, Phys. Status Solidi b **62**, 223.
Rossat-Mignod, J., J.C. Souillat and G. Quézel, 1974b, Phys. Status Solidi b **62**, 519.
Rotenberg, M., R. Bivins, N. Metropolis and J.K.J. Wooten, 1959, The 3-j and 6-j symbols (MIT Press, Cambridge, MA).
Rudowicz, C., 1985, Chem. Phys. **97**, 43.
Rudowicz, C., 1986a, Chem. Phys. **102**, 437.
Rudowicz, C., 1986b, J. Chem. Phys. **84**, 5045.
Rukmini, E., C.K. Jayasankar and M.F. Reid, 1994, J. Phys.: Condens. Matter **6**, 5919.
Saber, D., J. Dexpert-Ghys, P. Caro, A.M. Lejus and D. Vivien, 1985, J. Chem. Phys. **82**, 5648.
Saez-Puche, R., E. Antic-Fidancev, M. Lemaître-Blaise, P. Porcher, C. Cascales, C.M. Marcano and I. Rasines, 1989, J. Less-Common Met. **148**, 369.
Sarup, R., and M.H. Crozier, 1965, J. Chem. Phys. **42**, 371.
Saruwatari, M., K. Otsuka, S. Miyazawa, T. Yamada and T. Kimura, 1977, IEEE J. Quantum. Electron. **QE-13**, 836.
Saxe, J.D., J.P. Morley and F.S. Richardson, 1982, Mol. Phys. **47**, 407.
Sayre, E.V., and S. Freed, 1956, J. Chem. Phys. **24**, 1213.
Sayre, E.V., K.M. Sancier and S. Freed, 1955, J. Chem. Phys. **23**, 2060.
Schmid, B., B. Haelg, A. Furrer, W. Urland and R. Kremer, 1987, J. Appl. Phys. **61**, 3426.
Schoene, C.A., J.R. Quagliano and F.S. Richardson, 1991, Inorg. Chem. **30**, 3803.
Schultheiss, E., A. Scharmann and D. Schwabe, 1987, Phys. Status Solidi b **140**, 173.
Schwartz, R.W., 1975, Mol. Phys. **30**, 81.
Schwartz, R.W., 1976, Mol. Phys. **31**, 1909.
Schwartz, R.W., 1977, Inorg. Chem. **16**, 1694.
Schwartz, R.W., H.G. Brittain, J.P. Riehl, W. Yeakel and F.S. Richardson, 1977, Mol. Phys. **34**, 361.
Schwartz, R.W., T.R. Faulkner and F.S. Richardson, 1979, Mol. Phys. **38**, 1767.
Schwartz, R.W., A.K. Banerjee, A.C. Sen and M. Chowdhury, 1980, J. Chem. Soc. Faraday Trans. 2 **76**, 620.
Schwiesow, R.L., and H.M. Crosswhite, 1969a, J. Opt. Soc. Am. **59**, 592.
Schwiesow, R.L., and H.M. Crosswhite, 1969b, J. Opt. Soc. Am. **59**, 602.
Scott, P.D., 1970, Ph.D Thesis (Yale University).
Scott, P.D., H.E. Meissner and H.M. Crosswhite, 1969, Phys. Lett. **28A**, 489.
Seltzer, M.D., J.B. Gruber, M.E. Hills, G.J. Quarles and C.A. Morrison, 1993, J. Appl. Phys. **74**, 2821.
Seltzer, M.D., J.B. Gruber, G.H. Rosenblatt, C.A. Morrison and E.D. Filer, 1994, J. Appl. Phys. **75**, 280.
Sengupta, D., and J.O. Artman, 1970a, J. Chem. Phys. **53**, 838.

Sengupta, D., and J.O. Artman, 1970b, Phys. Rev. B **1**, 2986.

Sharipov, K.T., Y.P. Agureev, K.I. Petrov and N.V. Porotnikov, 1975, in: Spektroskopiya Kristallov, eds A.A. Kaminskii, Z.L. Morgenshtern and D.T. Sviridov (Nauka, Moscow).

Sharp, E.J., J.E. Miller, D.J. Horowitz, A. Linz and V. Belruss, 1974, J. Appl. Phys. **45**, 4974.

Shekun, L.Y., 1966, Sov. Phys. Solid State **8**, 1370.

Sievers, A.J., and A.M. Tinkham, 1963, J. Appl. Phys. **34**, 1235.

Singh, B.P., K.K. Sharma and I.S. Minhas, 1986, J. Phys. C **19**, 6655.

Sinha, S.P., 1976, Struct. Bonding (Berlin) **25**, 69.

Sinha, S.P., and E. Butter, 1969, Mol. Phys. **16**, 285.

Skripko, G.A., A.G. Makhanek and R.I. Gintoft, 1976, Zh. Prikl. Spektrosk. **24**, 968.

Song, Z., S. Lian, D. Ma, Y. Xu, Y. Gu, Y. Gui, D. Hua and S. Wang, 1984, Guangpuxue Yu Guangpu Fenxi **4**, 1.

Song, Z., D. Hua, S. Wang and Y. Gui, 1988, J. Chem. Phys. **89**, 5404.

Sovers, O.J., and T. Yoshioka, 1968, J. Chem. Phys. **49**, 4945.

Sovers, O.J., and T. Yoshioka, 1969, J. Chem. Phys. **51**, 5330.

Stephens, E.M., 1989, Gadolinium as an EPR probe, in: Lanthanide Probes in Life, Chemical and Earth Sciences, eds J.-C.G. Bünzli and G.R. Choppin (Elsevier, Amsterdam) p. 181.

Stephens, E.M., D.H. Metcalf, M.T. Berry and F.S. Richardson, 1991, Phys. Rev. B **44**, 9895.

Stevens, K.W.H., 1952, Proc. Phys. Soc. London Sect. A **65**, 209.

Stevens, S.B., C.A. Morrison, T.H. Allik, A.L. Rheingold and B.S. Haggerty, 1991, Phys. Rev. B **43**, 7386.

Stewart, G.E., 1985, Hyperfine Interact. **23**, 1.

Stöhr, J., and J.B. Gruber, 1971, J. Chem. Phys. **55**, 4457.

Stöhr, J., and J.B. Gruber, 1975, Chem. Phys. **7**, 336.

Stöhr, J., D.N. Olsen and J.B. Gruber, 1971, J. Chem. Phys. **55**, 4463.

Sztucki, J., and W. Stręk, 1986a, Chem. Phys. Lett. **125**, 520.

Sztucki, J., and W. Stręk, 1986b, Phys. Rev. B **34**, 3120.

Tagiev, B.G., S.A. Abushov, G.M. Niftiev, C.M. Briskina, V.F. Zolin, V.M. Markushev and F.S. Aidaev, 1985, Phys. Status Solidi a **89**, K191.

Taibi, M., J. Aride, E. Antic-Fidancev, M. Lemaître-Blaise and P. Porcher, 1989, Phys. Status Solidi a **115**, 523.

Taibi, M., E. Antic-Fidancev, J. Aride, M. Lemaître-Blaise and P. Porcher, 1993, J. Phys.: Condens. Matter **5**, 5201.

Taibi, M., J. Aride, E. Antic-Fidancev, M. Lemaître-Blaise and P. Porcher, 1994, Phys. Status Solidi a **144**, 453.

Tanner, P.A., 1985a, Mol. Phys. **54**, 883.

Tanner, P.A., 1985b, J. Chem. Soc. Faraday Trans. 2 **81**, 1285.

Tanner, P.A., 1986a, Mol. Phys. **57**, 737.

Tanner, P.A., 1986b, J. Chem. Phys. **85**, 2344.

Tanner, P.A., 1986c, Mol. Phys. **58**, 317.

Tanner, P.A., 1988, Mol. Phys. **63**, 365.

Tanner, P.A., C.K. Jayasankar and F.S. Richardson, 1988, Mol. Phys. **65**, 49.

Tanner, P.A., J.R. Quagliano and F.S. Richardson, 1991, J. Chem. Soc. Faraday Trans. 2 **87**, 1707.

Tanner, P.A., Y.-L. Liu, M. Chua and M.F. Reid, 1994a, J. Alloys & Compounds **207/208**, 83.

Tanner, P.A., V.V. Ravi Kanth Kumar, C.K. Jayasankar and M.F. Reid, 1994b, J. Alloys & Compounds **215**, 349.

Teste de Sagey, G., P. Porcher, G. Garon and P. Caro, 1982, in: The Rare Earths In Modern Science and Technology, Vol. 3, eds G.J. McCarthy, H.B. Silber and J.J. Rhyne (Plenum Press, New York) p. 127.

Thomas, K.S., S. Singh and G.H. Dieke, 1963, J. Chem. Phys. **38**, 2180.

Thompson, L.C., 1979, Complexes, in: Handbook on the Physics and Chemistry of Rare Earths, Vol. 3, eds K.A. Gschneidner Jr and L. Eyring (North-Holland, Amsterdam) ch. 25, p. 209.

Thompson, L.C., and S.C. Kuo, 1989, J. Less-Common Met. **148**, 173.

Thompson, L.C., O.A. Serra, J.P. Riehl, F.S. Richardson and R.W. Schwartz, 1977, Chem. Phys. **26**, 393.

Thompson, L.C., S.C. Kuo and H.-D. Amberger, 1991, Eur. J. Solid State Inorg. Chem. **28**, 187.

Tie, S., Q. Su and Y. Yu, 1995, J. Solid State Chem. **114**, 282.

Tinsley, B.M., 1963, J. Chem. Phys. **39**, 3503.

Tkachuk, A.M., A.K. Przhevusskii, L.G. Morozova, A.V. Poletimova, M.V. Petrov and A.M. Korovkin, 1986, Opt. Spectrosc. (USSR) **60**, 176.

Tofield, B.C., H.P. Weber, T.C. Damer and P.F. Liao, 1975, J. Solid State Chem. **12**, 207.

Toledano, J.C., 1972, J. Chem. Phys. **57**, 4468.

Tomaschek, R., 1932a, Physik. Z. **33**, 878.
Tomaschek, R., 1932b, Nature **130**, 740.
Trenam, R.S., 1953, Proc. R. Soc. London Ser. A **66**, 118.
Tucker, A.W., and M. Birnbaum, 1979, in: Proc. Int. Conf. Laser '78, December 11–15, Orlando, FL (STS Press, McLean, VA).
Urland, W., 1979, Chem. Phys. Letters **62**, 525.
Valon, P., J.C. Gacon, A. Vedrine and G. Boulon, 1977, J. Solid State Chem. **21**, 357.
Van Vleck, J.H., 1937, J. Phys. Chem. **41**, 67.
Varsanyi, F., and G.H. Dieke, 1962, J. Chem. Phys. **36**, 2951.
Veyssie, M., and B. Dreyfus, 1967, J. Phys. Chem. Solids **28**, 499.
Voloshin, V.A., N.A. Kulagin, L.N. Ovander and A.M. Prudnikov, 1976, Opt. Spectrosc. (USSR) **39**, 334.
Voron'ko, Y.K., A.A. Kaminskii and V.V. Osiko, 1966, Sov. Phys. JETP **22**, 295.
Voron'ko, Y.K., V.V. Osiko, N.V. Savost'yanova, V.S. Federov and I.A. Shcherbakov, 1973, Sov. Phys. Solid State **14**, 2294.
Wadsack, R.L., J.L. Lewis, B.E. Argyle and R.K. Chang, 1971, Phys. Rev. B **3**, 4342.
Wang, Q., Y. Gao and A. Bulou, 1995, J. Phys. Chem. Solids **56**, 285.
Weber, M.J., 1971, Phys. Rev. B **4**, 3153.
Weber, M.J., 1973, J. Appl. Phys. **44**, 3205.
Weber, M.J., 1979, Rare earth lasers, in: Handbook on the Physics and Chemistry of Rare Earths, Vol. 4, eds K.A. Gschneidner Jr and L. Eyring (North-Holland, Amsterdam) ch. 35.
Weber, M.J., and T.E. Varitimos, 1971, J. Appl. Phys. **42**, 4996.
Weber, M.J., M. Bass, T.E. Varitimos and D.P. Bua, 1973, IEEE J. Quantum Electron. **QE-9**, 1079.
Weissbluth, M., 1978, Atoms and Molecules (Academic Press, New York).
Weller, P.F., 1967, J. Electrochem. Soc. **114**, 609.
Wheeler, R.G., F.M. Reanes and E.J. Wachtel, 1968, J. Appl. Phys. **39**, 915.
Wong, E.Y., 1963, J. Chem. Phys. **39**, 2781.
Wong, E.Y., and I. Richman, 1962, J. Chem. Phys. **36**, 1889.
Wong, E.Y., O.M. Stafsudd and D.R. Johnston, 1963a, J. Chem. Phys. **39**, 786.
Wong, E.Y., O.M. Stafsudd and D.R. Johnston, 1963b, Phys. Rev. **131**, 990.
Wood, D.L., 1963, J. Chem. Phys. **39**, 1671.
Wortman, D.E., 1968, Phys. Rev. **175**, 488.
Wortman, D.E., 1972, J. Phys. Chem. Solids **33**, 311.
Wortman, D.E., and D. Sanders, 1970, J. Chem. Phys. **53**, 1247.
Wortman, D.E., and D. Sanders, 1971, J. Chem. Phys. **55**, 3212.
Wortman, D.E., R.P. Leavitt and C.A. Morrison, 1974, J. Phys. Chem. Solids **35**, 591.
Wortman, D.E., C.A. Morrison and R.P. Leavitt, 1975a, Harry Diamond Laboratories Report TR-1726, 13pp.
Wortman, D.E., C.A. Morrison and R.P. Leavitt, 1975b, Phys. Rev. B **12**, 4780.
Wunderlich, J.A., 1977, Ph.D Thesis (University of Southern California).
Wybourne, B.G., 1965, Spectroscopic Properties of Rare Earths (Wiley-Interscience, New York).
Yang, P., S. Li and Y. Wang, 1991, J. Phys.: Condens. Matter **3**, 483.
Yen, W.M., 1989, Laser spectroscopy, in: Handbook on the Physics and Chemistry of Rare Earths, Vol. 12, eds K.A. Gschneidner Jr and L. Eyring (North-Holland, Amsterdam) ch. 87, p. 433.
Yen, W.M., W.C. Scott and A.L. Schawlow, 1964, Phys. Rev. **136**, A271.
Yen, W.M., C.G. Levey, S. Huang and S.T. Lai, 1981, J. Lumin. **24&25**, 659.
Yeung, Y.Y., and D.J. Newman, 1987, J. Chem. Phys. **86**, 6717.
Zhang, Q., J.-P. Jouart, M. Bouffard and G. Mary, 1994, Phys. Status Solidi b **184**, 559.
Zimmermann, H., and R. Boyn, 1985, Phys. Status Solidi b **130**, 315.
Zverev, G.M., G.Y. Kolodnyi and A.I. Smirnov, 1967, Opt. Spectrosc. (USSR) **23**, 325.
Zverev, G.M., G.Y. Kolodnyi and A.M. Onischenko, 1970, Sov. Phys. JETP **30**, 435.

Handbook on the Physics and Chemistry of Rare Earths
Vol. 23
edited by K.A. Gschneidner, Jr. and L. Eyring

Chapter 156

PHOSPHIDES

Yurij KUZ'MA and Stepan CHYKHRIJ
Institute of Chemistry, Ivan Franko L'viv State University,
Kyrylo & Mefodij Str. 6, L'viv, 290005, Ukraine

Contents

Symbols and abbreviations

a, *b*, *c*	unit-cell dimensions in nm	ST	structure type
at.%	atomic percentage	V	unit-cell volume in nm^3
CN	coordination number	wt.%	weight percentage
CP	coordination polyhedron	X	p-element (P, As, Sb, Si, Ge)
HTM	high-temperature modification	*x*, *y*, *z*	atomic coordinates
LTM	low-temperature modification	*Z*	number of formula units in unit cell
M	transition metal	α, β, γ	unit-cell angles in degrees
R	reliability factor of crystal structure determination	δ	interatomic distance, nm
sp.gr.	space group		

Introduction

The present chapter consists of two main sections, presenting data about binary and ternary rare-earth phosphides, respectively. Section 1 deals with material on phase diagrams of R–P systems, the crystal structures of all known binary phosphides, their chemical properties, and methods of preparation. Section 2 contains similar information on ternary rare-earth phosphides, and additionally includes systematized data on physical properties and the valence state of lanthanoid atoms.

The crystallochemical peculiarities and structural relationships of the binary and ternary rare-earth phosphides are discussed from the viewpoint of the coordination of the phosphorus atoms.

1. Binary phosphides

The present section deals with the material on binary phosphides in the following order. Section 1.1 presents data about interactions in R–P systems and some phase diagrams. The systems are considered in order of increasing R atomic mass. Information about the structure type of binary phosphides and their lattice parameters is included in this part. There are also references to works concerned with the investigation of their physical properties. Section 1.2 describes the structure types to which R binary phosphides belong. Each structure type contains a structure projection and the coordination polyhedra of the phosphorus atoms. Crystallochemical regularities of binary phosphide structures are considered in sect. 1.3. Generalized data on the chemical properties of the binary phosphides, including some thermodynamic characteristics, are reported in sect. 1.4. Section 1.5 is concerned with methods of binary rare-earth phosphide synthesis.

1.1. *R–P systems*

1.1.1. *Sc–P*

Scandium phosphides have been obtained by heat treating mixtures of elemental components in evacuated silica tubes. Komissarova et al. (1965) established that scandium monophosphide has a melting point higher than 2300 K and begins to dissociate at $T \approx 1173$ K. Berger (1981) determined the crystal structure of Sc_3P which is of the Fe_3C-type with $a = 0.67540$, $b = 0.88449$, $c = 0.57662$ and of Sc_7P_3 of the Th_7Fe_3-type with $a = 0.89340$, $c = 0.57349$. Berger (1980) revealed the existence of two polymorphous modifications of the phosphide Sc_3P_2, one with the structure of Cr_3C_2 ($a = 0.69781$, $b = 0.37570$, $c = 1.43655$) and the other with the anti-Sb_2S_3 structure ($a = 1.01075$, $b = 0.36944$, $c = 1.0179$). All these structures were studied by the X-ray powder method without determination of the atomic parameters. Parthé and Parthé (1963) obtained scandium monophosphide ScP for the first time and determined that its crystal structure belonged to ST NaCl ($a = 0.5312$). Niessen and de Boer (1981) mention the phosphides ScP_2 and Sc_2P but data about their crystal structure are absent. Electric and magnetic properties of ScP were studied by Perkins et al. (1981) and Burdet et al. (1988); X-ray spectral investigation of ScP was performed by Myers et al. (1985).

1.1.2. *Y–P*

Iandelli (1961) obtained yttrium monophosphide YP for the first time and determined that it crystallizes with the NaCl structure: $a = 0.5662$. Franzen and Hariharan (1980) studied the thermal dissociation of YP. Information about phosphides Y_2P and YP_2 (Niessen and de Boer 1981) needs confirmation. Ren and Meng (1985) determined that YP is a semiconductor with a band gap of 1.0 eV.

1.1.3. *La–P*

Iandelli and Botti (1936) obtained the phosphide LaP, Hordijenko and Hol'nik (1977) determined its melting point as 3400 K. Kost et al. (1983) state that thermal dissociation of LaP begins higher than 1123 K. Thermal dissociation of LaP was studied by Franzen and Hariharan (1980). No homogeneity range was found for the monophosphide LaP in the temperature range 800–2450 K by Hol'nik et al. (1979); this has been confirmed by other researchers. From these data one can conclude that LaP has a constant composition.

Phosphide LaP_2 was obtained for the first time by von Schnering et al. (1975) and LaP_5 by Wichelhaus and von Schnering (1976). Both phosphides were synthesized by heat treating a correct mixture of the elemental components with the addition of KI and I_2 in evacuated silica tubes. Two-zone heating (1353–923 and 1023–853 K) and different duration of treatment (5 and 7 days) were used for LaP_2 and LaP_5, respectively. Wichelhaus and von Schnering (1975) synthesized phosphide LaP_7 by interaction of the components in a melted eutectic mixture KCl + NaCl at 813 K. Ono et al. (1974) determined that LaP_5 does not decomposed up to 973 K.

Iandelli and Botti (1936) determined a NaCl-type structure for LaP with $a = 0.6024$, it was confirmed by Ono et al. (1974) ($a = 0.60346$). Phosphide LaP_2 has two polymorphous modifications. Hayakawa et al. (1976) established that the LTM (up to 1023 K) of LaP_2 crystallized with the $LaAs_2$ structure ($a = 1.2530$, $b = 0.8881$, $c = 1.3967$) and for the HTM of LaP_2 they proposed an orthorhombic structure with $a = 0.8839$, $b = 0.8882$, $c = 1.3966$, and a possible space group Im2a or Imma. Neither of these structures are completely determined. By the X-ray single-crystal method von Schnering et al. (1975) investigated the HTM of LaP_2 and found a monoclinic structure of a new type: $a = 0.8883$, $b = 1.3942$, $c = 0.8825$, $\beta = 90.15°$, $R = 0.063$.

Using an X-ray single-crystal method Wichelhaus and von Schnering (1976) established that LaP_5 crystallizes in a monoclinic structure of a new type: $a = 0.9768$, $b = 0.9679$, $c = 0.5578$, $\beta = 105.25°$, $R = 0.051$. Ono et al. (1974) give the other lattice parameters for LaP_5 (without a complete structure determination): $a = 0.4971$, $b = 0.9613$, $c = 0.5534$, $\beta = 103.8°$. According to the last data the a parameter is half of that given by Wichelhaus and von Schnering (1976), all other parameters satisfactorily agree. Taking into account the complete structure investigation performed by Wichelhaus and von Schnering (1976) we prefer their results.

Phosphide LaP_7 has a novel structure type with $a = 0.7923$, $b = 1.1656$, $c = 0.6989$, $\beta = 93.24°$, $R = 0.028$ (Wichelhaus and von Schnering 1975).

Ren and Meng (1985) studied the electrical properties of LaP and established that it is a semiconductor with a bandgap of 1.46 eV.

1.1.4. *Ce–P*

Using the results of X-ray, densimetric and magnetic analysis Vasil'eva et al. (1970) and Hulliger and Ott (1978) observed that cerium monophosphide has a small homogeneity range at temperatures between 1073–1473 K, but the limits of this range were not determined. Hordijenko and Hol'nik (1977) established the melting point of CeP as 3253 K. CeP_5 is not decomposed up to 973 K (Ono et al. 1974). von Schnering et al. (1976) reported the existence of a phosphide CeP_7.

Iandelli and Botti (1936) determined that the crystal structure of CeP belongs to the NaCl-type with $a=0.591$; a more precise value of the lattice parameter, $a=0.5909$, is reported by Iandelli (1961). CeP undergoes a first-order phase transition at a pressure of 9.0 HPa which is accompanied by a decreasing unit-cell volume of 3% (Vedel et al. 1987). CeP, with a NaCl-type structure, remains up to 19 HPa and at 19–23 HPa two modifications, one with NaCl and the other with a CsCl structure, exist. Leger et al. (1987) determined that at normal pressure cerium atoms are in the valence state Ce^{3+} and at 9.0 HPa the charge of the latter changes to $Ce^{3.35+}$.

The crystal structure of the LTM of CeP_2 belongs to the ST $NdAs_2$: $a=0.4065$, $b=0.6580$, $c=1.0145$, $\beta=105.64°$ (Ono et al. 1974) or $a=0.40641$, $b=0.65826$, $c=1.01591$, $\beta=105.686°$ (Hassler et al. 1974). von Schnering and Hönle (1988) report that the HTM of CeP_2 has the LaP_2 structure. The lattice parameters of CeP_5 have been determined using the X-ray powder method: $a=0.5500$, $b=0.9624$, $c=0.4955$, $\beta=105.83°$, possible space group $P2_1/m$ or $P2_1$ (Ono et al. 1974); these values are close to the respective parameters of LaP_5 determined by the same authors. Perhaps the structure of CeP_5 belongs to the LaP_5-type (cell parameter a in this case must be doubled). Using an X-ray single-crystal method von Schnering et al. (1976) determined a LaP_7-type structure for the compound CeP_7.

1.1.5. *Pr–P*

The phase diagram of the Pr–P system was proposed by Mironov (1981) (fig. 1). Mironov (1984) reports that the homogeneity range of cerium monophosphide depends on the preparation method. At a saturation of metallic praseodymium by phosphorus the homogeneity range is described by the formula $PrP_{0.85-1.00}$, and at the phosphorus separation from monophosphide by the formula $PrP_{1.000-0.974}$. Hol'nik et al. (1979) confirmed that the homogeneity range includes the compositions PrP and $PrP_{0.974}$. Mironov (1988) determined that a dense layer of phosphorus defective PrP ($a=0.585$) is formed on the metal surface during the interaction of metallic praseodymium with phosphorus vapors; with further interaction the defectivity decreases and the lattice parameter a increases. Torbov et al. (1971) noted that thermal dissociation of PrP begins at 713 K.

Higher praseodymium phosphides PrP_2 and PrP_5 have been obtained by synthesis from the elemental components at 1273 K (Hassler et al. 1974) and at 973 K (Ono et al. 1974), respectively. Data about the existence of the phosphides $PrP_{2.5}$ (Torbov et al. 1974) and PrP_7 (von Schnering et al. 1976) need confirmation.

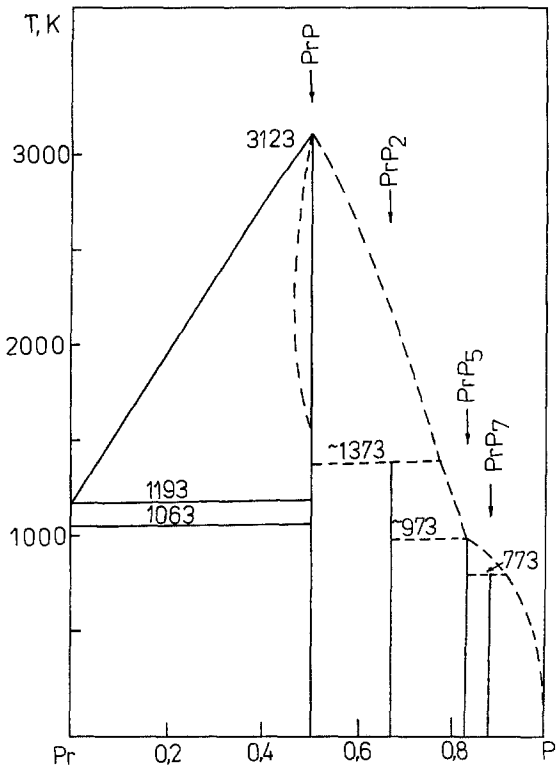

Fig. 1. Pr–P system.

Iandelli and Botti (1936) established the NaCl-type structure for PrP, $a = 0.5872$, Ono et al. (1974) report a refinement of the parameter, $a = 0.59143$. Hol'nik et al. (1979) indicate that the lattice parameter depends on the phosphorus content in the phosphide: at the composition $PrP_{0.974}$ $a = 0.5897$ and at PrP $a = 0.5903$.

The structure of PrP_2 was determined by Hassler et al. (1974) by powder method; it belongs to the $NdAs_2$-type with $a = 0.40315$, $b = 0.6553$, $c = 1.01046$, $\beta = 105.968°$. Using the X-ray powder method Ono et al. (1974) determined the lattice parameters of PrP_5 ($a = 0.5471$, $b = 0.9589$, $c = 0.4934$, $\beta = 103.68°$, possible sp.gr. $P2\bar{1}/m$ and $P2\bar{1}$), but a complete structure investigation was not carried out. Wittmann et al. (1977) report that the structure of PrP_5 belongs to the NdP_5-type. Using the X-ray single-crystal method von Schnering et al. (1976) established LaP_7-type structure for PrP_7.

1.1.6. *Nd–P*

The phase diagram of the Nd–P system (fig. 2) constructed using the results obtained by Samsonov et al. (1977, 1978) is given in Kost et al. (1983). The existence of the compound $NdP_{2.5}$ requires confirmation. Thermal dissociation of NdP begins at 653 K (Torbov et al. 1974). The phosphide NdP has been synthesized by heat treatment of the elemental components in an evacuated silica tube at 1023 K (Wichelhaus and von Schnering 1976).

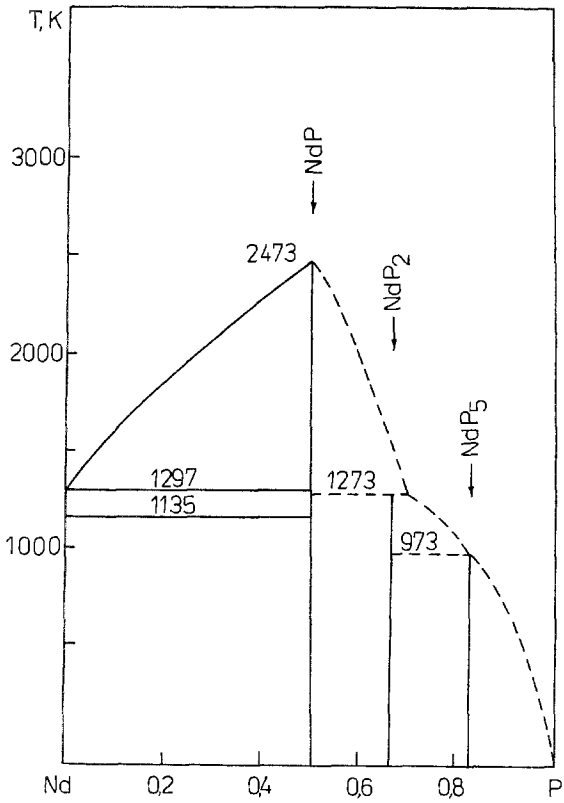

Fig. 2. Nd–P system.

Iandelli and Botti (1937) determined that NdP has the NaCl-type crystal structure with $a = 0.5838$. According to von Schnering and Hönle (1988) NdP_2 crystallizes with the $NdAs_2$ structure. Using a single-crystal method Wichelhaus and von Schnering (1976) determined the NdP_5 structure to be a new type with $a = 0.4938$, $b = 0.9551$, $c = 0.5444$, $\beta = 103.27°$, R = 0.037.

Niedzielski and Troć (1984) studied the magnetic susceptibility of a polycrystalline sample NdP in the temperature range 4.2–800 K and $H < 7$ kE using the Faraday method and found antiferromagnetic order at $T_N = 11$ K. Ren and Meng (1985) found NdP to be a semiconductor with a bandgap of 1.15 eV.

1.1.7. *Sm–P*

Hol'nik et al. (1977) investigated the homogeneity range of samarium monophosphide at temperatures of 1315–2022 K using mass-spectral and X-ray phase analysis and determined that it is described by formula $SmP_{1.000-0.982}$. Torbov et al. (1971) showed that thermal dissociation of SmP begins at 623 K. Wichelhaus and von Schnering (1976) obtained the phosphide SmP_5 by heat treatment of the elemental components

in an evacuated silica tube at 973 K during 5–7 days. Ono et al. (1974) note that the phosphide SmP_5 is decomposed above 973 K.

Iandelli (1956) found the NaCl-type structure for SmP with $a=0.5760$. The crystal structure of SmP_5 belongs to NdP_5-type with $a=0.4936$, $b=0.9508$, $c=0.5411$, $\beta=102.90°$ (Wichelhaus and von Schnering 1976).

The electrophysical properties of SmP were studied by Paderno et al. (1970), Ren and Meng (1985) determined that SmP is a semiconductor with a bandgap of 1.1 eV.

1.1.8. *Eu–P*

A number of compounds are reported in the Eu–P system, namely Eu_2P, Eu_4P_3, $EuP_{0.91}$, Eu_4P_5, $EuP_{1.82}$, $EuP_{2.75}$ (Mironov et al. 1975), Eu_3P_2 (Hulliger and Vogt 1970), Eu_5P_4 (von Schnering and Hönle 1988), EuP (Bruzzone et al. 1964), Eu_3P_4 (von Schnering et al. 1984), EuP_2 (Mironov and Brygalina 1973), two modifications of EuP_3 (von Schnering et al. 1976) and EuP_7 (von Schnering and Wittmann 1980). The composition of Eu_4P_3 and Eu_4P_5 was established by chemical analysis (Mironov et al. 1975) and they probably are identical with the compounds of similar composition Eu_3P_2 and Eu_3P_4 with determined crystal structures. Mironov and Brygalina (1974) measured the melting point of the phosphides Eu_3P_2 (1573 K), EuP (2473 K) and EuP_2 (1113 K); Eu_3P_4 is melted at 1220 K (von Schnering et al. 1984). Schmettow et al. (1984) investigated the kinetics of thermal decomposition of EuP_7 and EuP_3, which proceed by the following schemes: $EuP_7 \rightarrow EuP_3$ (637–795 K) $\rightarrow EuP_2$ (749–945 K) and $EuP_3 \rightarrow EuP_2$ (738–956 K) $\rightarrow$ Eu_3P_4 (788–949 K) $\rightarrow$ EuP (993–1227 K). Howell and Pytlewski (1970) found that the thermal dissociation of EuP begins at 1103 K. The temperature of the polymorphous transformation of EuP_3 is about 940 K (Schmettow et al. 1980).

Hulliger and Vogt (1970) determined an anti-Th_3P_4-type structure for compound Eu_3P_2, $a=0.5755$. von Schnering and Hönle (1988) reported that phosphide Eu_4P_3 belongs to the Th_3P_4-type structure and that Eu_5P_4 belongs to Eu_5As_4-type, but they do not determine their lattice parameters. EuP has the NaCl-structure with $a=0.5755$ (Bruzzone et al. 1964). Using an X-ray single-crystal method von Schnering et al. (1984) determined the crystal structure of Eu_3P_4 which belongs to the Sr_3As_4-type with $a=1.4050$, $b=1.7085$, $c=0.5738$, $R=0.044$. EuP_2 has its own structure type (mP18) (von Schnering and Hönle 1988). α-EuP_3 belongs to $EuAs_3$-type structure: $a=0.9068$, $b=0.7222$, $c=0.5598$ (von Schnering et al. 1976) and β-EuP_3 belongs to the $EuAs_3$-type: $a=1.123$, $b=0.7345$, $c=0.8394$, $\beta=103.34°$ (Chattopadhyay et al. 1988b). Using an X-ray single-crystal method von Schnering and Wittmann (1980) determined the EuP_7 structure as a new type: $a=1.1488$, $b=0.5700$, $c=1.0610$, $\beta=106.08°$, $R=0.031$.

Schmettow et al. (1984) estimated the standard enthalpy of formation of europium phosphides compared to EuP and concluded that α-EuP_3 and EuP_7 have high stability and EuP_2 is unstable. Mironov et al. (1975) investigated the magnetic properties of the europium phosphides and showed that EuP contains Eu^{3+} ions, Eu_3P_2 and EuP_2 – Eu^{2+} ions and the other phosphides are characterized by an intermediate valence of europium atoms. The magnetic behavior of α-EuP_3 at low temperature is very complicated

(Chattopadhyay et al. 1987a, 1988b,c). The Curie point of Eu_3P_2 is 25 K (Hulliger and Vogt 1970).

1.1.9. *Gd–P*

Two binary phosphides GdP and GdP_5 were found in the Gd–P system; both were obtained by heating a mixture of the elemental components in evacuated silica tubes. According to Menge and von Schnering (1976) GdP_5 has already formed at 873 K. The melting point of GdP was found by different authors to be from 2229 to 2773 K; these data are generalized by Kost et al. (1983). Mironov et al. (1971) note that homogeneity range of gadolinium monophosphide is described by formula $GdP_{1.00-0.96}$. Torbov et al. (1971) determined that the thermal dissociation of GdP begins at 603 K.

The crystal structure of GdP is of the NaCl-type with $a = 0.5723$ (Iandelli 1961). Menge and von Schnering (1976) determined that GdP_5 has the NdP_5 structure with $a = 0.4928$, $b = 0.9446$, $c = 0.5370$, $\beta = 102.58°$, $R = 0.039$.

Kost et al. (1983) have summarized the results on the electrical and magnetic properties of GdP. According to Menge and von Schnering (1976) GdP is paramagnetic with $\mu_{eff} = 7.83\ \mu_B$.

1.1.10. *Tb–P*

Two binary compounds, TbP and TbP_5, are known in the Tb–P system; TbP_5 was obtained by interaction of the elemental components in evacuated silica tubes at 773–1023 K (Wittmann et al. 1977). Reliable data about the homogeneity range of TbP are unknown. Thermal dissociation of TbP begins at 553 K (Torbov et al. 1971).

Olcese (1961) determined that the crystal structure of TbP belongs to the NaCl-type with $a = 0.5688$; these data are in good agreement with Iandelli (1961): $a = 0.5686$. Hulliger and Levy (1969) found that the cubic cell of TbP is deformed into a rhombohedral cell below 9.5 K. TbP_5 has the NdP_5-type structure (Wittmann et al. 1977).

Faffius and Kotzler (1983) measured the homogeneous magnetization of a TbP single crystal in the temperature range 5–14 K and in a magnetic field up to 50 kE and observed a first-order transition from a paramagnetic to an antiferromagnetic phase with a Néel temperature $T_N = 7.1$ K.

1.1.11. *Dy–P*

Two binary compounds, DyP and DyP_5, were found in the Dy–P system, their homogeneity ranges have not been determined. Phosphide DyP_5 was obtained by the same method as TbP_5. According to Torbov et al. (1971) the thermal dissociation of DyP begins at 523 K.

DyP is of the NaCl-type structure with $a = 0.5654$ (Iandelli 1961). Hulliger and Levy (1969) observed a tetragonal deformation of the DyP cell below 10 K and at 4.2 K the lattice parameters are: $a = 0.5655$, $c = 0.5638$. Wittmann et al. (1977) determined the NdP_5-type structure for the compound DyP_5.

Ren and Meng (1988) determined that DyP is an *n*-type semiconductor with a bandgap of 1.15 eV; some electrical parameters of DyP were also measured.

1.1.12. *Ho–P*

The compounds HoP and HoP_5 are obtained in Ho–P system; HoP_5 was obtained by the same method as TbP_5.

HoP has the NaCl-type structure with $a=0.5626$ (Iandelli 1961). Fischer et al. (1985) report HoP phase transitions at low temperatures connected with magnetic transformations. HoP_5 has an NdP_5-type structure (Wittmann et al. 1977).

1.1.13. *Er–P*

In the system Er–P, phosphides ErP and ErP_5 are known; the last was obtained by the same method as used for TbP_5.

Independently, Iandelli (1961) and Bruzzone (1961) determined an NaCl-type structure for ErP, $a=0.5606$. ErP_5 has the NdP_5-type structure (Wittmann et al. 1977).

1.1.14. *Tm–P*

The compounds TmP and TmP_5 are found in the system Tm–P. TmP_5 was obtained by the same method as for TbP_5.

Iandelli determined that TmP crystallized with the NaCl-type structure, $a=0.5573$. TmP_5 is of the NdP_5-type structure (Wittmann et al. 1977).

1.1.15. *Yb–P*

The compound Yb_3P_2 was synthesized for the first time by Pytlewski and Howell (1967). Wittmann et al. (1977) report two modifications of YbP_5 obtained by interaction of elemental components in evacuated silica tubes at 773–1023 K. At higher temperatures the compound YbP is formed. Torbov et al. (1971) determined that thermal dissociation of YbP begins at 1193 K.

YbP has the NaCl-type structure with $a=0.5554$ (Iandelli 1961). According to Wittmann et al. (1977) one of the modifications of YbP_5 has the NdP_5-type structure. The other modification of YbP_5, type (mP24), which was determined by the X-ray single-crystal method (von Schnering et al. 1976) is of a new type.

Vol and Kohan (1976) systematized the physical characteristics of YbP. Ren and Meng (1988) confirmed that YbP is a *n*-type semiconductor with a band gap of 1.30 eV. Bonville et al. (1988) studied the Mössbauer spectra of YbP in the temperature range 0.045–10 K.

1.1.16. *Lu–P*

Binary phosphides LuP and LuP_5 are known in the Lu–P system; LuP_5 was obtained by the same method as TbP_5.

Iandelli (1961) established the NaCl-type structure for LuP, $a=0.5533$; LuP_5 is of NdP_5-type structure (Wittmann et al. 1977).

1.2. *Crystal structure of binary phosphides*

The characteristics of the structure types of binary phosphides given in the text contain the following information: the name of the first representative of the ST and its Pearson symbol; reference; the figure number showing the structure; the space group and lattice constants. After that the table contains the atom identifications, the position in the space group and atomic parameters *x, y, z*; the last column lists the atoms forming the coordination arrangement of the central atom.

Each figure shows one projection of the unit cell, the coordination polyhedra of the phosphorus atoms and some structure peculiarities. In the case where atomic parameters of some phosphides are not refined they are given as for their respective prototype or other isotypic structure. STs are considered in order of increasing phosphorus content in the compound. The number near circles indicates the third coordinate of the atom.

Krypyakevych (1977) has proposed the systematics of structure types of intermetallic and related compounds based on the analysis of the coordination polyhedra of the smallest atom. This author distinguishes 17 groups to which the coordination polyhedra of the smallest atoms belong. In analyzing the crystal structures of intermetallic compounds some problems, connected with choice of the smallest atom, arise. In the case of the metal compounds with boron, carbon, silicon, and phosphorus the nonmetal element is always the smallest. Kuz'ma (1983) successfully used this concept for the analysis of the structure types of borides. In analyzing the structure types of the binary and ternary phosphides we will hold to the systematics developed by Krypyakevych (1977) also because the CPs of phosphorus atoms are given in the figures.

1.2.1. *Fe_3C, oP16*

Structure type Fe_3C (Villars and Calvert 1985; fig. 3, table 1) has space group Pnma, $a=0.67540$, $b=0.8449$, $c=0.57662$ (for Sc_3P) (Berger 1981).

Only one phosphide Sc_3P belongs to Fe_3C-type structure. The atomic parameters in Sc_3P are not refined. In the structure of Sc_3P (fig. 3) paired columns of deformed trigonal prisms are placed parallel to the *Y* axis. Phosphorus atoms occupy only half of the trigonal prisms, therefore in filled columns [PSc_6] and empty [$\square Sc_6$] prisms alternate with one another.

Table 1
Atomic parameters for Sc_3P[a]

Atom	Position	Fractional coordinates			Atomic arrangement
		x	*y*	*z*	
Sc1	4(*c*)	0.044	1/4	0.837	12Sc 2P
Sc2	8(*d*)	0.181	0.063	0.337	11Sc 2P
P	4(*c*)	0.881	1/4	0.431	6Sc

[a] Atomic coordinates are as for the structure Fe_3C (Villars and Calvert 1985).

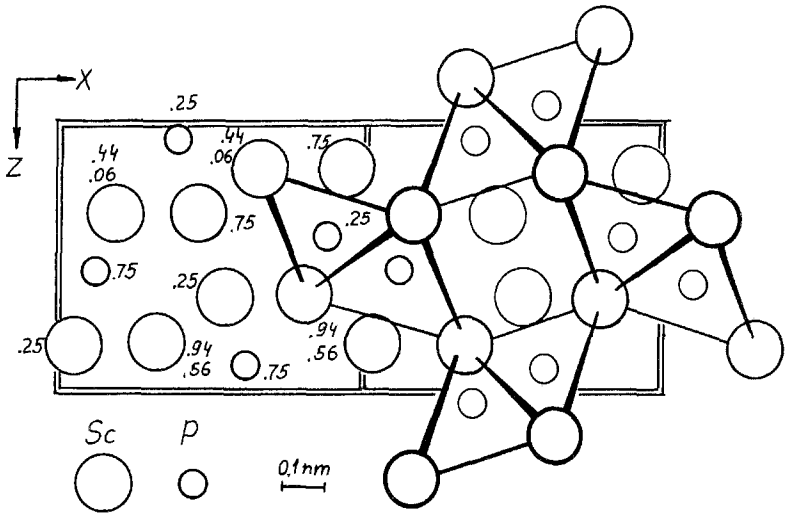

Fig. 3. Crystal structure of Sc_3P (ST Fe_3C) and stacking of trigonal prisms.

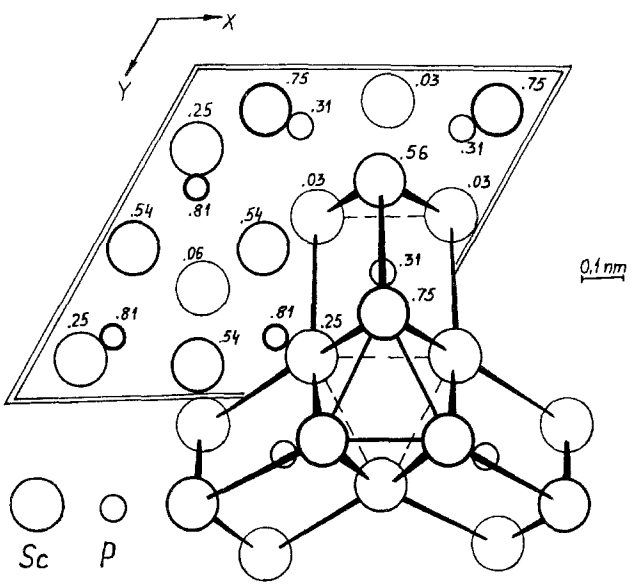

Fig. 4. Crystal structure of Sc_7P_3 (ST Th_7Fe_3) and joining of trigonal prisms [PSc_6] and empty octahedra [$\square Sc_6$].

1.2.2. *Th_7Fe_3, hP20*

Structure type Th_7Fe_3 (Florio et al. 1956; fig. 4, table 2) has space group $P6_3mc$, $a = 0.89340$, $c = 0.57349$ (for Sc_7P_3) (Berger 1981).

Table 2
Atomic parameters for Sc_7P_3 [a]

Atom	Position	Fractional coordinates			Atomic arrangement
		x	y	z	
Sc1	2(*b*)	1/3	2/3	0.060	12Sc 3P
Sc2	6(*c*)	0.126	0.874	0.250	11Sc 3P
Sc3	6(*c*)	0.544	0.456	0.030	11Sc 2P
P	6(*c*)	0.815	0.185	0.310	6Sc

[a] Atomic coordinates are as for the structure Th_7Fe_3 (Florio et al. 1956).

In the structure Sc_7P_3 (ST Th_7Fe_3) scandium atoms also form trigonal prisms joined with one another via edges of their bases. Triangular sides of these are joined in such a manner that trigonal prisms form empty octahedra (fig. 4). Trigonal prisms are occupied by phosphorus atoms and no P–P contacts occur. Besides that one can see empty octahedra in the structure of Sc_7P_3. Scandium atoms have CNs 15, 14 and 13.

1.2.3. *Cr_3C_2, oP20*

Structure type Cr_3C_2 (Meinhardt and Krisement 1960; fig. 5, table 3) has space group Pnma, $a=0.69781$, $b=0.37570$, $c=1.43655$ (for Sc_3P_2) (Berger 1980).

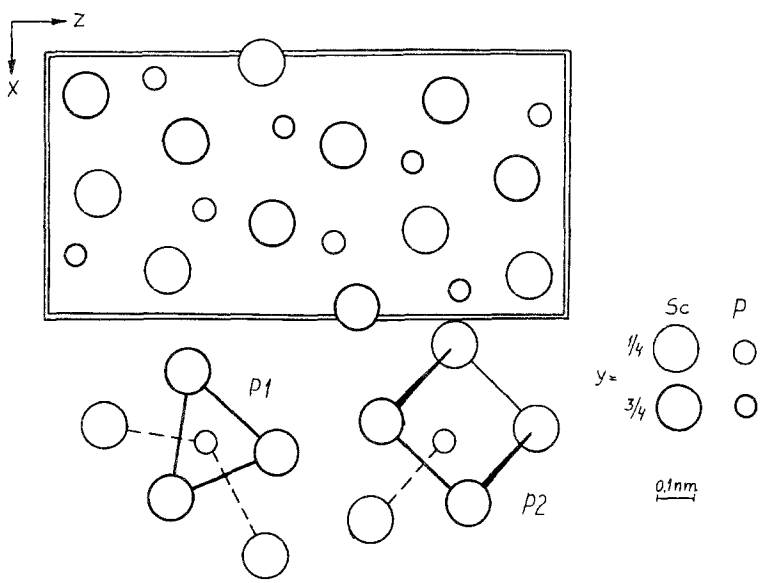

Fig. 5. Crystal structure of Sc_3P_2 (ST Cr_3C_2).

Table 3
Atomic parameters for Sc_3P_2 (ST Cr_3C_2)[a]

Atom	Position	Fractional coordinates			Atomic arrangement
		x	y	z	
Sc1	4(c)	0.030	1/4	0.406	9Sc 5P
Sc2	4(c)	0.175	1/4	0.770	8Sc 4P
Sc3	4(c)	0.850	1/4	0.930	6Sc 5P
P1	4(c)	0.092	1/4	0.204	8Sc
P2	4(c)	0.228	1/4	0.952	7Sc

[a] Atomic coordinates are as for the structure Cr_3C_2 (Meinhardt and Krisement 1960).

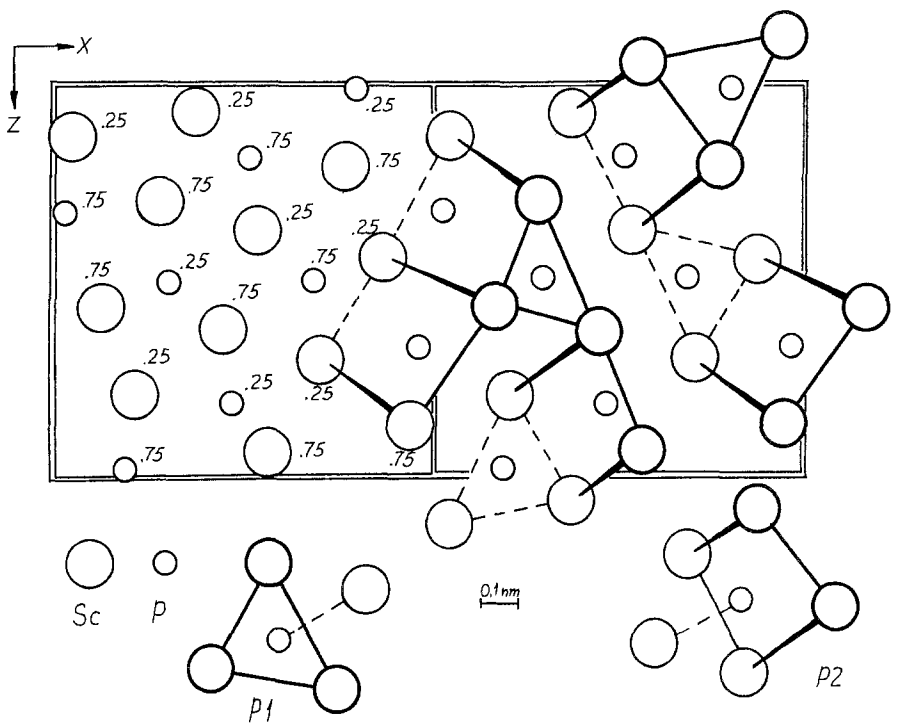

Fig. 6. Crystal structure of Sc_3P_2 (ST anti-Sb_2S_3) and stacking of trigonal prisms.

1.2.4. *anti-Sb_2S_3, oP20*

Structure type anti-Sb_2S_3 (Scavnicar 1960; fig. 6, table 4) has space group Pnma, $a = 1.01075$, $b = 0.36944$, $c = 1.01793$ (for Sc_3P_2) (Berger 1980).

The compound Sc_3P_2 has two modifications with the structures of Cr_3C_2 and anti-Sb_2S_3 (figs. 5, 6). These structure types are closely related; in both structures two-thirds of all the trigonal prisms formed by scandium atoms are filled with atoms of smaller size.

Table 4
Atomic parameters for Sc_3P_2 (ST anti-Sb_2S_3)[a]

Atom	Position	Fractional coordinates			Atomic arrangement
		x	*y*	*z*	
Sc1	4(*c*)	0.04668	1/4	0.12969	8Sc 5P
Sc2	4(*c*)	0.37613	1/4	0.06439	7Sc 5P
Sc3	4(*c*)	0.21613	1/4	0.79647	7Sc 5P
P1	4(*c*)	0.30851	1/4	0.49890	7Sc
P2	4(*c*)	0.47390	1/4	0.82207	7Sc

[a] Atomic coordinates are as for the structure Hf_3P_2 (Lundström 1968).

All trigonal prisms joined in columns are centered by phosphorus atoms, and the filled and empty trigonal prisms alternate in stacks. The allocation of columns and stacks of trigonal prisms in the structures is shown in figs. 5 and 6. The columns of trigonal prisms are connected with empty prisms and the smallest atoms (phosphorus) have no contact with one another.

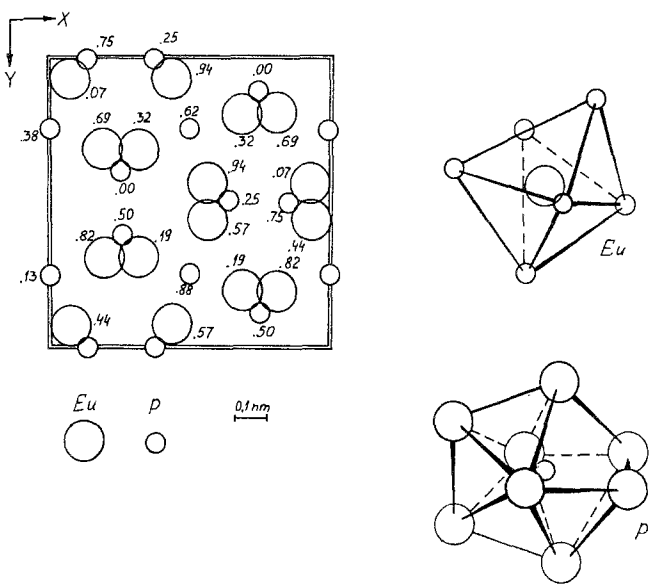

Fig. 7. Crystal structure of Eu_3P_2 (ST anti-Th_3P_4).

1.2.5. *anti-Th_3P_4, cI20*

Structure type anti-Th_3P_4 (Meisel 1939; fig. 7, table 5) has space group $I\bar{4}3d$, $a = 0.9026$ (for Eu_3P_2) (Hulliger and Vogt 1970).

Table 5
Atomic parameters for Eu_3P_2

Atom	Position	Fractional coordinates			Atomic arrangement
		x	y	z	
Eu	16(*c*)	0.065	0.065	0.065	6P
P[a]	12(*a*)	3/8	0	1/4	8Eu

[a] Occupancy 88%.

The crystal structure of the phosphide Eu_3P_2 (Hulliger and Vogt 1970) belongs to the anti-Th_3P_4 type (Meisel 1939). The europium atoms occupy the positions of the phosphorus atoms in Th_3P_4 and the P atoms occupy 88% of the positions of the Th atoms, as a result the composition of this europium phosphide is described by the formula Eu_3P_2. The CP of the phosphorus atoms – a normal 8-vertices polyhedron also occurs in the sheelite structure; the europium atoms are placed into a distorted octahedron (fig. 7). Krypyakevych (1962) considers ST anti-Th_3P_4 as a deformed packing of α-Fe-type cells, which are formed by ions of P^{3-} and Th^{4+} ions included in voids of such a packing. Interatomic distances between Eu and P atoms are shorter than the sum of the atomic radii of the respective elements: $\delta_{Eu-P} = 0.3311$ and 0.2953.

1.2.6. *NaCl, cF8*

Structure type NaCl (Bragg 1914; fig. 8, table 6) has space group Fm3m, $a = 0.60346$ (for LaP) (Ono et al. 1974).

All rare-earth monophosphides have the NaCl-type structure (Bragg 1914). It is characterized by octahedral coordination of phosphorus atoms (fig. 8). The interatomic distances ($\delta_{R-P} = 1/2a$) are close to the sum of atomic radii of the components.

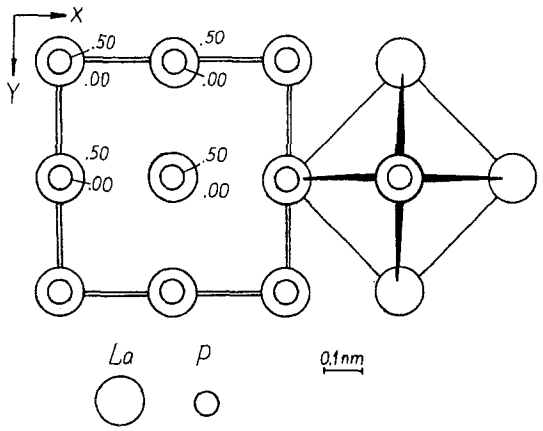

Fig. 8. Crystal structure of LaP (ST NaCl).

Table 6
Atomic parameters for LaP

Atom	Position	Fractional coordinates			Atomic arrangement
		x	*y*	*z*	
La	4(*a*)	0	0	0	6P
P	4(*b*)	1/2	1/2	1/2	6La

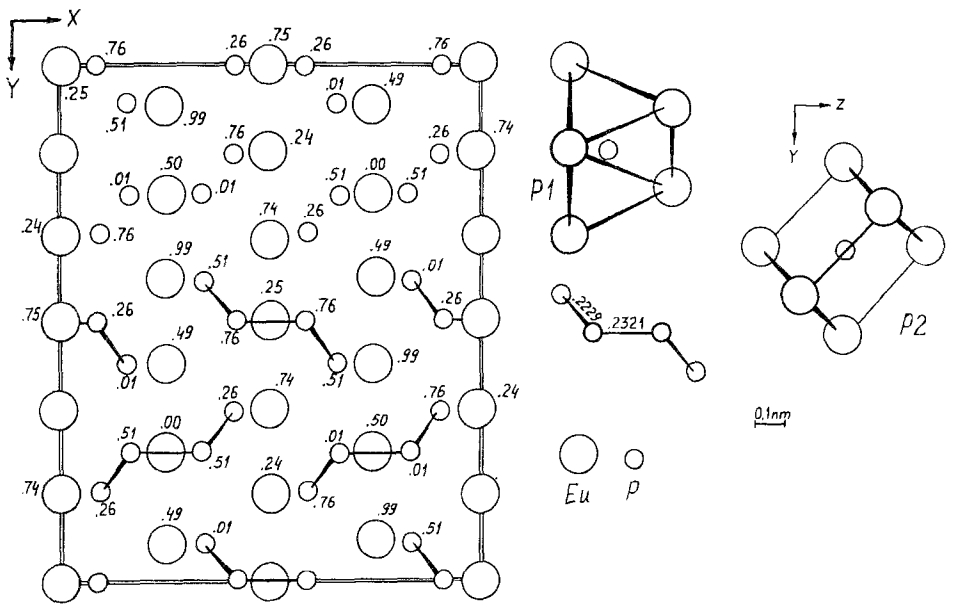

Fig. 9. Crystal structure of Eu_3P_4 (ST Sr_3As_4) and fragment of a chain of phosphorus atoms.

1.2.7. *Sr_3As_4, oF56*

Structure type Sr_3As_4 (Deller and Eisenmann 1977; fig. 9, table 7) has space group Fdd2, $a = 1.4050$, $b = 1.7085$, $c = 0.5738$ (for Eu_3P_4) (von Schnering et al. 1984).

The phosphide Eu_3P_4 has the ST Sr_3As_4 (von Schnering et al. 1984). The CPs of the phosphorus atoms are deformed trigonal prisms (one of the prisms edges is almost a right quadrangle) formed by europium atoms. The coordination environment of the phosphorus atoms includes other P atoms: one P1 and two P2 (fig. 9). Four phosphorus atoms are linked in a zigzag-like chain (fig. 9) which may be considered as a part of the framework from the α-$ThSi_2$ structure. Sr_3As_4 may then be considered as a defect variant of α-$ThSi_2$ ($Eu_3P_4\square_2$) (von Schnering et al. 1984). The interatomic distances of the respective atoms in the structure Eu_3P_4 vary between 0.4028 and 0.4082 (for Eu–Eu); 0.3202 and 0.2998 (Eu–P); $\delta_{P1-P2} = 0.2229$; $\delta_{P2-P2} = 0.2321$.

Table 7
Atomic parameters for Eu_3P_4

Atom	Position	Fractional coordinates			Atomic arrangement
		x	*y*	*z*	
Eu1	8(*a*)	0	0	1/4	8Eu 8P
Eu2	16(*b*)	0.24812	0.08229	0.99324	8Eu 8P
P1	16(*b*)	0.3399	0.9228	0.0079	6Eu 1P
P2	16(*b*)	0.5826	0.9999	0.2566	6Eu 2P

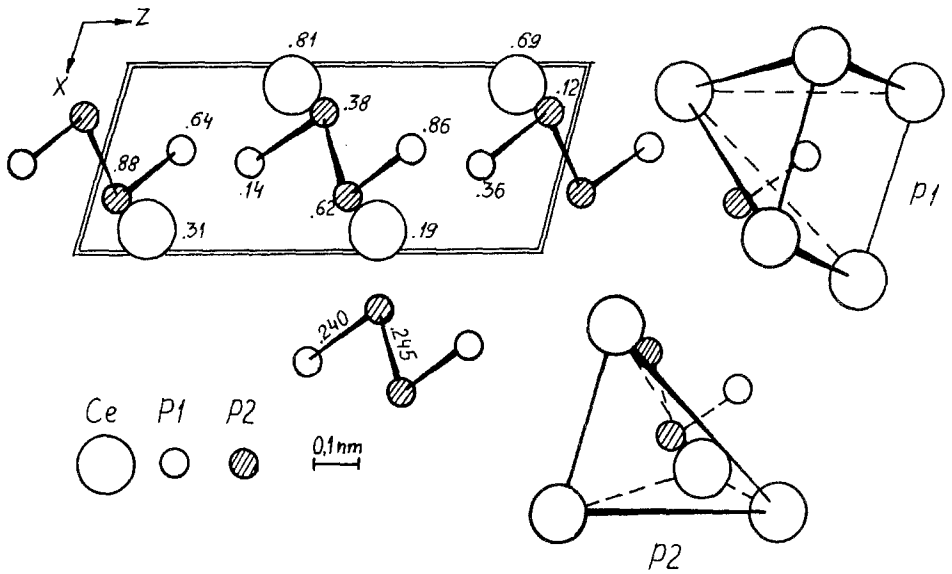

Fig. 10. Crystal structure of CeP_2 (ST $NdAs_2$) and fragment of a chain of phosphorus atoms.

Table 8
Atomic parameters for CeP_2 [a]

Atom	Position	Fractional coordinates			Atomic arrangement	
		x	*y*	*z*		
Ce	4(*e*)	0.9124	0.3126	0.1402		9P
P1	4(*e*)	0.4610	0.6436	0.1708	5Ce	1P
P2	4(*e*)	0.2727	0.3777	0.4503	4Ce	2P

[a] Atomic coordinates are as for the structure $NdAs_2$ (Villars and Calvert 1985).

1.2.8. *$NdAs_2$, mP12*

Structure type $NdAs_2$ (Villars and Calvert 1985; fig. 10, table 8) has space group $P2_1/c$, $a = 0.40641$, $b = 0.65826$, $c = 1.01591$, $\beta = 105.686°$ (for CeP_2) (Hassler et al. 1974).

The crystal structure of CeP_2 belongs to $NdAs_2$-type (fig. 10). The phosphorus atoms have CPs in the form of tetragonal pyramids (P1) and distorted tetrahedra (P2) with one or two additional phosphorus atoms, respectively (fig. 10). The phosphorus atoms form fragments of zigzag-like chains (fig. 10). The interatomic distances vary between 0.4064 and 0.3932 (Ce–Ce); 0.3127 and 0.2919 (Ce–P); $\delta_{P1-P2} = 0.2404$; $\delta_{P2-P2} = 0.2453$.

1.2.9. *LaP_2, mI48*

Structure type LaP_2 (von Schnering et al. 1975; fig. 11, table 9) has space group Ia, $a = 0.8883$, $b = 1.3942$, $c = 0.8825$, $\beta = 90.15°$.

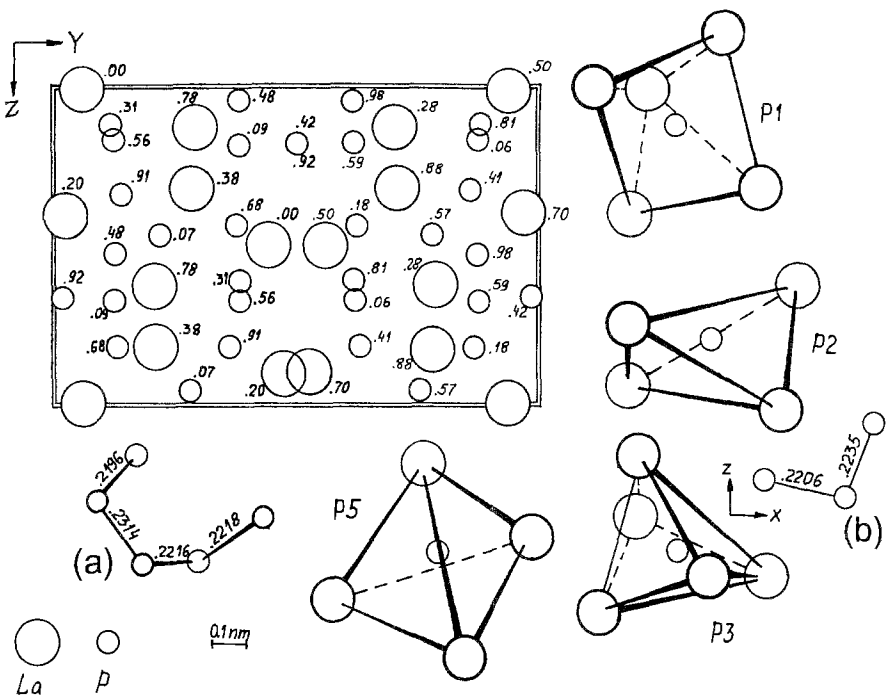

Fig. 11. Crystal structure of LaP_2 and method of joining of (a) five and (b) three phosphorus atoms.

The structure type LaP_2 (von Schnering et al. 1975) is characterized by a variety of phosphorus CPs, such as tetragonal pyramids (P1 and P8), trigonal bipyramids (P3 and P4) and distorted tetrahedra (all other P atoms). Some of them are shown in fig. 11. The phosphorus atoms are linked in groups consisting of five or three atoms (fig. 11). Interatomic distances are: $\delta_{La-La} = 0.4078–0.3848$; $\delta_{La-P} = 0.3195–0.2968$; $\delta_{P-P} = 0.2314–0.2197$.

Table 9
Atomic parameters for LaP_2

Atom	Position	Fractional coordinates			Atomic arrangement
		x	y	z	
La1	4(*a*)	0.20449	0.02279	0.39836	3La 9P
La2	4(*a*)	0.77735	0.20685	0.62875	3La 9P
La3	4(*a*)	0	0.05815	0	3La 9P
La4	4(*a*)	0.38055	0.28849	0.32170	3La 9P
P1	4(*a*)	0.3138	0.1168	0.1153	5La 1P
P2	4(*a*)	0.5582	0.1221	0.1593	4La 2P
P3	4(*a*)	0.6746	0.3723	0.4352	5La 1P
P4	4(*a*)	0.4842	0.3805	0.0289	5La 1P
P5	4(*a*)	0.4152	0.5052	0.1684	4La 2P
P6	4(*a*)	0.0859	0.3790	0.1766	4La 1P
P7	4(*a*)	0.0666	0.2177	0.4643	4La 2P
P8	4(*a*)	0.9126	0.1358	0.3184	5La 1P

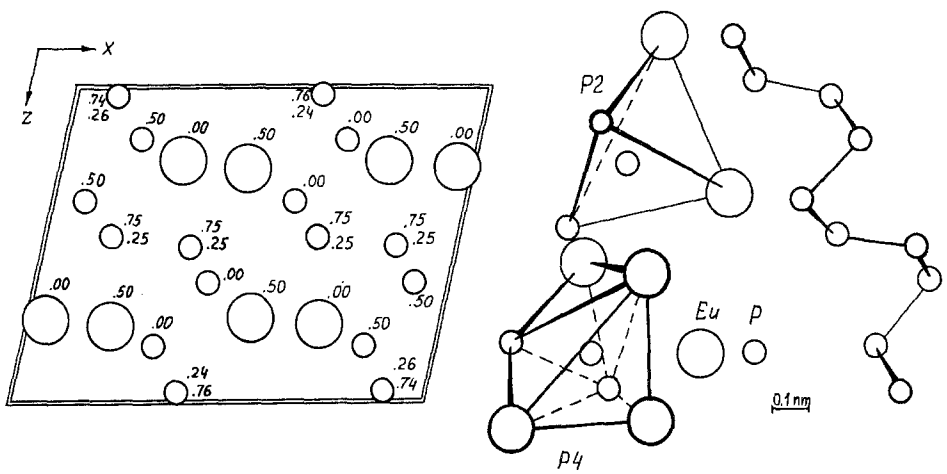

Fig. 12. Crystal structure of α-EuP_3 (ST BaP_3) and chain of phosphorus atoms.

1.2.10. *BaP_3, mC16*

Structure type BaP_3 (von Schnering and Dahlmann 1971; fig. 12, table 10) has space group C2/m, $a = 0.9068$, $b = 0.7222$, $c = 0.5598$, $\beta = 113.15°$ (for α-EuP_3) (von Schnering et al. 1976).

The crystal structure of α-EuP_3 belongs to the ST BaP_3 (von Schnering and Dahlmann 1971), but we have not found the data about the atomic parameters in the α-EuP_3 structure; fig. 12 shows the structure of α-EuP_3 with the atomic coordinates as for BaP_3. The phosphorus atoms have CPs in the form of trigonal bipyramids (P1) and distorted

Table 10
Atomic parameters for α-EuP_3

Atom	Position	Fractional coordinates			Atomic arrangement
		x	*y*	*z*	
Eu	4(*i*)	0.173	0	0.312	4Eu 9P
P1	4(*i*)	0.407	0	0.030	2Eu 3P
P2	8(*j*)	0.413	0.235	0.286	4Eu 2P

[a] Atomic coordinates are as for the structure BaP_3 (Villars and Calvert 1985).

tetrahedra (P2) (fig. 12). P1 atoms link P2 pairs forming a puckered network parallel to XY (fig. 12). The reported interatomic distances are in the range: $\delta_{Eu-P} = 0.3427–0.2990$; $\delta_{P-P} = 0.2250–0.2201$ (Bauhofer et al. 1985).

1.2.11. *SrP_3, mC32*

Structure type SrP_3 (Dahlmann and von Schnering 1973; fig. 13, table 11) has space group C2/m, $a = 1.123$, $b = 0.7345$, $c = 0.8394$, $\beta = 103.34°$ (for β-EuP_3) (Chattopadhyay et al. 1988c).

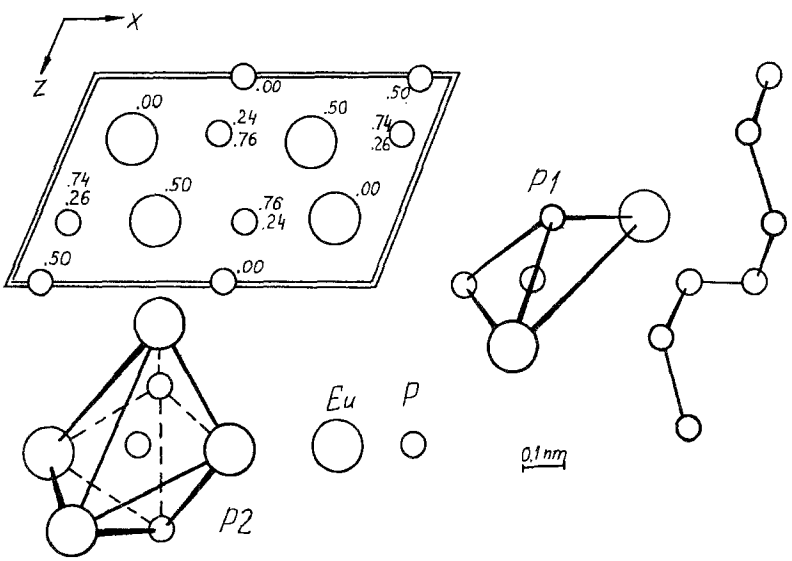

Fig. 13. Crystal structure of β-EuP_3 (ST SrP_3) and chain of phosphorus atoms.

The crystal structure of β-EuP_3 belongs to the ST SrP_3 (Dahlmann and von Schnering 1973), its projection is shown in fig. 13; the atomic coordinates as accepted for SrP_3. The CPs of the phosphorus atoms are trigonal bipyramids (P1 and P2) and distorted octahedra (P3 and P4) (fig. 13). The phosphorus atoms P1 and P3 form puckered six-member rings linked into a framework by P2 atoms. Besides that there occur contacts

Table 11
Atomic parameters for β-EuP_3 [a]

Atom	Position	Fractional coordinates			Atomic arrangement
		x	y	z	
Eu1	4(i)	0.2921	0	0.2243	4Eu 11P
Eu2	4(i)	0.9573	0	0.2591	5Eu 9P
P1	4(i)	0.6758	0	0.1645	2Eu 3P
P2	4(i)	0.5837	0	0.3672	2Eu 3P
P3	8(j)	0.0985	0.2622	0.0259	4Eu 2P
P4	8(j)	0.1485	0.2457	0.4879	4Eu 2P

[a] Atomic parameters are as for the structure SrP_3 (Villars and Calvert 1985).

between P2 and P4 atoms which form zigzag-like chains –P2–P4–P2–P4–. Interatomic distances are: $\delta_{Eu-P} = 0.3512–0.2999$, $\delta_{P-P} = 0.2224–0.2186$ (Bauhofer et al. 1985).

1.2.12. *NdP_5, mP12*

Structure type NdP_5 (Wichelhaus and von Schnering 1976; fig. 14, table 12) has space group $P2_1/m$, $a = 0.4938$, $b = 0.9551$, $c = 0.5444$, $\beta = 103.27°$.

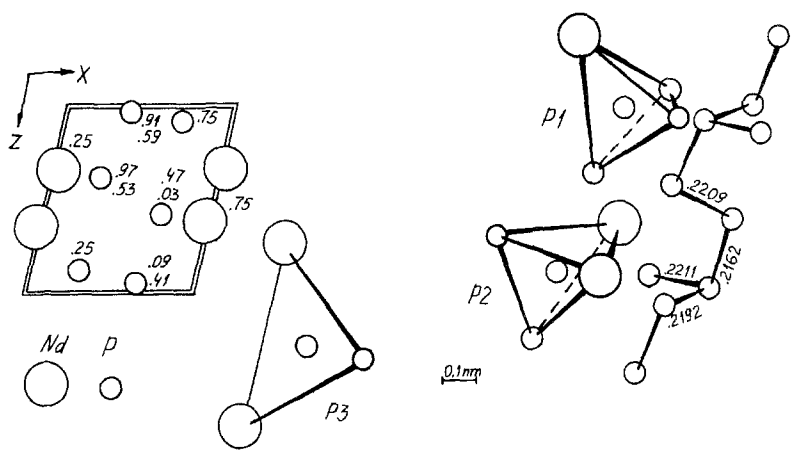

Fig. 14. Crystal structure of NdP_5 and framework of phosphorus atoms.

A projection of the crystal structure of NdP_5 (Wichelhaus and von Schnering 1976) is shown in fig. 14. The CPs of all phosphorus atoms are distorted tetrahedra formed by neodymium and phosphorus atoms (fig. 14). Zigzag-like chains of phosphorus atoms are joined with one another by P3 atoms and form a framework. No Nd–Nd contacts occur in NdP_5 structure. Interatomic distances are: $\delta_{Nd-P} = 0.3046–0.2991$; $\delta_{P-P} = 0.2211–0.2162$.

Table 12
Atomic parameters for NdP_5

Atom	Position	Fractional coordinates			Atomic arrangement	
		x	*y*	*z*		
Nd	2(*e*)	0.01903	1/4	0.35744		8P
P1	4(*f*)	0.3815	0.5903	0.0422	1Nd	3P
P2	4(*f*)	0.2899	0.5338	0.3991	2Nd	2P
P3	2(*e*)	0.2864	1/4	0.9092	2Nd	2P

1.2.13. *LaP_5, mP24*

Structure type LaP_5 (Wichelhaus and von Schnering 1976; fig. 15, table 13) has space group $P2_1/m$, $a = 0.9768$, $b = 0.9679$, $c = 0.5576$, $\beta = 105.25°$.

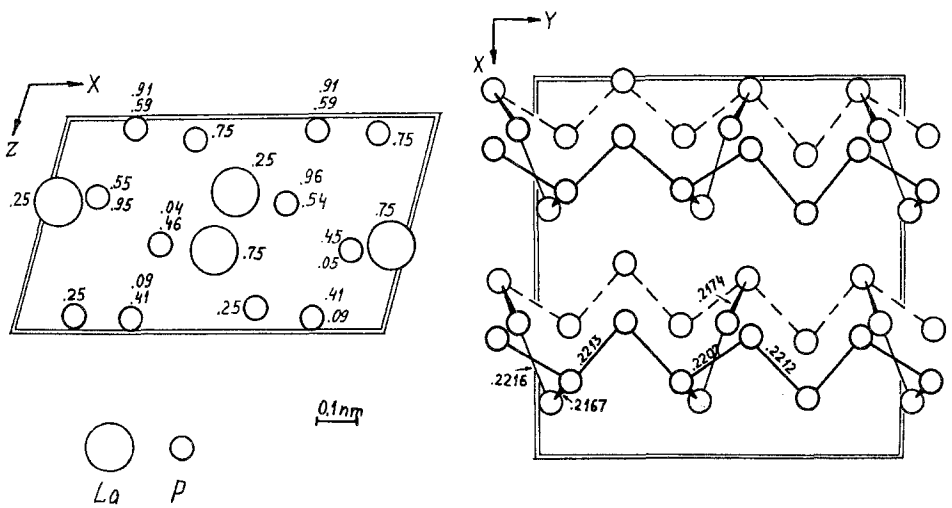

Fig. 15. Crystal structure of LaP_5 and framework of phosphorus atoms.

The structure type LaP_5 (Wichelhaus and von Schnering 1976) is closely related to the NdP_5-type and differs from it by a double lattice parameter *a* (fig. 15). In both structures the CPs of the phosphorus atoms and their bond types are identical. Interatomic distances are: $\delta_{La-P} = 0.3121$–0.3035; $\delta_{P-P} = 0.2216$–0.2167.

Table 13
Atomic parameters for LaP_5

Atom	Position	Fractional coordinates			Atomic arrangement	
		x	y	z		
La1	2(*e*)	0.03434	1/4	0.38966		8P
La2	2(*e*)	0.51321	1/4	0.36193		8P
P1	4(*f*)	0.1891	0.5942	0.0256	1La	3P
P2	4(*f*)	0.6895	0.5856	0.0494	1La	3P
P3	4(*f*)	0.1373	0.5447	0.3707	2La	2P
P4	4(*f*)	0.6562	0.5387	0.4110	2La	2P
P5	2(*e*)	0.1518	1/4	0.9418	2La	2P
P6	2(*e*)	0.6396	1/4	0.9165	2La	2P

1.2.14. *LaP_7, mP32*

Structure type LaP_7 (Wichelhaus and von Schnering 1976; fig. 16, table 14) has space group $P2_1/n$, $a=0.7923$, $b=1.1656$, $c=0.6989$, $\beta=93.24°$.

In the crystal structure of LaP_7 (Wichelhaus and von Schnering 1976) all the phosphorus atoms have CPs in the form of distorted tetrahedra of two kinds: $[PLaP_3]$ and $[PLa_2P_2]$ (fig. 16). The first are characteristic of atoms P1, P2, P5 and P7, and the second of P3, P4 and P6. The phosphorus atoms form a framework (fig. 16). The interatomic distances are: $\delta_{La-P}=0.3232–0.3061$. $\delta_{P-P}=0.2246–0.2172$.

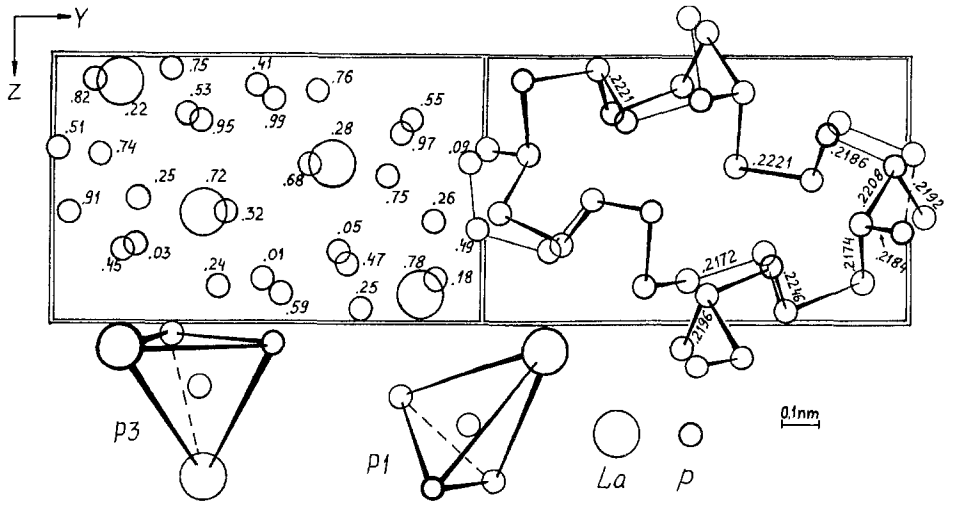

Fig. 16. Crystal structure of LaP_7 and framework of phosphorus atoms.

Table 14
Atomic parameters for LaP_7

Atom	Position	Fractional coordinates			Atomic arrangement	
		x	*y*	*z*		
La	4(*e*)	0.21745	0.15034	0.10282		10P
P1	4(*e*)	0.4080	0.4661	0.0968	1La	3P
P2	4(*e*)	0.7376	0.1144	0.3747	1La	3P
P3	4(*e*)	0.9531	0.3374	0.2501	2La	2P
P4	4(*e*)	0.8209	0.0984	0.0848	2La	2P
P5	4(*e*)	0.9934	0.5122	0.1552	1La	3P
P6	4(*e*)	0.5280	0.3105	0.2144	2La	2P
P7	4(*e*)	0.7516	0.2812	0.0368	1La	3P

1.2.15. *EuP_7, mP32*

Structure type EuP_7 (von Schnering and Wittmann 1980; fig. 17, table 15) has space group $P2_1/n$, $a = 1.1488$, $b = 0.5700$, $c = 1.0610$, $\beta = 106.08°$.

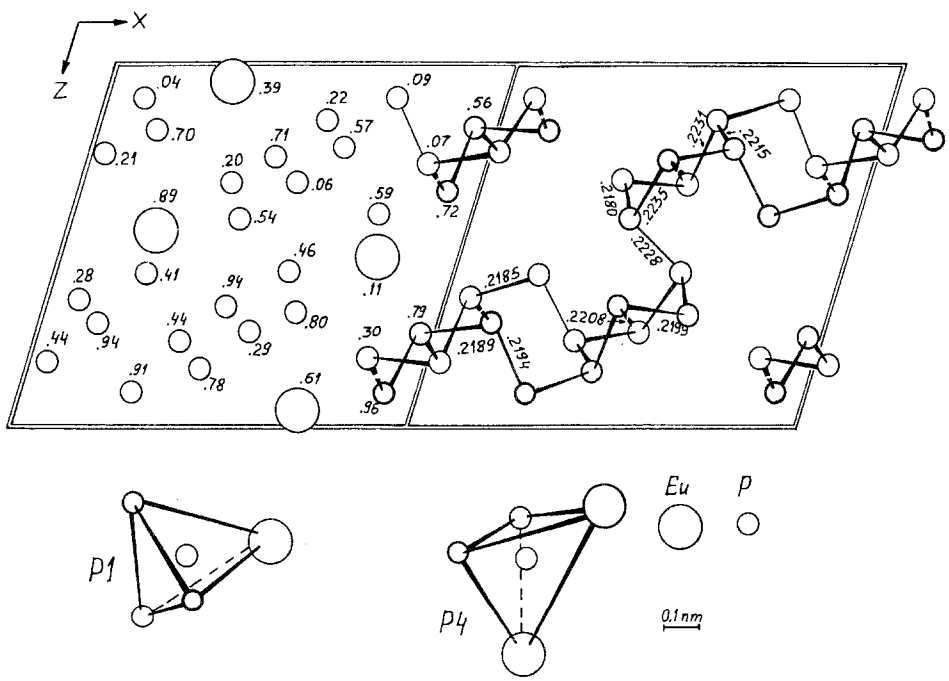

Fig. 17. Crystal structure of EuP_7 and framework of phosphorus atoms.

Table 15
Atomic parameters for EuP_7

Atom	Position	Fractional coordinates			Atomic arrangement	
		x	y	z		
Eu	4(*e*)	0.2863	0.3931	0.0376		9P
P1	4(*e*)	0.0837	0.0405	0.0796	1Eu	3P
P2	4(*e*)	0.5664	0.2176	0.1487	1Eu	3P
P3	4(*e*)	0.0293	0.2074	0.2453	1Eu	3P
P4	4(*e*)	0.3636	0.2031	0.3249	2Eu	2P
P5	4(*e*)	0.8621	0.0667	0.2763	1Eu	3P
P6	4(*e*)	0.7226	0.0940	0.0879	2Eu	2P
P7	4(*e*)	0.5418	0.0549	0.3308	1Eu	3P

The coordination of phosphorus atoms in the EuP_7-type structure (von Schnering and Wittmann 1980) is the same as in the LaP_7-structure (fig. 17). The phosphorus atoms are linked in ribbons of complicated configuration (fig. 17). The distances between the phosphorus atoms in the ribbons vary between 0.2235 and 0.2180, while those between phosphorus atoms from different ribbons are about 0.350. The interatomic distances Eu–P are 0.3262–0.3062.

1.3. *Crystallochemical regularities*

The reported data on the formation of binary rare-earth phosphides and their crystal structure provides an opportunity to make some generalizations. The data about compositions and structure types of all known binary rare-earth phosphides are listed in table 16.

Known scandium phosphides contain 50 or less at.% of phosphorus and in this way they differ in principle from other rare-earth phosphides. The crystal structures of scandium phosphides (except ScP) are characterized by a trigonal-prismatic coordination of phosphorus atoms. They are more closely related to the structures of the IVa transition-metal (Zr and Hf) phosphides than with the other rare-earth phosphides.

The greatest number of phosphides are known for europium, and, certainly, this is connected to the variable valence of europium. That is why the other binary phosphorus systems of the rare earths with probable variable valence require additional investigation, particularly the higher phosphides RP_7 of light rare earths. No promethium phosphides are known, but formation of PmP and PmP_5 compounds is very probable.

Phosphorus CPs in the structures of the binary rare-earth phosphides belong to six groups and the structure types belong to four of 17 groups distinguished by Krypyakevych (1977). The smallest atoms have only a few kinds of coordination polyhedra. The relationship of such a structure to a definite structure group is determined by the polyhedron with the fewest number of vertices. As one can see from table 17 there is

Table 16
Composition and structure types of binary rare-earth phosphides

Comp.	Str. type	Sc	Y	La	Ce	Pr	Nd	Pm	Sm	Eu	Gd	Tb	Dy	Ho	Er	Tm	Yb	Lu
R_3P	Fe_3C	■																
R_7P_3	Th_7Fe_3	■																
R_3P_2	Cr_3C_2	■																
	anti-Sb_2S_3	■																
	anti-Th_3P_4									■							■	
R_5P_4	Eu_5As_4									■								
RP	NaCl	■	■	■	■	■	■		■	■	■	■	■	■	■	■	■	■
R_3P_4	Sr_3As_4									■								
RP_2	$NdAs_2$				■	■	■											
	LaP_2			■	■													
RP_3	$EuAs_3$									■								
	SrP_3									■								
RP_5	NdP_5		■			■	■		■		■	■	■	■	■	■	■	■
	LaP_5			■	■													
	β-YbP_5																■	
RP_7	LaP_7			■	■	■												
	EuP_7									■								

Table 17
Coordination polyhedra of phosphorus atoms in the structures of binary rare-earth phosphides

ST	CP of P atom					
	normal polyhedron, 8 vertices	trigonal prism	octahedron	trigonal bipyramid	tetragonal pyramid	tetrahedron
Fe_3C		■				
Th_7Fe_3		■				
Cr_3C_2		■				
anti-Sb_2S_3		■				
anti-Th_3P_4	■					
NaCl			■			
Sr_3As_4		■				
$NdAs_2$					■	■
LaP_2				■	■	■
BaP_3			■	■		
SrP_3			■	■		
NdP_5						■
LaP_5						■
LaP_7						■
EuP_7						■

a regular change from the definite structure group to another group due to the increasing phosphorus content in the compound. In compounds with a P content up to 0.57 at.% the coordination environment of the phosphorus atoms are normal 8-vertices polyhedra and trigonal prisms. Only in monophosphides P atoms have octahedral coordination, and, together with a trigonal bipyramidal one in both EuP_3 modifications the CPs have six vertices. All phosphides with phosphorus content higher than 80 at.% are characterized by tetrahedral coordination of P atoms.

Analysis of the minimum interatomic distances in structures of binary phosphides (table 18) does not show any clear tendencies. The δ_{R-P} largely depends on the atomic radius of R and to a smaller degree on the phosphide composition. Hovewer, some increase of the minimum interatomic distances δ_{R-P} is observed in phosphides with higher phosphorus contents. The minimum value of the δ_{P-P} for most phosphides corresponds to the P–P distances in the phosphorus modifications, 0.221 (white phosphorus) and 0.224 (red phosphorus) with an average value of 0.2219 (Hittorf phosphorus)

Table 18
Minimum interatomic distances in the binary rare-earth phosphides

Phosphide	ST	Minimum δ	
		R–P	P–P
LaP	NaCl	0.3017	–
Eu_3P_4	Sr_3As_4	0.2998	0.2229
CeP_2	$NdAs_2$	0.2919	0.2404
LaP_2	LaP_2	0.2968	0.2196
α-EuP_3	BaP_3	0.2990	0.2201
β-EuP_3	SrP_3	0.2999	0.2186
NdP_5	NdP_5	0.2991	0.2162
LaP_5	LaP_5	0.3035	0.2167
LaP_7	LaP_7	0.3061	0.2172
EuP_7	EuP_7	0.3062	0.2180

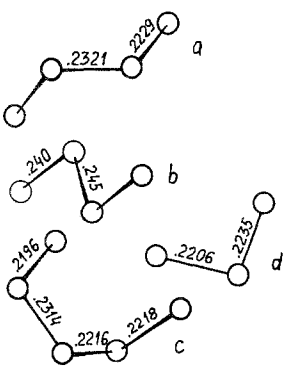

Fig. 18. Bond types of phosphorus atoms in the structures of (a) Eu_3P_4, (b) NdP_2 and (c, d) LaP_2.

(Krebs 1968). According to Pearson (1977) the covalent radius of the phosphorus atom in a single bond is 0.110.

In all binary rare-earth phosphides with a phosphorus content equal to or less than 50 at.% the phosphorus atoms are isolated and no P–P contact occurs. Chemical bonding between phosphorus atoms is observed in phosphides with higher phosphorus contents (figs. 18, 19). In these structures phosphorus atoms are linked to one another forming zigzag-like chains. Increasing the P content in compounds leads to the appearance of complicated frameworks (fig. 19). It is considered that separate groups of phosphorus atoms have a negative charge and form complicated anions. In the structure of monophosphides, phosphorus atoms are isolated and are in the P^{3-} valence state, and are compensated by R^{3+} cations. In the phosphide Eu_3P_4 the phosphorus anions have the composition P_4^{6-}. In LaP_2 (von Schnering et al. 1975) there exist two types of anions (P_3^{5-} and P_5^{7-}) which correspond to the phosphanes P_3H_5 and P_5H_7, respectively. Thus, the structure of LaP_2 may be considered as derivatives of those phosphanes ($La_4P_3P_5$). Using

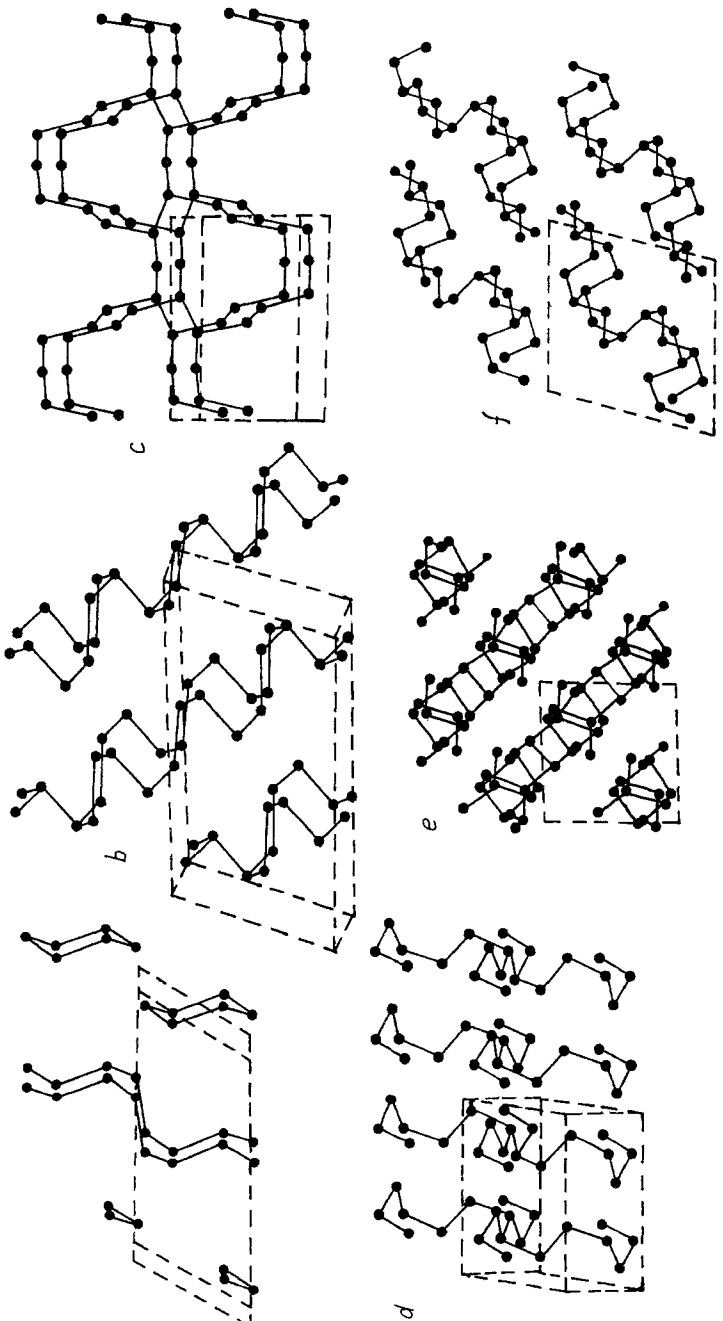

Fig. 19. Bond types of phosphorus atoms in the structures of (a) α-EuP_3, (b) β-EuP_3, (c) NdP_5, (d) LaP_5, (e) LaP_7 and (f) EuP_7.

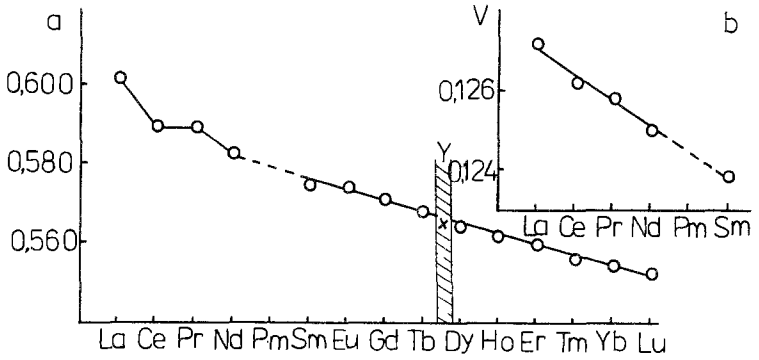

Fig. 20. (a) Lattice parameter a of rare-earth monophosphides and (b) unit cell volume of rare-earth pentaphosphides per one formula unit vs rare-earth atomic number.

a formal valence scheme penta and heptaphosphides may be considered as $R^{3+}(P_5)^{3-}$ and $R^{3+}(P_7)^{3-}$, respectively. Magnetic susceptibility measurements of GdP_5 at 298 K (Menge and von Schnering 1976) which allows calculating the effective magnetic moment of the gadolinium atom ($\mu_{exp} = 7{,}83\ \mu_B$) confirms the existence of Gd^{3+} ions.

Some information about the valence state of the lanthanoid atoms in their compounds shows the dependence of the lattice parameters due to the change of the R atomic number. All the rare earths may be considered for monophosphides with the NaCl-type structure (fig. 20). Using the listed data one can make conclusions about the R^{3+} valence state of all the rare earths. A small deviation from a linear dependence of the lattice parameter vs. atomic number is observed only for cerium monophosphide. This anomaly is probably due to an intermediate valence of cerium atoms between Ce^{3+} and Ce^{4+}. For the light rare-earth pentaphosphides we consider the change of the unit-cell volumes which correspond to one formula units. The variation is caused by the RP_5 phosphides belonging to two structure types with a different number of formula units per unit cell. As one can see (fig. 20b) a linear dependence indicates the trivalent state of the R atoms in these compounds.

Magnetic susceptibility measurements (Iandelli 1956, 1961) confirm the R^{3+} valence state of the rare-earth atoms in monophosphides. The magnetic behavior of all rare-earth monophosphides shows the Curie–Weiss law, except SmP and EuP which show Van Vleck paramagnetism.

The magnetic properties of the europium phosphides were especially studied in detail. Using the calculation of the effective magnetic moments of the europium atoms Mironov et al. (1975) determined the valence state of the europium atoms in phosphides: in EuP europium is almost solely in the Eu^{3+} state, in EuP_2 the valence state is Eu^{2+} and in Eu_3P_2 and Eu_4P_5 (there may be a question about the compound Eu_3P_4) europium atoms are in intermediate states between Eu^{2+} and Eu^{3+}. The existence of Eu^{2+} ions in Eu_3P_2 and EuP_2 was also shown by Hulliger and Vogt (1970) and Busch et al. (1971). von Schnering et al. (1984) note that the magnetic moment of europium in Eu_3P_4 ($\mu_{eff} = 7.94\ \mu_B$) is less than that for the Eu^{2+} ion; it may be rationalized by the presence of up to 5 at.% of Eu^{3+}.

Reliable data about the valence state of ytterbium atoms in their binary phosphides have not been found.

1.4. *Chemical properties of binary rare-earth phosphides*

The chemical properties of the binary rare-earth phosphides have been studied fully only for monophosphides, their thermodynamic characteristics have also been determined. Thermodynamic data of formation and atomization of the R monophosphides are listed in table 19.

Table 19
Standard enthalpy of formation and atomization (kJ/mol) of solid binary rare-earth phosphides

Compound	$-\Delta H^0_{298.15\,K}$	Reference(s)	$\Delta H^0_{atom.,298.15\,K}$	Reference(s)
ScP	343.5	Franzen et al. (1980)	940.98	Chua and Pratt (1974)
YP	412	Iandelli (1961)	1051	Chua and Pratt (1974)
LaP	319.66	Hordijenko (1988)	1082.6	Hordijenko (1989)
			1068.59	Hordijenko et al. (1979)
			1137.42	Franzen et al. (1980)
LaP_2	453	Niessen and de Boer (1981)		
CeP	313.8	Hordijenko (1988)	1097.14	Hordijenko et al. (1979)
PrP	356.9	Hordijenko (1988)		
NdP	346.9	Hordijenko (1988)	990.8	Hordijenko et al. (1979)
SmP	378.2	Hordijenko (1988)	842.6	Hordijenko (1989)
EuP	306.3	Hordijenko (1988)	797.9	Hordijenko and Mironov (1983)
GdP	313.8	Hordijenko et al. (1982)	1027.3	Hordijenko et al. (1982)
TbP	313.8[a]	Hordijenko (1988)		
DyP	315.1[a]	Hordijenko (1988)		
HoP	316.7[a]	Hordijenko (1988)		
ErP	318.8[a]	Hordijenko (1988)		
TmP	319.2[a]	Hordijenko (1988)		
YbP	320.9[a]	Hordijenko (1988)		
LuP	322.2[a]	Hordijenko (1988)	1066.9	Hordijenko et al. (1979)

[a] Predicted data.

Powders of the monophosphides (except EuP and, to some extent, LaP) are stable in air. Mironov et al. (1977) determined that rare-earth phosphides are oxidized in air above 673 K. The products of oxidation are complex phosphates and above 1223 K orthophosphates.

The chemical behaviors of some rare-earth monophosphides in different solvents are listed in table 20. Kost et al. (1983) showed that the monophosphides (except EuP) react slightly with water. Mineral acids (HNO_3, HCl) and CH_3COOH decompose

Table 20
Interaction of rare-earth monophosphides with some chemical reagents[a]

Phosphide	HNO_3		HCl		$HCl:HNO_3$	H_2SO_4		H_2O dist.	H_2O_2 3%	NaOH 5%	Reference(s)
	conc	1:1	conc	1:1		conc	1:1				
ScP	68.8	CS	78.5	CS	–	69.5	CS	2.1	–	NR	Komissarova et al. (1965)
LaP	CS	CS	CS	CS	CS	SS	SS	NR	NR	NR	Samsonov and Endrzeevskaja (1963)
CeP	CS	CS	CS	CS	–	–	CS	4.4	14	15.5	Sinitsina et al. (1970)
PrP	CS	CS	CS	CS	–	–	97	1.7	3.6	2.2	Sinitsina et al. (1970)
NdP	CS	CS	CS	CS	CS	SS	SS	NR	NR	NR	Endrzeevskaja and Samsonov (1965)
SmP	CS	CS	CS	CS	CS	–	–	0.3	0.4	0.4	Sinitsina et al. (1970)
YbP	CS	CS	CS	CS	–	390	CS	NR	NR	NR	Sinitsina et al. (1970)

[a] Powder; interaction time 1 hour. Abbreviations: CS, completely soluble; SS, slightly soluble; NR, no interaction.
Numbers indicate solubility in wt.% compared to initial mass of sample.

R monophosphides producing PH_3. Polyphosphides are stable in water and are dissolved only in oxidizing acids.

von Schnering et al. (1984) note that Eu_3P_2 hydrolyzes slightly. The products of its interaction with water and with H_2SO_4 are phosphine and diphosphine, respectively. LaP_2 may be kept in air and in water (von Schnering et al. 1975). Dilute acids interact by forming PH_3, P_2H_4 and solid phosphane. Interaction with dilute alkaline solutions proceeds slowly and also produces PH_3.

Single crystals of LaP_5 and NdP_5 are stable in dilute alkaline solution and non-oxydizing acids (Wichelhaus and von Schnering 1976). Single crystals of GdP_5 are stable in concentrated solutions of NaOH and HCl, but are slowly decomposed by concentrated HNO_3 (Menge and von Schnering 1976). The phosphide LaP_7 does not interact with dilute solutions of alkalis and non-oxidizing acids (Wichelhaus and von Schnering 1975).

In summary we can conclude that the chemical stability of binary rare-earth phosphides increases with increasing phosphorus content of the compounds.

1.5. *Preparation of binary rare-earth phosphides*

The direct methods based on interaction between the components at high temperatures are most frequently used for preparing binary rare-earth phosphides. As a rule, this interaction proceeds in evacuated silica tubes. Mixtures of the separate powders of metal and red (or white) phosphorus are placed into a tube and slowly heated up to 900–1200 K with further annealing for 50–100 hours at this temperature. The interaction between the components begins at a temperature of about 673 K and its velocity depends on many factors. It should be mentioned, that the temperature of synthesis is chosen according to the definite compounds which are to be obtained. Thus, for example the LaP_2 was obtained at 1453 K and LaP_5 at 1023–953 K. In general, phosphides with high phosphorus content are formed at relatively lower temperatures. The phosphides obtained may contain some oxide impurities which result from the presence of oxygen in the powders of the initial components and/or in silica. Very often mixtures of phosphides are obtained and they are difficult to separate.

Addition of iodine as a mineralizer accelerates the interaction between phosphorus and rare earths. For preparing single crystals of rare-earth phosphides suitable for further investigations, the product obtained was ground, pressed into pellets, and sealed in evacuated silica tubes with a small quantity of KI. The sealed ampoule was again treated at the annealing temperature. Wichelhaus and von Schnering (1975) used a eutectic mixture NaCl + KI for synthesizing LaP_7.

A variation of the direct method is a synthesis using two-temperature heating. A silica tube of about 20 cm in length containing the reaction components is placed in a furnace with a temperature gradient. The end of the ampoule with the rare earth is placed in the higher temperature zone and the other one with phosphorus (inserted in a small silica tube or in a crucible) in the lower temperature zone. By selecting the appropriate temperature gradient one can obtain an almost homogeneous phosphide of definite composition. von Schnering et al. (1975) synthesized LaP_2 using the temperature regime 1453–923 K. By

changing the temperature of the hot and cold zones one can also obtain phosphides of different stoichiometries. Ono et al. (1974) obtained different cerium phosphides at a constant temperature of the hot zone (973 K) and varying the temperature of the cold zone: 420 K, CeP; 420–470 K, $CeP + CeP_2$; 470–670 K, CeP_2; 670–870 K, CeP_5.

Another group of methods are those using chemical compounds containing rare earths or phosphorus. The deficiency of these methods is the formation of by-products which yield an impure phosphide.

Another possible method is the interaction of gaseous PH_3 with a rare-earth oxide which proceeds by the following scheme:

$$R_2O_3 + 2\,PH_3 = 2\,RP + 3\,H_2O.$$

Studying this reaction Samsonov et al. (1966), Mironov et al. (1966) and Mironov et al. (1971) determined that the reaction must proceed with a large excess PH_3 (exceeding 100–200 times) for suppressing the dissociation of RP and increasing the yield. The interaction proceeds at temperatures between 1173–1673 K, depending on the compounds taking part in the reaction. Samsonov et al. (1966), Mironov et al. (1966) and Samsonov and Endrzeevskaja (1963) note that relatively lower temperatures are used for reactions with metallic rare earths and higher temperatures are required for those with rare-earth oxides.

Yim et al. (1972) obtained scandium monophosphide by the reaction:

$$ScCl_3 + PH_3 = ScP + 3\,HCl.$$

Pytlewski and Howell (1967) proposed an original method of synthesizing europium and ytterbium phosphides RP and R_2P_3. For this purpose the rare earth was dissolved in liquid NH_3 and PH_3 was passed through the solution obtained. Thermal decomposition of the sediment $R(PH_2)_2 \times 7\,NH_3$ gives the respective phosphides.

2. Ternary and quaternary phosphides

2.1. *R–M–P and R–M–M′–P systems*

The first part of this section is concerned with the crystal structures of ternary and quaternary phosphides and the isothermal sections of ternary systems. Systems R–M–P are considered in order of increasing atomic number of rare earth and then transition metal. The crystallographic characteristics of the phosphides are listed in tables. For phosphide structures which have been refined by single-crystal methods, atomic parameters and *R*-values are given. Compounds in each system are considered in order of increasing phosphorus and then rare-earth content. A separate column in the table indicates the method used for preparing the phosphide.

Table 21
Compounds in the system Sc–M–P

Compound	Prep.[a]	Structure type	Lattice parameters			R	Reference(s)
			a	*b*	*c*		
$Sc_2Mn_{12}P_7$	1	$Zr_2Fe_{12}P_7$	0.9392	–	0.3562		Jeitschko et al. (1993)
$ScFe_4P_2$	3	$ZrFe_4Si_2$	0.6962	–	0.3622	0.014	Jeitschko et al. (1990)
$Sc_2Fe_{12}P_7$	3	$Zr_2Fe_{12}P_7$	–	–	–		Reinbold and Jeitschko (1987)
$ScFe_5P_3$	3	YCo_5P_3	–	–	–		Reinbold and Jeitschko (1987)
$Sc_2Co_{12}P_7$	3	$Zr_2Fe_{12}P_7$	0.8973	–	0.3531		Jeitschko and Reinbold (1985)
$ScCo_5P_3$	3	YCo_5P_3	1.1691	0.3583	1.0206		Jeitschko and Reinbold (1985)
$Sc_5Co_{19}P_{12}$	3	$Sc_5Co_{19}P_{12}$	1.1919	–	0.3592	0.023	Jeitschko and Reinbold (1985)
ScCoP	3	TiNiSi	0.6268	0.3750	0.7050		Jeitschko and Reinbold (1985)
$Sc_2Ru_{12}P_7$	2	$Zr_2Fe_{12}P_7$	0.9318	–	0.387	0.038	Ghetta et al. (1986)
ScRuP	2	ZrNiAl	0.6524	–	0.3610	0.040	Ghetta et al. (1986)
$ScCa_2Pt_7P_{\sim 3}$	1	$Eu_2Pt_7AlP_{\sim 3}$	0.4038	–	2.7027		Lux et al. (1991b)

[a] Methods of preparation: (1) ampoule synthesis from the pure components; (2) melting in arc furnace; (3) tin flux method; (4) other method.

2.1.1. *Sc–M–P*

Sc–M–P compounds are listed in table 21. No phase diagram of scandium-containing systems is reported. A continuous solid solution occurs between compounds ScP and ScAs (Yim et al. 1972). Jansen and Sperlich (1975) found continuous solid solution between the phosphides ScP and GdP.

2.1.2. *Y–M–P, Y–M–M′–P*

Y–M–(M′)P compounds are listed in table 22. Quinn and Weaver (1976) found a continuous solid solution between the monophosphides YP and TbP. Sampathkumaran et al. (1986) investigated single-phase polycrystalline samples $Y_{0.95}Eu_{0.05}Ni_2P_2$ and $Y_{0.95}Eu0_{.05}Pd_2P_2$; their phase composition was determined by X-ray analysis.

2.1.3. *R–M–P, R–M–M′–P (R = rare-earth metal of cerium group)*

R–M–(M′)P compounds with cerium-group rare earths are listed in table 23. Pavlov et al. (1991) studied the isothermal section of the system La–Mn–P at 1873 K and found two separate phases to exist in the liquid state at the temperatures investigated. Samples with 35 at.% of lanthanum contain two liquid phases and solid LaP.

The isothermal section of the La–Fe–P system in the range 0–75 at.% P (fig. 21a) has been determined using X-ray phase analysis (Chykhrij and Shevchuk 1993). Samples were prepared by arc melting (phosphorus content up to 30 at.%) or by heating in evacuated silica tubes (other part of the system) with further annealing at 870 K during 500 hours. Only one ternary compound $LaFe_2P_2$ appears in the phase diagram (fig. 21a). No solubility of the third component in binary compounds has been found.

Table 22
Compounds in the systems Y–M–P and Y–M–M′–P

Compound	Prep.[a]	Structure type	Lattice parameters			R	Reference(s)
			a	*b*	*c*		
$Y_2Fe_{12}P_7$		$Zr_2Fe_{12}P_7$	–	–	–		Raffius et al. (1991)
YFe_5P_3	3	YCo_5P_3	1.2008	0.3672	1.0423		Jeitschko et al. (1984)
YCo_5P_3	3	YCo_5P_3	1.1820	0.3666	1.0336	0.051	Meisen and Jeitschko (1984b)
YCo_3P_2	2	$HoCo_3P_2$	1.0600	0.3704	1.2248		Chykhrij et al. (1989b)
$Y_5Co_{19}P_{12}$	3	$Sc_5Co_{19}P_{12}$	1.2057	–	0.3679		Jakubowski-Ripke and Jeitschko (1988)
YNi_4P_2	2	$ZrFe_4Si_2$	0.7109	–	0.3600		Chykhrij et al. (1986)
$Y_2Ni_{12}P_7$	3	$Zr_2Fe_{12}P_7$	0.9076	–	0.3682		Jeitschko and Jaberg (1980b)
$Y_6Ni_{20}P_{13}$	3	$Y_6Ni_{20}P_{13}$	1.2677	–	0.3749	0.068	Chykhrij et al. (1985)
$Y_7Ni_{19}P_{13}$	4	$Zr_6Ni_{20}P_{13}$	1.2676	–	0.3747		Madar et al. (1985b)
YNiP	2	$Tb_{1-x}NiP$	0.3889	–	1.5620		Chykhrij et al. (1987)
YNi_2P_2	1	$CeAl_2Ga_2$	0.3859	–	0.9332		Jeitschko and Jaberg (1980a)
YCu_xP_y	1	orthorhomb.	~2.0	~0.55	~0.55		Möller and Jeitschko (1985)
$Y_5Ru_{19}P_{12}$	1	$Ho_5Ni_{19}P_{12}$	1.2531	–	0.3933		Ghetta et al. (1989)
YRu_2P_2	1,3	$CeAl_2Ga_2$	0.4030	–	0.9545		Jeitschko et al. (1987)
$Y_2Rh_{12}P_7$	1	$Zr_2Rh_{12}P_7$	0.9619	–	0.3792		Pivan et al. (1985c,d)
YPd_2P_2	1	$CeAl_2Ga_2$	0.4053	–	0.9850		Jeitschko and Hofmann (1983)
YPtP		YbPtP	0.4097	–	0.3865		Wenski and Mewis (1986c)
$YLiCu_2P_2$	1	$TbLiCu_2P_2$	0.3985	–	0.6570		Mahan and Mewis (1983)
$YCuZnP_2$	1	Ce_2S_2O	0.3983	–	0.6523	0.066	Klüfers et al. (1980), Mahan and Mewis (1983)

[a] Methods of preparation: (1) ampoule synthesis from the pure components; (2) melting in arc furnace; (3) tin flux method; (4) other method.

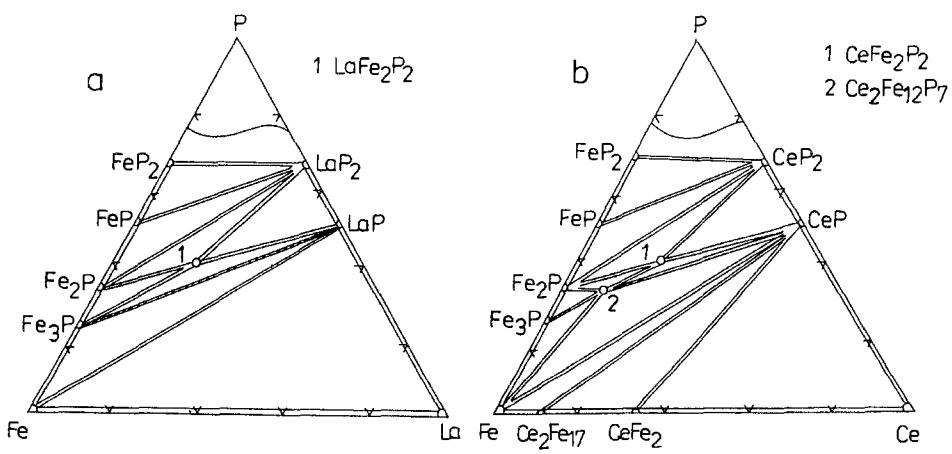

Fig. 21. (a) La–Fe–P and (b) Ce–Fe–P, isothermal sections at 870 K.

Table 23
Compounds in the systems R–M–P and R–M–M′–P (R = rare-earth metal of cerium group)

Compound	Prep.[a]	Structure type	Lattice parameters			R	Reference(s)
			a	*b*	*c*		
$LaLi_3P_2$	1	$LaLi_3P_2$	0.42508	–	0.6906	0.025	Grund et al. (1984)
$LaLi_2P_2$		Ce_2S_2O	0.4189	–	0.6834		Maslout et al. (1975)
$LaSiP_3$(P)	1	orthorhomb.	–	–	–		Ono et al. (1976)
$LaSiP_3$(X)	1	orthorhomb.	–	–	–		Ono et al. (1976)
$LaSiP_3$(F)	1	orthorhomb.	0.5968	0.5820	2.5269		Ono et al. (1976)
$LaSi_2P_6$	1	orthorhomb.	1.0150	2.8189	1.0384		Ono et al. (1976)
$La_2Fe_{25}P_{12}$	3	$La_2Fe_{25}P_{12}$	1.4756	1.8149	0.3636	0.038	Zimmer and Jeitschko (1992)
$LaFe_2P_2$	3	$CeAl_2Ga_2$	0.38407	–	1.0982	0.024	Jeitschko et al. (1985)
	3		0.38432	–	1.09871	0.057	Chykhrij and Shevchuk (1993)
$LaFe_4P_{12}$	1	$LaFe_4P_{12}$	0.78316	–	–	0.028	Jeitschko and Braun (1977)
$LaCo_5P_3$	2	$LaCo_5P_3$	0.3651	1.1573	1.1459	0.054	Davydov and Kuz'ma (1981)
$LaCo_8P_5$	3	$LaCo_8P_5$	1.0501	0.3596	0.9342	0.040	Meisen and Jeitschko (1984a)
$LaCo_2P_2$	3	$CeAl_2Ga_2$	0.38149	–	1.1019	0.011	Jeitschko et al. (1985)
$La_{0.2}Co_4P_{12}$	3	$LaFe_4P_{12}$	0.7745	–	–		Zemni et al. (1986)
$La_2Ni_{12}P_5$	1	$La_2Ni_{12}P_5$	1.0911	0.3696 $\beta = 108.02$	1.3174	0.028	Kuz'ma et al. (1993)
$LaNi_{10}P_4$	2	$LaNi_{10}P_4$	0.9310	0.3706	2.234	0.038	Babizhets'ky et al. (1992c)
~$LaNi_{11}P_5$	2		–	–	–		Babizhets'ky and Kuz'ma (1994)
~$LaNi_6P_3$	2		–	–	–		Babizhets'ky and Kuz'ma (1994)
$La_3Ni_{12}P_7$		$La_3Ni_{12}P_7$	0.3806	3.030	1.0730		Babizhets'ky et al. (1992b)
$LaNi_5P_3$	3	$LaCo_5P_3$	0.3642	1.1716	1.1494	0.070	Hofmann and Jeitschko (1984)
$La_3Ni_7P_5$	2	$Nd_3Ni_7P_5$	1.7004	–	0.3997		Chykhrij et al. (1989c)
LaNiP	2	$Tb_{1-x}NiP$	0.4024	–	1.6297		Chykhrij et al. (1987)
$LaNi_2P_2$	1	$CeAl_2Ga_2$	0.4007	–	0.9632		Jeitschko and Jaberg (1980a)
	3		0.4010	–	0.9604	0.016	Hofmann and Jeitschko (1984)
$La_6Ni_6P_{17}$	1	$La_6Ni_6P_{17}$	1.0168	–	–	0.023	Braun and Jeitschko (1978)
$La_5Cu_{19-x}P_{12}$	1	$Nd_5Cu_{19-x}P_{12}$	1.2769	–	0.3972		Oryshchyn et al. (1991a)
$LaCu_xP_y$	1	$CeCu_{1.12}P_{1.97}$	–	–	–		Möller and Jeitschko (1985)
$La_5Ru_{19}P_{12}$	1	$Sc_5Co_{19}P_{12}$	1.2647	–	0.4000		Ghetta et al. (1989)
LaRuP		PbFCl	–	–	–		Reehuis and Jeitschko (1990)
$LaRu_2P_2$	1,3	$CeAl_2Ga_2$	0.4031	–	1.0675	0.028	Jeitschko et al. (1987)
$LaRu_4P_{12}$	1	$LaFe_4P_{12}$	0.80561	–	–		Jeitschko and Braun (1977)
$La_6Rh_{32}P_{17}$	1	$La_6Rh_{32}P_{17}$	2.7054	–	0.3944	0.050	Pivan et al. (1988)
$LaRh_2P_2$	1	$CaBe_2Ge_2$	0.4189	–	0.9577		Madar et al. (1985a, 1987a)
LaPdP	1	ZrBeSi	0.4269	–	0.7909		Johrendt and Mewis (1990)
$LaPd_2P_2$	1	$CeAl_2Ga_2$	0.4188	–	0.9857		Jeitschko and Hofmann (1983)
$La_6Pd_6P_{17}$	1	$La_6Ni_6P_{17}$	1.0411	–	–		Jeitschko and Hofmann (1983)

Table 23, *continued*

Compound	Prep.[a]	Structure type	Lattice parameters			R	Reference(s)
			a	*b*	*c*		
$LaAg_xP_y$	1	tetrag.	~0.4	–	~2.0		Möller and Jeitschko (1985)
$LaAg_xP_y$	1	$CeCu_{1.12}P_{1.97}$	–	–	–		Möller and Jeitschko (1985)
$LaOs_4P_{12}$	1	$LaFe_4P_{12}$	0.80844	–	–		Jeitschko and Braun (1977)
$LaCuZnP_2$	1	Ce_2S_2O	0.4082	–	0.6742	0.055	Mahan and Mewis (1983)
$LaZnAgP_2$		Ce_2S_2O	0.4194	–	0.6817		Tejedor and Stacy (1990)
$(La,Ce)_{12}Rh_{30}P_{21}$	1	$(La,Ce)_{12}Rh_{30}P_{21}$	1.7475	–	0.3948	0.049	Pivan and Guerin (1986)
$CeLi_2P_2$		Ce_2S_2O	0.4189	–	0.6834		Maslout et al. (1975)
$CeSiP_3$	1	$CeSiP_3$	0.5861	2.5295	0.5712	0.048	Hayakawa et al. (1978)
$CeSiP_3$(F)	1	orthorhomb.	0.59059	0.57748	2.5069		Ono et al. (1976)
$CeSiP_3$(P)	1	orthorhomb.	0.58610	0.57119	2.5295		Ono et al. (1976)
$CeSi_2P_6$	1	orthorhomb.	1.0123	2.8071	1.0325		Ono et al. (1976)
$Ce_2Fe_{12}P_7$	3	$Zr_2Fe_{12}P_7$	0.9135	–	0.3677	0.029	Jeitschko et al. (1984)
$CeFe_2P_2$	3	$CeAl_2Ga_2$	0.38490	–	1.0280	0.016	Jeitschko et al. (1985)
$CeFe_4P_{12}$	1	$LaFe_4P_{12}$	0.77920	–	–		Jeitschko and Braun (1977)
	3		0.7792	–	–	0.022	Grandjean et al. (1984)
$Ce_2Co_{12}P_7$	3	$Zr_2Fe_{12}P_7$	0.90776	–	0.36553		Jeitschko et al. (1978)
$CeCo_5P_3$	3	YCo_5P_3	1.1817	0.3710	1.0404		Meisen and Jeitschko (1984b)
$CeCo_3P_2$	2	$HoCo_3P_2$	1.0634	0.3764	1.2349		Chykhrij et al. (1989b)
$CeCo_2P_2$	3	$CeAl_2Ga_2$	0.38973	–	0.9598	0.023	Jeitschko et al. (1985)
$Ce_{0.25}Co_4P_{12}$	3	$LaFe_4P_{12}$	0.7738	–	–	0.014	Zemni et al. (1986)
~$CeNi_2P$	2	–	–	–	–		Babizhets'ky and Kuz'ma (1994)
$Ce_9Ni_{26}P_{12}$	2	$Ce_9Ni_{26}P_{12}$	1.4260	–	0.3863	0.069	Babizhets'ky et al. (1992a)
$Ce_2Ni_{12}P_5$	1	$La_2Ni_{12}P_5$	1.0803	0.3684 $\beta = 107.74$	1.3161		Kuz'ma et al. (1993)
~$CeNi_{11}P_5$	2	–	–	–	–		Babizhets'ky and Kuz'ma (1994)
~$CeNi_6P_3$	2	–	–	–	–		Babizhets'ky and Kuz'ma (1994)
~$Ce_2Ni_5P_3$	2	–	–	–	–		Babizhets'ky and Kuz'ma (1994)
$Ce_2Ni_7P_4$	2	$Nd_2Ni_7P_4$	0.3769	0.9219	1.0414		Babizhets'ky and Kuz'ma (1994)
$Ce_6Ni_{15}P_{10}$	2	$Ce_6Ni_{15}P_{10}$	1.6637	–	0.3878		Babizhets'ky et al. (1993a)
$Ce_{20}Ni_{42}P_{30}$	2	$Sm_{20}Ni_{41.6}P_{30}$	2.0454	–	0.3892		Babizhets'ky and Kuz'ma (1994)
$Ce_2Ni_{12}P_7$	3	$Zr_2Fe_{12}P_7$	0.9094	–	0.3737		Jeitschko and Jaberg (1980b)
$CeNi_{5-x}P_3$ ($x = 0.1$)	2,3	$CeNi_{5-x}P_3$	2.4701	0.3785 $\beta = 105.2$	1.0619	0.067	Babizhets'ky et al. (1992d)
$Ce_7Ni_{19}P_{13}$	1	$Zr_6Ni_{20}P_{13}$	1.2766	–	0.3829		Madar et al. (1985b)
CeNiP	2	$Tb_{1-x}NiP$	0.3994	–	1.6085		Chykhrij et al. (1987)

Continued on next page

Table 23, *continued*

Compound	Prep.[a]	Structure type	Lattice parameters			R	Reference(s)
			a	*b*	*c*		
$CeNi_2P_2$	1	$CeAl_2Ga_2$	0.3955	–	0.9505		Jeitschko and Jaberg (1980a)
	3		0.3958	–	0.9489	0.015	Hofmann and Jeitschko (1984)
$Ce_6Ni_6P_{17}$	1	$La_6Ni_6P_{17}$	1.0116	–	–	0.046	Braun and Jeitschko (1978)
$Ce_5Cu_{19-x}P_{12}$	1	$Nd_5Cu_{19-x}P_{12}$	1.27294	–	0.39283		Oryshchyn et al. (1991a)
$CeCu_{1.12}P_{1.97}$	1	$CeCu_{1.12}P_{1.97}$	1.9649	0.5550	0.5522	0.024	Möller and Jeitschko (1985)
$Ce_2Cu_2P_{5-x}$ ($x=0.5$)	1	$Ce_2Cu_2P_{5-x}$	0.5522	0.5550	1.965		Möller and Jeitschko (1981)
$CeCu_xP_y$	1	tetrag.	~0.4	–	~2.0		Möller and Jeitschko (1985)
$Ce_5Ru_{19}P_{12}$	1	$Ho_5Ni_{19}P_{12}$	1.2546	–	0.3947		Ghetta et al. (1989)
$CeRu_2P_2$	1,3	$CeAl_2Ga_2$	0.4042	–	1.0134		Jeitschko et al. (1987)
$CeRu_4P_{12}$	1	$LaFe_4P_{12}$	0.80376	–	–		Jeitschko and Braun (1977)
$Ce_6Rh_{32}P_{17}$	1	$La_6Rh_{32}P_{17}$	2.6941	–	0.3926		Pivan et al. (1988)
$CeRh_2P_2$	1	$CaBe_2Ge_2$	0.4157	–	0.9501		Madar et al. (1985a)
			0.4146	–	0.9539		Madar et al. (1987a)
CePdP	1	ZrBeSi	0.4248	–	0.7799	0.05	Johrendt and Mewis (1990)
$CePd_2P_2$	1	$CeAl_2Ga_2$	0.4156	–	0.9887		Jeitschko and Hofmann (1983)
$Ce_6Pd_6P_{17}$	1	$La_6Ni_6P_{17}$	1.0339	–	–		Jeitschko and Hofmann (1983)
$CeAg_xP_y$	1	$CeCu_{1.12}P_{1.97}$	–	–	–		Möller and Jeitschko (1985)
$CeOs_4P_{12}$	1	$LaFe_4P_{12}$	0.80626	–	–		Jeitschko and Braun (1977)
$CeLiCu_2P_2$	1	$TbLiCu_2P_2$	0.4042	–	0.6718		Mahan and Mewis (1983)
CeCuZnP$_2$	1	Ce_2S_2O	0.4064	–	0.6697	0.056	Mahan and Mewis (1983)
$PrLi_2P_2$	4	Ce_2S_2O	0.4196	–	0.6821		Fischer and Schuster (1980)
$PrSiP_3$(F)	1	orthorhomb.	0.5871	0.5749	2.4972		Ono et al. (1976)
$PrSiP_3$(P)	1	orthorhomb.	0.5823	0.5687	2.5200		Ono et al. (1976)
$PrSi_2P_6$	1	orthorhomb.	1.0105	2.7938	1.0278		Ono et al. (1976)
$Pr_2Fe_{12}P_7$	3	$Zr_2Fe_{12}P_7$	0.92039	–	0.36878		Jeitschko et al. (1978)
$PrFe_2P_2$		$CeAl_2Ga_2$	0.3855	–	1.0323	0.011	Reehuis and Jeitschko (1987)
$PrFe_4P_{12}$	1	$LaFe_4P_{12}$	0.78149	–	–		Jeitschko and Braun (1977)
$Pr_2Co_{12}P_7$	3	$Zr_2Fe_{12}P_7$	0.91300	–	0.36606		Jeitschko et al. (1978)
$PrCo_5P_3$	3	YCo_5P_3	1.1911	0.3713	1.0449		Meisen and Jeitschko (1984b)
$PrCo_3P_2$	2	$HoCo_3P_2$	1.0735	0.3767	1.2370		Chykhrij et al. (1989b)
PrCoP	3	PbFCl	0.39229	–	0.8215		Reehuis and Jeitschko (1990)
$PrCo_8P_5$	3	$LaCo_8P_5$	1.0479	0.3570	0.9295		Reehuis et al. (1988b)
$PrCo_2P_2$	3	$CeAl_2Ga_2$	0.39000	–	0.9759	0.044	Jeitschko et al. (1985)
$Pr_xCo_4P_{12}$	3	$LaFe_4P_{12}$	0.7733	–	–		Zemni et al. (1986)
$Pr_9Ni_{26}P_{12}$	2	$Ce_9Ni_{26}P_{12}$	1.4298	–	0.3875		Babizhets'ky et al. (1992a)
$Pr_2Ni_{12}P_5$	1	$La_2Ni_{12}P_5$	1.0845	0.3683	1.3153		Kuz'ma et al. (1993)
				$\beta=107.67$			
$Pr_2Ni_{12}P_7$	3	$Zr_2Fe_{12}P_7$	0.9131	–	0.3756		Jeitschko and Jaberg (1980b)
$Pr_3Ni_7P_5$	2	$Nd_3Ni_7P_5$	1.6887	–	0.3969		Chykhrij et al. (1989c)

Table 23, *continued*

Compound	Prep.[a]	Structure type	Lattice parameters			R	Reference(s)
			a	*b*	*c*		
$Pr_7Ni_{19}P_{13}$	1	$Zr_6Ni_{20}P_{13}$	1.2820	–	0.3852		Madar et al. (1985b)
PrNiP	2	$Tb_{1-x}NiP$	0.3993	–	1.5975		Chykhrij et al. (1987)
$PrNi_2P_2$	1	$CeAl_2Ga_2$	0.3952	–	0.9493		Jeitschko and Jaberg (1980a)
$Pr_6Ni_6P_{17}$	1	$La_6Ni_6P_{17}$	1.0073	–	–		Braun and Jeitschko (1978)
$Pr_5Cu_{19-x}P_{12}$	1	$Nd_5Cu_{19-x}P_{12}$	1.2706	–	0.3924		Oryshchyn et al. (1991a)
$PrCu_xP_y$	1	$CeCu_{1.12}P_{1.97}$	–	–	–		Möller and Jeitschko (1985)
$Pr_5Ru_{19}P_{12}$	1	$Ho_5Ni_{19}P_{12}$	1.2579	–	0.3975		Ghetta et al. (1989)
$PrRu_2P_2$	1,3	$CeAl_2Ga_2$	0.4048	–	0.9974		Jeitschko et al. (1987)
$PrRu_4P_{12}$	1	$LaFe_4P_{12}$	0.80420	–	–		Jeitschko and Braun (1977)
$PrRh_2P_2$	1	$CaBe_2Ge_2$	0.4156	–	0.9513		Madar et al. (1985a, 1987a)
PrPdP	1	ZrBeSi	0.4232	–	0.7732		Johrendt and Mewis (1990)
$PrPd_2P_2$	1	$CeAl_2Ga_2$	0.4134	–	0.9879		Jeitschko and Hofmann (1983)
$PrAg_xP_y$	1	$CeCu_{1.12}P_{1.97}$	–	–	–		Möller and Jeitschko (1985)
$PrOs_4P_{12}$	1	$LaFe_4P_{12}$	0.80710	–	–		Jeitschko and Braun (1977)
$Nd_2Fe_{12}P_7$	3	$Zr_2Fe_{12}P_7$	0.91856	–	0.36769		Jeitschko et al. (1978)
$NdFe_4P_{12}$	1	$LaFe_4P_{12}$	0.78079	–	–		Jeitschko and Braun (1977)
$Nd_2Co_{12}P_7$	3	$Zr_2Fe_{12}P_7$	0.9106	–	0.36499		Jeitschko et al. (1978)
$NdCo_5P_3$	3	YCo_5P_3	1.1897	0.3708	1.0438		Meisen and Jeitschko (1984b)
$NdCo_3P_2$	2	$HoCo_3P_2$	1.0717	0.3759	1.2363		Chykhrij et al. (1989b)
NdCoP	3	PbFCl	0.39044	–	0.8173		Reehuis and Jeitschko (1990)
$NdCo_2P_2$	3	$CeAl_2Ga_2$	0.38941	–	0.9681		Jeitschko et al. (1985)
$Nd_xCo_4P_{12}$	3	$LaFe_4P_{12}$	0.7723	–	–		Zemni et al. (1986)
~$NdNi_2P$	2	–	–	–	–		Babizhets'ky (1995)
$Nd_9Ni_{26}P_{12}$	2	$Ce_9Ni_{26}P_{12}$	1.4312	–	0.3874		Babizhets'ky et al. (1992a)
$Nd_2Ni_{12}P_5$	1	$La_2Ni_{12}P_5$	1.0815	0.3677 $\beta = 107.71$	1.3142		Kuz'ma et al. (1993)
~$Nd_2Ni_6P_3$	2	–	–	–	–		Babizhets'ky (1995)
~$NdNi_{11}P_5$	2	–	–	–	–		Babizhets'ky (1995)
$Nd_2Ni_7P_4$	2	$Nd_2Ni_7P_4$	0.37588	0.9238	1.0413	0.054	Chykhrij et al. (1990)
$Nd_{20}Ni_{42}P_{30}$	2	$Sm_{20}Ni_{41.6}P_{30}$	2.0750	–	0.3898		Babizhets'ky (1995)
$Nd_2Ni_{12}P_7$	3	$Zr_2Fe_{12}P_7$	0.9111	–	0.3740		Jeitschko and Jaberg (1980b)
$Nd_5Ni_{19}P_{12}$	3	$Sc_5Co_{19}P_{12}$	1.2458	–	0.3834		Babizhets'ky et al. (1993a)
$Nd_7Ni_{19}P_{13}$	1	$Zr_6Ni_{20}P_{13}$	1.2800	–	0.3835		Madar et al. (1985b)
$Nd_3Ni_7P_5$	2	$Nd_3Ni_7P_5$	1.6679	–	0.3891	0.061	Chykhrij et al. (1989c)
NdNiP	2	$Tb_{1-x}NiP$	0.3991	–	1.5930		Chykhrij et al. (1987)
$NdNi_2P_2$	1	$CeAl_2Ga_2$	0.3942	–	0.9461		Jeitschko and Jaberg (1980a)
$Nd_5Cu_{19-x}P_{12}$ ($x = 1.2$)	1	$Nd_5Cu_{19-x}P_{12}$	1.2704	–	0.39098	0.059	Oryshchyn et al. (1991a)
$NdCu_xP_y$	1	$CeCu_{1.12}P_{1.97}$	–	–	–		Möller and Jeitschko (1985)
$Nd_5Ru_{19}P_{12}$	1	$Ho_5Ni_{19}P_{12}$	1.2561	–	0.3972		Ghetta et al. (1989)

Continued on next page

Table 23, *continued*

Compound	Prep.[a]	Structure type	Lattice parameters			R	Reference(s)
			a	*b*	*c*		
$NdRu_2P_2$	1,3	$CeAl_2Ga_2$	0.4046	–	0.9874		Jeitschko et al. (1987)
$NdRu_4P_{12}$	1	$LaFe_4P_{12}$	0.80364	–	–		Jeitschko and Braun (1977)
$Nd_2Rh_{12}P_7$	1	$Zr_2Rh_{12}P_7$	0.9600	–	0.3820		Pivan et al. (1985c,d)
$NdRh_2P_2$	1	$CaBe_2Ge_2$	0.4142	–	0.9488		Madar et al. (1985a, 1987a)
NdPdP	1	ZrBeSi	0.4219	–	0.7690		Johrendt and Mewis (1990)
$NdPd_2P_2$	1	$CeAl_2Ga_2$	0.4124	–	0.9878		Jeitschko and Hofmann (1983)
$NdOs_4P_{12}$	1	$LaFe_4P_{12}$	0.80638	–	–		Jeitschko and Braun (1977)
$Sm_2Mn_{12}P_7$		$Zr_2Fe_{12}P_7$	0.9510	–	0.3680		Ghetta (1987)
			0.9509	–	0.3679		Jeitschko et al. (1993)
$Sm_2Fe_{12}P_7$	3	$Zr_2Fe_{12}P_7$	0.91558	–	0.36653		Jeitschko et al. (1978)
SmFeP	3	PbFCl	0.38803	–	0.8198		Reehuis and Jeitschko (1990)
$SmFe_4P_{12}$	1	$LaFe_4P_{12}$	0.78029	–	–		Jeitschko and Braun (1977)
$Sm_2Co_{12}P_7$	3	$Zr_2Fe_{12}P_7$	0.90853	–	0.36330		Jeitschko et al. (1978)
$SmCo_5P_3$	3	YCo_5P_3	1.1878	0.3694	1.0402		Meisen and Jeitschko (1984b)
$SmCo_3P_2$	2	$HoCo_3P_2$	1.0660	0.3736	1.2307		Chykhrij et al. (1989b)
SmCoP	3	PbFCl	0.38845	–	0.8085		Reehuis and Jeitschko (1990)
$SmCo_2P_2$	3	$CeAl_2Ga_2$	0.38703	–	0.9566		Jeitschko et al. (1985)
~$SmNi_2P$	2	–	–	–	–		Babizhets'ky (1995)
$Sm_9Ni_{26}P_{12}$	2	$Ce_9Ni_{26}P_{12}$	1.42473	–	0.3847		Babizhets'ky et al. (1992a)
$SmNi_4P_2$	2	$SmNi_4P_2$	1.4185	1.0759	0.3744	0.041	Oryshchyn et al. (1988a)
~$Sm_2Ni_5P_3$	2	–	–	–	–		Babizhets'ky (1995)
$Sm_{20}Ni_{41.6}P_{30}$	2	$Sm_{20}Ni_{41.6}P_{30}$	2.0448	–	0.3877		Chykhrij et al. (1993)
$Sm_{15}Ni_{28}P_{21}$	2	$Tb_{15}Ni_{28}P_{21}$	2.4535	–	0.3880		Babizhets'ky (1995)
$Sm_2Ni_{12}P_7$	3	$Zr_2Fe_{12}P_7$	0.9088	–	0.3719		Jeitschko and Jaberg (1980b)
$Sm_7Ni_{19}P_{13}$	1	$Zr_6Ni_{20}P_{13}$	1.2748	–	0.3798		Madar et al. (1985b)
$Sm_3Ni_7P_5$	2	$Nd_3Ni_7P_5$	1.6626	–	0.3848		Chykhrij et al. (1989c)
SmNiP	2	$Tb_{1-x}NiP$	0.3948	–	1.5612		Chykhrij et al. (1987)
$SmNi_2P_2$	1	$CeAl_2Ga_2$	0.3919	–	0.9403		Jeitschko and Jaberg (1980a)
$Sm_5Cu_{19-x}P_{12}$	1	$Nd_5Cu_{19-x}P_{12}$	1.2659	–	0.3918		Oryshchyn et al. (1991a)
$SmCu_{1+x}P_{2-x}$	1	$HfCuSi_2$	0.3814	–	0.9759		Chykhrij et al. (1989a)
$SmCuP_2$	1	$SrZnBi_2$	0.3839	–	1.9431		Chykhrij (1990a,b)
$SmCu_xP_y$	1	orthorhomb.	~2.0	~0.55	~0.55		Möller and Jeitschko (1985)
$Sm_5Ru_{19}P_{12}$	1	$Ho_5Ni_{19}P_{12}$	1.2522	–	0.3959		Ghetta et al. (1989)
$SmRu_2P_2$	1,3	$CeAl_2Ga_2$	0.4035	–	0.9682		Jeitschko et al. (1987)
SmPdP	1	ZrBeSi	0.4198	–	0.7576		Johrendt and Mewis (1990)
$SmPd_2P_2$	1	$CeAl_2Ga_2$	0.4100	–	0.9866		Jeitschko and Hofmann (1983)
SmPtP	1	YbPtP	0.4146	–	0.3909		Wenski and Mewis (1986c)
$SmLiCu_2P_2$	1	$TbLiCu_2P_2$	0.4014	–	0.6634		Mahan and Mewis (1983)
$SmCuZnP_2$		Ce_2S_2O	0.4016	–	0.6592		Tejedor and Stacy (1990)

Table 23, *continued*

Compound	Prep.[a]	Structure type	Lattice parameters			R	Reference(s)
			a	*b*	*c*		
$SmZnAgP_2$		Ce_2S_2O	0.41247	–	0.66920	0.021	Tejedor and Stacy (1990)
$Eu_3Li_4P_4$		$Sr_3Li_4Sb_4$	1.4479	0.6711	0.4363		Hartweg (1987)
$Eu_3Na_2P_4$	4	Sm_5Ge_4	0.7298	1.5043	0.7881	0.041	Hönle et al. (1992)
$EuMn_2P_2$	1	Ce_2S_2O	0.4143	–	0.7034		Rühl and Jeitschko (1979)
$EuFe_2P_2$	1	$CeAl_2Ga_2$	0.3818	–	1.1224		Marchand and Jeitschko (1978)
			0.3818	–	1.1224	0.027	Reehuis and Jeitschko (1987)
$EuFe_4P_{12}$	1	$LaFe_4P_{12}$	0.78055	–	–		Jeitschko and Braun (1977)
$Eu_2Co_{12}P_7$	3	$Zr_2Fe_{12}P_7$	0.90753	–	0.36284		Jeitschko et al. (1978)
$EuCo_8P_5$	3	$LaCo_8P_5$	1.0526	0.3559	0.9321	0.028	Reehuis et al. (1988b)
$EuCo_2P_2$	1	$CeAl_2Ga_2$	0.37649	–	1.1348	0.047	Marchand and Jeitschko (1978)
$Eu_9Ni_{26}P_{12}$	2	$Ce_9Ni_{26}P_{12}$	1.4474	–	0.3873		Babizhets'ky et al. (1992a)
$Eu_2Ni_{12}P_5$	1	$La_2Ni_{12}P_5$	1.0784	0.3666 $\beta = 107.82$	1.3207		Kuz'ma et al. (1993)
~$EuNi_{10}P_4$	2	–	–	–	–		Babizhets'ky (1995)
~$Eu_2Ni_{11}P_5$	2	–	–	–	–		Babizhets'ky (1995)
~$Eu_2Ni_5P_3$	2	–	–	–	–		Babizhets'ky (1995)
$Eu_2Ni_7P_4$	2	$Nd_2Ni_7P_4$	0.3793	0.9280	1.0458		Babizhets'ky (1995)
$Eu_{20}Ni_{42}P_{30}$	2	$Sm_{20}Ni_{41.6}P_{30}$	2.0675	–	0.3947		Babizhets'ky (1995)
$Eu_2Ni_{12}P_7$	3	$Zr_2Fe_{12}P_7$	0.9115	–	0.3750		Jeitschko and Jaberg (1980b)
$EuNi_5P_3$		$LaCo_5P_3$	0.35986	1.17374	1.15230	0.021	Badding and Stacy (1987a)
$Eu_6Ni_{20}P_{13}$	2	$Zr_6Ni_{20}P_{13}$	1.2765	–	0.3799		Babizhets'ky (1995)
EuNiP	2	YbPtP	0.3939	–	0.8175		Babizhets'ky (1995)
$EuNi_2P_2$	1	$CeAl_2Ga_2$	0.3939	–	0.9482		Marchand and Jeitschko (1978)
	1		0.3938	–	0.9469	0.049	Jeitschko and Jaberg (1980a)
EuCuP		ZrBeSi	0.4123	–	0.8200		Tomuschat and Schuster (1981)
$EuCu_{1.75}P_2$		$CeAl_2Ga_2$	0.4110	–	0.9591	0.042	Mewis (1980a)
$EuZn_2P_2$	1	Ce_2S_2O	0.4087	–	0.7010		Klüfers et al. (1980)
$EuRu_2P_2$	1,2	$CeAl_2Ga_2$	0.4029	–	1.0772	0.018	Wenski and Mewis (1986a)
			0.4030	–	1.0785		Jeitschko et al. (1987)
$EuRu_4P_{12}$	1	$LaFe_4P_{12}$	0.80406	–	–		Jeitschko and Braun (1977)
EuPdP	1	γ-EuPtP	0.4150	–	0.8112		Johrendt and Mewis (1990)
$EuPd_2P_2$	1	$CeAl_2Ga_2$	0.4181	–	0.9742		Jeitschko and Hofmann (1983)
EuAgP		ZrBeSi	0.4395	–	0.8057		Tomuschat and Schuster (1981)
$EuOs_2P_2$		$CeAl_2Ga_2$	0.4037	–	1.0891		Jeitschko et al. (1987)
EuPtP	1	ZrBeSi	0.4086	–	0.8630		Wenski and Mewis (1986d)
EuPtP(α)	3	ZrBeSi	0.4086	–	0.8630	0.019	Lux et al. (1991a)
EuPtP(β)	3	ZrBeSi	0.4090	–	0.8384	0.012	Lux et al. (1991a)
EuPtP(γ)	3	γ-EuPtP	0.4103	–	0.8256	0.020	Lux et al. (1991a)
$EuPt_2P_{1.62}$	1	$EuPt_2P_{1.62}$	0.4143	–	1.9120	0.071	Wenski and Mewis (1986a)
$EuPt_{0.65}P_{1.35}$	1	AlB_2	0.4065	–	0.4290		Wenski and Mewis (1986b)

Continued on next page

Table 23, *continued*

Compound	Prep.[a]	Structure type	Lattice parameters			R	Reference(s)
			a	*b*	*c*		
$EuPt_{0.80}P_{1.20}$	1	AlB_2	0.4069	–	0.4337	0.057	Wenski and Mewis (1986b)
EuAuP		ZrBeSi	0.4313	–	0.8258		Tomuschat and Schuster (1981)
$Eu_2Na_4SiP_4$	4	Na_6ZnO_4	0.9251	–	0.7198		Hartweg (1987), von Schnering et al. (1988)
$Eu_2Na_4GeP_4$	4	Na_6ZnO_4	0.9317	–	0.7200		von Schnering et al. (1988)
$Eu_2Na_4SnP_4$	4	Na_6ZnO_4	0.9468	–	0.7287		von Schnering et al. (1988)
$Eu_2Na_4PbP_4$	4	Na_6ZnO_4	0.9272	–	0.7314		von Schnering et al. (1988)
$Eu_2Mg_{0.7}Pt_7P_{3.3}$	4	$Eu_2AlPt_7P_{\sim 3}$	0.4056	–	2.7000	0.051	Lux et al. (1991b)
$Eu_2AlPt_7P_{2.95}$	1	$Eu_2AlPt_7P_{\sim 3}$	0.4046	–	2.6850	0.026	Lux et al. (1991b)
$Eu_2MnPt_7P_{\sim 3}$	1	$Eu_2AlPt_7P_{\sim 3}$	0.4057	–	2.6817		Lux et al. (1991b)
$Eu_2FePt_7P{\sim}3$	1	$Eu_2AlPt_7P_{\sim 3}$	0.4050	–	2.6706		Lux et al. (1991b)
$Eu_2Zn_{\sim 1}Pt_{\sim 7}P_{\sim 3}$	1	$Eu_2AlPt_7P_{\sim 3}$	0.4060	–	2.6708		Lux et al. (1991b)

[a] Methods of preparation: (1) ampoule synthesis from the pure components; (2) melting in arc furnace; (3) tin flux method; (4) other method.

Babizhets'ky and Kuz'ma (1994) constructed the isothermal sections of the La–Ni–P system at 1070 K (samples with La content up to 33 at.%) and 670 K (the lanthanum-rich part of the system) (fig. 22) using X-ray phase analysis. No solid solutions based on binary compounds or homogeneity ranges of the ternary compounds have been found. $La_6Ni_6P_{17}$ prepared by the tin flux technique has not been obtained by heating the elemental components in evacuated silica tubes. Compound $La_3Ni_{12}P_7$ whose structure was determined using a single crystal from an arc-melted sample was not found in samples annealed at the temperature investigated.

Westerholt and Methfessel (1977) revealed the existence of a continuous solid solution $La_xPr_{1-x}P_{0.85}$ $(0 < x < 1)$ and measured the lattice parameters at different compositions. Myers and Narath (1973) reported a continuous solid solution between LaP and GdP.

Refinement of atomic occupations in $LaFe_2P_2$ and $LaCo_2P_2$ has shown their deficiencies for transition metal and phosphorus: 97.8% and 96.7%, respectively, in $LaFe_2P_2$ and 99.4% and 96.7%, respectively, in $LaCo_2P_2$ (Jeitschko et al. 1985).

Mendelejev et al. (1990) studied the isothermal section (1873 K) of Fe–P samples which were doped by up to 95 wt.% of rare-earth metal (including 25 wt.% of La and 50 wt.% of Ce). Two separate liquid phases with both low and high phosphorus content were shown to be in equilibrium with the rare-earth monophosphide.

Chykhrij and Shevchuk (1993) studied the phase diagram of the Ce–Fe–P system at 870 K (fig. 21b) using X-ray phase analysis. Samples for investigation were prepared by the same technique as La–Fe–P. The existence of two earlier known compounds $Ce_2Fe_{12}P_7$ and $CeFe_2P_2$ was confirmed while $CeFe_4P_{12}$ was not obtained in these synthesized samples. No visible solubility of a third component in the binary compounds was found.

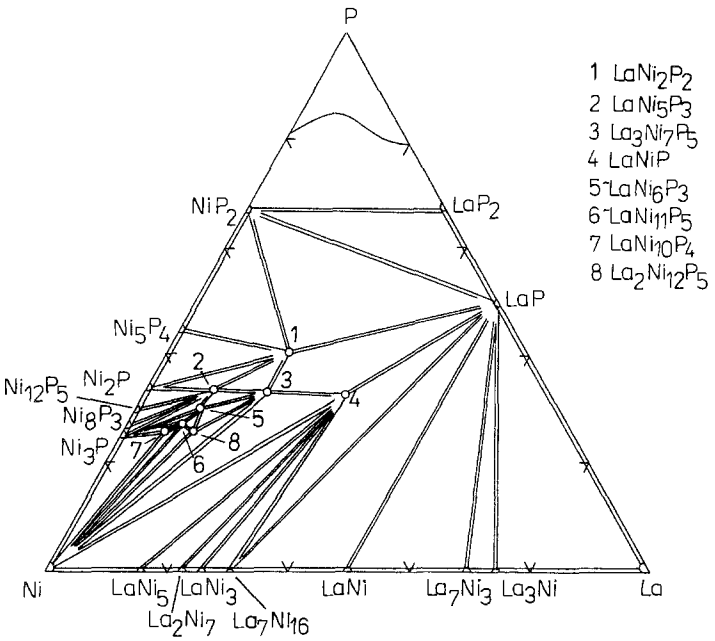

Fig. 22. La–Ni–P, isothermal sections at 1070 K (La content 0–33 at.%) and 870 K (33–100 at.% La).

Babizhets'ky and Kuz'ma (1994) constructed the phase diagram of the Ce–Ni–P system at 1070 K (the range with Ce content of 0–33 at.%) and 870 K (the rest of the system) (fig. 23). The compounds $CeNi_{5-x}P_3$ and $Ce_6Ni_6P_{17}$ were not found at the temperatures investigated; a single crystal of the former compound was extracted from an arc-melted sample. The latter was synthesized by the tin flux technique.

Babizhets'ky (1995) constructed the phase diagram for the Nd–Ni–P system at 1070 K (0–33 at.% of Nd) and 670 K (33–100 at.% of Nd) (fig. 24). The $Nd_5Ni_{19}P_{12}$ compound synthesized from liquid tin was not found in the samples investigated.

The phase diagram of the Sm–Ni–P system at 1070 K (0–33 at.% of Sm) and 670 K (33–100 at.% of Sm) has been constructed using X-ray phase analysis (Babizhets'ky 1995) (fig. 25).

Hönle et al. (1992) synthesized the compound $Na_2Eu_3P_4$ from mixture of Na_3P, EuP and red phosphorus. The constituent parts were placed into a niobium ampoule and sealed in an evacuated silica tube with further heating at 1143 K during two days. The composition of the compound was established using a chemical method. Thermogravimetric and mass-spectral investigations have shown that $Na_2Eu_3P_4$ loses Na^+ ions upon heating and is completely transformed into Eu_3P_4 at 873 K.

Babizhets'ky (1995) constructed the phase diagram of the Eu–Ni–P system at 1070 K (0–25 at.% of Eu) and 670 K (25–33 at.% of Eu) (fig. 26). $Eu_2Ni_{12}P_7$, obtained by the tin flux technique, was not found in the samples annealed at 1070 K.

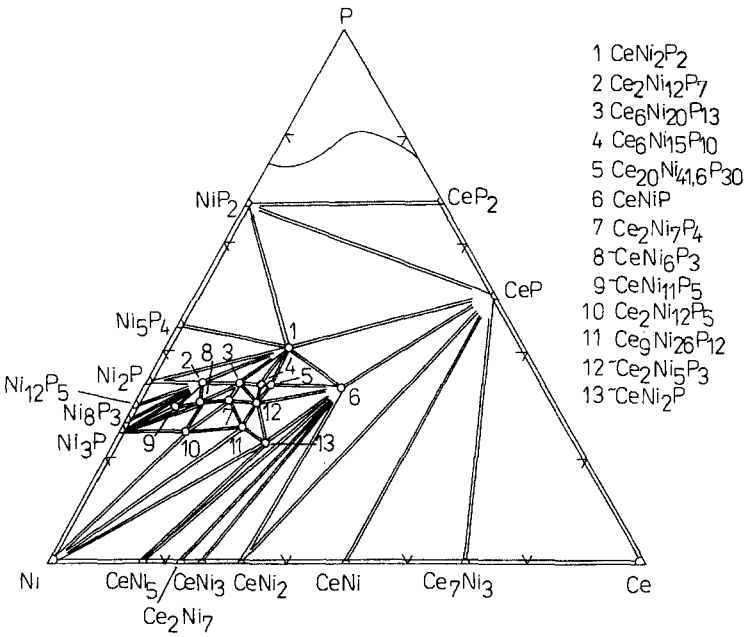

Fig. 23. Ce–Ni–P, isothermal sections at 1070 K (Ce content 0–33 at.%) and 870 K (33–100 at.% Ce).

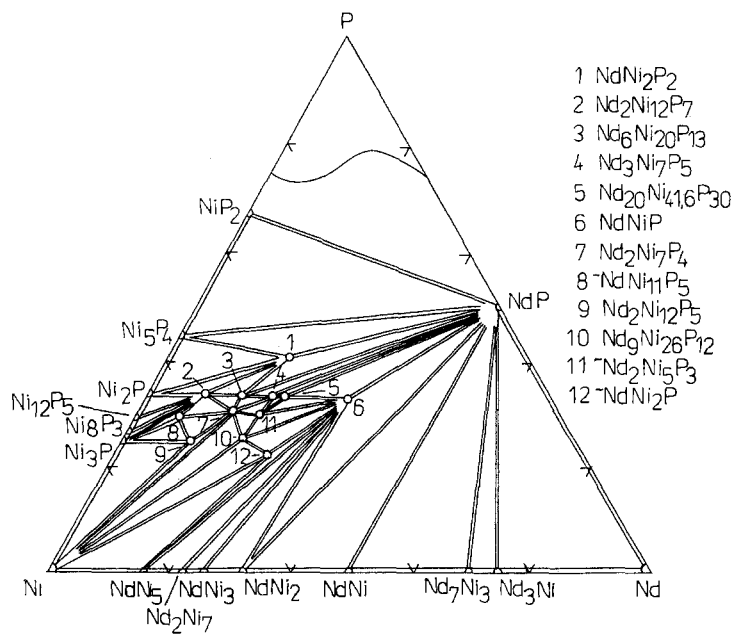

Fig. 24. Nd–Ni–P, isothermal sections at 1070 K (Nd content 0–33 at.%) and 670 K (33–100 at.% Nd).

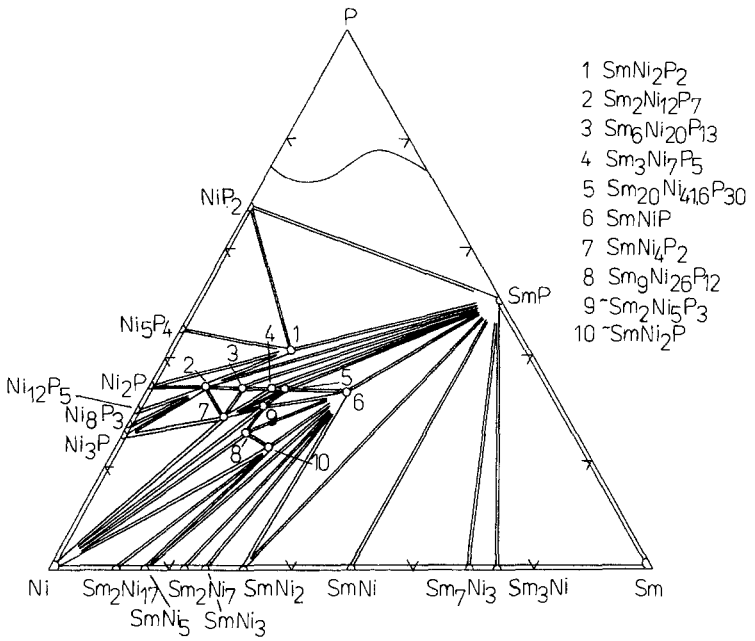

Fig. 25. Sm–Ni–P, isothermal sections at 1070 K (Sm content 0–33 at.%) and 670 K (33–100 at.% Sm).

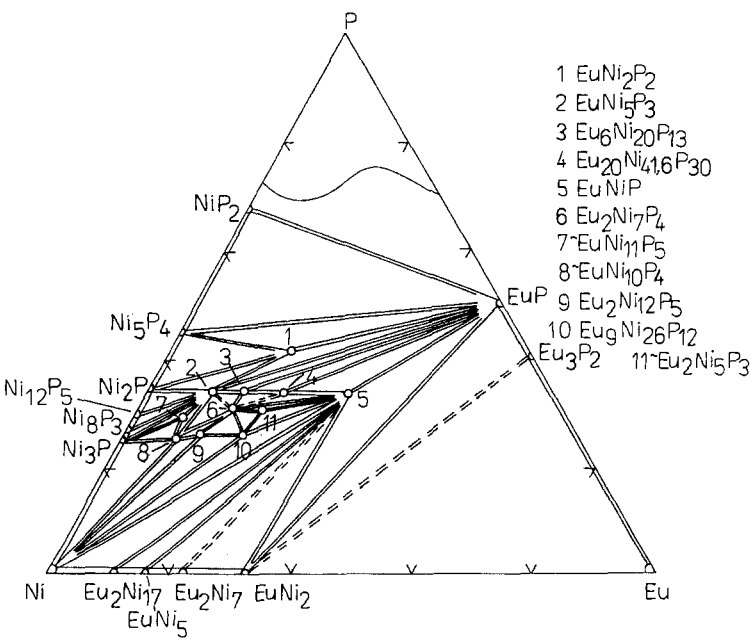

Fig. 26. Eu–Ni–P, isothermal sections at 1070 K (Eu content 0–33 at.%) and 670 K (33–100 at.% Eu).

The compound Eu(Pt, P)$_2$ has a variable composition $EuPt_{0.65-0.80}P_{1.35-1.20}$ (Wenski and Mewis 1986b). Substitution of platinum atoms by P slightly influences the lattice parameter a, and considerably decreases the parameter c (table 23).

Mörsen et al. (1988a) studied the ^{57}Fe Mössbauer spectra of the solid solution $EuCo_{2-x}Fe_xP_2$ ($x < 0.1$) at 20 K and 300 K.

The compound EuPtP dissolves Gd up to the composition $Eu_{\sim 0.5}Gd_{\sim 0.5}PtP$ with decreasing lattice parameters to $a = 0.4114$ and $c = 0.8156$ (Lux et al. 1991a). Substitution of half of the Eu atoms by Sr in α-EuPtP resulted in changing the lattice constants to $a = 0.4083$ and $c = 0.8867$.

2.1.4. *R–M–P, R–M–M′–P (R = rare-earth metal of yttrium group)*

R–M–(M′)P compounds with yttrium-group rare earths are listed in table 24. Oryshchyn et al. (1988b) constructed the isothermal section of the Gd–Si–P system at 1070 K (fig. 27a) using X-ray analysis; no ternary compounds or solid solutions were found.

Kuz'ma et al. (1986b) established the phase diagram of the Gd–Co–P system at 1070 and 870 K (fig. 27b) using the X-ray phase method. Assigning the crystal structure of $Gd_2Co_4P_3$ to the $Hf_2Co_4P_3$ type requires single-crystal confirmation.

Table 24
Compounds in the systems R–M–P and R–M–M′–P (R = rare-earth metal of yttrium group)

Compound	Prep.[a]	Structure type	Lattice parameters			R	Reference(s)
			a	b	c		
$Gd_2Mn_{12}P_7$	1	$Zr_2Fe_{12}P_7$	0.9492	–	0.3665		Jeitschko et al. (1993)
$Gd_2Fe_{12}P_7$	3	$Zr_2Fe_{12}P_7$	0.91448	–	0.36528		Jeitschko et al. (1978)
$GdFe_5P_3$	3	YCo_5P_3	1.2043	0.3683	1.0460	0.063	Jeitschko et al. (1984)
$Gd_2Co_{12}P_7$	3	$Zr_2Fe_{12}P_7$	0.90669	–	0.36230		Jeitschko et al. (1978)
$GdCo_5P_3$	3	YCo_5P_3	1.1859	0.3670	1.0355		Meisen and Jeitschko (1984b)
$Gd_5Co_{19}P_{12}$	3	$Sc_5Co_{19}P_{12}$	1.2104	–	0.3700		Jakubowski-Ripke and Jeitschko (1988)
$GdCo_3P_2$	3	$HoCo_3P_2$	1.0611	0.3727	1.2325		Jakubowski-Ripke and Jeitschko (1988)
	2		1.0618	0.3716	1.2263		Chykhrij et al. (1989b)
$Gd_2Co_4P_3$	2	$Hf_2Co_4P_3$	1.2261	–	0.3719		Kuz'ma et al. (1986a)
$GdNi_4P_2$	2	$ZrFe_4Si_2$	0.7128	–	0.3620		Chykhrij et al. (1986)
$Gd_2Ni_{12}P_7$	3	$Zr_2Fe_{12}P_7$	0.9085	–	0.3702		Jeitschko et al. (1978)
	3		0.9069	–	0.3690		Jeitschko and Jaberg (1980b)
$Gd_7Ni_{19}P_{13}$	1	$Zr_6Ni_{20}P_{13}$	1.2719	–	0.3777		Madar et al. (1985b)
$Gd_3Ni_7P_5$	2	$Nd_3Ni_7P_5$	1.6248	–	0.3819		Chykhrij et al. (1989c)
GdNiP	2	$Tb_{1-x}NiP$	0.3949	–	1.5503		Chykhrij et al. (1987)
	1		0.3888	–	0.9378		Marchand and Jeitschko (1978)
$GdNi_2P_2$	1	$CeAl_2Ga_2$	0.3892	–	0.9372		Jeitschko and Jaberg (1980a)
			0.3885	–	0.9378		Reehuis et al. (1991)
$GdCu_{1+x}P_{2-x}$	1	$HfCuSi_2$	0.3798	–	0.9730		Chykhrij et al. (1989a)

Table 24, *continued*

Compound	Prep.[a]	Structure type	Lattice parameters			R	Reference(s)
			a	*b*	*c*		
$GdCu_xP_y$	1	orthorhomb.	~2.0	~0.55	~0.55		Möller and Jeitschko (1985)
$Gd_5Ru_{19}P_{12}$	1	$Ho_5Ni_{19}P_{12}$	1.2501	–	0.3948		Ghetta et al. (1989)
$GdRu_2P_2$	1,3	$CeAl_2Ga_2$	0.4034	–	0.9634		Jeitschko et al. (1987)
$Gd_2Rh_{12}P_7$	1	$Zr_2Rh_{12}P_7$	0.9626	–	0.3790		Pivan et al. (1984a, 1985c,d)
GdPdP	1	ZrBeSi	0.4179	–	0.7507		Johrendt and Mewis (1990)
$GdPd_2P_2$	1	$CeAl_2Ga_2$	0.4081	–	0.9858		Jeitschko and Hofmann (1983)
GdPtP	1	YbPtP	0.4119	–	0.3904		Wenski and Mewis (1986c)
$Gd_4Co_{13}(Si,P)_9$		$Gd_4Co_{13}(Si,P)_9$	1.0419	–	0.3727	0.032	Jakubowski-Ripke and Jeitschko (1987)
$Tb_2Mn_{12}P_7$	1	$Zr_2Fe_{12}P_7$	0.9472	–	0.3651		Jeitschko et al. (1993)
$Tb_2Fe_{12}P_7$	3	$Zr_2Fe_{12}P_7$	0.91333	–	0.36460		Jeitschko et al. (1978)
$TbFe_5P_3$	3	YCo_5P_3	1.2013	0.3675	1.0436		Jeitschko et al. (1984)
$Tb_2Co_{12}P_7$	3	$Zr_2Fe_{12}P_7$	0.90557	–	0.36094		Jeitschko et al. (1978)
$TbCo_3P_3$	3	YCo_5P_3	1.1827	0.3667	1.0340		Meisen and Jeitschko (1984b)
$Tb_5Co_{19}P_{12}$	3	$Sc_5Co_{19}P_{12}$	1.2089	–	0.3689		Jakubowski-Ripke and Jeitschko (1988)
$TbCo_3P_2$	3	$HoCo_3P_2$	1.0586	0.3706	1.2267		Jeitschko and Jakubowski (1985)
$\sim Tb_{19}Ni_{54}P_{27}$	2	–	–	–	–		Chykhrij and Kuz'ma (1990)
$TbNi_4P_2$	2	$ZrFe_4Si_2$	0.7116	–	0.3614		Chykhrij et al. (1986)
$\sim Tb_{22}Ni_{49}P_{29}$	2	–	–	–	–		Chykhrij and Kuz'ma (1990)
$\sim Tb_{24}Ni_{45}P_{31}$	2	–	–	–	–		Chykhrij and Kuz'ma (1990)
$Tb_2Ni_{12}P_7$	3	$Zr_2Fe_{12}P_7$	0.9061	–	0.3688		Jeitschko and Jaberg (1980b)
$Tb_7Ni_{19}P_{13}$	1	$Zr_6Ni_{20}P_{13}$	1.2694	–	0.3756		Madar et al. (1985b)
$Tb_3Ni_7P_5$	2	$Nd_3Ni_7P_5$	1.6309	–	0.3815		Chykhrij et al. (1989c)
$Tb_{1-x}NiP$, ($x=0.05$)	2	$Tb_{1-x}NiP$	0.3922	–	1.5328		Chykhrij et al. (1987)
$TbNi_2P_2$	1	$CeAl_2Ga_2$	0.3870	–	0.9342		Jeitschko and Jaberg (1980a)
			0.38693	–	0.9361		Reehuis et al. (1991)
$\sim TbCu_3P_2$	1	–	–	–	–		Shouminsky et al. (1991)
$\sim TbCu_5P_3$	1	–	–	–	–		Shouminsky et al. (1991)
$\sim Tb_{17}Cu_{45}P_{38}$	1	–	–	–	–		Shouminsky et al. (1991)
$TbCu_{1.25}P_{1.75}$	1	$HfCuSi_2$	0.3774	–	0.9686		Chykhrij et al. (1989a)
$TbCu_xP_y$	1	orthorhomb.	~2.0	~0.55	~0.55		Möller and Jeitschko (1985)
$Tb_5Ru_{19}P_{12}$	1	$Ho_5Ni_{19}P_{12}$	1.2477	–	0.3944		Ghetta et al. (1989)
$TbRu_2P_2$	1,3	$CeAl_2Ga_2$	0.4028	–	0.9578		Jeitschko et al. (1987)
$Tb_2Rh_{12}P_7$	1	$Zr_2Rh_{12}P_7$	0.9624	–	0.3790		Pivan et al. (1985c,d)
TbPdP	1	TiNiSi	0.6926	0.4015	0.7710		Johrendt and Mewis (1990)
$TbPd_2P_2$	1	$CeAl_2Ga_2$	0.4056	–	0.9845		Jeitschko and Hofmann (1983)
TbPtP	1	YbPtP	0.4110	–	0.3872		Wenski and Mewis (1986c)
$TbLiCu_2P_2$	1	$TbLiCu_2P_2$	0.3994	–	0.6563	0.027	Mahan and Mewis (1983)

Continued on next page

Table 24, *continued*

Compound	Prep.[a]	Structure type	Lattice parameters			R	Reference(s)
			a	*b*	*c*		
$Tb_4Co_{13}(Si,P)_9$		$Gd_4Co_{13}(Si,P)_9$	–	–	–		Jakubowski-Ripke and Jeitschko (1987)
$Dy_2Mn_{12}P_7$	1	$Zr_2Fe_{12}P_7$	0.9470	–	0.3645		Jeitschko et al. (1993)
$Dy_2Fe_{12}P_7$	3	$Zr_2Fe_{12}P_7$	0.91148	–	0.36363		Jeitschko et al. (1978)
$DyFe_5P_3$	3	YCo_5P_3	1.1999	0.3666	1.0423		Jeitschko et al. (1984)
$Dy_2Co_{12}P_7$	3	$Zr_2Fe_{12}P_7$	0.90465	–	0.36016		Jeitschko et al. (1978)
$DyCo_5P_3$	3	YCo_5P_3	1.1820	0.3662	1.0327		Meisen and Jeitschko (1984b)
$Dy_5Co_{19}P_{12}$	3	$Sc_5Co_{19}P_{12}$	1.2066	–	0.3676		Jakubowski-Ripke and Jeitschko (1988)
$DyCo_3P_2$	3	$HoCo_3P_2$	1.0570	0.3698	1.2250		Jeitschko and Jakubowski (1985)
$DyNi_4P_2$	2	$ZrFe_4Si_2$	0.7109	–	0.3612		Chykhrij et al. (1986)
$Dy_2Ni_{12}P_7$	3	$Zr_2Fe_{12}P_7$	0.9054	–	0.3674		Jeitschko and Jaberg (1980b)
$Dy_7Ni_{19}P_{13}$	1	$Zr_6Ni_{20}P_{13}$	1.2674	–	0.3744		Madar et al. (1985b)
DyNiP	2	$Tb_{1-x}NiP$	0.3921	–	1.5283		Chykhrij et al. (1987)
$DyNi_2P_2$	1	$CeAl_2Ga_2$	0.3857	–	0.9332		Jeitschko and Jaberg (1980a)
			0.3857	–	0.9349		Reehuis et al. (1991)
$DyCu_{1+x}P_{2-x}$	1	$HfCuSi_2$	0.3763	–	0.9634		Chykhrij et al. (1989a)
$DyCu_xP_y$	1	orthorhomb.	~2.0	~0.55	~0.55		Möller and Jeitschko (1985)
$Dy_5Ru_{19}P_{12}$	1	$Dy_5Ru_{19}P_{12}$	1.2465	–	0.3940	0.044	Ghetta et al. (1989)
$DyRu_2P_2$	1,3	$CeAl_2Ga_2$	0.4024	–	0.9536		Jeitschko et al. (1987)
$Dy_2Rh_{12}P_7$	1	$Zr_2Rh_{12}P_7$	0.9595	–	0.3790		Pivan et al. (1985c,d)
DyPdP	1	TiNiSi	0.6877	0.4000	0.7711		Johrendt and Mewis (1990)
$DyPd_2P_2$	1	$CeAl_2Ga_2$	0.4042	–	0.9844		Jeitschko and Hofmann (1983)
DyPtP	1	YbPtP	0.4107	–	0.3850		Wenski and Mewis (1986c)
$Dy_4Co_{13}(Si,P)_9$		$Gd_4Co_{13}(Si,P)_9$	–	–	–		Jakubowski-Ripke and Jeitschko (1987)
$Ho_2Mn_{12}P_7$	1	$Zr_2Fe_{12}P_7$	0.9456	–	0.3636		Jeitschko et al. (1993)
$Ho_2Fe_{12}P_7$	3	$Zr_2Fe_{12}P_7$	0.91053	–	0.36340		Jeitschko et al. (1978)
$HoFe_5P_3$	3	YCo_5P_3	1.1988	0.3663	1.0410		Jeitschko et al. (1984)
$Ho_2Co_{12}P_7$	3	$Zr_2Fe_{12}P_7$	0.90383	–	0.35956		Jeitschko et al. (1978)
$HoCo_5P_3$	3	YCo_5P_3	1.1794	0.3653	1.0315		Meisen and Jeitschko (1984b)
$Ho_5Co_{19}P_{12}$	3	$Sc_5Co_{19}P_{12}$	1.2060	–	0.3670	0.033	Jakubowski-Ripke and Jeitschko (1988)
$HoCo_3P_2$	3	$HoCo_3P_2$	1.0560	0.3687	1.2233	0.055	Jeitschko and Jakubowski (1985)
$HoNi_4P_2$	2	$ZrFe_4Si_2$	0.7106	–	0.3609		Chykhrij et al. (1986)
$Ho_2Ni_{12}P_7$	3	$Zr_2Fe_{12}P_7$	0.9052	–	0.3669		Jeitschko and Jaberg (1980b)
	1		0.9063	–	0.3673	0.036	Pivan et al. (1986)
$Ho_5Ni_{19}P_{12}$	1	$Ho_5Ni_{19}P_{12}$	1.2288	–	0.3762	0.049	Pivan et al. (1984b, 1985a)
$Ho_{20}Ni_{66}P_{43}$	1	$Ho_{20}Ni_{66}P_{43}$	2.3095	–	0.3742	0.054	Pivan et al. (1984b, 1985b)

Table 24, *continued*

Compound	Prep.[a]	Structure type	Lattice parameters			R	Reference(s)
			a	*b*	*c*		
$Ho_6Ni_{20}P_{13}$	1	$Ho_6Ni_{20}P_{13}$	1.2677	–	0.3730	0.034	Pivan et al. (1984b, 1986)
$Ho_7Ni_{19}P_{13}$	1	$Zr_6Ni_{20}P_{13}$	1.2645	–	0.3731		Madar et al. (1985b)
HoNiP	2	$Tb_{1-x}NiP$	0.3917	–	1.5163		Chykhrij et al. (1987)
$HoNi_2P_2$	1	$CeAl_2Ga_2$	0.3844	–	0.9329		Jeitschko and Jaberg (1980a)
			0.38484	–	0.9338		Reehuis et al. (1991)
$HoCu_{1+x}P_{2-x}$	1	$HfCuSi_2$	0.3747	–	0.9623		Chykhrij et al. (1989a)
$HoCu_xP_y$	1	orthorhomb.	~2.0	~0.55	~0.55		Möller and Jeitschko (1985)
$Ho_5Ru_{19}P_{12}$	1	$Ho_5Ni_{19}P_{12}$	1.2457	–	0.3938		Ghetta et al. (1989)
$HoRu_2P_2$	1,3	$CeAl_2Ga_2$	0.4023	–	0.9499		Jeitschko et al. (1987)
$Ho_2Rh_{12}P_7$	1	$Zr_2Rh_{12}P_7$	0.9587	–	0.3789		Pivan et al. (1984a, 1985c,d)
HoPdP	1	TiNiSi	0.6853	0.3983	0.7702		Johrendt and Mewis (1990)
$HoPd_2P_2$	1	$CeAl_2Ga_2$	0.4022	–	0.9833		Jeitschko and Hofmann (1983)
$Ho_4Co_{13}(Si,P)_9$		$Gd_4Co_{13}(Si,P)_9$	–	–	–		Jakubowski-Ripke and Jeitschko (1987)
$Er_2Mn_{12}P_7$	1	$Zr_2Fe_{12}P_7$	0.9446	–	0.3629		Jeitschko et al. (1993)
$Er_2Fe_{12}P_7$	3	$Zr_2Fe_{12}P_7$	0.90978	–	0.36274		Jeitschko et al. (1978)
$ErFe_5P_3$	3	YCo_5P_3	1.1976	0.3657	1.0400		Jeitschko et al. (1984)
$Er_2Co_{12}P_7$	3	$Zr_2Fe_{12}P_7$	0.90252	–	0.35913	0.069	Jeitschko et al. (1978), Jeitschko and Jaberg (1980b)
$ErCo_5P_3$	3	YCo_5P_3	1.1784	0.36446	1.0300		Jakubowski-Ripke and Jeitschko (1988)
$Er_5Co_{19}P_{12}$	3	$Sc_5Co_{19}P_{12}$	1.2027	–	0.3659		Jakubowski-Ripke and Jeitschko (1988)
$Er_6Co_{30}P_{19}$	3	$Yb_6Co_{30}P_{19}$	1.4721	–	0.3589		Jeitschko and Jakubowski-Ripke (1993)
$ErCo_3P_2$	3	$HoCo_3P_2$	1.0546	0.3678	1.2201		Jeitschko and Jakubowski (1985)
$ErNi_4P_2$	2	$ZrFe_4Si_2$	0.7094	–	0.3605		Chykhrij et al. (1986)
$Er_2Ni_{12}P_7$	3	$Zr_2Fe_{12}P_7$	0.9037	–	0.3667	0.059	Jeitschko and Jaberg (1980b)
$Er_7Ni_{19}P_{13}$	1	$Zr_6Ni_{20}P_{13}$	1.2648	–	0.3721		Madar et al. (1985b)
ErNiP	2	$Tb_{1-x}NiP$	0.3905	–	1.5086		Chykhrij et al. (1987)
$ErNi_2P_2$	1	$CeAl_2Ga_2$	0.3830	–	0.9303		Jeitschko and Jaberg (1980a)
			0.38351	–	0.99313		Reehuis et al. (1991)
$ErCu_{1+x}P_{2-x}$	1	$HfCuSi_2$	0.3720	–	0.9622		Chykhrij et al. (1989a)
$ErCu_xP_y$	1	orthorhomb.	~2.0	~0.55	~0.55		Möller and Jeitschko (1985)
$ErRu_2P_2$	1,3	$CeAl_2Ga_2$	0.4022	–	0.9463		Jeitschko et al. (1987)
$Er_2Rh_{12}P_7$	1	$Zr_2Rh_{12}P_7$	0.9568	–	0.3780		Pivan et al. (1985c,d)
$Er_3Pd_7P_4$	1	$Er_3Pd_7P_4$	1.5180	0.3955 $\beta = 125.65$	0.9320	0.031	Johrendt and Mewis (1994)
ErPdP	1	TiNiSi	0.6826	0.3965	0.7689	0.034	Johrendt and Mewis (1990)
$ErPd_2P_2$	1	$CeAl_2Ga_2$	0.4022	–	0.9841		Jeitschko and Hofmann (1983)

Continued on next page

Table 24, *continued*

Compound	Prep.[a]	Structure type	Lattice parameters			*R*	Reference(s)
			a	*b*	*c*		
$Er_4Co_{13}(Si,P)_9$		$Gd_4Co_{13}(Si,P)_9$	–	–	–		Jakubowski-Ripke and Jeitschko (1987)
$Tm_2Mn_{12}P_7$	1	$Zr_2Fe_{12}P_7$	0.9438	–	0.3619		Jeitschko et al. (1993)
$Tm_2Fe_{12}P_7$	3	$Zr_2Fe_{12}P_7$	0.90898	–	0.36191		Jeitschko et al. (1978)
$TmFe_5P_3$	3	YCo_5P_3	1.1965	0.3652	1.0392		Jeitschko et al. (1984)
$Tm_2Co_{12}P_7$	3	$Zr_2Fe_{12}P_7$	0.90215	–	0.35867		Jeitschko et al. (1978)
$TmCo_5P_3$	3	YCo_5P_3	1.1776	0.3635	1.0293		Jakubowski-Ripke and Jeitschko (1988)
$Tm_5Co_{19}P_{12}$	3	$Sc_5Co_{19}P_{12}$	1.2004	–	0.3650		Jakubowski-Ripke and Jeitschko (1988)
$TmCo_3P_2$	3	$HoCo_3P_2$	1.0531	0.3666	1.2174		Jeitschko and Jakubowski (1985)
$Tm_6Co_{30}P_{19}$	3	$Yb_6Co_{30}P_{19}$	1.4709	–	0.3580		Jeitschko and Jakubowski-Ripke (1993)
$TmNi_4P_2$	2	$ZrFe_4Si_2$	0.7089	–	0.3603		Chykhrij et al. (1986)
$Tm_2Ni_{12}P_7$	3	$Zr_2Fe_{12}P_7$	0.9031	–	0.3664		Jeitschko and Jaberg (1980b)
$Tm_7Ni_{19}P_{13}$	1	$Zr_6Ni_{20}P_{13}$	1.2637	–	0.3713		Madar et al. (1985b)
TmNiP	2	$Tb_{1-x}NiP$	0.3893	–	1.5014		Chykhrij et al. (1987)
$TmNi_2P_2$	1	$CeAl_2Ga_2$	0.3823	–	0.9310		Jeitschko and Jaberg (1980a)
			0.38242	–	0.9304		Reehuis et al. (1991)
$TmCu_xP_y$	1	orthorhomb.	~2.0	~0.55	~0.55		Möller and Jeitschko (1985)
TmPdP	1	TiNiSi	0.6796	0.3949	0.7677		Johrendt and Mewis (1990)
TmPtP	1	YbPtP	0.4082	–	0.3791		Wenski and Mewis (1986c)
$Yb_2Mn_{12}P_7$	1	$Zr_2Fe_{12}P_7$	0.9437	–	0.3614		Jeitschko et al. (1993)
$Yb_2Fe_{12}P_7$	3	$Zr_2Fe_{12}P_7$	0.90914	–	0.36154		Jeitschko et al. (1978)
$YbFe_5P_3$	3	YCo_5P_3	1.1954	0.3647	1.0378		Jeitschko et al. (1984)
$Yb_2Co_{12}P_7$	3	$Zr_2Fe_{12}P_7$	0.90206	–	0.35788		Jeitschko et al. (1978)
$YbCo_5P_3$	3	YCo_5P_3	1.1756	0.3632	1.0273		Meisen and Jeitschko (1984b)
$Yb_5Co_{19}P_{12}$	3	$Sc_5Co_{19}P_{12}$	1.2002	–	0.3646		Jakubowski-Ripke and Jeitschko (1988)
$YbCo_3P_2$	3	$HoCo_3P_2$	1.0514	0.3657	1.2155		Jeitschko and Jakubowski (1985)
$Yb_6Co_{30}P_{19}$	3	$Yb_6Co_{30}P_{19}$	1.4703	–	0.3574	0.045	Jeitschko and Jakubowski-Ripke (1993)
$Yb_xCo_4P_{12}$	3	$LaFe_4P_{12}$	0.7718	–	–		Zemni et al. (1986)
$YbNi_4P_2$	2	$ZrFe_4Si_2$	0.7076	–	0.3592		Chykhrij et al. (1986)
$Yb_2Ni_{12}P_7$	3	$Zr_2Fe_{12}P_7$	0.9045	–	0.3649		Jeitschko et al. (1978)
	3		0.9038	–	0.3653		Jeitschko and Jaberg (1980b)
$Yb_6Ni_{20}P_{13}$	3	$Y_6Ni_{20}P_{13}$	1.2714	–	0.3731		Babizhets'ky et al. (1993a)
$Yb_7Ni_{19}P_{13}$	1	$Zr_6Ni_{20}P_{13}$	1.2676	–	0.3747		Madar et al. (1985b)

Table 24, *continued*

Compound	Prep.[a]	Structure type	Lattice parameters			R	Reference(s)
			a	*b*	*c*		
$YbNi_2P_2$	1	$CeAl_2Ga_2$	0.3833	–	0.9325		Marchand and Jeitschko (1978)
	1		0.3834	–	0.9323		Jeitschko and Jaberg (1980a)
$YbCu_{3-x}P_2$ ($x=0.4$)	1	$YbCu_3P_2$	0.3964	–	4.0296	0.075	Klüfers et al. (1979)
$YbCu_2P_2$	1	$YbCu_2P_2$	0.3951	–	5.946		Klüfers et al. (1979)
$YbZn_2P_2$	1	Ce_2S_2O	0.4035	–	0.6774	0.037	Klüfers et al. (1979)
$Yb_5Ru_{19}P_{12}$	1	$Ho_5Ni_{19}P_{12}$	1.2424	–	0.3928		Ghetta et al. (1989)
$YbRu_2P_2$	1,3	$CeAl_2Ga_2$	0.4026	–	0.9463		Jeitschko et al. (1987)
$Yb_2Rh_{12}P_7$	1	$Zr_2Rh_{12}P_7$	0.9582	–	0.3792		Pivan et al. (1985c,d)
YbPdP	1	TiNiSi	0.6776	0.3937	0.7670		Johrendt and Mewis (1990)
$YbPd_2P_2$	1	$CeAl_2Ga_2$	0.4088	–	0.9721		Jeitschko and Hofmann (1983)
YbPtP	1	YbPtP	0.4077	–	0.3777		Wenski and Mewis (1986c)
$YbLiCu_2P_2$	1	$TbLiCu_2P_2$	0.3949	–	0.6484		Mahan and Mewis (1983)
$YbMnCuP_2$	4	Ce_2S_2O	0.3960	–	0.6484		Mewis (1980b)
$YbCuZnP_2$	1	Ce_2S_2O	0.3946	–	0.6462	0.063	Klüfers et al. (1979)
$Lu_2Mn_{12}P_7$	1	$Zr_2Fe_{12}P_7$	0.9439	–	0.3613		Jeitschko et al. (1993)
$Lu_2Fe_{12}P_7$	3	$Zr_2Fe_{12}P_7$	0.90688	–	0.36180		Jeitschko et al. (1978)
$LuFe_5P_3$	3	YCo_5P_3	1.1948	0.3643	1.0372		Jeitschko et al. (1984)
$Lu_2Co_{12}P_7$	3	$Zr_2Fe_{12}P_7$	0.90001	–	0.35722		Jeitschko et al. (1978)
$LuCo_5P_3$	3	YCo_5P_3	1.1766	0.3628	1.0276		Meisen and Jeitschko (1984b)
$Lu_5Co_{19}P_{12}$	3	$Sc_5Co_{19}P_{12}$	1.1991	–	0.3641		Jakubowski-Ripke and Jeitschko (1988)
$LuCo_3P_2$	3	$HoCo_3P_2$	1.0520	0.3652	1.2138		Jeitschko and Jakubowski (1985)
$Lu_6Co_{30}P_{19}$	3	$Yb_6Co_{30}P_{19}$	1.4697	–	0.3571		Jeitschko and Jakubowski-Ripke (1993)
$LuNi_4P_2$	2	$ZrFe_4Si_2$	0.7065	–	0.3591		Chykhrij et al. (1986)
$Lu_2Ni_{12}P_7$	3	$Zr_2Fe_{12}P_7$	0.9022	–	0.3648		Jeitschko and Jaberg (1980b)
LuNiP	2	$Tb_{1-x}NiP$	0.3853	–	1.5033		Chykhrij et al. (1987)
LuPdP	1	TiNiSi	0.6760	0.3920	0.7662	0.050	Johrendt and Mewis (1990)
LuPtP	1	YbPtP	0.4071	–	0.3759		Wenski and Mewis (1986c)

[a] Methods of preparation: (1) ampoule synthesis from the pure components; (2) melting in arc furnace; (3) tin flux method; (4) other method.

Chykhrij (1988) constructed part of the phase diagram of the Tb–Co–P system (fig. 28a). Chykhrij and Kuz'ma (1990) established the phase diagrams of the Tb–{Cr, Fe, Co, Ni}–P systems (figs. 28–30) using X-ray and, partially, microstructural analysis. The compounds $TbFe_5P_3$ and $Tb_5Co_{19}P_{12}$ obtained from liquid tin, and $Tb_3Ni_7P_5$, obtained from liquid cadmium, were not found at the temperatures investigated.

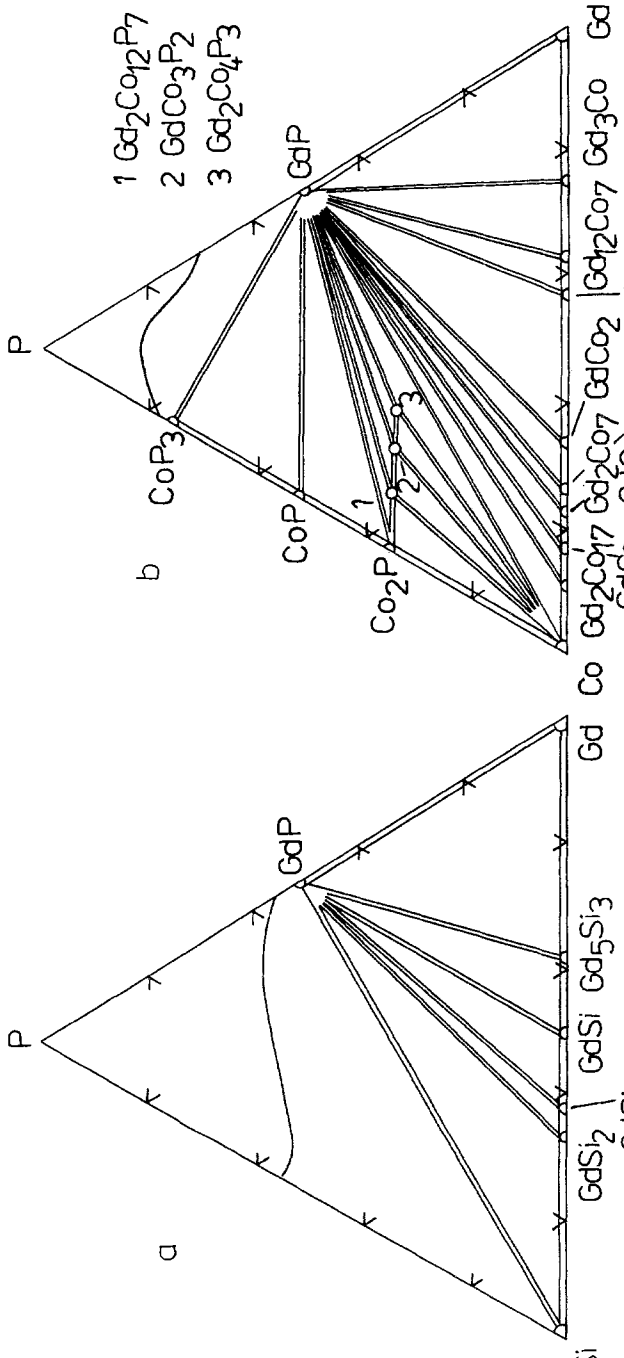

Fig. 27. (a) Gd–Si–P, isothermal section at 1070 K; (b) Gd–Co–P, isothermal section at 1070 K (0–33 at.% Gd) and 870 K (33–100 at.% Gd).

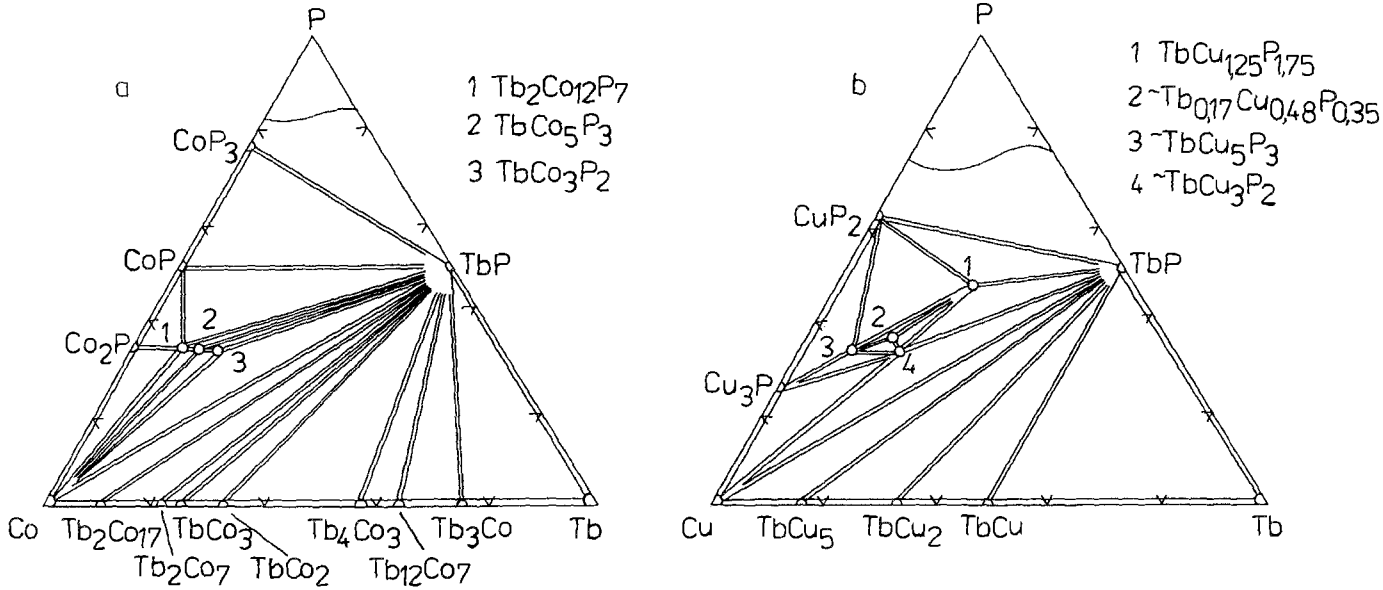

Fig. 28. (a) Tb–Co–P and (b) Tb–Cu–P, isothermal sections at 1070 K (0–33 at.% Tb) and 870 K (33–100 at.% Tb).

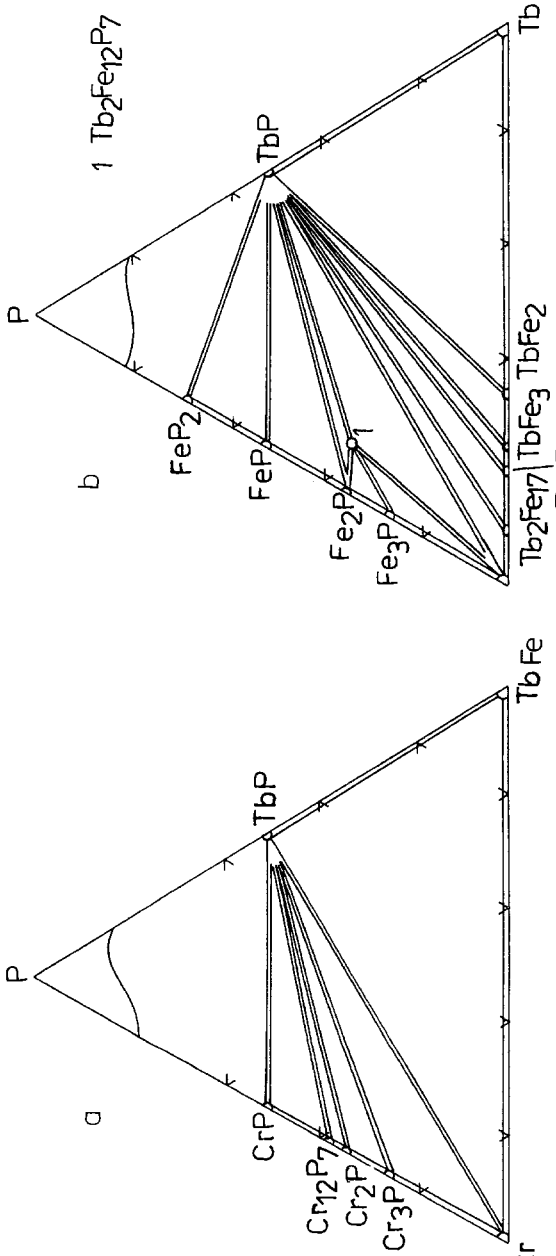

Fig. 29. (a) Tb–Cr–P, isothermal section at 1070 K; (b) Tb–Fe–P, isothermal sections at 1070 K (0–33 at.% Tb) and 870 K (33–100 at.% Tb).

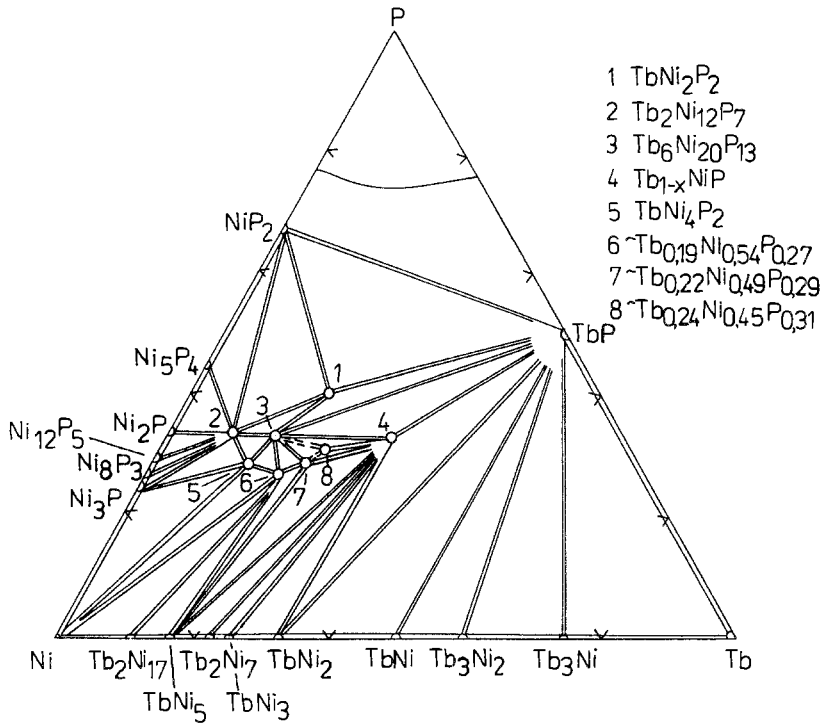

Fig. 30. Tb–Ni–P, isothermal sections at 1070 K (Tb content 0–33 at.%) and 870 K (33–100 at.% Tb).

Shouminsky et al. (1991) constructed the phase diagram of the Tb–Cu–P system at 1070 K in the range of 0–67 at.% of P (fig. 28b) using the X-ray phase method.

No phase diagrams of the {Dy, Ho, Er, Tm, Yb, Lu}–M–P systems have been studied. The crystallographic characteristics of all known ternary compounds are listed in table 24.

2.2. *Peculiarities of the interaction between components in the ternary R–M–P systems*

Some aspects of the interaction between components in the ternary systems R–M–P, where M is a transition metal, are considered by Kuz'ma et al. (1989), Oryshchyn et al. (1991b) and Kuz'ma et al. (1991). The characteristics of R–M–P systems are summarized in fig. 31. Phase diagrams are known for only 14 ternary systems, namely {La, Ce}–Fe–P, {La, Ce, Nd, Sm, Eu, Tb}–Ni–P, Gd–{Si, Co}–P and Tb–{Cr, Fe, Co, Cu}–P. Other systems were investigated only for the synthesis of phosphides with definite stoichiometric compositions.

The elements interacted in the systems investigated differ considerably from one another in electronic structure (f-, d- and p-elements), electronegativity and atomic radii. Sokolowskaya and Huzej (1986) consider that great difference in electronic structure of

	Li	Na	K	C	Si	Ge	Sn	Pb	Ti	V	Cr	Mn	Fe	Co	Ni	Cu	Zn	Zr	Nb	Mo	Tc	Ru	Rh	Pd	Ag	Cd	Hf	Ta	W	Re	Os	Ir	Pt	Au	Hg
Sc												1	3	4								2													
Y													2	3	6	1						2	1	1									1		
La	2				4								3	4	10	2						4	2	3	2						1				
Ce	1				4								3	5	15	4						3	2	3	1						1				
Pr	1				3								3	7	8	2						3	1	2	1						1				
Nd													2	6	13	2						3	2	2							1				
Pm																																			
Sm												1	3	5	11	4						2		2									1		
Eu	1	1										1	2	3	12	2	1					2		2	1						1		3	1	
Gd												1	2	5	6	2						2	1	2									1		
Tb												1	2	4	9	5						2	1	2									1		
Dy												1	2	4	5	2						2	1	2									1		
Ho												1	2	4	8	2						2	1	2											
Er												1	2	5	5	2						1	1	3											
Tm												1	2	5	5	1								1									1		
Yb												1	2	6	5	2	1					2	1	2									1		
Lu												1	2	5	3									1									1		

Fig. 31. Degree of investigation of R–M–P systems: shaded squares indicate compounds for which a phase diagram has been built; the number of ternary compounds found, if any, is given in the square.

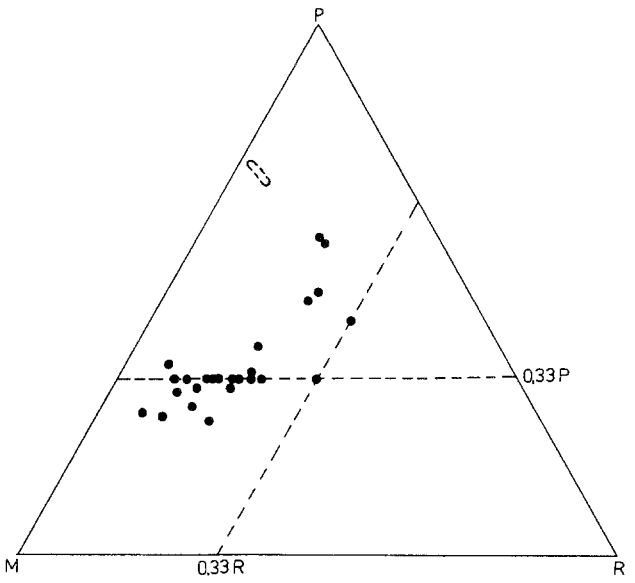

Fig. 32. Compositions of ternary compounds in R–M–P systems.

the interacted elements leads to the formation of compounds. Where close relationships exist (electronic structure, atomic radii) the trend to form solid solutions increases. At the same time the increasing differences in electronegativity of the interacted elements and their electronic structure (for example, s- and p-elements) causes the appearence of direct covalent and ionic-covalent bonds in the compound. And that, in turn, decreases the number of compounds in the system.

Kuz'ma et al. (1986a) and Lomnitskaya and Kuz'ma (1991a) showed that phosphorus behaves as a metallic element in ternary M–M′–P systems at low P content (up to 25 at.%), as indicated by the formation of phosphorus solid solutions in binary intermetallic compounds (e.g., Zr_2Fe, Zr_2Co). In ternary compounds phosphorus atoms occupy the same positions as iron triad metals in the structure. At phosphorus contents up to 33.3 at.%, metallic-type chemical bonds occur in the compounds, and there are no P–P contacts.

In the R–M–P systems investigated no solid solutions are found. Ternary compounds are characterized by their constant composition and, in their structure, a statistical distribution of the transition metal and phosphorus atoms is very rare. Only in the phosphides with the $HfCuSi_2$- and AlB_2-type structure do statistical distributions of copper (in former compounds) or platinum (in latter) and phosphorus atoms occur. This is the principal difference between the R–M–P and M–M′–P systems.

As illustrated in fig. 32, ternary compounds in R–M–P systems are situated in the part of the diagram system with 0–33.3 at.% of R. Substitution of R by a transition metal with a close atomic radius (Zr, Hf) does not cause an essential change in the number of ternary phosphides formed: La–Ni–P (10 compounds), Ce–Ni–P (15), Tb–Ni–P (9) and Zr–Ni–P (12). However, as was shown by Lomnitskaya and Kuz'ma (1991b), ternary

compounds in the Zr–Ni–P system are formed over the whole concentration region of the system. R–Ni–P systems are similar to R–M–B ones where ternary borides contain up to 37 at.% of R (Kuz'ma and Chaban 1990).

Phase diagrams of the Tb–M–P systems provide an opportunity to observe the influence of the M-component on the interaction in R–M–P systems. In Tb–Cr–P system no ternary compounds are formed, in Tb–Fe–P, 2; in Tb–Co–P, 4; in Tb–Ni–P, 9 and in Tb–Cu–P, 4. Since the differences in atomic radii and electronegativity of these transition metals are small, the main influence on the number of compounds formed must be the electronic structure of the metal. The number of compounds increases from Fe to Ni, moreover, these systems are characterized by forming isotypic (ST $Zr_2Fe_{12}P_7$) or structurally related compounds (see sect. 2.4). The system Tb–Cu–P strongly differs from iron triad metal-containing systems; no isotypic compounds are formed in the Tb–Cu–P and Tb–{Fe, Co, Ni}–P systems.

Substitution of the R element also affects the character of interaction in the systems. The number of compounds formed is 10 in La–Ni–P, 15 in Ce–Ni–P, 13 in Nd–Ni–P, 11 in Sm–Ni–P, 12 in Eu–Ni–P, and 9 in Tb–Ni–P. The number of compounds containing light rare earths is greater than in systems containing an R of the yttrium group.

2.3. *Structure types of ternary and quaternary phosphides*

The structure types of the ternary and quaternary phosphides are presented in order of increasing phosphorus content and at the same P content in order of increasing rare-earth content. Some closely related STs are also discussed. Information about the structure types of ternary phosphides is reported similarly as for binary phosphides above.

2.3.1. *$Eu_2Pt_7AlP_3$, tI28*

Structure type $Eu_2Pt_7AlP_3$ (Lux et al. 1991b; fig. 33, table 25) has space group I4/mmm, $a = 0.4046$, $c = 2.6850$.

Table 25
Atomic parameters for $Eu_2Pt_7AlP_3$

Atom	Position	Fractional coordinates			Atomic arrangement			
		x	y	z				
Eu	4(*e*)	0	0	0.3348	4Eu	9Pt		8P
Pt1	4(*e*)	0	0	0.2074	5Eu			5P
Pt2	2(*a*)	0	0	0		8Pt	4Al	
Pt3	8(*g*)	0	1/2	0.0705	2Eu	6Pt	2Al	2P
Al	2(*b*)	0	0	1/2		12Pt		
P1[a]	4(*d*)	1/2	0	1/4	4Eu	4Pt		4P
P2	4(*e*)	0	0	0.1195	4Eu	5Pt		

[a] Occupancy 48%.

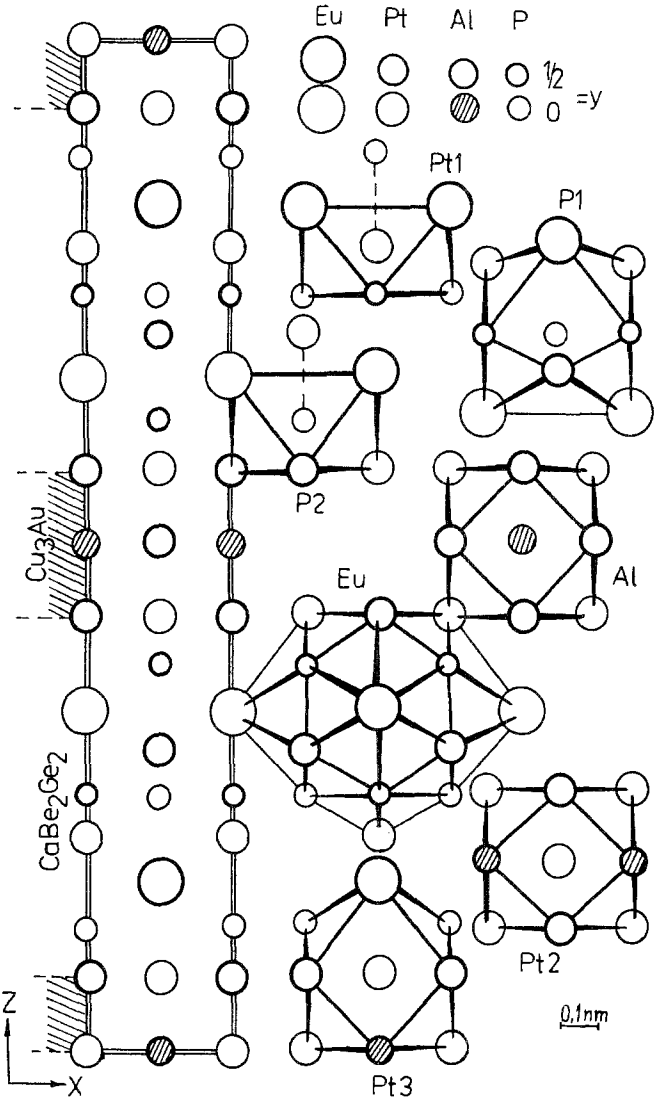

Fig. 33. Crystal structure of $Eu_2Pt_7AlP_3$ and CPs of atoms.

The crystal structure was determined by an X-ray single-crystal method, $R = 0.026$ (Lux et al. 1991b). ST $Eu_2Pt_7AlP_{\sim 3}$ is a combination of the STs $CaBe_2Ge_2$ and Cu_3Au (fig. 33). The atomic coordination of Pt2, Pt3, Al and P1 is a cubooctahedron or its distorted derivative; Pt1 and P2 atoms occupy an Archimedean cube with two or one additional atom outside the square faces, respectively. The shortest interatomic distances are: $\delta_{Eu-Pt1} = 0.3077$; $\delta_{Eu-P1} = 0.3046$; $\delta_{Pt2-P3} = 0.2771$; $\delta_{Pt3-Al} = 0.2771$; $\delta_{Pt1-P1} = 0.2324$. Isotypic compounds are $Eu_2Pt_{\sim 7}Mg_{\sim 1}P_{\sim 3}$ and $Eu_2Pt_7MP_{\sim 3}$ where M = Mn, Fe, Zn.

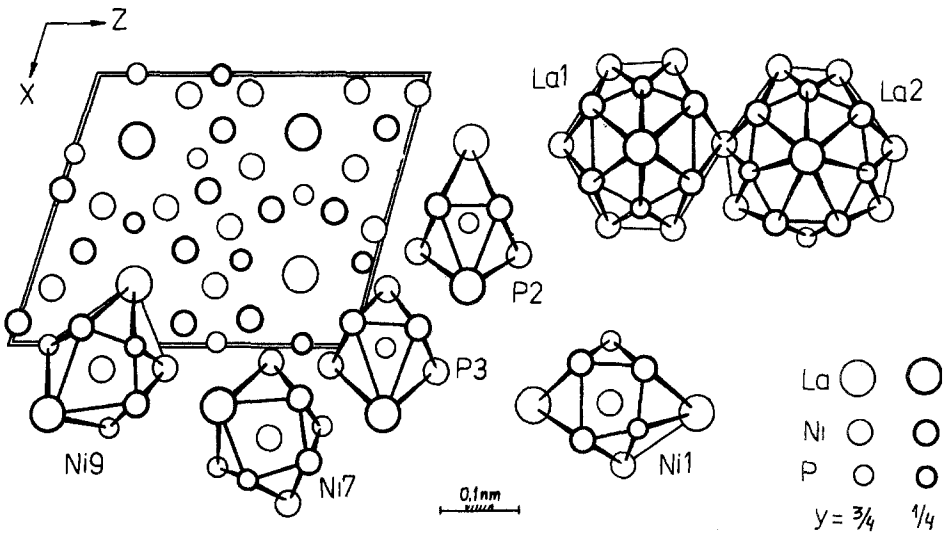

Fig. 34. Crystal structure of $La_2Ni_{12}P_5$ and CPs of atoms.

Table 26
Atomic parameters for $La_2Ni_{12}P_5$

Atom	Position	Fractional coordinates			Atomic arrangement		
		x	*y*	*z*			
La1	4(*e*)	0.22033	1/4	0.68325	2La	14Ni	4P
La2	4(*e*)	0.25165	1/4	0.18766	2La	14Ni	7P
Ni1	4(*e*)	0.2017	1/4	0.9183	2La	7Ni	3P
Ni2	4(*e*)	0.2134	1/4	0.4385	2La	7Ni	3P
Ni3	4(*e*)	0.4288	1/4	0.0141	1La	9Ni	2P
Ni4	4(*e*)	0.4350	1/4	0.4490	1La	9Ni	2P
Ni5	4(*e*)	0.5064	1/4	0.6588	3La	6Ni	3P
Ni6	4(*e*)	0.5106	1/4	0.8490	3La	6Ni	3P
Ni7	4(*e*)	0.6559	1/4	0.1341	2La	8Ni	2P
Ni8	4(*e*)	0.6562	1/4	0.4392	2La	8Ni	2P
Ni9	4(*e*)	0.9063	1/4	0.6950	3La	5Ni	4P
Ni10	4(*e*)	0.9201	1/4	0.0101	3La	5Ni	4P
Ni11	4(*e*)	0.9213	1/4	0.5099	3La	6Ni	3P
Ni12	4(*e*)	0.9375	1/4	0.2030	3La	6Ni	3P
P1	4(*e*)	0.0072	1/4	0.3782	2La	7Ni	
P2	4(*e*)	0.5495	1/4	0.2596	3La	6Ni	
P3	4(*e*)	0.6891	1/4	0.6130	2La	7Ni	
P4	4(*e*)	0.7007	1/4	0.9836	2La	7Ni	
P5	4(*e*)	0.9918	1/4	0.8712	2La	7Ni	

2.3.2. *$La_2Ni_{12}P_5$, mP76*

Structure type $La_2Ni_{12}P_5$ (Kuz'ma et al. 1993; fig. 34, table 26) has space group $P2_1/m$, $a=1.0911$, $b=0.3697$, $c=1.3174$, $\beta=108.02°$.

The crystal structure of $La_2Ni_{12}P_5$ was determined by an X-ray single-crystal method, $R=0.028$ (Kuz'ma et al. 1993). It is characterized by a trigonal-prismatic environment of all phosphorus atoms; typical CPs are shown in fig. 34. CNs of the lanthanum atoms are 20 and 23, all the nickel atoms have a CN 12. Interatomic distances have values in the following ranges: $\delta_{La-La}=0.3696$; $\delta_{La-Ni}=0.3650$–0.3029; $\delta_{La-P}=0.3129$–0.2993; $\delta_{Ni-Ni}=0.2923$–0.2378; $\delta_{Ni-P}=0.2420$–0.2142. Isotypic phosphides are found for Ce, Pr, Nd, Eu.

2.3.3. *$LaNi_{10}P_4$, oP60*

Structure type $LaNi_{10}P_4$ (Babizhets'ky et al. 1992c; fig. 35, table 27) has space group Pnma, $a=0.9310$, $b=0.3706$, $c=2.234$.

The crystal structure of $LaNi_{10}P_4$ was determined by an X-ray single-crystal method, $R=0.038$ (Babizhets'ky et al. 1992c). The XZ projection and typical coordination polyhedra are shown in fig. 35; all phosphorus atoms are situated in trigonal prisms formed by metal atoms. The interatomic distances are close to the sum of atomic radii of the corresponding elements, their minimum values are: $\delta_{La-Ni7}=0.3249$; $\delta_{La-P1}=0.3049$; $\delta_{Ni2-Ni3}=0.2452$; $\delta_{P1-Ni2,3}=0.219$.

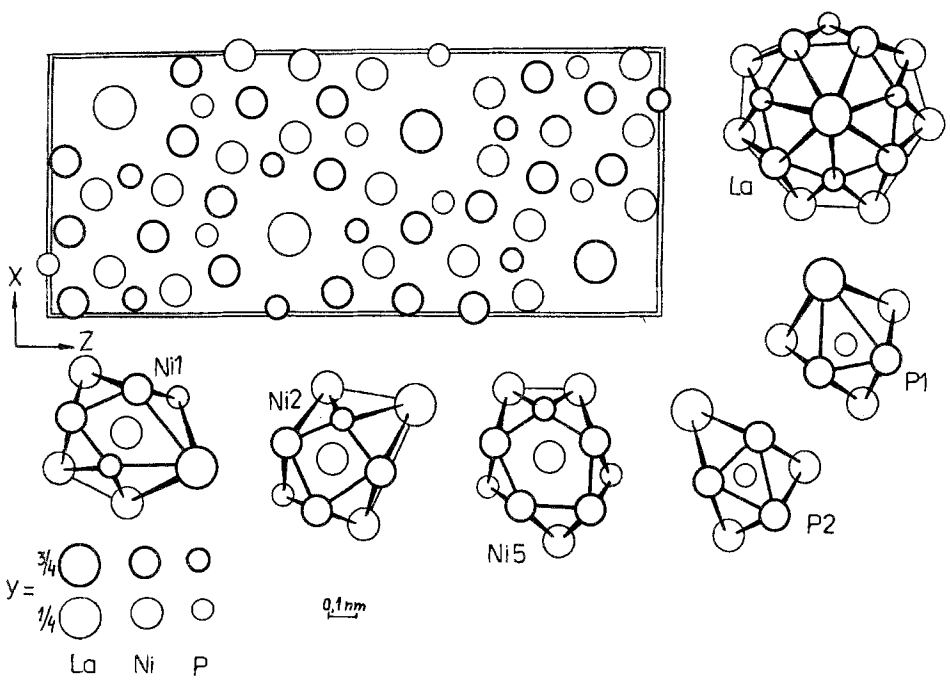

Fig. 35. Crystal structure of $LaNi_{10}P_4$ and CPs of atoms.

Table 27
Atomic parameters for $LaNi_{10}P_4$

Atom	Position	Fractional coordinates			Atomic arrangement		
		x	y	z			
La	4(*c*)	0.7997	1/4	0.1075	2La	12Ni	6P
Ni1	4(*c*)	0.0766	1/4	0.7786	2La	7Ni	3P
Ni2	4(*c*)	0.0959	1/4	0.2033	1La	8Ni	3P
Ni3	4(*c*)	0.1760	1/4	0.0987	1La	8Ni	3P
Ni4	4(*c*)	0.1913	1/4	0.5351	1La	9Ni	2P
Ni5	4(*c*)	0.2050	1/4	0.6710		10Ni	2P
Ni6	4(*c*)	0.3404	1/4	0.7839	2La	7Ni	3P
Ni7	4(*c*)	0.4173	1/4	0.9705	2La	8Ni	2P
Ni8	4(*c*)	0.4528	1/4	0.0822	1La	9Ni	2P
Ni9	4(*c*)	0.4628	1/4	0.5385	3La	5Ni	4P
Ni10	4(*c*)	0.9813	1/4	0.3078	1La	8Ni	3P
P1	4(*c*)	0.189	1/4	0.0008	2La	7Ni	
P2	4(*c*)	0.295	1/4	0.2555	1La	8Ni	
P3	4(*c*)	0.4370	1/4	0.6387	2La	7Ni	
P4	4(*c*)	0.979	1/4	0.6309	2La	7Ni	

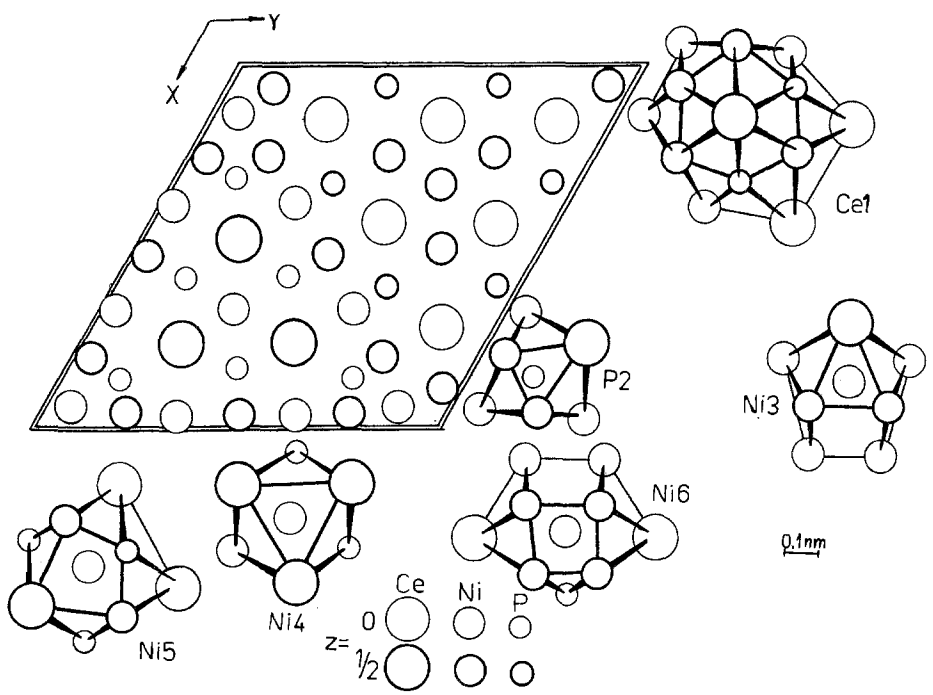

Fig. 36. Crystal structure of $Ce_9Ni_{26}P_{12}$ and CPs of atoms.

Table 28
Atomic parameters for $Ce_9Ni_{26}P_{12}$

Atom	Position	Fractional coordinates			Atomic arrangement		
		x	*y*	*z*			
Ce1	3(*j*)	0.1463	0.8537	0	4Ce	12Ni	4P
Ce2	3(*j*)	0.4241	0.5759	0	6Ce	10Ni	4P
Ce3	3(*k*)	0.7601	0.2399	1/2	4Ce	10Ni	6P
Ni1	1(*e*)	2/3	1/3	0	6Ce		3P
Ni2	1(*d*)	1/3	2/3	1/2	6Ce	3Ni	
Ni3	3(*k*)	0.057	0.943	1/2	2Ce	8Ni	
Ni4	3(*k*)	0.2417	0.7583	1/2	6Ce	1Ni	2P
Ni5	3(*k*)	0.5226	0.4774	1/2	4Ce	4Ni	4P
Ni6	3(*j*)	0.9368	0.0632	0	2Ce	10Ni	1P
Ni7	6(*l*)	0.957	0.337	0	4Ce	4Ni	4P
Ni8	6(*m*)	0.9532	0.746	1/2	3Ce	6Ni	3P
P1	3(*j*)	0.581	0.419	0	4Ce	5Ni	
P2	3(*j*)	0.851	0.149	0	2Ce	7Ni	
P3	6(*m*)	0.603	0.671	1/2	4Ce	5Ni	

2.3.4. *$Ce_9Ni_{26}P_{12}$, hP47*

Structure type $Ce_9Ni_{26}P_{12}$ (Babizhets'ky et al. 1992a; fig. 36, table 28) has space group $P\bar{6}m2$, $a = 1.4260$, $c = 0.3863$.

The structure was determined by Babizhets'ky et al. (1992a) using an X-ray single-crystal method, $R = 0.069$. All the cerium atoms have an environment in the form of a hexagonal prism with additional atoms outside all faces of the prism (fig. 36). Ni1, Ni2 and Ni4 are situated in cerium trigonal prisms with additional atoms outside the rectangular faces of the prism; Ni3 has a CN 10 and a coordination polyhedron as for Mn in the $MnAl_6$ structure; the CPs of Ni5, Ni7 and Ni8 are orthorhombic prisms with an additional four atoms outside the rectangular faces of the prism. Ni6 has a CN 13. The arrangement of all the phosphorus atoms is in the form of metallic trigonal prisms and CN 9. Interatomic distances in the $Ce_9Ni_{26}P_{12}$ structure are close to the sum of atomic radii of corresponding atoms; slightly shorter are the distances Ce1–Ni3 (0.292), Ni2–Ni4 (0.226), Ni1–P1 (0.213) and Ni4–P3 (0.215). Isotypic compounds are with Pr, Nd and Eu.

2.3.5. *$ZrFe_4Si_2$, tP14*

Structure type $ZrFe_4Si_2$ (Yarmolyuk et al. 1975; fig. 37, table 29) has space group $P4_2/mnm$, $a = 0.7116$, $c = 0.3614$ (for $TbNi_4P_2$) (Chykhrij et al. 1986).

The structure of $TbNi_4P_2$ was determined by the single-crystal X-ray method; the atomic parameters are refined to $R = 0.133$ (Chykhrij et al. 1986). Phosphorus atoms are situated in trigonal prisms formed by metal atoms (fig. 37). The shortest interatomic distances are: $\delta_{Tb-Ni} = 0.303$; $\delta_{Tb-P} = 0.282$; $\delta_{Ni-P} = 0.230$. Isotypic compounds are $ScFe_4P_2$ and RNi_4P_2 where R = Y, Gd, Dy–Lu.

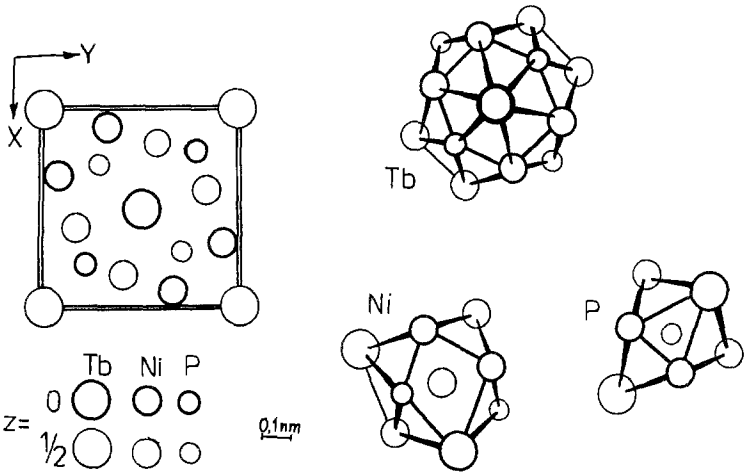

Fig. 37. Crystal structure of $TbNi_4P_2$ and CPs of atoms.

Table 29
Atomic parameters for $TbNi_4P_2$

Atom	Position	Fractional coordinates			Atomic arrangement		
		x	*y*	*z*			
Tb	2(*b*)	0	0	1/2	2Tb	12Ni	6P
Ni	8(*i*)	0.330	0.086	0	4Tb	5Ni	3P
P	4(*g*)	0.215	0.785	0	3Tb	6Ni	

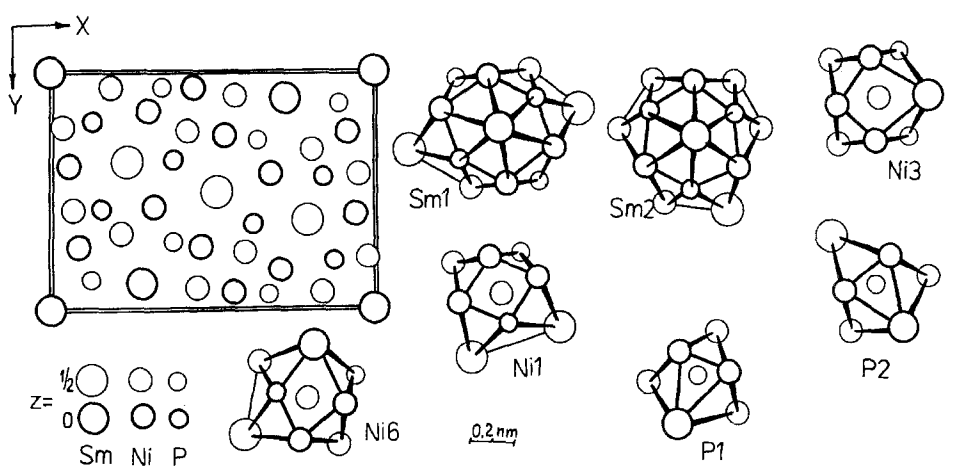

Fig. 38. Crystal structure of $SmNi_4P_2$ and CPs of atoms.

Table 30
Atomic parameters for $SmNi_4P_2$

Atom	Position	Fractional coordinates			Atomic arrangement		
		x	*y*	*z*			
Sm1	2(*a*)	0	0	0	4Sm	10Ni	6P
Sm2	4(*g*)	0.2768	0.8791	0	3Sm	11Ni	6P
Ni1	4(*g*)	0.0867	0.7473	0	2Sm	7Ni	3P
Ni2	4(*g*)	0.4369	0.0744	0	1Sm	9Ni	2P
Ni3	4(*g*)	0.0584	0.4027	0	2Sm	8Ni	2P
Ni4	4(*g*)	0.4634	0.7250	0	3Sm	6Ni	3P
Ni5	4(*g*)	0.3226	0.5699	0	5Sm	3Ni	4P
Ni6	4(*g*)	0.2949	0.1719	0	3Sm	5Ni	4P
P1	4(*g*)	0.1596	0.5662	0	2Sm	7Ni	
P2	4(*g*)	0.1292	0.2079	0	3Sm	6Ni	
P3	4(*g*)	0.3818	0.3617	0	4Sm	5Ni	

2.3.6. *$SmNi_4P_2$, oP42*

Structure type $SmNi_4P_2$ (Oryshchyn et al. 1988a; fig. 38, table 30) has space group Pnnm, $a=1.485$, $b=1.0759$, $c=0.3744$.

Oryshchyn et al. (1988a) determined the $SmNi_4P_2$ structure using the X-ray single-crystal method, $R=0.041$. The samarium atoms have a CN 20, all nickel atoms have a CN 12; phosphorus atoms are situated in metallic trigonal prisms with additional metal atoms outside rectangular faces of the prism (fig. 38). The shortest interatomic distances are: $\delta_{Sm1-Ni1}=0.2981$; $\delta_{Sm1-P2}=0.2892$; $\delta_{Ni2-Ni2}=0.2401$; $\delta_{Ni1-P1}=0.2207$.

2.3.7. *$Er_3Pd_7P_4$, mC28*

Structure type $Er_3Pd_7P_4$ (Johrendt and Mewis 1994; fig. 39, table 31) has space group C2/m, $a=1.5180$, $b=0.3955$, $c=0.9320$, $\beta=125.65°$.

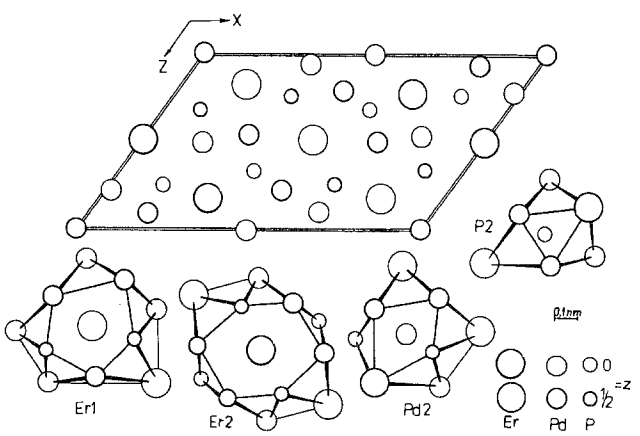

Fig. 39. Crystal structure of $Er_3Pd_7P_4$ and CPs of atoms.

Table 31
Atomic parameters for $Er_3Pd_7P_4$

Atom	Position	Fractional coordinates			Atomic arrangement		
		x	*y*	*z*			
Er1	4(*i*)	0.1806	0	0.1774	1Er	10Pd	4P
Er2	2(*d*)	0	1/2	1/2	2Er	10Pd	6P
Pd1	4(*i*)	0.3324	0	0.0772	4Er	5Pd	3P
Pd2	4(*i*)	0.0105	0	0.7848	4Er	5Pd	3P
Pd3	2(*b*)	0	1/2	0	4Er	6Pd	2P
Pd4	4(*i*)	0.1943	0	0.5283	5Er	3Pd	4P
P1	4(*i*)	0.1593	0	0.7520	4Er	5Pd	
P2	4(*i*)	0.6057	0	0.3188	3Er	6Pd	

Johrendt and Mewis (1994) studied the $Er_3Pd_7P_4$ structure by a single-crystal method, $R=0.031$. Erbium atoms are situated in distorted hexagonal and pentagonal prisms; palladium and phosphorus atoms are situated in orthorhombic and trigonal prisms, respectively. All prisms have additional atoms outside their rectangular faces. The shortest interatomic distances are: $\delta_{Er1-Pd1}=0.2949$; $\delta_{Er1-P1}=0.2897$; $\delta_{Pd2-Pd4}=0.2757$; $\delta_{Pd3-P2}=0.2417$. Band calculations show strong covalent Pd–P bonds and weak bonding interactions between Pd atoms with Pd–Pd distances shorter than 0.290.

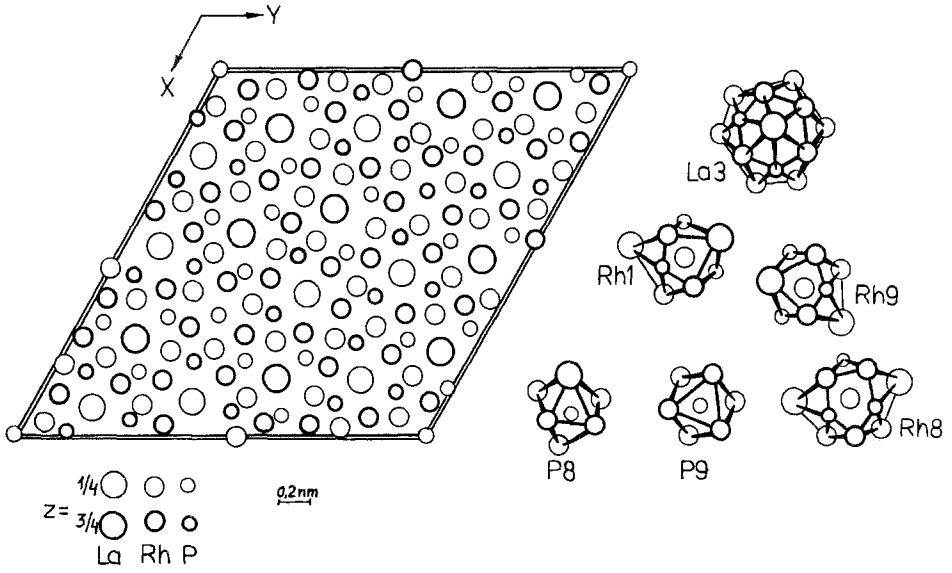

Fig. 40. Crystal structure of $La_6Rh_{32}P_{17}$ and CPs of atoms.

Table 32
Atomic parameters for $La_6Rh_{32}P_{17}$

Atom	Position	Fractional coordinates			Atomic arrangement		
		x	*y*	*z*			
La1	6(*h*)	0.23345	0.07604	1/4	2La	12Rh	6P
La2	6(*h*)	0.27870	0.83798	1/4	2La	12Rh	6P
La3	6(*h*)	0.90456	0.38550	1/4	2La	14Rh	4P
Rh1	6(*h*)	0.8027	0.0270	1/4	3La	5Rh	4P
Rh2	6(*h*)	0.0525	0.1668	1/4	3La	5Rh	4P
Rh3	6(*h*)	0.6663	0.8542	1/4	3La	5Rh	4P
Rh4	6(*h*)	0.7807	0.1157	1/4	3La	5Rh	4P
Rh5	6(*h*)	0.9440	0.9054	1/4	1La	7Rh	5P
Rh6	6(*h*)	0.4211	0.6952	1/4	1La	9Rh	5P
Rh7	6(*h*)	0.6373	0.3983	1/4	1La	7Rh	5P
Rh8	6(*h*)	0.2728	0.9702	1/4	2La	8Rh	5P
Rh9	6(*h*)	0.4993	0.2342	1/4	3La	5Rh	4P
Rh10	6(*h*)	0.1650	0.5689	1/4	3La	5Rh	4P
Rh11	6(*h*)	0.4885	0.3793	1/4	3La	5Rh	4P
Rh12	6(*h*)	0.3775	0.9630	1/4	2La	7Rh	3P
Rh13	6(*h*)	0.7308	0.6436	1/4	2La	7Rh	3P
Rh14	6(*h*)	0.5357	0.0016	1/4	3La	6Rh	3P
Rh15	6(*h*)	0.2822	0.4394	1/4	3La	6Rh	3P
Rh16	6(*h*)	0.6194	0.9661	1/4	2La	8Rh	2P
P1	6(*h*)	0.2578	0.2995	1/4	2La	7Rh	
P2	6(*h*)	0.7840	0.6019	1/4	2La	7Rh	
P3	6(*h*)	0.0902	0.2675	1/4	2La	7Rh	
P4	6(*h*)	0.0661	0.5095	1/4	2La	7Rh	
P5	6(*h*)	0.7919	0.4573	1/4	2La	7Rh	
P6	6(*h*)	0.0125	0.8779	1/4	2La	7Rh	
P7	6(*h*)	0.4621	0.7950	1/4	2La	7Rh	
P8	6(*h*)	0.9389	0.6173	1/4	2La	7Rh	
P9[a]	4(*f*)	1/3	2/3	0.870		6Rh	
P10[a]	2(*b*)	0	0	0		6Rh	

[a] Occupancy 50%.

2.3.8. *$La_6Rh_{32}P_{17}$, hP168*

Structure type $La_6Rh_{32}P_{17}$ (Pivan et al. 1988; fig. 40, table 32) has space group $P6_3/m$, $a = 2.7054$, $c = 0.3944$.

The structure of $La_6Rh_{32}P_{17}$ was determined by a single-crystal method, $R=0.050$ (Pivan et al. 1988). Lanthanum atoms have an atomic arrangement in the form of hexagonal prisms with all faces centered, their CN is 20 (fig. 40). Rh atoms have CP in the form of pentagonal (Rh6, Rh8) and orthorhombic prisms (another rhodium atom) with centered rectangular faces; Rh5 and Rh7 have a CN 13 and an orthorhombic-prismatic environment with one prism face centered by two phosphorus atoms. The phosphorus atoms (P1–P8) have trigonal-prismatic coordination. All atoms in the $La_6Rh_{32}P_{17}$ structure form two flat nets ($z=1/4$ and $z=3/4$) and only P9 ($z=0.870$) and P10 ($z=0$) are displaced from this arrangement and have octahedral coordination. The atomic positions of P9 and P10 are only half occupied. The shortest interatomic distances are: $\delta_{La2-Rh11}=0.3074$; $\delta_{La2-P2}=0.3007$; $\delta_{Rh4-Rh14}=0.2659$; $\delta_{Rh13-P2}=0.2226$. An isotypic compound is $Ce_6Rh_{32}P_{17}$.

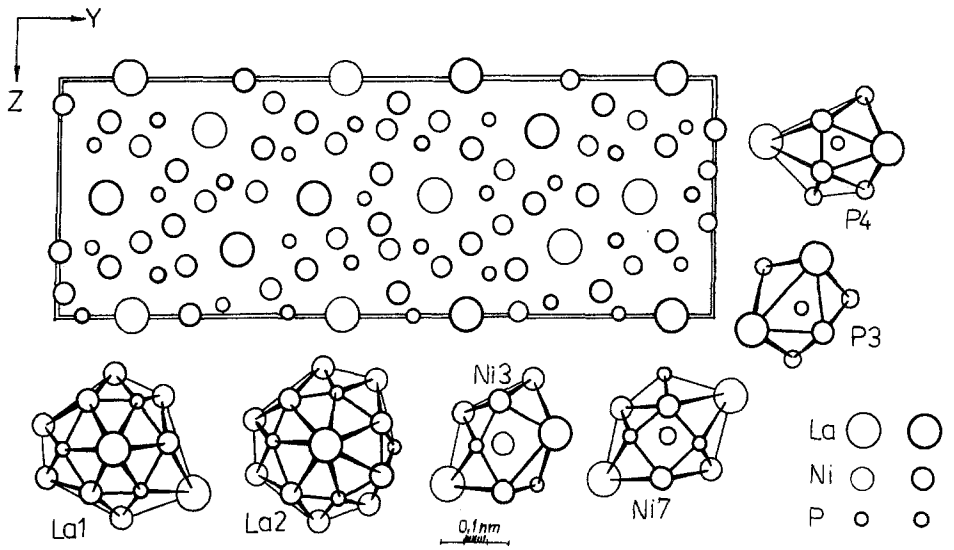

Fig. 41. Crystal structure of $La_3Ni_{12}P_7$ and CPs of atoms.

2.3.9. *$La_3Ni_{12}P_7$, oC88*

Structure type $La_3Ni_{12}P_7$ (Babizhets'ky et al. 1992b; fig. 41, table 33) has space group $Cmc2_1$, $a=0.3806$, $b=3.030$, $c=1.0730$.

The structure was determined by a single-crystal method, $R=0.040$ (Babizhets'ky et al. 1992b). La1 and La3 atoms have CNs of 20 and for La2 CN is 23. Nickel atoms (except Ni1) are situated in orthorhombic prisms with additional atoms outside the rectangular faces of the prisms (fig. 41). The atomic arrangement of Ni7 is a 13-vertices polyhedron. The phosphorus atoms have trigonal-prismatic coordination with 3 or 4 (P4) additional atoms. Interatomic distances are close to the sum of the respective atomic

Table 33
Atomic parameters for $La_3Ni_{12}P_7$

Atom	Position	Fractional coordinates			Atomic arrangement		
		x	y	z			
La1	4(*a*)	0	0.1148	0	3La	12Ni	6P
La2	4(*a*)	0	0.4300	0.0052	2La	14Ni	7P
La3	4(*a*)	0	0.7674	0.2752	3La	12Ni	5P
Ni1	4(*a*)	0	0.0131	0.1001	3La	5Ni	4P
Ni2	4(*a*)	0	0.1231	0.3054	3La	5Ni	4P
Ni3	4(*a*)	0	0.1923	0.1994	3La	6Ni	3P
Ni4	4(*a*)	0	0.2222	0.4774	3La	6Ni	3P
Ni5	4(*a*)	0	0.3220	0.1072	3La	5Ni	4P
Ni6	4(*a*)	0	0.4224	0.3128	3La	5Ni	4P
Ni7	4(*a*)	0	0.5004	0.2800	2La	6Ni	5P
Ni8	4(*a*)	0	0.5781	0.2039	3La	5Ni	4P
Ni9	4(*a*)	0	0.6741	0.3808	2La	7Ni	3P
Ni10	4(*a*)	0	0.6978	0.007	5La	3Ni	4P
Ni11	4(*a*)	0	0.8741	0.1979	4La	4Ni	4P
Ni12	4(*a*)	0	0.9861	0.3853	3La	5Ni	4P
P1	4(*a*)	0	0.0494	0.293	2La	7Ni	
P2	4(*a*)	0	0.2474	0.058	3La	6Ni	
P3	4(*a*)	0	0.3479	0.316	4La	5Ni	
P4	4(*a*)	0	0.5367	0.008	3La	6Ni	
P5	4(*a*)	0	0.6529	0.183	2La	7Ni	
P6	4(*a*)	0	0.8496	0.015	2La	7Ni	
P7	4(*a*)	0	0.9458	0.222	2La	7Ni	

radii; the shortest distances in $La_3Ni_{12}P_7$ structure are: $\delta_{La1-Ni6} = 0.2987$; $\delta_{Ni2-Ni3} = \delta_{Ni6-Ni7} = 0.239$; $\delta_{Ni11-P6} = 0.210$.

2.3.10. *$Nd_2Ni_7P_4$, oP26*

Structure type $Nd_2Ni_7P_4$ (Chykhrij et al. 1990; fig. 42, table 34) has space group $Pmn2_1$, $a = 0.37588$, $b = 0.9238$, $c = 1.0413$.

The structure was determined by a single-crystal method, $R = 0.0545$ (Chykhrij et al. 1990). All nickel atoms have CPs in the form of orthorhombic prisms with centered square faces, the phosphorus atoms are in trigonal prisms (fig. 42). The shortest interatomic distances are: $\delta_{Nd1-Nd1} = \delta_{Nd2-Nd2} = 0.3759$; $\delta_{Nd1-Ni6} = 0.2996$; $\delta_{Nd2-P3} = 0.287$; $\delta_{Ni3-Ni6} = 0.243$; $\delta_{Ni3-P3} = 0.216$.

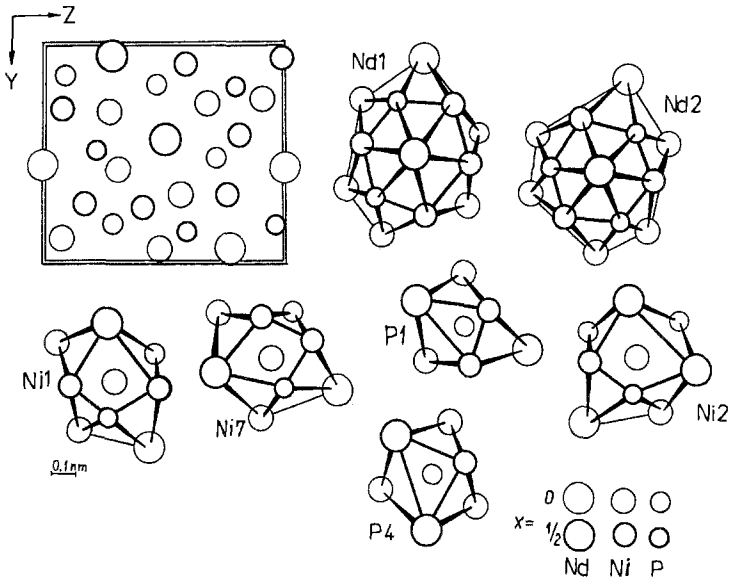

Fig. 42. Crystal structure of $Nd_2Ni_7P_4$ and CPs of atoms.

Table 34
Atomic parameters for $Nd_2Ni_7P_4$

Atom	Position	Fractional coordinates			Atomic arrangement		
		x	*y*	*z*			
Nd1	2(*a*)	0	0.5642	0	3Nd	12Ni	5P
Nd2	2(*a*)	0	0.9407	0.7819	3Nd	11Ni	6P
Ni1	2(*a*)	0	0.5825	0.3083	3Nd	6Ni	3P
Ni2	2(*a*)	0	0.3164	0.2633	5Nd	3Ni	4P
Ni3	2(*a*)	0	0.2539	0.9029	2Nd	7Ni	3P
Ni4	2(*a*)	0	0.9035	0.0817	4Nd	4Ni	4P
Ni5	2(*a*)	0	0.9431	0.4815	3Nd	5Ni	4P
Ni6	2(*a*)	0	0.2711	0.6698	3Nd	5Ni	4P
Ni7	2(*a*)	0	0.6958	0.5713	3Nd	6Ni	3P
P1	2(*a*)	0	0.517	0.719	3Nd	6Ni	
P2	2(*a*)	0	0.820	0.292	2Nd	7Ni	
P3	2(*a*)	0	0.157	0.092	2Nd	7Ni	
P4	2(*a*)	0	0.189	0.464	4Nd	5Ni	

2.3.11. *$Sm_{20}Ni_{41.6}P_{30}$, hP98*

Structure type $Sm_{20}Ni_{41.6}P_{30}$ (Chykhrij et al. 1993; fig. 43, table 35) has space group $P6_3/m$, $a = 2.0448$, $c = 0.3877$.

Chykhrij et al. (1993) determined the $Sm_{20}Ni_{41.6}P_{30}$ structure using a single-crystal method, $R = 0.049$. Samarium atoms have a CN of 20, the nickel atoms have 9, 12

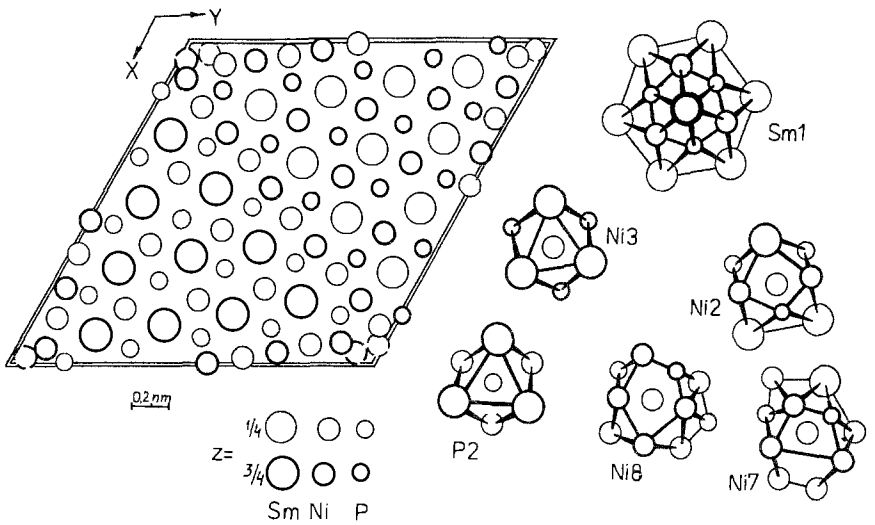

Fig. 43. Crystal structure of $Sm_{20}Ni_{41.6}P_{30}$ and CPs of atoms.

Table 35
Atomic parameters for $Sm_{20}Ni_{41.6}P_{30}$

Atom	Position	Fractional coordinates			Atomic arrangement		
		x	*y*	*z*			
Sm1	2(*c*)	1/3	2/3	1/4	8Sm	6Ni	6P
Sm2	6(*h*)	0.2981	0.8400	1/4	6Sm	8Ni	6P
Sm3	6(*h*)	0.5049	0.8781	1/4	6Sm	8Ni	6P
Sm4	6(*h*)	0.7106	0.9103	1/4	4Sm	10Ni	6P
Ni1	6(*h*)	0.2408	0.9532	1/4	4Sm	4Ni	4P
Ni2	6(*h*)	0.4472	0.9902	1/4	4Sm	4Ni	4P
Ni3	6(*h*)	0.7583	0.5874	1/4	6Sm		3P
Ni4	6(*h*)	0.7939	0.4172	1/4	6Sm		3P
Ni5	6(*h*)	0.9339	0.7949	1/4	3Sm	5Ni	4P
Ni6	6(*h*)	0.9726	0.6292	1/4	4Sm	4Ni	4P
Ni7[a]	6(*h*)	0.8726	0.9514	1/4	1Sm	10Ni	3P
Ni8[a]	6(*h*)	0.933	0.980	1/4		11Ni	3P
P1	6(*h*)	0.6810	0.6310	1/4	4Sm	5Ni	
P2	6(*h*)	0.7060	0.4530	1/4	6Sm	3Ni	
P3	6(*h*)	0.8390	0.8330	1/4	2Sm	7Ni	
P4	6(*h*)	0.8840	0.6680	1/4	4Sm	5Ni	
P5	6(*h*)	0.9180	0.4910	1/4	4Sm	5Ni	

[a] Occupancy 77% for Ni7 and 18% for Ni8.

and 15; all phosphorus atoms are in trigonal prisms formed by metal atoms (fig. 43). The interatomic distances are close to the sum of the respective atomic radii; the shortest δ_{Ni-P} is 0.215.

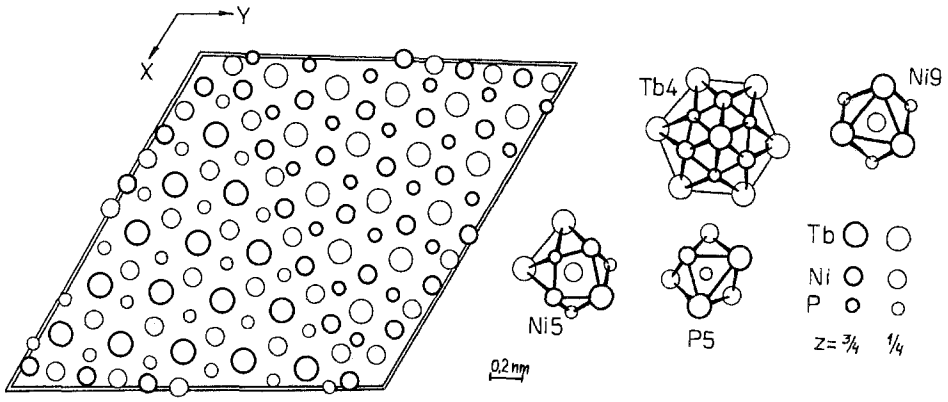

Fig. 44. Crystal structure of $Tb_{15}Ni_{28}P_{21}$ and CPs of atoms.

Table 36
Atomic parameters for $Tb_{15}Ni_{28}P_{21}$

Atom	Position	Fractional coordinates			Atomic arrangement		
		x	*y*	*z*			
Tb1	6(*h*)	0.0685	0.2417	1/4	4Tb	10Ni	6P
Tb2	6(*h*)	0.0955	0.4151	1/4	6Tb	8Ni	6P
Tb3	6(*h*)	0.2417	0.3866	1/4	6Tb	8Ni	6P
Tb4	6(*h*)	0.2665	0.5613	1/4	8Tb	6Ni	6P
Tb5	6(*h*)	0.4168	0.5335	1/4	6Tb	8Ni	6P
Ni1	2(*d*)	2/3	1/3	1/4	6Tb		3P
Ni2	6(*h*)	0.0349	0.1029	1/4	1Tb	7Ni	3P
Ni3	6(*h*)	0.1714	0.0559	1/4	3Tb	5Ni	4P
Ni4	6(*h*)	0.2012	0.2437	1/4	4Tb	4Ni	4P
Ni5	6(*h*)	0.3174	0.0316	1/4	4Tb	4Ni	4P
Ni6	6(*h*)	0.3691	0.3915	1/4	4Tb	4Ni	4P
Ni7	6(*h*)	0.4643	0.0093	1/4	4Tb	4Ni	4P
Ni8	6(*h*)	0.4917	0.1861	1/4	6Tb		3P
Ni9	6(*h*)	0.6411	0.1600	1/4	6Tb		3P
Ni10	6(*h*)	0.7877	0.1353	1/4	6Tb		3P
P1	6(*h*)	0.2850	0.1070	1/4	4Tb	5Ni	
P2	6(*h*)	0.4250	0.0770	1/4	4Tb	5Ni	
P3	6(*h*)	0.5750	0.0550	1/4	4Tb	5Ni	
P4	6(*h*)	0.6020	0.2220	1/4	6Tb	3Ni	
P5	6(*h*)	0.7260	0.0310	1/4	4Tb	5Ni	
P6	6(*h*)	0.7450	0.2040	1/4	6Tb	3Ni	
P7	6(*h*)	0.8660	0.0060	1/4	2Tb	7Ni	

2.3.12. *$Tb_{15}Ni_{28}P_{21}$, hP128*

Structure type $Tb_{15}Ni_{28}P_{21}$ (Chykhrij et al. 1993; fig. 44, table 36) has space group $P6_3/m$, $a=2.417$, $c=0.3825$.

The structure was determined by a single-crystal method, $R=0.044$ (Chykhrij et al. 1993). Terbium atoms have a CN of 20, the nickel atoms have a CN of 12 and 9, the phosphorus atoms occupy trigonal prisms formed by metal atoms; their CN is 9.

2.3.13. *$Zr_2Fe_{12}P_7$, hP21*

Structure type $Zr_2Fe_{12}P_7$ (Ganglberger 1968a; fig. 45, table 37) has space group $P\bar{6}$, $a=0.9025$, $c=0.3591$ (for $Er_2Co_{12}P_7$) (Jeitschko and Jaberg 1980b).

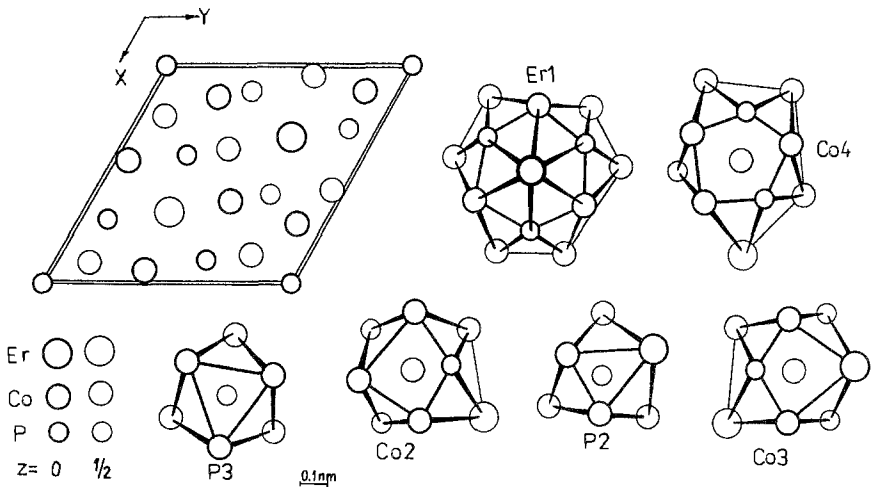

Fig. 45. Crystal structure of $Er_2Co_{12}P_7$ and CPs of atoms.

Table 37
Atomic parameters for $Er_2Co_{12}P_7$

Atom	Position	Fractional coordinates			Atomic arrangement		
		x	*y*	*z*			
Er1	1(*c*)	1/3	2/3	0		12Co	6P
Er2	1(*f*)	2/3	1/3	1/2		12Co	6P
Co1	3(*j*)	0.4345	0.0579	0	3Er	5Co	4P
Co2	3(*j*)	0.1530	0.2733	0	1Er	7Co	4P
Co3	3(*k*)	0.3815	0.4356	1/2	3Er	5Co	4P
Co4	3(*k*)	0.2333	0.1009	1/2	1Er	7Co	5P
P1	3(*j*)	0.4069	0.2952	0	2Er	7Co	
P2	3(*k*)	0.1188	0.4069	1/2	2Er	7Co	
P3	1(*a*)	0	0	0		9Co	

The crystal structure of $Zr_2Fe_{12}P_7$ has been determined by Ganglberger (1968a). The Zr atoms have a CN of 18, the nickel atoms 15 and 12 and phosphorus atoms 9. Among the ternary rare-earth phosphides the atomic parameters have been refined for $Sc_2Ru_{12}P_7$ (Ghetta et al. 1986), $Ce_2Fe_{12}P_7$ (Jeitschko et al. 1984), $Er_2Co_{12}P_7$ and $Er_2Ni_{12}P_7$ (Jeitschko and Jaberg 1980b) and $Ho_2Ni_{12}P_7$ (Pivan et al. 1986). The structure of $Zr_2Fe_{12}P_7$ is established for $R_2Fe_{12}P_7$ (R = Sc, Ce, Pr, Nd, Sm, Gd–Lu), $R_2Co_{12}P_7$ (R = Sc, Ce, Pr, Nd, Sm, Eu, Gd–Lu), $R_2Ni_{12}P_7$ (R = Y, Ce, Pr, Nd, Sm, Eu, Gd–Lu) and $Sc_2Ru_{12}P_7$.

2.3.14. *$Zr_2Rh_{12}P_7$, hP22*

Structure type $Zr_2Rh_{12}P_7$ (Pivan et al. 1984a; table 38) has space group $P6_3/m$, $a = 0.9516$, $c = 0.3773$.

The ST of $Zr_2Rh_{12}P_7$ was determined by a single-crystal method, $R = 0.040$ (Pivan et al. 1984a), but no rare-earth phosphide with this structure is completely determined with a refinement of the atomic parameters. The ST of $Zr_2Rh_{12}P_7$ is closely related to $Zr_2Fe_{12}P_7$ and differs by only one position of phosphorus atoms: the P3 atoms in $Zr_2Fe_{12}P_7$ occupy the position 1(*a*) 000 (sp.gr. P6) in the center of metal trigonal prisms while in $Zr_2Rh_{12}P_7$ the P2 atoms (half of them) occupy the position 2(*b*) (000 and 001/2) (sp.gr. $P6_3/m$). One can suppose that the P2 atoms oscillate along the sixth-order axis in trigonal prisms formed by the rhodium atoms. This is indicated by anisotropic thermal parameters: $U_{11} = U_{22} = 70$ while $U_{33} = 1700$. Phosphides $R_2Rh_{12}P_7$, where R is Y, Nd, Gd–Er or Lu, have the $Zr_2Rh_{12}P_7$-type structure.

Table 38
Atomic parameters for $Zr_2Rh_{12}P_7$

Atom	Position	Fractional coordinates			Atomic arrangement		
		x	*y*	*z*			
Zr	2(*c*)	1/3	2/3	1/4		12Rh	6P
Rh1	6(*h*)	0.4539	0.0722	1/4	3Zr	5Rh	4P
Rh2	6(*h*)	0.1515	0.2646	1/4	1Zr	5Rh	4P
P1	6(*h*)	0.4081	0.2869	1/4	2Zr	7Rh	
P2	2(*b*)	0	0	0		9Rh	

2.3.15. *YCo_5P_3, oP36*

Structure type YCo_5P_3 (Meisen and Jeitschko 1984a,b; fig. 46, table 39) has space group Pnma, $a = 1.1820$, $b = 0.3666$, $c = 1.0336$.

Meisen and Jeitschko (1984b) determined the structure of YCo_5P_3 by a single-crystal method, $R = 0.051$. The CN of the yttrium atoms is 18, cobalt atoms have CN 15 (Co1) or 12 (all other cobalt atoms) and phosphorus atoms have a CN of 9 (fig. 46). The shortest interatomic distances are: $\delta_{Y-Co} = 0.2918$; $\delta_{Y-P} = 0.2799$; $\delta_{Co-Co} = 0.2525$; $\delta_{Co-P} = 0.2170$.

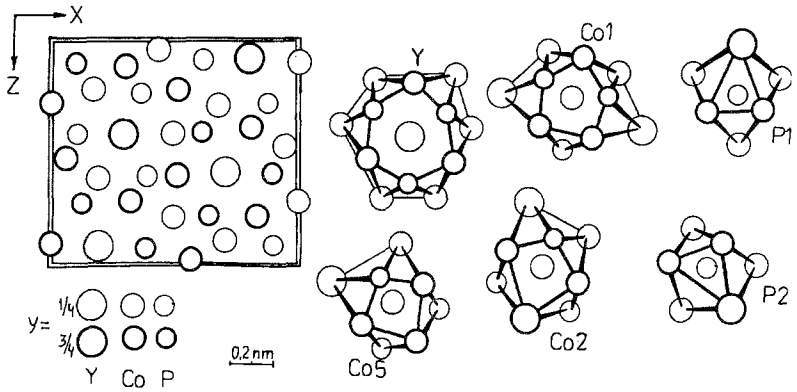

Fig. 46. Crystal structure of YCo_5P_3 and CPs of atoms.

Table 39
Atomic parameters for YCo_5P_3

Atom	Position	Fractional coordinates			Atomic arrangement		
		x	*y*	*z*			
Y	4(*c*)	0.2038	1/4	0.9170		12Co	6P
Co1	4(*c*)	0.4893	1/4	0.7864	2Y	8Co	5P
Co2	4(*c*)	0.9881	1/4	0.0933	3Y	5Co	4P
Co3	4(*c*)	0.6764	1/4	0.2801	3Y	5Co	4P
Co4	4(*c*)	0.1977	1/4	0.6175	3Y	5Co	4P
Co5	4(*c*)	0.4326	1/4	0.0332	1Y	7Co	4P
P1	4(*c*)	0.6127	1/4	0.0816	2Y	7Co	
P2	4(*c*)	0.3694	1/4	0.2304	2Y	7Co	
P3	4(*c*)	0.8906	1/4	0.8999	2Y	7Co	

Isotypic compounds are RFe_5P_3 (R = Sc, Y, Gd, Lu) and RCo_5P_3 (R = Sc, Ce, Pr, Nd, Sm, Gd–Lu).

2.3.16. *$CeNi_{5-x}P_3$, mC82*

Structure type $CeNi_{5-x}P_3$ (Babizhets'ky et al. 1992d; fig. 47, table 40) has space group C2/m, $a = 2.4701$, $b = 0.3785$, $c = 1.0619$, $\beta = 105.2°$.

Babizhets'ky et al. (1992d) determined the structure of $CeNi_{5-x}P3$ ($x = 0.1$) by a single-crystal method, $R = 0.071$. The Ce1 and Ce2 atoms have a CN of 20 and 23, respectively. Coordination polyhedron of Ni1–Ni4 and Ni6–Ni11 atoms is the orthorhombic prism and Ni5 has an atomic arrangement in the form of a pentagonal prism; all the phosphorus atoms have trigonal-prismatic coordination and a CN of 9; rectangular faces of all prisms are centered by additional atoms. The ideal structural order occurs with position 2(*c*) 001/2 occupied and Ni11 and Ni12 atoms absent. Incomplete occupation of positions

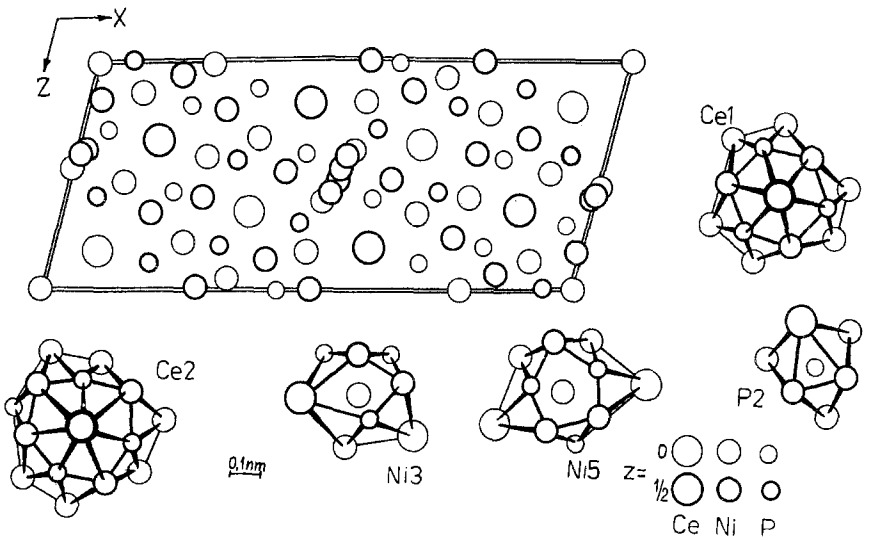

Fig. 47. Crystal structure of $CeNi_{5-x}P_3$ and CPs of atoms.

Table 40
Atomic parameters for $CeNi_{5-x}P_3$ ($x = 0.1$)

Atom	Position	Fractional coordinates			Atomic arrangement		
		x	y	z			
Ce1	4(*i*)	0.3552	0	0.6447	2Ce	12Ni	6P
Ce2	4(*i*)	0.0907	0	0.8443	2Ce	16Ni	5P
Ni1	2(*a*)	0	0	0	2Ce	6Ni	4P
Ni2	4(*i*)	0.2156	0	0.0046	2Ce	8Ni	
Ni3	4(*i*)	0.3351	0	0.3354	3Ce	5Ni	4P
Ni4	4(*i*)	0.6578	0	0.0606	3Ce	5Ni	4P
Ni5	4(*i*)	0.7570	0	0.2189	2Ce	8Ni	5P
Ni6	4(*i*)	0.5187	0	0.1685	1Ce	7Ni	4P
Ni7	4(*i*)	0.0960	0	0.1279	3Ce	5Ni	4P
Ni8	4(*i*)	0.8983	0	0.4801	2Ce	7Ni	3P
Ni9	4(*i*)	0.2447	0	0.4038	3Ce	5Ni	3P
Ni10[a]	4(*i*)	0.5173	0	0.3878	1Ce	9Ni	3P
Ni11[a]	4(*i*)	0.000	0	0.456	1Ce	8Ni	3P
Ni12[a]	8(*j*)	0.0057	0.223	0.417	1Ce	6Ni	5P
P1	4(*i*)	0.1907	0	0.193	2Ce	7Ni	
P2	4(*i*)	0.8023	0	0.4341	2Ce	7Ni	
P3	4(*i*)	0.4269	0	0.4088	2Ce	7Ni	
P4	4(*i*)	0.0466	0	0.289	2Ce	7Ni	
P5	4(*i*)	0.3097	0	0.1174	2Ce	7Ni	
P6	4(*i*)	0.5603	0	0.006	2Ce	7Ni	

[a] Occupancies: Ni10, 64%; Ni11, 24%; Ni12, 17%.

by Ni10–Ni12 atoms causes a deformation of coordination polyhedra of the respective atoms.

2.3.17. *$LaCo_5P_3$, oC36*

Structure type $LaCo_5P_3$ (Davydov and Kuz'ma 1981; fig. 48, table 41) has space group Cmcm, $a=0.3651$, $b=1.1573$, $c=1.1459$.

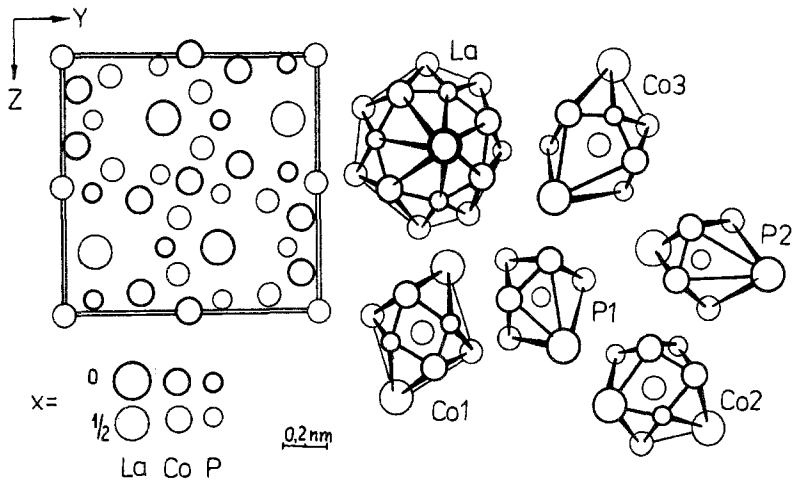

Fig. 48. Crystal structure of $LaCo_5P_3$ and CPs of atoms.

Table 41
Atomic parameters for $LaCo_5P_3$

Atom	Position	Fractional coordinates			Atomic arrangement		
		x	*y*	*z*			
La	4(*c*)	0	0.3884	1/4	2La	14Co	7P
Co1	4(*b*)	0	1/2	0	2La	6Co	4P
Co2	8(*f*)	0	0.0543	0.1429	3La	5Co	4P
Co3	8(*f*)	0	0.3023	0.5670	3La	5Co	4P
P1	8(*f*)	0	0.1176	0.5393	2La	7Co	
P2	4(*c*)	0	0.6117	1/4	3La	6Co	

The structure was determined by a single-crystal method, $R=0.054$ (Davydov and Kuz'ma 1981). The phosphorus atoms center distorted trigonal prisms $[La_2Co_4]$. Lanthanum, cobalt and phosphorus atoms have a CN of 23, 12 and 9, respectively. Some of the shortest interatomic distances are $\delta_{Co1-Co3}=0.241$; $\delta_{Co3-P1}=0.216$. Isotypic phosphides are $LaNi_5P_3$ and $EuNi_5P_3$. Badding and Stacy (1987a) studied the crystal

structure of $EuNi_5P_3$ which is of $LaCo_5P_3$-type but the reported atomic coordinates are displaced by 0 1/2 1/2 with respect to those of $LaCo_5P_3$. This was not taken into consideration by Villars and Calvert (1991) who regard $EuNi_5P_3$ as a new structure type.

2.3.18. *$Ho_5Ni_{19}P_{12}$, hP32*

Structure type $Ho_5Ni_{19}P_{12}$ (Pivan et al. 1985a; fig. 49, table 42) has space group $P\bar{6}2m$, $a=1.2288$, $c=0.3762$.

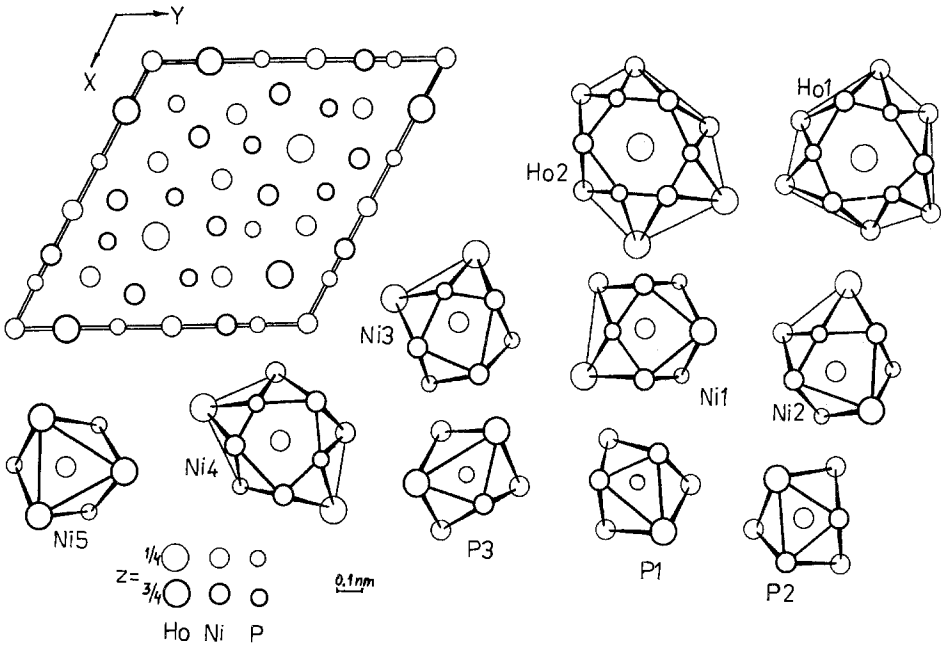

Fig. 49. Crystal structure of $Ho_5Ni_{19}P_{12}$ and CPs of atoms.

The structure of $Ho_5Ni_{19}P_{12}$ was determined by a single-crystal method, $R=0.049$ (Pivan et al. 1985a). It is closely related to the structure of $Hf_2Co_4P_3$ (Ganglberger 1968a,b): some of the largest atoms (Hf) are substituted by medium atoms (Ni). In $Ho_5Ni_{19}P_{12}$, phosphorus atoms are situated in trigonal prisms formed by metal atoms. The CN of holmium atoms is 18, nickel atoms have a CN of 15 (Ni4), 12 (Ni1–Ni3) or 9 (Ni5) and coordination polyhedra in the form of their respective prisms with additional atoms outside rectangular faces of the prisms. The shortest interatomic distances are: $\delta_{Ho1-Ni5}=0.2932$; $\delta_{Ho1-P2}=0.2847$; $\delta_{Ni1-Ni2}=0.2649$; $\delta_{Ni5-P3}=0.2227$. Isotypic phosphides are $R_5Ru_{19}P_{12}$ (R = Y, Ce, Pr, Nd, Sm, Gd, Tb, Dy, Ho, Er, Yb).

Oryshchyn et al. (1991a) studied the crystal structure of $Nd_5Cu_{19-x}P_{12}$ ($x=1.2$) ($R=0.059$) which may be considered as a defective variant of $Ho_5Ni_{19}P_{12}$. The position of Ni4 (in the $Ho_5Ni_{19}P_{12}$ structure) atoms is occupied by 60% copper atoms in $Nd_5Cu_{19-x}P_{12}$. Interatomic distances in $Nd_5Cu_{19-x}P_{12}$ are close to the sum of the

Table 42
Atomic parameters for $Ho_5Ni_{19}P_{12}$

Atom	Position	Fractional coordinates			Atomic arrangement		
		x	*y*	*z*			
Ho1	3(*g*)	0.8167	0	1/2		12Ni	6P
Ho2	2(*c*)	1/3	2/3	0	2Ho	10Ni	6P
Ni1	6(*k*)	0.8720	0.5146	1/2	3Ho	5Ni	4P
Ni2	6(*j*)	0.8152	0.1899	0	3Ho	5Ni	4P
Ni3	3(*g*)	0.2862	0	1/2	2Ho	6Ni	4P
Ni4	3(*f*)	0.4397	0	0	2Ho	8Ni	5P
Ni5	1(*a*)	0	0	0	6Ho		3P
P1	6(*k*)	0.5174	0.6859	1/2	2Ho	7Ni	
P2	3(*f*)	0.6420	0	0	2Ho	7Ni	
P3	3(*f*)	0.1730	0	0	4Ho	5Ni	

respective atomic radii; their minimum values are $\delta_{Nd1-Cu4} = 0.3100$; $\delta_{Nd2-P3} = 0.2920$; $\delta_{Cu3-Cu3} = 0.2603$; $\delta_{Cu4-P1} = 0.227$. Isotypic compounds are $R_5Cu_{19-x}P_{12}$ (R = La, Ce, Pr, Sm).

2.3.19. *$Sc_5Co_{19}P_{12}$, hP37*

Structure type $Sc_5Co_{19}P_{12}$ (Jeitschko and Reinbold 1985) has space group $P\bar{6}2m$, $a = 1.2124$, $c = 0.3633$.

The structure of $Sc_5Co_{19}P_{12}$ was determined by a single-crystal method, $R = 0.023$ (Jeitschko and Reinbold 1985). The ST of $Sc_5Co_{19}P_{12}$ differs from $Ho_5Ni_{19}P_{12}$ only by the 50% occupation of the atomic position 2(*b*) 00*z* ($z = 0.0827$) by cobalt atoms while in $Ho_5Ni_{19}P_{12}$ the nickel atoms occupy position 1(*a*) 000. The coordinates of all other atoms in both structures are very close. The shortest interatomic distances in $Sc_5Co_{19}P_{12}$ are $\delta_{Sc1-Co4} = 0.2686$; $\delta_{Sc2-P2} = 0.2791$; $\delta_{Co1-Co2} = 0.2597$; $\delta_{Co4-P1} = 0.2154$. Isotypic compounds are $R_5Co_{19}P_{12}$ (R = Y, Gd–Lu).

2.3.20. *$Zr_6Ni_{20}P_{13}$, hP39*

Structure type $Zr_6Ni_{20}P_{13}$ (Guerin et al. 1984; fig. 50, table 43) has space group $P\bar{6}$, $a = 1.2677$, $c = 0.3749$ (for $Y_6Ni_{20}P_{13}$) (Chykhrij et al. 1985).

The compounds $Zr_6Ni_{20}P_{13}$ (Guerin et al. 1984) and $Y_6Ni_{20}P_{13}$ (Chykhrij et al. 1985) were studied independently and have the same crystal structure, which will be called $Zr_6Ni_{20}P_{13}$-type. However, the atomic parameters in $Y_6Ni_{20}P_{13}$ and $Zr_6Ni_{20}P_{13}$ numerically differ from one another and Villars and Calvert (1991) regard these structures as two different STs. Madar et al. (1985b) obtained compounds with the composition $R_7Ni_{19}P_{13}$ and regarded their structure as $Zr_6Ni_{20}P_{13}$-type using the results of X-ray powder analysis. Samples with the ideal composition $R_6Ni_{20}P_{13}$ contain an admixture of the phase $R_2Ni_{12}P_7$. The present authors consider that it is necessary to carry out

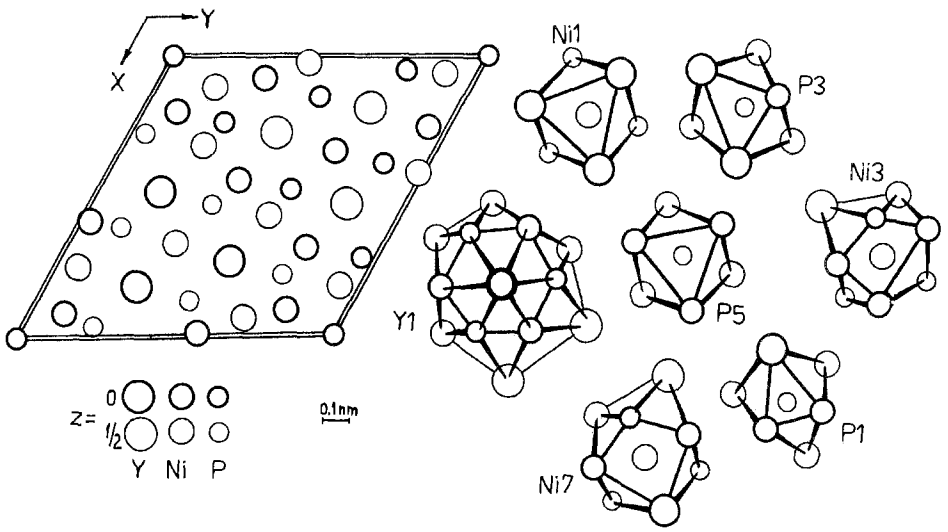

Fig. 50. Crystal structure of $Y_6Ni_{20}P_{13}$ and CPs of atoms.

Table 43
Atomic parameters for $Y_6Ni_{20}P_{13}$

Atom	Position	Fractional coordinates			Atomic arrangement		
		x	*y*	*z*			
Y1	3(*j*)	0.472	0.189	0	4Y	10Ni	6P
Y2	3(*k*)	0.531	0.812	1/2	4Y	10Ni	6P
Ni1	1(*c*)	1/3	2/3	0	6Y	3P	
Ni2	1(*d*)	2/3	1/3	1/2	6Y		3P
Ni3	3(*j*)	0.197	0.094	0	1Y	7Ni	4P
Ni4	3(*k*)	0.814	0.929	1/2		9Ni	5P
Ni5	3(*j*)	0.438	0.417	0	4Y	4Ni	4P
Ni6	3(*k*)	0.562	0.587	1/2	4Y	4Ni	4P
Ni7	3(*j*)	0.076	0.321	0	3Y	5Ni	4P
Ni8	3(*k*)	0.926	0.682	1/2	3Y	5Ni	4P
P1	3(*j*)	0.236	0.285	0	2Y	7Ni	
P2	3(*k*)	0.773	0.726	1/2	2Y	7Ni	
P3	3(*j*)	0.472	0.611	0	4Y	5Ni	
P4	3(*k*)	0.525	0.387	1/2	4Y	5Ni	
P5	1(*a*)	0	0	0		9Ni	

additional investigations of atomic distribution in the crystal structure of compounds obtained.

In the structure of $Y_6Ni_{20}P_{13}$ yttrium atoms have a CN of 20, Ni4 has 14, Ni3 and Ni5–Ni8 have 12 and Ni1–Ni2 have 9; their CPs are distorted prisms. The shortest interatomic distances are $\delta_{Y1-Y1}=0.373$; $\delta_{Y1-Ni2}=0.290$; $\delta_{Y-P}=0.281$; $\delta_{Ni3-Ni7}=0.251$; $\delta_{Ni3-P5}=0.215$. Isotypic compounds are $R_{6-7}Ni_{20-19}P_{13}$ (R = Ce, Pr, Nd, Sm, Eu, Gd, Tb, Dy, Ho, Er, Tm, Yb).

2.3.21. *$Ho_6Ni_{20}P_{13}$, hP46*

Structure type $Ho_6Ni_{20}P_{13}$ (Pivan et al. 1986; table 44) has space group $P6_3/m$, $a=1.2677$, $c=0.3730$.

Pivan et al. (1986) determined the structure of $Ho_6Ni_{20}P_{13}$ by a single-crystal method, $R=0.034$. The arrangement of all the atoms is similar to that in the $Zr_6Ni_{20}P_{13}$ structure. The shortest interatomic distances are $\delta_{Ho-Ni3}=0.2914$; $\delta_{Ho-P1}=0.2840$; $\delta_{Ni1-Ni4}=0.2471$; $\delta_{Ni5-P3}=0.2167$.

Table 44
Atomic parameters for $Ho_6Ni_{20}P_{13}$

Atom	Position	Fractional coordinates			Atomic arrangement		
		x	*y*	*z*			
Ho	6(*h*)	0.52969	0.81133	1/4	2Ho	10Ni	6P
Ni1	6(*h*)	0.75403	0.07386	1/4	3Ho	6Ni	4P
Ni2	6(*h*)	0.41554	0.97903	1/4	4Ho	4Ni	4P
Ni3	2(*d*)	2/3	1/3	1/4	6Ho		3P
Ni4[a]	6(*h*)	0.0923	0.8950	1/4	1Ho	7Ni	5P
Ni5[a]	6(*h*)	0.9267	0.0817	3/4		7Ni	4P
P1	6(*h*)	0.6139	0.1386	1/4	4Ho	5Ni	
P2	6(*h*)	0.9503	0.2326	1/4	2Ho	7Ni	
P3[a]	2(*a*)	0	0	3/4		9Ni	

[a] Occupancy 50%.

2.3.22. *$Ho_{20}Ni_{66}P_{43}$, hP36*

Structure type $Ho_{20}Ni_{66}P_{43}$ (Pivan et al. 1985b; fig. 51, table 45) has space group $P6_3/m$, $a=2.3095$, $c=0.3742$.

The structure of $Ho_{20}Ni_{66}P_{43}$ was determined by a single-crystal method, $R=0.054$. (Pivan et al. 1985b). The atomic coordination is the same as in the $Zr_2Fe_{12}P_7$ or $Zr_6Ni_{20}P_{13}$ structures. The shortest interatomic distances are $\delta_{Ho4-Ni11}=0.2865$; $\delta_{Ho2-P7}=0.2819$; $\delta_{Ni8-Ni9}=0.2477$; $\delta_{Ni8-P8}=0.2159$.

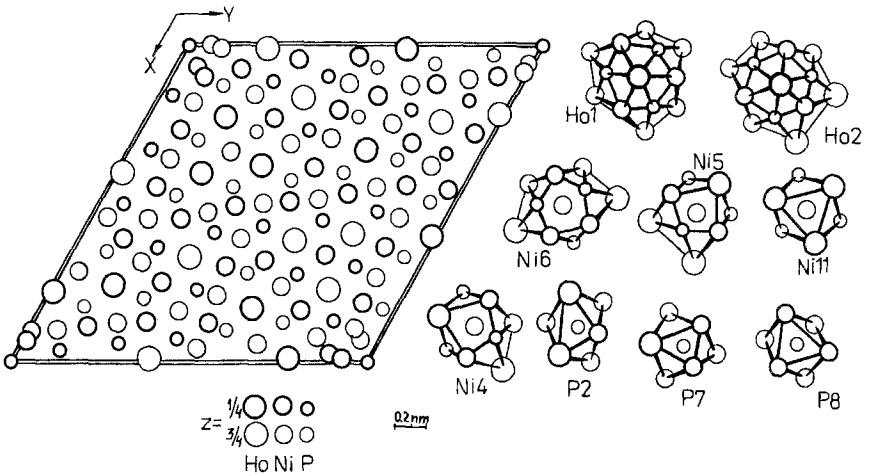

Fig. 51. Crystal structure of $Ho_{20}Ni_{66}P_{43}$ and CPs of atoms.

Table 45
Atomic parameters for $Ho_{20}Ni_{66}P_{43}$

Atom	Position	Fractional coordinates			Atomic arrangement		
		x	*y*	*z*			
Ho1	2(*c*)	2/3	1/3	3/4	2Ho	9Ni	6P
Ho2	6(*h*)	0.39587	0.01422	3/4	4Ho	10Ni	6P
Ho3	6(*h*)	0.23966	0.83412	3/4	4Ho	10Ni	6P
Ho4	6(*h*)	0.22099	0.99253	3/4	4Ho	10Ni	6P
Ni1	6(*h*)	0.3154	0.4472	3/4	3Ho	5Ni	4P
Ni2	6(*h*)	0.5383	0.0399	3/4	3Ho	5Ni	4P
Ni3	6(*h*)	0.8739	0.2353	3/4	4Ho	4Ni	4P
Ni4	6(*h*)	0.6851	0.2101	3/4	3Ho	5Ni	4P
Ni5	6(*h*)	0.7312	0.8894	3/4	4Ho	4Ni	4P
Ni6	6(*h*)	0.5504	0.1613	3/4	1Ho	10Ni	4P
Ni7	6(*h*)	0.3863	0.8774	3/4	2Ho	6Ni	4P
Ni8[a]	6(*h*)	0.9011	0.9128	3/4		*[b]	
Ni8[a]	6(*h*)	0.9316	0.0094	1/4		*[b]	
Ni9	6(*h*)	0.8957	0.0788	3/4		*[b]	
Ni10	6(*h*)	0.3003	0.5508	3/4	3Ho	5Ni	4P
Ni11	6(*h*)	0.7148	0.0513	3/4	6Ho		3P
P1	6(*h*)	0.8427	0.9653	3/4		*[b]	
P2	6(*h*)	0.8803	0.7035	3/4	4Ho	5Ni	
P3	6(*h*)	0.2723	0.3314	3/4	4Ho	5Ni	
P4	6(*h*)	0.3637	0.7717	3/4	2Ho	7Ni	
P5	6(*h*)	0.7276	0.5260	3/4	2Ho	7Ni	
P6	6(*h*)	0.4452	0.3478	3/4	4Ho	5Ni	
P7	6(*h*)	0.4295	0.5013	3/4	2Ho	7Ni	
P8[a]	2(*a*)	0	0	3/4		*[b]	

[a] Occupancy 50%. [b] CPs include atoms from partially occupied positions.

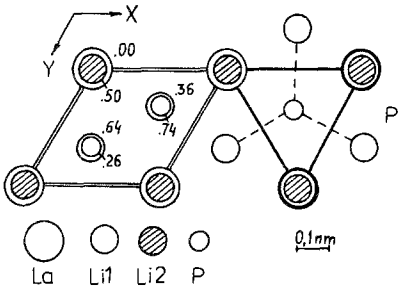

Fig. 52. Crystal structure of $LaLi_3P_2$ and CPs of atoms.

Table 46
Atomic parameters for $LaLi_3P_2$

Atom	Position	Fractional coordinates			Atomic arrangement		
		x	*y*	*z*			
La	1(*a*)	0	0	0		8Li	6P
Li1	2(*d*)	1/3	2/3	0.637	3La	6Li	
Li2	1(*b*)	0	0	1/2	2La	6Li	6P
P	2(*d*)	1/3	2/3	0.2594	3La	6Li	

2.3.23. *$LaLi_3P_2$, hP6*

Structure type $LaLi_3P_2$ (Grund et al. 1984; fig. 52, table 46) has space group $P\bar{3}m1$, $a=0.42508$, $c=0.6906$.

Grund et al. (1984) determined the structure of $LaLi_3P_2$ by a single-crystal method, $R=0.019$; the parameters of the Li atoms were refined by neutron diffraction for the isotypic compound YLi_3Sb_2. The La atoms have a CN of 14; their CP is a hexagonal prism $[Li_6P_6]$ with Li atoms outside the base faces. The Li2 atoms have the same coordination; Li1 and P atoms have a CN of 9 and trigonal-prismatic coordination with additional atoms outside the rectangular faces of the prism. The structure of $LaLi_3P_2$ is a superstructure of ST Fe_2Si (Kudielka 1977). It also may be considered as a structure that includes Li atoms in Ce_2O_2S-type (the other name $CaAl_2Si_2$) which is again a superstructure of La_2O_3. The shortest interatomic distances are $\delta_{La-Li2}=c/2$; $\delta_{La-P}=0.3038$; $\delta_{Li1-P}=0.256$.

2.3.24. *$TbLiCu_2P_2$, hP6*

Structure type $TbLiCu_2P_2$ (Mahan and Mewis 1983) has space group $P\bar{3}m1$, $a=0.3994$, $c=0.6563$.

Mahan and Mewis (1983) determined the $TbLiCu_2P_2$ structure by a single-crystal method, $R=0.027$. The ST $TbLiCu_2P_2$ is a superstructure of $LaLi_3P_2$ with copper atoms situated in the Li1 positions ($z=0.6559$); phosphorus atoms are in the positions 2(*d*) with $z=0.2593$. Atomic CNs and CPs are analogous with the $LaLi_3P_2$ structure. The shortest

interatomic distances are $\delta_{Tb-P} = 0.2866$; $\delta_{Cu-P} = 0.2370$; $\delta_{Cu-Li} = 0.2526$; $\delta_{Li-P} = 0.2795$. Isotypic compounds are $RLiCu_2P_2$ where R is Y, Ce, Sm, Yb.

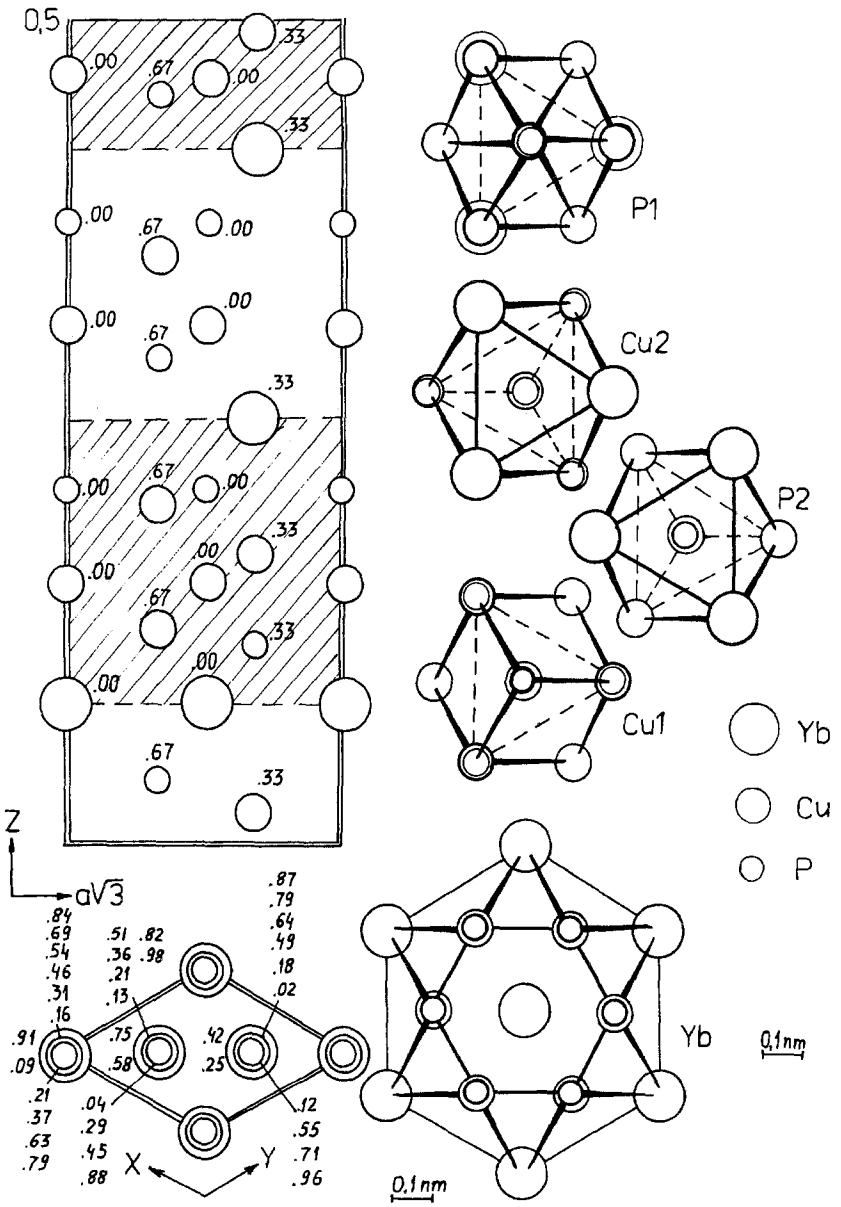

Fig. 53. Crystal structure of $YbCu_{3-x}P_2$ as a combination of structure blocks which occur in Cu_3P structures (Cu_2P-blocks, dark sections) and Ce_2O_2S structures (CuP-blocks, light sections), and CPs of atoms.

Table 47
Atomic parameters for $YbCu_{3-x}P_2$ ($x=0.4$)

Atom	Position	Fractional coordinates			Atomic arrangement		
		x	y	z			
Yb	6(*c*)	0	0	0.0759	6Yb	6Cu	6P
Cu1[a]	6(*c*)	0	0	0.1566		6Cu	4P
Cu2	6(*c*)	0	0	0.3116	3Yb	3Cu	4P
Cu3	6(*c*)	0	0	0.4621	3Yb	3Cu	4P
P1	6(*c*)	0	0	0.2137	3Yb	7Cu	
P2	6(*c*)	0	0	0.3722	3Yb	4Cu	

[a] Occupancy 56%.

2.3.25. *$YbCu_{3-x}P_2$ ($x=0.4$), hR12*

$YbCu_{3-x}P_2$ ($x=0.4$) (Klüfers et al. 1979; fig. 53, table 47) has space group $R\bar{3}m$, $a=0.3964$, $c=4.0296$.

Klüfers et al. (1979) determined the structure of $YbCu_{3-x}P_2$ ($x=0.4$) by a single-crystal method, $R=0.075$. It is built from atomic blocks occurring in Cu_3P (Cu_2P-blocks) and Ce_2O_2S (CuP-blocks) structures (fig. 53), which alternate regularly along the hexagonal Z axis. The Yb atoms have a CP similar to that of the aluminium atoms in AlB_2; all copper and P1 atoms have similar CPs (fig. 53). Atomic arrangement of P2 is an octahedron [Yb_3Cu_3] with one additional atom. The shortest interatomic distances are $\delta_{Yb-Cu3}=0.3127$; $\delta_{Yb-P2}=0.2732$; $\delta_{Cu1-Cu1}=0.2428$; $\delta_{Cu1-P1}=0.2301$.

2.3.26. *$HoCo_3P_2$, oP38*

Structure type $HoCo_3P_2$ (Jeitschko and Jakubowski 1985; fig. 54, table 48) has space group Pmmn, $a=1.0560$, $b=0.3688$, $c=1.2233$.

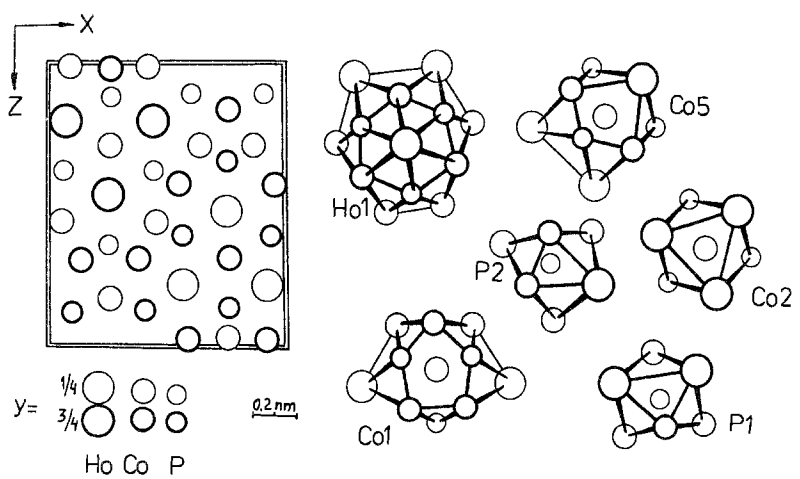

Fig. 54. Crystal structure of $HoCo_3P_2$ and CPs of atoms.

Table 48
Atomic parameters for $HoCo_3P_2$

Atom	Position	Fractional coordinates			Atomic arrangement		
		x	*y*	*z*			
Ho1	2(*b*)	1/4	3/4	0.47411	2Ho	12Co	6P
Ho2	4(*f*)	0.56773	1/4	0.79412	2Ho	12Co	6P
Co1	2(*a*)	1/4	1/4	0.8434	2Ho	8Co	5P
Co2[a]	4(*e*)	1/4	0.2172	0.2975	6Ho		3P
Co3	2(*b*)	1/4	3/4	0.0165	2Ho	6Co	4P
Co4	4(*f*)	0.0837	1/4	0.0067	3Ho	5Co	4P
Co5	4(*f*)	0.0464	1/4	0.5679	4Ho	4Co	4P
Co6	4(*f*)	0.6296	I/4	0.2929	3Ho	5Co	4P
P1	2(*a*)	1/4	1/4	0.1198	4Ho	6Co	
P2	2(*a*)	1/4	1/4	0.6532	2Ho	7Co	
P3	4(*f*)	0.0622	1/4	0.3828	4Ho	5Co	
P4	4(*f*)	0.5984	1/4	0.1075	2Ho	7Co	

[a] Occupancy 50%.

The structure was determined by a single-crystal method, $R=0.055$ (Jeitschko and Jakubowski 1985). Holmium atoms have a CN of 20, Co3–Co6 have 12, Co1 has 15, Co2 and all P atoms have a CN of 9 and a trigonal-prismatic arrangement with additional atoms outside the rectangular faces of the prisms. The shortest interatomic distances are $\delta_{Ho1-Co2}=0.2763$; $\delta_{Ho2-P4}=0.2815$; $\delta_{Co6-Co6}=0.2543$; $\delta_{Co2-P1}=0.2178$. Isotypic compounds are RCo_3P_2 where R = Y, Ce, Pr, Nd, Sm, Gd, Tb, Dy, Er, Tm, Yb, Lu.

2.3.27. *$Nd_3Ni_7P_5$, hP62*

Structure type $Nd_3Ni_7P_5$ (Chykhrij et al. 1989c; fig. 55, table 49) has space group $P6_3/m$, $a=1.6679$, $c=0.3891$.

Chykhrij et al. (1989c) determined the structure of $Nd_3Ni_7P_5$ by a single-crystal method, $R=0.061$. All phosphorus and Ni1 atoms are situated in trigonal prisms formed by the metal atoms. The shortest interatomic distances are $\delta_{Nd1-Ni1}=0.298$; $\delta_{Nd2-P2}=0.294$; $\delta_{Ni3-Ni5}=0.244$; $\delta_{Ni1-P3}=0.217$. Isotypic compounds are $R_3Ni_7P_5$ where R = La, Pr, Sm, Gd, Tb.

2.3.28. *$(La, Ce)_{12}Rh_{30}P_{21}$, hP64*

Structure type $(La, Ce)_{12}Rh_{30}P_{21}$ (Pivan and Guerin 1986) has space group $P6_3/m$, $a=1.7475$, $c=0.3948$.

Pivan and Guerin (1986) synthesized the compound $(La, Ce)_{12}Rh_{30}P_{21}$ from a mixture of constituent components with an atomic ratio 3:3:32:17; the structure was determined by a single-crystal method, $R=0.049$. The ST $(La, Ce)_{12}Rh_{30}P_{21}$ is closely related to

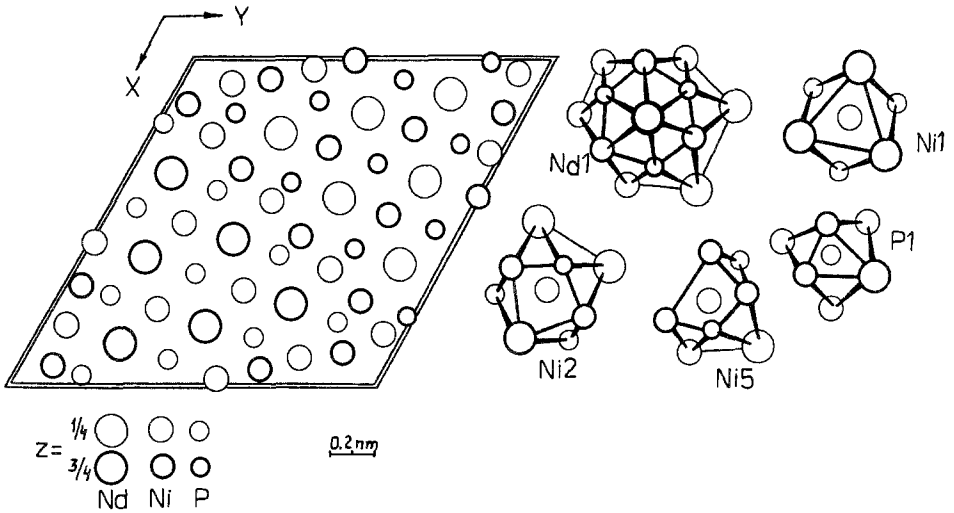

Fig. 55. Crystal structure of $Nd_3Ni_7P_5$ and CPs of atoms.

Table 49
Atomic parameters for $Nd_3Ni_7P_5$

Atom	Position	Fractional coordinates			Atomic arrangement		
		x	*y*	*z*			
Nd1	6(*h*)	0.2373	0.3582	1/4	4Nd	10Ni	6P
Nd2	6(*h*)	0.1748	0.5606	1/4	6Nd	8Ni	6P
Ni1	6(*h*)	0.5113	0.2272	1/4	6Nd		3P
Ni2	6(*h*)	0.4451	0.4335	1/4	4Nd	4Ni	4P
Ni3	6(*h*)	0.0432	0.3472	1/4	4Nd	4Ni	4P
Ni4	6(*h*)	0.2474	0.1765	1/4	3Nd	5Ni	4P
Ni5[a]	6(*h*)	0.0882	0.1475	1/4	1Nd	7Ni	3P
P1	6(*h*)	0.203	0.025	1/4	2Nd	7Ni	
P2	6(*h*)	0.464	0.075	1/4	4Nd	5Ni	
P3	6(*h*)	0.411	0.273	1/4	4Nd	5Ni	
P4	2(*c*)	2/3	1/3	1/4	6Nd	3Ni	

[a] Occupancy 67%.

ST $Nd_3Ni_7P_5$. The only differences are: the position of the Ni5 atoms is completely occupied by Rh atoms. The empty octahedra formed by the metal atoms are filled with the P5 atoms (position 2(*a*) 000). The shortest interatomic distances are $\delta_{R1-Rh4} = 0.3014$; $\delta_{R1-P3} = 0.3035$; $\delta_{Rh3-Rh5} = 0.2710$; $\delta_{Rh5-P3} = 0.2278$.

2.3.29. *$Ce_6Ni_{15}P_{10}$, hP68*

Structure type $Ce_6Ni_{15}P_{10}$ (Babizhets'ky et al. 1993a) has space group $P6_3/m$, $a=1.6637$, $c=0.3878$.

The structure of $Ce_6Ni_{15}P_{10}$ was determined by a single-crystal method, $R=0.042$ (Babizhets'ky et al. 1993a). It is also closely related to $Nd_3Ni_7P_5$. In $Nd_3Ni_7P_5$ the columns of octahedra [$\square Ni_6$] are filled with Ni6 atoms which occupy 22% of the positions 6(*h*) *xy*1/4 ($x=0.0412$, $y=0.0684$), while in $Ce_6Ni_{15}P_{10}$ these positions with close coordinates are fully occupied by nickel atoms. The atomic coordinates of all other atoms do not differ essentially from those in $Nd_3Ni_7P_5$. The shortest interatomic distances are $\delta_{Ce-Ni}=0.3009$; $\delta_{Ce-P}=0.3020$; $\delta_{Ni-Ni}=0.2765$; $\delta_{Ni-P}=0.2310$.

2.3.30. *$Hf_2Co_4P_3$, hP36*

Structure type $Hf_2Co_4P_3$ (Ganglberger 1968a,b) has space group $P\bar{6}2m$, $a=1.2261$, $c=0.3719$ (for $Gd_2Co_4P_3$) (Kuz'ma et al. 1986b).

The structure of compound $Gd_2Co_4P_3$ was determined by a powder method (Kuz'ma et al. 1986b) but intensity calculations have not been carried out because of the impurity of the sample. That is identification of $Gd_2Co_4P_3$ as the $Hf_2Co_4P_3$-type requires confirmation.

2.3.31. *TiNiSi, oP12*

Structure type TiNiSi (Schoemaker and Schoemaker 1965; fig. 56, table 50) has space group Pnma, $a=0.6826$, $b=0.3965$, $c=0.7689$ (for ErPdP) (Johrendt and Mewis 1990).

The structure type TiNiSi is a superstructure of anti-$PbCl_2$. Johrendt and Mewis (1990) determined the ErPdP structure by a single-crystal method, $R=0.046$. Phosphorus atoms fill the trigonal prisms, erbium and palladium atoms have a CN of 15 and 12, respectively. The shortest interatomic distances are $\delta_{Er-Pd}=0.2950$; $\delta_{Er-P}=0.2803$; $\delta_{Pd-Pd}=0.2981$; $\delta_{Pd-P}=0.2522$. Isotypic compounds are ScCoP and RPdP where R = Tb, Dy, Ho, Tm, Yb, Lu.

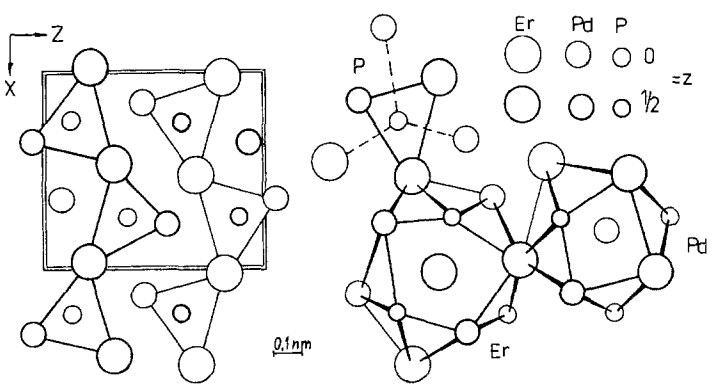

Fig. 56. Crystal structure of ErPdP and CPs of atoms.

Table 50
Atomic parameters for ErPdP

Atom	Position	Fractional coordinates			Atomic arrangement		
		x	*y*	*z*			
Er	4(*c*)	0.5314	1/4	0.6880	4Er	6Pd	5P
Pd	4(*c*)	0.6475	1/4	0.0619	6Er	2Pd	4P
P	4(*c*)	0.2495	1/4	0.1228	5Er	4Pd	

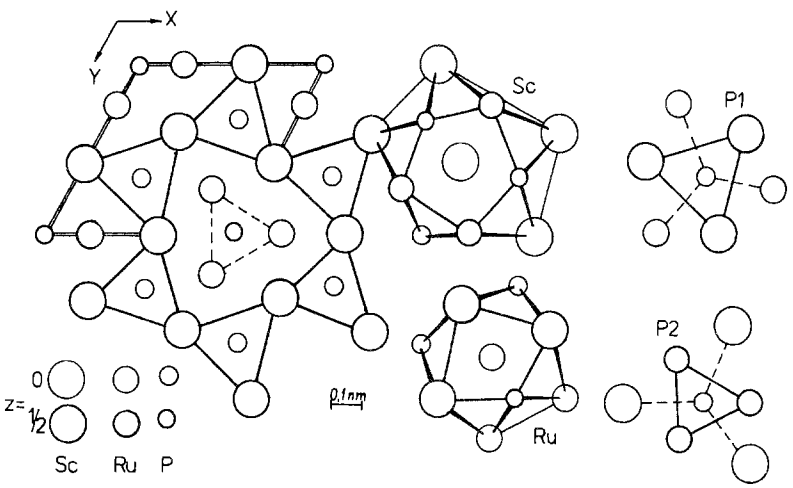

Fig. 57. Crystal structure of ScRuP and CPs of atoms.

Table 51
Atomic parameters for ScRuP

Atom	Position	Fractional coordinates			Atomic arrangement		
		x	*y*	*z*			
Sc	3(*g*)	0.5895	0	1/2	4Sc	6Ru	5P
Ru	3(*f*)	0.2447	0	0	6Sc	2Ru	4P
P1	2(*c*)	1/3	2/3	0	6Sc	3Ru	
P2	1(*b*)	0	0	1/2	3Sc	6Ru	

2.3.32. *ZrNiAl, hP9*

Structure type ZrNiAl (Krypyakevych et al. 1967; fig. 57, table 51) has space group $P\bar{6}2m$, $a=0.6524$, $c=0.3610$ (for ScRuP) (Ghetta et al. 1986).

Ghetta et al. (1986) determined the structure of ScRuP by a single-crystal method ($R=0.040$) and regarded its structure as of ZrRuSi type. In reality it belongs to structure

type ZrNiAl (superstructure of Fe_2P). In the structure of ScRuP the scandium and ruthenium atoms form columns of trigonal prisms which are centered by phosphorus atoms. Such columns are linked via common edges and form six-member channels which are filled with isolated columns of trigonal prisms. The shortest interatomic distances are $\delta_{Sc-Ru}=0.288$; $\delta_{Sc-P}=0.267$; $\delta_{Ru-Ru}=0.276$; $\delta_{Ru-P}=0.241$.

2.3.33. *AlB_2, hP3*

Structure type AlB_2 (Hofmann and Jäniche 1936; fig. 58, table 52) has space group P6/mmm, $a=0.4016$, $c=0.4163$ (for $EuPt_{0.65}P_{1.35}$) (Wenski and Mewis 1986b).

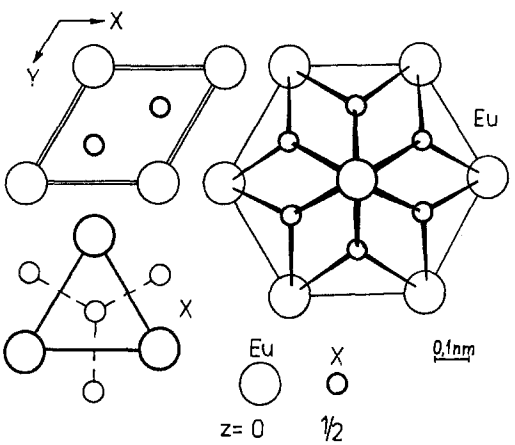

Fig. 58. Crystal structure of $EuPt_{0.65}P_{1.35}$ and CPs of atoms.

Table 52
Atomic parameters for $EuPt_{0.65}P_{1.35}$

Atom	Position	Fractional coordinates			Atomic arrangement	
		x	*y*	*z*		
Eu	1(*a*)	0	0	0	8Eu	12X
X[a]	2(*d*)	1/3	2/3	1/2	6Eu	3X

[a] X = 0.65Pt + 1.35P.

Wenski and Mewis (1986b) investigated single crystals of the compound $EuPt_{0.65}P_{1.35}$ ($R=0.057$). In the structure of EuX_2 (where X = 0.65Pt + 1.35P) europium atoms form layers of trigonal prisms which are centered by X atoms; all X atoms form a graphite-like net which is perpendicular to the *Z* axis. Interatomic distances are $\delta_{Eu-X}=0.3179$; $\delta_{X-X}=0.2347$.

2.3.34. *YbPtP, hP3*

Structure type YbPtP (Wenski and Mewis 1986c; table 53) has space group $P\bar{6}m2$, $a=0.4077$, $c=0.3777$.

Table 53
Atomic parameters for YbPtP

Atom	Position	Fractional coordinates			Atomic arrangement		
		x	*y*	*z*			
Yb	1(*a*)	0	0	0	8Yb	6Pt	6P
Pt	1(*d*)	1/3	2/3	1/2	6Yb		3P
P	1(*f*)	2/3	1/3	1/2	6Yb	3Pt	

Wenski and Mewis (1986c) determined the structure of YbPtP by a single-crystal method, $R = 0.050$. YbPtP is a first-order superstructure of the AlB_2-type: platinum and phosphorus atoms regularly occupy trigonal prisms formed by ytterbium atoms. Such regularity causes a decreasing symmetry with a transition from sp.gr. P6/mmm (ST AlB_2) to sp.gr. $P\bar{6}2m$ (ST YbPtP). Interatomic distances are $\delta_{Yb-Pt} = \delta_{Yb-P} = 0.3018$; $\delta_{Pt-P} = 0.2354$. Isotypic compounds are EuNiP and RPtP where R = Y, Sm, Gd, Tb, Dy, Tm, Lu.

2.3.35. *ZrBeSi, hP6*

Structure type ZrBeSi (Nielsen and Baenziger 1954; table 54) has space group $P6_3/mmc$, $a = 0.4248$, $c = 0.7799$ (for CePdP) (Johrendt and Mewis 1990).

The ST ZrBeSi (Nielsen and Baenziger 1954) differs from the ST AlB_2 by a double lattice parameter *c* and a regular distribution of small atoms. Johrendt and Mewis (1990) regard the crystal structure of the compounds RPdP (R = La, Ce, Pr, Nd, Sm, Gd) as the ST Ni_2In. The atomic arrangement of the smallest atoms in RPdP is a trigonal prism which is formed by R atoms (as it is in ZrBeSi), while in Ni_2In (or in its superstructure GeMnNi) the environment of the respective atoms is a trigonal bipyramid. Besides the *c/a* ratio in the Ni_2In-type structures is considerably lower than that in the ZrBeSi structure (~1.1–1.4 and 1.939, respectively). These considerations allow the possibility that RPdP compounds belong to the ZrBeSi type. The coordination polyhedra in RPdP are the same as those in the AlB_2 structure. The interatomic distances are $\delta_{Ce-Pd} = \delta_{Ce-P} = 0.3133$; $\delta_{Pd-P} = 0.2453$. Besides the above mentioned phosphide compounds the EuMP, where M = Cu, Ag, Au, Pt, have the crystal structure of ZeBeSi.

Table 54
Atomic parameters for CePdP

Atom	Position	Fractional coordinates			Atomic arrangement		
		x	*y*	*z*			
Ce	2(*a*)	0	0	0	8Ce	6Pd	6P
Pd	2(*c*)	1/3	2/3	1/4	6Ce		3P
P	2(*d*)	2/3	1/3	1/4	6Ce	3Pd	

Lux et al. (1991a) carried out a single-crystal investigation of EuPtP and showed that the P atoms are displaced from ideal positions with $z = 1/4$, but occupy 50% of the positions 4(*f*) 1/3 2/3 *z* with $z = 0.7408$ or $z = 0.7388$ in α-EuPtP and β-EuPtP, respectively. This considerably improves the thermal parameters of the phosphorus atoms. The deviation of the *z* coordinate from $z = 1/4$ influences the interatomic distances: in α-EuPtP $\delta_{Eu-P} = 0.3251$ and 0.3144; in β-EuPtP $\delta_{Eu-P} = 0.3221$ and 0.3096; $\delta_{Pt-P} = 0.2360$ and 0.2363 in α- and β-EuPtP, respectively. The results obtained agree with Mössbauer investigations (Lossau et al. 1989a) which indicate a variable valence of the europium atoms in the temperature range 4–300 K.

2.3.36. *γ-EuPtP, hP6*

Structure type γ-EuPtP (Lux et al. 1991a; table 55) has space group $P\bar{3}m1$, $a = 0.4103$, $c = 0.8256$.

Lux et al. (1991a) determined the γ-EuPtP structure by a single-crystal method at 180 K ($R = 0.044$). In γ-EuPtP both Pt and P atoms are displaced from the ideal positions with $z = 1/4$; this leads to a decreased symmetry compared to ST ZrBeSi. One can consider γ-EuPtP as a superstructure of $CaIn_2$ (Iandelli 1964). Interatomic distances are $\delta_{Eu1-Pt} = 0.3082$; $\delta_{Eu2-Pt} = 0.3204$; $\delta_{Eu1-P} = 0.3091$; $\delta_{Eu2-P} = 0.3195$; $\delta_{Pt-P} = 0.2370$.

Table 55
Atomic parameters for γ-EuPtP

Atom	Position	Fractional coordinates			Atomic arrangement		
		x	*y*	*z*			
Eu1	1(*a*)	0	0	0	8Eu	6Pt	6P
Eu2	1(*b*)	0	0	1/2	8Eu	6Pt	6P
Pt	2(*d*)	2/3	1/3	0.2388	8Eu		6P
P	2(*d*)	1/3	2/3	0.2404	8Eu	6Pt	

2.3.37. *$Tb_{1-x}NiP$ ($x = 0.05$), hP12*

Structure type $Tb_{1-x}NiP$ ($x = 0.05$) (Chykhrij et al. 1987; fig. 59, table 56) has space group $P6_3/mmc$, $a = 0.3922$, $c = 1.5328$.

Chykhrij et al. (1987) determined the structure of $Tb_{1-x}NiP$ by a single-crystal method; the atomic parameters were refined using powder intensities to $R = 0.075$. The structure of $Tb_{1-x}NiP$ is related to the ST AlB_2 and its derivatives. The nickel and phosphorus atoms occupy trigonal prisms formed by the terbium atoms. Villars and Calvert (1991) consider the $Tb_{1-x}NiP$ structure as belonging to MoC_{1-p}-type (Nowotny et al. 1954). However, this point of view is formal and is based on the same positions being occupied in the MoC_{1-p} and $Tb_{1-x}NiP$ structures. Considering $Tb_{1-x}NiP$ as belonging to the ST MoC_{1-p}, the Tb1 and Tb2 atoms occupy positions of the C1 and Mo1 atoms which are characterized by different environments including an octahedral one of C1. Besides, the existence of

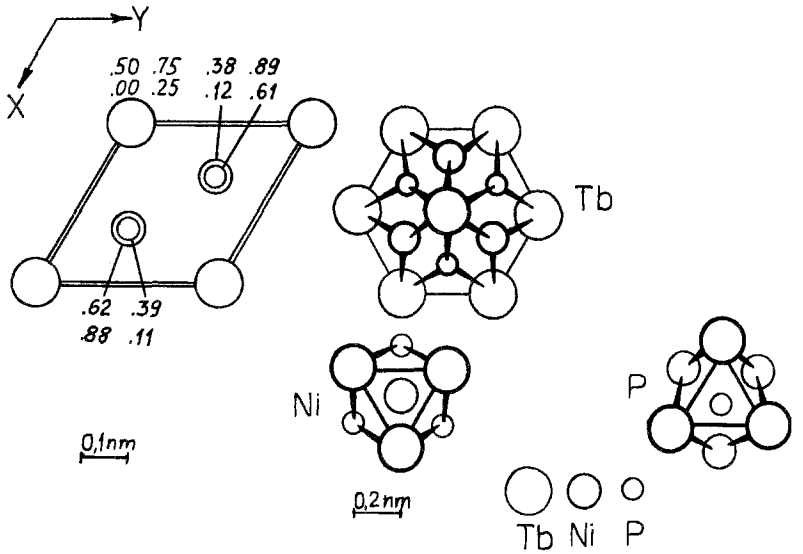

Fig. 59. Crystal structure of $Tb_{1-x}NiP$ and CPs of atoms.

Table 56
Atomic parameters for $Tb_{1-x}NiP$ ($x = 0.05$)

Atom	Position	Fractional coordinates			Atomic arrangement		
		x	y	z			
Tb1[a]	2(*a*)	0	0	0	8Tb	6Ni	6P
Tb2	2(*b*)	0	0	1/4	8Tb	6Ni	6P
Ni	4(*f*)	1/3	2/3	0.121	6Tb		3P
P	4(*f*)	1/3	2/3	0.610	6Tb	3Ni	

[a] Occupancy 90%.

MoC_{1-p} needs confirmation. The interatomic distances in $Tb_{1-x}NiP$ are $\delta_{Tb1-Tb2} = 0.383$; $\delta_{Tb1-Ni} = 0.293$; $\delta_{Tb1-P} = 0.282$; $\delta_{Ni-P} = 0.227$. Isotypic compounds are RNiP where R = Y, La, Ce, Pr, Nd, Sm, Gd, Dy, Ho, Er, Tm, Lu.

2.3.38. *PbFCl, tP6*

Structure type PbFCl (Nieuwenkamp and Bijvoet 1931; table 57) has space group P4/nmm, $a = 0.4062$, $c = 0.6752$ (for CeFeSi) (Bodak et al. 1970).

The ST PbFCl (Nieuwenkamp and Bijvoet 1931) is a superstructure of the ST Cu_2Sb (Westgren et al. 1929). Since no atomic parameters have been reported for ternary rare-earth phosphides we used data from the CeFeSi structure. The smallest atoms (P) occupy positions in the centers of Archimedean cubes formed by metal atoms. Known phosphides with the PbFCl-type structure are SmFeP, RCoP (R = Pr, Nd, Sm) and LaRuP.

Table 57
Atomic parameters for CeFeSi

Atom	Position	Fractional coordinates			Atomic arrangement		
		x	*y*	*z*			
Ce	2(*c*)	1/4	1/4	0.672	8Ce	4Fe	6Si
Fe	2(*a*)	3/4	1/4	0	4Ce	4Fe	4Si
Si	2(*c*)	1/4	1/4	0.175	5Ce	4Fe	

2.3.39. *$Gd_4Co_{13}(Si,P)_9$, hP26*

Structure type $Gd_4Co_{13}(Si,P)_9$ (Jakubowski-Ripke and Jeitschko 1987) has space group $P\bar{6}m2$, $a=1.0419$, $c=0.3727$.

Jakubowski-Ripke and Jeitschko (1987) determined the structure of $Gd_4Co_{13}(Si,P)_9$ by a single-crystal method, $R=0.032$, but atomic parameters are not reported. The Si:P ratio in the compound is 1:1. Isotypic compounds are $R_4Co_{13}(Si,P)_9$ where R = Tb, Dy, Ho, Er.

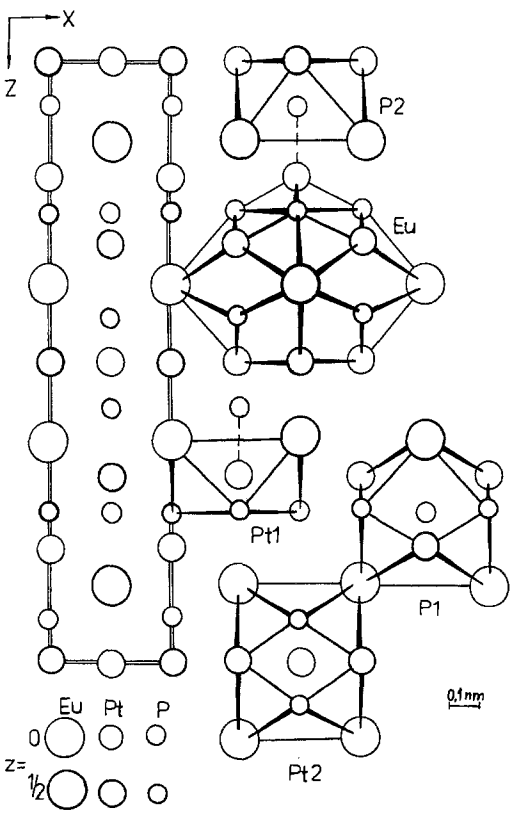

Fig. 60. Crystal structure of $EuPt_{1.62}P_2$ and CPs of atoms.

Table 58
Atomic parameters for $EuPt_2P_{1.62}$

Atom	Position	Fractional coordinates			Atomic arrangement		
		x	*y*	*z*			
Eu	4(*e*)	0	0	0.3704	4Eu	9Pt	6P
Pt1	4(*e*)	0	0	0.1953	4Eu		5P
Pt2	4(*c*)	1/2	0	0	4Eu	4Pt	4P
P1[a]	4(*d*)	1/2	0	1/4	4Eu	4Pt	4P
P2	4(*e*)	0	0	0.0742	4Eu	5Pt	

[a] Occupancy 62%.

2.3.40. *$EuPt_2P_{1.62}$, tI20*

Structure type $EuPt_2P_{1.62}$ (Wenski and Mewis 1986a–d; fig. 60, table 58) has space group I4/mmm, $a = 0.4143$, $c = 1.9120$.

Wenski and Mewis (1986a–d) determined the structure of $EuPt_2P_{1.62}$ by a single-crystal method, $R = 0.071$. The CP of the Eu atom is similar to that of Ce in $CeGa_2Al_2$ (fig. 60), P1 atoms fill a tetragonal prism with centered rectangular faces, P2 atoms have CPs in the form of an Archimedean cube with additional Pt atoms outside one of the square faces; Pt1 has an atomic environment similar to P2. The shortest interatomic distances are $\delta_{Eu-Pt1} = 0.3188$; $\delta_{Eu-P1} = 0.3097$; $\delta_{Pt2-Pt2} = 0.2930$; $\delta_{Pt1-P2} = 0.2320$.

2.3.41. *$Yb_6Co_{30}P_{19}$, hP55*

Structure type $Yb_6Co_{30}P_{19}$ (Jeitschko and Jakubowski-Ripke 1993; fig. 61, table 59) has space group $P\bar{6}$, $a = 1.4703$, $c = 0.3574$.

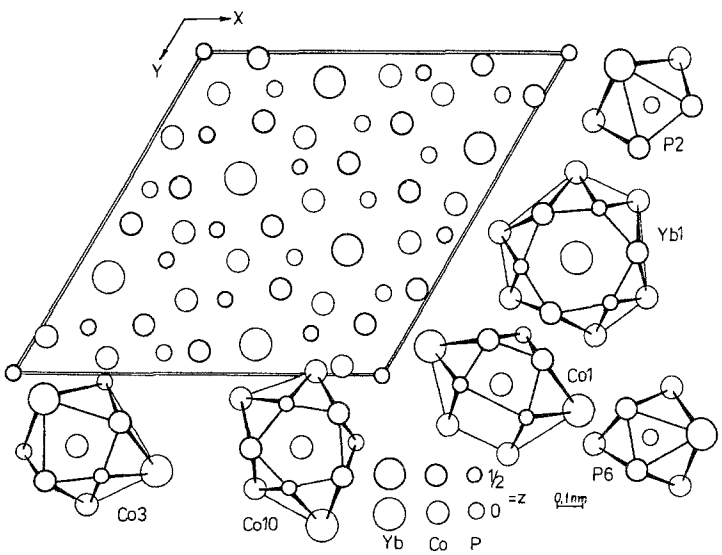

Fig. 61. Crystal structure of $Yb_6Co_{30}P_{19}$ and CPs of atoms.

Table 59
Atomic parameters for $Yb_6Co_{30}P_{19}$

Atom	Position	Fractional coordinates			Atomic arrangement		
		x	*y*	*z*			
Yb1	3(*k*)	0.3902	0.0959	1/2	2Yb	12Co	6P
Yb2	3(*j*)	0.6054	0.9032	0	2Yb	12Co	6P
Co1	3(*k*)	0.6554	0.2255	1/2	2Yb	6Co	5P
Co2	3(*j*)	0.3512	0.7734	0	2Yb	6Co	5P
Co3	3(*k*)	0.4615	0.9227	1/2	3Yb	5Co	4P
Co4	3(*j*)	0.5356	0.0696	0	3Yb	5Co	4P
Co5	3(*k*)	0.2702	0.2271	1/2	3Yb	5Co	4P
Co6	3(*j*)	0.7245	0.7745	0	3Yb	5Co	4P
Co7	3(*k*)	0.1496	0.4190	1/2	3Yb	5Co	4P
Co8	3(*j*)	0.8464	0.5866	0	3Yb	5Co	4P
Co9	3(*k*)	0.1581	0.0275	1/2	1Yb	7Co	4P
Co10	3(*j*)	0.8660	0.9775	0	1Yb	9Co	5P
P1	3(*k*)	0.4498	0.7665	1/2	2Yb	6Co	
P2	3(*j*)	0.5432	0.2251	0	2Yb	6Co	
P3	3(*k*)	0.1389	0.2596	1/2	2Yb	7Co	
P4	3(*j*)	0.8628	0.7445	0	2Yb	7Co	
P5	3(*k*)	0.4327	0.3767	1/2	2Yb	7Co	
P6	3(*j*)	0.5690	0.6335	0	2Yb	7Co	
P7	1(*b*)	0	0	1/2		9Co	

The structure of $Yb_6Co_{30}P_{19}$ was determined by a single-crystal method, $R=0.031$ (Jeitschko and Jakubowski-Ripke 1993). The CPs of the ytterbium, cobalt and phosphorus atoms are hexagonal (Yb), pentagonal (Co10), orthorhombic (all other Co atoms) and trigonal (P) prisms with centered rectangular faces. Base faces of the Yb CPs are also centered by additional atoms and the Co1 and Co2 CPs have two additional Co atoms outside one of the rectangular faces. The structure of $Yb_6Co_{30}P_{19}$ is analogous to $U_6Co_{30}Si_{19}$ (Yarmolyuk et al. 1980) which is described in sp.gr. $P6_3/m$. The shortest interatomic distances in $Yb_6Co_{30}P_{19}$ are $\delta_{Yb1-Co8}=0.288$; $\delta_{Yb1-P2}=0.2755$; $\delta_{Co3-Co7}=0.2471$; $\delta_{Co9-P7}=0.2151$. Isotypic compounds are $R_6Co_{30}P_{19}$ where R = Er, Tm, Lu.

2.3.42. *$LaCo_8P_5$, oP28*

Structure type $LaCo_8P_5$ (Meisen and Jeitschko 1984a,b; fig. 62, table 60) has space group Pmmn, $a=1.05101$, $b=0.3596$, $c=0.9342$.

Meisen and Jeitschko (1984a) determined the structure of $LaCo_8P_5$ by a single-crystal method, $R=0.040$. The structure is characterized by trigonal-prismatic coordination of the phosphorus atoms. Increasing the phosphorus content leads to the appearance of P–P contacts ($\delta_{P1-P1}=0.2485$). The stacking of trigonal prisms is shown in fig. 62. The

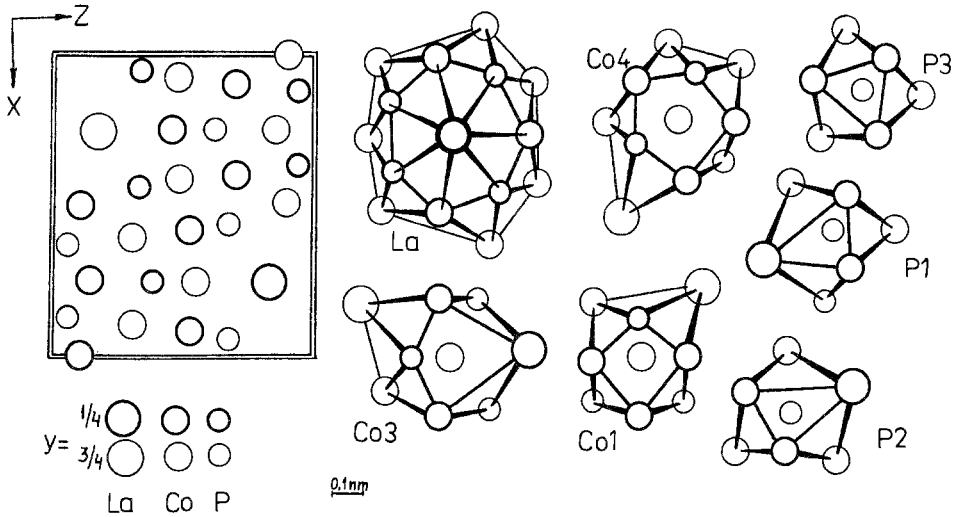

Fig. 62. Crystal structure of $LaCo_8P_5$ and CPs of atoms.

Table 60
Atomic parameters for $LaCo_8P_5$

Atom	Position	Fractional coordinates			Atomic arrangement		
		x	*y*	*z*			
La	2(*a*)	1/4	1/4	0.1762	2La	13Co	8P
Co1	4(*f*)	0.4181	1/4	0.4796	1La	7Co	4P
Co2	4(*f*)	0.4951	1/4	0.8897	3La	5Co	4P
Co3	4(*f*)	0.6065	1/4	0.3035	1La	9Co	5P
Co4	2(*a*)	1/4	1/4	0.8470	1La	6Co	5P
Co5	2(*b*)	1/4	3/4	0.4548	2La	6Co	4P
P1	4(*f*)	0.6317	1/4	0.0662	2La	6Co	1P
P2	4(*f*)	0.5592	1/4	0.6623	2La	7Co	
P3	2(*a*)	1/4	1/4	0.6137		9Co	

shortest interatomic distances are $\delta_{La-Co1}=0.3075$; $\delta_{La-P2}=0.3086$; $\delta_{Co1-Co1}=0.2517$; $\delta_{Co1-P3}=0.2165$. Isotypic compounds are $PrCo_8P_5$ and $EuCo_8P_5$.

2.3.43. *Na_6ZnO_4, hP22*

Structure type Na_6ZnO_4 (Kastner and Hoppe 1974; fig. 63, table 61) has space group $P6_3mc$, $a=0.9251$, $c=0.7198$ (for $Na_4Eu_2SiP_4$) (von Schnering et al. 1988).

The structure of $Na_4Eu_2SiP_4$ was determined by a single-crystal method (von Schnering et al. 1988) but atomic parameters are not reported. Tetrahedral SiP_4 fill hexagonal channels which are formed by Na and Eu atoms; part of the space in these channels

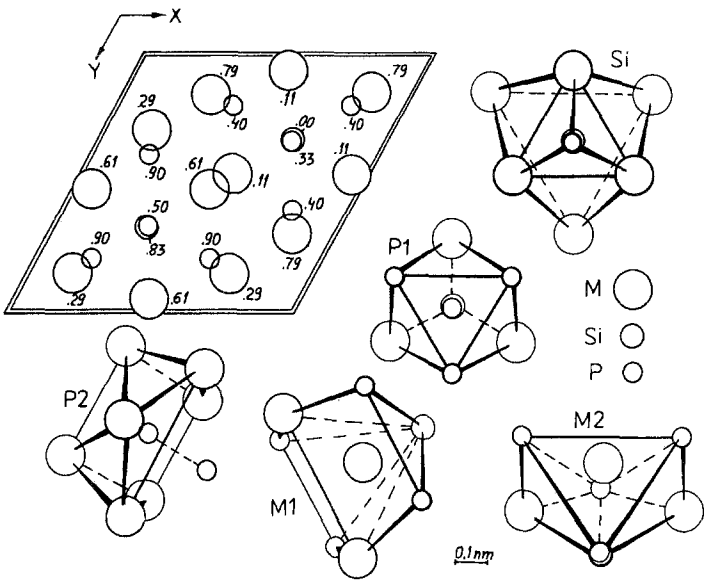

Fig. 63. Crystal structure of $Eu_2Na_4SiP_4$ and CPs of atoms.

Table 61
Atomic parameters for $Na_4Eu_2SiP_4$

Atom	Position	Fractional coordinates			Atomic arrangement		
		x	*y*	*z*			
M1[a]	6(*c*)	0.5292	0.4708	0.1127	2M	1Si	4P
M2[a]	6(*c*)	0.1445	0.8555	0.2855	3M	1Si	4P
Si	2(*b*)	1/3	2/3	0	6M		1P
P1	2(*b*)	1/3	2/3	0.3255	3M	1Si	3P
P2	6(*c*)	0.8082	0.1918	0.3967	7M		1P

[a] M1 = 1Na + 2Eu; M2 = 3Na.

is not filled. The P1 atoms have octahedral coordination with one additional atom and the P2 atoms have a trigonal-prismatic environment with two additional atoms (M and P1) outside the rectangular faces. Isotypic compounds are $Na_4Eu_2MP_4$ where M = Ge, Sn, Pb.

2.3.44. *$CeAl_2Ga_2$, tI10*

Structure type $CeAl_2Ga_2$ (Zarechnyuk et al. 1964; fig. 64, table 62) has space group I4/mmm, $a = 0.4010$, $c = 0.9604$ (for $LaNi_2P_2$) (Hofmann and Jeitschko 1984).

The ST $CeAl_2Ga_2$ (Zarechnyuk et al. 1964) (another name is $ThCr_2Si_2$, Sikirica and Ban 1964) is a superstructure of $BaAl_4$ (Andress and Alberti 1935). The structure of $CeAl_2Ga_2$ is built of layers of Archimedean cubes $[GaCe_4Al_4]$. The CPs are shown in

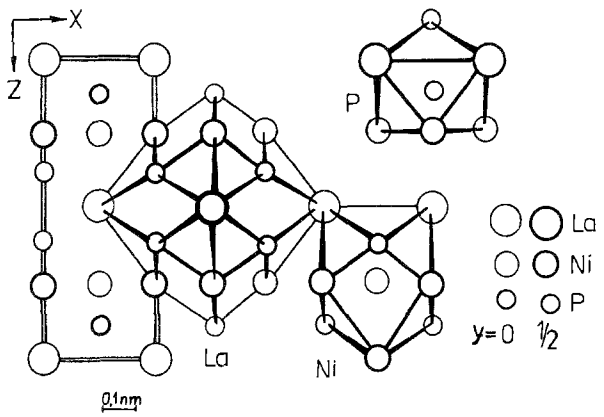

Fig. 64. Crystal structure of $LaNi_2P_2$ and CPs of atoms.

Table 62
Atomic parameters for $LaNi_2P_2$

Atom	Position	Fractional coordinates			Atomic arrangement		
		x	*y*	*z*			
La	2(*a*)	0	0	0	4La	8Ni	10P
Ni[a]	4(*d*)	0	1/2	1/4	4La	4Ni	4P
P[a]	4(*e*)	0	0	0.3700	4La	4Ni	1P

[a] Occupancy factors: Ni, 94.2%; P, 95.1%.

fig. 64. Isotypic phosphides are RFe_2P_2 (R = La, Ce, Pr, Eu), RCo_2P_2 (R = La, Ce, Pr, Nd, Sm, Eu), RNi_2P_2 (R = Y, La, Ce, Pr, Nd, Sm, Eu, Gd–Yb), $EuCu_{1.7}P_2$, RRu_2P_2 (R = Y, La, Ce, Pr, Nd, Sm, Eu, Gd–Er, Yb), RPd_2P_2 (R = Y, La, Ce, Pr, Nd, Sm, Eu, Gd–Er, Yb) and $EuOs_2P_2$.

2.3.45. *$CaBe_2Ge_2$, tP10*

Structure type $CaBe_2Ge_2$ (Eisenmann et al. 1972; fig. 65, table 63) has space group P4/nmm, $a = 0.4146$, $c = 0.9539$ (for $CeRh_2P_2$) (Madar et al. 1987a).

Madar et al. (1987a) determined the structure of $CeRh_2P_2$ by a single-crystal method, $R = 0.035$. The ST $CaBe_2Ge_2$ is closely related to the $CeAl_2Ga_2$-type; it is built from similar layers of Archimedean cubes but in a primitive unit cell. Rh1 and P1 have atomic arrangement in the form of an Archimedean cube with one additional atom outside the square face (fig. 65). The shortest interatomic distances are $\delta_{Ce-Rh1} = 0.3189$; $\delta_{Ce-P} = 0.3109$; $\delta_{Rh2-Rh2} = 0.2932$; $\delta_{Rh1-P2} = 0.2329$. Isotypic compounds are RRh_2P_2 where R = La, Pr, Nd.

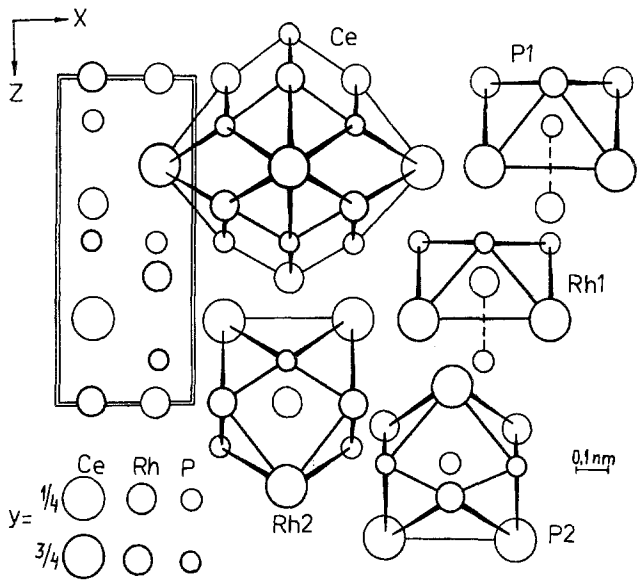

Fig. 65. Crystal structure of $CeRh_2P_2$ and CPs of atoms.

Table 63
Atomic parameters for $CeRh_2P_2$

Atom	Position	Fractional coordinates			Atomic arrangement		
		x	*y*	*z*			
Ce	2(*c*)	1/4	1/4	0.7429	4Ce	9Rh	9P
Rh1	2(*c*)	1/4	1/4	0.3888	4Ce		5P
Rh2	2(*a*)	3/4	1/4	0	4Ce	4Rh	4P
P1	2(*c*)	1/4	1/4	0.1390	4Ce	5Rh	
P2	2(*b*)	3/4	1/4	1/2	4Ce	4Rh	4P

2.3.46. *Ce_2S_2O, hP5*

Structure type Ce_2S_2O (Zachariasen 1949; fig. 66, table 64) has space group $P\bar{3}m1$, $a = 0.4196$, $c = 0.6821$ (for $PrLi_2P_2$) (Fischer and Schuster 1980).

The ST Ce_2S_2O (Zachariasen 1949) is a superstructure of anti-La_2O_3 (Pauling 1928); the other name is $CaAl_2Si_2$. The P atoms are situated in octahedra formed by La and Li atoms; one of the faces is centered by an additional Li atom. The shortest interatomic distances are $\delta_{Pr-P} = 0.2979$; $\delta_{Li-P} = 0.2546$. Isotypic rare-earth phosphides RLi_2P_2 (R = La, Ce, Pr), $EuMn_2P_2$, RZn_2P_2 (R = Eu, Yb), $RCuZnP_2$ (R = Y, La, Ce, Sm, Yb), $YbMnCuP_2$ and $SmZnAgP_2$.

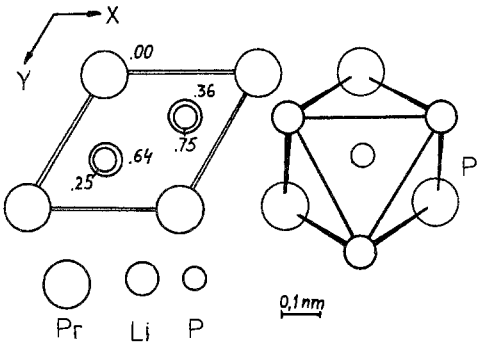

Fig. 66. Crystal structure of $PrLi_2P_2$ and CPs of atoms.

Table 64
Atomic parameters for $PrLi_2P_2$

Atom	Position	Fractional coordinates			Atomic arrangement		
		x	y	z			
Pr	1(*a*)	0	0	0		6Li	6P
Li	2(*d*)	1/3	2/3	0.6352	3Pr		3P
P	2(*d*)	1/3	2/3	0.2514	3Pr	3Li	

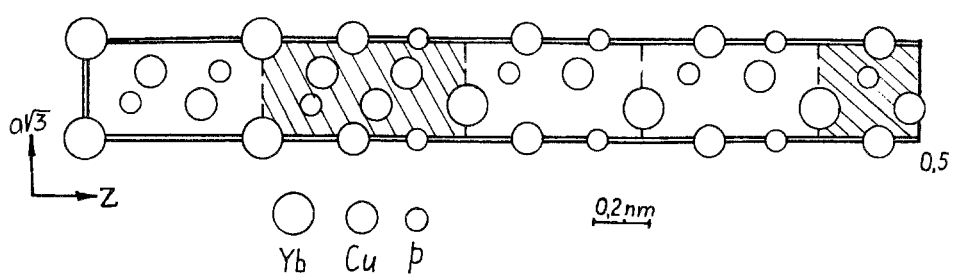

Fig. 67. Crystal structure of $YbCu_2P_2$ as a combination of structure blocks which occur in Cu_3P structures (Cu_2P-blocks, dark sections) and Ce_2O_2S structures (CuP-blocks, light sections).

2.3.47. *$YbCu_2P_2$, hR17*

Structure type $YbCu_2P_2$ (Klüfers et al. 1979; fig. 67, table 65) has space group $R\bar{3}m$, $a = 0.3951$, $c = 5.946$.

Klüfers et al. (1979) determined the structure of $YbCu_2P_2$ by a single-crystal method, $R = 0.076$; the exact composition of the compound is $YbCu_{2.27}P_2$. Similar to $YbCu_3P_2$ the structure of $YbCu_2P_2$ is built from atomic blocks which also occur in the Cu_3P and Ce_2O_2S structures (fig. 67). However, there are twice as many CuP-blocks as Cu_2P-blocks. All atoms have CPs analogous with those in $YbCu_3P_2$ (fig. 53). The shortest interatomic distances are $\delta_{Yb2-P2} = 0.2734$; $\delta_{Yb2-Cu2} = 0.3119$; $\delta_{Cu1-Cu1} = 0.2419$; $\delta_{Cu1-P1} = 0.2289$.

Table 65
Atomic parameters for $YbCu_2P_2$

Atom	Position	Fractional coordinates			Atomic arrangement		
		x	*y*	*z*			
Yb1	3(*a*)	0	0	0	6Yb	6Cu	6P
Yb2	6(*c*)	0	0	0.1054	6Yb	7Cu	6P
Cu1[a]	6(*c*)	0	0	0.1596	1Yb	6Cu	4P
Cu2[a]	6(*c*)	0	0	0.2637	3Yb	3Cu	4P
Cu3	6(*c*)	0	0	0.4749	3Yb	4Cu	3P
Cu4[a]	6(*c*)	0	0	0.3731	3Yb	3Cu	4P
P1	6(*c*)	0	0	0.1984	3Yb	7Cu	
P2	6(*c*)	0	0	0.4134	3Yb	4Cu	
P3	6(*c*)	0	0	0.3062	3Yb	4Cu	

[a] Occupancy 80%.

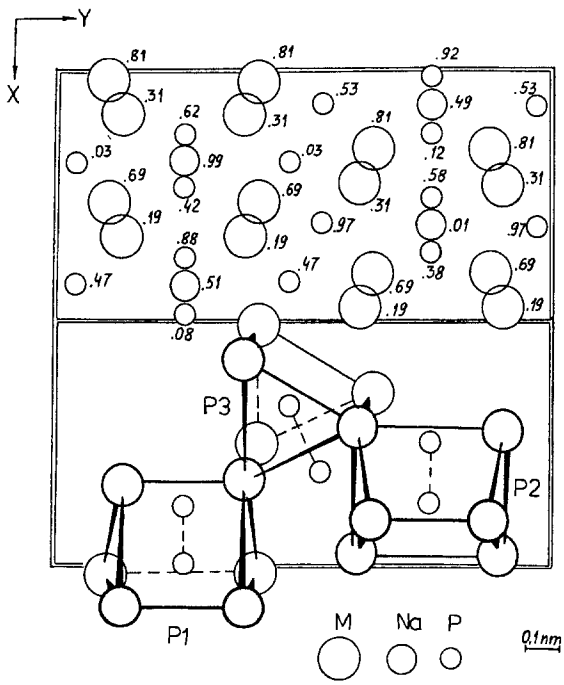

Fig. 68. Crystal structure of $Na_2Eu_3P_4$ and CPs of atoms.

2.3.48. *Sm_5Ge_4, oP36*

Structure type Sm_5Ge_4 (Smith et al. 1966; fig. 68, table 66) has space group Pnma, $a=0.7298$, $b=1.5043$, $c=0.7881$ (for $Na_2Eu_3P_4$) (Hönle et al. 1992).

Table 66
Atomic parameters for $Na_2Eu_3P_4$

Atom	Position	Fractional coordinates			Atomic arrangement		
		x	y	z			
M1[a]	8(*d*)	0.0366	0.10146	0.80841	7M	2Na	6P
M2[a]	8(*d*)	0.1837	0.12642	0.31435	8M	2Na	6P
Na	4(*c*)	0.3648	1/4	0.9920	8M		
P1	4(*c*)	0.4792	1/4	0.4197	6M		1P
P2	4(*c*)	0.2560	1/4	0.6200	6M		1P
P3	8(*d*)	0.3640	0.0352	0.0283	6M		1P

[a] M1 = 7.65Eu + 0.35Na; M2 = 4.30Eu + 3.70Na.

Hönle et al. (1992) determined the structure of $Na_2Eu_3P_4$ by a single-crystal method, $R = 0.041$. Phosphorus atoms have a CN of 9 and a CP in the form of distorted trigonal prisms with rectangular faces centered by metal or phosphorus atoms; the phosphorus atoms form pairs P_2 ($\delta_{P1-P2} = 0.2268$; $\delta_{P3-P3} = 0.2293$). The trigonal prism stacking in the structure of $Na_2Eu_3P_4$ is shown in fig. 68. Other shortest interatomic distances are $\delta_{M2-P3} = 0.2949$; $\delta_{Na-P1} = 0.2899$.

2.3.49. *$HfCuSi_2$, tP8*

Structure type $HfCuSi_2$ (Andrukhiv et al. 1975; fig. 69, table 67) has space group P4/nmm, $a = 0.3774$, $c = 0.9886$ (for $TbCu_{1.25}P_{1.75}$) (Chykhrij et al. 1989a).

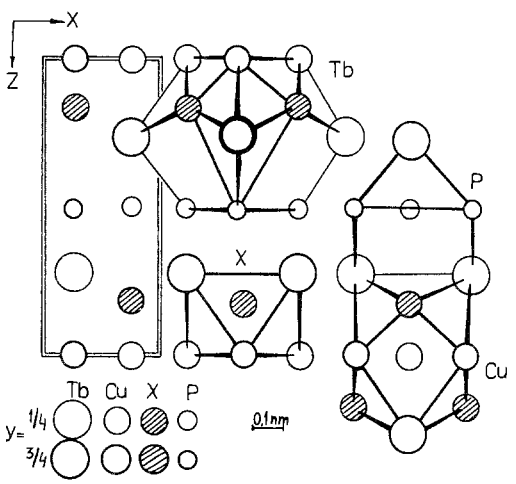

Fig. 69. Crystal structure of $TbCu_{1.25}P_{1.75}$ and CPs of atoms.

The structure of the compound $RCu_{1+x}P_{2-x}$ with $HfCuSi_2$-type was determined by the powder method, $R = 0.095$ for $TbCu_{1.25}P_{1.75}$ (Chykhrij et al. 1989a). It is desirable to confirm this structure by a single-crystal investigation. Phosphorus has an atomic

Table 67
Atomic parameters for $TbCu_{1.25}P_{1.75}$

Atom	Position	Fractional coordinates			Atomic arrangement			
		x	*y*	*z*				
Tb	2(*c*)	1/4	1/4	0.736	4Tb	4Cu	4X	4P
Cu	2(*a*)	3/4	1/4	0	4Tb	4Cu	4X	
P	2(*b*)	3/4	1/4	1/2	4Tb			4P
X[a]	2(*c*)	1/4	1/4	0.165	4Tb	4Cu		

[a] X = 0.5Cu + 1.5P.

arrangement in the form of an 8-vertices polyhedron and X atoms (a statistical mixture of 0.5Cu + 1.5P) have a CP in the form of Archimedean cube (fig. 69). The interatomic distances are close to the sum of the respective atomic radii. Isotypic compounds are $RCu_{1+x}P_{2-x}$ where R = Sm, Gd, Dy, Ho, Er.

2.3.50. *$SrZnBi_2$, tI16*

Structure type $SrZnBi_2$ (Cordier et al. 1976; fig. 70, table 68) has space group I4/mmm, $a = 0.3839$, $c = 1.9431$ (for $SmCuP_2$) (Chykhrij 1990a).

Chykhrij (1990a) determined the $SmCuP_2$ structure by a single-crystal method, the atomic parameters were refined using powder intensities to $R = 0.100$. The atomic arrangement around P1 and P2 is an 8-vertices polyhedron and Archimedean cube, respectively. The interatomic distances are close to the corresponding sum of atomic radii.

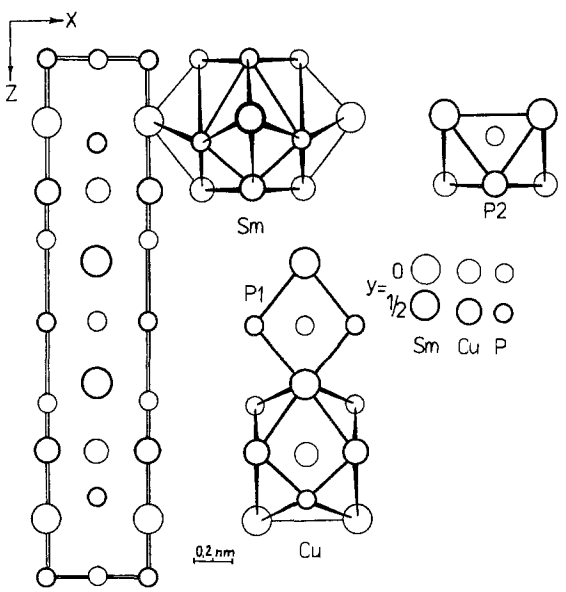

Fig. 70. Crystal structure of $SmCuP_2$ and CPs of atoms.

Table 68
Atomic parameters for $SmCuP_2$

Atom	Position	Fractional coordinates			Atomic arrangement		
		x	*y*	*z*			
Sm	4(*e*)	0	0	0.117	4Sm	4Cu	8P
Cu	4(*d*)	0	1/2	1/4	4Sm	4Cu	4P
P1	4(*c*)	0	1/2	0	4Sm		4P
P2	4(*e*)	0	0	0.342	4Sm	4Cu	

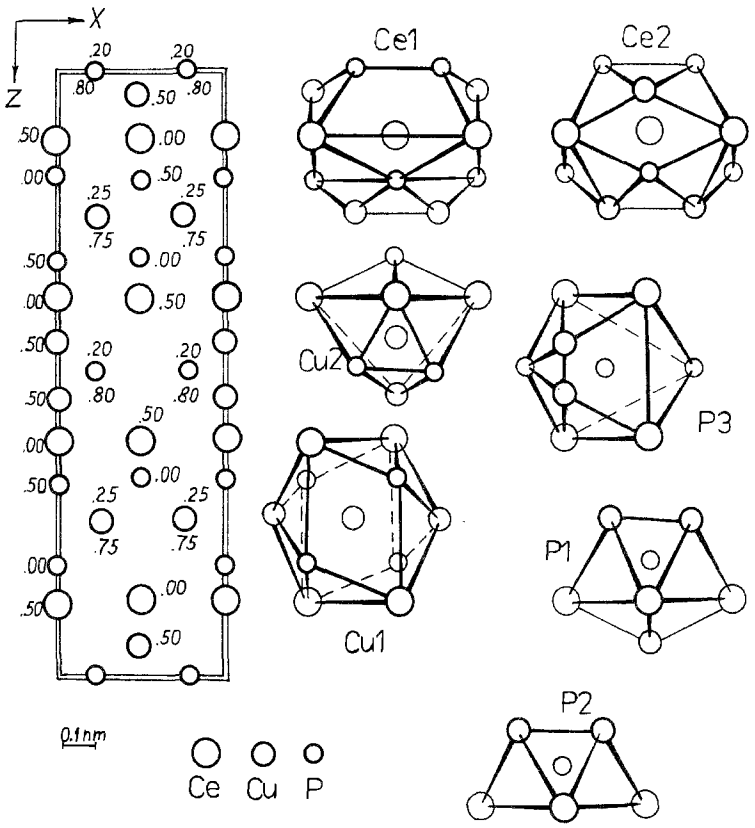

Fig. 71. Crystal structure of $CeCu_{1.12}P_{1.97}$ and CPs of atoms.

2.3.51. *$CeCu_{1.12}P_{1.97}$, oC36*

Structure type $CeCu_{1.12}P_{1.97}$ (Möller and Jeitschko 1985; fig. 71, table 69) has space group Cmmm, $a = 1.9649$, $b = 0.5550$, $c = 0.5522$.

Möller and Jeitschko (1985) determined the structure of $CeCu_{1.12}P_{1.97}$ by a single-crystal method, $R = 0.024$. The structure of $CeCu_{1.12}P_{1.97}$ is related to ST $CeAl_2Ga_2$. The

Table 69
Atomic parameters for $CeCu_{1.12}P_{1.97}$

Atom	Position	Fractional coordinates			Atomic arrangement		
		x	y	z			
Ce1	4(*h*)	0.11690	0	1/2	4Ce	6Cu	8P
Ce2	4(*g*)	0.37867	0	0	4Ce	6Cu	8P
Cu1	8(*m*)	1/4	1/4	0.2522	4Ce	2Cu	4P
Cu2[a]	4(*h*)	0.4543	0	1/2	4Ce	1Cu	5P
P1	4(*h*)	0.3240	0	1/2	4Ce	5Cu	
P2	4(*g*)	0.1771	0	0	4Ce	4Cu	
P3	8(*n*)	0	0.2262	0.2044	4Ce	2Cu	2P

[a] Occupancy 34%.

P3 atoms form flat 4-member chains which are linked by Cu2 atoms. The P1 and P2 atoms have an environment in the form of Archimedean cubes with an additional Cu atom outside the square basic face (for P1). The CP of P3 is a strongly distorted Archimedean cube. The existence of isotypic compounds $RCu_{1.12}P_{1.97}$ with R = La, Pr, Nd is noted, but their lattice parameters are not given.

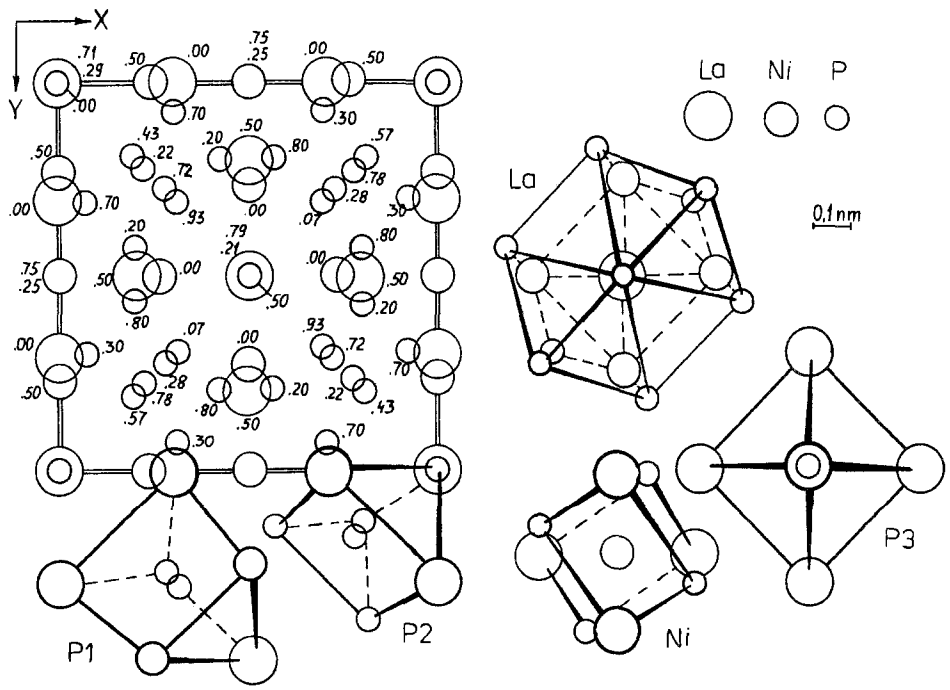

Fig. 72. Crystal structure of $La_6Ni_6P_{17}$ and CPs of atoms.

Table 70
Atomic parameters for $La_6Ni_6P_{17}$

Atom	Position	Fractional coordinates			Atomic arrangement		
		x	y	z			
La	12(e)	0.28997	0	0	1La	4Ni	9P
Ni	12(d)	1/4	1/2	0	4La		4P
P1	24(g)	0.20148	0.20148	0.43226	3La	2Ni	1P
P2	8(c)	0.21483	0.21483	0.21483	3La		3P
P3	2(a)	0	0	0	6La		

2.3.52. *$La_6Ni_6P_{17}$, cI58*

Structure type $La_6Ni_6P_{17}$ (Braun and Jeitschko 1978; fig. 72, table 70) has space group $I\bar{4}3m$, $a = 1.0168$.

Braun and Jeitschko (1978) determined the structure of $La_6Ni_6P_{17}$ by a single-crystal method, $R = 0.023$. The P1 and P2 atoms are situated in distorted trigonal prisms and the P3 atoms have octahedral coordination formed by lanthanum atoms (fig. 72). Three P1 and one P2 atom form a pyramid P_4. The shortest interatomic distances are $\delta_{La-P3} = 0.2949$; $\delta_{Ni-P1} = 0.2217$; $\delta_{P2-P3} = 0.2220$. Isotypic compounds are $Ce_6Ni_6P_{17}$, $Pr_6Ni_6P_{17}$, $La_6Pd_6P_{17}$ and $Ce_6Pd_6P_{17}$.

2.3.53. *$CeSiP_3$, oP40*

Structure type $CeSiP_3$ (Hayakawa et al. 1978; fig. 73, table 71) has space group $Pna2_1$, $a = 0.5861$, $b = 2.5295$, $c = 0.5712$.

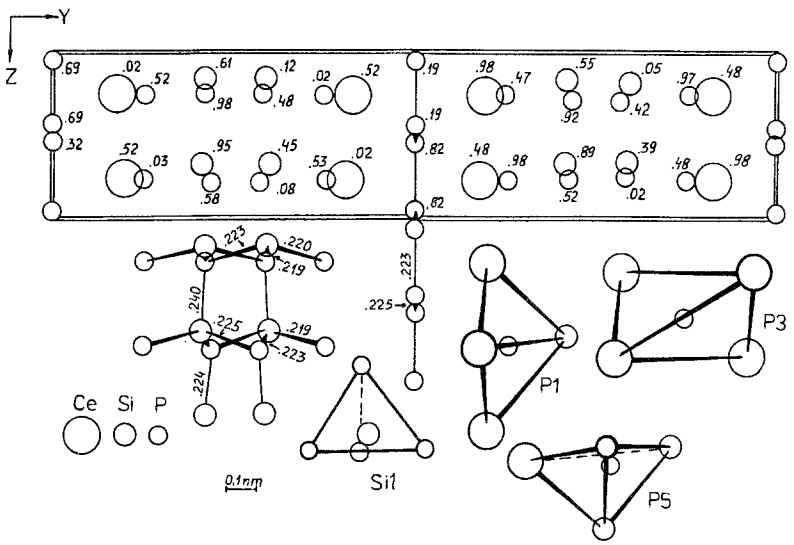

Fig. 73. Crystal structure of $CeSiP_3$, bond types of phosphorous atoms, and CPs of atoms.

Table 71
Atomic parameters for $CeSiP_3$

Atom	Position	Fractional coordinates			Atomic arrangement		
		x	y	z			
Ce1	4(*a*)	0.0229	0.0887	1/4			9P
Ce2	4(*a*)	0.5241	0.0978	0.7496			9P
Si1	4(*a*)	0.9449	0.2053	0.6613			4P
Si2	4(*a*)	0.6153	0.2086	0.1633			4P
P1	4(*a*)	0.5159	0.1270	0.2497	4Ce	1Si	
P2	4(*a*)	0.0278	0.1232	0.7456	4Ce	1Si	
P3	4(*a*)	0.3153	0.0034	0.5325	4Ce		2P
P4	4(*a*)	0.6877	0.9992	0.4398	4Ce		2P
P5	4(*a*)	0.5830	0.2158	0.7748	1Ce	3Si	
P6	4(*a*)	0.9807	0.2111	0.2430	1Ce	3Si	

Hayakawa et al. (1978) determined the structure of $CeSiP_3$ by a single-crystal method, $R=0.048$. The atoms P1 and P2 have coordination polyhedra in the form of distorted tetragonal pyramids and P3 and P4 atoms have tetrahedral environments formed by cerium atoms with two additional phosphorus atoms; the P5, P6 and all silicon atoms have a distorted tetrahedral coordination. The P1–P4 and silicon atoms form a fragment of framework and the P5–P6 atoms form a zigzag-like chain (fig. 73). The shortest interatomic distances are $\delta_{Ce2-P1}=0.2896$; $\delta_{Si1-P2}=0.2186$; $\delta_{P3-P4}=0.2248$.

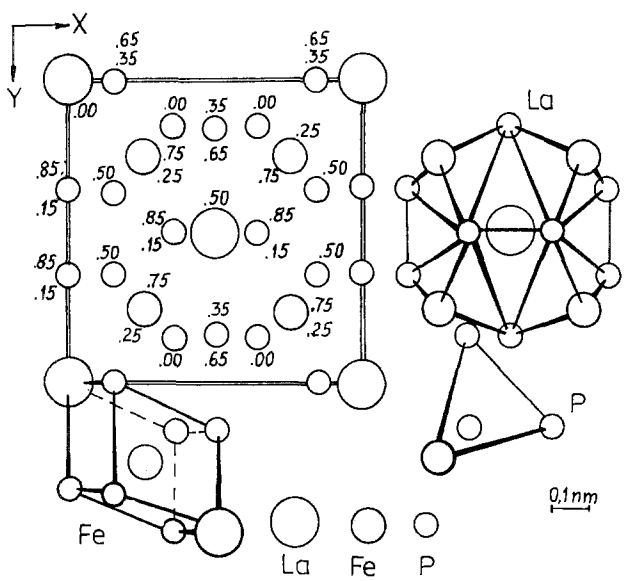

Fig. 74. Crystal structure of $LaFe_4P_{12}$ and CPs of atoms.

Table 72
Atomic parameters for $LaFe_4P_{12}$

Atom	Position	Fractional coordinates			Atomic arrangement		
		x	y	z			
La	2(*a*)	0	0	0		8Fe	12P
Fe	8(*c*)	1/4	1/4	1/4	2La		6P
P	24(*g*)	0	0.3539	0.1504		2Fe	2P

2.3.54. *$LaFe_4P_{12}$, cI34*

Structure type $LaFe_4P_{12}$ (Jeitschko and Braun 1977; fig. 74, table 72) has space group Im3, $a = 0.7832$.

Jeitschko and Braun (1977) determined the structure of $LaFe_4P_{12}$ by a single-crystal method, $R = 0.028$. $LaFe_4P_{12}$ may be considered to be of ST $CoAs_3$ with filled icosahedral holes by R atoms. The phosphorus atoms have their nearest environment in the form of a distorted tetrahedron with one additional La atom. Fe and P atoms form a polyanion $[Fe_4P_{12}]^{3-}$ with inserted La^{3+} ions. Interatomic distances are $\delta_{La-Fe} = 0.3391$; $\delta_{La-P} = 0.3012$; $\delta_{Fe-P} = 0.2259$; $\delta_{P-P} = 0.2288$ and 0.2356. Isotypic compounds are RFe_4P_{12} (R = Ce, Pr, Nd, Sm, Eu); RRu_4P_{12} (R = La, Ce, Pr, Nd, Eu); ROs_4P_{12} (R = La, Ce, Pr, Nd) and $R_xCo_4P_{12}$ (R = La, Ce, Pr, Nd, Yb; $x = 0.2$–0.25).

2.4. *Structure relationships of ternary and quaternary phosphides*

This section is devoted to the classification and structural relationships of ternary and quaternary rare-earth phosphides. The classification of the structures is accomplished using the same principles as for the binary phosphides, that is, by the form of the environment of the smallest (P) atoms (Krypyakevych 1977). One can observe the correlation between the phosphorus content and its atomic arrangement in the compound (table 73). Trigonal-prismatic coordination occurs in compounds with 26–36 at.% of P. In compounds with 33–50 at.% P an atomic arrangement in the form of an Archimedean cube dominates. Octahedral coordination is observed rarely, but over a wide concentration range (23–58 at.% P). In a number of structures trigonal-prismatic coordination dominates, but some octahedral holes may be occupied by P atoms (as observed in $(La, Ce)_{12}Rh_{30}P_{21}$). Tetrahedral coordination occurs only in compounds with a P content over 60 at.%.

Some structure types are very similar. For example, ST $Ho_5Ni_{19}P_{12}$ differs from $Sc_5Co_{19}P_{12}$ by only one position of the transition metal atoms: in the former compound nickel atoms occupy position 1(*a*) 000 and in the latter cobalt atoms half occupy the position 2(*b*) 00*z* ($z = 0.0827$) (sp.gr. $P\bar{6}2m$). STs $Nd_3Ni_7P_5$ (or $Nd_{12}Ni_{\sim 30}P_{20}$), $(La, Ce)_{12}Rh_{30}P_{21}$ and $Ce_6Ni_{15}P_{10}$ are also closely related: in $Nd_3Ni_7P_5$ empty octahedra occur with the center in the coordinate origin, in $(La, Ce)_{12}Rh_{30}P_{21}$ these octahedra have phosphorus atoms in their centers (position 2(*a*) 000) and in $Ce_6Ni_{15}P_{10}$ nickel atoms

Table 73
Classification of structure types of ternary and quaternary phosphides

CP of P atoms	ST
Trigonal prism	$La_2Ni_{12}P_5$, $LaNi_{10}P_4$, $Ce_9Ni_{26}P_{12}$, $ZrFe_4Si_2$, $SmNi_4P_2$, $Nd_2Ni_7P_4$, $Er_3Pd_7P_4$, $La_3Ni_{12}P_7$, $Sm_{20}Ni_{41.6}P_{30}$, $Tb_{15}Ni_{28}P_{21}$, $Yb_6Co_{19}P_{13}$, $Zr_2Fe_{12}P_7$, $Zr_2Rh_{12}P_7$, YCo_5P_3, $CeNi_{5-x}P_3$, $LaCo_5P_3$, $Ho_5Ni_{19}P_{12}$, $Sc_5Co_{19}P_{12}$, $Zr_6Ni_{20}P_{13}$, $Ho_6Ni_{20}P_{13}$, $Ho_{20}Ni_{66}P_{43}$, $LaLi_3P_2$, $TbLiCu_2P_2$, $Nd_3Ni_7P_5$, $Ce_6Ni_{15}P_{10}$, $Hf_2Co_4P_3$, TiNiSi, AlB_2, ZrNiAl, YbPtP, ZrBeSi, γ-EuPtP, $Tb_{1-x}NiP$, $LaCo_8P_5$, Sm_5Ge_4
Archimedean cube	PbFCl, $EuPt_2P_{1.62}$, $CeAl_2Ga_2$, $CaBe_2Ge_2$, $HfCuSi_2$, $CeCu_{1.12}P_{1.97}$, $SrZnBi_2$
Octahedron	$Eu_2Pt_7AlP_{\sim 3}$, $YbCu_{3-x}P_2$, $(La,Ce)_{12}Rh_{30}P_{21}$, Na_6ZnO_4, Ce_2S_2O, $YbCu_2P_2$, $La_6Ni_6P_{17}$
Tetrahedron	$CeSiP_3$, $LaFe_4P_{12}$

occupy 22% of the position 6(*h*) *xy*1/4, ($x = 0.0412$; $y = 0.0684$), sp.gr. $P6_3/m$, i.e. they are displaced from the centers of octahedra.

In some structures with the same compositions similar relationships resulted in a change of space group in which these compounds crystallize, for example $Zr_2Fe_{12}P_7$ ($P\bar{6}$)–$Zr_2Rh_{12}P_7$ ($P6_3/m$); $Zr_6Ni_{20}P_{13}$ ($P\bar{6}$)–$Ho_6Ni_{20}P_{13}$ ($P6_3/m$).

The peculiarities of a number of STs of ternary rare-earth phosphides require a critical examination of the data on their crystal structure. A great number of them are determined by the powder method which does not permit distinction between such small structure details.

All known structures of the ternary rare-earth phosphides with a phosphorus content close to 33.3 at.% (except $YbCu_3P_2$) are characterized by a metallic trigonal-prismatic arrangement of P atoms. Besides, these compounds have a number of common structure attributes:

– the rare-earth and transition-metal atoms exhibit the same or very similar coordination polyhedra and the same coordination numbers, respectively;

– all atoms form two flat nets mutually displaced by half of the shortest unit-cell dimension which corresponds to the height of a trigonal prism (0.36–0.4 nm);

– these trigonal prisms are assembled in columns stretched along the shortest unit-cell dimension and the columns themselves can link with one another via common rectangular faces or through common trigonal-prismatic edges, so that,

– no P–P contacts occur.

The existence of such common structure attributes gave an opportunity for numerous scholars to search for a unique scheme to describe these structures and predict new compounds. Thus, Madar et al. (1987b) used a crystallochemical model, based on metalloidal environment of the metal, for a uniform representation of the structures of ternary phases with a metal-to-nonmetal ratio close to 2:1. According to Madar et al. (1987b) the metal atoms may be situated in triangular prismatic, pyramidal, tetrahedral and triangular sites formed by P atoms, and their formal oxidation numbers are +3, +2, +1 and 0, respectively; for isolated (from one another) phosphorus atoms the formal

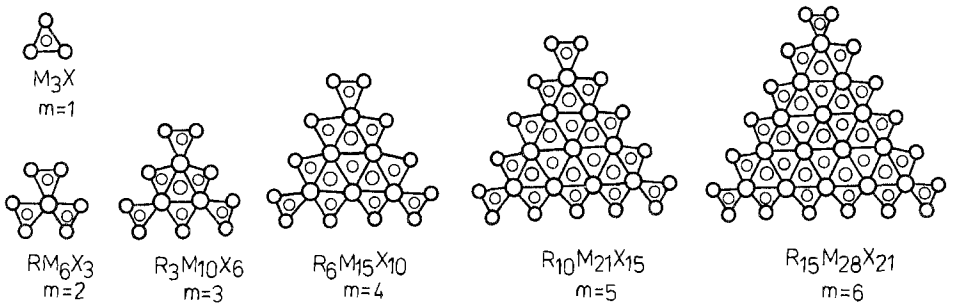

Fig. 75. Basic structure fragments in compounds belonging to a homologous family with metal-to-nonmetal ratio 2:1.

oxidation number is −3. Using such considerations the authors propose a scheme of valence compensation in the compounds belonging to specific families and predict a number of new compounds.

Pivan et al. (1987) consider the structure homogeneity of $(R, M)_2P$ phases and propose to describe them as formed from triangular units which occur in the structures "anti-AlB_2", Fe_2P, $Zr_2Fe_{12}P_7$, $Zr_6Ni_{20}P_{13}$, and $(La, Ce)_{12}Rh_{30}P_{21}$. Variation in the stacking of such fragments allows the description of a great number of phosphide and silicide structures and to predict a number of new compounds.

Earlier Yarmolyuk and Aksel'rud (1983) had proposed a general approach for the description of structures with a metal-to-nonmetal ratio of 2:1. The authors consider that the main characteristic feature of this structure family is the formation of slightly distorted hexagonal nets of metalloid atoms in the projection perpendicular to the smallest unit-cell direction. Proceeding from this consideration one can easily infer a great number of hexagonal structures by choosing a radius vector from the coordinate origin and taking into account the conditions mentioned above. For hexagonal structures, the unit-cell parameter a is determined from the ratio $a = a'\sqrt{K}$, where a' is the minimum period of the flat hexagonal net (distance between neighbouring metalloid atoms in planar net); K is the number of metalloid atoms in the unit cell.

For our structure description of the rare-earth phosphides we chose a similar approach based on the stacking of trigonal prisms formed by metal atoms; these determine the atomic arrangement of the phosphorus atoms. Isolated trigonal prism columns with phosphorus inside each prism, and/or their ensembles (fig. 75) are the basic structure fragments from which all structure types considered are built. The general chemical formula of such fragments may be written $R_{m(m-1)/2}M_{(m+1)(m+2)/2}P_{m(m+1)/2}$, where m is an integer and R and M correspond to the largest and medium-sized atoms, respectively.

The hexagonal structures form separate rows with the same stacking of the structure units; the composition of members of each row is described by a definite chemical formula.

The compounds Fe_2P (Rundqvist and Jellinek 1959, Carlsson et al. 1973), $Zr_2Fe_{12}P_7$ (Ganglberger 1968a), $Zr_6Ni_{20}P_{13}$ (Guerin et al. 1984), $(La,Ce)_{12}Rh_{30}P_{21}$ (Pivan and Guerin 1986), $Sm_{20}Ni_{41.6}P_{30}$ and $Tb_{15}Ni_{28}P_{21}$ (Chykhrij et al. 1993) form homologous

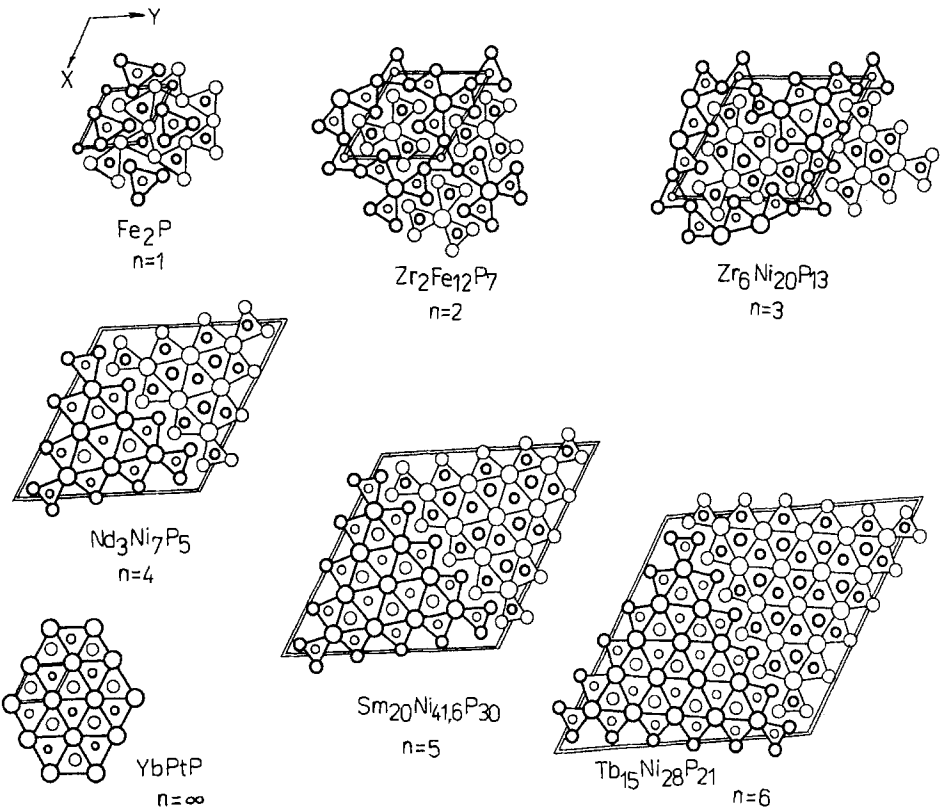

Fig. 76. Combination of structure units in phosphides with the general chemical formula $R_{n(n-1)}M_{(n+1)(n+2)}X_{n(n+1)+1}$.

rows with unit cells containing two identical units mutually displaced from $c/2$ (fig. 76). The general chemical formula of this series (without possible defects) may be written $R_{n(n-1)}M_{(n+1)(n+2)}X_{n(n+1)+1}$ (Pivan and Guerin 1986). The unit-cell dimension, a, of members of this series depends on n, the atomic fragment dimension (fig. 77). The average value of the parameter, a', for these structures is 0.357 (table 74). An increasing a' value is caused by the increasing content of the largest atoms. As a limiting member of this series one can consider the structure YbPtP (Wenski and Mewis 1986c) (fig. 77) with all trigonal prisms formed by R atoms and alternately filled with phosphorus and transition-metal atoms.

The unit cell of $Ho_{20}Ni_{66}P_{43}$ (Pivan et al. 1985b) contains close number of metalloid atoms as $Tb_{15}Ni_{28}P_{21}$ ($Z=2$) (Chykhrij et al. 1993) (the exception is a non-occupied position 2(*a*) 000 in the terbium compound), but the manner of trigonal prism stacking in the structures is different. The general chemical formula of members in the series with the same structure fragment stacking as in $Ho_{20}Ni_{66}P_{43}$ is $R_{n(n+1)}M_{(n+1)(n+6)}X_{n(n+3)+3}$ (Chykhrij et al. 1992) (fig. 78). The unit-cell content and lattice dimension, a, of members in this series are listed in table 75.

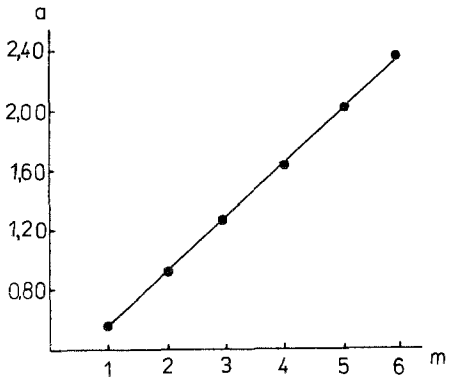

Fig. 77. Dependence of lattice parameter a on m for hexagonal structures with the general chemical formula $R_{m(m-1)}M_{(m+1)(m+2)}X_{m(m+1)+1}$.

Table 74
Determination of minimum period of flat hexagonal net for ternary rare-earth phosphides[a]

Compound	K	a	a'	Reference
$Tb_2Ni_{12}P_7$	7	0.9037	0.342	Jeitschko et al. (1978)
$Tb_6Ni_{20}P_{13}$	13	1.2694	0.352	Madar et al. (1985b)
$Tb_3Ni_7P_5$	21	1.6309	0.356	Chykhrij et al. (1989c)
$Sm_{20}Ni_{41.6}P_{30}$	31	2.0448	0.367	Chykhrij et al. (1993)
$Tb_{15}Ni_{28}P_{21}$	43	2.417	0.368	Chykhrij et al. (1993)

[a] $a'_{av} = 0.357$.

The general formula $R_{3n(n-1)}M_{3n(n+3)}X_{3n(n+1)+1}$ shows the unit-cell content of the other branch of this structure family. $Cr_{12}P_7$ (Chun and Carpenter 1979) and $Yb_6Co_{30}P_{19}$ (Jeitschko and Jakubowski-Ripke 1993) are the first representatives of this branch; further members will have the same form of structure fragment stacking but with different compositions (fig. 79, table 76).

Still one more homologous structure series compounds of Laue symmetry *6/mmm* form unit cells which contain two different structure units with the neighbour n values. The first representatives of this series are α-UCr_6P_4 (Brink and Jeitschko 1986, Jeitschko and Brink 1992) and $Zr_4Co_{13}Si_9$ (Gladyshevskii and Grin 1981) and probably the compound $Gd_4Co_{13}(Si, P)_9$ (Jakubowski-Ripke and Jeitschko 1987) has the same structure, but we have no data on the atomic parameters in this structure. The predicted composition in this series obeys the general formula $R_{n^2}M_{(n+2)^2-3}X_{(n+1)^2}$ (fig. 80, table 77).

The structure of $La_6Rh_{32}P_{17}$ is considered as belonging to a homologous family with a metal-to-nonmetal ratio of 2:1 with one non-occupied phosphorus position (Pivan et al. 1988).

Structures with infinite straight chains of these units have orthorhombic or monoclinic symmetry. An inventory of the orthorhombic structural examples actually known can be divided into three groups:

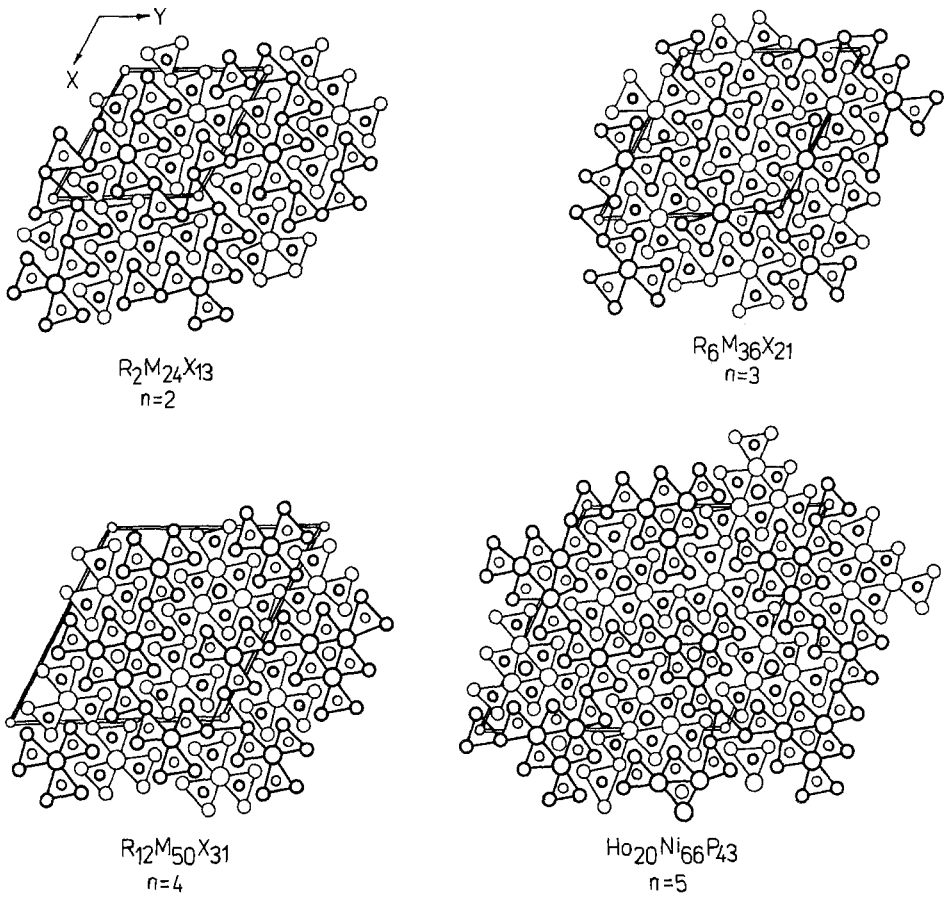

Fig. 78. Combination of structure units in ternary compounds with the general chemical formula $R_{n(n+1)}M_{(n+1)(n+6)}X_{n(n+3)+3}$.

Table 75
Unit cell content and lattice constant a of members of the series $R_{n(n+1)}M_{(n+1)(n+6)}X_{n(n+3)+3}$

n	Chemical formula	Structure type	a
0	M_6X_3	Fe_2P	0.5867
1	$M_{14}X_7$	–	0.90
2	$R_2M_{24}X_{13}$	–	1.26
3	$R_6M_{36}X_{21}$	–	1.60
4	$R_{12}M_{50}X_{31}$	–	1.95
5	$R_{20}M_{66}X_{43}$	$Ho_{20}Ni_{66}P_{43}$	2.3095

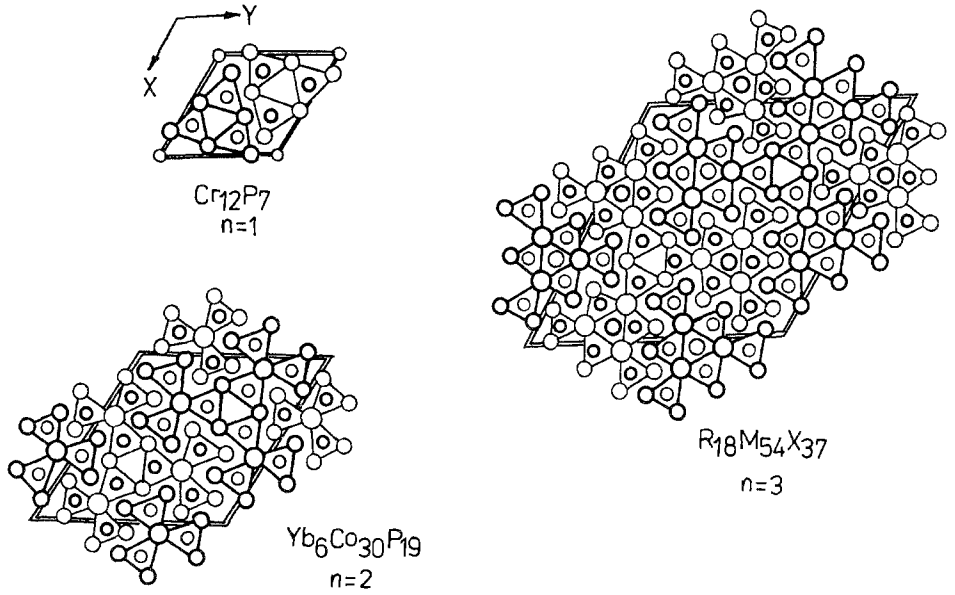

Fig. 79. Combination of structure units in ternary compounds with the general chemical formula $R_{3n(n-1)}M_{3n(n+3)}X_{3n(n+1)+1}$.

Table 76
Unit cell content and lattice constant a of members of the series $R_{3n(n-1)}M_{3n(n+3)}X_{3n(n+1)+1}$

n	Chemical formula	Structure type	a
1	$M_{12}X_7$	$Cr_{12}P_7$	0.8977
2	$R_6M_{30}X_{19}$	$Yb_6Co_{30}P_{19}$	1.4703
3	$R_{18}M_{54}X_{37}$	–	2.13
4	$R_{36}M_{84}X_{61}$	–	2.73

– structural examples with infinite linear chains are represented by Fe_2As (Elander et al. 1936), YNi_5Si_3 (Aksel'rud et al. 1976) and $HoCo_3P_2$ (Jeitschko and Jakubowski 1985) (fig. 81);

– UPt_2 (Villars and Calvert 1985) and $LaCo_5P_3$ (Davydov and Kuz'ma 1981) are the structural examples of infinite zigzag chains (shear after one unit) (fig. 82);

– anti-$PbCl_2$ (Co_2P, Rundqvist 1960) and YCo_5P_3 (Meisen and Jeitschko 1984b) represent structures with infinite zigzag chains with shear after two units (fig. 82).

The compound $CeNi_{5-x}P_3$ ($x=0.1$) (Babizhets'ky et al. 1992d) may be considered as a combination of chains as occur in YCo_5P_3 and $LaCo_5P_3$ (fig. 82).

The structure relationships of ternary rare-earth phosphides with metal-to-nonmetal ratio 2:1 are shown in fig. 83.

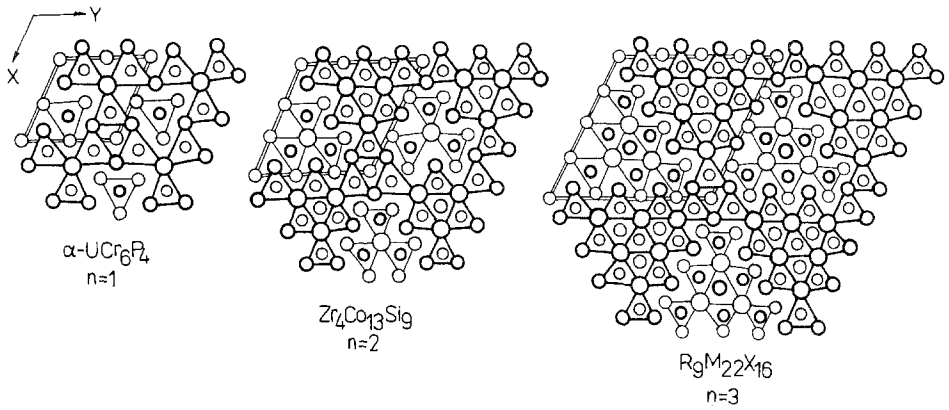

Fig. 80. Combination of structure units in ternary compounds with the general chemical formula $R_{n^2}M_{(n+2)^2-3}X_{(n+1)^2}$.

Table 77
Unit cell content and lattice constant a of members of the series $R_{n^2}M_{(n+2)^2-3}X_{(n+1)^2}$

n	Chemical formula	Structure type	a
1	RM_6X_4	α-UCr_6P_4	0.6877
2	$R_4M_{13}X_9$	$Gd_4Co_{13}(Si, P)_9$	1.0419
3	$R_9M_{22}X_{16}$	–	1.4
4	$R_{16}M_{33}X_{25}$	–	1.75

Decreasing phosphorus content in ternary rare-earth phosphides results in two possible changes in the structures:

– substitution of phosphorus atoms in trigonal prisms by transition-metal atoms; this is observed in the structure of $Ce_9Ni_{26}P_{12}$ (Babizhets'ky et al. 1992a) (fig. 84);

– variation of the mutual stacking and allocation of structure units. When the basic structure fragments associate with one another through a common vertex a transition metal from one could be substituted by an R-atom. Thus, the new structure fragments deriving from the basic, could be obtained and those that are known to exist are shown in fig. 85. The RM_4P_2, $R_2M_7P_4$, $R_3M_6P_4$ and $R_3M_{10}P_6$ structure units were detected for the first time in the compounds RNi_4P_2 (Chykhrij et al. 1986), $Nd_2Ni_7P_4$ (Chykhrij et al. 1990), $Er_3Pd_7P_4$ (Johrendt and Mewis 1994) and $SmNi_4P_2$ (Oryshchyn et al. 1988a), respectively (fig. 85).

The structure of $La_3Ni_{12}P_7$ (Babizhets'ky et al. 1992b) is formed by infinite chains of $LaNi_6P_3$ fragments with $La_2Ni_7P_4$ units inserted between the chains (fig. 86).

Upon further increasing transition-metal content (only nickel compounds are known) the fragment of face-centered cubic motif (half of a f.c.c. unit cell) is observed in the structures. Such extra nickel fragments are already known in compounds with a

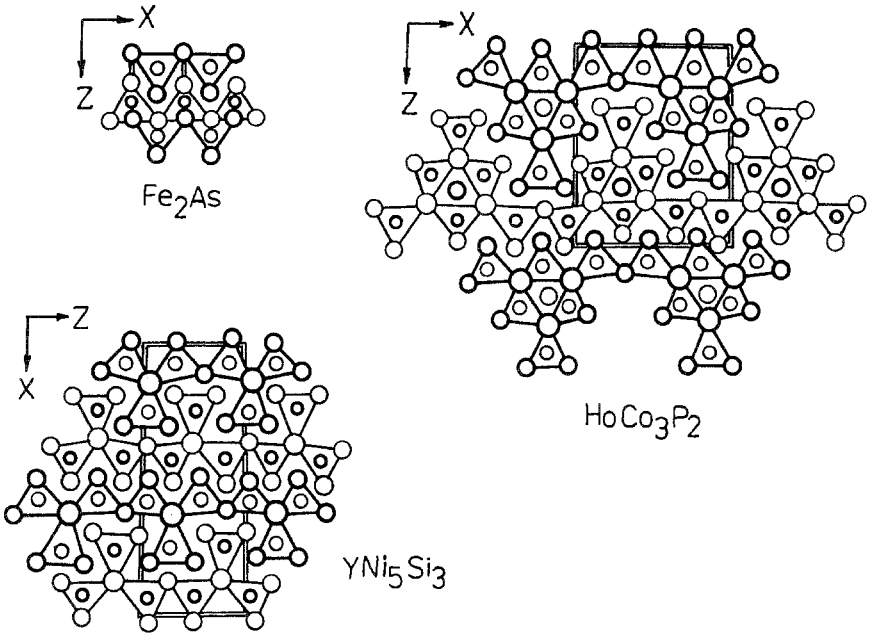

Fig. 81. Structural representation of Fe_2As, YNi_5Si_3 and $HoCo_3P_2$.

nickel content of 67.2 at.% ($SmNi_4P_2$) and higher. These are detected in the structure of $La_2Ni_{12}P_5$ (Kuz'ma et al. 1993) and $LaNi_{10}P_4$ (Babizhets'ky et al. 1992c) (fig. 86).

Compounds of RMP composition also have trigonal-prismatic coordination of phosphorus atoms, but a crystal structure complication is caused by multiplied increase of the lattice dimension c or by lowering the symmetry compared to the initial prototype AlB_2. Phosphorus atoms are always found in the centers of trigonal prisms and slightly influence the crystal structure modification. They especially influence the ratio of atomic radii of the R and M components (r_R/r_M). All ternary rare-earth phosphides of RMP composition may be divided into two groups. The first is formed by TiNiSi- and ZrNiAl-related compounds (ScCoP, RPdP where R = Tb–Lu; ScRuP). The r_R/r_M ratio for these compounds is in the range of 1.23–1.30 and it is close to the $r_M/r_{M'}$ ratio for ternary transition-metal phosphides (Lomnitskaya and Kuz'ma 1991a, Kuz'ma et al. 1989). The second group is formed by AlB_2-derivatives, namely AlB_2, YbPtP, ZrBeSi, β-EuPtP, γ-EuPtP and $Tb_{1-x}NiP$. Structure relationships of these structure types is shown in fig. 87. AlB_2-related structures have r_R/r_M ratio 1.25–1.56. So, a morphotropic transition between ST TiNiSi and ZrNiAl on the one hand, and the AlB_2-derivatives on the other, is caused by the ratio of atomic radii of the R and M components.

A gradual transformation from an octahedral coordination of phosphorus atoms to a trigonal-prismatic one is observed in La_2O_3-related structures. The La_2O_3 structure does not occur in ternary rare-earth phosphorus systems, but its isomorph superstructure Ce_2O_2S with the same symmetry and regular distribution of metal atoms does occur.

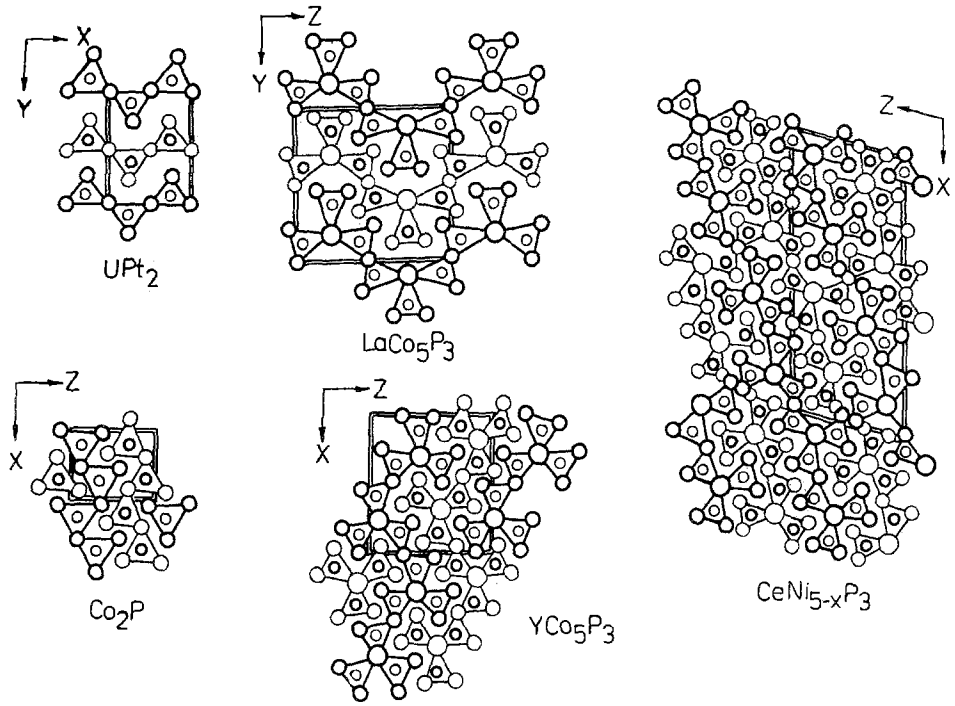

Fig. 82. Structural representation of UPt_2, $LaCo_5P_3$, Co_2P, YCo_5P_3 and $CeNi_{5-x}P_3$.

HEXAGONAL STRUCTURES

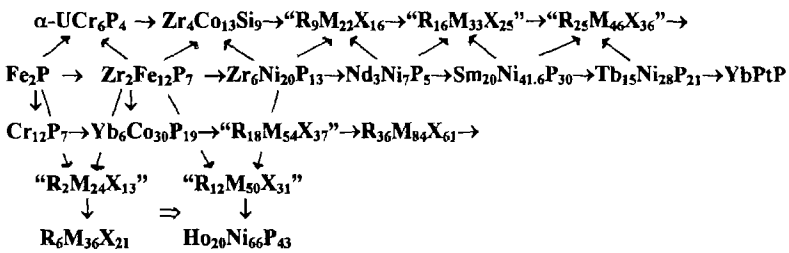

ORTHORHOMBIC STRUCTURES

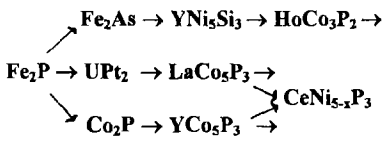

Fig. 83. Structure relations of ternary rare-earth phosphides with metal-to-nonmetal ratio 2:1.

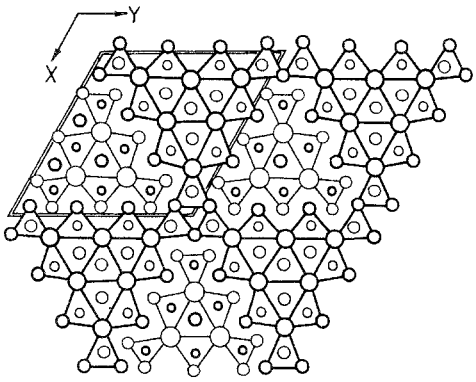

Fig. 84. Structural representation of $Ce_9Ni_{26}P_{12}$.

In $LaLi_3P_2$ an additional Li atom is inserted into a La_2O_3-type cell and $TbLiCu_2P_2$ possesses a similar unit cell (fig. 87). In the Ce_2O_2S-type structure octahedral coordination of the smallest atoms occurs and in $LaLi_3P_2$ and $TbLiCu_2P_2$ the coordination is trigonal-prismatic. Such changes correspond to the general tendency of having an octahedral environment of phosphorus atoms in compounds with higher P content.

The structure types PbFCl, $CeAl_2Ga_2$, $HfCuSi_2$, $SrZnBi_2$, $EuPt_2P_{1.62}$ and $CeCu_{1.12}P_{1.97}$ may be considered as layers of Archimedean cubes (A.c.), either empty or centered by the smallest atoms, along the Z axis (fig. 88). In the PbFCl-structure layers of filled A.c. alternate with layers of empty tetrahedra formed by the largest atoms. In phosphides with $CeAl_2Ga_2$ structure all the A.c. are filled with P atoms and in the $CaBe_2Ge_2$-type phosphides P atoms center only half of the A.c. and the other half is centered by transition-metal atoms; in the $HfCuSi_2$-type structure the A.c. filled by P atoms alternate with empty ones. The mutual allocation of the layers of Archimedean cubes is the same in all these structures. In $SrZnBi_2$ and $EuPt_2P_{1.62}$ the lattice parameter c is doubled; in the former compound the A.c. centered by phosphorus and transition-metal atoms alternate and in the latter compound the A.c. centered by phosphorus atoms alternate with empty ones. The structure of $CeCu_{1.12}P_{1.97}$ may be considered as an orthorhombic deformation of $SrZnBi_2$ with an additional position partially occupied by copper atoms. The motif of stacking of the A.c. is the same as that in $SrZnBi_2$ with additional copper atoms inside part of the empty A.c.

The structural and space group relationships of $LaFe_4P_{12}$ and other $CoAs_3$-related compounds has been determined by Jeitschko and Braun (1977) (fig. 89).

The greatest crystallochemical similarity of ternary rare-earth phosphides is observed in the structures of ternary uranium phosphides and silicides. In particular, both groups of compounds form homologous structure series with a metal-to-nonmetal ratio of 2:1. Yarmolyuk and Aksel'rud (1983) report the chemical formula $U_{n(n+1)}Co_{6(n^2+1)}Si_{4n^2+2}$ for the description of the unit-cell content of the compounds UCo_5Si_3 (Yarmolyuk et al. 1978), $U_6Co_{30}Si_{19}$ (Yarmolyuk et al. 1980) and $U_{10}Co_{51}Si_{33}$ (Aksel'rud et al. 1980). Brink and Jeitschko (1988) report the chemical formula $\square_{n(n+1)}A_{n(n-1)}T_{6(n^2+1)}X_{4n^2+3}$ for compounds $U_2Mo_{30}P_{19}$ (Brink and Jeitschko 1987), $U_6Mo_{60}P_{39}$ and $U_{12}Mo_{102}P_{67}$ (Brink

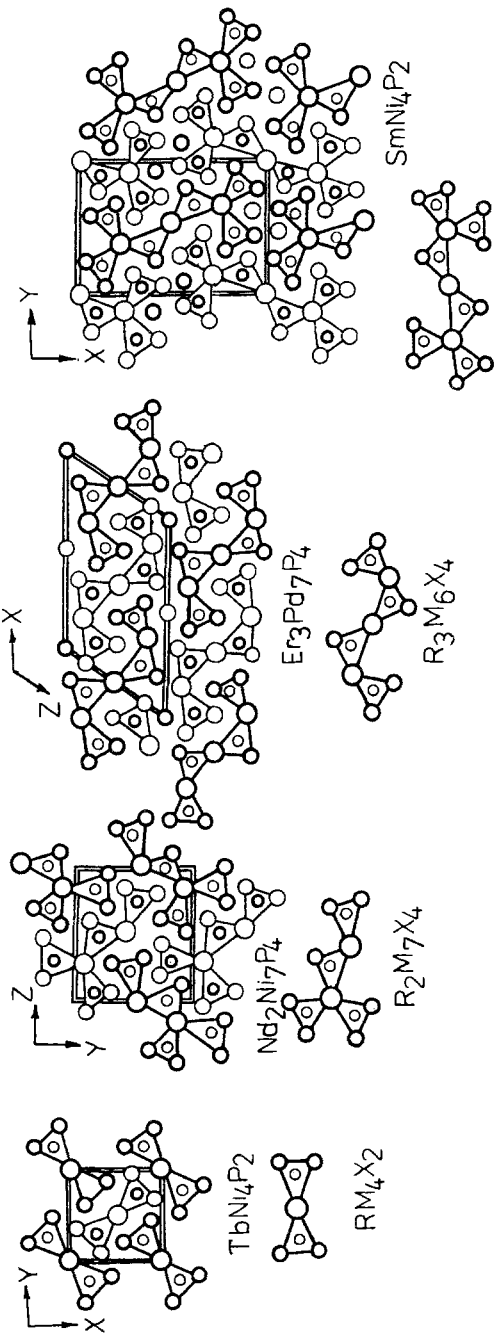

Fig. 85. Deriving structure units in ternary rare-earth and transition-metal structures with trigonal-prismatic coordination of phosphorus atoms, and structural representation of $TbNi_4P_2$, $Nd_2Ni_7P_4$, $SmNi_4P_2$ and $Er_3Pd_7P_4$.

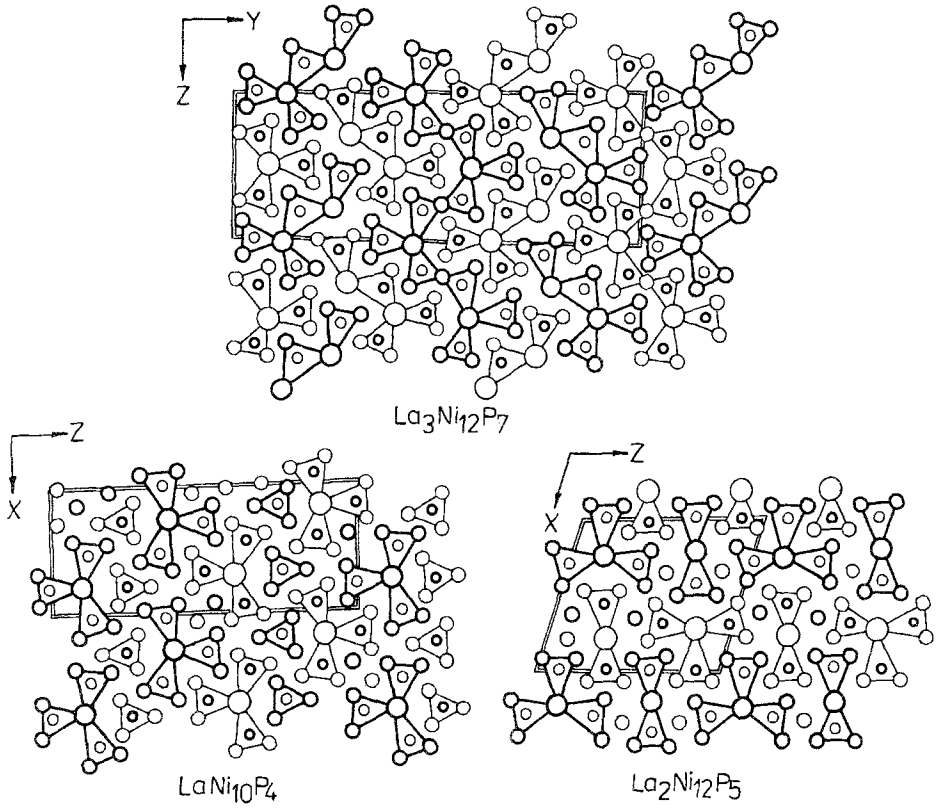

Fig. 86. Structural representation of $La_3Ni_{12}P_7$, $La_2Ni_{12}P_5$ and $LaNi_{10}P_4$.

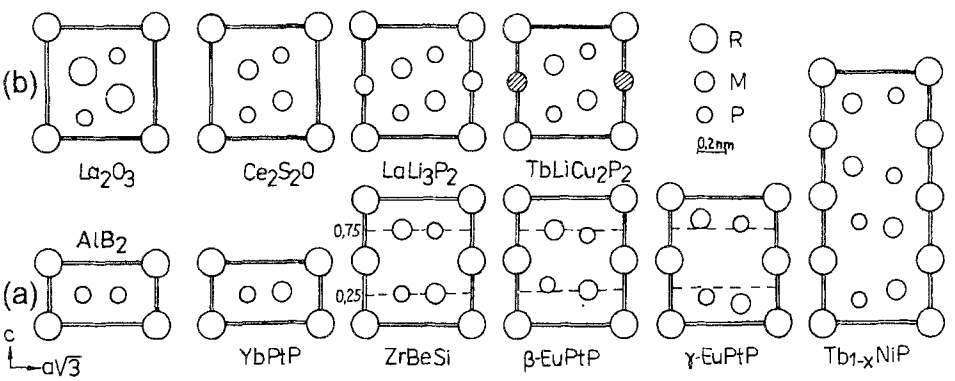

Fig. 87. Structural relations of (a) AlB_2-type and (b) La_2O_3-type related ternary rare-earth phosphides.

and Jeitschko 1988) and formula $\square_{3n(n+1)}A_{3n(n-1)}T_{18n^2+2}X_{12n^2+1}$ for an homologous series which is represented by $U_6Mo_{74}P_{49}$ (Brink and Jeitschko 1988).

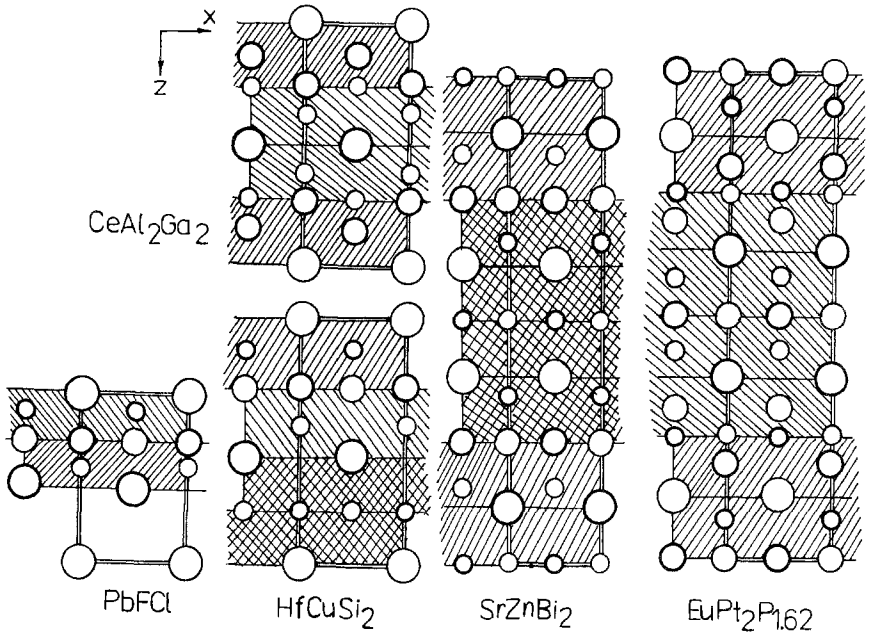

Fig. 88. Stacking of layers of Archimedean cubes in ternary rare-earth phosphides with $BaAl_4$-related structures.

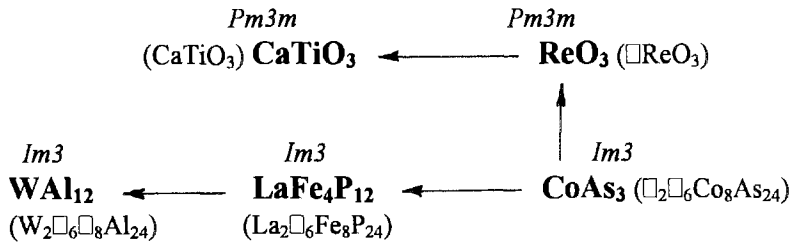

Fig. 89. Structural and space-group relations of $CoAs_3$-related compounds.

Structures consisting of the above mentioned structure fragments are known in the ternary systems R–Pd, Ru–Si.

Structures with trigonal-prismatic coordination of the smallest atoms occur widely in boron systems (Kuz'ma 1983), and silicon and germanium systems (Gladyshevskii and Bodak 1982, Bodak and Gladyshevskii 1985). A structural homologous serie with trigonal-prismatic coordination is known for the ternary cerium silicides; the general chemical formula for members of this series is $Ce_{2n^2+3n+2}(Ni, Si)_{2n^2+2}$ (Gladyshevskii and Bodak 1982). Trigonal prisms are formed only by cerium atoms and they are centered by a statistical mixture (Ni, Si). One can consider these structures as filled analogues of the S_2Th_7–$Rh_{20}Si_{13}$-series (Krypyakevych 1977).

In ternary rare-earth borides, trigonal-prismatic coordination of the smallest atoms remains to 67 at.% of B content, and B–B contacts occur in compounds with B content

higher than 50 at.% (Kuz'ma 1983). In these phosphides P–P bonds occur in compounds with a phosphorus content of 35.7 at.% ($LaCo_8P_5$) and higher and trigonal-prismatic coordination is observed up to 44.4 at.% of P ($Na_2Eu_3P_4$).

$BaAl_4$-related structures occur widely in the systems U–M–P and R–M–{B, Si, Ge}. In particular, in the system U–Cu–P the crystal structure of $BaAl_4$ derivatives, UCu_2P_2 (Zolnierek et al. 1987), $UCuP_2$ (Noël et al. 1987a) and $U_4Cu_4P_7$ (Noël et al. 1987b) have been determined.

Compounds with P content higher than 50 at.% have isotypic representatives among the respective pnictides (STs $LaFe_4P_{12}$, $La_6Ni_6P_{17}$) only.

2.5. *Physical properties of ternary rare-earth phosphides and the valence state of the rare-earth atoms*

2.5.1. *Magnetic properties and valence state of lanthanoid atoms*

The investigation of physical properties of ternary rare-earth phosphides is in progress. In this chapter published data concerning magnetic properties and the valence state of lanthanoid atoms in ternary rare-earth phosphides are brought together in tables according to their composition with increasing phosphorus content. Contradictory data and those not reflected in the tables are discussed separately. The character of changing unit-cell volumes for isotypic compounds indicates the valence state of rare-earth atoms shown as a plot of V vs. atomic number of R.

2.5.1.1. *$R_2Ni_{12}P_5$.* The data for $R_2Ni_{12}P_5$ are collected in table 78.

Table 78
Magnetic properties of $R_2Ni_{12}P_5$ compounds

Compound	Magnetic properties	T_C or T_N (K)	μ_{exp} (μ_B)	Valence state of R	Reference
$La_2Ni_{12}P_5$	Temperature-independent paramagnetism		–		Babizhets'ky et al. (1993b)
$Ce_2Ni_{12}P_5$	Curie–Weiss law		0.98	$Ce^{3+/4+}$	Babizhets'ky et al. (1993b)
$Pr_2Ni_{12}P_5$	Curie–Weiss law		3.51	Pr^{3+}	Babizhets'ky et al. (1993b)
$Eu_2Ni_{12}P_5$	Curie–Weiss law		3.80	Eu^{3+}	Babizhets'ky et al. (1993b)

2.5.1.2. *RNi_4P_2.* For compounds RNi_4P_2 (R = Y, Gd, Lu; table 79) anomalously high temperatures of magnetic ordering compared with other rare-earth phosphides are revealed by Chykhrij et al. (1991). The nature of magnetic order in these compounds is not ascertained. Taking into account cell volumes (fig. 90) we can make a supposition about normal R^{3+} valence states of all rare-earth atoms.

Table 79
Magnetic properties of RNi_4P_2 compounds

Compound	Magnetic properties	T_C or T_N (K)	μ_{exp} (μ_B)	Valence state of R	Reference
YNi_4P_2	Ferromagnetism	440		Y^{3+}	Chykhrij et al. (1991)
$GdNi_4P_2$	Antiferromagnetism	590		Gd^{3+}	Chykhrij et al. (1991)
$TbNi_4P_2$	Antiferromagnetism	730		Tb^{3+}	Chykhrij et al. (1991)
$DyNi_4P_2$	Ferromagnetism	610		Dy^{3+}	Chykhrij et al. (1991)
$HoNi_4P_2$	Antiferromagnetism	720		Ho^{3+}	Chykhrij et al. (1991)
$ErNi_4P_2$	Ferromagnetism	600		Er^{3+}	Chykhrij et al. (1991)
$TmNi_4P_2$	Ferromagnetism	450		Tm^{3+}	Chykhrij et al. (1991)
$YbNi_4P_2$	Ferromagnetism	600		Yb^{3+}	Chykhrij et al. (1991)
$LuNi_4P_2$	Ferromagnetism	390		Lu^{3+}	Chykhrij et al. (1991)

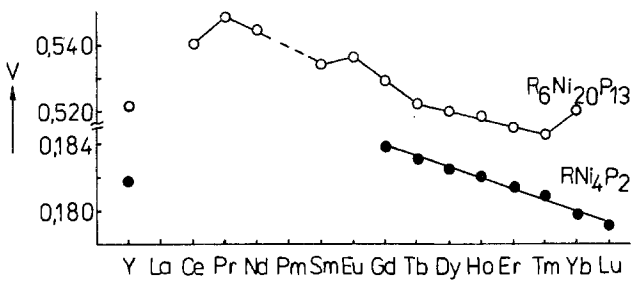

Fig. 90. Plot of unit cell volumes of RNi_4P_2 and $R_6Ni_{20}P_{13}$ compounds.

2.5.1.3. *$R_6Rh_{32}P_{17}$*. Pivan et al. (1988) revealed the absence of magnetic order of the transition-metal subcell and Pauli paramagnetism for $La_6Rh_{32}P_{17}$. The investigation of magnetic susceptibility of $Ce_6Rh_{32}P_{17}$ has shown that it does not fit a Curie–Weiss law and suggests strong crystal-field or Kondo effects.

2.5.1.4. *$R_2M_{12}P_7$*. The unit-cell plot of $R_2M_{12}P_7$ compounds (table 80; fig. 91) probably indicates a different valence state from R^{3+} for cerium (in compounds with Fe, Co, Ni, Rh), europium (with Ni) and ytterbium (with Rh and Ni) atoms. The magnetic moment on the transition-metal atoms is observed only in cobalt compounds, magnetic properties of all other $R_2M_{12}P_7$ compounds are caused by rare-earth atoms.

The compounds $R_2Mn_{12}P_7$ (R = Gd,Ho,Er,Tm) are paramagnetic at room temperature and show Curie–Weiss behavior down to about 200 K. The magnetic moments were proportional to the moments of the free R^{3+} ions. At lower temperatures the curves showed inconsistencies due to impurities (Jeitschko et al. 1993).

Attempts to study the properties of $Sc_2Co_{12}P_7$ were not succesful because of the great impurity of the samples (Raffius et al. 1991).

Table 80
Magnetic properties of $R_2M_{12}P_7$ compounds

Compound	Magnetic properties	T_C or T_N (K)	μ_{exp} [a] (μ_B)	Valence state of R	Reference
$Y_2Fe_{12}P_7$	Weak itinerant exchange				Raffius et al. (1991)
$Ce_2Fe_{12}P_7$	Intermediate valence of Ce			$Ce^{3+/4+}$	Reehuis and Jeitschko (1989)
$Ce_2Co_{12}P_7$	Ferromagnetism (Co)	48	1.21	$Ce^{3+/4+}$	Reehuis and Jeitschko (1989)
$Pr_2Fe_{12}P_7$	Pauli paramagnetism		3.8	Pr^{3+}	Reehuis and Jeitschko (1989)
$Pr_2Co_{12}P_7$	Ferromagnetism (Co)	136	(1.14) 3.5	Pr^{3+}	Reehuis and Jeitschko (1989)
$Pr_2Ni_{12}P_7$	Curie–Weiss law, antiferromagnetism (?)		3.51	Pr^{3+}	Zeppenfeld and Jeitschko (1993)
$Nd_2Fe_{12}P_7$	Pauli paramagnetism		3.8	Nd^{3+}	Reehuis and Jeitschko (1989)
$Nd_2Co_{12}P_7$	Ferromagnetism (Co)	140	(1.14) 3.5	Nd^{3+}	Reehuis and Jeitschko (1989)
$Nd_2Ni_{12}P_7$	Curie–Weiss law, antiferromagnetism (?)		3.2	Nd^{3+}	Zeppenfeld and Jeitschko (1993)
$Sm_2Fe_{12}P_7$	Van Vleck paramagnetism		2.0	Sm^{3+}	Reehuis and Jeitschko (1989)
$Sm_2Co_{12}P_7$	Ferromagnetism (Co), Van Vleck paramagnetism (Sm)	148	(1.14) 1.9	Sm^{3+}	Reehuis and Jeitschko (1989)
$Sm_2Ni_{12}P_7$	Van Vleck paramagnetism (Sm)		1.55	Sm^{3+}	Zeppenfeld and Jeitschko (1993)
$Eu_2Co_{12}P_7$	Ferromagnetism (Co) Van Vleck paramagnetism (Eu)	151	(1.14) 4.1	Eu^{3+}	Reehuis and Jeitschko (1989), Mörsen et al. (1988a)
$Gd_2Mn_{12}P_7$	Curie–Weiss law down to 200 K			Gd^{3+}	Jeitschko et al. (1993)
$Gd_2Fe_{12}P_7$	Pauli paramagnetism		7.8	Gd^{3+}	Reehuis and Jeitschko (1989)
$Gd_2Co_{12}P_7$	Ferromagnetism (Co)	145	(1.14) 8.1	Gd^{3+}	Reehuis and Jeitschko (1989)
$Gd_2Ni_{12}P_7$	Antiferromagnetism (Gd)	15	7.89	Gd^{3+}	Zeppenfeld and Jeitschko (1993)
$Tb_2Fe_{12}P_7$	Pauli paramagnetism		9.7	Tb^{3+}	Reehuis and Jeitschko (1989)
$Tb_2Co_{12}P_7$	Ferromagnetism (Co)	150	(1.14) 9.9	Tb^{3+}	Reehuis and Jeitschko (1989)
$Tb_2Ni_{12}P_7$	Methamagnetism	12	9.2	Tb^{3+}	Zeppenfeld and Jeitschko (1993)
$Dy_2Fe_{12}P_7$	Pauli paramagnetism		10.6	Dy^{3+}	Reehuis and Jeitschko (1989)
$Dy_2Co_{12}P_7$	Ferromagnetism (Co)	152	(1.14) 10.5	Dy^{3+}	Reehuis and Jeitschko (1989)
$Dy_2Ni_{12}P_7$	Ferromagnetism (Dy)	9	10.64	Dy^{3+}	Zeppenfeld and Jeitschko (1993)
$Ho_2Mn_{12}P_7$	Curie–Weiss law down to 200 K			Ho^{3+}	Jeitschko et al. (1993)
$Ho_2Fe_{12}P_7$	Pauli paramagnetism		10.9	Ho^{3+}	Reehuis and Jeitschko (1989)
$Ho_2Co_{12}P_7$	Ferromagnetism (Co)	152	(1.14) 10.4	Ho^{3+}	Reehuis and Jeitschko (1989)
$Ho_2Ni_{12}P_7$	Curie–Weiss law		10.7	Ho^{3+}	Pivan et al. (1986)
	Curie–Weiss law		10.44	Ho^{3+}	Zeppenfeld and Jeitschko (1993)
$Ho_2Rh_{12}P_7$	Antiferromagnetism (Ho)	2.7		Ho^{3+}	Pivan et al. (1985c)

continued on next page

Table 80, *continued*

Compound	Magnetic properties	T_C or T_N (K)	μ_{exp}[a] (μ_B)	Valence state of R	Reference
$Er_2Fe_{12}P_7$	Pauli paramagnetism		9.5	Er^{3+}	Reehuis and Jeitschko (1989)
$Er_2Mn_{12}P_7$	Curie–Weiss law down to 200 K			Er^{3+}	Jeitschko et al. (1993)
$Er_2Co_{12}P_7$	Ferromagnetism (Co)	146	(1.14) 7.4	Er^{3+}	Reehuis and Jeitschko (1989)
$Er_2Ni_{12}P_7$	Curie–Weiss law with magnetic order at $T < 2$ K		9.58	Er^{3+}	Zeppenfeld and Jeitschko (1993)
$Tm_2Mn_{12}P_7$	Curie–Weiss law down to 200 K			Tm^{3+}	Jeitschko et al. (1993)
$Tm_2Fe_{12}P_7$	Pauli paramagnetism		7.5	Tm^{3+}	Reehuis and Jeitschko (1989)
$Tm_2Co_{12}P_7$	Ferromagnetism (Co)	147	(1.14) 7.4	Tm^{3+}	Reehuis and Jeitschko (1989)
$Tm_2Ni_{12}P_7$	Curie–Weiss law with magnetic order at $T < 2$ K		7.54	Tm^{3+}	Zeppenfeld and Jeitschko (1993)
$Yb_2Fe_{12}P_7$	Pauli paramagnetism		4.5	Yb^{3+}	Reehuis and Jeitschko (1989)
$Yb_2Co_{12}P_7$	Ferromagnetism (Co)	134	(1.14) 4.2	Yb^{3+}	Reehuis and Jeitschko (1989)
$Yb_2Ni_{12}P_7$	Intermediate valence (Yb)		3.9	$Yb^{2+/3+}$	Zeppenfeld and Jeitschko (1993)
$Lu_2Fe_{12}P_7$	Weak itinerant exchange				Reehuis and Jeitschko (1989), Raffius et al. (1991)
$Lu_2Co_{12}P_7$	Ferromagnetism (Co)	150	1.14	Lu^{3+}	Reehuis and Jeitschko (1989)
$Lu_2Ni_{12}P_7$	Pauli paramagnetism		0	Lu^{3+}	Zeppenfeld and Jeitschko (1993)

[a] Values in parentheses are magnetic moments of the lanthanoid atoms in cobalt-containing compounds. These were calculated on the assumption that the cobalt atoms in these compounds have the same μ_{exp}(Co) as in $Lu_2Co_{12}P_7$: $\mu_{exp}(Co) = 1.14\,\mu_B$.

Mössbauer spectra indicate no magnetic order of Fe atoms in $Ce_2Fe_{12}P_7$ and $Gd_2Fe_{12}P_7$ (Reehuis and Jeitschko 1989). Magnetic susceptibility behavior of $Ce_2Fe_{12}P_7$ more closely resembles that of $Lu_2Fe_{12}P_7$ where Lu^{3+} does not carry a magnetic moment while for most $R_2Fe_{12}P_7$ compounds the Curie–Weiss law is observed. However, the absolute value of the magnetic susceptibility of $Ce_2Fe_{12}P_7$ is higher than that of $Lu_2Fe_{12}P_7$. This can be rationalized by both an intermediate or a tetravalent character of cerium atoms.

For $Ce_2Co_{12}P_7$ the Weiss constant (56 K) and $T_c = 48$ K differs considerably from that of other cobalt-containing phosphides (~150 K). It may indicate a valence state of cerium atoms different from 3+. The magnetic moment in this compound is slightly higher than that of Co atoms in $Lu_2Co_{12}P_7$, which may indicate a valence state of cerium atoms different from 4+ where Ce atoms are nonmagnetic. For all ferromagnetic compounds, $R_2Co_{12}P_7$, the magnetic moment of rare-earth atoms is calculated taking into account the magnetism of the Co atoms. The μ for Co is accepted as that for $Lu_2Co_{12}P_7$.

For $Sm_2Fe_{12}P_7$ Van Vleck paramagnetism is observed. Such temperature-independent contributions to the susceptibilities can also be assumed for the Sm^{3+} and Eu^{3+} ions

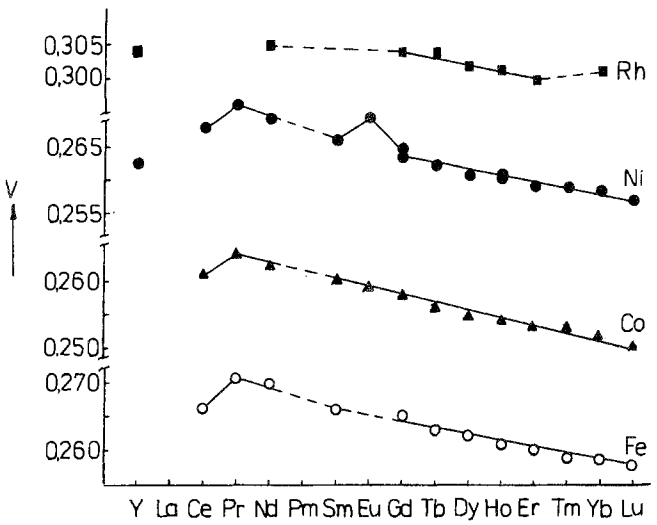

Fig. 91. Plot of unit cell volumes of $R_2M_{12}P_7$ compounds.

in cobalt-containing compounds, however, the magnetic behavior of these compounds is dominated by the cobalt atoms (Reehuis and Jeitschko 1989). The magnetic moment of the europium atoms in $Eu_2Co_{12}P_7$ ($\mu_{exp} = 4.1\,\mu_B$) is close to that expected for the Van Vleck ion Eu^{3+} ($\mu_{eff} = 3.52\,\mu_B$) and quite different from that of Eu^{2+} ($\mu_{eff} = 7.94\,\mu_B$) and "normal" Eu^{3+} ($\mu_{eff} = 0\,\mu_B$).

From the nickel compounds with the $Zr_2Fe_{12}P_7$-structure, $Sm_2Ni_{12}P_7$ shows Van Vleck paramagnetism, $Lu_2Ni_{12}P_7$ shows Pauli paramagnetism, while the magnetic susceptibility of the other phosphides obey the Curie–Weiss law resulting in magnetic moments corresponding to the free-ion values of the lanthanoid atoms. The ytterbium atoms in $Yb_2Ni_{12}P_7$ show mixed or intermediate valence behavior, while only a very small deviation of unit-cell volume from a linear dependency is observed for this compound (fig. 91). No magnetic order was observed for the praseodymium, neodymium, holmium, erbium and thulium compounds down to 2 K, while $Gd_2Ni_{12}P_7$ is antiferromagnetic, $Dy_2Ni_{12}P_7$ is ferromagnetic and $Tb_2Ni_{12}P_7$ is metamagnetic.

2.5.1.5. *$R_6Ni_{20}P_{13}$.* Proceeding from the unit-cell volumes of the $R_6Ni_{20}P_{13}$ compounds (fig. 90) we may expect the valence state of the R atoms to differ from 3+ for $Ce_6Ni_{20}P_{13}$ (3+/4+), $Eu_6Ni_{20}P_{13}$ and $Yb_6Ni_{20}P_{13}$ (both 2+/3+). The magnetic properties are studied only for $Ho_6Ni_{20}P_{13}$ (Pivan et al. 1986). They established antiferromagnetic order of the Ho subcell at 7.4 K; the magnetic moment of holmium atoms $\mu_{exp} = 10.52\,\mu_B$ is close to that for the Ho^{3+} ion ($\mu_{eff} = 10.60\,\mu_B$).

2.5.1.6. *$R_5M_{19}P_{12}$.* Data for $R_5M_{19}P_{12}$ compounds are given in table 81. A plot of the unit-cell volumes (fig. 92) suggests an intermediate-valence state of cerium atoms in these compounds. For copper compounds no physical property investigations were carried out.

Table 81
Magnetic properties of $R_5Ni_{19}P_{12}$ compounds

Compound	Magnetic properties	T_C or T_N (K)	μ_{exp} (μ_B)	Valence state of R	Reference
$La_5Ru_{19}P_{12}$	Temperature independent paramagnetism				Ghetta et al. (1989)
$Ce_5Ru_{19}P_{12}$	Temperature independent paramagnetism				Ghetta et al. (1989)
$Pr_5Ru_{19}P_{12}$	Non-linear behaviour of $1/\chi$ vs T		2.91	Pr^{3+}	Ghetta et al. (1989)
$Nd_5Ru_{19}P_{12}$	Non-linear behaviour of $1/\chi$ vs T		3.09	Nd^{3+}	Ghetta et al. (1989)
$Sm_5Ru_{19}P_{12}$	Temperature independent paramagnetism				Ghetta et al. (1989)
$Gd_5Ru_{19}P_{12}$	Paramagnetism with magnetic order at low temperature		8.23	Gd^{3+}	Ghetta et al. (1989)
$Tb_5Ru_{19}P_{12}$	Paramagnetism with magnetic order at low temperature		10.35	Tb^{3+}	Ghetta et al. (1989)
$Dy_5Ru_{19}P_{12}$	Paramagnetism with magnetic order at low temperature		10.96	Dy^{3+}	Ghetta et al. (1989)
$Ho_5Ru_{19}P_{12}$	Paramagnetism with magnetic order at low temperature		11.17	Ho^{3+}	Ghetta et al. (1989)
$Er_5Ru_{19}P_{12}$	Paramagnetism with magnetic order at low temperature		9.85	Er^{3+}	Ghetta et al. (1989)
$Yb_5Ru_{19}P_{12}$			4.46	Yb^{3+}	Ghetta et al. (1989)

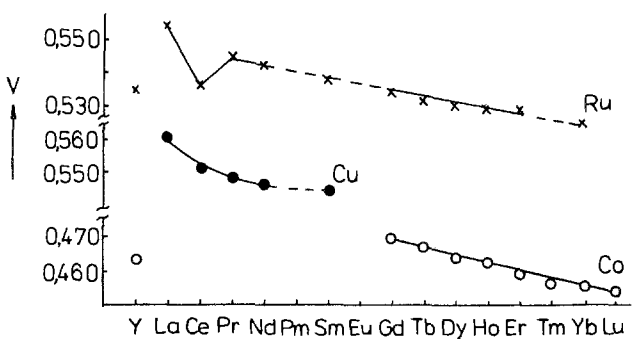

Fig. 92. Plot of unit cell volumes of $R_5M_{19}P_{12}$ compounds.

In $R_5Ru_{19}P_{12}$ the transition-metal atoms do not carry any magnetic moment, while in $R_5Co_{19}P_{12}$ cobalt atoms are magnetic (Ghetta et al. 1989).

2.5.1.7. *RM_5P_3.* In compounds with YCo_5P_3 structure (table 82), a plot of the unit-cell volumes (fig. 93) shows a deviation from linear dependence for $CeCo_5P_3$ and a small

Table 82
Magnetic properties of RM_5P_3 compounds

Compound	Magnetic properties	T_C or T_N (K)	μ_{exp} (μ_B)	Valence state of R	Reference
$HoFe_5P_3$	Ferromagnetism (Ho)	2	10.1	Ho^{3+}	Raffius et al. (1991)
$ErFe_5P_3$	Ferromagnetism (Er)	4	9.1	Er^{3+}	Raffius et al. (1991)
$TmFe_5P_3$	Ferromagnetism (Tm)	3	7.5	Tm^{3+}	Raffius et al. (1991)
$EuNi_5P_3$			8.1	Eu^{2+}	Badding and Stacy (1987a,b)

deviation for $LuCo_5P_3$. Such behavior of $LuCo_5P_3$ is explained by Jakubowski-Ripke and Jeitschko (1988) as a probable deviation from the ideal composition which may arise when lutetium atoms occupy the cobalt position with high coordination numbers.

The similarity in unit-cell volumes between $LaNi_5P_3$ and $EuNi_5P_3$ with the $LaCo_5P_3$-type structure suggests that the europium atoms are divalent, which has been confirmed by magnetic susceptibility measurements (Badding and Stacy 1987a,b).

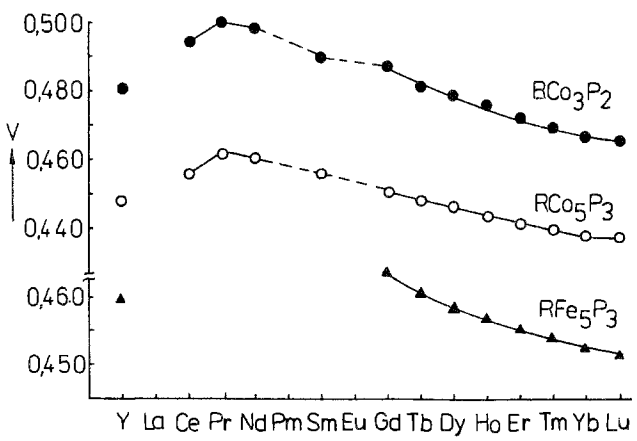

Fig. 93. Plot of unit cell volumes of RM_5P_3 and RCo_3P_2 compounds.

2.5.1.8. *RCo_3P_2.* From the plot of unit-cell volumes (fig. 93) one can predict a valence state different from 3+ for cerium atoms in $CeCo_3P_2$. The small deviation for $LuCo_3P_2$ is explained by Jeitschko and Jakubowski (1985) as similar to that for $LuCo_5P_3$.

2.5.1.9. *$YbCu_3P_2$ and $YbCu_2P_2$.* Klüfers et al. (1979) make a supposition about the trivalent state of ytterbium atoms in $YbCu_3P_2$ and $YbCu_2P_2$ based on the interatomic distances in the structures of these compounds.

2.5.1.10. *RCo_8P_5*. Data for RCo_8P_5 compounds are listed in table 83. For $PrCo_8P_5$ at low temperatures, ferromagnetic order is probable, considering the positive value of the Weiss constant (20 K) (Reehuis et al. 1988b).

Table 83
Magnetic properties of RCo_8P_5 compounds

Compound	Magnetic properties	T_C or T_N (K)	μ_{exp} (μ_B)	Valence state of R	Reference
$LaCo_8P_5$	Pauli paramagnetism				Reehuis et al. (1988b)
$PrCo_8P_5$	Curie–Weiss law		3.67	Pr^{3+}	Reehuis et al. (1988b)
$EuCo_8P_5$	Curie–Weiss law		7.70	Eu^{2+}	Reehuis et al. (1988b)

The valence state of Eu^{2+} in $EuCo_8P_5$ is confirmed by a Mössbauer study in the temperature range 4.2–300 K. Magnetic order at temperatures under 4.2 K is possible in $EuCo_8P_5$, as also indicated by the positive Weiss constant (+6 K) (Reehuis et al. 1988b).

2.5.1.11. *RMP*. Table 84 lists the data for RMP compounds. A valence state different from R^{3+} is expected for cerium and europium compounds from a cell volume plot (fig. 94). The europium valence in EuPtP, as examined by L_{III}-X-ray absorption and Mössbauer experiments (Lossau et al. 1989a) is a function of temperature and changes from 2.16 at 295 K to 2.40 at 4 K. In the region of the strongest temperature dependence of the valency the compound undergoes two first-order phase transitions at $T_1 = 235$ K and $T_2 = 190$ K characterized by discontinuities in the lattice constants and in the magnetic susceptibility. The first-order transition at T_2 is from β-EuPtP to γ-EuPtP, and the complex magnetic ordering is a property of γ-EuPtP (Lossau et al. 1989b). Mössbauer investigations (Lossau et al. 1989b) established three valence states of europium atoms: 10% of the europium ions order ferromagnetically at about $T_C = 25$ K, and 25% of the divalent europium ions show antiferromagnetic order at $T_N = 8.6$ K. The transition at 0.9 K is due to the magnetic ordering of a 40% fraction of europium ions having a valence of about 2.9 and therefore still having a magnetic moment of $0.8\,\mu_B$. However, it is also possible that at 0.9 K a rearrangement of the already ordered spins occurs, or that crystal-field effects become important at this temperature (Lossau et al. 1989b).

L_{III}-X-ray absorption and magnetic susceptibility measurements of $Eu_{0.5}Sr_{0.5}PtP$ have shown only one magnetic-order transition at 6.4 K and no first-order transition (Lossau et al. 1989b).

Lux et al. (1991a) examined the compounds $Eu_{1-x}Gd_xPtP$ and $Eu_{0.5}Sr_{0.5}PtP$ which have the same structures as α- or β-EuPtP, but do not undergo first-order phase transitions at $x > 0.05$. Their L_{III}-X-ray absorption and magnetic susceptibility studies have shown a dependence similar to that of EuPtP, but only one magnetic transition was found. The temperatures of antiferromagnetic order in these compounds depend on europium content and have the following values: 7.5 K (5% Gd), 6.8 K (10% Gd) and 6.4 K (50% Sr).

Table 84
Magnetic properties of RMP compounds

Compound	Magnetic properties	T_C or T_N (K)	μ_{exp} (μ_B)	Valence state of R	Reference
SmCoP	Ferromagnetism (Co)	85			Reehuis and Jeitschko (1990)
	Curie-like plus Van Vleck paramagnetism (Sm)		1.36	Sm^{3+}	
SmPtP	Temperature independent paramagnetism		1.43	Sm^{3+}	Kuss et al. (1987)
EuCuP	Ferromagnetism (Eu)	37	7.64		Tomuschat and Schuster (1984)
EuAgP	Ferromagnetism (Eu)	18	7.52		Tomuschat and Schuster (1984)
EuAuP	Ferromagnetism (Eu)	17	7.68		Tomuschat and Schuster (1984)
γ-EuPtP		0.9		$Eu^{2+/3+}$	Lossau et al. (1989b)
	Antiferromagnetism (Eu)	8.6			Lossau et al. (1989a,b)
	Ferromagnetism (Eu)	25			Lossau et al. (1989b)
α-EuPtP			7.46[a]	$Eu^{2+/3+}$	Lossau et al. (1989a)
EuPdP				$Eu^{2+/3+}$	Johrendt and Mewis (1990)
GdPtP	Antiferromagnetism (Gd)	65	7.8	Gd^{3+}	Kuss et al. (1987)
TbPtP	Ferromagnetism (Tb)	30	9.65	Tb^{3+}	Kuss et al. (1987)
TmPtP	Curie–Weiss law with magnetic order at $T < 10$ K		7.5	Tm^{3+}	Kuss et al. (1987)
YbPtP	Curie–Weiss law		4.4	Yb^{3+}	Kuss et al. (1987)
LuPtP	Pauli paramagnetism		0	Lu^{3+}	Kuss et al. (1987)

[a] At room temperature.

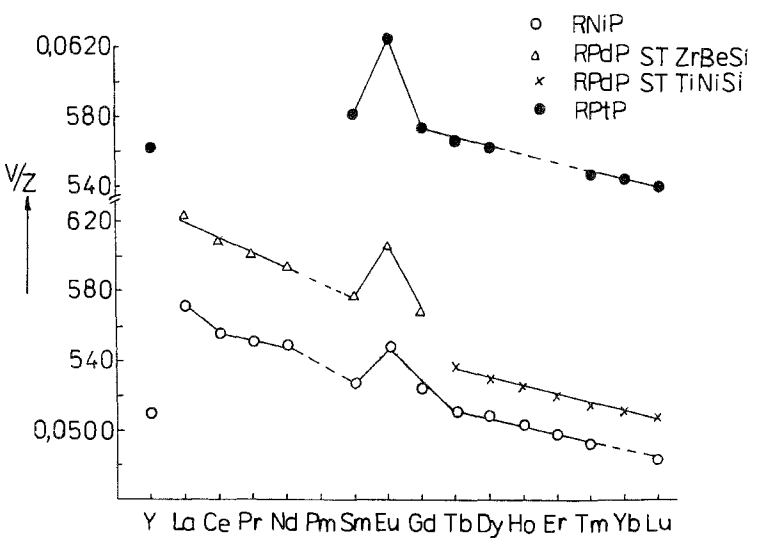

Fig. 94. Plot of one formula unit volume of RMP compounds.

Table 85
Magnetic properties of RM_2P_2 compounds

Compound	Magnetic properties	T_C or T_N (K)	μ_{exp} (μ_B)	Valence state of R	Reference
$LaFe_2P_2$	Pauli paramagnetism			La^{3+}	Mörsen et al. (1988b), Jeitschko et al. (1985)
$LaCo_2P_2$	Ferromagnetism (Co)	125	2.04	La^{3+}	Mörsen et al. (1988b)
$LaNi_2P_2$	Diamagnetism superimposed by slightly dependent Pauli paramagnetism			La^{3+}	Jeitschko and Reehuis (1987)
$LaRu_2P_2$	Diamagnetism			La^{3+}	Jeitschko et al. (1987)
$CeLi_2P_2$	Curie–Weiss law		2.52	Ce^{3+}	Zwiener et al. (1981)
$CeFe_2P_2$	Intermediate valence(Ce)			$Ce^{3+/4+}$	Reehuis and Jeitschko (1990)
$CeCo_2P_2$	Antiferromagnetism (Co)	440		$Ce^{3+/4+}$	Reehuis and Jeitschko (1990)
$CeNi_2P_2$	Intermediate valence (Ce)			$Ce^{3+/4+}$	Jeitschko and Reehuis (1987)
$CeRh_2P_2$	Interpretation of magnetic behaviour is complex				Madar et al. (1985a)
$PrLi_2P_2$	Curie–Weiss law		3.72	Pr^{3+}	Zwiener et al. (1981)
$PrFe_2P_2$	Antiferromagnetism (Pr) Ferromagnetism	27	3.6	Pr^{3+}	Reehuis and Jeitschko (1990)
$PrCo_2P_2$	Antiferromagnetism (Co) Ferromagnetism	304 19	3.08	Pr^{3+}	Reehuis and Jeitschko (1990)
$PrNi_2P_2$	Curie–Weiss law with magnetic order at $T < 12$ K		3.40	Pr^{3+}	Jeitschko and Reehuis (1987)
$PrRh_2P_2$	Van Vleck paramagnetism				Madar et al. (1985a)
$NdCo_2P_2$	Antiferromagnetism (Co)	309			Reehuis and Jeitschko (1990)
	Antiferromagnetism (Nd)	20		Nd^{3+}	Reehuis and Jeitschko (1990)
	Ferromagnetism (Nd)	<5			Reehuis and Jeitschko (1990)
			2.78	Nd^{3+}	Reehuis et al. (1993)
$NdNi_2P_2$	Curie–Weiss law with magnetic order at $T < 12$ K		3.47	Nd^{3+}	Jeitschko and Reehuis (1987)
$NdRh_2P_2$	Van Vleck paramagnetism				Madar et al. (1985a)
$SmCo_2P_2$	Antiferromagnetism (Co)	302			Reehuis and Jeitschko (1990)
	Curie-like plus Van Vleck paramagnetism (Sm)			Sm^{3+}	
$SmNi_2P_2$	Curie-like plus Van Vleck paramagnetism		1.50	Sm^{3+}	Jeitschko and Reehuis (1987)
$EuFe_2P_2$	Ferromagnetism (Eu)	27	7.74	Eu^{2+}	Mörsen et al. (1988b)
$EuCo_2P_2$	Antiferromagnetism (Eu)	67	6.9	Eu^{2+}	Reehuis et al. (1988a, 1992)
	Antiferromagnetism (Eu)	67	8.1	Eu^{2+}	Mörsen et al. (1988b)
$EuNi_2P_2$	Intermediate valence(Eu)		7.3	$Eu^{2+/3+}$	Mörsen et al. (1988b)
$EuZn_2P_2$			7.85	Eu^{2+}	Zwiener et al. (1981)
$EuPd_2P_2$				Eu^{2+}	Sampathkumaran et al. (1985a)

continued on next page

Table 85, *continued*

Compound	Magnetic properties	T_C or T_N (K)	μ_{exp} (μ_B)	Valence state of R	Reference
$EuRu_2P_2$	Ferromagnetism (Eu)	32	7.8	Eu^{2+}	Wenski and Mewis (1986a)
$EuPt_2P_{1.62}$	Antiferromagnetism (Eu)	17	7.6	Eu^{2+}	Wenski and Mewis (1986a)
$GdNi_2P_2$	Antiferromagnetism (Gd)	10.5 9.5	7.86	Gd^{3+}	Jeitschko and Reehuis (1987) Reehuis et al. (1991)
$TbNi_2P_2$	Paramagnetism with magnetic order at $T < 10$ K		9.61	Tb^{3+}	Jeitschko and Reehuis (1987)
	Antiferromagnetism (Tb)	10.5			Reehuis et al. (1991)
$DyNi_2P_2$	Paramagnetism with magnetic order at $T < 10$ K		10.55	Dy^{3+}	Jeitschko and Reehuis (1987)
	Antiferromagnetism (Dy)	5.0			Reehuis et al. (1991)
$ErNi_2P_2$	Paramagnetism with magnetic order at $T < 10$ K		9.38	Er^{3+}	Jeitschko and Reehuis (1987)
	Antiferromagnetism (Er)	2.2			Reehuis et al. (1991)
$YbNi_2P_2$	Intermediate valence Yb			$Yb^{2+/3+}$	Jeitschko and Reehuis (1987)
$YbZn_2P_2$	Intermediate valence Yb		2.65	$Yb^{2+/3+}$	Zwiener et al. (1981)

2.5.1.12. *RM_2P_2.* Data for RM_2P_2 compounds appear in table 85. Deviations from a linear dependence of the unit-cell volumes of compounds with the $ThCr_2Si_2$ and $CaBe_2Ge_2$-structures (fig. 95) are observed for lanthanum (with Fe, Co, Ru, Pd), cerium (with Fe, Co, Ni, Rh), europium (with Fe, Co, Ni, Ru, Rh, Pd) and ytterbium (with Ni, Ru, Pd) compounds. For $LaRu_2P_2$ and $LaPd_2P_2$ the decreasing and increasing of unit-cell volumes, respectively, are explained by deviations from the ideal composition (Jeitschko et al. 1987). The magnetic characteristics of $LaFe_2P_2$ and $LaCo_2P_2$ indicate the normal valence state, La^{3+}, for lanthanum atoms; Reehuis and Jeitschko (1990) explained the cell volume deviations mentioned previously for $LaFe_2P_2$ and $LaCo_2P_2$ by the increase of P–P distances (0.3176 and 0.3156, respectively), while that in $LaNi_2P_2$ is 0.2497. This leads to increasing cell parameter c and unit-cell volume.

The magnetic susceptibilities of $CeNi_2P_2$ and $YbNi_2P_2$ at $T > 50$ K are temperature independent and increase at lower temperatures (Jeitschko and Reehuis 1987). This is explained by deviations of the valence state of cerium and ytterbium from 3+ to 4+ and 2+, respectively.

An interpretation of the magnetic behavior of $CeRh_2P_2$ is not given; no ferromagnetic order was observed for any other RRh_2P_2 compound (Madar et al. 1985a).

Among all RM_2P_2 compounds magnetic order of the transition-metal subcell is observed only for cobalt-containing compounds. Reehuis et al. (1992) carried out a neutron diffraction study of the magnetic structure of $EuCo_2P_2$ and established that the cobalt atoms are not magnetic; μ_{eff} of europium atoms is 6.9 μ_B. The order of the Eu moments is ferromagnetic within the basal planes in agreement with the positive Weiss

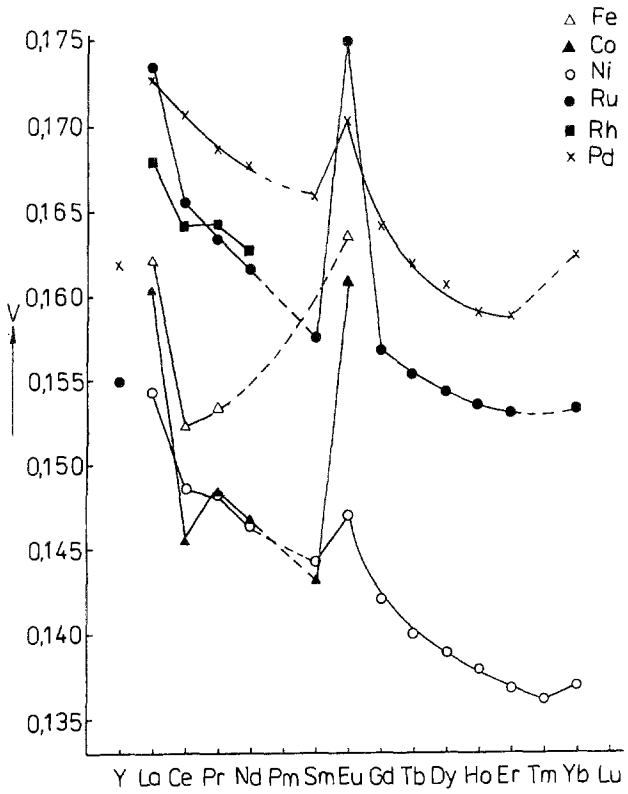

Fig. 95. Plot of unit cell volumes of RM_2P_2 compounds.

constant obtained from magnetic susceptibility measurements. Along the c-axis the order is that of an antiferromagnetic spiral and this agrees with the over-all antiferromagnetic behavior of the magnetic susceptibility.

Reehuis et al. (1993) carried out a neutron diffraction study of the magnetic order in the phosphides $PrCo_2P_2$ and $NdCo_2P_2$. In agreement with magnetic susceptibility data (Reehuis and Jeitschko 1990) the magnetic moments of both the Pr^{3+} ions and cobalt atoms of $PrCo_2P_2$ were found to order antiferromagnetically with different, well-defined Néel temperatures. In contrast, in $NdCo_2P_2$ only the magnetic moments of the cobalt atoms order at a well-defined Néel temperature, while the magnetic order of the Nd^{3+} moments is induced gradually at lower temperature with the same propagation vector through the magnetic order of the cobalt atoms. At low temperatures the magnetic moments of the cobalt atoms were found to be about $\mu_{exp} = 0.8\,\mu_B$ in both $PrCo_2P_2$ and $NdCo_2P_2$ compounds.

The compound $EuNi_2P_2$ shows no magnetic order down to 4.2 K (Mörsen et al. 1988b). From the slope of $1/\chi$ vs T plot Jeitschko and Reehuis (1987) obtained an effective magnetic moment of $\mu_{exp} = 7.43\,\mu_B$, while μ_{eff} for Eu^{2+} is $7.94\,\mu_B$ and for

Eu^{3+} it is 3.50 μ_B. Linear interpolation suggests a valence of 2.11 for Eu in $EuNi_2P_2$. From the deviation of the straight line in the cell dimensions europium valency may be 2.65 (Reehuis and Jeitschko 1987); from the L_{III}-X-ray absorption edge an intermediate valence of 2.46 is obtained (Warthmann et al. 1985); using Mössbauer spectra Nagarajan et al. (1985) have shown that the valence of Eu is increasing with decreasing temperature and becomes 2.25 at room temperature, while Nagarajan et al. (1981) obtained a value for Eu valence of 2.5 at room temperature.

Similar behavior of the europium valence occurs in dilute compounds $Eu_{0.05}Y_{0.95}Ni_2P_2$, where even at 4.2 K Eu is in a strongly mixed valence state (Sampathkumaran et al. 1986).

Contradictory data exist about the valence state of Eu atoms in $EuPd_2P_2$. The deviation of unit-cell volume (Jeitschko and Hofmann 1983), the europium L_{III}-edge X-ray absorption spectrum (Sampathkumaran et al. 1985b), and photoemission from the europium 3d core level (Wertheim et al. 1985) suggest a mixed valence, while magnetic susceptibility measurements (Sampathkumaran et al. 1984), the ^{151}Eu Mössbauer isomer shifts (Sampathkumaran et al. 1984, 1985b), and the photoemission of the 4f shell (Wertheim et al. 1985) indicate divalent europium. Similar behavior of europium atoms in the dilute compound $Eu_{0.05}Y_{0.95}Pd_2P_2$, in particular, L_{III}-edge subspectra indicate an identical relative weight of Eu^{2+} and Eu^{3+} to those in the concentrated compound $EuPd_2P_2$ (Sampathkumaran et al. 1986). This means that the occurrence of such final-state effects is not concerned with Eu–Eu interaction, but depends on the Eu–ligand interaction. Sampathkumaran et al. (1986) explained these effects by the promotion of shake-up 4f electrons into a ligand orbital, which is covalently mixed with europium 4f electrons in these compounds.

The magnetic behavior of $EuRu_2P_2$ indicates only a divalent state of europium atoms (Wenski and Mewis 1986a).

In the compound $YbZn_2P_2$ partial substitution of zinc atoms by copper leads to an increase of the ytterbium valence which rises to a value of 3+ at a composition of $YbCuZnP_2$ ($\mu_{eff} = 4.71\ \mu_B$) (Zwiener et al. 1981).

The magnetic susceptibility of $AgZnLaP_2$ depends very slightly on the temperature which is characteristic of diamagnetic semiconductors, while the magnetic susceptibility of $AgZnSmP_2$ is temperature independent and characteristic of paramagnetic compounds (Tejedor and Stacy 1990).

2.5.1.13. *$R_xU_{1-x}P$.* Niedzielski and Troć (1984) investigated the magnetic susceptibility of the solid solutions $Pr_xU_{1-x}P$ and $Nd_xU_{1-x}P$ and found antiferromagnetic order with Néel temperatures as follows: 30 and 20 K for praseodymium compounds with $x = 0.68$ and 0.28, respectively; and for $Nd_xU_{1-x}P$, 84, 60, 28 and 20 K at $x = 0.38$, 0.48, 0.68 and 0.78, respectively. Troć et al. (1978) built a magnetic diagram of the systems NdP–UP and PrP–UP.

2.5.1.14. *RM_4P_{12}.* Data for RM_4P_{12} compounds are collected in table 86. Deviations from a linear dependence of the unit-cell volumes of RM_4P_{12} compounds (fig. 96) probably

Table 86
Magnetic properties of RM_4P_{12} compounds

Compound	Magnetic properties	T_C or T_N (K)	μ_{exp} (μ_B)	Valence state of R	Reference
$LaFe_4P_{12}$	Pauli paramagnetism		1.46	La^{3+}	Grandjean et al. (1984)
$CeFe_4P_{12}$	Intermediate valence Ce		1.07	$Ce^{3+/4+}$	Grandjean et al. (1984)
$PrFe_4P_{12}$	Ferromagnetism	1.05		Pr^{3+}	Meisner (1981)
$PrRu_4P_{12}$	Ferromagnetism	0.35		Pr^{3+}	Meisner (1981)
$NdFe_4P_{12}$	Ferromagnetism	1.97		Nd^{3+}	Meisner (1981)
$NdRu_4P_{12}$	Ferromagnetism	1.51		Nd^{3+}	Meisner (1981)
$EuFe_4P_{12}$	Ferromagnetism (Eu)	100	6.2	$Eu^{2+/3+}$	Grandjean et al. (1983)

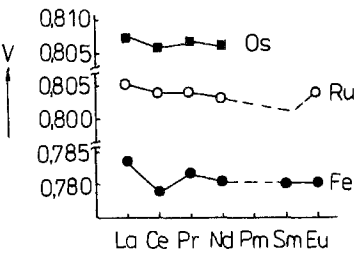

Fig. 96. Plot of unit cell volumes of RM_4P_{12} compounds.

indicate different valence states of cerium atoms from 3+ in $CeFe_4P_{12}$, $CeRu_4P_{12}$, $CeOs_4P_{12}$ (to 4+) and of europium atoms in $EuFe_4P_{12}$ and $EuRu_4P_{12}$ (Jeitschko and Braun 1977).

$CeFe_4P_{12}$ and $CeRu_4P_{12}$ do not undergo magnetic ordering down to 4.2 K (Meisner 1981). The nature of the magnetism in $PrRu_4P_{12}$ has not been explained.

Grandjean et al. (1984) have shown that relative quantities of the Eu^{2+} and Eu^{3+} in $EuFe_4P_{12}$ do not change with temperature. The Mössbauer spectra indicate their ratio as 1:1 because the valence of europium atoms is 2.5. Iron atoms in $EuFe_4P_{12}$ do not carry a magnetic moment and the magnetic behavior of this compound is connected with the ordering of europium subcell (Gerard et al. 1983). In $LaFe_4P_{12}$ the magnetic moment of the Fe atoms is less than 0.01 μ_B (Shenoy et al. 1982).

2.5.1.15. *$Eu(P,As)_3$.* Semimetallic $Eu(As_{1-x}P_x)_3$ with $x < 0.98$ is antiferromagnetically ordered with $T_N = 11.4$–8.5 K depending on x (Chattopadhyay et al. 1988a–c) with a phase transition in sine-wave amplitude-modulated phase, which is accompanied by a first-order transition into the helimagnetic phase (Chattopadhyay et al. 1987a,b). Bauhofer et al. (1985) connect antiferromagnetic order in these compounds with indirect interaction of europium atoms through nonmetallic atoms (P or As).

2.5.2. *Electrical properties*

The temperature dependence of the resistivity of ternary phosphides RNi_4P_2 (R = Y, Gd–Lu) in the range 77–290 K has shown typical metallic conductivity with resistivity values of about 200–600 mΩ cm (Chykhrij 1990b). The phosphides $R_2Ni_{12}P_5$ (R = La, Ce, Pr, Eu) demonstrate a similar character of conductivity and have absolute values of electrical resistivity in the same range with RNi_4P_2 compounds (Babizhets'ky et al. 1993b).

No transition to a superconductive state was found above 1.7 K for $Ce_2Fe_{12}P_7$ and $Lu_2Fe_{12}P_7$ (Reehuis and Jeitschko 1989) and $LaCo_8P_5$ (Reehuis et al. 1988b); above 2 K for $La_6Rh_{32}P_{17}$ and $Ce_6Rh_{32}P_{17}$ (Pivan et al. 1988); above 4.2 K for ScRuP and $Sc_2Ru_{12}P_7$ (Ghetta et al. 1986). The resistivity value of needle-like single crystals of $Ce_6Rh_{32}P_{17}$ was found to be 580 mΩ cm at 293 K and 495 mΩ cm at 2 K (Pivan et al. 1988). Pivan et al. (1986) determined that the temperature dependence of $Ho_6Ni_{20}P_{13}$ single crystals is typical of metallic conductors; the electrical conductivity of $Ho_2Ni_{12}P_7$ was measured only at room temperature.

The electrical properties of the phosphides $CuZnSmP_2$, $AgZnSmP_2$ and $AgZnLaP_2$ were investigated by Tejedor and Stacy (1990). The resistivity values of all three compounds are in the range of 0.1–0.2 mΩ cm, which is an indication that these materials are small band gap semiconductors. At temperatures above approximately 100 K the resistivity variation of $AgZnSmP_2$ and $CuZnSmP_2$ is much like that of a metal (increases with increasing temperature). This type of behavior is characteristic of heavily doped (generated) semiconductors. $AgZnLaP_2$ at $T > 100$ K exhibits typical semiconductor behavior (resistivity decreases with increasing temperature).

Investigations of the electrical properties of the compounds RM_2P_2 have shown metallic conductivity. The phosphide $LaRu_2P_2$ became a superconductor at 4.1 K (Jeitschko et al. 1987), while for YRu_2P_2 (Jeitschko et al. 1987), $LaFe_2P_2$ (Jeitschko et al. 1985), $LaNi_2P_2$ and $CeNi_2P_2$ (Jeitschko and Reehuis 1987) no transition to a superconductive state was found at temperatures above 1.8 K, and for $LuRh_2P_2$ (Madar et al. 1985a) no transition was found above 1.5 K.

Meisner (1981) found that $LaFe_4P_{12}$ and $LaRu_4P_{12}$ are superconductors at temperatures below 4.08 and 7.02–6.79, respectively. $CeFe_4P_{12}$, $CeRu_4P_{12}$, $PrFe_4P_{12}$ and $PrRu_4P_{12}$ do not undergo a transition into a superconductive state above 0.35 K, and $NdFe_4P_{12}$ and $NdRu_4P_{12}$ not above 1 K (Meisner 1981). Grandjean et al. (1984) established metallic conductivity for all RM_4P_{12} (M = Fe, Ru) compounds. Only $CeFe_4P_{12}$ is a semiconductor with a band gap of 0.015 eV (Meisner 1981).

Comparison of the plots of the unit-cell volumes of isotypic compounds with results determining the valence state of the lanthanoid atoms using physical methods, indicates a good correlation between these data. Among the compounds investigated the only exceptions are $EuFe_4P_{12}$ and $Yb_2Ni_{12}P_7$, where the cell volume indicates the trivalent state of europium and ytterbium atoms, while magnetic susceptibility measurements show intermediate valence of europium (Gerard et al. 1983) and ytterbium (Zeppenfeld and Jeitschko 1993) in these compounds. In all other cases deviations from the R^{3+} valence state which are indicated by the cell volumes of the compounds were confirmed by calcu-

lation of the magnetic moments for the lanthanoid atoms or by other methods. Moreover, using the value of the cell volume deviation one can estimate the value of the change from valence state of R^{3+} to R^{2+} or to R^{4+}. Thus, for the compounds EuM_2P_2 (M = Fe, Co, Ru) considerable deviation of the cell volume is connected with the divalent state of europium atoms, while for $EuNi_2P_2$, with an intermediate valence of Eu, the deviation is smaller.

Some correlation is observed between the phosphorus content in the compound and the valence of lanthanoid atoms. Estimating the values of deviations of the unit-cell volumes of europium compounds one can see that the Eu valence decreases from 3+ to 2+ with increasing phosphorus content in the compound and also with increasing europium content. At a P content less than or equal to 33.3 at.% the trivalent state of the Eu atoms is characteristic ($Eu_2Ni_{12}P_5$, $Eu_2Fe_{12}P_7$, $Eu_2Co_{12}P_7$); for $Eu_2Ni_{12}P_7$ and $Eu_6Ni_{20}P_{13}$ the deviation of the cell volume is small which indicates an intermediate valence of Eu as slightly different from 3+. All compounds of EuMP composition show an intermediate valence of the Eu atoms. In EuM_2P_2 compounds in most cases (beside $EuNi_2P_2$) the valence state Eu^{2+} is observed. At further increasing phosphorus content only the divalent state of Eu may be expected, but the exception is again $EuFe_4P_{12}$ with Eu in the intermediate valence state. Such unique behavior of $EuFe_4P_{12}$ may probably be connected with the structure of the polyanion $Fe_4P_{12}^{n-}$, which determines the charge of the R ion and decreases the influence of the R-ion size on the unit-cell volume.

For cerium compounds the valence state Ce^{3+} was found only for $CeLi_2P_2$, in all other cases Ce atoms are in the intermediate valence state between 3+ and 4+. Using values of deviations of unit-cell volumes one can make a supposition that the valence of the Ce atoms decreases with increasing P content.

A similar tendency of decreasing valence is observed for ytterbium compounds. In most compounds Yb atoms are in the normal trivalent state and only in compounds with 40 at.% of P an intermediate valence between 3+ and 2+ was found.

The influence of the transition-metal atoms on the valent state of the lanthanoids may be estimated with sufficient probability only for isotypic compounds, because the crystal structure of the compounds and, as mentioned above, the phosphorus content considerably influence it too. However, it should be mentioned that the smallest deviations from the normal state R^{3+} are observed for nickel compounds and considerably larger ones are observed for iron and cobalt compounds.

The most complete information is available about RM_2P_2 phosphides with the $ThCr_2Si_2$ structure. In particular, the crystal structure of cerium and europium compounds with Fe, Co and Ni is completely determined. The positive charge of the R-ion in these compounds must be compensated by a negative charge of the polyanion $[M_2P_2]^{n-}$. The value of the charge depends on the number of bonding electrons given by transition-metal atoms and P–P distance. The charge of the phosphorus ion may be changed from 4– (for covalently bonding P_2 pair) to 6– (for two independent P^{3-} ions). The P–P distance in the nickel compounds (table 87) indicates the existence of chemical bonding between the phosphorus atoms, but at a greater distance than in the covalent P–P bond (the covalent radius of the P atom is 0.110, Pauling 1970). As a result, the intermediate variant of the pair P_2^{5-} with two bonding and antibonding electrons is acceptable (Jeitschko and Reehuis 1987).

Table 87
Interatomic distances in compounds RM_2P_2 (R = Ce, Eu; M = Fe, Co, Ni)

Compound	δ_{P-P}	δ_{M-P}	δ_{M-M}	δ_{R-P}	Reference
$CeFe_2P_2$	0.2864	0.2236	0.2722	0.3075	Jeitschko et al. (1985)
$CeCo_2P_2$	0.2461	0.2271	0.2754	0.3016	Jeitschko et al. (1985)
$CeNi_2P_2$	0.2405	0.2299	0.2799	0.3046	Hofmann and Jeitschko (1984)
$EuFe_2P_2$	0.3268	0.2240	0.2699	0.3155	Reehuis and Jeitschko (1990)
$EuCo_2P_2$	0.3272	0.2233	0.2662	0.3125	Marchand and Jeitschko (1978)
$EuNi_2P_2$	0.2371	0.2296	0.2785	0.3026	Jeitschko and Jaberg (1980a)

Hofmann and Jeitschko (1984) have shown that nickel atoms form Ni–Ni bonds with one bonding electron per Ni atom and the proposed scheme of valence compensation as $R^{3+}Ni^{1+}Ni^{1+}P_2^{5-}$. Taking into account the intermediate valence of Ce and Eu atoms one can propose the following scheme for their compounds: $Ce^{3+/4+}Ni^{1+}Ni^{1+}P_2^{4-/5-}$ and $Eu^{2+/3+}Ni^{1+}Ni^{1+}P_2^{4-/5-}$. The charge of the P_2 ions varies slightly from –5 to –6 and –4 in Ce and Eu compounds, respectively, which is indicated by a small difference in the Ni–P distances (table 87) and again small deviations of cell volumes (fig. 95). The P–P distance in $EuFe_2P_2$ and $EuCo_2P_2$ (table 87) indicates the absence of bonding between the corresponding atoms, and proceeding from the divalent state of the Eu atoms we may write valence compensation as $Eu^{2+}M^{2+}M^{2+}P^{3-}P^{3-}$. For the compounds $CeFe_2P_2$ and $CeCo_2P_2$ the value of the negative charge of the P_2 pair increases from –5 to –6 which is indicated by the increasing P–P distance and it leads to increasing valence of the cerium atoms and to a respective decreasing of cell volume.

2.6. *Chemical properties*

Systematic investigation of the chemical properties of the ternary rare-earth phosphides has not been carried out. Some authors report chemical properties of some compounds.

The phosphide $LaLi_3P_2$ (Grund et al. 1984) is stable against air and water; $PrLi_2P_2$ (Fischer and Schuster 1980) is rapidly decomposed by water, its reaction with acids proceeds with the appearance of fire. $Na_2Eu_3P_4$ hydrolyzes in damp air (Hönle et al. 1992).

The phosphides RNiP are grey substances which are soluble in concentrated HCl and HNO_3 (Chykhrij et al. 1987); concentrated H_2SO_4 passivates their solubility, but moderate sulfuric acid (1:1) rapidly decomposes the RNiP compounds. Water solutions of the alkalies and ammonia do not decompose RNiP. Johrendt and Mewis (1990) have established that RPdP (R = La–Gd) are brown or grey-black finely-crystalline substances which are stable against air, moisture or dilute mineral acids. The RPdP (R = Tb–Lu) are decomposed by air and by reaction with HCl (1:1).

$EuZn_2P_2$, $YZnCuP_2$ (Klüfers et al. 1980), $LaZnCuP_2$, $CeZnCuP_2$ (Mahan and Mewis 1983) and $YbZnCuP_2$ (Mewis 1980b) are stable against air and moisture, the latter compound is easily decomposed by dilute mineral acids.

The phosphide $EuCu_{1.75}P_2$ (Mewis 1980a) does not react with dilute hydrochloric acid; $YbCu_3P_2$ (Klüfers et al. 1979) is stable against air, water and dilute mineral acids. The phosphides $SmCuZnP_2$, $SmAgZnP_2$ and $LaAgZnP_2$ (Tejedor and Stacy 1990) have melting points higher than 1370 K and do not react with water at room temperature.

2.7. *Preparation of ternary rare-earth phosphides*

The melting of previously pressed powders of the transition metals with pieces of rare-earth ingots protected in an argon atmosphere in an arc furnace produces the ternary rare-earth phosphides with low phosphorus content (up to 33.3 at.%). An excess of phosphorus is added to compensate for phosphorus losses during arc melting. Using such a method the phosphides $R_2Ni_{12}P_5$, RNi_4P_2, $R_3Ni_{12}P_7$, $R_9Ni_{26}P_{12}$ and some others have been obtained. This method was used for preparing samples with a P content of up to 33.3 at.% during the investigation of the phase diagrams of the R–M–P systems.

Another method used for the preparation of ternary phosphides is ampoule synthesis. Evacuated silica tubes with an inserted pressed mixture of the powder components are gradually heated up to 1000–1270 K, held at this temperature during 1–7 days and then slowly cooled or quenched. For obtaining samples containing chemically active rare earths the constituent components are placed into alumina crucibles and for lithium-containing samples they are placed into tantalum or niobium crucibles. Sometimes the silica tubes are filled with purified argon. By such a method $EuCu_{1.75}P_2$ (Mewis 1980a), RM_2P_2, $SmCuP_2$ (Chykhrij 1990a,b) and some others were obtained. The phosphides containing refractory or chemically inert metals are prepared by two steps: previously heated samples are crushed, pressed and again homogenized in evacuated silica tubes. The phosphides RPdP (Johrendt and Mewis 1990), RPtP (Wenski and Mewis 1986b–d) and some others were obtained using such a method.

Some authors use a combination of the two methods mentioned. At first, the rare earth and transition metals are melted in an arc or high-frequency furnace and then the alloy obtained is crushed and heat-treated in an evacuated silica tube with the required quantity of red phosphorus. By such a method the compounds RRh_2P_2 (Madar et al. 1987a,b) and $R_5Ru_{19}P_{12}$ (Ghetta et al. 1989) were obtained.

The third method is a tin flux technique. Mixtures of powder components are placed into alumina crucibles with 5–30 times excess tin and sealed in an evacuated silica tube. The silica tube and its content are heat treated at 770–1270 K during 6–120 hours and either rapidly or slowly cooled. After dissolving the ingot obtained in hydrochloric acid finely-crystalline ternary rare-earth phosphides are obtained. By such a method the majority of the ternary rare-earth phosphides are prepared by Jeitschko and colleagues. Oryshchyn and Chykhrij (1993) describe conditions for preparing the ternary rare-earth phosphides from a tin flux in detail. The same authors tested cadmium and indium as metal-solvents. The main disadvantage of the melting method is the fact that often phosphides with compositions differing from the initial mixture are obtained. Besides that, in four-component systems competing chemical reactions take place and binary compounds containing metals and metal-solvent or phosphorus are formed.

Oryshchyn and Chykhrij (1993) note that such by-products are Ni_3Sn_4, Ni_2P, CoP, Cu_5Sn_6 (solvent Sn) and Ni_3In_2 (solvent In).

For obtaining single crystals of the ternary rare-earth phosphides with high phosphorus content, heating with a temperature gradient in the presence of substances which may be transport agents is used. Single crystals of $SmCuP_2$ (Chykhrij 1990a) have been prepared using a temperature regime 1470–1370 K in the presence of I_2 or Br_2 as mineralizers.

References

Aksel'rud, L.G., V.I. Yarovets and O.I. Bodak, 1976, Kristallografiya **21**, 383. In Russian.

Aksel'rud, L.G., Ya.P. Yarmolyuk and E.I. Gladyshevskii, 1980, Dopov. Akad. Nauk Ukr. RSR, Ser. A **5**, 79. In Ukrainian.

Andress, K.R., and E. Alberti, 1935, Z. Metallkd. **27**, 126. In German.

Andrukhiv, L.S., L.O. Lysenko, Ya.P. Yarmolyuk and E.I. Gladyshevskii, 1975, Dopov. Akad. Nauk Ukr. RSR, Ser. A **7**, 645. In Ukrainian.

Babizhets'ky, V.S., 1995, Interaction of rare earth metals of cerium subgroup with nickel and phosphorus, Thesis for obtaining scientific degree of Candidate of Chemistry (Ivan Franko L'viv State University) 176pp. In Ukrainian.

Babizhets'ky, V.S., and Yu.B. Kuz'ma, 1994, Zh. Neorg. Khim. **39**, 322. In Russian.

Babizhets'ky, V.S., S.I. Chykhrij, S.V. Oryshchyn and Yu.B. Kuz'ma, 1992a, Zh. Neorg. Khim. **37**, 2660. In Russian.

Babizhets'ky, V.S., S.I. Chykhrij, S.V. Oryshchyn and Yu.B. Kuz'ma, 1992b, Dopov. Akad. Nauk Ukr. RSR **9**, 116. In Ukrainian.

Babizhets'ky, V.S., Yu.B. Kuz'ma, S.I. Chykhrij and S.V. Oryshchyn, 1992c, Dopov. Akad. Nauk Ukr. RSR **5**, 113. In Ukrainian.

Babizhets'ky, V.S., S.V. Oryshchyn, S.I. Chykhrij and Yu.B. Kuz'ma, 1992d, Kristallografiya **37**, 1024. In Russian.

Babizhets'ky, V.S., S.I. Chykhrij, S.V. Oryshchyn and Yu.B. Kuz'ma, 1993a, Ukr. Khim. Zh. **59**, 240. In Ukrainian.

Babizhets'ky, V.S., Yu.K. Gorelenko, Ya.F. Mykhal'sky, Yu.B. Kuz'ma and S.V. Oryshchyn, 1993b, Magnetic and electrical properties of the $Ln_2Ni_{12}P_5$ compounds (Ln = La, Ce, Pr, Nd, Eu), in: Abstracts of reports of the VIth Scientific–Technical Conference on Phosphorus, L'viv, 1993, p. 68. In Ukrainian.

Badding, J.V., and A.M. Stacy, 1987a, J. Solid State Chem. **67**, 354.

Badding, J.V., and A.M. Stacy, 1987b, Phys. Rev. B **35**, 8880.

Bauhofer, W., E. Gmelin, M. Möllendorf, R. Nesper and H.G. von Schnering, 1985, J. Phys. C **18**, 3017.

Berger, R., 1980, Acta Chem. Scand. Ser. A **34**, 231.

Berger, R., 1981, Acta Chem. Scand. Ser. A **35**, 635.

Bodak, O.I., and E.I. Gladyshevskii, 1985, Ternary Rare Earth Containing Systems (Vyshcha Shkola, L'viv) 328pp. In Russian.

Bodak, O.I., E.I. Gladyshevskii and P.I. Krypyakevych, 1970, Zh. Strukt. Khim. **11**, 305. In Russian.

Bonville, P., J.A. Hodges, F. Hulliger, P. Imbert, G. Jehanno, J.B. Marimon de Cunha and H.R. Ott, 1988, J. Magn. & Magn. Mater. **76**, 473.

Bragg, W.L., 1914, Proc. R. Soc. Ser. A **89**, 468.

Braun, D.J., and W. Jeitschko, 1978, Acta Crystallogr. B **34**, 2069.

Brink, R., and W. Jeitschko, 1986, Z. Kristallogr. **174**, 27. In German.

Brink, R., and W. Jeitschko, 1987, Z. Kristallogr. **178**, 34. In German.

Brink, R., and W. Jeitschko, 1988, Z. Kristallogr. **182**, 46. In German.

Bruzzone, G., 1961, Atti Accad. Naz. Lincei Cl. Sci. Fis. Mat. Nat. Rend. **31**, 260. In Italian.

Bruzzone, G., A.F. Ruggiero and G.L. Olcese, 1964, Atti Accad. Naz. Lincei Cl. Sci. Fis. Mat. Nat. Rend. **36**, 66. In Italian.

Burdet, J.K., B.A. Coddens and G.V. Kulkarni, 1988, Inorg. Chem. **27**, 3259.

Busch, G., M. Campagne, F. Hulliger and H.C. Siegmann, 1971, J. Phys. Chem. Solids **32**, 2173.

Carlsson, B., M. Gölin and S. Rundqvist, 1973, J. Solid State Chem. **8**, 57.

Chattopadhyay, T., H. Bartholin, J. Voiron, W. Bauhofer and H.G. von Schnering, 1987a, J. Magn. & Magn. Mater. **63–64**, 632.

Chattopadhyay, T., P.J. Brown and H.G. von Schnering, 1987b, Phys. Rev. B **36**, 7300.

Chattopadhyay, T., P.J. Brown and H.G. von Schnering, 1988a, Europhys. Lett. **6**, 89.

Chattopadhyay, T., P.J. Brown, P. Thalmeier, W. Bauhofer and H.G. von Schnering, 1988b, Phys. Rev. B **37**, 269.

Chattopadhyay, T., J. Voiron and H. Bartholin, 1988c, J. Magn. & Magn. Mater. **72**, 35.

Chua, K.S., and J.N. Pratt, 1974, Thermochim. Acta **8**, 409.

Chun, H.K., and G.B. Carpenter, 1979, Acta Crystallogr. **35**, 30.

Chykhrij, S.I., 1988, Interaction between components in system Tb–Co–P, in: Novelty in Obtaining and Utilization of Phosphides and Phosphorus Containing Alloys, ed. A.M. Kounayev (Nauka, Alma-Ata) pp. 116–118. In Russian.

Chykhrij, S.I., 1990a, Zh. Neorg. Khim. **35**, 1656. In Russian.

Chykhrij, S.I., 1990b, Phase equilibria and crystal structure of compounds in systems Tb–(Fe, Co, Ni)–P and related ones, Thesis for obtaining scientific degree of Candidate of Chemistry (Ivan Franko L'viv State University) 176pp. In Russian.

Chykhrij, S.I., and Yu.B. Kuz'ma, 1990, Zh. Neorgan. Khim. **34**, 3203. In Russian.

Chykhrij, S.I., and O.M. Shevchuk, 1993, Phase diagrams of the (La, Ce)–Fe–P systems, in: Abstracts of reports of the VIth Scientific–Technical Conference on Phosphorus, L'viv, 1993, p. 67. In Ukrainian.

Chykhrij, S.I., L.G. Aksel'rud, S.V. Oryshchyn and Yu.B. Kuz'ma, 1985, Dopov. Akad. Nauk Ukr. RSR, Ser. B **11**, 57. In Ukrainian.

Chykhrij, S.I., S.V. Oryshchyn and Yu.B. Kuz'ma, 1986, Dopov. Akad. Nauk Ukr. RSR Ser. A **7**, 79. In Ukrainian.

Chykhrij, S.I., S.V. Oryshchyn and Yu.B. Kuz'ma, 1987, Zh. Neorg. Khim. **32**, 2375. In Russian.

Chykhrij, S.I., Yu.B. Kuz'ma and S.V. Oryshchyn, 1989a, Dopov. Akad. Nauk Ukr. RSR Ser. B **3**, 63. In Ukrainian.

Chykhrij, S.I., S.V. Oryshchyn and Yu.B. Kuz'ma, 1989b, Izv. Akad. Nauk SSSR, Ser. Neorgan. Mater. **25**, 1380. In Russian.

Chykhrij, S.I., S.V. Oryshchyn, Yu.B. Kuz'ma and T. Glowiak, 1989c, Kristallografiya **34**, 1131. In Russian.

Chykhrij, S.I., Yu.B. Kuz'ma, S.V. Oryshchyn, B.V. Khabursky and V.S. Fundamenskii, 1990, Dopov. Akad. Nauk Ukr. RSR Ser. B **9**, 49. In Ukrainian.

Chykhrij, S.I., Yu.K. Gorelenko, S.V. Oryshchyn, R.V. Skolozdra and Yu.B. Kuz'ma, 1991, Fiz. Tverd. Tela **33**, 2752. In Russian.

Chykhrij, S.I., S.V. Oryshchyn and Yu.B. Kuz'ma, 1992, The structures of ternary rare earth and transition metal phosphides with metal to nonmetal ratio 2:1, in: Physical Chemistry and Technology of Phosphides and Phosphorus Containing Alloys, eds V.I. Trefilov and A.M. Kounayev (Gylym, Alma-Ata) pp. 163–173. In Russian.

Chykhrij, S.I., V.S. Babizhets'ky, S.V. Oryshchyn, L.G. Aksel'rud and Yu.B. Kuz'ma, 1993, Kristallografiya **38**, 262. In Russian.

Cordier, G., B. Eisenmann and H. Schäfer, 1976, Z. Anorg. Allg. Chem. **426**, 205. In German.

Dahlmann, W., and H.G. von Schnering, 1973, Naturwissenschaften **60**, 429. In German.

Davydov, V.N., and Yu.B. Kuz'ma, 1981, Dopov. Akad. Nauk Ukr. RSR Ser. A **1**, 81. In Ukrainian.

Deller, K., and B. Eisenmann, 1977, Z. Naturforsch. **32b**, 1368. In German.

Eisenmann, B., N. May, W. Müller and H. Schäfer, 1972, Z. Naturforsch. **27b**, 1155. In German.

Elander, M., G. Hägg and A. Westgren, 1936, Ark. Kemi Mineral. Geol. B **12**, 1.

Endrzeevskaja, S.N., and G.V. Samsonov, 1965, Zh. Obshch. Khim. **35**, 1983. In Russian.

Faffius, G., and J. Kotzler, 1983, Phys. Lett. A **93**, 423.

Fischer, H.O., and H.U. Schuster, 1980, Z. Naturforsch. **35b**, 1322. In German.

Fischer, P., A. Furrer, E. Kaldis, D. Kim, J.K. Kjems and P.M. Levy, 1985, Phys. Rev. B **31**, 456.

Florio, J.V., N.C. Beanziger and R.E. Rundle, 1956, Acta Crystallogr. **9**, 367.

Franzen, H.F., and A.V. Hariharan, 1980, J. Chem. Thermodynamics **12**, 975.

Franzen, H.F., A.V. Hariharan and I.A. Merrich, 1980, High Temp. Sci. **12**, 11.

Ganglberger, E., 1968a, Monatsh. Chem. **99**, 557. In German.

Ganglberger, E., 1968b, Monatsh. Chem. **99**, 559. In German.

Gerard, A., F. Grandjean, J.A. Hodges, D.J. Braun and W. Jeitschko, 1983, J. Phys. C **16**, 2797.

Ghetta, V., 1987, Cristallochimie des phases ternaires ($\square$, Ln, M)$_2$X, Thèse pour obtenir le titre de docteur

(L'Institut National Polytechnique de Grenoble) p. 40. In French.

Ghetta, V., P. Chaudouet, R. Madar, J.-P. Senateur and B. Lambert-Andron, 1989, J. Less-Common Met. **146**, 299.

Ghetta, V.P., P. Chaudouet, B. Lambert-Andron, M.-N. Deschizeaux-Cherny, R. Madar and J.-P. Senateur, 1986, C. R. Acad. Sci. Paris Ser. II **303**, 357.

Gladyshevskii, E.I., and O.I. Bodak, 1982, Crystal Chemistry of Compounds of Rare Earth Metals (Vyshcha Shkola, L'viv) 253pp. In Russian.

Gladyshevskii, E.I., and Yu.N. Grin, 1981, Sov. Phys. Crystallogr. **26**, 683.

Grandjean, F., A. Gerard, J.A. Hodges, D.J. Braun and W. Jeitschko, 1983, Hyperfine Interact. **15/16**, 765.

Grandjean, F., A. Gerard, D.J. Braun and W. Jeitschko, 1984, J. Phys. Chem. Solids **45**, 877.

Grund, I., H.-U. Schuster and P. Müller, 1984, Z. Anorg. Allg. Chem. **515**, 151.

Guerin, R., E. Ghadraoui, J.-Y. Pivan, J. Padiou and M. Sergent, 1984, Mat. Res. Bull. **19**, 1257.

Hartweg, M., 1987, Über physikalische Eigenschaften der Seltenerd-Pentaphosphide LnP_5, von CeP_2 und $LaAs_2$, sowie zur Kenntnis einiger neuer ternärer Alkalimetall-Europium-Pniktide, Diss. Dokt. Naturwiss. (Chemische Fakultät, Universität Stuttgart) 231pp. In German.

Hassler, E., T. Johnsson and S. Rundqvist, 1974, Acta Chem. Scand. Ser. A **28**, 123.

Hayakawa, H., K. Nomura and S. Ono, 1976, J. Less-Common Met. **44**, 327.

Hayakawa, H., S. Ono, A. Kabayashi and Y. Sasaki, 1978, Nippon Kagaku Kaishi **9**, 1214.

Hofmann, W., and W. Jäniche, 1936, Z. Metallkd. **28**, 1. In German.

Hofmann, W.K., and W. Jeitschko, 1984, J. Solid State Chem. **51**, 152.

Hol'nik, V.F., S.P. Hordijenko and K.E. Mironov, 1977, Homogeneity range of samarium monophosphide, in: Obtaining, Properties and Utilization of Phosphides (Naukova Dumka, Kiev) pp. 71–76. In Russian.

Hol'nik, V.F., S.P. Hordijenko and K.E. Mironov, 1979, Zh. Fiz. Khim. **53**, 490. In Russian.

Hönle, W., J. Lin, M. Hartweg and H.G. von Schnering, 1992, J. Solid State Chem. **97**, 1.

Hordijenko, S.P., 1988, Standard enthalpy of solid phosphides formation, in: Novelty in Obtaining and Utilization of Phosphides and Phosphorus Containing Alloys, Vol. 2 (Nauka, Alma-Ata) pp. 98–102. In Russian.

Hordijenko, S.P., 1989, Porosh. Metall. **5**, 64. In Russian.

Hordijenko, S.P., and V.F. Hol'nik, 1977, Thermodynamic functions of solid phosphides of cerium subgroup rare earth metals and gadolinium, in: Obtaining, Properties and Utilization of Phosphides (Naukova Dumka, Kiev) pp. 66–71. In Russian.

Hordijenko, S.P., and K.E. Mironov, 1983, Izv. Akad. Nauk SSSR, Neorg. Mater. **19**, 151. In Russian.

Hordijenko, S.P., B.V. Fenochka and G.Sh. Viksman, 1979, The Thermodynamics of Lanthanoid Compounds (Naukova Dumka, Kiev) pp. 136–152. In Russian.

Hordijenko, S.P., V.F. Hol'nik and K.E. Mironov, 1982, Izv. Akad. Nauk SSSR, Neorg. Mater. **18**, 1448. In Russian.

Howell, J.K., and L.L. Pytlewski, 1970, Inorg. Nucl. Chem. Lett. **6**, 681.

Hulliger, F., and P. Levy, 1969, Phys. Lett. A **28**, 471.

Hulliger, F., and H.R. Ott, 1978, Z. Phys. Chem. Abt. B **29**, 47.

Hulliger, F., and O. Vogt, 1970, Solid State Commun. **8**, 771.

Iandelli, A., 1956, Z. Anorg. Allg. Chem. **288**, 81. In German.

Iandelli, A., 1961, Cell dimensions and magnetic susceptibilities of the MX compounds of rare earths with P, As, Sb, Bi, S, Se and Te, in: Rare Earths Research (McMillan, New York) pp. 135–141.

Iandelli, A., 1964, Z. Anorg. Allg. Chem. **330**, 221. In German.

Iandelli, A., and E. Botti, 1936, Atti Accad. Naz. Lincei Cl. Sci. Fis. Mat. Nat. Rend. **24**, 459. In Italian.

Iandelli, A., and E. Botti, 1937, Atti Accad. Naz. Lincei Cl. Sci. Fis. Mat. Nat. Rend. **25**, 638. In Italian.

Jakubowski-Ripke, U., and W. Jeitschko, 1987, Z. Kristallogr. **178**, 116. In German.

Jakubowski-Ripke, U., and W. Jeitschko, 1988, J. Less-Common Met. **136**, 261.

Jansen, K., and G. Sperlich, 1975, Solid State Commun. **17**, 1179.

Jeitschko, W., and D.J. Braun, 1977, Acta Crystallogr. B **33**, 3401.

Jeitschko, W., and R. Brink, 1992, Z. Naturforsch. **47b**, 192. In German.

Jeitschko, W., and W.K. Hofmann, 1983, J. Less-Common Met. **95**, 317.

Jeitschko, W., and B. Jaberg, 1980a, J. Solid State Chem. **35**, 312.

Jeitschko, W., and B. Jaberg, 1980b, Z. Anorg. Allg. Chem. **467**, 95. In German.

Jeitschko, W., and U. Jakubowski, 1985, J. Less-Common Met. **110**, 339.

Jeitschko, W., and U. Jakubowski-Ripke, 1993, Z. Kristallogr. **207**, 69. In German.

Jeitschko, W., and M. Reehuis, 1987, J. Phys. Chem. Solids **48**, 667.

Jeitschko, W., and E.J. Reinbold, 1985, Z. Naturforsch. **40b**, 900. In German.

Jeitschko, W., D.J. Braun, R.H. Ashcraft and R. Marchand, 1978, J. Solid State Chem. **25**, 309.

Jeitschko, W., U. Meisen and U.D. Scholz, 1984, J. Solid State Chem. **55**, 331.

Jeitschko, W., U. Meisen, M.H. Möller and M. Reehuis, 1985, Z. Anorg. Allg. Chem. **527**, 73. In German.

Jeitschko, W., R. Glaum and L. Boonk, 1987, J. Solid State Chem. **69**, 93.

Jeitschko, W., T.J. Terbüchte, E.J. Reinbold, P.G. Polmeier and T. Vomhof, 1990, J. Less-Common Met. **161**, 125.

Jeitschko, W., P.G. Polmeier and U. Meisen, 1993, J. Alloys & Compounds **196**, 105.

Johrendt, D., and A. Mewis, 1990, Z. Naturforsch. **45b**, 1262. In German.

Johrendt, D., and A. Mewis, 1994, Z. Anorg. Allg. Chem. **620**, 561.

Kastner, P., and R. Hoppe, 1974, Z. Anorg. Allg. Chem. **409**, 69.

Klüfers, P., A. Mewis and H.U. Schuster, 1979, Z. Kristallogr. **149**, 211. In German.

Klüfers, P., H. Neumann, A. Mewis and H.U. Schuster, 1980, Z. Naturforsch. **35b**, 1317. In German.

Komissarova, L.N., A.A. Men'kov and L.M. Vasil'eva, 1965, Izv. Akad. Nauk SSSR Neorg. Mater. **1**, 1493. In Russian.

Kost, M.E., A.L. Shylov, V.I. Mikheeva, S.I. Uspenskaya, V.I. Novokshonov, K.E. Mironov, M.N. Abdusaljamova, A.A. Eliseev, H.M. Kuz'michova and G.B. Seifert, 1983, in: The Rare Earth Compounds, ed. I.V. Tananayev (Nauka, Moscow) pp. 94–144. In Russian.

Krebs, H., 1968, Grundzüge der Anorganischen Kristallchemie (Ferdinand Enke Verlag, Stuttgart) 304pp. In German.

Krypyakevych, P.I., 1962, Kristallografiya **7**, 686. In Russian.

Krypyakevych, P.I., 1977, Structure Types of Intermetallic Compounds (Nauka, Moscow) 288pp. In Russian.

Krypyakevych, P.I., V.Ya. Markiv and J.V. Mel'nyk, 1967, Dopov. Akad. Nauk. Ukr. RSR Ser. A, 750. In Russian.

Kudielka, H., 1977, Z. Kristallogr. **145**, 177. In German.

Kuss, M., G. Wenski, A. Mewis and H.U. Schuster, 1987, Z. Anorg. Allg. Chem. **553**, 156. In German.

Kuz'ma, Yu.B., 1983, Crystal Chemistry of Borides (Vyscha Shkola, Lvov) 160pp. In Russian.

Kuz'ma, Yu.B., and N.F. Chaban, 1990, Binary and Ternary Boron Containing Systems, Reference Book (Metallurgiya, Moscow) 320pp. In Russian.

Kuz'ma, Yu.B., Ya.F. Lomnitskaya and S.V. Oryshchyn, 1986a, The interaction of phosphorus with transition metals of IVa–VIa group elements and iron triad metals, in: Stable and Metastable Phase Equilibria in Metallic Systems, ed. M.E. Drits (Nauka, Moscow) p. 12–18. In Russian.

Kuz'ma, Yu.B., M.R. Ovod and V.N. Davydov, 1986b, Izv. Akad. Nauk SSSR Neorgan. Mater. **22**, 692. In Russian.

Kuz'ma, Yu.B., Ya.F. Lomnitskaya, S.V. Oryshchyn, O.N. Il'nitskaya and S.I. Chykhrij, 1989, New phosphides with transition and rare earth metals and their crystal structures, in: Collected Abstracts XI Int. Conf. on Phosphorus Chemistry, Tallinn, 1989, Vol. 2, ed. M. Veiderma (Academy of Sciences of Estonian SSR, Tallinn) p. 57.

Kuz'ma, Yu.B., S.I. Chykhrij and V.S. Babizhets'ky, 1991, The interaction of rare earth and transition metals with phosphorus, in: Int. Scientific–Technical Conf. Current Problems of Fundamental Sciences, Moscow, USSR, 1991, Collected Reports, ed. I.B. Fedorov, Vol. 5 (MGTU) p. 15–17. In Russian.

Kuz'ma, Yu.B., V.S. Babizhets'ky, S.I. Chykhrij, S.V. Oryshchyn and V.K. Pecharsky, 1993, Z. Anorg. Allg. Chem. **619**, 587.

Leger, J.M., I. Vedel, A.M. Redon and J. Rossat-Mignod, 1987, J. Magn. & Magn. Mater. **63–64**, 49.

Lomnitskaya, Ya.F., and Yu.B. Kuz'ma, 1991a, The interaction in ternary systems containing transition metals of IV–VI period and phosphorus, in: Phase Diagrams in Science of Materials, ed. V.N. Eremenko (IPM, Kiev) pp. 61–70. In Russian.

Lomnitskaya, Ya.F., and Yu.B. Kuz'ma, 1991b, Visn. L'viv. Derzh. Univ. Ser. Khim. **31**, 24. In Ukrainian.

Lossau, N., H. Kierspel, J. Langen, W. Schabitz, D. Wohlleben, A. Mewis and C. Sauer, 1989a, J. Phys. B Condens. Matter **74**, 227.

Lossau, N., H. Kierspel, G. Michels, F. Oster, W. Schlabitz, D. Wohlleben, C. Sauer and A. Mewis, 1989b, J. Phys. B Condens. Matter **77**, 393.

Lundström, T., 1968, Acta Chem. Scand. **22**, 2191.

Lux, C., A. Mewis, N. Lossau, G. Michels and W. Schlabitz, 1991a, Z. Anorg. Allg. Chem. **593**, 169. In German.

Lux, C., G. Wenski and A. Mewis, 1991b, Z. Naturforsch. **46b**, 1035. In German.

Madar, R., P. Chaudouet, D. Boursier, J.P. Senateur and B. Lambert, 1985a, Structural Chemistry and Physical Properties of Ternary Pnictides $RERh_2X_2$ (RE = Rare Earth, X = P, As), in: VIII Int. Conf. on Solid Compounds of Transition Elements, Vienna, Austria, 1985, Extended Abstracts, P4 A13.

Madar, R., P. Chaudouet, E. Dhahri, J.P. Senateur, R. Fruchart and B. Lambert, 1985b, J. Solid State Chem. **56**, 335.

Madar, R., P. Chaudouet, J.P. Senateur, S. Zemni and D. Tranqui, 1987a, J. Less-Common Met. **133**, 303.

Madar, R., V. Ghetta, E. Dhahri, P. Chaudouet and J.P. Senateur, 1987b, J. Solid State Chem. **66**, 73.

Mahan, A., and A. Mewis, 1983, Z. Naturforsch. **38b**, 1041. In German.

Marchand, R., and W. Jeitschko, 1978, J. Solid State Chem. **24**, 351.

Maslout, A.E., J.P. Motte, A. Courtois and C. Gleitzer, 1975, C. R. Acad. Sci. Paris C **280**, 21. In French.

Meinhardt, D., and O. Krisement, 1960, Z. Naturforsch. **15a**, 880. In German.

Meisel, K., 1939, Z. Anorg. Allg. Chem. **240**, 300. In German.

Meisen, U., and W. Jeitschko, 1984a, Z. Kristallogr. **167**, 135.

Meisen, U., and W. Jeitschko, 1984b, J. Less-Common Met. **102**, 127.

Meisner, G.P., 1981, Physica **108**, 763.

Mendelejev, V.A., A.V. Pavlov and Yu.I. Utochkin, 1990, Izv. Vyssh. Uchebn. Zaved. Chern. Met. **7**, 1. In Russian.

Menge, G., and H.G. von Schnering, 1976, Z. Anorg. Allg. Chem. **422**, 226. In German.

Mewis, A., 1980a, Z. Naturforsch. **35b**, 141. In German.

Mewis, A., 1980b, Z. Naturforsch. **35b**, 939. In German.

Mironov, K.E., 1981, Izv. Akad. Nauk SSSR Neorg. Mater. **17**, 197. In Russian.

Mironov, K.E., 1984, Zh. Neorg. Khim. **29**, 194. In Russian.

Mironov, K.E., 1988, Peculiarities of formation of rare earth phosphides at metals saturation by phosphorus and homogeneity ranges of rare earth monophosphides, in: Novelty in Obtaining and Utilization of Phosphides and Phosphorous Containing Alloys, ed. A.M. Kounayev (Nauka, Alma Ata) pp. 67–69. In Russian.

Mironov, K.E., and G.P. Brygalina, 1973, Europium diphosphide with semiconductor properties, in: Rare Earth Metals, Alloys and Compounds (Nauka, Moscow) p. 305. In Russian.

Mironov, K.E., and G.P. Brygalina, 1974, Izv. Akad. Nauk SSSR Neorg. Mater. **10**, 920. In Russian.

Mironov, K.E., I.G. Vasil'eva and E.D. Sinitsina, 1966, Izv. Acad. Nauk SSSR Neorgan. Mater. **2**, 1315. In Russian.

Mironov, K.E., G.P. Brygalina, I.G. Vasil'eva and E.D. Popova, 1971, Process of phosphidization of europium sesquialteral oxide, in: Metallothermic Processes in Chemistry and Metallurgy (Nauka, Novosibirsk) pp. 116–120. In Russian.

Mironov, K.E., G.P. Brygalina and V.N. Ikorskij, 1975, The dependence of magnetic properties of alloys in Eu–P system versus their composition, in: Alloys of Rare Earth Metals with Unique Physical and Chemical Properties (Nauka, Moscow) pp. 121–123. In Russian.

Mironov, K.E., I.G. Vasil'eva and G.P. Brygalina, 1977, Oxidation of rare earth phosphides, in: Semiconductive Materials and their Utilization (Voronezh State University) pp. 111–122. In Russian.

Möller, M.H., and W. Jeitschko, 1981, Acta Crystallogr. A **37**(Suppl.), 176.

Möller, M.H., and W. Jeitschko, 1985, Ternary Rare Earth Copper and Silver Pnictides with $ThCr_2Si_2$-related Structures, in: VIII Int. Conf. on Solid Compounds of Transition Elements, 1985, Vienna, Austria, Extended Abstracts, P4 A14.

Mörsen, E., B.D. Mosel, W. Müller-Warmuth, M. Reehuis and W. Jeitschko, 1988a, J. Phys. C **21**, 3133.

Mörsen, E., B.D. Mosel, W. Müller-Warmuth, M. Reehuis and W. Jeitschko, 1988b, J. Phys. Chem. Solids **49**, 785.

Myers, C.E., H.F. Franzen and J.W. Anderegg, 1985, Inorg. Chem. **24**, 1822.

Myers, S.M., and A. Narath, 1973, Phys. Rev. B **7**, 4776.

Nagarajan, R., E.V. Sampathkumaran, L.C. Gupta, R. Vijayaraghavan, V. Prabhawalkar, Bhaktdarshan and B.D. Padalia, 1981, Phys. Lett. A **84**, 275.

Nagarajan, R., G.K. Shenoy, L.C. Gupta and E.V. Sampathkumaran, 1985, J. Magn. Magn. Mater. **47–48**, 413.

Niedzielski, R., and R. Troć, 1984, Phys. Status Solidi **123**, 29.

Nielsen, J., and N. Baenziger, 1954, Acta Crystallogr. **7**, 132.

Niessen, A.K., and F.R. de Boer, 1981, J. Less-Common Met. **82**, 75.

Nieuwenkamp, W., and J.M. Bijvoet, 1931, Z. Kristallogr. **81**, 469. In German.

Noël, H., Z. Zolnierek, D. Kaczorowski and R. Troć, 1987a, J. Less-Common Met. **132**, 327.

Noël, H., Z. Zolnierek, D. Kaczorowski, R. Troć and J. Stępień-Damm, 1987b, J. Less-Common Met. **135**, 61.

Nowotny, N., H. Parthé, R. Kieffer and F. Benesovsky, 1954, Monatsh. Chem. **85**, 255. In German.

Olcese, G.L., 1961, Atti Accad. Naz. Lincei Cl. Sci. Fis. Mat. Nat. Rend. **30**, 195. In Italian.

Ono, S., K. Nomura and H. Hayakawa, 1974, J. Less-Common Met. **38**, 119.

Ono, S., H. Hayakawa and K. Nomura, 1976, Nippon Kagaku Kaishi **11**, 1700.

Oryshchyn, S.V., and S.I. Chykhrij, 1993, Obtaining single crystals of ternary rare earth and transition metal phosphides, in: Physical Chemistry and Technology of Phosphides and Phosphorus Containing Alloys, Vol. 1, eds V.I. Trefilov and A.M. Kounayev (Gylym, Alma-Ata) pp. 174–181. In Russian.

Oryshchyn, S.V., S.I. Chykhrij, T. Glowiak and Yu.B. Kuz'ma, 1988a, Dopov. Akad. Nauk Ukr. RSR Ser. B **3**, 54. In Ukrainian.

Oryshchyn, S.V., E.S. Shouminsky and Yu.B. Kuz'ma, 1988b, Vestn. L'vov. Univ. Ser. Khim. **29**, 42. In Russian.

Oryshchyn, S.V., S.I. Chykhrij, V.S. Babizhets'ky and Yu.B. Kuz'ma, 1991a, Dopov. Akad. Nauk Ukr. RSR **6**, 138. In Ukrainian.

Oryshchyn, S.V., S.I. Chykhrij and Yu.B. Kuz'ma, 1991b, The interaction of transition and rare earth metals with phosphorus, in: Refractory Compounds. Obtaining, Structure, Properties and Utilization, ed. T.Ya. Kosolapova (Naukova Dumka, Kiev) pp. 118–121. In Russian.

Paderno, Yu.B., V.L. Yurko and N.N. Tichonova, 1970, To the question of nature of samarium phosphide, in: Chemistry of Phosphides with Semiconductor Properties (Nauka, Novosibirsk) pp. 75–80. In Russian.

Parthé, Er., and Ed. Parthé, 1963, Acta Crystallogr. **16**, 71.

Pauling, L., 1928, Z. Kristallogr. **69**, 415. In German.

Pauling, L., 1970, General Chemistry (Mir, Moscow) 846pp. In Russian.

Pavlov, A.V., Yu.V. Kazakov and Yu.I. Utochkin, 1991, Izv. Vyssh. Uchebn. Zaved. Chern. Met. **11**, 94. In Russian.

Pearson, W.B., 1977, The Crystal Chemistry and Physics of Metals and Alloys, Vol. 1 (Mir, Moscow) 419pp. In Russian.

Perkins, P.G., A.K. Marwaha and J.P. Stewart, 1981, Theor. Chim. Acta **59**, 555.

Pivan, J.-Y., and R. Guerin, 1986, J. Less-Common Met. **120**, 247.

Pivan, J.-Y., R. Guerin and M. Sergent, 1984a, C.R. Acad. Sci. Paris, Ser. II **299**, 533. In French.

Pivan, J.-Y., R. Guerin and M. Sergent, 1984b, C.R. Acad. Sci. Paris, Ser. II **299**, 689. In French.

Pivan, J.-Y., R. Guerin and M. Sergent, 1985a, Inorg. Chim. Acta **109**, 221.

Pivan, J.-Y., R. Guerin and M. Sergent, 1985b, Mater. Res. Bull. **20**, 887.

Pivan, J.-Y., R. Guerin and M. Sergent, 1985c, New $R_2Rh_{12}X_7$ compounds structurally related to $Zr_2Fe_{12}P_7$ type, in: VIII Int. Conf. on Solid Compounds of Transition Elements, 1985, Vienna, Austria, Extended Abstracts, P4 A15.

Pivan, J.-Y., R. Guerin and M. Sergent, 1985d, J. Less-Common Met. **107**, 249.

Pivan, J.-Y., R. Guerin, J. Padiou and M. Sergent, 1986, J. Less-Common Met. **118**, 191.

Pivan, J.-Y., R. Guerin and M. Sergent, 1987, J. Solid State Chem. **68**, 11.

Pivan, J.-Y., R. Guerin, O. Pena, J. Padiou and M. Sergent, 1988, Mater. Res. Bull. **23**, 513.

Pytlewski, L.L., and J.K. Howell, 1967, Chem. Commun. **24**, 1280.

Quinn, R.K., and T.H. Weaver, 1976, J. Solid State Chem. **16**, 197.

Raffius, H., E. Mörsen, B.D. Mosel, W. Müller-Warmuth, T. Hillich, M. Reehuis, T. Volhof and W. Jeitschko, 1991, J. Phys. Chem. Solids **52**, 787.

Reehuis, M., and W. Jeitschko, 1987, Z. Kristallogr. **178**, 221. In German.

Reehuis, M., and W. Jeitschko, 1989, J. Phys. Chem. Solids **50**, 563.

Reehuis, M., and W. Jeitschko, 1990, J. Phys. Chem. Solids **51**, 961.

Reehuis, M., W. Jeitschko, M.H. Möller and P.J. Brown, 1988a, Z. Kristallogr. **182**, 218. In German.

Reehuis, M., W. Jeitschko, E. Mörsen and W. Müller-Warmuth, 1988b, J. Less-Common Met. **139**, 359.

Reehuis, M., T. Vomhof and W. Jeitschko, 1991, J. Less-Common Metals **169**, 139.

Reehuis, M., W. Jeitschko, M.H. Möller and P.J. Brown, 1992, J. Phys. Chem. Solids **53**, 687.

Reehuis, M., P.J. Brown, W. Jeitschko, M.H. Hönle and T. Vomhof, 1993, J. Phys. Chem. Solids **54**, 469.

Reinbold, E.J., and W. Jeitschko, 1987, Z. Kristallogr. **178**, 188. In German.

Ren, Y., and J. Meng, 1985, Investigation on the preparation and properties of rare earth monophosphides, in: New Frontiers in Rare Earth Science and Applications, Proc. Int. Conf. Beijing, September 10–14, 1985, Vol. 1 (Beijing) pp. 326–328.

Ren, Y., and J. Meng, 1988, J. Appl. Chem. (London) **5**, 39.

Rühl, R., and W. Jeitschko, 1979, Mat. Res. Bull. **14**, 513.

Rundqvist, S., 1960, Acta Chem. Scand. **14**, 1961.

Rundqvist, S., and F. Jellinek, 1959, Acta Chem. Scand. **13**, 425.

Sampathkumaran, E.V., B. Perscheid and G. Kaindl, 1984, Solid State Commun. **51**, 701.

Sampathkumaran, E.V., G. Kaindl, W. Krone, B. Perscheid and B. Vajayaraghavan, 1985a, Phys. Rev. Lett. **54**, 1067.

Sampathkumaran, E.V., B. Perscheid, W. Krone and G. Kaindl, 1985b, J. Magn. Magn. Mater. **47–48**, 407.

Sampathkumaran, E.V., G. Warthmann and G. Kaindl, 1986, J. Magn. Magn. Mater. **54–57**(Part 1), 347.

Samsonov, G.V., and S.N. Endrzeevskaja, 1963, Zh. Obshch. Khim. **33**, 2803. In Russian.

Samsonov, G.V., L.L. Verejkina, S.N. Endrzeevskaja and N.N. Tichonova, 1966, Ukr. Khim. Zh. **32**, 115. In Russian.

Samsonov, G.V., V.B. Chernohorenko and S.V. Muchnik, 1977, Present state and prospects of investigation and utilization of phosphides, in: Obtaining, Properties and Utilization of Phosphides (Naukova Dumka, Kiev) pp. 5–16. In Russian.

Samsonov, G.V., V.B. Chernohorenko and G.F. Kobzenko, 1978, Regularities of interaction of elements of Vb subgroup with neodymium, in: Refractory Compounds of Rare Earths (Donish, Dushanbe) pp. 98–103. In Russian.

Scavnicar, S., 1960, Z. Kristallogr. **114**, 85. In German.

Schmettow, W., D. Sommer, C. Mensing and H.G. von Schnering, 1980, Europium-Phosphid-Arsenid $EuP_{3-x}As_x$, in: 2. Vortragstag. Ges. Dtsch. Chem. Fachgruppe Festkörperchen (Stuttgart) Kurzref, p. 1. In German.

Schmettow, W., C. Mensing and H.G. von Schnering, 1984, Z. Anorg. Allg. Chem. **510**, 51.

Schoemaker, C.B., and D.P. Schoemaker, 1965, Acta Crystallogr. **18**, 900.

Shenoy, G.K., D.R. Noakes and G.P. Meisner, 1982, J. Appl. Phys. **53**(Part 2), 2628.

Shouminsky, Ye.S., S.I. Chykhrij and Yu.B. Kuz'ma, 1991, Visn. L'viv. Derzh. Univ. Ser. Khim. **31**, 29. In Ukrainiam.

Sikirica, M., and Z. Ban, 1964, Croat. Chem. Acta **36**, 151.

Sinitsina, E.D., I.H. Vasil'eva and K.E. Mironov, 1970, Chemical properties of cerium, praseodymium and ytterbium monophosphides, in: Chemistry of Phosphides with Semiconductor Properties (Nauka, Novosibirsk) pp. 71–74. In Russian.

Smith, G.S., Q. Johnson and A.G. Tharp, 1966, Acta Crystallogr. **22**, 269.

Sokolowskaya, E.M., and L.S. Huzej, 1986, Metallokhimiya (Izd. MGU, Moscow) 264pp. In Russian.

Tejedor, P., and A.M. Stacy, 1990, J. Solid State Chem. **89**, 227.

Tomuschat, C., and H.U. Schuster, 1981, Z. Naturforsch. **36b**, 1193. In German.

Tomuschat, C., and H.U. Schuster, 1984, Z. Anorg. Allg. Chem. **518**, 161. In German.

Torbov, V.I., L.A. Egorov, V.I. Chukalin and E.I. Jarembash, 1971, Izv. Akad. Nauk SSSR Neorg. Mater. 7, 1618. In Russian.

Torbov, V.I., V.I. Chukalin, V.N. Doronin, L.T. Nikolayeva and Z.S. Medvedyeva, 1974, Zh. Neorg. Khim. **19**, 39. In Russian.

Troć, R., R. Niedzielski, J. Lieciejewicz and A. Murasik, 1978, The magnetic phase diagram of UP–LP, in: Rare Earth and Actinides 1977, Inst. of Phys. Conf. Ser. **37**, 196.

Vasil'eva, I.G., K.E. Mironov and Yu.I. Mironov, 1970, Some properties of cerium monophosphide, in: Rare Earth Metals and their Compounds (Naukova Dumka, Kiev) pp. 160–165. In Russian.

Vedel, I., A.M. Redon, J. Rossat-Mignod, O. Vogt and J.M. Leger, 1987, J. Phys. C **20**, 3439.

Villars, P., and L.D. Calvert, 1985, Pearsons Handbook of Crystallographic Data for Intermetallic Phases (ASM, Ohio) 3 volumes, 3258pp.

Villars, P., and L.D. Calvert, 1991, Pearsons Handbook of Crustallographic Data for Intermetallic Phases, 2nd Ed. (ASM, Metals Park, OH) 4 volumes.

Vol, A.E., and I.K. Kohan, 1976, Structure and Properties of Binary Metal Systems, Vol. 3 (Nauka, Moscow) p. 682. In Russian.

von Schnering, H.G., and W. Dahlmann, 1971, Naturwissenschaften **58**, 623. In German.

von Schnering, H.G., and W. Hönle, 1988, Chem. Rev. **88**, 243.

von Schnering, H.G., and M. Wittmann, 1980, Z. Naturforsch. **35b**, 824. In German.

von Schnering, H.G., W. Wichelhaus and N.M. Schulze, 1975, Z. Anorg. Allg. Chem. **412**, 193. In German.

von Schnering, H.G., W. Wichelhaus and M. Wittmann, 1976, New polyphosphides of the rare earth metals, in: Reports 5th Int. Conf. on Solid Compounds of Transition Elements, Uppsala, Report II.68.

von Schnering, H.G., M. Wittmann and D. Sommer, 1984, Z. Anorg. Allg. Chem. **510**, 61. In German.

von Schnering, H.G., M. Hartweg, H. Kalpen, F.J. Nus and W. Hönle, 1988, Z. Kristallogr. **182**, 238. In German.

Warthmann, G., K.H. Frank, E.V. Sampathkumaran, B. Perscheid, G. Schmeister and G. Kaindl, 1985, J. Magn. Magn. Mater. **49**, 325.

Wenski, G., and A. Mewis, 1986a, Z. Naturforsch. **41b**, 38. In German.

Wenski, G., and A. Mewis, 1986b, Z. Anorg. Allg. Chem. **543**, 49. In German.

Wenski, G., and A. Mewis, 1986c, Z. Kristallogr. **174**, 200.

Wenski, G., and A. Mewis, 1986d, Z. Kristallogr. **176**, 125.

Wertheim, G.K., E.V. Sampathkumaran, G. Laubschat and G. Kaindl, 1985, Phys. Rev. B **31**, 6836.

Westerholt, K., and S. Methfessel, 1977, Physica B+C **86–88**, 1160.

Westgren, A., G. Hägg and S. Erikson, 1929, Z. Phys. Chem. B **4**, 453.

Wichelhaus, W., and H.G. von Schnering, 1975, Naturwissenschaften **62**, 180. In German.

Wichelhaus, W., and H.G. von Schnering, 1976, Z. Anorg. Allg. Chem. **419**, 77. In German.

Wittmann, M., W. Wichelhaus and G. Menge, 1977, Die Pentaphosphide der Seltenerdmetalle, in: 17 Hauptversammlung Gesellschaft der Deutscher Chemikersch, München, 1977 (Frankfurt/Main) p. 75. In German.

Yarmolyuk, Ya.P., and L.G. Aksel'rud, 1983, Kristallografiya **28**, 1111. In Russian.

Yarmolyuk, Ya.P., L.O. Lysenko and E.I. Gladyshevskii, 1975, Dopov. Akad. Nauk Ukr. RSR. Ser. A **3**, 281. In Ukrainian.

Yarmolyuk, Ya.P., L.G. Aksel'rud and E.I. Gladyshevskii, 1978, Kristallografiya **23**, 942. In Russian.

Yarmolyuk, Ya.P., L.G. Aksel'rud, V.S. Fundamenskii and E.I. Gladyshevskii, 1980, Kristallografiya **25**, 97. In Russian.

Yim, W.M., E.J. Stofko and R.T. Smith, 1972, J. Appl. Phys. **43**, 254.

Zachariasen, W.H., 1949, Acta Crystallogr. **2**, 60.

Zarechnyuk, O.S., P.I. Krypyakevych and E.I. Gladyshevskii, 1964, Kristallografiya **9**, 835. In Russian.

Zemni, S., D. Tranqui, P. Chaudouet, R. Madar and J.P. Senateur, 1986, J. Solid State. Chem. **65**, 1.

Zeppenfeld, K., and W. Jeitschko, 1993, J. Phys. Chem. Solids **54**, 1527.

Zimmer, B.I., and W. Jeitschko, 1992, Z. Kristallogr. **5**(Suppl.), 271. In German.

Zolnierek, Z., H. Noël and D. Kaczorowski, 1987, J. Less-Common Met. **128**, 265.

Zwiener, G., H. Neumann and H.U. Schuster, 1981, Z. Naturforsch. **36b**, 1195. In German.

Handbook on the Physics and Chemistry of Rare Earths
Vol. 23
edited by K.A. Gschneidner, Jr. and L. Eyring

Chapter 157

HALIDE VAPORS AND VAPOR COMPLEXES

S. BOGHOSIAN and G.N. PAPATHEODOROU
Institute of Chemical Engineering and High Temperature Chemical Processes, ICE/HT-FORTH and Department of Chemical Engineering, University of Patras, P.O. Box 1414, GR-26500 Patras, Greece

Contents

1. Introduction

The systematics of high-temperature metal halide vapors and vapor complexes have earlier been summarized in a number of review articles or monographs. Worth mentioning are the books by Schäfer (1964), Margrave (1967) and Hastie (1975) and a number of proceedings volumes, such as those edited by Hildenbrand and Cubicciotti (1978) and Hastie (1979). Schäfer (1976, 1983) reviewed the thermodynamics of metal chloride vapor complexes. Papatheodorou (1982) and Brooker and Papatheodorou (1983) gave an extensive account on the electronic, vibrational, thermodynamic and structural properties of transition and rare-earth metal halide vapor complexes. Finally, Hilpert (1989, 1990)

summarized the thermodynamics of the metal halide vapor complexes studied by Knudsen effusion mass spectrometry since the year 1980.

In the years after 1970, the vapor complexes gained in significance due to a series of important potential applications (Hastie 1975) related to new energy sources, energy conservation and to a number of recycling and/or separation processes. A sudden increase in the number of published articles was then observed which resulted in a significant improvement in the knowledge of the thermochemical properties of the rare-earth halide vapor complexes as well as to a much better understanding of their electronic and structural properties. A large number of new vapor complexes has been identified and the thermodynamics of their formation have been determined.

The aim of this chapter is to review the up to date available data of the simple rare-earth halide vapors and of the vapor complexes formed by the rare-earth halides with different complexing agents. First (sect. 2), the vaporization thermodynamics and structural trends of simple rare-earth halides will be addressed together with the characterization of gaseous homo-complexes. The summary of vapor complexes in binary systems of rare-earth halides with (principally) alkali halides, in which the total vapor pressures are low enough to permit the use of Knudsen effusion mass spectrometry will constitute a separate section (sect. 3). Some of these systems are characterized by *volatility enhancement factors* (see sect. 1.1) between 1 and 140, and are important for the development of high intensity discharge lamps. The discussion on vapor complexes involving the relatively volatile trichlorides of Al, In and Ga as complex forming agents ("carrier gases") and the presentation of vapor complex systems with volatility enhancement factors up to 10^{13} will then be presented (sect. 4). These systems, studied mainly by electronic absorption and fluorescence spectroscopy, had been given serious consideration as energy storage media for high power laser systems and for development of recycling/separation processes (sect. 1.2) thus making a natural choice for a separate section.

1.1. *Vapor complex formation*

Vapor complexation involving rare-earth halides can be classified depending on the type of the metal halide which plays the role of the *vapor complex forming agent* in two large categories represented by the following general reaction schemes:

$$m\,RX_3(\text{s or l}) + n\,MX(\text{s, l or g}) \rightleftharpoons M_nR_mX_{3m+n}(\text{g}), \tag{1}$$

where MX is (usually) an alkali halide and

$$m\,RX_3(\text{s}) + n\,A_2X_6(\text{g}) \rightleftharpoons R_mA_{2n}X_{3m+6n}(\text{g}), \tag{2}$$

where AX_3 is mainly a Group-IIIA halide (A = Al, In, Ga; X = Cl, Br, I).

In case (1) the alkali halide may be present both in the condensed and vapor phase, while the more volatile Group-IIIA halides (reaction 2) are in the gas phase. A large number of particular reactions of type (1) and (2) have been studied with a view both

to establish the formation and the stoichiometry of the gaseous complexes participating in the equilibrium vapors as well as to characterize their thermochemical, electronic and structural properties. Among the various experimental methods applied for the characterization of metal halide vapor complexes, the most widely used ones include Knudsen effusion mass spectrometry (Hilpert 1989, 1990), transpiration experiments (Wachter and Schäfer 1980), analysis of quenched equilibrium vapors (Wachter and Schäfer 1980), vapor density measurements using radioactive isotopes (Peterson et al. 1979), spectrophotometry (Øye and Gruen 1969), fluorescence spectroscopy (Carnall et al. 1978), total pressure measurements of equilibrium vapors (Datz et al. 1961), boiling point technique and condensate analysis (Mien-tseng and Novikov 1966) and chemical vapor transport (Schäfer 1964, 1974). By far the most extensive information on vapor composition and partial pressures has been obtained by Knudsen effusion mass spectrometry. Hilpert (1989, 1990) has demonstrated the potential of this method as exploited also by transpiration mass spectrometry for gas phase analysis.

While the value of m in reactions (1) and (2) has most commonly been assumed or found to be equal with *one*, often n has been shown to get more than one value in each binary system. In reactions of type (1) common values for n include 1 and 2 corresponding to MRX_4 and M_2RX_5 vapor complexes, while in reactions of type (2) n may obtain several values ($n=0.5$, 1, 1.5, 2, ...) corresponding to RAX_6, RA_2X_9 RA_3X_{12}, RA_4X_{15} type vapor complexes. Generally more than one complex is present in the equilibrium vapor mixture (see sect. 3.2, 4.1).

It has been established that the apparent volatilities of transition and rare-earth metal halides are increased by several orders of magnitude through reactions of type (1) and (2) giving rise to vapor complex formation. The enhancement of the vapor densities of transition metal and/or rare-earth metal ions has commonly (see for example Papatheodorou 1982) been reported in the form of the *volatility enhancement factor*. That is, when a reaction occurs between a solid rare-earth halide with low vapor pressure P_S (e.g. $NdCl_3$) and a more volatile salt (carrier gas) with partial pressure P (e.g. $AlCl_3$, NaCl), and the partial pressure of the vapor complex is P_C, then the volatility enhancement factor is determined at *unit pressure* of the carrier gas as:

$$r = P_C / P_S. \tag{3}$$

Depending on the system and temperature the values of r are up to ~140 for reactions with alkali halides (see sect. 3) but can reach values up to 10^{13} for reactions with aluminum halides (see sect. 4).

Of significant interest also are the thermochemical properties of single component rare-earth halide systems. Formation of gas phase homocomplexes (e.g R_2X_6 dimers) has been established for a limited number of rare-earth halides, which however at least for the chlorides and iodides are considered to represent the range of properties of the whole series (i.e., $ScCl_3$, $LaCl_3$, $EuCl_3$ and $LuCl_3$, and ScI_3, LaI_3, DyI_3, HoI_3 and TmI_3) indicating that formation of dimers can most likely be safely assumed as occurring also for the rest of the single component systems. Establishing the thermochemical properties

of the vapor complexes and determining the relative amounts of the species present in equilibrium vapors should naturally be based on accurate thermodynamic data concerning the pure systems.

1.2. *Applications*

Hastie (1975) has presented a detailed description of the applications involving metal halide vapor complexes in general, while more recent accounts are given by Schäfer (1976, 1983) and Papatheodorou (1982). Particular applications of rare-earth halide vapor complexes have been described separately. Thus, the role of rare-earth halide vapor complexes in the improvement of the luminous efficacy and color rendering index of metal halide lamps has been specifically addressed (see e.g. Hirayama et al. 1978b, 1980, Wesselink 1983, Van Erk and Rietveld 1987); the potential use of the rare-earth halide vapor complexes as laser media has been demonstrated (see e.g. Krupke 1976a–c, Hessler et al. 1977) and extensive studies of separation processes have recently been performed by Adachi's group (see e.g. Murase et al. 1993). A summary of the most characteristic applications of rare-earth halide vapor complexes will be presented in the present subsection. For further information the reader should refer to the articles cited under each application in order to access the original literature.

1.2.1. *Chemical synthesis-crystal growth*

A method for the preparation and purification of anhydrous rare-earth halides based in vapor complexation and chemical vapor transport has been developed which uses the rare-earth oxide as starting material. As an example, for preparing and purifying $SmCl_3$ (Papatheodorou and Kucera 1979), anhydrous and degassed Sm_2O_3 (~2 g) was placed in fused silica tubes (~1 cm i.d. × 20 cm long) containing an excess of aluminum chloride (~2 g). The evacuated and sealed tube was then placed in a furnace and the temperature was raised slowly (in 3–4 h) to 300°C. Near 200°C the following reaction began:

$$Sm_2O_3(s) + Al_2Cl_6(g, l) \rightarrow Al_2O_3(s) + 2SmCl_3(s). \tag{4}$$

The chlorination was completed within a few hours and the remaining excess of $Al_2Cl_6(g)$ created a pressure of ~2 atm in the tube. The tube was then placed in a tilted furnace where the lower part of the tube, containing the solids (Al_2O_3 + $SmCl_3$), was at 350°C and the upper part was near the melting point of aluminum chloride (180°C). With this thermal gradient "$SmCl_3$" was vapor transported according to the following reaction:

$$SmCl_3(s) + \tfrac{3}{2}Al_2Cl_6(g) \rightleftharpoons SmAl_3Cl_{12}(g), \tag{5}$$

and was deposited in the form of small yellow crystals (~0.1 mm × 1 mm) at the middle of the tube. Within 2 days the vapor transport yielded ~1 g of $SmCl_3$. By using the same procedure Papatheodorou and Kucera (1979) prepared and vapor transported $NdCl_3$, $NdBr_3$, $PrCl_3$, $ErCl_3$, YCl_3, $ThCl_4$, UCl_3 and UCl_4 by reacting the corresponding oxides

with Al_2Cl_6 or Al_2Br_6 [reactions like (4) and (5)] which they concluded were very general for the preparation of rare-earth and actinide halides. By appropriate control of the vapor transport rate small single crystals of the halides were obtained. More recently by using the same method $ScCl_3$, $LaCl_3$, $DyCl_3$, $GdCl_3$ and $LuCl_3$ have also been prepared and purified (Boghosian et al. 1995).

Preparation of iodides can also be performed by means of reaction (4) using rare-earth oxides and AlI_3 (Moyer 1978) or alternatively Al metal and I_2 as starting materials. For example, (Boghosian and Herstad 1994) for a small scale production, ~1 g of anhydrous and degassed terbium oxide was placed in a silica tube together with aluminum metal (~0.25 g) and iodine (~4 g). The tube was evacuated and sealed and the reaction mixture was heated to 250°C for 48 h. After the iodination of aluminum was completed the temperature was raised to 400°C for another 48 h. The reaction tube contained a condensed phase (Al_2O_3 + TbI_3) while gaseous Al_2I_6 and I_2 were also contained. The excess AlI_3 and I_2 were condensed away by applying a temperature gradient along the container sealed tube and the rare-earth iodide was separated and purified by repeated vacuum distillations.

1.2.2. *Chemical separations*

In the late 1960s Zvarova and Zvara (1969, 1970) as well as Zvarova (1973) demonstrated that a vapor transport process mediated by vapor complexation with Al_2Cl_6 can be used for gas-chromatographic separations of lanthanides and actinides based on differences in the volatility enhancement of the involved metal halides as well as differences in the affinity between individual complexes and column packings. The method appears to have potential for treating and separating nuclear fuel materials. For example, Papatheodorou (1982) has described a laboratory scale separation of ThO_2 and UO_2, in which reaction of the oxides with a mixture of Al_2Cl_6(g) and Cl_2(g) at 700 K, yields $ThCl_4$ and UCl_5, and subsequently $ThAl_2Cl_{10}$ and $UAlCl_8$, which can then be separated in a temperature gradient due to different apparent volatility enhancements and produce very pure and separated UCl_5 and $ThCl_4$ crystals.

More recently Adachi's group in Japan performed chemical vapor transport experiments and demonstrated the mutual separation of rare-earth chlorides in binary (Pr–Er, Pr–Sm and Pr–Nd) as well as in ternary (Pr–Gd–Er) systems based on the formation of $RAl_{2n}Cl_{6n+3}$ vapor complexes (see for example Murase et al. 1993, 1994a and references therein). Recovery of rare earths from the scrap of rare-earth intermetallic compounds was also performed from the same group of authors (Murase et al. 1995) along a well-controlled temperature gradient using either $AlCl_3$ or alkali chlorides as complex forming agents. Their apparatus, a sectional view of which is shown in fig. 1 consisted of two electric kanthal wound mullite tube (i.d. 35 mm) furnaces, A (length 180 mm) and B (length 500 mm). Furnace A was used to generate gaseous Al_2Cl_6 while furnace B comprised several divided heaters so to produce various heating zones and temperature gradients. $RAl_{2n}Cl_{6n+3}$ vapor complexes were formed above the boat containing the raw material (lanthanoid chloride or oxide mixtures) and carried along the furnace

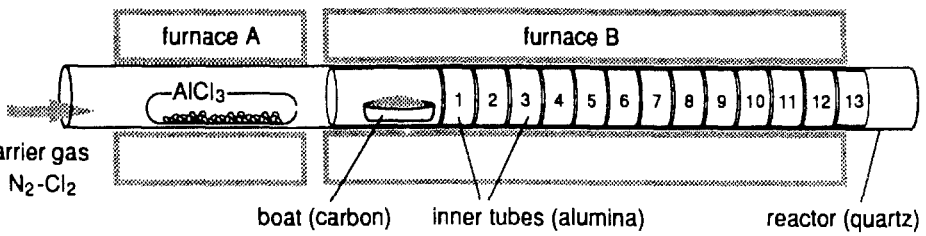

Fig. 1. Assembly of furnaces for the vapor transport and separation of rare-earth halides. The numbers 1–13 denote fraction numbers of separately heated zones (from Murase et al. 1994b).

by the carrier gas stream (N_2, Cl_2, Al_2Cl_6). Heavier rare-earth chlorides were readily transported and concentrated in deposits in lower temperature zones while lighter ones were selectively deposited in higher temperature zones.

1.2.3. *Metal halide lamps*

The importance of vapor complex formation in RX_3–MX binary systems [M = alkali metal, X = I (mainly) and Br] according to reaction (1) for the development of high intensity discharge lamps with high luminous efficacy and a good color rendering index was recognized a few decades ago and has triggered a lot of interest on the thermochemical properties and on the systematics of the vapor complexes between rare-earth iodides or bromides and the corresponding alkali halides. Hirayama et al. (1978b, 1980) and Hilpert (1989) have outlined descriptions of the role of these vapor complexes in metal halide lamps. The achieved progress has led to exploitation of modifications in the mercury lamp via additions of mixtures of metal halides. The rare-earth iodides ScI_3, DyI_3 and TmI_3 have already been used mixed with NaI in commercial lamps. Vapor complex compounds of the form $NaRI_4$ are the dominant species present in the equilibrium vapor of the high-temperature arc of these lamps (see fig. 2), thereby increasing the vapor density of desired radiative species in the discharge medium. Iodides have proven most satisfactory as lamp additives due to their compatibility with the silica arc tubes and with the tungsten electrodes and due to their higher vapor pressures when compared to the other halides.

For the efficient modelling of the metal halide lamps (Hirayama et al. 1980) it is important to establish both the composition of the gas phase (i.e. species present and partial pressures) in the arc tube over the condensed phase as well as the relevant thermochemical properties. Various reactions take place in the range of temperatures (i.e., from ~1000 K in the envelope to ~4000 K in the arc) of the tube (see fig. 2). The Na concentration in the arc tube is enhanced significantly by formation of Na_nRI_{3+n} vapor complexes, thereby resulting in higher efficiencies for generation of radiation emitted from excited Na atoms in the high-temperature arc column. Furthermore, when such reactions occur in the lamp envelope, rare-earth metal ions are introduced in the electric arc, resulting in better color rendition due to the rich emission spectra in the visible range possessed by these ions.

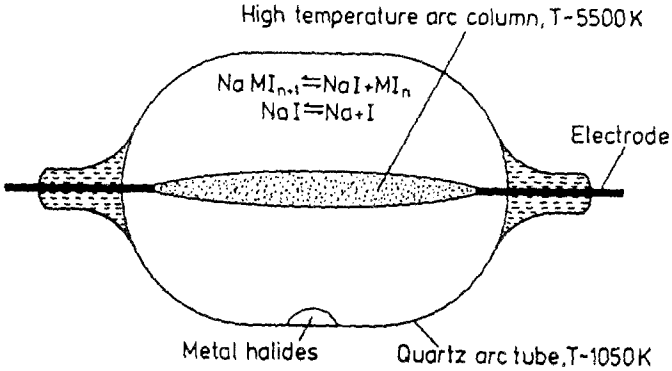

Fig. 2. Schematic representation of the arc tube of a metal halide lamp (from Hilpert 1989).

1.2.4. *Lasers based on vapor complexation*

A motivating factor for the increased emphasis for studying the vapor complexes formed between rare-earth chlorides and aluminum chloride has been the potential for their use as laser media. It has been suggested that rare-earth molecular vapors could overcome the low efficiency, high cost, and low duty cycle inherent in the very-high-power solid state rare-earth lasers used in laser fusion applications (see for example Krupke 1976a,c). One of the reasons for which the rare-earth vapor complexes have been selected among other groups of rare-earth vapors is their relatively high volatility. Volatility enhancement factors up to 10^{13} have been reported for $RCl_3(AlCl_3)_n$ vapor complexes (sect. 4) resulting in densities as high as 10^{18} rare-earth ions/cm^3 at 600 K, which is deemed sufficient for optical gain and high-energy storage. Therefore, studies of the optical and fluorescence properties of these vapors are of importance although there have been no reports for construction of high power lasers using these materials.

2. Vapors of simple rare-earth halides

The vaporization of rare-earth trihalides (RX_3) gives rise to the formation of mainly monomer vapor halide molecules, RX_3. In several cases however, vapor dimer homo-complexes (R_2X_6) have been identified (see e.g. Hastie et al. 1968). Gaseous divalent lanthanide halides (RX_2, R = Sm, Eu and Yb) exist predominantly as monomers, while CeF_4 is the only tetrahalide that vaporises congruently (Gibson and Haire 1988). The vaporization thermodynamics of rare-earth halides will be reviewed in the present section. Emphasis will be given to the collection of vapor pressure data as well as on the enthalpies and entropies of sublimation and dimerization. An account of the structural properties of rare-earth halide vapors will also be given.

Extensive descriptions of the high-temperature methods utilized for identifying the gaseous species and for establishing their thermochemical, structural, vibrational and electronic properties are given by Margrave (1967), Hastie (1975) and Hastie (1979). Hilpert (1990) underlined the potential of Knudsen effusion mass spectrometry as a tool

for both qualitative and quantitative analysis of high-temperature equilibrium vapors as well as for determining their thermochemical properties.

The vaporization thermodynamics of rare-earth halides have been the subject of numerous investigations in which the reported experimental data do not appear always to be reproducible among the various research groups. This is probably due to insufficient purity of the samples used, incompatibility of container materials and low accuracy of the measurements, specially where low partial pressures were involved. After Brown (1968) had given a very extensive coverage of the vaporization thermodynamics of rare-earth halides, numerous relevant studies dealing also with reinvestigations of previously studied systems appeared in the literature. Myers and Graves (1977a,b) reviewed and reported the data produced from the late 1960s up to 1976, while Hilpert (1990) summarized the rare-earth halide vaporization studies that took place since about the year 1980 by means of Knudsen effusion mass spectrometry. A recent compilation of the thermodynamic properties of inorganic substances (Barin 1993) includes most of the rare-earth halides in the vapor as well as in the condensed phases. From the Barin tables the thermodynamic functions of vaporization and the apparent vapor pressures over solid or liquid rare-earth halides can be estimated. The relevant literature is extensive and the reader will have to refer in certain cases to the previous reviews to find references to the original literature.

Trends in the sublimation enthalpies of lanthanide halides with a common anion according to which the enthalpies of sublimation decrease monotonically with the atomic number of the lanthanide (Shimazaki and Niwa 1962) should be taken under question since both Hirayama et al. (1975) as well as Myers and Graves (1977a,b) illustrated that there is no such monotonic trend at least for the case of chlorides, bromides and iodides. Furthermore, from a structural point of view, it seems that although the majority of the data supports slightly pyramidal RX_3 gaseous molecules, the question as to which rare-earth trihalides are planar (D_{3h} symmetry) and which are pyramidal (C_{3v} symmetry) does not appear to be fully settled experimentally. However, extended Huckel calculations (Myers et al. 1978) performed within the frame of molecular orbital methods on rare-earth trihalide molecules gave lower total valence electron energies for pyramidal geometries (C_{3v}) than for planar geometries (D_{3h}) in agreement with the experimental evidence. The important result of the above calculations is that all rare-earth halide molecules are predicted to possess pyramidal configurations. Calculated X–R–X bond angles corresponding to minimum energies were found to increase in the halogen series as well as with increasing atomic number of the lanthanide ranging from 91° for LaF_3 to 119° for LuI_3. Moreover, in agreement with the above calculations, empirical correlations based on polarizability models (Drake and Rosenblatt 1979) illustrated remarkable trends in the geometries of RF_3 and RCl_3 molecules according to which these molecules are likely to be pyramidal.

Finally, the crystal structure of the rare-earth trihalides and the coordination of the rare-earth ion in the crystal lattice represents substantial interest and it will be addressed, since it has been argued (Papatheodorou 1982) that the coordination of the metal atom in a series of transition and rare-earth metal halide vapor complexes is most probably preserved on going from the solid halide to the vapor complex molecule. In each group

of lanthanide halides, structural changes occur on going from LaX_3 to LuX_3 by following systematic trends according to which as the ionic radii get smaller along the lanthanide series, the structures change to less crowded ones. The changes in the coordination number are also related to the size of the halogen atoms, in such a way that large halogen atoms tend to limit the coordination around, particularly, the lanthanide metals with small ionic radii while small halogen atoms allow for larger coordination numbers.

2.1. *Fluorides*

Among the rare-earth halides, fluorides represent the most extensively studied systems with respect to the thermochemical properties of their vapors. Most of the studies took place in the period from the late 1960s to mid-1970s.

From the point of view of their crystal structures, while scandium trifluoride is cubic and the trifluorides of lanthanum to neodymium inclusive crystallize only in the LaF_3-type hexagonal symmetry, the trifluorides of yttrium and samarium to lutetium inclusive are dimorphic. These latter trifluorides crystallize in the orthorhombic YF_3-type at room temperature and undergo transitions to hexagonal phases at high temperatures. Brown (1968) reviewed some early crystal structure work, while Spedding and Henderson (1971) and Spedding et al. (1974) provided more precise data concerning the lattice parameters and transition temperatures (orthorhombic $\rightarrow$ hexagonal). The high precision powder data of Greis and Petzel (1974) are in good agreement with Spedding's lattice parameters.

Extensive studies have been performed for the determination of the vapor pressures and the vaporization thermodynamics of rare-earth fluorides. The majority of the data are based on mass spectrometric work and originate from the laboratories of Suvorov, Margrave and Searcy. Table 1 summarizes the reported vapor pressures and thermodynamic functions of sublimation, vaporization and (in two cases) dimerization of rare-earth fluorides. The data are not in full agreement in those cases that the same compound has been studied by different research groups. The reader should also refer to the articles of Myers and Graves (1977a,b) for selected third-law values for the enthalpy of sublimation, $\Delta H^0_{s,298}$.

Although the electron impact fragmentation patterns resulting from dissociative ionization of $RF_3(g)$ molecules appear to have been established (see for example Zmbov and Margrave 1968), a survey of the literature shows that the RF_3^+ fragment has not been detected in all cases, thus creating a possible source for the observed differences. Furthermore, it seems that the scarcity of reports concerning the identification of R_2F_6 dimer vapor molecules is due to the experimental difficulty in identifying fragments of the type $R_2F_n^+$ (due to insufficient sensitivity of the mass spectrometers used more than two decades ago) and not because the dimer species are actually not present in the equilibrium vapor. Indeed, progress in the instrumentation used in Knudsen effusion mass spectrometric studies of rare-earth halide vapors made the identification and the determination of thermochemical properties of R_2X_6 dimer molecules feasible even in bromide (see Hilpert et al. 1995) and iodide systems (see for example Hilpert 1990 and

Table 1
Vapor pressures and vaporization thermodynamics of rare-earth fluorides[a,b]

Substance	m.p. (K)	Ref.	Temperature range (K)	Ref.	Vapor species identified	$\log P_{atm} = -A/T(K) + B$		$RF_x(s) \rightleftharpoons RF_x(g)$		$RF_3(l) \rightleftharpoons RF_3(g)$		$2RF_3(g) \rightleftharpoons R_2F_6(g)$	
						A	B	$\Delta H^0_{s,T}$ [c]	$\Delta S^0_{s,T}$ [d]	$\Delta H^0_{v,T}$ [c]	$\Delta S^0_{v,T}$ [d]	$\Delta H^0_{d,T}$ [c]	$\Delta S^0_{d,T}$ [d]
ScF_3	1825	1	1159–1411	2	ScF_3	17774	8.698	340	167				
			1172–1402	3,4	ScF_3	19380	9.43	371	181				
			1223–1473	5				341	183				
			1335–1403	6				345	166				
YF_3	1428	7	1256–1434	3,4	YF_3	21850	9.77	419	187				
LaF_3	1766	7	1340–1650	8	LaF_3	21730	9.608	416	184				
			1200–1434	3,4	LaF_3	20200	8.20	387	157				
			1221–1736	9	LaF_3, La_2F_6			410	176			–298	–191
			1450	10	LaF_3			340	127				
CeF_3	1705	1	1373–1634	11	CeF_3	20460	9.205	392	176				
			1301–1485	4	CeF_3			382	(159)				
			1577	12	CeF_3, Ce_2F_6							–216	
			1450	10	CeF_3			383	161				
CeF_4			800–1123	13	CeF_4			209					
PrF_3	1672	7	1424–1586	14	PrF_3	21090	9.371	404	180				
			1327–1491	4	PrF_3			389	(159)				
			1340–1470	10	PrF_3	17923	7.066	345	140				
NdF_3	1650	7	1383–1520	15,4	NdF_3	18730	8.03	359	154				
			1450	10				341	136				
SmF_3	1573	1	1362–1506	4	SmF_3, SmF_2			405	188				
SmF_2	1690	16											
EuF_3	1549	16	1382–1522	4	EuF_3, EuF_2			385	(180)				
EuF_2	1689	16	1412–1612	17	EuF_2	20360	8.591	390	165				

continued on next page

Table 1, *continued*

Substance	m.p. (K)	Ref.	Temperature range (K)	Ref.	Vapor species identified	$\log P_{atm} = -A/T(K) + B$		$RF_x(s) \rightleftharpoons RF_x(g)$		$RF_3(l) \rightleftharpoons RF_3(g)$		$2RF_3(g) \rightleftharpoons R_2F_6(g)$	
						A	B	$\Delta H^0_{s,T}$ [c]	$\Delta S^0_{s,T}$ [d]	$\Delta H^0_{v,T}$ [c]	$\Delta S^0_{v,T}$ [d]	$\Delta H^0_{d,T}$ [c]	$\Delta S^0_{d,T}$ [d]
GdF_3	1504	16	1391–1527	4	GdF_3			378	(172)				
TbF_3	1450	1	992–1167	4	TbF_3			426	(197)				
DyF_3	1430	1	1314–1386	18	DyF_3	23250	10.720	446	206				
			1002–1170	4	DyF_3			450	207				
DyF_3(l)			1426–1622	18	DyF_3	18420	7.538			353	145		
HoF_3	1416	7,16	1278–1415	18	HoF_3	23090	10.650	442	204				
			1023–1180	4	HoF_3			447	209				
HoF_3(l)			1423–1499	18	HoF_3	18470	7.333			354	141		
ErF_3	1419	1	1314–1386	18	ErF_3	23390	10.680	448	205				
ErF_3(l)			1421–1521	18	ErF_3	19300	7.777			370	149		
TmF_3	1431	1	1273–1415	19	TmF_3	19600	8.24	376	158				
YbF_3	1435	1	1293–1428	19	YbF_3,YbF_2	18670	7.75	358	149				
YbF_3(l)			1548–1703	20	YbF_3,YbF_2	19100	7.54			366	144		
YbF_2	1680	16											
LuF_3	1457	7	1287–1450	19	LuF_3	21000	9.41	402	181				

continued on next page

Table 1, notes

[a] Reported vapor pressures are over the solid condensed phase unless indicated otherwise by "(l)". Listed values of enthalpy ($kJ\,mol^{-1}$) and entropy ($J\,mol^{-1}\,K^{-1}$) refer to the mean of the temperature range given. Parentheses denote estimated values.

[b] Scandium trifluoride is cubic. Yttrium trifluoride and the trifluorides of samarium to lutetium are dimorphic, possessing orthorhombic YF_3-type structure, at room temperature. Above their transition temperatures (see Brown 1968, Spedding et al. 1974 and Spedding and Henderson 1971) they transform to hexagonal. The high-temperature modifications of the trifluorides of samarium through holmium possess the LaF_3-type structure (Coordination Number of the rare-earth metal CN = 9), while the trifluorides of erbium through lutetium possess most probably the high-temperature YF_3-type hexagonal structure (CN = 9).

[c] In $kJ\,mol^{-1}$.

[d] In $J\,mol^{-1}\,K^{-1}$.

References

(1) Spedding et al. (1974)
(2) Rinehart and Behrens (1980)
(3) Kent et al. (1966)
(4) Zmbov and Margrave (1968)
(5) Rat'kovskii and Suvorov (1972)
(6) Petzel (1973)
(7) Spedding and Henderson (1971)
(8) Mar and Searcy (1967)
(9) Skinner and Searcy (1971)
(10) Suvorov et al. (1966)
(11) Lim and Searcy (1966)
(12) Roberts and Searcy (1972)
(13) Gibson and Haire (1988)
(14) Skinner and Searcy (1968)
(15) Zmbov and Margrave (1966)
(16) Brown (1968) and references therein
(17) Petzel and Greis (1972)
(18) Besenbruch et al. (1967)
(19) Zmbov and Margrave (1967)
(20) Biefeld and Eick (1975)

Table 2
Vibrational frequencies (in cm^{-1}) of pyramidal (C_{3v}) rare-earth trifluoride vapors[a,b,c]

Vapor molecule	$\nu_1(A_1)$	$\nu_2(A_1)$	$\nu_3(E)$	$\nu_4(E)$	Reference(s)
ScF_3	634	119	723	165	1
YF_3	597	95	595	140	1
	–	119	663	140	2
LaF_3	540	82	510	125	1
CeF_3	549	80	519	115	1
PrF_3	542	86	458	99	3,4
NdF_3	557	80	535	115	1
PmF_3	(560)	(90)	(535)	(124)	5
SmF_3	(564)	92	508	123	3,5
EuF_3	572	90	544	120	1
GdF_3	583	95	552	130	1
TbF_3	580	97	554	131	6
DyF_3	(581)	(98)	(561)	(133)	5
HoF_3	585	102	569	120	6
ErF_3	(589)	(102)	(571)	(137)	5
TmF_3	(593)	(103)	(576)	(139)	5
YbF_3	597	100	579	144	6
LuF_3	598	109	585	150	6

[a] Group theory classification of vibrational modes:
Pyramidal RF_3 (C_{3v} symmetry):
$\Gamma = 2A_1(R, IR) + 2E(R, IR)$;
Planar RF_3 (D_{3h} symmetry):
$\Gamma = A_1'(R) + 2A_2'(IR) + 2E'(R, IR)$

[b] IR studies of matrix-isolated rare-earth fluorides. Parentheses indicate estimated values.

[c] Although assignment is made on the basis of probable C_{3v} symmetry, planar D_{3h} symmetry has been argued at least for LaF_3, CeF_3, PrF_3, NdF_3, SmF_3 and EuF_3 (Hauge et al. 1971, Wesley and DeKock 1971, see also text).

References
(1) Hastie et al. (1975)
(2) Wesley and DeKock (1973)
(3) Wesley and DeKock (1971)
(4) Lesiecki et al. (1972)
(5) Myers and Graves (1977a)
(6) Hauge et al. (1971)

references therein), in which the high-mass $R_2I_n^+$-type fragments could be detected, in a mass range (around 900 amu) where the sensitivity of the mass spectrometers is low.

In contrast with the planar D_{3h} symmetries exhibited by the Group-IIIA (Al, Ga In) and Fe trihalides (Brooker and Papatheodorou 1983), most experimental structural work performed on rare-earth trifluorides is indicative of pyramidal C_{3v} geometries in accordance with the correlations outlined by Drake and Rosenblatt (1979) and the theoretical predictions of Myers et al. (1978). According to the latter calculations the F–R–F bond angles corresponding to minimum total electron energy are in the narrow range of 91° to 92° on going from La to Lu. Therefore, the vibrational frequencies of the rare-earth trifluoride vapors listed in table 2 are assigned on the basis of pyramidal geometry. Earlier, both planar D_{3h} (see for example Wesley and DeKock 1971) and pyramidal C_{3v} (Hauge et al. 1971,

Table 3
Vibrational frequencies (in cm^{-1}) of R_2F_6 dimers[a,b]

Molecule	$\nu_8(B_{1u})$	$\nu_9(B_{1u})$	$\nu_{13}(B_{2u})$	$\nu_{16}(B_{3u})$	$\nu_{17}(B_{3u})$	$\nu_{18}(B_{3u})$
Sc_2F_6	740	190	491	560	462	145
La_2F_6	532	166	378	542	323	
Ce_2F_6	404		359	448		

[a] Assignment is made for D_{2h} symmetry. Group theory classification of vibrational modes:
R_2F_6 dimer molecules (D_{2h} symmetry):
$\Gamma = 4A_{1g}(R) + 2B_{1g}(R) + 2B_{2g}(R) + B_{3g}(R) + A_u(IA) + 3B_{1u}(IR) + 2B_{2u}(IR) + 3B_{3u}(IR)$
[b] IR studies of matrix-isolated rare-earth fluorides. Data from Hastie et al. (1975)

Hastie et al. 1975) geometries have been supported based on interpretation of infrared spectral data of matrix-isolated RF_3 molecules that appear to be similar. The symmetric stretch ν_1 mode, which is IR-active only for the C_{3v} configuration has been measured for YF_3, LaF_3, CeF_3, NdF_3, EuF_3, GdF_3, TbF_3, HoF_3, YbF_3 and LuF_3 (Hauge et al. 1971). On the other hand, planar D_{3h} symmetries have been argued (Wesley and DeKock 1971) for LaF_3, CeF_3, PrF_3, NdF_3, SmF_3 and EuF_3. Although a clear assignment to the $\nu_1(ScF_3)$ mode has not been possible (Hastie et al. 1975), the pyramidal configuration for ScF_3 is supported from electric dipole deflection results (Kaiser et al. 1972). However, as stated by Yates and Pitzer (1979) there is far from a consensus on the structure of ScF_3. None the less the results of Kaiser et al. (1972) from their electric deflection study point to pyramidal geometries based on nonzero molecular dipole moments indicated by strong refocusing for ScF_3, YF_3, LaF_3, GdF_3 and LuF_3 and weaker refocusing for CeF_3, ErF_3 and TmF_3. Moreover the data for the PrF_3, NdF_3, TbF_3, DyF_3 and HoF_3 are interpreted in terms of C_{3v} structures arising from small distortions of the planar D_{3h} geometry.

Vibrational frequencies assigned to vapor R_2F_6 dimer molecules have been reported for the case of Sc_2F_6, La_2F_6 and Ce_2F_6 vapors trapped in inert matrices (Hastie et al. 1975). Table 3 summarizes the relevant data. As pointed out by Papatheodorou (1982) dimerization in the gas phase is likely to occur for trivalent metal halides, especially those of low molecular weight and low boiling points. From a structural point of view $M_2X_6(g)$ dimers are known to consist of two tetrahedra bridged by an edge (resulting in D_{2h} symmetry) with the exception of Au_2Cl_6 for which a planar gaseous structure has been found (Nalbandian and Papatheodorou 1992).

The difluorides of scandium, samarium, europium and ytterbium are known to exhibit bent C_{2v} structures. A bond angle of 135 deg has been estimated for ScF_2 based on the bond angles of neighbouring molecules (Hastie et al. 1969). Furthermore, relative IR intensities (Hastie et al. 1971, DeKock et al. 1972) have been used for determining a bond angle of 110 deg for EuF_2. Electric deflection results (Kaiser et al. 1972) confirm the highly bent structures of SmF_2, EuF_2 and YbF_2 indicated by relative infrared spectroscopic data. Previously, Brooker and Papatheodorou (1983) have summarized the vibrational frequencies of triatomic MX_2 metal halides. Table 4 lists the available IR data obtained from matrix isolated rare-earth difluorides.

Table 4
Vibrational frequencies (in cm^{-1}) of bent (C_{2v}) gaseous rare-earth difluorides[a,b]

Vapor molecule	ν_1	ν_2	ν_3	References
SmF_2	456	(114)	435	1, 2
EuF_2	435	(114)	456	1–3
YbF_2	476	(114)	462	1, 2

[a] Group theory classification of vibrational modes: Bent RF_2 (C_{2v} symmetry): $\Gamma = 2A_1(R, IR) + B_1(R, IR)$

[b] IR studies of matrix-isolated samples. Parentheses indicate estimated values.

References
(1) DeKock et al. (1972) (2) Kaiser et al. (1972) (3) Hastie et al. (1971)

2.2. *Chlorides*

The crystal structures and lattice parameters for the rare-earth chlorides have been reviewed earlier by Brown (1968). Scandium trichloride possesses the rhombohedral $FeCl_3$-type structure. The trichlorides of lanthanum to gadolinium inclusive possess the hexagonal UCl_3-type structure in which each metal atom is bonded to nine chlorine atoms (CN = 9). Terbium chloride and α-$DyCl_3$ possess the orthorhombic $PuBr_3$-type structure (CN = 8), while the trichlorides of yttrium and those of dysprosium (β-form) to lutetium inclusive possess the monoclinic $AlCl_3$-type structure (CN = 6). This structural change and variation in the coordination number of the metal atom is consistent with the contraction in ionic radius occurring along the lanthanide series.

Numerous papers dealing with high-temperature studies of rare-earth chloride vapors have been published, mainly before 1980. The aim of these studies was principally to characterize the thermochemical properties of the vapors, to determine the vapor species present and to a lesser extent establish their structural properties. Several methods including boiling point, effusion, effusion weight loss and Knudsen mass spectrometric techniques were used. However, as pointed out by Hastie et al. (1968), the reported vapor pressures and thermodynamics of vaporization are likely to be in considerable error due to, for instance, the tendency of rare-earth chlorides to form dimers in the vapor phase. Many of the methods used are insensitive to small concentrations of dimer species. Furthermore the reported data cannot be considered to be in agreement in cases where the system reported has been studied by different groups. Finally, attempts for third-law treatment of the available data (Myers and Graves 1977b) reveal significant variations for the $\Delta H^0_{s,298}$ values along the lanthanide series, which can not yet be considered as indicative of trends. Acquisition of accurate experimental molecular data (i.e. vibration frequencies) is essential before attempting a third-law treatment of the data. Table 5 summarizes the vapor pressures and vaporization thermodynamics of rare-earth chlorides. It is noteworthy that In the case of $ScCl_3$, Schäfer and Wagner (1979a) made the observation of the existence of the trimer Sc_3Cl_9 molecule.

Limited data exist on the geometries of gaseous rare-earth trichlorides. Electron diffraction measurements (Drake and Rosenblatt 1979 and references therein) indicate

Table 5
Vapor pressures and vaporization thermodynamics of rare-earth chlorides[a,b]

Substance	m.p. (K)	Ref.	b.p. (K)	Ref.	Temperature range (K)	Ref.	Vapor species identified	$\log P_{atm} = -A/T(K) + B$		$RCl_3(s) \rightleftharpoons RCl_3(g)$		$RCl_x(l) \rightleftharpoons RCl_x(g)$		$2RCl_3(g) \rightleftharpoons R_2Cl_6(g)$	
								A	B	$\Delta H^0_{s,T}$	$\Delta S^0_{s,T}$	$\Delta H^0_{v,T}$	$\Delta S^0_{v,T}$	$\Delta H^0_{d,T}$	$\Delta S^0_{d,T}$
$ScCl_3$	1239	1	1240	1	873–1233	2	$ScCl_3$, Sc_2Cl_6	14580	11.679						
					767–871	3	$ScCl_3$, Sc_2Cl_6, Sc_3Cl_9			244	174			−191	−123
YCl_3(l)	982	4	1761	5	1315–1650	5	YCl_3	15650	$28.363 - 6\log T$			300	120[d]		
YCl_3	920	6			780–1075	6	YCl_3, Y_2Cl_6			239	197			−117	
$LaCl_3$	1135	4	2023	4	1022–1110	7	$LaCl_3$	15796	11.828	299[c]	167[c]				
$LaCl_3$					1000–1100	8	$LaCl_3$, La_2Cl_6			310	178			−201	−125
$LaCl_3$(l)					1273–1673	9	$LaCl_3$	13930	7.31						
$LaCl_3$			1981	10	1275–1645	10	$LaCl_3$	16463	$28.093 - 6\log T$			315	109[d]		
$CeCl_3$	1090	4	2003	4	1012–1071	7	$CeCl_3$	15544	12.035	296[c]	174[c]				
$CeCl_3$(l)			1924	10	1275–1645	10	$CeCl_3$	16347	$28.203 - 6\log T$			313	113[d]		
$CeCl_3$					1000	8								(−188)	
$PrCl_3$	1059	4	1983	4	1002–1061	7	$PrCl_3$	15439	12.121	293[c]	174[c]				
$PrCl_3$(l)			1899	11	1374–1636	5	$PrCl_3$	16100	$28.149 - 6\log T$			308	112[d]		
$PrCl_3$					1000	8								(−180)	
$NdCl_3$	1031	4	1963	4	973–1032	7	$NdCl_3$	15145	12.014	288[c]	173[c]				
$NdCl_3$(l)			1903	10	1275–1645	10	$NdCl_3$	15769	$27.964 - 6\log T$			302	108[d]		
$NdCl_3$					1000	8								(−172)	
$NdCl_3$	1033	12			1055–1093	11	$NdCl_3$					251			
$SmCl_3$	955	4	dec.[f]		1000	8								(−146)	
$SmCl_2$	1132	4					$SmCl_2$	14770	$15.01 - 2.8\log T$						

continued on next page

Table 5, *continued*

Substance	m.p. (K)	Ref.	b.p. (K)	Ref.	Temperature range (K)	Ref.	Vapor species identified	$\log P_{atm} = -A/T(K) + B$		$RCl_3(s) \rightleftharpoons RCl_3(g)$		$RCl_x(l) \rightleftharpoons RCl_x(g)$		$2RCl_3(g) \rightleftharpoons R_2Cl_6(g)$	
								A	B	$\Delta H^0_{s,T}$	$\Delta S^0_{s,T}$	$\Delta H^0_{v,T}$	$\Delta S^0_{v,T}$	$\Delta H^0_{d,T}$	$\Delta S^0_{d,T}$
$EuCl_3$	dec.[f]		dec.[f]		1145–1290	8	$EuCl_2$					255			
$EuCl_3$ ($+LuCl_3$)					890–1080	8	$EuCl_3$, $EuCl_2$, Eu_2Cl_6 ($+LuCl_3$, Lu_2Cl_6, $EuLuCl_6$)								−134
$EuCl_2$	1011	4					$EuCl_2$	14770	$14.48 - 2.8\log T$						
$GdCl_3$(l)	875	4	1853	4	1369–1603	5	$GdCl_3$	15715	$28.034 - 6\log T$			301	111[d]		
$GdCl_3$					1000	8									(−172)
$GdCl_3$	882	12			963–1075	11	$GdCl_3$					238			
$GdCl_3$					1000–1200	12	$GdCl_3$					152	68		
$TbCl_3$(l)	855	4	1823	4	1326–1652	5	$TbCl_3$	14995	$27.779 - 6\log T$			287	107[d]		
$TbCl_3$					1000	8									(−180)
$DyCl_3$(l)	920	4	1812	5	1325–1620	5	$DyCl_3$	15064	$27.862 - 6\log T$			288	109[d]		
$DyCl_3$(l)[e]							$DyCl_3$	10810	5.9792						
$DyCl_3$					1000	8									(−167)
$HoCl_3$(l)	993	4	1796	10	1275–1645	10	$HoCl_3$	14946	$27.854 - 6\log T$			286	109[d]		
$HoCl_3$					1000	8									(−155)
$ErCl_3$(l)	1049	4	1769	10	1275–1645	10	$ErCl_3$	14816	$27.859 - 6\log T$			284	110[d]		
$ErCl_3$(l)					1292–1490	13	$ErCl_3$	11579	6.636			222	125		
$ErCl_3$					1000	8									(−142)
$TmCl_3$(l)	1097	4	1763	4	1275–1645	10	$TmCl_3$	14465	$27.690 - 6\log T$			277	107[d]		
$TmCl_3$					1000	8									(−126)
$YbCl_2$	975	4					$YbCl_2$	14770	$14.65 - 2.8\log T$						
$YbCl_3$	1138	4	dec.[f]		1000	8									(−117)

continued on next page

Table 5, *continued*

Substance	m.p. (K)	Ref.	b.p. (K)	Ref.	Temperature range (K)	Ref.	Vapor species identified	$\log P_{atm} = -A/T(K) + B$		$RCl_3(s) \rightleftharpoons RCl_3(g)$		$RCl_x(l) \rightleftharpoons RCl_x(g)$		$2RCl_3(g) \rightleftharpoons R_2Cl_6(g)$	
								A	B	$\Delta H^0_{s,T}$	$\Delta S^0_{s,T}$	$\Delta H^0_{v,T}$	$\Delta S^0_{v,T}$	$\Delta H^0_{d,T}$	$\Delta S^0_{d,T}$
$LuCl_3$ ($+EuCl_3$)	1198	4	1753	4	890–1080	8	$LuCl_3$, Lu_2Cl_6 ($+EuCl_3$, Eu_2Cl_6, $EuCl_2$, $EuLuCl_6$)			264				−197	
$LuCl_3$(l)			1695	10	1275–1645	10	$LuCl_3$	14718	$28.059 - 6\log T$			282	116[d]		

[a] Reported vapor pressures are over the solid condensed phase unless indicated otherwise by "(l)". Listed values of enthalpy (kJ mol^{-1}) and entropy (J mol^{-1} K^{-1}) refer to the mean of the temperature range given, unless indicated otherwise. Parentheses denote estimated values.

[b] Scandium trichloride possesses the rhombohedral $FeCl_3$-type structure. The trichlorides of lanthanum through gadolinium possess the hexagonal UCl_3-type structure (Coordination Number of lanthanide CN = 9). Terbium chloride and α-$DyCl_3$possess the orthorhombic $PuBr_3$-type structure (CN = 8), while the trichlorides of yttrium and those of dysprosium (β-form) to lutetium possess the monoclinic $AlCl_3$-type structure (CN = 6).

[c] Enthalpies of sublimation at the melting point

[d] Vaporization entropies at the boiling point.

[e] Data from Novikov and Shnyp (1971).

[f] Decomposes.

References

(1) Kubaschewski and Alcock (1979) and references therein
(2) Patrikeev et al. (1973)
(3) Schäfer and Wagner (1979a)
(4) Brown (1968) and references therein
(5) Dudchik et al. (1969a)
(6) McKinley (1965)
(7) Shimazaki and Niwa (1962)
(8) Hastie et al. (1968)
(9) Novikov and Tolmacheva (1965)
(10) Dudchik et al. (1969b)
(11) Ciach et al. (1973)
(12) Dienstbach and Blachnik (1978)
(13) Novikov and Gavryuchenkov (1965a)

Table 6
Vibrational frequencies (cm^{-1}) of pyramidal (C_{3v}) rare-earth trichloride vapors[a,b]

Vapor molecule	$\nu_1(A_1)$	$\nu_2(A_1)$	$\nu_3(E)$	$\nu_4(E)$	Reference
YCl_3	378[c]	78[c]	359[c]	59[c]	1
$LaCl_3$	324[c]		311[c]		1
	(335)	(51)	316[d]	(79)	2
$CeCl_3$	(335)	(52)	(319)	(80)	2
$PrCl_3$	(336)	(52)	320[d]	(80)	2
$NdCl_3$	349[c]	177[c]	306[c]	120[c]	3
	(301)	177[c]	349[c]	120[c]	3
	(336)	(53)	324[d]	(81)	2
$PmCl_3$	(377)	(54)	(322)	(82)	2
$SmCl_3$	(337)	(55)	(323)	(82)	2
$EuCl_3$	(338)	(55)	(324)	(83)	2
			331[d]		4
$GdCl_3$	(338)	(56)	326[d]	(84)	2
			332[d]		4
$TbCl_3$	(339)	(57)	(326)	(84)	2
$DyCl_3$	(340)	(58)	(328)	(85)	2
$HoCl_3$	(339)	(58)	(327)	(85)	2
			340[d]		4
$ErCl_3$	(340)	(59)	(329)	(86)	2
$TmCl_3$	(341)	(59)	(330)	(87)	2
$YbCl_3$	(341)	(60)	(331)	(87)	2
			346[d]		4
$LuCl_3$	(342)	(60)	(331)	(88)	2

[a] Parentheses indicate estimated values.
[b] Although assignment is made on the basis of probable C_{3v} symmetry, planar D_{3h} symmetry has been argued at least for $NdCl_3$ (Wells et al. 1977, see also text).
[c] Data from vapor IR studies.
[d] Data from matrix IR studies.

References
(1) Konings and Booij (1992)
(2) Myers and Graves (1977a) and references therein
(3) Wells et al. (1977)
(4) Loktyushina et al. (1984)

pyramidal structures for the substances studied, i.e. $GdCl_3$, $TbCl_3$ and $LuCl_3$. A Cl–Lu–Cl angle of 111° has been determined for $LuCl_3$ by gas phase electron diffraction (Giritcheva et al. 1974). However, based even on such limited experimental evidence, empirical polarizability correlations predict pyramidal geometries for all lanthanide trichlorides, while the essential qualitative features of the above experimental results are reproduced by the calculations of Myers et al. (1978).

A limited number of experimentally determined vibrational frequencies of rare-earth chlorides are available (see table 6). Myers and Graves (1977a) have given a

Table 7
Vibrational frequencies (in cm^{-1}) of bent (C_{2v}) gaseous rare-earth dichlorides[a,b]

Vapor molecule	ν_1	ν_2	ν_3	Reference
$ScCl_2$[c]				1
YCl_2				1
$SmCl_2$	247	(64)	283	2
$EuCl_2$	248	(64)	283	2
	271		282	3
$YbCl_2$	250	(64)	294	2
	282		294	3

[a] Group theory classification of vibrational modes:
Bent RCl_2 (C_{2v} symmetry): $\Gamma = 2A_1(R, IR) + B_1(R, IR)$;
Linear RCl_2 ($D_{\infty h}$ symmetry): $\Gamma = \Sigma_g^+(R) + \Sigma_u^+(IR) + \pi_u(IR)$.
[b] IR studies of matrix-isolated samples. Parentheses indicate estimated values.
[c] For $ScCl_2$ a linear $D_{\infty h}$ structure has been proposed.

References
(1) Drake and Rosenblatt (1979) and references therein
(2) Brooker and Papatheodorou (1983) and references therein
(3) Loktyushina et al. (1984)

list of estimated vibration frequencies on the basis of pyramidal RCl_3 molecules, the determination of which was based on a number of assumptions explained by the authors. These estimated values are included in table 6. As can be seen, the results of the high-temperature IR spectra of $LaCl_3$ (1400 K) and $NdCl_3$ (1275 K) are not in agreement with the estimated values. The high-temperature IR spectra of YCl_3 and $LaCl_3$ (Konings and Booij 1992) are indicative of a C_{3v} configuration while, despite the observed IR activity of all four fundamental modes in the IR spectra of $NdCl_3$ at 1275 K (Wells et al. 1977), the authors seem to be in favour of the planar geometry. However the frequencies listed in table 6 are assigned on the basis of C_{3v} symmetry.

The structural picture is better clarified for the dichlorides (see Drake and Rosenblatt 1979 and references therein). Scandium dichloride is known to be linear ($D_{\infty h}$) as indicated by matrix IR isotope shifts and selection rules, while YCl_2 is predicted to be bent (C_{2v} configuration). The known lanthanide dichlorides $SmCl_2$, $EuCl_2$ and $YbCl_2$ are bent (C_{2v}) and the Cl–R–Cl angles have been determined as 130°, 135° and 140°, respectively. Table 7 lists the vibrational frequencies of the dichlorides of Sm, Eu and Yb assigned on the basis of bent C_{2v} geometry.

The existence of dimer R_2Cl_6 species has been nicely demonstrated by Hastie et al. (1968) who studied the vapor phase over the representative solid/liquid chlorides $LaCl_3$, $EuCl_3$ and $LuCl_3$. They concluded that the proportion of dimer to monomer increases with increasing temperature and varies considerably with the nature of the metal. However there is still a critical lack of high-temperature measurements that will lead to reliable determinations of the thermochemical properties of the dimers.

2.3. *Bromides*

The crystal structures and lattice parameters of rare-earth bromides are rather well known (Brown 1968). The tribromides of lanthanum to praseodymium inclusive possess the hexagonal UCl_3-type structure (CN = 9). The tribromides of neodymium to europium inclusive possess the orthorhombic $PuBr_3$-type structure (CN = 8), while those of gadolinium to lutetium inclusive as well as those of scandium and yttrium possess the rhombohedral $FeCl_3$-type structure (CN = 6).

Among the rare-earth halides, bromides constitute the group of systems which are studied to a much lesser extend compared to fluorides, chlorides and iodides. It is noteworthy that after Makhmadmurodov et al. (1975a,b) published their results on vaporization thermodynamics of some rare-earth bromides it was very recently that an extensive well-documented Knudsen effusion mass spectrometric investigation of the $DyBr_3$ vaporization appeared in the literature (Hilpert et al. 1995). The successful characterization of the thermochemical properties of the dimer homocomplex $Dy_2Br_6(g)$ by Hilpert et al. is taken as an indication that further vaporization studies are required for most rare-earth bromide systems with a view to establish the probable existence of vapor dimer homocomplexes and determine their thermochemical properties. Table 8 summarizes the vapor pressures and vaporization thermodynamics of rare-earth bromides. Most likely the vapor pressures reported so far could be in considerable error since the formation of dimers has not been taken into account.

Gas-phase electron diffraction results confirmed pyramidal geometries for $LaBr_3$, $GdBr_3$ and $LuBr_3$ with Br–R–Br angles 115.1, 113.8 and 114.5°, respectively (Myers et al. 1978 and references therein). It can then be concluded that the pyramidal C_{3v} configuration is plausible for all lanthanide bromides, given that the above three compounds are expected to represent the range of properties for the whole series. The only gas phase IR spectroscopic study is the one on $NdBr_3$ (Wells et al. 1977) while some matrix-IR data are also reported $NdBr_3$, $GdBr_3$ and $LuBr_3$. Table 9 lists the available experimental and estimated vibrational frequencies of rare-earth bromides.

2.4. *Iodides*

The coordination of the lanthanide ions in the crystal lattice of lanthanoid iodides changes along the series from eight-fold to sixfold, the change occurring between NdI_3 and SmI_3. Thus the triiodides of lanthanum to neodymium inclusive possess the orthorhombic $PuBr_3$-type structure (CN = 8), while the triiodides of samarium to lutetium and those of scandium and yttrium possess the hexagonal BiI_3-type structure (CN = 6).

A summary of the available data on vaporization thermodynamics of rare-earth iodides is presented in table 10. Scandium iodide is by far the most extensively studied system due to its wide use in lamps. However, it was from a mass spectrometric study of Hirayama et al. (1976) on LaI_3, where the detection of appreciable amounts of $La_2I_6(g)$ made evident that chemical interaction occurred in the gas phase between the monomers and that the presumption of congruent vaporization for the rare-earth iodides should

Table 8
Vapor pressures and vaporization thermodynamics of rare-earth bromides[a,b]

Substance	m.p. (K)	Ref.	b.p. (K)	Ref.	Temperature range (K)	Ref.	Vapor species identified	$\log P_{atm} = -A/T(K) + B$		$RBr_3(s) \rightleftharpoons RBr_3(g)$		$RBr_x(l) \rightleftharpoons RBr_x(g)$		$2RBr_3(g) \rightleftharpoons R_2Br_6(g)$	
								A	B	$\Delta H^0_{s,T}$	$\Delta S^0_{s,T}$	$\Delta H^0_{v,T}$	$\Delta S^0_{v,T}$	$\Delta H^0_{d,T}$	$\Delta S^0_{d,T}$
$ScBr_3$		1							13785	11.4					
$YBr_3(l)$	1186	1	1646	2	1208–1523	2	YBr_3	13390	$24.213 - 5\log T$			199	121		
$LaBr_3$	1062	1	1853	1	1002–1052	3	$LaBr_3$	15446	9.687	297[c]	183[c]				
$CeBr_3$	1006	1	1833	1	943–992	3	$CeBr_3$	14990	9.453	286[c]	180[c]				
$PrBr_3$	964	1	1823	1	924–973	3	$PrBr_3$	14916	9.627	284[c]	183[c]				
$NdBr_3$	955	1	1813	1	889–948	3	$NdBr_3$	14829	9.674	283[c]	184[c]				
$SmBr_3$	dec.		dec.												
$SmBr_2$	942	1													
$EuBr_2(l)$	956	4			1185–1568	4	$EuBr_2$	12730	5.03			244	96		
$GdBr_3(l)$	1043	1	1763	1	1220–1532	5	$GdBr_3$	13603	$23.916 - 5\log T$			204	116		
$TbBr_3(l)$	1101	1	1763	4	1219–1536	5	$TbBr_3$	13301	$23.876 - 5\log T$			200	115		
$DyBr_3$	1152	1	1753	1	803–1053	6	$DyBr_3$	13821	9.375	264.5	179.5			−208	−145
							Dy_2Br_6[d]	16770	11.173						
$DyBr_3(l)$					1220–1535	5	$DyBr_3$	13349	$24.004 - 5\log T$			199	118		
$HoBr_3(l)$	1192	1	1679	2	1208–1523	2	$HoBr_3$	13418	$24.117 - 5\log T$			200	120		
$ErBr_3(l)$	1196	1	1733	1	1242–1506	5	$ErBr_3$	13330	$24.207 - 5\log T$			198	122		
$TmBr_3(l)$	1227	1	1713	1	1252–1482	5	$TmBr_3$	12915	$23.999 - 5\log T$			190	118		
$YbBr_3$	dec.		dec.												
$YbBr_2$	886	1													
$LuBr_3(l)$	1298	1	1683	1	1305–1468	5	$LuBr_3$	12812	$24.123 - 5\log T$			188	122		

continued on next page

Table 8, notes

[a] Reported vapor pressures are over the solid condensed phase unless indicated otherwise by "(l)". Listed enthalpy ($kJ\,mol^{-1}$) and entropy ($J\,mol^{-1}\,K^{-1}$) values refer to the mean of the temperature range given, unless indicated otherwise.

[b] The tribromides of lanthanum through praseodymium possess the hexagonal UCl_3-type structure (Coordination Number of lanthanide CN = 9). The tribromides of neodymium through europium possess the orthorhombic $PuBr_3$-type structure (CN = 8), while those of gadolinium through lutetium as well as those of scandium and yttrium possess the rhombohedral $FeCl_3$-type structure (CN = 6).

[c] Enthalpies and entropies of sublimation at the melting point.

[d] Data from Hilpert et al. (1995).

References

(1) Brown (1968) and references therein
(2) Makhmadmurodov et al. (1975a)
(3) Shimazaki and Niwa (1962)
(4) Haschke and Eick (1970)
(5) Makhmadmurodov et al. (1975b)
(6) Hilpert et al. (1995)

Table 9
Vibrational frequencies (in cm^{-1}) of pyramidal (C_{3v}) rare-earth tribromide vapors[a,b]

Vapor molecule	$\nu_1(A_1)$	$\nu_2(A_1)$	$\nu_3(E)$	$\nu_4(E)$	Reference
$LaBr_3$	(265)	(41)	(252)	(63)	1
$CeBr_3$	(265)	(41)	(252)	(63)	1
$PrBr_3$	(265)	(42)	(253)	(64)	1
$NdBr_3$	220[c]	107[c]	188[c]	80[c]	2
	(171)	107[c]	220[c]	80[c]	2
			234[d]		3
	(266)	(42)	(254)	(64)	1
$PmBr_3$	(266)	(43)	(255)	(65)	1
$SmBr_3$	(267)	(43)	(256)	(65)	1
$EuBr_3$	(267)	(44)	(257)	(66)	1
$GdBr_3$	(268)	(44)	(257)	(66)	1
			238[d]		3
	(210)	(41)	(240)	(56)	3
$TbBr_3$	(268)	(45)	(258)	(67)	1
$DyBr_3$	(269)	(45)	(259)	(67)	1
$HoBr_3$	(269)	(46)	(260)	(68)	1
$ErBr_3$	(270)	(46)	(261)	(68)	1
$TmBr_3$	(270)	(47)	(261)	(69)	1
$YbBr_3$	(271)	(47)	(262)	(69)	1
$LuBr_3$	(271)	(48)	(263)	(70)	1
			245[d]		3
	(220)	(43)	(250)	(60)	3

[a] Parentheses indicate estimated values.
[b] Although assignment is made on the basis of probable C_{3v} symmetry, planar D_{3h} symmetry has been argued at least for $NdBr_3$ (see also text).
[c] Data from vapor IR studies.
[d] Data from matrix IR studies.

References
(1) Myers and Graves (1977a) and references therein
(2) Wells et al. (1977)
(3) Loktyushina and Mal'tsev (1984)

be seriously questioned. By paying special attention and scanning the appropriate mass ranges with increased sensitivity it was indeed possible to detect $R_2I_n^+$-type fragments and identify dimer species in large amounts also in the ScI_3, DyI_3, HoI_3 and TmI_3 systems. Significant amounts of gaseous Sc_2I_6 have been identified by Hirayama et al. (1978a), Dettingmeijer et al. (1985) as well as Hilpert et al. (1985) in the equilibrium vapors over solid scandium iodide. However due to differences in the adopted assumptions about fragmentation patterns and ionization cross section ratios, the monomer-dimer content of the vapor is not certain. For example, at 800 K the mole fraction of the dimer according to the above authors is 0.04, 0.19 and 0.05, respectively. Hildenbrand et al. (1990) attempted

Table 10
Vapor pressures and vaporization thermodynamics of rare-earth iodides[a–c]

Substance	m.p. (K)	Ref.	b.p. (K)	Ref.	Temperature range (K)	Ref.	Vapor species identified	$\log P_{atm} = -A/T(K)+B$		$nRI_3(s) \rightleftharpoons R_nI_{3n}(g)$		$RI_x(l) \rightleftharpoons RI_x(g)$		$2RI_3(g) \rightleftharpoons R_2I_6(g)$	
										$\Delta H^0_{s,T}$	$\Delta S^0_{s,T}$	$\Delta H^0_{v,T}$	$\Delta S^0_{v,T}$	$\Delta H^0_{d,T}$	$\Delta S^0_{d,T}$
								A	B						
ScI_3	1193	1			1012–1178	2	ScI_3	13348	11.289	255	216				
ScI_3					766–872	3	ScI_3, Sc_2I_6	13622[M]	11.62[M]	265	213			–206	–184
							Sc_2I_6	16501[D]	13.80[D]	316					
ScI_3					1000–1175	4	(ScI_3)			248	207			–198	–175
							(Sc_2I_6)			297	239				
ScI_3					785–900	5	ScI_3, Sc_2I_6	12307[M]	9.575[M]	234	183				
							Sc_2I_6	15623[D]	13.093[D]	298					
ScI_3					734–835	6	ScI_3, Sc_2I_6	12470[M]	10.16[M]	239	211[d]			–190[d]	–165[d]
							Sc_2I_6	15470[D]	12.62[D]	296					
ScI_3					700–900	7	ScI_3, Sc_2I_6	12533[T]	10.20[T]	222	172				
							Sc_2I_6			262					
YI_3	1238	1	1583	1			YI_3	11706	6.659						
LaI_3	1045	1	1678	1	891–1008	8	LaI_3, La_2I_6	15784[T]	11.091[T]	302	212	205[c]		–192	–149
							La_2I_6			322[f]		234[e]			
LaI_3					953–1012	9	LaI_3	15397	9.964	292[g]	188[g]				
CeI_3	1039	1	1673	1	870–1015	10	CeI_3	14858	10.27	285	197				
PrI_3	1010	1	1653	1	841–1032	10,11	PrI_3	15821	10.87	293	208				
PrI_3					933–1012	9	PrI_3	14640	9.822	276[g]	183[g]				
NdI_3	1057	1	1643	1	857–1037	10,11	NdI_3	15037	10.63	288	203				
NdI_3					953–1002	9	NdI_3	14495	9.594	273[g]	180[g]				

continued on next page

Table 10, *continued*

Substance	m.p. (K)	Ref.	b.p. (K)	Ref.	Temperature range (K)	Ref.	Vapor species identified	$\log P_{atm} = -A/T(K) + B$		$nRI_3(s) \rightleftharpoons R_nI_{3n}(g)$		$RI_x(l) \rightleftharpoons RI_x(g)$		$2RI_3(g) \rightleftharpoons R_2I_6(g)$	
								A	B	$\Delta H^0_{s,T}$	$\Delta S^0_{s,T}$	$\Delta H^0_{v,T}$	$\Delta S^0_{v,T}$	$\Delta H^0_{d,T}$	$\Delta S^0_{d,T}$
SmI_3	1123	1	dec.[b]												
SmI_2(l)	793	1	1932	1	1008–1155	12	SmI_2	13367	6.92			256	133		
EuI_3	dec.		dec.												
EuI_2	853	1										224[i]			
GdI_3	1198	1	1613	1	917–1025	10	GdI_3	16009	11.55	307	221				
TbI_3	1230	1	1603	1	889–995	10	TbI_3	14021	9.70	269	185				
DyI_3	1251	1	1593	1	843–1060	10	DyI_3	14085	9.79	270	188				
DyI_3					900–1100	13	DyI_3, Dy_2I_6	14969[M]	10.63[M]	275				−225	−179
							Dy_2I_6	18030[D]	12.02[D]	348					
HoI_3	1267	1	1573	1	924–1029	10	HoI_3	15586	11.18	298	214				
HoI_3					935–1055	14	HoI_3, Ho_2I_6	12918[M]	8.51[M]	265				−203	
							Ho_2I_6	15224[D]	9.25[D]	330					
ErI_3	1288	1	1553	1	898–1016	10	ErI_3	15122	10.90	290	209				
TmI_3	1294	1	1533	1	867–990	10	TmI_3	14952	10.86	286	208				
TmI_3					874–1032	15	TmI_3, Tm_2I_6	11946[M]	7.652[M]	227	142			−169	−89
							Tm_2I_6	15075[D]	10.666[D]	286	199				
YbI_3	dec.		dec.												
LuI_3	1323	1	1483	1											

continued on next page

Table 10, notes

[a] Reported vapor pressures are over the solid condensed phase unless indicated otherwise by "(l)". Listed enthalpy ($kJ\,mol^{-1}$) and entropy ($J\,mol^{-1}\,K^{-i}$) values refer to the mean of the temperature range given, unless indicated otherwise.

[b] The triiodides of lanthanum through neodymium possess the orthorhombic $PuBr_3$-type structure (CN = 8), while the triiodides of samarium to lutetium and those of scandium and yttrium possess the hexagonal BiI_3-type structure (CN = 6).

[c] In cases where both dimer and monomer species have been detected, the capital superscripts M and D indicate the particular *A* and *B* values derived for the monomer and the dimer, while T indicates that although the dimer species has been identified, the derived equation reflects the *total* vapor pressure.

[d] At 298 K.

[e] At 1059 K.

[f] At 1017 K.

[g] Enthalpies and entropies of sublimation at the melting point.

[h] Decomposes.

[i] Value from Hirayama et al. (1974).

References

(1) Brown (1968) and references therein
(2) Fischer et al. (1939)
(3) Hirayama et al. (1978a)
(4) Work (1980)
(5) Dettingmeijer et al. (1985)
(6) Hilpert et al. (1985)
(7) Hildenbrand et al. (1990)
(8) Hirayama et al. (1976)
(9) Shimazaki and Niwa (1962)
(10) Hirayama et al. (1975)
(11) Hirayama and Camp (1972)
(12) Hirayama et al. (1974)
(13) Kaposi et al. (1983a)
(14) Kaposi et al. (1986)
(15) Dettingmeijer and Dielis (1988)

Table 11
Vibrational frequencies (in cm^{-1}) of pyramidal (C_{3v}) rare-earth triiodide vapors[a,b]

Vapor molecule	$\nu_1(A_1)$	$\nu_2(A_1)$	$\nu_3(E)$	$\nu_4(E)$	Reference
ScI_3	153[c]				1
LaI_3	(186)	(28)	(177)	(44)	2
CeI_3	(186)	(28)	(178)	(44)	2
PrI_3	(186)	(28)	(179)	(45)	2
NdI_3	182[d]	98[d]	141[d]	72[d]	3
	(133)	98[d]	195[d]	72[d]	3
			192[e]		4
	(187)	(29)	(179)	(45)	2
PmI_3	(187)	(29)	(180)	(45)	2
SmI_3	(188)	(30)	(180)	(46)	2
EuI_3	(188)	(30)	(181)	(46)	2
GdI_3	(188)	(31)	(181)	(46)	2
			194[e]		4
TbI_3	(189)	(31)	(182)	(47)	2
DyI_3	(189)	(32)	(182)	(47)	2
HoI_3	(190)	(32)	(183)	(48)	2
			196[e]		4
ErI_3	(190)	(33)	(184)	(48)	2
TmI_3	(191)	(33)	(184)	(48)	2
YbI_3	(191)	(34)	(185)	(49)	2
LuI_3	(191)	(34)	(185)	(49)	2
			198[e]		4

[a] Parentheses indicate estimated values.
[b] Although assignment is made on the basis of probable C_{3v} symmetry, planar D_{3h} symmetry has been argued at least for NdI_3 (Wells et al. 1977).
[c] Data from vapor Raman study.
[d] Data from vapor IR studies.
[e] Data from matrix IR studies.

References
(1) Metallinou et al. (1991)
(2) Myers and Graves (1977a) and references therein
(3) Wells et al. (1977)
(4) Loktyushina and Mal'tsev (1984)

an assessment on the thermochemical properties of scandium iodide vapors. The largest extent of dimerizatrion has been reported by Dettingmeijer and Dielis (1988) for thulium iodide vapors in equilibrium with the solid, where the mole fraction of $Tm_2I_6(g)$ was found in the range between 0.25 at 900 K and 0.41 at 1000 K. Finally, since the range of properties of the rare-earth triiodides is to a considerable extend represented by the members of the series for which dimer species have been identified (ScI_3, LaI_3, DyI_3, HoI_3 and TmI_3), it can be safely assumed that dimers are likely to exist also in the systems studied before 1976.

Little is known in terms of structural and spectroscopic properties of the rare-earth iodides. High-temperature absorption spectra of gaseous NdI_3 and $NdBr_3$ (Gruen and DeKock 1966) exhibited a complex band with unusually high oscillator strength located between 16 000–17 000 cm^{-1} as the most prominent feature, which was assigned to the hypersensitive transition $^4I_{9/2} \rightarrow {}^4G_{5/2}$ (see sect. 4.2). Electron diffraction measurements (see Drake and Rosenblatt 1979 and references therein) indicate that the triiodides studied (PrI_3, NdI_3, GdI_3 and LuI_3) are pyramidal. Furthermore, calculated I–R–I angles corresponding to minimum total valence electron energy (Myers et al. 1978) are slightly below 120°, ranging between 114° and 119° on going from La to Lu.

The lack of experimentally determined vibrational frequencies is critical also in the group of rare-earth iodides. Values for the asymmetric stretching frequency, ν_3, have been reported from matrix-IR work for NdI_3, GdI_3, HoI_3 and LuI_3 (Loktyushina and Mal'tsev 1984). The only high-temperature spectroscopic work concerns the IR spectra of NdI_3 (Wells et al. 1977) and the observation of the $\nu_1(ScI_3)$ mode from a vapor Raman study of the CsI–ScI_3 binary system (Metallinou et al. 1991). Table 11 summarizes the available experimental and estimated vibrational frequencies of the rare-earth iodides.

2.5. *Comments*

Before closing this section it should be pointed out that the present review of the vaporization thermodynamics and structural trends of rare-earth halides reveals that several of the single-component systems should be reinvestigated with a view both to establishing the existence of dimer species in the equilibrium vapors, if they exist, and to refine the relevant vapor pressure data. Furthermore, the thermochemical properties of the vapors need to be studied more thoroughly in order to identify possible trends in the vaporization thermodynamics. Finally, a clear, unambiguous high-temperature and/or matrix isolation spectroscopic (Raman and IR) characterization of the vibrational properties of the rare-earth halide vapors still remains to be realized before their structural picture is fully settled and a reliable third-law treatment of the data is attempted.

3. Rare-earth halide vapor complexes with monovalent and divalent metal halides

By the mid-1970s several vapor complexes of rare-earth chlorides and alkali chlorides had been identified, while the knowledge about bromide and iodide vapor complexes was virtually non-existent. However, in the last two decades iodide vapor complexes have gained in significance due to their application in metal halide lamps (see sect. 1.2). Vapor complex compounds of the form MRI_4 (M = alkali metal, R = rare earth) are the dominant species present in the equilibrium vapor of the high-temperature arc of these lamps, thereby increasing the density of desired radiative species in the discharge medium.

A summary of the vapor complexes formed in rare-earth halide/alkali halide binary systems according to the general reaction scheme (1) (sect. 1.1) is given in the present section. Studied systems involving divalent metal halides include only the $ScCl_3$–$MgCl_2$

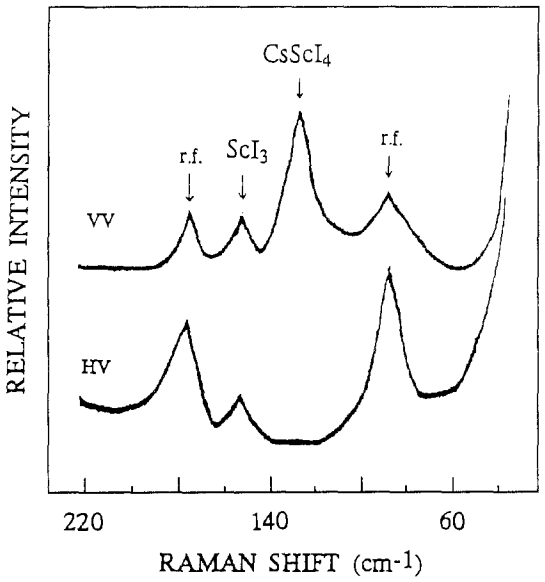

Fig. 3. Raman spectra of the gas phase over an equimolar ScI_3–CsI mixture at 800°C. (from Metallinou et al. 1991).

and ScI_3–SnI_2 binary mixtures and will also be covered in this section. The majority of the data originate from Knudsen effusion mass spectrometry. Methods like torsion-mass-effusion, vapor pressure measurements by the boiling point technique, transpiration experiments and chemical analysis of quenched equilibrium vapors have been also applied to a considerable extent (see sect. 1). Gas phase spectrophotometry has been used for studying the equilibrium vapors over CeI_3–CsI, NdI_3–CsI (Liu and Zollweg 1974), NdI_3–MI, where M = Li, Cs (Foosnaes 1979, Foosnaes and Øye 1981) and NdI_3–TlI (Knapstad et al. 1987). The only information originating from high-temperature vibrational spectroscopy is the Raman spectrum of equilibrium vapors over an equimolar CsI–ScI_3 mixture at 800°C (Metallinou et al. 1991), shown in fig. 3, where the ν_1 modes of "tetrahedral" ScI_4 in $CsScI_4$(g) and of ScI_3(g) are indicated. Unfortunately, slow attack of the quartz cell from ScI_3 results in the appearance of resonance fluorescence bands (labeled "r.f.") due to a Si–Sc–I species which obscures the remaining spectral features. It would be useful however to extend such studies in chloride and bromide systems, where less of an attack is expected.

3.1. *Knudsen effusion mass spectrometry*

Hilpert (1989, 1990) has given extensive descriptions of the instrumentation involved in Knudsen effusion mass spectrometric investigations of high-temperature metal halide vapor complexes and has presented also the principles involved for identifying gaseous species and determining partial pressures and thermodynamic quantities. The reader should refer to the above articles and references cited therein in order to address descriptions of instrumental aspects and of particular types of Knudsen cells.

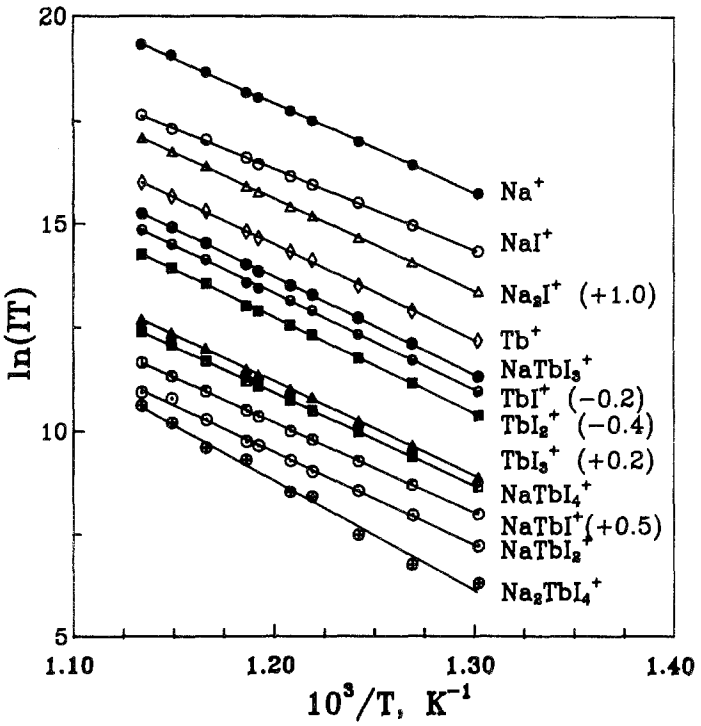

Fig. 4. Plots of $\ln(IT)$ for the ions over an equimolar TbI_3–NaI mixture. Electron energy, 50 eV (from Boghosian and Herstad 1994).

3.1.1. *Identification of gaseous species*

The molecular beam generated by the gaseous species effusing out of the Knudsen cell through the orifice (which can be knife-edged or cylindrical) does not alter the thermodynamic equilibrium in the Knudsen cell. It then enters the cross beam electron impact ion source, whereby fragmentation occurs and the fragments are detected mass spectrometrically. Proper assignment of the observed fragment ions to their molecular precursors is the essential step for the identification of the gaseous species present in equilibrium vapors. The general procedure for interpreting experimental mass spectrometric results has been summarized by Grimley (1967) and Hilpert (1989).

The temperature dependence of the ion intensities, I_i, is plotted as $\ln(I_i T)$ vs $1/T$; see for example fig. 4, where such plots are shown for the ions observed over an equimolar NaI–TbI_3 mixture (Boghosian and Herstad 1994). The plots concerning the $NaTbI_n^+$ ($n = 1$, 2, 3, 4) are essentially parallel, indicating that the ions originate from the same parent molecule, namely $NaTbI_4$(g). Considering the less abundant $Na_2TbI_4^+$ion, an assignment to a parent molecule has been more difficult since this fragment might have been derived from either Na_2TbI_5(g) or $Na_2Tb_2I_8$(g). A relevant discussion on assignments of $A_2MX_4^+$-type fragments in alkali halide/metal trihalide systems follows in sect. 3.2.

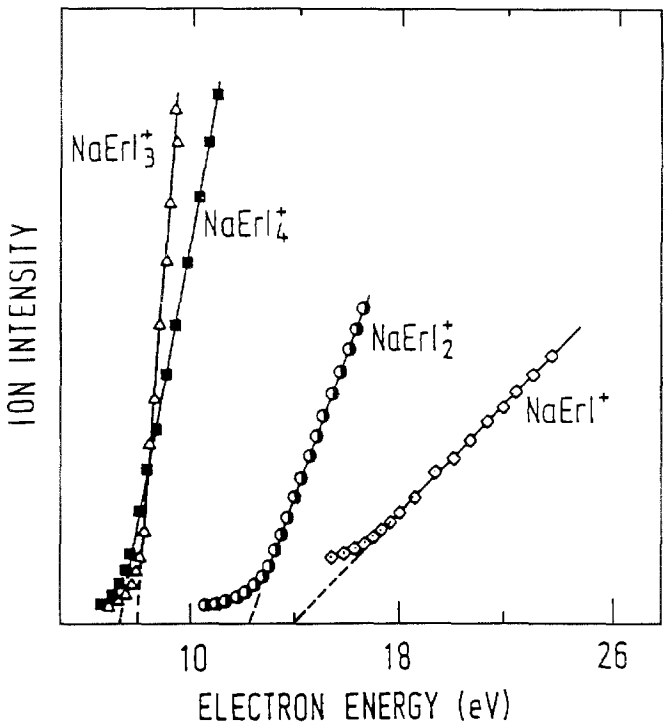

Fig. 5. Ionization efficiency curves for the ions $NaErI^+$, $NaErI_2^+$, $NaErI_3^+$ and $NaErI_4^+$ (from Metallinou et al. 1990).

Figure 5 shows typical ionization efficiency curves obtained by electron impact fragmentation of gas samples effusing from a Knudsen cell containing an equimolar NaI–ErI_3 mixture (Metallinou et al. 1990). As expected (Grimley 1967 and Hilpert 1989) the measured appearance potentials increase with increasing degree of fragmentation. Various aspects concerning determination of appearance potentials as well as calibration procedures of electron energy scale are treated extensively in the literature (see e.g. Franklin et al. 1969, Moore 1970, Rosenstock et al. 1977, Levin and Lias 1982).

3.1.2. *Partial pressures and thermodynamic quantities*

In several cases, an ion may have two different neutral precursors. In such a case it is necessary to determine the contribution of each gaseous species to the apparent intensity of each fragment. Well established techniques are described by Hilpert (e.g. see Hilpert 1989, 1990 for details, and Hilpert and Miller 1988, 1990) as well as by Schäfer (see for example Schäfer and Wagner 1979a). However, as pointed out by Hildenbrand et al. (1990), a number of questionable assumptions and particularly those about fragmentation patterns and relative ionization cross section ratios tend to create confusion about the content of the equilibrium vapors. The partial pressure of each gaseous species, i, at temperature T is given generally by the summation $P_i = \left[k \sum (I_i T)\right] / \sigma_i$, where k is the

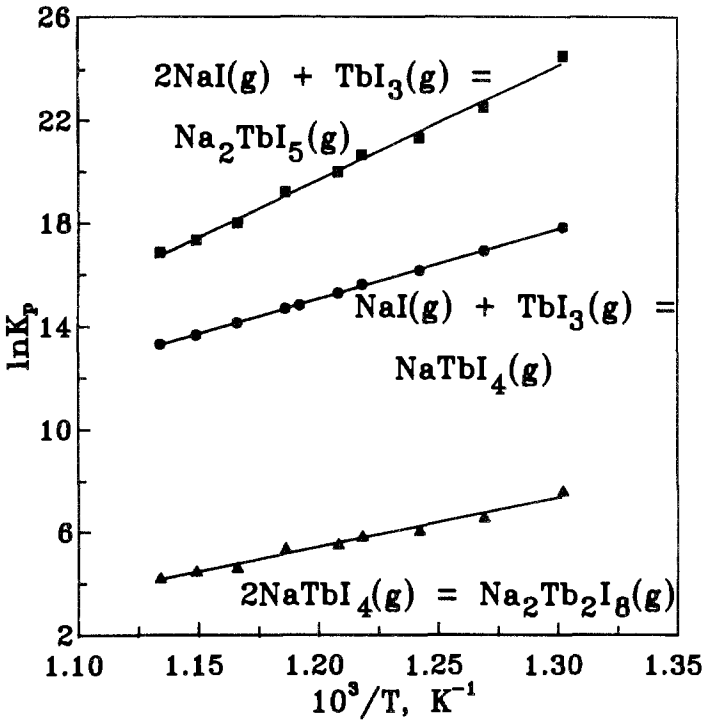

Fig. 6. Temperature dependence of equilibrium constants of reactions in the NaI–TbI_3 system (from Boghosian and Herstad 1994).

pressure calibration factor and σ_i is the ionization cross section of the species i. The ionization cross sections of gaseous molecules can be determined from atomic cross sections by using the additivity rule. Atomic cross sections are reported for ionization energies in the range 0 to 220 eV in steps of 1 eV (Mann 1967, 1970) and methods for ion intensity scale calibration are treated by Grimley (1967).

After determining the partial pressures of the gaseous species, the equilibrium constants, K_P, the enthalpies and the entropies of the considered equilibria are readily obtained from $\ln K_P$ vs. $1/T$ plots. For example, the mass spectrometric data of equilibrium vapors over the equimolar NaI–TbI_3 mixture were interpreted (Boghosian and Herstad 1994) in terms of the equilibrium

$$NaI(g) + TbI_3(g) \rightleftharpoons NaTbI_4(g), \tag{6}$$

while one of the following possible equilibria had also to be considered, accounting for the detection of the $Na_2TbI_4^+$ fragment:

$$2NaI(g) + TbI_3(g) \rightleftharpoons Na_2TbI_5(g) \quad \text{and} \quad 2NaTbI_4(g) \rightleftharpoons Na_2Tb_2I_8(g). \tag{7,8}$$

Figure 6 shows the temperature dependence of the equilibrium constants of reactions (6)–(8). The enthalpy and the entropy of the gaseous equilibria are determined from the slope and the intersect of the plots, respectively.

3.2. *Summary of vapor complexes studied in MX–RX_3 and MX_2–RX_3 systems*

A summary of the characterization and the thermodynamics of vapor complexes in MX–RX_3 and MX_2–RX_3 systems is presented in table 12. The table lists in separate columns the predominant vapor complex species identified in each studied system, the particular gaseous complex formation reactions considered, the thermodynamic quantities (ΔH^0, ΔS^0) and the volatility enhancement factors (see sect. 1.1) which are calculated from the treatment of the data. In all systems studied the 1:1 MRX_4 vapor molecule is the dominant complex species present formed according to reaction (1) with $m=n=1$. In several systems however, M_2RX_5 complex molecules have been identified, formed according to reaction (1) with $m=1$, $n=2$. These include Li_2ScCl_5, Cs_2ScCl_5 (Schäfer and Wagner 1979a,b), Na_2ScCl_5, K_2ScCl_5, Rb_2ScCl_5 (Wagner and Schäfer 1979b–d), Na_2ScI_5 (Hilpert and Miller 1990, Hildenbrand et al. 1990), Na_2TbI_5 (Boghosian and Herstad 1994), Na_2DyBr_5 (Hilpert and Miller 1994), Na_2DyI_5 (Hilpert and Miller 1988, Gavrilin et al. 1987) and Na_2HoI_5 (Gavrilin et al. 1987). Dimer $M_2R_2X_8$ complexes have also been postulated, including $Li_2Sc_2Cl_8$, $Cs_2Sc_2Cl_8$ (Schäfer and Wagner 1979a,b), $Na_2Sc_2Cl_8$, $K_2Sc_2Cl_8$, $Rb_2Sc_2Cl_8$ (Wagner and Schäfer 1979b–d), $Na_2Tb_2I_8$ (Boghosian and Herstad 1994) and $Na_2Er_2I_8$ (Metallinou et al. 1990).

A literature survey concerning the identification of M_2RX_5 and/or $M_2R_2X_8$-type vapor complexes indicates that assigning the $M_2RX_4^+$-type complex fragments has been somewhat controversial. For example, the $M_2AlF_4^+$ (M = Li, Na, K) fragments have been assigned (Sidorov and Sholts 1972) to $M_2Al_2F_8$ complexes (Li_2AlF_5 is also mentioned), the $M_2AlCl_4^+$ (M = Li, Na, K) ions have been attributed to $M_2Al_2Cl_8$ (Gesenhues and Wendt 1984). In the $ScCl_3$–MCl (M = Li, Na, K, Rb, Cs) systems the $M_2ScCl_4^+$ fragment has been detected in all cases and both M_2ScCl_5 and $M_2Sc_2Cl_8$ vapor complexes have been postulated. In alkali iodide–rare-earth iodide systems the $M_2RI_4^+$ fragment has not been detected by all authors (e.g. Kaposi et al. 1983b, 1988), while in systems where it has been observed along with the $M_2RI_3^+$ fragment, M_2RI_5 was assumed as the parent molecule (Gavrilin et al. 1987). Finally, whereas the Na_2ScI_5 (Hilpert and Miller 1990), Na_2DyI_5 (Hilpert and Miller 1988), Na_2DyBr_5 (Hilpert and Miller 1994) and $Na_2Er_2I_8$ (Metallinou et al. 1990) have been reported as the molecular precursors of their respective $Na_2RI_4^+$ fragments, there could be no easy discrimination for the presence of Na_2TbI_5 or $Na_2Tb_2I_8$ in the NaI–TbI_3 system (Boghosian and Herstad 1994).

From the ΔH and ΔS values listed in table 12 it follows that the thermodynamic quantities of reaction (1) are:

$$RX_3(g) + MX(g) \rightleftharpoons MRX_4(g), \qquad \begin{cases} \Delta H_9^0 \approx -240 \pm 40\ \text{kJ mol}^{-1}, \\ \Delta S_9^0 \approx -135 \pm 20\ \text{J mol}^{-1}\ \text{K}^{-1}, \end{cases} \tag{9}$$

$$RX_3(g) + 2MX(g) \rightleftharpoons M_2RX_5(g), \qquad \begin{cases} \Delta H_{10}^0 \approx -380 \pm 25\ \text{kJ mol}^{-1}, \\ \Delta S_{10}^0 \approx -270 \pm 30\ \text{J mol}^{-1}\ \text{K}^{-1}. \end{cases} \tag{10}$$

Certain indicative trends can possibly be derived concerning the thermodynamic characteristics of the dissociation of $MRX_4(g)$. The ΔH_9^0 values indicate that the stabilities of

Table 12
Characterization and thermodynamics of vapor complexes of rare-earth halides with monovalent and divalent metal halides

System	Temperature range (K)	Predominant vapor complex species identified	Reaction	Thermodynamic quantities[a]		Volatility enhancement		Reference
				ΔH_T^0	ΔS_T^0	r[b]	T (K)	
ScF_3–NaF	1169	$NaScF_4$				21	1169	Sidorov et al. (1970)
$ScCl_3$–LiCl	689–840	$LiScCl_4$,	$ScCl_3(g)+LiCl(g) \rightleftharpoons LiScCl_4(g)$	–232	–147	140	700	Schäfer and Wagner (1979a)
		Li_2ScCl_5,	$ScCl_3(g)+2LiCl(g) \rightleftharpoons Li_2ScCl_5(g)$	–387	–234			
		$Li_2Sc_2Cl_8$	$2LiScCl_4(g) \rightleftharpoons Li_2Sc_2Cl_8(g)$	–156	–142			
$ScCl_3$–NaCl	760–892	$NaScCl_4$, Na_2ScCl_5, $Na_2Sc_2Cl_8$	$ScCl_3(g)+NaCl(g) \rightleftharpoons NaScCl_4(g)$	–237	–137	15	700	Wagner and Schäfer (1979b)
$ScCl_3$–KCl	735–890	$KScCl_4$, K_2ScCl_5, $K_2Sc_2Cl_8$	$ScCl_3(g)+KCl(g) \rightleftharpoons KScCl_4(g)$	–234	(-125)			Wagner and Schäfer (1979c)
$ScCl_3$–RbCl	742–896	$RbScCl_4$, Rb_2ScCl_5, $Rb_2Sc_2Cl_8$	$ScCl_3(g)+RbCl(g) \rightleftharpoons RbScCl_4(g)$	–226	–125			Wagner and Schäfer (1979d)
$ScCl_3$–CsCl	748–901	$CsScCl_4$, Cs_2ScCl_5, $Cs_2Sc_2Cl_8$	$ScCl_3(g)+CsCl(g) \rightleftharpoons CsScCl_4(g)$	–227	–122			Schäfer and Wagner (1979b)
$ScCl_3$–$MgCl_2$	780–909	$MgScCl_5$,	$ScCl_3(g)+MgCl_2(g) \rightleftharpoons MgScCl_5(g)$	–185	–118			Wagner and Schäfer (1979a)
		Mg_2ScCl_7,	$ScCl_3(g)+Mg_2Cl_4(g) \rightleftharpoons Mg_2ScCl_7(g)$	–198				
		$MgSc_2Cl_8$	$Sc_2Cl_6(g)+MgCl_2(g) \rightleftharpoons MgSc_2Cl_8(g)$	–200				
ScI_3–LiI	690–790	$LiScI_4$	$ScI_3(g)+LiI(g) \rightleftharpoons LiScI_4(g)$			60	770	Hirayama et al. (1977)
ScI_3–NaI	910–1000	$NaScI_4$	$ScI_3(g)+NaI(g) \rightleftharpoons NaScI_4(g)$			7.5	910	Hirayama et al. (1977)
ScI_3–NaI	715–800	$NaScI_4$	$ScI_3(g)+NaI(g) \rightleftharpoons NaScI_4(g)$	–356		27	770	Hirayama et al. (1980)

continued on next page

Table 12, *continued*

System	Temperature range (K)	Predominant vapor complex species identified	Reaction	Thermodynamic quantities[a]		Volatility enhancement		Reference
				ΔH_T^0	ΔS_T^0	r[b]	T (K)	
ScI_3–NaI	613–848	$NaScI_4$,	$ScI_3(g)+NaI(g) \rightleftharpoons NaScI_4(g)$	−223	−154	19	700	Hilpert and Miller (1990)
		Na_2ScI_5	$ScI_3(g)+2NaI(g) \rightleftharpoons Na_2ScI_5(g)$	−378	−289			
ScI_3–NaI	709–924	$NaScI_4$, Na_2ScI_5	$ScI_3(g)+NaI(g) \rightleftharpoons NaScI_4(g)$	−218	−142	44	800	Hildenbrand et al. (1990)
ScI_3–CsI	715–800	$CsScI_4$	$ScI_3(g)+CsI(g) \rightleftharpoons CsScI_4(g)$			17	770	Hirayama et al. (1977)
ScI_3–CsI	1075	$CsScI_4$						Metallinou et al. (1991)
ScI_3–SnI_2	726–873	$SnScI_5$	$ScI_3(g)+SnI_2(g) \rightleftharpoons SnScI_5(g)$	−164	−168	17	770	Miller and Hilpert (1987)
YF_3–NaF	1169	$NaYF_4$						Sidorov et al. (1970)
LaF_3–NaF	1169	$NaLaF_4$						Sidorov et al. (1970)
$LaCl_3$–NaCl	1375–1625	$NaLaCl_4$	$LaCl_3(g)+NaCl(g) \rightleftharpoons NaLaCl_4(g)$	−292	−137	3	1425[c]	Novikov and Tolmacheva (1965)
$LaCl_3$–KCl	1275–1425	$KLaCl_4$	$LaCl_3(g)+KCl(g) \rightleftharpoons KLaCl_4(g)$	−257	−136			Novikov and Baev (1964)
LaI_3–CsI	910–1000	$CsLaI_4$				14	1000[c]	Hirayama et al. (1980)
$CeCl_3$–KCl	1275–1425	$KCeCl_4$	$CeCl_3(g)+KCl(g) \rightleftharpoons KCeCl_4(g)$	−255	−136			Novikov and Baev (1964)
CeI_3–CsI	910–1000	$CsCeI_4$	$CeI_3(g)+CsI(g) \rightleftharpoons CsCeI_4(g)$	−280		3.5	1000[c]	Hirayama et al. (1980)
$PrCl_3$–KCl	1275–1425	$KPrCl_4$	$PrCl_3(g)+KCl(g) \rightleftharpoons KPrCl_4(g)$	−248	−136			Novikov and Baev (1964)
$NdCl_3$–NaCl	1375–1575	$NaNdCl_4$	$NdCl_3(g)+NaCl(g) \rightleftharpoons NaNdCl_4(g)$	−257	−136	1.2	1375[c]	Gavryuchenkov and Novikov (1966)
$NdCl_3$–KCl	1275–1425	$KNdCl_4$	$NdCl_3(g)+KCl(g) \rightleftharpoons KNdCl_4(g)$	−248	−136			Novikov and Baev (1964)
NdI_3–CsI	1075–1180	$CsNdI_4$	$NdI_3(g)+CsI(g) \rightleftharpoons CsNdI_4(g)$	−238	−117	7	1000[c]	Liu and Zollweg (1974)
NdI_3–CsI	1150–1250	$CsNdI_4$	$NdI_3(g)+CsI(g) \rightleftharpoons CsNdI_4(g)$	−205	−93	8.9	1100[c]	Foosnaes (1979)
NdI_3–LiI	1050–1240	$LiNdI_4$	$NdI_3(g)+LiI(g) \rightleftharpoons LiNdI_4(g)$	−211	−115	7.5	1100[c]	Foosnaes and Øye (1981)
NdI_3–TlI	950–1150	$TlNdI_4$	$NdI_3(g)+TlI(g) \rightleftharpoons TlNdI_4(g)$	−200	−140	22	1000[c]	Knapstad et al. (1987)

continued on next page

Table 12, *continued*

System	Temperature range (K)	Predominant vapor complex species identified	Reaction	Thermodynamic quantities[a]		Volatility enhancement		Reference
				ΔH_T^0	ΔS_T^0	r[b]	T (K)	
$GdCl_3$–ACl (A = Li, Na)	970	$AGdCl_4$						Ciach et al. (1973)
$GdCl_3$–LiCl	1275–1425	$LiGdCl_4$	$GdCl_3(g) + LiCl(g) \rightleftharpoons LiGdCl_4(g)$	–232	–116			Patrikeev et al. (1973)
$GdCl_3$–ACl (A = Na, K, Cs)	1113–1163	$AGdCl_4$						Dienstbach and Blachnik (1978)
TbI_3–NaI	765–885	$NaTbI_4$,	$TbI_3(g) + NaI(g) \rightleftharpoons NaTbI_4(g)$	–225	–144	58	825	Boghosian and Herstad (1994)
		Na_2TbI_5,	$TbI_3(g) + 2NaI(g) \rightleftharpoons Na_2TbI_5(g)$	–372	–282			
		$Na_2Tb_2I_8$	$2NaTbI_4(g) \rightleftharpoons Na_2Tb_2I_8(g)$	–159	–146			
$DyCl_3$–LiCl	1275–1525	$LiDyCl_4$	$DyCl_3(g) + LiCl(g) \rightleftharpoons LiDyCl_4(g)$	–291	–170	1.5	1333[c]	Novikov and Shnyp (1973)
$DyCl_3$–NaCl	1000–1275	$NaDyCl_4$	$DyCl_3(g) + NaCl(g) \rightleftharpoons NaDyCl_4(g)$	–250	(-125)	154	1000[c]	McPhail et al. (1984)
$DyCl_3$–KCl	1000–1275	$KDyCl_4$						McPhail et al. (1984)
$DyCl_3$–NaI	1000–1275	$NaDyI_xCl_{4-x}$						McPhail et al. (1984)
$DyCl_3$–CsCl		$CsDyCl_4$	$DyCl_3(g) + CsCl(g) \rightleftharpoons CsDyCl_4(g)$	–267	–149			Novikov and Shnyp (1971)
$DyBr_3$–NaBr	763–1009	$NaDyBr_4$,	$DyBr_3(g) + NaBr(g) \rightleftharpoons NaDyBr_4(g)$	–236	–133	7.8	905	Hilpert and Miller (1994)
		Na_2DyBr_5	$DyBr_3(g) + 2NaBr(g) \rightleftharpoons Na_2DyBr_5(g)$	–404	–274			
DyI_3–NaI	860–920	$NaDyI_4$	$DyI_3(g) + NaI(g) \rightleftharpoons NaDyI_4(g)$	–198	–119	1.5	900	Kaposi et al. (1983b)
DyI_3–NaI	635–710	$NaDyI_4$	$DyI_3(g) + NaI(g) \rightleftharpoons NaDyI_4(g)$	–238	–140			Kaposi et al. (1988)
DyI_3–NaI	743–933	$NaDyI_4$,	$DyI_3(g) + NaI(g) \rightleftharpoons NaDyI_4(g)$	–211	–119	15	800	Hilpert and Miller (1988)
		Na_2DyI_5	$DyI_3(g) + 2NaI(g) \rightleftharpoons Na_2DyI_5(g)$	–372	–269			
DyI_3–NaI	770–870	$NaDyI_4$,	$DyI_3(g) + NaI(g) \rightleftharpoons NaDyI_4(g)$	–199[d]				Gavrilin et al. (1987)
		Na_2DyI_5	$DyI_3(g) + 2NaI(g) \rightleftharpoons Na_2DyI_5(g)$	–392[d]				

continued on next page

Table 12, *continued*

System	Temperature range (K)	Predominant vapor complex species identified	Reaction	Thermodynamic quantities[a]		Volatility enhancement		Reference
				ΔH_T^0	ΔS_T^0	r[b]	T (K)	
DyI_3–NaI–CsI	860–1060	$NaDyI_4$, $CsDyI_4$						Kaposi et al. (1984)
		$NaCsDyI_5$	$NaI(g) + CsDyI_4(g) \rightleftharpoons NaCsDyI_5(g)$	−14				
		Na_2CsDyI_6	$Na_2I_2(g) + CsDyI_4(g) \rightleftharpoons Na_2CsDyI_6(g)$	−53				
		$NaCs_2DyI_6$	$CsI(g) + NaCsDyI_5(g) \rightleftharpoons NaCs_2DyI_6(g)$	−142				
		$Na_3Cs_2DyI_8$	$Na_2I_2(g) + NaCs_2DyI_6(g) \rightleftharpoons Na_3Cs_2DyI_8(g)$	−151				
DyI_3–CsI	880–1000	$CsDyI_4$	$DyI_3(g) + CsI(g) \rightleftharpoons CsDyI_4(g)$	−182	−157	1.2	900	Kaposi et al. (1983b)
HoI_3–NaI	770–870	$NaHoI_4$,	$HoI_3(g) + NaI(g) \rightleftharpoons NaHoI_4(g)$	−202[d]				Gavrilin et al. (1987)
		Na_2HoI_5	$HoI_3(g) + 2NaI(g) \rightleftharpoons Na_2HoI_5(g)$	−342[d]				
$ErCl_3$–NaCl	1275–1475	$NaErCl_4$	$ErCl_3(g) + NaCl(g) \rightleftharpoons NaErCl_4(g)$	−264	−142	1.6	1275[d]	Novikov and Gavryuchenkov (1965b)
$ErCl_3$–KCl	1275–1425	$KErCl_4$	$ErCl_3(g) + KCl(g) \rightleftharpoons KErCl_4(g)$	−249	−136			Novikov and Baev (1964)
$ErCl_3$–KCl	1225–1500	$KErCl_4$	$ErCl_3(g) + KCl(g) \rightleftharpoons KErCl_4(g)$	−247	−134			Novikov and Gavryuchenkov (1965a)
ErI_3–NaI	830–950	$NaErI_4$,	$ErI_3(g) + NaI(g) \rightleftharpoons NaErI_4(g)$	−244	−163	50	825	Metallinou et al. (1990)
		$Na_2Er_2I_8$	$2NaErI_4(g) \rightleftharpoons Na_2Er_2I_8(g)$	−200	−187			
$LuCl_3$–LiCl	1275–1525	$LiLuCl_4$	$LuCl_3(g) + LiCl(g) \rightleftharpoons LiLuCl_4(g)$	−258	−150			Shnyp and Novikov (1972)
$LuCl_3$–CsCl	1275–1525	$CsLuCl_4$	$LuCl_3(g) + CsCl(g) \rightleftharpoons CsLuCl_4(g)$	−222	−129			Shnyp and Novikov (1972)

[a] Values of enthalpy (kJ mol^{-1}) and entropy (J mol^{-1} K^{-1}) are given at the mean of the temperature range given, unless indicated otherwise. Parentheses denote estimated values.

[b] r is the approximate volatility enhancement factor in *one* atmosphere of carrier gas and at the temperature indicated in the next column.

[c] Volatility enhancement over $MLnX_4(l)$.

[d] At 298 K.

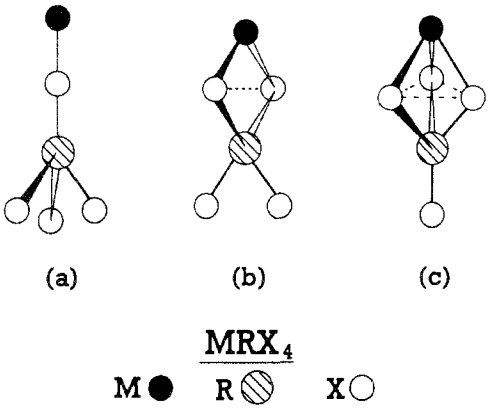

Fig. 7. Molecular models for the MRX_4-type rare-earth halide vapor complexes. (a) C_{3v} symmetry; (b) C_{2v} symmetry; (c) C_{3v} symmetry.

this type of complexes can be considered similar. However, for chlorides, which are by far the most extensively studied systems, the enthalpy values listed in table 12 point to a weak tendency of decreasing stability of the complex when the alkali chloride is changed from LiCl to CsCl. Furthermore, for a fixed alkali chloride a decreasing stability of the vapor complex is inferred on changing the rare-earth chloride in the sequence $LaCl_3$–$LuCl_3$.

The ΔS values of formation of $MRX_4(g)$ and $M_2RX_5(g)$ molecules from their gaseous constituents according to reactions (9, 10) are in conformity with the generalization rules set up by Hastie (Hastie 1975) on the thermodynamics of metal halide vapor complex formation reactions according to which values of -125 ± 20 and $251\pm20\,J\,mol^{-1}\,K^{-1}$ are predicted for $A+B=C$ and $2A+B=C$ type gaseous reactions, respectively.

From a structural point of view, there are three possible configurations for the MRX_4 complex molecules (Papatheodorou 1982), as shown in fig. 7, with the alkali atom situated at an apex (structure a, C_{3v} symmetry), an edge (structure b, C_{2v} symmetry) or a face (structure c, C_{3v} symmetry) of a RX_4 tetrahedron. Naturally, the presented results originating from mass spectrometric investigations cannot provide bases for any structural discriminations between the molecular models of fig. 7. However, *ab initio* molecular orbital calculations performed for the $MAlF_4$ (M=Li, Na) vapor complexes indicated that energetically the most stable structures are (i) for $LiAlF_4$ the edge-bridged "b" (C_{2v}) geometry and (ii) for $NaAlF_4$ the face-bridged "c" (C_{3v}) geometry (Curtiss 1979, 1993).

4. Rare-earth halide vapor complexes with Group-IIIA halides

The formation of vapor complexes between the transition and rare-earth metal halides and the "acidic" trihalides of Al, Ga, In and Fe resulting in enhanced apparent volatilities is recognized as a common phenomenon (see e.g. Papatheodorou 1982, Brooker and Papatheodorou 1983). Among the Group-IIIA halides, aluminum chloride has been by far the most widely used *vapor complex forming agent* in this respect, while $AlBr_3$, $GaCl_3$, $InCl_3$ and $FeCl_3$ have been also used to a lesser extent.

An overview of the thermodynamics of vapor complexation will be given in sect. 4.1. The electronic absorption spectra and the systematics of the possible structures of vapor complexes will be discussed in sect. 4.2. Finally, an account of results from fluorescence spectroscopy will be presented in sect. 4.3.

4.1. *Thermodynamic considerations*

The majority of the data originate from gas phase spectrophotometry (see e.g. Øye and Gruen 1969, Papatheodorou and Kucera 1979, Foosnaes and Øye 1983) whereby partial pressures of identified species, thermodynamic quantities and volatility enhancement factors could be effectively determined for reaction (2). Moreover, temperature-dependent alterations in the abundance of the various species as well as structural changes of vapor complexes could be inferred by appropriate treatment of absorption band intensities (see e.g. Berg and Papatheodorou 1980 and Papatheodorou 1982). Other methods for characterizing rare-earth halide complexes with Group-IIIA halides have been applied to a lesser extent and include mass spectrometry (Schäfer and Florke 1981), entrainment and quenching experiments (Cosandey and Emmenegger 1979) and radiochemistry (Steidl et al. 1983a,b). Finally, numerous laboratory studies dealing with chemical vapor transport reactions of rare-earth chlorides mediated by Group-IIIA metal (mainly aluminum) chloride have been performed leading to transport and purification of the rare-earth chlorides (see sect. 1.2 and e.g. Schäfer 1964, 1974) as well as to mutual rare-earth separation (see for example Murase et al. 1993 and references therein).

Table 13 summarizes the available data from studies of characterization of vapor complexes in divalent and trivalent rare-earth halide/Group-IIIA halide systems (RX_2–AX_3 and RX_3–AX_3). Separate columns list the predominant vapor complex species identified in each studied system, the thermodynamic quantities (ΔH^0, ΔS^0) for the particular gaseous complex formation reactions considered and the volatility enhancement factors (see sect. 1.1) which are calculated from the treatment of the data. It is evident that several complexes are present in the equilibrium vapors formed according to the general reaction (2) with $m=1$ and $n=\frac{1}{2}$, 1, $\frac{3}{2}$ and 2. Figure 8 shows a characteristic example of the variation of partial pressures of vapor complexes resulting from temperature-dependent equilibrium shifts in the $NdCl_3$–$GaCl_3$ system (Kulset 1986). As expected at high temperatures the predominant species is the low molecular weight 1:1 vapor complex.

A critical evaluation of the thermodynamic data in table 13 does not yield any accurate systematics. Within the errors involved for the different experimental techniques it can be concluded that at least for the systems with aluminum chloride (RCl_3–$AlCl_3$), the thermodynamics of formation have rather common values for the various rare-earth chlorides involved. Thus for the values of $n=\frac{1}{2}$, 1 and $\frac{3}{2}$ the thermodynamic quantities of reaction (2) are:

$$\begin{aligned} &RCl_3(s) + \tfrac{1}{2}Al_2Cl_6(g) \rightleftharpoons RAlCl_6(g); \quad R = Sc, Eu, Gd, Tm, Yb, \\ &\Delta H^0_{11} \approx 155 \pm 10\,\mathrm{kJ\,mol^{-1}}, \quad \Delta S^0_{11} \approx 135 \pm 15\,\mathrm{J\,mol^{-1}\,K^{-1}}, \end{aligned} \tag{11}$$

Table 13
Characterization and thermodynamics of vapor complexes of rare-earth halides with Group-IIIA metal trihalides

Reaction	System	Temperature range (K)	Predominant vapor complex species	Thermodynamic quantities[a]		Volatility enhancement		Method[c] (Reference)
				ΔH_T^0	ΔS_T^0	r[b]	T (K)	
$RCl_2(s) + nAl_2Cl_6(g) \rightleftharpoons RAl_{2n}Cl_{6n+2}(g)$	$SmCl_2$–$AlCl_3$	600–800	$SmAl_{2n}Cl_{6n+2}$			10^{10}	650	AS (Papatheodorou and Kucera 1979)
	$EuCl_2$–$AlCl_3$	640–825	$EuAl_3Cl_{11}$	70	71	10^{12}	700	AS (Sorlie and Øye 1978)
			$EuAl_4Cl_{14}$	36	19			
	$EuCl_2$–$AlCl_3$	475–850	$EuAlCl_5$	(238)[d]	(127)[d]			CVT (Lange and Bärnighausen 1993)
			$EuAl_2Cl_8$	(53)[d]	(44)[d]			
			$EuAl_3Cl_{11}$	(69)[d]	(71)[d]			
			$EuAl_4Cl_{14}$	(35)[d]	(17)[d]			
$RCl_3(s) + nA_2Cl_6(g) \rightleftharpoons RA_{2n}Cl_{6n+3}(g)$	$ScCl_3$–$AlCl_3$	730–830	$ScAlCl_6$	166	140			MS (Schäfer and Florke 1981)
	YCl_3–ACl_3 (A = Al, Fe)	870–770	$YA_{2n}Cl_{6n+3}$					CVT (Schäfer 1974)
	$LaCl_3$–$AlCl_3$	725–1000	$LaAl_{2n}Cl_{6n+3}$					CVT (Schäfer 1974)
	$NdCl_3$–$AlCl_3$	500–900	$NdAl_3Cl_{12}$	45	10	10^{13}	600	AS (Øye and Gruen 1969)
			$NdAl_4Cl_{15}$	7	−52			
	$NdCl_3$–$AlCl_3$	500–725	$NdAl_{2n}Cl_{6n+3}$					F,CVT (Boghosian et al. 1995)
	$NdCl_3$–$GaCl_3$	600–1000	$NdGaCl_6$	147	109	$\sim 10^{13}$	600	AS (Foosnaes and Øye 1983)
			$NdGa_2Cl_9$	106	52			
			$NdGa_3Cl_{12}$	65	25			
			$NdGa_4Cl_{15}$	21	−43			

continued on next page

Table 13, *continued*

Reaction	System	Temperature range (K)	Predominant vapor complex species	Thermodynamic quantities[a]		Volatility enhancement		Method[c] (Reference)
				ΔH_T^0	ΔS_T^0	r[b]	T (K)	
$RCl_3(s)+nA_2Cl_6(g) \rightleftharpoons RA_{2n}Cl_{6n+3}(g)$ (*cont'd*)	$NdCl_3$–$GaCl_3$	800–1400	$NdGaCl_6$	172	118	~10^4	1050	AS (Kulset 1986)
			$NdGa_2Cl_9$	120	76			
			$NdGa_3Cl_{12}$	67	27			
			$NdGa_4Cl_{15}$	33	–29			
	$SmCl_3$–$AlCl_3$	600–800	$SmAl_3Cl_{12}$	28	–4			AS (Papatheodorou and Kucera 1979)
	$EuCl_3$–$AlCl_3$	475–850	$EuAlCl_6$	(150)[d]	(125)[d]			CVT (Lange and Bärnighausen 1993)
			$EuAl_2Cl_9$	(85)[d]	(46)[d]			
			$EuAl_3Cl_{12}$	(26)[d]	(-11)[d]			
			$EuAl_4Cl_{15}$	(0)[d]	(-64)[d]			
	$GdCl_3$–$AlCl_3$	700–800	$GdAl_3Cl_{12}$	~34	10			E,Q (Cosandey and Emmenegger 1979)
	$GdCl_3$–$AlCl_3$	450–1000	$GdAlCl_6$	166[d]	149[d]	~10^{12}	600	RC (Steidl et al. 1983a)
			$GdAl_2Cl_9$	105[d]	65[d]			
			$GdAl_3Cl_{12}$	31[d]	–7[d]			
			$GdAl_4Cl_{15}$	0[d]	–54[d]			
	$GdCl_3$–$FeCl_3$	700–800	$GdFe_3Cl_{12}$	~53				E,Q (Cosandey and Emmenegger 1979)
	$TbCl_3$–$AlCl_3$	800	$TbAl_{2n}Cl_{6n+3}$					AS,F (Caird et al. 1981a,b)
	$DyCl_3$–$AlCl_3$[e]	500–700	$DyAl_{2n}Cl_{6n+3}$					F,CVT (Boghosian et al. 1995)
	$HoCl_3$–$AlCl_3$	500–800	$HoAl_3Cl_{12}$	11	–18	~10^{11}	600	AS (Hoekstra et al. 1978)
	$HoCl_3$–$AlCl_3$[e]	500–700	$HoAl_{2n}Cl_{6n+3}$					F (Boghosian et al. 1995)

continued on next page

Table 13, *continued*

Reaction	System	Temperature range (K)	Predominant vapor complex species	Thermodynamic quantities[a] ΔH_T^0	ΔS_T^0	Volatility enhancement r[b]	T (K)	Method[c] (Reference)
$RCl_3(s)+nA_2Cl_6(g) \rightleftharpoons RA_{2n}Cl_{6n+3}(g)$ *(cont'd)*	$ErCl_3$–$AlCl_3$	525–800	$ErAl_3Cl_{12}$, $ErAl_4Cl_{15}$					AS,F (Berg and Papatheodorou 1980, Papatheodorou and Berg 1980)
	$ErCl_3$–$AlCl_3$	525–800	$ErAl_{2n}Cl_{6n+3}$					AS (Carnall et al. 1978)
	$ErCl_3$–$GaCl_3$	750–1000	$ErGaCl_6$, $ErGa_3Cl_{12}$, $ErGa_4Cl_{15}$					AS,F (Berg and Papatheodorou 1980, Papatheodorou and Berg 1980)
	$ErCl_3$–$InCl_3$	900–1100	$ErInCl_6$, $ErIn_3Cl_{12}$					AS,F (Berg and Papatheodorou 1980, Papatheodorou and Berg 1980)
	$TmCl_3$–$AlCl_3$	450–1000	$TmAlCl_6$	153[d]	128[d]	$\sim 10^{10}$	600	RC (Steidl et al. 1983a)
			$TmAl_2Cl_9$	91[d]	50[d]			
			$TmAl_3Cl_{12}$	28[d]	−10[d]			
			$TmAl_4Cl_{15}$	0[d]	−67[d]			
	$YbCl_3$–$AlCl_3$	500–1000	$YbAlCl_6$	150[d]	124[d]	$\sim 10^{14}$	600	RC (Steidl et al. 1983b)
			$YbAl_2Cl_9$	88[d]	48[d]			
			$YbAl_3Cl_{12}$	28[d]	−12[d]			
			$YbAl_4Cl_{15}$	0[d]	−66[d]			
$NdI_3(g)+nAlI_3(g) \rightleftharpoons NdAl_nI_{3n+3}(g)$	NdI_3–AlI_3	900–1370	$NdAlI_6$	−186	−128			AS (Kulset 1986)
			$NdAl_2I_9$	−62	−27			

[a] Enthalpy (kJ mol^{-1}) and entropy (J mol^{-1} K^{-1}) values are given at the mean of the temperature range given, unless indicated otherwise. Parentheses denote estimated values.

[b] r is the approximate volatility enhancement factor in *one* atmosphere of carrier gas and at the temperature given in the next column.

[c] Abbreviations: AS, spectrophotometry; CVT, chemical vapor transport; MS, mass spectrometry; F, fluorescence; E, entrainment; Q, quenching; RC, radiochemistry.

[d] At 298 K.

[e] Preliminary results.

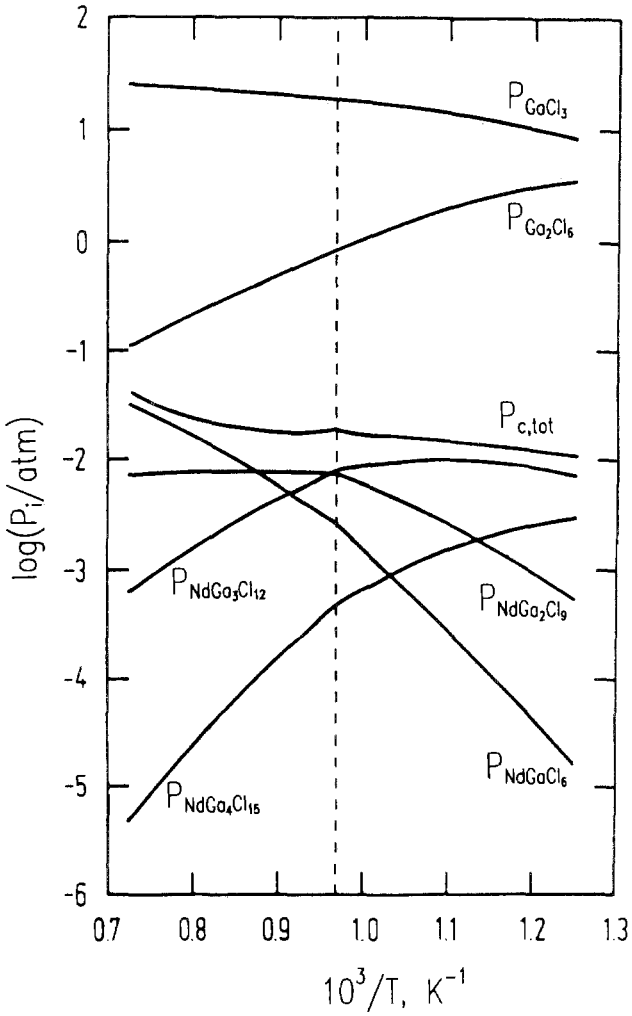

Fig. 8. Temperature dependence of equilibrium partial pressures of the $NdGaCl_6$, $NdGa_2Cl_9$, $NdGa_3Cl_{12}$ and $NdGa_4Cl_{15}$ vapor complexes. $P^0_{Ga_2Cl_6} = 9.72 \times 10^{-3} T$. The dashed line indicates the melting point of $NdCl_3$ (from Kulset 1986).

$$RCl_3(s) + Al_2Cl_6(g) \rightleftharpoons RAl_2Cl_9(g); \quad R = Eu, Gd, Tm, Yb,$$
$$\Delta H^0_{12} \approx 93 \pm 10\,\text{kJ mol}^{-1}, \quad \Delta S^0_{12} \approx 52 \pm 10\,\text{J mol}^{-1}\,\text{K}^{-1}, \tag{12}$$

$$RCl_3(s) + \tfrac{3}{2}Al_2Cl_6(g) \rightleftharpoons RAl_3Cl_{12}(g), \quad R = Sm, Eu, Gd, Tm, Yb,$$
$$\Delta H^0_{13} \approx 28 \pm 5\,\text{kJ mol}^{-1}, \quad \Delta S^0_{13} \approx -8 \pm 5\,\text{J mol}^{-1}\,\text{K}^{-1}. \tag{13}$$

The enthalpy and entropy of $HoAl_3Cl_{12}$ and $NdAl_3Cl_{12}$ complexes deviate from the values established by all other systems.

The small and "common" enthalpy value of reaction (13) suggests that the bonding of the lanthanide atom in the vapor complex does not change drastically relative to that in the corresponding solid RCl_3. On the other hand the coordination number of lanthanide in solid neodymium, samarium, europium and gadolinium trichlorides is CN = 9, while that in the solid thulium and ytterbium trichlorides is CN = 6 (see sect. 2). Thus it seems that like in the case of vapor complexation of transition metal chlorides (Papatheodorou and Capote 1978, Papatheodorou 1982) the coordination number of R is preserved on going from the $RCl_3(s)$ to the RAl_3Cl_{12} vapor complex. This supports the structural models inferred from the analysis of the hypersensitive electronic transitions discussed in sect. 4.2.

Finally, it should be pointed out that the data in table 13 and the semi-quantitative comparisons along the lanthanide series performed by Murase et al. (1993), suggest that the *volatility enhancement* increases from the lighter to the heavier lanthanides.

4.2. *Electronic absorption spectroscopy and structural implications*

4.2.1. *Trivalent lanthanides*

Lanthanide ions (R^{3+}) are characterized by ground electronic configurations of n-equivalent 4f electrons which are spatially contained within the exterior closed $5s^25p^6$ shells. This shielding of the open $4f^n$ configuration of the R^{3+} ions ensures that the electronic orbital wave functions will not be significantly affected by the environment and therefore the energies of the f ← f transitions will be varied only to a minor extent by the electrostatic field of the ligands. When the R^{3+} ions are incorporated into a molecular structure lacking inversion symmetry, the ligand fields perturb the 4f orbitals slightly, break the parity selection rule forbidding electric dipole transitions among $4f^n$ states and induce a rich spectrum of weak UV, Vis and IR bands which are however insensitive to the chemical environment and/or the host medium. The intensities, however, of the *hypersensitive* transitions are known to depend drastically on both ligand field and structural alterations (Jørgensen and Judd 1964). These transitions have been the subject of many research efforts and have been treated extensively (see e.g. Reisfeld and Jørgensen 1977, Henrie et al. 1976, Peacock 1975). The intensities of experimentally observed "forbidden" transitions in lanthanide spectra can be interpreted by the Judd–Ofelt theory (Judd 1962 and Ofelt 1962) in terms of a forced electric-dipole mechanism in which states of opposite parity are mixed into the 4f configuration. The Judd–Ofelt intensity analysis of experimental data from lanthanide spectra leads (see e.g. Krupke 1976c) to the determination of the Ω_t intensity parameters (Ω_2, Ω_4 and Ω_6) in terms of which numerous transitions of the lanthanide ions can to some extent be described and understood (Papatheodorou 1982).

According to Jørgensen and Judd (1964) the hypersensitive transition intensities increase when the lanthanide is surrounded by a field of decreasing symmetry. When the lanthanide itself lies on a center of symmetry, the hypersensitive band intensity is zero (apart from vibronic intensity). This has been established from studies of lanthanide crystals of high symmetry (Dieke 1968).

Table 14
High-intensity absorption bands of lanthanide (III) vapors and vapor complexes

System	Predominant vapor species	T (K)	σ_{max} (10^3 cm^{-1})	ε_{max} (L/mol cm)	f $\times 10^6$	$\Omega_i \times 10^{20}$ (cm^2)			Assignment[a]	Reference
						Ω_2	Ω_4	Ω_6		
$NdCl_3$–$AlCl_3$	$NdAl_3Cl_{12}$, $NdAl_4Cl_{15}$	500–900	17.03	18.8		18.0	4.8	3.9	$^4G_{5/2} \leftarrow {}^4I_{9/2}$	Øye and Gruen (1969), Jacobs et al. (1977)
$NdCl_3$–$AlCl_3$(l)	[Nd–Al–Cl(l)[b] (Nd/Al = 1/4)]	500	17.04	19.3					$^4G_{5/2} \leftarrow {}^4I_{9/2}$	Boghosian et al. (1995)
$NdCl_3$–$GaCl_3$	$NdGa_3Cl_{12}$, $NdGa_4Cl_{15}$, $NdGaCl_6$, $NdGa_2Cl_9$	600–1000	16.98[600]–16.87[900][c]	22.0					$^4G_{5/2} \leftarrow {}^4I_{9/2}$	Foosnaes and Øye (1983)
$NdCl_3$–$GaCl_3$	$NdGa_3Cl_{12}$, $NdGa_4Cl_{15}$, $NdGaCl_6$, $NdGa_2Cl_9$	800–1400	16.89[800]–16.69[1400][c]	19.0[800]–29.4[1400][d]					$^4G_{5/2} \leftarrow {}^4I_{9/2}$	Kulset (1986)
NdI_3–AlI_3	$NdAlI_6$	900–1370	16.35	3					$^4G_{5/2} \leftarrow {}^4I_{9/2}$	Kulset (1986)
	$NdAl_2I_9$			180						
$NdCl_3$	$NdCl_3$	1250–1400	16.77	13[1300]–22[1400][d]					$^4G_{5/2} \leftarrow {}^4I_{9/2}$	Kulset (1986)
$NdBr_3$	$NdBr_3$	1470	16.47	115	330	180	9	9	$^4G_{5/2} \leftarrow {}^4I_{9/2}$	Gruen (1971), Gruen et al. (1967)
NdI_3	NdI_3	1150–1460	16.347	347	530	270	9	9	$^4G_{5/2} \leftarrow {}^4I_{9/2}$	Gruen (1971), Gruen et al. (1967)
NdI_3–CsI	$CsNdI_4$	~1200	16.606	116					$^4G_{5/2} \leftarrow {}^4I_{9/2}$	Liu and Zollweg (1974), Foosnaes (1979)
NdI_3–LiI	$LiNdI_4$	1050–1240	16.555	97					$^4G_{5/2} \leftarrow {}^4I_{9/2}$	Liu and Zollweg (1974), Foosnaes and Øye (1981)
NdI_3–TlI	$TlNdI_4$	1100–1180	16.540	97					$^4G_{5/2} \leftarrow {}^4I_{9/2}$	Foosnaes (1979)
$SmCl_3$–$AlCl_3$	$SmAl_3Cl_{12}$	650–750	24.63	6.4[650]–5.6[750][c]					$^6P_{3/2} \leftarrow {}^6H_{5/2}$	Papatheodorou and Kucera (1979)

continued on next page

Table 14, *continued*

System	Predominant vapor species	T (K)	σ_{max} (10^3 cm^{-1})	ε_{max} (L/mol cm)	f $\times 10^6$	$\Omega_i \times 10^{20}$ (cm^2)			Assignment[a]	Reference
						Ω_2	Ω_4	Ω_6		
$HoCl_3$–$AlCl_3$	$HoAl_3Cl_{12}$	550–750	21.93		137	62.1	6.7	2.5	$^5G_6 \leftarrow {}^5I_8$	Hoekstra et al. (1978)
$HoCl_3$–$AlCl_3$(l)	[Ho–Al–Cl(l)[b] (Ho/Al = 1/3)]	500	21.78	25.2					$^5G_6 \leftarrow {}^5I_8$	Boghosian et al. (1995)
$ErCl_3$–$AlCl_3$	$ErAl_3Cl_{12}$, $ErAl_4Cl_{15}$	~650	19.10	22	24	25.8	2.7	2.0	$^2H_{11/2} \leftarrow {}^4I_{15/2}$	Carnall et al. (1978), Berg and Papatheodorou (1980)
$ErCl_3$–$GaCl_3$	$ErGa_3Cl_{12}$, $ErGa_4Cl_{15}$, $ErGaCl_6$	575–775	19.15[575]–19.11[775][c]	25[575]–26.5[775][d]	25 26.5				$^2H_{11/2} \leftarrow {}^4I_{15/2}$	Berg and Papatheodorou (1980), Papatheodorou (1982)
$ErCl_3$–$InCl_3$	$ErIn_3Cl_{12}$, $ErInCl_6$	900–1100	19.13[900]–19.10[1100][c]	29[900]–36[1100][d]	29 41.5				$^2H_{11/2} \leftarrow {}^4I_{15/2}$	Berg and Papatheodorou (1980), Papatheodorou (1982)
$ErBr_3$	$ErBr_3$	1378	19.19	50	57.5	60	1.5	1.6	$^2H_{11/2} \leftarrow {}^4I_{15/2}$	Gruen (1971), Gruen et al. (1967)
ErI_3	ErI_3	1267	19.0	53	95.5	106	6.4	1.6	$^2H_{11/2} \leftarrow {}^4I_{15/2}$	Gruen (1971), Gruen et al. (1967)

[a] Hypersensitive transitions except for Sm(III).
[b] Preliminary results from Raman and UV/Vis spectroscopic studies of $LnCl_3$–$AlCl_3$ molten mixtures.
[c] Band maximum shifts to lower energies with increasing temperature.
[d] Molar absorptivity increases with increasing temperature.
[e] Molar absorptivity decreases with increasing temperature.

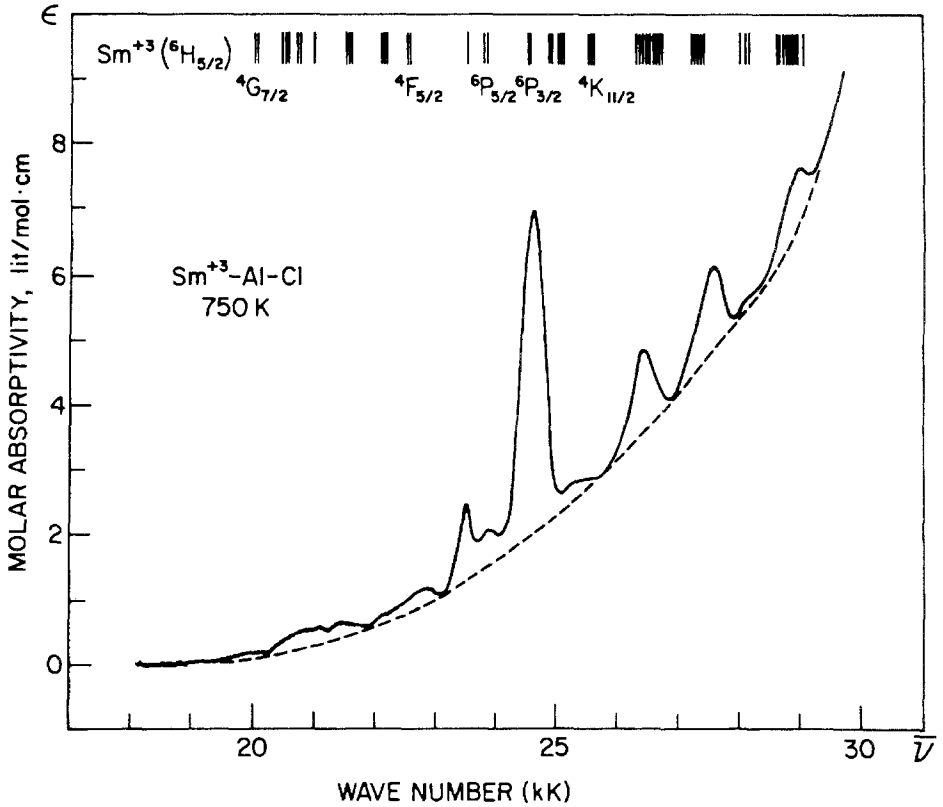

Fig. 9. Molar absorptivity of $SmAl_3Cl_{12}$(g) (from Papatheodorou and Kucera 1979).

Finally, experimental results point to the following outline behavior of the hypersensitive band intensities as affected from the chemical environment of the lanthanide ions (Henrie et al. 1976, Peacock 1975): (i) the intensity of a given hypersensitive transition in a halide compound of constant structure appears to increase in the order $I^- > Br^- > Cl^- > F^-$; (ii) hypersensitivity is proportional to the nephelauxetic ratio and possibly to the R–X covalency (Henrie and Choppin 1968, Mehta et al. 1971) and (iii) a correlation exists between the hypersensitive intensities and the electron donating ability (basicity) of the ligand according to which the more basic the ligand the more intense the hypersensitive band.

Table 14 summarizes the trivalent lanthanide halide vapor complexes which have been studied by means of spectrophotometry. Among the binary systems involving Group-IIIA trihalides, chlorides are by far the most extensively studied systems. The overall spectra of vapor complexes are similar to those observed in aqueous solutions (Carnall 1979) or in other (e.g. glass) media (Reisfeld 1975) in terms of transition energies but the hypersensitive transition intensities were found to vary. However, the hypersensitive Nd^{3+} intensity ($^4G_{5/2} \leftarrow {}^4I_{9/2}$) of the Nd–Al–Cl vapor complexes compares well with the result

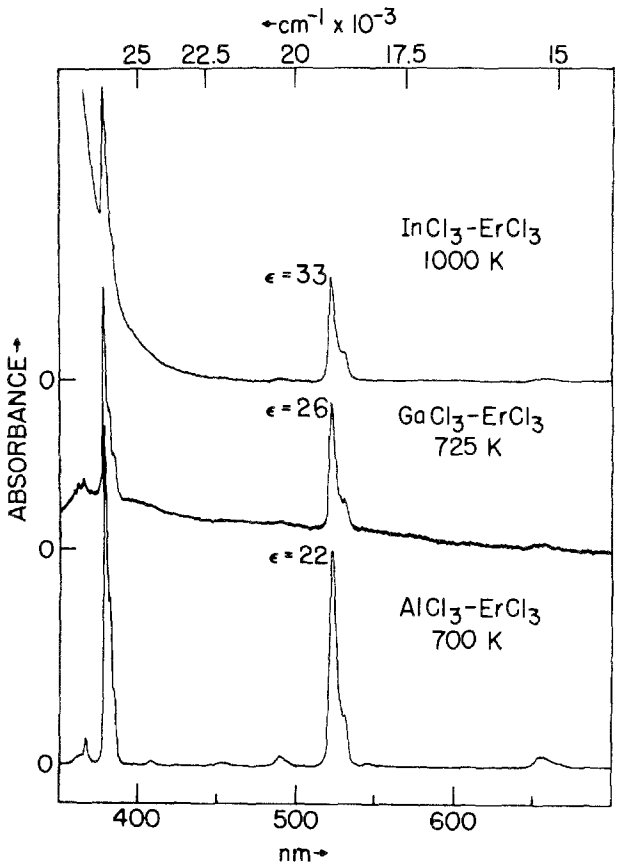

Fig. 10. Absorption spectra of the Er–Cl–Al, Er–Cl–Ga and Er–Cl–In vapor complexes (Berg and Papatheodorou 1980).

of a UV/Vis spectrum obtained from a dilute $NdCl_3$–$AlCl_3$ molten mixture at 225°C (Boghosian et al. 1995), where formation of a stable Nd–Al–Cl liquid complex compound with Nd/Al = 1/4 is known to occur (Murase et al. 1994). As discussed below, on absence of evidence to the contrary, this can be interpreted as indicating similar coordination (i.e. coordination number) around the Nd^{3+} ion in the vapor and liquid Nd–Al–Cl complexes.

Figure 9 shows an example of the similarities between the energy levels of Sm(III) in crystals (vertical lines at the top of fig. 9) and the spectral region involving non-hypersensitive transitions of the $SmAl_3Cl_{12}$ vapor complex (Papatheodorou and Kucera 1979). Generally, only small shifts in band positions have been observed on going from the solid, aqueous solution or liquid complex into the vapor complex. Nonetheless, the intensities of hypersensitive transitions vary even within a group of homologous vapor complexes. Thus, as shown in fig. 10, for the $ErCl_3$–ACl_3 (A = Al, Ga, In) complexes

(Berg and Papatheodorou 1980) the intensities of the two hypersensitive transitions in the regions ~19 100 cm^{-1} and ~26 300 cm^{-1}, increase in the sequence In > Ga > Al.

4.2.2. *Hypersensitivity and structural implications*

For a given lanthanide involved in more than one vapor molecule, certain trends can be deduced for the hypersensitive band intensities based on the experimental data (table 14). For example, data on $NdCl_3$–ACl_3 (A = Al, Ga), NdI_3–MI (M = Li, Cs) and $ErCl_3$–ACl_3 (A = Al, Ga, In) indicate that the band intensities (i.e. ε_{max} or f) decrease with increasing polarizing power (i.e. Z/r) of the countercation. Such a decrease has been observed also for lanthanide hypersensitive transitions in different environments and is attributed to the decreasing electron donating ability of the ligand. Thus, the high-charge, small-ionic-radius countercation polarizes the halide, diminishing its basicity and reducing the hypersensitive band intensity (Henrie et al. 1976).

Generally, the data in table 14 are in agreement with the general observations (i)–(iii) mentioned above. Moreover, it is evident that hypersensitive band intensities for vapors like NdI_3 possessing only terminal halogen atoms (i.e. high basicity) are higher than those for vapors involving halogen bridges (e.g. $CsNdI_4$). Furthermore, in most cases, hypersensitivity and molar absorption coefficients do not seem to be affected significantly from changes in temperature and/or pressure of the complex forming agent. Exceptions to this are the marked temperature-dependent features observed for the following vapor complex systems: NdI_3–AlI_3 (Kulset 1986), $ErCl_3$–$InCl_3$ (Berg and Papatheodorou 1980) and $NdCl_3$–$GaCl_3$ (Foosnaes and Øye 1983, Kulset 1986), and, to a lesser extent, $ErCl_3$–$GaCl_3$ (Berg and Papatheodorou 1980). Thermodynamic measurements indicate (table 13) that temperature-dependent equilibrium shifts in these systems lead to thermal dissociation of vapor complexes at high temperatures and to formation of RA_2X_9 and/or RAX_6 molecules.

Thus far there is no structural (e.g. Raman spectroscopic) information available on the lanthanide halide vapor complexes. However, on the basis of the structural information on transition metal halide vapor complexes (Papatheodorou 1982, Papatheodorou and Capote 1978) it is reasonable to assume that the structures of $RX_3 \cdot x\,AX_3$ vapor complexes consist mainly of recurring AX_4 tetrahedra which can bond to the rare-earth atom by a face, an edge or a corner. This is illustrated in fig. 11 where possible sets of structures for different x values are presented. In the "ring" type structures R_x ($x = 1, 2, 3, \ldots$) the lanthanide ion is tetracoordinated with two terminal and two bridging halogen atoms and is bound to the AX_4 by either an edge ($x = 1$) or a corner ($x \geqslant 2$). This bonding arrangement and coordination within the ligand fraction of the molecule is similar to that found in R_2X_6 and A_2X_6 (A = Al, Ga, In, Fe) vapors. In the "cluster" type structures (fig. 11) K_x, K_3' and S_x, the lanthanide ion preserves the coordination found in the solid chlorides (e.g., sixfold for an end lanthanide chloride, eightfold for a middle lanthanide chloride and ninefold for an early lanthanide chloride, see sect. 2) and is bound to AX_4 by an edge (e.g K_3 or S_4 structure) or a face (e.g. K_3' or S_3) and/or involves bidentate A_2X_7 bridging (e.g. K_4).

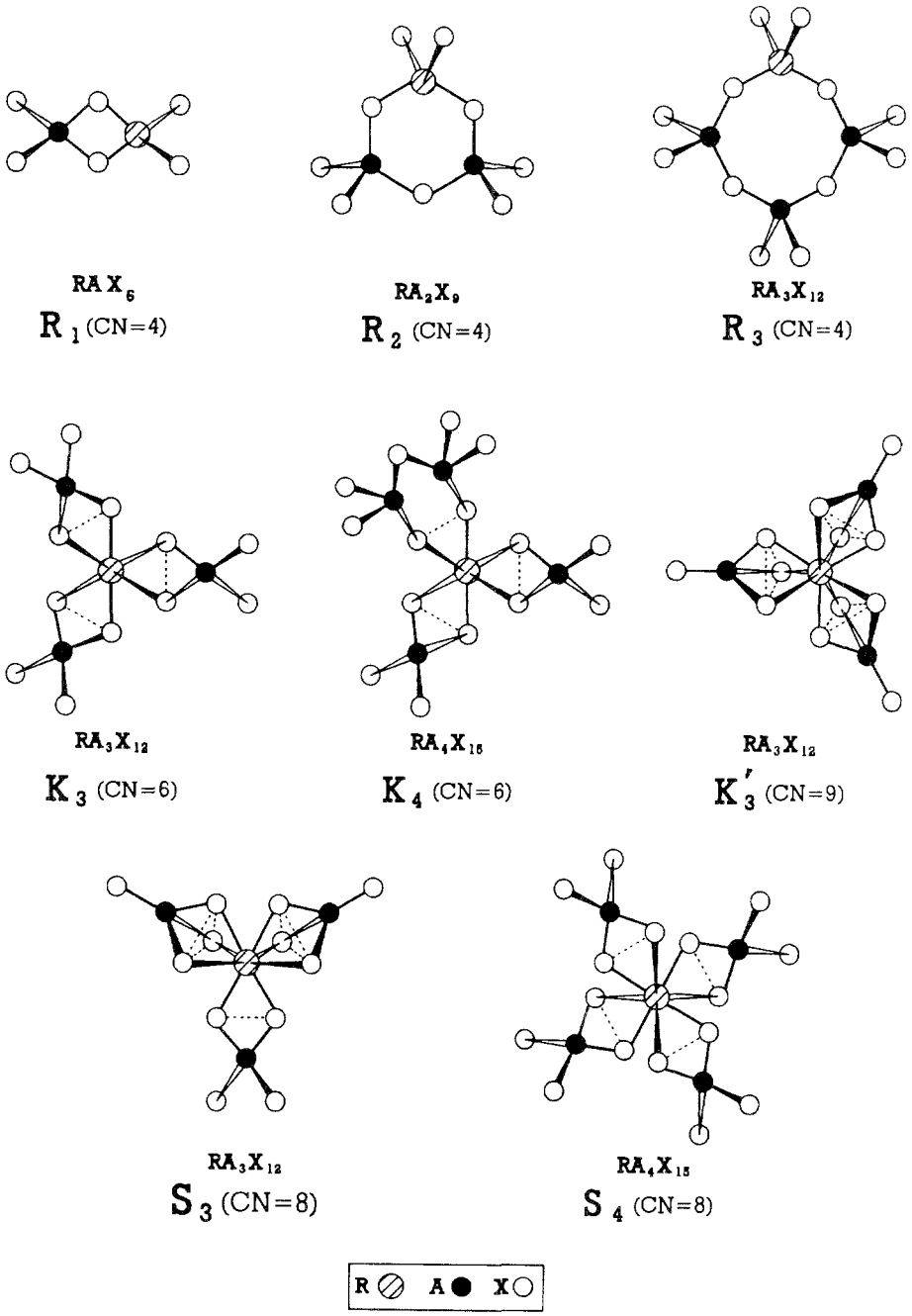

Fig. 11. Molecular models for $RA_{2n}X_{6n+3}$-type rare-earth halide vapor complexes.

"Ring" type structures can be easily extended to higher than $x=3$ values and may include more than one four-coordinate lanthanide ion per molecule. For example a $2RX_3 \cdot 2AX_3$ molecule could have a structure similar to R_3. The six-coordinated K_x structures can also be extended for $x \geqslant 4$ by inclusion of A_2X_7 bidentate units in the molecule. However, because of charge distribution and steric requirements, the nine-coordinated K_3' structure cannot be extended to higher x values.

Regardless of the structure (i.e. R_x, K_x, K_3' or S_x) of the $RX_3 \cdot xAX_3$ complexes the A–X interaction will decrease the basicity of the ligand coordinated to R in the sequence In > Ga > Al, and thus the intensity of hypersensitive transitions are expected to decrease in the same sequence. The data presented in table 14 and the above discussion support this view, but no definite conclusions about the type of species and their structures can be made. In relation, however, to the proposed structures in fig. 11 the following statements can be made and might be helpful in choosing certain molecular structures for the lanthanide halide vapor complexes:

(i) If the equilibrium vapor in lanthanide halide/metal halide systems contain species from only one of the proposed structure series [i.e. R_x ($x=1, 2, 3, \ldots$ or K_x ($x=3, 4$) or K_3'], then the ligand basicity and coordination number will not change along the series, and the hypersensitive band intensities will be rather insensitive to the relative concentrations of the different species. In such a case, hypersensitivity and molar absorption coefficients are expected to be independent of both temperature and/or total pressure.

(ii) If, on the other hand, equilibrium shifts involve crossing from one structure to another (e.g. dissociation of K_3' to R_1) then the coordination number and the average basicity of the ligands is altered (e.g. bridging halogens become terminal) and the hypersensitive band intensities will be, in contrast to (i) above, more sensitive to the relative concentrations of the abundant species. In other words, temperature (and/or pressure) dependence is expected when both R_x and K_x (or K_3' or S_x) type structures are simultaneously present in the vapor.

For the data in table 14, case (ii) appears to apply to the $ErCl_3$–ACl_3 and $NdCl_3$–ACl_3 systems, suggesting the following structures for the vapor molecules involved:

$ErGaCl_6$, $ErInCl_6$, $NdGaCl_6$: R_1;

$NdGa_2Cl_9$: R_2;

$ErAl_3Cl_{12}$, $ErGa_3Cl_{12}$, $ErIn_3Cl_{12}$, $NdAl_3Cl_{12}$, $NdGa_3Cl_{12}$: K_3 or K_3';

$ErAl_4Cl_{15}$, $ErGa_4Cl_{15}$, $NdAl_4Cl_{15}$, $NdGa_4Cl_{15}$: K_4.

Furthermore, if the solid halide-to-vapor complex reaction occurs with preservation of the lanthanide metal coordination (see sect. 4.1) then it is more likely that ErA_3Cl_{12}(A = Al, Ga, In), $HoAl_3Cl_{12}$, $TmAl_3Cl_{12}$ and $YbAl_3Cl_{12}$ possess the K_3 configuration while the NdA_3Cl_{12}(A = Al, Ga), $SmAl_3Cl_{12}$, $EuAl_3Cl_{12}$ and $GdAl_3Cl_{12}$ are likely to possess the K_3' configuration. Vapor complexes of the RAl_3X_{12} type formed by $TbCl_3$ and the tribromides of Nd to Eu are more likely to have an S_3 (or S_4) structure since the CN in the corresponding solid halide is eight.

Finally, the only well-studied iodide system, NdI_3–AlI_3, appears to deviate from the above rules. Two vapor complexes are formed, $NdAlI_6$ and $NdAl_2I_9$, of which the former has presumably a R_1 structure while for the latter a configuration with low symmetry is anticipated (Kulset 1986).

4.2.3. *Divalent lanthanides*

Divalent lanthanide halide complexes studied by absorption spectroscopy involve the Sm(II)–Al–Cl and Eu(II)–Al–Cl vapor complexes. The data are interpreted by the presence of $EuAl_3Cl_{11}$ and $EuAl_4Cl_{14}$ vapor molecules (Sorlie and Øye 1978) while the stoichiometries of the $SmCl_2$–$AlCl_3$ vapor complexes are not known (Papatheodorou and Kucera 1979). Spectra of divalent lanthanides are expected to exhibit weak Laporte-forbidden 4f ← 4f transitions and relatively strong bands arising from 5d ← 4f, 6s ← 4f, ... transitions. Such transitions are observed in the near-UV region in spectra of both Sm(II)–Al–Cl and Eu(II)–Al–Cl vapor complexes (figs. 12 and 13).

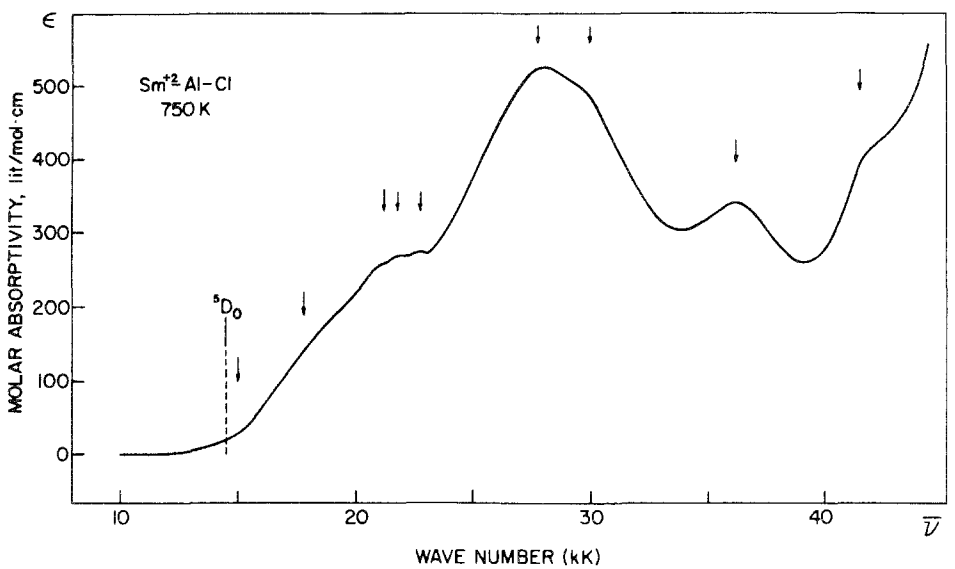

Fig. 12. Molar absorptivity of the Sm(II)–Cl–Al vapor complex(es) (from Papatheodorou and Kucera 1979).

The observed absorption bands of Eu(II) in the vapor complexes are caused by a $4f^6 5d \leftarrow 4f^7(^8S_{7/2})$ transition and are known from spectra of Eu(II)-doped crystals and of Eu(II) dissolved in water and molten salts (see Sorlie and Øye 1978 and references therein). Small temperature-dependent variations in the molar absorptivity were also observed. The splitting of the two bands, 6300 cm^{-1}, is equal to the ligand field splitting, 10 Dq, of the 5d energy level. This splitting is not sensitive to the ligand field and therefore no conclusions could be drawn on the coordination number. The spectra of the Sm(II)–Al–Cl complex(es) appear more complicated, and transitions to 6s and/or 6p levels may

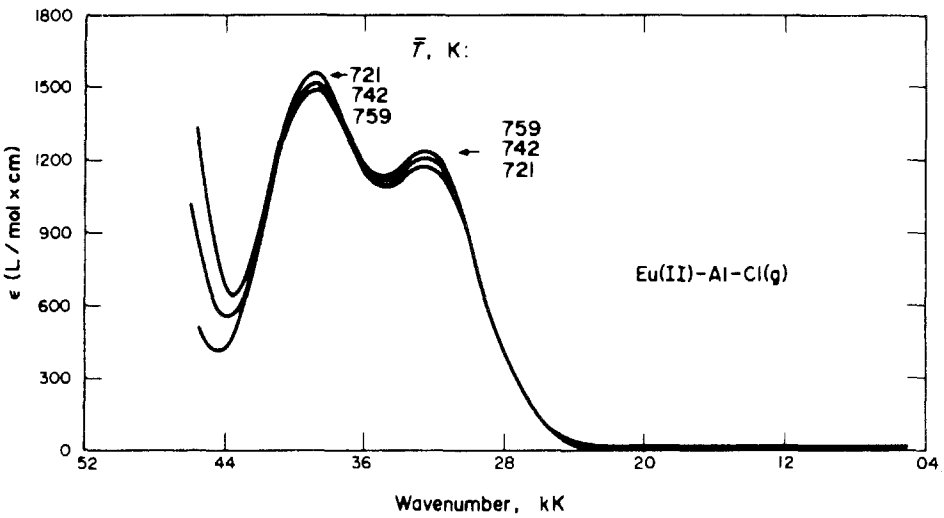

Fig. 13. Molar absorptivity of the Eu(II)–Cl–Al vapor complexes (from Sorlie and Øye 1978).

occur. The molar absorptivity is independent of temperature. No structural interpretations could be inferred for both Sm(II)–Al–Cl and Eu(II)–Al–Cl vapor complexes.

4.3. *Fluorescence spectroscopy*

Following absorption of energy by a lanthanide ion (R^{3+}), excited electronic state relaxation can occur by both radiative and non-radiative modes and the total lifetime of an excited state can be expressed as the inverse sum of the rates due to radiative and non-radiative processes. The importance of realizing the possible paths of excited state relaxation was recognized while evaluating the lanthanide halide vapor complexes as potential laser media (sect. 1.2). In few cases, optical excitation of lanthanide halide vapor complex systems has led to fluorescence with excited state lifetimes that approached their pure radiative limits (see e.g. Hessler et al. 1977, Caird et al. 1981b). Extensive calculation of fluorescence characteristics have been reported to date for the $NdAl_{2n}Cl_{6n+3}$ (Krupke 1976b, Jacobs et al. 1977), $ErAl_{2n}Cl_{6n+3}$ (Carnall et al. 1978), $HoAl_{2n}Cl_{6n+3}$ (Hoekstra et al. 1978) and $TbAl_{2n}Cl_{6n+3}$ (Caird et al. 1981b) vapor complexes.

Measurements of the fluorescence spectra and fluorescence decay kinetics of the $TbAl_{2n}Cl_{6n+3}$ vapor complex(es) have been performed in the 350–700 nm range (Hessler et al. 1977, Carnall et al. 1978, Caird et al. 1981a–c). Fluorescence was excited using a pulsed xenon flashlamp and the principal lines in the spectra were identified as emission from the $^5D_4$, $^5D_3$ and $^5G_6$ levels of the Tb^{3+} ion. Figure 14 shows the fluorescence spectrum from the $^5D_4$ level to the ground state ^7F_J multiplet. Hessler et al. (1977) discussed the temperature dependence of the fluorescence lifetime, while Caird et al. (1981a–c) were the first to apply the Judd–Ofelt theory of forced electric dipole transitions to combined absorption and fluorescence data sets.

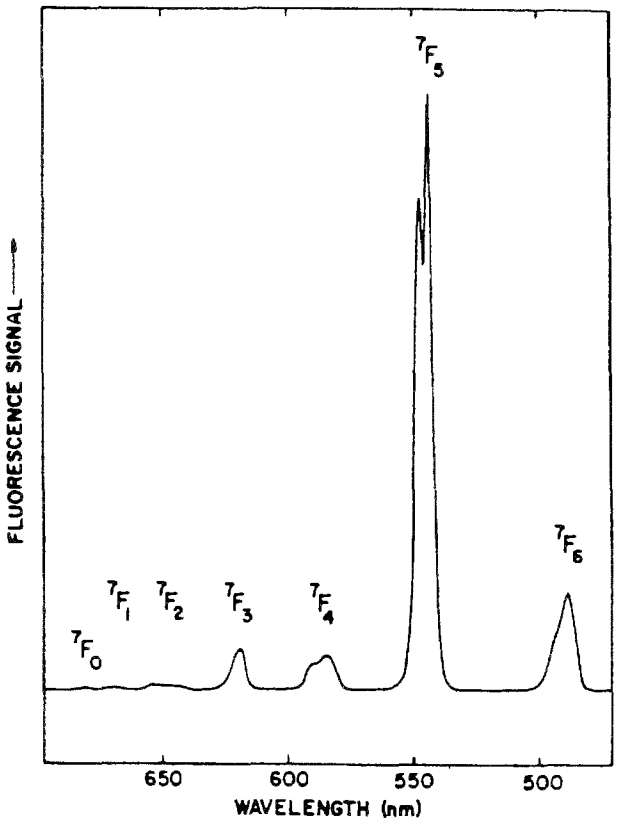

Fig. 14. Fluorescence spectrum of the Tb^{3+} ($^5D_4$) energy level in the $TbAl_{2n}Cl_{6n+3}$ vapor complex(es) (from Caird et al. 1981b).

Fluorescence lifetime studies have been also performed in the $NdAl_{2n}Cl_{6n+3}$ vapor complex(es) (Krupke 1976b, Jacobs et al. 1977). The Nd^{3+} $^4F_{3/2}$ state was populated via a rapid non radiative process subsequent to optical excitation at 531 nm performed by means of a Nd^{3+}:YAG laser. The authors then monitored fluorescence intensities from the Nd^{3+} $^4F_{3/2} \rightarrow {}^4I_{9/2}$ and $^4F_{3/2} \rightarrow {}^4I_{11/2}$ transitions and determined fluorescence lifetimes; they discussed several mechanisms accounting for non-radiative deactivation and for the observed temperature dependence of the measured radiative lifetimes.

During attempts to study the resonance Raman spectra of the R–A–Cl (A = Al, Ga, In) vapor complexes by laser excitation near hypersensitive bands, Papatheodorou and Berg (1980) and Boghosian et al. (1995) have observed resonance fluorescence due to $4f^n$ transitions of R^{3+} (R = Er, Nd, Dy, Ho) in the vapor complexes. Raman scattering from the $A_2Cl_6(g)$–$ACl_3(g)$ carrier gas molecules which are the predominant species in the equilibrium vapor mixture was also observed. Thus laser excitation of the Er–A–Cl (A = Al, Ga, In) vapor mixture with the 647.1, 530.9 and 520.8 nm Kr^+ laser lines in the

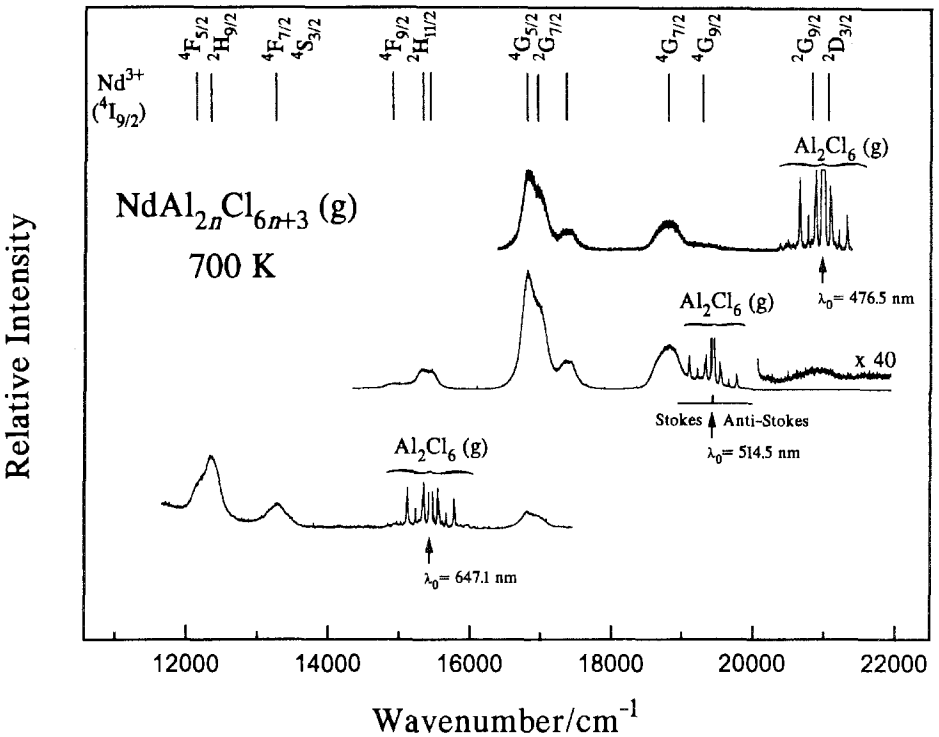

Fig. 15. Raman and fluorescence spectra of Nd–Cl–Al vapors at 700 K using different excitation laser lines (from Boghosian et al. 1995).

temperature range 475–1100 K gave rise to fluorescence due to the $^2H_{11/2} \rightarrow {}^4I_{15/2}$ and $^4S_{3/2} \rightarrow {}^4I_{15/2}$ f → f Er^{3+} transitions.

Similar was the situation for the $NdAl_{2n}Cl_{6n+3}$ vapor complex(es) where excitation with different Ar^+ and Kr^+ laser frequencies (see fig. 15) gave the fluorescence components of the well-known energy levels of the $4f^3$ Nd^{3+} configuration (Pelletier-Allard et al. 1990). An assignment of the transitions observed is given in fig. 15. Fluorescence bands were also observed in the "anti-Stokes" side of the spectra at energies as much as 1500 cm^{-1} higher than the energy of the excitation source. At the temperatures of the experiment $kT < 500$ cm^{-1} and thermal excitation is relatively low, which indicates that absorption of radiation involves also levels higher than the $^4I_{9/2}$ ground state.

Finally, laser excitation of the equilibrium vapor mixture in the Dy–Al–Cl system induced fluorescence due to $4f^9$ transitions of Dy^{3+} in the $DyAl_{2n}Cl_{6n+3}$ vapor complex(es). Figure 16 shows an example of the bands observed upon excitation of the Dy–Al–Cl vapors at 600 K with the 457.9 nm Ar^+ laser which resulted in optical pumping within the Dy^{3+} $^4I_{15/2}$ level. An assignment of the bands is given at the top of fig. 16. The envelopes of the $^4I_{15/2} \rightarrow {}^6H_{15/2}$ and $^4F_{9/2} \rightarrow {}^6H_{15/2}$ fluorescence bands appear in the spectra at ~21 900 and 20 700–21 000 cm^{-1}, respectively. Superimposed on these

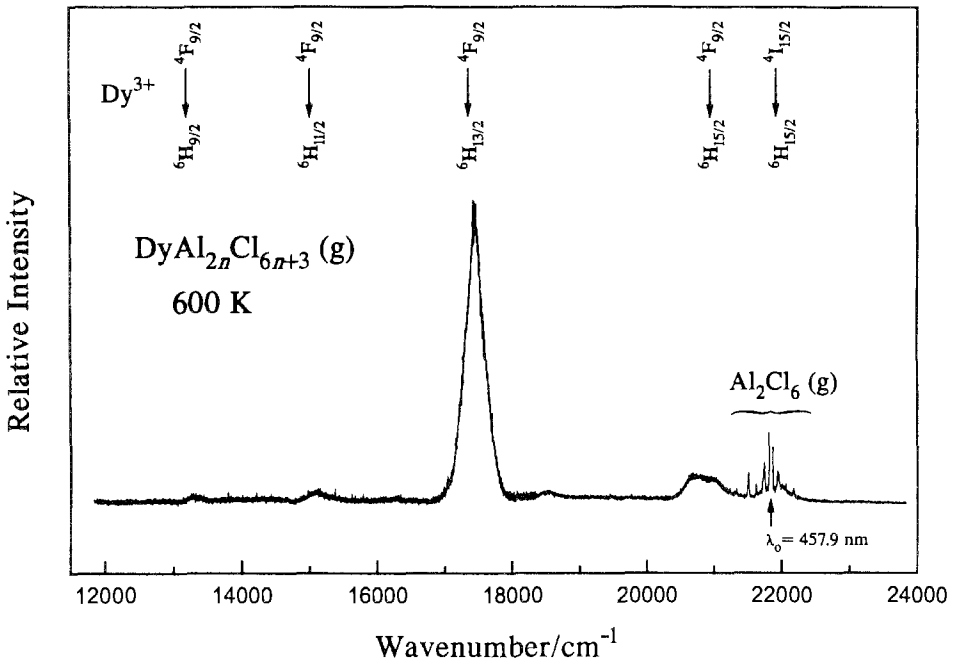

Fig. 16. Raman and fluorescence spectra of Dy–Cl–Al vapors at 600 K (from Boghosian et al. 1995).

bands are the Stokes and anti-Stokes Raman bands due to Al_2Cl_6(g). However, the most prominent feature of the spectrum is the strong band at 17 468 cm^{-1} which (together with the 15 100 and 13 300 cm^{-1} bands) is not due to transitions terminating in the ground Dy^{3+} $^6H_{15/2}$ state. Based on studies of fluorescence spectra of Dy^{3+} in fluoride crystals (Xu et al. 1984, Jagannath et al. 1979) an assignment of the observed bands is shown in fig. 16.

5. Concluding remarks

The pioneer work of Schäfer (1964) has created a new field of chemistry involving gaseous reactions and chemical transport of inorganic materials at high temperatures. Rare earths enter the field in the sixties and seventies and useful thermodynamic and spectroscopic information has been obtained particularly in systems related to high efficiency halide lamps and lasers. It should be pointed out however that, the characterization of certain high-temperature species (dimers, vapor complexes etc) and their thermochemical properties are not established with certainty. This holds especially for the RX_3–AX_3 systems studied spectrophotometrically where modelling and certain assumptions are required for deriving the thermodynamics of the assumed species (sect. 4). Furthermore the spectroscopic techniques used so far do not give adequate

information for the determination of the structures of the rare-earth halide vapor complexes (sect. 4.2, 4.3).

A better understanding of the thermodynamic, spectroscopic and structural properties of these equilibrium vapor mixtures and the establishment of their systematics requires further careful investigations which could involve:

(i) matrix-isolation IR and Raman studies for determining the predominant vibrational frequencies of the simple rare-earth halide vapors and possibly of the vapor complexes (e.g. Huglen et al. 1978);

(ii) in situ high-temperature vapor Raman and IR investigations for measuring the vibrational frequencies of the RX_3 and MRX_4 species (e.g. Metallinou et al. 1991, Konings and Booij 1992);

(iii) studies of related systems in the condensed phase, mainly in molten and glassy states (e.g. Murase et al. 1994);

(iv) extension of the research effort to rare-earth bromide systems with MBr and ABr_3 as carrier gases (e.g. Hilpert et al. 1995);

(v) use of modern computational chemistry techniques for establishing the optimum structures for the RX_3–AX_3 vapor complex systems (e.g. Curtiss 1993).

References

Barin, I., 1993, Thermochemical Data of Pure Substances (VCH Verlagsgesellschaft, Weinheim).

Berg, R.W., and G.N. Papatheodorou, 1980, Inorg. Chim. Acta **45**, L211.

Besenbruch, G., T.V. Charlu, K.F. Zmbov and J.L. Margrave, 1967, J. Less-Common Met. **12**, 375.

Biefeld, R.M., and H.A. Eick, 1975, J. Chem. Phys. **63**, 1190.

Boghosian, S., and O. Herstad, 1994, Polyhedron **13**, 1639.

Boghosian, S., G.D. Zissi and G.N. Papatheodorou, 1995, work in progress.

Brooker, M.H., and G.N. Papatheodorou, 1983, in: Advances in Molten Salt Chemistry, Vol. 5, ed. G. Mamantov (Elsevier, New York) p. 27.

Brown, D., 1968, Halides of the Lanthanides and Actinides (Wiley-Interscience, New York).

Caird, J.A., W.T. Carnall, J.P. Hessler and C.W. Williams, 1981a, J. Chem. Phys. **74**, 798.

Caird, J.A., W.T. Carnall, J.P. Hessler and C.W. Williams, 1981b, J. Chem. Phys. **74**, 805.

Caird, J.A., W.T. Carnall and J.P. Hessler, 1981c, J. Chem. Phys. **74**, 3225.

Carnall, W.T., 1979, in: Handbook on the Physics and Chemistry of Rare Earths, Vol. 3, eds K.A. Gschneidner Jr and L. Eyring (North-Holland, Amsterdam) p. 171.

Carnall, W.T., J.P. Hessler, H.R. Hoekstra and C.W. Williams, 1978, J. Chem. Phys. **68**, 4304.

Ciach, S., A.J.C. Nicholson, D.L. Swingler and P.J. Thistlethwaite, 1973, Inorg. Chem. **12**, 2072.

Cosandey, M., and F.P. Emmenegger, 1979, J. Electrochem. Soc. **126**, 1601.

Curtiss, L.A., 1979, Chem. Phys. Lett. **68**, 225.

Curtiss, L.A., 1993, in: Molten Salt Chemistry and Technology/1993, eds M.L. Saboungi and S. Kojima (The Electrochemical Society, Pennington, NJ) PV 93-9, p. 31.

Datz, S., W.T. Smith Jr and E.H. Taylor, 1961, J. Phys. Chem. **34**, 558.

DeKock, C.W., R.D. Wesley and D.D. Ratke, 1972, High Temp. Sci. **4**, 41.

Dettingmeijer, J.H., and H.R. Dielis, 1988, J. Less-Common Met. **139**, 331.

Dettingmeijer, J.H., H.R. Dielis, B.J. De Maagt and P.A.M. Vermeulen, 1985, J. Less-Common Met. **107**, 11.

Dieke, G.H., 1968, Spectra and Energy Levels of Rare Earth Ions in Crystals (Wiley-Interscience, New York).

Dienstbach, F., and R. Blachnik, 1978, Z. Anorg. Allg. Chem. **442**, 135.

Drake, M.C., and G.M. Rosenblatt, 1979, J. Electrochem. Soc. **126**, 1387.

Dudchik, G.P., O.G. Polyachenok and G.I. Novikov, 1969a, Russ. J. Inorg. Chem. **14**, 1669.

Dudchik, G.P., O.G. Polyachenok and G.I. Novikov, 1969b, Russ. J. Phys. Chem. **43**, 1203.

Fischer, W., R. Gewehr and H. Wingchen, 1939, Z. Anorg. Allg. Chem. **242**, 161.

Foosnaes, T., 1979, Gas Complexation of Neodymium Halides, Ph.D. Thesis (University of Trondheim, Trondheim, Norway).

Foosnaes, T., and H.A. Øye, 1981, Acta Chem. Scand. A **35**, 81.

Foosnaes, T., and H.A. Øye, 1983, Inorg. Chem. Scand. **22**, 3873.

Franklin, J.L., J.G. Dillard, H.M. Rosenstock, J.T. Herron, K. Draxl and F.H. Field, 1969, Ionization potentials, appearance potentials and heats of formation of gaseous positive ions, NSRDS-NBS 26 (NBS, Washington, DC).

Gavrilin, E.N., N.S. Chilingarov, E.V. Skokan, I.D. Sorokin, O. Kaposi and L.N. Sidorov, 1987, Russ. J. Phys. Chem. **61**, 1203.

Gavryuchenkov, F.G., and G.I. Novikov, 1966, Russ. J. Inorg. Chem. **11**, 810.

Gesenhues, U., and H. Wendt, 1984, Z. Phys. Chem. N. F. **142**, 93.

Gibson, J.K., and R.G. Haire, 1988, J. Less-Common Met. **144**, 123.

Giritcheva, N.I., G.V. Giritchev, K.S. Krasnov, E.Z. Zasorin and V.P. Spiridonov, 1974, in: Proc. 11th Rare Earth Res. Conf., p. 1087.

Greis, O., and T. Petzel, 1974, Z. Anorg. Allg. Chem. **403**, 1.

Grimley, R.T., 1967, in: The Characterization of High Temperature Vapors, ed. J.L. Margrave (Wiley, New York) p. 195.

Gruen, D.M., 1971, in: Progress in Inorganic Chemistry, Vol. 14, ed. S.J. Lippard (Wiley-Interscience, New York) p. 119.

Gruen, D.M., and C.W. DeKock, 1966, J. Chem. Phys. **45**, 455.

Gruen, D.M., C.W. DeKock and R.L. McBeth, 1967, Adv. Chem. Ser. **71**, 102.

Haschke, J.M., and H.A. Eick, 1970, J. Phys. Chem. **74**, 1806.

Hastie, J.W., 1975, High Temperature Vapors (Academic Press, New York).

Hastie, J.W., ed., 1979, Proc. 10th Materials Symp. on High Temperature Metal Halide Chemistry (NBS Publication, Washington, DC).

Hastie, J.W., P. Ficalora and J.L. Margrave, 1968, J. Less-Common Met. **14**, 83.

Hastie, J.W., R.H. Hauge and J.L. Margrave, 1969, Chem. Commun., p. 1453.

Hastie, J.W., R.H. Hauge and J.L. Margrave, 1971, High Temp. Sci. **3**, 56.

Hastie, J.W., R.H. Hauge and J.L. Margrave, 1975, J. Less-Common Met. **39**, 309.

Hauge, R.H., J.W. Hastie and J.L. Margrave, 1971, J. Less-Common Met. **23**, 359.

Henrie, D.E., and G.R. Choppin, 1968, J. Chem. Phys. **49**, 477.

Henrie, D.E., R.L. Fellows and G.R. Choppin, 1976, Coord. Chem. Rev. **18**, 199.

Hessler, J.P., F. Wagner Jr, C.W. Williams and W.T. Carnall, 1977, J. Appl. Phys. **48**, 3260.

Hildenbrand, D.L., and D.D. Cubicciotti, eds, 1978, High Temperature Metal Halide Chemistry (The Electrochemical Society, Pennington, NJ).

Hildenbrand, D.L., K.H. Lau, T.D. Russell, E.G. Zubler and C.W. Struck, 1990, J. Electrochem. Soc. **137**, 1618.

Hilpert, K., 1989, J. Electrochem. Soc. **136**, 2099.

Hilpert, K., 1990, Structure & Bonding (Berlin) **73**, 97.

Hilpert, K., and M. Miller, 1988, High Temp. High Pressures **20**, 231.

Hilpert, K., and M. Miller, 1990, J. Electrochem. Soc. **137**, 1618.

Hilpert, K., and M. Miller, 1994, J. Electrochem. Soc. **141**, 2769.

Hilpert, K., L. Bencivenni and B. Saha, 1985, Ber. Bunsenges. Phys. Chem. **89**, 1292.

Hilpert, K., M. Miller and F. Ramondo, 1995, J. Chem. Phys. **102**, 6194.

Hirayama, C., and F.E. Camp, 1972, J. Chem. Eng. Data **17**, 415.

Hirayama, C., P.M. Castle, R.W. Liebermann, R.J. Zollweg and F.E. Camp, 1974, Inorg. Chem. **13**, 2804.

Hirayama, C., J.F. Rome and F.E. Camp, 1975, J. Chem. Eng. Data **20**, 1.

Hirayama, C., G.L. Carlson, P.M. Castle, J.F. Rome and W.E. Snider, 1976, J. Less-Common Met. **45**, 293.

Hirayama, C., P.M. Castle, C.S. Liu and R.J. Zollweg, 1977, J. Illum. Eng. Soc. **6**, 209.

Hirayama, C., P.M. Castle, W.E. Snider and R.L. Kleinosky, 1978a, J. Less-Common Met. **57**, 69.

Hirayama, C., C.S. Liu and R.J. Zollweg, 1978b, in: High Temperature Metal Halide Chemistry, eds D.L. Hildenbrand and D.D. Cubicciotti (The Electrochemical Society, Pennington, NJ) PV 78-1, p. 71.

Hirayama, C., C.S. Liu and R.J. Zollweg, 1980, J. Light & Vis. Env. **4**, 17.

Hoekstra, H.R., J.P. Hessler, C.W. Williams and W.T. Carnall, 1978, in: High Temperature Metal Halide Chemistry, eds D.L. Hildenbrand and D.D. Cubicciotti (The Electrochemical Society, Pennington, NJ) PV 78-1, p. 123.

Huglen, R., S.J. Cyvin and H.A. Øye, 1978, in: High Temperature Metal Halide Chemistry, eds D.L. Hildenbrand and D.D. Cubicciotti (The Electrochemical Society, Pennington, NJ) PV 78-1, p. 352.

Jacobs, R.R., W.F. Krupke, J.P. Hessler and W.T. Carnall, 1977, Opt. Commun. **21**, 395.

Jagannath, H., A. Sivaram, D. Ramachandra Rao and P. Venkateswarlu, 1979, Chem. Phys. Lett. **63**, 90.

Jørgensen, C.K., and B.R. Judd, 1964, Mol. Phys. **8**, 281.

Judd, B.R., 1962, Phys. Rev. **127**, 750.

Kaiser, E.W., W.E. Falconer and W. Klamperer, 1972, J. Chem. Phys. **56**, 5392.

Kaposi, O., L. Lelik and K. Balthazar, 1983a, High Temp. Sci. **16**, 299.

Kaposi, O., L. Lelik and K. Balthazar, 1983b, High Temp. Sci. **16**, 311.

Kaposi, O., J. Sjilagyi and L. Lelik, 1984, High Temp. Sci. **18**, 67.

Kaposi, O., Zs. Ajtony, A. Popovic and J. Marsel, 1986, J. Less-Common Met. **123**, 199.

Kaposi, O., L. Bencze and Zs. Ajtony, 1988, in: High Temperature Lamp Chemistry II, Vol. PV 88-4, ed. E.G. Zubler (The Electrochemical Society, Pennington, NJ) p. 70.

Kent, R.A., K.F. Zmbov, A.S. Kana'an, G. Besenbruch, J.D. McDonald and J.L. Margrave, 1966, J. Inorg. Nucl. Chem. **28**, 1419.

Knapstad, B., T. Østvold and H.A. Øye, 1987, Acta Chem. Scand. **A41**, 98.

Konings, R.J.M., and A.S. Booij, 1992, J. Mol. Struct. **271**, 183.

Krupke, W.F., 1976a, Opt. Commun. **18**, 182.

Krupke, W.F., 1976b, in: Proc. 2nd Summer Colloquium on Electronic Transition Lasers, ed. J.I. Steinfeld (MIT Press, Cambridge, MA) p. 148.

Krupke, W.F., 1976c, in: Lawrence Livermore Laboratory Report, UCID 16993 (University of California, Livermore, CA).

Kubaschewski, O., and C.B. Alcock, 1979, in: Metallurgical Thermochemistry, ed. G.V. Raynor (Pergamon Press, Oxford).

Kulset, N., 1986, High Temperature Study of Neodymium Halide Gas Complexes, Ph.D. Thesis (University of Trondheim, Trondheim, Norway).

Lange, F.Th., and H. Bärnighausen, 1993, Z. Anorg. Allg. Chem. **619**, 1747.

Lesiecki, M., J.W. Nibler and C.W. DeKock, 1972, J. Chem. Phys. **57**, 1352.

Levin, R.D., and S.G. Lias, 1982, Ionization potentials and appearance potential measurements 1971–1981, NSRDS-NBS 71 (NBS, Washington, DC).

Lim, M., and A.W. Searcy, 1966, J. Phys. Chem. **70**, 1762.

Liu, C.S., and R.J. Zollweg, 1974, J. Chem. Phys. **60**, 2384.

Loktyushina, N.S., and A.A. Mal'tsev, 1984, Russ. J. Phys. Chem. **58**, 1602.

Loktyushina, N.S., S.B. Osin and A.A. Mal'tsev, 1984, Russ. J. Inorg. Chem. **29**, 986.

Makhmadmurodov, A., G.P. Dudchik and O.G. Polyachenok, 1975a, Russ. J. Phys. Chem. **49**, 1270.

Makhmadmurodov, A., G.P. Dudchik and O.G. Polyachenok, 1975b, Russ. J. Phys. Chem. **49**, 1599.

Mann, J.B., 1967, J. Chem. Phys. **46**, 1646.

Mann, J.B., 1970, in: Recent Developments in Mass Spectrometry, eds K. Ogata and T. Hayakawa (University of Tokyo Press) p. 814.

Mar, R.W., and A.W. Searcy, 1967, J. Phys. Chem. **71**, 888.

Margrave, J.L., 1967, The Characterization of High Temperature Vapors (Wiley, New York).

McKinley, J.D., 1965, J. Chem. Phys. **42**, 2245.

McPhail, D.S., M.G. Hocking and J.H.E. Jeffes, 1984, Int. J. Mass Spectrom. Ion Proc. **59**, 261.

Mehta, P.C., S.S.L. Surana, M.P. Bhutra and S.P. Tandon, 1971, Spectrosc. Lett. **4**, 181.

Metallinou, M.M., O. Herstad, T. Østvold and G.N. Papatheodorou, 1990, Acta Chem. Scand. **44**, 683.

Metallinou, M.M., L. Nalbandian, G.N. Papatheodorou, W. Voigt and H.H. Emons, 1991, Inorg. Chem. **30**, 4260.

Mien-tseng, S., and G.I. Novikov, 1966, Russ. J. Inorg. Chem. **11**, 270.

Miller, M., and K. Hilpert, 1987, Ber. Bunsenges. Phys. Chem. **91**, 642.

Moore, C.E., 1970, Ionization potentials and ionization limits derived from the analysis of optical spectra, NSRDS-NBS 34 (NBS, Washington, DC).

Moyer, J.W., 1978, in: High Temperature Metal Halide Chemistry, eds D.L. Hildenbrand and D.D. Cubicciotti (The Electrochemical Society, Pennington, NJ) PV 78-1, p. 147.

Murase, K., K. Shinozaki, Y. Hirashima, K. Machida and G. Adachi, 1993, J. Alloys & Compounds **198**, 31 and references therein.

Murase, K., G. Adachi, G.D. Zissi, S. Boghosian and G.N. Papatheodorou, 1994, J. Non-Cryst. Solids **180**, 88.

Murase, K., K. Machida and G. Adachi, 1994a, Chem. Lett., p. 1297.

Murase, K., K. Nishikawa, K. Machida and G. Adachi, 1994b, Chem. Lett., p. 1845.

Murase, K., K. Machida and G. Adachi, 1995, J. Alloys & Compounds **217**, 218.

Myers, C.E., and D.T. Graves, 1977a, J. Chem. Eng. Data **22**, 436.

Myers, C.E., and D.T. Graves, 1977b, J. Chem. Eng. Data **22**, 440.

Myers, C.E., L.J. Norman II and L.M. Loew, 1978, Inorg. Chem. **17**, 1581.

Nalbandian, L., and G.N. Papatheodorou, 1992, Vib. Spectrosc. **4**, 25.

Novikov, G.I., and A.K. Baev, 1964, Russ. J. Inorg. Chem. **9**, 905.

Novikov, G.I., and F.G. Gavryuchenkov, 1965a, Russ. J. Inorg. Chem. **10**, 909.

Novikov, G.I., and F.G. Gavryuchenkov, 1965b, Russ. J. Inorg. Chem. **10**, 1469.

Novikov, G.I., and V.A. Shnyp, 1971, Russ. J. Phys. Chem. **45**, 1681.

Novikov, G.I., and V.A. Shnyp, 1973, Russ. J. Phys. Chem. **47**, 915.

Novikov, G.I., and V.D. Tolmacheva, 1965, Russ. J. Inorg. Chem. **10**, 1472.

Ofelt, G.S., 1962, J. Chem. Phys. **37**, 511.

Øye, H.A., and D.M. Gruen, 1969, J. Am. Chem. Soc. **91**, 2229.

Papatheodorou, G.N., 1982, in: Current Topics in Materials Science, Vol. 10, ed. E. Kaldis (North-Holland, Amsterdam) p. 249.

Papatheodorou, G.N., and R.W. Berg, 1980, Chem. Phys. Lett. **75**, 483.

Papatheodorou, G.N., and M.A. Capote, 1978, J. Chem. Phys. **69**, 2067.

Papatheodorou, G.N., and G.H. Kucera, 1979, Inorg. Chem. **18**, 385.

Patrikeev, Yu.B., G.I. Novikov and N.V. Badivskaya, 1973, Russ. J. Phys. Chem. **47**, 1236.

Peacock, R.D., 1975, Struct. Bonding **22**, 83.

Pelletier-Allard, N., R. Pelletier and J. Shertzer, 1990, J. Chem. Phys. **93**, 14.

Peterson, E.J., J.A. Caird, J.P. Hessler, H.R. Hoekstra and C.W. Williams, 1979, J. Chem. Phys. **83**, 2458.

Petzel, T., 1973, Z. Anorg. Allg. Chem. **395**, 1.

Petzel, T., and O. Greis, 1972, Z. Anorg. Allg. Chem. **388**, 137.

Rat'kovskii, I.A., and A.V. Suvorov, 1972, Obshch. Prikl. Khim. **5**, 56.

Reisfeld, R., 1975, Struct. Bonding (Berlin) **22**, 123.

Reisfeld, R., and C.K. Jørgensen, 1977, Lasers and Excited States of Rare Earths (Springer, Berlin).

Rinehart, G.H., and R.G. Behrens, 1980, J. Less-Common Met. **75**, 65.

Roberts, J.A., and A.W. Searcy, 1972, High Temp. Sci. **4**, 411.

Rosenstock, H.M., K. Draxl, B.W. Steiner and J.T. Herron, 1977, J. Phys. Chem. Ref. Data **6**.

Schäfer, H., 1964, Chemical Transport Reactions (Academic Press, New York).

Schäfer, H., 1974, Z. Anorg. Allg. Chem. **403**, 116.

Schäfer, H., 1976, Angew. Chem. **88**, 775.

Schäfer, H., 1983, Adv. Inorg. Chem. **26**, 201.

Schäfer, H., and U. Florke, 1981, Z. Anorg. Allg. Chem. **479**, 89.

Schäfer, H., and K. Wagner, 1979a, Z. Anorg. Allg. Chem. **450**, 88.

Schäfer, H., and K. Wagner, 1979b, Z. Anorg. Allg. Chem. **451**, 61.

Shimazaki, E., and K. Niwa, 1962, Z. Anorg. Allg. Chem. **314**, 21.

Shnyp, V.A., and G.I. Novikov, 1972, Russ. J. Phys. Chem. **46**, 315.

Sidorov, L.N., and V.B. Sholts, 1972, Int. J. Mass. Spectrom. Ion Phys. **8**, 437.

Sidorov, L.N., V.P. Shcheredin and P.A. Akishin, 1970, Russ. J. Phys. Chem. **44**, 885.

Skinner, H.B., and A.W. Searcy, 1968, J. Phys. Chem. **72**, 3375.

Skinner, H.B., and A.W. Searcy, 1971, J. Phys. Chem. **75**, 108.

Sorlie, M., and H.A. Øye, 1978, J. Inorg. Nucl. Chem. **40**, 493.

Spedding, F.H., and D.C. Henderson, 1971, J. Chem. Phys. **54**, 2476.

Spedding, F.H., B.J. Beaudry, D.C. Henderson and J. Moorman, 1974, J. Chem. Phys. **60**, 1578.

Steidl, G., K. Bachmann and F. Dienstbach, 1983a, J. Phys. Chem. **87**, 5010.

Steidl, G., F. Dienstbach and K. Bachmann, 1983b, Polyhedron **2**, 727.

Suvorov, A.V., E.A. Krzhizhanovskaya and G.I. Novikov, 1966, Zh. Neorg. Khim. **11**, 2685.

Van Erk, W., and T. Rietveld, 1987, Philips J. Res. **42**, 102.

Wachter, H., and H. Schäfer, 1980, Z. Anorg. Allg. Chem. **471**, 38.

Wagner, K., and H. Schäfer, 1979a, Z. Anorg. Allg. Chem. **450**, 107.

Wagner, K., and H. Schäfer, 1979b, Z. Anorg. Allg. Chem. **450**, 115.

Wagner, K., and H. Schäfer, 1979c, Z. Anorg. Allg. Chem. **451**, 57.

Wagner, K., and H. Schäfer, 1979d, Z. Anorg. Allg. Chem. **452**, 83.

Wells Jr, J.C., J.B. Gruber and M. Lewis, 1977, Chem. Phys. **24**, 391.

Wesley, R.D., and C.W. DeKock, 1971, J. Chem. Phys. **55**, 3866.

Wesley, R.D., and C.W. DeKock, 1973, J. Phys. Chem. **77**, 466.

Wesselink, G.A., 1983, Philips J. Res. **38**, 166.

Work, D.E., 1980, J. Less-Common Met. **69**, 383.

Xu, L.-W., H.M. Crosswhite and J.P. Hessler, 1984, J. Chem. Phys. **81**, 698.

Yates, J.H., and R.M. Pitzer, 1979, J. Chem. Phys. **70**, 4049.

Zmbov, K.F., and J.L. Margrave, 1966, J. Chem. Phys. **45**, 3167.

Zmbov, K.F., and J.L. Margrave, 1967, J. Less-Common Met. **12**, 494.

Zmbov, K.F., and J.L. Margrave, 1968, Adv. Chem. Ser. **72**, 267.

Zvarova, T.S., 1973, Radiochim. Acta **15**, 542.

Zvarova, T.S., and I. Zvara, 1969, J. Chromatogr. **44**, 604.

Zvarova, T.S., and I. Zvara, 1970, J. Chromatogr. **49**, 290.

Handbook on the Physics and Chemistry of Rare Earths
Vol. 23
edited by K.A. Gschneidner, Jr. and L. Eyring

Chapter 158

MARINE CHEMISTRY AND GEOCHEMISTRY OF THE LANTHANIDES

R.H. BYRNE[1] and E.R. SHOLKOVITZ[2]
[1] *Department of Marine Science, University of South Florida, 140 Seventh Avenue South, St. Petersburg, FL 33701, USA*
[2] *Department of Marine Chemistry and Geochemistry, Woods Hole Oceanographic Institution, Woods Hole, MA 02543, USA*

Contents

1. Introduction

This handbook article combines an up-to-date tabulation of the lanthanide composition of the "ocean" with a description of lanthanide distributions in the context of physical, chemical and biogeochemical processes controlling these distributions. The focus of this chapter is water column biogeochemistry. While pore waters and hydrothermal waters will be considered in this article, the extensive literature on the lanthanide geochemistry of minerals and marine sediments will not be discussed.

In order to appreciate and understand the ocean chemistry of the lanthanides, one must be aware of the central role of rivers and estuaries in shaping the input of lanthanides to the sea. Rivers are the major source of lanthanides to the oceans, and modification of lanthanide fluxes to the ocean via riverine and estuarine processes will constitute an important aspect of this review.

This article has two broad divisions, reflecting the research directions of its authors. One division covers elemental distributions and physical forms of lanthanides in rivers, estuaries and oceans. The emphasis here is on lanthanide abundances in space and time and the general processes responsible for absolute and relative lanthanide concentrations. The second division centers on the aquatic chemistry of lanthanides. This section's emphasis is physical chemistry and covers solution complexation, surface complexation (sorption), and the coupling which exists between physical chemistry and lanthanide distributions.

The tabulation of published data on the concentration of rare earth elements and the Nd isotopic composition of natural waters is published separately in a Woods Hole Oceanographic Institution (WHOI) Technical Report (Sholkovitz 1996). In this Handbook article these data tables will be referred to as tables A1 through A14. These "A" tables include data for rivers, estuaries, seawater, enclosed basins, anoxic basins, pore waters and hydrothermal waters. The tabulated data are also contained on *Microsoft Excel* files included on a disk as part of the Technical Report. Readers can receive a copy of the Technical Report by writing to the following address:

The Document Library
Woods Hole Oceanographic Institution, MS 8
Woods Hole, MA 02543, USA.

2. The marine chemistry of the lanthanides

The objective of this section is to introduce some of the broad characteristics and properties of lanthanides in seawater along with the rationale for studying the lanthanide composition of natural waters. The themes developed below will be expanded upon in subsequent sections.

The lanthanides are composed of a group of fourteen elements (La, Ce, Pr, Nd, Sm, Eu, Gd, Tb, Dy, Ho, Er, Tm, Yb and Lu). Pm, a lanthanide between Nd and Sm which can be produced by nuclear reactions, does not exist in nature in significant concentrations. The lanthanides will be referred to as lights, middles and heavies. This division is arbitrary and is based on the separations used in many preconcentration methods (lights = La, Ce and Pr; middles = Nd, Sm, Eu, Gd and Tb; heavies = Dy, Ho, Er, Tm, Yb and Lu). In many examples from the literature in this article, Nd is used to represent the light elements and Er the heavy elements.

There are anthropogenic sources of lanthanides to the atmosphere (and presumably to the ocean) in the form of particles produced during the cracking of oil and the combustion of oil and gasoline products (Olmez and Gordon 1985, Olmez et al. 1991, Kitto et al. 1992, Brown et al. 1991). Many petroleum-cracking catalysts and products are highly enriched in La, Ce and Nd. Olmez and Gordon (1985) argued for long-range transport of oil-combustion products with light-lanthanide enrichment from the Asian continent to Hawaii across the Pacific Ocean. The input of anthropogenic lanthanides to the oceans, while poorly known, is probably negligible with respect to crustal sources delivered by rivers and the atmosphere. No additional discussion of anthropogenic sources and processes will be presented in this article.

A major objective of chemical oceanography is to understand processes controlling the concentration, distribution, speciation and flux of elements in the oceans. In practice, this objective applies to trace elements (e.g., metals and nutrients) as they are involved in a large set of biogeochemically-driven reactions. Uptake by biota in surface waters and remineralization in deep water is a classic example. How can the study of lanthanides contribute to the above objective? The answer lies in the fundamental chemical properties of the lanthanides (Elderfield 1988). The unique and chief attraction of using lanthanides to address geochemical and oceanographic problems is that they form a coherent group of trace elements whose chemical properties change systematically across the series from La to Lu. This group effect and the varying redox state of Ce allows the lanthanides to be utilized as probes of many fundamental reactions and processes operating on trace elements in natural waters, including rivers, estuaries and oceans. Specific processes include adsorption to mineral and organic surfaces of suspended and sinking particles, complexation to inorganic and organic ligands in solution, particle-particle interactions such as formation of colloids, oxidation-reduction by biota and photochemistry, incorporation into biogenic, diagenetic and authigenic minerals and water/rock interactions in hydrothermal systems.

The interplay of surface and solution chemistry is a fundamental process underlying the cycling of trace elements in the oceans (e.g., Balistrieri et al. 1981, Hunter 1983, Nyffeler et al. 1984, Honeyman and Santschi 1988). The extent to which trace elements are bound to different types of inorganic and biogenic particles (colloidal, suspended and large fast-sinking types) will affect their removal rates and the composition of seawater. Removal by particles also affects other major oceanic processes such as remineralization in the water column, diagenesis in the sediments and preservation of the sedimentary record. One outstanding question is: "To what extent do solution/surface partitioning

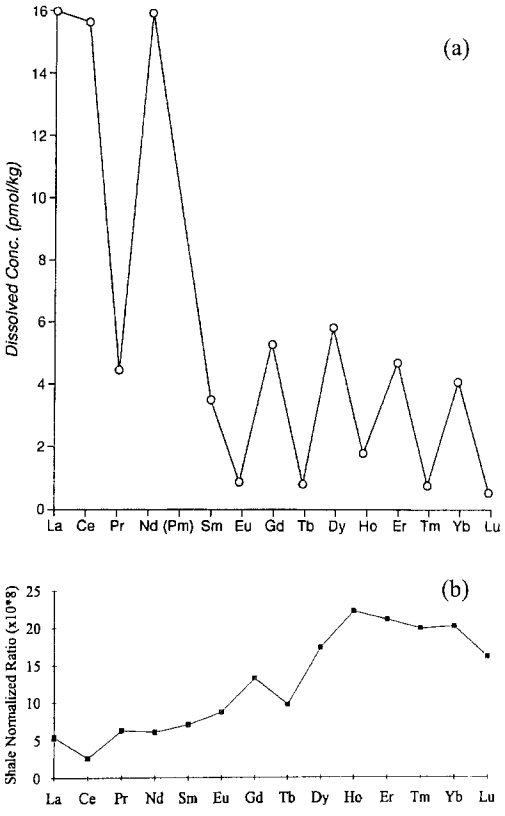

Fig. 1. (a) The concentration of dissolved lanthanides in the surface waters of the Sargasso Sea. A composite of data measured by TIMS (Sholkovitz and Schneider 1991) and INAA (De Baar et al. 1983). Note classic saw-tooth abundance pattern. Pm does not exist in nature. (b) Shale-normalized pattern of the composite seawater shown in (a) using shale concentrations of table 1. Tb, being inconsistent, probably reflects an incorrect concentration of the seawater.

processes influence the relative concentrations of metals in seawater?" The group effect of lanthanide chemistry is ideally suited to addressing this basic question.

With the exception of cerium, the lanthanides have a trivalent oxidation state in most natural waters. As a result of the f-electron shell being progressively filled, there is a gradual decrease in ionic radius across the series ("lanthanide contraction"). In seawater, lanthanide-carbonate ion complexes are the dominant dissolved species, and there is a systematic increase in extent of carbonate complexation from the light to heavy trivalent lanthanides (Cantrell and Byrne 1987a, Byrne and Kim 1990, Lee and Byrne 1993a). Increased complexation from La to Lu leads to a decrease in the proportions of free ions across the series. This change in speciation, in turn, results in mass fractionation defined here as the variation in the relative lanthanide concentrations through biogeochemical reactions operating within the water column and between ocean basins. Hence, the fractionation will reflect, in part, the competition between adsorption to surface sites and complexation to ligands in solution (Byrne and Li 1995).

Fractionation of the lanthanides is a major theme of the literature and hence this article. Fractionation in natural waters is often quantified by computing shale-normalized ratios

Table 1
Lanthanide concentrations of shale in the marine literature

	La	Ce	Pr	Nd	Sm	Eu	Gd	Tb	Dy	Ho	Er	Tm	Yb	Lu
ppm	41	83	10.1	38	7.5	1.61	6.36	1.23	5.49	1.34	3.75	0.63	3.51	0.61
μmol/kg	295	592	71.7	263	49.9	10.6	40.4	7.74	33.8	8.12	22.4	3.73	20.4	3.49

and comparing shale-normalized patterns. [Most studies of rocks and minerals prefer normalization to chondrite (Henderson 1984)]. Shale is representative of the lanthanide composition of the upper crust (Taylor and McLennan 1985). Normalization to shale accomplishes two tasks. First it removes the naturally occurring saw-tooth distribution in the absolute abundance of the lanthanides. As illustrated in fig. 1a for Sargasso Sea seawater, the absolute abundance of the lanthanides has the classic odd–even pattern found in all natural materials (Henderson 1984). Note that the seawater concentrations decrease between the light and heavy elements (in this case from 16 to 0.5 pmol/kg). Normalization to shale as illustrated in fig. 1b results in the typical pattern for seawater – a large depletion in Ce and a heavy-element enrichment. The second task of shale normalization is to represent the abundance of a sample *relative* to that of the upper crust of the continents. In that sense, shale patterns also serve as source signatures (fig. 1b). Different shale concentrations have been used for normalization. In this article the shale concentrations are the mean values of the North American, European and Russian shale composite presented by De Baar (1983). This composition, presented in table 1, has been adopted by many (but not all) marine geochemists (Sholkovitz et al. 1989 and references therein). Other shale compositions used for normalization can be found in Taylor and McLennan (1985) and Piepgras and Jacobsen (1992).

While Ce(III) has a solution chemistry similar to its trivalent lanthanide neighbors (La and Pr), its oxidation to Ce(IV) results in the formation of an insoluble oxide. In many cases, Ce is compared to La and Nd as Pr cannot be measured by isotope dilution mass spectrometry (sect. 3). Because trivalent La, Ce, Pr and Nd have such similar aquatic chemistries, geochemists have focused on this suite of elements to understand more about oxidation-reduction reactions in seawater and in seafloor minerals like manganese nodules. Unlike redox-sensitive elements which do not have closely allied chemistries (e.g., Fe, Mn, U, V, Cr), the chemical coherence of the trivalent lanthanides allows the redox chemistry of Ce to be viewed in the perspective of strictly trivalent neighbors. Thus, anomalous concentrations of Ce reflect redox reactions. It is important to note that the Ce(III)/Ce(IV) redox potential lies between that of Fe(II)/Fe(III) and Mn(II)/Mn(IV) (Elderfield and Sholkovitz 1987, Elderfield 1988). Due to their redox cycles in natural waters and sediments, Fe and Mn are notable in being two of the most geochemically-active and important elements. The formation and dissolution of Mn and Fe oxides control the cycling of many trace elements without multiple redox states; the strictly trivalent lanthanides are a good example of this coupling. Ce, independent of the other lanthanides also exhibits an active redox-driven geochemistry in natural waters and sediments.

The anomalous behavior of Ce has been quantified by defining the Ce anomaly in terms of shale-normalized compositions as follows:

$$\text{Ce anomaly} = 3\,[\text{Ce}]_n / \left[2\,[\text{La}]_n + [\text{Nd}]_n\right],$$

where n refers to the shale-normalized ratios. Where Pr data are available, the Ce anomaly is defined with respect to La and Pr. In many waters studies, where the data come from isotope dilution mass spectrometry, the nearest heaviest neighbor to Ce is Nd. A value of 1 for the anomaly means that Ce is not fractionated relative to the crustal composition. A depletion of Ce relative to its lanthanide(III) neighbors yields values less than 1, so called negative Ce anomalies. Positive anomalies have values greater than 1. Eu anomalies are defined in a similar manner (Eu anomaly $= 2\,[\text{Eu}]_n / \left[[\text{Sm}]_n + [\text{Gd}]_n\right]$) by comparing Eu with its two neighbors Sm and Gd. Because Eu anomalies are associated with hydrothermal waters and basalt, both shale-normalized values and chondrite-normalized values of Sm, Eu and Gd are used in the literature.

Processes invoked to explain the development of Ce anomalies include (1) biologically-mediated oxidation of Ce(III) to Ce(IV) in coastal and open oceans (Moffett 1990, 1994a,b, Sholkovitz and Schneider 1991, Sholkovitz et al. 1994); (2) Ce(III)–Ce(IV) redox shifts across anoxic/oxic interfaces in the water columns of marine basins (De Baar et al. 1988, German and Elderfield 1989, Schijf et al. 1991, Sholkovitz et al. 1992); and (3) the development of the largest Ce anomalies in rivers with the highest pH (Goldstein and Jacobsen 1988a,b, Elderfield et al. 1990). Each of these subjects will be covered in more depth in subsequent sections.

Europium redox changes [Eu(II)/Eu(III)] are restricted to the high temperatures and pressures associated with the formation of minerals and rocks and hydrothermal waters (Henderson 1984, Henderson and Pankhurst 1984, Taylor and McLennan 1985). The only seawater samples to show an Eu anomaly (a negative one in this case) were surface waters reported in Elderfield and Greaves (1982) for a site off northwest Africa. They attributed this feature to the eolian transport and dissolution of Saharan dust. The most notable Eu anomalies are associated with hydrothermal waters venting to the seafloor. Venting waters are characterized by large positive Eu anomalies as the result of water/basalt reactions (e.g, German et al. 1990, Klinkhammer et al. 1994a). Further discussion of the Eu anomaly will be limited to hydrothermal fluids for which there are systematic studies of lanthanide geochemistry (sect. 7.3).

3. Methods of analysis

There appears to be only one review-type article on the analytical techniques used to measure lanthanides in natural materials. This is Henderson and Pankhurst's (1984) chapter in *Rare Earth Element Geochemistry* (Henderson 1984) on the analytical chemistry of lanthanides in rocks, minerals and water. *A Handbook of Silicate Rock Analysis* by Potts (1987) covers the principles and instrumentation used in the mass

spectrometric analyses of lanthanides. Two more recent publications provide detailed descriptions for the measurement of lanthanide concentrations in seawater by thermal ionization mass spectrometry (Greaves et al. 1989, Schneider and Palmieri 1994). This section contains references most relevant to this section's topic, the measurement of lanthanide concentration in natural waters (rain, river, estuary and ocean).

The measurement of lanthanides represents a challenge as their dissolved concentrations are extremely low, 0.5–20 pmol/kg in open ocean water. For the analysis of a 1–2 liter sample of seawater, only 0.1–3 ng of each lanthanide is being measured. Particulate concentrations are a factor of 5–10 lower. At natural water levels, pre-concentration and purification steps must precede the instrumental measurement. Great care must be taken not to contaminate the samples during collection, storage and analysis and to maintain low blanks in the analytical solutions and steps. All of this has been accomplished and several laboratories are producing high quality data for seawater and other natural waters.

As in other fields of aquatic chemistry, advances in analytical methods catalyze a better understanding of the distributions of the lanthanides and the processes responsible for their sources, abundance and oceanic cycles. A major breakthrough came with the publication of Elderfield and Greaves's (1982) paper in which the first vertical distributions in the ocean (Atlantic Ocean) showed that lanthanide profiles have vertical structure in response to biogeochemical cycling. Co-precipitation with iron oxyhydroxides was used by Elderfield and Greaves (1982) as the pre-concentration step and cation exchange was used to purify the lanthanides. This work involved the first use of isotope dilution thermal ionization mass spectrometry (ID-TIMS) for the analysis of dissolved lanthanides. A detailed description of these methods modified for seawater from Thirlwall's (1982) detailed procedure for measuring the lanthanide concentrations of rocks, can be found in Elderfield and Greaves (1983) and Greaves et al. (1989). Prior to Elderfield and Greaves (1982), there were only two publications on the measurement of lanthanides in a few samples of seawater; both employed instrumental neutron activation analysis (INAA) (Goldberg et al. 1963, Høgdahl et al. 1968). The paper by Goldberg et al. (1963) appears to be the first with data on the lanthanide concentrations of seawater; examination of their analytical protocol demonstrates the heroic efforts required to make these measurements. While De Baar improved the analysis of seawater by INAA (De Baar et al. 1983, 1985a,b, De Baar 1984), this method lacks the precision of ID-TIMS. The latter technique constitutes the most precise method for the measurement of those lanthanides for which there exist enriched isotopes (McLaren et al. 1990). Not only is mass spectrometry a more sensitive means of detection, isotope dilution provides a built-in yield monitor for calculating concentrations (Heumann 1992).

Further improvements in the analysis of lanthanides in seawater by ID-TIMS were made (Sholkovitz and Schneider 1991, Piepgras and Jacobsen 1992, Schneider and Palmieri 1994) by separating the lanthanides into three or four groups prior to the mass spectrometric measurements. The lanthanide data of Piepgras and Jacobsen (1992) from the Pacific Ocean are significantly smoother than those of earlier studies (using ID-TIMS and INAA). This improved precision (reported measurement errors, based on counting statistics only, are better than 1%) has important consequences with respect to interpreting

oceanographic processes. Greaves et al. (1989) also reported a reproducibility of <1% except for La, Yb and Lu at 2–3%. Neither study reported replicate measurements of the same seawater samples. Greaves et al. (1989) compared their concentrations of Nd and Sm with those of Piepgras and Wasserburg (1983). While both used ID-TIMS, their profiles from the Northeast Atlantic were collected at different locations (about 200 km apart) and at different times. Despite these differences, their concentrations agreed to within 1%; this value was derived by comparing the averaged concentrations of their water column Nd and Sm values (table 6 of Greaves et al. 1989). Sholkovitz and Schneider (1991) compared their lanthanide concentrations of Sargasso Sea water (ID-TIMS) with those measured by INAA by De Baar et al. (1983). With the exception of Ce, for which there was a major analytical problem with INAA (De Baar 1991), good agreement was observed for many elements even though these samples were collected nine years apart from different locations.

Replicate analyses of identical samples represent a more pragmatic view of the errors achieved by ID-TIMS. Triplicate analyses of filtered Chesapeake Bay water provide one example (Sholkovitz et al. 1992). With exception of Nd at 5%, the other nine lanthanides had a precision of better than 3%; many were below 1.4%. Replicate analysis of two coastal seawater samples showed similar precisions; although most all of the lanthanides had precisions better than 2%, many were below 1% (Sholkovitz 1993).

With the recent development of inductively coupled plasma mass spectrometry (ICP-MS) as a powerful method for the measurement of trace elements (Colodner et al. 1994), this technique has been applied to the analysis of lanthanides in seawater and fresh waters (Hall et al. 1995, Kawabata et al. 1991, Shabani et al. 1990, 1992, Shabani and Masuda 1991, Möller et al. 1992, Westerlund and Öhman 1992, Esser et al. 1994, Klinkhammer et al. 1994b). ICP-MS has two advantages over TIMS. One is speed of analysis and the second is the ability to measure all the lanthanides. Presently, ID-TIMS yields higher precisions on the measurement of lanthanide concentrations in seawater than does ICP-MS. Piepgras and Jacobsen (1992) and Sholkovitz et al. (1994) have argued that this higher precision is required to interpret the small vertical variations in open ocean profiles. Speed is an obvious advantage when a large number of samples is required to determine the spatial and temporal variations of lanthanides in rivers, estuaries and oceans. Using isotope dilution, TIMS yields data only for ten elements: La, Ce, Nd, Sm, Eu, Gd, Dy, Er, Yb and Lu. Enriched isotopes of these elements are commercially available; the other lanthanides are monoisotopic and thus cannot be measured by the ID mode. Having data on all the lanthanides, as opposed to just the ten ID-determined elements, can be an advantage for studying the aquatic chemistry of lanthanides. For example, a more accurate measure of the cerium anomaly requires data for Pr as well as La and Ce. Likewise, normalizations to shale and chondrite are more complete when using all the lanthanides. Nevertheless, while our current understanding of the aquatic geochemistry of the lanthanides is improved by having concentration data on all, not just the ten ID-measurable lanthanides, it is the quality and the precision of data which are most critical for interpreting lanthanide distributions in natural waters.

Measurement of lanthanides in seawater by both ID-TIMS and ICP-MS requires pre-concentration and isolation steps. New and different procedures for these steps have been developed and successfully applied by Shabani and Masuda (1991), Shabani et al. (1990, 1992), Esser et al. (1994) and Hall et al. (1995). Most studies have employed internal standards (i.e., Lu) for determining recovery efficiencies and external calibrations to determine the concentrations. Esser et al. (1994) applied isotope dilution (ID–ICP–MS) which eliminates the need for internal or external standards.

Studies by Möller et al. (1992) and Westerlund and Öhman (1992) reported precisions of 5–15% RSD for lanthanides in seawater using ICP-MS. Esser et al. (1994) reported a 4–10% RSD based on a triplicate analysis of 1 liter samples of seawater using ID-ICP-MS. Shabani et al. (1992) reported better precisions using ICP-MS without isotope dilution: 1–5% RSD for a quadruplicate analysis of 1 liter samples and 0.5–2% RSD for a quadruplicate analysis of 5 liter samples of seawater. The precision of their data for all the lanthanides match those obtained with ID-TIMS, but their methods have not yet been applied to a vertical profile in the oceans. Only Klinkhammer et al. (1994b) have directly compared lanthanide concentrations using ID-TIMS and ICP-MS measurements. Using a suite of hydrothermal waters from seafloor vents, they concluded that ID-TIMS is more precise than ICP-MS (1 vs. 3%) and that ICP-MS is accurate at the 6% (2σ) level with respect to ID-TIMS. ICP-MS has worked well for hydrothermal solutions where lanthanide concentrations are greatly enriched over those of seawater (Klinkhammer et al. 1994b). One author of this article (ERS) has concluded through comparative studies that ICP-MS is suitable for river waters with high concentrations but not suitable for seawater where concentrations are 5–20 times lower and vertical gradients are small (Schneider and Palmieri 1994).

In what areas of marine geochemistry will advances in methodology significantly improve our knowledge of the processes operating on the lanthanides? As emphasized in this section, advances in analytical techniques over the past decade and a half have lead to a large increase in our understanding of the aquatic chemistry of lanthanides (and other trace elements). Improvements in both TIMS and ICP-MS analysis and the technology of ICP mass spectrometers will continue. The development of magnetic sector ICP mass spectrometers (Walder et al. 1993) combining the speed of ICP-MS with the higher resolution of magnetic sector separation is a prime example. Improvements in the efficiency of introducing samples to the plasma will further increase the signal and precision. The sensitivity and precision of ICP-MS measurements will soon match that of TIMS, leading to shorter analysis time and more samples being analyzed. This, in turn, should lead to a better understanding of the processes responsible for the temporal and spacial variability of lanthanides in rivers, estuaries and seawater.

The pore water composition of lanthanides is poorly characterized. Low concentrations and small volumes of pore water samples (typically 10–50 ml) combine to make detection difficult. Only the lanthanide-enriched pore waters of anoxic coastal and estuarine sediments have been measured at a few sites (sect. 6). Currently, the pore water chemistry of lanthanides in non-coastal marine sediments is unknown. The field of lanthanide pore water chemistry remains an important challenge.

4. Physical chemistry of the lanthanides in seawater

4.1. *Solution chemistry*

Descriptions of the molecular behavior of the lanthanides in seawater are generally based upon observations made in simple synthetic solutions rather than seawater itself. Compilations of lanthanide stability constants obtained in simple solutions commonly employ data from experiments in which lanthanides have been studied one at a time or as a group of no more than a few elements. Since great importance is attached to lanthanide behavior in the context of comparative chemistries, it is important that the results of various experiments are analyzed in a manner which preserves comparative aspects of lanthanide behavior. Thus, when stability constant data are combined toward the end of producing a critically selected database for a given ligand, it is most desirable to employ data sets in which all lanthanides were studied, using a consistent set of procedures. While this situation is common for lanthanide complexation with organic ligands, it is frequently the case that lanthanide complexation constants for important inorganic ligands have been obtained for only a few lanthanides. In cases where a variety of investigators have determined lanthanide stability constants for a limited number of elements, important comparative chemical features can be obscured. In such cases, within a limited framework of direct observations, linear free-energy relationships can be used (Lee and Byrne 1992, 1993a,b, Byrne and Li 1995) as a guide to comparative chemistries. In the text which follows we have compiled stability constants for inorganic lanthanide complexes which are potentially significant in seawater. Selected stability constant data are then used to construct speciation schemes and distribution models appropriate to seawater.

4.2. *Lanthanide complexation in seawater*

Seawater contains a complex mixture of anions capable of complexing the lanthanides. Potentially important inorganic lanthanide complexes include those with PO_4^{3-}, CO_3^{2-}, HPO_4^{2-}, SO_4^{2-}, OH^-, F^-, $H_2PO_4^-$, $SiO(OH)_3^-$, Cl^- and $B(OH)_4^-$. Since the salinity (S) of the ocean varies within a relatively small range, $34 \leqslant S \leqslant 36$ for 98% of the ocean's volume (Montgomery 1958), the ionic strength of seawater remains close to 0.70 mol kg^{-1}. Although only a small fraction of the ocean's volume has a temperature as high as 20°C (Pickard and Emery 1982), most lanthanide equilibrium data have been obtained at temperatures between 20°C and 25°C. In practice, this does not create an appreciable problem since the enthalpies of reaction for the lanthanides are generally small (Choppin 1980, Grant et al. 1988). In the following section, recommended lanthanide stability constants appropriate to 0.70 mol kg^{-1} ionic strength and 25°C are presented. Earlier critical assessments upon which the following treatment is based include those of Turner et al. (1981), Byrne et al. (1988), Wood (1990) and Millero (1992).

4.2.1. *Lanthanide complexation with phosphate*

There are very few measurements upon which an assessment of lanthanide phosphate stability constants can be based (Byrne and Bingler 1989). The recommended constants

Table 2
Complexation constant estimates for MPO_4^0 formation at 0.7 mol kg^{-1} ionic strength and 25°C[a]

Metal (M)	$\log_{PO_4}\beta_1$	Metal (M)	$\log_{PO_4}\beta_1$
La	8.06	Tb	9.49
Ce	8.45	Dy	9.62
Pr	8.70	Ho	9.69
Nd	8.88	Er	9.79
Sm	9.21	Tm	9.92
Eu	9.32	Yb	10.04
Gd	9.30	Lu	10.09

[a] Estimates expressed in terms of free-ion concentrations:
$_{PO_4}\beta_1 = [MPO_4^0][M^{3+}]^{-1}[PO_4^{3-}]^{-1}$, where [ ] denotes free-ion concentration.

provided in table 2 are based on the work of Byrne et al. (1991) and Lee and Byrne (1992). The latter work utilized linear free-energy relationships to estimate lanthanide phosphate stability constants from $CePO_4^0$ and $GdPO_4^0$ complexation results (Byrne et al. 1991).

The results shown in table 2 indicate that lanthanide phosphate complexes are relatively minor species in seawater. Total phosphate concentrations in seawater are as large as 3×10^{-6} mol kg^{-1} only in the deep ocean and can approach nanomolar concentrations in surface waters. Of the total phosphate, approximately one third is present as free HPO_4^{2-} (Millero and Schreiber 1982) and the remaining two thirds is ion-paired with Na^+, Ca^{2+}, and Mg^{2+}. Since $\log [PO_4^{3-}][H^+]/[HPO_4^{2-}] \approx -11.2$ at 25°C and $\mu = 0.7$ mol kg^{-1} (Atlas et al. 1976), it follows that the concentration of free phosphate ion ($[PO_4^{3-}]$) in seawater is generally much smaller than 1×10^{-9} mol kg^{-1}. Although the pH of surface waters is relatively high (pH ≈ 8.2), surface seawater is sufficiently depleted in nutrients, including phosphate, that phosphate complexation of lanthanides in the upper oceanic water column is essentially negligible. In deep water, which is enriched in regenerated nutrients and may have free HPO_4^{2-} concentrations on the order of 1×10^{-6} mol kg^{-1}, other factors limit the significance of MPO_4^0 formation. The influence of pressure on the reaction $HPO_4^{2-} + M^{3+} \rightleftharpoons MPO_4^0 + H^+$, favoring formation of highly charged, electrostricted species (e.g. M^{3+}), in concert with lower pH (higher $[H^+]$ than in surface waters) serves to minimize the significance of phosphate complexation throughout the ocean's volume. The investigation of $GdHPO_4^{2+}$ formation constants of Bingler and Byrne (1989) indicated that $_{HPO_4}\beta_1(Gd)$ and $_{H_2PO_4}\beta_1(Gd)$, expressed in terms of free-ion concentrations ([ ]) at 25°C and 0.7 mol kg^{-1} ionic strength, are $\log {}_{HPO_4}\beta_1(Gd) \approx 4$ and $\log {}_{H_2PO_4}\beta_1(Gd) \leqslant 1.8$. Since the free-ion concentration of HPO_4^{2-} in seawater is no larger than approximately 1×10^{-6} mol kg^{-1}, it is clear that lanthanide complexes involving HPO_4^{2-} and $H_2PO_4^-$ in seawater should be negligible.

4.2.2. *Lanthanide complexation with CO_3^{2-}*

The work of Turner et al. (1981) was the first to indicate the importance of carbonate complexation in the marine chemistry of the lanthanides. The lanthanide carbonate

Table 3a
Complexation constant estimates for MCO_3^+ and $M(CO_3)_2^-$ formation at 0.7 mol kg^{-1} ionic strength and 25°C[a]

Metal	$\log_{CO_3}\beta_1$(M)	$\log_{CO_3}\beta_2$(M)	Metal	$\log_{CO_3}\beta_1$(M)	$\log_{CO_3}\beta_2$(M)
La	5.43	9.64	Tb	6.26	11.16
Ce	5.71	10.26	Dy	6.31	11.29
Pr	5.87	10.54	Ho	6.35	11.34
Nd	5.98	10.72	Er	6.42	11.52
Sm	6.19	11.00	Tm	6.50	11.66
Eu	6.26	11.03	Yb	6.59	11.84
Gd	6.13	10.98	Lu	6.60	11.91

[a] Estimates expressed in terms of free carbonate ion concentrations:
$_{CO_3}\beta_1(M) = [MCO_3^+][M^{3+}]^{-1}[CO_3^{2-}]^{-1}$ and $_{CO_3}\beta_2(M) = [M(CO_3)_2^-][M^{3+}]^{-1}[CO_3^{2-}]^{-2}$.

formation constant behavior predicted by Turner et al. (1981) was based upon carbonate–oxalate stability constant relationships for divalent metals. Direct experimental complexation observations (Ciavatta et al. 1981, Lundqvist 1982, Ferri et al. 1983) indicate that linear free-energy relationships based on the behavior of divalent metals considerably underestimate the magnitude of lanthanide carbonate stability constants. To a much greater extent than predicted by the model of Turner et al. (1981), carbonate complexes dominate the solution speciation of lanthanides in seawater. In order to assess the comparative solution complexation behavior of lanthanides in seawater, Cantrell and Byrne (1987a,b) investigated cerium, europium, and ytterbium complexation by CO_3^{2-}. The formation constants for lanthanides not directly measured were approximated using a quadratic relationship to express lanthanide formation constants as a function of lanthanide atomic number. Recently, Lee and Byrne (1993a) made direct measurements of the carbonate complexation behavior of Ce, Eu, Gd, Tb and Yb. In this work, the formation constants of lanthanides which were not assessed directly were estimated using multiple linear free-energy relationships. The results of these assessments appropriate to 25°C and 0.70 mol kg^{-1} ionic strength are shown in table 3a.

Use of table 3a in calculations of lanthanide seawater complexation requires that the total inorganic carbon concentration of seawater (C_T) be partitioned into dissolved aqueous carbon dioxide (CO_{2aq}), bicarbonate (HCO_3^-) and carbonate (CO_3^{2-}). Since only a small fraction (~14%) of CO_3^{2-} in seawater is in the form of free ions, with the remainder being ion-paired as $NaCO_3^-$, $CaCO_3^0$ and $MgCO_3^0$, use of table 3a constants requires an assessment of carbonate and bicarbonate ion-pairing equilibria. Table 3b shows a more convenient stability constant formulation wherein lanthanide carbonate stability constants are expressed in terms of total (free plus ion-paired) carbonate ion concentrations in seawater ($[CO_3^{2-}]_T$). These results can be compared with direct observations of europium carbonate complexation in synthetic seawater (Lee and Byrne 1994). The $GdCO_3^+$ and $Gd(CO_3)_2^-$ formation constant results of Lee and Byrne (1994), expressed in terms of

Table 3b
Complexation constant estimates for MCO_3^+ and $M(CO_3)_2^-$ formation in salinity 35 seawater at 25°C[a]

Metal (M)	$\log {}^{SW}_{CO_3}\beta_1(M)$	$\log {}^{SW}_{CO_3}\beta_2(M)$
La	4.57	7.92
Ce	4.85	8.54
Pr	5.01	8.82
Nd	5.12	9.00
Sm	5.33	9.28
Eu	5.40	9.31
Gd	5.27	9.26
Tb	5.38	9.44
Dy	5.45	9.57
Ho	5.49	9.62
Er	5.56	9.80
Tm	5.64	9.94
Yb	5.73	10.12
Lu	5.74	10.19

[a] Estimates expressed in terms of total carbonate ion concentrations:
${}^{SW}_{CO_3}\beta_1(M) = [MCO_3^+][M^{3+}]^{-1}[CO_3^{2-}]_T^{-1}$ and ${}^{SW}_{CO_3}\beta_2(M) = [M(CO_3)_2^-][M^{3+}]^{-1}[CO_3^{2-}]_T^{-2}$, where
$[CO_3^{2-}]_T = [CO_3^{2-}] + [NaCO_3^-] + [CaCO_3^0] + [MgCO_3^0]$.

total carbonate ($[CO_3^{2-}]_T$), are in good agreement with the predictions shown in table 3b: $\log {}^{SW}_{CO_3}\beta_1(Gd) = 5.19$ and $\log {}^{SW}_{CO_3}\beta_2(Gd) = 9.18$.

Lanthanide carbonate complexation in seawater is strongly dependent on pH. The total carbonate ion concentration of seawater ($[CO_3^{2-}]_T$) is related to pH and the total inorganic carbon content of seawater (C_T), through

$$C_T = [CO_3^{2-}]_T \left(1 + [H^+]_T/K_2 + [H^+]_T^2/K_1K_2\right),$$

where $[H^+]_T$ is a total hydrogen ion concentration ($[H^+]]_T \approx [H^+] + [HSO_4^-]$), and the dissociation constants for carbonic acid (K_1) and bicarbonate (K_2) in seawater on this pH scale (Dickson 1993) are given in Dickson and Goyet (1994). At $S = 35$ and 25°C, $\log K_1 = -5.856$ and $\log K_2 = -8.925$. A typical value of C_T for seawater is 2×10^{-3} mol kg^{-1}, and seawater pH generally varies within the range $7.3 \leqslant pH_T \leqslant 8.3$ (with highest values at the surface, lower values at depth, and lowest values in waters strongly depleted of oxygen). Following the above C_T–$[CO_3^{2-}]$–pH relationship, at $pH_T = 8$ the total carbonate ion concentration of seawater is calculated as $\log [CO_3^{2-}]_T = -3.676$. Comparison with table 3b then shows that, under these conditions,

$$[LaCO_3^+] / [La^{3+}] \approx 7.8, \qquad [La(CO_3)_2^-] / [La^{3+}] \approx 3.70$$

while

$$[LuCO_3^+] / [Lu^{3+}] \approx 116, \qquad [Lu(CO_3)_2^-] / [Lu^{3+}] \approx 689.$$

Table 4
Comparison of Eu(III) carbonate complexation constants at 25°C and zero ionic strength

$\log\beta_1^0$	$\log\beta_2^0$	Source	Method
8.00	13.38	Lundqvist (1982)[a]	solvent exchange
7.88	13.1	Cantrell and Byrne (1987a)[b]	solvent exchange
–	13.1	Thompson and Byrne (1988)[b]	spectrophotometry
8.08	12.78	Chatt and Rao (1989)[c]	solvent exchange
7.91	13.07	Rao and Chatt (1991)[b]	solvent exchange
8.06	12.91	Rao and Chatt (1991)[c]	solvent exchange
7.95	13.4	Lee and Byrne (1993a)[b]	solvent exchange

[a] Recalculated (Rao and Chatt 1991) using specific-interaction theory.
[b] Calculated using an ion-pairing model.
[c] Calculated using specific-interaction theory.

Since carbonate complexation is the dominant factor influencing comparative lanthanide solution behavior in seawater, critical evaluation of lanthanide carbonate complexation constants is very important to assessment of lanthanide seawater speciation. Most of the comparisons shown in table 4 were obtained via solvent-exchange analysis. Some insight into systematic differences in formation constant estimates attributable to experimental procedure can be gained by comparing the potentiometrically derived yttrium carbonate stability constant of Spahiu (1985) with the solvent-exchange result of Liu and Byrne (1995). The results of Spahiu (1985), corrected to 0.7 mol dm^{-3} ionic strength (Liu and Byrne 1995), $\log {}^{SW}_{CO_3}\beta_1(Y) = 5.49$, is in fair agreement with the direct estimate of Liu and Byrne (1995), $\log {}^{SW}_{CO_3}\beta_1(Y) = 5.26$. Other formation constant estimates available for comparison with solvent-exchange results include the potentiometrically derived $_{CO_3}\beta_1(La)$ result of Ciavatta et al. (1987) and the $_{CO_3}\beta_1(Ce)$ result of Ferri et al. (1983), obtained through solubility analysis. These results, obtained at 25°C and 3 mol dm^{-3} ionic strength, $\log\beta_1(La) = 5.67$ and $\log\beta_1(Ce) = 6.30$, are not fully consistent with the result of Spahiu (1985), $\log {}_{CO_3}\beta_1(Y) = 6.02$, for the same conditions. Based on linear free-energy analysis (Lee and Byrne 1992) and the expectation that yttrium carbonate formation constants will lie between those of Tb (Cantrell and Byrne 1987a, Liu and Byrne 1995) and Ho (Lee and Byrne 1993a), La and Ce carbonate complexation constants should be considerably smaller than those of yttrium. Thus, lanthanide stability constants obtained through potentiometry and solubility analysis, while generally concordant in terms of absolute magnitudes, do not provide the coherent picture of comparative lanthanide complexation which is obtained through solvent exchange analysis with multiple lanthanides. Nevertheless, since solubility and potentiometric analyses produce even larger lanthanide carbonate stability constants than are obtained by solvent exchange analysis, the conclusion that carbonate complexes dominate the speciation of lanthanides in seawater is strongly supported by both solubility studies and potentiometric investigations.

Table 5
Complexation constant estimates for MSO_4^+ at 25°C and 0.7 mol kg^{-1} ionic strength[a]

Metal (M)	$\log_{SO_4}\beta_1$(M)	Metal (M)	$\log_{SO_4}\beta_1$(M)
La	1.95	Tb	1.97
Ce	1.92	Dy	1.95
Pr	1.95	Ho	1.92
Nd	1.97	Er	1.92
Sm	2.00	Tm	1.92
Eu	2.00	Yb	1.91
Gd	1.99	Lu	1.85

[a] Estimates expressed in terms of free sulfate ion concentrations:
$_{SO_4}\beta_1(M) = [MSO_4^+][M^{3+}]^{-1}[SO_4^{2-}]^{-1}$.

4.2.3. *Lanthanide complexation by SO_4^{2-}*

While lanthanide phosphate and carbonate stability constants increase substantially between La and Lu, the complexation behavior of lanthanides with sulfate changes very little across the lanthanide series. This difference in complexation constant trends is consistent with inner sphere (CO_3^{2-}) versus outer sphere (SO_4^{2-}) complexation behavior (Byrne and Li 1995). Stability constants for lanthanide sulfate complexes at 25°C and zero ionic strength could be well represented as $\log {}_{SO_4}\beta_1^0(M) = 3.60 \pm 0.08$. The recommended stability constants (25°C, 0.7 mol kg^{-1} ionic strength) shown in table 5 are based upon the works of Spedding and Jaffe (1954) and Powell (1974). Following the activity coefficient estimates of Millero and Schreiber (1982) and Cantrell and Byrne (1987a), lanthanide sulfate stability constants, expressed in terms of free-ion concentrations, were calculated as $\log {}_{SO_4}\beta_1 = \log {}_{SO_4}\beta_1^0 - 1.67$.

Since the free sulfate ion concentration in seawater ($S = 35$) is on the order of 0.0095 mol kg^{-1} and varies with temperature by no more than approximately 20%, the concentration of lanthanide sulfate species in seawater remains nearly constant relative to free metal ion concentrations ($[MSO_4^+]/[M^{3+}] \approx 0.8$). Consideration of the formation of $M(SO_4)_2^-$ species in seawater, with zero ionic strength formation constants on the order of $\log {}_{SO_4}\beta_2^0 \leqslant 5.2$, results in predicted $M(SO_4)_2^-$ concentrations which are on the order of 10% as large as free lanthanide ion concentrations in seawater.

4.2.4. *Lanthanide hydrolysis*

Thorough compilations of lanthanide hydrolysis data are given by Rizkalla and Choppin (1991), and Baes and Mesmer (1976). Lanthanide hydrolysis constants are potentially the most controversial constants used in inorganic lanthanide speciation calculations. The hydrolysis constant estimates shown in table 6 are based on the assessment by Lee and Byrne (1992) and were derived from the recommended constants of Baes and Mesmer (1976). The hydrolysis constants of Lee and Byrne (1992) at 25°C and zero ionic strength are larger than the $\log \beta_1^0$ estimates of Millero (1992) by about 0.2 units, and are in

Table 6
Lanthanide hydrolysis constants at 25°C and 0.7 mol kg^{-1} ionic strength[a]

Metal (M)	$\log {}^{*}\beta_1$(M)	Metal (M)	$\log {}^{*}\beta_1$(M)
La	−9.20	Tb	−8.40
Ce	−8.95	Dy	−8.35
Pr	−8.81	Ho	−8.32
Nd	−8.70	Er	−8.27
Sm	−8.50	Tm	−8.22
Eu	−8.44	Yb	−8.14
Gd	−8.47	Lu	−8.13

[a] Estimates expressed in terms of free-ion concentrations. Following the work of Byrne et al. (1988), the relationship between hydrolysis constants at zero ionic strength ($^{*}\beta_1^0$(M)) and hydrolysis constants at 0.7 mol kg^{-1} ionic strength is given as
$\log {}^{*}\beta_1(\mathrm{M}) = \log {}^{*}\beta_1^0(\mathrm{M}) - 0.54$, where ${}^{*}\beta_1(\mathrm{M}) = [\mathrm{MOH}^{2+}][\mathrm{H}^{+}][\mathrm{M}^{3+}]^{-1}$.

general agreement with the lower-bound hydrolysis constant estimates in the compilation of Rizkalla and Choppin (1991). In contrast to the very small temperature dependence for most lanthanide equilibrium constants, lanthanide hydrolysis constants are expected to increase strongly with increasing temperature. Based on the work of Baes and Mesmer (1981), the enthalpy change appropriate to lanthanide hydrolysis has been estimated (Byrne et al. 1988) as 14 kcal/mole. Consequently, using the hydrolysis constant data shown in table 6, hydrolysis constants at temperature T (K) can be estimated as

$$\log {}^{*}\beta_1 = \log {}^{*}\beta_1(298.15\,\mathrm{K}) + 10.26 - 3059.4\,T^{-1}.$$

A reasonable upper-bound pH for seawater at 25°C is pH = −log [H$^+$] = 8.35. The hydrolysis constant estimate for lutetium then indicates that $[\mathrm{LuOH}^{2+}]/[\mathrm{Lu}^{3+}] \leqslant 1.7$. Seawater pH increases by approximately 0.014 units for a 1°C decrease in temperature. Considering both the 14 kcal/mole enthalpy change for lanthanide hydrolysis and the increase in seawater pH with decreasing temperature, the extent of Lu hydrolysis at 0°C is estimated as $[\mathrm{LuOH}^{+}]/[\mathrm{Lu}^{3+}] \leqslant 0.4$. Although larger lanthanide hydrolysis constant estimates (Rizkalla and Choppin 1991) will result in a greater predicted degree of lanthanide hydrolysis, it is clear that the concentrations of hydrolyzed lanthanide species in seawater are comparable to the concentrations of free lanthanide ions only in relatively warm (e.g., $t > 20$°C) surface water.

4.2.5. *Lanthanide complexation by F^- and Cl^-*

Previous assessments of lanthanide fluoride stability constants appropriate at 25°C and zero ionic strength indicate that $\log_F\beta_1^0$ is on the order of 4 or less for all lanthanides. The works of Walker and Choppin (1967) and Bilal and co-workers (Bilal et al. 1979, Bilal and Becker 1979, Bilal and Koss 1980, Bilal 1980, Bilal and Becker 1980, Becker

Table 7
Lanthanide fluoride stability constants at 25°C and 0.7 mol kg^{-1} [a]

Metal (M)	$\log_F\beta_1(M)$	Metal (M)	$\log_F\beta_1(M)$
La	2.57	Tb	3.32
Ce	2.76	Dy	3.29
Pr	2.88	Ho	3.27
Nd	2.97	Er	3.26
Sm	3.17	Tm	3.26
Eu	3.24	Yb	3.30
Gd	3.21	Lu	3.29

[a] Constants expressed in terms of free-ion concentrations:
${}_F\beta_1(M) = [MF^{2+}][M^{3+}]^{-1}[F^-]^{-1}$.

and Bilal 1985) are in reasonable agreement for the light lanthanides (La–Eu) when the data of Bilal and coworkers are corrected for chloride ion-pairing (Lee and Byrne 1993c). For the heavy rare-earth elements (Tb–Lu), the formation constant data of Walker and Choppin (1967) and Bilal and co-workers (Bilal et al. 1979, Bilal and Becker 1979, Bilal and Koss 1980, Bilal 1980, Bilal and Becker 1980, Becker and Bilal 1985) show different trends. The formation constants of Walker and Choppin (1967) increase across the entire lanthanide series, whereas the formation constants of Bilal and co-workers (Bilal et al. 1979, Bilal and Becker 1979, Bilal and Koss 1980, Bilal 1980, Bilal and Becker 1980, Becker and Bilal 1985) increase between La and Dy and then decrease between Dy and Lu. The analysis by Lee and Byrne (1993c) is in good agreement with the La–Tb formation constant behavior found by Walker and Choppin (1967), but for heavier lanthanides (Tb–Lu), indicates that fluoride stability constants are nearly constant. Recommended formation constants, which follow from the analysis by Lee and Byrne (1993c) are given in table 7.

The total fluoride concentration of seawater is 7×10^{-5} mol kg^{-1} at a salinity of 35. The free concentration of fluoride is approximately 3.5×10^{-5} with the remainder being present as MgF^+. The formation constants given in table 7 then indicate that $[MF^{2+}]/[M^{3+}] < 0.1$ for all lanthanides.

The lanthanide chloride stability constants which are recommended for seawater speciation calculations are shown in table 8. The $\log_{Cl}\beta_1$ values shown in table 8 were calculated from the data of Mironov et al. (1982) and are nearly identical to the $\log_{Cl}\beta_1$ values used by Lee and Byrne (1993c) to correct the fluoride stability constant data of Bilal and co-workers (Bilal et al. 1979, Bilal and Becker 1979, Bilal and Koss 1980, Bilal 1980, Bilal and Becker 1980, Becker and Bilal 1985) for chloride ion pairing.

Since the concentration of Cl^- in $S = 35$ seawater is 0.56 mol kg^{-1}, the concentration ratio $[MCl^{2+}]/[M^{3+}]$ for the lanthanides ranges from 0.22 for La to 0.12 for Lu. The $[MCl^{2+}]/[M^{3+}]$ estimates which follow from table 8 are a factor of two to three smaller than the estimates ($[MCl^{2+}]/[M^{3+}] \approx 0.5$) of Millero (1992) for salinity 35 seawater.

Table 8
Complexation constant estimates for MCl^{2+} at 25°C and 0.7 mol kg^{-1} ionic strength[a]

Metal (M)	$\log_{Cl}\beta_1$(M)	Metal (M)	$\log_{Cl}\beta_1$(M)
La	−0.41	Tb	−0.57
Ce	−0.42	Dy	−0.59
Pr	−0.44	Ho	−0.59
Nd	−0.48	Er	−0.62
Sm	−0.52	Tm	−0.63
Eu	−0.55	Yb	−0.63
Gd	−0.57	Lu	−0.66

[a] Estimates expressed in terms of free-ion concentrations:
$_{Cl}\beta_1(M) = [MCl^{2+}][M^{3+}]^{-1}[Cl^-]^{-1}$.

4.2.6. *Other inorganic lanthanide species*

Seawater contains bicarbonate ions at concentrations on the order of 2×10^{-3} mol kg^{-1}. The formation constant results of Ciavatta et al. (1981) and Spahiu (1985) at 3 mol kg^{-1} ionic strength indicate that $\log_{HCO_3}\beta_1 = 1.3$ for both La^{3+} and Y^{3+}. The results of Cantrell and Byrne (1987a) and Lee and Byrne (1993a) at 0.7 mol kg^{-1} ionic strength indicate that lanthanide bicarbonate stability constants, expressed in terms of free concentrations, are on the order of $\log_{HCO_3}\beta_1 = 1.8$. Corrected to zero ionic strength, the Ciavatta et al. (1981) and Spahiu (1985) results are $\log_{HCO_3}\beta_1^0 \approx 2.4$. The results obtained by Cantrell and Byrne (1987a) and Lee and Byrne (1993a) for Ce, Eu, Gd, Tb and Yb are consistent with the estimate $\log_{HCO_3}\beta_1^0 \approx 2.7$. These estimates indicate that $[MHCO_3^{2+}]/[M^{3+}]$ concentration ratios for lanthanides are on the order of 0.10 in seawater. Lanthanide bicarbonate stability constants appropriate to seawater ionic strength, estimated using the results and procedures of Lee and Byrne (1993a), are given in table 9.

Table 9
Complexation constant estimates for $MHCO_3^{2+}$ formation at 0.7 mol l^{-1} ionic strength and 25°C[a]

Metal (M)	$\log_{HCO_3}\beta_1$	Metal (M)	$\log_{HCO_3}\beta_1$
La	1.63	Tb	1.84
Ce	1.75	Dy	1.74
Pr	1.79	Ho	1.67
Nd	1.81	Er	1.61
Sm	1.83	Tm	1.56
Eu	1.83	Yb	1.56
Gd	1.86	Lu	1.51

[a] Estimates expressed in terms of free-ion concentrations:
$_{HCO_3}\beta_1 = [MHCO_3^{2+}][M^{3+}]^{-1}[HCO_3^-]^{-1}$.

Byrne and Cantrell (1996) recently examined the complexation of Eu^{3+} by $B(OH)_4^-$ ions. This solvent-exchange analysis indicated $\log {}_{B(OH)_4}\beta_1 \approx 3$, at 25°C and $\mu = 0.7\,\text{mol dm}^{-3}$. Since the total boron concentration of seawater is $4.2\times10^{-4}\,\text{mol kg}^{-1}$ at salinity 35, and the boric acid dissociation constant is approximately $\log {}_{B(OH)_3}K = -8.7$, the total (free plus ion-paired) borate concentration in seawater is generally less than $1\times10^{-4}\,\text{mol kg}^{-1}$. In view of borate ion pairing equilibria (whereby $[B(OH)_4^-] < [B(OH)_4^-]_T$), these results indicate that lanthanide borate complexation is of little importance in seawater: $[MB(OH)_4^{2+}] / [M^{3+}] \leqslant 0.10$.

4.3. *Lanthanide seawater speciation models*

The total dissolved lanthanide content of seawater is partitioned into individual species contributions using the following relationship

$$M_T = [M^{3+}]\left(1 + B_0 + {}^{SW}_{CO_3}\beta_1 [CO_3^{2-}]_T + {}^{SW}_{CO_3}\beta_2 [CO_3^{2-}]_T^2 + \beta_1^* [H^+]^{-1}\right), \quad (1)$$

where $B_0 = {}_{Cl}\beta_1 [Cl^-] + {}_{SO_4}\beta_1 [SO_4^{2-}] + {}_{F}\beta_1 [F^-] + {}_{HCO_3}\beta_1 [HCO_3^-]$, brackets ([ ] and [ ]$_T$) denote free and total concentrations, and the formation constants (${}_L\beta_n$) appropriate to the above equation are given in tables 3b, 5, 6, 7, 8 and 9. For simplicity, the contributions of minor pH-dependent species such as MPO_4^0, $M(B(OH)_4)^{2+}$ and $MHPO_4^{2+}$ are not shown in eq. (1). The term B_0 is comprised of minor species whose concentrations are essentially independent of pH. Figure 2 shows the concentrations of MCl^{2+}, MSO_4^+, MF^{2+} and

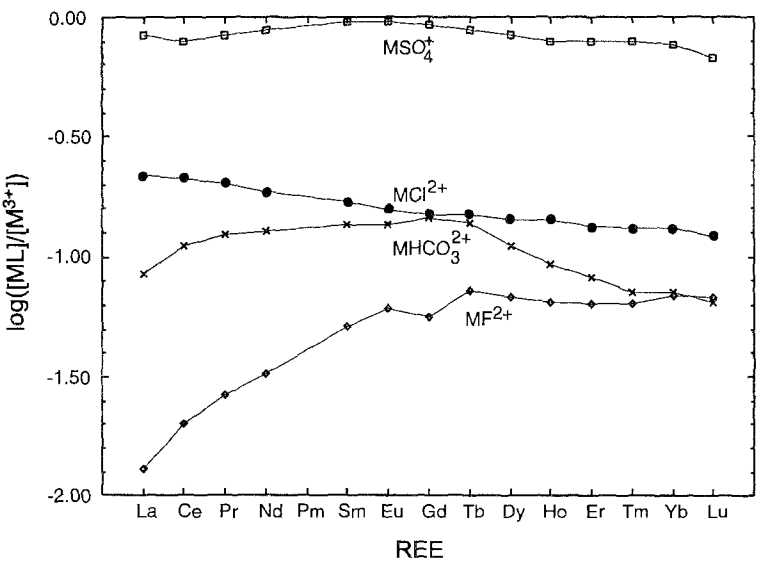

Fig. 2. The concentrations of MCl^{2+}, MSO_4^+, MF^{2+}, and $MHCO_3^{2+}$ are expressed relative to free lanthanide concentrations in seawater at 25°C and salinity equal to 35.

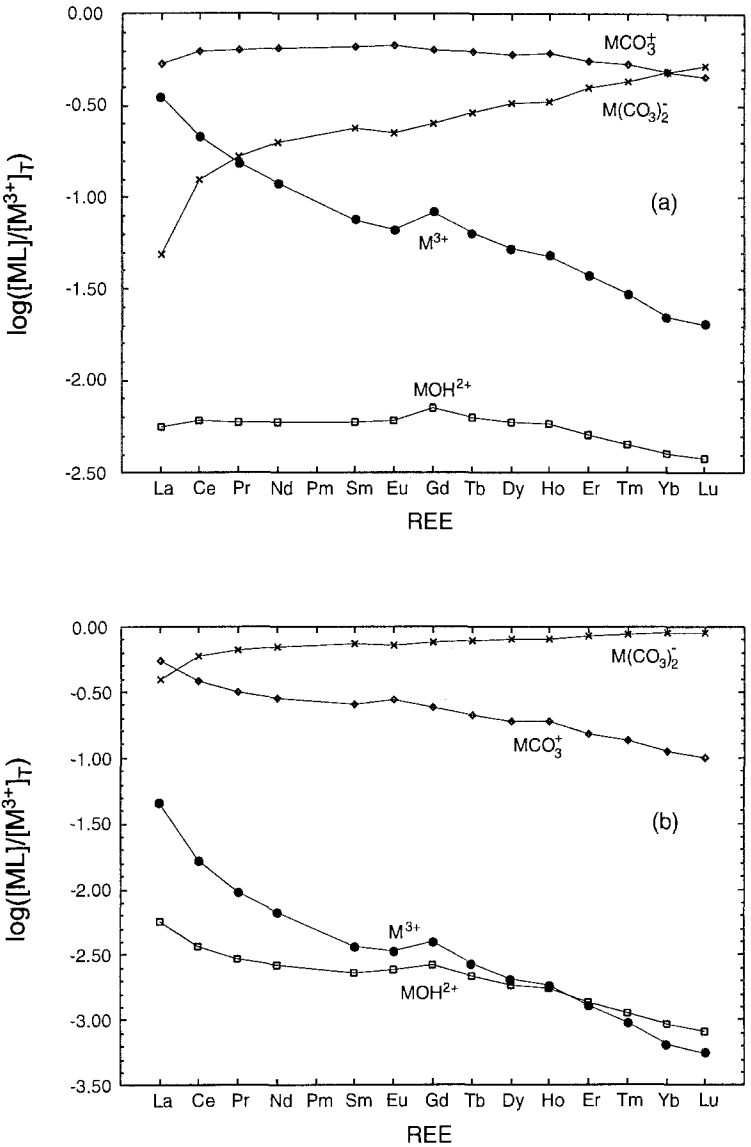

Fig. 3. The concentrations of MCO_3^+, $M(CO_3)_2^-$, MOH^{2+}, and M^{3+} are expressed as fractions of the total concentration of each lanthanide. Figure 3a shows results at pH = 7.4 and figure 3b shows results at pH = 8.3.

$MHCO_3^{2+}$ expressed in terms of $[M^{3+}]$, as a function of lanthanide atomic number. Figure 2 indicates that the sum concentrations of MCl^{2+}, MSO_4^+, $MHCO_3^{2+}$ and MF^{2+} are nearly identical to the concentrations of free lanthanide ions in seawater.

In contrast to the small variations in extent of lanthanide complexation for weakly complexing ions (SO_4^{2-}, Cl^-, F^- and HCO_3^-), the extent of complexation of lanthanides

by carbonate ions changes by more than an order of magnitude between La and Lu. Figures 3a and 3b show the extent of complexation of the lanthanides as MCO_3^+, $M(CO_3)_2^-$ and MOH^{2+} species at high and low pH in seawater. Figure 3a shows that at the lowest pH encountered in seawater (pH = 7.4) lanthanide complexation is dominated by the carbonate species MCO_3^+. The concentrations of lanthanide hydroxide species are approximately two orders of magnitude smaller than the concentration of MCO_3^+ for all lanthanides. Figure 3b shows that at the highest pH(25°C) encountered in seawater (pH = 8.3) lanthanide complexation is dominated by the carbonate species $M(CO_3)_2^-$. The concentrations of lanthanide hydroxide species are generally two or more orders of magnitude smaller than the concentration of $M(CO_3)_2^-$. Figure 4 (overleaf) shows the speciation of La and Lu in seawater (25°C, $S = 35$) as a function of pH. Comparison of figs. 4a and 4b demonstrates that the role of phosphate in lanthanide complexation increases strongly between La and Lu.

4.4. *Lanthanide complexation by organic ligands*

The solution complexation of many metals in seawater is profoundly influenced by organic ligands (Bruland 1989, Donat and van den Berg 1992, Donat et al. 1994, Donat and Bruland 1995, Rue and Bruland 1995, van den Berg 1984). It has not, however, been shown that organic ligands in seawater appreciably influence the solution complexation of lanthanides. Instead, organic ligands are expected to strongly influence the marine behavior of the lanthanides through the role of organics in lanthanide surface complexation.

It has been proposed (Schindler 1975, Balistrieri et al. 1981, Whitfield and Turner 1987), that metal ion sorption on particles settling through the oceanic water column constitutes a dominant mechanism for removal of metals from seawater. The variety of particles present in seawater potentially provides for very diverse and complex metal interactions with particle surfaces in the ocean. However, adsorbed organics appear to be capable of dramatically transforming the surface characteristics of particles in natural waters (Davis 1984, Hunter and Liss 1979). Adsorbed organic matter may contribute a chemical character to particle surfaces which is largely based on the functional group chemistries of organic ligands. Byrne and Kim (1990) observed that the affinity of lanthanides for surfaces can be strongly affected by thin organic coatings. Glass surfaces rapidly acquire an organic coating subsequent to immersion in seawater, and then exhibit (Byrne and Kim 1990) an adsorptive behavior typical of organic-rich surfaces (enhanced light lanthanide adsorption) (Bingler et al. 1989, Stanley and Byrne 1990) rather than glass surfaces (enhanced heavy lanthanide adsorption). The marine environment is organic-rich, and with a mean residence time for ocean particles on the order of two to ten years (Balistrieri et al. 1981, Whitfield and Turner 1987), organic surfaces should play a prominent role in lanthanide ocean chemistry.

The functional-group chemistries involved in lanthanide complexation by organic ligands on particle surfaces is not presently known. However, some insight into the general character of lanthanide complexation by organic ligands can be gained by examining

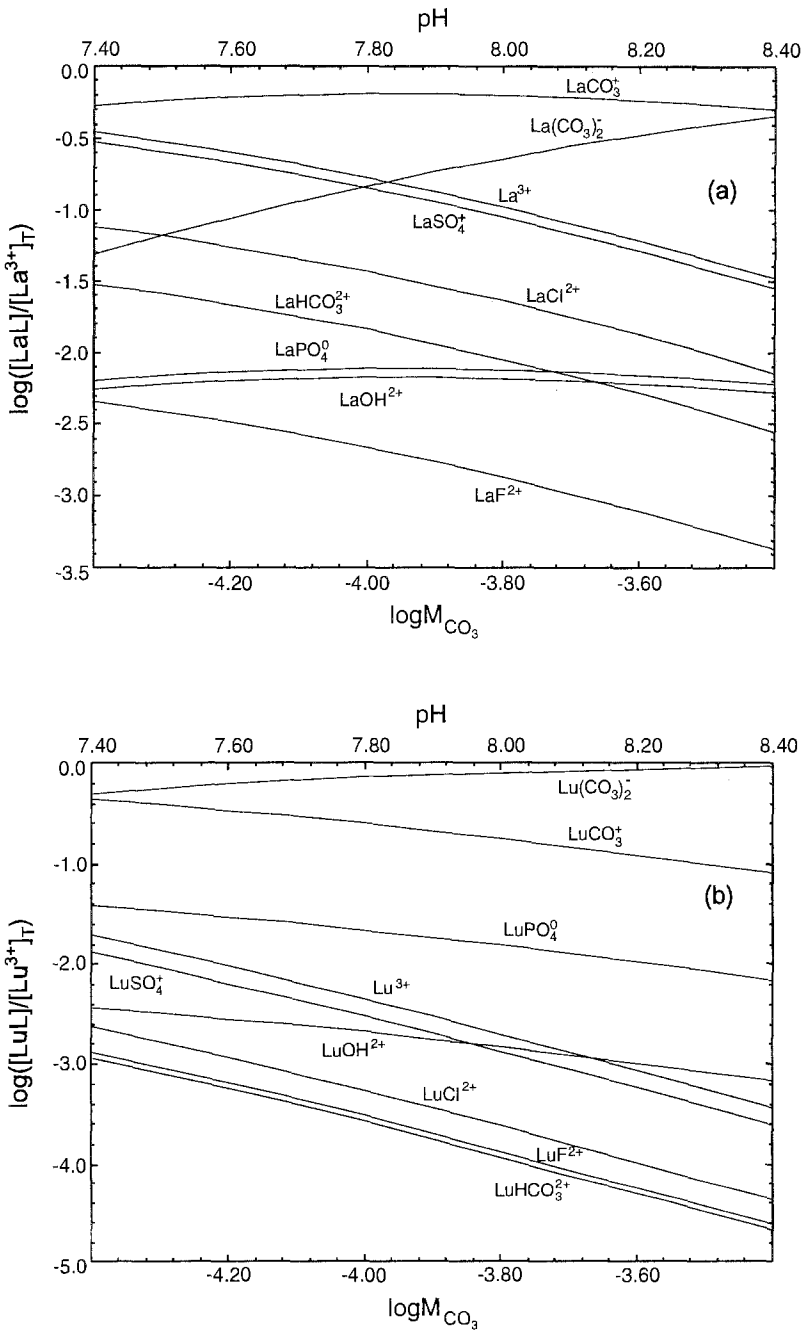

Fig. 4. Species distributions (25°C, $S=35$) are shown for La (fig. 4a) and Lu (fig. 4b) as a function of pH and carbonate ion concentration. This figure was constructed assuming a total bicarbonate ion concentration equal to 2×10^{-3} mol kg^{-1}.

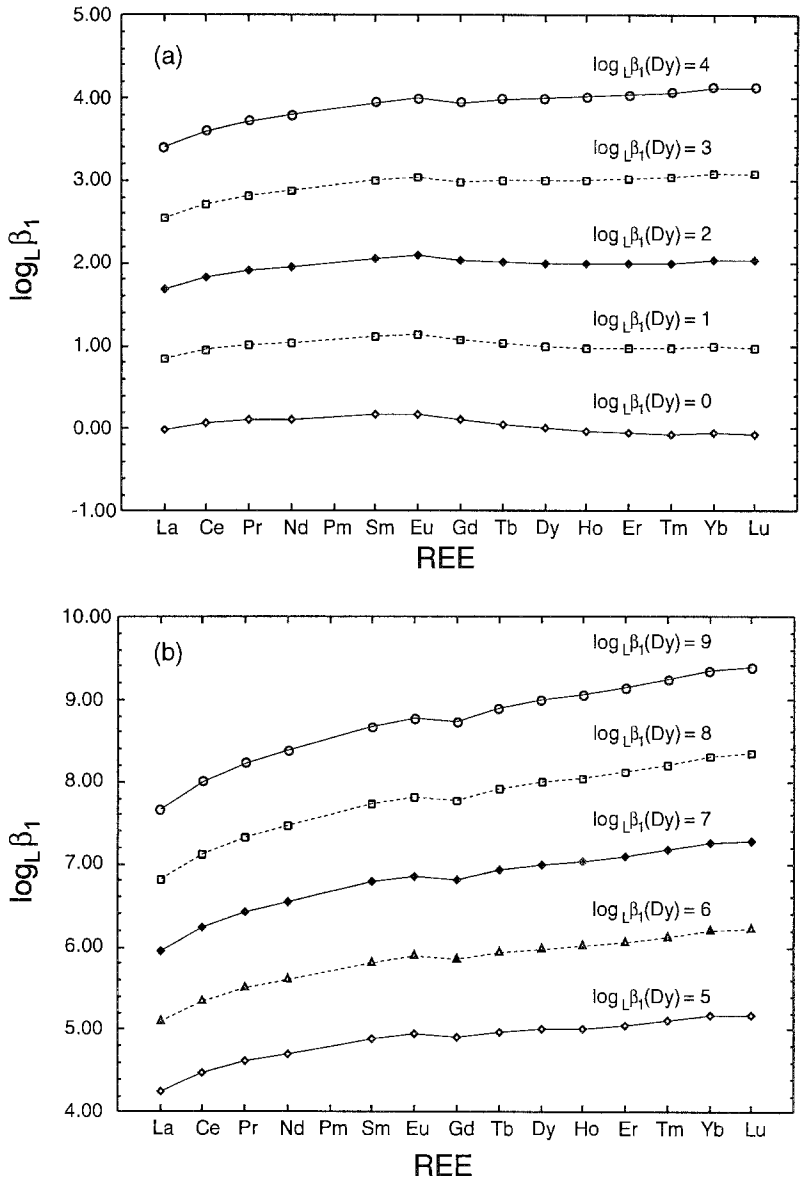

Fig. 5. Predicted lanthanide formation constants obtained in the linear free-energy relationship (LFER) analysis of Byrne and Li (1995) are shown as a function of atomic number and the magnitude of $\log_L\beta_1(\mathrm{Dy})$ for a given ligand (L).

organic-ligand stability constant compilations. In fig. 5, we have summarized the average character of lanthanide complexation by organic ligands through the use of linear free-energy relationships (Byrne and Li 1995). The relationships shown in fig. 5 are based on

the behavior of 101 organic ligands (Martell and Smith 1974, 1977, 1982, Smith and Martell 1975, 1989). Strong differences in lanthanide stability constant behaviors are observed with increasing lanthanide–ligand affinities. In fig. 5, the general magnitudes of metal–ligand affinities are expressed in terms of the stability constants of Dy (Byrne and Li 1995). For very weak ligands (e.g., $\log {}_{L}\beta_1(Dy) \approx 0$), lanthanide complexation constants change only weakly between La and Lu, and in fact decrease between Tb and Lu. For lanthanide stability constants on the order of 10^4 (i.e., $\log {}_{L}\beta_1(Dy) = 4$), stability constants increase between La and Gd and are essentially invariant between Tb and Lu. For larger stability constants (i.e., $\log {}_{L}\beta_1(Dy) > 6$), lanthanide stability constants strongly increase across the lanthanide series in two steps, La to Gd, and Gd to Lu. Gadolinium, at the junction of those two steps, appears to have an anomalously low stability constant relative to its neighbors, Eu and Tb.

Although fig. 5 reasonably well captures the average complexation behavior of the lanthanides with organic ligands, it should be noted that extreme exceptions to the average behaviors depicted in fig. 5 are not uncommon. As an example, whereas the stability constants for DTPA, with $\log {}_{L}\beta_1(Dy) \approx 22$, are expected (through LFER predictions) to increase by nearly an order of magnitude between Dy and Lu, a decrease of $\log {}_{DTPA}\beta_1(M)$ between Dy and Lu by 0.5 units is actually observed (Byrne and Li 1995, Martell and Smith 1977). Deviations between predictions and observations are less marked in the case of simple organic and inorganic ligands. Comparison of fig. 5 with formation constant trends for Cl^-, SO_4^{2-}, F^- and CO_3^{2-} indicates a general accord between LFER predictions and experimental observations when molecular mechanics is not important in metal–ligand affinities.

4.5. *Lanthanide solubility in seawater*

The solubility of lanthanide hydroxides decreases by nearly five orders of magnitude between La and Lu. Solubility products, expressed as $K^0_{SP}(M) = [M^{3+}][H^+]^{-3}$ at zero ionic strength and 25°C vary between $\log K^0_{SP}(La) = 20.3$ and $\log K^0_{SP}(Lu) = 14.5$ (Baes and Mesmer 1976). Since the pH of seawater normally ranges between approximately 7.4 and 8.3, these solubility products are far too large for lanthanide hydroxides to exert solubility controls on lanthanides in seawater.

Another plausible control on lanthanide solubility in seawater includes the formation of lanthanide carbonates (Choppin 1986, 1989). Previous determinations of lanthanide carbonate solubility products include the works of Jordanov and Havezov (1966) and Firsching and Mohammadzadel (1986). In the former study lanthanide solubility products expressed as $K^0_{SP}(M) = [M^{3+}]^2[CO_3^{2-}]^3$ at 25°C and zero ionic strength, were found to increase from $\log K^0_{SP}(La) = -33.4$ to $\log K^0_{SP}(Yb) = -31.1$. In the latter study, calculated solubility products at 25°C and zero ionic strength ranged between $\log K^0_{SP}(La) = -30$ and $\log K^0_{SP}(Gd) = -35.5$. Choppin (1986) indicated that these solubility products would decrease by roughly one order of magnitude subsequent to consideration of the influence of solution complexation in the calculations of Firsching and Mohammadzadel. Choppin (1986) calculated a $\log K^0_{SP}(Nd)$ result appropriate to the Firsching and Mohammadzadel

(1986) work as $\log K^0_{SP}(Nd) = -35.3$. This result is in good accord with solubility products obtained for neighboring elements in other studies. Ferri and Salvatore (1983) and Ferri et al. (1983) reported $\log K^0_{SP}(La) = -35.3$ and $\log K^0_{SP}(Ce) = -35.5$. Thus, the preponderance of evidence suggests that $M_2(CO_3)_{3(s)}$ solubility products are such that $\log K^0_{SP}(M) \geqslant -35.5$. Solubility products of this magnitude would support free lanthanide ion concentrations in seawater which are three or more orders of magnitude larger than those observed. Consequently, precipitation of carbonates is not expected in seawater.

Lanthanide phosphate solubility products are very low (Tananaev and Vasil'eva 1963, Tananaev and Petushkova 1967) and phosphate precipitation has been suggested (Jonasson et al. 1985, Byrne and Kim 1993) to exert significant controls on lanthanide concentrations in seawater and other natural waters. Lanthanide phosphate solubility products of fresh precipitates at 25°C and zero ionic strength were reported to range between $\log K^0_{SP}(Ce) = -24.3$ and $\log K^0_{SP}(Yb) = -23.3$ (Byrne and Kim 1993). The solubility products of coarse crystalline precipitates are substantially lower. The work of Jonasson et al. (1985) suggests that lanthanide phosphate solubility products decrease between La and Nd and subsequently increase between Nd and Er. The lanthanide solubility products obtained by Firsching and Brune (1991) plotted against lanthanide atomic number are generally on the order of $\log K^0_{SP} = -25.5$ but exhibit a maximum at Tb and Dy ($\log K^0_{SP}(Tb, Dy) = -24.4$). The analysis by Byrne and Kim (1993) indicated that the activity products of lanthanide ions and phosphate ions in seawater at depths below about 300 m are approximately constant and are equal to or greater than previously reported solubility products. In the work of Byrne and Kim (1993), it was noted that lanthanide phosphate precipitation should not involve the formation of pure phases. Due to similar ionic radii and similar solubility products for adjacent lanthanides, lanthanide phosphates should occur as co-precipitates which incorporate all lanthanides. The co-precipitation experiments of Byrne and Kim (1993) indicated that lanthanide phosphate co-precipitation occurs in a manner which enriches solutions with heavy lanthanides relative to light lanthanides. Thus, lanthanide co-precipitation processes are consistent with observed shale-normalized enrichments of the heavy lanthanides in seawater (fig. 1b).

4.6. *Lanthanide distribution models*

Lanthanide distribution models (Elderfield 1988, Byrne and Kim 1993, Erel and Morgan 1991, Erel and Stolper 1993) provide a basis for the comparative shale-normalized lanthanide concentrations (lanthanide fractionations) which are observed in the oceans. Lanthanide fractionation models are formulated in terms of competitive complexation equilibria involving, on one hand, solution complexation, and on the other, surface complexation on marine particles. Following the developments of Elderfield (1988) and Byrne and Kim (1993), shale-normalized lanthanide concentrations $(M_T)_{SN}$ in seawater can be expressed as

$$\log (M_T)_{SN} = \log \sum_{nj} \left(1 + {}_{L_j}\beta_n(M) \left[L_j\right]^n\right) - \log \bar{K}(M) + \text{constant}, \tag{2}$$

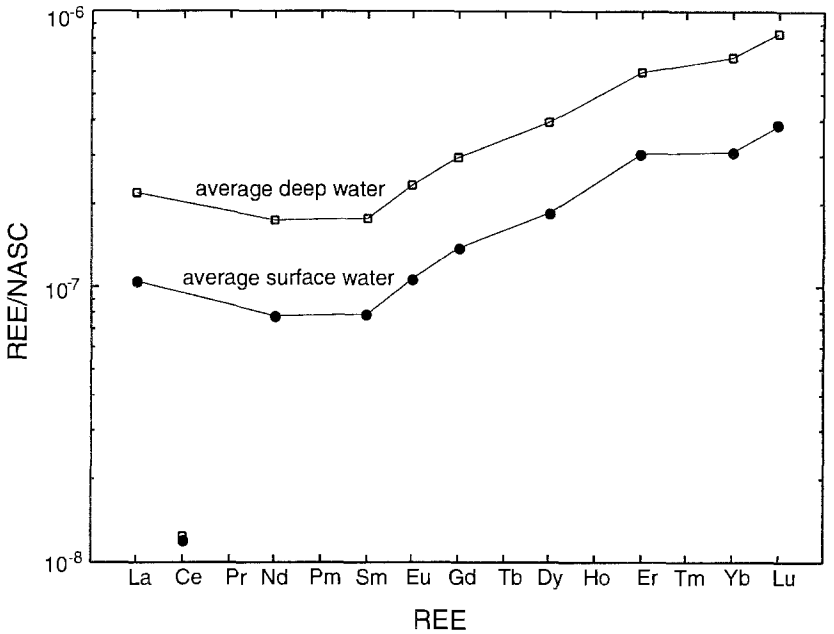

Fig. 6a. Lanthanide concentrations in seawater normalized to North American Shale Composite (Piepgras and Jacobsen 1992) are shown for average deep water and average surface water.

where the summation term depicts lanthanide solution complexation in seawater and $\overline{K}$(M) is a surface complexation constant for metal M. Many of the solution complexation terms ${}_{Lj}\beta_n$(M) in eq. (2) have been experimentally determined, while the $\log \overline{K}$(M) term is a subject of conjecture. Two approaches to estimation of $\log \overline{K}$(M) values have been used. The $\log \overline{K}$(M) values in eq. (2) have been assumed to exhibit (a) an atomic-number variation appropriate to oxide surfaces and metal ion hydrolysis constant behavior (Elderfield 1988, Erel and Stolper 1993) or (b) an atomic-number variation appropriate to the behavior of organic ligands (Elderfield 1988, Byrne and Kim 1990). Predicted variations in $(M_T)_{SN}$, using surface complexation behavior predicted from either hydrolysis constants or organic ligand complexation constants, are quite similar. The calculations by Elderfield (1988) and Byrne and Kim (1990) produce the heavy-lanthanide enrichments which are a ubiquitous feature of lanthanides in seawater, and provide evidence for small La enrichments in seawater relative to the neighboring trivalent lanthanides, Pr and Nd. Essentially all previous assessments of lanthanide distributions using eq. (2) or equivalent formulations (Elderfield 1988, Byrne and Kim 1990, Piepgras and Jacobsen 1992, Erel and Stolper 1993) have been based on the carbonate stability constants of Cantrell and Byrne (1987a). It is important to note that previous predictions of lanthanum enrichments, relative to Pr, Nd, Sm, etc., are then based on estimated rather than directly measured $\log {}_{CO_3}\beta_n$(La) values. The work of Lee and Byrne (1993a) provided refined estimates of $\log {}_{CO_3}\beta_n$(La) based on linear free-energy relationships. However,

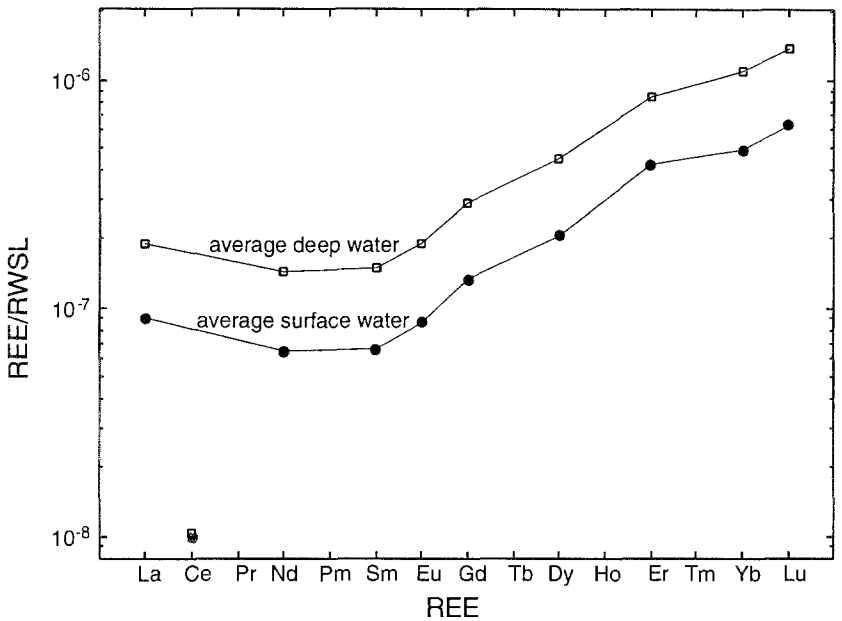

Fig. 6b. Lanthanide concentrations in seawater normalized to river water suspended load (Piepgras and Jacobsen 1992) are shown for average deep water and average surface water.

in the absence of direct comparative ${}_{CO_3}\beta_n(M)$ measurements for La and its neighbors, considerable uncertainties remain in $\log(M_T)_{SN}$ predictions derived using eq. (2).

Figures 6a and b provide the results of direct $\log(M_T)$ observations for average deep water and average surface water (a) normalized to North American Shale Composite ($\log(M_T)_{SN}$) and (b) normalized to river water suspended load (Piepgras and Jacobsen 1992). Figure 6c shows the $\log \sum_{nj}(1 + {}_{L_j}\beta_n(M)[L_j]^n)$ term in eq. (2) calculated at pH 8.3, 7.9 and 7.4. The calculated differences (eq. 2) between fig. 6a and 6b normalized $\log(M_T)$ values and fig. 6c $\log \sum_{nj}(1 + {}_{L_j}\beta_n(M)[L_j]^n)$ values provide the comparative magnitudes of the $\log \overline{K}(M)$ terms shown in eq. (2). The $\log \overline{K}(M)$ curves shown in figs. 7a and b were obtained assuming a pH equal to 7.9 and a total bicarbonate concentration equal to 2×10^{-3} mol kg^{-1}. Additional calculations indicate that the principal features of fig. 7 are insensitive to pH within the normal pH range of seawater. The shapes of the formation constant depictions in figs. 7a and b deviate significantly from the average behaviors of organic ligands depicted in figs. 5a and b (note that the absolute magnitudes of the vertical scale in figs. 7a,b are not significant due to the undetermined constant in eq. 2). Nevertheless, the $\log \overline{K}(M)$ trends shown in fig. 7 are within the range of behaviors observed for organic ligands (Byrne and Li 1995). The trends shown in fig. 7 would be typical of monocarboxylate ligands were it not for the very low $\log \overline{K}(La)$ values compared to those of Nd. Direct determinations of all lanthanide carbonate complexation constants (including those of La) may indicate that the $\log {}_{CO_3}\beta_n(La)$ estimates of Lee and Byrne (1993a) are too small. Larger $\log {}_{CO_3}\beta_n(La)$ estimates relative

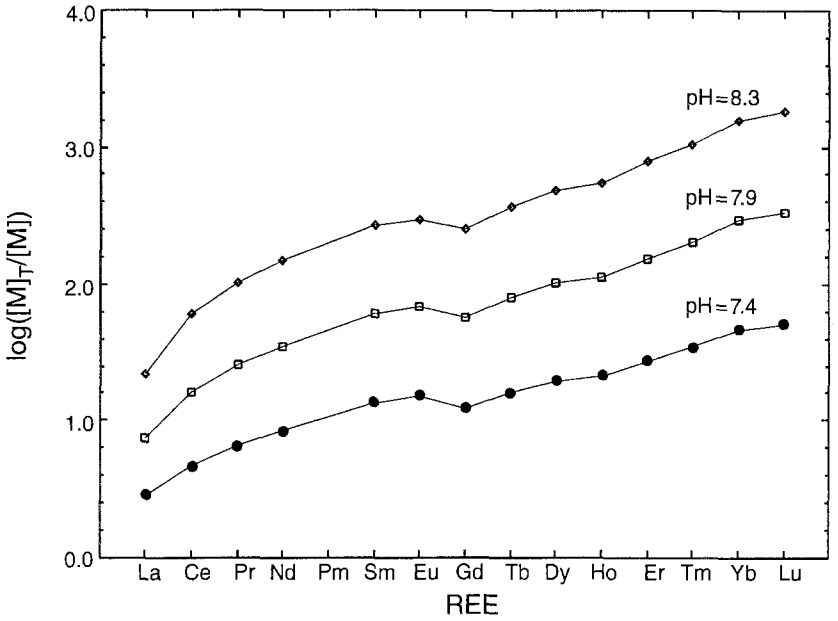

Fig. 6c. The lanthanide solution complexation term, $\log \sum_{nj} \left(1 + {}_{L_j}\beta_n(\mathrm{M})\,[L_j]^n\right)$, is shown for seawater ($S = 35$, 25°C) and three values of pH. The bicarbonate ion concentration in this figure is equal to 2×10^{-3} mol kg^{-1}.

to Ce, Pr and Nd would make the trends shown in fig. 7 more closely resemble a typical monocarboxylic acid. Alternatively the trends shown in fig. 7 may well-represent a surface complexation behavior which deviates from the average patterns shown in fig. 5. In addition to emphasizing the importance of direct $\log {}_{CO_3}\beta_n(\mathrm{M})$ evaluations for all lanthanides, future efforts to model lanthanide distributions in the oceans must extend lanthanide surface complexation observations (Byrne and Kim 1990, Koeppenkastrop et al. 1991, Koeppenkastrop and DeCarlo 1993) to include a wide variety of fresh, natural surfaces.

Principal reported features of shale-normalized lanthanide distributions in seawater include (a) La enrichments relative to heavier neighboring elements, (b) pronounced Ce depletions relative to neighboring elements, (c) Gd enrichments relative to its immediate neighbors, and (d) heavy-lanthanide enrichments relative to the light lanthanides. Whereas simple thermodynamic models are capable of explaining all of these features semiquantitatively, it has proven difficult to construct models which closely reproduce all observed distributional features. Lanthanide fractionation models which reasonably depict heavy-lanthanide enrichment in seawater underestimate the fractionation of La relative to its heavier neighbors. Two possible model refinements can be suggested which might improve the coherence of predictions and observations. Fractionation models should be constructed which examine lanthanide distributions in terms of multi-step fractionation, beginning in rivers (Elderfield 1988, Sholkovitz 1995) and continuing in seawater. As

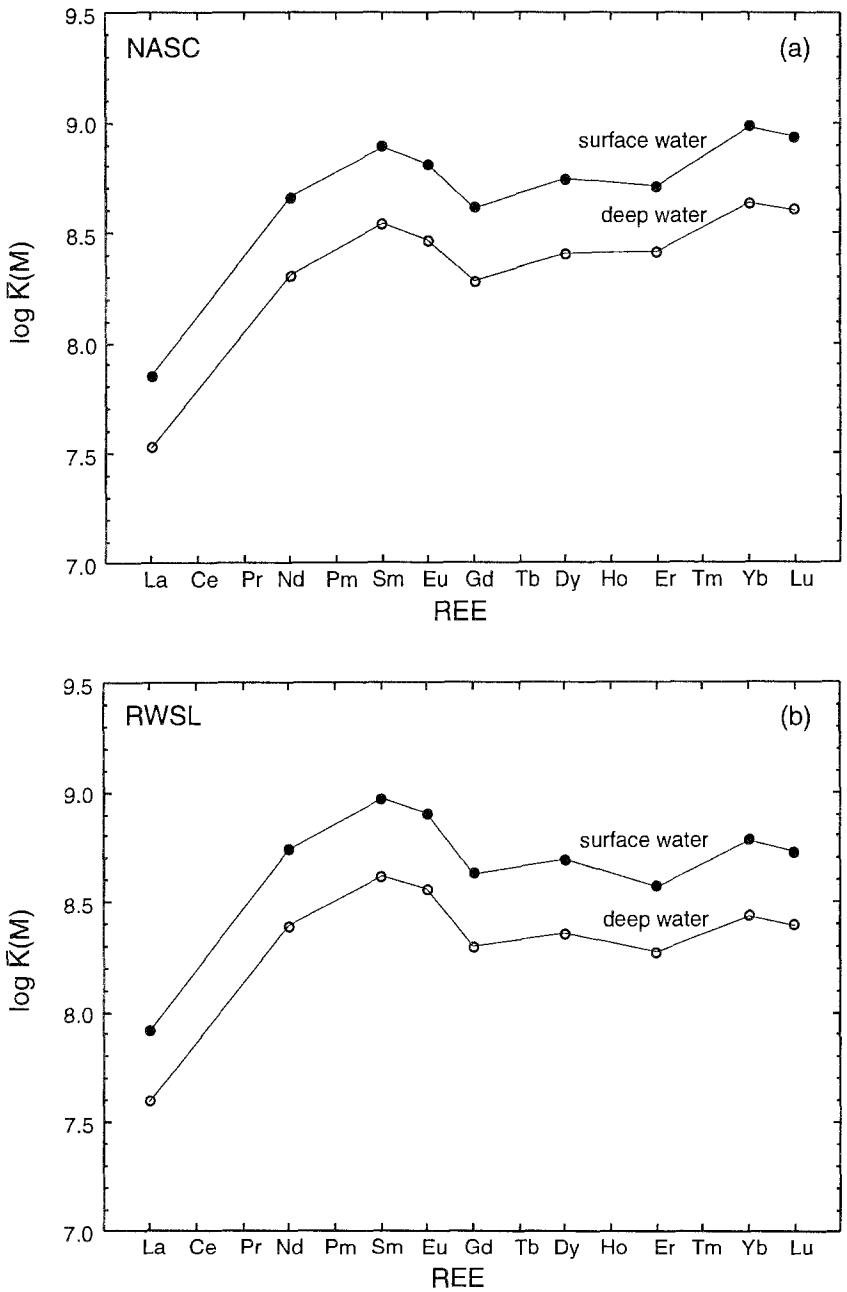

Fig. 7. Predicted $\log \overline{K}(M)$ values (eq. 2) consistent with figs. 6a–c are shown for pH = 7.9. Figure 7a shows data using the NASC normalization and fig. 7b shows the results obtained for a river water suspended load normalization.

a further means of accounting for observed lanthanide fractionation, it should be noted that lanthanide phosphate precipitation (co-precipitation) may support La enrichments in solution, relative to its neighbors. The lanthanide phosphate solubility data of Jonasson et al. (1985) indicated that the solubility product of lanthanum phosphate is larger than that of neodymium phosphate by more than an order of magnitude. This observation is consistent with the recent work of Liu and Byrne (1996) wherein lanthanide phosphate solubility products decrease between La and Nd, and thereafter increase with increasing atomic number.

Equilibrium predictions of Ce concentrations in seawater combine Ce(III) speciation calculations with the following redox equation (Elderfield 1988, De Baar et al. 1991):

$$Ce^{3+} + 2H_20 \leftrightharpoons CeO_2 + 4H^+ + e^-, \tag{3}$$

where CeO_2 is considered to be very insoluble. Calculations involving eqs. (1) and (3) indicate that the total equilibrium concentration of Ce in seawater should be on the order of 10^{-15} mol kg^{-1}. Since observed concentrations are three to four orders of magnitude larger than equilibrium predictions, kinetic factors must control Ce seawater concentrations (Elderfield 1988). The work of Moffett (1990, 1994a,b) indicates that Ce(III) oxidation kinetics is the rate-determining step in removal of Ce from seawater, and that Ce(III) oxidation is biologically mediated.

Gadolinium enrichments in seawater relative to its immediate neighbors have appeared as a common feature of shale-normalized lanthanide distributions in seawater (De Baar et al. 1985a,b, 1991). However, this "anomalous" behavior of Gd relative to its neighbors is less conspicuous in recent high-quality data (Piepgras and Jacobsen 1992, Bertram and Elderfield 1993, German et al. 1995) obtained by thermal ionization mass spectrometry. The investigation by Kim et al. (1991) examined the distribution of Eu, Gd, and Tb between seawater and the macroalgae *Ulva lactuca* L. Positive Gd fractionations were observed for low seawater carbonate concentrations and negative fractionations were found for high carbonate concentrations. These observations were shown to be consistent with predictions based on eqs. (1) and (2) and $\overline{K}$(M) values appropriate to monocarboxylic acids (Martell and Smith 1977). Gadolinium complexation constants which are smaller than values based on interpolations between Eu and Tb are a common feature of compiled lanthanide stability constant data. It is also observed that the magnitudes of deviations between interpolated and directly measured constants are largest for strongly complexing ligands. Consequently, it is predicted (Kim et al. 1991) that positive Gd fractionations are promoted by surface ligands which have large effective complexation constants [large $\overline{K}$(M)].

Gadolinium anomalies have occasionally been conceptualized as a particular example of the "tetrad" effect (Masuda and Ikeuchi 1979, Masuda et al. 1987), wherein patterns in lanthanide stability constants are developed in response to enhanced stability of lanthanide 4f shells which are quarter, half and three quarter filled. In the recent analysis by McLennan (1994), the existence of a "tetrad" effect in natural systems was termed ambiguous. The stability constant analysis of Byrne and Li (1995) provided no prominent

evidence for a "tetrad" effect in the aqueous complexation behavior of organic ligands. Examination of fig. 5b provides muted evidence for stability constant patterns involving four-element lanthanide subseries (e.g. for $\log {}_L\beta_1(\mathrm{Dy}) = 9$, La, Ce, Pr, Nd; (Pm), Sm, Eu, Gd; Gd, Tb, Dy, Ho; Er, Tm, Yb, Lu. However, quantification of such suggested patterns is presently uncertain.

Heavy-lanthanide enrichments in seawater are reasonably explained by eqs. (1) and (2) wherein the extent of lanthanide solution complexation increases between La and Lu to a much greater degree than is the case for surface complexation. It is probable that competitive solution/surface complexation exerts the dominant role in heavy-lanthanide enrichments in seawater. However, it should be noted, as well, that lanthanide phosphate co-precipitation also appears to promote heavy-lanthanide enrichments in solution. Although the existence of lanthanide phosphate precipitation in seawater has not been directly demonstrated, such controls are consistent with observed total lanthanide concentrations in some environments (Byrne and Kim 1993, Johannesson et al. 1995) and are consistent, as well, with the general features of lanthanide fractionation in the oceans.

5. Inputs of lanthanides to seawater: rivers and estuaries

5.1. *Lanthanide composition and aquatic chemistry of river water*

Transport by rivers is the major source of dissolved and particulate lanthanides to the oceans. In addition, reactions between river water and seawater in estuaries modify the flux and composition of lanthanides reaching the oceans. Hence, a discussion of the marine geochemistry of lanthanides requires an overview of the composition and aquatic chemistry of rivers and estuaries. This section will focus on dissolved lanthanide concentration in rivers. The first lanthanide data on the dissolved and particulate composition of river water (Gironde, France) appeared in the article by Martin et al. (1976). After a gap of one decade and the application of ID-TIMS analyses to water, a series of papers reported high quality data on the dissolved and particulate composition of lanthanides in river water. Major contributions in this field of study include Goldstein and Jacobsen (1987, 1988a,b), Elderfield et al. (1990) and Sholkovitz (1992b, 1995). The latter paper, *The aquatic chemistry of rare-earth elements in rivers and estuaries,* incorporates new data into a synthesis of the current state of knowledge.

Tabular compilations of dissolved and particulate data for rivers appear in tables A1 and A2 respectively. The focus of this section will be on papers cited above. Other papers with dissolved data include Keasler and Loveland (1982), Hoyle et al. (1984), Sholkovitz and Elderfield (1988), Sholkovitz et al. (1992) and Stordal and Wasserburg (1986). [The poor quality of data in Keasler and Loveland (1982) has been previously noted (Elderfield et al. 1990)]. Papers containing data on the composition of suspended matter include Martin et al. (1976), Martin and Meybeck (1979), Thomas and Martin

(1982), Hoyle et al. (1984), Gordeev et al. (1985), Goldstein and Jacobsen (1988a,b), Somayajulu et al. (1993) and Sholkovitz (1995).

A major conclusion from the literature on rivers is that chemical weathering reactions on the continents leads to extensive fractionation between the dissolved lanthanide composition of river waters and the lanthanide composition of suspended riverine particles and continental rocks. Solution and surface chemistry play a major role in establishing the lanthanide composition of freshwater. Both the concentration and the extent of fractionation of dissolved lanthanides in river waters are dependent on pH and on the presence of colloidal particles. High-pH waters have the lowest dissolved lanthanide concentrations, the most fractionated composition and the most well-developed Ce anomalies. A large proportion of the dissolved lanthanide inventory in river waters exists as fine colloidal particles which undergo large scale coagulation in estuaries. Hence, fractionation of trivalent lanthanides and redox forms [Ce(III), Ce(IV)] must be interpreted in view of low-temperature weathering of rocks, soils and minerals, and riverine processes.

Rivers drain different geological and urban terrain and exhibit large ranges in discharge, concentrations of suspended and colloidal particles and chemical composition. Given the diversity and individuality in rivers, readers must be wary of generalizations based on the chemical features of any one river. Moreover, with respect to their lanthanide composition, the global coverage of rivers is poor. Rivers show large temporal variations in the chemical composition of their dissolved matter. As time-series data for rivers are lacking, it is currently impossible to quantify temporal variability in the lanthanide composition of river water. Having provided these geochemical caveats, we will focus on the larger rivers of the world and draw some general conclusions which are well established in the literature.

Fractionation of the lanthanides is often quantified by shale-normalized patterns. Normalization to shale represents an abundance *relative* to that of the upper crust of the continents. A flat shale pattern for river suspended particles would indicate a composition similar to that of averaged continental crust. To study fractionation in rivers, it is also instructive to normalize the dissolved composition to that of suspended particles on the assumption that the particles better represent the solids being weathered in the watershed.

(1) *River waters have dissolved lanthanide compositions which are strongly fractionated with respect to continental crust.* This feature is illustrated in fig. 8 which shows the shale patterns of Amazon, Mississippi, Fly (Papua New Guinea) Rivers and the "averaged world river water composition" estimated by Goldstein and Jacobsen (1988a). Dissolved compositions here refer to 0.22 μm filtrates. All rivers have dissolved compositions significantly different from that of the upper continental crust. The Mississippi River is similar in relative abundance to that of the averaged world rivers and has a shale ratio which increases progressively across the series. In marked contrast, the Amazon and Fly Rivers are characterized by large enrichments centered in the middle of the lanthanides. Rivers draining volcanic rock have light-enriched patterns (Goldstein and Jacobsen 1988a; data not plotted). Shale patterns of suspended particles from the same suite of rivers are

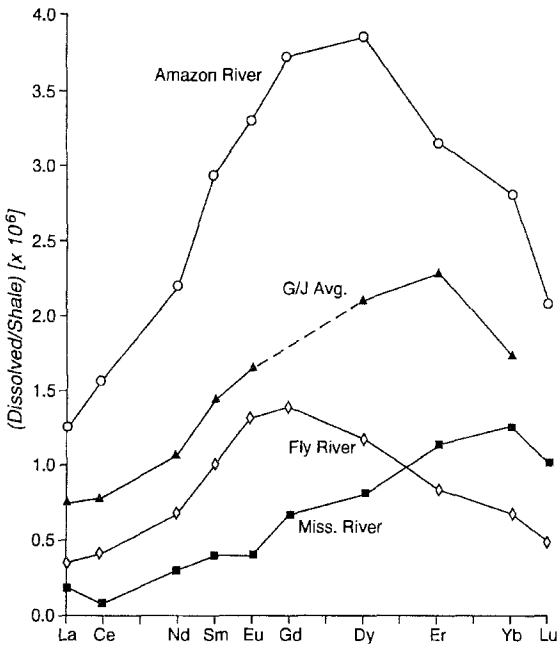

Fig. 8. Shale-normalized lanthanide compositions of 0.22 μm filtrates of the Amazon, Fly (Papua New Guinea) and Mississippi River waters. Amazon and Mississippi data from Sholkovitz (1993, 1995); Fly River data from unpublished work of Sholkovitz. "G/J Avg." refers to the averaged river water composition of Goldstein and Jacobsen (1988a).

presented in fig. 9. A general observation is that river particles are characterized by a slight depletion in the heavy lanthanides. The compositions of river suspended particles are more similar to one another and the upper crust than they are to their dissolved counterparts. Hence, a major conclusion is that dissolved lanthanides of rivers are strongly fractionated with respect to their source particles and rocks. The degree of this fractionation differs greatly between the major rivers of the world (i.e., Amazon vs. Mississippi).

(2) *The concentrations and fractionations of lanthanides dissolved in river waters are highly pH-dependent.* This conclusion is based on both field and experimental data, and figures illustrating this point can be found in Goldstein and Jacobsen (1988b), Elderfield et al. (1990) and Sholkovitz (1995). Higher pH results in lower concentrations. As an example, Elderfield et al. (1990) reported that the concentration of dissolved Nd ranges from 100 to 3000 pmol/kg over a pH range of 9.5 to 5.5. Higher pH also results in more fractionated compositions, specifically the enrichment in the heavy lanthanides as defined by shale-normalized patterns. Elderfield et al. (1990) reported that the dissolved Er/Nd (mole) ratio increases by a factor of 10 (0.03 to 0.3) as the pH increases from 6.0 to 8.0. With increasing pH the order of lanthanide adsorption onto river particle surfaces is light > middle > heavy. With decreasing pH, lanthanides are released from surfaces in the same order, light > middle > heavy (Sholkovitz 1995). Hence, the composition of lanthanides in the dissolved form of river waters is mainly controlled by surface reactions

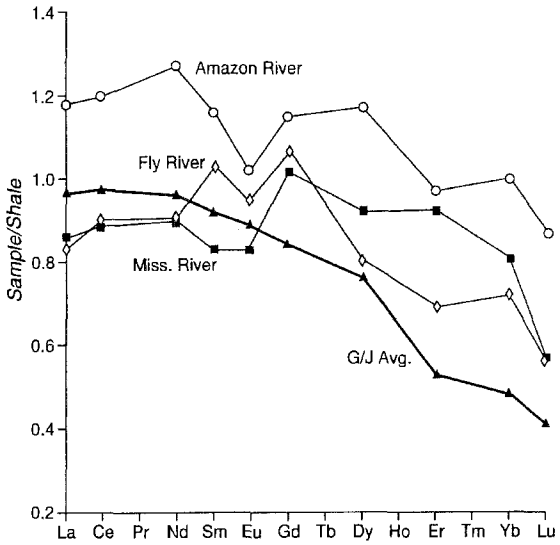

Fig. 9. Shale-normalized lanthanide compositions of river suspended particles (>0.22 μm) of the Amazon, Fly (Papua New Guinea) and Mississippi River waters. See fig. 8 for more details.

where pH is a master variable in establishing the absolute and relative lanthanide abundance. The order of fractionation associated with adsorption and release at different pHs is consistent with chemical models of lanthanide partitioning between solutions and surfaces (sect. 4).

(3) *Within the dissolved matter of river waters, Fe–organic colloids are major carriers of lanthanides, and colloidal lanthanides are strongly fractionated with respect to the dissolved and solution phases in river water* (Goldstein and Jacobsen 1987, Elderfield et al. 1990, Sholkovitz 1992b, 1995). This observation explains the highly correlated relationship between the dissolved concentrations of lanthanides and Fe in river waters. Filtration with progressively finer pore sizes results in filtrates with lanthanides which are lower in absolute concentrations and more fractionated. As an example, the Nd concentrations in filtered Connecticut River water decrease from 576 to 179 to 87 pmol/kg for <0.22 μm pore-size membranes and 50K and 5K molecular weight ultrafilters (Sholkovitz 1995). Studies employing ultrafiltration of river water allow direct comparisons of colloid composition and dissolved lanthanide composition (Sholkovitz 1995). Figure 10 compares lanthanides in colloidal particles (5K and 50K ultrafiltration) with dissolved lanthanides (<0.22 μm) in the Connecticut River (Sholkovitz 1995) and shows a 10-fold fractionation between these two phases. Note that with respect to the dissolved phase, colloidal particles are progressively enriched in the light lanthanides and ultrafiltrates are heavy-lanthanide enriched. These results show that river waters, stripped of their suspended particles and colloidal particles, have lanthanide compositions which are strongly evolved (heavy-enriched) relative to the composition of rocks in their watersheds. As argued by Goldstein and Jacobsen (1987, 1988a) and by Elderfield et al. (1990), solution chemistry, not rock

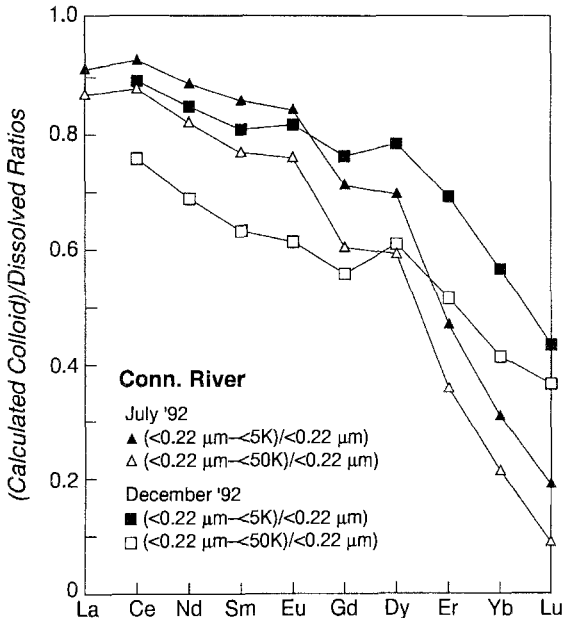

Fig. 10. The "calculated" lanthanide concentrations of river colloids normalized against the dissolved (0.22 μm filtrate) lanthanide concentrations for the Connecticut River water collected on 20 July 1992 and on 17 December 1992. From Sholkovitz (1995). "Dissolved" refers to <0.22 μm filtrate and "calculated colloid" refers to the difference between the dissolved composition and the composition of two ultrafiltrates (5K and 50K nominal wt. cut-offs).

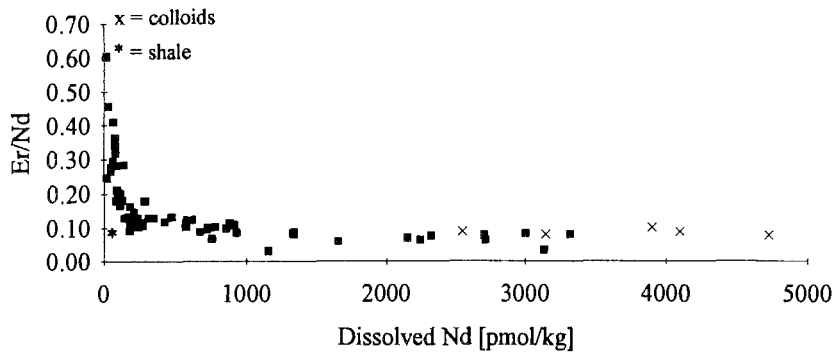

Fig. 11. River water data: a plot of dissolved Nd concentrations vs. the Er/Nd (mole) ratio. Also included are data for colloidal particles extracted from the Connecticut and Hudson Rivers. Data from a compilation in table A1. Text contains more details.

composition of the drainage basin, is the most important factor in establishing the dissolved lanthanide composition of river waters.

The importance of colloids on the lanthanide composition of rivers waters was developed in Elderfield et al. (1990) who suggested that lanthanides are contained in three pools: particles, colloids and solution. The combination of the latter two pools determined the lanthanide composition reported as dissolved concentrations (i.e., 0.22 and 0.45 μm filtrates). In fig. 11 we have up-dated their plot of Nd versus the Er/Nd (mole) ratio of river waters using data collated in table A1. This

plot contains all the available dissolved data (mostly 0.22 and 0.45 μm filtrates) plus a limited amount of data from > 5K and > 50K colloids extracted from the Connecticut and Hudson Rivers (Sholkovitz 1995). The outstanding feature of this plot is the curved relationship. That is, the Er/Nd ratios are not constant but rather decrease markedly in a curved manner as the dissolved Nd concentration increases. The largest decrease occurs from 50 to 350 pmol/kg of Nd. Above Nd concentrations of about 1000 pmol/kg, the Er/Nd ratio levels off at values between 0.06 and 0.09. The colloids have Er/Nd (0.08–0.10) ratios which lie on the flat part of the plot and which are similar to those upper crust (shale ≈ 0.08). This figure reinforces an earlier point that the dissolved matter of river water can be highly fractionated from the lanthanide composition of the crust and of the bedrock of a river's watershed. Elderfield et al. (1990) interpreted the curvature in this plot to reflect the addition of colloids to the solution pool as Nd concentration increases. That is, rivers with high dissolved Nd concentrations also have larger proportions of colloidal Nd. Data on colloids in this plot support that idea. Based on their Er/Nd ratios, the river colloids appear to be fine crustal material. As the colloidal pool becomes less abundant, the dissolved concentrations decrease and the dissolved composition becomes enriched in the heavy lanthanides (increasing the Er/Nd/ratio to values as high as 0.6). These rivers have pHs in the high end (8–9) of the observed range. In contrast, rivers with more crustal ratios have low pHs (4–6). This reinforces a previous point that the higher-pH rivers have the most fractionated lanthanide compositions.

(4) *The dissolved phase Ce anomaly of river waters is pH-dependent.* In general, higher-pH rivers have more negative Ce anomalies (along with more fractionated lanthanide compositions). The Amazon River water has a value of 0.98 (little fractionation from the crustal value of 1) while the Mississippi River water has the most negative (0.37) anomaly reported for river waters (fig. 8) (Goldstein and Jacobsen 1987, 1988a, Elderfield et al. 1990, Sholkovitz 1993). One explanation is that there is oxidation of dissolved Ce(III) to particulate Ce(IV) oxides in the Mississippi River where high (8.0) pH and an abundance of surface sites promote oxidation and adsorptive removal from the dissolved pool. The microbial oxidation of Ce(III) to Ce(IV) has been measured in seawater (Moffett 1990) and estuarine waters (Moffett 1994a,b) and inferred for the Amazon estuary (Sholkovitz 1993).

In summary, several avenues of research would make valuable additions to our knowledge of the aquatic chemistry of lanthanides in rivers. A study of the oxidation kinetics of Ce(III) in freshwater has not been reported. The control of pH, particles and bacterial reactions on the development of Ce anomalies needs study. Water/rock reactions on the continents are poorly understood. There have been no studies of lanthanides in streams of small watersheds which undergo different degrees and types of chemical weathering. Temporal compositional variations in response to daily and seasonal changes in river properties (e.g., rainfall, discharge, solute composition and pH) are unknown. Comparison of watersheds with different rock types (i.e., granite vs. basalt) would provide insights into weathering processes and the aquatic chemistry of the lanthanides. Field data

of this type could be used to guide speciation models appropriate to low ionic strength systems.

5.2. *The estuarine chemistry of the lanthanides*

Estuaries are one of the two interfaces between the continents and oceans, the ocean/air interface being the other. Estuaries can be viewed as highly complex biogeochemical reactors which modify the flux and composition of trace elements delivered by rivers to the ocean. It can be argued that the complexity of estuaries exceeds that of other aquatic systems such as lakes, ground waters, rivers and the oceans. This complexity not only extends to the types of reactions but also to the dynamics of the reactions and the accompanying hydrology. When rivers mix with sea water to form estuarine waters, there are large changes in three basic properties – pH, salinity, suspended particle concentration – which play important roles in establishing the concentration and speciation of trace elements. Important reactions operating on trace elements in estuaries include: coagulation of river-borne colloids, desorption off river particles, diagenetic release from sediments, adsorption onto particles and sediments and uptake by biota. The dynamics of these reactions become complex when interactions with large scale temporal variability in hydrographic processes are considered; these include river discharge, tidal and wind mixing and currents. Large hydrographic variability occurs on the times scales of hours to seasons. Hence, the kinetics of biogeochemical reactions are superimposed on hydrographic dynamics. Most estuarine sampling provides only snap-shots of a trace elements distribution. This certainly applies to the lanthanides.

The field of estuarine chemistry has developed within marine geochemistry. A principal focus in this field is elucidation of the processes which modify the concentration and composition of trace elements during the mixing of river water and sea water. Here the lanthanides can be well used to understand how reactions fractionate trace elements. The results of both field and laboratory studies will be discussed. The latter allow controlled experiments to simulate natural reactions.

The first report on the estuarine distribution and chemistry of lanthanides was published for the Gironde estuary by Martin et al. (1976). This work pointed to the reactive nature of these elements during estuarine mixing, specifically the removal of dissolved lanthanides from river water. Papers on the estuarine chemistry of the lanthanides are few in number and include: Martin et al. (1976), Hoyle et al. (1984), Goldstein and Jacobsen (1988c), Sholkovitz and Elderfield (1988), Elderfield et al. (1990), Sholkovitz et al. (1992) and Sholkovitz (1992b, 1993, 1995). The subject of these works, reactivity of dissolved and colloidal phases, is the focus of this section. While there are no review articles on the estuarine chemistry of lanthanides, Elderfield et al. (1990) and Sholkovitz (1995) provide the most comprehensive overviews. Papers on lanthanides in suspended particles and sediments (Gordeev et al. 1985, Sholkovitz 1990, Somayajulu et al. 1993) will not be discussed here.

Estuarine data are compiled in table A3 which includes unpublished data for the Fly River in Papua New Guinea (Sholkovitz, in preparation). As with river studies, data on

estuaries are limited in geographic and temporal coverage. Except for one time-series station in Chesapeake Bay (Sholkovitz et al. 1992), there are no lanthanide seasonal variability data for an estuary.

The main features of the estuarine chemistry of lanthanides are as follows:

(1) River water concentrations are significantly higher than those of seawater.
(2) There is large-scale coagulation of dissolved (<0.22 μm) lanthanides at low (0–5) salinity whereby a large percentage of the lanthanides is removed from the dissolved phase of river waters. Hence, lanthanides are highly non-conservative and have a similar behavior to that of iron and humic acids.
(3) Coagulation is caused by salting out of river-borne colloid-containing lanthanides. This removal process leads to lanthanide fractionation.
(4) Sediments of the seaward, high-salinity regions of estuaries are a source of dissolved lanthanides to coastal seawater. Fractionation accompanies this release of lanthanides from sediments.
(5) Cerium anomalies develop under different types of conditions. The development of sub-oxic and anoxic conditions leads to the preferential release of Ce to estuarine waters. Chesapeake Bay is a classic example of this process (Sholkovitz et al. 1992). In regions of high biological productivity, there is biologically-mediated removal of dissolved cerium through an oxidative process. This has been observed in the Amazon estuary (Sholkovitz 1993).

Dissolved lanthanide concentrations of river waters greatly exceed those of seawater. Goldstein and Jacobsen's (1988a) world average river concentration for Nd is 280 pmol/kg while the seawater concentration range is 5–15 pmol/kg. For the Amazon River, this difference is even greater, 500–600 pmol/kg compared to 15 pmol/kg for high salinity Atlantic seawater transported onto the Amazon shelf (Sholkovitz 1993).

The Amazon and Fly River (Papua New Guinea) estuaries serve as good examples of the five features outlined above. The salinity distribution of dissolved Nd (<0.22 μm) in fig. 12 is representative of the other trivalent lanthanides. This figure contains data for both surface and deep waters; the bottom part B is an expanded scale for $S > 3$ samples. The Fly and Amazon data sets have Nd–salinity distributions for surface waters which are remarkably similar and exhibit the same two major features: (1) removal of dissolved lanthanides in the low (0–5) salinity region and (2) desorption in the seaward region. Hence, it appears that the removal process and the release process (desorption) are decoupled.

The large-scale removal of dissolved lanthanides in the low salinity region is an ubiquitous feature of estuaries (Martin et al. 1976, Goldstein and Jacobsen 1988c, Sholkovitz and Elderfield 1988, Elderfield et al. 1990, Sholkovitz et al. 1992, Sholkovitz 1993, 1995). As illustrated for the Amazon and Fly (fig. 12), the Nd concentrations of surface waters decrease sharply between the river ($S \approx 0$) and a salinity of 5–7. In the case of the Amazon, Nd removal represents approximately 95% of the river-borne dissolved flux. Of all the trace element distributions reported for estuaries, the lanthanides stand out as being the most similar to dissolved Fe and humic acids, both of which undergo extensive removal in estuaries. Since there is also a strong correlation between

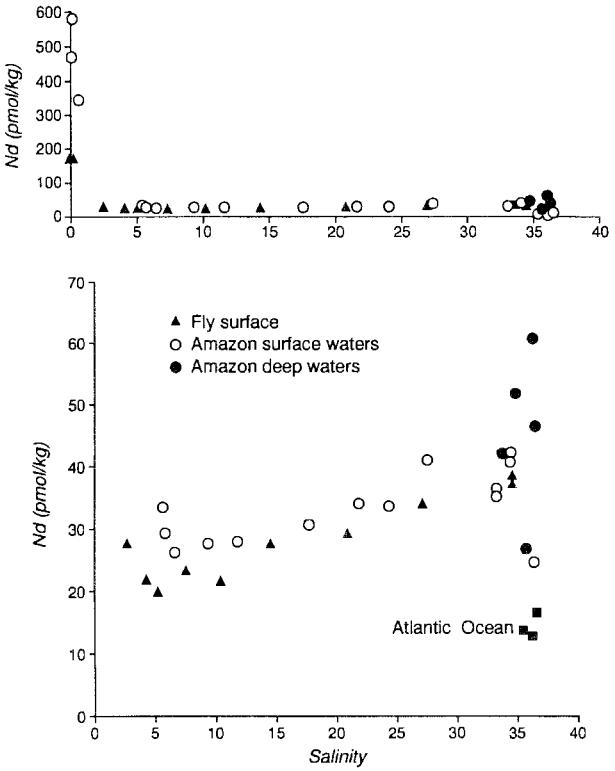

Fig. 12. Dissolved Nd concentration vs. salinity for the Amazon and Fly (Papua New Guinea) River estuaries. The bottom part is an expanded (> salinity 3) section of the top part. The bottom part also contrasts the surface and deep waters from the Amazon Estuary and shows the concentration of the open ocean Atlantic surface waters which are transported into the Amazon estuary. Amazon data from Sholkovitz (1993); Fly data from unpublished work of Sholkovitz.

the concentrations of dissolved Fe and lanthanides in rivers, the estuarine chemistry of lanthanides is seen to be tightly coupled to that of Fe and humic acids (Elderfield et al. 1990). Since Fe, humic acids and lanthanides predominately exist as colloids in river water (Sholkovitz 1976, 1992b, 1995), it is understandable that salt-induced coagulation would be responsible for their removal in the low salinity region of estuaries. The existence of this coagulation process has been confirmed in laboratory simulations of estuarine mixing (Elderfield et al. 1990, Sholkovitz 1995).

The removal of lanthanides in the low-salinity region of estuaries is accompanied by fractionation. The removal of river-borne dissolved lanthanides decreases between La and Lu. For the Amazon, the removal percentage ranges from 95 to 86%. As summarized in Sholkovitz (1995), other estuaries exhibit larger ranges in this type of fractionation. This pattern of fractionation is consistent with the observed fractionation of colloids within the dissolved phase of river water (sect. 5.1). Since river colloids are enriched in light lanthanides, coagulation results in the removal order of light > middle > heavy.

An important observation emerging from estuarine studies is that estuarine reactions not only markedly reduce riverine lanthanide fluxes but also modify the relative abundance of dissolved lanthanides reaching the oceans. The preferential removal of light elements at low salinity creates an "effective" river composition (that reaching the ocean after modification in estuaries) which is evolved toward that of seawater, which has a heavy-lanthanide enriched shale pattern. This conclusion assumes that no other processes are returning the river-borne lanthanides to the oceans.

The release of lanthanides in the outer regions of estuaries is a newly observed feature, first reported for the Amazon by Sholkovitz (1993). As shown for both the Fly and Amazon estuaries in fig. 12, surface water concentrations of Nd gradually increase by 20 pmol/kg (from 20 to 40 pmol/kg) between 5 and 35 salinity. Hence, Nd concentrations in high-salinity shelf waters are three to eight times larger than those of open ocean water adjacent to the coastal regions. Moreover, three of five near-bottom Amazon samples have higher (1.5–2 times) Nd concentrations than surface waters at comparable salinities. These observations suggest that estuarine sediments are a source of dissolved lanthanides to coastal waters and the oceans. Neither the mechanisms nor the fluxes associated with this release have been studied or quantified. However, available evidence suggests that fractionation during the release of lanthanides from estuarine sediments (Sholkovitz 1993) creates a preferential release of heavy lanthanides. The whole question of release and fractionation in estuarine regions is critical to understanding the processes controlling the oceanic composition and residence times of the lanthanides. It appears that the combination of removal in low-salinity waters and release in high-salinity waters contributes to the evolution of the heavy-lanthanide enriched composition, characteristic of seawater.

In the Amazon estuary enhanced removal of dissolved Ce (relative to trivalent La and Nd) occurs in the low-salinity zone and in the zone of high biological productivity at a salinity of 18–26 (Sholkovitz 1993). These two regions have Ce-anomaly salinity gradients which are attributable to biogeochemical reactions rather than mixing. The largest change in the Ce anomaly (0.99 to 0.30) occurs between the freshwater and a salinity of 6, the same region where all the dissolved lanthanides undergo extensive removal. Over this salinity range the calculated percent removals for dissolved La, Ce and Nd are 95%, 97% and 95% respectively. The 2% higher value for Ce translates into large differences in Ce anomalies. Sholkovitz (1993) suggested that the colloidal properties of river water are responsible for the fractionation of Ce in the low-salinity region of the Amazon. This feature does not appear in the Fly River estuary. There are insufficient data from other estuaries to generalize about these processes.

In the Amazon estuary the second large gradient in the Ce anomaly occurs between a salinity of 20 and 28 where the value drops from 0.64 to 0.42. The sharp decrease in the anomaly at a salinity of 20 is driven by a combination of a Ce decrease and a continued rise in La and Nd concentrations. The large decreases in Ce and in the Ce anomaly are coincident with a large decrease in nutrient concentrations (phosphate and nitrate) and an increase in chlorophyll-*a*. As these latter two gradients reflect enhanced biological productivity, Sholkovitz (1993) argued that there is biologically-mediated oxidation of

dissolved Ce(III) to particulate Ce(IV) occurring in this estuary. This process has been experimentally documented for the open ocean and coastal water (Moffett 1990) and estuaries (Moffett 1994a,b). While not observed from the field data of other estuaries, the development of Ce anomalies in the mid-region of the Amazon estuary may reflect its high biological productivity.

The effect of sub-oxic and anoxic conditions on lanthanide distributions in estuaries is very pronounced and will be discussed in sect. 7.

In summary, the lanthanides undergo an array of reactions in estuaries which affect both their absolute and relative lanthanide abundances. Hence, estuaries are excellent natural laboratories to test and study the influence of aquatic geochemical processes on lanthanide fractionation. To what extent does fractionation in estuaries control the composition of seawater? Is the release of dissolved lanthanides from estuarine shelf sediments a quantitatively important process with respect to the ocean budget and composition? Answers to these and other related questions will require more detailed study and modeling.

6. The oceanic chemistry of the lanthanides: distributions, biogeochemical cycles, mass fractionation, Ce redox reactions and Nd isotopes

6.1. *Introduction*

This section describes and discusses lanthanide distributions in the oceans and the biogeochemical and physical processes responsible for these distributions. Three interrelated subjects will be developed. These are (a) profiles of lanthanide concentrations in the water column and their variations within and between ocean basins, (b) the redox geochemistry of Ce as revealed by vertical and horizontal variations in the Ce anomaly and (c) the inter-oceanic mass fractionation of the strictly trivalent lanthanides.

Since the first reliable measurements of seawater by Elderfield and Greaves (1982), approximately 25 publications have been reported on the distribution of lanthanide concentrations in the oceans and inland seas. Table A4 provides a bibliography of these papers sorted by region (Atlantic, Indian, Pacific and Arctic Oceans and the Mediterranean, Black and Baltic Seas). There are also approximately ten papers which have focused on the Nd isotopic composition of seawater; they usually report the concentration of Nd and Sm. These papers also listed in table A5.

Five papers form the core of this section's discussion: Elderfield (1988), Piepgras and Jacobsen (1992), Bertram and Elderfield (1993), Sholkovitz et al. (1994) and German et al. (1995). While other papers make important contributions and will be mentioned to different extents, these five papers provide the most detailed coverage of this subject. Elderfield (1988) reviewed the field using data from papers prior to 1988. The two detailed profiles from Piepgras and Jacobsen (1992) best illustrate vertical distributions in the North Pacific Ocean. Bertram and Elderfield (1993) used all existing data including their detailed study of the Indian Ocean to provide a broad discussion of the distribution and fractionation of lanthanides in the world's oceans. The study by Sholkovitz et al. (1994)

used chemical digestion techniques to show that surface coatings on suspended particles are responsible for the removal and fractionation of lanthanides from seawater. Building on a vertical profile from the South Atlantic Ocean, German et al. (1995) discuss mass fractionation of the lanthanides between the three oceans, and the oxidative removal of dissolved Ce as deep waters evolve with transport between the three oceans.

To help readers locate sample sites discussed in the text, fig. 13 provides a world map with station locations listed in tables A4 and A5. The figure shows the locations of surface water samples and vertical profile samples for which lanthanide data are reported in the literature. The numbers next to references refer to location numbers on the map. Studies plotted include both those that measure a group of lanthanides as well as those that report only Nd isotopes and Nd and Sm concentrations. Table A5 distinguishes between those two types of studies, again by referencing to a common location number. Table A5 also lists the analytical methods used (ICP-MS versus TIMS) and the type of analysis made (lanthanide series vs. Sm–Nd only in Nd isotope papers). Tables A6, A7 and A8 contain the lanthanide data (dissolved and particulate matter) for the Atlantic, Pacific and Indian Ocean respectively. Table A9 contains Elderfield's unpublished data for the Pacific Ocean (H. Elderfield, Department of Earth Sciences, Cambridge University, England). His data are unique in providing a transect of surface samples across the Pacific Ocean. As Elderfield is presently interpreting the oceanographic significance of these data, his unpublished data will not be discussed in this article, and readers are requested to consult Elderfield prior to using these data in publications. Data for the Arctic Ocean are presented in table A10. Although studies of the Mediterranean and Baltic Seas will not be discussed in this article, data from these regions are included in table A11. Data in all tables are reported in units of pmol/kg seawater.

A comparison of profiles from one station in the western North Pacific (Piepgras and Jacobsen 1992) and one station from the South Atlantic Ocean (German et al. 1995) are used below to introduce the major features (fig. 14) of oceanic lanthanide distributions. The following characteristics summarize the major features of lanthanides in the oceans:

(1) *Vertical profiles of the dissolved concentrations of all the lanthanides, except Ce, are characterized by low values in the upper ocean and increasing values with increasing water depth.* With the exception of profiles from the well-mixed water column of the Arctic (Westerlund and Öhman 1992), this feature is ubiquitous in the three major oceans. Profiles in fig. 14 point to large and variable vertical gradients between surface and deep waters. In the Pacific profile of station 271-1 the Nd concentration increases from 5 pmol/kg in surface water to 35 pmol/kg in deep waters. As indicated in fig. 14, the magnitude of the surface depletion (and hence deep-water enrichment) varies from region to region. This figure also shows that there are large differences in the vertical gradients within a single profile (e.g., the South-Atlantic station) and between regions. With respect to regional differences, the gradient in Nd is much steeper in the upper 3000 m of western North Pacific than it is in the South Atlantic. A gradient increase below 3000 m at the South-Atlantic site results in a similar deep to surface water ratio for Nd at these two locations.

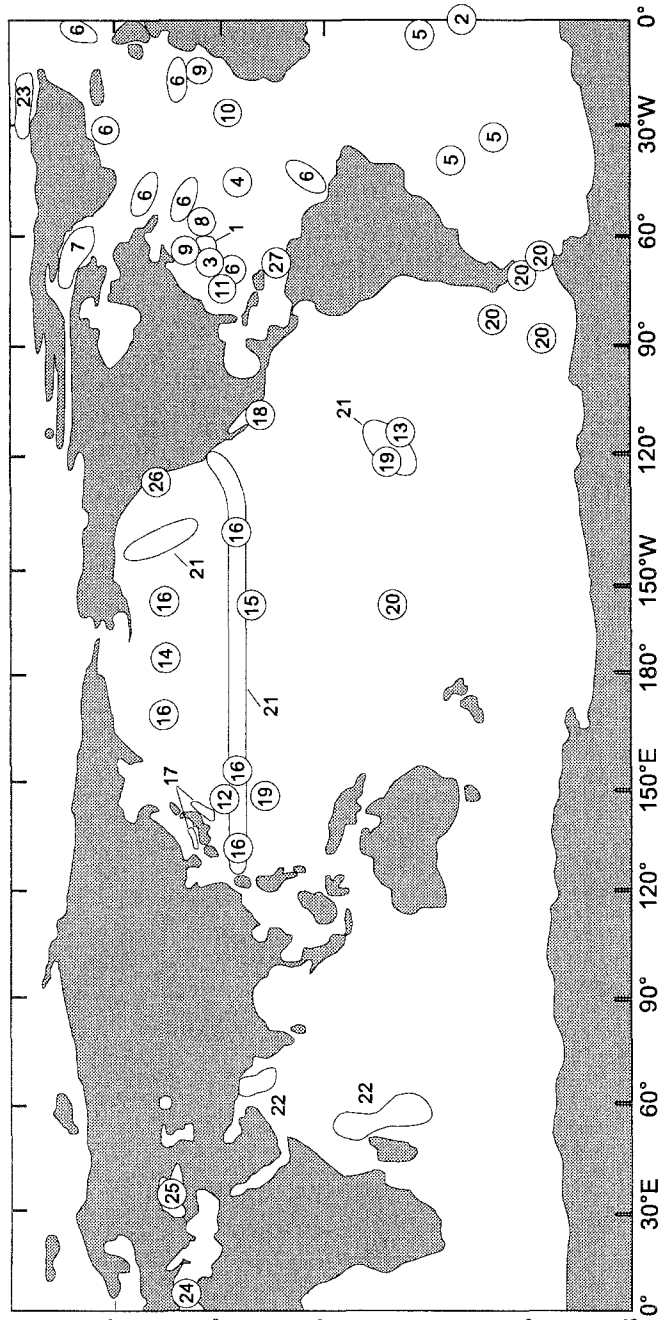

Fig. 13. World map for lanthanide data in the literature. See the text for explanation.

Atlantic Ocean
1. Jeandel et al. (1995)
2. German et al. (1995)
3. Sholkovitz et al. (1994)
4. Mitra et al. (1994)
5. Jeandel (1993)
3. De Baar (1991)
3. Sholkovitz and Schneider (1991)
6. Piepgras and Wasserburg (1987)
7. Stordal and Wasserburg (1986)
8. De Baar et al. (1983)
9. Piepgras and Wasserburg (1983)
10. Elderfield and Greaves (1982)
11. Piepgras and Wasserburg (1980)

Pacific Ocean
12. Zhang et al. (1995)
13. Möller et al. (1994)
14. Shimizu et al. (1994)
15. Esser et al. (1994)
16. Piepgras and Jacobsen (1988, 1992)
17. Tanaka et al. (1990)
18. De Baar et al. (1985a)
19. Klinkhammer et al. (1983)
20. Piepgras and Wasserburg (1982)
20. Piepgras et al. (1979)
Piepgras and Wasserburg (1980)
21. Elderfield, in preparation

Indian Ocean
22. Bertram and Elderfield (1993)
22. German and Elderfield (1990)

Arctic Ocean
23. Westerlund and Öhman (1992)

Mediterranean Sea
24. Greaves et al. (1991)
24. Spivack and Wasserburg (1988)

Anoxic Basins
25. Schijf et al. (1991)
25. German et al. (1991)
26. German and Elderfield (1989)
27. De Baar et al. (1988)

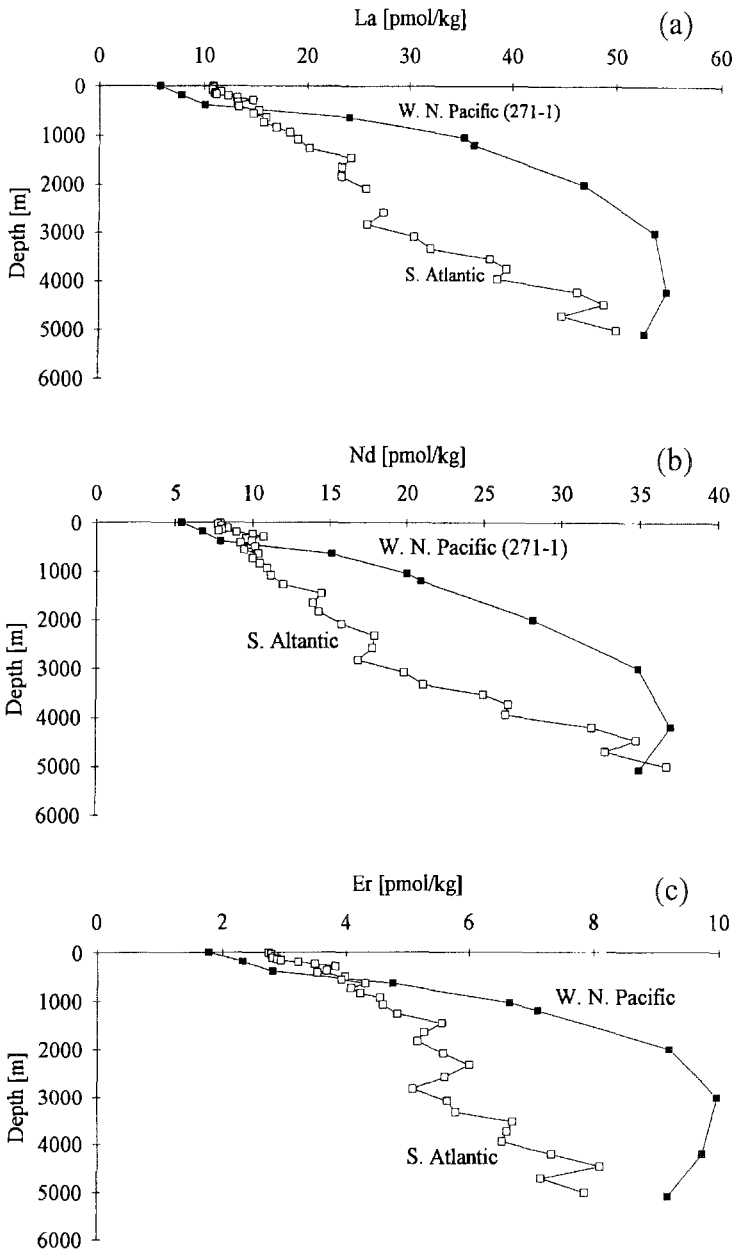

Fig. 14. Two vertical profiles of dissolved La, Nd, Er, and Ce concentrations and the Ce anomaly, parts a–e respectively: a comparison of the South Atlantic station of German et al. (1995) and the western North Pacific station (#271-1) of Piepgras and Jacobsen (1992).

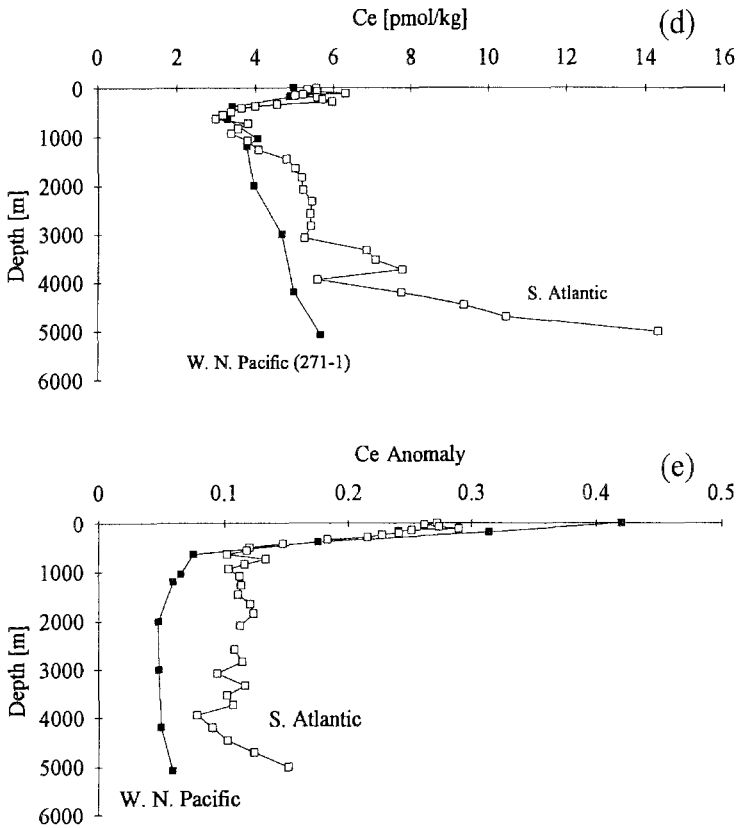

Fig. 14 (continued).

(2) *Dissolved Ce, in marked contrast to its strictly trivalent neighbors, typically decreases in concentration with depth in the upper 1000 m of the water column* (fig. 14). Below about 1 km Ce concentration profiles display a variety of distributions. Ce concentrations can remain constant, decrease slightly or increase to various degrees as illustrated in fig. 14d. There are large regional variations in Ce concentrations and in Ce anomalies. The Ce anomaly is a revealing indicator of processes operating on this redox-sensitive lanthanide; this parameter directly compares the distribution of Ce to its strictly trivalent neighbors. As demonstrated in fig. 14e for the western North Pacific and South Atlantic Oceans, the Ce anomaly rapidly decreases (becomes increasingly negative) in the upper 1000 m followed by relatively constant values to 5000 m.

(3) *Mass fractionation of the strictly trivalent lanthanides in the oceans is a feature which uniquely characterizes these trace elements* (Bertram and Elderfield 1993, German et al. 1995). Mass fractionation – variation in relative lanthanide concentrations through biogeochemical reactions – occurs within the water column

and between ocean basins. Inter-oceanic mass fractionation provides a global view of the fundamental processes operating on trace elements in concert with their marine biogeochemical cycle. A major characteristic of lanthanides in the oceans is their deep-water concentration decrease with the following order: Pacific > Indian > Atlantic Oceans. Accompanying this change in the absolute concentrations of all the lanthanides (except Ce) is a change in the relative abundance of the lanthanides. Heavy-lanthanide concentrations increase with respect to the light lanthanides as the deep waters age in their passage between ocean basins. This feature is apparent when one compares the deep-water concentrations of La and Nd with the concentration of Er for the South-Atlantic and western North-Pacific stations (fig. 14). The concentrations of La and Nd are approximately equal in both basins whereas the concentration of the heavy element Er is 15–20% higher in the deep water of the western North Pacific.

(4) *Ce undergoes an active redox chemistry in the upper oceans.* Experiments have shown that the oxidation of dissolved Ce(III) to particulate Ce(IV) oxides is microbially mediated and related to the redox chemistry of Mn (Moffett 1990, 1994a,b). High surface water concentrations of dissolved Ce (fig. 14d) appear to reflect oxidative removal at depth and reductive solubilization near the surface. Profiles of surface-bound Ce on suspended particles confirm that there is in situ oxidation of dissolved Ce(III) to particulate Ce(IV) in the upper oceans (Sholkovitz et al. 1994).

(5) *There is slow but progressive oxidation of dissolved Ce(III) to particulate Ce(IV) in the deep waters as they age in transport from the North Atlantic to the North Pacific and Indian Oceans* (Elderfield 1988, German et al. 1995). This redox-driven oxidation is reflected in the development of more negative Ce anomalies along the path of deep water transport. This feature is apparent when one compares the deep water samples of the western North Pacific with those of the South Atlantic (figs. 14d, e). Between these two locations the Ce anomalies change by about 50% (from 0.12 to 0.06).

6.2. *Profiles and cycles*

The partitioning of trace elements between particles and seawater is controlled by an interplay of surface and solution chemistry. Surface binding and solution complexation are fundamental processes underlying the profiles and cycling of trace elements in the oceans. The extent to which trace elements are bound to different types of inorganic and biogenic particles (colloidal, suspended and large fast-sinking types) will affect their removal rates, remineralization in the water column and the composition of seawater. One outstanding question with respect to particle/solution interactions is the extent to which trace elements fractionate during the partitioning process(es). Fractionation is defined here as a relative change in the lanthanide composition of solutions or particles due to biogeochemical reactions. As noted in sect. 2, the lanthanides have chemical properties which make them

an excellent natural probe of particle/solution interactions and redox reactions at surfaces. Moreover, group coherence makes them especially useful indicators of fractionation.

Two case studies, one from the North Atlantic and the other from the North Pacific Ocean, are presented below.

6.2.1. *Case study I – Sargasso Sea (western North Atlantic Ocean)*

Sholkovitz et al. (1994) compared the lanthanide composition of seawater with that of coatings on suspended particles. A conceptual picture of lanthanides cycling in seawater (Sholkovitz et al. 1994) with a focus on the role of particle surface coatings as active sites for the removal, remineralization and fractionation of trivalent lanthanides and oxidation of Ce(III), is reproduced in fig. 15. To compare the composition of surface coatings to the underlying mineral matrix, Sargasso Sea suspended particles were sequentially digested with three chemical treatments (acetic acid, mild HCl/HNO_3 and $HF/HNO_3/HCl$ in a reaction bomb). The latter two treatments dissolve detrital minerals while the acetic acid treatment removes surface coatings (organic matter and Mn oxides).

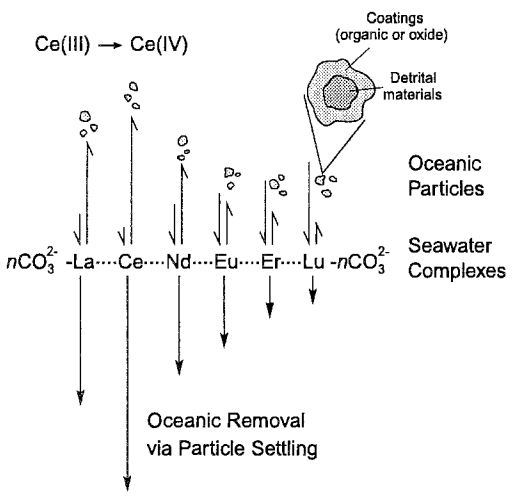

Fig. 15. Schematic model of lanthanide fractionation between particles and seawater reproduced from Sholkovitz et al. (1994). Main features include (1) the systematic variation in the relative affinity of lanthanide(III) for complexation to solution carbonates and binding to particles, (2) the enhanced formation of particulate Ce due to the oxidation of Ce(III) to Ce(IV) and (3) presence of surface active coatings on detrital particles. These features lead to fractionation of lanthanides between seawater and particles and to fractionation via the settling of large sinking particles.

Shale-normalized data from a 255 m sample illustrate the major features observed by Sholkovitz et al. (1994) (fig. 16). Included in this comparison is the lanthanide composition of dust collected in Bermuda within a few months of the water sample collection (Sholkovitz et al. 1993). The major observation is that surface coatings have a lanthanide composition which is distinct from that of seawater, dust and the two mineral phases of the suspended particles. The mineral matrix of suspended particles and the atmospheric dust are similar in composition. Both mineral matrices have crust-like patterns indicating a detrital source from the atmosphere. About 40–70% of the lanthanides are contained in the acetic acid digest; the strong acid digest carries 10–30% and the bomb digest carries 15–25%. At the heavy end of the series (Yb and Lu) the three fractions contribute equal proportions. These observations indicate that the surface

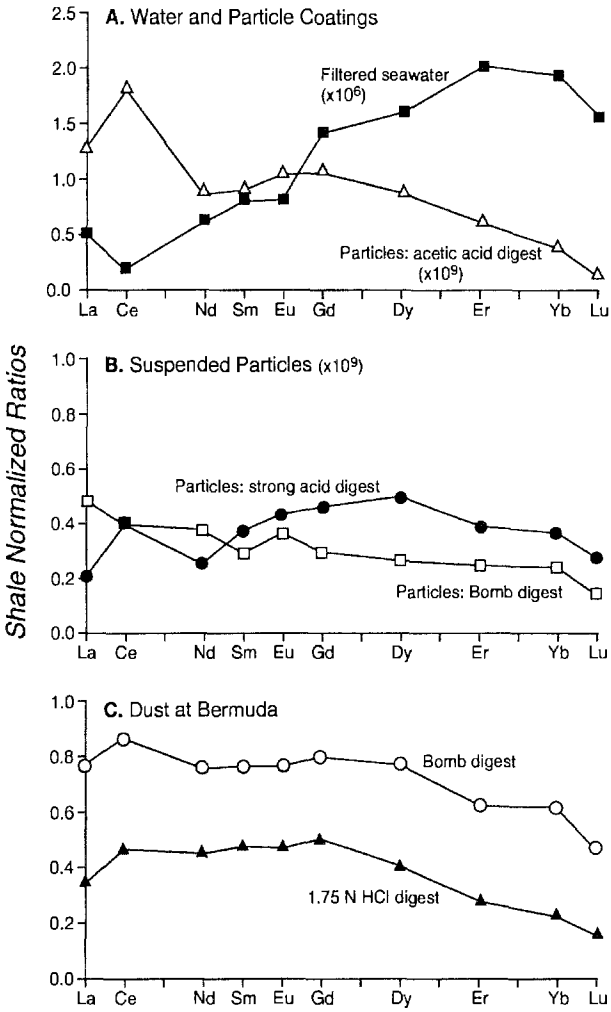

Fig. 16. (a, b) Shale-normalized ratios of filtered seawater and suspended particles from a sample collected at 255 m in the Sargasso Sea in April 1989. Results from three sequential digestions of the suspended particles (acetic acid, strong acid and bomb) are compared. (c) Shale-normalized ratio of dust collected at Bermuda in August 1989. Dust data from Sholkovitz et al. (1993) include the results of a mild digestion with dilute HCl and a strong acid digestion in bomb.

coatings of suspended particles in surface waters carry a large inventory of the particulate lanthanides. These results suggest that atmospheric particles delivered to the Sargasso Sea surface become coated with organic matter and Mn-oxides. These coatings, in turn, remove and fractionate lanthanides from seawater.

To reinforce the arguments for the role of surface coatings in lanthanide cycling, the compositional patterns of fig. 16 can be considered in more detail. The filtered seawater

has a shale-pattern typical of seawater (a large negative Ce anomaly within an overall enrichment of the heavy lanthanides). In marked contrast, the acetic acid digest is enriched in the light lanthanides and exhibits a large positive Ce anomaly. A large decrease in shale-normalized ratios occurs at the heavy end of the series (from Gd to Lu). Hence, the acetic acid digest has a pattern which is the mirror image to that of seawater. Both the strong acid and bomb digests have fairly flat patterns indicative of crust-like compositions. This is consistent with the major fraction of Al being in these two digestions (Landing and Lewis 1991) and not in the acetic acid digest. The bomb digests of both the suspended particles and Bermuda dust show a subtle but systematic decrease from La to Lu (figs. 16b,c). This compositional similarity between dust at Bermuda and the mineral matrix of suspended particles indicates a common (atmospheric) source of minerals to the Sargasso Sea. An African source of mineral dust to Sargasso Sea is well documented (e.g., Prospero and Ness 1986, Prospero et al. 1987).

The lanthanide compositions of acetic acid digests normalized to filtered seawater (fig. 17) for Sargasso Sea samples collected between 60 and 2000 m (Sholkovitz et al. 1994) exhibit two main features: (1) a systematic and 10-fold decrease in the ratios from La to Lu excluding Ce and (2) large positive anomalies in normalized Ce below 105 m. The large size of the Ce peaks results from the combination of Ce removal from the dissolved phase and Ce uptake by the particle coatings. The seawater-normalized plots of all samples fall closely together even though the absolute concentrations show large variations within the 2000 m profile. Fractionation can be assessed by comparing the acetic acid digest/seawater ratios for La and Yb. The mean and standard deviations for the nine samples are 1.85(0.39) for La and 0.27(0.05) for Yb. Thus a 7-fold difference in the partitioning of La relative to Yb, when surface coatings are normalized against their respective seawater concentrations, provides a convincing case for fractionation – the preferential uptake of the lightest trivalent lanthanides.

The shift from no Ce anomalies in the 60 m and 105 m samples to large positive anomalies in samples at 150 m and below is a unique feature of this data set (fig. 17). The development of large positive anomalies (ratio of coating to seawater composition) provides convincing evidence that the surface coatings are active sites for the oxidation of dissolved Ce(III) to particulate Ce(IV) in the upper oceans.

Vertical profiles from the Sargasso Sea (Sholkovitz et al. 1994) are shown in figs. 18 and 19. Figure 18 contains dissolved La, Ce and Nd profiles and fig. 19 shows Mn profiles for both filtered seawater and the acetic acid digest of suspended particles. The main feature of dissolved lanthanide profiles is the contrast between Ce and its trivalent neighbors, La and Nd, in the upper 550 m. There is extensive depletion of dissolved Ce (15.7 pmol/kg at 15 m to 6.3 pmol/kg at 550 m) while La and Nd concentrations show little variation over this depth range. Ce reaches a minimum at 750 m and then increases slightly at greater depths. There is also extensive downward depletion of dissolved Mn over the upper 250 m. The profile of dissolved Mn differs from that of Ce in that Mn reaches a minimum concentration at a much shallower depth (250 m vs. 750 m). The removal of Ce from the dissolved phase leads to the development of increasingly negative Ce anomalies with depth. Surface waters have anomalies of 0.45 while the 750 m sample

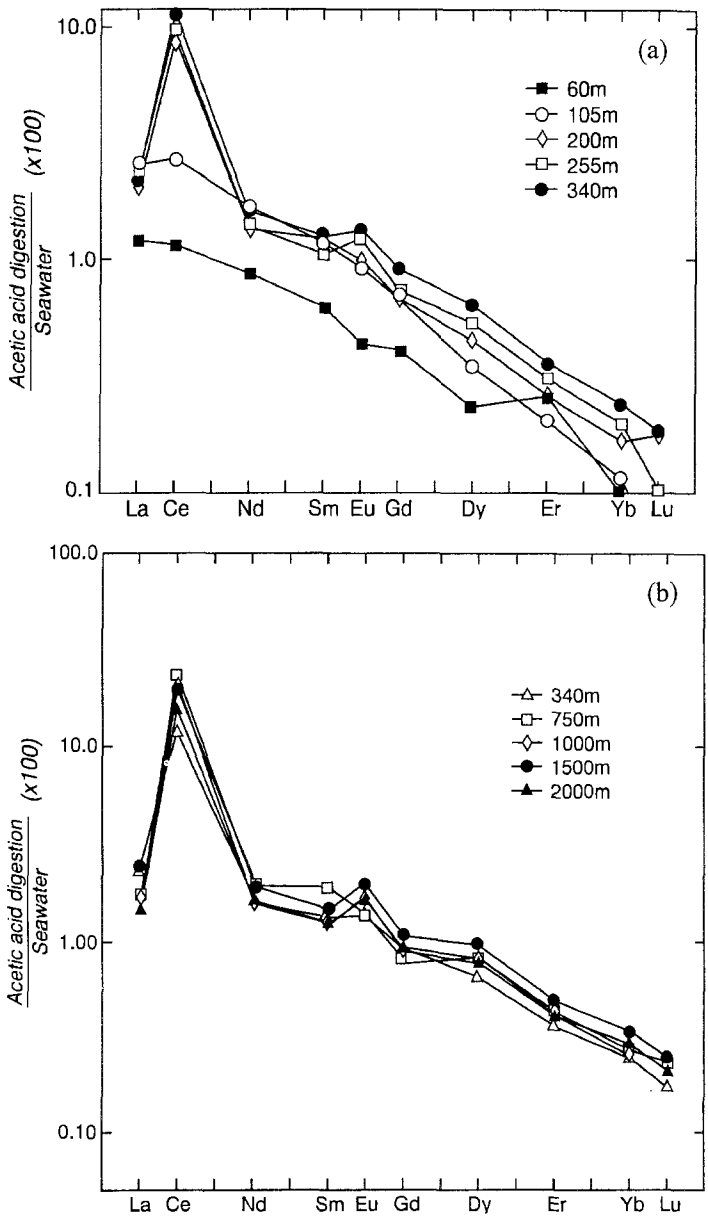

Fig. 17. The lanthanide composition of acetic acid digestions of suspended particles normalized to the composition of filtered Sargasso Sea seawater, (a) for samples in the upper 340 m and (b) for samples between 340 m and 2000 m. Note log scale. From Sholkovitz et al. (1994).

has a value of 0.18. Trivalent lanthanide concentrations, as illustrated by La and Nd, increase between 500 and 1000 m and then level off. As already documented in fig. 14,

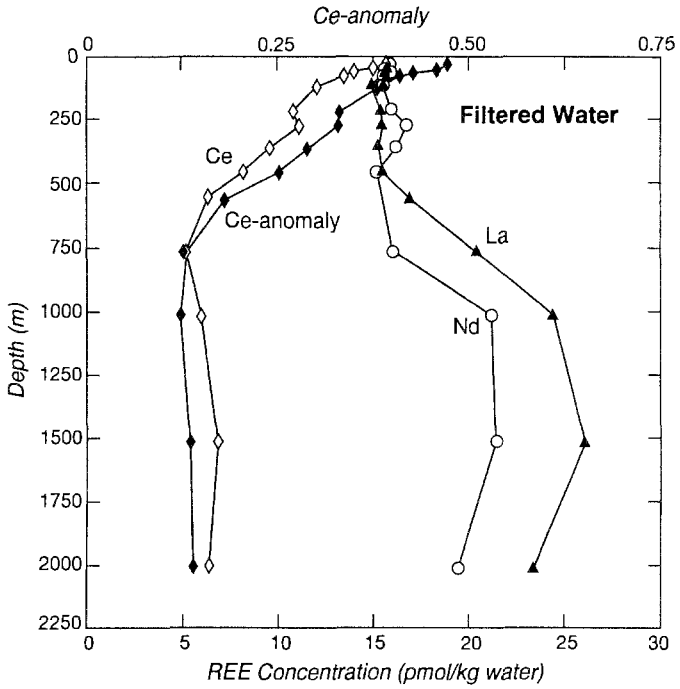

Fig. 18. Vertical profiles of dissolved (<0.22 μm) La, Ce and Nd from the Sargasso Sea. The profile of the calculated Ce anomaly is also shown. From Sholkovitz et al. (1994).

the remineralization of trivalent lanthanides in the deep water is a constant feature of oceanic profiles (e.g., Elderfield and Greaves 1982, De Baar et al. 1985a,b, Elderfield 1988, Piepgras and Jacobsen 1992, Bertram and Elderfield 1993).

Large vertical gradients of particle-bound La, Ce and Nd and Ce anomalies are seen (fig. 20) in acetic acid digestions. La and Nd concentrations double between 60 m and 105 m and then increase gradually with depth. Ce concentrations increase about 7-fold between 60 m and 225 m and then remain fairly uniform (the high value at 550 m being an exception). The in-growth of Ce onto particle surfaces mirrors the depletion of dissolved Ce (fig. 18). A major feature of this data set is the shift from negative to positive Ce anomalies between 105 and 150 m. The acetic acid digests of the 60 and 105 m particles have anomalies of 0.44 and 0.47 (like seawater) while samples below 200 m have values of 1.4–1.6. These data confirm prior experimental studies (Moffett 1990) that there is in situ oxidation of dissolved Ce(III) to particulate Ce(IV) in the upper water column of the Sargasso Sea. The production of particles with positive Ce anomalies corresponds with the production of a sub-surface maximum in particulate Mn and a minimum of dissolved Mn (fig. 19). As the acetic acid digest carries the major portion of the particulate Mn signal, this phase must be Mn oxyhydroxide formed within the water column. This oxidation of dissolved Mn(II) to particulate Mn(IV) is a well documented feature of the Sargasso Sea (Sunda et al. 1983, Sunda and Huntsman 1988).

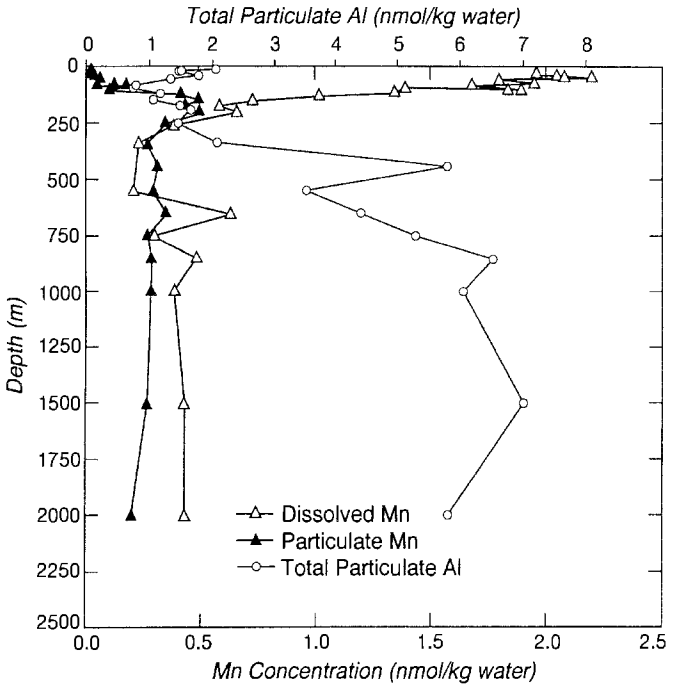

Fig. 19. Vertical profiles in the Sargasso Sea of dissolved Mn and total particulate Mn and Al. A high dissolved value (2.7 μmol/kg) at 440 m was measured but not plotted. For almost all the samples, over 90% of the particulate Mn concentration is carried in the phase released by the acetic acid digestion; in contrast, the major portion of particulate Al is carried in the strong acid and bomb digestions (Landing and Lewis 1991). From Sholkovitz et al. (1994).

In summary, profiles of dissolved and particulate lanthanide concentrations in the Sargasso Sea (Sholkovitz et al. 1994) provide the following conclusions:

(1) The extensive fractionation of trivalent lanthanides between Sargasso Sea water and suspended particles can be qualitatively explained by a solution/surface competition model (fig. 15). The progressive decrease from La to Lu in the extent to which dissolved lanthanides are removed by suspended particles results from an increase in the solution complexation constants as predicted by chemical models (e.g., sect. 4 of this chapter; Erel and Morgan 1991, Erel and Stolper 1993, Byrne and Li 1995).

(2) Acetic acid digestions of suspended particles demonstrate that removal and fractionation of lanthanides in seawater are caused by processes which result in particle surface coatings. In contrast, the detrital phases have dust and crust-like lanthanide compositions indicative of a continental source.

(3) The oxyhydroxides of Mn provide important surface sites for the oxidation of dissolved Ce(III) to particulate Ce(IV) and the fractionation of trivalent lanthanides during sorption. Oxidative processes become important at water depths between

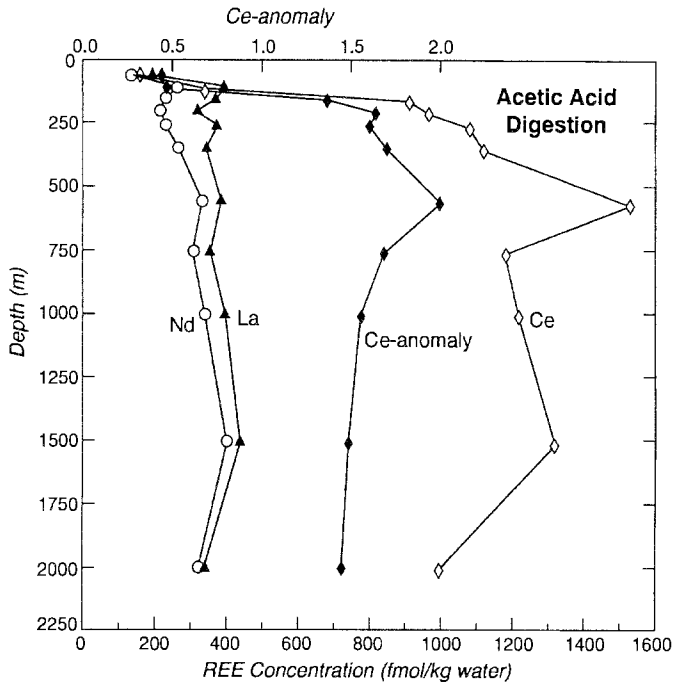

Fig. 20. Vertical profiles of La, Ce and Nd concentrations from the acetic acid digestion of suspended particles from the Sargasso Sea. The Ce anomaly profile is also shown. From Sholkovitz et al. (1994).

100 to 200 m, in concert with oxidation of dissolved Mn(II) to particulate Mn(IV) oxides. Organic matter coatings may also play a key role in the cycling of the lanthanides.

Jeandel et al. (1995) used a different approach (Nd isotopes) to study the water column cycling of the lanthanides in the Sargasso Sea. They measured the Nd isotopic composition of small suspended particles and large sinking particles and compared their results with previously published data for filtered seawater (Piepgras and Wasserburg 1987). They concluded that there is reversible exchange of Nd between suspended particles and seawater. The uptake of Nd onto the surfaces of suspended particles and the reversible exchange of Nd during the remineralization of sinking particles were used by these authors to explain both the observed Nd isotopic variations within water column of the Sargasso Sea and between the three ocean basins (sect. 6.7 covers Nd isotopes in more detail). Reversible exchange between seawater and particles is consistent with the observation of Sholkovitz et al. (1994) that the surface coatings of suspended particles are responsible for the removal, release and fractionation of lanthanides in the oceans. Jeandel et al. (1995) also concluded that approximately 50% of the particulate Nd leaving the surface is remineralized in deep waters.

6.2.2. *Case study II – North Pacific Ocean*

The behavior of lanthanides in the North Pacific allows insights into important oceanographic processes operating on these trace elements. The following discussion is centered on two detailed vertical profiles (Piepgras and Jacobsen 1988, 1992) from the western North Pacific Ocean. Station 39-1 lies at 47°N and station 271-1 lies at 24°N; both lie at about the same longitude (161 and 150°E respectively). Their data come from the analyses of unfiltered samples. The vertical profiles of La and Yb are compared in fig. 21; this figure also compares the vertical profiles of the La/Yb ratio and of the Nd isotopic composition. Figure 22 compares the vertical profiles of Nd with those of salinity, silica and phosphate.

Profiles at both Pacific stations exhibit a familiar distribution of surface depletion and deep water enrichment in the concentrations of lanthanides. The two profiles have deep waters with approximately the same concentrations of La and Yb (and other lanthanides). What distinguishes the two profiles is the composition of the upper (<1000 m) water column (fig. 21a). Station 271-1 at 24°N has much lower surface concentrations of lanthanides than does station 39-1 at 47°N. For La this difference is 6 vs. 23 pmol/kg and for Yb this difference is 2 vs. 5 pmol/kg. Piepgras and Jacobsen (1992) argued that this difference reflects the presence of different water masses in the upper water column of these sites. Hence, they ruled out a direct biogeochemical cause. Their evidence for a hydrographic explanation includes large differences in temperature–salinity properties and in Nd isotopic composition (fig. 21c) for depths < 1000 m. The major inter-station differences in nutrient concentrations and gradients are an important feature, not previously explored. Surface waters of the 24°N station (fig. 22) are almost completely depleted in phosphate (0.03), silicate (1.5) and nitrate (1.5) concentrations (μmol/kg); nitrate profiles are not plotted but they are similar in shape to phosphate. This 24°N station with depleted nutrient levels is characterized by lower concentrations of lanthanides. In contrast, the 47°N station with higher lanthanide concentrations, has much higher surface water concentrations of phosphate (1.18), silicate (17.8) and nitrate (12.4). The large inter-station differences in nutrient concentrations could reflect a different set of biological processes such as higher phytoplankton productivity at the 24°N station, driving down the nutrient levels. Hence, biogeochemical processes, as well as hydrographic ones, may be responsible for the inter-station variations in lanthanide distributions. With this alternative in mind the profiles of La/Yb ratios can be examined (fig. 21b). This ratio exhibits large vertical variations at both stations. At the 47°N station the La/Yb ratio continuously decreases (6.5 to 4.5) from the surface to a depth of 2 km; this is followed by a continuous increase to 5.5 at a depth of 5.5 km. The 24°N station has a more complicated distribution. Its La/Yb ratio reaches a low value (4.2) in the surface and increases to a value of 5.4 at 1000 m; below 1000 m the profile at 24°N is similar to that of the 47°N station. Piepgras and Jacobsen (1992) interpreted the La/Yb divergence in the upper 1000 m to water mass differences. An alternative explanation is that depletion of lanthanide concentrations by biological processes in the upper water column of the 24°N station leads to the preferential removal of the light lanthanides relative to the heavy

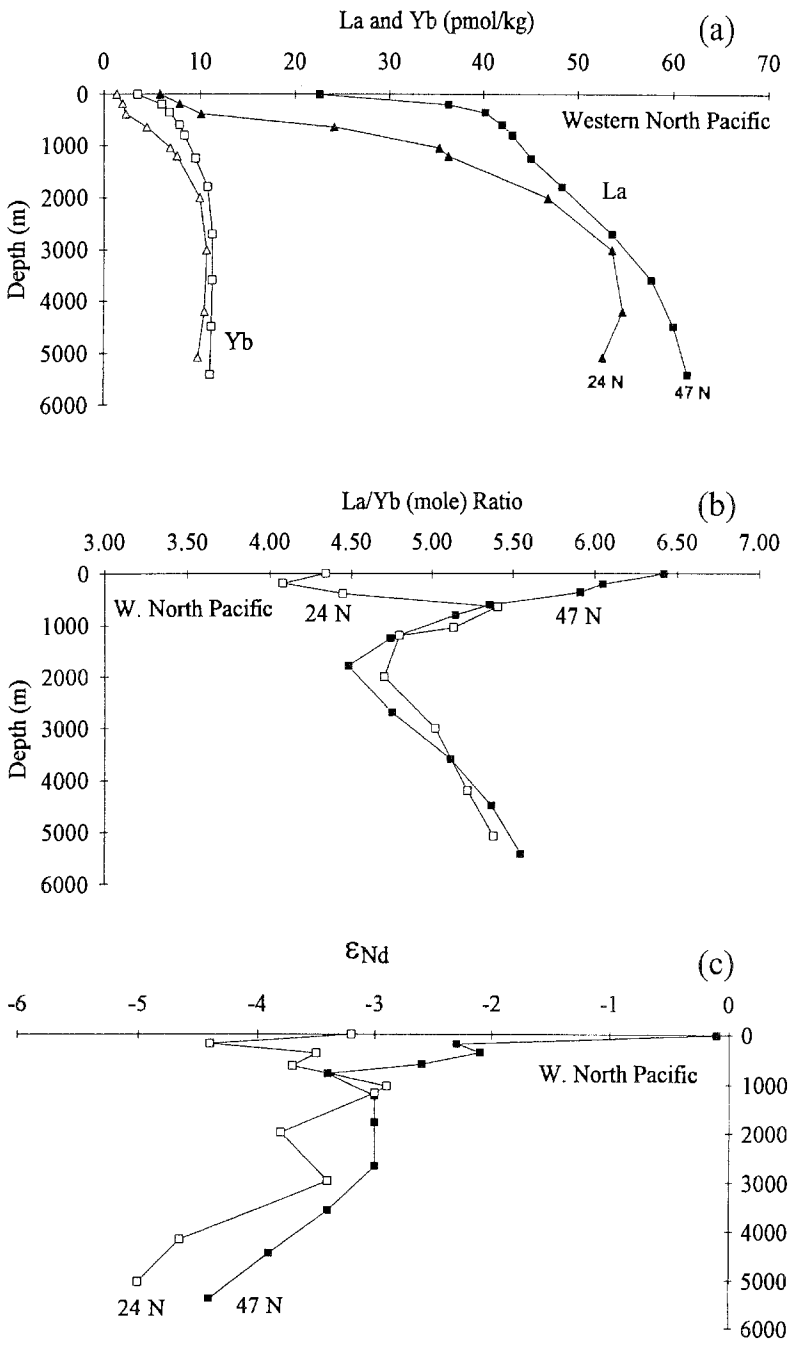

Fig. 21. Profiles from the water (unfiltered) column in the western North Pacific Ocean. Comparison of Sta. 39-1 at 47°N with Sta. 271-1 at 24°N. Data from Piepgras and Jacobsen (1992). (a) La and Yb concentrations, (b) La/Yb (mole) ratio and (c) Nd isotopic composition in ε_{Nd} units.

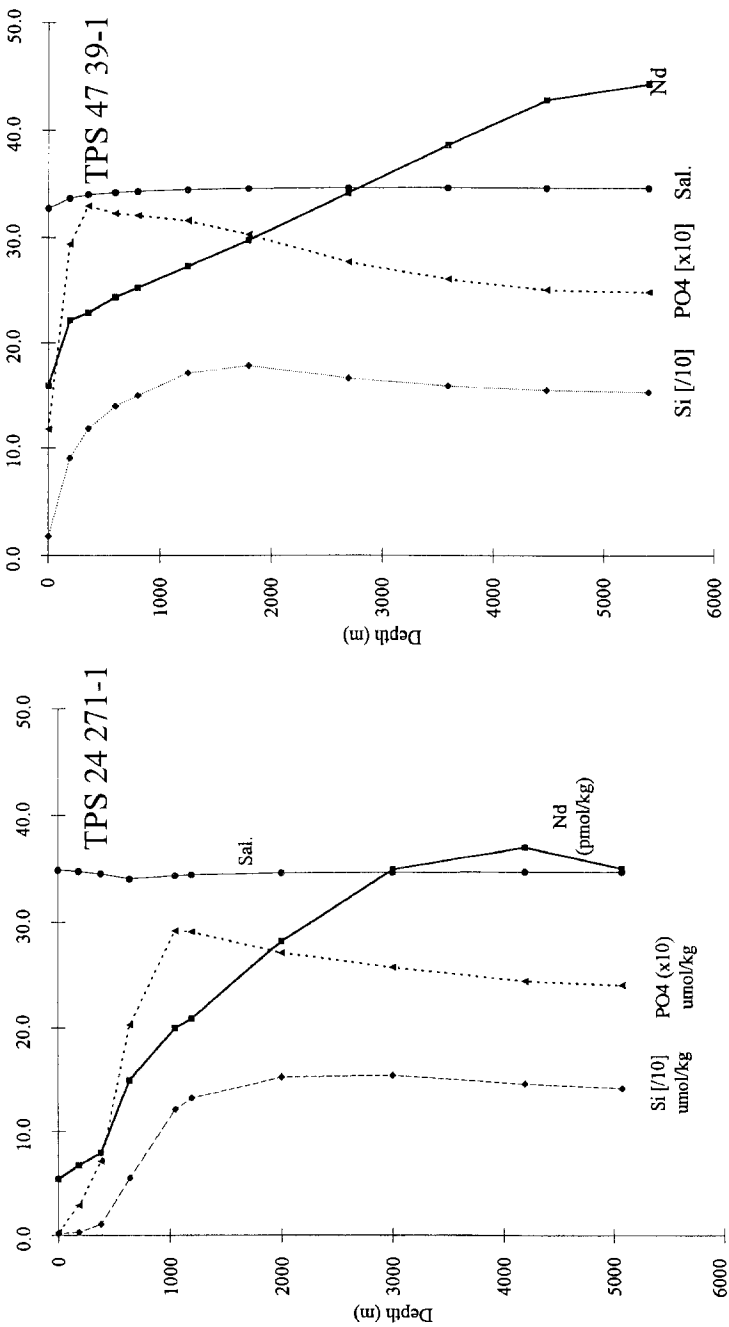

Fig. 22. Profiles from the water (unfiltered) column in the western North Pacific Ocean. Comparison of Nd, salinity and the nutrients, phosphate and silica from Sta. 271-1 at 24°N with Sta. 39-1 at 47°N. Data from Piepgras and Jacobsen (1992). Nitrate closely follows the distribution of phosphate.

lanthanides. Fractionation of this type is consistent with the previously discussed study of the Sargasso Sea where surface coatings of surface particles are preferentially enriched in the lightest lanthanides.

Future studies will be needed to resolve the role of hydrography and biogeochemistry in controlling the absolute and relative abundance of the lanthanides in the seawater. Time-series studies in regions with large seasonal cycles in biological productivity and nutrient distributions are required. The North Atlantic Bloom Experiment is a prototype for such a study. The results of this experiment in the eastern North Atlantic demonstrated that a large spring bloom of phytoplankton reduces nutrient levels and produces a bloom of sinking biogenic particles (Honjo and Manganini 1993). Determining the extent of fractionation during a spring bloom would add greatly to our knowledge of the marine chemistry of lanthanides.

6.3. *Lanthanide–nutrient relationships*

The oceanic profiles of many trace elements (e.g., Cd, Cu, Zn) closely resemble those of the nutrients (silica, nitrate and phosphate). Like nutrients, the concentration profiles of these metals are characterized by surface water depletion and deep water enrichment. This observation has lead to the well-established concept that the cycling of many trace metals in the water column is driven by the biological cycle. That is, the production of biogenic particles in the surface waters reduces nutrients and metals to low levels, and subsequent remineralization of biogenic particles at depth release silica, nitrate, phosphate and trace metals back to the water column. In detail, the remineralization of silica differs from that of nitrate and phosphate. Silica is associated with skeletal matter (hard parts) of siliceous plankton while nitrate and phosphate are accumulated in the organic tissue (soft parts) of plankton. This type of fractionation leads to a shallow-water (upper 1000 m) regeneration of nitrate and phosphate as organic matter is decomposed. Silica, in contrast, has a deep-water enrichment as siliceous tests are transported to depth and are less rapidly dissolved than the organic matter components of the sinking biogenic material. Figure 22, with profiles from the western North Pacific Ocean, illustrates the shallow water and deep water regeneration of phosphate and silica. Trace metals and nutrients in the oceans are strongly correlated as for example Cd profiles which are almost identical to those of phosphate. Hence, Cd is incorporated into the organic component of plankton and predominately regenerated in the upper part of the water column. In contrast, Zn has a Si-like profile suggesting a deep water regeneration following its incorporation into siliceous skeletal matter.

The relationship between dissolved lanthanides and nutrients has received considerable discussion in the literature. Unlike for many other trace metals, there appears to be no metabolic requirement for lanthanides by plankton. At pmol/kg levels such a requirement is unlikely. Hence, surface water depletion must reflect a general type of "scavenging" onto newly formed surfaces (plankton). The extremely low concentrations of lanthanides in the calcium carbonate or siliceous skeletal matter of plankton suggest that such

incorporation is not an important process in controlling the water column profiles of lanthanides (Palmer 1985, Elderfield et al. 1981).

Bertram and Elderfield (1993) used data from the Atlantic, Pacific and Indian Ocean to produce plots of Si verses Nd, Er and the Ce anomaly (fig. 23). As noticed earlier by De Baar et al. (1983, 1985a,b), Klinkhammer et al. (1983), Elderfield (1988) and others, the heavy lanthanides are more closely related (in a statistical sense) to silica than are the lighter elements. A comparison of Nd and Er vs. Si brings out this point (fig. 23). Because the vertical profiles of dissolved lanthanides are most similar to profiles of Si (as compared to nitrate and phosphate), lanthanide–Si relationships have been used to suggest that there is a biogeochemical coupling between the two cycles. De Baar et al. (1983, 1985a,b) argued that uptake and release from biogenic silica is responsible for the vertical distribution of lanthanides. More recent studies have argued that the lanthanides are not simply cycled along with biogenic silica (Klinkhammer et al. 1983, Piepgras and Jacobsen 1992, Bertram and Elderfield 1993, Sholkovitz et al. 1994). As noted by Piepgras and Jacobsen (1992) and illustrated in fig. 22, "In general, the REE concentrations increase downward long after Si and PO_4^{3-} have reached their respective deep-water maxima. This observation in itself indicates an independent behavior between REE and nutrients. We also find that Er–Si relationships vary with location in agreement with the observations made by Klinkhammer et al. (1983)". This variation of Er–Si was noted by Bertram and Elderfield (1993) and is apparent from their compilation of data in fig. 23. They also point out that, unlike nutrients and many trace metals, surface water concentrations of the lanthanides do not reach zero values (fig. 10). Bertram and Elderfield (1993) concluded "... in detail, the description of linear stoichiometry is a simplification and there is a significant range in values (Er/Si ratios) both within and between oceans." They then note that "... it is intriguing that small average interoceanic differences in $\Delta Er/\Delta Si$ in deep waters are such that they increase in the following sequence: Atlantic < Indian < Pacific, that is in the direction of deep water movement. This may indicate small systematic differences in regeneration behavior, but there is considerable scatter in the data and a larger data set is needed to test this hypothesis."

The study by Sholkovitz et al. (1994) emphasized the role of sorption to suspended particles in the marine chemistry of the lanthanides. They concluded that "It is difficult to reconcile a geochemical coupling between Si and REEs. Our data point to the uptake and release of REEs from surface coatings ("soft" parts) while Si is released from dissolved siliceous plankton ("hard" parts) in deep waters ...".

Summing up this subsection, while the lanthanides most closely resemble Si in profile shape, the silica regeneration cycle does not control the distribution of lanthanides in the oceanic water column. The evidence suggests that the lanthanides are removed from surface waters through a scavenging process onto the surfaces of biogenic particles and particles of air-borne dust which become coated in surface waters with Mn oxides and organic matter. The lanthanides are then released to the deeper water as small particles aggregated in surface waters and form larger sinking particles which are bacterially decomposed. The study of Nd isotopes in seawater and particles supports this process. While driven by the biological/nutrient cycle, the incorporation of lanthanides into either

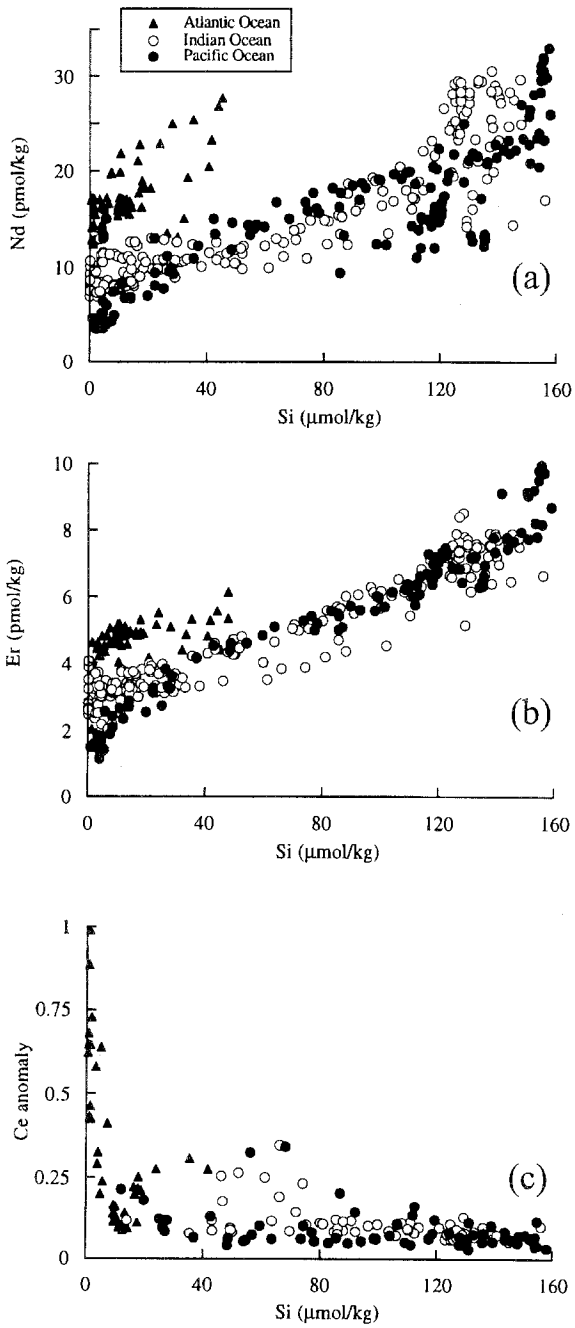

Fig. 23. Plots vs. dissolved Si for (a) Nd, (b) Er, and (c) Ce anomaly for the Atlantic, Indian, and Pacific oceans. Data from this study and from Elderfield and Greaves (1982), De Baar et al. (1983, 1985a,b), Klinkhammer et al. (1983), Palmer (1983), Elderfield (1988), Piepgras and Jacobsen (1988, 1992), Greaves et al. (1989, 1991), German and Elderfield (1990), Sholkovitz and Schneider (1991), and Dickie and Elderfield (unpublished data). From Bertram and Elderfield (1993).

the organic tissue or the skeletal matter of the biogenic particles is not the dominant process. Hence, one would not expect the vertical distributions of the lanthanides to exactly follow those of the nutrients. Rather one might expect profiles with a shape broadly like those of nutrients, that is, surface depletion and deep water enrichments associated with particle remineralization in the water column.

6.4. *Mass fractionation*

Interelement lanthanide fractionation in the oceans allow insights into basic processes controlling the concentrations and relative abundance of trace elements. The best synthesis of lanthanide fractionation in the oceans appears in Bertram and Elderfield (1993). This subsection relies heavily on this paper and focuses on strictly trivalent elements.

Figures 23 and 24 (from Bertram and Elderfield 1993) illustrate interelement fractionations. "There is a clear regional variation between oceans [fig. 23]. Surface water concentrations of both Er and Nd increase in the following sequence: Atlantic > Indian > Pacific ... This is the reverse of the situation in the deep waters of the oceans. ... deep waters concentration of the REEs increase in the following sequence: Atlantic < Indian < Pacific. The oceanwide trend in surface waters REE concentrations suggests that the primary control is that of REE input from the continents rather than scavenging efficiency for REE removal." Studies of Nd isotopes confirm this key point – continents as the dominant source of lanthanides to oceans (sect. 5.1).

Bertram and Elderfield (1993) point out the major features with respect to fractionation. As expected from their close positions in the lanthanide series, the oceanic distributions of Nd and Sm are tightly coupled. Sm and Nd molar ratios range between 0.181 and 0.203, with very minor variability and a mean value equal to 0.189. Sm/Nd ratios decrease in the following sequence: Atlantic (0.203 ± 0.009, mean and standard deviation) > Indian Ocean (0.196 ± 0.013) > Pacific (0.181 ± 0.024). Thus, the inter-basin differences are not significant relative to the range for each ocean. Since the Sm/Nd ratio for average shale is identical to the oceanic mean but is smaller than Sm/Nd for dissolved lanthanides ($Sm/Nd \approx 0.25$) in many rivers (Elderfield et al. 1990), oceans are fractionated relative to the dissolved river input with a small enrichment in Nd relative to Sm (Bertram and Elderfield 1993).

Bertram and Elderfield (1993) note that "In contrast to Sm–Nd, there is significant fractionation of Nd relative to Er. ... A comparison of the major oceans shows that there is separation of Er and Nd, and average Er/Nd ratios increase in the following sequence: Atlantic (0.26 ± 0.06) < Indian Ocean (0.34 ± 0.05) < Pacific (0.35 ± 0.09). The contrast between the oceans can be seen from fig. 25. Because of mixing of oceanic deep waters, it is to be expected that ratios of each ocean overlap. The range of each ocean also reflects the increasing HREE enrichment with depth seen in REE abundance patterns [*not shown*]. The oceanic mean Er/Nd is 0.32. This compares with 0.084 for average shale. In REE-poor rivers, the dissolved Er/Nd ratio is about 0.25; seawaters are Er-enriched relative to Nd as compared with this value. In summary, Sm/Nd ratios are very similar everywhere in the oceans. On average, the world ocean has the same Sm/Nd as average shale but

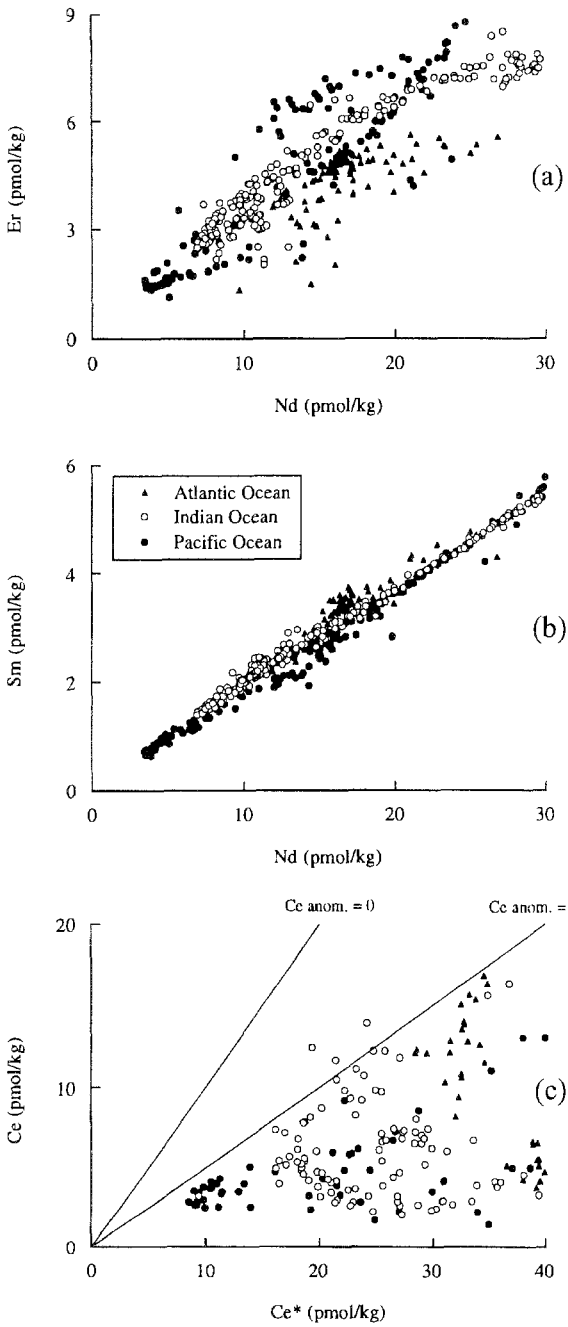

Fig. 24. Lanthanide interelement ratios: (a) Sm vs. Nd, (b) Er vs. Nd, and (c) Ce vs. Ce* for the Atlantic, Indian, and Pacific oceans. $Ce^* = Ce_{shale}\,[2(La/La_{shale}) + (Nd/Nd_{shale})]/3$, where the subscripts refer to concentrations in shale. Data as in fig. 23. From Bertram and Elderfield (1993).

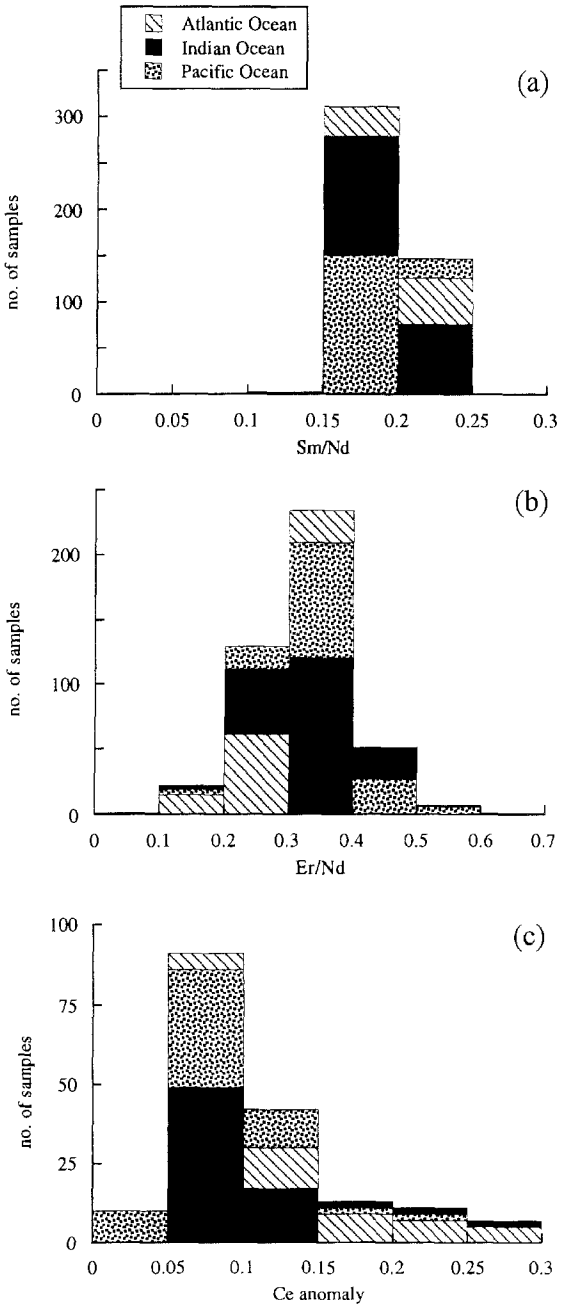

Fig. 25. Histograms showing lanthanide interelement fractionation for the Atlantic, Indian, and Pacific oceans (data as in fig. 24): (a) Sm/Nd ratio; (b) Er/Nd ratio; and (c) Ce anomaly. From Bertram and Elderfield (1993).

Table 10
River and ocean compositions: Nd, Er and Er/Nd ratio

	Nd (pmol/kg)	Er (pmol/kg)	Er/Nd (molar)
1. Goldstein and Jacobsen (1988a)			
Average dissolved river water	284	50.6	0.179
"Effective" dissolved river water	114	30.8	0.270
2. Bertram and Elderfield (1993)			
Oceanic mean			0.321
Atlantic Ocean			0.260
Indian Ocean			0.340
Pacific Ocean			0.350
3. Shale (table 1)			0.084

has a lower ratio than river waters. In contrast, seawater Er/Nd ratios are on average nearly four times higher than shales (40% higher than river waters), and they increase in the following sequence: rivers < Atlantic < Indian < Pacific, consistent with removal of Nd from seawater relative to Er in the direction of deep water flow."

This last point describes one of the important and distinctive features with respect to the distribution and geochemical cycling of lanthanides in the oceans, that is, the inter-ocean fractionation of lanthanides. Arguments about the extent of fractionation rely on knowing the composition of lanthanides reaching the oceans via the rivers. As discussed in earlier sections, weathering on continents and reactions in estuaries cause fractionation within the dissolved component of the river water. Returning to the Er/Nd ratio as proxy for fractionation, table 10 compares the oceanic data of Bertram and Elderfield (1993) with the river data of Goldstein and Jacobsen (1988a). It is important to emphasize that both sets of data represent "average" compositions. The effective river load refers to the dissolved concentrations of Nd and Er reaching the oceans after the lanthanides undergo removal in estuaries. As the light elements are removed to a larger extent than the heavy elements, significant fractionation occurs between the rivers and the oceans. Goldstein and Jacobsen (1988a), using estuarine removal factors of 60 and 40% for Nd and Er respectively, concluded that the average Er/Nd ratio increases from a river value of 0.179 to an effective river value of 0.270. This is a large shift. The effective river ratio of 0.270 is much closer to that of mean ocean water (0.321) and similar to that of the Atlantic Ocean (0.260). The Atlantic ratio clearly reflects a continental source. Both the river and effective river ratios greatly exceed that of shale (0.084), indicating the enrichment of heavy elements over light elements during weathering and estuarine transport.

As noted above, the river and effective river Er/Nd ratios are calculated using an average riverine composition and an estimate of estuarine removal; data from relatively

few rivers and estuaries are extrapolated to yield global values (Goldstein and Jacobsen 1988a). Figure 11 shows Er/Nd ratios for the dissolved component of river waters plotted against the concentration of dissolved Nd. These data come from the most recent compilation of river data (see sect. 5). The Er/Nd ratio has a large range (0.05–0.5) and, as noted by Elderfield et al. (1990), the Er/Nd vs. Nd plot has strong curvature. The ratio approaches the shale value (0.084) as dissolved Nd concentrations increase. This feature is interpreted as reflecting the increasing inventory of clay-like colloidal particles in rivers with increasing dissolved lanthanide concentrations. This figure emphasizes the great variability of river composition. Uncertainty in river composition has a large effect on interpretations of mass fractionation in the oceans. While averaged compositions allow the development of an ocean-wide view of fractionation, one should realize how little is known about the composition of river input and fractionation within estuaries and the coastal region. The poorly documented composition of rivers draining into the Pacific Ocean and uncertainties (Goldstein and Jacobsen 1988a, Elderfield et al. 1990, Sholkovitz 1995) in the extent of release (Sholkovitz 1993, 1995) of dissolved lanthanides from estuarine coastal sediments add substantial uncertainty to characterizations of the mass fractionation of lanthanides.

The vertical profiles of the Er/Nd ratio for different ocean basins are compared in fig. 26. This type of presentation allows a closer inspection of fractionation within and between ocean basins. Profiles include those from the eastern North Atlantic off NW Africa (Elderfield and Greaves 1982), the Sargasso Sea near Bermuda (Sholkovitz et al. 1994, plus new unpublished data for samples at 3 and 4 km), the South Atlantic (German et al. 1995), the Indian Ocean (Sta. 1507 from Somali Basin, Bertram and Elderfield 1993) and two stations from the western North Pacific (Piepgras and Jacobsen 1992). The Er/Nd ratio in deep waters (arbitrarily taken here as >3 km) increases from a low 0.1 off NW Africa to a high 0.28 in the western North Pacific. Waters of the South Atlantic have a ratio between that of the Sargasso Sea and the western North Pacific, and the Indian-Ocean ratio is slightly smaller than that of the western North Pacific. The deep water off NW Africa has a Er/Nd ratio which is close to that of shale, reflecting a continental source (Elderfield and Greaves 1982). Data for the Arctic Ocean (Westerlund and Öhman 1992) show Er/Nd ratios approximately equal to 0.2 below 3 km.

Water column profiles of the Er/Nd ratio have a complex structure (fig. 26). Many profiles (e.g., Indian and Pacific Ocean) are characterized by a large maximum in Er/Nd in the upper 1–2 km region of the water column. Below this depth range, all profiles show a large decrease in Er/Nd with increasing depth. The upper ocean variability probably reflects local effects such as input of African dust to the eastern North Atlantic leading to shale-like ratios in surface waters (Elderfield and Greaves 1982). As both water mass mixing and water column geochemistry operate on lanthanide distributions, the comparative contributions of hydrographic effects and geochemical effects on curvature in Er/Nd profiles are not well defined (Piepgras and Jacobsen 1992, Bertram and Elderfield 1993, German et al. 1995).

Figure 27a compares the vertical distributions of Nd and Er in the South Atlantic and fig. 27b shows these same data in a plot which normalizes the Nd and Er concentrations

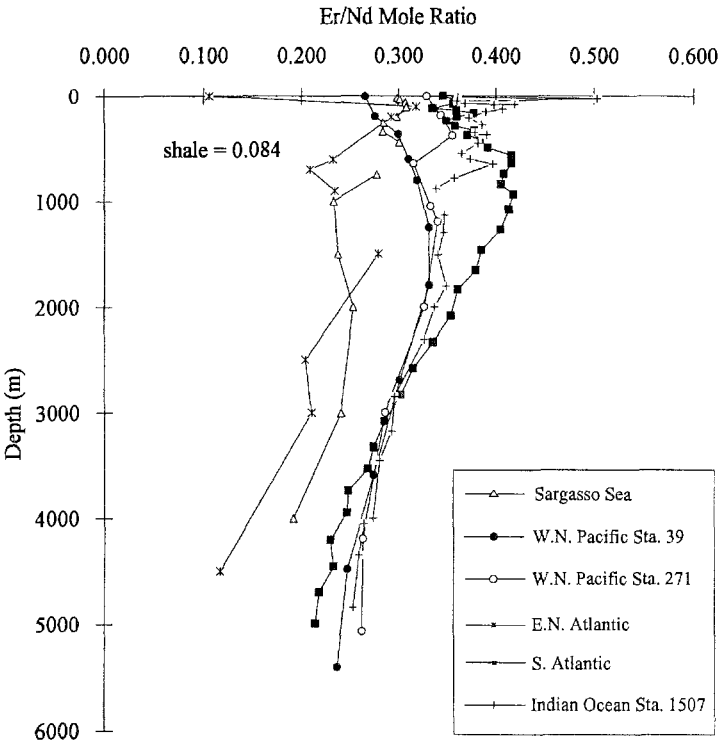

Fig. 26. A comparison of vertical profiles of the Er/Nd (mole) ratio for seawater from the Atlantic, Indian and Pacific Oceans. Stations shown in legend. Shale ratio is 0.084. Data from Elderfield and Greaves (1982), Sholkovitz and Schneider (1991), Piepgras and Jacobsen (1992), Bertram and Elderfield (1993) and German et al. (1995).

to surface water values. In deep water the light elements have larger vertical gradients than do the heavy elements. In this particular profile, Nd increases by a factor of 2.5 between 3 to 5 km while Er increases by only 50%. This relative increase of Nd over Er drives the large decrease in Er/Nd below 1000 m. Over the upper 1000 m there is a preferential increase of Er leading to a maximum in the Er/Nd ratio at about 1 km. Observed decreases in heavy(III)/light(III) ratios with increasing depth have been reported frequently (fig. 26) and have been interpreted as being controlled by a biogeochemical cycle (Elderfield and Greaves 1982, De Baar et al. 1985a,b, Elderfield 1988, Bertram and Elderfield 1993). The maximum in the Er/Nd ratio can be interpreted as being caused by (1) preferential removal of light elements by suspended particles in the productive surface waters and (2) preferential release of light elements off sinking particles in deep (>1 km) waters.

As developed in sect. 6.2, Sholkovitz et al. (1994) noted that there is systematic fractionation between the surface coatings of suspended particles and filtered seawater (fig. 17). Observation of surface coatings allows insight into particle/solution interactions responsible for fractionation. Vertical profiles of the La/Nd and La/Yb ratios of filtered

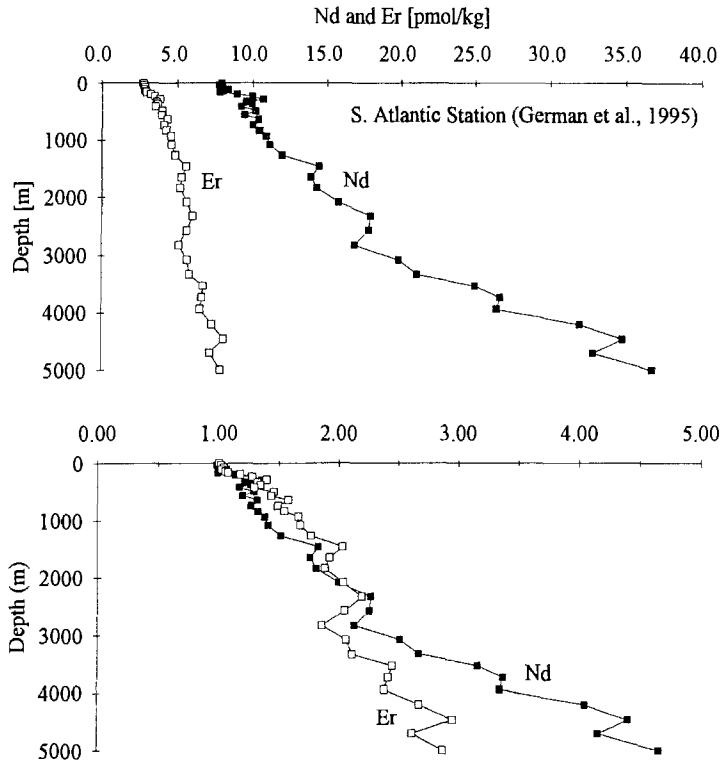

Fig. 27. Vertical profiles for a station in the South Atlantic Ocean (data from German et al. 1995): (a) dissolved concentrations of Nd and Er and (b) dissolved concentrations of Nd and Er normalized to their respective concentrations in the surface (3 m) water.

seawater and acetic acid digests (oxide and organic coatings) for suspended particles from the Sargasso Sea (figs. 28 and 29) indicate preferential removal of light lanthanides(III) onto surface coatings in the upper few hundred meters is followed by the preferential release of light lanthanides(III) at depth (Sholkovitz et al. 1994). The La/Nd ratio provides a good contrast to the La/Yb ratio as La and Nd should exhibit less fractionation due to their more similar masses. The La/Yb ratio in particle coatings increases by a factor of 1.6 between 60 and 105 m reflecting the preferential removal of light lanthanides in the upper oceans. Between 105 and 550 m this ratio reverses direction and decreases sharply (by 3.2-fold), indicating the preferential release of light lanthanides during remineralization. Between 550 and 2000 m the La/Yb ratio does not change appreciably. The La/Yb ratio of the filtered seawater, while more subtle in its vertical variation, does show systematic changes. These changes are in the opposite direction to those of the acetic acid digestions. The La/Yb seawater ratio decreases in the upper 100 m (4.0 to 3.6) and then increases to a value of 5.1 at 2000 m. While the La/Yb ratios of seawater and particle coatings are converging at depth due to fractionation during remineralization, the coatings remain

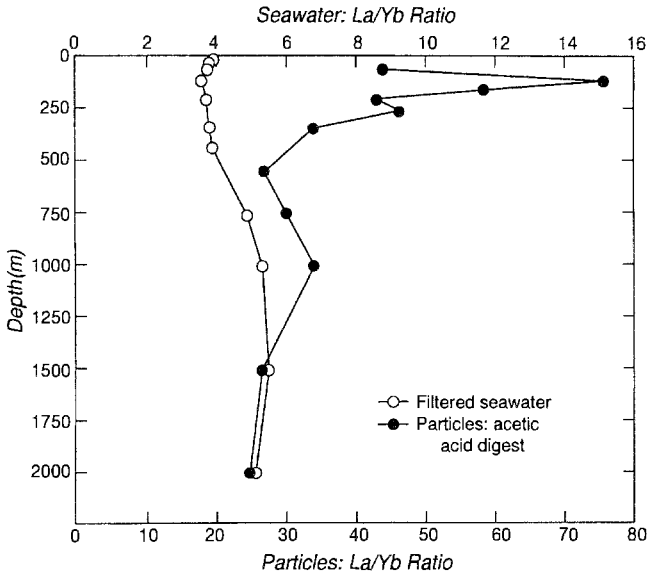

Fig. 28. Vertical profiles of the La/Yb ratios of filtered seawater and the acetic acid digestions of suspended particles from the Sargasso Sea. From Sholkovitz et al. (1994).

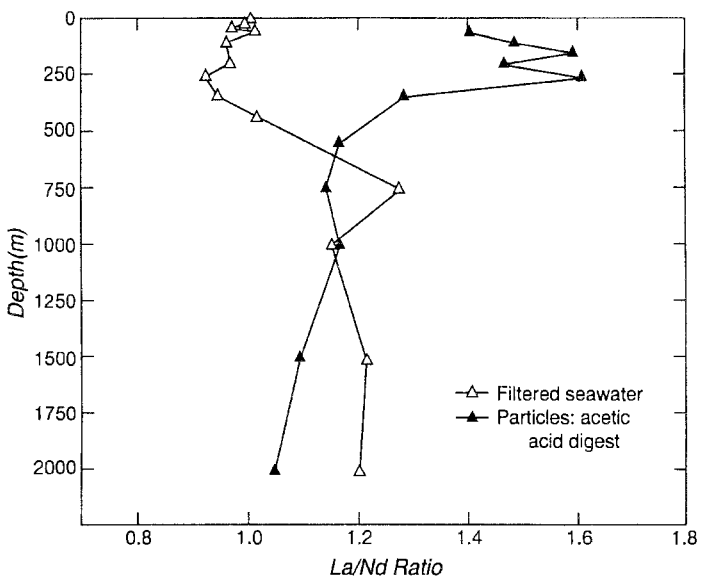

Fig. 29. Vertical profiles of the La/Nd ratios of filtered seawater and the acetic acid digestions of suspended particles from the Sargasso Sea. From Sholkovitz et al. (1994).

significantly more light-lanthanide enriched throughout the 2000 m section. As predicted, variations in the La/Nd ratios are smaller than their La/Yb counterparts. Although

Table 11
Dissolved lanthanide concentrations (pmol/kg) in the ocean water masses[a]

Water mass	La	Ce	Nd	Sm	Eu	Gd	Dy	Er	Yb	Lu	Ce anomaly	Er/Nd
AAIW	15	3.1	9.5	1.8	0.50	3.0	3.8	3.9	3.9	0.66	0.12	0.41
CDW	29	6.6	17	3.1	0.86	5.3	6.6	6.7	7.2	1.1	0.13	0.39
NADW	29	5.4	21	4.1	1.1	6.3	6.4	5.5	5.4	0.88	0.10	0.26
AABW	54	12	38	7.1	1.8	8.8	9.7	8.4	8.5	1.4	0.12	0.22
PDW	54	5.9	36	6.8	1.8	9.7	11	9.8	11	1.9	0.06	0.27

[a] Data reproduced from German et al. (1995).

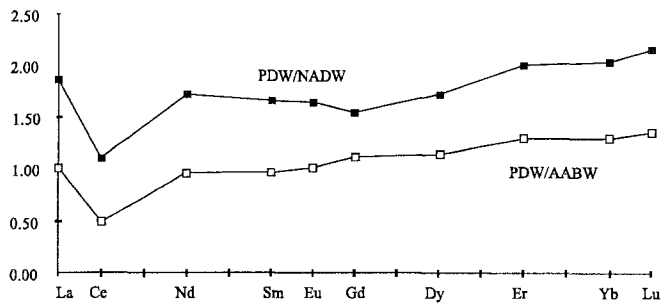

Fig. 30. A comparison of the lanthanide composition of the Pacific Deep Water (PDW) with the composition of North Atlantic Deep Water (NADW) and the composition of Antarctic Bottom Water (AABW). Plots of PDW/NADW ratios and PDW/AABW ratios. Data for water masses from German et al. (1995).

La/Nd variations are small, they are measurable and systematic. Between the surface and 250 m, preferential removal of La relative to Nd by surface coatings (La/Nd increases from 1.4 to 1.6) is mirrored by a small decrease in the La/Nd ratio (1.00 to 0.92) of the filtered seawater. Between 250 and 550 m the seawater ratio reverses directions indicating the preferential release of La off particles to the seawater. Below 1000 m the La/Nd ratios of the two phases converge and cross. This convergence and cross-over of La/Nd ratios from starting ratios of 1.0 and 1.6 in the surface waters exemplifies the active nature of fractionation resulting from surface/solution interactions. This cross-over is not observed for the La/Yb ratio as these two lanthanides exhibit a greater extent of fractionation between seawater and surface coatings.

An increase in Er/Nd ratios along the path of deep water flow is a major feature of deep waters. Bertram and Elderfield (1993) suggested that this increase is caused by preferential removal of dissolved light elements (e.g., Nd) along the transport path. Using the end-member concentrations (table 11) reported by German et al. (1995), fig. 30 provides a comparison of lanthanide concentrations in Pacific Deep Water, North Atlantic Deep Water and Antarctic Bottom Water. Excluding Ce from the discussion, there is no removal of the light lanthanides (e.g., Nd) along the path of transport. Rather, the light elements either remain constant or increase slightly. In contrast, the heavy elements do increase

more than the light elements between the NADW and PDW. In the plot of PDW/NADW composition ratios, there is a continual decrease from La (1.9) to the middle element Gd (1.5) and then a continual increase to the heaviest element Lu (2.2). Taken at face value, the PDW/NADW comparison suggests that all lanthanide concentrations increase between the deep waters of the North Atlantic and North Pacific by 1.5–2.2 times. This pattern suggests that the middle lanthanides undergo a smaller increase, and the light and heavy elements are slightly enriched, suggesting fractionation during transport. A comparison of PDW/AABW compositions shows a continual increase across the series starting with a ratio of 1.0 for La to a ratio of 1.4 for Lu. In detail, this comparison shows a flat pattern from La to Eu. From Eu to Lu the ratio increases continuously, suggesting that there is a preferential increase in the heavier lanthanides along this section of deep water transport. A more quantitative analysis of fractionation in the oceans would require a complex mixing model and more profiles.

In summary, the mass fractionation of the lanthanides remains an intriguing process controlled by complex reactions between surfaces and solution. Deciphering fractionation processes is complicated by hydrography and the variable composition of the river sources. With a growing knowledge of the solution chemistry of lanthanides in seawater (e.g. Erel and Stolper 1993, Byrne and Li 1995), it may be possible to develop a global model which incorporates geochemistry and water mass mixing in absolute and relative abundance predictions for the lanthanides. A larger coverage of the water column from the world's oceans would promote progress toward this goal.

6.5. *Suspended and trapped particles*

There have been only a few studies of the lanthanide composition of particles in the oceans. We will distinguish suspended particles collected in bottles from settling particles collected in sediment traps. Sediment trap data have been reported by Murphy and Dymond (1984), Masuzawa and Koyama (1989) and Fowler et al. (1992). Suspended-particle compositions have been reported for anoxic basins by De Baar et al. (1988) and German and Elderfield (1989, 1990). The only data for oceanic suspended particles are those of Bertram and Elderfield (1993) for the Indian Ocean and Sholkovitz et al. (1994) and Jeandel et al. (1995) for the Sargasso Sea (N. Atlantic). The latter study only measured Nd concentrations on suspended and trapped particles. A fuller discussion of the results and interpretations of particle studies is by Sholkovitz et al. (1994). A brief overview follows.

Sediment trap data provide a means of quantifying fractionation between solution and particle phases and for determining in situ processes such as remineralization and downward flux. The most comprehensive study is that by Fowler et al. (1992), who deployed traps at depths of 200, 500, 1000 and 2000 m in the northwest Mediterranean Sea. They report lanthanide data for material collected for six thirteen-day deployments over a total period of 10 weeks. Their samples were digested in strong acid (HNO_3/HF) using microwave heating. By way of example, consider samples collected between 18 June and 1 July 1990. Their 200 m trap had a crust-like composition while their 2000 m trap was both elevated in lanthanide concentrations and highly fractionated. This fractionation

takes the form of a positive Ce anomaly (1.18) and a large enrichment in the light lanthanides. Many of Fowler et al.'s deep traps from other time periods have similar fractionated compositions. Fowler et al. (1992) noted that the extent of fractionation in sediment-trapped material is much less well developed in the deep water samples after a phytoplankton bloom. The bloom yields a large increase in total sediment trap flux throughout the water column. After a high-flux period, deep samples show Ce anomalies that are negative and shale-normalized patterns for trivalent lanthanides that are flat. The authors suggested that the extent of fractionation is indirectly related to the residence time and size of particles in the water column. That is, short residence times of fast sinking particles lead to little fractionation between particles and seawater whereas longer residence times of small, slowly sinking particles lead to extensive fractionation of lanthanide(III) and the biologically mediated oxidation of Ce(III) on surfaces. Hence, it was proposed that the extent of fractionation is a kinetically controlled interaction between solution and particle phases. This conclusion was also reached by Koeppenkastrop et al. (1991) and Koeppenkastrop and DeCarlo (1992, 1993) based on laboratory uptake experiments using inorganic oxides of Mn and lanthanide radiotracers in a seawater medium. More field studies are needed to confirm the interpretations of Fowler et al. (1992).

Masuzawa and Koyama (1989) attributed the positive Ce anomalies of their sediment trap samples (Japan Sea) to a biologically-mediated oxidation process associated with the presence of Mn oxide particles. This process is discussed in detail in the subsection on Ce redox chemistry. The shale-normalized patterns of Masuzawa and Koyama (1989) do not show any consistent form from which to draw conclusions about lanthanide(III) fractionation. Only their 2750 m sample is slightly light-element enriched; the other four samples have flat or heavy-enriched patterns. Sediment trap particles from the eastern equatorial Pacific Ocean (Murphy and Dymond 1984) are strikingly different in that their shale-normalized patterns are like those of seawater: heavy-lanthanide enrichment and negative Ce anomalies.

One difficulty in interpreting particle data lies in the complexity of the particle phases. A second difficulty lies in the fact that different researchers use different dissolution procedures; hence direct comparisons are not usually possible. The results and interpretation of the study of the Sargasso Sea by Sholkovitz et al. (1994) are described in detail near the beginning of this section. These authors used a set of chemical digestions steps and concluded that a large part of the lanthanide inventory on suspended particles resides on surface coatings of Mn oxides and organic matter. Hence, more emphasis should be placed in the future on studying the phase distribution of lanthanides. This is a very difficult area of research but one which is necessary in order to understand those processes causing uptake, remineralization and fractionation of lanthanides as seawater and particles chemically interact in the water column. Similarly, the study of sediment trap particles offers opportunities to decipher key parts of the marine geochemical cycle of the lanthanides. Comparisons of dissolved, suspended and trapped material, like the one carried out for Nd and Nd isotopes by Jeandel et al. (1995), under different oceanic conditions, should prove valuable in better quantifying recycling rates, extent of fractionation, residence times and sediment input rates.

6.6. *Cerium redox cycles in the ocean*

Cerium, the only lanthanide with redox transformations at ambient oceanic conditions, has been exploited by geochemists to learn more about redox-controlled reactions in seawater. Background on the redox chemistry of Ce is presented in sect. 2. To emphasize a previous point, the Ce anomaly allows one to focus on the redox-controlled reactions of Ce by comparing its concentration to those of near neighbors (La and Nd in most cases cited next) which undergo no redox transformations. This section will focus on cerium and the Ce anomaly in open ocean seawater. The dynamic nature of the Ce redox chemistry in anoxic basins and pore waters will be discussed in the next section.

Goldberg et al. (1963) first recognized that Ce is depleted in seawater relative to its lanthanide neighbors. Carpenter and Grant (1967) carried out the first process-oriented study of Ce redox chemistry using radioactive tracers. Like Goldberg et al. (1963), they also used large volumes (100 l) of seawater to determine Ce concentrations. While both studies were pioneering, it was not until the development of more sensitive analytical methods that the Ce redox chemistry of natural waters could be understood. The following two subsections will focus on the processes operating in the upper oceans and the deep water.

6.6.1. *Upper ocean processes*

The existence of maxima in Ce anomalies in surface waters and marked decreases in the upper water column are universal features of water column profiles. This is illustrated in fig. 31 for three different regions of the world's oceans, the Sargasso Sea, the South Atlantic and the western North Pacific. The upper 750–1000 m of the water column is characterized by large gradients, termed "ceroclines" by Sholkovitz and Schneider (1991); profiles below this boundary are fairly constant in their Ce-anomaly values. Surface water anomalies cover a wide range of values (0.18 to 0.75) indicative of large regional differences. All surface water values remain below a value of 1. Hence, Ce is uniformly depleted relative to La and Nd leading to the long-known (Goldberg et al. 1963) negative shale-normalized Ce anomalies in seawater. The large Ce gradients in the upper ocean are accompanied by increasingly negative anomalies with depth. Below 1000 m the anomalies level off at values between 0.07 and 0.15. The South Atlantic profile shows a small increase in the anomaly between 4000 and 5000 m. This increase (0.05 units) coincides with a large increase (through a near-bottom gradient) in the concentrations of all the lanthanides. German et al. (1995) suggested that this gradient in the Ce anomaly reflects a benthic source with a more shale-like composition and/or bottom water with a different lanthanide composition.

The Ce-anomaly gradient in the upper water column has been studied in some detail using both field and experimental observations. Decreases in the anomaly usually reflect (a) a decrease in Ce concentration only or (b) a decrease in Ce coinciding with increases in La and Nd concentrations. An example of a type "a" profile comes from the Sargasso Sea (fig. 18) where Ce concentrations decrease in the upper 500 m by about 10 pmol/kg while La and Nd concentrations remains rather constant. Type "b" profiles exist in the South

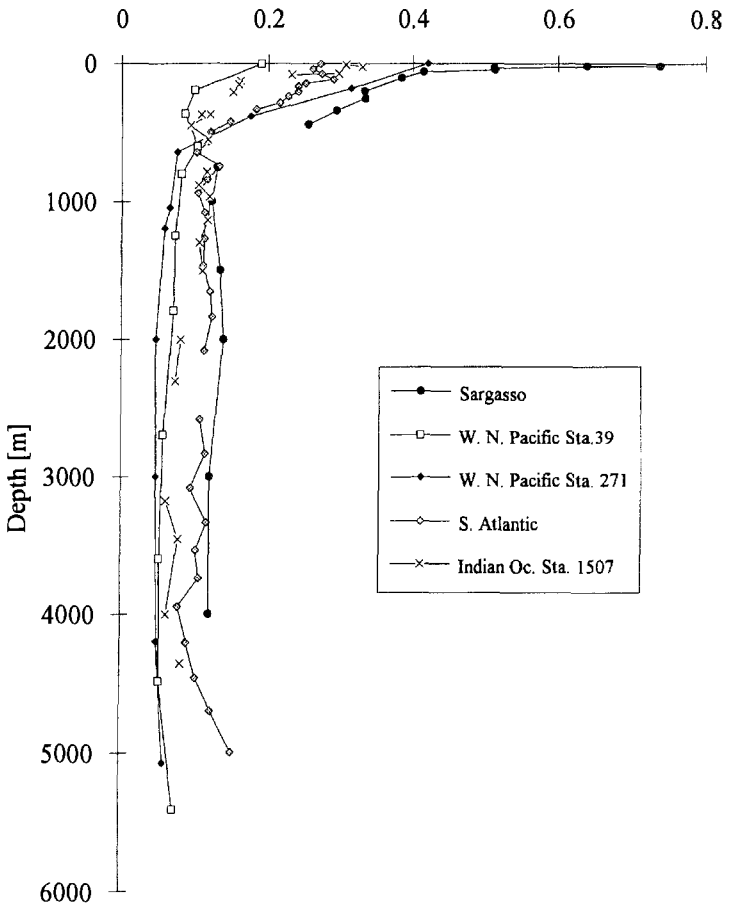

Fig. 31. A comparison of vertical profiles of the Ce anomaly for seawater from the Atlantic, Indian and Pacific Oceans. Stations shown in legend. Data from Elderfield and Greaves (1982), Sholkovitz and Schneider (1991), Piepgras and Jacobsen (1992) and German et al. (1995).

Atlantic Ocean and the western North Pacific Ocean (as described in fig. 14). In both cases it is clear that Ce in upper water column is being removed from the dissolved phase. The study of particle surface coatings by Sholkovitz et al. (1994), (discussed in sect. 6.2), demonstrates in-situ oxidation of dissolved Ce to particulate Ce. As shown in fig. 20 with a Sargasso Sea profile, there is a large continuous increase in Ce associated with the surface coatings of suspended particles between surface and 500 m water. The in-growth of Ce in the upper 500 m of the water column corresponds with the subsurface maximum in particulate Mn oxyhydroxide (fig. 19), suggesting that the oxidation of Ce(III) is directly coupled to the redox chemistry of Mn.

Moffett (1990, 1994a,b) applied a series of laboratory experiments to study the redox chemistry of Ce in seawater. This chemical approach complements the field approach

described above. His studies focused on determining the chemical and biochemical processes responsible for the upper ocean gradients in Ce and Ce anomalies. Moffett made use of radioisotopes (^{139}Ce and ^{152}Eu) to follow the redox reactions of Ce in natural waters; Eu served as a control against which the redox-driven aspects of the Ce cycle can be measured. To investigate the hypothesis that the redox chemistry of Mn in the upper oceans controls that of Ce, Moffett also used ^{54}Mn as a radiochemical probe in experiments designed to compare and to contrast the oxidation and reduction rates of Ce and Mn.

Building on the Mn oxidation rate experiments of Sunda et al. (1983) and Sunda and Huntsman (1988), Moffett (1990) used incubation experiments to determine the rates of Ce(III) and Mn(II) oxidation in Sargasso Sea samples. He observed that Ce(III) and Mn(II) have similar oxidation characteristics. From a comparison of experiments using poisoned and unpoisoned samples, Moffett (1990) showed that, like Mn, the oxidation of Ce is microbially mediated. No abiotic oxidation was observed. A second key observation is that the oxidation rate of both elements has a strong depth dependence: slow in the mixed layer and much faster in the lower euphotic zone. The rate of Ce(III) oxidation gradually increased from insignificant values at 20 m to 0.3% per day at 60 m and 0.7% per day at 200 m. The rate of Ce(III) oxidation is photosensitive whereby sunlight inhibits oxidation. This effect has been documented for Mn. Photoinhibition of Ce oxidation is consistent with field observations which show that Ce surface coating of Sargasso Sea particles commences below a depth of about 100 m (figs. 17 and 20). Reduction of Mn(IV) and Ce(IV) oxides represents the second half of their redox cycles. While the photoreduction of particulate Mn(IV) oxides in the upper oceans has been confirmed to be a key part of the cycling of Mn (Sunda et al. 1983, Sunda and Huntsman (1988), the reduction of particulate Ce(IV) to dissolved Ce(III) has not been studied. Photoreduction of Ce along with photoinhibition of Ce(III) oxidation, could serve to maintain Ce concentration maxima in the upper ocean and the large Ce-anomaly gradient observed in nature (fig. 31). This cycle would be similar to the one proposed for Mn whereby Ce(III) would be oxidized to particulate Ce(IV) below some photoactive threshold depth, and particulate Ce(IV) would be reduced to dissolved Ce(III) above this depth. Again, this cycle fits the profiles of dissolved and particulate Ce observed in the oceans.

The rate of Ce oxidation is three to four times slower than that of Mn in the 100–200 m zone of the Sargasso Sea. This difference in rates is consistent with water column profiles which show that Mn concentration gradients in the upper 200 meters are approximately 2.5 times larger than those of Ce (figs. 18 and 19). Moffett (1990) also compared the oxidation of Ce in Sargasso Sea seawater with that of a coastal site (Vineyard Sound, MA, USA). The rate of microbial oxidation of Ce was about 50 times faster than the highest measured rate in the Sargasso Sea. The increased rates of microbial oxidation and adsorption of Ce were attributed to the higher concentration of biogenic particles in this coastal site.

Further investigation (Moffett 1994a,b) of the relationship between Ce and Mn oxidation in the coastal zone (Vineyard Sound and Chesapeake Bay) showed that the

specific rates of Ce(III) and Mn(II) oxidation co-vary over a wide range of environments and values, and indicate the existence of a mechanistic relationship. "The results are consistent with a common oxidative pathway for Ce and Mn ... non-biological Ce oxidation on freshly formed Mn oxides is unlikely" (Moffett 1994a). The oxidation of Ce is closely coupled to the microbially-mediated oxidation of dissolved Mn(II) to particulate Mn(IV) oxides. Data can be modeled (Moffett 1994a) by a set of chemical reactions and rate equations in which Ce(III) in solution is first rapidly adsorbed to Mn(IV) oxide particles and then slowly microbially oxidized to particulate Ce(IV). In a study of Chesapeake Bay, Moffett (1994b) showed that the rate of Ce oxidation was several orders of magnitude higher during the warm summer months than in the cold winter months. "The seasonal differences probably reflect strong seasonal variations in the abundance of Mn-oxidizing bacteria.... The specific rates of oxidation for both elements (Ce and Mn) were over 1000 times higher than those measured in the Sargasso Sea. However, the specific rates for Ce(III) and Mn(II) were similar to each other. This fact, coupled with similar spatial and temporal trends for specific oxidation rates, suggests a common mechanism of oxidation of both elements which may be significant in a wide range of marine environments" (quote from abstract of Moffett 1994b).

Masuzawa and Koyama (1989) reported positive Ce anomalies on settling particles collected in sediment traps deployed in the Japan Sea. They noted a strong relationship between excess (excess being that quantity over and above that contained in detrital minerals) solid phase Ce and Mn concentrations and suggested that the formation of particulate Mn(IV) oxides is a key process responsible for the preferential removal of Ce from the water column.

6.6.2. *Ce redox chemistry in deep waters*

The oxidative removal of Ce from the deep ocean has been addressed in several studies (Elderfield 1988, Bertram and Elderfield 1993, German et al. 1995). As briefly mentioned earlier in this section and illustrated in figs. 14 and 31, the deep waters of the Pacific Ocean have a more negative Ce anomaly than do the deep waters of Atlantic Ocean. German et al. (1995) compiled all the existing data for Ce anomalies of deep waters (<1000 m) of the Atlantic, Pacific and Indian Oceans and plotted these values against silica concentrations (fig. 32). To quote German et al. (1995), "A trend of more negative Ce anomaly with increasing dissolved Si concentrations is seen, indicating progressive Ce fractionation along the flow direction of oceanic deep waters. Because fractionation of dissolved Ce from its trivalent REE neighbors can only be effected by oxidation of dissolved Ce^{3+} and precipitation of some insoluble Ce(IV)-oxide phase, the observed trend in Ce/Ce^* values provides evidence that dissolved Ce^{3+} oxidation occurs over the mixing time of the deep ocean.". From an earlier compilation of the same data Elderfield (1988) estimated that the oxidation rate of Ce(III) in the direction of deep water flow was similar in magnitude to the input rate of dissolved Ce(III) from the rivers. One cautionary remark with respect to interpreting the trend of fig. 32 is the fact that the Ce anomaly only decreases by a small (0.10 to 0.05) amount over the major part of the deep-water transport

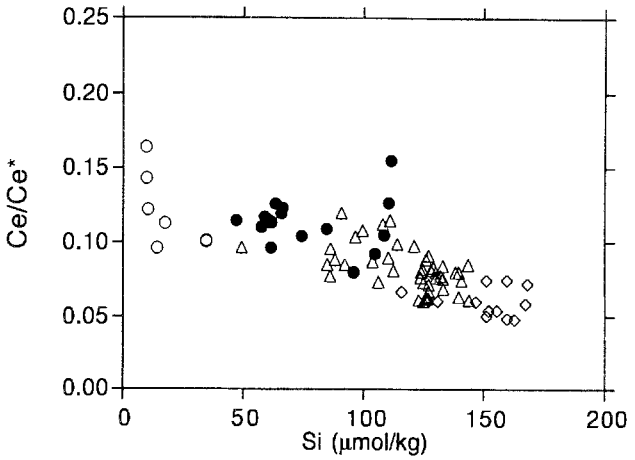

Fig. 32. Plot of Ce/Ce* vs. dissolved Si concentrations from the North Atlantic Ocean (open circles, Greaves et al. 1991, Mitra et al. 1994); from the southeastern Atlantic Ocean (solid circles, German et al. 1995); from the Indian Ocean (open triangles, Bertram and Elderfield 1993); and from the Pacific Ocean (open diamonds, Piepgras and Jacobsen 1992). Linear regression of the data (excluding AABW-influenced southeastern Atlantic bottom waters) yields the equation $Ce/Ce^* = 0.136 - 0.000463\,[Si]$ $(r^2 = 0.67)$. From German et al. (1995).

path. The different ocean basins have a cluster of data points along the trend. German et al. (1995) have measured and calculated the end-member Ce anomalies of the major deep water masses; the North Atlantic Deep Water and the Pacific Deep Water, for example, have values of 0.12 and 0.06 respectively. It is a tribute to their analytical methods, that small differences in inter-ocean composition can be measured.

Ce-anomaly data presented by Bertram and Elderfield (1993) are shown in figs. 23 and 24. These two figures demonstrate that the majority of ocean samples (surface and deep) have anomalies below 0.5 with no correlation between Ce concentration and the Ce anomaly. The histogram in fig. 25 shows the distribution of values in the three oceans. Bertram and Elderfield (1993) concluded that the average Ce anomalies of deep waters decrease in the following sequence: Atlantic (0.16 ± 0.05) > Indian (0.09 ± 0.02) and Pacific (0.08 ± 0.03). They also noted that the anomaly values of rivers (0.3–1.2) are more positive than those of surface seawater which, in turn, exceed those of deep waters. Hence, there is large scale oxidative removal of dissolved Ce(III) from the upper oceans and additional removal along the flow of deep water between the ocean basins.

6.7. *The Nd and Ce isotopic composition of the oceans*

The objective of this section is to provide a short overview of the Nd isotopic composition of the oceans. Nd isotopes have been applied to a large range of problems in earth science (see books by Henderson 1984 and Taylor and McLennan 1985). When combined with the signature of lanthanide concentrations, the Nd isotopic composition of rocks and minerals is an excellent indicator of differentiation and chemical evolution of the earth

and of the provenance and age of detrital minerals. The study of Nd isotopes in river and seawater naturally evolved from studies on the geochemistry of petrogenesis (Goldstein and Jacobsen 1987, 1988b). This evolution was driven, in part, by the development of analytical methods. Articles by Piepgras and Jacobsen (1988), Bertram and Elderfield (1993) and Jeandel et al. (1995) provide a good background and discussion on the subject of the Nd isotopic composition of the oceans.

A suite of publications describing Nd isotopes in seawater followed the first measurements by Piepgras et al. (1979). These works include Andersson et al. (1992), Bertram and Elderfield (1993), Elderfield (1988), Henry et al. (1994), Jeandel (1993), Jeandel et al. (1995), Piepgras and Jacobsen (1988), Piepgras and Wasserburg (1980, 1982, 1983, 1985, 1987), Piepgras et al. (1979), Shimizu et al. (1994), Spivack and Wasserburg (1988) and Stordal and Wasserburg (1986). The studies by Goldstein and Jacobsen (1987, 1988b) are key ones with respect to the Nd isotopic composition of river water. Isotopic measurements of Mn nodules, sediments and dust also contribute greatly to our understanding of the Nd isotopic composition of seawater (e.g., Albarède and Goldstein 1992, Alpin et al. 1986, Frost et al. 1986, Goldstein and O'Nions 1981, Goldstein et al. 1984, Jones et al. 1994, McLennan et al. 1990, Naki et al. 1993, O'Nions et al. 1978). Papers on sedimentary phases will not be discussed.

Nd isotopic composition measurement of seawater is difficult. Difficulties arise from the need to collect high-precision Nd isotope ratios on samples with only a small amount of Nd (approximately 2 ng per kg of seawater vs. 40 μg Nd per gram of continental crust). Typically, the lanthanides are extracted and pre-concentrated from 10–30 kg samples of seawater, and Nd is separated from its neighbors. The $^{143}Nd/^{144}Nd$ ratio is measured by thermal ionization mass spectrometry (e.g., Piepgras et al. 1979, Piepgras and Jacobsen 1988, Bertram and Elderfield 1993).

Isotopic fractionation of Nd occurs within rocks. One of the isotopes of Sm, ^{147}Sm, undergoes alpha decay (half-life of 1.06×10^{11} years) to ^{143}Nd. Because of fractionation within the earth, different rocks have evolved with different ratios of Sm to Nd. Fractionation of lanthanides during the crystallization of rock has segregated materials into light depleted oceanic mantle and light enriched continental crust, each with distinctive Sm/Nd and ages. Hence, the combination of radioactive decay and source rocks with different Sm/Nd leads to rocks with different Nd isotopic compositions or different ratios of radiogenic ^{143}Nd to non-radiogenic ^{144}Nd. The isotopic composition ($^{143}Nd/^{144}Nd$) variations are expressed as

$$\varepsilon_{Nd}(0) = \left(\frac{(^{143}Nd/^{144}Nd)_{meas.}}{0.512636} - 1 \right) \times 10000,$$

where 0.512636 is the present-day value for CHUR (Chondritic Uniform Reservoir).

Oceanic crustal rocks are characterized by positive ε_{Nd} values (0 to + 10). In marked contrast, the continental crust has negative values (−10 to −30). Hence, the weathering of different rock types delivers Nd, in dissolved and particulate river matter, with regionally distinct isotopic compositions (Goldstein and Jacobsen 1987, 1988b). Rivers

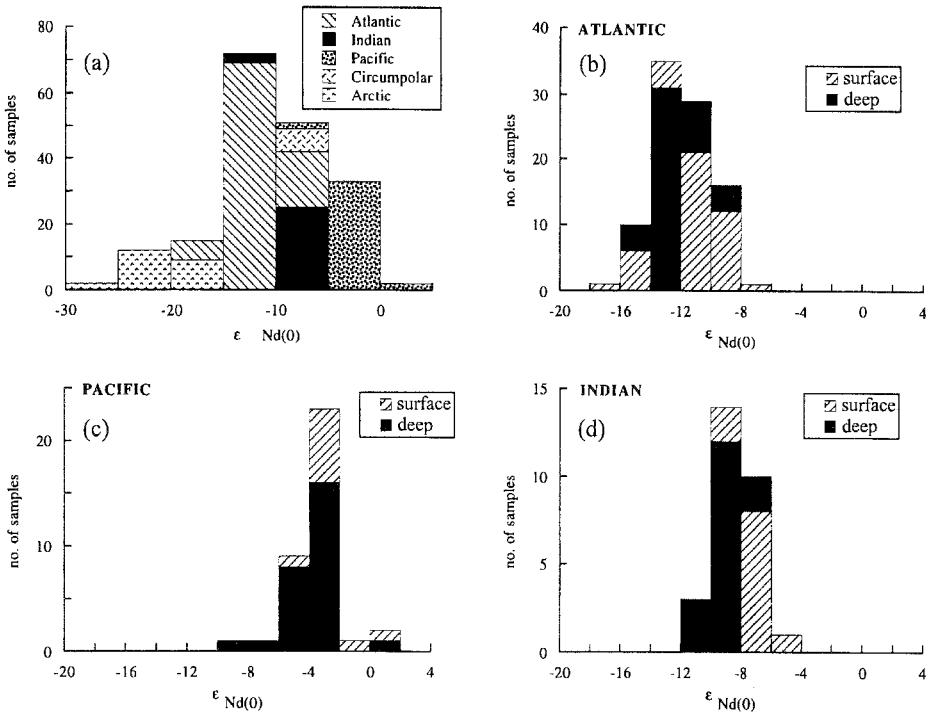

Fig. 33. Histograms of neodymium isotopic compositions: (a) compilation of all oceanic data; (b–d) comparison of surface (<1 km) and deep waters (>1 km) for Atlantic, Indian, and Pacific Oceans, respectively. From Bertram and Elderfield (1993).

draining into the Atlantic Ocean have been estimated to have a weighted average of $\varepsilon_{Nd}(0) = -10.8$ to -12.6 while values for rivers draining into the Pacific are much lower, -2.9 to -3.7 (Goldstein and Jacobsen 1987). Rivers entering the Indian Ocean have an intermediate averaged composition (-9). Dissolved matter and particulate matter in rivers are isotopically similar. The regional differences in source composition reflect the relative importance of continental and oceanic crust weathered around each ocean basin. For example, the Pacific Ocean receives river water draining both old continental crust of China ($\varepsilon_{Nd}(0) \approx -10$ to -12) and young volcanic islands (e.g., Japan, Philippines) with positive values of $\varepsilon_{Nd}(0)$. Rivers entering the Atlantic Ocean drain old continental crust, an extreme example being the -20 values reported for $\varepsilon_{Nd}(0)$ of Baffin Bay in Canada (Stordal and Wasserburg 1986).

The major observation is that each major ocean basin is characterized by a distinct Nd isotopic composition. There is some overlap in deep waters due to mixing of water masses. The averaged values of Atlantic, Indian and Pacific Ocean are -12, -8 and -3 (Piepgras et al. 1979, Piepgras and Wasserburg 1980, 1983, Piepgras and Jacobsen 1988, Bertram and Elderfield 1993). This inter-ocean difference is presented in histograms for surface and deep waters (fig. 33). The isotopic composition of seawater reflects the averaged Nd

isotopic composition of dissolved river Nd entering the three ocean basins; the ε_{Nd} values are estimated to be −12.6, −8.7 and −2.9 respectively (Goldstein and Jacobsen 1987, 1988b). Hence, the inter-oceanic variation can be qualitatively explained by variations in Nd isotopic composition of river waters which, in turn, reflect the isotopic composition of the land masses being weathered.

In order to maintain inter-ocean differences in Nd isotopic composition, the ocean residence time (replacement time) of dissolved Nd must be shorter (i.e., <1000 years) than the mixing time of the ocean water. In this regard, it is instructive to compare the Nd and Sr isotopic composition of the oceans. In marked contrast to Nd, the Sr isotopic composition of seawater is exactly the same in all three ocean basins even though the river sources to each ocean are isotopically different in both Sr and Nd (Goldstein and Jacobsen 1987). Because Sr has a very long (~10^6 years) residence time relative to the mixing time of the oceans, the Sr isotopic composition of the oceans is uniform.

A fundamental dilemma arises when trying to reconcile the inter-ocean variations in the isotopic composition of Nd with the estimated long oceanic residence time of Nd (Goldstein and Jacobsen 1987, Bertram and Elderfield 1993). Goldstein and Jacobsen (1988b) calculated a 7100 year ocean residence time based on the *effective* river water flux of Nd. The effective flux is the total dissolved river flux minus the removal of dissolved Nd during estuarine mixing. The authors employed a 70% removal in their calculations. An earlier estimate of the oceanic residence time of Nd by Elderfield and Greaves (1982) yielded a value of about 4400 year. This value, based on an effective river flux, is derived using a river dissolved Nd concentration of 1010 pmol/kg, a value which greatly exceeds the 280 pmol/kg world river average value used by Goldstein and Jacobsen (1988a). On the good assumption that the latter is a better estimate, the 4400 year Nd residence time of Elderfield and Greaves (1982) would increase to 15 000 years. Hence, it appears, based solely on river input of dissolved Nd, that the oceanic residence time of Nd (and other lanthanides) greatly exceeds the 500–1000 year mixing time of ocean water.

Jeandel et al. (1995) concluded that 50% of the particulate Nd leaving the surface is remineralized back to the deep waters and estimated a "scavenged Nd residence time of approximately 1900 y ...". They reached these conclusions from a vertical transport model which used their measurements of the Nd isotopic composition of small suspended particles and large sinking particles in the Sargasso Sea. The uptake of Nd onto the surfaces of suspended particles and the reversible exchange of Nd during the remineralization of sinking particles was used by these authors to explain Nd isotopic variations within the water column of the Sargasso Sea and between the three ocean basins.

Goldstein and Jacobsen (1987, 1988b) concluded that an additional source of Nd to the oceans is required in order to lower the residence time by a factor of about 10 and maintain the inter-oceanic variations in the Nd isotopic composition. The missing source(s) of Nd to the three oceans would need to be isotopically different, like those of the averaged river fluxes. The authors argued that neither hydrothermal nor atmospheric sources are quantitatively important, leaving the dilemma unresolved. Estimates of atmospheric fluxes resulted in only a doubling of the total dissolved Nd flux to the

oceans (Sholkovitz et al. 1993, Greaves et al. 1994). As pointed out by Goldstein and Jacobsen (1987), Naki et al. (1993) and Jones et al. (1994), dust reaching the North Pacific Ocean is derived mainly from the continental soils of China and, as a consequence, has an Nd isotopic composition ($\varepsilon_{Nd} \approx -10$) which is quite different from that ocean's composition (−2 to −5). These authors concluded that dissolution of Nd from Asian dust is not a quantitatively important process. Furthermore, Jones et al. (1994) disagreed with the conclusion of Albarède and Goldstein (1992) that the Nd isotopic composition of the oceans is controlled by the release of Nd from eolian detrital sediments. From their detailed synthesis of the processes responsible for the Nd isotopic composition of the Pacific Ocean, Jones et al. (1994) argued that neither the dissolution of Asian dust reaching the central Pacific Ocean nor dissolution of margin sediments from volcanic islands are important sources of dissolved Nd to the North Pacific. Recently, Bertram and Elderfield (1993) constructed a seven-box model for the Nd isotopic composition of the oceans. They concluded that "... interoceanic variations in neodymium compositions and Nd concentrations cannot be reconciled unless particle–water exchange is invoked, unless inputs to the oceans are much larger than currently envisioned." Based on estuarine studies, Sholkovitz (1993, 1995) suggested that the release of Nd from coastal estuarine sediments may be a major unrecognized source of dissolved Nd to the oceans; this explanation was also invoked by Jones et al. (1994). However, there are no reliable estimates of sedimentary fluxes of dissolved Nd. The sources and processes maintaining inter-ocean differences in Nd isotopic composition require further quantification. In particular, studies in the western North Pacific Ocean are important as this is a region with high weathering rates and isotopically different sources.

Many studies have applied inter-ocean differences of Nd isotopes as tracers for global or basin-wide ocean circulation. Key references include Bertram and Elderfield (1993), Elderfield (1988), Jeandel (1993), Piepgras and Jacobsen (1988), Piepgras and Wasserburg (1980, 1982, 1983, 1985, 1987), and Piepgras et al. (1979). By way of example, the radiogenic signature of North Atlantic deep water can be used to trace deep and bottom water circulation through the southern oceans and into the Pacific Ocean. On a smaller scale, there is vertical structure in the Nd isotopic composition of seawater within individual profiles. This structure has been interpreted to reflect the different sources of water (e.g., Piepgras and Jacobsen 1988). This point is illustrated in sect. 6.2 in which a case study of the western North Pacific Ocean is presented (fig. 21).

There is a small and emerging literature on the isotopic systematics of Ce in the oceans. Elderfield (1992), in a short overview of this subject, raises points of concern with respect to interpreting the isotopic data. Recently, Shimizu et al. (1994) presented data on the Ce isotopic composition of the oceans. An earlier paper from the same group reported on the Ce isotopic composition of ferromanganese nodules (Amakawa et al. 1991). The La–Ce isotopic system is based on the decay of ^{138}La to ^{138}Ce with a half-life of 2.5×10^{11} years. Hence, the application behind the Ce isotopic system is similar to that of the Nd isotopic system. For example, as with Nd and Sr isotopes, continental and ocean crust have different Ce isotopic compositions. In principle, these differences can be exploited as a new indicator of the sources of lanthanides (Ce) to seawater and

to authigenic minerals such as in Mn nodules. Because the redox shift of Ce makes this lanthanide more mobile than the others, the Ce isotopic composition should help to constrain the source and cycling of Ce in the oceans. In practice, the measurement of the Ce isotopic composition of seawater is more difficult than that of the Nd isotopes (Shimizu et al. 1994). Given the small number of papers on this subject, this article will not provide a fuller discussion of Ce isotopes.

In summary, the distinct Nd isotopic composition of the major ocean basins and the rivers feeding these basins make Nd unique amongst other tracers. This feature has been exploited as provenance indicators of wind- and ocean-borne sediments, as tracers for water circulation within and between ocean basins and as probes for particle–solution interactions in seawater. Reliable values for ocean residence times of the lanthanides are still needed. The inter-oceanic differences in Nd isotopic composition suggest short residence times whereas river/estuarine studies points to long residence times. This dilemma has lead to the hypothesis that Nd (and other lanthanides) are being added to the oceans from the sediments.

7. Lanthanide cycling in anoxic marine basins, pore waters and hydrothermal waters

7.1. *Anoxic marine basins*

Redox potential (oxidation–reduction) is considered a master variable with respect to controls on the concentration and speciation of many trace elements in natural waters (Stumm and Morgan 1981). Shifts between oxic, suboxic and anoxic conditions represent one of nature's most dramatic chemical variations. The response of lanthanides to variations in redox conditions has been studied in many of the world's classic anoxic and suboxic basins. These include: (1) the Black Sea (German et al. 1991, Schijf et al. 1991, 1994, Schijf and De Baar 1995), (2) Saanich Inlet (Canada) (German and Elderfield 1989), (3) Chesapeake Bay (Sholkovitz and Elderfield 1988, Sholkovitz et al. 1992), (4) the Cariaco Trench (De Baar et al. 1988), (5) the Mediterranean Sea (Schijf et al. 1995) and (6) the northwest Indian Ocean (German and Elderfield 1990). The latter two regions are located on ocean shelves while the first three basins are estuarine and coastal. Data from the papers cited above are compiled in table A12.

The objective of this section is to describe the major features of lanthanides in the water column of anoxic basins and briefly discuss the mechanisms responsible for spatial and temporal variations. Two examples will be used, the Black Sea and Chesapeake Bay. The next subsection on lanthanides in pore waters follows naturally in that many of the processes operating in anoxic water columns occur in marine sediments.

The following features emerge from all studies of lanthanides in anoxic marine basins:

(1) The transition from oxic to anoxic conditions results in large increases in the dissolved concentrations of all lanthanides. Sharp gradients develop across oxic/anoxic boundaries.

(2) The increase in concentration between oxic and anoxic waters is accompanied by large scale fractionation of the trivalent-only lanthanides. Although these elements have no redox chemistry of their own, their absolute and relative abundance are altered by variations in redox conditions, in particular the cycling of iron and manganese.
(3) Cerium, with its own redox chemistry, undergoes extensive fractionation between oxic and anoxic waters. Ce is preferentially released to anoxic water as it is reduced from particulate Ce(IV) to dissolved Ce(III). Hence, large Ce anomalies develop across redox boundaries.
(4) A time-series study of Chesapeake Bay demonstrated that the dissolved lanthanides have a large seasonal cycle in both the water column and pore water in response to the development of anoxia in the spring and reoxygenation in the fall (Sholkovitz et al. 1992). Short-term variations in fractionation accompany the release and removal of lanthanides from the water column under seasonally-varying redox conditions.

Before presenting two case studies, it is instructive to consider De Baar et al.'s (1988) geochemical cycle for lanthanides in anoxic basins. They proposed that the oxides of Fe and/or Mn scavenge dissolved lanthanides from oxic seawater, transport them downward on sinking particles and release them to suboxic and anoxic waters as the oxides themselves are reduced to dissolved Fe(II) and Mn(II). Hence, the strictly-trivalent lanthanides are coupled to the active redox chemistry and cycles of Fe and Mn. In the De Baar et al. (1988) model, fractionation occurs during the redox cycling of Fe and Mn because the heavier lanthanides form stronger complexes with ligands in solution leaving the lighter lanthanides preferentially adsorbed to the oxide surfaces. This difference in binding of lanthanides to the surface of oxide particles is critical in that it results in the preferential removal of dissolved light lanthanides above the oxic/anoxic boundary and their preferential release below the boundary. In essence, there is a distillation of lanthanides driven by a combination of solution chemistry and the formation, transport and dissolution of Fe/Mn oxides in anoxic basins.

Figure 34 (from German et al. 1991) shows a series of vertical profiles from the Black Sea where the dissolved oxygen concentration reaches undetectable values at 90–100 m. Note the large gradients in dissolved Fe and Mn across the oxic/anoxic boundary. The production of high concentrations of hydrogen sulfide in the anoxic waters results in the removal of dissolved Fe as insoluble iron sulfides; the formation of particulate Mn oxides in the water column above the oxic/anoxic boundary (not shown) is a prominent feature of the profile. As illustrated with Nd and Er, the concentrations of strictly-trivalent dissolved lanthanides decrease slightly from the oxic surface waters to the anoxic boundary and then increase markedly (3-to-4-fold) across the oxic/anoxic boundary. The decrease in the upper region is attributed to the scavenging of dissolved lanthanides by Mn oxide particles. The large increase in anoxic waters is attributed to the release of Mn oxide-bound lanthanides as this carrier phase is reduced to soluble Mn(II). Different opinions have been published as to the relative importance of the Mn and Fe cycles on the lanthanide cycles in anoxic basins (Sholkovitz 1992a, German et al. 1992). Nevertheless, the main conclusion remains that the distribution and cycling of the lanthanides are closely

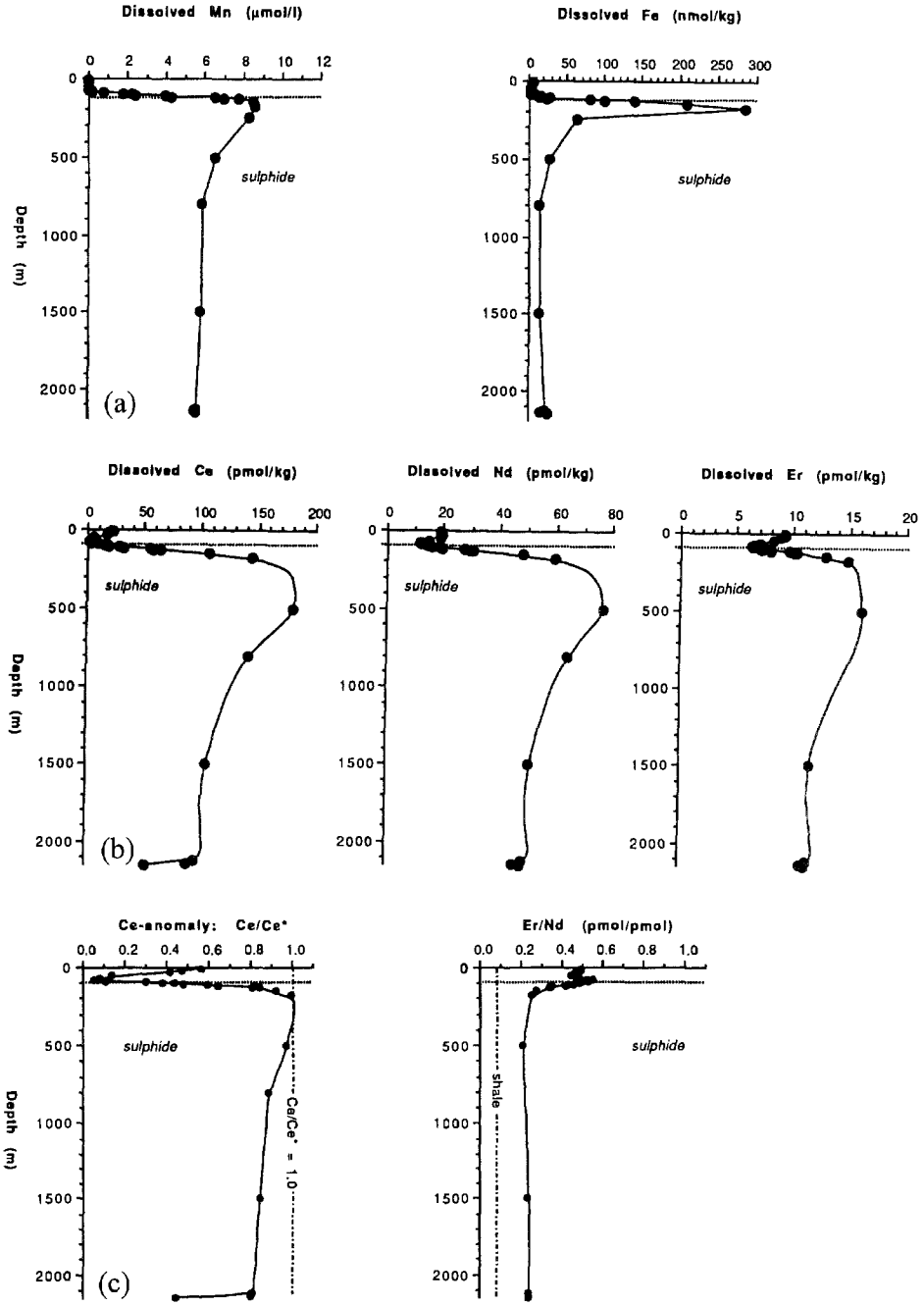

Fig. 34. Vertical profiles of dissolved trace metals at station BS3-6: (a) Mn and Fe (data from Lewis and Landing 1991); (b) Ce, Nd, and Er; (c) the Ce anomaly: Ce/Ce* (after De Baar et al. 1985a) and Er/Nd. The dashed line represents the depth of the sulfide interface. From German et al. (1991).

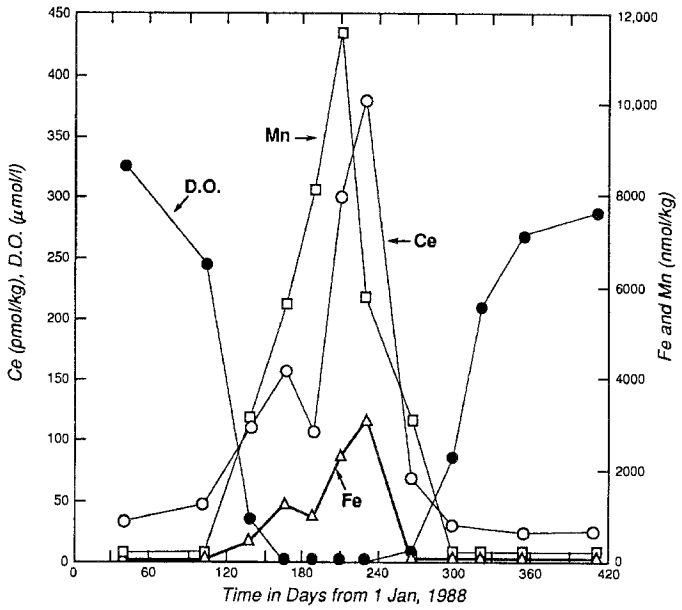

Fig. 35. Concentration of dissolved oxygen, and dissolved Fe, Mn, and Ce in the bottom water (28 m) as a function of time for the CHEER time-series study of Chesapeake Bay. From Sholkovitz et al. (1992).

associated with the redox cycles of Mn and/or Fe. The depth plot of the Nd/Er ratio exhibits extensive fractionation as lanthanides are removed from the oxic waters and released to anoxic waters. The Nd/Er ratio increases 3-to-4-fold across the boundary and into the upper part of the anoxic water column. This change reflects the preferential release of the lighter lanthanides in anoxic waters. As shown by German et al. (1991) (their fig. 2), the shape of the shale-normalized patterns also changes from the oxic upper waters to the lower anoxic waters. The former are strongly heavy-lanthanide enriched (as is typical of ocean water) and the latter are flatter in response to the preferential release of the lighter lanthanides. Hence, fractionation within the trivalent lanthanides is such that the extent of release increases from Lu to La (light > middle > heavy). This observation is consistent with the fractionation model described earlier in this section.

Chesapeake Bay, with its seasonally anoxic deep waters, is an excellent natural laboratory to study the coupling between redox conditions and lanthanide cycling. Vertical profiles of other anoxic basins have only yielded a snap-shot of dynamic geochemical and physical systems. Sholkovitz et al. (1992) carried out a time-series sampling study (called CHEER) of one deep basin in Chesapeake Bay in order to document the response of lanthanides to seasonally-varying redox conditions. Their bottom water data are presented in figs. 35–37, and their pore water data are discussed in the next section. The dissolved oxygen time series in fig. 35 shows that the bottom waters go anoxic in the summer and are reoxygenated in the fall. The dissolved concentrations of elements with a redox chemistry, Fe, Mn and Ce, all exhibit large increases as anoxia develops

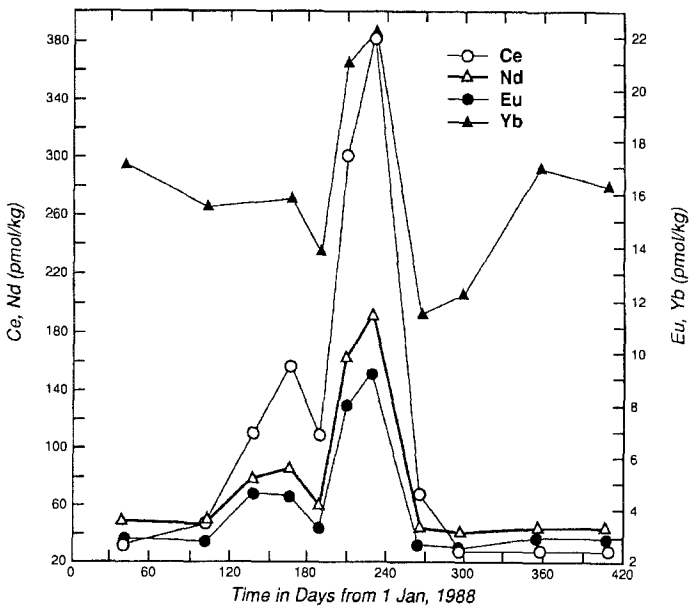

Fig. 36. Concentration of dissolved Ce, Nd, Eu, and Yb in the bottom water (28 m) as a function of time for the CHEER time-series study of Chesapeake Bay. From Sholkovitz et al. (1992).

and sharp decreases during reoxygenation. As illustrated for Nd, Eu and Yb in fig. 36, the strictly trivalent dissolved lanthanides also show well-developed seasonal cycles. Their concentrations increase in response to anoxia and decrease with reoxygenation in the fall. The closure on the year time series is excellent. There is a very high correlation between the time-series cycles of dissolved Fe and the lanthanides. It appears that iron oxide phases are controlling the release and removal of dissolved lanthanides in association with the seasonal redox cycle of iron.

Large scale fractionation accompanies the seasonal cycle of the dissolved lanthanide concentrations in Chesapeake Bay. This is illustrated in fig. 37 which presents the time series of the Nd/Yb ratio for bottom waters (and upper pore waters). This light to heavy lanthanide ratio increases in the spring and is followed by an equally large decrease in the fall. At its maximum in the summer, the Nd/Yb ratio is three times greater than its winter baseline ratio. Hence, the lighter lanthanides are preferentially released in the spring and summer and then preferentially removed in the fall.

Shale-normalized patterns quantify the extent of fractionation during periods of anoxia as illustrated by the water column data collected from different depths of Chesapeake Bay on 26 July 1988 (fig. 38). The oxic surface water exhibits a heavy-enrichment and large negative Ce anomaly while anoxic bottom water has an almost flat pattern and a small negative Ce anomaly. Hence the lanthanide composition shifts away from the heavy-enriched pattern of oxic seawater toward one that is more crust-like. As redox conditions become more reducing, the relative order of trivalent lanthanide release to the

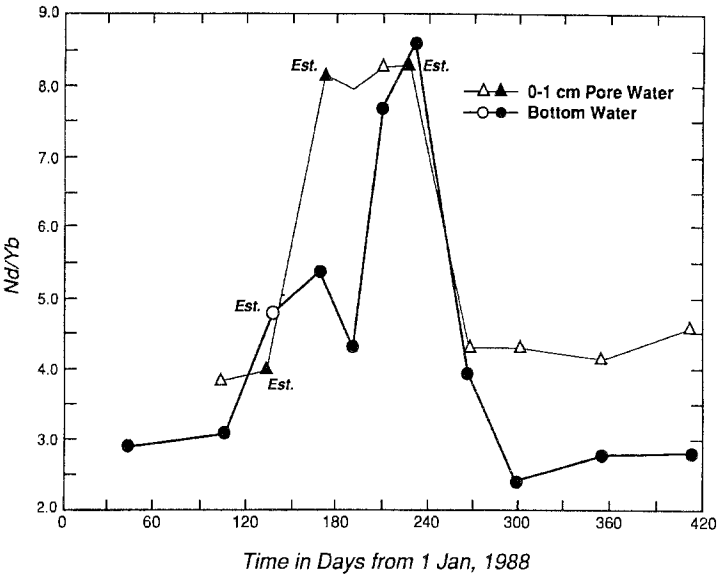

Fig. 37. Temporal variation of the Nd/Yb ratio in the bottom water and upper porewater for the CHEER time-series study of Chesapeake Bay. Four symbols refer to "estimated" values, as the heavy-lanthanide (Yb) fractions from these samples were lost (see sect. 3). The Yb concentrations were estimated by using the shale-normalized patterns generated from the light lanthanide and middle lanthanide fractions and extrapolating to Yb. This leads to good (±10%) estimates as the lanthanide patterns are smooth (see fig. 7). From Sholkovitz et al. (1992).

deep water is light > middle > heavy. The top plot in fig. 38 shows that the anoxic waters relative to oxic surface water are systematically and progressively enriched toward the light trivalent lanthanides. Lu concentrations barely increase whereas La is ten-fold higher in the anoxic waters. During reoxygenation in the fall the order of lanthanide removal from the deep waters remains the same, light > middle > heavy. After reoxygenation in the fall, the shale pattern returns to that of oxic seawater. This type of fractionation is consistent with the model of De Baar et al. (1988) in which the formation of oxides of Fe and Mn preferentially removes the lighter lanthanides from oxic seawater and the reductive solubilization of these oxides releases this fractionated composition to anoxic waters.

Ce anomalies are major features of anoxic basins. The Black Sea Ce anomaly has two sharp gradients, one between the oxic surface waters and the anoxic/oxic boundary and one across the anoxic/oxic boundary (fig. 34). The first gradient reflects the preferential removal of dissolved Ce by the formation of Mn oxide particles above the anoxic boundary. This removal includes both the oxidation of dissolved Ce(III) to particulate Ce(IV) and the adsorption of Ce(III) onto oxide surfaces. These processes lower the Ce anomaly to 0.1, a value much smaller than that of the surface water (0.6). The second gradient is extremely large, 0.1–1.0, and reflects the preferential release of dissolved Ce to the anoxic waters. This release is driven by the reduction of Ce(IV)-enriched oxide particles and by the release of Ce(III) bound to dissolving oxide particles.

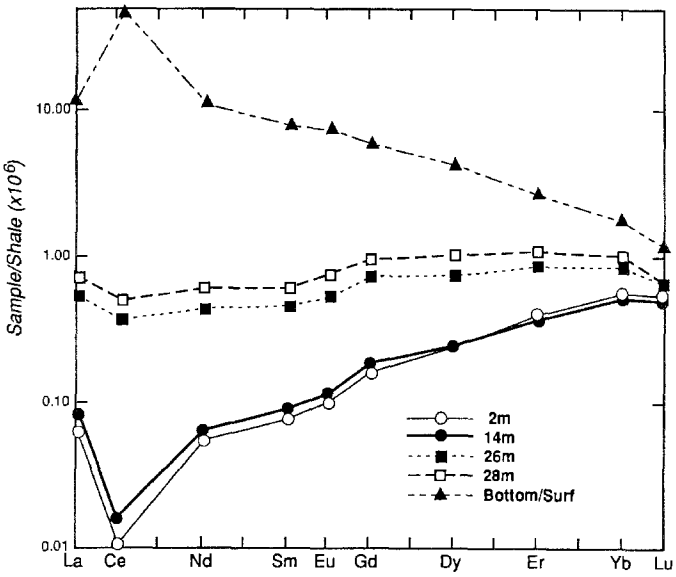

Fig. 38. Shale-normalized lanthanide patterns for CHEER 6 (26 July 1988) filtered samples; comparison of oxic surface waters, anoxic bottom waters, and anoxic upper porewater. Also shown is the pattern resulting from the normalization of the lanthanide concentrations of the anoxic bottom waters relative to the lanthanide concentrations of the oxic surface waters. From Sholkovitz et al. (1992).

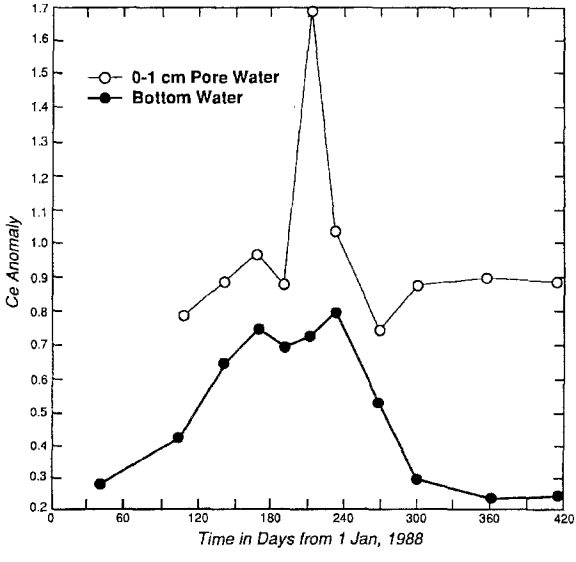

Fig. 39. Temporal variation of the Ce anomaly in the bottom water and upper porewater for the CHEER time-series study of Chesapeake Bay. From Sholkovitz et al. (1992).

In Chesapeake Bay there are large seasonal variations in the Ce anomaly as illustrated in fig. 39 reproduced from Sholkovitz et al. (1992). The bottom waters exhibit a

three-fold change in response to seasonal anoxicity. The anomaly increased from 0.28 in February 1988 to a maximum of 0.80 in August. By October the Ce anomaly had returned to 0.29. Even though the bottom waters remain anoxic for about 100 days in the summer, the Ce anomaly levels off between 0.7 and 0.8 and never exceeds 1 over this period of time. The snap-shot of the Bay on 26 July 1988 shows the shift from Ce-depleted oxic surface waters to anoxic deep waters which have become preferentially enriched in Ce compared to La and Nd (fig. 38).

In summary, the Chesapeake Bay time series demonstrates the large dynamic range over which the Ce anomaly can vary in response to seasonal anoxia. The concentration and composition of the strictly-trivalent lanthanides are sensitive to redox conditions. Concentrations increase under anoxic conditions. The lanthanides undergo an active geochemical cycle in anoxic marine basins in association with the redox cycles of Mn and Fe. Extensive fractionation occurs as dissolved lanthanides and Ce are released to anoxic waters and removed from oxic waters. To date, models of lanthanide cycling and fractionation in anoxic marine basins are qualitative. There has been no attempt to merge (1) the solution/surface chemistry of the lanthanides, (2) the redox cycling of Mn and Fe and (3) the physical dynamics of anoxic water columns. Lanthanide modeling for permanently and seasonally anoxic basins is a challenging future task. The required kinetic model would go beyond the equilibrium type models currently available for lanthanides in oxic seawater. The complexity of coastal anoxic basins makes such modeling difficult. Models of lanthanide cycling and fractionation would provide a great leap forward in understanding the coupling between basic chemistry and natural water chemistry.

7.2. *The lanthanide composition of marine pore waters*

What are pore waters and why are their compositions important with respect to the marine geochemistry of the lanthanides? The term "pore waters" (or alternatively, interstitial waters) refers to the waters contained within the pores of sediments. Pore waters are extracted by different types of procedures. Centrifugation and squeezing of sediments are two common methods. The latter is accomplished by using hydraulic systems or gas pressure systems. In all methods the extracted waters are rapidly filtered (typically 0.22 or 0.45 μm pore size) to yield dissolved matter for analysis.

The reason that the chemical composition of pore waters is studied is that these fluids are sensitive indicators of post-deposition reactions occurring in sediments (i.e., diagenesis). Given the high weight ratio of sediment to pore water, pore water composition is a more sensitive indicator of reactions than solid phase compositions. Hence, an increase of pore water concentrations reflects the diagenetic degradation of organic and mineral matter. Likewise, a depletion in concentrations can reflect processes such as in-situ formation of minerals, adsorption and consumption. This view is a simplified one; in practice the variations in pore water composition and concentrations are controlled by a complex set of reactions involving many types of solid phases, bacterially-driven decomposition of organic matter and water transport. Most studies of pore waters focus

on vertical profiles. Not only do concentration profiles provide information about the progression of diagenetic reactions upon burial of sediment, but they allow geochemists to determine the flux of elements across the sediment/water interface. Gradients in pore water concentrations are needed to calculate the rate and direction of trace element transport between seawater and sediments. Hence, pore water studies provide data critical to quantifying one part of the marine geochemical cycle of the lanthanides.

As described in sect. 3, small sample volumes (usually 10–50 ml) and low concentrations make it extremely difficult to measure the lanthanide concentrations of pore waters. Just as lanthanide concentrations in the water column increase several-fold under conditions of low or no oxygen, lanthanides in pore waters respond to redox conditions. There are a small number of studies of lanthanides in pore waters and they focus on sub-oxic and anoxic environments of estuaries and coastal regions. These include Chesapeake Bay (Sholkovitz and Elderfield 1988, Sholkovitz et al. 1992); Buzzards Bay (Elderfield and Sholkovitz 1987, Sholkovitz et al. 1989) and Saanich Inlet (German and Elderfield 1989). The first published paper on lanthanides in pore waters is less than a decade old (Elderfield and Sholkovitz 1987). All the above studies used ID-TIMS as the method of analysis. Pore water data are compiled in table A13.

There is only one paper with data on the pore water composition of deep ocean sediments deposited under oxygenated water (Ridout and Pagett 1984). This paper mostly deals with extraction methods and provides poorly documented lanthanide data for a single sample. It is fair to state the lanthanide composition and chemistry of oxic marine sediments is unknown.

Three major observations emerge from the studies of pore waters in anoxic or sub-oxic basins. Each of the following points will be briefly expanded upon in this section.

(1) Sub-oxic and anoxic conditions in the sediments lead to lanthanide concentrations which are significantly higher than those of seawater in the overlying oxic water column.
(2) There is a large degree of fractionation across the trivalent lanthanides during their diagenesis.
(3) Cerium concentrations are preferentially enriched as this element has a redox chemistry in natural waters.

Pore water results from a 72 cm sediment core from Buzzards Bay (MA, USA) provide good examples of the main features outlined above (Sholkovitz et al. 1989). This profile (not reproduced here) shows that there is a large enrichment of the all lanthanide elements in the upper half of the profile followed by the preferential removal of light and middle lanthanides in the lower part of the core. The diagenetic release in the upper half is also accompanied by the preferential release of the light and middle lanthanides. Hence, there is active diagenetic chemistry with fractionation occurring during the release and removal stages. Nd, for example, increases 16-fold in the upper half of the core (from 77 pmol/kg in the 14 m water column sample to about 1200 pmol/kg for the 40 cm pore water). Nd then decreases to about 500 pmol/kg at 72 cm. The mole ratio of Nd/Yb, indicative of fractionation between the light and heavy lanthanides, varies by a factor of 2–3 over this core. The Nd/Yb ratio increases from 5–7 in the oxic water

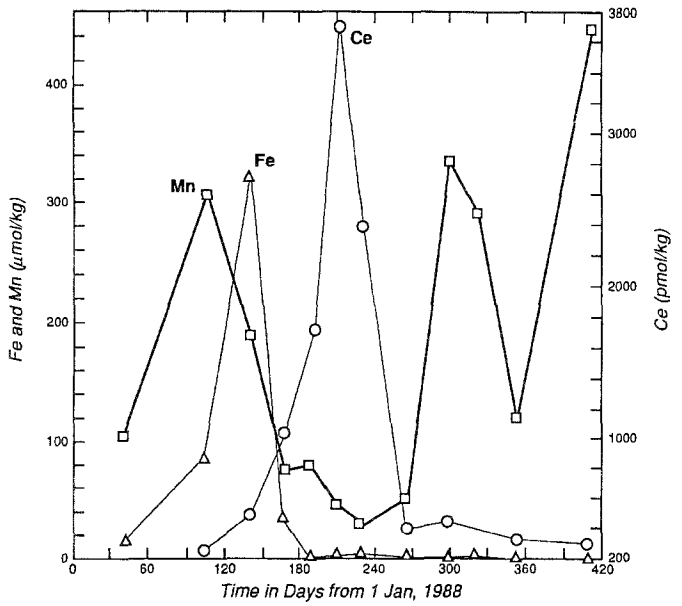

Fig. 40. Concentration of dissolved Fe, Mn, and Ce in the upper porewater (0–1 cm) as a function of time for the CHEER time-series study of Chesapeake Bay. From Sholkovitz et al. (1992).

column to a maximum of 13 in the 25 cm anoxic pore water; with further diagenesis this ratio returns to 6 at 72 cm. With a 31-fold increase in concentration over 40 cm, Ce undergoes a greater degree of remobilization than the other lanthanides. The shift from a negative (0.68) Ce anomaly in the water column to positive values (1.2–1.8) in the pore waters indicates that Ce is being preferentially remobilized as a results of the reduction of particulate Ce(IV) to dissolved Ce(III).

A strong seasonality was also observed for the pore water composition of upper (0–1 cm) Chesapeake Bay sediments (figs. 39–41). For example, the Nd concentration of surface pore water increases 6-fold as anoxic conditions develop in the spring and summer and then decreases markedly and rapidly during the reoxygenation of the Bay's bottom waters in the Fall. During the summer Nd pore water concentrations are 10-fold larger than those of the bottom waters, reflecting the sensitive response of pore water composition to varying redox conditions. The Bay's bottom waters exhibit a tight correlation between lanthanide and Fe variations (fig. 35). In contrast, variations in the lanthanide concentrations of the upper pore water, including those of Ce, lag variations of Fe by approximately 50 days (fig. 40). This decoupling between lanthanides and Fe in the pore waters is explained in terms of a redox front which moves upward from the sediment to the bottom waters in the spring and summer (Sholkovitz et al. 1992).

Pore waters also exhibit large scale fractionation of lanthanides during release and removal processes. This is demonstrated by the time-series variations in Nd/Yb ratios (fig. 37). The summertime development of anoxic conditions results in the

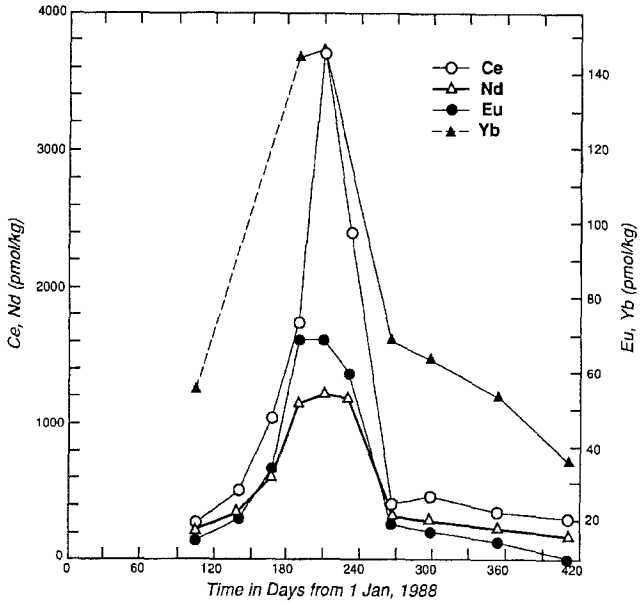

Fig. 41. Concentration of dissolved Ce, Nd, Eu, and Yb in the upper porewater (0–1 cm) as a function of time for the CHEER time-series study of Chesapeake Bay. Dashed line for Yb indicates that no heavy-lanthanide fraction was measured for samples on days 138 and 166. From Sholkovitz et al. (1992).

preferential release of light lanthanides (increasing the Nd/Yb ratio by a factor of 3) to the surface pore waters. This fractionation operates in reverse (shown by the decreasing Nd/Yb ratio) during the removal of lanthanides from the pore waters in fall and winter.

In summary, the lanthanides undergo large scale diagenetic reactions under sub-oxic and anoxic conditions. Pore water concentrations increase greatly over those of oxic seawater. Large cerium anomalies develop and large scale fractionation occurs as the strictly-trivalent lanthanides are added to and removed from pore waters. These features develop in vertical profiles within sediments and in surface sediments exposed to seasonally varying redox conditions.

The application of lanthanides as indicators of paleoredox conditions must take into consideration their diagenetic chemistry (German and Elderfield 1990). More sensitive analytical methods are required before the lanthanide pore water chemistry of deep ocean sediments can be studied. This research subject is challenging and would provide answers to the transport rate of lanthanides across the sediment/water interface in pelagic environments.

7.3. *Lanthanides in marine hydrothermal waters*

The venting of hydrothermal waters to the oceans through the seafloor is one of the major discoveries in modern oceanography. Hydrothermal systems have allowed geochemists to study two fundamental classes of reactions: (1) water/rock interactions at

high temperatures and (2) hydrothermal water/seawater interactions at low temperatures. The first type of interaction is more geological in nature, in that hydrothermal fluids have reacted with basalt at high temperatures prior to being vented to the oceans. The second type of interaction takes place in the ocean as a plume of hydrothermal water mixes with bottom water at low temperatures. Both types of interactions produce a suite of reactions and products. The systematics of lanthanide geochemistry in both types of hydrothermal interactions have been presented in a series of papers. These studies include German et al. (1990), Klinkhammer et al. (1983, 1994a,b), Michard (1989), Michard et al. (1983), Michard and Albarède (1986), Mitra et al. (1994), Piepgras and Wasserburg (1985), and Rudnicki and Elderfield (1993). Concentrations have been measured by both TIMS and ICP-MS. Hydrothermal data are compiled in table A14.

The following points summarize the major observations and conclusions of hydrothermal studies.

(1) The reactions of magmatic water with basalt lead to hydrothermal fluids with lanthanide end-member concentrations which are much greater than seawater. For example, the average fluid composition reported by Klinkhammer et al. (1994a) has lanthanide concentrations which are 10–100 times higher than Goldstein and Jacobsen's (1988a) average seawater (2.5 km) composition; Eu is 2100 times higher in the hydrothermal fluid!

(2) The lanthanide composition of hydrothermal waters differs significantly from that of basalt and seawater. The leaching of lanthanides from basalt results in large scale fractionation whereby hydrothermal end-member waters are strongly enriched in the light lanthanides and have extremely large positive Eu anomalies. Eu anomalies provide unique compositional signatures of hydrothermal waters. These features are illustrated in fig. 42 using the data of Klinkhammer et al. (1994a) and German et al. (1990). Average fluid composition (Klinkhammer et al. 1994a) is normalized to chondrite and seawater and plotted on a log scale. The fluid/chondrite patterns are characterized by large positive Eu anomalies superimposed on a systematic decrease from La to Er (fig. 42a). The shale-normalized patterns of a TAG vent fluid and ambient seawater are strikingly different (fig. 42b). The latter is heavy-enriched with a large negative Ce anomaly while the vent fluid is heavy depleted with a huge positive Eu anomaly. As concluded by Klinkhammer et al. (1994a), "The REE patterns of deep-sea hydrothermal fluids are remarkably similar, regardless of seafloor setting." They also concluded that the reaction with MORB (Mid-Ocean Ridge Basalt) plagioclase is critical in establishing the fractionated composition (including the positive Eu anomalies) of hydrothermal fluids.

(3) Upon venting to the ocean, there is almost total removal of hydrothermally-derived lanthanides (Rudnicki and Elderfield 1993). Dissolved lanthanides of both hydrothermal and seawater origin are scavenged by iron oxide particles which form when dissolved Fe(II) from reducing venting water oxidizes in seawater. There is a strong correlation between particulate Fe and lanthanide concentrations (German et al. 1990). The removal of hydrothermally-derived lanthanides in plumes over vent sites has been modeled by Rudnicki and Elderfield (1993). Rapid

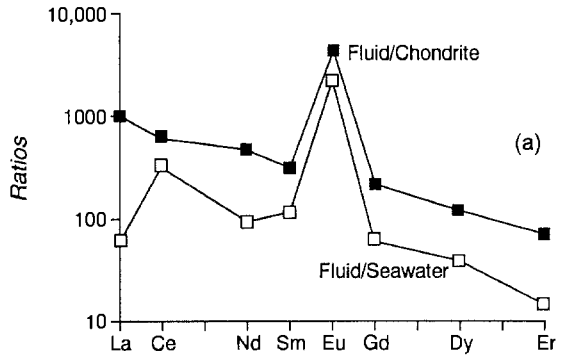

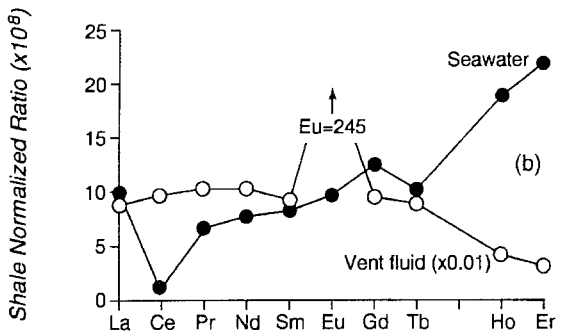

Fig. 42. (a) The ratio of vent fluid composition (TAG hydrothermal vent field in the North Atlantic Ocean) to that of chondrite and that of ambient seawater. Note log scale. (b) Shale-normalized patterns of vent water and ambient seawater. Data from German et al. (1990).

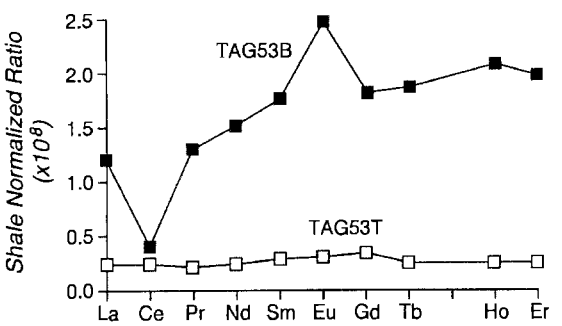

Fig. 43. Shale-normalized ratios of suspended particles from the TAG site. "T" refers to sample collected above of the plume (ambient type seawater) and "B" refers to particles collected in the plume. Data from German et al. (1990).

quantitative, near-vent removal of hydrothermal lanthanides means that this source does not affect the lanthanide composition of the oceans. In fact, formation of oxides removes dissolved lanthanides from ambient seawater. Measurements of particulate lanthanide concentrations near and above vent sites have been reported by German et al. (1990) and Klinkhammer et al. (1994a). As illustrated in fig. 43 with data from the TAG site in the North Atlantic Ocean, suspended particles in plumes (TAG53B sample) have shale-normalized patterns which exhibit heavy-enrichment, negative Ce anomalies and positive Eu anomalies. The Eu anomaly

indicates a hydrothermal fluid source while the first two features indicate a seawater source. Hence, plume particles are scavenging lanthanides from both venting fluid and ambient seawater. In contrast, particles above the plume at this site (TAG53T sample) and other sites have a flat shale pattern indicating the presence of continental detrital minerals.

In summary, extensive research has been carried out on the lanthanide geochemistry of marine hydrothermal vent systems. Lanthanides are good indicators of water/rock reactions between hydrothermal fluids and basalt, and reactions between Fe oxide particles and seawater. While the lanthanides undergo an active geochemical cycle in and above venting fluids, this cycle is not quantitatively significant with respect to river water fluxes and oceanic cycles and inventory.

References

Albarède, F., and S.L. Goldstein, 1992, Geologica **20**, 761.

Alpin, A., A. Michard and F. Albarède, 1986, Earth Planet. Sci. Lett. **81**, 7.

Amakawa, H., J. Ingri, A. Masuda and H. Shimizu, 1991, Earth Planet. Sci. Lett. **105**, 554.

Andersson, P.S., G.J. Wasserburg and J. Ingri, 1992, Earth Planet. Sci. Lett. **113**, 459.

Atlas, E., C. Culberson and R.M. Pytkowicz, 1976, Mar. Chem. **4**, 243.

Baes, C.F., and R.E. Mesmer, 1976, The Hydrolysis of Cations (Wiley, New York) 489pp.

Baes, C.F., and R.E. Mesmer, 1981, Am. J. Sci. **281**, 935.

Balistrieri, L., P.G. Brewer and J.W. Murray, 1981, Deep-Sea Res. **28A**, 101.

Becker, P., and B.A. Bilal, 1985, J. Solution Chem. **14**, 407.

Bertram, C.J., and H. Elderfield, 1993, Geochim. Cosmochim. Acta **57**, 1957.

Bilal, B.A., 1980, in: The Rare Earths in Modern Science and Technology (Plenum Press, New York) pp. 83–86.

Bilal, B.A., and P. Becker, 1979, J. Inorg. Nucl. Chem. **41**, 1607.

Bilal, B.A., and P. Becker, 1980, in: The Rare Earths in Modern Science and Technology, eds G.J. McCarthy, J.J. Rhyne and H.B. Silber (Plenum Press, New York) pp. 117–120.

Bilal, B.A., and V. Koss, 1980, J. Inorg. Nucl. Chem. **42**, 629.

Bilal, B.A., F. Herrmann and W. Fleischer, 1979, J. Inorg. Nucl. Chem. **41**, 347.

Bingler, L.S., and R.H. Byrne, 1989, Polyhedron **8**, 1315.

Bingler, L.S., R.H. Byrne, G.A. Vargo and C.R. Tomas, 1989, Chem. Spec. Bioavailability **1**, 103.

Brown Jr, J.A., F.W. Kunz and R.K. Belitz, 1991, J. Anal. At. Spectrom. **6**, 393.

Bruland, K.W., 1989, Limnol. Oceanogr. **34**, 269.

Byrne, R.H., and L.S. Bingler, 1989, Geochim. Cosmochim. Acta **53**, 1475.

Byrne, R.H., and K.J. Cantrell, 1996, in preparation.

Byrne, R.H., and K.-H. Kim, 1990, Geochim. Cosmochim. Acta **54**, 2645.

Byrne, R.H., and K.-H. Kim, 1993, Geochim. Cosmochim. Acta **57**, 519.

Byrne, R.H., and B.Q. Li, 1995, Geochim. Cosmochim. Acta, **59**, 4575.

Byrne, R.H., L.R. Kump and K.J. Cantrell, 1988, Mar. Chem. **25**, 163.

Byrne, R.H., J.H. Lee and L.S. Bingler, 1991, Geochim. Cosmochim. Acta **55**, 2729.

Cantrell, K.J., and R.H. Byrne, 1987a, Geochim. Cosmochim. Acta **51**, 597.

Cantrell, K.J., and R.H. Byrne, 1987b, J. Solution Chem. **16**, 555.

Carpenter, J.H., and V.E. Grant, 1967, J. Mar. Res. **25**, 228.

Chatt, A., and R.R. Rao, 1989, Mat. Res. Soc. Symp. Proc. **127**, 897.

Choppin, G.R., 1980, Lanthanide and Actinide Chemistry and Spectroscopy, ACS Symp. Series **131**, 137.

Choppin, G.R., 1986, J. Less-Common Met. **126**, 307.

Choppin, G.R., 1989, Mar. Chem. **28**, 19.
Ciavatta, L., D. Ferri, I. Grenthe, F. Salvatore and K. Spahiu, 1981, Acta Chem. Scand. A **35**, 403.
Ciavatta, L., M. Iuliano and R. Porto, 1987, Polyhedron **6**, 1283.
Colodner, D., V. Salters and D.C. Duckworth, 1994, Anal. Chem. **66**, 1079A.
Davis, J.A., 1984, Geochim. Cosmochim. Acta **48**, 679.
De Baar, H.J.W., 1983, The marine geochemistry of the rare-earth elements, Ph.D. Thesis (MIT/WHOI Joint Program in Oceanography) 278pp.
De Baar, H.J.W., 1984, in: Proc. Int. Symp. on the Use and Development of Low and Medium Flux Research Reactors, Atomkernenergie-Kerntechnik **44**(Suppl.), 702–709.
De Baar, H.J.W., 1991, Geochim. Cosmochim. Acta. **55**, 2981.
De Baar, H.J.W., M.P. Bacon and P.G. Brewer, 1983, Nature **301**, 324.
De Baar, H.J.W., M.P. Bacon, P.G. Brewer and K.W. Bruland, 1985a, Geochim. Cosmochim. Acta **49**, 1943.
De Baar, H.J.W., P.G. Brewer and M.P. Bacon, 1985b, Geochim. Cosmochim. Acta **49**, 1961.
De Baar, H.J.W., C.R. German, H. Elderfield and P. van Gaans, 1988, Geochim. Cosmochim. Acta **52**, 1203.
De Baar, H.J.W., J. Schijf and R.H. Byrne, 1991, Eur. J. Solid State Inorg. Chem. **28**, 357.
Dickson, A.G., 1993, Mar. Chem. **44**, 131.
Dickson, A.G., and C. Goyet, 1994, Handbook of Methods for the Analysis of the Various Parameters of the Carbon Dioxide System in Sea Water, version 2, ORNL/CDIAC-74 (US Department of Energy, Washington, DC).
Donat, J.R., and K.W. Bruland, 1995, in: Trace Elements in Natural Waters, eds B. Salbu and E. Steinnes (CRC Press, Boca Raton, FL) ch. 11.
Donat, J.R., and C.M.G. van den Berg, 1992, Mar. Chem. **38**, 69.
Donat, J.R., K.A. Lao and K.W. Bruland, 1994, Anal. Chim. Acta **284**, 547.
Elderfield, H., 1988, Philos. Trans. R. Soc. London A **325**, 105.
Elderfield, H., 1992, Earth Planet. Sci. Lett. **111**, 557.
Elderfield, H., and M.J. Greaves, 1982, Nature **296**, 214.
Elderfield, H., and M.J. Greaves, 1983, Trace Metals in Sea Water (Plenum Press, New York) pp. 427–445.
Elderfield, H., and E.R. Sholkovitz, 1987, Earth Planet. Sci. Lett. **82**, 280.
Elderfield, H., C.J. Hawkesworth, M.J. Greaves and S.E. Calvert, 1981, Geochim. Cosmochim. Acta **45**, 513.
Elderfield, H., R. Upstill-Goddard and E.R. Sholkovitz, 1990, Geochim. Cosmochim. Acta **54**, 971.
Erel, Y., and J.J. Morgan, 1991, Geochim. Cosmochim. Acta **55**, 1807.
Erel, Y., and E.M. Stolper, 1993, Geochim. Cosmochim. Acta **57**, 513.
Esser, B.K., A. Volpe, J.M. Kenneally and D.K. Smith, 1994, Anal. Chem. **66**, 1736.
Ferri, D., and F. Salvatore, 1983, Acta Chem. Scand. A **37**, 531.
Ferri, D., I. Grenthe, S. Hietaanen and F. Salvatore, 1983, Acta Chem. Scand. A **37**, 359.
Firsching, F.G., and S.N. Brune, 1991, J. Chem. Eng. Data **36**, 93.
Firsching, F.G., and J. Mohammadzadel, 1986, J. Chem. Eng. Data **31**, 40.
Fowler, S.W., T.F. Hamilton, R.D. Peinert, J. La Rose and J.-L. Teyssie, 1992, EROS 2000: Third Workshop on the North-west Mediterranean Seas (Water Pollution Research Reports, Commission European Communities).
Frost, C.D., R.K. O'Nions and S.L. Goldstein, 1986, Earth Planet. Sci. Lett. **55**, 45.
German, C.R., and H. Elderfield, 1989, Geochim. Cosmochim. Acta **53**, 2561.
German, C.R., and H. Elderfield, 1990, Geochim. Cosmochim. Acta **54**, 1929.
German, C.R., G.P. Klinkhammer, J.M. Edmond, A. Mitra and H. Elderfield, 1990, Nature **345**, 516.
German, C.R., B.P. Holliday and H. Elderfield, 1991, Geochim. Cosmochim. Acta **55**, 3553.
German, C.R., B.P. Holliday and H. Elderfield, 1992, Geochim. Cosmochim. Acta **56**, 4309.
German, C.R., T. Masuzawa, M.J. Greaves, H. Elderfield and J.M. Edmond, 1995, Geochim. Cosmochim. Acta **59**, 1551.
Goldberg, E.D., M. Koide, R.A. Schmitt and R.H. Smith, 1963, J. Geophys. Res. **68**, 4209.
Goldstein, S.J., and S.B. Jacobsen, 1987, Chem. Geol. **66**, 245.
Goldstein, S.J., and S.B. Jacobsen, 1988a, Earth Planet. Sci. Lett. **89**, 35.
Goldstein, S.J., and S.B. Jacobsen, 1988b, Earth Planet. Sci. Lett. **87**, 249.
Goldstein, S.J., and S.B. Jacobsen, 1988c, Earth Planet. Sci. Lett. **88**, 241.

Goldstein, S.L., and R.K. O'Nions, 1981, Nature **292**, 324.

Goldstein, S.L., R.K. O'Nions and P.J. Hamilton, 1984, Earth Planet. Sci. Lett. **70**, 221.

Gordeev, V.V., A.Z. Miklishansky, A.A. Migdisov and V.E. Artemyev, 1985, SCOPE/UNEP Sonderband Heft **58**, 225.

Grant, P.M., P.A. Baisden, W.F. Kinard and R.A. Torres, 1988, Inorg. Chem. **27**, 1156.

Greaves, M.J., H. Elderfield and G.P. Klinkhammer, 1989, Anal. Chim. Acta **218**, 265.

Greaves, M.J., M.D. Rudnicki and H. Elderfield, 1991, Earth Planet. Sci. Lett. **103**, 169.

Greaves, M.J., P.J. Statham and H. Elderfield, 1994, Mar. Chem. **46**, 255.

Hall, G.E.M., J.E. Vaive and J.W. McConnell, 1995, Chem. Geol. **120**, 91.

Henderson, P., ed., 1984, Rare Earth Element Geochemistry (Elsevier, New York) 510pp.

Henderson, P., and R.J. Pankhurst, 1984, Rare Earth Element Geochemistry (Elsevier, New York) p. 467.

Henry, F., C. Jeandel, B. Dupré and J.-F. Minster, 1994, Mar. Chem. **45**, 283.

Heumann, K.G., 1992, Int. J. Mass. Spectrom. Ion Phys. **118**, 575.

Høgdahl, O.T., S. Melson and V.T. Bowen, 1968, Trace inorganics in water, Adv. Chem. Ser. **73**, 308–325.

Honeyman, B.D., and P.H. Santschi, 1988, Environ. Sci. Technol. **22**, 862.

Honjo, S., and S.J. Manganini, 1993, Deep-Sea Res. **40**, 587.

Hoyle, J., H. Elderfield, A. Glenhill and M.J. Greaves, 1984, Geochim. Cosmochim. Acta **48**, 143.

Hunter, K.A., 1983, Deep-Sea Res. **30**, 669.

Hunter, K.A., and P.S. Liss, 1979, Nature **282**, 823.

Jeandel, C., 1993, Earth Planet. Sci. Lett. **117**, 581.

Jeandel, C., J.K. Bishop and A. Zindler, 1995, Geochim. Cosmochim. Acta **59**, 535.

Johannesson, K.H., W.B. Lyons, K.J. Stetzenbach and R.H. Byrne, 1995, Aquat. Geochem. **1**, 157.

Jonasson, R.G., G.M. Bancroft and H.W. Nesbitt, 1985, Geochim. Cosmochim. Acta **49**, 2133.

Jones, C.E., A.N. Halliday, D.K. Rea and R.M. Owen, 1994, Earth Planet. Sci. Lett. **127**, 55.

Jordanov, N., and I. Havezov, 1966, Z. Anorg. Allg. Chem. **347**, 101.

Kawabata, K., Y. Kishi, O. Kawaguichi, H. Watanabe and Y. Inoue, 1991, Anal. Chem. **63**, 2137.

Keasler, K.M., and W.D. Loveland, 1982, Earth Planet. Sci. Lett. **61**, 68.

Kim, K.-H., R.H. Byrne and J.H. Lee, 1991, Mar. Chem. **36**, 107.

Kitto, M.E., D.L. Anderson, G.E. Gordon and I. Olmez, 1992, Environ. Sci. Technol. **26**, 1375.

Klinkhammer, G.P., H. Elderfield and A. Hudson, 1983, Nature **305**, 185.

Klinkhammer, G.P., H. Elderfield, J.M. Edmond and A. Mitra, 1994a, Geochim. Cosmochim. Acta **58**, 5105.

Klinkhammer, G.P., C.R. German, H. Elderfield, M.J. Greaves and A. Mitra, 1994b, Mar. Chem. **45**, 179.

Koeppenkastrop, D., and E.H. DeCarlo, 1992, Chem. Geol. **95**, 251.

Koeppenkastrop, D., and E.H. DeCarlo, 1993, Environ. Sci. Technol. **27**, 1796.

Koeppenkastrop, D., E.H. DeCarlo and M. Roth, 1991, J. Radioanal. Nucl. Chem. **152**, 337.

Landing, W.M., and B.L. Lewis, 1991, Analysis of marine particulate and colloidal material for transition metals, in: Marine Particles: Analysis and Characterization, eds D.C. Hurd and D.W. Spencer, Geophysical Monograph 63 (AGU), pp. 263–272.

Lee, J.H., and R.H. Byrne, 1992, Geochim. Cosmochim. Acta **56**, 1127.

Lee, J.H., and R.H. Byrne, 1993a, Geochim. Cosmochim. Acta **57**, 295.

Lee, J.H., and R.H. Byrne, 1993b, Mar. Chem. **44**, 121.

Lee, J.H., and R.H. Byrne, 1993c, J. Solution Chem. **22**, 751.

Lee, J.H., and R.H. Byrne, 1994, Geochim. Cosmochim. Acta **58**, 4009.

Lewis, B.L., and W.M. Landing, 1991, Deep-Sea Res. **38**, S773–S803.

Liu, X.W., and R.H. Byrne, 1995, Mar. Chem. **51**, 213.

Liu, X.W., and R.H. Byrne, 1996, in preparation.

Lundqvist, R., 1982, Acta Chem. Scand. A **36**, 741.

Martell, A.E., and R.M. Smith, 1974, Critical Stability Constants, Vol. 1: Amino Acids (Plenum Press, New York).

Martell, A.E., and R.M. Smith, 1977, Critical Stability Constants, Vol. 3: Other Organic Ligands (Plenum Press, New York).

Martell, A.E., and R.M. Smith, 1982, Critical Stability Constants, Vol. 5: First Supplement (Plenum Press, New York).

Martin, J.M., and M. Meybeck, 1979, Mar. Chem. **7**, 173.

Martin, J.M., O.T. Høgdahl and J.C. Phillippot, 1976, J. Geophys. Res. **81**, 3119.

Masuda, A., and Y. Ikeuchi, 1979, Geochem. J. **13**, 19.

Masuda, A., O. Kawakami, Y. Domoto and T. Takenaka, 1987, Geochem. J. **21**, 119.

Masuzawa, T., and M. Koyama, 1989, Geophys. Res. Lett. **16**, 503.

McLaren, J.W., K.W.M. Siu, J.W. Lam, S.N. Willie, P.S. Maxwell, A. Palepu, M. Koether and S.S. Berman, 1990, Fresenius Z. Anal. Chem. **337**, 721.

McLennan, S.M., 1994, Geochim. Cosmochim. Acta **58**, 2025.

McLennan, S.M., S.R. Taylor, M.T. McCulloch and J.B. Maynard, 1990, Geochim. Cosmochim. Acta **54**, 2015.

Michard, A., 1989, Geochim. Cosmochim. Acta **53**, 745.

Michard, A., and F. Albarède, 1986, Chem. Geol. **55**, 51.

Michard, A., F. Albarède, G. Michard, J.F. Minster and J.L. Charlou, 1983, Nature **303**, 795.

Millero, F.J., 1992, Geochim. Cosmochim. Acta **56**, 3123.

Millero, F.J., and D.R. Schreiber, 1982, Am. J. Sci. **282**, 1508.

Mironov, V.E., N.I. Avramenko, A.A. Koperin, V.V. Blokhin, M.Yu. Eike and I.D. Isayev, 1982, Koord. Khim. **8**, 636.

Mitra, A., H. Elderfield and M.J. Greaves, 1994, Mar. Chem. **46**, 217.

Moffett, J.W., 1990, Nature **345**, 421.

Moffett, J.W., 1994a, Limnol. Oceanogr. **39**, 1309.

Moffett, J.W., 1994b, Geochim. Cosmochim. Acta **58**, 695.

Möller, P., P. Dulski and J. Luck, 1992, Spectrochim. Acta Part B **47**, 1379.

Möller, P., P. Dulski and M. Bau, 1994, Chem. Erde **54**, 129.

Montgomery, R.B., 1958, Deep-Sea Res. **5**, 134.

Murphy, K., and J. Dymond, 1984, Nature **307**, 444.

Naki, S., A.N. Halliday and D.K. Rea, 1993, Earth Planet. Sci. Lett. **119**, 143.

Nyffeler, U.P., Y.-H. Li and P.H. Santschi, 1984, Geochim. Cosmochim. Acta **48**, 1513.

Olmez, I., and G.E. Gordon, 1985, Science **229**, 966.

Olmez, I., E.R. Sholkovitz, D. Hermann and R.P. Eganhouse, 1991, Environ. Sci. Technol. **25**, 310.

O'Nions, R.K., S.R. Carter, R.S. Cohen, N.M. Evensen and P.J. Hamilton, 1978, Nature **273**, 435.

Palmer, M.R., 1983, Rare earth elements and Nd and Sr isotopes in the Atlantic Ocean, Ph.D. Thesis (Leeds University).

Palmer, M.R., 1985, Earth Planet. Sci. Lett. **73**, 285.

Pickard, G.L., and W.J. Emery, 1982, Descriptive Physical Oceanography (Pergamon Press, Oxford).

Piepgras, D.J., and S.B. Jacobsen, 1988, Geochim. Cosmochim. Acta **52**, 1373.

Piepgras, D.J., and S.B. Jacobsen, 1992, Geochim. Cosmochim. Acta **56**, 1851.

Piepgras, D.J., and G.J. Wasserburg, 1980, Earth Planet. Sci. Lett. **50**, 128.

Piepgras, D.J., and G.J. Wasserburg, 1982, Science **217**, 207.

Piepgras, D.J., and G.J. Wasserburg, 1983, J. Geophys. Res. **88**, 5997.

Piepgras, D.J., and G.J. Wasserburg, 1985, Earth Planet. Sci. Lett. **72**, 341.

Piepgras, D.J., and G.J. Wasserburg, 1987, Geochim. Cosmochim. Acta **51**, 1257.

Piepgras, D.J., G.J. Wasserburg and E.J. Dasch, 1979, Earth Planet. Sci. Lett. **45**, 223.

Potts, P.J., 1987, A Handbook of Silicate Rock Analysis (Chapman and Hall, London).

Powell, H.K.P., 1974, J. Chem. Soc. Dalton Trans., p. 1108.

Prospero, J.M., and R.T. Ness, 1986, Nature **320**, 735.

Prospero, J.M., R.T. Ness and M. Uematsu, 1987, J. Geophys. Res. **92**, 14723.

Rao, R.R., and A. Chatt, 1991, Radiochim. Acta **54**, 181.

Ridout, P.S., and R.M. Pagett, 1984, Mar. Chem. **15**, 193.

Rizkalla, E.N., and G.R. Choppin, 1991, in: Handbook on the Physics and Chemistry of Rare Earths, Vol. 15, eds K.A. Gschneidner Jr and L. Eyring (North-Holland, Amsterdam) ch. 103.

Rudnicki, M.D., and H. Elderfield, 1993, Geochim. Cosmochim. Acta **57**, 2939.

Rue, E., and K.W. Bruland, 1995, Mar. Chem. **50**, 117.

Schijf, J., and H.J.W. De Baar, 1995, Geochim. Cosmochim. Acta **59**, 3503.

Schijf, J., H.J.W. De Baar, J.R. Wijbrans and W.M. Landing, 1991, Deep-Sea Res. **38**(Suppl. 2), 805.

Schijf, J., H.J.W. De Baar and F.J. Millero, 1994, Mar. Chem. **46**, 345.

Schijf, J., H.J.W. De Baar and F.J. Millero, 1995, Geochim. Cosmochim. Acta **59**, 3285.

Schindler, P.W., 1975, Thalassia Jugosl. **11**, 101.

Schneider, D.L., and J.M. Palmieri, 1994, A method for the analysis of rare earth elements in natural waters by isotope dilution mass spectrometry, Woods Hole Oceanographic Institution Technical Report No. 94-06, 39pp.

Shabani, M.B., and A. Masuda, 1991, Anal. Chem. **63**, 2099.

Shabani, M.B., T. Akagi, H. Shimizu and A. Masuda, 1990, Anal. Chem. **62**, 2709.

Shabani, M.B., T. Akagi and A. Masuda, 1992, Anal. Chem. **64**, 737.

Shimizu, H., K. Tachikawa, A. Masuda and Y. Nozaki, 1994, Geochim. Cosmochim. Acta **58**, 323.

Sholkovitz, E.R., 1976, Geochim. Cosmochim. Acta **40**, 831.

Sholkovitz, E.R., 1990, Chem. Geol. **88**, 333.

Sholkovitz, E.R., 1992a, Geochim. Cosmochim. Acta **56**, 4305.

Sholkovitz, E.R., 1992b, Earth Planet. Sci. Lett. **114**, 77.

Sholkovitz, E.R., 1993, Geochim. Cosmochim. Acta **57**, 2181.

Sholkovitz, E.R., 1995, Aquat. Geochem. **1**, 1.

Sholkovitz, E.R., 1996, WHOI Tech. Report, to be published.

Sholkovitz, E.R., and H. Elderfield, 1988, Global Biogeochem. Cycles **2**, 157.

Sholkovitz, E.R., and D.L. Schneider, 1991, Geochim. Cosmochim. Acta. **55**, 2737.

Sholkovitz, E.R., D.J. Piepgras and S.B. Jacobsen, 1989, Geochim. Cosmochim. Acta **53**, 2847.

Sholkovitz, E.R., T.J. Shaw and D.L. Schneider, 1992, Geochim. Cosmochim. Acta **56**, 3389.

Sholkovitz, E.R., T.M. Church and R. Arimoto, 1993, J. Geophys. Res. **98**, 20587.

Sholkovitz, E.R., W.M. Landing and B.L. Lewis, 1994, Geochim. Cosmochim. Acta **58**, 1567.

Smith, R.M., and A.E. Martell, 1975, Critical Stability Constants, Vol. 2: Amines (Plenum Press, New York).

Smith, R.M., and A.E. Martell, 1989, Critical Stability Constants, Vol. 6: Second Supplement (Plenum Press, New York).

Somayajulu, B.L.K., J.M. Martin, D. Eisma, A.J. Thomas, D.V. Borole and K.S. Rao, 1993, Mar. Chem. **43**, 83.

Spahiu, K., 1985, Acta Chem. Scand. A **39**, 33.

Spedding, F.H., and S. Jaffe, 1954, J. Am. Chem. Soc. **76**, 882.

Spivack, A.J., and G.J. Wasserburg, 1988, Geochim. Cosmochim. Acta **52**, 2767.

Stanley, J.K., and R.H. Byrne, 1990, Geochim. Cosmochim. Acta **54**, 1587.

Stordal, M.C., and G.J. Wasserburg, 1986, Earth Planet. Sci. Lett. 77, 259.

Stumm, W., and J.J. Morgan, 1981, Aquatic Chemistry, 2nd Ed. (Wiley-Interscience, New York).

Sunda, W.G., and S.A. Huntsman, 1988, Deep-Sea Res. **35**, 1297.

Sunda, W.G., S.A. Huntsman and G.R. Harvey, 1983, Nature **301**, 234.

Tanaka, M., H. Shimizu and A. Masuda, 1990, Geochem. J. **24**, 39.

Tananaev, I.V., and S.M. Petushkova, 1967, Russ. J. Inorg. Chem. **12**, 39.

Tananaev, I.V., and V.P. Vasil'eva, 1963, Russ. J. Inorg. Chem. **8**, 555.

Taylor, S.R., and S.M. McLennan, 1985, The Continental Crust: Its Composition and Evolution (Blackwell Science Publishers, Oxford) 312pp.

Thirlwall, M.F., 1982, Chem. Geol. **35**, 155.

Thomas, A.J., and J.M. Martin, 1982, SCOPE/UNEP Sonderband Heft **25**, 555.

Thompson, S.W., and R.H. Byrne, 1988, Anal. Chem. **60**, 19.

Turner, D.R., M. Whitfield and A.G. Dickson, 1981, Geochim. Cosmochim. Acta **45**, 855.

van den Berg, C.M.G., 1984, Mar. Chem. **15**, 1.

Walder, A.J., D. Koller, N.M. Reed, R.C. Hutton and P.A. Freedman, 1993, J. Anal. At. Spectr. **8**, 1037.

Walker, J.B., and G.R. Choppin, 1967, Adv. Chem. Ser. **71**, ch. 10.

Westerlund, S., and P. Öhman, 1992, Deep-Sea Res. **39**, 1613.

Whitfield, M., and D.R. Turner, 1987, in: Aquatic Surface Chemistry, ed. W. Stumm (Wiley, New York).

Wood, S.A., 1990, Chem. Geol. **82**, 159.

Zhang, J., H. Amakawa and Y. Nozaki, 1995, Geophys. Res. Lett. **21**, 2677.

AUTHOR INDEX

SUBJECT INDEX